中国气象局气候研究开放实验室

# 论文汇编

第十四卷

(2011)

下册

LCS

气候研究开放实验室

# 内 容 简 介

本文集收录了2011年度中国气象局气候研究开放实验室在国内外核心期刊发表的学术论文103篇。其中上册49篇，下册54篇。内容涉及气候监测、气候诊断、气候预测、气候模式模拟、气候变化及其影响评估、历史气候及人类活动影响等研究领域。

## （下 册）


50. 气候变暖对我国南方水稻可种植区的影响 …… 宋艳玲　刘　波　钟海玲　(473)
51. Rain-season trends in precipitation and their effect in different climate regions of China during 1961-2008 …… Yanling Song, Christine Achberger and Hans W Linderholm　(479)
52. Changes of Accumulated Temperature, Growing Season and Precipitation in the North China Plain from 1961 to 2009 …… SONG Yanling, ZHAO Yanxia and WANG Chunyi　(487)
53. 城市扩展影响下的气象观测和气温变化特征分析 …… 孙朝阳　邵全琴　刘纪远　匡文慧　(497)
54. 2010 年西北太平洋热带气旋活动特征及成因的初步分析 …… 孙　冷　(507)
55. Study on Climatic Characteristics of China-Influencing Tropical Cyclones …… SUN Linhai, AI Wanxiu, SONG Wenling, et al　(514)
56. 基于非线性相似度量方法研究中国季节划分 …… 孙树鹏　张　璐　侯　威　封国林　(520)
57. 全球平均温度序列的比较 …… 唐国利　王绍武　闻新宇　黄建斌　(527)
58. ENSO 与青藏高原积雪的关系及其对我国夏季降水异常的影响 …… 陶亦为　孙照渤　李维京　李伟平，等　(532)
59. 不同排放情景下模拟的 21 世纪东亚积雪面积变化趋势 …… 汪　方　丁一汇　(542)
60. 长江中下游汛期降水优化多因子组合客观定量化预测研究 …… 王启光　封国林　郑志海　支　蓉　(551)
61. 全球气候变暖原因的争议 …… 王绍武　罗　勇　赵宗慈　闻新宇　黄建斌　(562)
62. 近 50 a 江淮地区 6—7 月降水特征分析 …… 王　勇　李清泉　沈新勇　(568)
63. Radiative forcing and climate response due to black carbon in snow and ice …… Wang Z L, Zhang H and Shen X S　(574)
64. 中国冰冻日数的气候及变化特征分析 …… 王遵娅　(583)
65. 2010 年中国气候概况 …… 王遵娅　曾红玲　高　歌　陈　峪，等　(594)
66. 我国冰冻日出现的气象条件分析及其判别模型 …… 王遵娅　赵珊珊　张　强　(601)
67. 非球形沙尘气溶胶光学特性的分析 …… 卫晓东　张　华　(607)
68. 新疆 21 世纪气候变化的高分辨率模拟 …… 吴　佳　高学杰　石　英　Filippo Giorgi　(615)
69. 三峡水库气候效应及 2006 年夏季川渝高温干旱事件的区域气候模拟 …… 吴　佳　高学杰　张冬峰　石　英　GIORGI F　(624)
70.《生物多样性公约》下的气候变化问题：谈判与焦点 …… 吴　军　张称意　徐海根　(633)
71. 我国北方沙尘天气的气候成因分析 …… 吴占华　任国玉　徐卫丽　刘瑞兰　(637)
72. 青藏高原东北部土壤冻融过程的数值模拟 …… 夏　坤　罗　勇　李伟平　(644)
73. Simulation of freezing and melting of soil on the northeast Tibetan Plateau …… XIA Kun, LUO Yong, LI WeiPing　(655)
74. 卫星遥感海表温度资料和高度计资料的变分同化 …… 肖贤俊　何　娜　张祖强　刘怀明　王东晓　(666)
75. Analogue-Dynamical Prediction of Monsoon Precipitation in Northeast China Based on Dynamic and Optimal Configuration of Multiple Predictors …… XIONG Kaiguo, FENG Guolin, HUANG Jianping and CHOU Jifan　(674)

76. Quantifying uncertainty in the impacts of climate change on river discharge in sub-catchments of the Yangtze and Yellow River Basins, China …… H Xu, R Y Taylor and Y Xu (685)
77. 33 年来中国铁路运输行业的大气污染物排放 …… 徐雨晴 何吉成 王长科 (697)
78. 不同温室气体排放情景下未来中国地面气温变化特征 …… 闫冠华 李巧萍 邢 超 (704)
79. 动态最优多因子组合的华北汛期降水模式误差估计及预报 …… 杨 杰 王启光 支 蓉 封国林 (715)
80. 北京地区极端温度事件的变化趋势和年代际演变特征 …… 杨 萍 刘伟东 侯 威 (728)
81. 我国降水和气温的分级概率时空分布特征 …… 杨小波 陈丽娟 刘芸芸 (733)
82. 11 月气候异常型及前期环流信号 …… 杨小波 王永光 梁潇云 (745)
83. 小兴安岭红松径向生长对未来气候变化的响应 …… 尹 红 王 靖 刘洪滨 黄 磊 朱海峰 (753)
84. 近 48 年华东地区地面太阳总辐射变化特征和影响因子分析 …… 尹 青 张 华 何金海 (761)
85. Diurnal Variations of Summer Precipitation in the Beijing Area and the Possible Effect of Topographyand Urbanization …… YIN Shuiqing, LI Weijing, Deliang CHEN, et al (771)
86. 我国热带气旋潜在影响力指数分析 …… 尹宜舟 肖风劲 罗 勇 赵珊珊 (781)
87. 2008 年“2.28”低纬高原强对流成因诊断与数值模拟 …… 尤 红 肖子牛 艾永智 (790)
88. 中国旱涝格局演变(1961—2050 年)及其对水资源的影响 …… 翟建青 曾小凡 姜 彤 (797)
89. 历史极端雨涝事件研究——1823 年我国东部大范围雨涝 …… 张德二 陆龙骅 (803)
90. 天山乌鲁木齐河源 1 号冰川致冷效应的小气候观测 …… 张东启 明 镜 魏文寿 (810)
91. 一种处理漫射因子的新方法 …… 张 峰 张 华 沈钟平 卫晓东 (819)
92. PFCs 和 SF_6 的辐射强迫与全球增温潜能 …… 张 华 吴金秀 沈钟平 (823)
93. Simulation of direct radiative forcing of aerosols and their effects on East Asia climate using an interactive AGCM-Aerosol coupled system …… H Zhang, Z L Wang, Z Z Wang, et al (832)
94. A study of the radiative forcing and global warming potentials of hydrofluorocarbons …… Hua Zhang, Jinxiu Wu, Peng Lu (851)
95. Radiative forcing and global warming potential of perfluorocarbons and sulfur hexafluoride …… ZHANG Hua, WU JinXiu and SHEN ZhongPing (861)
96. 城市化对北京气象站极端气温指数趋势变化的影响…… 张 雷 任国玉 刘 江, 等 (870)
97. Changes in precipitation extremes over Eastern China simulated by the Beijing Climate Center Climate System Model (BCC_CSM1.0)…… Li Zhang, Min Dong, Tongwen Wu (880)
98. 北半球平流层大气环流转型的基本气候特征 …… 张 灵 李维京 陈丽娟 (899)
99. Interdecadal Change of the Relationship Between the Tropical Indian Ocean Dipole Mode and the Summer Climate Anomaly in China …… ZHAO Shanshan, ZHOU Tianjun, YANG Xiuqun, ZHU Yimin, et al (909)
100. 全球大风在减少吗 …… 赵宗慈 罗 勇 江 滢 (922)
101. 冬季澳大利亚东侧海温与长江流域夏季降水的联系及可能物理机制 …… 周波涛 (925)
102. Change in extreme temperature event frequency over mainland China, 1961—2008 …… Yaqing Zhou, Guoyu Ren (932)
103. 基于偏态分布的百分位估计公式的建立 …… 周 云 侯 威 钱忠华 何文平 (947)

www.climatechange.cn



文章编号：1673-1719 (2011) 04-0259-06

# 气候变暖对我国南方水稻可种植区的影响

宋艳玲，刘 波，钟海玲

（中国气象局国家气候中心，北京 100081）

**摘 要**：利用我国南方稻区214站1961—2009年逐日气象资料，研究气候变化对南方水稻可种植区的影响。研究结果显示：气候变暖使南方稻区活动积温（日平均气温≥10 ℃）明显增加，49年增加了324.4 ℃·d。同时水稻生长季长度也明显延长，49年延长了17.9 d。双季稻可种植区北界明显北移，三季稻可种植区北界略有北移，20世纪60—80年代，双季稻可种植区仅限于长江以南地区，但21世纪初以来的10年双季稻可种植区北界移到长江以北，即向北推移近300 km，从而使新增双季稻可种植区扩展到四川东北部、贵州东部、重庆、湖北大部、安徽中部以及江苏南部。

**关键词**：气候变暖；水稻；可种植区；中国南方

**中图分类号**：P467/S511 **文献标识码**：A

## 引 言

中国是世界上最大的稻米生产国和消费国，水稻种植面积在世界产稻国中位居第二，总产量居世界之首。中国水稻种植面积约占粮食总种植面积的27.4%，而年稻谷产量占粮食总产量的37.1%[1]。

水稻的生长发育受到气候条件的制约，水稻的纬向分布就是气候和大气条件以及光周期作用的结果[2]，季节降水量和它的分布都是影响水稻生长发育的重要因子[3]。短时期的气象灾害（如干旱、暴雨洪涝）、年际气候变率、大尺度的环流变化（如ENSO）和气候变化都能对水稻生长发育及其分布产生重大影响[4]。

IPCC第四次评估报告表明，全球平均地表温度自1861年以来持续升高，100年来（1906—2005年）增加了（0.74 ± 0.18）℃[5]。我国的气候也发生了明显的变化，百年来中国年平均气温升高0.4～0.8 ℃，其中以近50年变暖更为明显，达0.6～1.1 ℃[6−8]。20世纪50年代以来降水的变化趋势对所选取的时段和地区比较敏感，1951—2002年全国平均降水量变化趋势不显著，但1956—2002年间呈微弱上升趋势。20世纪后半叶，长江中下游地区暴雨日数呈增多趋势[9]。

气候变化对我国水稻种植业影响的深度和广度是当前科学界必须认真对待并加以解决的重大课题。本文利用1961—2009年我国南方（35°N以南）214站逐日气象数据，重点分析南方稻区活动积温、水稻生长季长度、年降水量及高温日数变化趋势，研究1961年以来气候变化对我国南方水稻可种植区的影响，探讨我国南方稻区应对气候变化的措施。

**收稿日期**：2011-03-23； **修回日期**：2011-04-14
**资助项目**：国家科技支撑计划课题（2007BAC29B05）；公益性行业（气象）科研专项（GYHY201106021）
**第一作者**：宋艳玲（1974—），女，副研究员，从事气候变化对农业影响研究。E-mail: songyl@cma.gov.cn

## 1 资料与方法

### 1.1 数据来源

本文利用中国气象局国家气象信息中心提供的1961—2009年753站逐日平均气温、最高气温和降水量资料，首先对原始数据进行质量控制，即当站点数据序列少于49年或缺测资料超过5%时，此站点数据被剔除，对缺测资料少于5%的站点数据用临近站点相同时间的数据进行插值。经过处理后，选出中国南方稻区数据质量较好的214站用于分析研究，站点分布见图1。

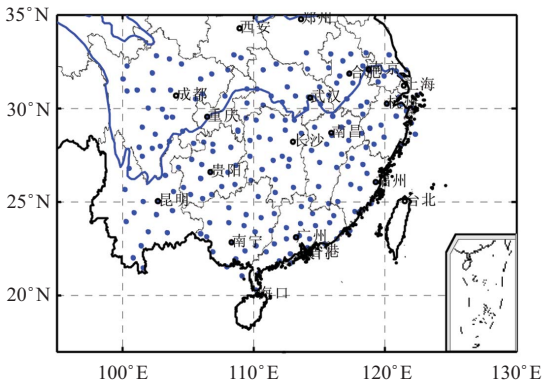


图1 研究区域及气象站点分布

Fig. 1 The research region and the locations of 214 weather stations

### 1.2 指标和计算方法

南方水稻可种植区指标。活动积温是指植物在整个生长期中高于生物学最低温度之和，即大于某一临界温度（本文取10 ℃）的日平均气温的总和。参照程式华等[10]的研究，以活动积温达到7000 ℃·d作为三季稻可种植区的积温指标，以活动积温达到5300 ℃·d作为双季稻可种植区的积温指标。

生长季长度指标。由于气候变化对不同地区生长季产生明显影响，近年来关于生长季的定义和变化规律研究很多。例如Linderholm[11]给出了目前国际上常用的5种生长季的定义方法。本研究采用程式华等[10]给出的我国南方水稻生长季长度指标，即日平均气温稳定通过≥10 ℃始现期至≥20 ℃终现期的间隔天数。

高温指标。夏季，长江以南大部地区早稻大多处于抽穗扬花和灌浆成熟期，经常受到高温天气的影响。本文以日最高气温≥35 ℃的日数作为高温指标。

此外，本研究中南方稻区活动积温变化趋势、水稻生长季长度变化趋势分析采用线性趋势分析，并利用Mann-Kendall趋势检验方法[12]进行检验，信度水平大于95%。

## 2 结 果

### 2.1 活动积温变化

如图2所示，1961—2009年，我国南方稻区活动积温增加了324.4 ℃·d，其中20世纪60—80年代活动积温变化趋势不明显，20世纪90年代以来，活动积温明显增加。例如20世纪60年代我国南方稻区平均活动积温为5712.8 ℃·d，2001—2009年上升到5980.8 ℃·d，比60年代增加了268.0 ℃·d。1991—2009年这19年间，有16年活动积温超过常年值。其中1998年活动积温最高，达到6144.9 ℃·d。

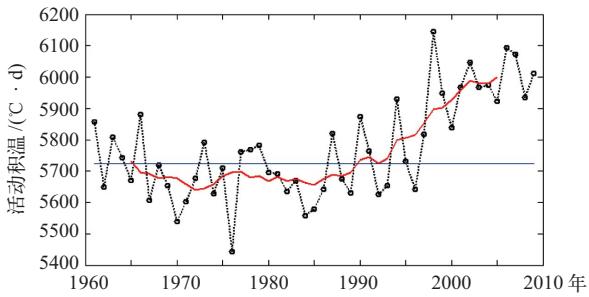


图2 1961—2009年我国南方稻区活动积温历年变化

Fig. 2 Yearly variation of the accumulated temperature in the southern China rice growing area from 1961 to 2009

热量资源影响水稻分布和分区。20世纪60—80年代，我国热量资源分布变化不大：年活动积温在7000 ℃·d以上的地区主要为华南中南部；年活动积温在5300～7000 ℃·d的地区包括湖南大部、江西、浙江中南部、福建大部、湖北东南部、四川和重庆的部分地区和云南南部（图略）。20世纪90年代以来，5300 ℃·d双季稻可种植区北界和7000 ℃·d三季稻可种植区北界逐渐北移。与1960年代相比，2001—2009年双季稻可种植区北界向北推移超过了

www.climatechange.cn



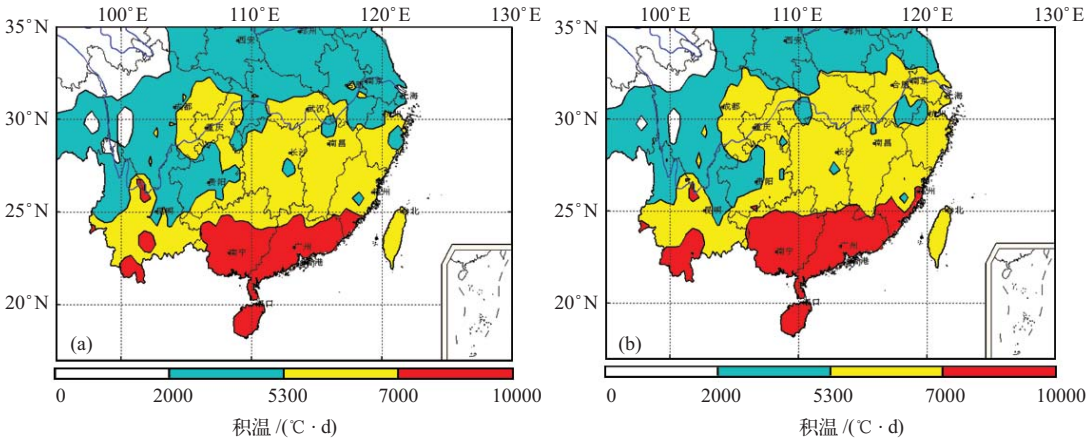


图 3　1961 — 1970 年 (a) 和 2001 — 2009 年 (b) 中国南方稻区活动积温分布（红色为三季稻可种植区，黄色为双季稻可种植区，蓝色为单季稻可种植区）

Fig. 3　The distribution of accumulated temperature over the southern China rice growing area in (a) 1961−1970 and (b) 2001−2009 (The cultivable areas for single harvest rice, double harvest rice and triple harvest rice are blue, yellow and red shaded, respectively)

两个纬距，约300 km（图3）。新增的双季稻可种植区包括四川东部、重庆大部、贵州东部、湖北大部、安徽中部和江苏南部。

## 2.2　水稻生长季长度变化

生长季长度也决定着水稻的分布，在我国华南稻区早稻一般2月下旬开始播种，晚稻11月上旬成熟；江南稻区早稻一般3月中旬播种，晚稻10月中旬成熟。

1961—2009年，我国南方稻区水稻生长季长度明显延长（图4），49年延长17.9 d。其中20世纪60—80年代，水稻生长季长度变化趋势不明显，20世纪90年代以来水稻生长季长度明显延长。20世纪60年代水稻平均生长季长度仅为214.9 d；2000—2009年水稻生长季长度增加为231.4 d，比60年代增加了16.5 d。

我国三季稻区水稻生长季长度一般在270 d以上，双季稻区在200 d以上；因而，水稻生长季长度在270 d以上一般可种植三季稻，在200 d以上可种植两季稻[10]。

图5显示，从水稻生长季长度的角度来看，随着气候变暖我国三季稻可种植区范围变化不大，但双季稻可种植区北界明显北移，特别是21世纪以来，北移范围非常明显。20世纪60—70年代，我国双季稻可种植区一般分布在长江以南地区，21世纪以来，双季稻可种植区北界移到长江以北，包括四川东北部、贵州东部、重庆、湖北大部、安徽中部以及江苏南部。

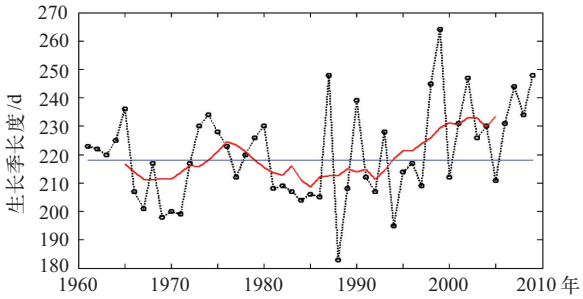


图 4　1961 — 2009 年我国南方稻区水稻生长季长度历年变化（红线表示 9 年滑动平均）

Fig. 4　Yearly variation of the length (days) of the growing season in the southern China rice growing area from 1961 to 2009

## 2.3　年降水量变化

我国双季稻区和三季稻区年降水量一般需要1000 mm以上[10]。研究表明，气候变暖对我国南方稻区降水量影响不大。20世纪60年代，南方稻区平均降水量为1379 mm，70年代、80年代和90年代，降水量持续增多，分别为1412、1435和1491 mm，21世纪以来，降水量略有减少，为1431 mm（图略）。

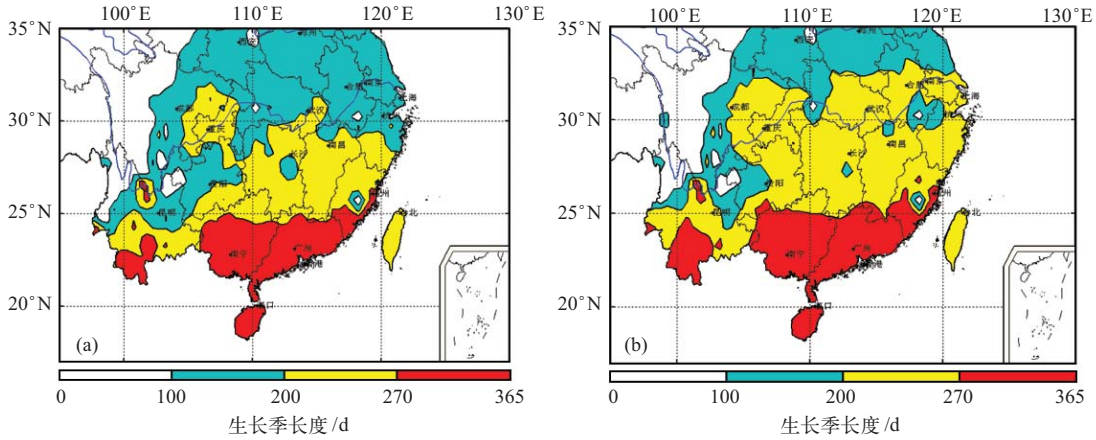


图 5 1961 — 1970 年 (a) 和 2001 — 2009 年 (b) 中国南方稻区水稻生长季长度分布（红色为三季稻可种植区，浅黄色为双季稻可种植区，蓝色为单季稻可种植区）

Fig. 5 The distribution of growing season length (days) over the southern China rice growing area in (a) 1961−1970 and (b) 2001−2009 (The cultivable areas for single harvest rice, double harvest rice and triple harvest rice are blue, yellow and red shaded, respectively)

另外，20 世纪 60 年代，我国海南大部、广西东部、广东、福建、江西等地年降水量在 1500 mm 以上，南方其余大部稻区年降水量为 1000～1500 mm；21 世纪以来，浙江、安徽、江西年降水量在 1500 mm 以上的地区明显减少，四川和云南年降水量为 1000～1500 mm 的地区略有减少（图略）。

综合考虑南方稻区活动积温、水稻生长季长度和年降水量（图 6），发现 1961 — 2009 年气候变暖使双季稻可种植区北界明显北移，20 世纪 60—80 年代，双季稻可种植区仅限于长江以南地区，但 21 世纪前 10 年双季稻可种植区北界移到长江以北，其北界向北推移近 300 km，从而使新增双季稻可种植区扩展到四川东北部、贵州东部、重庆、湖北大部、安徽中部以及江苏南部。

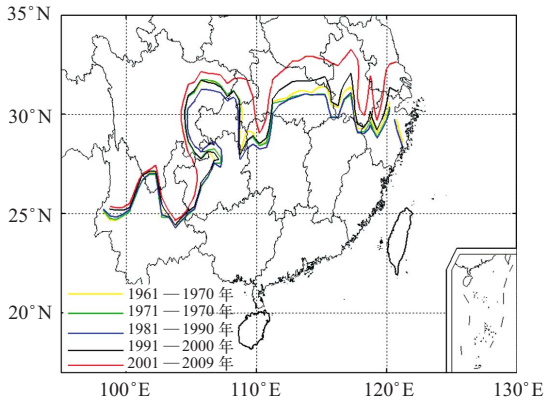


图 6 1961 — 2009 年不同年代我国南方双季稻可种植区北界变化

Fig. 6 The northern limit of double harvest rice for different decades in the southern China during 1961−2009

## 2.4 高温日数变化

夏季高温天气偏多一方面会导致水稻抽穗至成熟期时间缩短，叶片同化能力降低；另一方面会导致水稻空秕率有不同程度的增加，影响水稻的产量和质量。由于江南和华南水稻种植制度不同，高温天气影响也不同，因此分别讨论江南和华南地区高温日数变化规律（表 1）。

江南。分析显示：夏季（6 — 8 月）江南平均高温日数有 14.7 d，2001 年以来，高温日数明显增多，其中6月下旬和7月下旬增加趋势明显。6月下旬，江南地区水稻一般处于分蘖期，7 月下旬处于孕穗抽穗期，高温天气增多会对水稻孕穗抽穗产生不利影响。

华南。6 月，华南开始出现高温天气。总体上，华南地区夏季平均高温日数有 11.8 d，2001 年以来，高温日数明显增多，特别是 6 月下旬至 8 月上旬。

夏季高温日数明显增多，早稻灌浆期热害日益突出，不仅影响水稻产量，也会影响稻米质量，因此需迫切培育耐热品种和研究减轻高温危害的技术措施。

www.climatechange.cn



表 1　1961—2009 年江南和华南 6—8 月逐旬高温日数

Table 1　Dekad high temperature ( ≥ 35℃) days in the Jiangnan and Huanan regions during 1961−2009

d

| 地区 | 时段 | 1961—1970 年 | 1971—1980 年 | 1981—1990 年 | 1991—2000 年 | 2001—2009 年 |
|---|---|---|---|---|---|---|
| 江南 | 6 月上旬 | 0.3 | 0.2 | 0.4 | 0.3 | 0.3 |
| | 6 月中旬 | 0.5 | 0.6 | 0.4 | 0.3 | 0.8 |
| | 6 月下旬 | 0.8 | 0.7 | 0.6 | 0.7 | 1.7 |
| | 7 月上旬 | 1.4 | 2.5 | 1.8 | 1.4 | 2.8 |
| | 7 月中旬 | 3.6 | 2.1 | 3.3 | 2.8 | 3.4 |
| | 7 月下旬 | 4.3 | 3.1 | 2.5 | 3.8 | 4.5 |
| | 8 月上旬 | 3.1 | 3.3 | 2.6 | 2.8 | 2.9 |
| | 8 月中旬 | 2.6 | 1.4 | 1.8 | 1.4 | 1.8 |
| | 8 月下旬 | 2.7 | 1.4 | 1.0 | 1.1 | 2.1 |
| 华南 | 6 月上旬 | 0.3 | 0.2 | 0.3 | 0.9 | 0.4 |
| | 6 月中旬 | 0.4 | 0.7 | 0.6 | 0.5 | 0.5 |
| | 6 月下旬 | 0.8 | 0.7 | 1.0 | 0.7 | 1.5 |
| | 7 月上旬 | 1.1 | 1.7 | 1.5 | 1.2 | 2.1 |
| | 7 月中旬 | 1.8 | 1.9 | 2.2 | 1.6 | 3.0 |
| | 7 月下旬 | 2.5 | 1.9 | 2.1 | 2.4 | 3.1 |
| | 8 月上旬 | 1.4 | 1.2 | 2.1 | 1.9 | 2.7 |
| | 8 月中旬 | 1.4 | 0.9 | 1.9 | 1.4 | 1.8 |
| | 8 月下旬 | 1.7 | 0.8 | 1.2 | 1.5 | 1.8 |

## 3　结论与讨论

研究表明，1961—2009 年，气候变暖使我国南方稻区活动积温增加，49 年增加了 324.4 ℃·d。同时水稻生长季长度也明显延长，1961—2009 年水稻生长季长度延长了 17.9 d。双季稻可种植区北界明显北移，三季稻可种植区北界略有北移，20 世纪 60—80 年代，双季稻可种植区仅限于长江以南地区，但 21 世纪前 10 年双季稻可种植区北界移到长江以北，其北界向北推移近 300 km，从而使新增双季稻可种植区扩展到四川东北部、贵州东部、重庆、湖北大部、安徽中部以及江苏南部。赵锦等[13]研究也发现气候变暖使我国南方一年两熟和三熟种植北界明显北移。

气候变暖使南方双季稻可种植区明显扩大，然而在实际生产中，一个地区的种植制度和种植方式不仅取决于气候条件还要考虑当地的农业生产技术水平、农业投入、土壤、作物品种特性和政府政策引导等。如我国南方 20 世纪 60 年代末开始大规模推广双季稻，至 1976 年水稻总面积达 $3.62 \times 10^7$ $hm^2$，其后双季稻种植面积逐年减少[14]，特别是 20 世纪 90 年代以来我国南方双季稻种植面积持续减少[15]。尹昌斌等[16]认为这一变化的主要原因为稻谷价格过低，而陈风波等[17]对这个时期江汉平原稻农行为的研究表明稻农非农化程度越高，双季稻改单季稻的可能性就越大，说明非农活动的增加导致农业劳动力的减少也是种植模式变化的一个重要原因。由此可见，虽然气候变暖使南方双季稻可种植区明显扩大，而在实际生产中，受政府政策引导、稻米价格和农业劳动力减少等的影响，双季稻实际种植面积呈减少趋势。

气候变暖使我国南方稻区热量资源增加，为充分利用光热资源、提高复种指数创造了条件，应着力解决扩大双季稻生产的机械化问题。同时，随着

气候变暖，早稻灌浆期热害日益突出，也迫切需要加快选育耐热早稻品种，减轻高温危害。■

## 参考文献

[1] 中国农业年鉴编辑委员会 . 中国农业年鉴 [M]. 中国农业出版社 , 2008: 179−180

[2] Leff B, Ramankutty N, Foley J A. Geographic distribution of major crops across the world [J]. Global Biogeochem, 2004, 18, GB1009

[3] Olesen J E, Bindi M. Consequences of climate change for European agriculture productivity, land use and policy [J]. Eur Agron, 2002, 16: 239−262

[4] Tubiello F N.Climate variability and agriculture: perspectives on current and future challenges[M]// Night B K. Impact of climate change, variability and weather fluctuations on crops and produce markets. Cambridge, UK: Cambridge University Press, 2005: 45−63

[5] IPCC. Climate change 2007: the physical science basis: summary for policymakers. Contribution of working group I to the fourth assessment report of the Intergovernmental Panel on Climate Change [M]. Cambridge, UK: Cambridge University Press, 2007

[6] Hulme M, Wigley T, Jiang Tao, *et al.* Climate change due to the greenhouse effects and its impacts and its implications for China [J]. A Banson Production (UK), 1992: 53

[7] 王绍武 , 赵宗慈 . 未来 50 年中国气候变化趋势的初步研究 [J]. 应用气象学报 , 1995, 6 (3): 333−342

[8] 魏凤英 , 曹鸿兴 . 20 世纪我国气候增暖进程的统计事实 [J]. 应用气象学报 , 2003, 14 (1): 79−86

[9] 翟盘茂 , 任福民 , 张强 . 中国降水极值变化趋势检测 [J]. 气象学报 , 1999, 57 (2): 208−216

[10] 程式华 , 李建 . 现代中国水稻 [M]. 北京：金盾出版社 , 2007: 90−93

[11] Linderholm H W. Growing season changes in the last century[J]. Agricultural and Forest Meteorology, 2006, 137: 1−14

[12] Yue S, Pilon P, Cavadias G. Power of the Mann-Kendall and Spearman's rho tests for detecting monotonic trends in hydrological series[J]. Journal of Hydrology, 2002, 259: 254−271

[13] 赵锦 , 杨晓光 , 刘志娟 , 等 . 全球气候变暖对中国种植制度可能影响 II. 南方地区气候要素变化特征及对种植制度界限可能影响 [J]. 中国农业科学 , 2010, 43 (9): 1860−1867

[14] 王平 , 黄耀 , 张稳 . 1955 — 2005 年中国稻田甲烷排放估算 [J]. 气候变化研究进展 , 2009, 5 (5): 291−297

[15] 陈风波 . 水稻种植模式变迁对中国南方地区水稻产量的影响 [J]. 新疆农垦经济 , 2007, 8: 6−9

[16] 尹昌斌 , 陈印军 , 杨瑞珍 . 长江中下游地区稻田改制的倾向与动力 : 来自农户调查的实证分析 [J]. 中国农业资源与区划 , 2003, 2: 30−33

[17] 陈风波, 丁士军. 农村劳动力非农化与种植模式变迁: 以汉江平原稻农水稻种植为例 [J]. 南方经济 , 2006, 9: 43−52

# Impact of Global Warming on the Rice Cultivable Area in Southern China in 1961−2009

Song Yanling, Liu Bo, Zhong Hailing

(*National Climate Centre, China Meteorological Administration, Beijing* 100081*, China*)

**Abstract:** Using the daily weather data from 214 stations over southern China rice growing area during 1961−2009, impact of global warming on the rice cultivable area in southern China was studied. The results show that the accumulated temperature in rice-growing areas across southern China obviously increased in the period of 1961−2009, it increased up to 5980.8 ℃·d in 2001−2009, 268.0 ℃·d higher than that in the 1960s. Correspondingly, the rice growing season has clearly prolonged up to 231.4 d, 16.5 d longer than that in the 1960s. And the growing boundary for double-cropping rice apparently shifted northwards, and one for triple-cropping rice slightly shifted northwards. From the 1960s to 1980s, the double-cropping rice grew only in the areas south of the Yangtze River. However in the recent 10 years, the cultivable area for double-cropping rice has extended even north of the Yangtze River, i.e., the northern boundaries have advanced northwards approximately 300 km, extending to northeastern Sichuan, eastern Guizhou, Chongqing, most Hubei, central Anhui, as well as southern Jiangsu.

**Key words:** global warming; rice; cultivable area; southern China

Environ. Res. Lett. **6** (2011) 034025 (8pp) doi:10.1088/1748-9326/6/3/034025

# Rain-season trends in precipitation and their effect in different climate regions of China during 1961–2008

**Yanling Song[1,3], Christine Achberger[2] and Hans W Linderholm[2]**

[1] National Climate Centre, China Meteorological Administration, 100081 Beijing, People's Republic of China
[2] Department of Earth Sciences, University of Gothenburg, Box 460, 405 30 Gothenburg, Sweden

E-mail: songyl@cma.gov.cn

Received 12 May 2011
Accepted for publication 11 August 2011
Published 30 August 2011
Online at stacks.iop.org/ERL/6/034025

**Abstract**
Using high-quality precipitation data from 524 stations, the trends of a set of precipitation variables during the main rain season (May–September) from 1961 to 2008 for different climate regions in China were analysed. However, different characteristics were displayed in different regions of China. In most temperate monsoon regions (north-eastern China), total rain-season precipitation and precipitation days showed decreasing trends; positive tendencies in precipitation intensity were, however, noted for most stations in this region. It is suggested that the decrease in rain-season precipitation is mainly related to there being fewer rain days and a change towards drier conditions in north-eastern China, and as a result, the available water resources have been negatively affected in the temperate monsoon regions. In most subtropical and tropical monsoon climate regions (south-eastern China), the rain-season precipitation and precipitation days (11–50, with >50 mm) showed slightly positive trends. However, precipitation days with ⩽10 mm decreased in these regions. Changes towards wetter conditions in this area, together with more frequent heavy rainfall events causing floods, have a severe impact on peoples' lives and socio-economic development. In general, the rain-season precipitation, precipitation days and rain-season precipitation intensity had all increased in the temperate continental and plateau/mountain regions of western China. This increase in rain-season precipitation has been favourable to pasture growth.

**Keywords:** precipitation, trend analysis, rain season, China

## 1. Introduction

Changes in total and extreme precipitation have attracted much attention in research as well from the general public during recent years. A large number of studies focusing on precipitation changes during the past 50–100 years have generally concluded that changes in precipitation extremes have occurred worldwide during the past century, associated with increasing mean temperatures (e.g. Trenberth 1999, Easterling *et al* 2000, Beniston and Stephenson 2004).

In their Fourth Assessment Report, The Intergovernmental Panel on Climate Change (IPCC 2007) presented a global synthesis of precipitation trends since 1900 based on the current knowledge. The general picture that emerged was significantly increased precipitation in eastern parts of North and South America, northern Europe and northern and central Asia, whereas drying has been observed in the Sahel region,

[3] Address for correspondence: National Climate Centre, China Meteorological Administration, Zhong-Guan-Cun-Nan-Da-Jie 46, Haidian, Beijing 100081, People's Republic of China.

 © 2011 IOP Publishing Ltd Printed in the UK

the Mediterranean, southern Africa and parts of southern Asia.

The climate across China varies considerably and the country can be divided into several climate zones, which are mainly influenced by the Asian monsoon systems and the Tibetan Plateau (Domroes and Peng 1988, Ye and Gao 1979, Ding and Murakami 1994). Due to the large number of people living in the country, minor changes in the climate already have a profound impact on the people's livelihood. For instance, since Chinese agriculture is highly dependent on irrigation (48% of the cultivated area in 2006 was equipped with some kind of irrigation system (FAO 2011)), climate induced changes in the irrigation demand may have considerable impact on agricultural production (see e.g. Thomas 2008). Recent climate change and its various kinds of impact on, e.g., ecosystems, society, agriculture and water availability have therefore attracted much attention from a broad climate research community. There is, however, a constant need to monitor and analyse ongoing climate changes as new climate data become available.

The general aim of this study is to analyse ongoing precipitation changes in the rain season (May–September) using high-quality precipitation observations from 1961 to 2008, thereby providing an update of existing studies regarding precipitation variability across China. More specifically, the objectives of the paper are to analyse trends in the rain season of total precipitation, the number of days with light ($\leqslant$10 mm), moderate (11–50 mm) and heavy (>50 mm) precipitation, as well as precipitation intensity in different climate regions of China. The practical implications of changes in these parameters are also discussed, since many previous studies touch on this issue to a considerably lesser extent.

This letter is organized in the following manner. Section 2 provides climatological background information and section 3 briefly describes the data and methods. In section 4 the results are presented and section 5 links the findings to existing studies and discusses implications of changes in the rain season. Section 6 summarizes the main conclusions.

## 2. Background

In general, the rainy season occurs from May to September. It starts with a period of pre-monsoonal rain over South China in early April, and from May through August the summer monsoon rain belt moves northward to the Yangtze river basin (June) and finally to northern China (July). When the monsoon ends in August, the rain belt moves back to southern China. Due to the migration of the monsoon across China, the length of the rain season differs between southern and northern China, and rainfall amounts vary greatly among different regions depending on topography and distance to the ocean. In the subtropical and tropical monsoon climates of south-eastern China, annual rainfall amounts range from 1000 to 2000 mm. Here rice can grow in most regions. In the temperate monsoon climates of north-eastern China, annual rainfall amounts are considerably smaller, ranging from 400 to 800 mm, which is sufficient for growing corn, winter wheat and soya beans. Here, spring droughts are frequent, and as a result irrigation

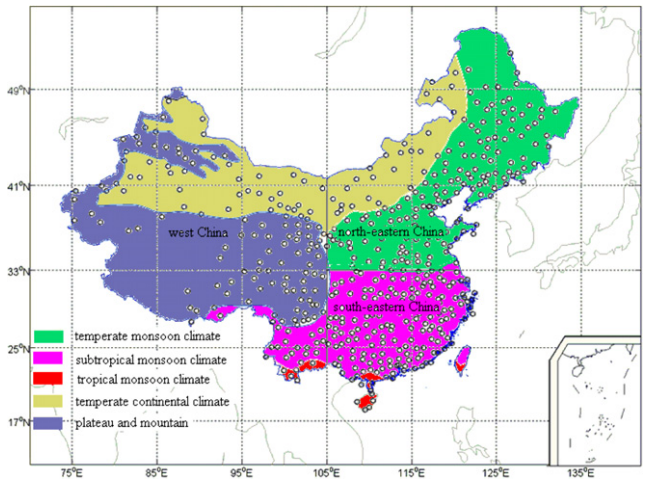


**Figure 1.** The distribution of climate regions in China and the locations of the 524 stations used in this study.

is necessary for agriculture during periods of drought. In the temperate continental climates, as well as the plateau and mountain regions, of western China, annual rainfall amounts are as low as 50–400 mm. Here, the vegetation ranges from forests to grasslands, and to deserts, depending on the humidity conditions (figure 1).

Besides the large variability in the spatial precipitation distribution, long-term changes in Chinese precipitation are evident (Ding and Sun 2003, Kripalani and Kulkarni 2001, Wang *et al* 1981, 2000, Zhai and Ren 1999, Zhao *et al* 2005, Ren *et al* 2000). Zhai *et al* (2005) analysed the trend in normalized annual precipitation anomalies as well as some annual extremes (daily precipitation >50 and >100 mm) for the period 1951–95 using 296 stations in China. While no obvious trends in the annual precipitation in China as a whole were found, the number of days with rainstorms (daily precipitation >50 mm) had decreased in northern China. These findings were later confirmed by Zhai *et al* (2005), using a larger station network (530 stations). Ren *et al* (2000) showed an increasing trend in summer precipitation over the middle to lower reaches of the Yangtze river, and a decreasing trend over the Yellow river basin, but virtually no change at higher latitudes. Examining the relationship between long-term summer precipitation change and the large-scale monsoon circulation features, Ding *et al* (2008, 2009) found that a significant weakening of the East Asian summer monsoon has led to reduced precipitation in North China. Shen (2010) studied 50 yr of water resource changes in different Chinese river basins, and found that rainfall had decreased in the Hai and Liao river basins as well as in parts of the Yellow river basin, while rainfall had increased in most regions in southern China, parts of northwest China and the northern part of northeast China. In addition, numerous studies have dealt with precipitation variability in specific regions, such as the Tarim river basin (Xu *et al* 2006, 2010), the Dongjiang river basin (e.g. Liu *et al* 2010) and the Pearl river basin (e.g. Zhang *et al* 2010).

## 3. Data and methods

### *3.1. Precipitation data*

In order to investigate the change of rain-season (May to September) precipitation in different climate regions of China, a data set of daily precipitation, obtained from 740 stations, covering mainland China for the period 1961–2008, was used. It included almost all national climate stations, and was developed at the Climate Data Centre (CDC) of the China Meteorological Administration. Only station series with a low rate of missing data (⩽5%) were chosen, forming a subset of 524 stations that were found to be suitable and were subsequently used in the analysis (figure 1).

### *3.2. Statistical analysis*

To assess the spatial and temporal distributions of rain-season precipitation changes in China, total precipitations, precipitation intensities and numbers of days with precipitation exceeding certain thresholds were calculated, from 1961 to 2008. Precipitation intensity is the amount of precipitation collected per unit time interval and is here defined as the total precipitation in the rain season divided by the number of precipitation days (with >0 mm) for individual stations. The precipitation days were subdivided into three groups depending on precipitation amounts, where ⩽10 mm characterizes light rain, 11–50 mm moderate rain and >50 mm heavy rain, according to the meteorological regulations of China. In China, daily rainfall >50 mm can induce breakage of reservoirs and, causing floods, lead to serious threats to people's safety and the economy (Li *et al* 2009a).

Changes in the total amount of rain-season precipitation may have different causes. They may be caused either by variations in the number of precipitation days or by variations in the precipitation intensity, or by both, and studying both factors gives possibilities for better understanding the individual contributions to changes in rain-season precipitation of these factors during the rainy season. For each precipitation variable, linear trends over time for the 1961–2008 periods were calculated for each climate station and the significance was tested using the Mann–Kendall trend test (Yue *et al* 2002).

## 4. Results

### *4.1. Rain-season total precipitation changes*

The results from the trend analysis of total precipitation in the rain season are shown in figure 2. Averaged over all stations, a general increasing tendency in rain-season precipitation between 1961 and 2008 was seen, although large interannual variability is evident (figure 2(a)). The magnitude and sign of the observed trends varies across China (figure 2(b)). In general, a majority of the stations located in the temperate monsoon climate experienced decreasing rain-season precipitation trends, while in general they increased in the other climate regions.

In the regions west of 105°E, most stations showed tendencies, i.e. non-significant trends, for increased rain-season precipitation over the analysed period. Positive

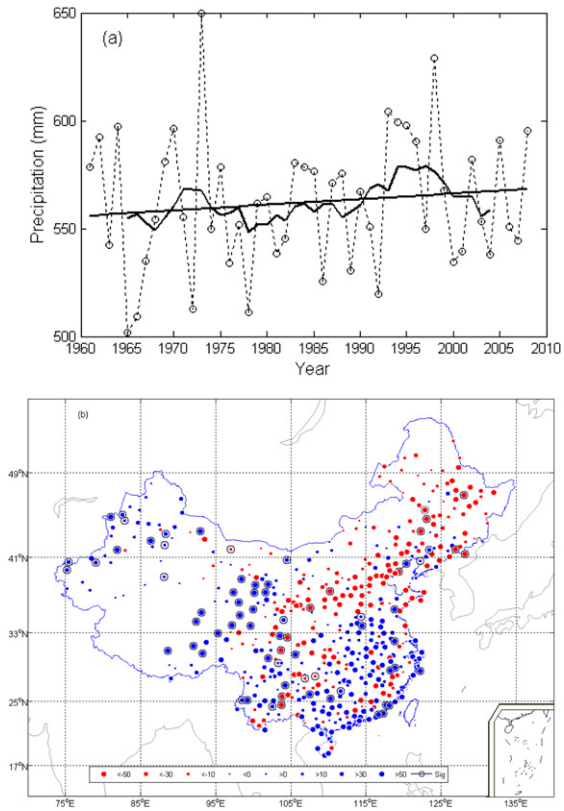


**Figure 2.** (a) Averaged time series of precipitation (mm) and (b) regional distribution of precipitation trends from 1961–2008 over China (mm). ((a) Dotted lines: interannual variability, solid lines: 9 yr moving average and trend line).

tendencies for rain-season precipitation were found at 68% of the stations (106 out of 156 stations). Furthermore, significant trends in rain-season precipitation, ranging from 18.9 to 355.9 mm, were found at 22% of the stations. The two largest significant trends appeared in the records of Jiali (30.66°N, 93.28°E) and Wudaoliang (35.22°N, 93.08°E) with linear significant increasing trends of 60.8% and 107.8% respectively.

In south-eastern China, east of 105°E and south of 33°N, 57% of the stations (118 out of 177 stations) showed positive rain-season precipitation tendencies, while significant positive trends were only found at 3 stations (figure 2(b)). In north-eastern China, east of 105°E and north of 33°N, negative rain-season precipitation tendencies were found at 82% of the stations (157 out of 191 stations), and significant negative trends of precipitation were found at 13 stations (6.8%), ranging from −94.1 to −177.4 mm.

Overall, the total rain-season precipitation increased by 12.6 mm (2.2%) during 1961–2008 in the whole of China (change is non-significant). The general picture that emerges is a change towards a slightly wetter rain-season climate in western China, belonging to temperate continental and plateau/mountain climates, as well as large parts of the south-eastern part of the country (subtropical and tropical monsoon climate). During the same period the north-eastern regions, mainly belonging to the temperate monsoon climate, became drier.

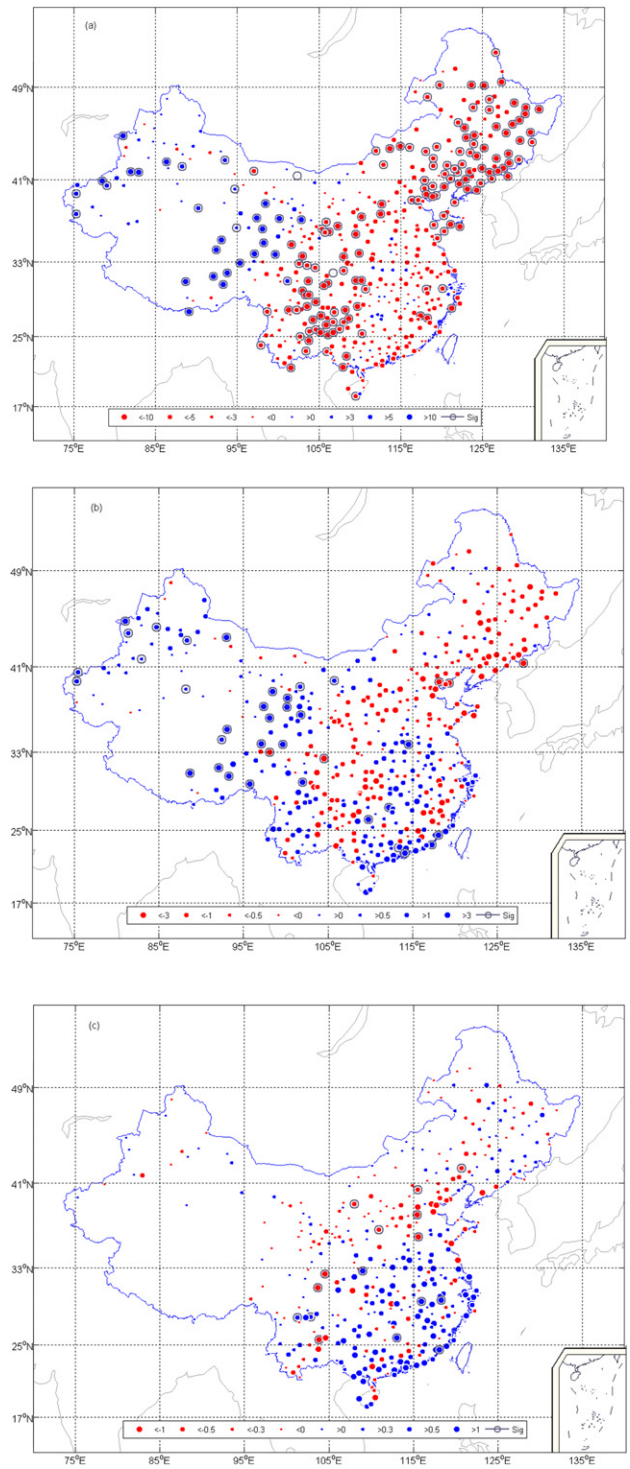


**Figure 3.** Change of precipitation days ((a) daily precipitation 0–10 mm, (b) daily precipitation 11–50 mm, (c) daily precipitation >50 mm) in the rain season from 1961 to 2008 over China.

### *4.2. Change in the number of rain-season precipitation days*

The trends in the number of days with precipitation over a certain threshold (i.e. ⩽10, 11–50 and >50 mm) are shown in figure 3.

For China as a whole, the results indicate that the precipitation days with 0–10 mm decreased by 2.8 days from 1961 to 2008 (non-significant). There is a clear spatial pattern with decreasing number of precipitation days with ⩽10 mm in most of the regions in north-eastern and south-eastern China, while in western China, the number of rain days increased. In north-eastern China, the precipitation days with ⩽10 mm decreased considerably. Here 95.8% of the stations (number of stations) displayed negative tendencies, and 42.4% showed significant negative trends corresponding to a reduction of 6 to 19.2 days. In south-eastern China, 16% of the stations (28 stations) displayed significant negative trends, and 88.7% of the stations showed negative tendencies. In contrast, the precipitation days with ⩽10 mm increased in western China: 73% of all stations (156 stations) displayed positive tendencies, but only 18% of stations (28 stations) showed significant positive trends (figure 3(a)).

Figure 3(b) shows the trends in precipitation days with 11–50 mm. In total, they increased slightly by 0.1 days for the whole of China. Similar to the trends in precipitation days with ⩽10 mm, the precipitation days with 11–50 mm in western China increased to 66% of the 103 stations, the increase being significant at 16% of the stations (25 stations). In south-eastern China, 54% of the stations showed positive tendencies, with significant trends at 6 stations (177 stations), while the remaining stations displayed negative tendencies. In north-eastern China, precipitation days with 11–50 mm decreased at most stations (71.2%), but significant trends were only found at 3 stations.

The trends of precipitation days with >50 mm during 1961–2008 are shown in figure 3(c), where the results show an increase by 0.16 days for the whole of China. In western China, the rain-season precipitation is usually less than 400 mm, which results in very few days that are precipitation days with >50 mm. In south-eastern China, precipitation days with >50 mm increased by 0.41 days, and 70% of the 156 stations showed positive tendencies, significant at 5 stations. In north-eastern China, precipitation days with >50 mm decreased by 0.14 days, and most stations (61.8%) displayed negative tendencies, including 6 stations with significant negative trends.

Overall, the trends in precipitation days varied across China. In north-eastern China, precipitation days showed considerably decreasing trends; in particular, about a half of the stations displayed decreasing trends significantly for light rainfall (0–10 mm). In south-eastern China, the precipitation days with 0–10 mm also decreased, while the precipitation days with >50 mm increased considerably in most parts of the regions. In western China, the precipitation days increased significantly during 1961–2008. These results therefore indicate a decrease in light rainfall in northeast and southeast China, while heavy rainfalls have been increasing in most regions of south-eastern China.

### *4.3. Change of precipitation intensity in the rain season*

A time series of precipitation intensity averaged for all 524 Chinese stations from 1961 to 2008 is shown in figure 4(a). The precipitation intensity increased significantly by, on average, 0.79 mm day$^{-1}$, but the increase was not continuous throughout the whole period. While there was a slight

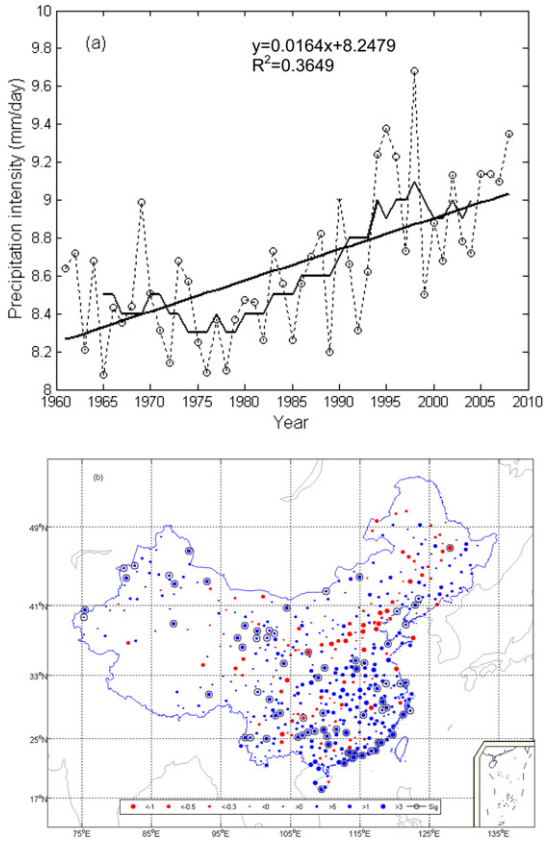


**Figure 4.** (a) Averaged time series of precipitation intensity and (b) regional distribution of precipitation intensity trends from 1961 to 2008 over China ((a) dotted lines: interannual variability, solid lines: 9 yr moving average and trend line).

decrease in precipitation intensity in the 1970s, an increasing trend started in the 1980s resulting in a precipitation intensity of about 9.0 mm day$^{-1}$ during 2001–8 compared to about 8.3 mm day$^{-1}$ in the 1970s.

The regional distribution of precipitation intensity trends in China from 1961–2008 is shown in figure 4(b). The precipitation intensity increased in western and south-eastern China, where 67.3% and 83.6% of the stations respectively displayed increasing tendencies. Out of these stations, 16.0% and 16.3% of the stations (for western and south-eastern China respectively) showed significant positive trends, from 0.9 to 6.2 mm day$^{-1}$. Positive tendencies in precipitation intensity were also noted for 61.8% of the stations in northeast China. These results indicate that, in general, precipitation intensity increased in the whole of China, especially in the south-eastern parts.

Regarding the relation between rain-season precipitation, precipitation days and precipitation intensity, it is clear that the increase in rain-season precipitation in the south-eastern regions of China is associated with more intense precipitation overcompensating for the rainfall deficit due to there being fewer rain days with $\leqslant$10 mm. The decrease in rain-season precipitation in north-eastern China is mainly related to there being fewer light rain days (with $\leqslant$10 mm) in combination with the decreased precipitation intensity. However, there are also stations in this region where precipitation intensity instead increased. This indicates that more intensive precipitation does not compensate for the rainfall deficit due to a decrease in the frequency of precipitation days with $\leqslant$10 mm. In western China the total number of precipitation days increased in accordance with positive trends in both precipitation intensity and precipitation days.

## 5. Discussion

### *5.1. Rain-season precipitation changes in China during 1961–2008*

The results showed that the total rain-season precipitation had increased by 12.6 mm during the 48 yr period averaged over China (table 1). While the rain-season precipitation showed different trends in different regions, in western and south-eastern parts of China, the precipitation gave increased tendencies, while in north-eastern China, the precipitation showed decreased tendencies.

In western and south-eastern China, 67.9% and 57% of stations showed tendencies for increased precipitation respectively, where 22% of stations showed significant positive trends in western China, and 6.8% in southeast China. Gong and Ho (2002) pointed out that the summer rainfall (from June to August) over the Yangtze river valley (south-eastern China) had increased over the last few decades, which could be related to changes in the subtropical high over the Northwest Pacific. On the basis of data from China, Korea, and Japan, Qian *et al* (2003) suggested that increasing summer precipitation in southern China could be linked to the multi-decadal variation of the monsoon circulation in eastern Asia. Moreover, a weakening in the East Asian summer monsoon, accompanied by a southward shift in the major monsoon rain belt from northern to southern China, has been observed since the end of 1970s (IPCC 2007).

The results from most regions of temperate monsoon climate clearly indicated trends towards drier rainy seasons, where 82% of the stations showed tendencies for decreasing rain-season precipitation (figure 2). This result agrees with the findings of an apparent summer precipitation decrease in northern China during the past few decades (Chen *et al* 1991, Xu *et al* 1992, Chen *et al* 2005). This may be related to a significant weakening of the East Asian summer monsoon in the last decades, which has decreased the northward moisture transport, leading to a deficit in moisture supply for precipitation in northern China (Ding *et al* 2008).

The trends in precipitation days also varied among different climate regions. In north-eastern China, the temperate monsoon climate regions, the precipitation days analyses indicated that the number of days with light, moderate and heavy precipitation has decreased in most of the area. This is in agreement with the results of Wang *et al* (2006) who calculated the change in the number of rain days with >0 mm in China over the last 40 yr, and found a decreasing number of rain days in northern China. In western China, the region with the smallest number of rain days with >50 mm, those with $\leqslant$10 mm and 11–50 mm increased significantly, suggesting that the $P_{RS}$ increase is partly due to the increase of light

**Table 1.** Linear trends of total precipitation, number of precipitation days and precipitation intensity of the rain season over the whole of China, and stations with significant trends in different climate regions from 1961 to 2008. (Bold: significant trends with $p < 0.05$, italic: stations with decreasing trends, black: stations with increasing trends.)

| | Trends over the whole of China | Stations with significant trends in Northeast China (⩾105°E, ⩾33°N) | Stations with significant trends in Southeast China (⩾105°E, <33°N) | Stations with significant trends in western China (<105°E) |
|---|---|---|---|---|
| Total precipitation | 12.6 mm, 2.2% | *13 stations, 6.8%* | **3 stations, 1.4%** | **35 stations, 22.4%** |
| Precipitation days with >0 mm | −2.8 days | *81 stations, 42.4%* | *28 stations, 15.8%* | **28 stations, 17.9%** |
| Precipitation days with >10 mm | 0.1 days | *3 stations, 1.6%* | **6 stations, 3.4%** | **25 stations, 16%** |
| Precipitation days with >50 mm | 0.16 days | *6 stations, 3.1%* | **5 stations, 2.8%** | — |
| Precipitation intensity | **0.79 mm day$^{-1}$** | **11 stations, 5.8%** | **29 stations, 16.4%** | **25 stations, 16%** |

and moderate rain days. Fu *et al* (2008) also pointed that the days of light rain were increasing in number in western China during 1961–2005. In south-eastern China, the spatial distribution of precipitation day trends varies with precipitation intensity. Here, the precipitation days with light rainfall were clearly decreasing in number, while the precipitation days with heavy rain, often inducing floods, have increased in number. One implication of this change is that the risk for floods and droughts has increased in south-eastern China.

The precipitation intensity increased significantly by 0.79 mm day$^{-1}$ over the whole of China in 1961–2008. Furthermore, this was reinforced in western and south-eastern China, which may lead to more floods in south-eastern China.

The observed precipitation changes are very likely to continue in the future due to global warming. According to the IPCC's Fourth Assessment Report (IPCC 2007) increasing summer precipitation and more extreme rainfall events, associated with tropical cyclone changes, are likely to occur in South East Asia. Since precipitation over South East Asia is strongly controlled by the strength of the Asian monsoon systems, any circulation changes here will have a considerable impact. Although global climate model (GCM) simulations project a weakening of the Asian summer monsoon circulation by the end of the 21st century, enhanced moisture convergence in a warmer atmosphere probably dominates over the weaker circulation, giving rise to enhanced precipitation. Also, Sun and Ding (2009), using the latest generation of coupled climate models, projected a reinforcement of the East Asian monsoon systems around the 2040s, which would mean that the precipitation over the whole of China would be increased.

### *5.2. Implications of rain-season precipitation changes*

Changes in the precipitation conditions and characteristics during the rainy season have a direct impact on the hydrological cycle, as well as on the temporal and spatial distributions of rainfall across China. This in turn has a wide range of practical implications. Decreasing precipitation will have a considerable impact on the water availability for, e.g., agriculture, industrial production and drinking water demand, especially in regions where water resources are already limited. Increasing the total precipitation, together with an increased frequency of heavy rainfall events, on the other hand may cause repeated damage, e.g. due to flooding, mudflows or landslides. In addition, changes in the spatial and temporal distributions of rainfall across China affect the balance between water resources and demands. A number of socio-economic consequences related to precipitation changes in China are discussed below.

In northeast China, decreasing rain-season precipitation will have a strong impact on the water resources. During 1951–2000, about 40% of the total 10 000 km of rivers had been changed from having runoff throughout the year to seasonal runoff. During the same time the averaged annual inflow to the Pacific Ocean decreased by 80% compared to the 1950s. Furthermore, compared to the 1950s, wetland areas decreased from 10 000 to 1000 km$^2$ in northeast China (Jia *et al* 2002). On the basis of a study of the groundwater level from a network of 600 shallow groundwater observation wells in Hebei, a province of Northeast China, Liu *et al* (2001) pointed out that the average depth of the groundwater had, on average, decreased from 7.23 m in 1983 to 11.52 m in 1993, yielding a decline of 0.43 m yr$^{-1}$. This was partly related to the decreased precipitation amounts during the rainy season.

Changes in water resources and surface hydrology are a result of the combined effects involving climate changes and various human activities. To what degree the examples mentioned above are caused by climate variability and/or various human activities is hard to estimate. Shen (2010) mentions that landscape changes alter the rainfall–runoff relationship, which may result in considerable reductions in water resources. This has been observed in major Chinese river basins over the past 50 years. In an attempt to separate the impact of climate change and human activities on runoff in the Dongjian river basin, Liu *et al* (2010) found that they separately accounted for approximately 50% of the runoff changes during the low-flow period. However, Li *et al* (2009b) found that climate variability had a stronger impact than land use changes when studying the surface hydrology of the Heihe catchment on the Loess plateau.

In the subtropical and tropical monsoon climate regions of China, precipitation often exceeds 1000 mm during the rainy season and floods occur frequently. The total rain-season precipitation, and the number of precipitation days with >50 mm as well as precipitation intensity showed positive trends, which have induced more floods. As a result, people's lives and socio-economic development have been strongly influenced by the increase in heavy rainfall events as well as occasions with floods and mudslides. For example, Ye *et al* (2009) found that the flood days had been increasing in

number since the 1990s in Hubei and Chongqing, provinces of south-eastern China. The data provided by the Ministry of Agriculture of China showed that the crop land affected by floods was 282.9 kha and 274.5 kha in the 1960s and 1970s respectively in southern China, while it amounted to 703.2 kha in the 1990s and 459.5 kha in 2001–8 (www.moa.gov.cn/). Also, mudslides related to floods have had a significant impact on people's welfare. For instance, a heavy downpour occurred on 13 June 2006 in Wangmo, a county in southern China, where the precipitation amounted to 196 mm in 4 h, and the results of this event included a mountain flood where 30 people died and 24 people went missing (NCC 2006, 2008). Moreover, heavy rainfalls also have an impact on the socio-economic activities in urban areas. The accelerated urbanization in China went hand in hand with increasing population and decreasing vegetation coverage. The urban rainwater discharges mainly through underground pipelines, and during heavy rainfall events, the drainage capacity of these underground pipelines is not sufficient, frequently causing floods within urban areas. For instance, Shanghai, the largest city of southern China with a population of 19.2 million, was hit by very heavy rainfall on 25 August 2008 receiving 117.5 mm in 1 h. The downpour produced a rainwater volume that exceeded the city's drainage capacity and as a consequence more than 150 roads were deeply inundated with water at a maximum depth at 1.5 m. As a consequence, numerous roads were closed for 10 h, and 138 flights were delayed (NCC 2008). At present, most Chinese cities are applying heavy rainfall prevention standards developed 30 years ago, and they cannot rapidly adapt to changed climate conditions. The results of our investigation point towards the need to include heavy rainfall extremes into the prevention standards when these cities are rebuilt, to be able to cope with changed climate conditions.

In temperate continental climate regions as well as plateau and mountain climate regions of China, the climate is rather dry, and vegetation varies from forests to grasslands, and to deserts. An increase in the total precipitation and number of precipitation days as well as precipitation intensity in this area is considered as favourable for growing pasture.

## 6. Conclusions

China, a large developing country, is dominated by tropical and subtropical monsoon climates in the south-eastern area, a temperate monsoon climate in the north-eastern area, as well as plateau and mountain climates in the west. Using high-quality precipitation data from 524 stations over China, the trends of total precipitation, number of precipitation days (with 0–10, 11–50 and >50 mm) and precipitation intensity during the rainy season were analysed, from 1961 to 2008.

Averaged over the whole of China, the results showed that total rain-season precipitation had increased by 12.6 mm, and the numbers of precipitation days with 11–50 mm and >50 mm were increased slightly, by 0.1 days and 0.16 days respectively, while the precipitation intensity had increased significantly by 0.79 mm day$^{-1}$ during the 48 yr period. The precipitation intensity has increased across the whole of China, especially in south-eastern China, but deviations from this general trend were found depending on region and rainfall statistics.

In most temperate monsoon regions, east of 105°E and north of 33°N, total rain-season precipitation has been decreasing during 1961–2008; furthermore, the number of precipitation days with ⩽10, 11–50 and >50 mm all showed decreasing tendencies for most stations, and the number of precipitation days with ⩽10 mm experienced significant negative trends at 42.4% of 191 stations, while positive tendencies in precipitation intensity were noted for most stations in northeast China. These results indicate that the decrease in total precipitation in north-eastern China is mainly related to there being fewer rain days. As a result, the water resources in temperate monsoon climate regions have been strongly influenced, since river runoff and water reservoirs are mainly fed from rainfall during the rainy season. Because 42% of the total arable area needs irrigation in the temperate monsoon climate regions, any change towards drier conditions will have a strong impact on the water demand in agriculture.

In most regions characterized by subtropical and tropical monsoon climate in China, east of 105°E and south of 33°N, the total number of days and number of precipitation days (11–50, with >50 mm) showed positive trends. Moreover, the precipitation intensity showed significant increasing trends at 16.3% of the stations, possibly inducing more floods. Changes towards wetter conditions in this area, together with more frequent heavy rainfall events causing floods as well as mudslides, will severely impact people's lives and socio-economic development. This is obvious from several extreme events that have occurred during the past few years.

In most of the temperate continental regions, as well as the plateau and mountain regions, of China, west of 105°E, the total rain-season precipitation, the number of precipitation days and the precipitation intensity have all increased. Here 22.4% of stations showed significant increasing trends for $P_{RS}$, ranging from 18.9 to 355.9 mm, which is considered as favouring pasture growth.

## Acknowledgments

This work was supported by 'The Impact of Meteorological Disasters on Agriculture in China under Climate Change' from CMA (GYHY201106021), the National Science and Technology Ministry (2007BAC29B04) of China, and the Swedish International Development Cooperation Agency SIDA (project SWE-2009-245).

## References

Beniston M and Stephenson D B 2004 Extreme climatic events and their evolution under changing climatic conditions *Glob. Planet. Change* **44** 1–9

Chen L X, Shao Y N, Zhang Q F, Ren Z H and Tian G S 1991 Preliminary analysis of climatic change during the last 39 years in China *Q. J. Appl. Meteorol.* **2** 164–73 (Chinese with English abstract)

Chen Y, Gao G, Ren G Y and Liao Y M 2005 Spatial and temporal variation of precipitation over ten major basins in China between 1956 and 2000 *J. Nat. Resource* **20** 637–43 (Chinese with English abstract)
Ding Y H and Murakami M 1994 *The Asian Monsoon.* (Beijing: China Meteorological Press) (in Chinese)
Ding Y H and Sun Y 2003 Inter-decadal variation of the temperature and precipitation patterns in East Asian monsoon region *(ISCC): Proc. Int. Symp. on Climate Change (Beijing, 31 March–3 April 2003)* WMO/TD-No. 1172 66–71
Ding Y H, Sun Y, Wang Z Y, Zhu Y X and Song Y F 2009 Inter-decadal variation of the summer precipitation in China and its association with decreasing Asian summer monsoon. Part II: Possible causes *Int. J. Climatol.* **29** 1926–44
Ding Y H, Wang Z Y and Ying S 2008 Inter-decadal variation of the summer precipitation in East China and its association with decreasing Asian summer monsoon. Part I: Observed evidences *Int. J. Climatol.* **28** 1139–61
Domroes M and Peng G 1988 *The Climate of China* (Berlin: Springer) p 361
Easterling D R, Meehl G A, Parmesan C, Changnon S A, Karl T R and Mearns L O 2000 Climate extremes: observations, modeling, and impacts *Science* **289** 2068–74
FAO (Food and Agricultural Organization) 2011 *Aquastat FAO's Information System on Water and Agricultural* (www.fao.org/nr/water/aquastat/countries/china/index.stm, accessed 11.05.2011)
Fu Q L, Lin X and Qian W H 2008 The temporal and spatial characteristics of graded summer rain days over China *J. Trop. Meteorol.* **24** 367–73
Gong D-Y and Ho C-H 2002 Shift in the summer rainfall over the Yangtze river valley in the late 1970s *Geophys. Res. Lett.* **29** 1436
IPCC 2007 *Climate Change 2007: Impacts, Adaptation and Vulnerability. Contribution of Working Group II to the Fourth Assessment Report of the Intergovernmental Panel on Climate Change* ed M L Parry, O F Canziani, J P Palutikof, P J van der Linden and C E Hanson (Cambridge: Cambridge University Press)
Jia J, Yu J and Liu C 2002 Groundwater regime and calculation of yield response in North China Plain: a case study of Luancheng County in Hebei Province *J. Geograph. Sci.* **12** 217–25
Kripalani R H and Kulkarni A 2001 Monsoon rainfall variations and teleconnections over south and East Asia *Int. J. Climatol.* **21** 603–16
Li C Y, Huang R H and Chou J H 2009a *The Study of Meteorological Disasters and Chinese Response* (China Meteorological Press) pp 33–51
Li Z, Liu W, Zhang X and Zheng F 2009b Impact of land use and climate variability on hydrology in an agricultural catchment on the Loess plateau of China *J. Hydrol.* **377** 35–42
Liu C M, Yu J J and Kendy E 2001 Groundwater exploitation and its impact on the environment in the North China Plain *Water Int.* **26** 265–72
Liu D, Chen X, Lian Y and Lou Z 2010 Impact of climate change and human activities on surface runoff in the Donjiang river basin of China *Hydrol. Process.* **24** 1487–95
NCC 2006 *The Impact of Climate in 2006* (China's Meteorological Press) p 45 (in Chinese)
NCC 2008 *The Impact of Climate in 2008* (China's Meteorological Press) p 36 (in Chinese)
Qian W H, Hu Q, Zhu Y F and Lee D K 2003 Centennial-scale dry–wet variations in east Asia *Clim. Dyn.* **21** 77–89
Ren G Y, Wu H and Chen Z H 2000 Spatial patterns of change trend in rainfall of China *Q. J. Appl. Meteorol.* **11** 322–30
Shen D 2010 Climate change and water resources: evidence and estimate in China *Curr. Sci.* **98** 1063–8
Sun Y and Ding Y H 2009 A projection of future changes in summer precipitation and monsoon in East Asia *Sci. China Ser.* D **39** 1487–504
Thomas A 2008 Agricultural irrigation demand under present and future climate scenarios in China *Glob. Planet. Change* **60** 306–26
Trenberth K E 1999 Conceptual framework for changes of extremes of the hydrological cycle with climate change *Clim. Change* **42** 327–39
Wang D J, Chen L and Ding Y G 2006 The change trend in rainfall, wet days of China in recent 40 years and the correlation between the change trend and the change of globe temperature *J. Trop. Meteorol.* **3** 3–12 (Chinese with English abstract)
Wang S W, Gong D Y, Ye J L and Chen Z H 2000 Seasonal precipitation series of Eastern China since 1880 and the variability *Acta Geograph. Sin.* **55** 281–93 (in Chinese)
Wang S W, Zhao Z C and Chen Z H 1981 Reconstruction of the summer rainfall regime for the last 500 years in China *Geophys. J.* **52** 117–22
Xu C, Chen Y, Li W and Chen Y 2006 Climate change and hydrological process response in the Tarim river basin over the past 50 years *Chin. Sci. Bull.* **51** 25–36
Xu G C, Yao H and Li S 1992 The changes of present precipitation and historical drought frequency in arid and semi-arid regions of China *Acta Meteorol. Sin.* **50** 378–82 (Chinese with English abstract)
Xu Z, Liu Z, Fu G and Chen Y 2010 Trends of major hydroclimatic variables in the Tarim river basin during the past 50 years *J. Arid Environ.* **74** 256–67
Ye D X, Zhang Q, Zhou X K and Chen X Y 2009 Changing trends of major meteorological disasters in recent decades over Three Gorges reservoir area *Resources Environ. Yangtze Basin* **18** 296–300
Ye D Z and Gao Y X 1979 *Meteorology of Qinghai-Xizang (Tibet) Plateau* (Beijing: Science Press) p 45 (in Chinese)
Yue S, Pilon P and Cavadias G 2002 Power of the Mann–Kendall and Spearman's rho tests for detecting monotonic trends in hydrological series *J. Hydrol.* **259** 254–71
Zhai P, Zhang X, Wan H and Pan X 2005 Trends in precipitation and frequency of daily precipitation extremes over China *J. Clim.* **18** 1096–108
Zhai P M and Ren F M 1999 On change of China's maximum and minimum temperatures in 1951–90 *Acta Meteorol. Sin.* **13** 278–90
Zhang Q, Jiang T, Chen Y D and Chen X 2010 Changing properties of hydrological extremes in south China: natural variations or human influences? *Hydrol. Process.* **24** 1421–32
Zhao Z C, Ding Y H, Luo Y and Wang S W 2005 Recent studies on attributions of climate change in China *Acta Meteorol. Sin.* **19** 389–400

# Changes of Accumulated Temperature, Growing Season and Precipitation in the North China Plain from 1961 to 2009*

SONG Yanling[1†](宋艳玲), ZHAO Yanxia[2](赵艳霞), and WANG Chunyi[3](王春乙)

1 *National Climate Center, China Meteorological Administration, Beijing* 100081

2 *Chinese Academy of Meteorological Sciences, China Meteorological Administration, Beijing* 100081

3 *Hainan Provincial Meteorological Service, Hainan* 570203

(Received December 29, 2009; in final form March 28, 2011)

**ABSTRACT**

Using the high-quality observed meteorological data, changes of the thermal conditions and precipitation over the North China Plain from 1961 to 2009 were examined. Trends of accumulated temperature and negative temperature, growing season duration, as well as seasonal and annual rainfalls at 48 stations were analyzed. The results show that the accumulated temperature increased significantly by 348.5°C day due to global warming during 1961–2009 while the absolute accumulated negative temperature decreased apparently by 175.3°C day. The start of growing season displayed a significant negative trend of –14.3 days during 1961–2009, but the end of growing season delayed insignificantly by 6.7 days. As a result, the length of growing season increased by 21.0 days. The annual and autumn rainfalls decreased slightly while summer rainfall and summer rainy days decreased significantly. In contrast, spring rainfall increased slightly without significant trends. All the results indicate that the thermal conditions were improved to benefit the crop growth over the North China Plain during 1961–2009, and the decreasing annual and summer rainfalls had no direct negative impact on the crop growth. But the decreasing summer rainfall was likely to influence the water resources in North China, especially the underground water, reservoir water, as well as river runoff, which would have influenced the irrigation of agriculture.

**Key words:** North China Plain, agriculture, climate change

**Citation:** Song Yanling, Zhao Yanxia, and Wang Chunyi, 2011: Changes of accumulated temperature, growing season and precipitation in the North China Plain from 1961 to 2009. *Acta Meteor. Sinica*, **25**(4), 534–543, doi: 10.1007/s13351-011-0412-1.

## 1. Introduction

At present, 40% of the earth's land surface is cropland and pasture (Foley et al., 2005). In developing countries, nearly 70% of people live in rural areas where agriculture is the largest supporter of livelihoods. For China, as a large developing country, the total population reached 13 billion with 73% of them pursuing agriculture, and the cropland was 1.2 billion ha in 2008 (CMA, 2009). About 20% of the global population lives in China supported by only 7% of the world's cultivated land. Although Chinese agriculture has undergone tremendous structural changes over the past decades, the average staple crop productivity has doubled in 25 years while the population increased by 25% (NBSC, 2009). Until now, agriculture is still the most important industry for China since it supplies food for the 13-billion population.

The interannual, monthly, and daily distributions of climate variables (e.g., temperature and precipitation) affect a number of physical, chemical, and biological processes that influence the productivity of agriculture. The latitudinal distribution of crop is affected by the current climatic and atmospheric conditions, as well as the photoperiod (e.g., Leff et al., 2004). The total seasonal precipitation as well as its variability pattern are both of major importance to agriculture (Olessen and Bindi, 2002). Short-term natural extremes such as droughts and floods, interannual

*Supported by the National Science and Technology Support Program of China (2007BAC29B05), China Meteorological Administration Special Public Welfare Research Fund for Meteorological Profession (GYHY200806008 and GYHY201106021).

†Corresponding author: songyl@cma.gov.cn.

©The Chinese Meteorological Society and Springer-Verlag Berlin Heidelberg 2011

and decadal climate variations, as well as large-scale circulation changes, i.e., the El Niño/Southern Oscillation (ENSO), all have important effects on crops. Over the North China Plain, crop growth and productivity are also strongly influenced by weather, especially temperature and precipitation, which determine both phenological development and growth rate of crops (Bauer et al., 1984). In particular, Chinese agriculture is strongly affected by the East Asian monsoon system, which often causes regional and large-scale droughts or low temperature. As a result, the agriculture production fluctuates interannually with varying meteorological conditions.

In addition to interannual variability, regional climate in China is undergoing a change. The average annual temperature in China as a whole has increased by 1.5°C during 1961–2009 (NCC, 2010), while the total precipitation has decreased over the last 50 years (Zhai et al., 1999, Song et al., 2005). It is doubtless that the agriculture meteorological resources are changing greatly due to the climate change. Many studies in China have focused on temperature change (Gao et al., 2001; Hulme et al., 1994; Tao et al., 2004; Xu et al., 2005; Zhao et al., 2003), but relatively few studies have dealt with the change of other agriculture meteorological resources.

In this paper, based on the observed daily meteorological data, the changes of agro-climate resources, including accumulated temperature, absolute accumulated negative temperature in winter, the start, end, as well as length of growing season, and seasonal and annual precipitation, were analyzed in the North China Plain from 1961 to 2009. Particularly, the possible influence of thermal conditions and precipitation on agriculture and irrigation was discussed. Then, some insights for agricultural decision making were provided.

## 2. Material and methods

### *2.1 Study area*

The North China Plain includes Hebei, Beijing, Tianjin, Henan, Shanxi, and Shandong, covers temperate, semi-humid, and monsoon-controlled climatic zones with an annual mean temperature of 10–15°C. Summers are rainy and hot (monthly mean temperatures range from 22 to 28°C), whereas winters are dry and cold (monthly mean temperatures range from –10 to 1°C). The total annual precipitation generally ranges from 400 to 800 mm (CMA, 2000), depending on circulation patterns and topographic features, with only about 90 mm in spring. Furthermore, strong East Asian monsoons often bring colder winters (Tao et al., 2004), while dust storms and droughts occur frequently during springtime.

In the North China Plain, the agriculture production amounts to 1.38 billion ton, 26.2% of the total production in whole China in 2008 (NBSC, 2009). In this region, the winter wheat, maize, cotton, as well as potato can be planted, and the total arable area amounts to 26.5 million hectares, of which 61.3% was irrigated agriculture in 2008 (NBSC, 2009).

### *2.2 Methods*

Using the daily meteorological data provided by the China Meteorological Administration (CMA), accumulated temperature and negative temperature, start and end of growing season, and growing season time-span were calculated. Then, the precipitation affecting agriculture irrigation and crop growth was analyzed (Table 1). Linderholm (2006) supplied 5 definitions of the start and end of the growing season, and we use $T_{\mathrm{mean}} \geqslant 5°\mathrm{C}$ after frost and the first frost in autumn in this paper, which were proved to be suitable in China (Song et al., 2010).

**Table 1.** Definitions of accumulated temperatures and growing season. Ground minimum temperature $\leqslant 0°\mathrm{C}$ is used as a frost criterion

| | Index | Definition |
|---|---|---|
| 1 | Accumulated temperature | $T_{\mathrm{mean}} \geqslant 5°\mathrm{C}$ during January–December |
| 2 | Accumulated negative temperature | $T_{\mathrm{mean}} < 0°\mathrm{C}$ during December–February |
| 3 | Start of growing season | 5 days with $T_{\mathrm{mean}} \geqslant 5°\mathrm{C}$ (after frost) |
| 4 | End of growing season | First autumn frost ($T_{\mathrm{mean}} \leqslant 0°\mathrm{C}$) |
| 5 | Length of growing season | 5 days with $T_{\mathrm{mean}} \geqslant 5°\mathrm{C}$ (after frost)/first autumn frost |

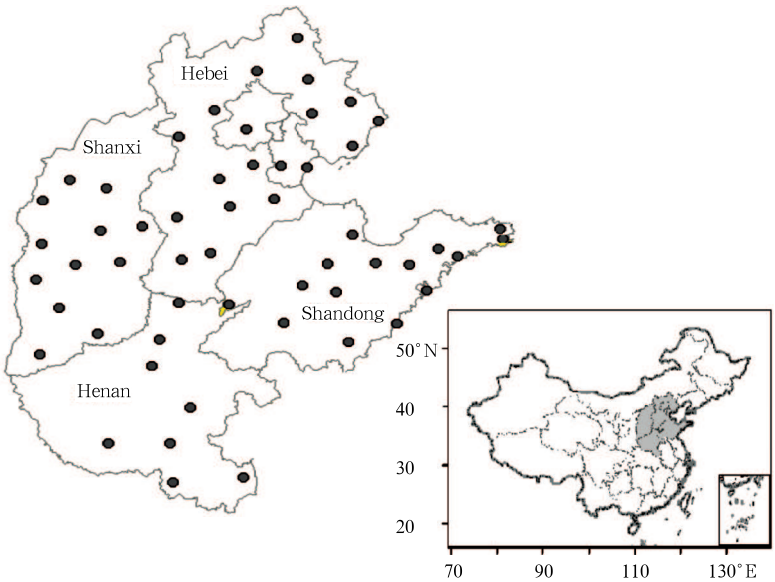


**Fig. 1.** The location of the stations over the North China Plain.

### *2.3 Data*

In order to investigate the change of agro-climate resources, the daily mean temperature, precipitation, and daily ground minimum temperature data provided by the CMA for the period 1961–2009 were used. Only station series covering 49 yr and having a low rate of missing data ($\leqslant$ 5%) were chosen. Special attention was paid to the thermal conditions and precipitation changes. Out of all the 82 stations over the North China Plain, only 48 stations were found to be suitable and were used in the analysis (Fig. 1). The linear trends of accumulated temperature, growing season length, and precipitation were analyzed by using the Mann-Kendall trend test with the 95% significance level (Yue et al., 2002).

## 3. Results

### *3.1 Accumulated temperature*

Accumulated temperature influences plant growth and development. Crops flower and mature until accumulated temperature amounts to a threshold that meets the crop's need. For example, winter wheat and maize are the main crops over the North China Plain; winter wheat matures when the accumulated temperature amounts to 1800–2500 °C day with accumulated negative temperature higher than –400°C day for winter dormancy, while summer maize matures until the accumulated temperature changes between 2500 and 2800 °C day, and spring maize needs 2000–3600 °C day to mature. In the North China Plain, summer maize is usually planted after winter wheat is ripe, so it often cannot mature completely when autumn comes.

In the North China Plain, the mean accumulated temperature was increasing significantly by 348.5°C day due to global warming during 1961–2009 (Fig. 2b). For example, the mean accumulated temperature was 4528.4°C day in the 1960s, 4521.6 and 4568.3°C day for the 1970s and 1980s, respectively, while it amounted to 4702.0°C day in the 1990s, 4796.8°C day during 2001–2009. Furthermore, 43 stations showed significant positive trends, with trend values > 500 °C day at 3 stations. The strongest trend was found in Xingtai, Hebei Province, being 632.6°C day (Fig. 2a). As a result, the winter wheat and summer maize can have more thermal to grow due to increased accumulated temperature.

The agriculture region in the North China Plain encloses temperate, semi-humid, and monsoon-controlled climatic zones. The growth and yields of winter wheat in this region were usually affected by freezing injury in winter. Freezing injury induced by

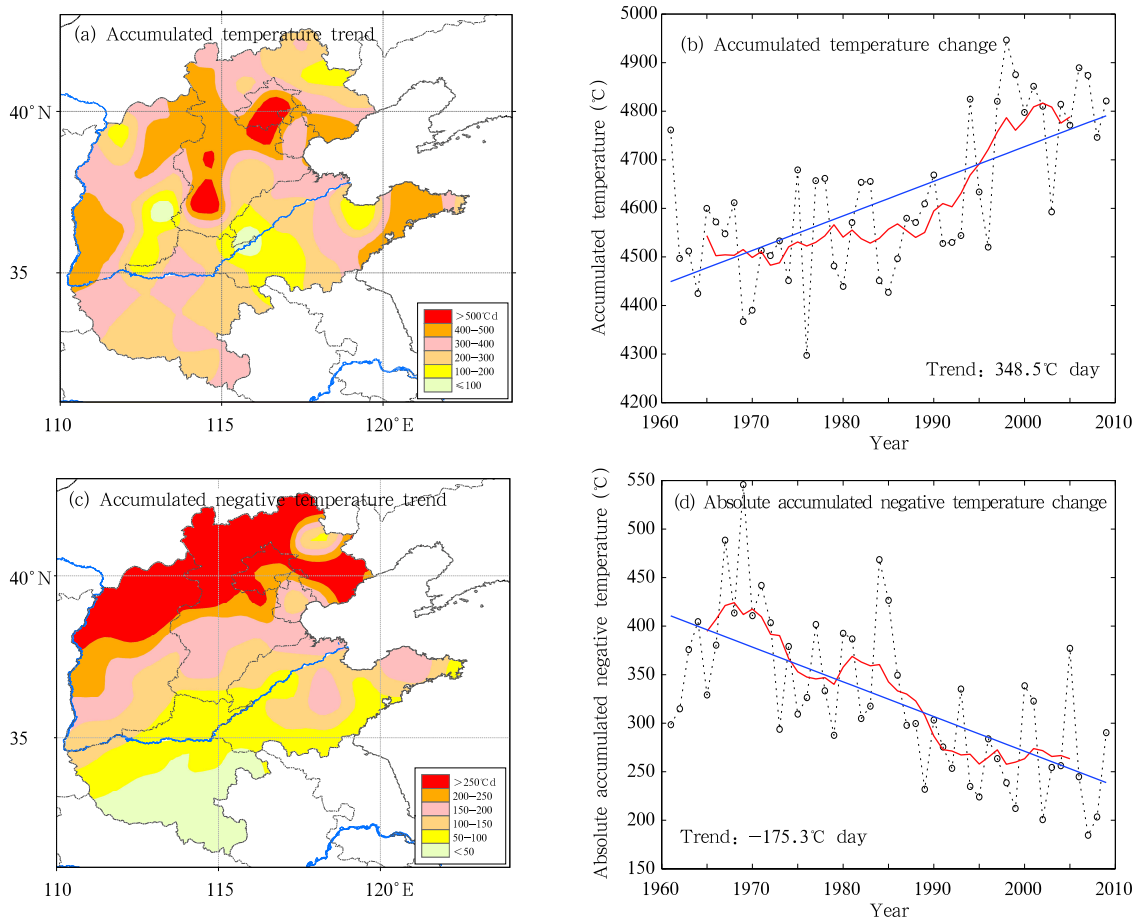


**Fig. 2.** Regional distributions of the trends of accumulated temperature (a) and negative temperature (c), and temporal distributions of accumulated temperature (b) and negative temperature (d) in North China from 1961 to 2009. Dotted lines denote interannual variability, straight lines indicate trend, and curves represent 10-yr moving average.

cold winds from Mongolia often happens in North China. For example, freezing injury persisted in each of the 5 winters during 1949–1953, and the yields of winter wheat decreased by 30% in Beijing. About 30% of the winter wheat was killed due to freezing injury in Hebei in 1980 (Jin, 1996).

Figures 2c and 2d show the features of the accumulated negative temperature in the North China Plain. The absolute value of accumulated negative temperature $\sum(0–t)$ decreased apparently by 175.3°C day (Fig. 2d). It amounted to 259.4 °C day during 2001–2009, which was only 65.5% of that in the 1960s. Furthermore, all the stations showed increasing trends in accumulated negative temperature, with 45 stations having significant trends. As we know, the freezing injury to winter wheat is induced by low temperature. It may be alleviated partly if absolute accumulated negative temperature is decreased. Song et al. (2006) found that the damage to winter wheat caused by freezing injury had been thus alleviated, based on simulations by a crop model. Jin (1996) also pointed out that the freezing injury had been alleviated in winter over the North China Plain.

### *3.2 Thermal growing season*

In this study, we utilize the same growing season (GS) indices as those used by Walther and Linderholm (2006) for the Greater Baltic Area, northern Europe, to calculate the trends in start, end, and length of the GS in China. In general, a $T_{\mathrm{mean}}$ threshold is used to identify a certain number of consecutive days in order to determine the start/end of the GS. The GS start

is defined as the date when the ensuing 5-day running mean $T_{\text{mean}} \geqslant 5°\text{C}$ after the last frost, and the GS end is defined as the first frost day. Here, ground minimum temperature $\leqslant 0°\text{C}$ was used as a frost criterion. After computing the particular start and end, GS length was then calculated as the number of days between these two dates.

To understand the temporal and spatial distributions of the GS in North China, average start, end, and length of GS were calculated for the 1971–2000 reference period using the above indices. The results (Table 2) show that GS starts on the 70th–90th Julian day on average (around March) in most parts of North China, and averagely GS ends on the 290th–305th Julian day (around October). The GS length was found to be about 210–240 days for most parts of North China.

Significant trends ranging from –22.7 to –7.0 days in the start of the GS during 1961–2009 appeared at 33 stations out of 48 stations (figure omitted). The largest significant trend was found in Jinan, Shandong Province, with a linear trend of –22.2 days over the study period. Twenty-three stations showed trends exceeding two weeks. Furthermore, 15 stations displayed negative and insignificant trends of an earlier start of the GS. No stations showed positive trends of delayed GS. Averagely, the start of GS displayed significant negative trends by –14.3 days during 1961–2009.

During 1961–2009, significant positive trends in GS end were only found at 3 of the 48 stations in the North China Plain, ranging from +6.9 to +11.4 days (figure omitted). Insignificant positive trends were found at 17 stations, with values less than +6.7 days. Insignificant negative trends were found at 25 stations. Overall, the end of GS delayed in significantly by 6.7 days.

As seen in Fig. 3a, significant positive trends of 20–27.3 days in the length of GS in 1961–2009 were found at 21 stations (43.8% of the 48 stations). Twenty-four stations showed insignificant positive trends of less than 20 days. Over the North China Plain as a whole, the mean GS length increased by 21.0 days on average (Fig. 3b). The largest significant trend in GS length occurred in Wuzai, Shanxi Province with an increase of 27.3 days. These results were in agreement with earlier findings of extended GS length elsewhere during the 20th century for most of the Northern Hemisphere (Penuelas et al., 2002; Frich et al., 2002; Parmesan and Yohe, 2003; Root et al., 2003; Menzel, 2003; IPCC, 2007).

### *3.3 Precipitation change*

In the North China Plain, droughts often occurred on the regional scale and seriously influenced winter wheat and maize yields. The annual precipitation in this region is about 580 mm while the spring precipitation is only 90 mm, 16% of the total. In spring,

**Table 2.** Changes of accumulated temperatures, growing season, and precipitation in North China from 1961 to 2009.

| | 1960s | 1970s | 1980s | 1990s | 2001–2009 | Trends during 1961–2009 |
|---|---|---|---|---|---|---|
| Accumulated temperature (°C day) | 4528.4 | 4521.6 | 4568.3 | 4702.0 | 4796.8 | **348.5** |
| Absolute value of accumulated negative temperature (°C day) | 396.2 | 356.9 | 338.6 | 266.0 | 259.4 | **–175.3** |
| Start of growing season (Julian day) | 79.9 | 78.7 | 76.9 | 72.9 | 66.2 | **–14.3** |
| End of growing season (Julian day) | 294.6 | 294.1 | 296.1 | 295.9 | 301.9 | 6.7 |
| Lengh of growing season (day) | 214.7 | 215.4 | 219.2 | 223.0 | 235.0 | **21.0** |
| Annual precipitation (mm) | 626.8 | 593.3 | 587.2 | 576.3 | 594.4 | –39.2 |
| Precipitation in spring (mm) | 92.6 | 81.8 | 96.0 | 95.0 | 99.2 | 17.0 |
| Precipitation in summer (mm) | 400.0 | 390.2 | 358.9 | 355.0 | 356.7 | –59.7 |
| | | | | | | **–70.8(1962–2006)** |
| Precipitation in autumn (mm) | 126.9 | 111.8 | 110.4 | 107.0 | 112.7 | –19.3 |
| Annual precipitation days | 73.7 | 71.0 | 78.6 | 73.7 | 76.5 | 3.7 |
| Precipitation days in spring | 16.7 | 15.2 | 18.2 | 17.1 | 16.8 | 1.2 |
| Precipitation days in summer | 35.8 | 35.4 | 33.2 | 31.9 | 32.2 | **–5.3** |
| Precipitation days in autumn | 18.8 | 17.5 | 18.0 | 17.2 | 17.0 | –2.5 |

Bold figures indicate significant trends with $p < 0.05$

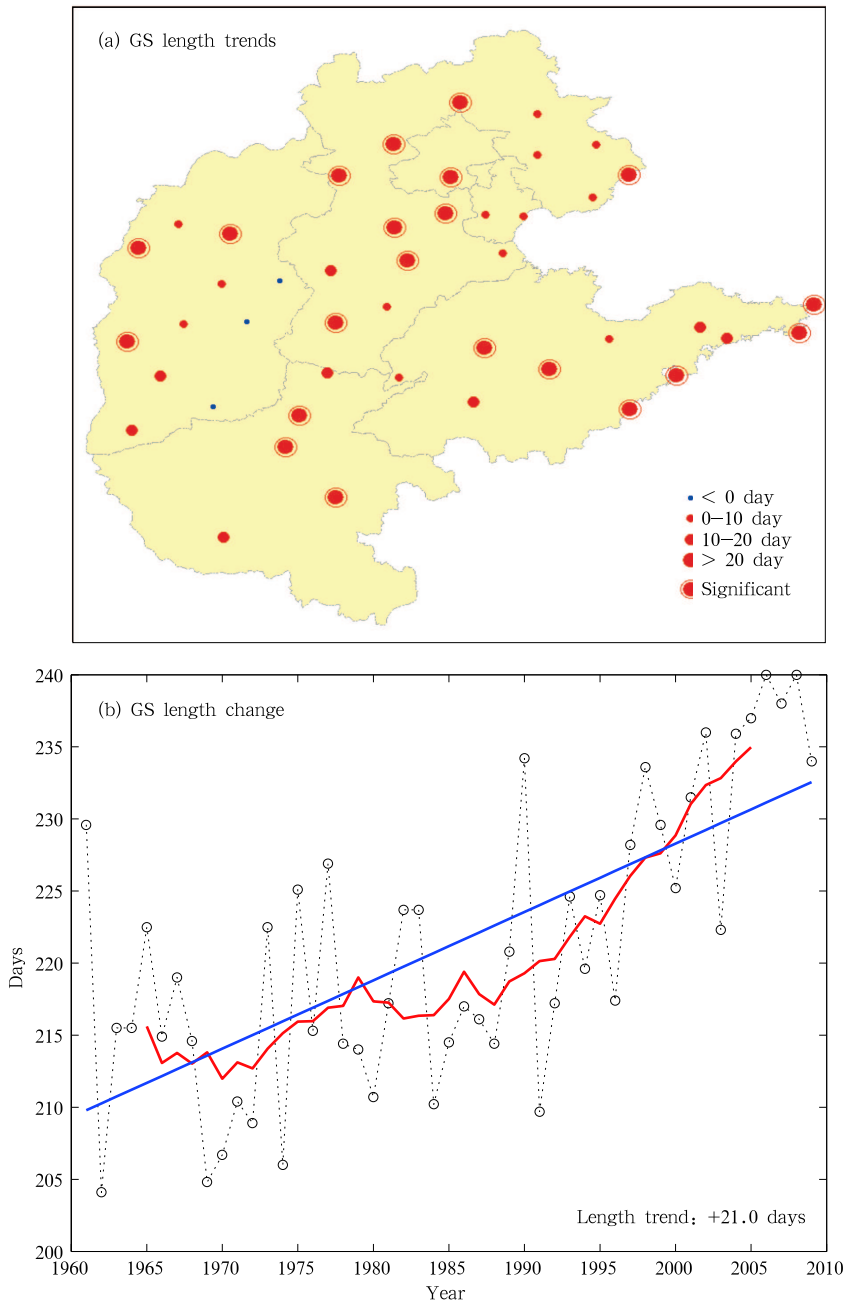


**Fig. 3.** (a) Regional distribution of trends of GS length, and (b) change of GS length over North China from 1961 to 2009. In (a), the dot with an outside circle denotes a trend value at the 95% significance level. In (b), dotted lines indicate interannual variability, straight lines denote trend, and curves represent 10-yr moving average.

winter wheat was tasseling, flowering, and filling, needing more water for maturity than other crops, and maize as well as potato began to grow. The droughts often happened due to less precipitation in spring, and the yields of winter wheat as well as the growth of spring maize and potato were often influenced strongly. Therefore, it was necessary to study the changes of precipitation in the North China Plain.

Figure 4 and Table 2 show the precipitation changes in North China during 1961–2009. It is seen that the annual precipitation was 585.6 mm in the normal years during 1971–2000, and it decreased slightly

by 39.2 mm with no significant trends. For example, the annual precipitation was 626.8 mm in the 1960s, and it decreased continuously in the 1970s, 1980s, and 1990s, being 593.3, 587.2 and 576.3 mm, respectively. In spring, the normal-year precipitation of this season was only 90.4 mm, which often induced droughts in the North China Plain. Table 2 shows that the spring rainfall increased by 17.0 mm during 1961–2009. Although the trend was not significant, the rainy days also increased slightly. This was a good trend which can have positive influences on the growth of crops. The normal summer rainfall was 368.0 mm, about 63% of the annual rainfall. The results indicate that summer rainfall decreased insignificantly by 59.7 mm during 1961–2009, with a significant decreasing trend of 70.8 mm during 1962–2006. Furthermore, summer

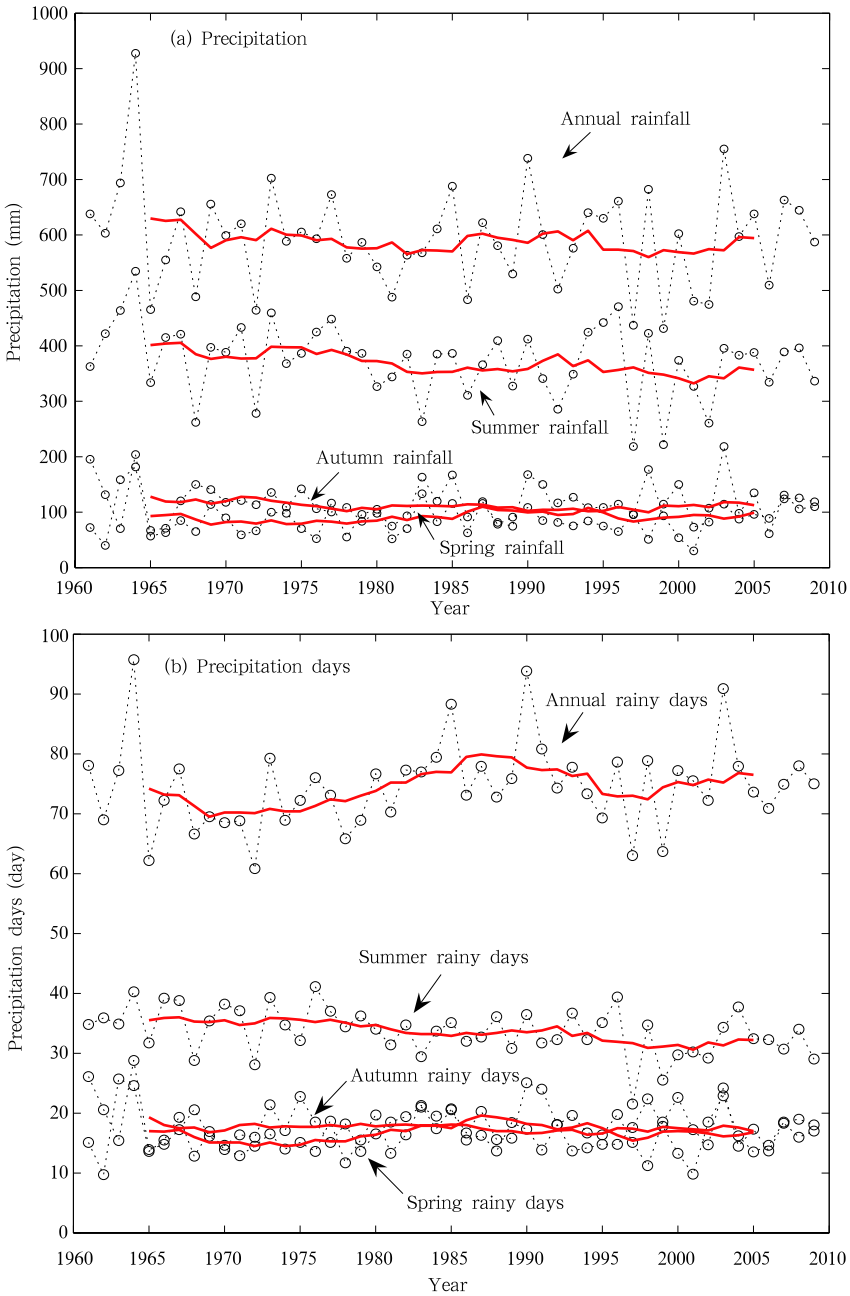


**Fig. 4.** Changes of precipitation and precipitation days for spring, summer, autumn, and annual total in North China during 1961–2009. Dotted lines indicate interannual variability and solid lines represent 10-yr moving average.

rainy days also decreased significantly by 5.3 days from 1961 to 2009. In summer, the winter wheat becomes mature, and spring maize, summer maize as well as potato are growing; they need about 200–300-mm precipitation to grow well. Thus, the decreasing summer rainfall generally can still support the growth of crops in the North China Plain. As a result, the decreasing summer rainfall had no direct negative impact on the growth of crops. The normal autumn precipitation was 109.7 mm, and it also decreased slightly.

As a whole, the annual and autumn rainfalls decreased slightly and the summer rainfall as well as the summer rainy days decreased significantly, but they can still support the crop growth in the North China Plain. Furthermore, the spring precipitation increased slightly, but with no significant trends. These results indicate that the changes of precipitation had no apparent negative impacts on crop growth over North China. This is in agreement with Song et al. (2005), who pointed out that the winter wheat production was not influenced apparently by the decreasing precipitation, based on the simulation by a crop model.

## 4. Conclusions and discussion

Over the North China Plain, the crop growth and productivity were strongly influenced by weather, especially temperature and precipitation. Therefore, this study examined the change of these agriculture meteorological resources in this region and provided insights for future agricultural decision making.

The results show that the accumulated temperature was increasing significantly by 348.5°C day due to global warming during 1961–2009, and it amounted to 4796.8 °C day during 2001–2009 over the North China Plain. At the same time, the absolute value of accumulated negative temperature was decreasing apparently by 175.3 °C day during 1961–2009, and it amounted to 259.4 °C during 2001–2009, only 65.5% of that in the 1960s. For the thermal growing season, the start of growing season displayed significant negative trends by –14.3 days during 1961–2009, and the end of growing season delayed insignificantly by 6.7 days. As a result, the length of growing season increased significantly by 21.0 days from 1961 to 2009.

The above results indicate that the thermal condition was improved to benefit the crop growth over the North China Plain during 1961–2009. Provided that an extension of the growing season is accompanied by increased temperatures, such an increase in the length of growing season may advance the potential crop production at high latitudes and promote the potential number of harvests and hence seasonal yields for perennial forage crops (Berner et al., 2004). In the 1960s and 1970s, in Shandong, Hebei, Shanxi, and Henan provinces, summer maize was planted after maturity of winter wheat, and it often could not mature fully when the first frost came. In the 1980s and 1990s, the accumulated temperature and growing season length increased. As a result, the summer maize had more thermal and time to grow, so the production of summer maize increased. Furthermore, the damage to winter wheat induced by freezing injury also happened in the 1960s and 1970s. Now, the absolute value of accumulated negative temperature decreased, so the freezing damage to winter wheat was alleviated.

The annual and autumn rainfalls decreased slightly and the summer rainfall as well as the summer rainy days decreased significantly, but they can still support the crop growth in the North China Plain. Furthermore, spring precipitation increased slightly, although with no significant trends. These results indicate that the changes of precipitation generally had no negative impacts on crop growth.

However, decreasing summer precipitation influenced strongly the water resources in North China. Because the runoff of rivers and water of reservoirs originate mainly from summer rainfall. For example, the water areas of Miyun and Huairou reservoirs, the largest reservoirs of Beijing (NCC, 2008), increased by about 10% because of more summer rainall in 2008. Contrarily, the runoff of rivers and water of reservoirs can be impacted negatively by decreased summer rainfall. During 1951–2000, about 40% of the rivers in length of 10000 km or more had been changed to be seasonal rivers in the North China Plain, and the average annual inflow to the Pacific Ocean decreased by 80% compared with that in 1950. Compared with the

1950s, the wetland decreased from 10000 to 1000 km$^2$, which was just 10% of that in the 1950s (Jia et al., 2002). Liu et al. (2001) pointed out that the average groundwater level dropped from 7.23 m in 1983 to 11.52 m in 1993 with a declining rate of 0.43 m yr$^{-1}$, based on surface observations from 600 shallow groundwater wells.

These studies indicated that the water resources decreased partly because of the decreasing summer rainfall. As a result, the irrigation of agriculture would be influenced. As we know, 61.3% of the total arable land needs to be irrigated over the North China Plain, and the water for irrigation mainly comes from rivers, reservoirs, as well as underground water in this region. Furthermore, the decreasing level of groundwater will also cause some ecological problems. Thus, this study on the changes of the agriculture meteorological resouces in the North China Plain is of practical significance.

## REFERENCES


Bauer, A., C. Fanning, J. W. Enz, and C. V. Eberlein, 1984: Use of growing degree-days to determine spring wheat growth stages. *North Dakota State Univ. Agricultural Extension Bulletin*, EB-37.

Berner, J., T. V. Callaghan, H. Huntington, et al., 2004: *Impacts of a Warming Arctic: Arctic Climate Impact Assessment*. Cambridge University Press, 1020 pp.

CMA (China Meteorological Administration), 2000: *Atlas of China*. Sinomaps Press, 251 pp. (in Chinese)

CMA (China Ministry of Agriculture), 2009: *China Agriculture Yearbook 2009*. China Agriculture Publishing House, 619 pp. (in Chinese)

Foley, J., R. DeFries, G. Asner, et al., 2005: Global consequences of land use. *Science*, **309**, 570–574.

Frich, P., L. Alexander, P. Della-Marta, et al., 2002: Observed coherent changes in climatic extremes during the second half of the twentieth century. *Climate Res.*, **19**, 193–212.

Gao, Xuejie, Zhao Zongci, and Ding Yihui, 2001: Climate change due to greenhouse effects in China as simulated by a regional climate model. *Adv. Atmos. Sci.*, **18**(6), 1224–1230.

Hulme, M, Z. Zhao, and T. Jiang, 1994: Recent and future climate change in East Asia. *Int. J. Climatol.*, **14**, 637–658.

IPCC (Intergovernmental Panel on Climate Change), 2007: *Climate Change: Impacts, Adaptation and Vulnerability*. Contribution of Working Group II to the Fourth Assessment Report of the Intergovernmental Panel on Climate Change. Cambridge University Press, Cambridge, UK, 976 pp.

Jia, J., J. Yu, and C. Liu, 2002: Groundwater regime and calculation of yield response in North China Plain: A case study of Luancheng County in Hebei Province. *J. Geogr. Sci.*, **12**(2), 217–225.

Jin Shanbao, 1996: *Winter Wheat in China*. China Agriculture Publishing House, Beijing, 766–768. (in Chinese)

Leff, B., N. Ramankutty, and J. Foley, 2004: Geographic distribution of major crops across the world. *Global Biogeochem. Cy.*, **18**, GB1009.

Linderholm, H., 2006: Growing season changes in the last century. *Agricultural and Forest Meteorology*. **137**, 1–14.

Liu, C., J. Yu, and K. Eloise, 2001: Groundwater exploitation and its impact on the environment in the North China Plain. *Water International*, **26**(2), 265–272.

Menzel, A., 2003: Phenological anomalies in Germany and their relation to air temperature and NAO. *Climatic Change*, **57**, 243–263.

NBSC (National Bureau of Statistics of China), 2009: *China Statistical Yearbook-2009*. China Statistics Press, 780 pp. (in Chinese)

NCC (National Climate Center), 2008: *China Climate Impact Assessment*. China Meteorological Press, 140 pp. (in Chinese)

NCC (National Climate Center), 2010: The Bulletin of the Influence of Climate Change on Agriculture in China, National Climate Center, 34 pp. (in Chinese)

Olesen, J., and M. Bindi, 2002: Consequences of climate change for European agriculture productivity, land use and policy. *Eur. J. Agron.*, **16**, 239–262.

Parmesan, C., and G. Yohe, 2003: A globally coherent fingerprint of climate impacts across natural systems. *Nature*, **421**, 37–42.

Penuelas, J., I. Filella, and P. Comas, 2002: Changed plant and animal life cycles from 1952 to 2000 in the Mediterranean region. *Global Change Biology*, **8**, 531–544.

Root, T., J. Price, K. Hall, et al., 2003: Fingerprints of global warming on wild animals and plants. *Nature*, **421**, 57–60.

Song, Y., E. Simelton, D. Chen, and W. Dong, 2005: Influence of climate change on winter wheat in North China during 1950–2000. *Acta Meteor. Sinica*, **19**(4), 501–510.

——, D. Chen, and W. Dong, 2006: Influence of climate on winter wheat productivity in different climate regions of China, 1961–2000. *Climate Res.*, **32**, 219–227.

——, H. Linderholm, D. Chen, and A. Walther, 2010: Trends of the thermal growing season in China during 1951–2007. *Int. J. Climatol.*, **30**, 33–43.

Tao, F., Z. Yokozawa, Y. Zhang, et al., 2004: Variability in climatology and agricultural production in China in association with the East Asian summer monsoon and El Niño/Southern Oscillation. *Climate Res.*, **28**, 23–30.

Walther, A., and H. W. Linderholm, 2006: A comparison of growing season indices for the Greater Baltic Area. *Int. J. Biometeorology*, **51**, 107–118, doi: 10.1007/s00484-006-0048-5.

Xu, Ying., Zhao Zongci, Luo Yong et al., 2005: Climate change projections for the 21st century by the NCC/IAP T63 model with SRES scenarios. *Acta Meteor. Sinica*, **19**(4), 407–417.

Yue, S., P. Pilon, and G. Cavadias, 2002: Power of the Mann-Kendall and Spearman's rho tests for detecting monotonic trends in hydrological series. *J. Hydrology*, **259**, 254–271.

Zhai Panmao, Ren Fumin, and Zhang Qiang, 1999: Detection of trends in China's precipitation extremes. *Acta Meteor. Sinica*, **57**(2), 208–216. (in Chinese)

Zhao, Z., Akimasa Sumi, and Chikako Harada, 2003: Projections of extreme temperature over East Asia for the 21st century as simulated by the CCSR/NIES2 couple model. *Proceeding of International Symposium on Climate Change*. WMO and CMA, Eds., China Meteorological Press, Beijing, 158–164.

孙朝阳，邵全琴，刘纪远，等. 2011. 城市扩展影响下的气象观测和气温变化特征分析 [J]. 气候与环境研究，16 (3)：337－346. Sun Chaoyang, Shao Quanqin, Liu Jiyuan, et al. 2011. Characteristics of air temperature change affected by urban expansion in China [J]. Climatic and Environmental Research (in Chinese), 16 (3): 337－346.

# 城市扩展影响下的气象观测和气温变化特征分析

孙朝阳[1,2,3] 邵全琴[1] 刘纪远[1] 匡文慧[1]

1 中国科学院地理科学与资源研究所，北京 100101
2 中国科学院研究生院，北京 100049
3 国家气候中心，北京 100081

**摘 要** 基于20世纪70年代的MSS (Multi-Spectral Scanner) 影像、1990年前后的TM (Thematic Mapper) 影像、2000年和2005年前后的ETM (Enhanced Thematic Mapper) 影像，对全国700多个地面气象观测站的历史时期下垫面属性进行判别，得到中国自上世纪70年代以来“进城”的气象站点，并通过电话咨询验证，最终确定“进城”且周边探测环境明显改变、气象观测受到城市化影响的站点。在此基础上，对中国各气象站点气温观测值的年际和季节变化进行了分析，通过“进城”站点和全部站点的气温变化趋势的比较，得出“进城”站点的气温变化率高于全国气象站点的平均变化率，从而验证了基于遥感影像的气象站点判别的有效性，并得出“进城”气象站点的气温观测数据在城市环境的影响下比其它站点增长的更多的结论。

**关键词** 城市扩展 气象站点“进城” 遥感判别 气温变化特征分析
**文章编号** 1006－9585 (2011) 03－0337－10 **中图分类号** P412.11 **文献标识码** A

# Characteristics of Air Temperature Change Affected by Urban Expansion in China

SUN Chaoyang[1,2,3], SHAO Quanqin[1], LIU Jiyuan[1], and KUANG Wenhui[1]

1 *Institute of Geographic Sciences and Natural Resources Research, Chinese Academy of Sciences, Beijing* 100101
2 *Graduate University of Chinese Academy of Sciences, Beijing* 100049
3 *National Climate Center, Beijing* 100081

**Abstract** The underlying surface of more than 700 national meteorological stations in different historical periods is distinguished based on the MSS (Multi-Spectral Scanner) images of the 1970s, TM (Thematic Mapper) images around 1990, and ETM (Enhanced Thematic Mapper) images around 2000 and 2005. The stations with apparent changes in their underlying surface and surrounding building environment are picked out and verified by telephone consultation. Based on the discriminant result, annual and seasonal change characteristics of air temperature are analyzed, and it is concluded that the change rate at air temperature of the stations "entering city" is higher than that at the other stations. The result validates the discriminant method based on RS (Remote Sensing) images, and con-

**收稿日期** 2009－07－13收到，2011－02－27收到修定稿
**资助项目** 国家科技支撑计划项目2006BAC08B00，国家重点基础研究发展规划项目2009CB421105，中国科学院知识创新工程重要方向项目KZCX2-YW-305-3，中国－瑞典国际合作项目2006-24724-44416-13
**作者简介** 孙朝阳，男，博士，工程师，研究方向为城市遥感和GIS。E-mail：sunchaoy@cma.gov.cn
**通讯作者** 邵全琴，E-mail：shaoqq@lreis.ac.cn



万方数据

forms that the observed air temperature at the stations "entering city" increase more than the other stations affected by the urban circumstance.

**Key words** urban expansion, meteorological stations "entering city", remote sensing discriminant, characteristic analysis of air temperature change

# 1 引言

地面气象观测数据长期以来广泛应用于生产、生活和科学研究各个领域，除了气象和气候研究以外，还在遥感参数反演的地面验证、生态模型驱动、生态环境评估等研究中扮演着重要的角色（赵天保等，2004；杨虎和杨忠东，2006；徐新良等，2007；朱怀松等，2007）。地面气象观测数据的准确性直接影响了这些研究的开展和可信度，而地面气象观测非常容易受到下垫面环境状态改变等因素的影响。因此，研究气象站点下垫面环境的历史变迁及其对地面气象观测的干扰具有重要的意义（He et al.，2007）。

中国自1951年以来在全国各地共建设了700多个基本、基准气象观测站，到2008年总数已增加至756个。在这期间，许多台站发生过业务改变、台站迁移等，有的已经撤站取消，有的是新建站点，2008年尚在业务运行的有727个（李庆祥和李伟，2007）。

中国气象局（2003）在其先后颁布的《地面气象观测规范》中规定，气象站点在选址时必须符合观测技术上的要求，应设在能较好地反映本地较大范围气象要素特点的地方，避免局部地形的影响。但是，中国自实行改革开放政策以来，整个社会经济高速发展，特别是城市建设和城市化进程日益加快，20世纪70年代末以后，气象站点逐步经历了被动"进城"的过程。特别是东部沿海和经济发展较快的地区，原本处于郊区或城市边缘的气象站点逐渐被高大密集的建筑包围起来，从而影响了气象站点的观测环境，使得观测数据逐渐失去区域上的代表性。观测环境的破坏严重影响到气象数据的代表性和连续性，从而影响到气象数据服务本身以及其它科学研究，带来不同程度的误差甚至是错误（Kalnay and Cai，2003；任慧龙等，2004；Li et al.，2004）。

世界气象组织对气象数据收集的一个最基本技术要求是气象站的站址要基本固定，只有站址固定，气象数据才能进行历史对比、分析，得出的气象信息才符合准确性、连续性、可比性和代表性的要求。然而，中国的气象站点在经历被动"进城"以后，一方面受到城市化带来的各种环境效应的干扰，另一方面，气象站也面临着被迫搬家的局面。这两种情况都会给气象观测的连续性带来一定程度的影响。

本研究以中国的基本、基准气象站点为对象，采用遥感影像的人工判读方式，对气象站点自上世纪70年代以来下垫面的变化情况进行全面的调查和研究。在此基础上，分析对比"进城"和未"进城"站点的气温变化特征，以此来揭示气象站点"进城"对气象观测的影响。

# 2 气象站点下垫面判别

## 2.1 数据

### 2.1.1 遥感影像

本研究收集到20世纪70年代末的MSS（Multi-Spectral Scanner）影像、1990年前后的TM（Thematic Mapper）影像、2000年和2005年前后的ETM（Enhanced Thematic Mapper）影像，一部分数据来自中国科学院资源环境数据中心，一部分是通过美国马里兰大学提供的镜像下载得到。影像数据覆盖了全国气象站点，是判别气象站点下垫面属性的主要依据。

### 2.1.2 中国地面气候资料

本研究采用的气温数据是由中国气象局提供的中国地面气候资料日值数据集中全国756个气象站点1951～2007年的逐日气温数据。该数据集还提供了各气象站点的地理位置、观测起始年份以及缺测情况等信息。

该数据经过了严格的质量控制和检查，统计结果经过极值检验和时间一致性检验人工抽查，确保数据无误。

本研究在对气温变化特征进行分析时，选取



万方数据

了 1978～2007 年有完整记录的 608 个气象站点的数据，从而保证了所采用数据的完整性，并对个别出现异常观测值的站点进行了剔除。

## 2.2 方法

根据中国气象局提供的全国气象站点的地理坐标，首先对气象站点进行了空间化和投影变换，使用 GIS 空间位置查询方法查找出气象站点所在的遥感影像图幅编号（图 1）。本研究中所获取的遥感影像都已进行了理论和人工校正，并且在以往的研究中得到了很好的验证（王思远和刘纪远，2001；刘纪远等，2003，2008；高志强和刘纪远，2006），气象站点的空间分布数据与遥感影像的匹配度比较高。

通过人工判读的方式，对全国 700 多个气象站点在 20 世纪 70 年代末、1990 年、2000 年和 2005 年几个时期的下垫面属性进行判别。

如图 2 所示，首先以 2000 年这一期的遥感影像判别为起点。在判别的过程中，首先排除明显不在城市附近的气象站点，将其确定为未“进城”站点，将明显进入城市区域的站点确定为“进城”站点，位于城市边缘的站点则暂时定为不确定站点，将根据该站点的年平均气温变化曲线图和电话咨询的结果进一步确定。

对于未“进城”和不确定的气象站点，需要进一步应用 2005 年遥感影像来判别，而已“进城”气象站点则需要继续用 1990 年遥感影像来判别，以进一步明确其“进城”时期。以此类推，最终得到 4 类判别结果：2000 年以后“进城”站点、20 世纪 90 年代“进城”站点、80 年代“进城”站点、70 年代“进城”站点和不能确定的站点。

图 3 和图 4 是各时期“进城”站点的示例，从影像截图上可以清晰地看到城市边界的扩张和气象站点被动“进城”的过程，同样它们的年平均气温变化曲线也反映了在相应的“进城”时期年平均气温有明显的增长趋势。图 3 中，银川站的年平均气温在 1998 年以后基本上保持在 10 ℃以上，而之前的年平均气温均在 10 ℃以下，与其周边的非城市站点陶乐相比，气温变化趋势基本一致，但是在 2003 年以后银川的年平均气温开始上升，而陶乐保持稳定；图 4 中的廊坊站的年平

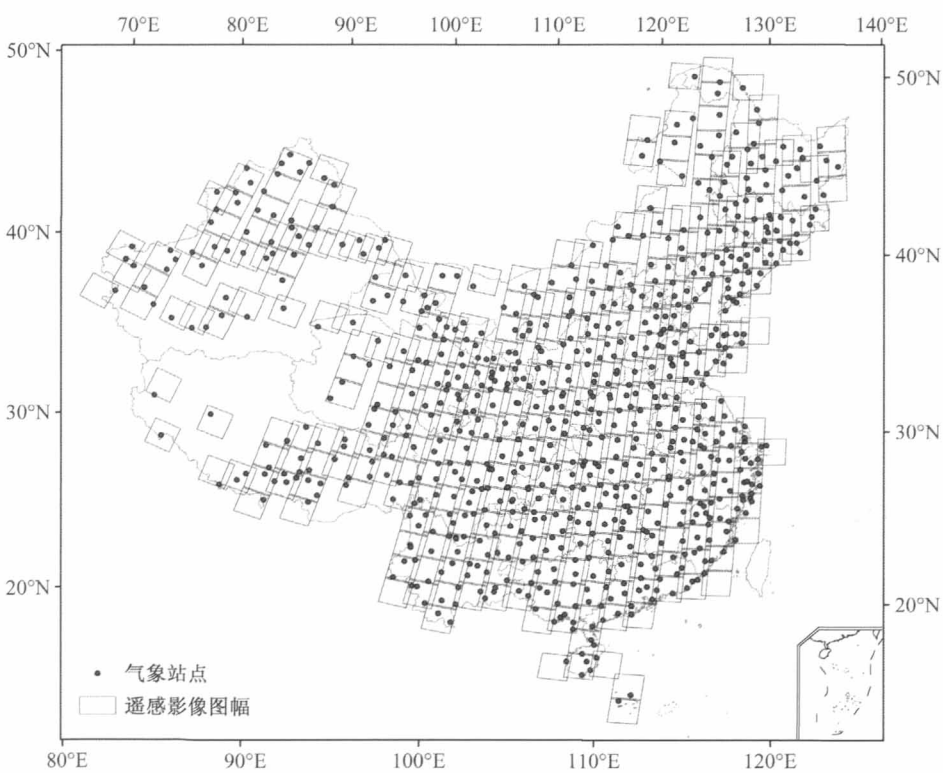


图 1　全国气象站点及其所在遥感影像图幅分布

Fig. 1　The distribution of meteorological stations and the RS (Remote Sensing) images



万方数据

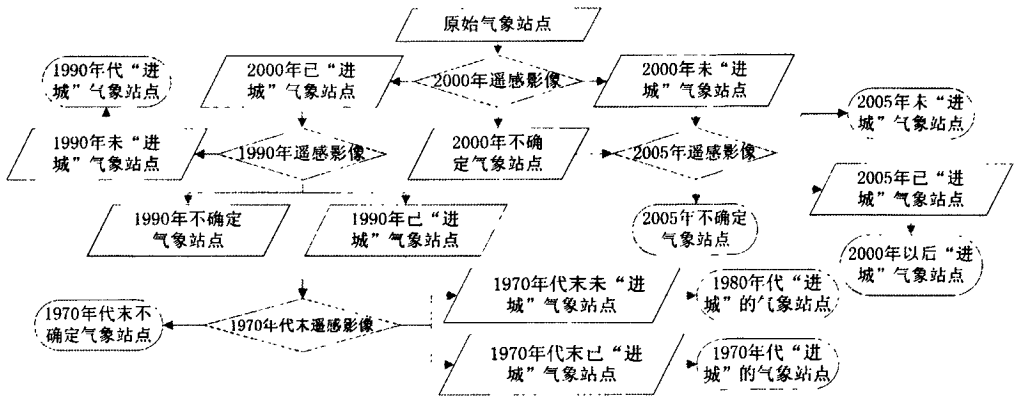


图2 基于遥感影像判别"进城"站点的流程

Fig. 2 Flow chart of distinguishing the stations based on RS images

均气温在1992年后有了明显上升，而天津站则保持缓慢增长上下波动。

对以上的判别结果，均需要进行电话咨询，以验证站点是否"进城"并确定其具体的"进城"和受影响的时期。针对是否进城（进城时间）、是否受影响和是否搬迁（搬迁时间）这几个问题，对影像判别的结果进行了进一步的验证和修正。

通过电话咨询，发现主要存在以下几种情况：(1) 站点确实已经被城市"包围"，观测明显受到影响，已经选定新的站址，着手搬迁；(2) 站点确实已经被城市"包围"，观测明显受到影响，但是还没有明确的搬迁计划；(3) 站点虽然已经"进城"，但是采取了一定的保护性措施，周边环境尚未对观测造成很大影响；(4) 站点目前并未"进城"，但是城市化的趋势必然会很快波及观测场周围；(5) 站点未"进城"，未来的城市建设会遵守相关保护法规，受影响的可能性不大。结合之前的影像判别结果，最终得出了各个时期"进城"站点的数目（表1）。

**表1 气象站点"进城"判别结果分类统计**

**Table 1 Statistics of the consultation result by telephone**

| | 进城站点总数 | 受影响站点数 |
|---|---|---|
| 20世纪70年代 | 37 | 3 |
| 20世纪80年代 | 40 | 19 |
| 20世纪90年代 | 51 | 26 |
| 2000年后 | 18 | 16 |
| 总计 | 146 | 64 |

### 2.3 判别结果

截止到目前，进城站点总数为146，占全部站点近20%。20世纪70年代末，进城站点只有37个，其中有3个站点已经被城区包围，且明显会受到周边建筑及其可能带来的城市热岛效应的影响；80年代进城站点的总数达到77个，受影响的站点增加到22个；90年代进城站点总数为128个，受影响站点增加至48个；2000年以后受影响的站点增加到64个。

如图5，进入20世纪80年代以后，"进城"和受到城市影响的站点都显著增加。通过电话咨询验证了解到，多数站点已经开始计划搬迁新址，有些站点正在着手搬迁，并且在新老观测位置上同时进行对比观测。在调查中也了解到近年来全国气象部门对气象站点的搬迁做了统一的规划和部署，最近几年已经成功搬迁了部分站点。同时，《气象法》和《气象探测环境和设施保护法》的颁布和有力执行，使得近年来各地政府部门在进行城市规划和建设时，充分考虑到对气象台站周边环境的保护，因此，2000年以后"进城"的气象站点数开始减少。但是，城市扩张和城市化的进程会随着社会经济的快速发展而加剧，气象站点被动"进城"这一现象仍是一个必须关注和解决的严峻问题。

## 3 "进城"气象站点的气温变化特征分析

全球和区域上的气候变化是当前的研究热点，气温变化是气候变化研究中的一项重要指标和内容。当气象站点被动"进城"以后，必然会受到



万方数据

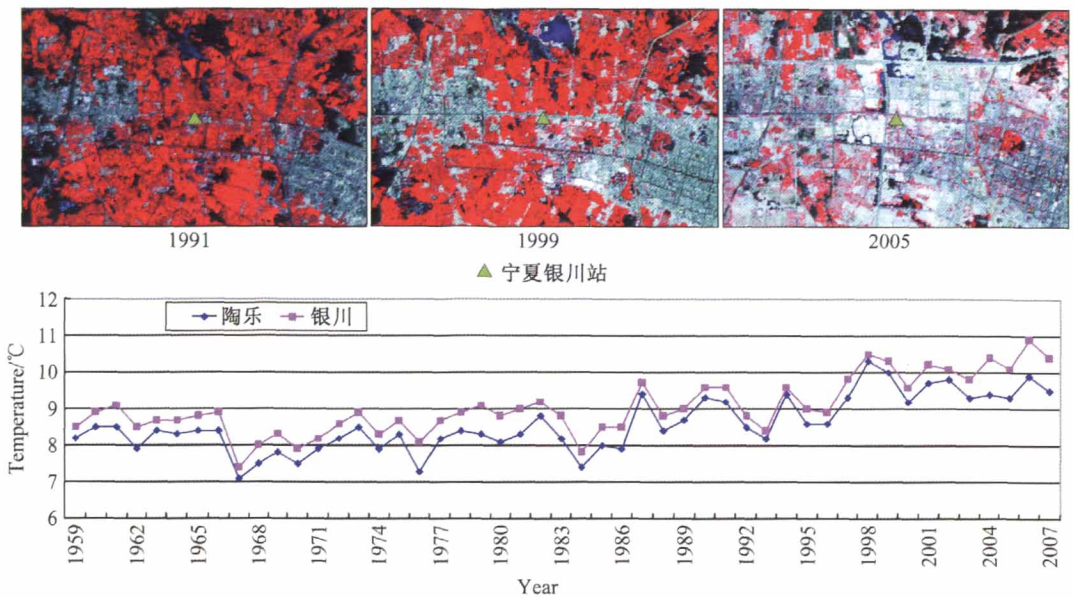


图 3　宁夏银川站进城前（1991、1999 年）后（2005 年）的卫星图像（上图）及其与周边未进城站点（陶乐站）的年平均气温变化趋势对比（下图）

Fig. 3　The satellite images of Yinchuan station, Ningxia before (1991, 1999) and after (2005) "entering city" (up) and it's annual average air temperature trend compared with that of the non-urban station (Taole) near it (bottom)

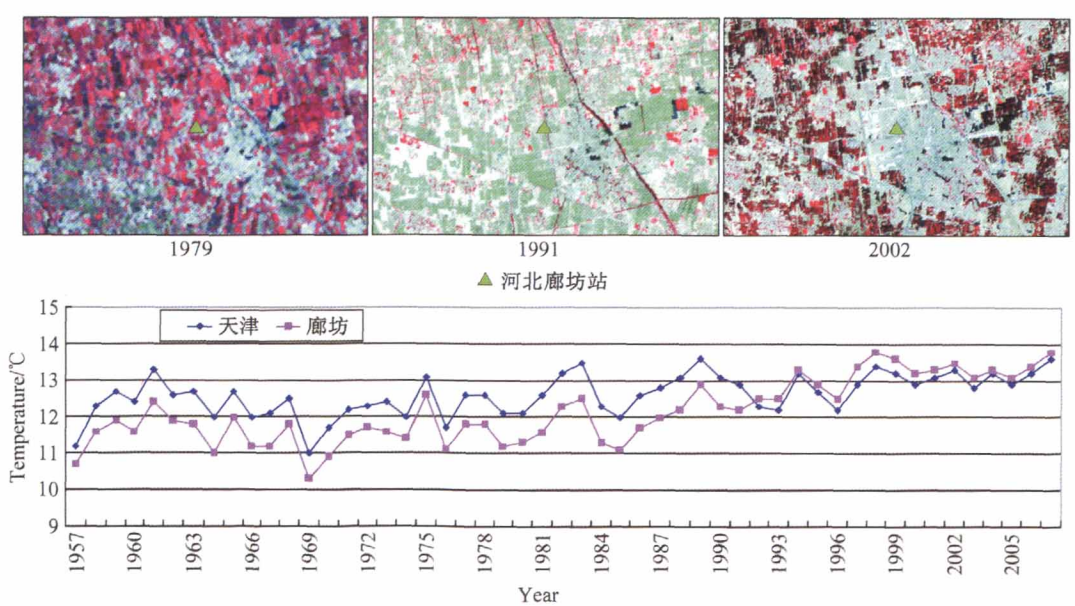


图 4　河北廊坊站进城前（1979 年）后（1991、2002 年）的卫星图像（上图）及其与周边未进城站点（天津站）的年平均气温变化趋势对比（下图）

Fig. 4　The satellite images of Langfang station, Hebei before (1979) and after (1991, 2002) "entering city" (up) and it's annual average air temperature trend compared with that of the non-urban station (Tianjin) near it (bottom)

城市建筑和周边环境的影响，特别是城市热岛效应对气温的影响尤其显著，对气温数据的观测会产生很大的扰动（Balling et al.，1990）。

### 3.1　年平均气温特征分析

本研究计算了气象站点的年平均气温、年平均最高气温、年平均最低气温和年平均温差的线



万方数据

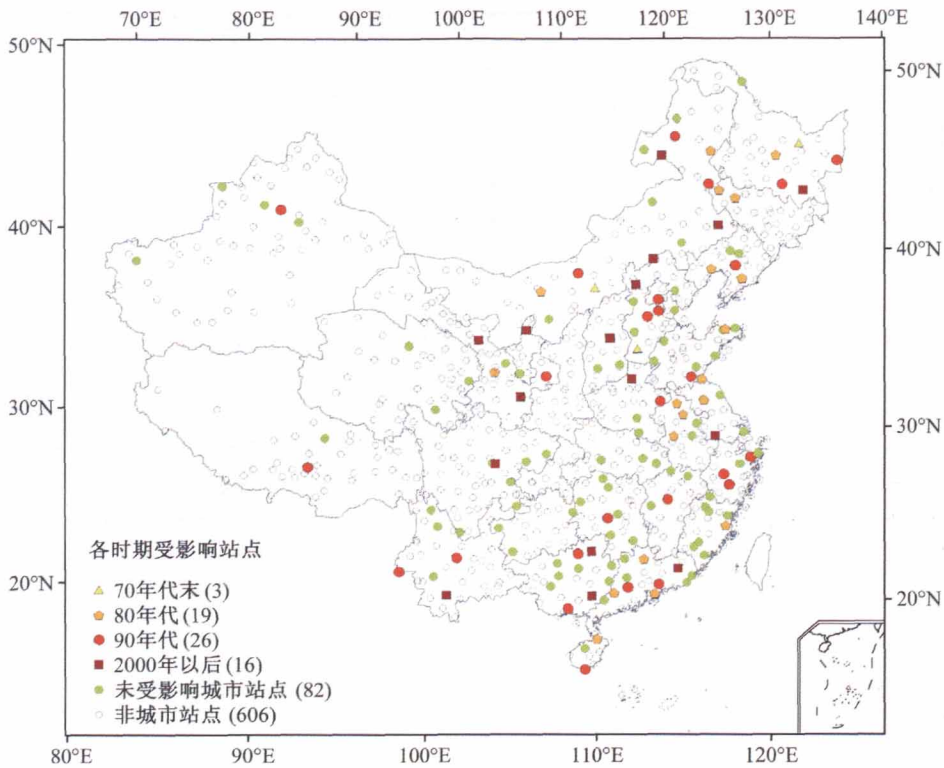


图5 20世纪70年代以来各时期"进城"和受城市影响的站点

Fig. 5 The stations "entering city" and affected by city since the 1970s

性倾斜率，从"进城"气象站点与未"进城"的站点的对比中可以发现："进城"且受城市化影响的站点的气温变化趋势更加明显。

从表2中可以看出，全部站点的年平均气温呈上升趋势，这与国内外学者关于全球变暖这一认识是一致的（曾昭美等，2003；任国玉等，2005a，2005b），其中最高气温的增长幅度略低于最低气温的增长，因此平均温差一直在缩小。从全部站点、未受影响的"进城"站点和受影响的"进城"站点三者的统计值的对比可以得出：未受影响的"进城"站点的气温变化趋势与全部站点的平均值基本持平，而受影响的"进城"站点的气温变化则明显高于平均水平。从而证明气象站点"进城"的确对气温观测产生了明显的影响，也同时表明基于遥感影像和电话咨询验证进行气象站点"进城"的判别是有效的。

**表2 气象站点年平均气温线性变化趋势**

**Table 2 The linear trend of annual average air temperature**

℃·(10 a)$^{-1}$

| | 年平均气温 | 年平均最高气温 | 年平均最低气温 | 年平均温差 |
|---|---|---|---|---|
| 全部站点 | 0.444 | 0.429 | 0.501 | −0.072 |
| 未受影响的"进城"站点 | 0.457 | 0.432 | 0.513 | −0.081 |
| 受影响的"进城"站点 | 0.544 | 0.448 | 0.660 | −0.212 |

### 3.2 季节平均气温特征分析

年平均气温只能粗略反映各个气象站点及其所代表的周边区域气温的总体变化趋势，气温的年内变化，则可以通过分析季节平均数据来得出（Aesawy and Hasanean，1998）。

本研究结合中国的季节分布特点，将上一年度12月和当年的1月、2月定义为冬季，随后是春季（3～5月）、夏季（6～8月）和秋季（9～11月）。针对各季节的平均气温、平均最高气温、平均最低气温和平均温差，进行了与年平均数据相同的分析。

从表3的统计结果可以得出，气温变化在季节上的差异比较明显。总体上来说春季最为显著，夏季的变化最小。这与周连童和黄荣辉（2003）、任国玉等（2005a）和康丽华等（2006，2009）等研究结果基本上是一致的。受影响的"进城"站点的季节平均气温的变化仍然高于未受影响的"进



万方数据

表 3　气象站点季节平均气温线性变化趋势

Table 3　The linear trend of seasonal average air temperature　　℃ · (10 a)$^{-1}$

| | 平均气温 | | | | 平均最高气温 | | | | 平均最低气温 | | | | 平均温差 | | | |
|---|---|---|---|---|---|---|---|---|---|---|---|---|---|---|---|---|
| | 冬季 | 春季 | 夏季 | 秋季 | 冬季 | 春季 | 夏季 | 秋季 | 冬季 | 春季 | 夏季 | 秋季 | 冬季 | 春季 | 夏季 | 秋季 |
| 全部站点 | 0.493 | 0.498 | 0.300 | 0.433 | 0.435 | 0.508 | 0.294 | 0.442 | 0.571 | 0.534 | 0.362 | 0.470 | −0.136 | −0.027 | −0.068 | −0.028 |
| 未受影响的“进城”站点 | 0.471 | 0.566 | 0.272 | 0.455 | 0.381 | 0.617 | 0.241 | 0.441 | 0.558 | 0.562 | 0.349 | 0.494 | −0.177 | 0.055 | −0.108 | −0.053 |
| 受影响的“进城”站点 | 0.617 | 0.592 | 0.367 | 0.545 | 0.443 | 0.528 | 0.331 | 0.450 | 0.766 | 0.710 | 0.441 | 0.630 | −0.323 | −0.182 | −0.111 | −0.179 |

城”站点和全部站点的平均值。气温在季节上的变化趋势跟年平均气温的变化基本上是一致的。但是，秋冬季节受影响的“进城”站点的气温变化比其它站点更为显著，而春夏季节的差异略小。

### 3.3　典型站点的对比分析

在前面的研究中，对年平均气温和季节平均气温的线性变化趋势的分析中已经清楚地对比出“进城”和未“进城”站点之间的差异。但是考虑到全国站点的地域分布较广，南北和东西的气候差异显著，平均值只能反映气温变化的相对高低。因此，在全国的各个气候分区内选取了部分“进城”站点和离该站点最近的 2 个站点，对它们最近 30 年的年平均气温和变化趋势进行直接的对比。

从全国的气象站点所覆盖的气候分区中选择中温带干旱区、高原温带亚干旱区、中温带湿润区、暖温带亚湿润区、北亚热带湿润区、中亚热带湿润区、南亚热带湿润区、边缘热带湿润区这 8 个主要分区，分别挑选 1 组站点。其中包括 1 个受影响的“进城”站点和离此站点最近的 2 个未受影响站点，优先选择 1 个未受影响的“进城”站点和 1 个非城市站点。

图 6 中的 8 组站点的对比均表现出同样的特征，受影响的“进城”站点的气温变化倾斜率高于未受影响的站点。但是在不同气候区，气象站点的气温变化率的绝对值有着明显差异。在中温带干旱区和边缘热带湿润区，年平均气温变化较为平缓，“进城”站点比其它站点略高，气温变化趋势非常接近；而北亚热带湿润区的站点均呈现较高的增温趋势。

## 4　讨论和结论

### 4.1　讨论

以往的研究通常忽视了气象站点的“进城”现象，或将这些受干扰的站点数据生硬地去掉，这都会使区域气温评价产生偏差。因此，如何保留和修正这些受干扰站点的数据，使其不仅能继续代表城市的气温特点，又能反映周边一定区域的气温特点，是一项值得探索的有意义的研究。

从本文的研究结果来看，经历过“进城”的站点约占总数近 20%，可见城市化对地面气象观测的影响不可小视。如果不排除或者剔除城市化对气温数据的高估作用，对中国近几十年的气温升高进行评估时，必然会造成一定程度的高估。因此，这种由城市化带来的区域气温高估作用有待进一步深入的研究。

另外，气象站点“进城”发生的时期不同，其受影响的程度和过程也不尽相同，不同地区、不同城市类型、不同城市化发展模式下都可能造成不同的结果。深入研究这一问题，有助于人们今后在进行城市规划时解决如何保护气象观测场所周边的探测环境和如何保证气象观测的连续性和稳定性这类问题。

总之，气象站点被动“进城”的现象应该得到国家相关部门的高度重视，特别是在气象观测和城市建设两方面如何协调这一点上，必须尽快制定出合理有效的对策。为保证我国气象事业以及其它相关研究的稳定发展和进步，加强站点的保护，积极应对已经出现的问题是十分重要的。

### 4.2　结论

最近 30 年来，气象站点被动“进城”的现象确实存在，并且显著影响了“进城”站点的气象观测数据。气象站点周边探测环境的变化不仅干扰了站点的观测数据本身，对整个国家的气象观测工作造成了一定程度的混乱，也对区域气候研究产生了不可低估的影响。

“进城”气象站点的年平均气温变化率明显高于全国气象站点的平均水平，当将这些观测数据



万方数据

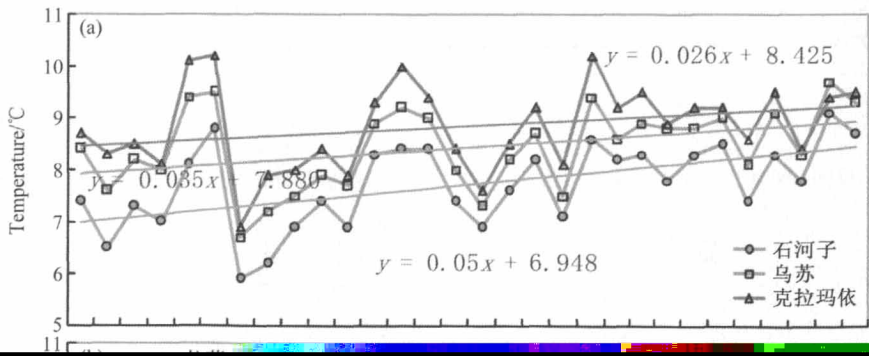
(a)
Temperature/°C
y = 0.026x + 8.425
y = 0.035x + 7.880
y = 0.05x + 6.948
石河子
乌苏
克拉玛依



万方数据

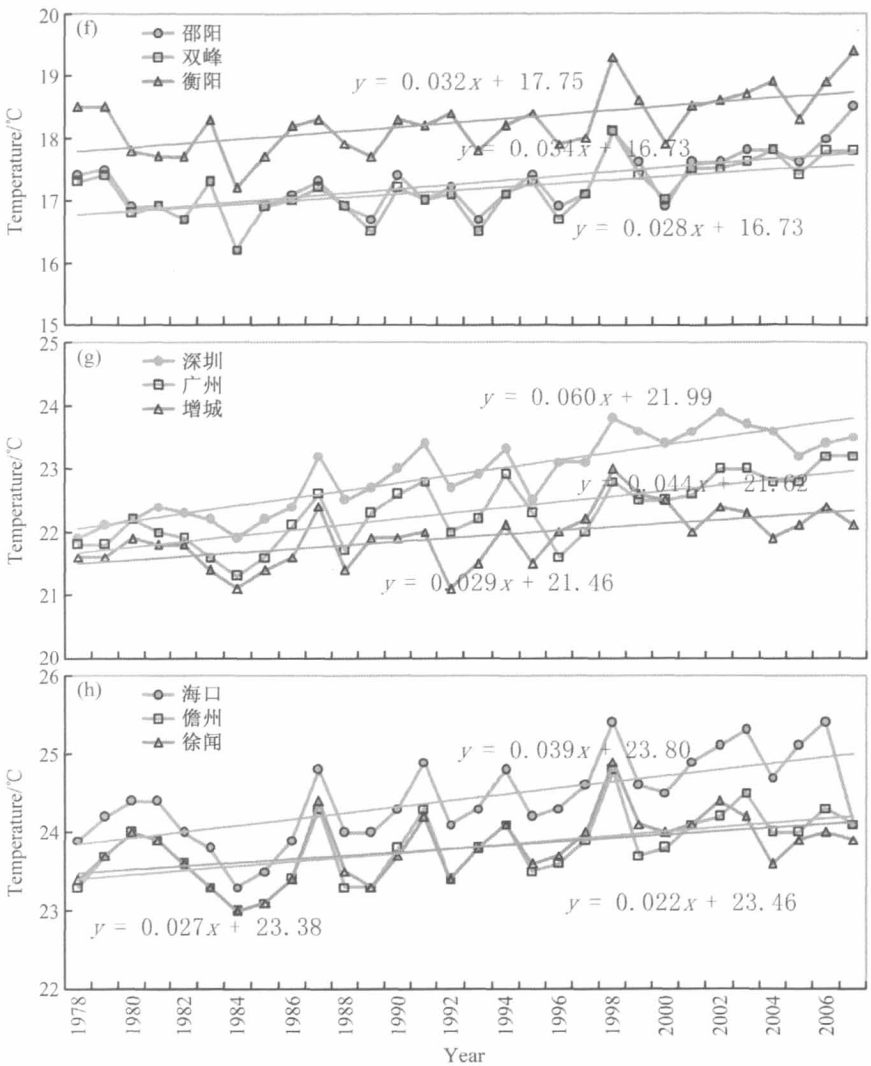


图 6　不同气候区“进城”站点和非城市站点年平均气温变化趋势对比：(a) 中温带干旱区（石河子、乌苏、克拉玛依）；(b) 高原温带亚干旱区（拉萨、泽当、尼木）；(c) 中温带湿润区（鞍山、沈阳、本溪）；(d) 暖温带亚湿润区（太原、阳泉、榆社）；(e) 北亚热带湿润区（溧阳、常州、吴县东山）；(f) 中亚热带湿润区（邵阳、双峰、衡阳）；(g) 南亚热带湿润区（深圳、广州、增城）；(h) 边缘热带湿润区（海口、儋州、徐闻）

Fig. 6　Comparison of annual average air temperature trend in different climate zones: (a) Middle warm temperate and arid zone (Shihezi, Wusu, Kelamayi); (b) plateau warm temperate and semi-arid zone (Lasa, Zedang, Nimu); (c) middle warm temperate and humid zone (Anshan, Shenyang, Benxi); (d) warm temperate and semi-humid zone (Taiyuan, Yangquan, Yushe); (e) north subtropical and humid zone (Liyang, Changzhou, Dongshan); (f) middle subtropical and humid zone (Shaoyang, Shuangfeng, Hengyang); (g) South subtropical and humid zone (Shenzhen, Guangzhou, Zengcheng); (h) marginal tropical and humid zone (Haikou, Danzhou, Xuwen)

应用到区域上的研究时，周边区域的气温必然会被“高估”，从而不仅失去了区域上的代表性，也会对长时间序列历史气温变化趋势分析造成不可忽视的干扰。

气象站点的气温变化率与其所在的地理位置即气候分区有着一定的联系，但是本研究还未进行更深入的研究，尚不能定论。

## 参考文献 (References)

Aesawy A M, Hasanean H M. 1998. Annual and seasonal climatic analysis of surface air temperature variations at six southern Mediterranean stations [J]. Thero. Appl. Climatol., 61: 55 - 68.

Balling R C, Skindlov J A, Phillips D H, et al. 1990. The impact of increasing summer mean temperatures on extreme maximum



万方数据

and minimum temperatures in Phoenix, Arizona [J]. J. Climate, 3: 1491 - 1494.

He J, Liu J, Zhuang D, et al. 2007. Assessing the effect of land use/land cover change on the change of urban heat island intensity [J]. Theor. Appl. Climatol., 90: 217 - 226.

Kalnay E, Cai M. 2003. Impact of urbanization and land-use change on climate [J]. Nature, 423: 528 - 531.

Li Q, Zhang H, Liu X, et al. 2004. Urban heat island effect on annual mean temperature during the last 50 years in China [J]. Theor. Appl. Climatol., 79: 165 - 174.

高志强，刘纪远. 2006. 1980～2000年中国LUCC对气候变化的响应 [J]. 地理学报，61 (8): 865 - 872. Gao Zhiqiang, Liu Jiyuan. 2006. The LUCC responses to climatic changes in China from 1980 to 2000 [J]. Acta Geographica Sinica (in Chinese), 61 (8): 865 - 872.

康丽华，陈文，魏科. 2006. 我国冬季气温年代际变化及其与大气环流异常变化的关系 [J]. 气候与环境研究，11 (3): 330 - 339. Kang Lihua, Chen Wen, Wei Ke. 2006. The interdecadal variation of winter temperature in China and its relation to the anomalies in atmospheric general circulation [J]. Climatic and Environmental Research (in Chinese), 11 (3): 330 - 339.

康丽华，陈文，王林，等. 2009. 我国冬季气温的年际变化及其与大气环流和海温异常的关系 [J]. 气候与环境研究，14 (1): 45 - 53. Kang Lihua, Chen Wen, Wang Lin, et al. 2009. Interannual variations of winter temperature in China and their relationship with the atmospheric circulation and sea surface temperature [J]. Climatic and Environmental Research (in Chinese), 14 (1): 45 - 53.

李庆祥，李伟. 2007. 近半个世纪中国区域历史气温网格数据集的建立 [J]. 气象学报，65 (2): 293 - 300. Li Qingxiang, Li Wei. 2007. Construction of the gridded historical temperature dataset over China during the recent half century [J]. Acta Meteorologica Sinica (in Chinese), 65 (2): 293 - 300.

刘纪远，张增祥，庄大方，等. 2003. 20世纪90年代中国土地利用变化时空特征及其成因分析 [J]. 地理研究，22 (1): 1 - 12. Liu Jiyuan, Zhang Zengxiang, Zhuang Dafang, et al. 2003. A study on the spatial-temporal dynamic changes of land-use and driving forces analyses of China in the 1990s [J]. Geographical Research (in Chinese), 22 (1): 1 - 12.

刘纪远，徐新良，邵全琴. 2008. 近30年来青海三江源地区草地退化的时空特征 [J]. 地理学报，63 (4): 364 - 376. Liu Jiyuan, Xu Xinliang, Shao Quanqin. 2008. The spatial and temporal characteristics of grassland degradation in the three-river headwaters region in Qinghai province [J]. Acta Geographica Sinica (in Chinese), 63 (4): 364 - 376.

任国玉，初子莹，周雅清，等. 2005a. 中国气温变化研究最新进展 [J]. 气候与环境研究，10 (4): 701 - 716. Ren Guoyu, Chu Ziying, Zhou Yaqing, et al. 2005a. Recent progresses in studies of regional temperature changes in China [J]. Climatic and Environmental Research (in Chinese), 10 (4): 701 - 716.

任国玉，徐铭志，初子莹，等. 2005b. 近54年中国地面气温变化 [J]. 气候与环境研究，10 (4): 717 - 727. Ren Guoyu, Xu Mingzhi, Chu Ziying, et al. 2005b. Changes of surface air temperature in China during 1951 - 2004 [J]. Climatic and Environmental Research (in Chinese), 10 (4): 717 - 727.

任慧龙，谷富生，张雪梅. 2004. 浅析地面气象数据的质量控制 [J]. 山西气象，2004 (3): 45 - 46. Ren Huilong, Gu Fusheng, Zhang Xuemei. 2004. Brief analysis of quality control of ground meteorological data [J]. Shanxi Meteorological Quarterly (in Chinese), (3): 45 - 46.

王思远，刘纪远. 2001. 中国土地利用时空特征分析 [J]. 地理学报，56 (6): 631 - 639. Wang Siyuan, Liu Jiyuan. 2001. Analysis on spatial-temporal features of land use in China [J]. Acta Geographica Sinica (in Chinese), 56 (6): 631 - 639.

徐新良，刘纪远，曹明奎，等. 2007. 近期气候波动与LUCC过程对东北农田生产潜力的影响 [J]. 地理科学，27 (3): 318 - 324. Xu Xinliang, Liu Jiyuan, Cao Mingkui, et al. 2007. Impact of recent climate fluctuation and LUCC process on potential for crops in northeast China [J]. Scientia Geographica Sinica (in Chinese), 27 (3): 318 - 324.

杨虎，杨忠东. 2006. 中国陆地区域陆表温度业务化遥感反演算法及产品运行系统 [J]. 遥感学报，10 (4): 600 - 607. Yang Hu, Yang Zhongdong. 2006. A modified land surface temperature split window retrieval algorithm and its application over China [J]. Journal of Remote Sensing (in Chinese), 10 (4): 600 - 607.

曾昭美，严中伟，叶笃正. 2003. 20世纪两次全球增暖事件的比较 [J]. 气候与环境研究，8 (3): 319 - 330. Zeng Zhaomei, Yan Zhongwei, Ye Duzheng. 2003. Two global warming events in the 20th century [J]. Climatic and Environmental Research (in Chinese), 8 (3): 319 - 330.

赵天保，艾丽坤，冯锦明. 2004. NCEP再分析资料和中国站点观测资料的分析与比较 [J]. 气候与环境研究，9 (2): 278 - 293. Zhao Tianbao, Ai Likun, Feng Jinming. 2004. An Intercomparison between NCEP reanalysis and observed data over China [J]. Climatic and Environmental Research (in Chinese), 9 (2): 278 - 293.

中国气象局. 2003. 地面气象观测规范 [M]. 北京：气象出版社，5 - 8. China Meteorological Administration. 2003. Criterion of Ground Meteorological Observation [M]. Beijing: China Meteorological Press, 5 - 8.

周连童，黄荣辉. 2003. 关于我国夏季气候年代际变化特征及其可能成因的研究 [J]. 气候与环境研究，8 (3): 274 - 290. Zhou Liantong, Huang Ronghui. 2003. Research on the characteristics of international variability of summer climate in China and its possible cause [J]. Climatic and Environmental Research (in Chinese), 8 (3): 274 - 290.

朱怀松，刘晓锰，裴欢. 2007. 热红外遥感反演地表温度研究现状 [J]. 干旱气象，25 (2): 17 - 21. Zhu Huaisong, Liu Xiaomeng, Pei Huan. 2007. Summary on retrieval land surface temperature using thermal infrared remote sensing [J]. Arid Meteorology (in Chinese), 25 (2): 17 - 21.



万方数据

孙冷. 2010年西北太平洋热带气旋活动特征及成因的初步分析[J]. 气象,2011,37(8):929-935.

# 2010年西北太平洋热带气旋活动特征及成因的初步分析*

孙 冷

国家气候中心,北京 100081

**提 要:** 文章用热带气旋资料和NCAR/NCEP再分析资料等,对2010年西北太平洋和南海热带气旋活动特征进行分析,总结有五方面的特点:(1)编号最少,登陆比例最高;(2)生成时间集中,生成位置偏西;(3)强台风和短生命期热带气旋比例偏高;(4)初台偏晚,终台偏晚;(5)登陆前少后多,登陆地点相对集中。另外,还对热带气旋活动特征的成因进行了初步研究。结果表明:(1)东印度洋持续偏暖是导致编号热带气旋异常偏少的重要原因;厄尔尼诺事件的滞后影响也是重要外强迫因素之一。(2)大气环流异常是造成热带气旋活动异常的直接原因,表现在副热带高压偏强偏西,季风槽位置异常偏西,垂直风切变偏大等几方面因素的综合影响。

**关键词:** 热带气旋,活动特征,成因分析,大气环流

# Analysis of Features and Causation for Tropical Cyclone Activities over the Western North Pacific in 2010

SUN Leng

National Climate Centre, Beijing 100081

**Abstract:** Characteristics and causation for tropical cyclone (TC) activities over the Western North Pacific (WNP) and the South China Sea (SCS) in 2010 were analyzed by using the data of TCs, reanalysis data of NCEP/NCAR in this paper. TC activities are characterized by (1) forming the least, and the highest percentages of landing, (2) concentrated and westward genesis, (3) higher proportion of strong TCs and short life cycle TCs, (4) the later for the first TC and last TC, and (5) TC landing fewer in July—August and more than normal in September, 5 of 7 TCs landing on Fujian. The causes were studied and the results were listed as follows. Firstly, the warm mode in the East Indian Ocean in 2010 was one of the key extra forcing factors resulting in the least TC genesis in WNP and SCS in 2010, especially the lag response of extratropical atmosphere to El Nino. Secondly, the atmospheric circulation abnormity was the key reasons. It showed the combined impacts of multi-factors including the larger and stronger Northwest Pacific subtropical high extending abnormally west, the abnormally westward monsoon trough and large vertical shear anomalies.

**Key words:** tropical cyclones (TCs), features, causation analysis, atmospheric circulation

* 公益性行业(气象)科研专项(HX-GYHY200806009)和科技部科技支撑项目(2009BAC51B02)共同资助
2011年3月3日收稿; 2011年5月31日收修定稿
作者:孙冷,主要从事极端气候事件监测与成因分析研究. Email:sunleng@cma.gov.cn



© 1994-2011 China Academic Journal Electronic Publishing House. All rights reserved. http://www.cnki.net

## 引 言

热带气旋(以下简记为TC)是影响我国的主要气象灾害之一,在其活动过程中,常伴随有狂风、暴雨、巨浪和风暴潮,对我国沿海地区的人畜造成生命威胁,使财产和经济遭受严重损失。但带来破坏性的同时,TC带来的降水也能缓解旱情,减轻高温热浪天气的影响。如1002号台风康森导致海南省90.5万人受灾,2人死亡,直接经济损失1.3亿元,但其带来的降水对缓和海南等地前期的旱情和解除华南前期持续了半个月之久的高温天气十分有利。随着科技水平的提高,关于TC的研究越来越受到关注,在其发生、发展和影响机理方面,前人已经做了很多工作[1-7]。

西北太平洋和南海是全球TC发生频数最多、分布范围最广的海域,其TC的活动特征、影响利弊和成因分析是气象工作者一直都十分关注且持续不断研究的问题。概括说来,前人的一些研究工作较多集中于某个因素异常对TC产生的影响,也有很多是从气候学的角度,考查大尺度环流及大气遥相关对TC生成频数和生成位置的月、季、年或年际变化的影响。研究成果表明,厄尔尼诺与南方涛动(ENSO)、对流活动、季风槽、副热带高压、垂直风切变、热带大气季节内振荡(MJO)等海温和大气环流因子都对TC活动存在影响[8-14];但其中对某些问题还存在分歧,特别是对多个因素同时出现异常,各个因素所起作用的研究涉及不多,这方面仍然需要更多深入细致的探索。

2010年西北太平洋和南海生成的TC活动特征显著,本文在总结分析其活动特点的基础上,主要着重从气候背景和年代际变化,热力(海洋)和动力(副热带高压、季风、垂直风切变)等多个因素综合影响的角度,试图揭示其活动特征的可能成因,为进一步做好TC的监测预测工作提供参考。

## 1 资料与方法

文中使用了1949—2010年TC资料,其中1949—2009年TC资料取自中国气象局编写的《热带气旋年鉴》,2010年TC资料取自中国气象局中央气象台提供的2010年西北太平洋和南海热带气旋纪要表和热带气旋路径资料,TC等级使用2006年开始实行的国家标准。文中所统计的西北太平洋和南海TC包括日界线以西、赤道以北范围内生成的TC(中心附近最大风力≥8级,即17.2 m·s$^{-1}$)。为了分析大尺度环境对热带气旋的影响,本文还使用了由美国气象环境预报中心(NCEP)和美国国家大气研究中心(NCAR)联合制作的空间分辨率为2.5°×2.5°的NCEP/NCAR再分析数据集中月平均风场和位势高度场的再分析资料;美国国家海洋大气局(NOAA)公布的空间分辨率为2°×2°的月平均表层海温资料(NOAA Extended Reconstructed SST V2)。副热带高压强度和副热带高压西伸脊点指数采用国家气候中心定义的西北太平洋副热带高压活动指数。文中提及的TC资料常年值和大尺度物理量异常所使用的气候态为30年(1971—2000年)资料平均值。

## 2 2010年西北太平洋和南海TC活动特征

### 2.1 编号最少,登陆比例最高

2010年,在西北太平洋和我国南海海域总共有14个编号TC,与1998年频数相同,均为历史编号最少年,较常年偏少13个;有7个TC登陆我国,登陆个数同常年,但登陆个数与编号个数的比例为历史最高(图1)。

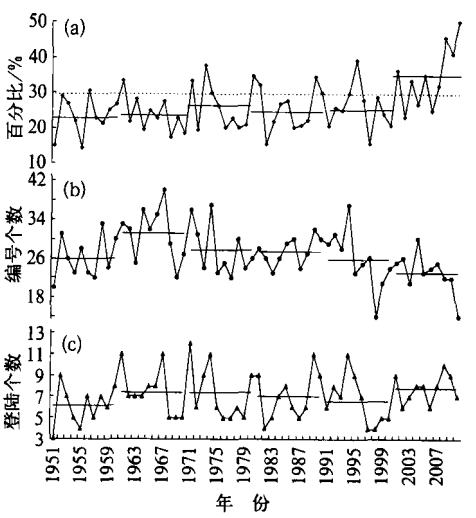


图1 1951—2010年西北太平洋和南海热带气旋登陆个数(c)和编号个数(b)及登陆占编号百分比(a)

Fig. 1 Series of TCs landing (c) and numbered (b) on China, forming in the WNP and SCS and their percentages (a) during 1951—2010



© 1994-2011 China Academic Journal Electronic Publishing House. All rights reserved. http://www.cnki.net

与全球 TC 活动总体偏少的特点一致,2010 年上半年西北太平洋和我国南海 TC 活动异常偏少,7 月 11 日之前仅有 1 个 TC 编号。与 1949 年以来的 TC 活动情况相比,历史上只有 1975 和 1998 年第二号热带气旋生成晚于 7 月 12 日,其中 7502 号热带气旋 Mamie 生成于 7 月 25 日,9802 号强热带风暴 Otto 生成于 8 月 1 日。前期编号异常偏少,也是 2010 年西北太平洋和南海 TC 活动的特点之一。

## 2.2　生成时间较为集中,生成位置总体偏西

2010 年 TC 生成时间较为集中,除 1001 号热带气旋于 3 月 24 日生成外,其余 13 个编号 TC 均在 7—10 月生成,占全年总数的 93%(表 1)。其中 8 月生成的 TC 最多(5 个),其次是 9 月(4 个),但均较常年偏少。

**表 1　2010 年西北太平洋和南海编号和登陆热带气旋频数与常年值比较**

**Table 1　Numbers of TCs numbered and landing on China, forming in the WNP and SCS and their anomalies in 2010**

| | 编号 | | 登陆 | |
|---|---|---|---|---|
| 上半年 | 1 个 | 偏少 3 个 | 0 个 | 偏少 1 个 |
| 7 月 | 2 个 | 偏少 2 个 | 2 个 | 接近常年 |
| 8 月 | 5 个 | 偏少 1 个 | 1 个 | 偏少 1 个 |
| 9 月 | 4 个 | 偏少 1 个 | 3 个 | 偏多 1 个 |
| 10 月 | 2 个 | 偏少 2 个 | 1 个 | 接近常年 |
| 全年 | 14 个 | 偏少 13 个 | 7 个 | 接近常年 |

2010 年在西北太平洋和我国南海海域生成的 14 个 TC 均在 145°E 以西的范围内(图 2),生成位置总体上显著偏西,生成位置最东的 1012 号强台风马勒卡(Malakas)于 9 月 21 日在西北太平洋洋面上(18°N、144.9°E)生成。其中有 4 个 TC 在我国南海海域生成,占总数的 28.6%,比例明显高于多年平均值的 18.3%[15]。另外,由于 TC 生成位置总体偏西,因而 TC 运动轨迹相对较短。从运动轨迹来看,2010 年 TC 多西行、西北行、偏北行或北上路径,当然也有个别曲折路径,如 1013 号台风鲇鱼(Megi,图 2)。

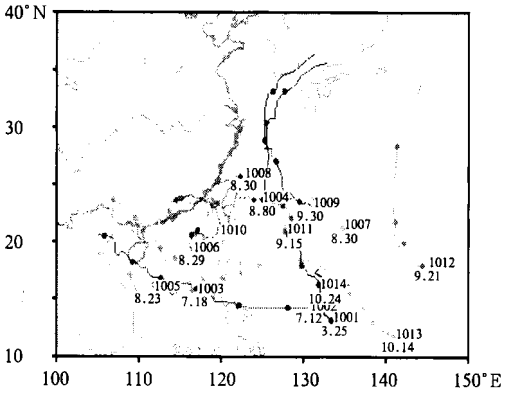


图 2　2010 年西北太平洋和南海 14 个编号热带气旋路径图

Fig. 2　Tracks of 14 numbered TCs forming in the WNP and SCS in 2010

## 2.3　强台风和短生命期 TC 比例偏高

从编号 TC 的强度来看,有 2 个热带风暴、4 个强热带风暴、3 个台风、3 个强台风和 2 个超强台风,其中强热带风暴和强台风所占比例较常年(26.6%和 17%)偏高。超过三分之一的 TC 为强台风以上,即中心附近最大风力在 14 级以上(≥41.5 m·s$^{-1}$),所占比例较常年(33.6%)偏高。强台风和超强台风基本上是在初秋季节的 9—10 月份生成。

2010 年西北太平洋和南海 TC 活动的另一特征是持续时间普遍较短,半数 TC 生命期为 2～4 天,生命期为 5 和 6 天的 TC 各 3 个,仅 1013 号台风鲇鱼生命期最长,长达 11 天。

## 2.4　初台偏晚,终台偏晚

第一个登陆我国的 1002 号台风康森(Conson)于 7 月 12 日上午生成,16 日 19 时 50 分在海南三亚附近登陆,登陆时间比常年初台日期(7 月 1 日)偏晚 15 天。初台偏晚,加上前期编号也异常偏少,进入台汛期偏晚,这与 2010 年季节延迟的天气气候特征相一致,也是 2010 年西北太平洋和南海 TC 活动的另一特点。

最后一个登陆我国的 1013 号超强台风鲇鱼(Megi)于 10 月 23 日中午在福建省漳浦县登陆,比常年终台日期偏晚 19 天。

## 2.5　登陆 TC 前少后多,影响相对集中

2010 年共有 7 个 TC 登陆我国东南沿海,其中前 2 个分别登陆海南和广东,后 5 个都登陆福建,包括 1 个两次登陆的,先在台湾登陆。与常年相比,前期登陆 TC 偏少,入秋后偏多,登陆地点相对集中,影响偏南,主要对我国华南沿海城市有明显的风雨影响,对华东影响较弱,灾情总体偏轻。

7 月登陆我国的 TC 个数接近常年(表 1),除"康森"外,还有 1003 号热带气旋灿都(Chanthu)于 7 月 22 日下午在广东吴川登陆。8 月登陆 TC 个数较常年偏少,仅 1008 号热带风暴南川(Namtheun)于 8 月 31 日夜在福建惠安登陆。9 月是登陆 TC 最



© 1994-2011 China Academic Journal Electronic Publishing House. All rights reserved.　http://www.cnki.net

多的月份，有3个TC登陆我国，较常年偏多1个，分别是1006号强热带风暴狮子山(Lionrock)于9月2日晨在福建省漳浦县登陆，1010号台风莫兰蒂(Meranti)于9月10日凌晨在福建省石狮市登陆，1011号超强台风凡亚比(Fanapi)先于9月19日上午在台湾花莲登陆，后于20日晨在福建省漳浦县再次登陆。10月登陆TC也与常年接近，仅1013号超强台风鲇鱼(Megi)登陆福建。

另外，值得一提的是1006号、1008号和1007号强台风圆规(Kompasu)生命期出现交叠现象，并同时对我国沿海地区产生影响。历史上在西北太平洋和我国南海海域三旋同现的现象并不罕见，但同时影响我国却并不多见，这也是2010年西北太平洋和南海TC活动的特点之一。

## 3 热带气旋活动特征的可能成因

众所周知，TC发生发展需要特定的气候背景场，既要考虑动力学因素，又要考虑热力学条件，而且TC生成还和大尺度环流条件有着密切的关系[16-18]。不同时空尺度的天气气候系统之间，存在着明显的层次性，较大的系统对于较小的系统，在一定条件下往往具有着极为重要的控制作用或调制作用[19]。TC活动也是如此，它必然会受到月、季尺度海洋下垫面环境和大气环流的影响[9]，同时，年际、年代际背景也反映出其活动特征的持续性及多时空尺度因子的综合影响。除海洋等热力环境因素的影响外，造成2010年西北太平洋热带气旋活动异常的主要原因是大气环流的异常。这些大气环流异常主要表现在西北太平洋副热带高压偏强偏西，东亚季风异常偏弱，缺少越赤道气流的辐合，季风槽异常偏西，热带气旋活动区域对流弱，垂直风切变偏大等几方面因素的综合影响，以下分别从年代际背景、海温、ENSO事件、副热带高压、季风槽和垂直风切变等几个方面来初步分析2010年TC活动特点的成因，重点分析TC生成少且位置偏西的可能成因。

### 3.1 编号少且登陆比例偏高的年代际背景

从图1可以看出，TC生成频数存在着明显的年际和年代际变化，TC常年值为27个，但多TC年和少TC年之间差别很大，1967年编号TC最多(40个)，2010年和1998年最少(14个)。1949年到2010年62年间编号TC频数偏高的年份有27个，偏低的年份有35个。20世纪60年代编号TC频数偏多明显[20-21]，70—80年代略偏多，而20世纪50年代和90年代以后偏少，21世纪前10年编号TC频数明显偏少。近50年西北太平洋及南海编号TC年频数具有明显减少的趋势，且自20世纪90年代中期以来基本处于偏少的年代际背景中。

登陆我国的TC频数长期变化趋势不显著，主要呈现年际和阶段性变化特征，但登陆TC占编号TC的比例呈现明显的上升趋势。登陆我国的TC常年值为7个，多年和少年之间差别也很大，1971年最多(12个)，1950和1951年最少(3个)。21世纪前10年处于偏多时段，特别是2007—2009年连续3年偏多。由于登陆偏多而编号偏少，最近几年西北太平洋和南海TC频数变化最明显的特征就是登陆比例呈现上升趋势，特别是进入21世纪以后这种上升趋势非常显著。可见，2010年处于编号TC偏少且登陆TC比例偏高的年代际背景下。

TC活动的年际变化某种程度上受海温和ENSO循环的影响。研究表明，ENSO事件[22]主要影响西北太平洋TC的生成位置偏东或偏西[12,23-26]，而东印度洋海温偏低或偏高则影响TC生成频数的多少；拉尼娜(La Nina)年TC生成位置多数位于145°E以西地区，且强台风以上的TC个数偏少[23]，2010年的TC活动特征充分验证了这些统计规律。通过与历史上ENSO事件演变特征的比较分析，发现1951年以来出现与2010年的海表降温过程类似特征的有5年，均是在厄尔尼诺事件(El Nino)结束当年2—6月后进入La Nina状态，并继续发展形成了La Nina事件。在这些海温变化相似年中，除1970年编号TC频数同常年外，1973、1995、1998和2007年编号TC频数均少于常年。1998与2010年最为相似，编号TC均为最少。可见，2010年编号TC频数偏少符合海温相似年频数变化的规律，也符合El Nino次年西北太平洋及南海TC生成频数多数偏少的规律[19]。另外，TC活动的年代际变化主要是由于全球变暖背景下大气环流变化造成的，特别是与20世纪70年代以后西北太平洋副热带高压面积不断扩大且强度增强有关[16,27-28]。

### 3.2 东印度洋海温偏高

TC是海气相互作用的产物，海温异常对TC生成有重要影响。2009年6月至2010年4月赤道中东太平洋发生了一次中等强度的中部型El Nino事件(图3)，对此次暖事件的滞后响应，2010年上半年印度洋出现全区一致持续偏暖模态，7—10月为持续4个月的印度洋偶极(IOD)负位相。2010年1—10月东印度洋(10°S～22.5°N、75°～100°E)海温持



© 1994-2011 China Academic Journal Electronic Publishing House. All rights reserved. http://www.cnki.net

续偏高(图 4),这是导致西北太平洋和中国南海编号 TC 偏少的重要原因。因为东印度洋海温偏高会通过对流加热机制激发大气暖性开文波东传,使赤道西太平洋海平面气压下降,对流层低层向赤道地区辐合,相应地引起赤道外的同期响应,导致西北太平洋和中国南海 TC 活动区域形成反气旋(图 5),从而抑制了 TC 的生成。

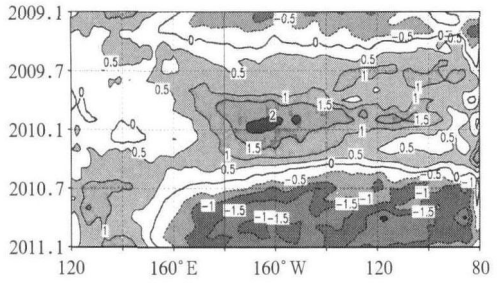


图 3　赤道(5°S～5°N)太平洋海表温度距平时间-经度剖面(单位:℃)

Fig. 3　Time-longitude section of equatorial sea surface temperature (SST) anomalies (unit:℃) averaged over 5°S－5°N

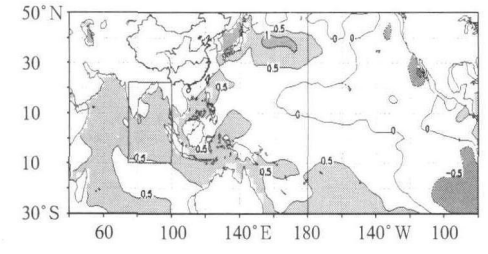


图 4　2010 年 1—10 月平均海表温度距平(单位:℃),方框区域为东印度洋(10°S～22.5°N、75°～100°E)

Fig. 4　SST anomalies (unit: ℃) during January—October 2010, the rectangle region denoting the East Indian Ocean (10°S－22.5°N,75°－100°E)

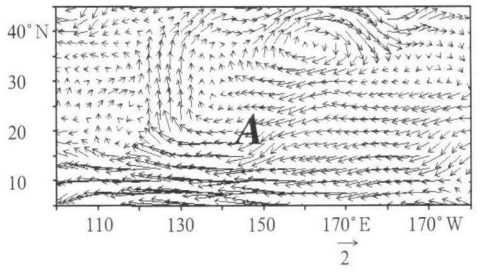


图 5　2010 年 7—10 月西北太平洋和南海 850 hPa 风场距平(单位:m·s$^{-1}$),A 表示反气旋

Fig. 5　850 hPa wind anomalies (unit:m·s$^{-1}$) in the WNP and SCS during July－October 2010, A denoting anticyclone

### 3.3　西太平洋副热带高压偏强偏西

2010 年热带大气对 ENSO 事件响应迅速,但热带外大气响应滞后。7 月虽已进入 La Nina 状态,但 6—9 月西北太平洋的大气状态仍主要表现为前期 El Nino 事件的滞后响应。通常热带外大气对 La Nina 的滞后响应为 3～4 个月,最早 2 个月[29-30]。2010 年 1—9 月,西北太平洋呈现典型 El Nino 次年大气特征。从 500 hPa 位势高度场上可以看出,西太平洋副热带高压(10°N 以北,110°E～180°)表现为强度持续偏强、西伸脊点位置持续偏西的特点,特别是夏季西太平洋副热带高压强度历史排名第一(图 6),强于此前 TC 活动最少的 1998 年。由于西北太平洋和南海在强大的副热带高压控制下,下沉气流异常强(图 7),抑制了对流活动的发展,导致 2010 年 TC 活动季节内在西北太平洋和我国南海海域生成 TC 个数异常偏少。另外,副热带高压外围的气流对 TC 的运动具有引导作用,偏强偏西的副热带高压也是导致 2010 年 TC 多西行、西北行或北上路径,进而登陆或影响我国的因素之一。

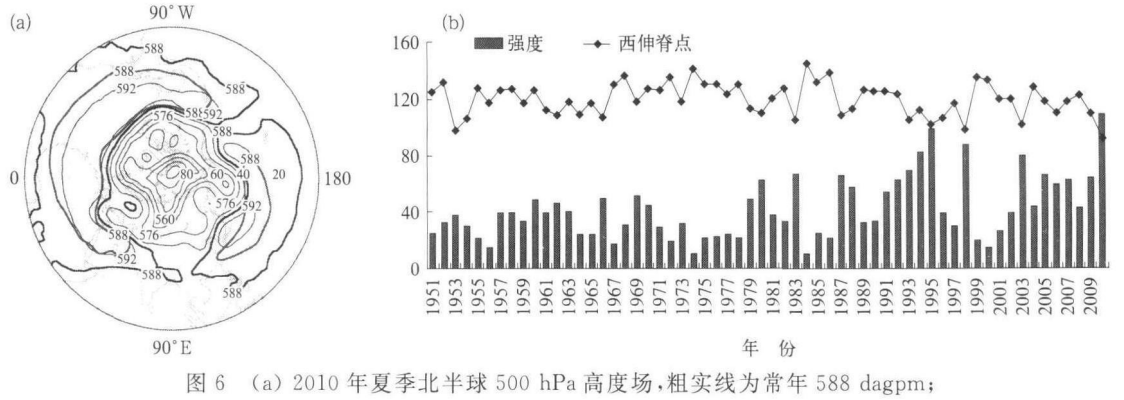


图 6　(a) 2010 年夏季北半球 500 hPa 高度场,粗实线为常年 588 dagpm;(b)1951－2010 年夏季西北太平洋副热带高压强度和西伸脊点指数演变

Fig. 6　Seasonal mean 500 hPa geopotential heights for the summer 2010 of the Northern Hemisphere and 588 dagpm of climatology in bold lines (a), and series of indices for the WNP subtropical high intensity and western ridge point in the summer during 1951－2010 (b)



© 1994-2011 China Academic Journal Electronic Publishing House. All rights reserved.　http://www.cnki.net

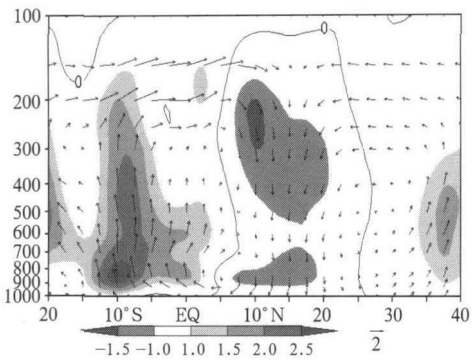


图7 2010年7—10月西太平洋(120°～170°E)矢量风距平气压-纬度剖面(单位:m·s$^{-1}$)
阴影区表示垂直速度(0.01 m·s$^{-1}$)

Fig. 7 Pressure-latitude section of vectors of combined anomalous meridional wind and vertical velocity (unit: m·s$^{-1}$) averaged over the West Pacific (120°−170°E) from July to October 2010
the shading area denoting the pressure vertical velocity (0.01 m·s$^{-1}$)

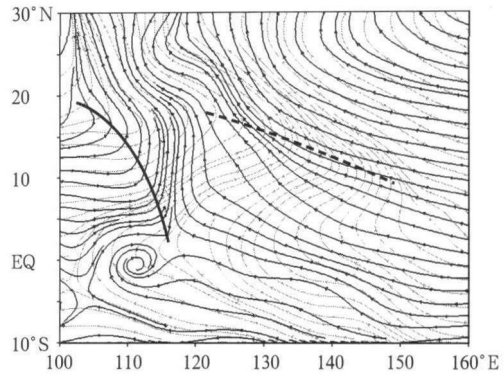


图8 7—10月850 hPa流场
粗实线表示2010年季风槽位置,
粗虚线表示常年季风槽位置

Fig. 8 Composite 850 hPa wind (streamline) during July−October with monsoon trough marked for 2010 by the bold solid line and the normal year averaged over 1971−2000 by the bold dash line

### 3.4 季风槽位置偏西

研究表明:80%～90%的TC发生在热带辐合区里[31],通常,西北太平洋和南海有70%以上的TC生成于季风槽中[8,32-34]。西北太平洋季风槽是夏季北半球的西南季风或越赤道气流与副高南侧之东南信风辐合而形成的低压带,属于热带辐合带的一部分[35]。2010年,南海夏季风为1951年来最弱;东亚副热带夏季风(6—8月)的强度也显著偏弱。7—10月季风槽主体位于南海上空,季风槽位置较常年同期异常偏西(图8),同时赤道西太平洋附近盛行平直偏东风,使得常年季风槽活跃的菲律宾以东洋面非常不利于气旋性涡旋生成,这是造成2010年编号TC总体上位于145°E以西地区的主要原因。

### 3.5 垂直风切变偏大

影响TC生成的另一个关键环境因素就是垂直风切变,即高低层(200与850 hPa)纬向风之差。图9中所示2010年7—10月西北太平洋和中国南海TC活动区域垂直风切变普遍偏大,限制了TC上层暖心的发展,不利于涡旋的形成[36],导致编号TC总体偏少。2010年在西北太平洋和我国南海海域生成的14个TC均在145°E以西的范围内,基本上都在垂直风切变小于4 m·s$^{-1}$或负值的区域(图9a),垂直风切变距平小于12 m·s$^{-1}$的区域(图9b)。由于生成位置总体上显著偏西,加上副热带环流季节内变化特征的有利配合,有利于TC登陆我国沿海地区,这也是TC生成总数少而登陆个数却正常的重要原因。

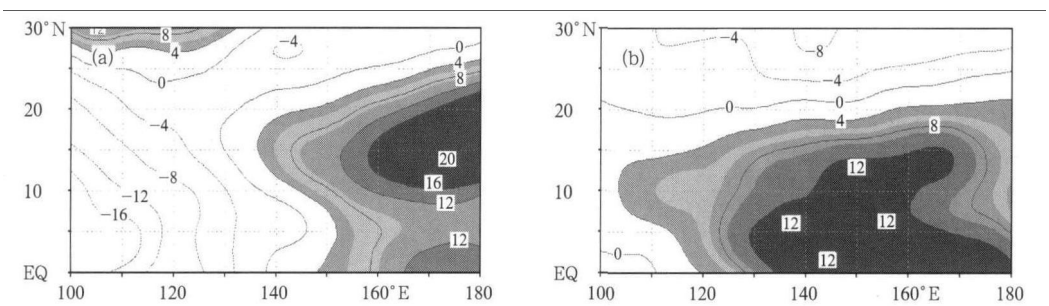


图9 2010年7—10月西北太平洋热带气旋活动区高低层纬向风垂直切变($U_{200\ hPa}-U_{850\ hPa}$)(a)与距平(b)(单位:m·s$^{-1}$)

Fig. 9 Vertical wind shear (a) and anomalies (b) ($U_{200\ hPa}-U_{850\ hPa}$) of the WNP during July−October 2010 (unit: m·s$^{-1}$)

## 4 结 论

2010年西北太平洋和南海生成的TC具有编号最少,登陆比例最高;生成时间集中,生成位置偏西;强台风和生命周期短的TC比例偏高;初台偏晚,终台偏晚;登陆前少后多,登陆地点集中,影响偏南等特点。在这五个方面特点中,编号最少且生成



© 1994-2011 China Academic Journal Electronic Publishing House. All rights reserved. http://www.cnki.net

位置总体上显著偏西的特点更为突出,究其可能成因主要有以下几方面。

(1) 从年代际背景来看,近 50 年西北太平洋及南海编号 TC 年频数具有明显减少的趋势,且自 20 世纪 90 年代中期以来基本处于偏少时段,2010 年处于编号 TC 偏少、登陆比例偏高的年代际背景中。

(2) 从海洋角度来看,2010 年 1—10 月东印度洋海温持续偏高,是导致西北太平洋和中国南海编号 TC 偏少的重要原因;2009 年 6 月至 2010 年 4 月赤道中东太平洋发生的中等强度中部型厄尔尼诺事件也是导致前期编号 TC 异常偏少的重要外强迫因素之一。

(3) 大气环流异常是造成 TC 活动异常的直接原因。主要表现为西北太平洋副热带高压偏强偏西,季风槽位置异常偏西,垂直风切变偏大等几方面因素的综合影响。同时环流异常也影响 TC 的运动路径,副热带高压南侧的东风气流容易引导 TC 以西行、西北行或北上路径进入我国沿海地区,有利于 TC 登陆我国,这也是 TC 编号少而登陆并不少的重要原因。

## 参考文献


[1] 陈联寿,丁一汇. 西太平洋热带气旋概论[M]. 北京:科学出版社,1979:399-410.

[2] 陈联寿,孟智勇. 我国热带气旋研究十年进展[J]. 大气科学,2001,25(3):420-432.

[3] 李崇银. 厄尔尼诺与西太平洋热带气旋活动[J]. 科学通报,1985,14:1087-1089.

[4] 李崇银. 厄尔尼诺与南海热带气旋活动[J]. 热带气象,1986,2(2):39-48.

[5] 何敏,龚振淞,徐明,等. 高低层纬向风异常与西北太平洋热带气旋生成年频数关系的研究[J]. 热带气象学报,2007,23(3):277-283.

[6] 李春晖,刘春霞,程正泉. 近 50 年南海热带气旋时空分布特征及其海洋影响因子[J]. 热带气象学报,2007,23(4):341-347.

[7] 陈联寿. 热带气象灾害及其研究进展[J]. 气象,2010,36(7):101-110.

[8] Gray W M. The formation of tropical cyclones[J]. Meteorology and Atmospheric Physics,1998,67:37-69.

[9] 张庆红,郭春蕊. 热带气旋生成机制的研究进展[J]. 海洋学报(中文版),2008,30(4):1-11.

[10] 杨桂山,施雅风. 西北太平洋热带气旋频数的变化及与海表温度的相关研究[J]. 地理学报,1999,54(1):22-29.

[11] Fu B,Li T, Peng M S,et al. Analysis of tropical cyclogenesis in the western North Pacific for 2000 and 2001[J]. Weather and Forecasting,2007,22:763-780.

[12] Wang B, Chan JCL. How strong ENSO events affect tropical storm activity over the western North Pacific[J]. Journal of Climate,2002,15:1643-1658.

[13] 王会军,范可. 西北太平洋台风生成频次与南极涛动的关系[J]. 科学通报,2006,21:2910-2914.

[14] 王会军,孙建奇,范可. 北太平洋涛动与台风和飓风频次的关系的研究[J]. 中国科学(D 辑),2007,37:966-973.

[15] 李雪,任福民,杨修群,等. 南海和西北太平洋热带气旋活动的区域性差异分析[J]. 气候与环境研究,2010,15(4):504-510.

[16] 丁一汇. 影响西太平洋台风形成的大尺度环流条件[J]. 海洋学报,1983,5(5):561-574.

[17] 雷小途,陈联寿. 热带气旋的登陆及其与中纬度环流系统相互作用的研究[J]. 气象学报,2001,59(5):602-615.

[18] 雷小途,陈联寿. 大尺度环境场对热带气旋影响的动力分析[J]. 气象学报,2001,59(4):429-439.

[19] 黄勇,李崇银,王颖. 2006 年西北太平洋热带气旋生成频数和源地异常的成因分析[J]. 热带气象学报,2008, 24(6):590-598.

[20] 李春晖,刘春霞,程正泉. 近 50 年南海热带气旋时空分布特征及其海洋影响因子[J]. 热带气象学报,2007, 23(4):341-347.

[21] Zhao X, Chu P-S. Bayesian change point analysis for extreme events (Typhoons, heavy rainfall, and heat waves): An RJMCMC approach[J]. Journal of Climate, 2010, 23: 1034-1046.

[22] 李晓燕,翟盘茂. ENSO 事件指数与指标研究[J]. 气象学报,2000,58(1):102-109.

[23] Zhan R,Wang Y,Lei X. Contributions of ENSO and East Indian Ocean SSTA to the interannual variability of Northwest Pacific tropical cyclone frequency[J]. Journal of Climate, 2011,24:509-521.

[24] Chen T-C,Weng S-P,Yamazaki N, et al. Interannual variation in the tropical cyclone formation over the western North Pacific[J]. Monthly Weather Review,1998,126:1080-1090.

[25] Chen T-C, Wang S-Y, Yen M-C. Interannual variation of the tropical cyclone activity over the western North Pacific[J]. Journal of Climate,2006,19:5709-5720.

[26] Chia H H, Ropelewski C F. The interannual variability in the genesis location of tropical cyclones in the Northwest Pacific [J]. Journal of Climate,2002,15:2934-2944.

[27] 陈光华,黄荣辉. 西北太平洋热带气旋和台风活动若干气候问题的研究[J]. 地球科学进展,2006,21(6):610-616.

[28] 应明,余晖. 2009 年西北太平洋热带气旋活动的若干特点分析[J]. 气象,2011,37(4):454-461.

[29] 张志华,黄刚. 不同类型 El Nino 事件及其与我国夏季气候异常的关系[J]. 南京气象学院学报,2008,31(6):782-789.

[30] 薛峰,刘长征. 中等强度 ENSO 对中国东部夏季降水的影响及其与强 ENSO 的对比分析[J]. 科学通报,2007,S2(23):2798-2850.

[31] 伍荣生,徐亚梅. 南半球冷空气入侵与热带气旋的形成[J]. 气象学报,2003,61(5):540-547.

[32] McBride J L. Tropical cyclone formation, Chapter 3, Global Perspectives on Tropical Cyclones[M]. WMO/TD No. 693. WMO, Geneva, Switzerland,1995.

[33] 王磊,陈光华,黄荣辉. 2009. 影响登陆我国不同区域热带气旋活动的大尺度环流定量分析[J]. 大气科学,33(5):916-922.

[34] 黄荣辉,陈光华. 西北太平洋热带气旋移动路径的年际变化及其机理研究[J]. 气象学报,2007,65(5):683-694.

[35] 申松林,江静. 西北太平洋台风频数异常年的气候背景分析[J]. 气象,2010,36(5):64-70.

[36] Demaria M. The effect of vertical shear on tropical cyclone intensity change[J]. Journal of the Atmospheric Sciences,1996, 53(14):2076-2088.




© 1994-2011 China Academic Journal Electronic Publishing House. All rights reserved.　http://www.cnki.net

Article ID: 1006-8775(2011) 02-0181-06

# STUDY ON CLIMATIC CHARACTERISTICS OF CHINA-INFLUENCING TROPICAL CYCLONES

SUN Lin-hai (孙林海)[1], AI Wan-xiu (艾万秀)[1], SONG Wen-ling (宋文玲)[1], WANG Yong-mei (王咏梅)[2]

(1. National Climate Center, Beijing 100081 China; 2. Yuncheng Weather Bureau, Yuncheng, Shanxi 044000 China)

**Abstract:** Analysis of the climatic characteristics of the tropical cyclones that affect China yields several interesting features. The frequency of these tropical cyclones tended to decrease from 1951 to 2005, with the lowest frequency in the past ten years. The decrease in the frequency of super typhoons is particularly significant. The main season of tropical cyclone activities is from May to November, with an active period from July to September. There are three obvious sources of these tropical cyclones and they vary with seasons and decades. Their movement has also changed with seasons. On average, these tropical cyclones affect China for 5.6 months annually and the period of influence decreases in the past decades. An analysis of daily data indicates that the days of typhoon influence are shorter in winter and spring and longer in summer. The frequency of tropical cyclones is the largest over southeastern China, decreasing northwestward. Taiwan is the region that is affected by tropical cyclones most frequently. The average annual precipitation associated with tropical cyclones has also decreased gradually northwestward from southeastern China.

**Key words:** tropical cyclones affecting China; climatic characteristics; period of influence

**CLC number:** P435 **Document code:** A **doi:** 10.3969/j.issn.1006-8775.2011.02.011

## 1 INTRODUCTION

Typhoons are among the most damaging natural disasters in the world. They bring about strong winds and heavy rains and cause economic losses and casualties. More than 500 million people in the world are affected by typhoons by varying degrees each year, and China is one of the countries that suffer tremendous typhoon damage[1]. Tropical cyclones (TCs) that affect China (to be referred to as "these TCs" hereafter) originate mainly from the northwestern Pacific Ocean[1, 2]. In the past years, more and more research interest has been given to the climatic characteristics of the northwestern Pacific TCs[3]. It is known that there exist obvious interannual and interdecadal variations in TC activities[4, 5], including the landfall typhoons[6-8]. Previous studies have also analyzed the winds and precipitation associated with tropical storms and the spatiotemporal characteristics of the heavy rain and strong winds over China from 1951 to 2000[9]. It is found that the characteristics of TC activities are different in different phases. The time of landing in Fujian and Zhejiang provinces is later than that in southern China, though the former involves stronger typhoons[10]. While many previous studies have focused on landfall typhoons, other typhoons that do not make landfall may also exert serious impacts on China and it is necessary to understand the characteristics of all these TCs.

For this study, the data of the TCs over the northwestern Pacific and the South China Sea are from the Shanghai Typhoon Institute of the China Meteorological Administration (CMA), and the data of these TCs are from the National Climate Center, CMA[11, 12]. We refer to these TCs as those that originate over northwestern Pacific or the South China Sea and bring precipitation to the mainland, Hainan, and Taiwan of China.

## 2 CHANGES OF THE FREQUENCY IN THE DECADAL, INTER-ANNUAL AND MONTHLY VARIATION

There were 1943 TCs over the Northwestern

**Received** 2010-02-25; **Revised** 2011-02-19; **Accepted** 2011-04-15

**Foundation item:** National Natural Science Foundation of China (41005051); Applicability of various multi-model ensemble approaches in seasonal precipitation prediction

**Biography:** SUN Lin-hai, Senior Engineer, M.S., primarily undertaking research on short-term climate prediction.

**Corresponding author:** SUN Lin-hai, e-mail: slh@cma.gov.cn



© 1994-2011 China Academic Journal Electronic Publishing House. All rights reserved. http://www.cnki.net

Pacific and South China Sea from 1951 to 2005, including 938 TCs, which affected China. The annual average is 17 (Fig. 1). Only nine TCs affected China in 1997, the least number for the time from 1951 to 2005. 1971 is the year with the largest number of these TCs (27). They tended to decrease in the past 55 years, and the trend is -1.03/10 yr (surpassing the significance test at the 0.01 level). Changes of these TCs are not as remarkable as the generation of TCs on the decadal scale, slightly decreasing in a process of fluctuation. These TCs are more than normal before the early 1970s. The annual frequency change has stronger variation in the early 1970s to the 1990s. It is less than normal since the 1990s with the least period after the year 2000. The characteristics of these TCs changing on the decadal scale are similar to those of the landing TCs in China.

There are significant seasonal variations with these TCs and single-peak distribution occurs on the monthly scale with the extreme value lying in August (figure omitted). China is affected by TCs to varying extent for almost all year around, and 98% of the TCs concentrate in May to November. The active TC season spans from July to September. The TC number also occurs the most in August, taking up 27% of the total. China is affected on average by 4.6 TCs in August over the past 55 years. TCs have 18.1% and 21.5% of the chance in July and September to affect China. Only one such TC occurs in January and February separately. Not a single one occurs in March and it is the only month in the whole year that China is free of any influence from TCs.

Figure 2 shows the curves of the dates of cyclogenesis for the first and the last yearly TC affecting China and the duration (in days) for such TCs to influence the precipitation over China in 1951 to 2005. The ordinate is for the calendar days on which these TCs occurred. We can see from the figure that most of the yearly first TCs occur from April to June and the yearly last ones from October to December. The average date (from 1971 to 2000) of the first yearly TCs is May 23th and that of the last ones is November 8th. The influence lasts 5.6 months in length. It is shown that the length of influence (in days) is decreasing with the trend for the past 55 years. We found that there are three or four days of influence every month from May to October and two days of influence in the other months, as shown in the monthly variation (figure omitted) of the number of TC affecting days (in terms of the maximum precipitation days recorded at observation stations) in 1951 to 2005. There are more days of influence in summer and autumn than in spring and winter. The maximum number of days of influence occurs in August, which is longer than four days and the shortest is in December, which is less than two days.

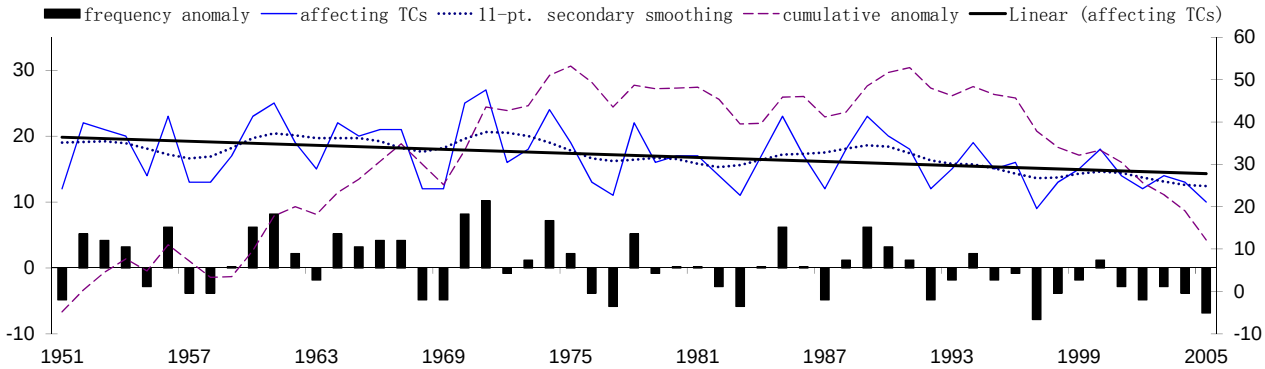


Fig. 1.Variations of cumulative anomalies (right ordinate) and annual frequency (left ordinate) of the tropical cyclones affecting China from 1951 to 2005. Abscissa: year; ordinate: number of TCs

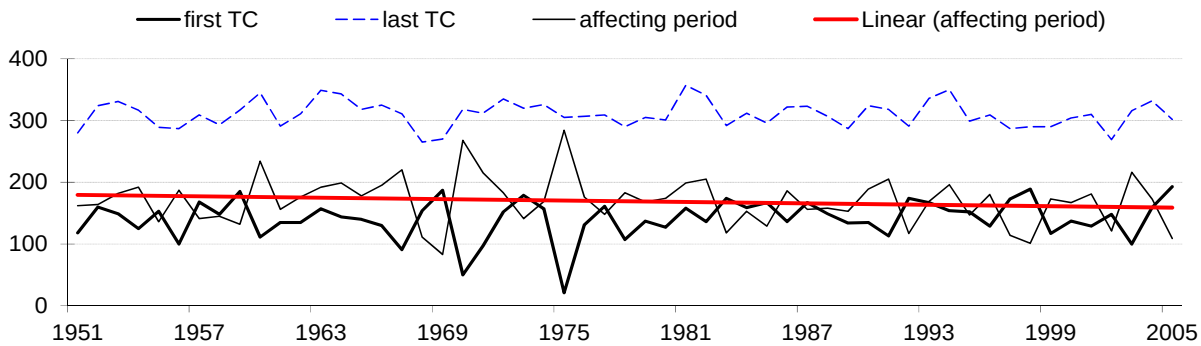


Fig. 2. Year-to-year variations of the occurring dates of the annually first and last tropical cyclones affecting China and the length of their influence from 1951 to 2005. Abscissa: year

## 3 VARIATIONS OF TROPICAL CYCLONES WITH DIFFERENT INTENSITY



© 1994-2011 China Academic Journal Electronic Publishing House. All rights reserved. http://www.cnki.net

Taking into account the disasters inflicted by TCs with different intensity, we analyze typhoons, strong typhoons, and super typhoons, based on intensity. From the linear trend line of annual change in the number of typhoons (TY, figure omitted), strong typhoons (STY, figure omitted) and super typhoons (super TY, Fig. 3), we can see that the number of these typhoons increases mildly during the past 55 years at a rate of 0.20 every ten years. STY decreases by a rate of 0.15 every ten years, and both of them pass the significance test. The decrease in the frequency of super TYs, at a rate of 0.4 every ten years, is particularly significant (surpassing the significance test at the 0.01 level). The average number is three in the 1950s and 1960s and less than one in the past ten years.

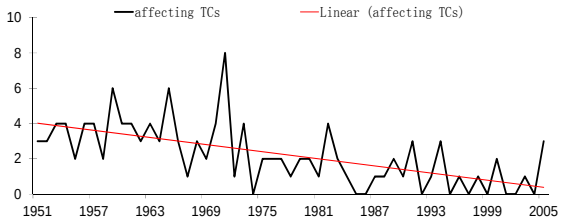


Fig. 3. Frequency of super typhoons among the tropical cyclones affecting China from 1951 to 2005. Abscissa: year

## 4 INTENSITY CHANGE OF THE TROPICAL CYCLONES

We refer to the intensity of these TCs as the minimum pressure and maximum wind speed near the center during the period of influence. The average intensity of these TCs is based on the average of all records from 1951 to 2005. The extreme intensity is expressed by the maximum value among all these TCs for each year. Fig. 4 shows the intensity variability of these TCs during their period of influence from 1951 to 2005. The average of the minimum pressure shows no significant change, and the extreme of the minimum has an increasing trend. The minimum of the minimum pressure has large annual fluctuations in the late 1950s to 1970s and shows an increasing trend after the late 1970s. The average of the maximum wind speed shows no significant change, similar to the averaged minimum pressure during the period of influence, but the extreme value of the maximum wind speed has a reducing trend. The analysis shows that there is a decreasing trend with the extreme intensity of these TCs during the period of influence in the past 55 years.

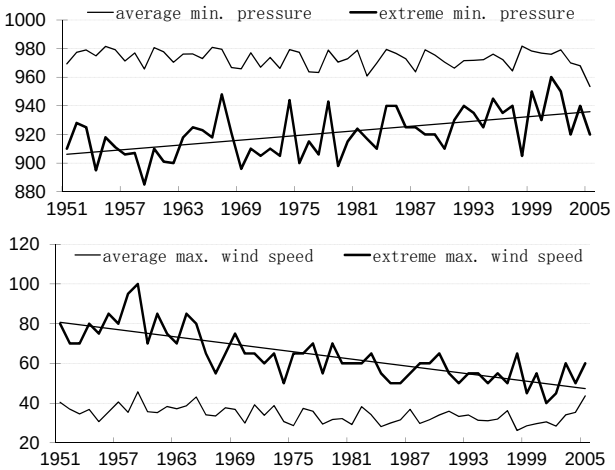


Fig. 4. Evolution of average minimum pressure and its extreme values (upper panel, in unit of hPa), and average maximum wind speed and its extreme values (lower panel, m/s), during the period of influence of the tropical cyclones affecting China

Figure 5 shows the monthly variability of the intensity of these TCs during the period of influence from 1951 to 2005. The monthly change of the averaged minimum pressure, in the range of 953–990 hPa, is not very dramatic (figure omitted). The average of the minimum pressure is lower in summer and autumn than in winter and spring. The monthly averaged maximum wind speed does not change significantly during the period of influence with the range between 28–45 m/s. There is obvious seasonal variability with the extreme of maximum wind speed; decreasing intensity occurs from January to May, increasing intensity occurs from June to October, with the peak of intensity in August, and the extreme maximum wind speed at 100 m/s. In summary, the extreme intensity of these TCs has obvious seasonal variation. The extreme intensity is stronger in summer and autumn than in winter and spring.

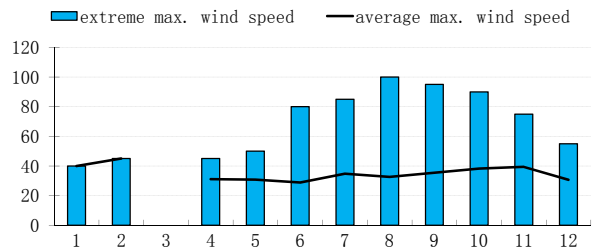


Fig. 5. Month-to-month evolution of average maximum wind speed and its extreme values (m/s) for the tropical cyclones affecting China during the period of influence

## 5 SOURCES OF THE TROPICAL CYCLONES

Figure 6 shows the frequency of these TCs which generated from 1951 to 2005; it is 938 in total within the 2.5° longitude ×2.5° latitude gridpoint boxes. The



© 1994-2011 China Academic Journal Electronic Publishing House. All rights reserved. http://www.cnki.net

TCs that bring precipitation to China mostly originate in the region west of 150° E and between 5–20° N. There were three obvious centers of cyclonegenesis, which distributed in the central part of the South China Sea, the eastern region of Philippine Islands and the western waters of the Caroline Islands. Main cyclonegenesis for these TCs happens in the South China Sea, with the maximum frequency within 2.5° longitude ×2.5° latitude gridpoint boxes being 35, and the other two sources being 20 and 18 respectively.

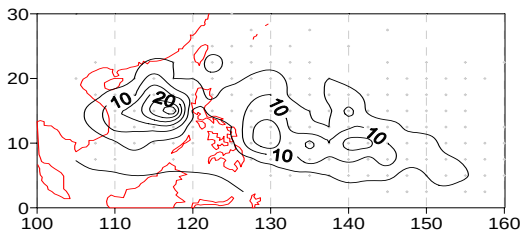


Fig. 6. Frequency of cyclogenesis of the tropical cyclones affecting China

Figure 7 shows the monthly variation of the average location of the cyclonegenesis by latitude and longitude. Seasonally, the source varies zonally and toward the north from January to August. Its average latitudinal position is the northernmost in August (16.5° N). The source position withdraws southward monthly from September to December. April to May and October to November are the obvious phases of the variability of the source position. Longitudinally, the position is more eastern than normal (in the vicinity of 140° E) in fall and winter and pushes westward to around 125° E in summer, and is more western than normal from May to September to 125–133° E.

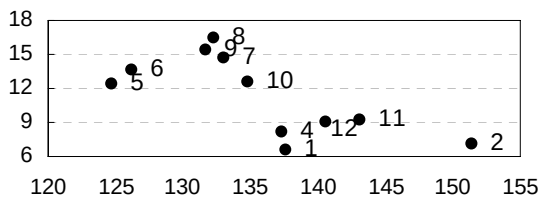


Fig. 7. Monthly longitudinal and latitudinal variations of average position of the tropical cyclones affecting China in terms of source of cyclogenesis Abscissa: longitude; ordinate: latitude

The average source position of these TCs has decadal shifts (table omitted). The average position from 1951 to 2005 is 132.5° E, 14.4° N. The source was located more westward than normal in the 1950s, and more eastward and southward than normal from the 1960s to 1970s, became more northward after the 1980s, and was more northward and westward than normal after the 1990s. The source position of these TCs shows obvious changes on the decadal scale, shifting from westward to eastward positions and then from eastward to westward positions, and from southward to northward positions during the last 55 years.

## 6 TRACKS OF THE TROPICAL CYCLONES

The tracks of these TCs vary regularly, reflecting the different characters of the scope and extent by which they affect China in different seasons. Here only the characters in their active period are given. The tracks are much more northward in July and August than in the preceding period, with most of them located south of 22° N and moving westward. The tracks are mainly (1) westward, entering the northern South China Sea and landing in Hainan Province and south of China, (2) northwestward, landing in Taiwan Island and southeast of China, and entering the inland areas of China, and (3) northward over the offshore area, with most of them moving across the East China Sea and landing in the Korean Peninsula, and some of them moving to the northwest, landing in the coast of Shandong and Liaoning Provinces, but seldom reaching Mongolia and the central region of Northeast China. TCs affected large areas, including the coastal areas in the southeast, south and east of China in July and August. The tracks of these TCs are more southward in September than in the previous two months and mainly move westward south of 20° N. The movement of TCs changes with seasons. The tracks of TCs are more southward in winter and spring when there is little influence of TCs but they are more northward in summer when there is severe influence of TCs.

## 7 FREQUENCY OF THE TROPICAL CYCLONES AND DISTRIBUTION OF THEIR PRECIPITATION

The frequency of TC influence is referred to as the annual average frequency of the stations which are affected by these TCs. Fig. 8 shows the distribution of influence frequency and annual average precipitation averaged from 1971 to 2000. According the analysis, we can obtain the following characteristics about the range and extent of these TCs.



© 1994-2011 China Academic Journal Electronic Publishing House. All rights reserved. http://www.cnki.net

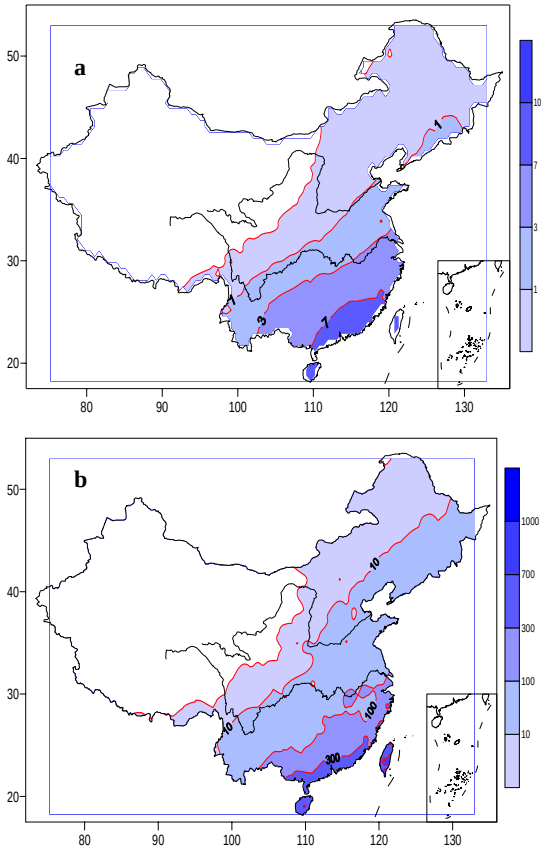


Fig. 8. Frequency of tropical cyclone influence (a, times/year) and spatial distribution of annul mean precipitation from tropical cyclones (b, unit: mm) from 1971 to 2000

(1) The influence is huge in time span and area, with these TCs affecting most of the central and eastern China (except the northwestern China and most of southwestern China).

(2) The annual average frequency of these TCs shows a zonal distribution that decreases from the southeast to the northwest.

(3) The areas most severely influenced by these TCs include the provinces of Taiwan, Hainan, Guangdong and Fujian (Fig. 8a). Of all, Taiwan is the region affected by these TCs most frequently, almost 10 times yearly in some parts of the island. Most of the area in the southern part of the middle and lower reaches of the Yangtze River, northern South China and southeastern Southwest China are affected three to seven times per year on average. The southeast part of Northeast China, the southern part of North China, Shandong Peninsula, the basins of the Yellow River and Huaihe River, the area comprising the middle and lower reaches of the Yangtze River and the Huaihe River basin, the middle reach of Yangtze River, the southern part of Southwest China are affected one to three times a year on average. Most of Northeast China, most of North China, and eastern Northwest China are affected less than once per year.

(4) Precipitation caused by these TCs reduces gradually from the southeast coast to the northwest inland areas. The maximum precipitation occurs in the central and eastern Taiwan Island and part of Hainan Province with the annual average rainfall above 700 mm and more than 1000 mm in some parts of Taiwan. The precipitation is 300 to 700 mm over the southeast coast of China, most of Hainan and western Taiwan. Northern South China and areas south of Yangtze River receives 100 to 300 mm of precipitation. The precipitation is 10 to 100 mm over the western and northern parts of the area south of the middle and lower reaches of the Yangtze River, most of Yunnan-Guizhou Plateau, the basins of the Yangtze and Huaihe Rivers in Jiangsu and Anhui provinces, the basins of Yellow River and Huaihe River, the central and southern part of North China, and the east and south of Northeast China. It is less than 10 mm over the central and eastern parts of Inner Mongolia region, western North China, eastern Northwest China and eastern Southwest China.

## 8 SUMMARIES

From the analysis above, the main conclusions are as follows.

(1) The frequency of the TCs affecting China tended to decrease from 1951 to 2005, with the lowest frequency appearing in the past 10 years. The decrease in the frequency of super typhoons is particularly significant.

(2) These TCs have obvious seasonal variations. The main season of TC activities is from May to November, with an active period from July to September.

(3) The extreme intensity of these TCs has obvious seasonal variations, being stronger in summer and autumn than in winter and spring.

(4) There were three obvious sources of these TCs varying with seasons and decades, which distribute in the central part of the South China Sea, the eastern region of Philippine Islands and the western waters of the Caroline Islands. Seasonal variation of the sources is zonal, with northward shifting from January to August and moving back southward monthly from September to December. The source position of these TCs changes obviously in decades, shifting from westward to eastward positions and then from eastward to westward positions, and from southward to northward positions during the last 55 years.

(5) The movement of TCs has also changed with seasons. The tracks of TCs are more southward in winter and spring when there is little influence of TCs but they more northward in summer when there is severe influence of TCs.

(6) The average date (from 1971 to 2000) of the first TC affecting China is May 23th and the last one is November 8th. On average, these TCs affect China for 5.6 months and the influence periods reduce with the decreasing trend during the past 55 years.



© 1994-2011 China Academic Journal Electronic Publishing House. All rights reserved. http://www.cnki.net

(7) The annual average frequency of these TCs showed a zonal distribution that decrease from the southeast to the northwest. Areas that are most severely influenced by these TCs include the provinces of Taiwan, Hainan, Guangdong and Fujian. Taiwan is the location these TCs affect with the highest frequency. The frequency of being affected by these TCs is almost 10 times per year in some regions of Taiwan. Precipitation caused by these TCs reduces gradually from the southeast to the northwest along the coast.

## REFERENCES:

[1] CHEN Lian-shou, DING Yi-hui. Introduction to the Western Pacific Typhoons [M]. Beijing: Science Press, 1979, 22-26.

[2] WANG Ji-zhi. Typhoon Activity in Northwestern Pacific for the Latest Hundred Years [M]. Beijing, China Ocean Press, 1991: 57-95.

[3] CHEN Min, ZHENG Yong-guang, TAO Zu-yu. An analysis on tropical cyclones' climatic feature in the western north Pacific for 1949-1996 [J]. J. Trop. Meteor., 1999, 15(1): 10-16.

[4] ZHANG Guang-zhi, ZHANG Xian-gong, WEI Feng-ying. A study on the variations of annual frequency for tropical cyclones in northwest pacific during the last hundred years [J]. J. Trop. Meteor., 1995, 11(4): 315-323.

[5] MU Hai-zhen, TU Qi-pu. Climatological characteristics of tropical cyclone activities in the west Pacific [J]. J. Nanjing Inst. Meteor., 2000, 23(1): 81-86.

[6] LI Ying, CHEN Lian-shou, ZHANG Sheng-jun. Statistical characteristics of tropical cyclone making landfalls on China [J]. J. Trop. Meteor., 2004, 20(1): 14-22.

[7] JIN Rong-hua, GAO Shuan-zhu, GU Hua, et al. An analysis on characteristics of landing and going north typhoons and its causes during 1975-2005 [J]. Meteor. Mon., 2006, 32(7): 33-39.

[8] WENG Xiang-yu, YE Meng, HE Xia-jiang. Analysis of characteristics of precipitation induced by tropical cyclones landfalling in west Guangdong [J]. J. Trop. Meteor., 2005, 21(3): 301-308.

[9] Shanghai Typhoon Institute of the China Meteorological Administration. Climatological Atlas for Tropical Cyclones Affecting China [M]. Shanghai: Shanghai Typhoon Institute of the China Meteorological Administration. 2007.

[10] LIN Hui-juan, ZHANG Yao-cun. Climatic features of the tropical cyclone influencing China and its relationship with the sea surface temperature in the Pacific Ocean [J]. J. Trop. Meteor., 2004, 20(2): 218-224.

[11] REN Fu-Min, WANG Yong-mei, WANG Xiao-ling, et al. Estimating tropical cyclone precipitation from station observations [J]. Adv. Atmos. Sci., 2007, 24(4): 700-711.

[12] WANG Yong-mei, REN Fu-min, WANG Xiao-ling, et al. The Study on the objective technique for partitioning tropical cyclone precipitation in China [J]. Meteor. Mon., 2006, 32(3): 6-10.

**Citation:** SUN Lin-hai, AI Wan-xiu, SONG Wen-ling et al.. Study on climatic characteristics of China-influencing tropical cyclones. *J. Trop. Meteor.*, 2011, 17(2): 181-186.



© 1994-2011 China Academic Journal Electronic Publishing House. All rights reserved. http://www.cnki.net

# 基于非线性相似度量方法研究中国季节划分*

孙树鹏[1)] 张 璐[1)] 侯 威[2)†] 封国林[2)3)]

1)(兰州大学大气科学学院,兰州 730000)

2)(国家气候中心,北京 100081)

3)(北京师范大学全球变化与地球系统科学研究院,地表过程与资源生态国家重点实验室,北京 100875)

(2010 年 3 月 9 日收到;2010 年 5 月 24 日收到修改稿)

利用中国气象局 1961—2008 年 752 个站点的候平均气温、气压、相对湿度和降水量资料,运用候平均气温划分方法、非线性相似度量方法和季节内离差最优分割方法,对中国的四季进行了划分,并研究了中国四季起始时间的空间分布. 用多要素构造了描述气候状态的变量,以气候状态在不同季节间的转折变化为切入点,并与传统季节划分方法进行了对比研究,验证了非线性相似度量方法的可行性,得到了以下研究结果:一是多要素比单一的温度要素更全面贴切地描述气候状态的变化,划分结果更体现出大气环流形势和大气活动中心等的季节变化;二是从气候状态转折角度考虑季节划分是可行的,揭示了季节转换时大气系统的调整和转折变化,体现了大气系统在季节内保持相对平稳的特征,在季节间发生较大的调整的观测事实.

**关键词:** 季节划分, 非线性相似度量方法, 季节内离差最优分割法

**PACS:** 92.05.Fg, 92.60.Ry

## 1. 引 言

早在 1934 年,张宝堃[1]提出采用当地候平均气温来划分四季;张家诚和林之光[2]、缪启龙和王勇[3]先后利用该方法研究了中国的四季分布情况;1956 年刘匡南和钨鸿勋[4]从周期降水总量、气温的演变、活动中心的变化等角度探讨了中国的季节划分问题;曾庆存等[5—7]提出利用两个场的相关系数作为其相似性度量指标,并由此定义大气环流的季节划分标准;董文杰等[8]根据各测站多年平均温度序列定义了适合其自身季节变化的温度判据,并考察了季节变化对全球增暖的响应.

季节变化可以看做是当地的天气气候系统在太阳辐射和下垫面性质等外强迫影响下,受大尺度甚至全球天气气候状态影响而发生的自身性质的演变. 季节变化除了受太阳直射角变化影响外,更主要是受大气环流和天气系统变化的影响,所以季节变化体现在天气气候系统的各个方面,包括温度、气压、相对湿度、风和降水量等各气象要素. 本文选取候平均气温、气压、相对湿度和降水量等四个要素,然后以其经验正交函数(EOF)分解第一特征向量所占总体解释方差的百分比为权重系数,构造气候状态变量 $\boldsymbol{F}$ 来考察天气气候系统的季节变化. 气候状态的演变在季节内相对平稳,在季节间有较大的转折变化,因此本文以气候状态在不同季节间的转折变化为切入点,考虑气候状态与四季典型状态之间相似性度量的变化情况进行季节划分的研究,且与"候平均气温划分方法"和"季节内离差最优分割法"进行了对比分析.

## 2. 资料和方法

### 2.1. 资料

资料来源于国家气象信息中心提供的中国 752 个地面气象观测站气候资料数据集. 资料预处理如下:1)选择满足 1961—2008 年连续观测要求的站

* 国家自然科学基金(批准号:40875040,40930952)、公益性行业(气象)科研专项基金(批准号:GYHY200806005)和国家重点基础研究发展计划(批准号:2006CB400503)资助的课题.

† 通讯联系人. E-mail: houwei@cma.gov.cn

©2011 中国物理学会 Chinese Physical Society 

点,经检验有 388 个站点的日平均气压、平均气温、平均相对湿度和日降水量四个要素满足要求,个别缺测用插值方法补齐;2)按照每旬两候、每年 72 候划分,计算候平均值;3)将上述候平均资料插值到范围为 15°N—55°N,70°E—140°E 分辨率为 2.5° × 2.5°的网格. 需要说明的是,388 个站点的分布是东部密集西部稀疏,青藏高原西部区域几乎没有站点,因此本文主要研究区域是青藏高原中部以东的中国大部分地区.

## 2.2. 方法

### 2.2.1. 非线性相似度量方法

非线性相似度量方法是基于非线性转折检测的相似性度量季节划分方法,利用多气象要素构造气候状态变量 $\boldsymbol{F}$,并提取其在四个季节的典型状态,然后分别计算各时段 $\boldsymbol{F}$ 与四季典型状态之间的相关系数作为其相似性度量,并利用非线性转折检测方法把该序列的转折点作为季节交替的界限. 具体步骤如下.

1)构造气候状态变量 $\boldsymbol{F}$. 为全面体现气候状态的季节变化,采用候平均的气温、气压、相对湿度和降水量等四个要素从多要素角度进行季节划分. 由于各要素对季节变化的贡献和响应程度不同,故对以上四个要素分别进行 EOF 分解,以其第一特征向量所占总体解释方差的百分比为权重系数,构造气候状态变量 $\boldsymbol{F}=(\alpha_1 P,\alpha_2 T,\alpha_3 H_{\mathrm{R}},\alpha_4 R)$,其中 $P,T,H_{\mathrm{R}},R$ 分别为气压、气温、相对湿度和降水量,在本文中相对应的权重系数分别为:$\alpha_1=0.805,\alpha_2=0.976,\alpha_3=0.451,\alpha_4=0.776$.

2)提取气候状态变量 $\boldsymbol{F}$ 在四个季节的典型状态. 对于单站点或某区域可以从经验角度来计算提取,但因全国范围气压、降水等的时空分布差异很大,无法直接确定,所以先利用相似性度量方法初步划分四季,然后对各地分别选取其最合适的四季典型时段及其对应的 $\boldsymbol{F}$ 典型状态.

取 1 月份和 7 月份多年平均值 $\boldsymbol{F}_{\mathrm{w}}$ 和 $\boldsymbol{F}_{\mathrm{s}}$,分别作为冬季和夏季的典型气候状态. 首先计算并消去其公共部分 $\boldsymbol{F}^*=\frac{1}{2}(\boldsymbol{F}_{\mathrm{w}}+\boldsymbol{F}_{\mathrm{s}})$ 得到偏差量 $\boldsymbol{F}'_{\mathrm{w}}$ 和 $\boldsymbol{F}'_{\mathrm{s}}$,并计算气候状态变量的偏差量 $\boldsymbol{F}'$,其中 $\boldsymbol{F}'=\boldsymbol{F}-\boldsymbol{F}^*$. 利用曾庆存和张邦林[5]提出的两个场相似性度量指标的计算方法,得到 $\boldsymbol{F}'$ 与 $\boldsymbol{F}'_{\mathrm{w}}$ 的相关系数 $r$

$$r\equiv(\boldsymbol{F}',\boldsymbol{F}'_{\mathrm{w}})/[\,\|\boldsymbol{F}'\|\cdot\|\boldsymbol{F}'_{\mathrm{w}}\|\,]. \qquad (1)$$

(1)式右端各变量均为矢量,则内积$(\boldsymbol{F}',\boldsymbol{F}'_{\mathrm{w}})$即为矢量的标量积,范数可通过内积得到 $\|\boldsymbol{F}'\|^2=(\boldsymbol{F}',\boldsymbol{F}')$. 参照文献[5]的划分标准,当 $0.5<r\leqslant 1$ 时,为冬季;当 $-0.5\leqslant r\leqslant 0.5$ 时,为春季或秋季过渡季节;当 $-1\leqslant r<-0.5$ 时,为夏季.

在上述初步划分的基础上,对每个站点取各季节中间的 4—6 候,计算得到四季的典型状态 $\boldsymbol{F}_{\mathrm{spr}}$(春季),$\boldsymbol{F}_{\mathrm{sum}}$(夏季),$\boldsymbol{F}_{\mathrm{fal}}$(秋季)和 $\boldsymbol{F}_{\mathrm{win}}$(冬季).

3)在每两个相邻季节间利用相似性度量方法,计算并得到各时段 $\boldsymbol{F}$ 与上述四季典型状态间的相似性度量序列. 如在确定春夏季交替日期时,利用 $\boldsymbol{F}_{\mathrm{spr}}$ 和 $\boldsymbol{F}_{\mathrm{sum}}$,计算并消去其公共部分 $\boldsymbol{F}^*_{\mathrm{ss}}=\frac{1}{2}(\boldsymbol{F}_{\mathrm{spr}}+\boldsymbol{F}_{\mathrm{sum}})$,得到 $\boldsymbol{F}'_{\mathrm{spr}}$ 和 $\boldsymbol{F}'_{\mathrm{sum}}$. 按照(1)式计算 $\boldsymbol{F}'$ 与 $\boldsymbol{F}'_{\mathrm{sum}}$(或 $\boldsymbol{F}'_{\mathrm{spr}}$)之间的相关系数,得到春夏季的相似性度量序列.

4)检测转折点,确定季节交替时间. 由于季节内气候状态变化相对平稳,季节间存在一定程度的转折,故对上述四条序列的相应时间段进行转折检测,即可得到相应季节的起始时间. 检测转折有多种方法[9—26],本文采用变点检测方法[10—13],这是一种对时间序列检测转折点简单却行之有效的方法. 步骤如下:

i)将序列$\{x_i\mid i=1,2,\cdots,N\}$从小到大按顺序排列,由此得到每个元素的顺序位置(秩序,rank),记为序列$\{r_i\mid i=1,2,\cdots,N\}$;

ii)对秩序序列$\{r_i\mid i=1,2,\cdots,N\}$计算每个元素的前 $n$ 项和,有

$$W_j=\sum_{i=1}^{j}r_i \qquad (j=1,2,\cdots,N-1); \qquad (2)$$

iii)对序列$\{x_i\mid i=1,2,\cdots,N\}$中的每个元素位置,计算

$$2W_j-j(N+1) \qquad (j=1,2,\cdots,N-1); \qquad (3)$$

iv)设

$$K_{m,n}=\max|2W_j-j(N+1)| \qquad (j=1,2,\cdots,N-1), \qquad (4)$$

其中,最大值 $K_{m,n}$ 所在的位置 $j$ 即为该序列转折变点所在的位置.

### 2.2.2. 季节内离差最优分割方法

由于季节发生改变时,地面形势和各要素时空分布发生显著改变,而在季节内则保持相对的稳定. 因此可以利用气候状态变量 $\boldsymbol{F}$ 在季节内的离差变化进行季节划分,即最优分割法,它是针对有序样本序列利用各时段内数据的方差来表征数据的变化幅度进行分类的一种统计方法[27].

## 3. 中国四季的划分结果和比较

### 3.1. 候平均气温划分方法

对中国多年平均(1961—2008 年)的候平均气温,按照张宝堃[1]提出的方法和标准进行划分,即候平均气温小于10 ℃为冬季,10—22 ℃为春季或秋季,大于22 ℃为夏季,由此得到四季起始候数的分布(图略,记为方法一). 其主要分布规律:1)中国的春、夏两季是从南方先开始,然后逐步向北推进;秋、冬两季则先从北方开始,然后逐步向南推进;2)中国四季的起始时间纬向带状分布特征比较明显,南方和北方四季起始时间差异较大;3)在一定程度上体现了海陆位置和海拔等的影响,如夏季从长江中游地区向北推进到华北时,在沿海地区稍有滞后;4)一般来讲,春、秋两季是过渡季节,夏、冬两季是比较典型的季节,而该方法对冬和夏两季划分时,在华南、东北和高原地区等不能给出较恰当的划分结果,说明该方法存在一定的局限性.

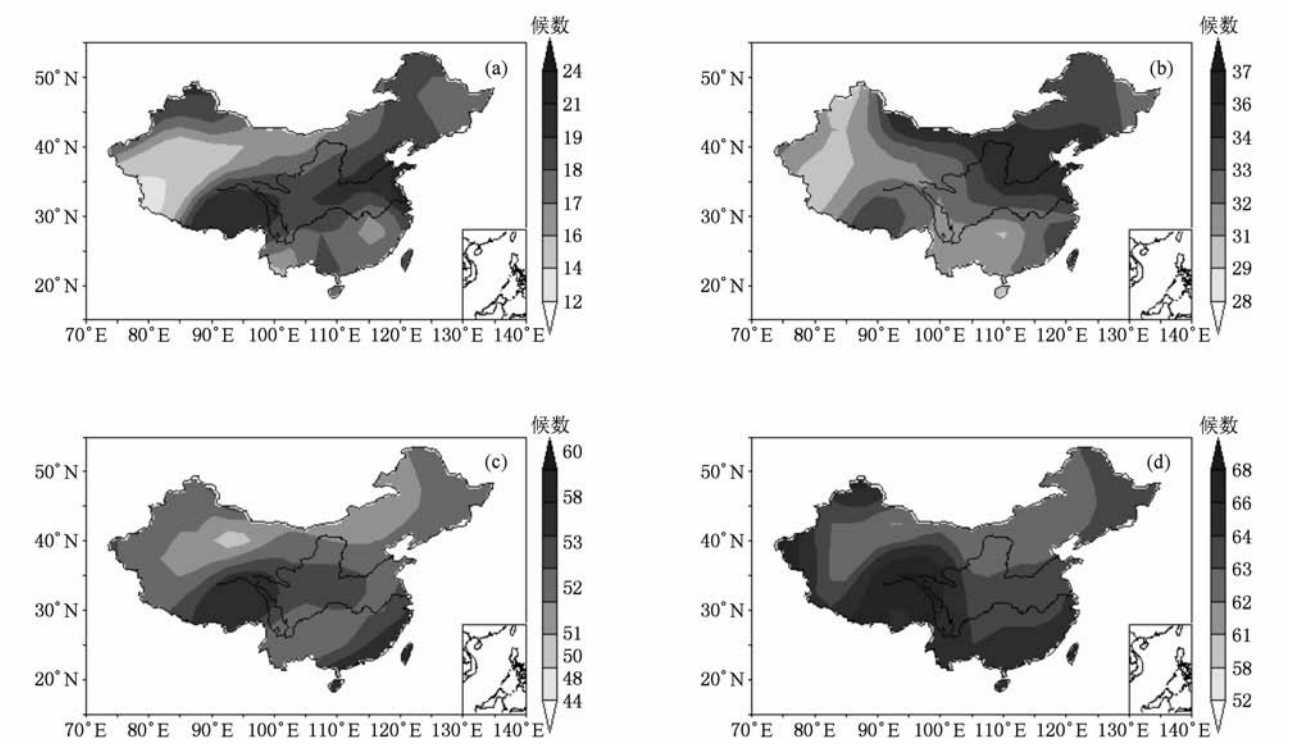


图1 由方法二得到的中国多年平均四季起始候数分布图 (a)春季,(b)夏季,(c)秋季,(d)冬季

### 3.2. 非线性相似度量方法

利用中国多年(1961—2008 年)的候平均气温、气压、相对湿度和降水量,按照非线性相似度量方法得到四季起始候数的分布(图1,记为方法二). 由图1 可见,1)春、夏两季起始时间分布较为类似,秋、冬两季分布相似. 中国地处东亚季风区,在夏半年盛行夏季风,冬半年盛行冬季风,分别对应一种相对稳定的环流形势. 而春和秋两季是过渡季节,是地面环流调整并趋于稳定的时期. 由图1(a),(b)可见,春、夏两季首先从华南地区开始,然后向北推进,华北地区北部及其周边地区开始最晚,这与夏季环流形势的建立和向北推进相一致. 而东北东部和北部地区略早于华北北部地区,可能是因为季风性夏季环流向北推进影响该地之前,东北地区的东部和北部的局地环流形势和天气气候特征已经基本趋于稳定. 秋、冬两季的分布图则反映了冬季环流形势建立和逐步向南推进的过程. 2)方法二的划分结果区域特征更加明显,受太阳直射角影响的纬向带状分布特征被弱化. 由于是从多要素角度考虑气候状态的季节变化,比方法一更凸显了天气气候系统在季节转换时的影响,体现了各地气候状

态的季节变化特征. 3)方法二从各区域的局地气候特征出发,确定出符合当地四季典型特征的气候状态变量 $\boldsymbol{F}$,从而进行四季划分. 充分反映了山脉、海陆位置等对局地气候状态变化的影响.

### 3.3. 方法二与方法一的比较

方法一采用单要素固定阈值进行季节划分,方法二利用多要素从局地气候特征转折角度确定季节起始时间,为进一步比较两种方法,给出其差值的空间分布(图2). 由图2(a)可见春季在长江中下游和黄河两侧及中间地带,两种方法的结果比较接近,相差在 ±2 候以内. 但在中国北方和西北大部分地区,方法一比方法二春季起始晚,在华南地区则较早,相差在6候以上. 图2(b)为夏季分布图,方法一比方法二提前2候以上,南岭地区甚至提前6候以上. 且方法一对于青藏高原和东北北部的部分地区不能很好地划分出夏季;而对于华北平原南部到华南大部分地区而言,两种方法差别较小. 这是因为如果单纯从温度的角度分析,海南和华南部分地区很早(最早2,3月份)就达到夏季的标准,然而这时控制该地的夏季环流形势还没有真正建立起来. 由图2(c),(d)可见,在中国北方和西北地区秋、冬两季方法一比方法二早2候以上,而在华南地区则晚2候以上,在华南沿海、东北北部和高原地区甚至相差6候以上,这主要是由方法一的单一划分标准所致.

方法二较方法一更突出地考虑了季节间气候状态的转折变化. 因为季节交替过程中有一些天气过程反复发生,气候状态多变,可能导致单要素序列出现一些振荡变化,这时利用阈值便不易确定出季节分界,而方法二可以通过非线性转折检测方法更准确地确定季节交替时间.

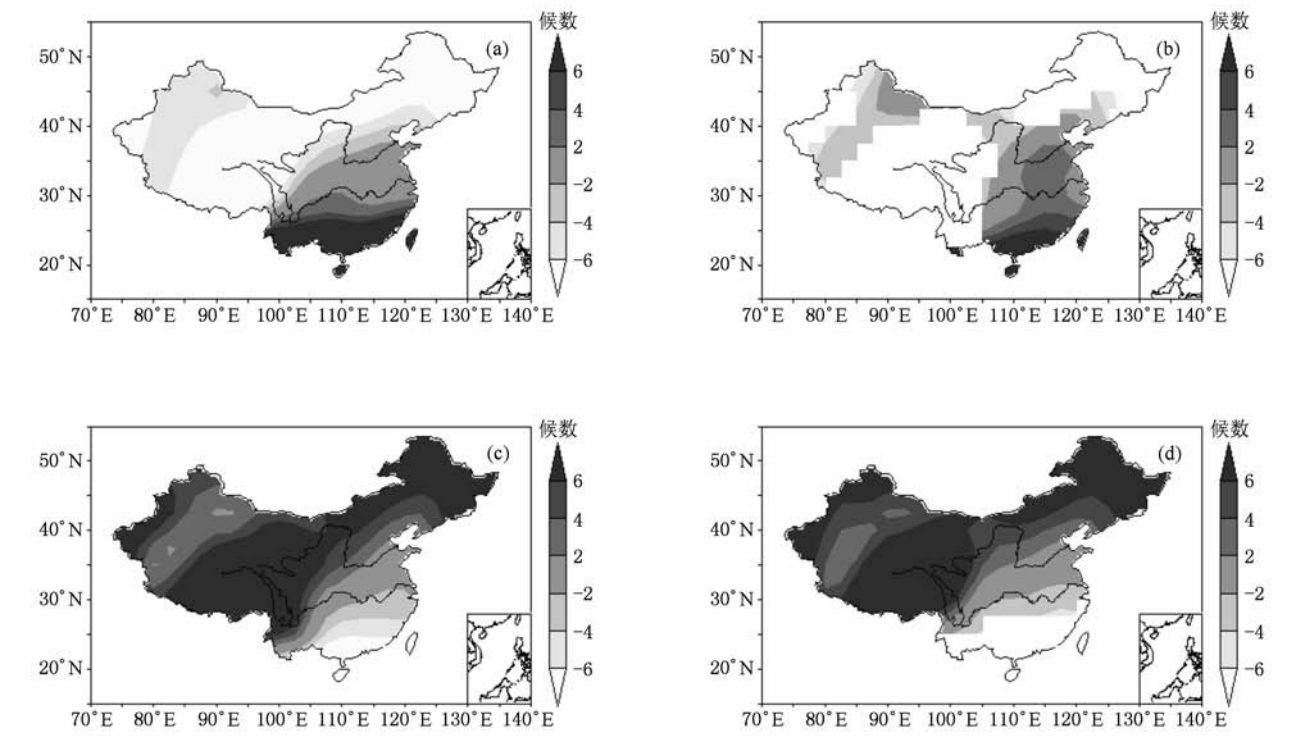


图2 由方法二减方法一得到的中国多年平均四季起始候数差值分布图 (a)春季,(b)夏季,(c)秋季,(d)冬季

### 3.4. 季节内离差最优分割法

利用中国多年(1961—2008年)的候平均气温、气压、相对湿度和降水量,采用多要素的最优分割法,从一年中气候状态的总体变化角度进行季节划分,得到春夏秋冬四季起始候数的分布图(图3,记为方法三). 由图3可见,1)方法三与方法二结果大致相似,四季的起始候数分布都反映了较明显的区域特征,体现了气候状态变化对季节变化的影响,验证了利用多要素并从季节间气候状态转折的角度进行季节划分的可行性. 2)反映了中国春、夏两季先从南方开始然后向北推进,但北方和华北地区

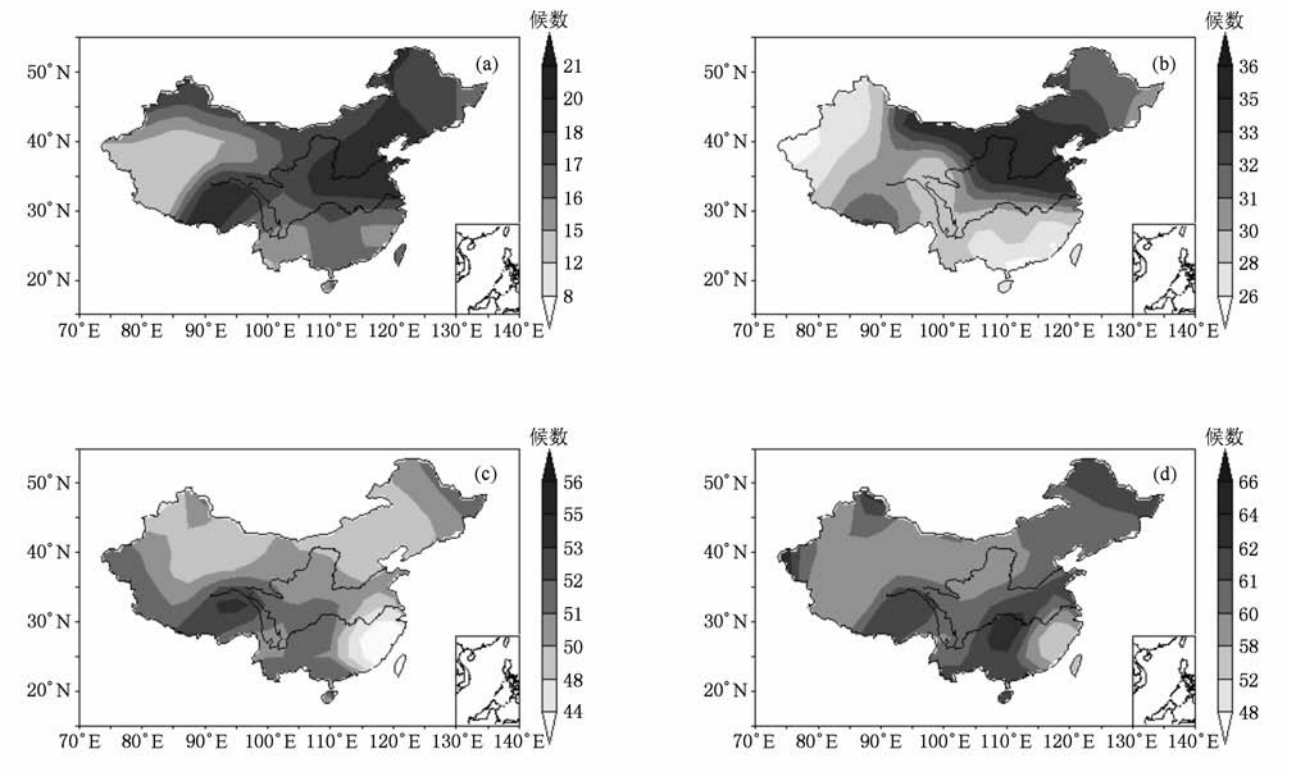


图3 由方法三得到的中国多年平均四季起始候数分布图 (a)春季,(b)夏季,(c)秋季,(d)冬季

要稍迟于东北地区,反映了不同地域局地典型季节气候状态的差异. 3)该方法在对中国东南部地区进行季节划分未能通过显著性水平 0.05 的统计检验,不能得到恰当的划分结果,显示了该方法的局限性. 这可能是因为该地区受北方冬季环流形势影响较弱,而受海洋的外强迫影响相对较强,尤其进行多年平均处理后秋、冬两季的气候状态变化幅度相对较小,从离差角度难以区分明显的季节变化.

### 3.5. 三种方法的比较

方法一采用气温单要素来描述气候状态的季节变化,其划分结果纬向带状分布特征比较明显,方法二和方法三则采用气温、气压、相对湿度和降水量等多要素,构建了气候状态变量 $\boldsymbol{F}$ 来描述天气气候系统的季节变化,多要素比单一温度要素更全面准确地刻画局地气候状态的变化特征,因此方法二和方法三的结果更体现出大气系统的影响范围和变化特征,强化了区域特征的局地影响.

方法一对全国采用同一个阈值标准(10℃/22℃)进行划分,而中国幅员辽阔,南北各地气温变化差异较大,所以划分结果南方与北方季节起始时间差异较大、梯度较为明显,且在华南、东北和青藏高原地区不能很好地区分出冬季或夏季. 方法二则针对各地的局域气候变化特征,从其多年平均的气候状态中确定各个季节典型的气候状态和划分标准,方法三从各地年尺度气候状态变化角度进行划分. 这样使得它们对各地的适用性更好,在东北和青藏高原等地区也有较好的适用性. 受相同属性天气气候系统控制的区域,其四季典型气候状态较为接近,所以在方法二和方法三的结果中区域性特征比较明显,南北变化梯度相对较小,更多地反映了大尺度天气气候系统对季节变化的影响. 相对于方法一,方法二和方法三之间的差异较小. 方法二与方法三划分结果中国大部分地区都在 3 候以内,但方法三在对有些地区(中国东南沿海部分地区)进行划分时不能很好地通过统计检验,这是该方法的一个缺陷.

综上所述,本文认为方法二即非线性相似度量方法是一个更为客观的季节划分方法,该方法利用多要素并从季节间气候状态转折的角度进行季节划分,得到的中国四季起始时间分布,比较符合各地天气气候系统的季节变化特征,对全国各地不同气候区适用性都比较好.

## 4. 结论和讨论

分别利用候平均气温划分方法、非线性相似度量方法和季节内离差最优分割方法对中国进行四季划分. 方法一得到的结果纬向带状分布特征比较明显,南方与北方差异较大;方法二和方法三利用多 要素构建气候状态变量,更全面准确地描述气候状态的季节变化特征,划分结果强化了区域特征的局地影响,南方与北方差异相对较小,更贴近季节环流形势的变化. 相比于方法一,方法二和方法三的突出之处在于可以从季节间气候状态转折角度考虑季节划分,更好地反映大气系统在季节内保持相对平稳,在季节间发生较大的调整的观测事实. 但因方法三对于有些地区还存在适用的局限性,所以本文认为方法二即非线性相似度量方法,是一个较为客观可行的季节划分方法.


[1] Zhang B K 1934 *Acta Geog. Sin.* **1** 1 (in Chinese) [张宝堃 1934 地理学报 **1** 1]

[2] Zhang J C, Lin Z G 1985 *Climate of China* (Shanghai: Shanghai Scientific and Technical Publishers) p55 (in Chinese) [张家诚、林之光 1985 中国气候(上海:上海科学技术出版社) 第 55 页]

[3] Miu Q L, Wang Y 2007 *Annual Conference of China Meteorological Society* Guangzhou, November 23—25, 2007 p693 (in Chinese) [缪启龙、王 勇 2007 中国气象学会 2007 年年会 第 693 页]

[4] Liu K N, Wu H X 1956 *Acta Meteorol. Sin.* **27** 219 (in Chinese) [刘匡南、邬鸿勋 1956 气象学报 **27** 219]

[5] Zeng Q C, Zhang B L 1992 *Chin. J. Atmos. Sci.* **16** 641 (in Chinese) [曾庆存、张邦林 1992 大气科学 **16** 641]

[6] Zhang B L, Zeng Q C 1998 *Chin. J. Atmos. Sci.* **22** 129 (in Chinese) [张邦林、曾庆存 1998 大气科学 **22** 129]

[7] Xue F, Lin Y H, Zeng Q C 2002 *Chin. J. Atmos. Sci.* **26** 307 (in Chinese) [薛 峰、林一骅、曾庆存 2002 大气科学 **26** 307]

[8] Dong W J, Jiang Y D, Yang S 2010 *Clim. Change* **99** 81

[9] Feng G L, Dong W J, Gong Z Q, Hou W, Wan S Q, Zhi R 2006 *Nonlinear Theories and Methods on Spatial-Temporal Distribution of the Observational Data* (Beijing: Metrological Press) p7 (in Chinese) [封国林、董文杰、龚志强、侯 威、万仕全、支 蓉 2006 观测数据非线性时空分布理论和方法(北京:气象出版社) 第 7 页]

[10] Pettitt A N 1979 *Appl. Statist.* **28** 126

[11] Pettitt A N 1980 *Biometrika* **67** 79

[12] Pettitt A N 1980 *J. Statist. Comput. Simul.* **11** 261

[13] Wei F Y 1999 *Modern Technology of Statistical Climate Detection and Prediction* (Beijing: China Meteorological Press) p72 (in Chinese) [魏凤英 1999 现代气候统计诊断与预测技术(北京:气象出版社)第 72 页]

[14] Feng G L, Gong Z Q, Dong W J, Li J P 2005 *Acta Phys. Sin.* **54** 5494 (in Chinese) [封国林、龚志强、董文杰、李建平 2005 物理学报 **54** 5494]

[15] Feng G L, Gong Z Q, Zhi R 2008 *Acta Meteorol. Sin.* **66** 892 (in Chinese) [封国林、龚志强、支 蓉 2008 气象学报 **66** 892]

[16] Hou W, Feng G L, Dong W J, Li J P 2006 *Acta Phys. Sin.* **55** 2663 (in Chinese) [侯 威、封国林、董文杰、李建平 2006 物理学报 **55** 2663]

[17] Gong Z Q, Feng G L, Dong W J, Li J P 2006 *Acta Phys. Sin.* **55** 3181 (in Chinese) [龚志强、封国林、董文杰、李建平 2006 物理学报 **55** 3181]

[18] Wang Q G, Zhang Z P 2008 *Acta Phys. Sin.* **57** 1976 (in Chinese) [王启光、张增平 2008 物理学报 **57** 1976]

[19] Feng G L, Dong W J, Jia X J, Cao H X 2002 *Acta Phys. Sin.* **51** 1181 (in Chinese) [封国林、董文杰、贾晓静、曹鸿兴 2002 物理学报 **51** 1181]

[20] Feng G L, Dai X G, Wang A H, Chou J F 2001 *Acta Phys. Sin.* **50** 606 (in Chinese) [封国林、戴新刚、王爱慧、丑纪范 2001 物理学报 **50** 606]

[21] He W P, Feng G L, Wu Q, Wan S Q, Chou J F 2008 *Nonlin. Processes Geophys.* **15** 601

[22] Zhi R, Lian Y, Feng G L 2007 *Acta Phys. Sin.* **56** 1837 (in Chinese) [支 蓉、廉 毅、封国林 2007 物理学报 **56** 1837]

[23] Xiong K G, Yang J, Wan S Q, Feng G L, Hu J G 2009 *Acta Phys. Sin.* **58** 2843 (in Chinese) [熊开国、杨 杰、万仕全、封国林、胡经国 2009 物理学报 **58** 2843]

[24] He W P, Feng G L, Dong W J, Li J P 2005 *Chin. Phys.* **14** 21

[25] Zhi R, Gong Z Q 2008 *Acta Phys. Sin.* **57** 4629 (in Chinese) [支 蓉、龚志强 2008 物理学报 **57** 4629]

[26] Hou W, Feng G L, Gao X Q, Chou J F 2005 *Acta Phys. Sin.* **54** 2441 (in Chinese) [侯威、封国林、高新全、丑纪范 2005 物理学报 **54** 2441]

[27] Huang J Y 1990 *Meteorological Statistical Analysis and Prediction* (Beijing: China Meteorological Press) p265 (in Chinese) [黄嘉佑 1990 气象统计分析与预报方法(北京:气象出版社)第 265 页]

# A non-linear similarity method for season division in China*

Sun Shu-Peng[1)] Zhang Lu[1)] Hou Wei[2)†] Feng Guo-Lin[2)3)]

1) (*College of Atmospheric Sciences, Lanzhou University, Lanzhou* 730000, *China*)

2) (*National Climate Center, Beijing* 100081, *China*)

3) (*State Key Laboratory of Earth Surface Processes and Resource Ecology, College of Global Change and Earth System Science, Beijing Normal University, Beijing* 100875, *China*)

(Received 9 March 2010; revised manuscript received 24 May 2010)

Abstract

Using the daily observational data of temperature, pressure, relative humidity and precipitation in 752 stations of China from 1961 to 2008, three methods of division of season, i. e. Zhang's method, non-linear similarity method and Fisher optimal dissection method are applied to different meteorological elements fields of China. Results indicate that division of season through multi-variables methods is more reasonable than single variable ones, especially in non-linear similarity method and Fisher optimal dissection method. When considering the seasonal climate transition between successive seasons, the results are in good accordance with actual observations. As a result we recommend the non-linear similarity method as a better way of season division.

**Keywords**: season division, non-linear similarity method, Fisher optimal dissection method

**PACS**: 92.05.Fg, 92.60.Ry

* Project supported by the National Natural Science Foundation of China (Grant Nos. 40875040, 40930592), the Special Scientific Research Fund of Meteorological Public Welfare Profession of China (Grant No. GYHY200806005) and the State Key Development Program for Basic Research of China (Grant No. 2006CB400503).

† Corresponding author. E-mail: houwei@cma.gov.cn

www.climatechange.cn



文章编号：1673-1719 (2011) 02-0085-05

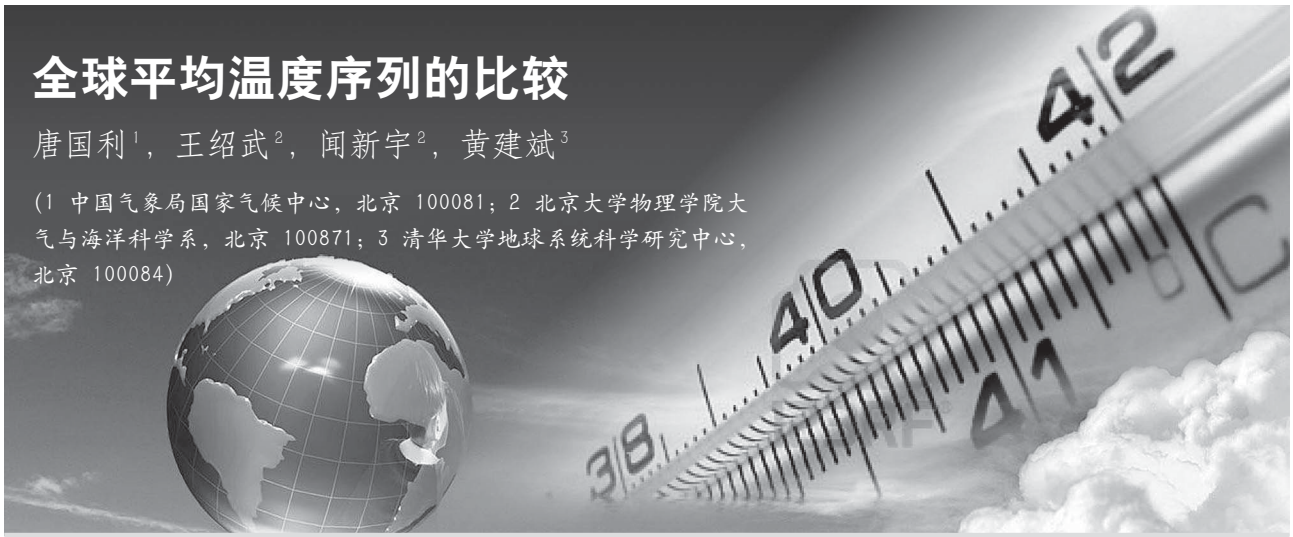

# 全球平均温度序列的比较

唐国利[1]，王绍武[2]，闻新宇[2]，黄建斌[3]

(1 中国气象局国家气候中心，北京 100081；2 北京大学物理学院大气与海洋科学系，北京 100871；3 清华大学地球系统科学研究中心，北京 100084)

**摘 要**：着重评述了目前国际上常用的3个全球平均温度序列：HadCRUT3、NCDC及GISS。后两个序列1982年之后引入了卫星观测资料。NCDC对资料作了插补，建立了1880—2009年覆盖面完整的序列。HadCRUT3序列所显示的近10年变暖的停滞可能主要是缺少极区资料造成的。NCDC与GISS两个序列依然保持约0.1 ℃/10a的增温。3个序列1910—2009年的变暖趋势十分接近，在0.70～0.75 ℃/100a之间。

**关键词**：全球平均；温度；HadCRUT3；NCDC；GISS

**中图分类号**：P467 **文献标识码**：A

## 引 言

建立一个能代表全球平均温度变化的时间序列是气候变化研究的基本任务，只有建立了这样的序列才能更准确地判断全球气候变暖。同时，确定全球气候变暖的程度、空间分布特征以及随时间的变化特征又是气候变化归因研究的基础。因此，对全球平均温度序列及其资料和方法进行分析具有重要意义。

全球平均温度的研究始于19世纪后期，随着观测资料的不断积累和研究的展开，陆续有不少学者建立了全球平均温度序列，并不断进行改进和完善[1−3]。大体可将全球平均温度序列的研究划分为3个阶段：1970年代之前、1980—1990年代以及2000年代。前两个阶段可以称为早期，第三个阶段称为现代。

## 1 早期研究

第一个阶段的研究可以认为是开创性的。出于了解全球气候是否存在变暖或变冷趋势的需要，从19世纪后期开始就有人研究全球平均温度。到20世纪中期，先后有30多位作者建立了自己的全球平均温度序列[1−3]，其中Mitchell[4]的工作最具有代表性。由于当时所能使用的资料仅有100～200个测站，只能按纬度带求平均，例如每30个纬度计算一个平均值，将每5年平均与1880—1884年的平均进行比较。由于只有陆地及少数岛屿测站，因此只能反映陆面气温的变化。尽管如此，Mitchell[4]在1960年代初就确认了1940年代的变暖。从观测事实分析的角度看，

**收稿日期**：2010-07-16； **修回日期**：2010-09-03

**资助项目**：国家重点基础研究发展规划项目(973)课题（2010CB428401）；国家“十一五”科技支撑计划项目“气候变化的检测和预估技术研究”（2007BAC03A01）；中国气象局气候变化专项（540000G010C01）

**第一作者**：唐国利（1960—），男，正研级高工，主要从事气候和气候变化研究。E-mail: tanggl@cma.gov.cn

这应该是全球变暖研究的一个良好开端。

1980—1990年代应用的测站数大为增加，Jones等[5-6]、Hansen等[7]及Vinnikov等[8]先后建立了全球温度序列。他们应用的测站数见表1。

表1 1980年代全球温度序列应用的测站数

Table 1 Numbers of meteorological stations used for the reconstruction of global mean temperature series in 1980s

| 作者 | 北半球 | 南半球 | 全球 |
|---|---|---|---|
| Jones等[5-6] | 2666 | 610 | 3276 |
| Hansen等[7] | 1902 | 738 | 2640 |
| Vinnikov等[8] | 301 | 265 | 566 |

当时的月平均温度资料主要是世界天气记录（World Weather Records）和每月世界气候资料（Monthly Climatic Data for the World）。3个序列的分析方法各不相同，Jones等[5-6]首先建立5°×10°（纬度×经度）格点温度序列，再按纬度面积加权求半球及全球平均，60°S以南无记录。Hansen等[7]则把全球分为面积相等的80个区，先建立每个区的序列，再合成为半球及全球序列。Vinnikov等[8]应用的测站相对较少，先计算每30个纬度带的平均，再建立半球及全球平均，南半球仅到60°S。

尽管这3个序列应用的测站数差异较大，分析方法也不相同，但是得到的全球平均温度序列相关系数很高，在0.94～0.95之间[5, 8]。这一时期的特点是建立了对陆地面积有较好代表性的温度序列，但是尚未引进海面温度观测资料。

## 2 现代全球温度序列

仅有陆地上的观测资料显然不具有全球代表性。第三个阶段的特点就是在序列中引入海洋资料。最初曾试图应用甲板上观测的气温，继而发现这样的观测受甲板反射影响较大，以后又试验用夜间甲板上观测的气温，但最后证明还是海温有较好的代表性[9-10]。现在的全球温度序列都采用陆面气温观测与海面温度（SST）观测结合得到全球平均温度，也称为地球表面温度（earth surface temperature）。下面分别概述目前比较常用的3个全球平均温度序列。

### 2.1 HadCRUT3序列

CRU（Climatic Research Unit）指英国东英吉利大学气候研究部，该研究部整理了全球陆地气温序列[11]。应用5159个测站，其中4167个站有1961—1990年的记录。剔除距平>5σ的数据，按网格面积加权计算5°×5°（经度×纬度）格点平均，得到北半球和南半球的序列，然后再合成为全球平均。这个陆地序列与哈德莱中心（Hadley Centre）的SST结合形成HadCRUT2。

后来CRU的资料又有所改进，并进行了不确定性分析、讨论了误差范围，再与改进的哈德莱中心的SST序列合并形成目前政府间气候变化专门委员会（IPCC）引用的HadCRUT3[12]。陆地测站为4500个，其空间分辨率不再限于固定的5°×5°（经度×纬度）格点，更便于与模式结果比较。

陆面气温变化的不确定性主要来源于3个方面：1) 测站温度误差，包括观测误差、均一性误差、标准值误差及计算误差；2) 资料覆盖误差；3) 偏差误差，如城市热岛效应。值得一提的是资料覆盖误差，利用50年模拟给出的具有完全覆盖面的再分析资料，可以计算与实际覆盖面相同的面积所得平均温度与完全覆盖面平均温度的差，由此估计资料覆盖不全的影响。关于城市化问题，强调主要考虑城市/农村的对比，但是城市与农村的分类会影响对比结果。在建立序列过程中，剔除了部分城市测站，另有部分测站的序列通过质量控制和均一化处理过程订正。在总不确定性估计中，城市热岛效应导致的误差从1900年开始1σ的标准值为0.055 ℃/100a。这3个不确定性加在一起大约造成温度的低频变化有±0.1 ℃的振幅，形成一个宽约0.2 ℃的范围，即95%误差区间，20世纪中期以来这个范围缩小到0.10～0.15 ℃宽。海温的改进见文献[13]。

### 2.2 NCDC序列

NCDC（National Climatic Data Center）指美国国家气候资料中心。NCDC序列是一个覆盖面完整的序列[14]，全球平均按5°×5°网格面积加权平均得到。其SST的处理很有代表性[15-16]，不仅考虑了观测技术的变化，而且引入了卫星资料。对1941年之

www.climatechange.cn



前的海温去掉约 0.3 ℃的负偏差，因为那时多采用吊桶打水的方式测量温度，而第二次世界大战之后则改用抽水方式测量温度，从而避免了提水过程中蒸发造成的降温。应用 1982 年以后的卫星资料对 SST 序列作插补，具体做法是把温度序列分为高频与低频两部分，低频部分用 10°经纬度格点、15 年滤波，高频部分用滤波后的高频距平，采用 EOT（经验正交遥相关）[17]分析，低频及高频两部分分别内插后再合并，得到完整的 SST 序列。

陆面温度资料来自 GHCN（全球历史气候资料网）[18]，使用了其中的 4400 个测站，以 1961—1990 年为基准期。

### 2.3　GISS 序列

GISS（Goddard Institute for Space Studies）即美国宇航局戈达德空间研究所。Hansen 等[19]把 GISS 序列延伸到 2009 年并对序列的建立与延伸作了全面的回顾，同时还与 HadCRUT3 及 NCDC 两个序列进行了比较。新的 GISS 序列陆面气温资料也来源于 GHCN[18]，选用其中 6300 个测站，剔除距平 > 2.5$\sigma$的记录，并用距格点 1200 km 之内的测站内插，权重与距格点的距离成反比，测站在格点上权重取 1，在 1200 km 处取 0。全球平均方法为先计算 90°～23.6°S、23.6°S～0°、0°～23.6°N 和 23.6°～90°N 4 个纬度带的平均，然后按 0.3：0.2：0.2：0.3 的权重进行面积加权平均。序列有两方面改进：一是过去用纬圈平均求半球或全球平均时以纬圈内有记录的面积为权重，现在则用整个纬圈面积为权重；二是城市化订正，美国区域城、乡划分以卫星观测的夜光为标准，低于 32 μW/(m$^2$·sr·μm) 为农村，高于此值为城市，对美国之外的区域则依人口划分。在未订正情况下 1900—2009 年美国平均增温 0.70 ℃，订正后为 0.64 ℃。而就全球平均温度来看，城市化的影响约为 0.01 ℃，这与全球变暖幅度相比微不足道。

SST 使用哈德莱中心的资料[10]，1982 年之后用经过船舶及浮标站校正的卫星资料[20]，通常写做 HadISST+OISST。

## 3　序列比较

图 1[19]给出 1880—2009 年 HadCRUT3，NCDC 及 GISS 3 个全球平均温度序列。表 2 为本文作者根据上述 3 个序列计算得到的每 10 年的平均温度距平（相对于 1961—1990 年平均值）和近 100 年（1910—2009 年）变化趋势。从图 1 和表 2 可见，3 个序列十分接近。在前 40 年 10 年平均温度距平相差 0.1 ℃左右，20 世纪中期降到 0.05 ℃左右，近 50 年在 0.05 ℃以下。1910—2009 年变暖趋势为 0.70～0.75 ℃/100a。

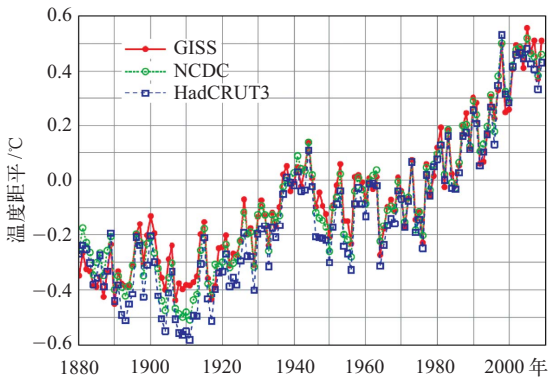


图 1　1880—2009 年全球平均温度距平序列（相对于 1961—1990 年）[19]

Fig. 1　Global mean temperature anomalies for 1880−2009 (relative to 1961−1990) [19]

比较 3 个序列还可以看到一个有意思的现象，HadCRUT3 序列显示 1998 年是最暖年，而 GISS 和 NCDC 序列则显示 2005 年是最暖年，而且 2005 年以来 GISS 序列明显高于 HadCRUT3（图 2a）。造成这一现象的原因，可能主要是 HadCRUT3 序列缺少北极的资料，而这一地区近 10 年的增暖非常显著[19]。有些作者根据 1999—2008 年 HadCRUT3 序列显示的微弱增温认为近 10 年气候变暖停滞了[21−22]。为了分析近 10 年的变化，本文分别计算了 3 个序列 2000—2009 年的增温趋势，结果显示，GISS 和 NCDC 序列分别为 0.12 ℃/10a 和 0.07 ℃/10a，而 HadCRUT3 序列只有 0.03 ℃/10a。上述结果表明，覆盖北极地区的 GISS 序列和 NCDC 序列比 HadCRUT3 序列显示出更强的增暖。文献[19]把 GISS 序列按 HadCRUT3 的格点重新平均后与 HadCRUT3 的结果十分接近

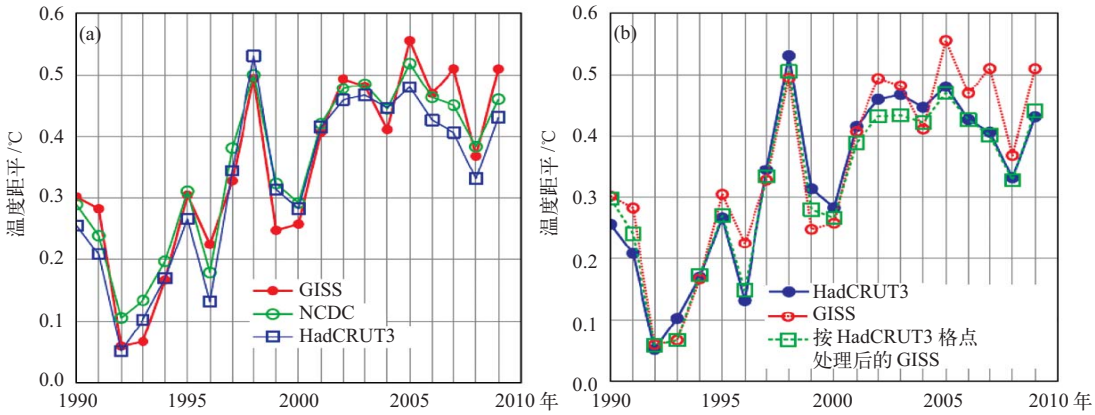


图 2 1990—2009 年全球平均温度距平（相对于 1961—1990 年）[19]

Fig. 2 Global surface temperature anomalies for 1990–2009 (relative to 1961–1990) [19]

表 2 1880—2009 年全球平均温度距平（单位：℃）（相对于 1961—1990 年平均值）及 1910—2009 年变化趋势（单位：℃/100a）

Table 2 Global surface temperature anomalies of decadal average (unit: ℃) during 1880–2009 (relative to 1961–1990) and the trend for 1910–2009 (unit: ℃/100a)

| 时间段 | HadCRUT3 | NCDC | GISS |
|---|---|---|---|
| 1880 年代 | −0.30 | −0.26 | −0.34 |
| 1890 年代 | −0.39 | −0.33 | −0.32 |
| 1900 年代 | −0.44 | −0.38 | −0.33 |
| 1910 年代 | −0.43 | −0.37 | −0.34 |
| 1920 年代 | −0.30 | −0.25 | −0.24 |
| 1930 年代 | −0.13 | −0.10 | −0.11 |
| 1940 年代 | −0.07 | −0.02 | −0.03 |
| 1950 年代 | −0.16 | −0.12 | −0.09 |
| 1960 年代 | −0.12 | −0.07 | −0.08 |
| 1970 年代 | −0.09 | −0.06 | −0.07 |
| 1980 年代 | 0.08 | 0.10 | 0.11 |
| 1990 年代 | 0.24 | 0.27 | 0.25 |
| 2000 年代 | 0.41 | 0.44 | 0.45 |
| 1910—2009 年 | 0.75 | 0.72 | 0.70 |

（图 2b）。这也进一步证明了资料覆盖面不全导致 HadCRUT3 序列近 10 年的增暖偏弱。

## 4 小 结

全球平均温度序列是气候变化检测和归因研究的重要基础。从早期只有少量陆地和岛屿测站到后来引入海洋和卫星资料，全球平均温度研究经历了 3 个发展阶段，其资料质量、空间覆盖和分析方法都有很大改进和提高。本文着重评述和比较了目前国际上常用的 3 个全球平均温度序列，分析表明：3 个序列总体上基本一致，但是早期的差异相对较大，前 40 年每 10 年平均温度距平相差 0.1 ℃左右；各序列给出的近百年（1910—2009年）变暖趋势十分接近，幅度在 0.70～0.75 ℃/100a 之间。不过，根据 2000—2009 年的计算结果，GISS 序列和 NCDC 序列比 HadCRUT3 序列显示出更强的增暖。对各序列资料覆盖范围的分析表明，HadCRUT3 序列缺少北极地区的资料可能是造成这一差异的主要原因。这一现象不仅突出说明了资料覆盖的重要性，而且也在一定程度上解释了 3 个序列早期的差别。■

### 参考文献

[1] Wigley T M L, Angell J K, Jones P D. Analysis of the temperature record [C]// MacCracken M C, Luther F M. Detecting the climatic effects of increasing carbon dioxide, DOE/ER-0235. Washington, DC: US Department of Energy, 1985: 55–90

[2] Ellsaesser H W, MacCracken M C, Walton J J, *et al*. Global climatic trends as revealed by the recorded data [J]. Rev Geophy, 1986, 24: 745–792

[3] Hansen J, Lebedeff S. Global trends of measured surface air temperature [J]. J Geophys Res, 1987, 92: 13345–13372

[4] Mitchell J M. Recent secular changes of global temperature [J]. Ann N Y Acad Sci, 1961, 95 : 235–250

[5] Jones P D, Raper S C B, Bradley R S, *et al*. Northern Hemisphere surface air temperature variations: 1851–1984 [J]. J Climate Appl Meteor, 1986, 25: 161–179

www.climatechange.cn



[6] Jones P D, Raper S C B, Wigley T M L. Southern Hemisphere surface air temperature variations: 1851−1984 [J]. J Climate Appl Meteor, 1986, 25: 1213−1230

[7] Hansen J, Lebedeff S. Global surface temperature: update through 1987 [J]. Geophys Res Lett, 1988, 15: 323−326

[8] Vinnikov K Y, Groisman P Y, Lugina K M. Empirical data on contemporary global climatic changes (temperature and precipitation) [J]. J Climate, 1990, 3: 662−677

[9] Parker D E, Jones P D, Bevan A, *et al*. Interdecadal changes of surface temperature since the 19th century [J]. J Geophys Res, 1994, 99: 14373−14399

[10] Rayner N A, Parker D E, Horton E B, *et al*. Global analyses of sea surface temperature, sea ice, and nigh marine air temperature since the late nineteenth century [J]. J Geophys Res, 2003, 108, 4407, doi: 10.1029/2002 J D002670

[11] Jones P D, Moberg A. Hemispheric and large-scale surface air temperature variations: an extensive revision and an update to 2001[J]. J Climate, 2003, 16: 206−223

[12] Brohan P, Kennedy J J, Harris I, *et al*. Uncertainty estimates in regional and global observed temperature changes: a new data set from 1850 [J]. J Geophys Res, 2006, 111, D12106, doi: 101029/2005 J D006548

[13] Rayner N A, Brohan P, Parker D E, *et al*. Improved analyses of changes and uncertainties in sea-surface temperature measured in-situ since the mid-nineteenth century [J]. J Climate, 2006, 19: 446−469

[14] Smith T M, Reynolds R W. A global merged land-air-sea surface temperature reconstruction based on historical observations (1880−1997) [J]. J Climate, 2005, 18: 2021−2036

[15] Smith T M, Reynolds R W. Extended reconstruction of global sea surface temperatures based on COADS data (1854−1997) [J]. J Climate, 2003, 16: 1495−1510

[16] Smith T M, Reynolds R W. Improved extended reconstruction of SST (1854−1997) [J]. J Climate, 2004, 17: 2466−2477

[17] van den Dool H M, Saha S, Johansson Å. Empirical orthogonal teleconnections [J]. J Climate, 2000, 13: 1421−1435

[18] Peterson T C, Vose R S. An overview of the global historical climatology network temperature database [J]. Bull Amer Meteor Soc, 1997, 78: 2837−2849

[19] Hansen J, Ruedy R, Sato M, *et al*. Global surface temperature change [J]. Rev Geophys, 2010, 48, RG4004, doi: 10.1029/2010RG000345

[20] Reynolds R W, Rayner N A, Smith T M, *et al*. An improved in situ and satellite SST analysis for climate [J]. J Climate, 2002, 15: 1609−1625

[21] Knight J, Kennedy J, Folland C, *et al*. Do global temperature trends over the last decade falsify climate prediction? [J]. Bull Amer Meteor Soc, 2009, 90 (8): S22−23

[22] Kerr R A. What happened to global warming? Scientists say just wait a bit [J]. Science, 2009, 326: 28−29

# Comparison of Global Mean Temperature Series

Tang Guoli[1], Wang Shaowu[2], Wen Xinyu[2], Huang Jianbin[3]

(1 *National Climate Center, China Meteorological Administration, Beijing* 100081, *China*; 2 *Department of Atmospheric and Oceanic Sciences, School of Physics, Peking University, Beijing* 100871, *China*; 3 *The Center for Earth System Science Studies, Tsinghua University, Beijing* 100084, *China*)

**Abstract:** Studies on the reconstruction of global mean temperature series are reviewed. Three series, HadCRUT3, NCDC, and GISS, are described in detail. Satellite data have been used since 1982 in the latter two series. NCDC series provides the most complete coverage among the three series by using statistic interpolation technique. It is found that the pause of global warming in 2000−2009, which is revealed in HadCRUT3 series, is caused by the incompleteness of data coverage. Missing of data over the Arctic reduced the positive anomaly of global mean temperature, for where the local warming was very high recently. GISS and NCDC series show much higher warming trends during the last 10 years. Three series give the nearly same warming trend (0.70−0.75 ℃ /100a) of global mean temperature for 1910−2009.

**Key words:** global mean; temperature; HadCRUT3; NCDC; GISS

陶亦为,孙照渤,李维京,等. ENSO与青藏高原积雪的关系及其对我国夏季降水异常的影响[J]. 气象,2011,37(8):919-928.

# ENSO与青藏高原积雪的关系及其对我国夏季降水异常的影响*

陶亦为[1,2] 孙照渤[1] 李维京[2] 李伟平[2] 左金清[2,3]

1 南京信息工程大学大气科学学院,南京 210044

2 国家气候中心,北京 100081

3 兰州大学大气科学学院,兰州 730000

**提 要**:文章利用1979—2005年Niño3区海温时间序列资料和中国雪深时间序列资料,分析了Niño3区海温与青藏高原积雪之间的关系,两者对我国夏季降水的影响以及两者共同作用下对我国夏季降水的影响。分析结果表明:当前期冬春季Niño3区SST为强暖(强冷)事件与高原积雪显著偏多(显著偏少)共同作用的配置下,我国东部夏季雨带往往偏南(偏北)。从月时间尺度方面,揭示了前期冬春季ENSO和冬春季青藏高原积雪对我国长江以南地区降水异常的影响在夏季各月是不一致的,前期冬春季逐月Niño3区SST和冬春季逐月高原积雪对长江以南地区6月的降水都为正相关,而对8月的降水都为反相关,并且春季逐月Niño3区SST和冬春季逐月高原积雪对长江以南地区7月的降水也都为正相关,另外,春季Niño3区SST和春季高原积雪对长江以南地区6月和7月降水更为重要。

**关键词**:冬春积雪,青藏高原,ENSO,夏季降水,SST

# Relationships Between ENSO and Qinghai-Tibetan Plateau Snow Depth and Their Influences on Summer Rainfall Anomalies in China

TAO Yiwei[1,2] SUN Zhaobo[1] LI Weijing[2] LI Weiping[2] ZUO Jinqing[2,3]

1 College of Atmospheric Sciences, Nanjing University of Information Science and Technology, Nanjing 210044

2 National Climate Centre, Beijing 100081

3 College of Atmospheric Sciences, Lanzhou University, Lanzhou 730000

**Abstract**: Based on the sea surface temperature (SST) in Niño3 region and snow depth from 1979 to 2005, relationships between ENSO and Qinghai-Tibetan Plateau (QXP) snow depth and their influences on summer rainfall in China were investigated, respectively. In addition, the joint influence of ENSO and QXP snow on summer rainfall in China was also analyzed.

The results showed that the summer rainbelt in eastern China often moved southward (northward) only when a strong warm (strong cold) ENSO event and a heavy (light) QXP snow occurred simultaneously during previous winter and spring. Moreover, the monthly Niño3 SST and QXP snow during previous winter and spring both had a positive correlation with the June rainfall over southward of the Yangtze River, while they both had a negative correlation with August rainfall over southward of the Yangtze River. Furthermore, the monthly Niño3 SST during previous spring and the QXP snow during previous winter and spring both had a positive correlation with the July rainfall over southward of the Yangtze River. Moreover, the Niño3 SST and QXP snow during spring had a more important impact on June and July rainfall anomalies over southward of the Yangtze River. It clearly indicated that the impacts of previous ENSO and QXP snow on monthly rainfall anomalies over

* 国家科技支撑计划(2007BAC29B04)资助

2010年6月12日收稿; 2011年5月15日收修定稿

第一作者:陶亦为,主要从事短期气候预测研究. Email:taoyiwei@hotmail.com



© 1994-2011 China Academic Journal Electronic Publishing House. All rights reserved. http://www.cnki.net

southward of the Yangtze River are different for each summer month.

**Key words**: winter and spring snow depth, Qinghai-Tibetan Plateau (QXP), ENSO, summer rainfall, SST (sea surface temperature)

## 引 言

中国是个自然灾害频发的国家，而其中由夏季降水丰欠产生的洪涝与干旱气象灾害占所有自然灾害中的比例很大，所以研究我国夏季降水的发生、发展和影响有着重要意义。影响我国夏季降水的因素比较复杂，赵振国等[1]曾把影响中国汛期旱涝的因素归纳为海温异常现象（El Nino Southern Oscillation, ENSO）、青藏高原热状况、亚洲季风、中纬度阻塞高压和西太平洋副热带高压这5个最重要的因子。肖子牛[2]在总结我国短期气候监测预测业务进展也指出，气候预测主要以物理统计方法为主，分析影响中国气候异常的各种物理因素及其前兆信号，以分析海温、雪盖、季风、阻高、副高等因子对中国汛期旱涝的影响为基础做气候预测。然而各个因子的复杂影响使得对我国夏季降水的季节预测一直是个难题。尤其是前期青藏高原积雪异常引起的下垫面热力变化对夏季环流系统和天气气候都有显著的影响。刘晓冬[3]提出积雪以其高反射率、热传导性差、融化过程吸收大量热量等特性通过改变下垫面热状况和大气冷热源从而影响大气的各种热力和动力过程。近年来很多气象科学工作者对青藏高原冬春季积雪对我国夏季降水也有比较深入的研究。朱玉祥等[4]研究表明在年代际尺度上，青藏高原大气热源和冬春积雪与中国东部降水型的年代际变化（南涝北旱）有很好的相关。韦志刚等[5]研究指出高原冬春多（少）雪年高原和我国东部地区气温偏低（高）、陆海温差的偏小（大）会延迟（促进）东亚夏季风的到来，一定程度上减弱（增强）了东亚季风的强度，因而西太平洋副高偏南（北），造成我国夏季雨带的变化。宋文玲等[6]统计分析结果指出冬季青藏高原积雪异常偏多时，夏季雨带位置偏南，长江流域容易发生洪涝灾害。

ENSO事件是另一个对我国汛期降水季节预测的重要参考因子。朱益民等[7]指出ENSO是热带太平洋地区海气系统年际气候变率的最强信号，它不仅对区域气候而且对全球气候异常都有明显的影响。许多气象工作者都研究发现ENSO事件对我国东部夏季降水有着重要影响，汪靖等[8]研究结果表明ENSO事件是影响江淮入梅早晚较强的前兆信号。前期冬春季出现ENSO暖位相时有利于入梅开始偏晚，ENSO冷位相出现时入梅往往偏早。赵振国[9]研究指出我国夏季雨带的位置与ENSO事件发生有着较好的关系，在厄尔尼诺当年我国夏季主要雨带偏南，在拉尼娜当年我国夏季主要雨带偏北。程炳岩等[10]研究指出，Niño3区SST与川渝地区降水存在较好的相关关系，在1960—1986年呈正相关关系，1987—2006年为负相关关系。

综上所述，我国学者对于青藏高原积雪与ENSO对我国夏季降水的异常影响分别进行了大量研究工作，但两因子之间的关系如何？这两个因子的共同作用对我国夏季降水有什么样的影响？对夏季各月降水影响又是怎样？本文是在前人研究工作的基础上，首先系统研究了ENSO与高原积雪的关系，并重点探讨了两者共同作用下对我国夏季降水异常的影响，此外还初步分析了高原积雪与ENSO在相同配置的共同作用下影响我国夏季降水异常的机理。

## 1 资料和方法

本文所用资料主要包括：(1)美国国家环境预报中心(NCEP)的再分析资料，时间跨度为1978年12月至2005年12月，包括高空各等压面2.5°×2.5°经纬度格点的高度、纬向风及垂直速度 $w$ 等要素；(2)国家气候中心提供的1979—2005年覆盖全中国的160个主要站点的夏季逐月降水资料；(3)由美国气候预测中心(CPC)提供Niño3区海表面温度(SST)指数资料；(4)青藏高原地区积雪资料数据来源于国家自然科学基金委员会“中国西部环境与生态科学数据中心”(http://westdc.westgis.ac.cn)，时间为1978年11月至2005年12月。该积雪资料[11]是利用美国国家冰雪数据中心(NSIDC)处理的1978年以来逐日被动微波遥感SMMR(1978—1987年)和SSM/I(1987—2005年)卫星资料进行反演得到的，在反演计算过程中利用了我国地面台站观测积雪深度的实测数据进行订正，并且这套资料分辨率较高，能更好地反映高原积雪的变化信息。



© 1994-2011 China Academic Journal Electronic Publishing House. All rights reserved. http://www.cnki.net

对于我国夏季雨带的划分参考了孙林海等[12]对我国东部季风区夏季降水的分类，降水型分为 2 类 4 型，分别为第 1 类代表南北多中间少的降水分布形态，分别为 1a 和 1d 类雨型，1a 主要雨带在黄河流域至华北一带，1d 主要雨带在华南、江南一带；第 2 类代表南北少中间多的降水分布形态，分别为 2b 和 2c 类雨型，2b 主要雨带位于黄河与长江之间，2c 主要雨带位于长江流域一带，可以说 1a 与 2b 雨型主要雨带偏北，1d 与 2c 雨型主要雨带偏南。

本文研究中采用的方法主要有 Mann-Kendall 突变检验法、相关分析和合成分析等方法。为了讨论 ENSO 与青藏高原积雪之间的关系及对我国东部夏季降水的影响，主要利用 1978/1979—2005 年逐日的中国雪深长时间序列数据集，计算得到 12 月至次年 5 月青藏高原主体范围(27.5°～37.5°N、80°～100°E)区域平均后经过标准化的指数，定义为青藏高原积雪深度指数(以下简称积雪指数)，并分别得到冬季(12 月至翌年 2 月)和春季(3—5 月)积雪指数。此外，对 1978/1979—2005 年 9 月至次年 5 月的 Niño3 区 SST 指数进行标准化处理，定义为 Niño3 区海温距平指数(以下简称 SSTA 指数)，并分别得到秋季、冬季和春季 SSTA 指数。为了清楚地表达 ENSO 与青藏高原积雪的异常程度，分别对 SSTA 指数和积雪指数的异常程度进行了定义(表 1)。

**表 1　SSTA 指数与积雪指数异常程度的定义**

**Table 1　The definition of anomalous extent of SSTA and snow depth**

| 指数 | <−1 | <−0.5 | −1～−0.5 | −0.5～0 | 0～0.5 | 0.5～1 | >0.5 | >1 |
|---|---|---|---|---|---|---|---|---|
| SSTA | 强冷事件 | 偏冷 | 略偏冷 | 正常偏冷 | 正常偏暖 | 略偏暖 | 偏暖 | 强暖事件 |
| 积雪 | 显著偏少 | 偏少 | 略偏少 | 正常偏少 | 正常偏多 | 略偏多 | 偏多 | 显著偏多 |

## 2　结果与讨论

### 2.1　ENSO 与青藏高原积雪的关系

#### 2.1.1　ENSO 与青藏高原积雪的年代际关系

Mann-Kendall 突变检验法(M-K 方法)是一种非参数统计检验方法，其优点是不需要样本遵从一定的分布，也不受少数异常值的干扰，而且计算简单，可以明确突变的开始时间[13]。积雪指数经 M-K 突变检验(图 1)，UF 与 UB 两条曲线在 1993 年相交，青藏高原积雪深度在 1993 年发生突变，1993 年以前积雪偏少，在 1993 年以后高原积雪呈整体增加趋势。Min Ho Kwon 等[14]研究也指出在 20 世纪 90 年代中期亚洲夏季环流存在突变，亚洲夏季环流的突变是否与高原积雪有关，这还需要进一步研究。

图2分别是1979—2005年冬春季积雪指数的

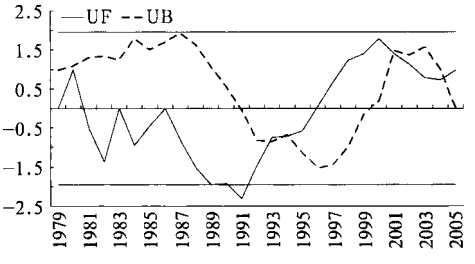


图 1　1979—2005 年积雪指数 M-K 突变检验

水平实线为 $\alpha=0.05$ 显著性水平临界值

Fig. 1　The M-K abrupt test of snow depth index during 1979—2005

The solid lines indicate the 0.05 significance level

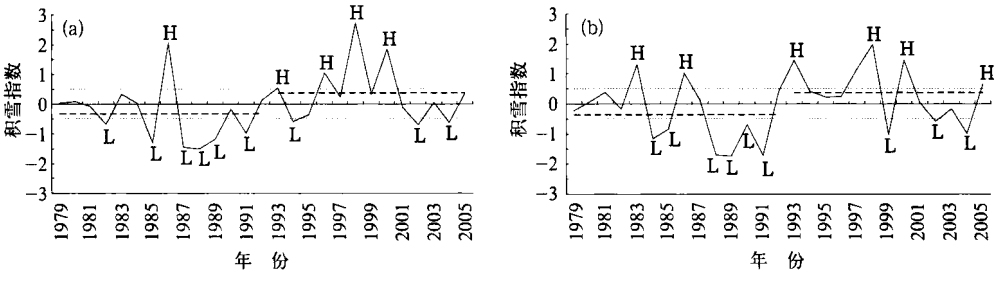


图 2　1979—2005 年冬季(a)和春季(b)积雪指数的年际演变曲线

H 表示积雪偏多年，L 表示积雪偏少年

Fig. 2　Annual variations of the snow depth index in (a) winter and (b) spring during 1979—2005

H and L indicate the years with heavy and light snow, respectively



© 1994-2011 China Academic Journal Electronic Publishing House. All rights reserved.　http://www.cnki.net

年际演变曲线，由图 2a 可见，1986、1993、1996、1998、2000 年为冬季积雪偏多，其中 1993 年以后(包括 1993 年)有 4 次，1982、1985、1987、1988、1989、1991、1994、2002 和 2004 年为冬季积雪偏少，其中 1993 年以前有 6 次。由图 2b 可见，1983、1986、1993、1998、2000、2005 年为春季积雪偏多，其中 1993 年以后(包括 1993 年)有 4 次，1984、1985、1988、1989、1990、1991、1999、2002 和 2004 年为春季积雪偏少，其中 1993 年以前有 6 次。另外图 2 中长虚线分别为 1993 年以前高原积雪距平平均和 1993 以后高原积雪距平平均，可以看出冬春季高原积雪在 1993 年以前积雪偏少，在 1993 年以后积雪开始增多，从 1979—2005 年冬春季青藏高原积雪呈整体增加的年代际变化趋势。

图 3 是 1979—2005 年冬春季 SSTA 指数与积雪指数 9 年滑动的演变曲线。冬季 SSTA 指数在 20 世纪 80 年代初至 80 年代末为减小趋势，80 年代末到 90 年代初 SSTA 指数呈增加趋势，积雪指数在 20 世纪 80 年代初至 90 年代初为平缓减小趋势，处于积雪偏少阶段，两者在 1994 年至 1996 年左右都呈增加趋势，随后冬季 SSTA 指数到 90 年代末呈减小趋势，在 2000 年初呈增加趋势，而冬季积雪指数在 1998 年升至高点后变化平缓，处于积雪偏多阶段(图 3a)。春季 SSTA 指数与积雪指数在 20 世纪 80 年代初到 80 年代末都呈减小趋势，80 年代末至 90 年代初又都呈增加趋势，从 1993 年至 1996 年都呈增加趋势，然后一直到 2000 年都呈减小趋势，21 世纪初又都为增加趋势(图 3b)。可以看出春季 SSTA 指数与积雪指数年代际变化具有一致性。

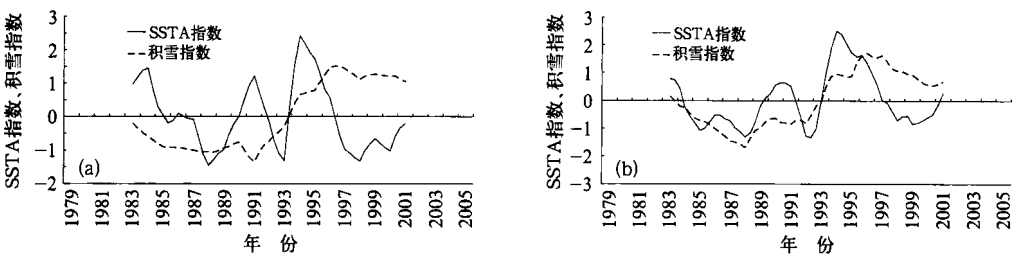


图 3 1979—2005 年冬季(a)和春季(b)SSTA 指数与积雪指数 9 年滑动的演变曲线

Fig. 3 Time series of 9-year running mean of the SSTA and snow depth indices in (a) winter and (b) spring during 1979—2005

### 2.1.2 ENSO 与青藏高原积雪的年际变化关系

图 4 是 1979—2005 年冬春季 SSTA 指数与积雪指数的年际演变曲线，为了更清楚地表明 SSTA 指数和积雪指数之间的年际关系特征，对于 Niño3 区 SST 偏暖(偏冷)的年份定义为 H(L)，并标在同期积雪指数曲线上。在冬季 Niño3 区 SST 偏暖的 6 年里，1998 年高原积雪偏多，1983、1992 和 2003 年为正常偏多，而 1987 年冬季高原积雪显著偏少，1995 年为正常偏少；冬季 Niño3 区 SST 偏冷的 9 年里，在 1985 和 1989 年这两年冬季高原积雪偏少，1994 和 2001 年为正常偏少，而 1986、1996 和 2000 年高原冬季积雪却显著偏多，1997 和 1999 年为正常偏多(图 4a)。可以看出冬季 Niño3 区 SST 冷暖位相与冬季高原积雪异常的对应关系并不好。在春

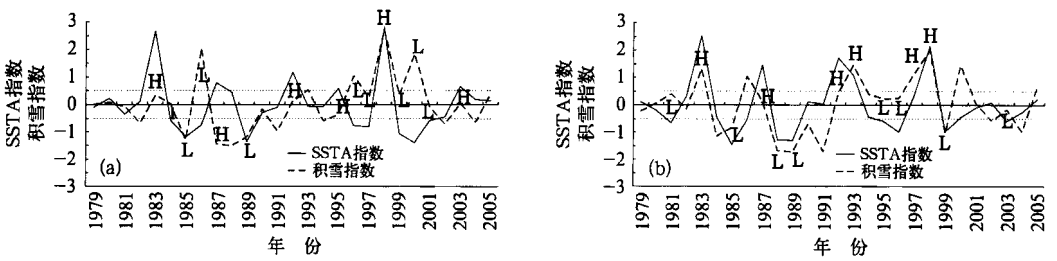


图 4 1979—2005 年冬季(a)和春季(b)SSTA 指数与积雪指数的年际演变曲线

H 表示 SST 偏暖年，L 表示 SST 偏冷年

Fig. 4 Annual variations of the SSTA and snow depth indices in (a) winter and (b) spring during 1979—2005

H and L indicate the years with warm and cold SST, respectively



© 1994-2011 China Academic Journal Electronic Publishing House. All rights reserved. http://www.cnki.net

季 Niño3 区 SST 偏暖的 6 年里，1983、1992、1993、1997 和 1998 年这 5 年春季高原积雪都偏多，1987 年高原积雪为正常偏多；在春季 Niño3 区 SST 偏冷的 8 年里，1985、1988、1989 和 1999 年这 4 年春季高原积雪都偏少，2003 年为正常偏少，而 1981、1995 和 1996 年积雪为正常偏多(图 4b)。春季 Niño3 区 SST 冷暖位相与春季高原积雪异常的对应关系比较好，并且当春季 Niño3 区 SST 偏暖时春季积雪指数都为正值，春季高原积雪往往都偏多。

### 2.1.3　ENSO 与青藏高原积雪冬季和春季的年际变化关系

图 5 是 1978/1979—2005 年冬春季逐月 SSTA 指数和积雪指数年际演变曲线。由图 5a 可见，Niño3 区 SST 异常的持续性比较好，一般冬季 Niño3 区 SST 偏暖(偏冷)，春季 Niño3 区 SST 也偏暖(偏冷)，对于冬季 Niño3 区 SST 为强暖状态和强冷状态这种异常的持续性会更好，如 1983、1992 和 1998 年冬季 Niño3 区 SST 为强暖状态，春季 SST 也为强暖状态；1985、1989 和 1999 年冬季 Niño3 区 SST 强冷状态，春季 SST 也为强冷状态或略偏暖。由图 5b 可见，青藏高原积雪异常的持续性并不好，冬季高原积雪偏多(偏少)，春季高原积雪不一定偏多(偏少)。但对于前期冬季高原积雪显著偏多的年份后期春季高原积雪也偏多，具有一定的异常持续性。如 1986、1998 和 2000 年冬季 12—2 月积雪指数都显著偏多，春季 3—5 月积雪也都偏多。

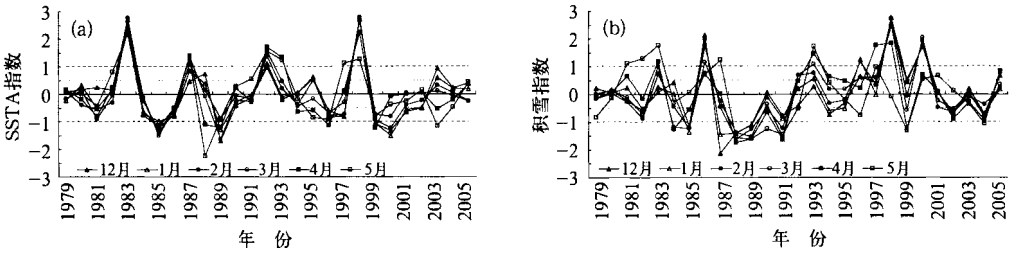


图 5　1978/1979—2005 年冬春季逐月 SSTA 指数(a)和积雪指数(b)年际演变曲线

Fig. 5　Annual variations of the monthly (a) SSTA and (b) snow depth indices in winter and spring during 1979—2005

为了讨论前期和同期的 SSTA 指数与积雪指数的关系，分别计算 1978/1979—2005 年前期秋季和同期冬、春季 SSTA 指数与积雪指数之间的相关系数(表 2)。由表 2 可见，冬季积雪指数与前期秋季和同期冬季 SSTA 指数相关并不好；而春季积雪指数与前期冬季和同期春季的 SSTA 指数相关比较好，尤其是与同期春季 SSTA 指数相关系数可以通过 0.01 显著性检验。

**表 2　1978/1979—2005 年前期秋季和同期冬、春季 SSTA 指数与积雪指数之间的相关系数**

**Table 2　Correlations between SSTA and snow depth indices during 1978/1979—2005**

| 季节 | SSTA 指数 | | |
|---|---|---|---|
| | 秋季 | 冬季 | 春季 |
| 冬季 | 0.170 | 0.175 | |
| 春季 | 0.321 | ***0.381*** | ***0.588*** |

注：粗斜体表示通过 0.05 显著性水平检验

Bold italic indicates passing through the test at 0.05 significance level

### 2.1.4　ENSO 与青藏高原积雪的月时间尺度关系

为了进一步说明在月时间尺度上 ENSO 与青藏高原积雪两者之间的关系，分别用 1978/1979—2005 年 9 月至次年 5 月前期秋季和同期冬、春季逐月的 SSTA 指数与积雪指数逐月计算两者之间的相关系数(表 3)。从表 3 可看出，冬季 12 月至次年 2 月积雪指数与前期和同期的 SSTA 指数相关并不好，所有组合都没有通过 0.05 显著性水平检验，说明冬季高原积雪与前期和同期 Niño3 区 SST 是相对独立的两个因子。春季 3 和 4 月积雪指数与前期冬季的 SSTA 指数相关较好，部分可以通过 0.05 的显著性水平检验，3、4 和 5 月的积雪指数分别与前一个月和同期的 SSTA 指数有比较好的相关性，尤其是 3、4 和 5 月积雪指数与同期的 3、4 和 5 月 SSTA 指数之间的相关系数很高，都可以通过 0.01 的显著性水平检验。

综上所述，无论是从季节时间尺度还是从月时间尺度来看，冬季积雪指数与前期和同期的 SSTA 指数相关性并不好，可以认为冬季青藏高原积雪与 Niño3 区 SST 是两个相对独立的因子；而对于春季积雪指数，它与前期冬季和同期春季 SSTA 指数有着比较好的相关性，尤其是与同期春季SSTA指数



© 1994-2011 China Academic Journal Electronic Publishing House. All rights reserved.　http://www.cnki.net

表3 同表2,但为月指数

Table 3 Same as Table 2, but for monthly indices

| 月份 | SSTA指数 | | | | | | | | |
|---|---|---|---|---|---|---|---|---|---|
| | 9月 | 10月 | 11月 | 12月 | 1月 | 2月 | 3月 | 4月 | 5月 |
| 12月 | 0.092 | 0.090 | 0.091 | 0.095 | | | | | |
| 1月 | 0.141 | 0.166 | 0.170 | 0.169 | 0.147 | | | | |
| 2月 | 0.190 | 0.269 | 0.291 | 0.282 | 0.280 | 0.332 | | | |
| 3月 | 0.236 | 0.351 | ***0.382*** | 0.378 | 0.365 | ***0.395*** | ***0.498*** | | |
| 4月 | 0.216 | 0.332 | ***0.381*** | ***0.385*** | 0.369 | 0.352 | ***0.455*** | ***0.565*** | |
| 5月 | 0.073 | 0.150 | 0.177 | 0.210 | 0.202 | 0.194 | 0.320 | ***0.475*** | ***0.543*** |

注:粗斜体表示通过0.05显著性水平检验

Bold italic indicates passing through the test at 0.05 significance level

之间,具有很好的相关性。

## 2.2 ENSO与青藏高原积雪异常的共同作用对我国夏季雨带的影响

### 2.2.1 ENSO与我国夏季雨带的关系

表4是1979—2005年冬春季SSTA指数和积雪指数与夏季雨带的分布统计,由表4可见,当冬春季Niño3区SST为正常偏暖(正常偏冷)的年份或者略偏暖(略偏冷)的年份,夏季雨带与Niño3区SST异常对应关系不显著,主要雨带偏北和偏南的概率相当;当冬春季Niño3区SST为强暖事件(强冷事件)时,夏季雨带一般偏南(偏北)。

下面从月时间尺度来看前期ENSO对我国东部地区夏季雨带的影响,分别对长江以南地区(20°~30°N、110°~125°E)范围内32个站点的夏季6、7和8月降水做平均,定义为南方降水指数,计算前期冬春季逐月SSTA指数与夏季逐月南方降水指数之间的相关系数(表5),由表5可见,前期冬春季逐月SSTA指数与6月南方降水指数之间为正相关,其中3和4月的相关比较好;前期冬季SSTA指数与7月南方降水指数之间为负相关,春季SSTA指数与7月南方降水指数之间为正相关,其中在5月SSTA指数与7月南方降水指数之间的相关关系要比其他月的相对要好;前期冬春季SSTA指数与8月南方降水指数之间都为负相关,其中2、3和4月SSTA指数与8月南方降水指数之间相关比较好。可以推论得到,冬春季Niño3区SST偏暖(偏冷),长江以南地区6月降水偏多(偏少),并且Niño3区春季SST对长江以南地区6月与7月的降水的影响要比冬季明显,而冬春季Niño3区SST偏暖(偏冷),长江以南地区8月降水偏少(偏多)。

表4 1979—2005年冬春季SSTA指数和积雪指数与夏季雨带的分布统计

Table 4 Occurrences of rainfall regime according to anomalies of Niño3 SSTA and QXP snow depth indices during 1979—2005

| 指数 | 夏季雨带偏北比例 | | | 夏季雨带偏南比例 | | |
|---|---|---|---|---|---|---|
| | <−1 | −1~−0.5 | −0.5~0 | 0~0.5 | 0.5~1 | >1 |
| 冬季SSTA | 3/4 | 1/5 | 2/7 | 1/5 | 1/3 | 2/3 |
| 春季SSTA | 3/3 | 3/6 | 3/6 | 4/7 | / | 4/5 |
| 冬季积雪 | 3/4 | 2/5 | 2/4 | 4/9 | 1/1 | 3/4 |
| 春季积雪 | 3/4 | 2/5 | 3/3 | 5/8 | 0/1 | 5/6 |

表5 1978/1979—2005年冬春季逐月SSTA指数与夏季南方降水之间的相关系数

Table 5 Correlations between monthly SSTA index and rainfall over southern China during 1978/1979—2005

| 月份 | SSTA指数 | | | | | |
|---|---|---|---|---|---|---|
| | 12月 | 1月 | 2月 | 3月 | 4月 | 5月 |
| 6月 | 0.366 | 0.351 | 0.362 | ***0.392*** | ***0.419*** | 0.328 |
| 7月 | −0.182 | −0.117 | −0.054 | 0.081 | 0.146 | 0.346 |
| 8月 | −0.371 | −0.365 | ***−0.402*** | ***−0.387*** | ***−0.432*** | −0.336 |

注:粗斜体为通过0.05显著性水平检验

Bold italic indicates passing through the test at 0.05 significance level



© 1994-2011 China Academic Journal Electronic Publishing House. All rights reserved. http://www.cnki.net

2.2.2　青藏高原积雪与我国夏季雨带的关系

上面已经讨论过冬春季青藏高原积雪在 1993 年以前积雪偏少，在 1993 年以后高原积雪呈整体增加趋势，对比我国夏季雨带的分布，在 1993 年以前的 14 年里偏北类雨型总共有 9 年，占 64%，1993 年以后的 13 年里偏南类雨型总共有 8 年，占 62%，可以看出随着青藏高原积雪的增加，我国夏季雨带逐渐偏南。另外，从表 4 可以看出，当冬春季高原积雪为正常偏多（正常偏少）的年份或者略偏多（略偏少）的年份，夏季雨带与高原积雪对应关系也并不显著，主要雨带偏北和偏南的概率相当，当冬春季高原积雪显著偏多（显著偏少）的年份，夏季雨带一般偏南（偏北）。

**表 6　同表 5，但为积雪指数与夏季南方降水指数之间的相关系数**

**Table 6　The same as Table 5, but for correlations between QXP snow depth index and rainfall over southern China**

| 月份 | 积雪指数 | | | | | |
|---|---|---|---|---|---|---|
| | 12 月 | 1 月 | 2 月 | 3 月 | 4 月 | 5 月 |
| 6 月 | ***0.399*** | ***0.417*** | ***0.431*** | ***0.559*** | ***0.589*** | 0.340 |
| 7 月 | 0.013 | 0.125 | 0.219 | 0.244 | 0.354 | 0.266 |
| 8 月 | −0.112 | −0.134 | −0.208 | −0.173 | −0.190 | −0.180 |

注：粗斜体为通过 0.05 显著性水平检验

Bold italic indicates passing through the test at 0.05 significance level

另外，从月时间尺度来看，计算前期冬春季逐月积雪指数与夏季逐月南方降水指数之间的相关系数（表 6），由表 6 可见，前期冬春季逐月积雪指数与 6 和 7 月南方降水指数都为正相关，其中 12 月至次年 4 月的积雪指数与 6 月南方降水指数之间的相关关系比较好，特别是春季 3 和 4 月积雪指数与 6 月南方降水指数之间的相关系数可以通过 0.01 的显著性检验。此外，3、4 和 5 月积雪指数与 7 月南方降水指数相关性与冬季相比相对较好。前期冬春季逐月积雪指数与 8 月南方降水指数之间都为负相关。说明前期高原冬春季积雪偏多（偏少），长江以南地区 6 和 7 月降水偏多（偏少），而对于 8 月则是相反的，此外还可以看到高原春季积雪对长江以南地区 6 和 7 月降水影响要强于冬季。

2.2.3　ENSO 与青藏高原积雪异常的共同作用对我国夏季雨带的影响

图 6 是 1979—2005 年冬春季 SSTA 指数与积雪指数的散点分布图。图 6a 是冬季 SSTA 指数与积雪指数散点分布，第一象限夏季偏南雨型年占 3/6，其中只有 1998 年一年为冬季 Niño3 区 SST 强暖事件与高原积雪显著偏多的配置，夏季主要雨带偏南，其余为冬季 SST 略偏暖或正常偏暖与高原积雪略偏多或正常偏多的年份，夏季雨带偏南偏北的概率相当；第三象限夏季偏北雨型年占了 3/8，其中有 1985 和 1989 年两年为冬季 Niño3 区 SST 强冷事件与高原积雪显著偏少的配置，夏季主要雨带都偏北，其余为冬季 Niño3 区 SST 略偏冷或正常偏冷与高原积雪略偏少或正常偏少的年份，夏季雨带偏南年占 5/6。图 6b 是春季 SSTA 指数与积雪指数散点分布，第一象限偏南雨型年占 5/7，其中 1983、1993 和 1998 年三年为春季 Niño3 区 SST 强暖事件与高原积雪显著偏多的配置，这三年夏季主要雨带都偏南，其余为春季 Niño3 区 SST 略偏暖或正常偏暖与高原积雪略偏多或正常偏多的年份，夏季雨带偏南偏北的概率相当；第三象限偏北雨型占了 6/7，其中有 1988 和 1989 年两年为春季 Niño3 区 SST 强冷事件与春季高原积雪显著偏少的配置，并且夏季主要雨带都偏北，其余为春季 Niño3 区 SST 略偏冷或正常偏冷与高原积雪略偏少或正常偏少的年份，大部分年份夏季雨带偏北。此外，从图 6 还可以看到，对于在第二象限（第四象限）也就是前期冬春季 Niño3 区 SST 偏暖或正常偏暖（偏冷或正常偏冷）与高原积雪偏少或正常偏少（偏多或正常偏多）的配置下我国夏季雨带的分布并不好确定，我国夏季雨带可能偏北也可能偏南。

综上所述，当 Niño3 区 SST 与青藏高原积雪共同作用时，前期冬春季 SST 略偏暖或正常偏暖（略偏冷或正常偏冷）与积雪略偏多或正常偏多（略偏少或正常偏少）的配置下，夏季雨带往往具有不确定性，主要雨带偏北和偏南的概率相当；当前期冬春季 SST 偏暖或正常偏暖（偏冷或正常偏冷）与积雪偏少或正常偏少（偏多或正常偏多）的配置下，夏季雨带的分布也并不好确定。只有当前期冬春季 Niño3 区SST为强暖（强冷）事件与高原积雪显著偏多（显



© 1994-2011 China Academic Journal Electronic Publishing House. All rights reserved.　http://www.cnki.net

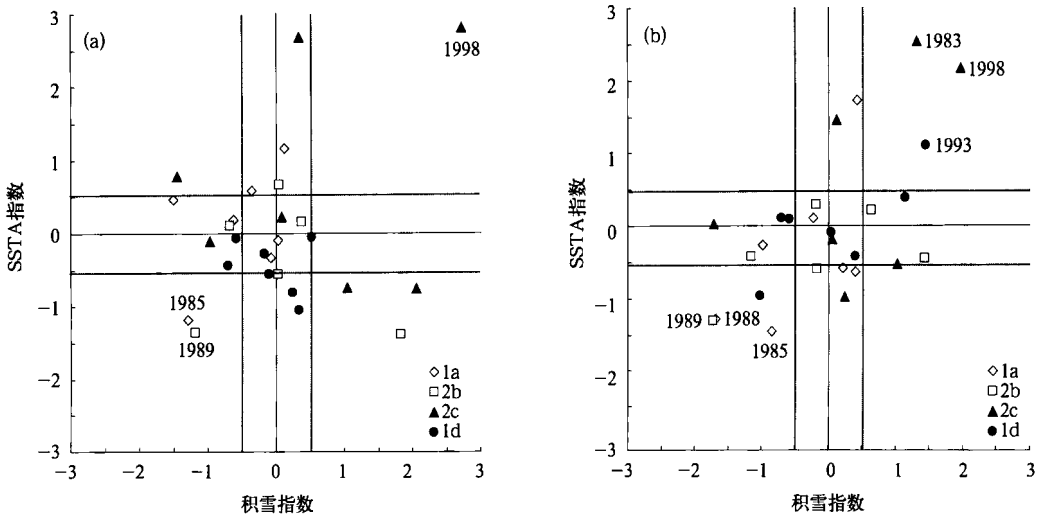


图6 1979—2005年冬季(a)和春季(b)SSTA指数与积雪指数的散点分布图

其中菱形为1a雨型,正方形为2b雨型,三角形为2c雨型,圆形为1d雨型

Fig. 6 Scatterplots of SSTA and snow depth indices in (a) winter and (b) spring during 1979—2005

diamond-type indicates rainfall regime 1a, square 2b, triangle 2c, and round 1d

著偏少)的配置下,我国东部夏季雨带往往偏南(偏北)。

## 2.3 青藏高原积雪与ENSO影响夏季降水机理的初步分析

前面已经讨论过春季Niño3区SST与高原积雪对长江以南地区6和7月降水影响更为重要,并且前期春季Niño3区SST强暖(强冷)事件与高原积雪显著偏多(显著偏少)的配置下,我国东部夏季雨带往往偏南(偏北)。根据再分析资料,对前期春季Niño3区SST强暖事件与高原积雪显著偏多配置(简称共同强正异常年)的1983、1993和1998年3年进行合成,对前期春季Niño3区SST强冷事件与高原积雪显著偏少配置(简称共同强负异常年)的1985(春季高原积雪接近于显著偏少)、1988和1989年3年进行合成,分析前期春季Niño3区SST强暖(强冷)事件与高原积雪显著偏多(显著偏少)配置下的夏季对流层中低层的环流背景。图7是1979—2005年春季Niño3区SSTA与青藏高原积雪共同作用下夏季500 hPa高度场的合成。由图7a可见,共同强正异常年对应的夏季500 hPa环流场合成,副热带高压偏西,其中587 dagpm等高线西伸至110°E左右的陆地上。廖荃荪等[15]指出西太平洋副热带高压强度和位置的变化是影响我国夏季雨带分布最重要的因素之一,对我国东部夏季降水的影响很大。在这种西太平洋副热带高压西伸的环流形势

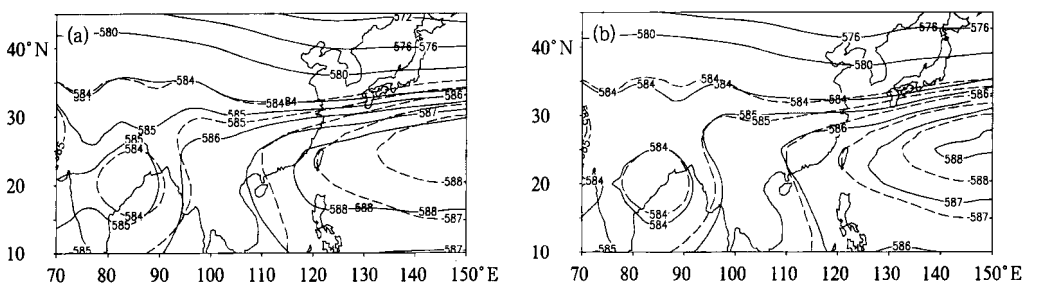


图7 春季Niño3区SST与青藏高原积雪共同作用下夏季500 hPa高度场的合成(单位:dagpm)

(a) SSTA和积雪均为强正异常,(b)SSTA和积雪均为强负异常

虚线为1979—2005年的气候平均

Fig. 7 Composites of summer 500 hPa geopotential height by different phase coupling of the Niño3 SST and QXP snow depth in spring (unit:dagpm),(a)strong warm SST and heavy snow, (b)strong cold SST and light snow

Dashed line indicates the climate mean during 1979—2005



© 1994-2011 China Academic Journal Electronic Publishing House. All rights reserved. http://www.cnki.net

下,沿副热带高压西侧的偏南气流可以从海面上带来充沛的水汽,有利于夏季南方地区降水,使我国夏季雨带偏南。由图 7b 可见,共同强负异常年对应的夏季 500 hPa 环流场合成,副热带高压偏东,587 dagpm 等高线东退至 125°E 左右的海洋上,这种环流形势不利于从海上来水汽向南方地区输送,使我国夏季南方降水偏少。

下面分别取高原主体的北边界(37.5°N)和南边界(27.5°N),并且用共同强正异常年相减共同强负异常年,讨论春季 Niño3 区 SST 强暖(强冷)事件与高原积雪显著偏多(显著偏少)的配置下夏季垂直纬圈环流特征。图 8 是春季 Niño3 区 SST 与青藏高原积雪共同作用下夏季沿 37.5°N 的垂直纬圈环流。由图 8 可见,沿 37.5°N 纬圈在高原西部和东部为相对下沉运动,高原中部为相对上升运动,在 105°～120°E 的我国北方地区从 300～800 hPa 共同强正异常年相对于共同强负异常年存在深厚的相对下沉运动,这不利于我国北方地区降水,可见共同强正异常年夏季北方偏干少雨。夏季沿 27.5°N 垂直纬圈环流(图略),高原整体为相对下沉运动,在东部 100°～120°E 的我国长江以南地区从 300～700 hPa 为深厚的相对上升运动,这种形势有利于我国长江以南地区降水,共同强正异常年我国南方降水偏多,雨带偏南。可以看出,共同强正异常年在我国北方为下沉运动,使我国北方夏季干旱少雨,在我国南方则为上升运动,有利于降水,使我国南方夏季多雨,共同强负异常年则与之相反。

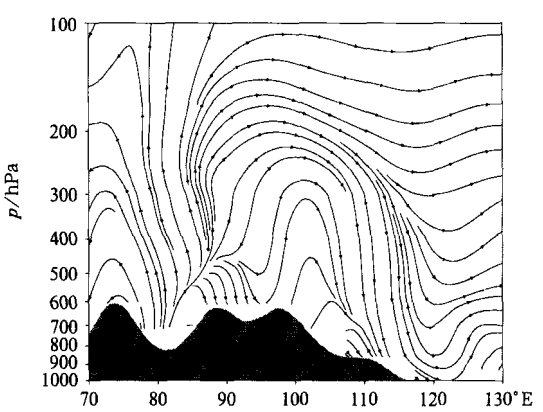


图 8　春季 Niño3 区 SST 与青藏高原积雪共同作用下夏季沿 37.5°N 的垂直纬圈环流
共同强正异常年减去共同强负异常年

Fig. 8　Difference of the vertical-zonal circulation along 37.5°N between years with warm SST and heavy snow and with cold SST and light snow

## 3　结　论

本文利用 1979—2005 年 Niño3 区海温时间序列资料和中国雪深时间序列资料,分析研究了 ENSO 与高原积雪的关系,以及两者共同作用下对我国夏季降水的异常影响;还初步分析了高原积雪与 ENSO 影响我国夏季降水异常的机理。得到的主要结论如下。

(1) 青藏高原积雪深度在 1993 年发生突变,1979—2005 年青藏高原冬春季积雪呈现整体增加的年代际变化趋势。对比冬春季 SSTA 指数与积雪指数年代际关系,可以看出春季 SSTA 指数与积雪指数年代际变化具有一致性。

(2) Niño3 区 SST 异常持续性比较好;青藏高原积雪异常持续性并不好,但前期冬季积雪显著偏多时,春季高原积雪也往往偏多。另外,无论是从季节时间尺度还是从月时间尺度来看,冬季积雪指数与前期和同期的 SSTA 指数相关性不好;而对于春季积雪指数,它与前期冬季和同期春季 SSTA 指数有着比较好的相关性,尤其与同期春季 SSTA 指数相关最好,春季 Niño3 区 SST 偏暖时春季高原积雪往往都偏多。

(3) 前期冬春季逐月 Niño3 区 SST 和高原积雪与长江以南地区 6 月的降水都为正相关,与 8 月降水都为反相关,另外,春季逐月 Niño3 区海温和冬春季逐月高原积雪与长江以南地区 7 月也为正相关。说明 ENSO 与青藏高原冬春季积雪对我国长江以南地区夏季降水异常的影响在各个月份是不一致的。

(4) 当冬春季 Niño3 区 SST 为强暖事件(强冷事件)的年份,夏季雨带一般偏南(偏北);当冬春季高原积雪显著偏多(显著偏少)的年份,夏季雨带也一般偏南(偏北)。说明在强 ENSO 事件或强高原积雪异常的背景下,前期 ENSO 或者高原积雪异常对我国夏季雨带影响是很显著。尤其是两种强异常叠加一起时,即前期冬春季 Niño3 区 SST 为强暖(强冷)事件与高原积雪显著偏多(显著偏少)共同作用的配置下,夏季雨带往往偏南(偏北)。说明只有当冬春季达到强 ENSO 事件和高原积雪显著异常的共同作用下,对我国夏季雨带的影响最为显著。

(5) 当前期春季 Niño3 区 SST 强暖事件与高原积雪显著偏多的配置下,我国北方地区为下沉运



© 1994-2011 China Academic Journal Electronic Publishing House. All rights reserved.　http://www.cnki.net

动，使我国北方地区夏季干旱少雨，在我国南方地区为上升运动，并且副热带高压偏西，有利于向我国南方地区输送水汽，使夏季雨带偏南；当前期春季Niño3区SST强冷事件与高原积雪显著偏少的配置下，我国北方为上升运动，我国南方地区为下沉运动，并且副热带高压偏东，使夏季雨带偏北。

## 参考文献


[1] 赵振国，等. 影响中国汛期降水和长江流域旱涝的主要物理因素的综合分析[C]//1998年特大暴雨（洪涝）学术研讨会论文摘要汇编. 北京：中国气象学会，1999.

[2] 肖子牛. 我国短期气候监测预测业务进展[J]. 气象，2010，36(7)：21-25.

[3] 刘晓东. 冰雪变化对大气环流和天气气候的影响[J]. 地球科学进展，1989，4(6)：53-56.

[4] 朱玉祥，丁一汇，徐怀刚. 青藏高原大气热源和冬春积雪与中国东部降水的年代际变化关系[J]. 气象学报，2007，65(6)：946-958.

[5] 韦志刚，陈文，黄荣辉. 青藏高原冬春积雪异常影响中国夏季降水的数值模拟[J]. 高原山地气象研究，2008，28(1)：1-7.

[6] 宋文玲，袁景凤，陈兴芳. 冬季高原积雪异常与1998年长江洪水关系的分析[J]. 气象，2000，26(2)：11-14.

[7] 朱益民，杨修群，陈晓颖，等. ENSO与中国夏季年际气候异常关系的年代际变化[J]. 热带气象学报，2007，23(2)：105-116.

[8] 汪靖，何金海，刘宣飞，等. 江淮入梅异常的强信号及其对入梅的影响[J]. 气象，2008，34(6)：35-40.

[9] 赵振国. 中国夏季旱涝及环境场[M]. 北京：气象出版社，1999：8-9.

[10] 程炳岩，郭渠，孙卫国. 川渝地区降水变化与Niño3区SST的关系及其稳定性分析[J]. 气象，2010，36(3)：27-33.

[11] Che Tao, Li Xin, Jin Rui, et al. Snow depth derived from passive microwave remote-sensing data in China[J]. Annals of Glaciology, 2008, 49: 145-154.

[12] 孙林海，赵振国，许力，等. 中国东部季风区夏季雨型的划分及其环流成因分析[J]. 应用气象学报，2005，16(增刊)：56-62.

[13] 魏凤英. 现代气候统计诊断与预测技术[M]. 北京：气象出版社，2007：63-66.

[14] Min Ho Kwon, Jong-Ghap Jhun, Kyung-Ja Ha. Decadal change in east Asian summer monsoon circulation in the mid-1990s[J]. Geophysical Research Letters, 2007, 34: 1-6.

[15] 廖荃荪，赵振国. 7—8月西太平洋副热带高压的南北位置异常变化及其对我国天气的影响[M]//章基嘉，黄荣辉. 长期天气预报和日地关系研究. 北京：海洋出版社，1992：131-139.




© 1994-2011 China Academic Journal Electronic Publishing House. All rights reserved. http://www.cnki.net

第 30 卷 第 4 期
2011 年 8 月

高 原 气 象
PLATEAU METEOROLOGY

Vol. 30 No. 4
August, 2011

汪方，丁一汇. 不同排放情景下模拟的 21 世纪东亚积雪面积变化趋势[J]. 高原气象，2011，30(4)：869－877

# 不同排放情景下模拟的 21 世纪东亚积雪面积变化趋势

汪 方， 丁一汇

（国家气候中心，北京 100081）

**摘 要**：利用 WCRP CMIP3 气候模式对 SRES A2、A1B 和 B1 排放情景下东亚地区积雪面积的未来变化趋势进行了预测，结果表明，未来东亚地区积雪面积将呈现减少趋势，在同一种排放情景下，春季的减小趋势最大，冬季次之，秋季再次之，夏季最小。比较不同区域之间的积雪面积变化，冬、春季青藏高原积雪面积变化趋势要明显大于东亚大陆北部，秋季二者差异不大。对不同排放情景而言，SRES A2 情景减小趋势最大，A1B 次之，B1 最小。地表气温和降雪量变化是造成积雪面积减小的主要原因，但在不同的区域和季节，对积雪面积变化趋势的贡献有明显差异。

**关键词**：东亚；积雪面积；气候模式

**文章编号**：1000-0534(2011)04-0869-09 **中图分类号**：P426.63$^{+}$5 **文献标识码**：A

## 1 引言

积雪作为冰雪圈中覆盖面积最广、季和年际变化最明显的组成部分，对地球气候起着十分重要的调节作用。一方面，积雪的存在会减小地表的辐射收支，对局地气温起到明显的降温作用；另一方面，积雪又会对局地的水分平衡和水循环产生影响，而这两方面的作用又必然会对大气环流和气候变化产生重要影响[1]。

作为全球重要的积雪区，欧亚大陆尤其是青藏高原（下称高原）积雪对亚洲及中国气候有着重要影响。目前已有大量关于积雪的空间分布和年代际变化特征的研究[2－5]。欧亚大陆积雪与亚洲季风之间关系十分密切，普遍认为欧亚大陆积雪增加会导致亚洲夏季风减弱或者推迟爆发，但这种关系十分复杂[6]。同样，高原积雪也对亚洲夏季风有着类似的影响机制[7－10]。高原冬季雪盖异常会影响东亚冬季风的异常，进而对我国夏季风雨带分布产生影响[11]。关于积雪和中国降水之间的关系，研究发现，欧亚大陆和高原积雪异常与中国夏季降水之间存在着重要联系[12－13]，欧亚大陆和高原冬、春季雪盖对我国夏季旱涝有重要的影响，是汛期降水预测的一个重要因子[14]。诊断研究表明[15]，在年代际尺度上，高原大气热源和冬、春季积雪与中国东部降水型的年代际变化（南涝北旱）有很好的相关。模拟研究也表明[16]，高原冬季多雪，是引起中国东部夏季降水出现“南涝北旱”的一个重要原因。此外，欧亚大陆积雪异常还会对大气环流产生重要影响[17－18]。这些都说明积雪变化对亚洲及中国气候变化的重要性，而未来积雪将如何变化，将对东亚季风及气候产生直接的影响。

IPCC 第四次评估报告[19]指出，受全球变暖影响，21 世纪积雪面积预计将大范围减少，在 SRES B2 情景下，到 21 世纪末北半球年平均积雪面积预计将减少 13%。而在北美大陆，SRES A1B 情景下积雪面积也将显著减少[20]。但东亚区域未来积雪面积将如何变化，目前还鲜有类似的研究。鉴于此，本文利用多个气候模式结果检验了气候模式对东亚积雪面积的模拟性能，并重点在东亚区域和季节尺度上分析全球变暖背景下 21 世纪积雪面积的可能变化趋势。

## 2 资料选取和方法介绍

### 2.1 资料选取

积雪面积的表示方法通常有两种，一是实际面

**收稿日期**：2010-04-14；**改回日期**：2010-06-01
**基金项目**：“十一五”国家科技支撑项目(2007BAC03A01)资助
**作者简介**：汪方(1974－)，男，湖北宜昌人，高级工程师，主要从事气候变化及其模拟研究. E-mail：fangwang@cma.gov.cn



© 1994-2011 China Academic Journal Electronic Publishing House. All rights reserved. http://www.cnki.net

积(单位：$km^2$)，二是积雪覆盖度(即单位网格内积雪覆盖面积占整个格点面积的比例，单位：%)，气候模式通常采用后者表征积雪面积。用到的模式结果来源于WCRP CMIP3多模式数据集，在23个全球耦合模式中选取在SRES A2、A1B和B1三种排放情景下(分别代表高、中、低排放情景)均有完整积雪面积输出的8个模式用于本文分析，即CGCM3.1(T47)(加拿大)、CSIRO－Mk3.0(澳大利亚)、CSIRO－Mk3.5(澳大利亚)、GISS－ER(美国)、INM－CM3.0(俄罗斯)、MIROC3.2(medres)(日本)、MRI－CGCM2.3.2(日本)和CCSM3(美国)。有关模式的具体信息可参见网址：http://www－pcmdi.llnl.gov/ipcc/model_documentation/ipcc_model_documentation.php。选取的资料为“20世纪气候模拟”(20C3M)试验以及SRES A2、B1和A1B三种排放情景下给出的20和21世纪月平均积雪面积、地表气温、降雪量等模式输出结果。积雪面积验证资料采用NOAA月平均积雪面积资料(1971年1月－1995年9月)，该资料由NOAA EASE－Grid(等面积可扩充地球网格)周积雪面积观测资料转换而来，资料说明及下载见网址：http://www－pcmdi.llnl.gov/ipcc/model_documentation/ipcc_model_documentation.php。

需要指出的是，尽管还有其他积雪资料可以选择，如台站观测、微波遥测等，要么观测要素为雪深，与积雪面积不匹配；要么观测开始时间晚，序列长度不能满足本文研究的需要，因此这里仍选取NOAA观测资料作为模式验证资料。

### 2.2 方法介绍

由于不同模式的空间分辨率差异较大，为便于集合以及同观测资料进行比较，将模式结果和观测资料采用双线性插值方法插值到统一的2.5°×2.5°经纬网格上。多模式集合由单个模式结果对应时间和空间点求算术平均得到：

$$S_{i,j,t,e}=\frac{1}{N}\sum_{m=1}^{N}S_{i,j,t,m}, \qquad (1)$$

其中：$N$为模式个数(本文为8)；$S_{i,j,t,m}$为第$m$个模式、某格点(第$i$个经度、第$j$个纬度)处、第$t$个时间的积雪面积；$S_{i,j,t,e}$为对应时间该空间点的多模式集合(平均)积雪面积。

除用线性回归方法来提取积雪面积变化的线性趋势外，本文还用到了经验正交函数(EOF)分解、多元线性回归等方法。此外，本文中时间变化曲线均在原始序列的基础上进行了九点二次平滑[21]。

考虑到积雪分布和季节变化，选取高原(27.5°～40°N，70°～105°E)和东亚大陆北部(40°～60°N，70°～140°E)两个关键区来研究东亚未来积雪面积变化。时间上采用常用的季节划分方式，即3～5月代表春季(MAM)，6～8月代表夏季(JJA)，9～11月代表秋季(SON)，12～2月代表冬季(DJF)。

## 3 全球气候模式对东亚地区积雪面积的模拟

比较NOAA的观测结果(图1，此处仅给出夏、冬季图)，可以看出，多模式集合基本模拟出了积雪面积的主要空间分布特征，夏季积雪主要位于高原，而秋、冬、春季扩展到整个东亚大陆北部地区。但与NOAA相比，还存在明显的模拟偏差，尤其是夏季高原周边从帕米尔高原到喜马拉雅山一线和念青唐古拉山东段多雪及高原腹地少雪的空间分布特征，不仅没有模拟好，甚至还有些相反的趋势，这可能是由于地形和下垫面复杂地区的积雪面积时空变率较大，而当前气候模式分辨率普遍较低，对次网格积雪过程模拟的不好有关。此外，秋、冬、春季在高原表现出与夏季一致的模拟偏差，同时，冬、春季在东亚大陆北部地区积雪面积模拟的偏少。值得注意的是，冬季在中国大陆中部地区出现了一个十分明显的正偏差，这可能会造成模式对积雪面积趋势进行预测时出现虚假的趋势。

从区域平均来看，不同模式在各个季节均表现出较大的不确定性(图2，仅给出冬季图)。春季，多模式集合(NOAA)给出的积雪面积在东亚大陆北部和高原分别为44%(43%)和40%(25%)；秋季分别为31%(25%)和26%(16%)；冬季分别为76%(80%)和57%(32%)；夏季，积雪主要位于高原，多模式集合为8%，略小于NOAA的13%。总的来说，东亚大陆北部的积雪面积模拟更接近于NOAA观测资料，而高原的秋、冬、春季模式集合要明显大于NOAA观测，夏季则比观测的略小。

积雪面积变化受气温、融雪速度以及降雪量等诸多不确定因素的影响，这给气候模式对积雪面积的年际变化及其趋势的模拟造成了很大的不确定性。从图2中可以看出，不同模式对冬季积雪面积年际变化的模拟表现出较大的不一致性，只有极少数模式与NOAA具有显著相关性。从线性趋势来看(1971－1994年共24年资料)(表1)，除东亚大陆北部秋季外，多模式集合对趋势符号的模拟完全



© 1994-2011 China Academic Journal Electronic Publishing House. All rights reserved. http://www.cnki.net

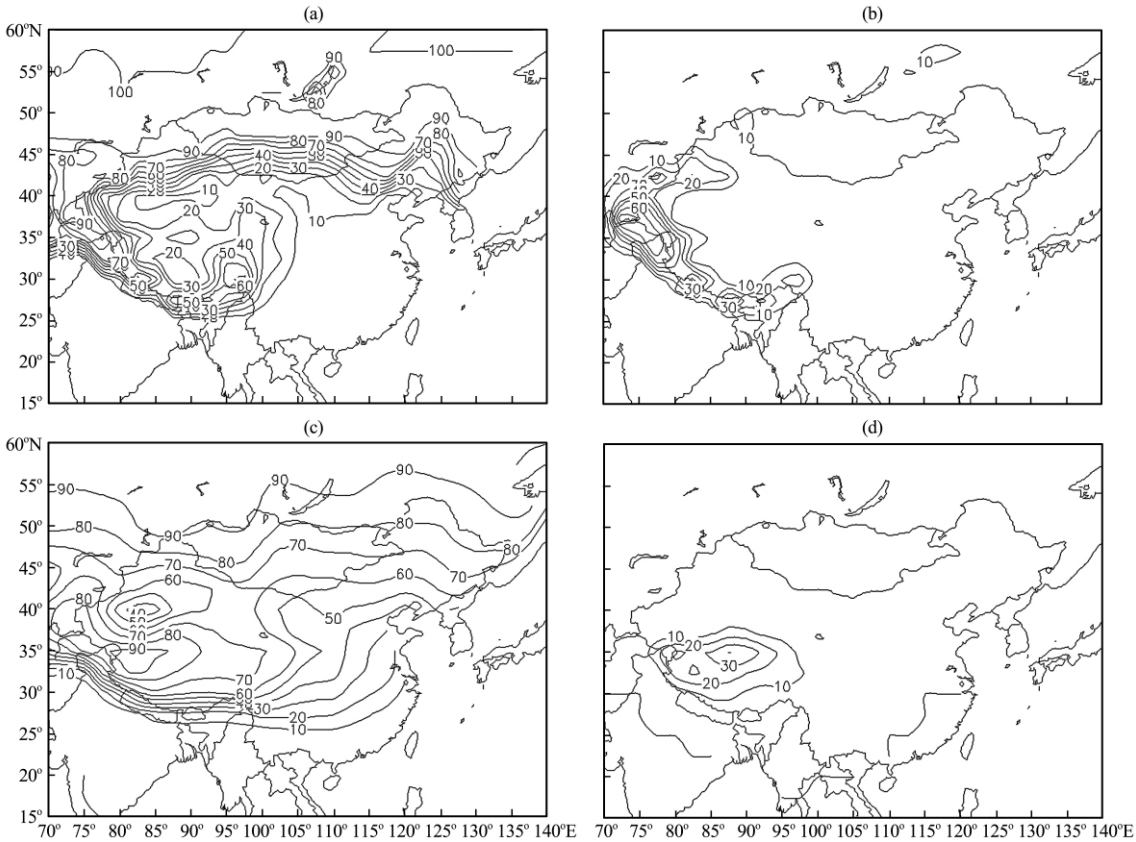


**图 1**　NOAA(a, b)**和多模式集合**(c, d)**的东亚多年平均冬季**(a, c)**和夏季**(b, d)**积雪面积分布**(**单位**：%)

Fig. 1　Distribution of multi-year mean of snow cover fraction in winter (a, c) and summer (b, d) in East Asia for NOAA(a, b) and multi-model ensemble(c, d). Unit: %

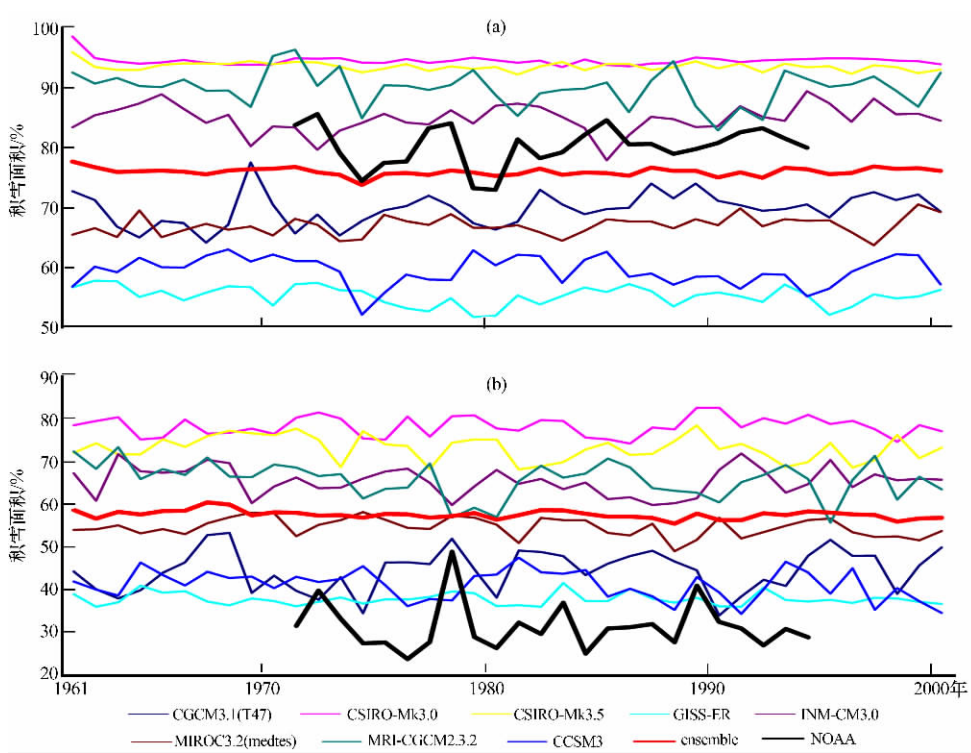


**图 2**　1961－2000 **年冬季**(a)**东亚大陆北部和**(b)**高原积雪面积变化**(**单位**：%)

Fig. 2　Variations of snow cover fraction in northern East Asia (a) and Qinghai-Xizang Plateau (b) in winter from 1961 to 2000. Unit: %



© 1994-2011 China Academic Journal Electronic Publishing House. All rights reserved.　http://www.cnki.net

表 1 1971－1994 年积雪面积线性趋势(单位:%·(10 a)$^{-1}$)

Table 1 Linear trend(unit: %·(10 a)$^{-1}$) of snow cover fraction from 1971 to 1994

| | NH_MAM | NH_SON | NH_DJF | TB_MAM | TB_SON | TB_DJF | TB_JJA |
|---|---|---|---|---|---|---|---|
| 集合 | －0.04 | 0.13 | 0.17 | －0.39 | －0.56 | －0.14 | －0.25 |
| NOAA | －2.65 | －1.88 | 0.67 | －6.57 | －2.76 | －0.61 | －3.87 |

注：NH 代表东亚大陆北部，TB 代表高原

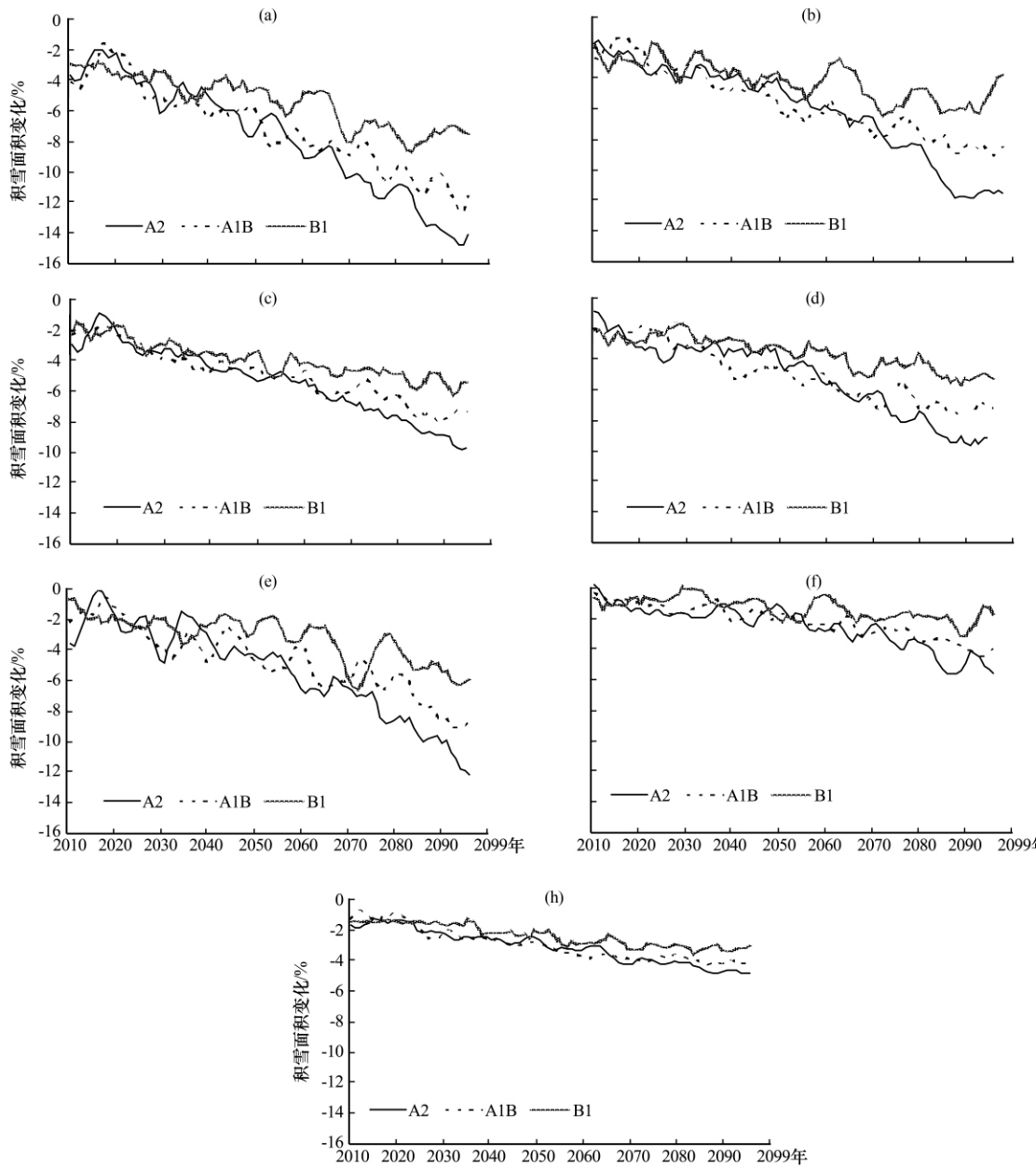


图 3 不同排放情景下多模式集合的 2010－2099 年高原和东亚大陆北部积雪面积变化(单位：%)

相对于 1961－2000 年平均. (a)TB_MAM, (b) NH_MAM, (c) TB_SON, (d) NH_SON, (e) TB_DJF, (f) NH_DJF, (g) TB_JJA

Fig. 3 Variations of snow cover fraction of Qinghai-Xizang Plateau and northern East Asia in 2010－2099 for multi-model ensemble under different scenarios. Unit: %, compared to average of 1961－2000

正确，但在量级上模式模拟的与 NOAA 相比还有较大的差距。

需要指出的是，NOAA 观测资料本身存在分辨率低、受云影响较大等缺点，尤其是 1981 年前后统计方法的改变，前后积雪面积存在几十到 $3\times10^4$ km$^2$ 的误差[3]，因此，仅用 NOAA 观测资料来验证



© 1994-2011 China Academic Journal Electronic Publishing House. All rights reserved. http://www.cnki.net

模式，可能存在较大的不确定性。此外，台站观测研究表明，高原从 20 世纪 60 年代中期到 80 年代末积雪呈现出明显的增加趋势，90 年代后又表现出减少的趋势[3,22]，本文模式虽未能模拟出高原积雪的这种变化，不过台站观测的是雪深，与本文的积雪面积并不等同，在此仅作为参考。

尽管模式对积雪面积年代际变化的模拟能力较差，但考虑到 21 世纪气温的持续升高是影响积雪面积变化的显著因子，这可能会弱化其他不确定因素的影响，因此，下面仍用模式结果来对 21 世纪东亚积雪面积变化趋势进行预测。

## 4　东亚地区未来积雪面积的可能变化

### 4.1　积雪面积变化趋势

图 3 给出了不同排放情景下多模式集合的 2010－2099 年高原和东亚大陆北部两个关键区积雪面积的变化曲线。从图 3 中可以看出，两个关键区未来积雪面积在所有季节都呈现显著的下降趋势。在 SRES A2 情景下，高原上春、夏、秋、冬四个季节的线性趋势分别为－1.42，－0.42，－0.90 和－1.16%·(10 a)$^{-1}$；对于 A1B 情景，线性趋势分别为－1.06，－0.39，－0.69 和－0.82%·(10 a)$^{-1}$；对于 B1 情景，线性趋势分别为－0.62，－0.26，－0.44 和－0.50%·(10 a)$^{-1}$。而在东亚大陆北部，在 SRES A2 情景下，春、秋、冬季三个季节(东亚大陆北部夏季几乎没有积雪存在，此处不予考虑)的线性趋势分别为－1.17，－0.93 和－051%·(10 a)$^{-1}$；对于 A1B 情景，线性趋势分别为－0.86，－0.70 和－0.41%·(10 a)$^{-1}$；对于 B1 情景，线性趋势分别为－0.40，－0.39 和－0.20%·(10 a)$^{-1}$(以上趋势均通过了 99%信度)。可以看出，不论对于哪个区域或季节，积雪面积的线性趋势都是 A2 情景最大，A1B 次之，B1 最小。而在同一种排放情景下，春季的减小趋势最大，其次是冬季，秋季次之，夏季最小。而不同区域之间比较，冬、春季高原积雪面积变化趋势要明显大于东亚大陆北部，秋季二者差异不大。

为了分析不同排放情景下的积雪面积变化差异，计算了不同情景下的标准差变化曲线(图略)，发现标准差在 2050 年前增加幅度较小，不同情景间差异不大，而在 2050 年以后呈快速增加趋势，说明积雪面积对排放情景的响应程度在 2050 年以后出现了明显分叉。进一步分析不同排放情景下 2050 年前后的积雪变化趋势，发现 SRES A2 情景下，东亚大陆北部的秋、冬、春季以及高原的冬季的积雪面积减小趋势在 2050 年后有一个突然加速的过程(前后趋势相差在 3 倍左右)，而在 A1B 和 B1 情景下减小趋势增加幅度不大(高原的夏、秋季减小趋势反而变缓)。

由于不同模式之间具有较大的不确定性，需要验证不同模式对集合所预测的积雪面积变化趋势是否具有一致性。为此，比较不同气候模式预估积雪面积的未来变化趋势发现，SRES A2 情景下(图 4)，NH(MAM)、NH(SON)、NH(DJF)、TB(MAM)、TB(SON)、TB(DJF)和 TB(JJA)分别有 8(8)①，8(8)，7(5)，8(8)，8(8)，8(8)和 8(6)个模式趋势为负值；对于 SRES A1B 情景，分别有 8(8)，8(8)，6(5)，8(8)，8(8)，7(7)和 8(6)个模式趋势为负值；而 SRES B1 情景下分别有 8(6)，8(7)，6(4)，8(6)，8(7)，8(5)和 8(7)个模式趋势为负值。总的来看，绝大多数模式在预测东亚未来积雪面积减小趋势上表现出了较好的一致性，模式间的差异较小。

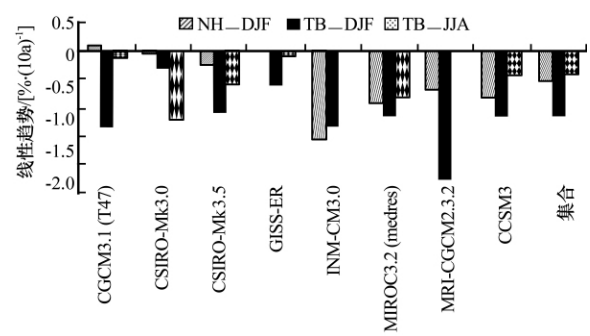


图 4　SRES A2 情景下不同气候模式模拟的 2010－2099 年积雪面积线性趋势(单位：%·(10 a)$^{-1}$)

Fig. 4　Linear trend of snow cover fraction in 2010－2099 simulated by different models under SRES A2 scenario. Unit: %·(10 a)$^{-1}$

为了进一步研究未来积雪面积变化的时空特征，对多模式集合的未来百年年平均积雪面积进行 EOF 分解，结果发现(图 5)，第一特征向量的方差贡献高达 74.4%，在整个东亚地区表现为以高原为中心的正值分布，对应的时间系数在整个 21 世纪呈明显的减小趋势，并在 2050－2060 年之间由正位相转变为负位相。第二特征向量在高原及以东地区为负，而在东亚大陆北部地区为正，解释方差为

① ( )内数字表示趋势为负的模式中达到 99%信度的模式个数，下同。



© 1994-2011 China Academic Journal Electronic Publishing House. All rights reserved.　http://www.cnki.net

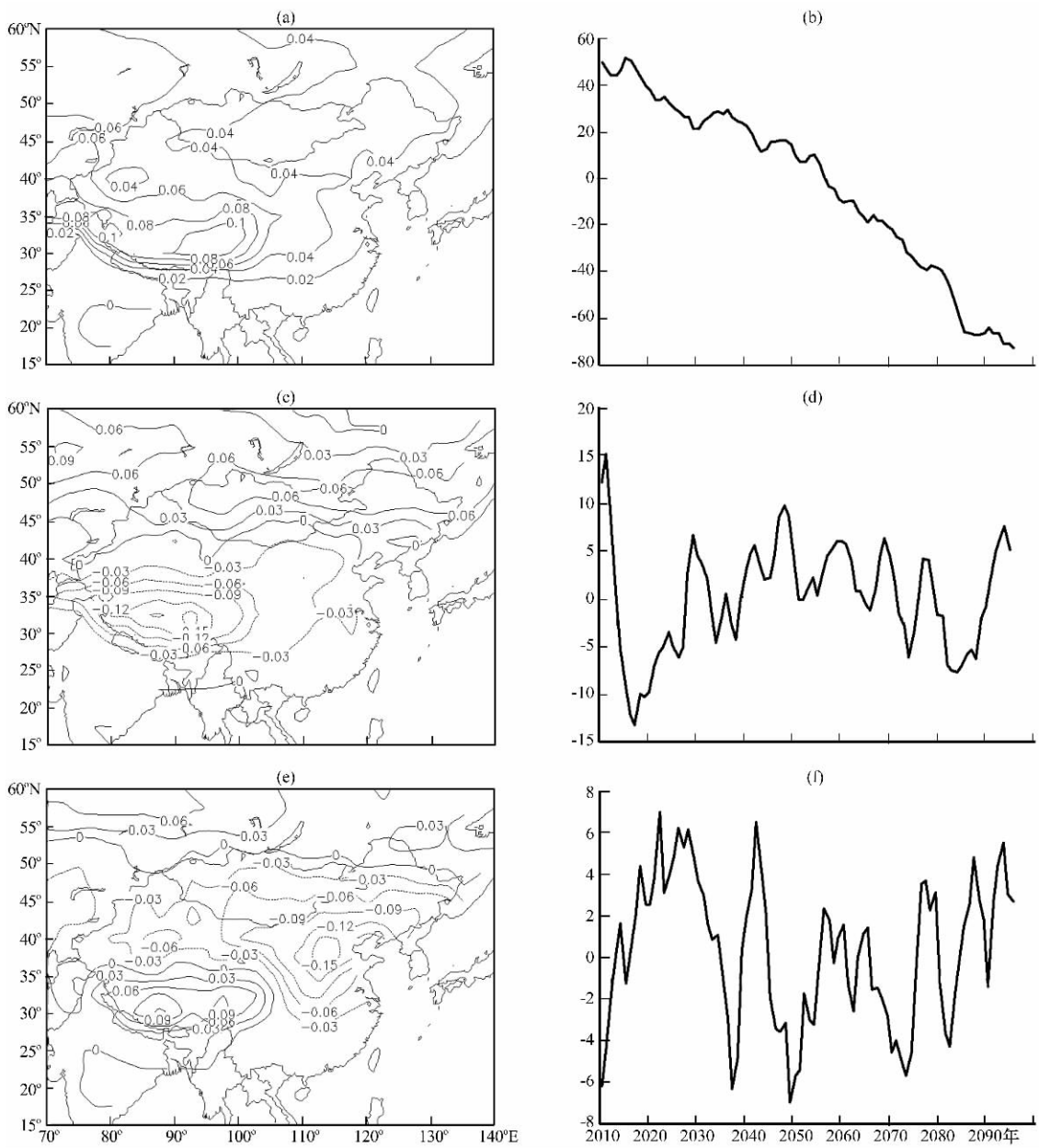


**图 5 2010—2099 年东亚地区积雪面积变化的 EOF 分析**

(a)、(b) 第一模态空间分布和时间系数，(c)、(d) 第二模态空间分布和时间系数，(e)、(f) 第三模态空间分布和时间系数

Fig. 5 EOF analysis of snow cover fraction in East Asia region from 2010 to 2099. (a), (b) spatial distribution and time coefficient for the first mode, (c), (d) spatial distribution and time coefficient for the second mode, (e), (f) spatial distribution and time coefficient for the third mode

3.6%。第三特征向量在以华北为中心的我国北方地区为负值，高原和东亚大陆北部为正值，解释了2.4%的方差贡献。第二和第三特征向量的时间系数均没有明显的线性趋势，但表现出明显的年代际扰动。

需要指出的是，尽管第二和第三特征向量方差贡献较小，但其较强的年代际波动可能和东亚季风气候的年际变化存在联系，这有待于进一步研究。

### 4.2 积雪面积变化的主要原因

积雪面积变化的原因很多，但最重要的因子是地表气温，尤其是未来气候的持续变暖将是积雪面积减少的直接原因(以 SRES A2 情景为例进行说明，下同)。表 2 分别给出了两个关键区 2010—2099 年地表气温和降雪量的线性趋势。对于地表气温，线性趋势在 0.44～0.58 ℃·(10 a)$^{-1}$之间，



© 1994-2011 China Academic Journal Electronic Publishing House. All rights reserved. http://www.cnki.net

表 2　SRES A2 情景下 2010－2099 年地表气温($T$)和降雪量($P$)线性趋势

Table 2　Linear trend of surface air temperature($T$) and snowfall($P$) during 2010－2099 under SRES A2 scenario

| | NH_MAM | NH_SON | NH_DJF | TB_MAM | TB_SON | TB_DJF | TB_JJA |
|---|---|---|---|---|---|---|---|
| $T$/(℃·(10 a)$^{-1}$) | 0.45 | 0.51 | 0.58 | 0.51 | 0.47 | 0.55 | 0.44 |
| $P$/[mm·(10 a)$^{-1}$] | －3.64 | －3.02 | 3.03 | －7.68 | －6.40 | －0.29 | －3.39 |

注：说明同表 1

表 3　回归方程(1)中回归系数

Table 3　Coefficients in equation (1)

| | NH_MAM | NH_SON | NH_DJF | TB_MAM | TB_SON | TB_DJF | TB_JJA |
|---|---|---|---|---|---|---|---|
| $a$ | －2.63 | －1.00 | －1.24 | －2.58 | －1.18 | －1.80 | －0.02 |
| $b$ | 0.003 | 0.13 | 0.08 | 0.01 | 0.06 | 0.08 | 0.14 |

注：说明同表 1

表 4　SRES A2 情景下地表气温和降雪量对积雪面积趋势的贡献(单位：%·(10 a)$^{-1}$)

Table 4　Contribution (unit: %·(10 a)$^{-1}$) linear trend of surface air temperature and snowfall to snow cover fraction under SRES A2 scenario

| | NH_MAM | NH_SON | NH_DJF | TB_MAM | TB_SON | TB_DJF | TB_JJA |
|---|---|---|---|---|---|---|---|
| $T$ | －1.18 | －0.51 | －0.72 | －1.30 | －0.56 | －0.99 | －0.01 |
| $P$ | －0.01 | －0.40 | 0.25 | －0.08 | －0.38 | －0.02 | －0.48 |

注：说明同表 1

总体表现为冬季增温最快，春、秋季次之，夏季最小。分析积雪面积与地表气温之间的变化关系，发现积雪面积和地表气温之间呈显著的负相关，相关系数均在－0.9 以上。这充分说明全球气候变暖造成的积雪融化速度加快是积雪面积减少的主要原因。降雪量作为对积雪的补充，也会对积雪面积的变化产生一定影响。从未来降雪量的线性趋势可以看出，在不同的区域降雪量的变化差异较大，除东亚大陆北部冬季降雪量增加(3.03 mm·(10 a)$^{-1}$)外，其余均呈减少趋势，其中高原春、秋季减少最快，分别达到－7.68 mm·(10 a)$^{-1}$和－6.40 mm·(10 a)$^{-1}$；而冬季减少趋势最小，仅为－0.29 mm·(10 a)$^{-1}$，降雪量变化的差异可能对不同区域和季节的积雪面积变化产生不同的影响。

考虑到积雪面积与地表气温及降雪量之间都具有较好的线性关系，利用多元线性回归方法建立线性回归方程如下(为方便了解温度和降水对积雪面积变化的贡献，回归时将常数项强制设为零)：

$$SN = aT + bP, \tag{1}$$

回归系数见表 3。经检验，这 7 组方程均在 $a=0.01$ 显著性水平之上，且气温和降雪均对积雪面积的变化具有显著作用，能够很好地拟合出未来积雪面积的变化。从上述回归方程可以看出，温度的升高对积雪面积的减少起到正贡献，而降雪量的增加则会对积雪进行补充，延缓积雪面积的减小。在不考虑降雪变化的情况下，相同升温带来的积雪面积减小在春季最大(东亚大陆北部和高原分别达到－2.63%·℃$^{-1}$和－2.58%·℃$^{-1}$)，其次是秋、冬季，而在高原夏季最小，仅为－0.08%·℃$^{-1}$。相反，在不考虑温度变化的情况下，高原春季以及东亚大陆北部的秋季积雪面积对降雪量的响应最敏感，超过了 0.1%·mm$^{-1}$；而东亚大陆北部春季最小，仅为 0.003%·mm$^{-1}$。总的来看，在不同的区域和季节，积雪面积变化对地表气温和降雪量的响应表现了较大的差异。

综合温度和降雪量两个因素，可以很好地解释未来不同区域和季节积雪面积变化的差异，为此，计算了地表气温和降雪量对积雪面积趋势的贡献(表 4)。春季，东亚大陆北部和高原积雪面积变化对温度的响应程度最大，但高原降雪量对积雪面积的贡献要远大于东亚大陆北部，因此高原春季的积雪面积减小趋势最大，东亚大陆北部春季次之；秋季，地表气温和降雪量的贡献相当，秋季东亚大陆北部和高原积雪面积减小趋势比较接近；冬季，高原地表气温对积雪面积的贡献明显大于东亚大陆北部，同时，东亚大陆北部冬季降雪量增加，高原冬



© 1994-2011 China Academic Journal Electronic Publishing House. All rights reserved.　http://www.cnki.net

季变化较小，造成高原冬季积雪面积的变化要远大于东亚大陆北部冬季；夏季，高原积雪面积对地表气温的响应很小，积雪面积变化主要由降雪量较少引起的。

## 5 结论与讨论

利用 WCRP CMIP3 气候模式对当前东亚地区积雪面积的模拟能力和不同排放情景下积雪面积的未来变化趋势进行了研究，得到以下主要结论：

（1） 气候模式对当前东亚地区积雪面积的多年平均分布特征具备了一定的模拟能力，但还存在明显的差距，尤其是在复杂地形的高原地区。模式对积雪面积的年际变化模拟较差，多模式集合尽管能模拟出区域平均的积雪面积线性变化趋势的符号，但在量级上和 NOAA 观测资料还有较大的差距。

（2） 未来东亚地区积雪面积将呈现出一致减少的趋势。在同一种排放情景下，春季的减小趋势最大，冬季次之，秋季再次之，夏季最小。而不同区域之间比较，冬、春季高原积雪面积变化趋势要明显大于东亚大陆北部，秋季二者差异不大。而对不同排放情景而言，SRES A2 情景减小趋势最大，A1B 次之，B1 最小。

（3） 地表气温和降雪量变化是造成积雪面积减小的主要原因，但在不同的区域和季节，它们对积雪面积变化趋势的贡献有明显差异。

已有的研究表明，东亚积雪面积的减少必将对东亚气候造成重要影响。首先，积雪面积减小造成地表反照率减小，从而增加地表的辐射收支，引起局部的进一步升温，反过来升温又会造成积雪面积的进一步减小，这种积雪和气候之间的正反馈会加强温室气体引起的气候变暖，但这种正反馈的强度有多大还有待进一步研究。最近，孙颖等[23]通过研究 IPCC AR4 气候模式预测结果，指出未来东亚季风环流和降水都将加强或增加，并且我国东部雨型的偶极型分布将转变为全面多雨型，从现有的研究关系来分析，这可能和东亚积雪的减少存在一定的内在联系，有必要进一步研究。

需要指出的是，受模拟能力的限制以及排放情景的不确定性，气候模式对积雪过程的模拟还存在较大差距，因此，本文的研究结果仅代表当前气候模式对未来积雪面积变化的模拟水平，随着积雪过程等物理机制的进一步完善，对积雪乃至气候变化的认识必将进一步提高。

## 参考文献


[1] Vavrus S. The role of terrestrial snow cover in the climate system[J]. Climate Dynamics，2007，29(1)：73－78.

[2] 韦志刚，吕世华. 青藏高原积雪的分布特征及其对地面反照率的影响[J]. 高原气象，1995，14(1)：67－73.

[3] 韦志刚，黄荣辉，陈文，等. 青藏高原地面站积雪的空间分布和年代际变化特征[J]. 大气科学，2002，26(4)：496－508.

[4] 柯长青，李培基. 青藏高原积雪分布与变化特征[J]. 地理学报，1998，53(3)：209－215.

[5] 李培基. 高亚洲积雪监测[J]. 冰川冻土，1996，18(增刊)：105－114.

[6] 杨琨，武炳义. 欧亚大陆积雪与亚洲季风关系研究进展[J]. 气象科技，2009，37(3)：263－270.

[7] 朱玉祥，丁一汇. 青藏高原积雪对气候影响的研究进展和问题[J]. 气象科技，2007，35(1)：1－8.

[8] 张顺利，陶诗言. 青藏高原积雪对亚洲夏季风影响的诊断及数值研究[J]. 大气科学，2001，25(3)：372－390.

[9] 杨梅学，姚檀栋. 青藏高原雪盖对亚洲季风影响进展[J]. 冰川冻土，1998，2(2)：186－191.

[10] 范广州，罗四维，吕世华. 青藏高原冬季积雪异常对东、南亚夏季风影响的初步数值模拟研究[J]. 高原气象，1997，16(2)：140－152.

[11] 陈乾金，高波，张强. 青藏高原冬季雪盖异常与冬夏季风变异及其相互联系的物理诊断研究[J]. 大气科学，2000，24(4)：477－492.

[12] Wu Bingyi，Yang Kun，Zhang Renhe. Eurasian snow cover variability and its association with summer rainfall in China [J]. Adv Atmos Sci，2009，26(1)：31－44.

[13] 彭京备，陈烈庭，张庆云. 青藏高原异常雪盖和 ENSO 的多尺度变化及其与中国夏季降水的关系[J]. 高原气象，2005，24(3)：366－377.

[14] 陈兴芳，宋文玲. 欧亚和青藏高原冬春季积雪与我国夏季降水关系的分析和预测应用[J]. 高原气象，2000，19(2)：214－223.

[15] 朱玉祥，丁一汇，徐怀刚. 青藏高原大气热源和冬春积雪与中国东部降水的年代际变化关系[J]. 气象学报，2007，65(6)：946－958.

[16] 朱玉祥，丁一汇，刘海文. 青藏高原冬季积雪影响我国夏季降水的模拟研究[J]. 大气科学，2009，33(5)：903－915.

[17] 陈海山，孙照渤. 欧亚积雪异常分布对冬季大气环流的影响 I 观测研究[J]. 大气科学，2003，27(3)：304－316.

[18] 陈海山，孙照渤，朱伟军. 欧亚积雪异常分布对冬季大气环流的影响 II 数值模拟[J]. 大气科学，2003，27(5)：847－860.

[19] IPCC. Climate Change 2007：The Physical Science Basis[R]. Contribution of Working Group I to the Fourth Assessment Report of the Intergovernmental Panel on Climate Change. Cambridge，UK and New York，USA：Cambridge University Press，2007.

[20] Frei A，Gong G. Decadal to century scale trends in north american snow extent in coupled atmosphere-ocean general circulation models[J]. Geophys Res Lett，2005，32 (18)，L18502.




© 1994-2011 China Academic Journal Electronic Publishing House. All rights reserved. http://www.cnki.net

[21] 魏凤英. 现代气候统计诊断预测技术[M]. 北京：气象出版社，1999：1－269.
[22] 雷俊，方之芳. 青海地区常规观测积雪资料对比及积雪变化趋势研究[J]. 高原气象，2008，27(1)：58－67.
[23] 孙颖，丁一汇. 未来百年东亚夏季降水和季风预测的研究[J]. 中国科学(D 辑)，2009，39(11)：1487－1504.

# Trend of Snow Cover Fraction in East Asia in 21th Century under Different Scenarios

WANG Fang,　DING Yi-hui
(*National Climate Center*, *Beijing* 100081, *China*)

**Abstract**: Using the snow cover fraction (SNC) output by 8 WCRP CMIP3 climate models under SRES A2, A1B and B1 scenarios, the trend of SNC in East Asia in future is analyzed. Results show that SNC is likely to decrease in East Asia continent, where SNC decreases the fastest in spring(MAM), then winter(DJF) and autumn(SON), and the slowest in summer(JJA), under the same scenario. In spring and winter, the SNC decreases faster in Qinghai-Xizang Plateau than in northern East Asia, while in autumn there is little difference between them. As for different scenarios, SRES A2 has the largest decrease trend, then A1B, and B1 has the least trend. The decrease of SNC is mainly caused by the changes of surface air temperature and snowfall, but they have different contributions to SNC trend in different regions and seasons.

**Key words**: East Asia; Snow cover fraction; Climate model



© 1994-2011 China Academic Journal Electronic Publishing House. All rights reserved.　http://www.cnki.net

王启光，封国林，郑志海，等. 2011. 长江中下游汛期降水优化多因子组合客观定量化预测研究 [J]. 大气科学，35 (2)：287－297. Wang Qiguang，Feng Guolin，Zheng Zhihai，et al. 2011. A study of the objective and quantifiable forecasting based on optimal factors combinations in precipitation in the middle and lower reaches of the Yangtze River in summer [J]. Chinese Journal of Atmospheric Sciences (in Chinese)，35 (2)：287－297.

# 长江中下游汛期降水优化多因子组合客观定量化预测研究

王启光[1] 封国林[2,3] 郑志海[2] 支蓉[2]

1 兰州大学大气科学学院，兰州 730000
2 国家气候中心气候研究开放实验室，北京 100081
3 中国科学院大气物理研究所东亚区域气候—环境重点实验室，北京 100029

**摘 要** 针对长江中下游区域汛期降水模式预报误差，利用历史资料的有用信息订正模式预报误差。根据国家气候中心预测室提供的 74 项环流特征量和美国国家海洋和大气管理局发布的 40 项气候指数，确定降水预报误差场的相似年份，利用相似年的降水误差场对模式结果进行相似误差订正，有别于传统的模式系统误差订正。研究发现，相似误差订正效果明显优于系统误差订正。在此基础上，对前期因子进行筛选，确定相似误差场的多因子优化组合，并结合加权集合平均的方法，提出了基于优化多因子组合的客观定量化预测（OQF）技术。2003～2009 年 7 年的独立样本回报结果表明，基于优化多因子组合的 OQF 方案具有较高的预报技巧，平均距平相关系数为 0.43。最后对历史资料中误差场间的距平相关系数进行分析，发现确定误差场相似年的关键技术还有待于进一步完善，并指出了改进方法的可能途径。

**关键词** 客观定量化预测 优化多因子组合 长江中下游汛期降水 模式预报误差
**文章编号** 1006－9895 (2011) 02－0287－11 **中图分类号** P426 **文献标识码** A

# A Study of the Objective and Quantifiable Forecasting Based on Optimal Factors Combinations in Precipitation in the Middle and Lower Reaches of the Yangtze River in Summer

WANG Qiguang[1]，FENG Guolin[2,3]，ZHENG Zhihai[2]，and ZHI Rong[2]

1 *College of Atmospheric Sciences*，*Lanzhou University*，*Lanzhou* 730000
2 *Laboratory for Climate Studies*，*National Climate Center*，*China Meteorological Administration*，*Beijing* 100081
3 *Key Laboratory of Regional Climate-Environment for Temperate East Asia*，*Institute of Atmospheric Physics*，*Chinese Academy of Sciences*，*Beijing* 100029

**Abstract** A new approach to improve precipitation in the Yangtze River in summer by using the useful historical data is suggested. The outcomes of the model can be improved by determining the years in which there are similar prediction error fields of precipitation based on 74 circulation characteristic indexes of Weather Diagnostic Forecasting

**收稿日期** 2010－05－18，2010－08－12 收修定稿
**资助项目** 公益性行业科研专项 GYHY200806005、GYHY201106016，国家自然科学基金资助项目 40875040、40930952、41005041，国家科技支撑计划 2007BAC29B01、2009BAC51B04



**作者简介** 王启光，男，博士研究生，主要从事短期气候预测研究。E-mail：photon316@163.com
**通讯作者** 封国林，E-mail：fenggl@cma.gov.cn

Room of National Climate Center and 40 climate indexes of NOAA, and then the fields are integrated to revise the output errors of the model. The results show that the revised errors using the above method are better than system ones. On the basis of the above conclusions, the objective and quantifiable forecasting (OQF) technique can be established. The steps are selecting pre-factors, determining optimal factor combinations (OFC) of the analogy forecasting error fields, and using the method of weighted average integration. It shows that the technique of OQF based on OFC has a better prediction skill to the regression results of independent samples between 2003 and 2009. Finally, the anomaly correlation coefficient (ACC) of historical data in the error field is analyzed. It is found that the determining of the analogy error field in different years can be improved more, and the possible way to improve is to be discussed.

**Key words** objective and quantifiable forecasting, optimal factors combinations, the precipitation in the middle and lower reaches of the Yangtze River in summer, the error of model forecast

## 1 引言

夏季旱涝异常分布对国民经济特别是对农业生产影响极大，是中央领导和各级政府极为关注的重要问题，也是众多气象学家长期以来研究的主要科学难题。中国汛期降水一个非常显著的特点是年际变化大，影响因素多种多样，特别是长江中下游地区，影响因素更为复杂多变，汛期降水有时可能是部分因素甚至是个别因素起主要作用，有时又可能是多种因素共同作用的结果。因此，长江中下游地区汛期降水预测具有很大的挑战性，这一科学难题吸引了众多科学家参与，几十年来取得了一系列研究成果。早在 20 世纪 50 年代，以陶诗言等（1958）为代表的气象学家从东亚大气环流和天气过程的变化角度研究长江流域的汛期降水，指出长江中下游汛期降水是亚洲大气环流季节变化的典型表现。20 世纪 80 年代，陈隆勋（1984）、Tao and Chen（1987）进一步提出，东亚夏季风系统内存在热带辐合带和长江中下游汛期降水锋带。海温变化尤其是 ENSO 事件作为大气环流变化的背景场，对长江中下游夏季降水有较为重要的影响。黄荣辉和孙凤英（1994）研究表明，热带西太平洋和赤道中、东太平洋海温异常偏低，致使菲律宾周围的热带西太平洋对流活动很弱，从而造成副热带高压偏南。吴国雄和刘还珠（1995）的研究表明，长江中下游的旱涝与中国近海海温（南海、印度洋等）关系密切。最近，Zhou and Wang（2006）研究了北半球春季 Hadley 环流对长江流域夏季降水的可能影响，指出春季 Hadley 环流变化可以激发印度洋和南海海表温度异常，该异常从春季一直持续到夏季，反过来引起东亚夏季环流异常，进而影响到长江流域夏季降水。范可（2006）研究表明，北半球春季正的南极涛动有利于长江中下游降水，在春、夏两季中，南半球在整个对流层中持续异常增温，季风推动力减弱，长江中下游易出现涝年。Sun et al.（2009）对南极涛动作用机制进行了深入研究，揭示了北半球春季南极涛动对夏季西太平洋副热带高压（下称西太副高）的可能影响途径。刘芸芸和丁一汇（2009）分别从时间和空间角度分析了西北太平洋夏季风与中国长江流域夏季降水的联系，发现二者存在显著的负相关关系。鲍名（2009）从中期天气过程的角度分析了近八年不利于长江中下游梅雨的主要因子。目前面临的主要问题是：影响长江中下游区域汛期旱涝的影响因子众多，如何利用这些多因子优化组合来提高该地区汛期降水的预报水平？

当前的相关研究表明，动力和统计相结合是提高短期气候预测准确率比较有效的途径之一（Barnett and Preisendorfer，1978；Chao et al.，1982；Huang et al.，1993；van den Dool，1994）。围绕两者如何有效结合的问题，国内外开展了广泛的研究，如集合预报技术、物理模型预测技术以及模式后处理等（范可等，2007，2008；Wang and Fan，2009；柯宗建等，2009；庄照荣等，2010）。其中，在气候模式预报基础上结合物理统计方法，利用历史资料信息对模式误差进行预报是引人注目的研究方向。顾震潮（1958）早在 1958 年就提出将数值预报从初值问题改为演变问题，指出了数值天气预报中使用历史资料的重要性和可行性；丑纪范（1974，1986）从理论上探讨了在长期预报中实现动力和统计相结合的做法；曹鸿兴（1993）提出一种基于大气自记忆原理的方法，从而把大气运动方程推广为包含多时次观测的自忆性方程；封国林等（2001）、Feng and Dong（2003）、Feng et al.（2004）提出了一种回溯阶差分格式方法，给出了由过去时次

资料动态求取记忆函数的方法；任宏利和丑纪范（2005，2007a，2007b）、任宏利等（2006）和郑志海等（2009）提出和发展了一种适用于动力季节预测的相似误差订正方法，预报结果显示该方法能有效提高热带降水和环流的预报技巧。但是对于长江中下游地区汛期降水而言，其预测水平有待进一步提高。

本文基于历史相似信息对动力模式的误差进行预报的思路，采用优化多因子组合的方式确定相似误差场，进一步发展了相似误差的提取技术。同时基于 3 种不同多因子优化组合选取相似误差场，并进行加权集合平均处理，提出了客观定量化预测（Objective and Quantifiable Forecasting，简称 OQF）方法。该方法从数值预报模式出发，以推导出的动力相似预报方程作为理论依据，将日益丰富的历史资料相似信息有效地运用到不断完善的数值模式中，利用已知的历史相似信息估计当前未知的模式预报误差。采用多个前期因子综合判断历史相似，选取了具有针对性的历史相似年，在不改变动力模式框架的基础上，有效地改进了模式的预测效果。利用该方法对长江中下游地区（27.5°N～32.5°N，110°E～122.5°E）2003～2009 年共 7 年的汛期降水进行了独立样本回报试验，结果表明该方法可以明显改善汛期降水预测效果，最后指出了 OQF 方法可能的改进思路。

## 2　资料和方法

### 2.1　资料介绍

利用国家气候中心（NCC）全球气候业务模式生成的 1983～2009 年共 27 年回报和预报数据资料集，选用 2 月底起报的 48 个初始场每年 6～8 月集合平均结果。将美国气候预报中心组合降雨分析（CMAP）资料的总降水量作为实况观测资料（本文研究区域包含 18 个格点），结合 27 年模式回报数据中的汛期预报降水场计算汛期降水预报误差场，并以 1983～2002 年资料计算气候平均态。利用国家气候中心气候系统诊断预测室提供的 74 项环流特征量以及美国国家海洋和大气管理局（NOAA）发布的 40 项气候指数作为因子选取误差场相似年。本文独立样本回报指的是在不包含预报年及其以后年份资料信息前提下所进行的回报检验。

### 2.2　相似误差订正原理

大气数值预报模式可以简化表示为：

$$\begin{cases}\dfrac{\partial \psi}{\partial t}+L(\psi)=0,\\ \psi(x,t_0)=\psi_0(x),\end{cases}\tag{1}$$

其中，$\psi(x,t)$ 为模式预报变量，$x$ 和 $t$ 分别表示空间坐标和时间，$L$ 是 $\psi$ 的微分算子，对应于实际的数值模式。$t_0$ 为初始时刻，$\psi_0$ 为初值。

长期业务预报的经验表明，在相似的初始场和边界条件下，大气状况的演变在一定的时间尺度范围内也具有一定的相似性（任宏利和丑纪范，2007a）。因此，在相似动力模式中可以将当前的预报场 $\psi$ 看成是历史相似 $\widetilde{\psi}$ 加上一个小扰动 $\hat{\psi}$，即 $\psi=\widetilde{\psi}+\hat{\psi}$。将历史参考态 $\widetilde{\psi}$ 代入式（1），有：

$$\begin{cases}\dfrac{\partial \widetilde{\psi}}{\partial t}+L(\widetilde{\psi})=E(\widetilde{\psi}),\\ \widetilde{\psi}(x,0)=\widetilde{\psi}_0(x),\end{cases}\tag{2}$$

其中，$E$ 为模式的误差算子。式（2）结合式（1）经过一系列变换（郑志海等，2009），得到模式预报结果为：

$$\hat{P}(\psi_0)=P(\psi_0)+\breve{P}(\widetilde{\psi}_j)-P(\widetilde{\psi}_j),\tag{3}$$

其中，$\hat{P}(\psi_0)$ 为进行误差项相似估计的情况下所得到的预报结果，$P(\psi_0)$ 为数值预报模式对当前初值 $\psi_0$ 的预报结果，$\breve{P}(\widetilde{\psi}_j)$ 为历史相似对应的实况，$P(\widetilde{\psi}_j)$ 为历史相似初值的预报结果。该方程的本质是引入历史相似对应的预报误差信息来估计当前的预报误差，即式（3）右端的 $\breve{P}(\widetilde{\psi}_j)-P(\widetilde{\psi}_j)$，从而减小数值模式误差，将动力预报问题转化为预报误差的估计问题。

### 2.3　检验标准

本文回报结果采用 WMO 推荐的标准化检验方案，利用常用的距平相关系数（ACC）和均方根误差（RMSE）。考虑到沿纬圈的情况，ACC 计算标准如下：

$$Q(j)=\frac{\sum_{i=1}^{N_j}[F(i,j)-C(i,j)-M_{\mathrm{f}}(j)][A(i,j)-C(i,j)-M_{\mathrm{a}}(j)]}{\sqrt{\sum_{i=1}^{N_j}[F(i,j)-C(i,j)-M_{\mathrm{f}}(j)]^2\sum_{i=1}^{N_j}[A(i,j)-C(i,j)-M_{\mathrm{a}}(j)]^2}},\tag{4}$$

其中，$Q(j)$ 为 ACC 的值，$F(i,j)$ 为预报值，$A(i,j)$ 为实况，$C(i,j)$ 为气候平均态，且有

$$\begin{cases} M_f(j) = \dfrac{1}{N_j}\sum_{i=1}^{N_j}[F(i,j)-C(i,j)], \\ M_a(j) = \dfrac{1}{N_j}\sum_{i=1}^{N_j}[A(i,j)-C(i,j)]. \end{cases} \tag{5}$$

考虑纬度订正后的 $ACC$ 值为

$$Q = \frac{1}{K}\sum_{j=1}^{N} P(j)\ \cos\theta_j, \tag{6}$$

其中，$K = \sum_{j=1}^{N}\cos\theta_j$，对高斯纬圈而言，$\theta_j$ 为高斯纬度。ACC 是预报的气候距平与实况的气候距平之间位相误差的度量，当两距平之间位相完全相同或相反，ACC 评分为 1 或−1。

第 $j$ 纬圈上的 RMSE 值为

$$R(j) = \sqrt{\frac{1}{N_j}\sum_{i=1}^{N_j}[F(i,j)-A(i,j)]^2}, \tag{7}$$

其中，$R(j)$ 为 RMSE 的值。考虑纬度订正后总的 RMSE 值为

$$R = \frac{1}{K}\sum_{j=1}^{N} R(j)\cos\theta_j, \tag{8}$$

RMSE 越小，表示模式的预报效果越好，当预报值与实况完全一致时其值为 0。

## 3 相似误差订正方法的改进

### 3.1 单因子相似误差订正

本文首先尝试从相关系数的角度入手，选取合适的前期因子进行相似误差订正。基于第 2 节相似误差订正原理，利用国家气候中心预测室提供的 74 项环流特征量和 NOAA 的 40 项气候指数进行相似降水误差场的选取。首先，将降水误差场进行经验正交（EOF）分解（黄嘉佑，1990；施能，1992），计算第一主分量时间系数与各个指数的相关系数，在通过 95%信度检验的因子集中寻找前期关键因子。由于各项指数在不同月份对长江中下游区域的降水影响可能不同，因此本文由 114 项指数可以构造出样本量为 114×12＝1368 逐月变化的因子集。确定合适的前期关键因子之后，计算单个前期关键因子预报当年的值与其他年份值的欧氏距离并进行比较，根据距离越小则判断为越相似的原则，确定预报误差场的相似年。为了保证预报误差场质量，每个前期关键因子选取了 4 个相似年（任宏利和丑纪范，2007a）的降水误差场进行等权重线性误差估计。比较发现，相关系数高的因子其交叉检验的订正效果未必就好，例如选取相关系数最高的 8 月份大西洋副高北界指数作为前期因子（相关系数为 0.63），得到相似误差订正 27 年交叉检验 ACC 仅为 0.11（图略）。

表 1 列出了针对长江中下游汛期降水利用单个前期因子进行 27 年交叉检验 ACC 排名前五位因子，研究发现，单因子相似误差订正的平均 ACC 相对于系统误差订正有明显提高，比仅利用相关系数选取的订正更有优势。例如，利用前期 10 月份全球平均陆地海洋温度指数进行相似误差订正的 27 年平均 ACC 为 0.32，比系统误差订正的−0.01 提高了 0.33。

**表 1 单因子 27 年交叉检验相似误差订正平均 ACC 排序**

**Table 1 The rank of the average ACC (anomaly correlation coefficient) of single factor in 27 years through the cross-examination of analogue error correction (only top five factors are listed)**

| 因子 | 月份 | ACC |
|---|---|---|
| 全球平均陆地海洋温度指数 | 10 | 0.32 |
| 北美副高强度指数 | 9 | 0.31 |
| 西太平洋副高面积指数 | 12 | 0.30 |
| 太平洋副高强度指数 | 8 | 0.29 |
| 热带北大西洋指数 | 10 | 0.29 |

### 3.2 多因子相似误差订正

一般而言，不同的单个前期因子在交叉检验时对相同年份的 ACC 提高是不同的，具有一定的偶然性，在实际操作过程中很难预先确定预报年前期起主导作用的关键因子，因此有必要考虑将多个因子组合起来选取相似误差场，为此进行了如下试验。

多因子相似误差订正的具体做法是，将各因子序列标准化后，利用 EOF 分解提取解释方差占 80%的主分量，然后根据各主分量的时间系数来确定 4 个降水误差场相似年，进而得到 27 年相似误差订正的交叉检验的结果。采用式（9）选取 4 个相似年对应的模式误差场的平均值作为预报年的相似误差场。

$$D = \left(\frac{\sum_{i=1}^{k} w_i(\phi'_{ij}-\phi'_{ik})^2}{\sum_{i=1}^{k} w_i}\right)^{\frac{1}{2}}, \tag{9}$$

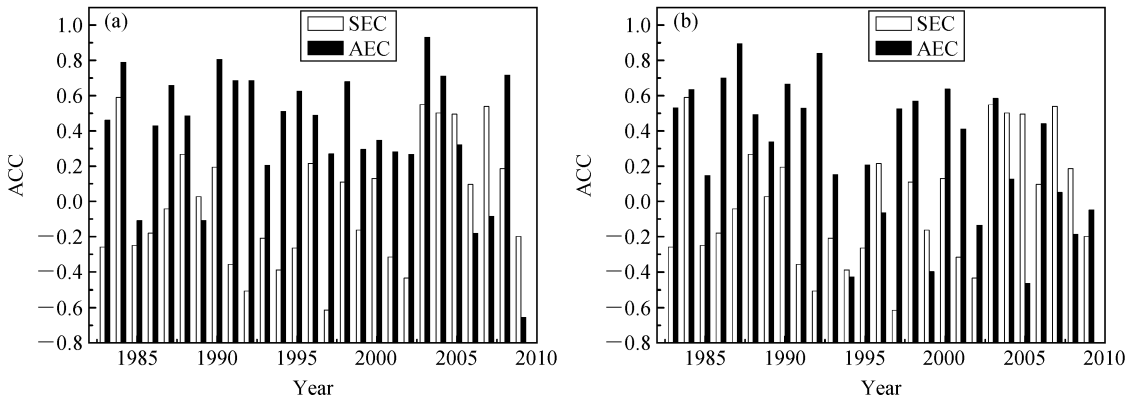


图 1　利用全球平均陆地海洋温度指数和北美副高强度指数双因子及结合西太副高面积指数三因子相似误差订正（AEC）与系统误差订正（SEC）结果比较：(a) 双因子 ACC；(b) 三因子 ACC

Fig. 1　Comparison between analogue error correction (AEC) and systematic error correction (SEC) for ACC through (a) double factors and (b) triple factors, the double factors are global average land - ocean temperature index and the strength of subtropical high in North America, the triple ones plus the western Pacific subtropical high area index

式中，$D$ 为提取的各主分量时间系数间的欧氏距离，$\phi'$ 代表各主分量的时间系数。$j$ 和 $k$ 分别代表两个不同时刻，$w_i$ 为权重系数，取各主分量的解释方差，欧氏距离越小则说明越相似。这里采用 EOF 分解可以消除因子之间可能存在的相互影响和联系，从而避免多因子线性相关导致的误差非线性增长，并且降低了因子场的维数。

图 1a 为采用表 1 中全球平均陆地海洋温度指数和北美副高强度指数这前两个因子相似误差订正结果，图 1b 为采用全球平均陆地海洋温度指数、北美副高强度指数及西太副高面积指数进行三因子相似误差订正结果。从图 1a、b 可以发现采用双因子和三因子的相似误差订正得到的交叉检验平均 ACC 都比系统误差订正要高，双因子组合订正后的 27 年平均 ACC 达到 0.39，三因子组合订正后的 27 年平均 ACC 达到 0.29。这两种因子组合相似误差订正的效果呈现一定的年代际特征，双因子组合订正效果明显的阶段处于 27 年的中后期的 15 年中（1990～2004 年），三因子组合订正效果明显的阶段主要集中在前期的 11 年（1983～1993 年），这说明不同因子组合对不同降水预测时段具有一定的针对性。从交叉检验的结果可以发现，采用双因子相似误差订正的效果要优于单因子和三因子组合，这恰恰印证了“对线性系统资料用得越多越好，对非线性系统则不然，有巧不在多”（丑纪范和任宏利，2006）这一结论。因此，采用多因子组合的方法进行相似误差订正可以取长补短，在一定程度上提高预报效果。因而本文接下来的工作就是寻找合适的、有针对性的因子组合方案，从而确定更为合适的预报年的相似误差场。

### 3.3　基于优化多因子组合的 OQF 方法

多因子相似误差订正的组合选择方案：首先将单因子相似误差订正交叉检验的平均 ACC 按从大到小排序，ACC 最大值因子作为起始因子，将因子从两个开始逐步累加，得到预报年前期历史交叉检验 ACC 评分最高的双因子组合，然后再添加第三个因子，使得此种情况下预报年前期历史交叉检验 ACC 评分最高，依此类推逐步增加因子个数。将降水预报年之前的历年交叉检验平均 ACC 作为判断组合优劣的标准，可以得到较为稳定的交叉检验的相似误差订正效果（图 2）。从图 2 中可以看出，2003～2009 年前期历史交叉检验的 ACC 开始时随因子个数的增多而增大，但当因子个数达到 10 个以上时，增大趋势逐渐变缓，趋于平稳的状态，因此，在选定因子组合的时候可以考虑取前 10 个因子。但是，在研究中发现选择的前 10 个因子中往往存在历年平均 ACC 为负值的单因子，考虑到该部分因子对误差场相似年的确定会提供虚假信息，有必要予以剔除。

图 3 给出了在 ACC 排序的基础上对因子进行进一步筛选，将单因子前期历史交叉检验中 ACC 高于 0.1 以上的因子作为前期关键因子，再进行以上逐步累加的过程，选取不同因子个数组合下预报年前期历史交叉检验 ACC 最高的因子组合，从而

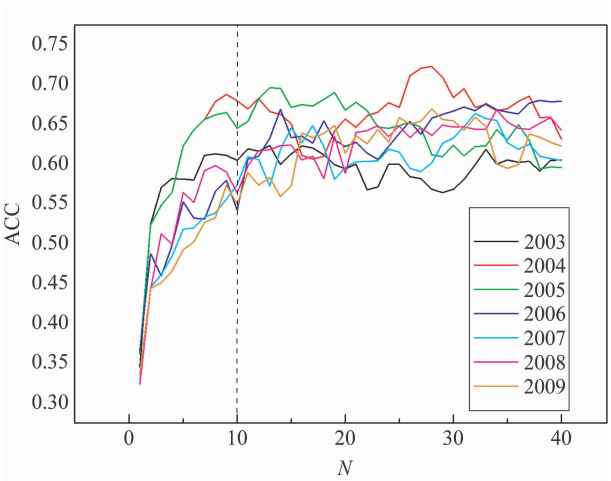


图 2 2003～2009 年的逐步累加的前期因子组合个数（N）与预报年之前年份交叉检验 ACC 关系

Fig. 2 The relationship between the number (N) of accumulated pre-factors and the ACC in the years before forecasting through cross-examination from 2003 to 2009

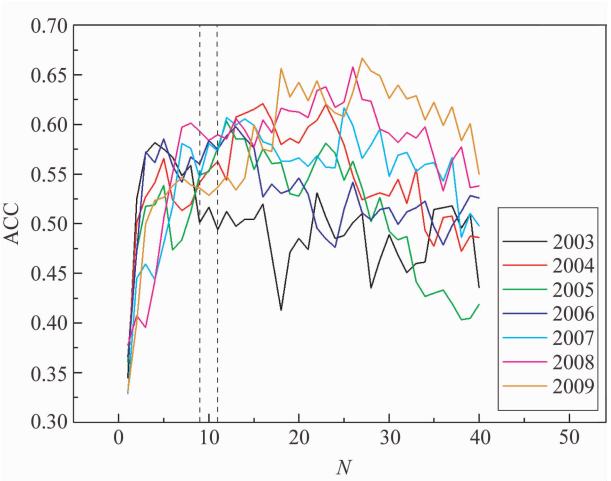


图 3 2003～2009 年优化配置的前期因子组合个数与预报年之前年份交叉检验 ACC 关系

Fig. 3 The same as Fig. 6, but for the relationship between the number of optimal factor combinations (OFC) and the ACC

得到优化多因子组合。

图 3 显示在经过进一步筛选的因子集中，当因子组合个数达到 10 个左右时，2003～2009 年的前期历史交叉检验 ACC 基本都会达到一个比较平稳的值，其中，2003 年在 12 个以上因子组合的时候平均 ACC 随因子个数的增加呈现下降趋势，其他年份在因子个数累加到 20 个左右时平均 ACC 也都呈现出衰减的趋势。因此本文分别选取 9、10、11 个优化多因子组合确定误差场相似年，既可保证所选因子组合在前期历史交叉检验中订正效果明显，又可通过三种不同的优化多因子组合提取有一定区别的相似年误差场，从而在一定程度上克服以往误差场相似年固定为 4 个的局限性。

表 2 以 2007～2009 年为例，列出了采用 9、10、11 个优化多因子组合选取的误差场相似年，可以看出，尽管采用的因子个数不同，但所选取的误差场相似年有很多都重复出现，例如 2007 年的误差场相似年中，2004、1995 这两年重复出现了三次，2006年和1988年重复出现了两次。其他年份选取的误差场相似年也都存在类似的情况，这说明优化多因子组合选取相似误差场的性能是稳定的。因此，本文在进行相似误差场合成的过程中，把三种优化多因子组合选取的相似年误差场进行集合平均，并且根据误差场相似年重复出现的次数，将各相似年误差场赋予 $n(i)/12$ 的权重系数，其中 $n(i)$ 为误差场相似年重复出现的次数，分母 12 为三种情况的优化多因子组合选取的 12 个误差场相似年，这有利于克服进行误差场合成时没有考虑欧氏距离差异的缺点。最后，将加权集合平均相似误差场与模式预报的降水场合成，形成该区域汛期降水的 OQF 结果（流程如图 4 所示），具体步骤如下：

第 1 步：根据 CMAP 历年降水资料和历年模式回报结果得到汛期降水历年模式预测误差；

第 2 步：将 114 项指数在预测年（例如 2009 年）的 1 月份因子和前一年（2008 年）的 2～12 月份的因子作为预测年前期因子，利用各单因子以交叉检验的方式对模式结果进行相似误差订正，与 CMAP 降水资料对比，得到单因子相似误差订正的 26 年（1983～2008）平均 ACC 排序；

**表 2 2007～2009 年不同因子个数的优化多因子组合选取的误差场相似年**

**Table 2 The analogue years of 2007 to 2009 in error fields on different numbers of OFC**

| | 9 个因子 | 10 个因子 | 11 个因子 |
|---|---|---|---|
| 2007 年 | 2004、1995、1999、2006 | 1995、1988、2004、2006 | 1995、1988、2004、1994 |
| 2008 年 | 2005、1991、1985、2004 | 2001、2005、1985、2000 | 2005、1985、2001、1993 |
| 2009 年 | 2001、1991、1992、1989 | 2001、1992、1989、2008 | 2001、1991、1992、2008 |

第 3 步：选取 26 年平均 ACC 大于 0.1 的因子进行优化组合，将其中 ACC 最大值因子作为组合的首因子，根据双因子对 1983～2008 年交叉检验的平均 ACC 值的大小判断第二个因子，依此类推得到前 11 个优化多因子组合；

第 4 步：对前 9、10、11 个优化多因子组合，采用 EOF 分解提取解释方差占 80%的主分量，由式（9）得到每种因子组合选取的 4 个相似年，结合历年模式误差分别选取相似误差场；

第 5 步：将各相似年误差场根据重复出现的次数加权集合平均，结合2009年模式预测结果，得到基于优化多因子组合的 OQF 方法预测的 2009 年汛期降水状况。

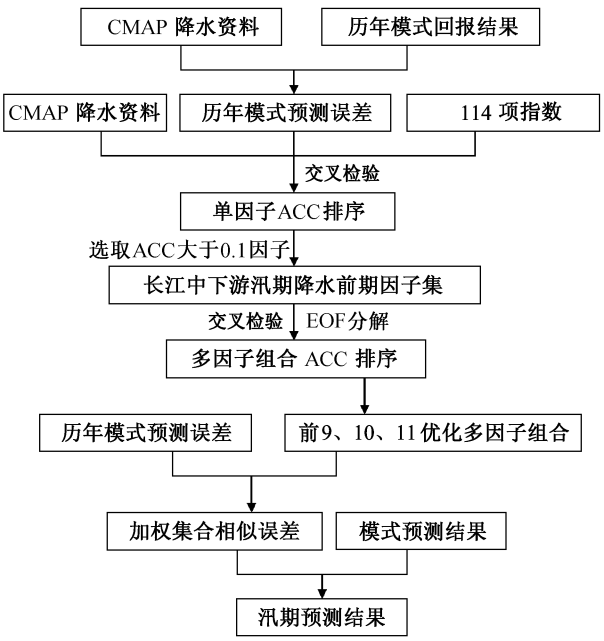


图 4　OQF 方法流程图

Fig. 4　The flow chart of OQF method

## 4　独立样本回报效果

为检验 OQF 方法的效果，本文利用该方法对 2003～2009 年进行了独立样本回报检验，各年 ACC 评分和 RMSE 如图 5 所示。

图 5a 给出了基于优化多因子组合的 OQF 方法回报的降水场的 7 年 ACC，可以发现，7 年回报结果 ACC 分别为 0.58、0.49、0.76、0.09、0.55、0.04、0.47。7 年平均 ACC 为 0.43，相比于系统误差订正的 7 年 ACC 平均值 0.28 有了明显提高，并且除 2006 年和 2008 年外，其余 5 年利用 OQF 方法的 ACC 均高于系统误差订正。图 5b 是采用两种误差订正方法后的历年均方根误差，其平均值也从系统误差订正的 99.48 减小到 OQF 方法的 92.63，尤其在 2003、2004、2005 和 2009 年 4 年中 OQF 方法的均方根误差比系统误差订正的结果明显减小，体现出利用 OQF 方法对该地区汛期降水有较高的预测技巧。

### 4.1　2009 年独立样本回报年优化多因子组合及其订正效果

本节将以 2009 年为例，详细分析基于优化多因子组合的 OQF 方法的订正效果。这里采用的优化多因子组合如表 3 所示。11 个因子主要集中在 7、8、10 三个月，以北半球环流指数为主，还涉及到表征热带中东太平洋海表温度的指数。

在表 2 最后一行列出了利用优化多因子组合选取的2009年误差场相似年，从中可以看出，虽然

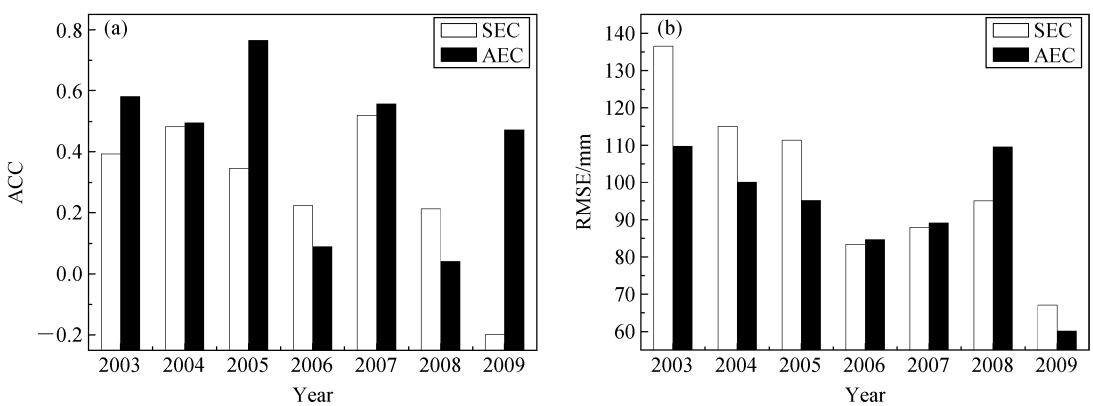


图 5　2003～2009 年 OQF 方法与系统误差订正的独立样本回报比较：(a) ACC；(b) RMSE

Fig. 5　The independent sample regression outcomes of OQF technique and system error correction from 2003 to 2009: Comparison of the two methods on (a) ACC and on (b) root mean square error

表 3 2009 年前期优化多因子组合

Table 3 The pre-OFC in 2009

| 序号 | 月份 | 因子 | 单因子 ACC |
|---|---|---|---|
| 1 | 10 | 全球平均海陆温度指数 | 0.34 |
| 2 | 8 | 南海副高北界 | 0.23 |
| 3 | 8 | 南海副高脊线 | 0.29 |
| 4 | 2 | 大西洋欧洲环流型 E | 0.12 |
| 5 | 7 | 热带中太平洋 SST | 0.10 |
| 6 | 7 | 大西洋欧洲区极涡强度指数 4 区 | 0.16 |
| 7 | 8 | 全球平均角动量 | 0.14 |
| 8 | 10 | 西太平洋副高面积指数 | 0.14 |
| 9 | 4 | 北半球极涡中心位置 | 0.12 |
| 10 | 10 | 北半球副高面积指数 | 0.12 |
| 11 | 9 | 大西洋欧洲区极涡面积指数 | 0.11 |

利用不同个数的前期因子组合，但是选取的相似年基本类似，例如 2001、1991、2008、1989 年都重复出现，其中 2001 年在三种情况下都出现，这说明了优化多因子组合选取误差场相似年的稳定性。

图 6 给出了 2009 年降水距平百分率回报与实况的比较，长江中下游地区 2009 年汛期降水总体呈现东多西少的分布，该区域中包含的湖南、湖北、安徽、江西等地区降水普遍偏少，在浙江西部和东部钱塘江口降水也偏少，仅在江苏南部和浙江中东部区域降水偏多，区域总体较平均态偏少（图 6a）。系统误差订正后模式预报的区域降水总体偏多，并且东少西多，仅在浙江东北部出现了降水偏少的情况，与实况降水场的 ACC 为－0.15，和实况基本相反（图 6b）。采用优化多因子组合相似误差订正后模式预报的区域降水分布呈现东多西少的分布型，与实况的降水分布型较为吻合，与实况降水场的 ACC 为 0.47，达到了较好的预测效果。但是在该区域西北部 OQF 方法预测的降水仍然比实际偏多。

## 4.2 误差场相似年选取的探讨

从以上研究可以看出，利用优化多因子组合选取的相似年误差场订正模式预报结果，可以改进长江中下游区域的汛期降水预报效果，提高预报技巧。但是这里选取的误差场是否就是历史资料中最优的误差场组合，需要进一步验证，以期对 OQF 方法的改进提供一定的思路。因此，本节计算了 2003～2009 年各年模式误差场与其前期历年模式误差场的 ACC，通过计算可知 ACC 为正值的年份均在 10 个以上，表 4 仅依次列出了 ACC 靠前的 4

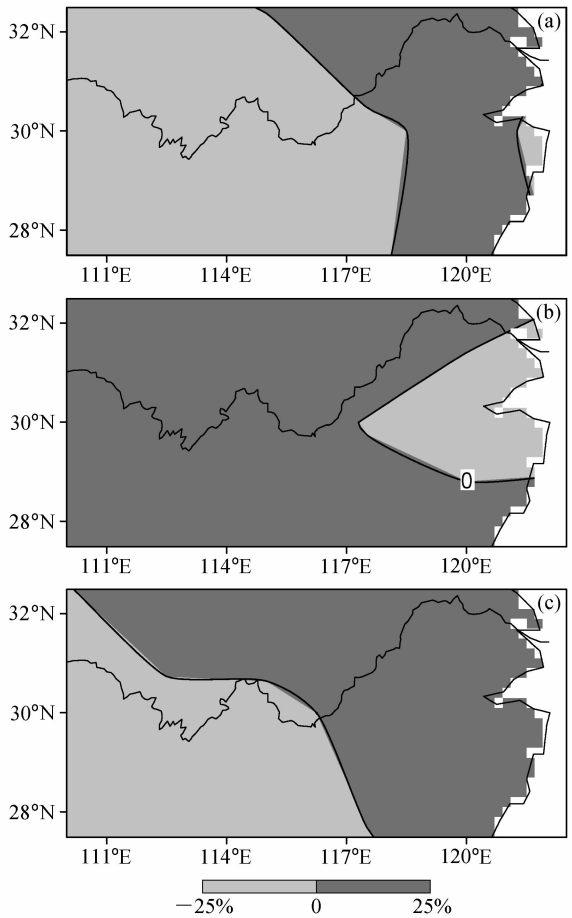


图 6 2009 年独立样本回报结果比较：(a) 降水距平百分率实况；(b) 系统误差订正后模式预报的降水距平百分率；(c) 优化多因子组合相似误差订正后模式预报的降水距平百分率

Fig. 6 Comparisons of the independent sample regression outcomes in 2009 between (a) precipitation anomaly percentage of the in-situ observation, (b) that revised by systematic error correction, and (c) that revised by OFC analogue error correction

个相似年份，以及各相似年误差场与回报年误差场 ACC 评分。

从表 4 中可以发现，2003～2009 年各年的实际误差场在历史上都可以找到 ACC 比较高的误差场第一相似年，最小为对应 2009 年与 1990 年的 0.53，最大为对应 2003 年与 1991 年的 0.87。即使第四相似年误差场与回报年误差场 ACC 最小值也可达到 0.38（2004 年与 1998 年）。表 4 中的“集合平均”为相似误差订正的预报结果与当年汛期降水实况的 ACC，7 年 ACC 均值为 0.79，远高于优化多因子组合相似误差订正的 0.43。当然，此种情况在理想的状况下才会出现，如以 2009 年为例，四个理想相似年分别为 1990 年、1984 年、2005 年、

**表 4　2003～2009 年模式误差场与其前期各年模式误差场距平相关系数前四位**

**Table 4　The top four ACC of actual error fields and their top four pre-analogue years error fields from 2003 to 2009**

| | 第一相似年 | | 第二相似年 | | 第三相似年 | | 第四相似年 | | 集合平均 |
|---|---|---|---|---|---|---|---|---|---|
| | 年 | ACC | 年 | ACC | 年 | ACC | 年 | ACC | ACC |
| 2003 年 | 1991 | 0.87 | 1984 | 0.84 | 1987 | 0.71 | 1986 | 0.70 | 0.89 |
| 2004 年 | 1988 | 0.64 | 1996 | 0.58 | 2002 | 0.43 | 1998 | 0.38 | 0.67 |
| 2005 年 | 1990 | 0.74 | 2000 | 0.71 | 1984 | 0.68 | 1989 | 0.58 | 0.87 |
| 2006 年 | 1997 | 0.65 | 1994 | 0.63 | 2002 | 0.53 | 1992 | 0.47 | 0.78 |
| 2007 年 | 2004 | 0.68 | 2005 | 0.58 | 2003 | 0.54 | 1986 | 0.51 | 0.81 |
| 2008 年 | 1996 | 0.72 | 1986 | 0.67 | 2007 | 0.67 | 2003 | 0.66 | 0.84 |
| 2009 年 | 1990 | 0.53 | 1984 | 0.47 | 2005 | 0.46 | 2001 | 0.42 | 0.68 |

2001 年，此种情况下 ACC 可以达到 0.68，与采用优化多因子组合选取的相似年比较，仅有 2001 年是相同的，且为理想情况下的第四相似年。通过该部分的分析可以得知，虽然历史资料中存在很好的相似误差场，但实际选取的各相似年误差场经常会出现 ACC 为负值的情况，说明利用相似误差订正方法提高区域降水预报技巧还有较大的提升空间，选取误差场相似年的工作还存在需要改进之处。本文仅考虑前期因子某个月的状况，没有涉及因子出现异常的情况，而因子异常往往会对区域降水产生较明显的影响，因此，下一步工作将主要针对因子在一定时间段内的演化情况来选取误差场相似年并考虑因子出现异常的状况。

## 5　结论与讨论

本文首先利用单因子相似误差订正的方法改进长江中下游地区降水预报效果，结果表明该方法可以提高该区域汛期降水预报技巧。在此基础上，根据独立样本回报年前期交叉检验的 ACC 评分，对因子进行优化组合，并且采用加权集合平均的方法对相似年误差场进行合成，提出了基于优化多因子组合的 OQF 方法。2003～2009 年 7 年的独立样本回报结果显示，利用 OQF 方法得到的相似误差订正的 7 年 ACC 均值为 0.43，比系统误差订正提高了 0.15，使得模式预测效果得到明显改善。以 2009 年为例研究了优化多因子组合及其选取的相似年状况，比较了相似误差场间的关系，发现选取的相似年误差场与 2009 年降水误差场有较好的匹配关系。从以上研究结果可知，OQF 方法是针对模式误差利用历史资料进行预报的有效方法，但该方法所选取的因子组合与长江中下游地区汛期降水之间产生关系的物理机制需要进一步深入研究。本文最后从理想试验的角度出发，分别计算了 2003～2009 年与其前期逐年误差场的 ACC，研究发现，各年在历史资料中都可以寻找到 4 个比较匹配的误差场相似年，从而获得优良的模式订正效果，显示了选取误差场相似年的工作还存在较大的改进余地。

## 参考文献（References）

Barnett T P, Preisendorfer R W. 1978. Multifield analog prediction of short-term climate fluctuations using a climate state vector [J]. J. Atmos. Sci., 35 (10): 1771－1787.

鲍名. 2009. 从中期天气过程看近几年长江中下游梅雨偏少的原因 [J]. 大气科学, 33 (4): 708－718.　Bao M. 2009. Causes of deficit Meiyu over the middle and lower reaches of the Yangtze River in the last several years viewed from medium range weather process [J]. Chinese Journal of Atmospheric Sciences (in Chinese), 33 (4): 708－718.

丑纪范. 1974. 天气数值预报中使用过去资料的问题 [J]. 中国科学 (A 辑), 6 (11): 635－644.　Chou J F. 1974. A problem of using past data in numerical weather forecasting [J]. Science in China (Ser. A) (in Chinese), 6 (11): 635－644.

丑纪范. 1986. 为什么要动力—统计相结合? ——兼论如何结合 [J]. 高原气象, 5 (4): 367－372.　Chou J F. 1986. Why to combine dynamical and statistical methods together? —Also discuss how to combine [J]. Plateau Meteorology (in Chinese), 5 (4): 367－372.

丑纪范, 任宏利. 2006. 数值天气预报——另类途径的必要性和可行性 [J]. 应用气象学报, 17 (2): 240－244.　Chou J F, Ren H L. 2006. Numerical weather prediction—Necessity and feasibility of an alternative methodology [J]. Journal of Applied Meteorological Science (in Chinese), 17 (2): 240－244.

559 Chao J P, Guo Y F, Xin R N. 1982. A theory and method of long-range numerical weather forecasts [J]. J. Meteor. Soc. Japan, 60: 282－291.

曹鸿兴. 1993. 大气运动的自忆性方程 [J]. 中国科学 (B辑), 23 (1): 104-112. Cao Hongxing. 1993. The equations of atmospheric self-memorial [J]. Science in China (Ser. B) (in Chinese), 23 (1): 104-112.

陈隆勋. 1984. 东亚季风环流系统的结构及其中期变动 [J]. 海洋学报, 6 (6): 744-758. Chen L X. 1984. The configuration of the East Asian monsoon circulation and its medium-term oscillation [J]. Acta Oceanologica Sinica (in Chinese), 6 (6): 744-758.

封国林, 曹鸿兴, 魏凤英, 等. 2001. 长江三角洲汛期预报模式的研究及其初步应用 [J]. 气象学报, 59 (2): 206-212. Feng G L, Cao H X, Wei F Y, et al. 2001. On area rainfall integration prediction and its application [J]. Acta Meteorologica Sinica (in Chinese), 59 (2): 206-212.

Feng G L, Dong W J. 2003. Evaluation of the applicability of a retrospective scheme based on comparison with several difference schemes [J]. Chinese Phys., 12: 1076-1086.

Feng G L, Dong W J, Jia X J. 2004. Application of retrospective time integration scheme to the prediction of torrential rain [J]. Chinese Phys., 13: 413-422.

范可. 2006. 南半球环流异常与长江中下游夏季旱涝的关系 [J]. 地球物理学报, 49 (3): 672-679. Fan K. 2006. Atmospheric circulation anomalies in the Southern Hemisphere and summer rainfall over Yangtze River valley [J]. Chinese J. Geophys. (in Chinese), 49 (3): 672-679.

范可, 王会军, Choi Y J. 2007. 一个长江中下游夏季降水的物理统计预测模型 [J]. 科学通报, 52 (24): 2900-2905. Fan K, Wang H J, Choi Y J. 2007. A physically-based statistical forecast model for the mid-lower reaches of the Yangtze River valley summer rainfall [J]. Chinese Science Bulletin (in Chinese), 52 (24): 2900-2905.

范可, 林美静, 高煜中. 2008. 用年际增量方法预测华北汛期降水 [J]. 中国科学 (D辑), 地球科学, 38 (11): 1452-1459. Fan K, Lin M J, Gao Y Z. 2008. Forecasting the summer rainfall in North China using the year-to-year increment approach [J]. Science in China (Ser. D) (in Chinese), 38 (11): 1452-1459.

顾震潮. 1958. 天气数值预报中过去资料的使用问题 [J]. 气象学报, 29 (3): 176-184. Gu Z C. 1958. On the utilization of past data in numerical weather forecasting [J]. Acta Meteorologica Sinica (in Chinese), 29 (3): 176-184.

Huang J P, Yi Y H, Wang S W, et al. 1993. An analogue-dynamical long-range numerical weather prediction system incorporating historical evolution [J]. Quart. J. Roy. Meteor. Soc., 119: 547-565.

黄嘉佑. 1990. 气象统计分析与预报方法 [M]. 北京: 气象出版社, 182-188. Huang J Y. 1990. Statistical Analysis and Forecasting Method in Meteorology (in Chinese) [M]. Beijing: China Meteorological Press (in Chinese), 182-188.

黄荣辉, 孙凤英. 1994. 热带西太平洋暖池的热状况及其上空的对流活动对东亚夏季气候异常的影响 [J]. 大气科学, 18 (2): 141-151. Huang R H, Sun F Y. 1994. Impacts of the thermal state and the convective activities in the Tropical western warm pool on the summer climate anomalies in East Asia [J]. Chinese Journal of Atmospheric Sciences (Scientia Atmospherica Sinica) (in Chinese), 18 (2): 141-151.

柯宗建, 张培群, 董文杰, 等. 2009. 最优子集回归方法在季节气候预测中的应用 [J]. 大气科学, 33 (5): 994-1002. Ke Z J, Zhang P Q, Dong W J, et al. 2009. An application of optimal subset regression in seasonal climate prediction [J]. Chinese Journal of Atmospheric Sciences (in Chinese), 33 (5): 994-1002.

刘芸芸, 丁一汇. 2009. 西北太平洋夏季风对中国长江流域夏季降水的影响 [J]. 大气科学, 33 (6): 1225-1237. Liu Y Y, Ding Y H. 2009. Influence of the western North Pacific summer monsoon on summer rainfall over the Yangtze River basin [J]. Chinese Journal of Atmospheric Sciences (in Chinese), 33 (6): 1225-1237.

任宏利, 丑纪范. 2005. 统计—动力相结合的相似误差订正法 [J]. 气象学报, 63 (6): 988-993. Ren H L, Chou J F. 2005. Analogue correction method of errors by combining both statistical and dynamical methods together [J]. Acta Meteorologica Sinica (in Chinese), 63 (6): 988-993.

任宏利, 张培群, 李维京, 等. 2006. 基于多个参考态更新的动力相似预报方法及应用 [J]. 物理学报, 55 (8): 4388-4396. Ren H L, Zhang P Q, Li W J, et al. 2006. A new method of dynamical analogue prediction based on multi-reference-state updating and its application [J]. Acta Physica Sinica (in Chinese), 55 (8): 4388-4396.

任宏利, 丑纪范. 2007a. 数值模式的预报策略和方法研究进展 [J]. 地球科学进展, 22 (4): 376-385. Ren H L, Chou J F. 2007a. Study progress in prediction strategy and methodology on numerical model [J]. Advances in Earth Science (in Chinese), 22 (4): 376-385.

任宏利, 丑纪范. 2007b. 动力相似预报的策略和方法研究 [J]. 中国科学 (D辑), 37 (8): 988-993. Ren H L, Chou J F. 2007b. Strategy and methodology of dynamical analogue prediction [J]. Science in China (Ser. D) (in Chinese), 37 (8): 988-993.

施能. 1992. 气象统计预报中的多元分析方法 [M]. 北京: 气象出版社, 210-227. Shi N. 1992. The Multianalysis Method of Meteorological Research and Prediction (in Chinese) [M]. Beijing: China Meteorological Press (in Chinese), 210-227.

Sun J Q, Wang H J, Yuan W. 2009. A possible mechanism for the co-variability of the boreal spring Antarctic Oscillation and the Yangtze River valley summer rainfall [J]. International Journal of Climatology, 29: 1276-1284.

陶诗言, 赵煜佳, 陈晓敏. 1958. 东亚的梅雨期与亚洲上空大气环流季节变化的关系 [J]. 气象学报, 29 (2): 119-134. Tao S Y, Zhao Y J, Chen X M. 1958. The relationship between May-Yu in Far East and the behaviour of circulation over Asia [J]. Acta Meteorologica Sinica (in Chinese), 29 (2): 119-134.

Tao S Y, Chen L X. 1987. A review of recent research on the East

Asian Summer Monsoon in China [M]// Monsoon Meteorology. Oxford University Press, 60－92.

van den Dool H M. 1994. Searching for analogues, how long must we wait? [J]. Tellus, 46A: 314－324.

吴国雄，刘还珠. 1995. 降水对热带海表温度异常的邻域响应 I：数值模拟 [J]. 大气科学，19 (4)：422－434.　Wu G X, Liu H Z. 1995. Neighbourhood response of rainfall to tropical sea surface temperature anomalies. Part I: Numerical experiment [J]. Chinese Journal of Atmospheric Sciences (Scientia Atmospherica Sinica) (in Chinese), 19 (4): 422－434.

Wang H J, Fan K. 2009. A new scheme for improving the seasonal prediction of summer precipitation anomalies [J]. Wea. Forecasting, 24: 548－554.

郑志海，任宏利，黄建平. 2009. 基于季节气候可预报分量的相似误差订正方法和数值试验 [J]. 物理学报，58 (10)：7359－7367. Zheng Z H, Ren H L, Huang J P. 2009. Analogue correction of errors based on seasonal climatic predictable components and numerical experiments [J]. Acta Physica Sinica (in Chinese), 58 (10): 7359－7367.

Zhou B T, Wang H J. 2006. Relationship between the boreal spring Hadley circulation and the summer precipitation in the Yangtze River valley [J]. J. Geophys. Res., 111: D16109, doi: 10.1029/2005JD007006.

庄照荣，薛纪善，李兴良，等. 2010. GRAPES 全球模式的模式误差估计 [J]. 大气科学，34 (3)：591－598.　Zhuang Z R, Xue J S, Li X L, et al. 2010. Estimation of model error for the global GRAPES model [J]. Chinese Journal of Atmospheric Sciences (in Chinese), 34 (3): 591－598.

第7卷 第2期
2011年3月
气候变化研究进展
ADVANCES IN CLIMATE CHANGE RESEARCH
Vol. 7 No. 2
March 2011

文章编号：1673-1719 (2011) 02-0079-06

# 全球气候变暖原因的争议

王绍武[1]，罗 勇[2,3]，赵宗慈[2,3]，闻新宇[1]，黄建斌[3]

（1 北京大学物理学院大气与海洋科学系，北京 100871；2 中国气象局国家气候中心，北京 100081；3 清华大学地球系统科学研究中心，北京 100084）

**摘 要**：综合分析了政府间气候变化专门委员会（IPCC）与非政府间国际气候变化专门委员会（NIPCC）针锋相对的观点：是人类活动还是自然因素主导了过去近百年的气候变化。指出20世纪中期以来温度变化的事实支持人类活动影响的观点，但是在近百年中自然因素如太阳活动、火山活动或大洋热盐环流的变化，对温度的年代际变化有重要影响。有充分的古气候与古太阳活动资料证明过去千年中的中世纪暖期及小冰期，过去万年中的冷事件与太阳活动有密切关系。这说明在历史气候变化中太阳活动有重要影响。目前一种占优势的观点认为银河宇宙线影响了低云量使气候变冷，但是影响机制还有待于进一步研究。

**关键词**：气候变暖；原因；争议；温室效应；太阳活动；银河宇宙线

**中图分类号**：P467　　**文献标识码**：A

## 引 言

全球气候变暖是当前国内外研究的热点问题，也是最有争议性的问题。争议范围之广，超出了早先人们的想象。从最根本的问题——气候是否变暖了，气候变暖的原因是什么，如何应对气候变暖，如何控制温室气体的排放使变暖达不到阈值，直到阈值是不是2 ℃。可以说几乎在每个环节上均有争议。本文将讨论争议的核心问题：气候为什么变暖？

## 1 争议的焦点

以IPCC为代表，其第四次评估报告（AR4[1]）指出："20世纪中期以来观测到的全球平均温度的上升，非常可能是由观测到的人类活动产生的温室气体增加造成的"；并且指出"这个结论比第三次评估报告（TAR[2]）前进了一步"。那时认为"近50年观测到的大部分变暖可能是由温室气体浓度增加造成的"。根据IPCC AR4，"非常可能"指可能性在90%以上，"可能"则指66%以上。也就是说从IPCC TAR到IPCC AR4对变暖是由温室气体增加造成的可能性的评估从 >66% 提高到 >90%。而另一方面NIPCC的决策者摘要[3]，标题就是："自然，而不是人类活动主导着气候"。显然这是与IPCC针锋相对的观点。下面就分别研究这两种观点各有什么证据，以及存在的问题。

**收稿日期**：2010-07-16；**修回日期**：2010-07-27
**资助项目**：国家重点基础研究计划：过去2000年典型暖期的形成机制及影响研究（2010CB950104）
**第一作者**：王绍武（1932—），男，教授，主要从事气候学方面的研究。E-mail: swwang@pku.edu.cn

## 2 温室效应理论的证据

历届 IPCC 报告均认为全球气候变暖是人类活动造成的温室效应加剧的结果，而且对这个论断持日益强硬态度。但是，回顾一下，究竟有什么证据支持这种观点呢？大体上可以分为两个方面：观测事实与模拟研究。

### 2.1 观测事实

温室效应理论认为人类活动造成的气候变暖应该是全球性的、四季都存在的、每天最高温度与最低温度均上升的一种几乎无所不在的普遍性变暖。但是，从理论上讲，高纬、特别是冬季温度上升更多。日最低温度上升应该超过最高温度。这些推测基本上得到了观测资料的证实。图 1 与图 2 给出 Hansen 等[4]到 2009 年的全球温度资料。图 1 为 1970—2000 年代平均温度距平，图右上角的数字为全球平均温度距平，可见近 40 年变暖十分明显。2000 年代除东南极沿岸和大洋上小范围为负距平外，陆上普遍变暖，北半球高纬尤甚。1990 年代也是一个暖的 10 年，但是温暖程度低于 2000 年代。图 2 为近 60 年四季温度变化趋势，右上角为全球平均趋势。各季平均变暖在 0.60～0.65 ℃，季节分布比较均匀。北半球冬季（12、1、2 月）欧亚大陆北部及北美大陆北部增温最明显，南半球冬季（6—8 月）南极沿岸变暖最强。

此外，气温日较差（DTR）有减小趋势[1]，与温室效应理论一致。但 IPCC AR4 的 DTR 减小趋势低于 IPCC TAR，80% 可以从云盖及降水量变化得到解释。根据卫星观测，1979—2005 年全球地面到 10 km 的对流层温度均保持普遍上升趋势，而平流层温度则处于下降中[1]，这也同温室效应理论一致。只有一个分歧就是，根据模式模拟，温室效应加剧后在热带对流层上层温度上升应高于地面，这一点却没有得到观测证实，因此成为 NIPCC 攻击 IPCC 的一个论据。近来 Allen 等[5]用热成风理论及相关观测资料推导出热带（20°N～20°S）对流层上层的温度，结果显示变暖幅度超过了地面。Thorne[6]指出，1979—2005 年 200 hPa 高度的温度增量达到（0.40 ± 0.29）℃/10a，超过了同期地面温度增量（0.13 ℃/10a）。利用风垂直切变与温度的水平梯度更精确地计算对流层上层的温度，这是一项值得注意的新研究。但是，

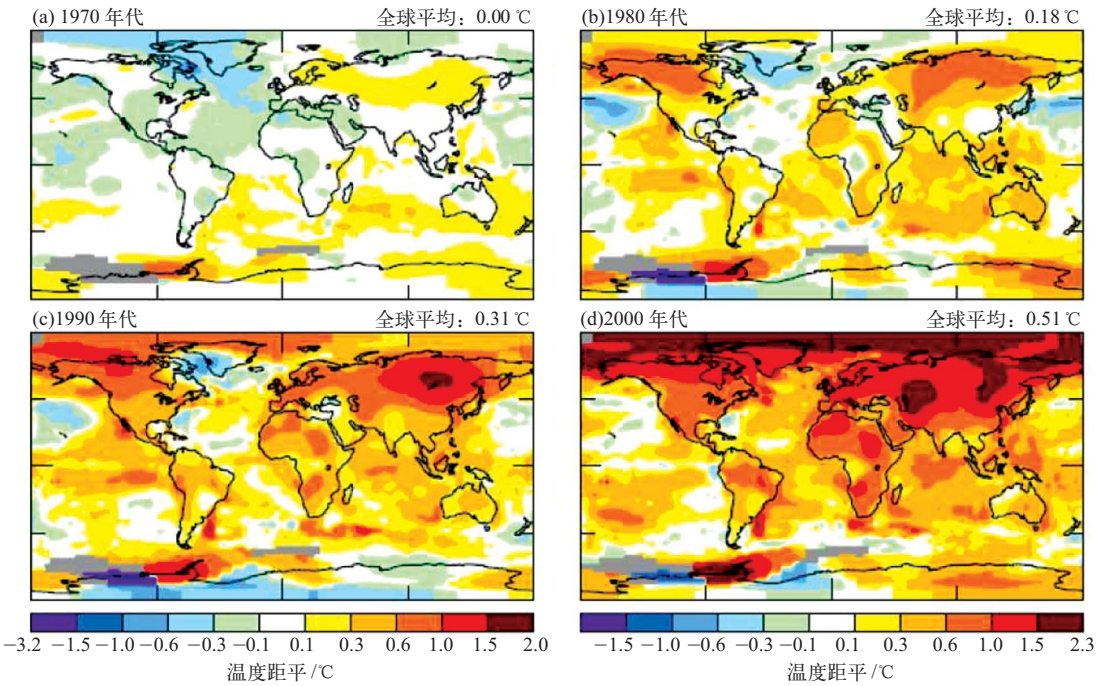


图 1 1970 — 2000 年代平均温度距平（相对于 1951 — 1980 年）[4]

Fig. 1 Decadal mean temperature anomalies from 1970s to 2000s (reference to 1951−1980) [4]

www.climatechange.cn



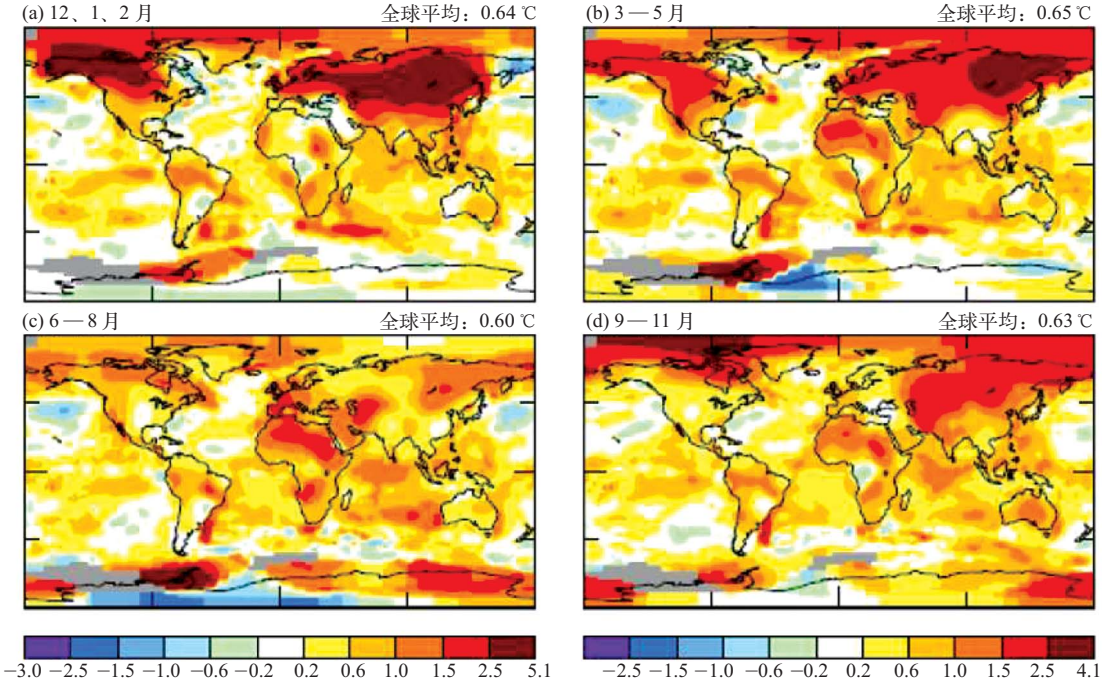


图 2　1950—2009 年四季温度变化趋势（单位：℃/60a）[4]

Fig. 2　Average trends of seasonal temperature for the period of 1950−2009 (unit: ℃/60a) [4]

为什么温度观测显示不出这样的结果还不清楚。

### 2.2　模拟研究

这里分析近百年温度变化的模拟研究。如果我们能在给定温室气体强迫的情况下模拟出全球平均温度变化，则可以更进一步确认这个变化是人类活动造成的。为了更好地模拟全球平均温度变化，IPCC AR4 用海气耦合模式，综合考虑温室气体、气溶胶、火山活动、太阳辐照度、$O_3$ 等因素模拟了 20 世纪全球平均地表温度变化。除 1930 年代后期至 1940 年代中期的温度峰值、1950 年代初期和中期的两个谷值未能模拟出来之外，1960 年之后模拟的较好。而且，如果不加入人类活动影响，则模拟不出 20 世纪后期的变暖，这证明温室效应在 20 世纪后半叶的变暖中起主导作用。这也是 IPCC AR4 提高人类活动影响可能性评估的主要依据。此外 IPCC AR4 还列举了 2002—2007 年完成的 12 个模式模拟的近千年温度变化，包括 6 个 GCM（大气环流或耦合环流模式），4 个 EMIC（中等复杂程度气候系统模式）及 2 个 EBM（能量平衡模式）。这些模式在考虑火山活动与太阳活动的强迫时能模拟出 12—14 世纪的变暖及 15、17、19 世纪的寒冷。对 20 世纪也能模拟出 1940 年代的暖及 20 世纪最后 30 年的变暖。这些模拟研究表明，温室效应确实是 20 世纪后半叶气候变暖的主要原因。但是，在对过去千年的模拟中，自然因素如火山活动与太阳活动则是驱动气候变化的主要因素。

## 3　太阳活动影响的证据

从19世纪末到20世纪初就有不少学者研究太阳活动与地球气候的关系。但是，太阳活动对地球气候影响的假设始终受到很大怀疑。其最主要的原因有两个：1) 太阳黑子变化的基本周期为 11 年左右，而地球上的各种气候指标，很少有持续较长时间的 11年周期，偶然有某个局地气候指数在1～2个或2～3 个 11 年周期内与太阳黑子变化有关，但是这种关系大多不能持久；2) 太阳活动影响地球气候的途径不清楚。先是把太阳辐照度（TSI）当作一个常数，称为太阳常数，后来证明，太阳常数是变化的，但是 11 年周期的振幅只有 0.1%。因此，我们要看一看有什么现代的资料突破了过去的概念。

### 3.1 MWP及LIA

鉴于地球气候缺少11年周期，我们着重讨论年代际尺度及百年尺度。最近的千年包括了两个地球气候的重要时期，中世纪暖期（MWP）和小冰期（LIA）。由于这两个时期主要发生在人类活动影响微弱的工业化之前，所以，大多数学者都同意是自然原因造成了MWP及LIA。其中首选的自然原因就是太阳活动。图3给出Kikby[7]总结的近千年温度变化与太阳活动。图3 (a)为近千年温度变化，右纵坐标为格陵兰两个钻孔（GRIP和Dye3）的温度。在图中作者标出的MWP为公元1000—1250年，LIA为公元1450—1850年。图3 (b)给出银河宇宙线（GCR）序列，MWP期间GCR弱，说明太阳活动强，而LIA期间GCR强，太阳活动弱。图3 (c)为委内瑞拉热带安第斯山冰川活动，湖泊沉积磁导率（SI）高表示气候冷湿，冰川前进。LIA期间高纬寒冷、亚非季风区干旱、赤道辐合带（ITCZ）南移。反映了以GCR为代表的太阳活动与地球气候的密切关系。

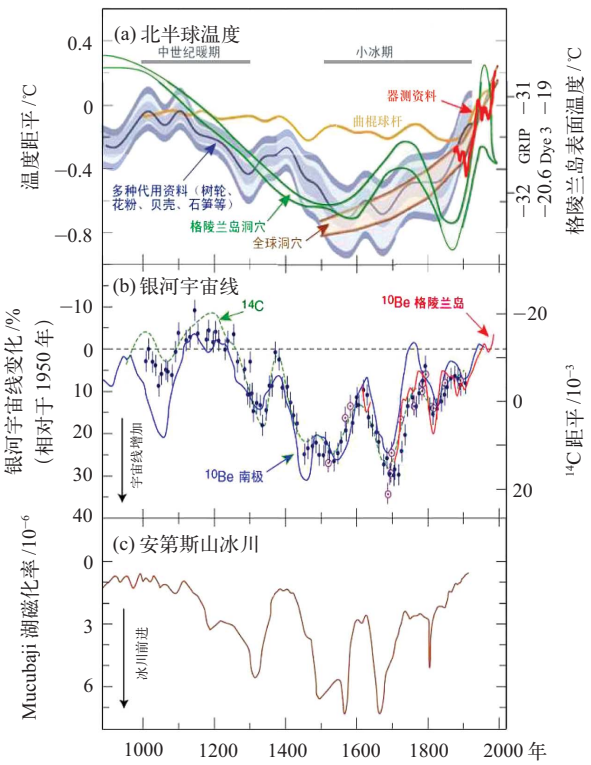


图3 近千年温度变化(a)、银河宇宙线变化 (b)及热带安第斯山冰川活动(c)（向下为前进）[7]

Fig. 3 (a) Temperature, (b) galactic cosmic ray, and (c) tropical Andean glacier changes during the last millennium [7]

### 3.2 全新世气候突变

Bond等[8]根据北大西洋流冰碎屑（IRD）指出全新世北大西洋有8次流冰事件（常称冷事件），由近及远编号为1至8次冷事件。后来发现小冰期的特征也与之类似，所以也算作一次冷事件，编号为0。因此，全新世11.5 kaBP至今共9次冷事件。大量的研究表明冷事件与北半球乃至全球气候异常有密切的关系[9−12]。Wang[13]曾经对冷事件的年代学及气候影响进行了综合分析，指出发生冷事件时北半球中高纬特别是西北欧气候冷干，但中欧及西欧夏季湿润。亚非季风区夏季风降水减少，从东非沿岸向东穿过阿拉伯海到南亚，再向东到东亚干旱，中国南部的石笋记录反映干旱事件与北大西洋冷事件有很好的对应关系[12]。

早在1973年，Denton等[14]就提出太阳活动减弱可能是全新世气候突变的原因。Bond等[15]用$^{14}C$、$^{10}Be$代表太阳活动，用4个海洋沉积记录得到综合指数。将$^{14}C$、$^{10}Be$和综合指数均去掉趋势并做70年滤波（图4），两个太阳活动指数与综合指数的相关系数分别达到0.44和0.56，9次冷事件均与太阳活动

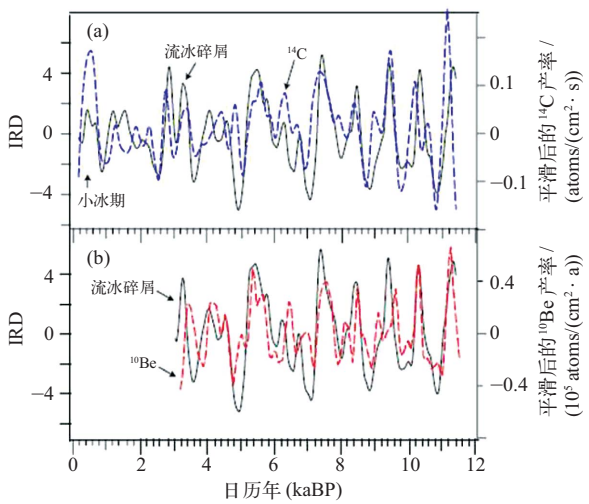


图4 全新世代表北大西洋冷事件的流冰碎屑（IRD）和太阳活动（$^{14}C$和$^{10}Be$）[15]

Fig. 4 Ice-rafted debris (IRD), which is representative of the cold events over the North Atlantic Ocean, and solar activity ($^{14}C$ and $^{10}Be$) [15]

www.climatechange.cn



谷值（GCR 峰值）对应，这表明太阳活动减弱可能是冷事件形成的原因。

### 3.3　太阳活动影响地球气候的途径与机制

太阳活动影响地球气候的途径有3个[16]：TSI的变化、太阳紫外线变化及GCR变化。关于第1种途径，由于已经有了两个半11年周期TSI的直接观测，早已证实太阳常数不是一个真正的常数，但是随11年周期的变化只有0.1%[17]，这大约只能造成0.1 ℃的温度变化[18]，不足以解释观测到的气候变化。在几百年的过程中，TSI的变化可能要大一些，根据太阳黑子的变化推算18世纪至今TSI仅增加0.5 W/m$^2$，相当于大气顶部的辐射强迫增加0.08 W/m$^2$。假定气候敏感度为0.7 ℃/(W/m$^2$)，则18世纪至今TSI的变化仅能造成0.06 ℃的温度变化，比这段时间观测到的升温0.6 ℃要小一个量级[19]。因此，目前越来越多的气候学家与天文学家不再认为这是太阳活动影响地球气候的主要途径。

第2种途径的主要依据是太阳活动11年周期中紫外线（UV）谱段的辐射强度变化剧烈[20]。不同学者估计不尽相同，最高估计从太阳活动11年周期极大年（M年）到极小年（m年）可变化7%。太阳活动强时UV增加，使平流层变暖、$O^3$增加。平流层通过热辐射及动力学过程影响对流层。对太阳活动影响地球气候的这种途径的物理机制还研究的不够，观测证据也不充分，例如$O^3$浓度与太阳活动关系的证据也有分歧。

对第3种途径的研究较多。观测证明，随太阳活动11年周期，GCR可变化15%，地球低云量可变化1.7%，相当辐射强迫1 W/m$^2$。$CO_2$的辐射强迫只有1.66 W/m$^2$，相比之下GCR的影响也足够大[21]。GCR影响地球气候的机制还在研究之中，GCR如何影响大气的低云量，目前有3种设想：增加凝结核[22]、雷暴起电[23]和气旋中形成冰晶[24−25]。Carslaw等[16]认为关键是GCR影响云滴数量及云中冰晶，并为此设计了两种机制：离子气溶胶清洁空气机制及接近云离子气溶胶机制。当然，目前还不能认为这是一种成熟的理论。因此，可以认为人们发现的太阳活动与古气候的关系，还只是一种可能性。究竟太阳活动对地球气候的影响有多大，可能在多大程度上抵消或加强温室效应的影响还是一个有待研究的问题。

## 4　结 论

(1) 20世纪中期以来温度变化的空间分布、季节变化、气温日较差变化均支持温室效应加剧可能是气候变暖的原因，近30年的气候变暖与温室效应加剧的模拟研究结果一致。

(2) 近百年温度变化中1940年代的高温、1950—1970年代的降温无法用温室气体的变化解释，这表明自然因素，如太阳活动、火山活动乃至大洋热盐环流在年代际温度变化中有重要的作用。

(3) 有充分的证据表明在近千年中MWP及LIA的形成可能与太阳活动的变化有关。全新世北大西洋冷事件与$^{14}C$及$^{10}Be$所揭示的太阳活动减弱有明显的关系。

(4) 太阳辐照度的变化不足以解释相应的气候变化。目前，大多数学者注意到银河宇宙线的作用，太阳活动减弱，银河宇宙线增强，地球大气低云量增加，使气候变冷。但是影响机制尚有待于进一步研究。

(5) 究竟太阳活动以及其他自然因素能在多大程度上抵消或加强温室效应的影响，是一个需要进一步研究的问题。■

### 参考文献


[1] Solomon S, Qin D, Manning M, *et al*. Climate change 2007: the physical science basis. Contribution of working group I to the fourth assessment report of the Intergovernmental Panel on Climate Change [M]. Cambridge, UK, and New York, USA: Cambridge University Press, 2007

[2] Houghton J T, Ding Y, Griggs D J, *et al*. Climate change 2001: the scientific basis. Contribution of working group I to the third assessment report of the Intergovernmental Panel on Climate Change [M]. Cambridge, UK, and New York, USA: Cambridge University Press, 2001

[3] Singer S F. Nature, not human activity, rules the climate: summary for policymakers of the report of the Nongovernmental International Panel on Climate Change [M]. Chicago: The Heartland Institute, 2008

[4] Hansen J, Ruedy R, Sato M, *et al*. Global surface temperature change [R/OL]. [2010-06-01]. http://www. columbia.edu/~jehl/

[5] Allen R, Sherwood S C. Warming maximum in the tropical upper troposphere deduced from thermal winds [J]. Nature Geoscience, 2008, 1: 399−413

[6] Thorne D W. The answer is blowing in the wind [J]. Nature Geoscience,

2008, 1: 347−348

[7] Kikby J. Cosmic rays and climate [J]. Surv Geophys, 2007, 28: 333−375

[8] Bond G, Showers W, Cheseby M, *et al*. A pervasive millennial-scale cycle in North Atlantic Holocene and glacial climate [J]. Science, 1997, 278: 1257−1266

[9] Mayewski P A, Rohling E E, Stager J C, *et al*. Holocene climate variability[J]. Quat Res, 2004, 62: 243−255

[10] Morrill C, Overpeck J T, Cole J E. A synthesis of abrupt changes in the Asian summer monsoon since the last deglaciation [J]. The Holocene, 2003, 13: 465−476

[11] Staubwasser M. An overview of Holocene South Asian monsoon records: monsoon domains and regional contrasts [J]. J Geol Soc India, 2006, 68: 433−446

[12] Wang Yongjin, Cheng Hai, Edwards R L. The Holocene Asian monsoon: links to solar changes and North Atlantic climate [J]. Science, 2005, 308: 854−857

[13] Wang Shaowu. Holocene cold events in the North Atlantic: chronology and climatic impact [J]. Chinese Quat Sci, 2009, 29 (6): 1146−1153

[14] Denton G H, Karlén W. Holocene climatic variations: their pattern and possible cause [J]. Quat Res, 1973, 3 (1): 155−205

[15] Bond G, Kromer B, Beer J, *et al*. Persistent solar influence on North Atlantic climate change during the Holocene [J]. Science, 2001, 294: 2130−2135

[16] Carslaw K S, Harrison R G, Kirkby J. Cosmic rays, clouds and climate [J]. Science, 2002, 298: 1732−1736

[17] Fröhlich C, Lean J. Solar radiative output and its variability: evidence and mechanisms [J]. The Astron Astrophys Rev, 2004, 12: 273−320

[18] Wigley T M L, Raper S C B. Climatic change to solar irradiative changes [J]. Geophys Res Lett, 1990, 17: 2169−2172

[19] Foukal P, Fröhlich C, Spruit H, *et al*. variations in solar luminosity and their effect on earth's climate [J]. Nature, 2006, 443: 161−166

[20] Haigh J D. The impact of solar variability on climate [J]. Science, 1996, 272: 981−984

[21] Svensmark H. Cosmoclimatology: a new theory emerges [J]. A&G, 2007, 48: 118−124

[22] Dikinson R E. Solar variability and the lower atmosphere [J]. Bull Amer Meteorol Soc, 1975, 56 (12): 1240−1248

[23] Markson R, Muir M. Solar wind control of the earth's electric field [J]. Science, 1980, 206: 979−990

[24] Tinsley B A, Deen G W. Apparent tropospheric response to MeV-GeV particle flux variations: a connection via electrofreezing of supercooled water in high-level clouds? [J]. J Geophys Res, 1991, 96 (D12): 22283−22296

[25] Tinsley B A. Correlations of atmospheric dynamics with solar wind-induced changes of air-earth current density into cloud [J]. J Geophys Res, 1996, 101 (D23): 29701−29714

# Debates on the Cause of Global Warming

Wang Shaowu[1], Luo Yong[2,3], Zhao Zongci[2,3], Wen Xinyu[1], Huang Jianbin[3]

(1 *Department of Atmospheric and Oceanic Sciences, School of Physics, Peking University, Beijing* 100871*, China*; 2 *National Climate Center, China Meteorological Administration, Beijing* 100081*, China*; 3 *The Center for Earth System Science Studies, Tsinghua University, Beijing* 100084*, China*)

**Abstract:** The controversial points of views of IPCC and NIPCC are reviewed. IPCC holds that the global warming is caused by the anthropogenic effect. However, NIPCC says, nature, not human activity, rules the climate. Observations of temperatures in the last one hundred years or so support the hypothesis of the anthropogenic impact, but natural factors such as solar activity, volcanism, and thermohaline circulation also take part in the modulation of temperature changes, especially in frequency band of inter-decadal variability. There is pervasive evidence for solar or cosmic ray forcing of the climate in time scale of last 1 ka to 10 ka, which proves that solar activity played an important role in the formation of MWP or LIA, and the cold events over the North Atlantic in the Holocene, though the mechanism responsible for the linkage of solar activity to the earth's climate is to be understood. Recently, the point of view that galactic cosmic rays can impact low clouds, thus resulting in climate cooling, is prevailing. However, its influencing mechanism is remained to be further investigated.

**Key words:** global warming; causes; debates; greenhouse effect; solar activity; galactic cosmic ray

王勇,李清泉,沈新勇. 近50 a江淮地区6—7月降水特征分析. 气象科学,2011,31(1):73-78. Wang Yong, Li Qingquan, Shen Xinyong. The characteristics of summer rainfall in the Yangtze-huaihe river basin in June and July of the recent 50 a. Scientia Meteorologica Sinica, 2011,31(1):73-78.

# 近50 a江淮地区6—7月降水特征分析

王勇[1,2] 李清泉[3] 沈新勇[2]
(1 江苏省防雷中心,南京 210009)(2 南京信息工程大学 气象灾害省部共建教育部重点实验室,南京 210044)
(3 国家气候中心,北京 100081)

**摘要** 用江淮地区147个气象站1956—2005年逐日降水资料,结合NCEP/NCAR 850 hPa风场再分析资料以及ERSST海温资料,对江淮地区夏季6—7月降水时空及其相关的海温特征进行了诊断分析。结果表明:江淮地区一致性偏多或偏少分布是6—7月降水的主要模态;从长期趋势来看,江淮地区6—7月降水表现为显著的增加趋势,另外近50a来,该区6—7月降水主要以年代际振荡为主;前期春季(3—5月)及其同期夏季(6—7月)中国邻近海域海表温度以及850 hPa风场同江淮地区夏季6—7月降水存在着显著的关系。

**关键词** 降水;诊断分析;趋势
**分类号** P463.1 **文献标识码** A

# The characteristics of summer rainfall in the Yangtze-huaihe river basin in June and July of the recent 50 a

**Wang Yong**[1] **Li Qingquan**[2] **Shen Xinyong**[1]
(1 *Jiangsu Lightning Protection Center*, *Nanjing* 210009, *China*)
(2 *Key Laboratory of Meteorological Disaster of Ministry of Education*, *Nanjing University of Information Science & Technology*, *Nanjing* 210044, *China*) (3 *National Climate Center*, *CMA*, *Beijing* 100081, *China*)

**Abstract** Based on the 1956—2005 summer daily precipitation of 147 Chinese stations supplied by the National Meteorological Information Center, features of the summer rainfall have investigated in the Yangtze-huaihe river basin, features of atmospheric circulation and sea surface temperature (SST) have been studied based on 850 hPa wind of NCEP/ NCAR reanalysis datasets and ERSST data. Results show that consistent anomalous distribution character is the main mode of the June-July rainfall in the Yangtze-huaihe river basin. The June-July rainfall in the Yangtze-huaihe river basin, in the long-term, exhibits a significant increasing trend and possesses a leading character of inter-annual oscillation in the past 50 a. There are good relationships between June-July rainfall in the Yangtze-huaihe river basin and the SST in the adjacent ocean of China as well as the 850 hPa wind in both preceding spring and corresponding summer.

**Key words** Rainfall; Diagnostic analysis; Trend

**收稿日期**:2009-06-06;**修改稿日期**:2010-03-18

**第一作者简介**:王勇(1980-),男,江苏南京,硕士生,主要从事极端气候方面的研究. wangyong_jsnj@126.com
**通讯作者**:沈新勇,教授,shenxy@nuist.edu.cn

## 引 言

早在1930s,竺可桢[1]就对江淮地区夏季降水做了研究,他指出江淮地区夏季降水显著的气候学特征是年际差异,并具有明显的年代际变化和趋势变化。而后来不少研究指出[2-3],江淮地区的夏季降水实际上就是东亚夏季风推进的产物,其季节内变化与东亚夏季风的进退紧密相关。尹树新等[4]认为夏季风的差异是影响中国江淮地区严重旱涝的重要因素;吴志伟等[5]研究也表明长江中下游地区旱涝并存与东亚夏季风的强度存在着显著的关系,也有研究表明[6],赤道东太平洋海温对江淮流域夏季旱涝存在显著的影响。海温异常作为气候异常的一个主要因子,其通过长期的海气相互作用影响后期环流背景,从而影响次年降水的异常。数值试验结果也表明[7-8],热带海温异常尤其是热带太平洋海温异常对中国江淮流域降水有很大的影响。江淮地区是旱涝灾害频发的地区,淮河流域夏季降水异常与印度西南季风、东亚副热带季风以及冷空气有密切关系[9],其中旱涝灾害大多发生在6—7月梅雨期间,江淮梅雨量与该地区夏季6—7月累积降水量的相关系数达到0.8以上[10],所以研究江淮地区降水特征一直是气象学者研究的重要课题之一。

然而,由于资料和方法上的差异,许多研究得到的结果也是不尽相同。并且以往的研究工作大多是分析梅雨的气候特征及形成原因[3,7-8],本文根据降水距平值选取6—7月为重点分析月份,其中包括梅雨时段的降水;为了能更加显著地突出降水的基本特征,同时使用的是逐日资料而非往常惯用的逐月资料。鉴于以上两点考虑,本文利用逐日降水资料,分析了江淮地区6—7月降水的基本气候特征,并且通过讨论6—7月降水异常与海温、风场等因素之间的关系,初步探求江淮地区降水的成因。

## 1 资料和方法

使用了国家气象信息中心提供的1956—2005年江淮地区逐日降水量资料,以及同时段NCEP/NCAR 2.5°×2.5°的逐月850 hPa风场再分析资料、NOAA 2°×2°逐月的海表面温度资料。

江淮区域的范围划分参考殷永红[11]的定义,即选取(28~34 °N、110 °E)以东范围内的陆地为江淮区域。对逐日降水资料做了质量控制,删除了资料序列长度过短或缺测过多的站点,对资料中缺测进行的检查方法是:如果1 a内缺测超过35 d(大于1 a内实际观测日数的10%)时,该年不参加计算。当站点无缺测超过40 a,这个站点予以保留。经过上述处理以后,选取了147站的逐日降水资料。

图1给出了江淮地区147站50 a平均的逐日降水距平曲线图。可以看出,一般情况下,江淮流域4—9月降水在年平均值以上。11—2月降水最小(小于1个负标准偏差),6—7月降水最大(大于一个正标准偏差),峰值出现在6月中旬左右。这主要是因为6月份副热带高压还较为偏南,江淮大部分地区处在副高的北侧,暖湿气流影响下,水汽充足,降水充沛。到了7月上旬左右,副热带高压北跳而控制了江淮大部,使其在副高的控制之中而高温少雨。因此本文重点分析该地区6—7月的降水特征。此外,文中还运用了经验正交函数(EOF)分解、小波分析、相关分析等方法分析了江淮地区的降水特征。

## 2 江淮地区6—7月降水的时空分布特征

### 2.1 空间分布特征

对江淮地区1956—2005年6—7月降水作EOF分析,有81个站点符合EOF时间序列要求。从第一模态(图2a)来看,整个江淮地区表现为一致的正值区,其中荷载区主要位于江淮地区中部,这说明江淮地区夏季一般受相同的天气系统影响,出现降水的步调是一致的,其中中部地区夏季降水最容易发生异常。第二模态(图2b)基本上以长江为分界线,其南北表现为反向变化特征,这主要同季风以及副高的南北移动和西伸东进有着密切的联系。由于前两个模态累计总方差贡献率已超过了41%,说明这两个空间型基本可以反映江淮地区6—7月降水的

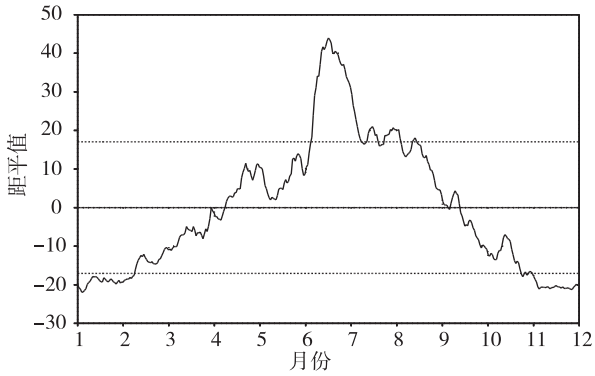


图1 1956—2005年各月江淮地区逐日降水距平年变化曲线,图中点线表示标准差

Fig. 1 The annual change of daily precipitation anomaly in the Yangtze-huaihe river basin from 1956 to 2005

主要空间特征。

## 2.2　时间演变特征

图 3 是 EOF 前两个模态时间系数序列以及线性拟合曲线。从图 3a 可以看出,第一模态降水时间序列表现出长期增加趋势,这表明江淮地区 6—7 月降水呈明显的增多趋势。但是,从图中也可以看到,近 5 a 降水量却明显偏少的。从图 3b 可以看出,在 1960s、1970s 以及 1990s 该序列以偏正值为主,而 1980s 以偏负值为主,结合该模态空间分布可以表明,1960s、1970s 以及 1990s 江淮偏北地区夏季降水偏少,而偏南地区偏多,而1980s恰恰相反,即 1960s、1970s 以及 1990s 江淮的南部地区偏少,而江淮的北部地区偏多。但从长期趋势来看该序列表现为较弱的增加趋势。

## 2.3　周期性特征

图 4 为 EOF 前两个模态时间系数的 Morlet 小波能谱等值线图(点区域为受边瓣效应影响的区域),从图 4a 可以看出,江淮地区 6—7 月降水 EOF 第一模态主要以年代际振荡为主,其中 1965—1975 年间以准 6 a 振荡周期,1975 年以后以 3 ~ 4 a 周期振荡为主。而从图 4b 可以看出 EOF 第二模态在 1985 年以后表现出了显著的准 6a 周期振荡。通过以上的分析可以看出,江淮地区 6—7 月降水存有明显的年代际振荡。

# 3　江淮地区 6—7 月降水与海温及低层风场的关系

## 3.1　降水第一主模态

图 5 给出了江淮地区 6—7 月降水 EOF 第一模态时间系数同太平洋海温前期春季(3—5 月)(图 5a)及同期(6—7 月)(图 5b)的回归系数空间分布。从图 5a 可以看出,6—7 月份,赤道大部分地区为正

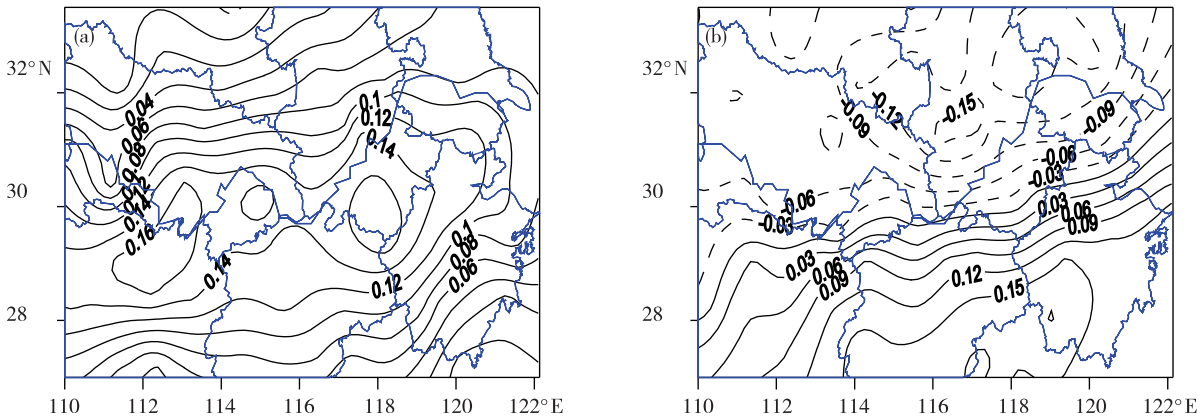


图 2　江淮地区 6—7 月降水 EOF 前两个模态
(a)第一模态(方差贡献 25.8%);(b)第二模态(方差贡献 15.3%)
Fig. 2　The first two modes of EOF in the Yangtze-huaihe river basin in June and July
(a) the first mode (variance contribution 25.8%); (b) the second mode (variance contribution 15.3%)

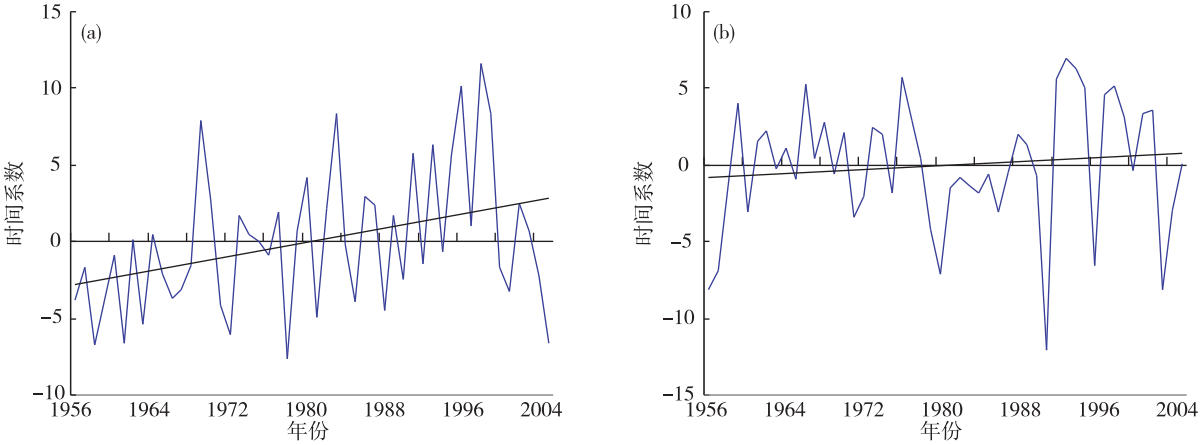


图 3　江淮地区夏季降水 EOF 前两个模态时间系数 (a)第一模态;(b)第二模态
Fig. 3　The time coefficients of EOF1 and EOF2 of summer rainfall in the Yangtze-huaihe river basin(a) first mode; (b) second mode

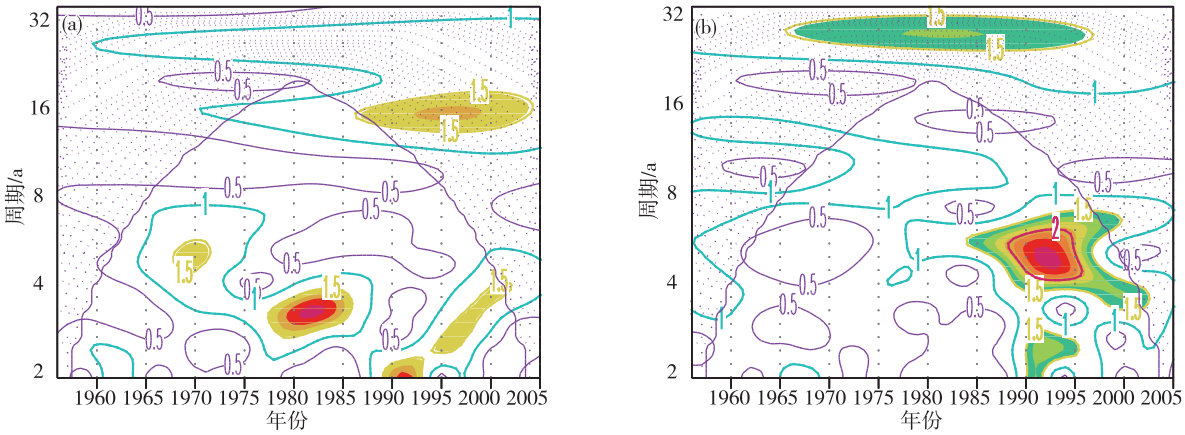


图 4 EOF 前两个模态时间系数 Morlet 小波能谱图
(阴影表示能量大于 2.0 的区域)(a)第一模态;(b)第二模态
Fig. 4 Energy spectrum of the Morlet wavelet transform of the time coefficients of EOF1 and EOF2 (Areas with the energy more than 2.0 are shaded) (a) first mode; (b) second mode

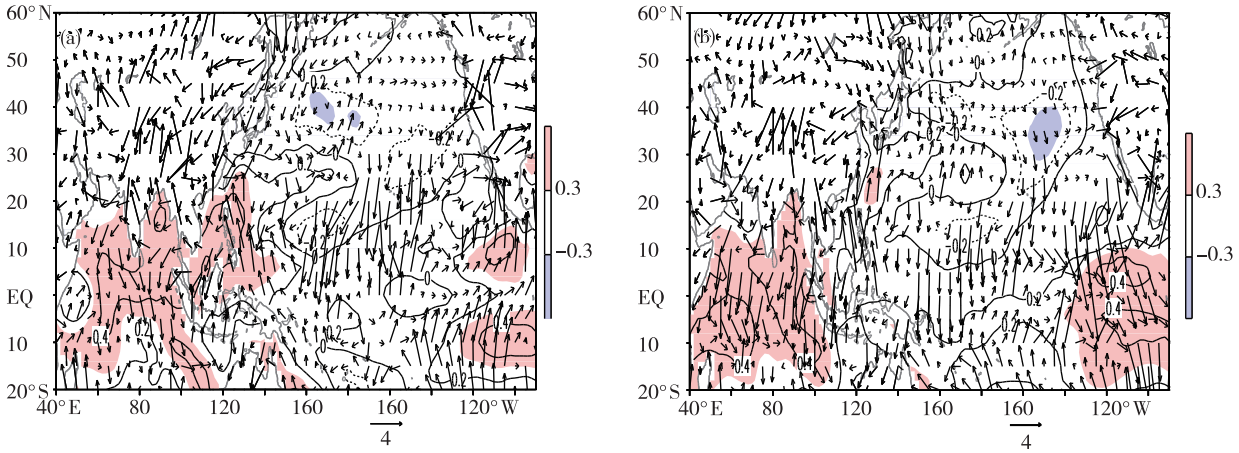


图 5 江淮地区 6—7 月降水第一模态的 850 hPa 风场(矢量)和海表温度距平相关(等值线)
(a)同期(6—7 月);(b)前期(3—5 月);(阴影表示通过 0.05 的显著性检验)
Fig. 5 Correlations of wind fields at 850 hPa (vector) with surface temperature anomaly (contour line) of the first mode in the Yangtze-huaihe river basin in June and July. (a) the same term (in June and July); (b) the earlier term (in March and May) (Areas with 0.05 significance level are shaded)

相关,其中显著正相关区域位于印度洋及赤道东太平洋地区,而北太平洋主要为负相关,其中显著负相关区域位于夏威夷群岛东北部。春季(3—5 月)海温特点与夏季 6—7 月相似,赤道大部分地区为正相关,而 10 °N 以北地区为负相关。但是赤道东太平洋地区的显著正相关区范围比 6—7 月大,显著负相关区的位置西退至北美西部(30 ~ 40 °N、140 ~ 150 °E)的太平洋海域附近。结合 EOF 第一模态空间分布可以得知,当前期春季及其夏季赤道印度洋及赤道东太平洋地区海温表现为正异常,而春季夏威夷群岛东北部海温表现为负异常时,夏季北美西部(30 ~ 40 °N、140 ~ 150 °E)的太平洋海域附近表现为负异常时,江淮地区夏季降水则显著偏多;反之亦然。

充足的水汽输送是形成降水的必要条件,而 850 hPa 风场可以清楚地反映出水汽输送特征,图 5 同时也给出了 EOF 第一模态时间系数同前期春季(3—5 月)和同期(6—7 月)850 hPa 风场。从图 5a 可以看出,夏季中国东海以东为一反气旋流场,而江淮地区为一气旋流场,这样从我国南海有明显在的南风向北水汽输送通道。而图 5b 同图 5a 在江淮地区及其邻近海区流场很相似,中国南海也存在很明显的偏南风水汽输送通道。结合 EOF 第一模态空间分布得知,当前期春季到夏季东海以东维持明显的反气旋环流,而江淮地区为气旋环流时,由于从中国南海水汽输送通道明显,使得江淮地区夏季降水偏多;反之亦然。

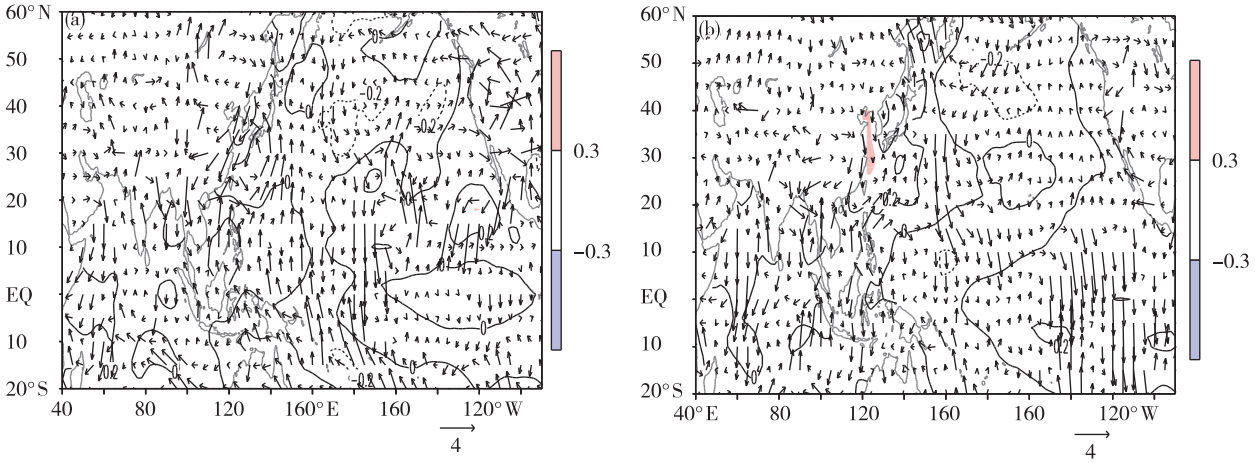


图 6　江淮地区 6—7 月降水第二模态的 850 hPa 风场(矢量)和海表面温度距平相关(等值线)
(a)同期(6—7 月);(b)前期(3—5 月);(阴影表示通过 0.05 的显著性检验)
Fig. 6　Correlations of wind fields at 850 hPa(vector) with surface temperature anomaly(contour line) of the second mode in the Yangtze-huaihe river basin in June and July. (a)the same term (in June and July); (b)the earlier term (in March and May)
(Areas with 0.05 significance levels are shaded)

## 3.2　降水第二模态

图 6 为江淮地区夏季降水第二模态时间系数同前期春季(3—5 月)(图 6a)和同期(6—7 月)(图 6b)的回归系数空间分布和 850 hPa 风场分布图。从夏季降水和海温的关系来看,图 6a 可以看出,北太平洋为负相关,而其余海区基本都为正相关区,只是所有海区的相关性都不显著,而从图 6b 同图 6a 表现为相似特点,所以我们可以得出,中国邻近海区的海温异常对江淮地区夏季降水的 EOF 第二模态的影响不显著。

低层风场上看,同期 6—7 月(图 6a)反气旋流场主要位于巴士海峡及其以东区域,江淮地区北部主要为偏西或偏北风,而南部以偏南偏东风为主,而前期 3—5 月(图 6b)与同期 6—7 月也表现为相似特点,并且风的强度更加偏大,结合 EOF 第二模态我们可以得知,当从春季到夏季巴士海峡附近维持明显的反气旋环流,而江淮地区北部由于存在偏西或偏北环流,使得该区域水汽输送不足,夏季降水偏少,而江淮地区南部由于存在偏南或偏东风,充足的水汽输送使得该区域夏季降水偏多,反之亦然。

# 4　结　论

本文利用江淮地区 1956—2005 年 147 站 50 a 逐日降水资料,计算逐日降水距平和标准偏差,同时分析了该地区 6—7 月的降水特征。得出以下结论:

(1)江淮地区降水一致性偏多或偏少分布是 6—7 月降水的一个主要模态;该地区南北反向变化特征是 6—7 月降水的另一个分布模态。

(2)从长期趋势来看,江淮地区 6—7 月降水有明显的增加趋势;近 50a 来该区 6—7 月降水主要以年代际振荡为主。

(3)当前期春季及同期夏季印度洋及赤道东太平洋地区海温表现为正相关,而春季夏威夷群岛东北部海温表现为负相关,夏季北美西部(30 ~ 40 °N、140 ~ 150 °E)的太平洋海域附近表现为负相关时,江淮地区夏季降水则显著偏多;反之亦然。

(4)当前期春季到夏季东海以东维持反气旋环流,而江淮地区为气旋环流时,由于从中国南海存在明显的偏南风水汽输送通道,使得江淮地区夏季降水偏多,反之亦然。当从春季到夏季巴士海峡附近维持反气旋环流,而江淮地区北部存在偏西或偏北环流,使得该区域水汽输送不足,夏季降水偏少,而江淮地区南部由于存在偏南或偏东环流,充足的水汽输送使得该区域夏季降水偏多;反之亦然。

## 参　考　文　献

[1]　竺可祯. 东南季风与中国之雨量. 地理学报,1934,1(1):1-27.
Zhu Kezheng. Southeastern monsoon and precipitation in China. Acta Geographica Sinica (in Chinese),1934,1(1):1-27.

[2]　涂长望,黄士松. 中国夏季风之进退. 气象学报,1944,18:1-20.
Tu Changwang, Huang Shisong. The advance and withdraw of Chinese summer monsoon. Acta Meteorologica Sinica (in Chinese),1944,18:1-20.

[3]　刘明丽,王谦谦. 江淮梅雨期极端降水的气候特征. 南京气象学院学报,2006,29(5):666-681.　Liu Mingli, Wang Qianqian. Climatic characteristics of the extreme precipitation in Jianghuai region. Journal of Nanjing Institute of Meteorology (in Chinese), 2006,29(5): 666-681.

[4] 尹树新,江燕如. 季风异常与江淮地区旱涝关系. 南京气象学院学报,1993,16(1):89-296. Yin Shuxin, Jiang Yanru. The relationship between the abnormality monsoon and the drought flood anomalies in Jianghuai region. Journal of Nanjing Institute of Meteorology(in Chinese), 1993,16(1):89-296.

[5] 吴志伟,何金海,李建平,等. 长江中下游夏季旱涝并存及其异常海气特征分析. 大气科学,2006,30(4):570-577. Wu Zhiwei, He Jinhai, Li Jianping, et al. The summer drought-flood coexistence in the middle and lower reaches of the Yangtze river and analysis of its air-sea background features in anomalous years. Chinese Journal of Atmospheric Sciences(in Chinese), 2006,30(4):570-577.

[6] 励申申,寿绍文. 赤道东太平洋海温与我国江淮流域夏季旱涝的成因分析. 应用气象学报,2000,11 (3):331-338. Li Sensen, Shou Saowen. Equatorial eastern Pacific SST and analysis on causes of summer floods/ droughts in the Changjiang and Huaihe river basins. Quarterly Journal of Applied Meteorological Science (in Chinese),2000,11(3):331-338.

[7] 徐海明,何金海,董敏. 江淮入梅的年际变化及其与北大西洋涛动和海温异常的联系. 气象学报,2001,59(6):694-706. Xu Haiming, He Jinhai, Dong Min. Interannual variability of the Meiyu onset and its association with north Atlantic oscillation and SSTA over north Atlantic. Acta Meteorologica Sinica (in Chinese),2001,59(6):694-706.

[8] 宗海锋,张庆云,彭京备. 江淮流域梅雨的多尺度特征及其与全球海温的关系. 气候与环境研究,2005,10 (1):101-114. Zong Haifeng, Zhang Qingyun, Peng Jingbei. Multiple scale characteristics for precipitation over the Yangtze river valley during the Meiyu period and their relationships with the global sea surface temperature. Climatic and Environmental Research (in Chinese), 2005,10(1):101-114.

[9] 王慧,王谦谦. 近49年来淮河流域降水异常及其环流特征. 气象科学,2002,22(2):149-158. Wang Hui, Wang Qianqian. The precipitation anomality and the circulation characteristics in the region of Huaihe River in recent 49 years. Scientia Meteorologica Sinica(in Chinese), 2002,22(2):149-158.

[10] 徐海明,何金海,姚永红. 江淮入梅的年际变化与前冬环流的联系及其可能成因. 南京气象学院学报, 1999,22(2):246-253. Xu Haiming, He Jinhai, Yao Yonghong. Interannual variability of the Meiyu onset and its association with the atmospheric circulation in the previous winter and possible causes. Journal of Nanjing Institute of Meteorology ( in Chinese),1999,22(2):246-253.

[11] 殷永红,倪允琪,史历. 江淮流域夏季降水异常及与全球中低纬海温异常关系的诊断研究. 南京大学学报,2001,37(3):358-368. Yin Yonghong, Ni Yunqi, Shi Li. A diagnosis of the relationships between the summer precipitation anomaly in Jianghuai region and the middle-high latitude SST anomalies. Journal Nanjing University(in Chinese),2001,37(3):358-368.

ADVANCES IN ATMOSPHERIC SCIENCES, VOL. 28, NO. 6, 2011, 1336–1344

# Radiative Forcing and Climate Response Due to Black Carbon in Snow and Ice

WANG Zhili[1,2,3] (王志立), ZHANG Hua*[3] (张 华), and SHEN Xueshun[4] (沈学顺)

[1] *Center for Atmosphere Watch and Services, Chinese Academy of Meteorological Sciences, China Meteorological Administration, Beijing* 100081

[2] *Graduate University of Chinese Academy of Sciences, Beijing* 100049

[3] *National Climate Center, China Meteorological Administration, Beijing* 100081

[4] *State Key Laboratory of Severe Weather, Chinese Academy of Meteorological Sciences, Beijing* 100081

(Received 9 December 2010; revised 14 April 2011)

**ABSTRACT**

The radiative forcing and climate response due to black carbon (BC) in snow and/or ice were investigated by integrating observed effects of BC on snow/ice albedo into an atmospheric general circulation model (BCC_AGCM2.0.1) developed by the National Climate Center (NCC) of the China Meteorological Administration (CMA). The results show that the global annual mean surface radiative forcing due to BC in snow/ice is +0.042 W m$^{-2}$, with maximum forcing found over the Tibetan Plateau and regional mean forcing exceeding +2.8 W m$^{-2}$. The global annual mean surface temperature increased 0.071°C due to BC in snow/ice. Positive surface radiative forcing was clearly shown in winter and spring and increased the surface temperature of snow/ice in the Northern Hemisphere. The surface temperatures of snow-covered areas of Eurasia and North America in winter (spring) increased by 0.83°C (0.6°C) and 0.83°C (0.46°C), respectively. Snowmelt rates also increased greatly, leading to earlier snowmelt and peak runoff times. With the rise of surface temperatures in the Arctic, more water vapor could be released into the atmosphere, allowing easier cloud formation, which could lead to higher thermal emittance in the Arctic. However, the total cloud forcing could decrease due to increasing cloud cover, which will offset some of the positive feedback mechanism of the clouds.

**Key words**: black carbon, snow/ice, radiative forcing, climate effects

**Citation**: Wang, Z. L., H. Zhang, and X. S. Shen, 2011: Radiative forcing and climate response due to black carbon in snow and ice. *Adv. Atmos. Sci.*, **28**(6), 1336–1344, doi: 10.1007/s00376-011-0117-5.

## 1. Introduction

Black carbon (BC), an important component of atmospheric aerosols, is produced by the incomplete combustion of hydrocarbon-containing materials including fossil fuels, biofuels, and biomass (IPCC, 2001; 2007). Bond et al. (2004) estimated the total global emission of BC to be ∼8 Tg C yr$^{-1}$, with contributions of 4.6 Tg C yr$^{-1}$ from fossil fuel and biofuel combustion and 3.3 Tg C yr$^{-1}$ from open biomass burning. Four main areas are large sources of BC: Eastern China, Western Europe, South America, and central Africa. Other important sources are southern North America and Australia (Streets et al., 2003; IPCC, 2007). Not only can BC directly alter the radiation balance of Earth's atmospheric system, it may also indirectly affect regional or global climate by changing the microphysical properties of clouds in terms of cloud condensation nuclei (CCN) or ice nuclei (IPCC, 2007; Wang et al., 2009; Zhang et al., 2009). BC in air can be transported long distances by atmospheric circulation and deposited onto snow and/or ice surfaces by rainout, washout, and dry deposition. Even very small quantities of BC can reduce the albedo of

*Corresponding author: ZHANG Hua, huazhang@cma.gov.cn

© China National Committee for International Association of Meteorology and Atmospheric Sciences (IAMAS), Institute of Atmospheric Physics (IAP) and Science Press and Springer-Verlag Berlin Heidelberg 2011

snow/ice because of the high albedo of pristine snow at visible wavelengths, the multiple scattering properties of snowpack, and the large difference of mass absorption coefficients between BC and snow/ice (Warren and Wiscombe, 1980; Flanner et al., 2007). Reduced albedo means increased absorption of solar radiation by the snow/ice and thus accelerated melting (referred to as the "snow/ice albedo mechanism") (Hansen and Nazarenko, 2004; Jacobson, 2004; Flanner et al., 2007).

A number of studies have measured BC concentrations in snow/ice and have analyzed the effects of BC on surface albedo (e.g., Warren, 1982; Noone and Clarke, 1988; Grenfell et al., 2002). Warren and Wiscombe (1980) found that snow albedo may be reduced by 1% if the BC concentration reaches 15 ng $g^{-1}$. Light et al. (1998) calculated that sea-ice albedo could be reduced by up to 30% with a BC concentration of 150 ng $g^{-1}$. In the Tibetan Plateau region, large amounts of BC attach to the snow and/or ice, increasing the absorption of solar radiation and the thermal radiation emission from the Earth. The results measured by Xu et al. (2006) showed that the highest mean BC content in snow/ice was 79.2 ng $g^{-1}$ in the northeast Himalaya, and the lowest content was 4.3 ng $g^{-1}$ in the western Himalaya. Ming et al. (2008) reported that the average BC concentration in snow/ice of the Everest region from 1951 to 2001 was $\sim$16 ng $g^{-1}$ and the largest radiative forcing by BC in snow/ice in the summer of 2001 exceeded +4.5 W $m^{-2}$. In many snow-covered regions in the Northern Hemisphere, snow and ice begin to melt heavily in March and April, but because these months precede the agricultural season, tremendous amounts of snow/ice water resources are lost before they can be used (Thompson et al., 2003; Barnett et al., 2005). Snow is an important source of surface runoff and soil moisture. Changes in the radiative properties of snow can thus have important impacts on the radiation balance and the water balance of the Earth's surface and the hydrological cycle. From a global perspective, the decrease of snow/ice albedo due to BC and the resultant rise in surface temperature can accelerate the global melting of glaciers and can contribute greatly to global warming. The effects of BC in snow/ice on radiative flux have also been simulated using climate models (Hansen and Nazarenko, 2004; Hansen et al., 2007; Flanner et al., 2007; Koch et al., 2009; Rypdal et al., 2009). Those studies estimated that global annual mean radiative forcing due to BC in snow/ice ranges between +0.007 and +0.16 W $m^{-2}$, and they showed that the efficacy of climate forcing to change global surface temperature by the snow/ice albedo mechanism is higher than that of $CO_2$. Some uncertainties about this research remain, such as limited observational data, mixed states of BC and snow/ice particles, different parameterizations of models, and so on. The IPCC (2007) also indicated that the level of scientific understanding of the forcing by BC in snow/ice is still low, and that further studies are therefore needed.

In the present study, radiative forcing by BC in snow/ice and the climate response to this forcing were studied using the second-generation AGCM developed by the National Climate Center (NCC) of the China Meteorological Administration (CMA), called the BCC_AGCM2.0.1. Section 2 describes the model and experimental design. Section 3 contains the calculation methods of the radiative forcing of BC in snow/ice and analyzes its effect on global climate. Finally, conclusions and discussion are presented in section 4.

## 2. Model Description and Experimental Design

### 2.1 *Basic model description*

The BCC_AGCM2.0.1 was developed by the National Climate Center of the China Meteorological Administration (NCC/CMA) based on the Community Atmosphere Model Version 3 (CAM3) of the U.S. National Center for Atmospheric Research (NCAR). The model uses horizontal triangular truncation at wavenumber 42 (T42, $\sim$2.8°×2.8°) and a vertical hybrid $\sigma$-pressure coordinate, which includes 26 vertical layers with the top layer at a pressure of 2.9 hPa. The model uses the same radiation scheme as that used in CAM3; both models divide the whole shortwave region into 19 spectral bands and use a two-stream $\delta$-Eddington approximation (Briegleb, 1992). This scheme takes atmospheric absorption due to gases such as $H_2O$, $CO_2$, $O_3$, and $O_2$ into account and also considers multiple-scattering and absorption processes due to aerosols such as sulfate, BC, organic carbon, dust, and sea salt. The model was coupled with the Community Land Model (CLM3), in which snow is a forecast variable. The simulation of snow takes into account the interactions between snowfall and melting and between new snow and old snow, as well as the integration, compression, and deformation processes among snow layers (Oleson et al., 2004). The sea-ice concentration and thickness are prescribed in the model. The shortwave region is divided into two spectral bands in the CLM3 and the sea-ice model including visible $\lambda<0.7$ $\mu$m and near-infrared $\lambda\geqslant0.7$ $\mu$m. Monthly mean climatological data from 1971 to 2000 on a Gaussian grid, obtained from National Centers for Environmental Prediction (NCEP) reanalysis products, were used as the initial

model field, and the geographical distribution of sea surface temperature was prescribed based on the 21-year climatology for 1981–2001 (available online from http://www/ccsm.ucar.edu/models/atmcam/docs/description). The climatologic field of the aerosol species considered in this study used monthly mean aerosol mass concentrations from the Model for Atmospheric Chemistry to Transport (MATCH) (Rasch et al., 1997), and their optical properties were described by Zhang et al. (2009). The aerosol distribution reasonably agreed with observations (Collins et al., 2001, 2002).

Compared with CAM3, many parameterizations were changed in BCC_AGCM2.0.1. The dynamics in the model differ significantly from the Eulerian spectral formulation of the dynamical equations in CAM3, and a reference stratified atmospheric temperature and a reference surface pressure were introduced into the model governing equations to improve calculation of the pressure gradient force and the gradients of surface pressure and temperature (Wu et al., 2010). The major modifications to the model physics include a new convection scheme (Zhang and Mu, 2005), a dry adiabatic adjustment scheme in which potential temperature is conserved (Yan, 1987), a modified scheme to calculate sensible heat and moisture fluxes over open

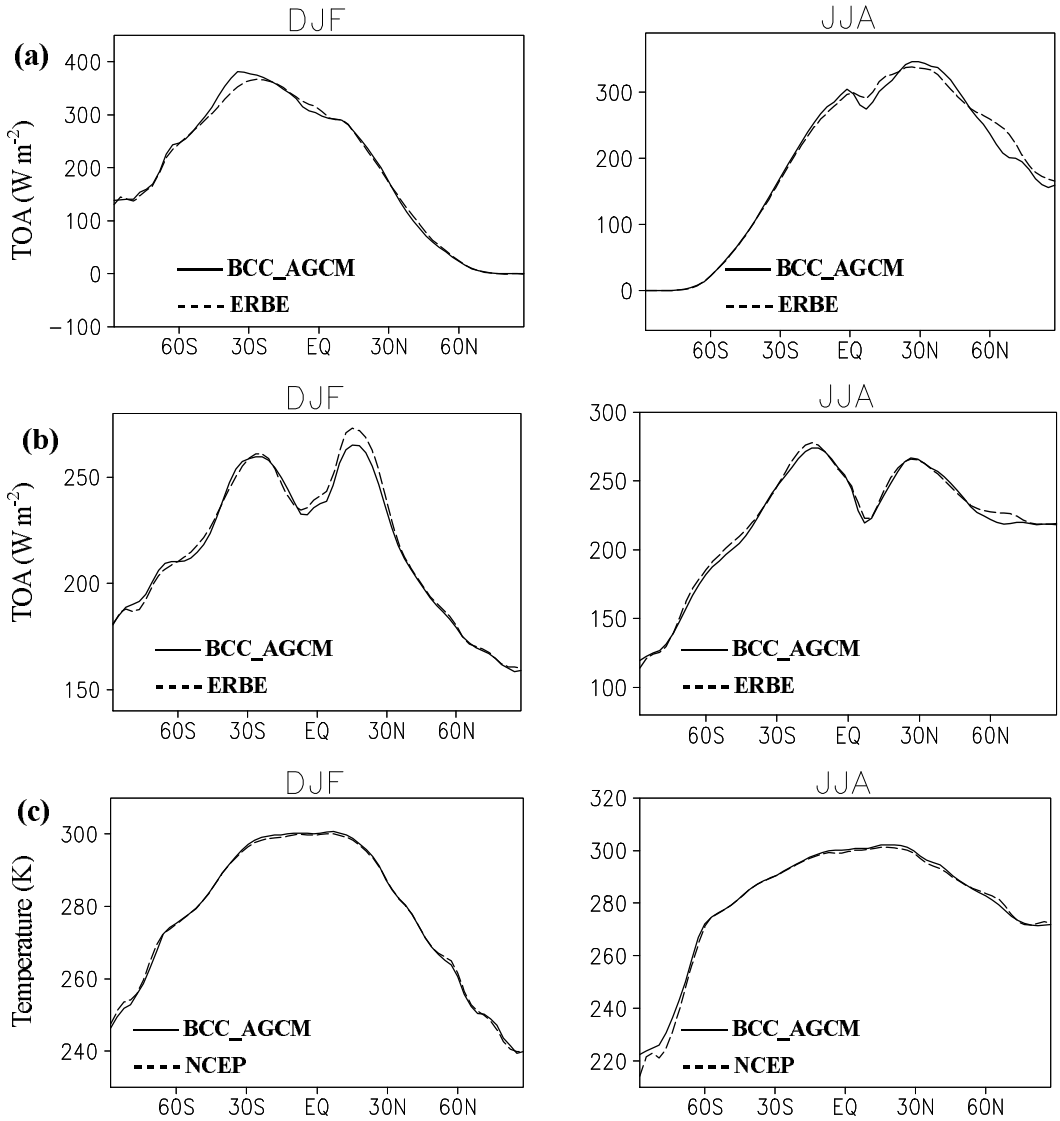


**Fig. 1.** The comparison of zonal mean of (a) net shortwave flux at the TOA (units: W $m^{-2}$), (b) upward longwave flux at the TOA (units: W $m^{-2}$), and (c) surface temperature (units: K) between the simulation and observations/reanalysis data. DJF and JJA represent winter and summer, respectively.

ocean that considers the effect of ocean waves on latent and sensible heat fluxes (Wu et al., 2010), and an empirical equation to compute the snow cover fraction (Wu and Wu, 2004). The model provides overall improvements to climate simulation in comparison with CAM3, especially for simulating the tropical maximum and the subtropical minimum of precipitation, wind stress, and sensible and latent heat fluxes at the ocean surface (Wu et al., 2010; Wang et al., 2010). Figure 1 gives the seasonal changes of the zonal mean of net shortwave flux and upward longwave flux at the top of the atmosphere (TOA) and surface temperature simulated by BCC_AGCM2.0.1. For comparison, observations from the Earth Radiation Budget Experiment (ERBE; Harrison et al., 1990) and reanalysis data from National Center for Environmental Prediction (NCEP; Kistler et al., 2001) are also presented. As shown in Fig. 1, latitudinal and seasonal patterns of the simulation are consistent with the observations or the NCEP data, and there are no large differences between them except that the simulated net shortwave flux at the TOA in summer (June, July, August: JJA) in the high-latitude region and the simulated upward longwave flux at the TOA in winter (December, January, February: DJF) in the tropical region in the Northern Hemisphere were underestimated in comparison with ERBE data.

### 2.2 *Experimental design*

Observations and simulations have shown that the effects of BC on snow/ice albedo are mainly concentrated at wavelengths <0.9 $\mu$m (Warren and Wiscombe, 1980; Jacobson, 2004; Flanner et al., 2007). Hansen and Nazarenko (2004) summarized the BC amounts in snow/ice samples from various sites in Alaska, Canada, Greenland, Sweden, and Eurasia, and in the sea ice of the central Arctic. They calculated the effects of BC on snow/ice albedo in the different regions and found that, with wavelength $\lambda$<0.77 $\mu$m, snow/ice albedos were reduced by 2.5% at the Arctic, by 5% for land-surface snow in the Northern Hemisphere, and by 1% for snow/ice in the Southern Hemisphere except at the South Pole. Ming et al. (2009) also analyzed the effects of BC in snow/ice on albedo at many sites in western China and the Tibetan Plateau. Their results showed albedo reduction due to BC in snow/ice of 6% at Haxilegen (43.73°N, 84.46°E) and Miaoergou (43.06°N, 94.32°E), 5% at Lanong (30.42°N, 90.57°E), and 4% at Mushitage (38.28°N, 75.02°E). The mean reduction of albedo among these sites was close to 5% in visible, which was consistent with the results of Hansen and Nazarenko (2004).

Firstly, two simulation experiments were conducted in this study to examine the climate response due to BC in snow/ice. In the control experiment (EXP1), no effect of BC on the snow/ice albedo was included. In the second experiment (EXP2), albedo decrease in snow/ice was specified at $\lambda$<0.7 $\mu$m according to the calculated results of Hansen and Nazarenko (2004) and Ming et al. (2009) described above (i.e., the snow/ice albedo in the Arctic decreased by 2.5%; the snow albedo on land in the Northern Hemisphere decreased by 5%, and the snow/ice albedo in the Southern Hemisphere, except the South Pole, decreased by 1%). In EXP2, the instantaneously radiative forcing caused by BC in snow/ice was also calculated. In addition, we conducted another experiment (EXP3) to calculate the instantaneously radiative forcing when simultaneously considering the BC in snow/ice and in the atmosphere. The difference between the results of the EXP1 and EXP2 was regarded as the effect of BC in snow/ice on climate. In each experiment, we ran the BCC_AGCM2.0.1 for 11 years, with the first year as the spin-up time. The results for the last 10 years were averaged and analyzed for this study.

## 3. Results

### 3.1 *Surface radiative forcing* ($F_s$) *of BC in snow/ice*

Figure 2a shows the annual mean distribution of BC column burden used in this model. The largest column burden of BC occurs over East Asia with a maximum value >2.7 mg m$^{-2}$. This high value was most likely attributed to a rapid industrial development in southeastern China in recent years. Other regions with large column burdens include India, Western Europe, some of the west coast of Central Africa, and central South America. There was also a relatively high column burden in the southern part of North America and in Australia.

BC deposits on snow/ice surfaces reduce their albedo and increase their absorption of solar radiation, so that positive radiative forcing is produced on the Earth's surface. The annual mean distribution of surface radiative forcing shown in Fig. 2b reveals that the maximum forcing in the Northern Hemisphere occurs over the Tibetan Plateau (30°–40°N, 80°–100°E), where regional mean forcing reaches +2.8 W m$^{-2}$, which is similar to the result calculated by Flanner et al. (2007) using BC emission list data (Bond et al., 2004). The maximum radiative forcing on Greenland also exceeds +2.0 W m$^{-2}$. At the two major regions of snow cover in Eurasia and North America, the annual mean surface radiative forcing is +0.2 W m$^{-2}$ to +2.0 W m$^{-2}$. The mean value for sea ice at the Arctic pole is approximately +0.8 W m$^{-2}$, and forcing is also distributed with a small range in the

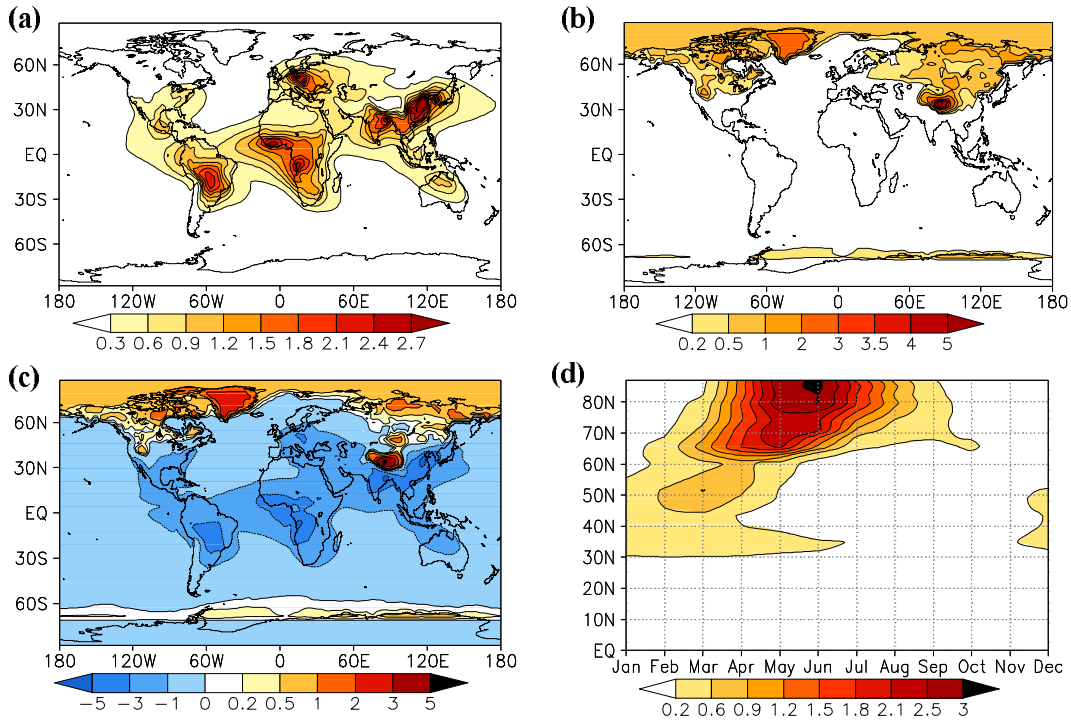


**Fig. 2.** Annual mean distribution of (a) BC column burden (units: mg m$^{-2}$), (b) surface radiative forcing due to BC in snow/ice and (c) BC in snow/ice and atmosphere, and (d) the seasonal change of zonal mean surface radiative forcing due to BC in snow/ice (units: W m$^{-2}$).

Southern Hemisphere. The global annual mean of surface radiative forcing calculated in this study was +0.042 W m$^{-2}$, which is smaller than the result of Hansen and Nazarenko (2004).

Figure 2c shows the annual mean distribution of total surface radiative forcing due to BC in snow/ice and in atmosphere. When simultaneously considering the BC in the atmosphere, the ranges of positive surface forcing greatly decrease in Eurasia and North America, but it barely affects the forcing in Tibetan Plateau and the Arctic pole, where the regional annual mean forcing rates are +2.5 W m$^{-2}$and +0.7 W m$^{-2}$, respectively.

The magnitude of surface radiative forcing by BC in snow/ice is determined by the concentration of BC in the snow/ice, the surface-incident solar flux, and the snow cover (Flanner et al., 2007). The seasonal change of zonal mean surface radiative forcing by BC in snow/ice is shown in Fig. 2d. Distinct forcing is shown in the region 30°–50°N in winter; over time, large values of radiative forcing gradually move northward with large amounts of solar radiation flux and snow cover. In summer, the radiative forcing at high-latitude areas of the Northern Hemisphere reach their maximum values (>+1.8 W m$^{-2}$ in most regions) due to the large amounts of BC emissions and the accumulation of BC by melting snow. Although the BC concentration in snow/ice is low and the surface-incident solar flux drops in the Arctic, the zonal mean values and range of radiative forcing are still large due to the large extent of snow/ice cover. In autumn, although BC emission is still high, radiative forcing is very small because snow pack has not yet accumulated.

### 3.2 *Climate response*

The effects on annual mean surface temperature from BC in snow/ice are shown in Fig. 3. The surface

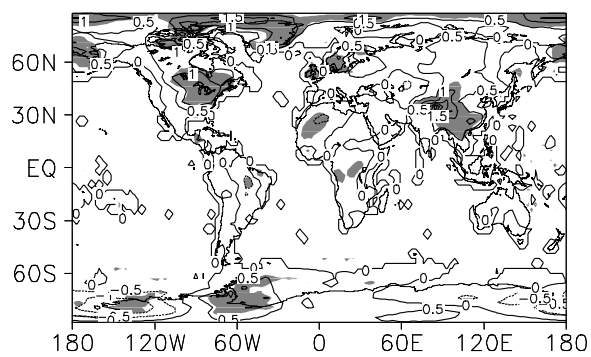


**Fig. 3.** The effect of BC in snow/ice on annual mean surface temperature (units: °C) (The shaded areas shows the confidence exceeds 95% using a $t$-test).

temperatures of snow-covered areas on land and of sea-ice-covered areas show an obvious increase due to the enhanced absorption of solar radiation caused by BC in snow/ice. The mean surface temperature of snow/ice on the Tibetan Plateau, the area with the largest radiative forcing, increased by 1.6°C. At the two major snow-covered regions of Eurasia and North America, temperature increases were ∼0.5°C and were >1°C in northern Canada and the eastern United States. In the area of Arctic sea-ice cover, a temperature increase of 1°C is shown. Furthermore, the results indicate that global annual mean surface temperature increased by ∼0.071°C due to BC in snow/ice. The changes of simulated surface temperature exceeded the 95% confidence level ($t$-test) over most areas of the Arctic sea ice, Tibetan Plateau, and North America. In China, recent observational studies have also shown that >80% of glaciers are receding (Xiao et al., 2007). Increased surface temperatures due to BC in snow/ice will further accelerate the melting of snow/ice under global warming due to $CO_2$.

Garrett and Zhao (2006) pointed out that anthropogenic aerosol could be transported to the Arctic through atmospheric circulation and could change the microphysical and radiative properties of clouds there, leading to an increase in surface longwave fluxes and contributing to the rise of Arctic surface temperatures. Figure 4a shows the effect of BC in snow/ice on annual zonal means of total cloud cover and net longwave flux at the surface. As shown in this figure, BC in snow/ice can also lead to an increase in surface longwave flux in the Arctic, where the maximum value exceeds +1 W m$^{-2}$ at 85°N. This increase is due to the warmer surface temperature, which causes more water vapor to be released into the atmosphere, allowing for easier cloud formation, which could result in higher thermal emittance arriving at the surface in the Arctic. Consequently, this positive feedback mechanism will further accelerate Arctic warming. But increasing cloud cover will decrease net cloud forcing in the Arctic (Fig. 4b), and this will offset some of the positive feedback mechanism of clouds.

Figure 5 presents the seasonal changes of zonal mean differences of surface temperature and snowmelt rate caused by BC in snow/ice. The temporal and spatial distributions of the differences of surface temperature and snowmelt rate are very consistent with those of surface radiative forcing. With the emergence of surface positive radiative forcing in winter, surface temperature significantly increased on land areas with snow/ice cover in the Northern Hemisphere. The mean increase in the surface temperature of snow in winter

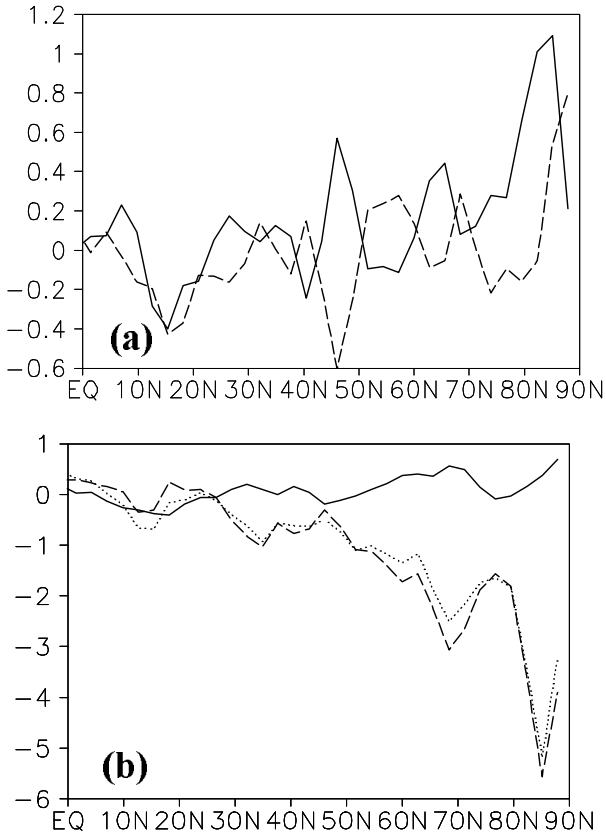


**Fig. 4.** The effect of BC in snow/ice on annual zonal means of (a) total cloud cover (%; dashed line) and net longwave flux at surface (units: W m$^{-2}$; solid line) and (b) shortwave cloud forcing (dashed line), longwave cloud forcing (solid line) and net cloud forcing (dot line; units: W m$^{-2}$).

and spring was ∼0.6°C. Two areas with large values were centered at 50°–70°N in February and at 70°–80°N in April, showing temperature increases of 1°C. The former could be caused by the model system errors, because it was not consistent with small surface radiative forcing during this time (Fig. 2b), and it had a low confidence level ($t$-test). At the Arctic pole, where perennial sea ice exists, the temperature of the sea-ice surface increased by >0.5°C in all seasons, with maximum increase of 2.5°C in September and October (Fig. 5a). Such increases will further accelerate ice melt in the Arctic. For regions north of the Arctic Circle, the surface temperature still increased during some periods without solar radiation, which may be a consequence of thermal inertia or could be dynamical in nature (Flanner et al., 2007). As shown in Fig. 5b, snowmelt rates obviously increased at the early melting stage in mid- and high-latitude areas of the North-

**Table 1.** Global and regional climate responses to BC in snow/ice.

| | Surface radiative Forcing (W m$^{-2}$) | Surface temperature (°C) | Snow cover ratio ($10^{-3}$) | Snow depth (mm) | Ice amount on land (kg m$^{-2}$) |
|---|---|---|---|---|---|
| Eurasia | 0.57/0.90/0.42 | 0.83/0.60/0.39 | –18.2/− 26.2/−15.7 | –12.6/−19.9/− 13.6 | –3.86/−8.02/−5.13 |
| North America | 0.26/0.44/0.19 | 0.83/0.46/0.47 | –43.0/− 33.5/− 31.5 | –27.2/−40.0/ −26.2 | –10.3/ −20.8/−11.7 |
| Global | 0.013/0.094/0.025 | 0.094/0.089/0.071 | –6.70/−8.65/−7.39 | –8.91/−12.6/−10.7 | –9.97/−14.5/−10.7 |

Note: *The three values represent the winter and spring seasons and the annual mean changes of these physical variables, respectively. The geographic ranges for Eurasia and North America are (30°–70°N, 20°–130°E) and (30°–70°N, 60°–130°W), respectively.

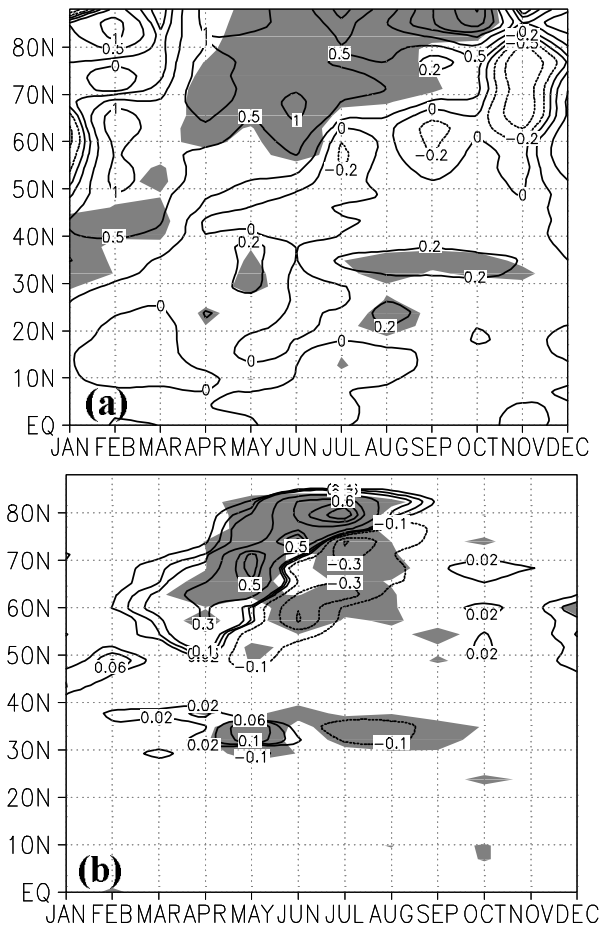


**Fig. 5.** Seasonal changes of zonal mean differences of (a) surface temperature (units: K) and (b) snow melt rate (units: mm d$^{-1}$) caused by the BC in snow/ice (The shaded areas shows the confidence exceeds 95% using a $t$-test).

ern Hemisphere, but they decreased due to the presence of less snow in the late melting stage. Corresponding to the temporal and spatial changes of temperature, the snowmelt rate on land in the Northern Hemisphere also increased obviously in winter and spring, which may shift peaks in river runoff to winter and early spring, away from summer and autumn when water demand is highest in these regions. Water storage capacities in these regions are not sufficient, and thus the earlier melting of snow/ice is expected to worsen water supply problems in the future (Barnett et al., 2005).

Eurasia and North America are the two major regions of snow cover on land, and increased snow/ice melting in these regions will have substantial impacts on local production and livelihoods. Table 1 lists the effects of BC in snow/ice on several important physical parameters worldwide and in the above two major snowpack regions. The seasonal mean values in winter and spring and the annual mean values of the snow cover ratio, snow depth, and ice amount in Eurasia and North America decreased due to the increased surface temperature. Flanner et al. (2009), from analysis of Jones (CRU) Air Temperature Anomalies Version 3 (CRUTEM3), showed that springtime surface temperatures on land north of 30°N over Eurasia and North America increased by 0.59°C (10 yr)$^{-1}$ and 0.23°C (10 yr)$^{-1}$, respectively, from 1979 to 2000. The surface temperatures increased by 0.6°C and 0.46°C over Eurasia and North America due to BC in snow/ice in this study, respectively, which could have contributed to the observational warming in those areas.

## 4. Conclusions

This study examined the radiative forcing of BC in snow/ice and its climatic effects by integrating the BC effects on snow/ice albedo calculated from observational data by Hansen and Nazarenko (2004) and Ming et al. (2009) into the BCC_AGCM2.0.1 developed by the NCC/CMA. Annual mean surface radiative forcing due to BC in snow/ice was calculated as approximately +0.042 W m$^{-2}$, which is smaller than the result reported by Hansen and Nazarenko (2004) because the impact of albedo is only considered at $\lambda$<0.7 $\mu$m in this work. The maximum annual mean surface forcing in

the Northern Hemisphere was shown over the Tibetan Plateau, where regional mean forcing exceeded +2.8 W $m^{-2}$; this finding is similar to that calculated by Flanner et al. (2007) using the BC emission list (Bond et al., 2004). At the two major regions of snow cover in Eurasia and North America, annual mean surface radiative forcing due to BC in snow/ice ranged from +0.2 W $m^{-2}$ to approximately +2.0 W $m^{-2}$. In the Arctic, the mean value for sea ice was approximately +0.8 W $m^{-2}$. When simultaneously considering the BC in atmosphere, the ranges of positive surface forcing obviously decreased in Eurasia and North America, but it has hardly affected the forcing in Tibetan Plateau and Arctic pole.

Clear increases in surface temperatures were shown for land areas with snow cover and sea areas with ice cover due to the enhanced absorption of solar radiation caused by BC in snow/ice. The annual mean increases of temperature in snow-covered areas were estimated to be ∼1.6°C on the Tibetan Plateau, 0.5°C for most of Eurasia and North America, and >1°C in areas of northern Canada and the eastern United States. The corresponding zonal mean values around the Arctic pole reach 1°C, and the global annual mean value increased by 0.071°C. Therefore, with the rise of surface temperature in the Arctic, more water vapor could be released into the atmosphere, allowing for easier cloud formation, which could lead to higher thermal emittance arriving at the surface in the Arctic. However, the net cloud forcing could be decreased due to the increasing of cloud cover, which will offset some of the positive feedback mechanism of the clouds.

Positive surface radiative forcing by BC in snow/ice occurs in winter and spring, leading to increased surface temperature on land areas with snow and ice in the Northern Hemisphere. Surface temperatures of continental Eurasia and North America increased by 0.6°C and 0.46°C in spring, respectively. Corresponding to the seasonal changes of temperature, the snowmelt rate on land in the Northern Hemisphere clearly increased in winter and spring, which could lead to earlier peaks of river runoff in late winter and early spring. Because water storage capacities are not sufficient, much of the winter and spring runoff would flow directly to the oceans. Snow and ice water sources, which have already decreased, would be further lost to human use because the earlier peaks would not coincide with peak usage demands.

Finally, some uncertainty remains regarding sources in this study's simulations. First, the data of BC concentration in snow/ice were from limited sites; errors may be introduced by using the changes of albedos calculated in these sites to represent the changes of regional albedo. Second, the vertical distribution of BC in snow/ice, the mixed state of BC, and snow/ice particles and the climatic data set used to initialize and force the model may all affect the simulated results of this study. Therefore, we hope to obtain more data and more accurate parameterizations in the future and to apply them to further AGCM modeling.

***Acknowledgements.*** This work was financially supported by the National Basic Research Program of China (Grant Nos. 2010CB955608 and 2011CB403405), the Public Meteorology Special Foundation of MOST (Grant No. GYHY200906020).

## REFERENCES

Barnett, T. P., J. C. Adam, and D. P. Lettenmaier, 2005: Potential impacts of a warming climate on water availability in snow-dominated regions. *Nature*, **438**, 303–309.

Bond, T. C., D. G. Streets, K. F. Yarber, S. M. Nelson, J.-H. Woo, and Z. Klimont, 2004: A technology-based global inventory of black and organic carbon emissions from combustion. *J. Geophys. Res.*, **109**, D14203, doi: 10.1029/2003JD003697.

Briegleb, B. P., 1992: Delta-Eddington approximation for solar radiation in the NCAR Community Climate Model. *J. Geophys. Res.*, **97**, 7603–7612.

Collins, W. D., P. J. Rasch, B. E. Eaton, B. V. Khattatov, J.-F. Lamarque, and C. S. Zender, 2001: Simulating aerosols using a chemical transport model with assimilation of satellite aerosol retrievals: Methodology for INDOEX. *J. Geophys. Res.*, **106**, 7313–7336.

Collins, W. D., P. J. Rasch, B. E. Eaton, D. W. Fillmore, J. T. Kiehl, C. T. Beck, and C. S. Zender, 2002: Simulation of aerosol distributions and radiative forcing for INDOEX: Regional climate impacts. *J. Geophys. Res.*, **107**, doi: 10.1029/2001JD001365.

Flanner, M. G., C. S. Zender, P. G. Hess, N. M. Mahowald, T. H. Painter, V. Ramanathan, and P. J. Rasch, 2009: Springtime warming and reduced snow cover from carbonaceous particles. *Atmos. Chem. Phys.*, **9**, 2481–2497.

Flanner, M. G., C. S. Zender, J. T. Randerson, and P. J. Rasch, 2007: Present-day climate forcing and response from lack carbon in snow. *J. Geophys. Res.*, **112**, D11202, doi: 1 0.1029/2006JD008003.

Garrett, T. J., and C. Zhao, 2006: Increased Arctic cloud longwave emissivity associated with pollution from mid-latitudes. *Nature*, **440**, 787–789.

Grenfell, T. C., B. Light, and M. Sturm, 2002: Spatial distribution and radiative effects of soot in the snow and sea ice during the SHEBA experiment. *J. Geophys. Res.*, **107**(10), 8032, doi: 10.1029/2000JC000414.

Hansen, J., and L. Nazarenko, 2004: Soot climate forcing via snow and ice albedos. *Proc. Natl. Acad. Sci.*, **101**(2), 423–428.

Hansen, J., and Coauthors, 2007: Climate simulations for 1880–2003 with GISS modelE. *Climate Dyn.*, **29**,

661–696, doi: 10.1007/s00382-007-0255-8.

Harrison, E. F., P. Minnis, B. R. Barkstrom, V. Ramanathan, R. D. Cess, and G. G. Gibson, 1990: Seasonal variation of cloud radiative forcing derived from the earth radiation budget experiment. *J. Geophys. Res.*, **95**, 18687–18703.

IPCC, 2001: *Climate Change 2001: The Scientific Basis. Contribution of Working Group I to the Third Assessment Report of the Intergovernmental Panel on Climate Change*, Houghton et al., Eds., Cambridge University Press, Cambridge, 881pp.

IPCC, 2007: *Climate Change 2007: The Physical Science Basis. Contribution of Working Group I to the Fourth Assessment Report of the Intergovernmental Panel on Climate Change*, Solomon et al., Eds., Cambridge University Press, Cambridge, 131–217.

Jacobson, M. Z., 2004: Climate response of fossil fuel and biofuel soot, accounting for soot's feedback to snow and sea ice albedo and emissivity. *J. Geophys. Res.*, **109**, D21201, doi: 10.1029/2004JD004945.

Kistler, R., and Coauthors, 2001: The NCEP–NCAR 50–Year Reanalysis: Monthly means CD–ROM and documentation. *Bull. Amer. Meteor. Soc.*, **82**, 247–267.

Koch, D., S. Menon, A. D. Genio, R. Ruedy, I. Alienov, and G. A. Schmidt, 2009: Distinguishing aerosol impacts on climate over the past century. *J. Climate*, **22**, 2659–2677.

Light, B., H. Eicken, G. A. Maykut, and T. C. Grenfell, 1998: The effect of included particulates on the spectral albedo of sea ice. *J. Geophys. Res.*, **103**, 27739–27752.

Ming, J., H. Cachier, C. Xiao, D. Qin, S. Kang, S. Hou, and J. Xu, 2008: Black carbon record based on a shallow Himalayan ice core and its climatic implications. *Atmos. Chem. Phys.*, **8**, 1343–1352.

Ming, J., C. Xiao, H. Cachier, D. Qin, X. Qin, Z. Li, and J. Pu, 2009: Black Carbon (BC) in the snow of glaciers in west China and its potential effects on albedos. *Atmospheric Research*, **92**, 114–123.

Noone, K. J., and A. D. Clarke, 1988: Soot scavenging measurements in Arctic snowfall. *Atmos. Environ.*, **22**, 2773–2778.

Oleson, K. W., and Coauthors, 2004: Technical description of the community land model (CLM). Tech. Rep. NCAR/TN-461+STR, 174pp.

Rasch, P. J., N. W. Mahowald, and B. E. Eaton, 1997: Representations of transport, convection, and the hydrologic cycle in chemical transport models: Implications for the modeling of short lived and soluble species. *J. Geophys. Res.*, **102**, 28127–28138.

Rypdal, K., N. Rive, T. K. Berntsen, Z. Klimont, T. K. Mideksa, G. Myhre, and R. B. Skeie, 2009: Costs and global impacts of black carbon abatement strategies. *Tellus*, **61B**, 625–641.

Streets, D. G., and Coauthors, 2003: An inventory of gaseous and primary aerosol emissions in Asia in the year 2000. *J. Geophys. Res.*, **108**(D21), 8809, doi: 10.1029/2002JD003093.

Thompson, L. G., E. M. Thompson, M. E. Davis, P.-N. Lin, K. Henderson, and T. A. Mashiotta, 2003: Tropical glacier and ice core evidence of climate changes on annual to millenial time scales. *Climatic Change*, **59**, 137–155.

Wang, Z. L., H. Zhang, X. S. Shen, S. L. Gong, and X. Y. Zhang, 2010: A modeling study of aerosol indirect effects on global climate with an AGCM. *Adv. Atmos. Sci.*, **27**(5), 1064–1077, doi: 10.1007/s00376-010-9120-5.

Wang, Z. L., P. W. Guo, and H. Zhang, 2009: The numerical study of direct radiative forcing due to black carbon and its effects on the summer precipitation in China. *Climatic and Environmental Research*, **14**(2), 161–171. (in Chinese)

Warren, S., 1982: Optical properties of snow. *Rev. Geophys.*, **20**, 67–89.

Warren, S., and W. Wiscombe, 1980: A model for the spectral albedo of snow. II: Snow containing atmospheric aerosols. *J. Atmos. Sci.*, **37**, 2734–2745.

Wu, T., and G. Wu, 2004: An empirical formula to compute snow cover fraction in GCMs. *Adv. Atmos. Sci.*, **21**, 529–535.

Wu, T., and Coauthors, 2010: The Beijing Climate Center atmospheric general circulation model: Description and its performance for the present-day. *Climate Dyn.*, **34**, 123–147, doi: 10.1007/s00382-008-0487-2.

Xiao, C., and Coauthors, 2007: Observed changes of cryosphere in China over the second half of the $20^{th}$ century: An overview. *Annals of Glaciology*, **46**, 382–390.

Xu, B., T. Yao, X. Liu, and N. Wang, 2006: Elemental and organic carbon measurements with a two-step heating-gas chromatography system in snow samples from the Tibetan Plateau. *Annals of Glaciology*, **43**, 257–262.

Yan, H., 1987: Design of a nested fine-mesh model over the complex topograph, Part two: parameterization of the subgrid physical processes. *Plateau Meteorology*, **6**(Suppl.), 64–139. (in Chinese)

Zhang, G. J., and M. Mu, 2005: Effects of modifications to the Zhang-McFarlane convection parameterization on the simulation of the tropical precipitation in the National Center for Atmospheric Research Community Climate Model, version 3. *J. Geophys. Res.*, **110**, D09109, doi: 10.1029/2004JD005617.

Zhang, H., Z. L. Wang, P. W. Guo, and Z. Z. Wang, 2009: A modeling study of the effects of direct radiative forcing due to carbonaceous aerosol on the climate in East Asia. *Adv. Atmos. Sci.*, **26**(1), 57–66, doi: 10.1007/s00376-009-0057-5.

王遵娅. 2011. 中国冰冻日数的气候及变化特征分析 [J]. 大气科学，35 (3)：411－421. Wang Zunya. 2011. Climatic characters and changes of ice-freezing days in China [J]. Chinese Journal of Atmospheric Sciences (in Chinese)，35 (3)：411－421.

# 中国冰冻日数的气候及变化特征分析

王遵娅

国家气候中心，北京 100081

**摘 要** 利用 1954～2009 年中国台站雨凇和雾凇日数统计分析了中国冰冻日数的气候及变化特征。中国的冰冻主要出现在新疆、西北东部、内蒙古东部、东北、华北、淮河流域及江南一带，年均冰冻日数一般有 1～5 天，5 天以上的重冰区主要分布在新疆北部、陕西南部、东北中部、华北东部、秦岭、云南东北部、贵州等地。雨凇大都出现在我国南方地区，而雾凇主要出现在我国北方地区。冰冻主要发生在 11 月至次年 3 月，尤其是冬季。中国冰冻、雨凇和雾凇日数在 1954～2009 年间出现了显著减少的变化趋势，并在 1990 年代初突变减少，雾凇的减少趋势较雨凇明显。中国冰冻、雨凇和雾凇日数的减少与气温的显著上升及相对湿度和风速的显著减小关系密切。另外，冰冻（雨凇、雾凇）日数与亚洲极涡的面积和强度，乌拉尔山和贝加尔湖阻塞高压的强度及西太平洋副高的面积、强度和位置均具有显著的相关关系。1954－2009 年间，亚洲极涡面积显著减小且强度减弱，乌拉尔山和贝加尔湖阻塞高压显著增强，西太平洋副高面积缩小、强度减弱并明显西伸。这些变化可能引起了我国冰冻（雨凇、雾凇）日数的大幅减少。

**关键词** 冰冻 雨凇 雾凇 变化趋势 大气环流指数

**文章编号** 1006－9895 (2011) 03－0411－11 **中图分类号** P461 **文献标识码** A

# Climatic Characters and Changes of Ice-Freezing Days in China

WANG Zunya

*National Climate Center*, *China Meteorological Administration*, *Beijing* 100081

**Abstract** Climatic characters and changes of ice-freezing days in China are analyzed based on the daily rime and glaze observational dataset at 743 stations in China from 1954 to 2009. It is found that ice-freezing occurs mainly in Xinjiang, eastern Northwest China, eastern Inner Mongolia, Northeast China, North China, the Huaihe River valley and the region to the south of the Yangtze River, with the rime being almost in the southern part of China while the glaze in the northern part. Annual ice-freezing day generally ranges from 1 to 5 days and heavy ice-freezing regions scatter in northern Xinjiang, southern Shannxi, central Northeast China, eastern North China, Qinling mountain range, northeastern Yunnan, Guizhou, and so on. During 1954 to 2009, the ice-freezing days show a significant decreasing trend and an abrupt change point is observed in the early 1990s, with the decreasing amplitude of rime days greater than that of glaze days. This decrease in ice-freezing days has close relevance with the obvious increase in the temperature and decrease in the relative humidity and the wind speed. Additionally, the ice-freezing days are closely related to the extent and intensity of Asian polar vortex, the intensity of the Ural blocking high and the Baykal blocking high, as well as the extent, intensity and location of the western Pacific subtropical high. Further, during 1954－2009, the extent and the intensity of Asian polar vortex decreased, and the Ural and Baykal blocking

**收稿日期** 2010－06－25，2010－12－09 收修定稿



**资助项目** 国家自然科学基金资助项目 40905036，国家科技支撑计划 2007BAC29B06

**作者简介** 王遵娅，女，高级工程师，研究方向为气候学和短期气候变化。E-mail：wangzy@cma.gov.cn

highs intensified, the extent and the intensity of the western Pacific subtropical high decreased while the subtropical high shifted more westward. These changes in general circulation may cause the significant decrease in ice-freezing (glaze, rime) days in China.

**Key words** ice-freezing, glaze, rime, climatic character, changing trend

## 1 引言

2008年1月10日至2月2日我国大部尤其是南方地区遭受了历史罕见的低温雨雪冰冻灾害。持续而大范围的冰冻天气使贵州、湖南、广西、云南等省的输电线网受到沉重打击，对社会和人民生活造成了巨大损害（王遵娅等，2008；王凌等，2008），引起了各方学者的关注，对其产生原因进行了多方面的研究（陶诗言和卫捷，2008；丁一汇等，2008；李崇银等，2008；陶祖钰等，2008；张庆云等，2008；Wen et al.，2009；谭桂荣等，2010）。随着电力、通讯网络的快速发展，冰冻作为一种重要气象灾害对我国社会经济的影响越来越大，因而有必要对冰冻的气候及变化特征，其产生原因、机理和影响进行更为深入的研究，以便为防灾减灾提供依据和参考。

前人的一些研究表明，冰冻现象主要由雨凇、雾凇、湿雪冻结等天气状况造成（Makkonen，2000）。中国大部地区的冰冻天气以雨凇和雾凇为主，这在我国的云、贵、川、粤北等地区是较为常见的，尤其是在严冬和初春季节（谭冠日等，1985；王守礼，1993）。20世纪90年代初，张家诚（1991）对中国雨凇和雾凇的分布特征进行统计发现，中国年平均雨凇日数在南方较北方多，雾凇日数北方多于南方，雨凇和雾凇都是潮湿地区较干旱地区多，山区比平原多。湖南省冰区分布与山地走向一致，从20世纪70年代起冰冻天气的频次和强度都有减小趋势（李军等，2004）；贵州省冰冻日数从西向东、从中部向南北两侧递减，20世纪80年代开始冰冻日数逐年减少（杨利群，1999；张宇发，1999）；三峡地区是我国典型的雾凇覆冰区，海拔高度超过800 m的垭口及风口覆冰特别严重（蒋兴良等，1998）。最近，赵珊珊等（2010）的研究表明，我国大部地区冰冻天气发生频次减少而强度增强。

由于冰冻天气在中国的分布具有较强的区域性特征，因而针对冰冻天气的研究也多以局地分析为主，缺乏对中国冰冻天气分布及变化特征等的全面了解。针对这个问题，本文将对中国雨凇和雾凇的空间分布及不同时间尺度的变率进行较为全面和细致的分析。

## 2 资料和方法

本文主要利用中国743站雨凇和雾凇的天气现象资料，时间长度为1954～2009年。该资料由国家气象信息中心整编，进行了初步的质量控制，在计算之前，我们还对资料长度短于30年的站点进行了剔除，最终利用699个站点的资料进行本文的分析。分析中，若某站某日有雨凇或雾凇发生，则定义该日为一个冰冻日。

本文所用的分析方法包括线性趋势分析、小波分析、相关分析等。

## 3 气候特征

图1显示了中国年冰冻日数的气候平均值（1971～2000年平均，下同），从图中可以看到，四川东部、云南大部、广东南部、广西南部、海南等地为无冰区，经统计共有142站；年平均冰冻日数在1天以下的少冰区主要分布在内蒙古西部和东南部、青海大部、西藏东南部、广东北部、广西北部、长江三角洲等地，共181站；年冰冻日数在1天以上的站点分布在新疆、西北东部、内蒙古东部、东北、华北、淮河流域及江南一带，其中冰冻日数在1～5天的站点最多，有227站，5～10天，10～30天和30天以上的站点数分别有51、45和23站，主要分布在新疆北部、陕西南部、东北中部、华北东部、秦岭、云南东北部、贵州等地，大部分的重冰区，尤其是年冰冻日数在30天以上的站点都分布在海拔较高的山地区域。统计发现，全国有51.7%的站点平均每年会出现1天以上的冰冻，其中年均冰冻日数在5天以上的站点占全国总站数的17.7%；而48.3%的站点无冰或少冰。

为了进一步了解雨凇和雾凇各自的分布特点，我们对中国各站的年均雨凇和雾凇日数进行了分析。如图2所示，中国大部地区都没有或基本没有

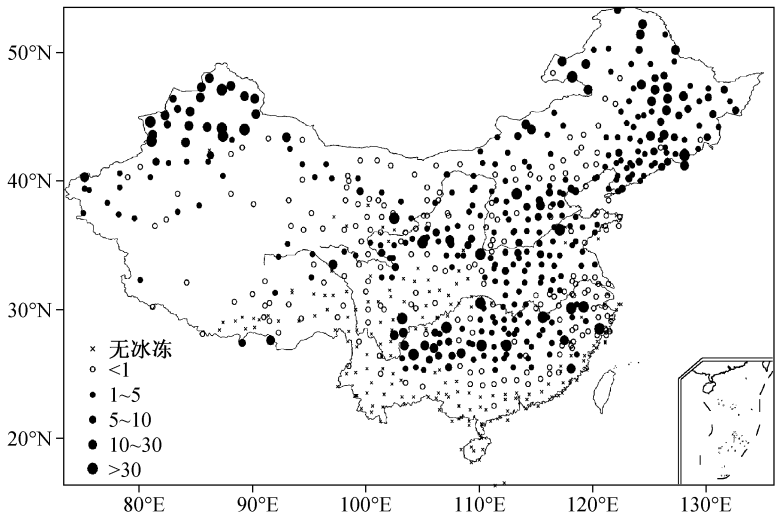


图 1　中国年冰冻日数（单位：d）

Fig. 1　Distribution of annual ice-freezing days at each station of China (units: d)

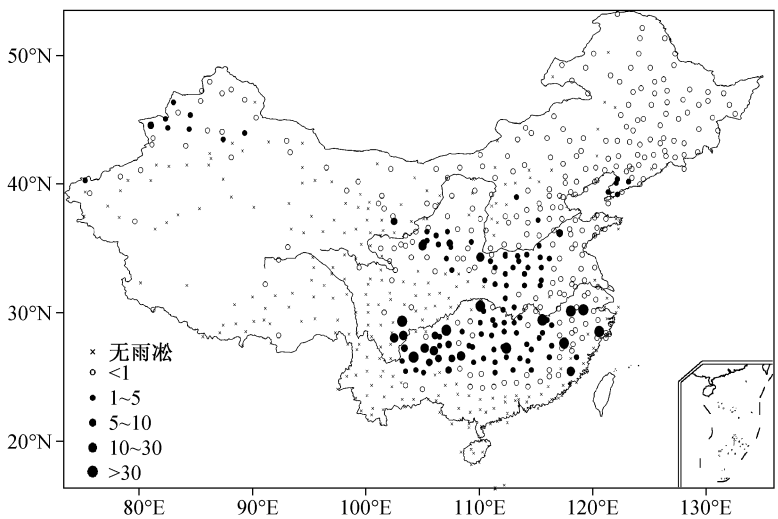


图 2　中国年雨凇日数（单位：d）

Fig. 2　Distribution of annual glaze days at each station of China (units: d)

雨凇发生，其中无雨凇站点 272 个，年均雨凇日数在 1 天以下的站点 279 个；而年均雨凇日数在 1 天以上的站点 118 个，仅占全国总站数的 17.6%，主要分布在我国南方地区，尤其是长江以南一带，包括云南、贵州、江西、湖南、浙江、福建等省。而我国北方地区偶发雨凇，仅在新疆西北部和辽宁南部部分站点的年均雨凇日数在 1 天以上。另外，秦岭山区、湖北、河南等地的年均雨凇日数也有 1～5 天。值得注意的是，中国年均雨凇日数在 5 天以上的站点仅 30 站，集中分布在云南东北部和贵州等地。

对雾凇而言，在进行统计的 669 站中，有 269 个站点的年均雾凇日数在 1 天以上，占 40.2%，主要分布在长江以北地区，包括新疆、东北、华北东部、淮河流域、秦岭山区等地（图 3），且雾凇日数在 5 天以上的站点共 99 站，占统计总站数的 14.8%，集中在新疆北部、东北中部、华北东部、秦岭山区一带，而长江以南地区仅个别站点出现雾凇，年均雾凇日数均在 30 天以上，其余大部分站点没有雾凇发生或年均雾凇日数在 1 天以下。

图 4 显示了中国各站海拔高度与冰冻日数的关系，可以清楚地看到，冰冻日数在 20 天以上的站

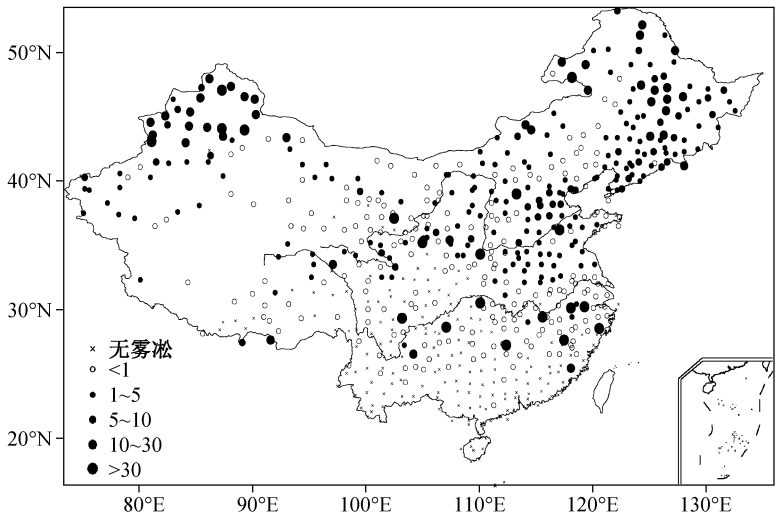


图 3 中国年雾凇日数（单位：d）

Fig. 3 Distribution of annual rime days at each station of China (units: d)

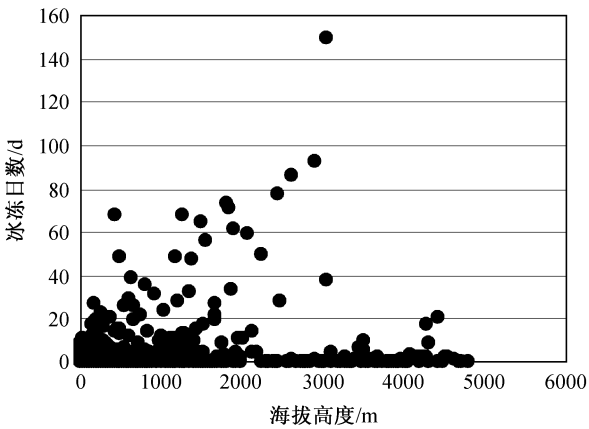


图 4 中国各站海拔高度与冰冻日数的分布

Fig. 4 Distribution of altitude and ice-freezing days at each station of China

点其冰冻日数与海拔高度呈明显的线性关系，即海拔高度越高则冰冻日数越多。实际上，高山是冰冻的频发地区，如四川峨眉山的年均冰冻日数达 150 天左右，山西五台山在 90 天左右，浙江天目山在 60 天以上等。但我们也能注意到，很多 2000 m 以上站点的冰冻日数并不多，甚至有的站点并不出现冰冻天气。这是由于很多站点虽然地处高原或山地，但由于空气湿度、气温、所在地点的坡度坡向等条件不适合雨凇或雾凇的生成，这样的站点就会少发生甚至不发生冰冻。对雨凇和雾凇分别进行同样的分析也能得到相似的结果。

从冰冻日数在各月的分布情况看（图 5），冰冻主要发生在 11 月至次年 3 月，尤其是 12 月至次年 2 年的隆冬季节，其中以 1 月最多，2 月和 12 月次之，3 月和 11 月也较多，7 月和 8 月没有冰冻发生。另外可以注意到，雾凇日数总体而言多于雨凇日数，雾凇在 12 月和 1 月最为频发，而雨凇在 1 月和 2 月最多。

## 4 变化特征及周期分析

图 6a 显示了 1954～2009 年中国平均冰冻、雨凇和雾凇日数的逐年演变。统计发现，三者的全国平均日数分别为 4.9 天、1.1 天和 3.9 天。从图 6a 可以非常清楚地看到，三者都在这几十年间出现了明显减少，其中冰冻日数的减少趋势最为显著，线性变化趋势系数为－0.9 d/10a。雾凇日数的减少较雨凇明显，其线性变化趋势系数分别为－0.78 d/10a 和－0.17 d/10a。并且，冰冻、雨凇、雾凇日数都在 20 世纪 90 年代初出现突变（显著减少），由之前的以正距平为主变为之后以负距平为主。为了确定突变点，我们对中国年冰冻日数序列进行了 Mann-Kendall 检验（简称 MK 检验）。这是一种非参数突变检验方法，最初由 Mann (1945) 发展用于检测序列的变化趋势，后 Goossens and Berger (1986) 将其发展成一种能检测气候突变的新方法。从图 6b 可以看到，中国的冰冻日数自 1957 年左右开始减少，至 1968 年左右统计曲线超过 95%的信度检验线，表明从此时起冰冻日数显著减少。并且，两条统计曲线在 1990 年相交，按照符淙斌和王强 (1992) 的补充说明，虽然交点在信度区间之

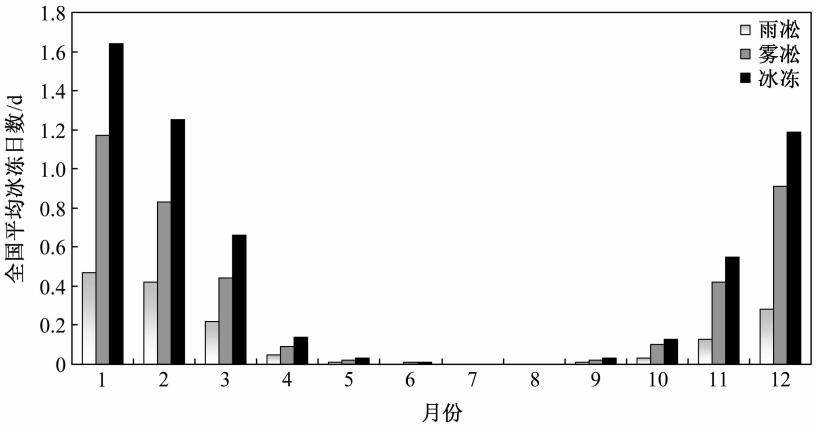


图 5　中国月平均冰冻日数（单位：d）

Fig. 5　Monthly ice-freezing days averaged over China (units: d)

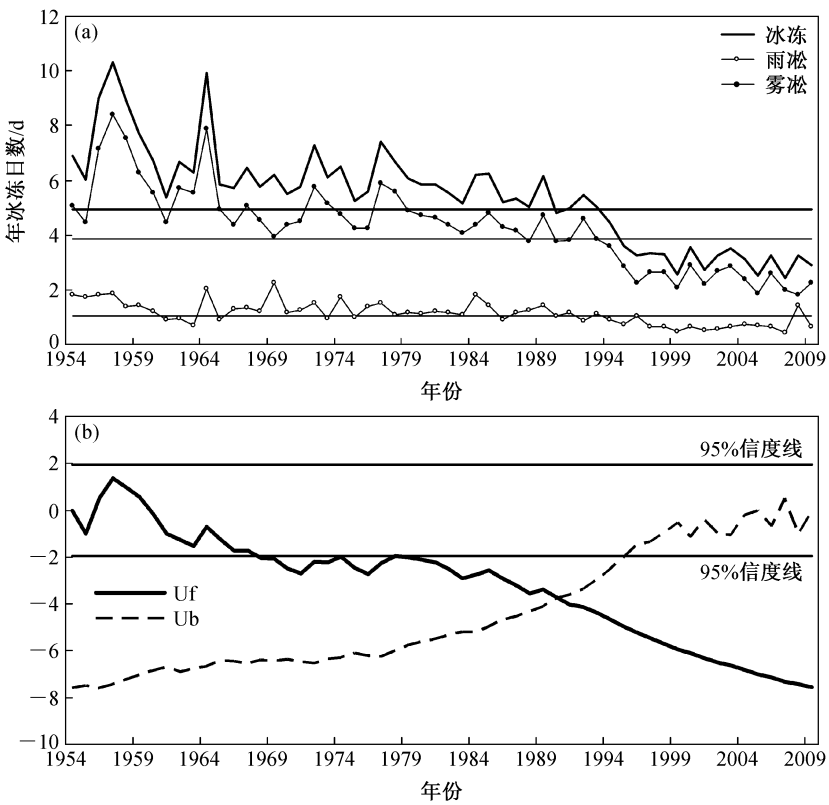


图 6　1954～2009 年中国年冰冻、雨凇、雾凇日数序列(a)和中国年冰冻日数的 MK 检验(b)

Fig. 6　(a) Time series of annual ice-freezing days, glaze days, and rime days averaged over China from 1954 to 2009 and (b) the Mann-Kendall test of annual ice-freezing days

外，但根据冰冻日数序列判断，这是一真实突变点。为了进一步验证该突变点的可靠性，我们还利用滑动 $t$ 检验和 Yamamoto 方法对序列进行了分析，两种方法检测到的突变点均在 1994 年。综上，1990 年代初中国年均冰冻日数发生了突变减少。分别对中国年雾凇和雨凇日数序列进行突变点检验发现，其变化特征与冰冻日数相似，并且也是在 1990 年代初出现突变减少。

从图 6a 还可以注意到，2008 年的雨凇日数较常年偏多，并且是自 1994 年以来唯一出现的正距

平值，而雾凇日数没有表现出偏多的情况，这表明2008年给我国造成大范围灾害和损失的冰冻灾害主要是由雨凇造成。2008年初，在强拉尼娜事件背景下，欧亚中高纬地区的大尺度环流异常稳定使冷空气不断自西北向东南输送，同时孟加拉湾和南海的暖湿空气不断北上，冷暖气流在中国南方地区频繁交汇，使对流层中低层形成逆温层和局地经向环流产生异常，从而在长江及其以南出现了大范围且长时间的雨凇天气（丁一汇等，2008；张庆云等，2008；杨贵名等，2008）。这在近些年是很罕见的。很有意思的是，无论是2008年的雨凇日数还是冰冻日数，在历史上都不算特别多，但造成的损失之大，灾害之重是历史罕见的，这虽然与冰冻在南方的长时间持续有关，但也在很大程度上体现了社会经济高速发展下电力通讯设施在自然灾害面前的脆弱性。另外，我们简要分析了中国平均冰冻、雾凇、雨凇日数与气温的相关关系（表1），可以看到冰冻、雾凇、雨凇日数与日平均气温、日最高气温和日最低气温均成显著的负相关关系，相关系数大都在－0.7以上，通过了99%的信度检验，这表明近几十年来中国冰冻日数的减少与气温的显著升高有密切关系。另外，中国冰冻、雨凇和雾凇日数与相对湿度和平均风速均呈显著的正相关关系，通过了99%的信度检验。1954～2009年，无论是中国平均相对湿度还是平均风速都出现了显著的下降趋势，这也与中国冰冻、雨凇和雾凇日数的减少有一定关系。

**表1 中国平均冰冻、雾凇、雨凇日数与气温、相对湿度和平均风速的相关系数**

**Table 1 Correlation coefficients between annual ice-freezing days, rime days, and glaze days in China with daily temperature, daily maximum temperature, daily minimum temperature, daily relative humidity, and daily wind speed**

| | 日平均气温 | 日最高气温 | 日最低气温 | 相对湿度 | 平均风速 |
|---|---|---|---|---|---|
| 冰冻日数 | －0.79 | －0.73 | －0.78 | 0.60 | 0.70 |
| 雾凇日数 | －0.74 | －0.65 | －0.74 | 0.58 | 0.67 |
| 雨凇日数 | －0.77 | －0.80 | －0.70 | 0.50 | 0.62 |

上面的分析显示中国平均冰冻、雨凇和雾凇日数在近几十年出现了显著减少，下面我们将进一步讨论各站的变化情况。考虑到一些站点无冰或少冰，因而在讨论各站冰冻日数的变化趋势时仅对年均冰冻、雨凇和雾凇日数大于1天的站点进行分析。从图7a可以看到，大部分站点的冰冻日数在1954～2009年都出现了显著的减少趋势，尤其是在新疆北部和东北中部一带，线性变化趋势系数小于－5 d/10a，而大部分站点的线性变化趋势系数在0到－2.5 d/10a之间。雨凇日数的减少趋势大都在0到－1 d/10a之间，云南东北部和贵州北部小于－1 d/10a（图7b）。大部站点的雾凇日数也在1954～2009年间也呈现出显著的减少趋势，线性变化趋势系数一般在0到－2.5 d/10a之间，趋势系数小于－2.5 d/10a的站点主要分布在新疆北部、内蒙古东北部和东北西部等地，这与冰冻日数的情况相似（图7c）。

除长期变化趋势外，我国的冰冻日数还存在明显的年际和年代际变化周期。图8显示了对冰冻日数进行小波分析的结果，可以看到，20世纪70年代中期以前中国的冰冻日数具有显著的2～4年和4～8年周期。对雨凇日数进行小波分析的结果表明，其具有显著的2～4年和准20年周期，而雾凇日数的2～4年和4～8年周期也通过了显著性检验（图略）。

## 5 冰冻日数与大尺度环流指数的关系

为了了解影响中国冰冻日数的大尺度环流因子，我们对冰冻日数与一些主要大尺度环流指数的相关关系进行了分析。前文已指出中国冰冻主要发生在冬春季节，而以往的研究发现北极涛动（AO）（龚道溢和王绍武，2003）、冬季风（施能，1996）及欧亚—太平洋遥相关（EUP）（Wallace and Gutzler，1981）对东亚冬季气候有非常重要的影响，本文则首先计算了这3个指数与中国冰冻日数的相关关系。年冰冻日数与年AO指数，冬季风指数和冬季EUP指数的相关系数分别为－0.21，－0.11和0.14，均没有通过信度检验，表明这3项指数与中国冰冻日数的相关关系不明显。

极涡和阻塞高压是与东亚气候关系密切的中高纬环流系统，为了讨论其与中国冰冻日数的关系，我们计算了亚洲极涡强度和面积指数（王遵娅和丁一汇，2009）及乌拉尔、鄂霍次克和贝加尔阻塞高压指数与中国冰冻、雨凇和雾凇日数的相关系数。乌拉尔（40°N～50°N，40°E～70°E）、鄂霍次克（50°N～60°N，120°E～150°E）和贝加尔（50°N～60°N，80°E～110°E）阻塞高压指数分别为500 hPa

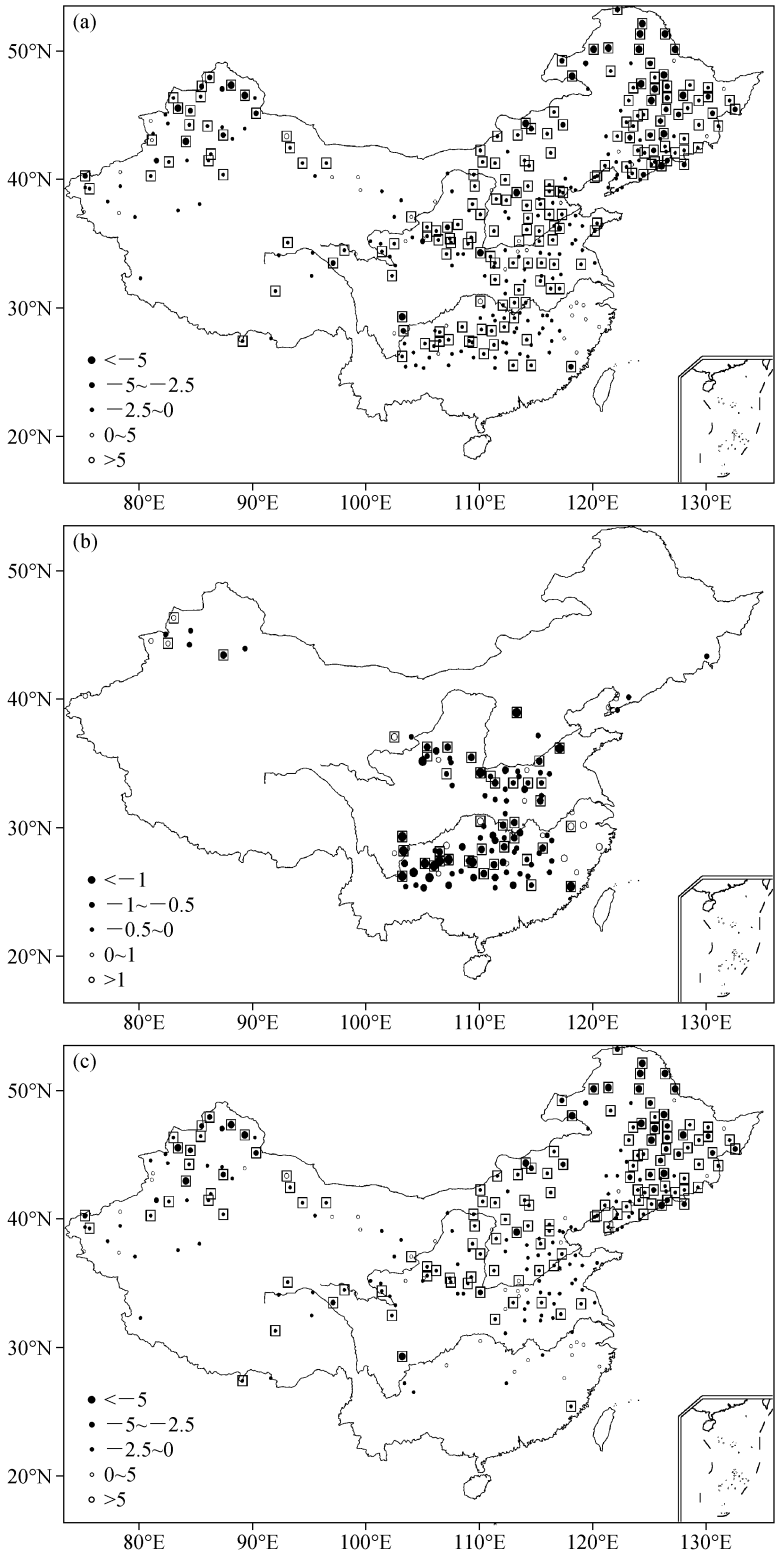


图 7　1954～2009 年中国各站冰冻 (a)、雨凇 (b) 和雾凇 (c) 日数线性变化趋势系数分布 (单位：d/10a)。方框表示通过了 95%的显著性检验

Fig. 7　Linear trend coefficients of (a) ice-freezing days, (b) rime days, and (c) glaze days at the stations of China from 1954 to 2009 (units: d/10a). The square frames denote exceeding the 95% confidence level

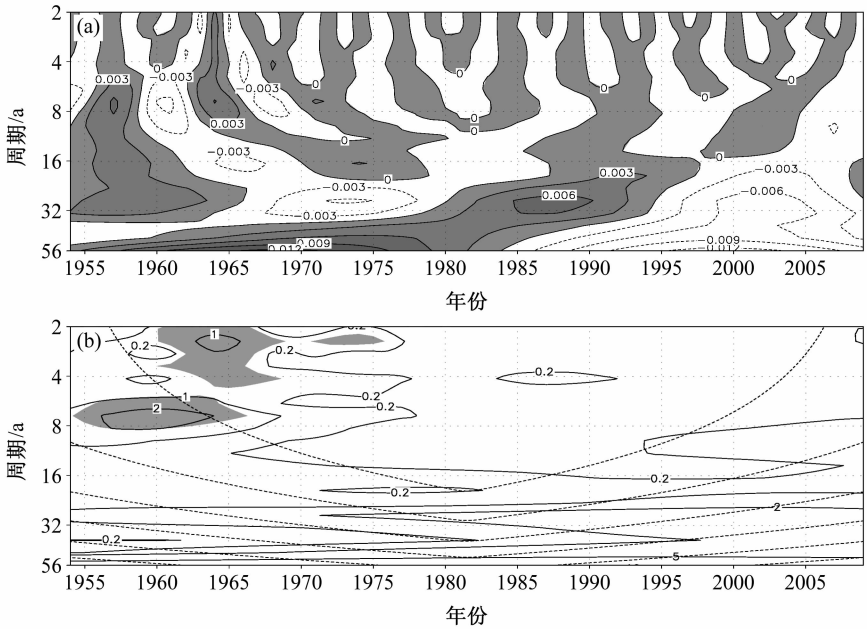


图 8 中国冰冻日数序列的小波实部（a，阴影为正值区）和显著性检验（b，阴影表示通过了 90%的显著性检验）

Fig. 8 (a) Real part (the shaded area denotes positive values) and (a) significance test (the shaded area denotes exceeding the 90% confidence level) of time series of ice-freezing days in China

相应区域平均的高度标准化值（赵振国，1999）。如表 2 所示，冰冻、雨凇和雾凇日数与亚洲极涡的面积和强度指数呈显著的正相关关系，即亚洲极涡面积偏大，强度偏强则我国冰冻、雨凇和雾凇日数多，并与欧亚中高纬地区的阻塞高压呈负相关关系，其中与乌拉尔和贝加尔阻塞高压的负相关系数通过了 95%的显著性检验，但与鄂霍次克海阻塞高压的相关关系不显著。进一步的分析表明，1954～2009 年间亚洲极涡面积和强度指数都出现了显著的减弱，而乌拉尔和贝加尔阻塞高压显著增强，这可能引起了冰冻、雨凇和雾凇日数在近几十年的显著减少。

**表 2 极涡指数和阻塞高压指数与中国冰冻、雨凇、雾凇日数的相关系数**

**Table 2 Correlation coefficients between annual indices of polar vortex and blocking highs with annual ice-freezing, rime, and glaze days in China**

| | 亚洲极涡 | | 阻塞高压 | | |
|---|---|---|---|---|---|
| | 面积指数 | 强度指数 | 乌拉尔 | 鄂霍次克 | 贝加尔 |
| 冰冻日数 | 0.62* | 0.36* | −0.60* | −0.24 | −0.49* |
| 雨凇日数 | 0.58* | 0.19 | −0.33* | −0.22 | −0.49* |
| 雾凇日数 | 0.58* | 0.37* | −0.62* | −0.22 | −0.46* |

注：* 表示通过了 95%的信度检验。

西太平洋副热带高压作为影响东亚气候的重要中低纬环流系统，可能也与我国冰冻日数的多寡有一定关系，因而分析了西太平洋指数与冰冻日数的相关关系。根据赵振国（1999）的定义，西太平洋副热带高压的面积指数为 5°×10°网格的 500 hPa 平均环流图上 10°N 以北，110°E～180°范围内 588 dagpm 等值线包括的网格点数；强度指数为 588 dagpm 等值线内各格点的平均高度值编码（588 编码为 1，589 编码为 2，590 编码为 3，以此类推）之和；脊线指数为 110°E～150°E 范围内副高脊线与每隔 5°的 9 条经线焦点的平均纬度值；北界指数为副高北侧 588 dagpm 等值线（东西 2 个脊点间）与每隔 5°的 9 条经线交点的纬度平均值；西伸脊点指数为 90°E ～180°范围内 588 dagpm 等值线最西位置所在的经度。表 3 显示了 1954～2009 年西太平洋副高各项指数与中国年冰冻、雨凇、雾凇日数的相关关系。可以看到，西太平洋副高面积和强度指数与冰冻、雨凇、雾凇日数均具有很显著的负相关关系，表明冬季副高面积偏小，强度偏弱有利于我国冰冻日数偏多。并且，副高西伸脊点指数与冰冻、雨凇、雾凇日数呈显著的正相关关系，表明副高偏西有利于我国雨凇、雾凇等冰冻天气。但西太平洋副高脊线和北界指数与我国冰冻日数的关系不

密切。分析还发现，1954～2009 年西太平洋副高面积和强度指数均表现出非常显著的下降趋势，而西伸脊点指数显示出显著的上升趋势，这种变化与我国冰冻（雨凇、雾凇）日数的明显减少关系密切。

**表 3　西太平洋副热带高压指数与中国冰冻、雨凇、雾凇日数的相关系数**

**Table 3　Correlation coefficients between annual indices of the western Pacific subtropical high and annual ice-freezing, rime, and glaze days in China**

| | 面积指数 | 强度指数 | 脊线指数 | 北界指数 | 西伸脊点指数 |
|---|---|---|---|---|---|
| 冰冻日数 | −0.51* | −0.46* | −0.08 | −0.06 | 0.35* |
| 雨凇日数 | −0.48* | −0.44* | −0.12 | −0.19 | 0.40* |
| 雾凇日数 | −0.49* | −0.43* | −0.06 | −0.02 | 0.31* |

注：* 表示通过了 95%的信度检验。

## 6　主要结论

通过对中国近几十年来冰冻的气候及变化特征的分析可以看到：

（1）中国的冰冻主要出现在新疆、西北东部、内蒙古东部、东北、华北、淮河流域及江南一带，年均冰冻日数一般有 1～5 天，5 天以上的重冰区主要分布在新疆北部、陕西南部、东北中部、华北东部、秦岭、云南东北部、贵州等地，30 天以上的站点大都位于海拔较高的山地区域；其余地区无冰或少冰，站点占全国统计站点的 48.3%。

（2）中国冰冻的空间分布具有区域性强的特征，雨凇大都出现在我国南方地区，尤其是长江以南的云南、贵州、江西、湖南、浙江、福建等地，而雾凇主要出现我国北方地区，以新疆北部、东北中部、华北东部、秦岭山区一带最多。冰冻主要发生在 11 月至次年 3 月，尤其是冬季。雾凇在 12 月和 1 月最为频发而雨凇在 1 月和 2 月最多。

（3）中国冰冻日数具有显著的 2～4 年和 4～8 年周期，雾凇也是如此，而雨凇具有显著的 2～4 年周期。中国冰冻、雨凇和雾凇日数在 1954～2009 年间出现了显著减少的变化趋势，并在 1990 年左右突变减少，雾凇的减少趋势较雨凇明显。雾凇减少趋势最明显的地区在新疆北部和东北中部一带，雨凇在云南东北部和贵州北部。

（4）中国冰冻日数的减少与气温的显著上升及相对湿度和风速的明显减小关系密切。并且，冰冻日数与亚洲极涡的面积和强度，乌拉尔和贝加尔阻塞高压的强度及西太平洋副高的面积、强度和位置均具有显著的相关关系。1954～2009 年间，亚洲极涡面积减小，强度减弱；乌拉尔和贝加尔阻塞高压明显增强；西太平洋副高面积减小，强度减弱，且西伸脊点显著偏西，这些变化可能引起了我国冰冻（雨凇、雾凇）日数的大幅减少。

## 参考文献（References）

丁一汇，王遵娅，宋亚芳. 2008. 中国南方 2008 年 1 月罕见低温雨雪冰冻灾害发生的原因及其与气候变暖的关系［J］. 气象学报，66（5）：808－825.　Ding Y H，Wang Z Y，Song Y F. 2008. Causes of the unprecedented freezing disaster in January 2008 and its possible association with the global warming［J］. Acta Meteorologica Sinica（in Chinese），66（5）：808－825.

符淙斌，王强. 1992. 气候突变的定义和检测方法［J］. 大气科学，16（4）：482－493.　Fu C B，Wang Q. 1992. The definition and detection of the abrupt climatic change［J］. Chinese Journal of Atmospheric Sciences（Scientia Atmospherica Sinica）（in Chinese），16（4）：482－493.

龚道溢，王绍武. 2003. 近百年北极涛动对中国冬季气候的影响［J］. 地理学报，58（4）：559－568.　Gong D Y，Wang S W. 2003. Influence of Arctic oscillation on winter climate over China［J］. Acta Geographica Sinica（in Chinese），58（4）：559－568.

Goossens C H，Berger A. 1986. Annual and seasonal climatic variations over the Northern Hemisphere and Europe during the last centrury［J］. Ann. Geophys.，4：385－400.

李崇银，杨辉，顾薇. 2008. 中国南方雨雪冰冻异常天气原因的分析［J］. 气候与环境研究，13（2）：113－122.　Li C Y，Yang H，Gu W. 2008. Cause of severe weather with cold air，freezing rain and snow over South China in January 2008［J］. Climatic and Environmental Research（in Chinese），13（2）：113－122.

李军，禹伟，许源，等. 2004. 基于湖南省冰冻分布及气候特征的思考［J］. 湖南电力，24（2）：16－19.　Li J，Yu W，Xu Y，et al. 2004. Analysis of frost distribution and its characteristics in Hunan［J］. Hunan Electric Power（in Chinese），24（2）：16－19.

蒋兴良，孙才新，顾乐观，等. 1998. 三峡地区导线覆冰的特性及雾凇覆冰模型［J］. 重庆大学学报（自然科学版），21（2）：16－19.　Jiang X L，Sun C X，Gu L G，et al. 1998. Power lines icing characteristics of the Three Gor-

ges District and a model of the accumulation of ice on electric on electric power lines [J]. Journal of Chongqing University (Natural Science Edition) (in Chinese), 21 (2): 16 - 19.

Makkonen L. 2000. Models for the growth of rime, glaze, icicles and wet snow on structure [J]. Phil. Trans. R. Soc. Lond. A, 358: 2913 - 2939.

Mann H B. 1945. Non-parametric tests against trend [J]. Econometrika, 13: 245 - 259.

施能. 1996. 近 40 年东亚冬季风强度的多时间尺度变化特征及其与气候的关系 [J]. 应用气象学报, 7 (2): 175 - 182. Shi N. 1996. Features of the East Asian winter monsoon intensity on multiple time scale in recent 40 years and their relation to climate [J]. Quarterly Journal of Applied Meteorology (in Chinese), 7 (2): 175 - 182.

谭冠日, 严济远, 朱瑞兆. 1985. 应用气候 [M]. 上海: 上海科学技术出版社, 3 - 56. Tan G R, Yan J Y, Zhu R Z. 1985. Applied Climatology (in Chinese) [M]. Shanghai: Shanghai Science and Technology Press, 3 - 56.

谭桂容, 陈海山, 孙照渤, 等. 2010. 2008 年 1 月中国低温与北大西洋涛动和平流层异常活动的联系 [J]. 大气科学, 34 (1): 175 - 183. Tan G R, Chen H S, Sun Z B, et al. 2010. Linkage of the cold event in January 2008 over China to the North Atlantic Oscillation and stratospheric circulation anomalies [J]. Chinese Journal of Atmospheric Sciences (in Chinese), 34 (1): 175 - 183.

陶诗言, 卫捷. 2008. 2008 年 1 月我国南方严重冰雪灾害过程分析 [J]. 气候与环境研究, 13 (4): 337 - 350. Tao S Y, Wei J. 2008. Severe snow and freezing-rain in January 2008 in the southern China [J]. Climatic and Environmental Research (in Chinese), 13 (4): 337 - 350.

陶祖钰, 郑永光, 张小玲. 2008. 2008 年初冰雪灾害和华南准静止锋 [J]. 气象学报, 66 (5): 850 - 854. Tao Z Y, Zheng Y G, Zhang X L. 2008. Southern China quasi-stationary front during ice-snow disaster of January 2008 [J]. Acta Meteorologica Sinica (in Chinese), 66 (5): 850 - 854.

Wallace J M, Gutzler D S. 1981. Teleconnection in the geopotential height field in the Northern Hemisphere [J]. Mon. Wea. Rev., 109: 784 - 812.

王凌, 高歌, 张强, 等. 2008. 2008 年 1 月我国大范围低温雨雪冰冻灾害分析 I. 气候特征与影响评估 [J]. 气象, 34: 95 - 100. Wang L, Gao G, Zhang Q, et al. 2008. Analysis of the severe cold surge, ice-snow and frozen disasters in South China during January 2008: I. Climatic features and its impact [J]. Meteorological Monthly (in Chinese), 34: 95 - 100.

王守礼. 1993. 云南高海拔地区电线覆冰问题研究 [M]. 昆明: 云南科技出版社, 7 - 44. Wang S L. 1993. Study of the Wire Ice Coating in the High Altitude Regions of Yunnan Province (in Chinese) [M]. Kunming: Yunnan Science and Technology Press, 7 - 44.

王遵娅, 张强, 陈峪, 等. 2008. 2008 年初我国低温雨雪冰冻灾害的气候特征 [J]. 气候变化研究进展, 4: 63 - 67. Wang Z Y, Zhang Q, Chen Y, et al. 2008. Characters of meteorological disasters caused by the extreme synoptic process in early 2008 over China [J]. Advances in Climate Research (in Chinese), 4: 63 - 67.

王遵娅, 丁一汇. 2009. 夏季亚洲极涡的长期变化对东亚环流和水汽收支的影响 [J]. 地球物理学报, 52 (1): 20 - 29. Wang Z Y, Ding Y H. 2009. Impacts of the long-term change of the summer Asian polar vortex on the circulation system and the water vapor transport in East Asia [J]. Chinese. J. Geophys. (in Chinese), 52 (1): 20 - 29.

Wen M, Yang S, Kumar A, et al. 2009. An analysis of the large-scale climate anomalies associated with the snowstorms affecting China in January 2008 [J]. Mon. Wea. Rev., 137: 1111 - 1131, doi: 10.1175/2008MWR2638.1.

杨利群. 1999. 贵州暴雨洪涝、秋绵雨和凝冻的气候特征及灾情分析 [J]. 贵州气象, 23 (4): 3 - 8. Yang L Q. 1999. Climatic characters and situation analysis of rainstorm and flood, autumn persistent rainfalls and rime in Guizhou [J]. Journal of Guizhou Meteorology (in Chinese), 23 (4): 3 - 8.

杨贵名, 孔期, 毛冬艳, 等. 2008. 2008 年初"低温雨雪冰冻"灾害天气的持续性原因分析 [J]. 气象学报, 66 (5): 836 - 849. Yang G M, Kong Q, Mao D Y, et al. 2008. Analysis of the long-lasting cryogenic freezing rain and snow weather in the beginning of 2008 [J]. Acta Meteorologica Sinica (in Chinese), 66 (5): 836 - 849.

张家诚. 1991. 中国气候总论 [M]. 北京: 气象出版社, 199 - 201. Zhang J C. 1991. Pandect of Climate in China (in Chinese) [M]. Beijing: China Meteorological Press, 199 - 201.

张庆云, 宣守丽, 彭京备. 2008. La Niña 年冬季亚洲中高纬环流与我国南方降雪异常关系 [J]. 气候与环境研究, 13 (4): 385 - 394. Zhang Q Y, Xuan S L, Peng J B. 2008. Relationship between Asian circulation in the middle-high latitude and snowfall over South China during La Niña events [J]. Climatic and Environmental Research (in Chinese), 13 (4): 385 - 394.

张宇发. 1999. 贵州气候灾害近 50 年变化趋势 [J]. 成都气

象学院学报，14 (1)：88－92. Zhang Y F. 1999. Variation trend of climatic calamities in the past 50 years in Guizhou [J]. Journal of Chengdu Institute of Meteorology (in Chinese)，14 (1)：88－92.

赵珊珊，高歌，张强，等. 2010. 中国冰冻天气的气候特征 [J]. 气象，36 (3)：34－38. Zhao S S，Gao G，Zhang Q，et al. 2010. Climatic characteristics of freezing weather in China [J]. Meteorological Monthly (in Chinese)，36 (3)：34－38.

赵振国. 1999. 中国夏季旱涝及环境场 [M]. 北京：气象出版社，45 － 50. Zhao Z G.. 1999. Study on Summer Flood and Drought in China and the Relating Circulation Factors (in Chinese) [M]. Beijing：China Meteorological Press，45－50.

王遵娅,曾红玲,高歌,等. 2010年中国气候概况[J]. 气象,2011,37(4):439-445.

# 2010年中国气候概况*

王遵娅 曾红玲 高 歌 陈 峪 司 东 刘 波
国家气候中心,北京 100081

**提 要**:2010年,中国年平均气温较常年偏高0.7 ℃,是1961年以来第10个最暖年,夏季气温达1961年以来历史同期最高。年降水量681 mm,比常年偏多11.1%,为1961年以来第2多。年内,极端天气气候事件频发:西南地区发生历史罕见秋冬春特大干旱。东北、华北发生近40年罕见冬春持续低温,新疆北部出现有气象记录以来最为严重的雪灾。5—7月华南、江南遭受14次暴雨袭击,7月中旬至9月上旬北方和西部地区遭受10次暴雨袭击,10月海南出现历史罕见持续性强降水过程,甘肃舟曲等地因局地强降水引发严重山洪、泥石流、滑坡等地质灾害。夏季高温频繁,强度强,范围大,初夏东北多地最高气温突破历史极值。热带气旋登陆比例高,影响区域集中,台风灿都、凡亚比造成损失较重。重庆出现近20余年来最严重风雹灾害,人员伤亡大。春季,强沙尘暴影响范围广,横扫21省(区、市)。2010年,中国气象灾害属于21世纪以来最为严重的年份,直接经济损失和死亡人数均为近10年来最多。

**关键词**:降水,气温,极端天气气候事件

## Climatic Characters in 2010' China

WANG Zunya ZENG Hongling GAO Ge CHEN Yu SI Dong LIU Bo
National Climate Center, Beijing 100081

**Abstract**: In 2010, the annual mean temperature was 0.7 ℃ higher than normal, which ranked the 10th warmest year since 1961. And it was the warmest summer mean temperature since 1961. Annual precipitation in China was 681 mm, 11.1% more than normal, which ranked the second most since 1961. During this year, extreme weather and climate events happened frequently. Southwest China experienced the rare severe autumn—winter—spring drought. In winter and spring, unusual persistent low temperature hit Northeast and North China. The most serious snowstorm attacked northern Xinjiang, which broke the historical record. From May to July, heavy rainstorm attacked southern China 14 times. From mid July to early September, severe rainstorm and induced flood attacked northern and western China 10 times. In early and mid October, seldom consecutive heavy rainstorm appeared in Hainan Province. Serious geological hazards such as mountain torrents, mud-rock flow and mudslide happened in Zhugqu of Gansu Province and other sporadic places. In summer, frequent hot waves happened widely and intensely. In early summer, the weather in Northeast China was very hot and the maximum temperature in many areas broke historical records. The number of tropical cyclones was below normal, while the proportion of landing was high. The affected regions concentrated in South China. Typhoons Chanthu and Fanapi brought serious losses. The worst strong wind and hail hazards in recent 20 years occurred in Chongqing and caused heavy casualties. In spring, the strong dust storm affected 21 provinces. In general, in 2010, the losses caused by meteorological hazards were the most since 2000. The direct economic losses and mortalities or the missing caused by meteorological hazards were the most in recent 10 years.

**Key words**: precipitation, mean temperature, extreme weather and climate events

* 国家自然科学基金(40905036)与科技部科技支撑项目(2007BAC29B06)共同资助
2011年2月10日收稿; 2011年3月21日收修定稿
第一作者:王遵娅,主要从事气候学和短期气候变化研究工作. Email: wangzy@cma.gov.cn



© 1994-2011 China Academic Journal Electronic Publishing House. All rights reserved. http://www.cnki.net

# 引 言

中国是世界上气象灾害最严重的国家之一，每年各种灾害性天气气候事件给社会、经济和生态环境都造成了很大影响和损失。尤其是在全球气候变暖的背景下，一些极端天气气候事件可能出现增强增多的变化趋势[1]。为了更好的防灾减灾，首先就要对我国气候及其异常特点进行监测，对各类灾害性天气气候事件进行总结和灾情分析，一方面为今后的防灾减灾措施提供参考，另一方面为全面评估中国的气候变化特征提供素材。

以往的一些综述和研究对前期中国的气候特征进行了阐述[2-7]，而本文着重对刚刚过去的2010年中国气温和降水的时空特征，以及年内发生的一些重大灾害性天气气候事件特征及影响进行综述[8-9]。

本文的结果主要使用中国607个站点的逐日平均气温、日最高气温、日最低气温和日降水量资料分析得到，资料由国家气象信息中心提供。气候平均值(即：常年值)采用1971—2000年平均值。

# 1 2010年中国气候概况

## 1.1 气温

2010年，中国年平均气温9.5 ℃，较常年偏高0.7 ℃，为1961年以来第10高值，也是1997年以来连续第14个偏高年份(图1)。1961—2010年，中国年平均气温表现出了显著升高趋势，线性变化趋势系数为0.3 ℃/10年，通过了0.05的显著性水平检验。尤其是20世纪80年代末以后，大多数年份的平均气温都较气候平均值偏高。从空间分布上看(图2)，除东北及河北东北部、新疆北部偏低外，全

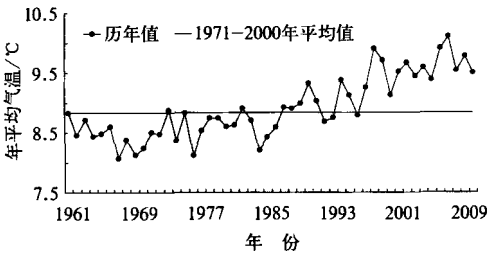


图1 1961—2010年中国年平均气温序列(单位：℃)

Fig. 1 Time series of annual mean temperature in China from 1961 to 2010 (unit: ℃)

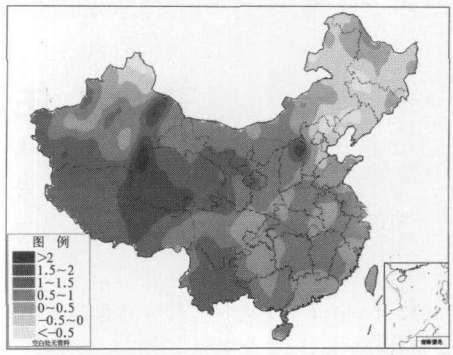


图2 2010年中国年平均气温距平分布(单位：℃)

Fig. 2 Annual mean temperature anomalies (℃) over China in 2010

国大部地区气温偏高，其中青藏高原及新疆南部和东部、甘肃中部、宁夏大部、云南、四川南部等地偏高1～2 ℃。

对四季而言，春季气温偏低、冬夏秋均偏高，夏季气温为1961年以来历史同期最高。冬季(2009年12月至2010年2月)，中国平均气温－3.6 ℃，较常年同期(－4.3 ℃)偏高0.7 ℃。春季(2010年3—5月)，中国平均气温9.5 ℃，比常年同期偏低0.1 ℃，为1997年以来首次低于常年。夏季(2010年6—8月)，中国平均气温21.5 ℃，比常年同期偏高1.1 ℃，为1961年以来历史同期最高值(图3)。从夏季气温异常的空间分布看，全国气温均偏高或接近常年同期，其中西北大部、东北中部和北部及内蒙古、西藏、四川西部、江苏南部等地偏高1～2 ℃，部分地区偏高2 ℃以上(图4)。秋季(2010年9—11月)，中国平均气温10.2 ℃，比常年同期偏高1.0 ℃。

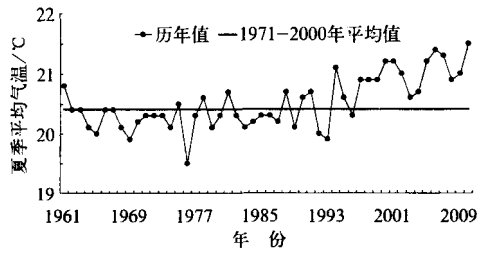


图3 1961—2010年中国夏季平均气温序列(单位：℃)

Fig. 3 Time series of summer mean temperature in China from 1961 to 2010 (unit: ℃)

2010年，中国平均年高温日数11.1天，较常年(7.0天)偏多4.1天，为1961年以来最多。南方大



© 1994-2011 China Academic Journal Electronic Publishing House. All rights reserved. http://www.cnki.net

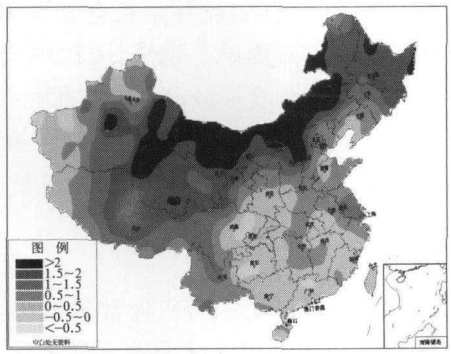


图 4　2010 年中国夏季平均气温距平分布(单位:℃)
Fig. 4　Summer mean temperature anomalies (℃) over China in 2010

部、华北中西部、黄淮西部及新疆东部、内蒙古中西部和东北部、黑龙江西北部等地偏多 5～15 天,其中江西中南部、湖南南部、福建西南部、海南北部等地偏多 15 天以上。全年共有 185 站日最高气温突破历史极值(图 5),其中有 56 站日最高气温超过 40 ℃。

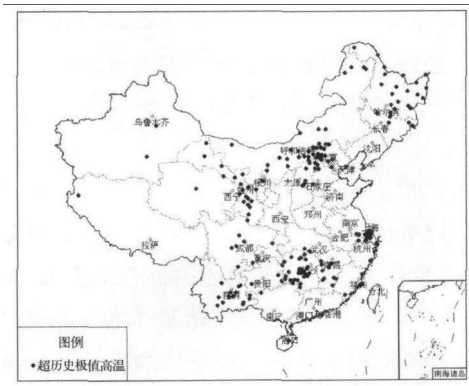


图 5　2010 年中国日最高气温突破历史极值的站点分布
Fig. 5　Stations with daily maximum temperature breaking historical records over China in 2010

另外,2010 年中国极端低温事件多发,全年共有 42 站日最低气温突破历史极值,主要出现在黑龙江、河北、内蒙古等地。

### 1.2　降水

2010 年,中国平均年降水量 681 mm,比常年偏多 11.1%,为 1961 年以来第二多(图 6)。1961—2010 年,中国平均年降水量的变化趋势不明显,没有通过显著性检验。与常年相比,除内蒙古东部、云南中东部等地降水偏少 10%～50%外,全国大部地区降水偏多或接近常年,其中东北中南部、西北中西部、江南大部及黑龙江东部、河北北部、山东北部、河南中西部、陕西南部、内蒙古西部、安徽南部、湖北东部、福建大部、广东西部、广西东部、海南大部、云南西北部、西藏东部和西部偏多 10%～50%,新疆、青海、辽宁、吉林的部分地区偏多 50%以上(图 7)。

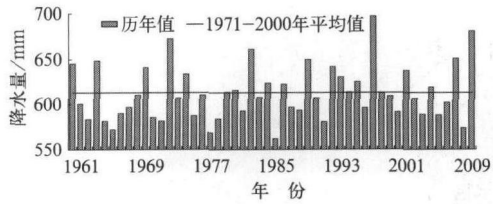


图 6　1961—2010 年中国年总降水量序列(单位:mm)
Fig. 6　Time series of annual precipitation (mm) in China from 1961 to 2010

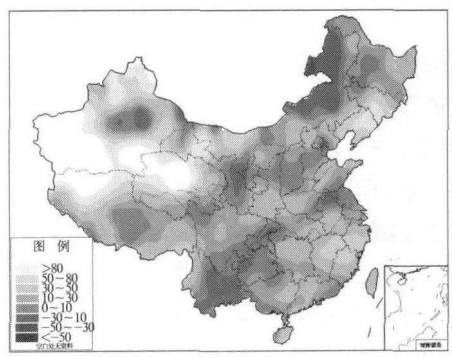


图 7　2010 年中国年降水量距平百分率分布(单位:%)
Fig. 7　Percentage of annual precipitation anomalies (%) over China in 2010

中国四季降水均偏多,其中春季降水量为 1961 年以来历史同期次多。冬季,中国平均降水量 43.7 mm,比常年同期偏多 14.2%。春季,中国平均降水量 168.4 mm,较常年同期偏多 21%,为 1961 年以来历史同期次多(图 8)。从春季降水量距平百分率分布图(图 9)上可以看到,除西藏南部、云南北部、贵州中部、海南等地降水偏少 30%～50%外,全国其余大部地区春季降水偏多或接近常年同期,其中北方大部地区,江淮南部、江南大部及山东东部、西藏东部偏多 30%以上,部分地区甚至偏多 1～2 倍。

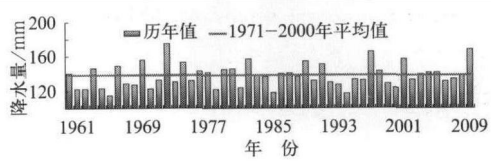


图 8　1961—2010 年中国春季降水量序列(单位:mm)
Fig. 8　Time series of precipitation (mm) in spring in China from 1961 to 2010



© 1994-2011 China Academic Journal Electronic Publishing House. All rights reserved.　http://www.cnki.net

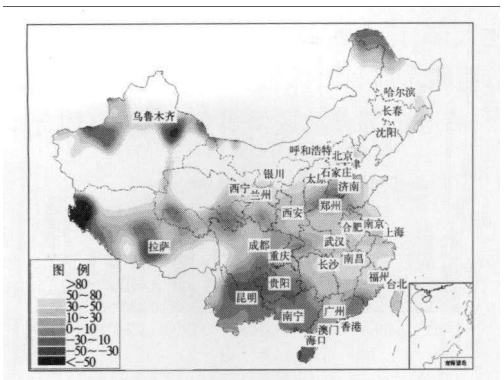


图9 2010年中国春季降水量距平百分率分布(单位:%)

Fig. 9 Percentage of precipitation anomalies (%) over China in spring 2010

夏季,中国平均降水量323.9 mm,比常年同期偏多2.6%。秋季,中国平均降水量139.4 mm,较常年同期偏多15.9%,为1984年以来最大值。

2010年,全国共出现暴雨1540站日,比常年(1267站日)偏多21.5%,为1961年以来第三多。暴雨主要出现在东北南部、秦岭至黄河下游及其以南地区,暴雨日数普遍较常年偏多。全国共有98站的日降水量突破历史极值(图10),其中27站日降水量超过250 mm,海南琼海(701.9 mm)、广东惠东(718.5 mm)等站日降水量超过600 mm。

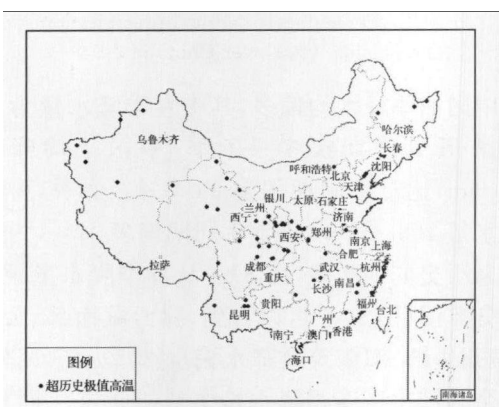


图10 2010年中国日降水量突破历史极值的站点分布

Fig. 10 Stations with daily rainfall amounts breaking historical records over China in 2010

## 2 主要天气气候事件

2010年,中国旱涝灾害相连,冷热时空交替明显,极端天气气候事件频发。区域性严重干旱、多流域暴雨洪涝、强降雨引发的地质灾害、暴雪和低温冷冻害、高比例登陆台风、大范围持续高温热浪、频繁的沙尘天气过程、局地强对流等给社会经济和人民生命财产安全带来严重影响。据统计,2010年气象灾害及次生灾害造成的直接经济损失和死亡(失踪)人口均为近10年来最多。总体而言,2010年中国气象灾害为进入21世纪以来最为严重的年份。

### 2.1 干旱

2010年,中国干旱受灾面积较常年偏小,且明显小于2009年,但区域性和阶段性干旱严重,属干旱灾害中等年份(图11)。

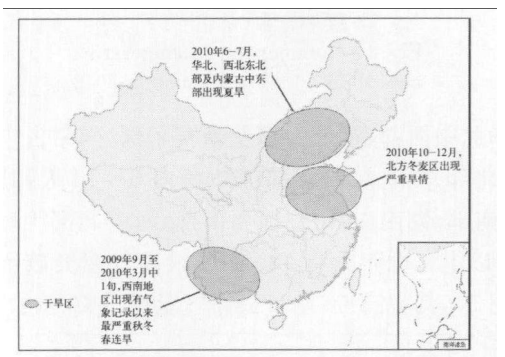


图11 2010年中国主要干旱事件示意图

Fig. 11 Sketch map of drought events in China 2010

2009年9月至2010年3月中旬,云南、贵州、四川南部、重庆南部、广西北部持续少雨,气温偏高,降水量比常年同期偏少30%~80%,云南、贵州降水量均为有气象观测记录以来最少值,平均气温分别为历史同期最高和第三高值。西南地区出现有气象记录以来最严重的秋冬春连旱。

6—7月,华北西部、西北东北部以及内蒙古大部降水量较常年同期偏少30%~80%;内蒙古平均降水量为1961年以来历史同期最少。同时,上述大部地区气温偏高2~4 ℃。长时间高温少雨导致华北、西北东北部及内蒙古中东部出现不同程度干旱,内蒙古中东部、河北西部、山西、陕西北部等地一度出现重旱,局部地区达特旱。内蒙古中东部部分地区干旱持续到10月上旬。

10—12月,华北中南部、黄淮、江淮北部降水量较常年同期偏少50%以上,其中山东省平均降水量为1961年以来历史同期次少,山西第三少,江苏为第四少值。同时,黄淮西部及河北西部、安徽北部等地气温偏高1~2 ℃。由于高温少雨,华北、黄淮、江淮大部干旱迅速发展。2010年底气象干旱监测显示,华北大部、黄淮、江淮北部及陕西大部等地存在



© 1994-2011 China Academic Journal Electronic Publishing House. All rights reserved. http://www.cnki.net

中度以上干旱,其中山西大部、山东、河南、安徽北部、江苏北部达到重旱以上等级,对农业生产造成一定影响。

## 2.2 暴雨洪涝

2010 年,中国暴雨过程频繁,降雨强度大,导致多流域汛情并发,滑坡和泥石流等次生灾害严重。

1 月 1 日至 3 月 16 日,江淮、江南降水过程频繁,江苏、安徽、江西、浙江、福建 5 省平均降水量达 313 mm,较常年同期偏多 61%,为 1961 年以来历史同期次多;平均降水日数偏多。受连续集中降水的影响,江西、浙江等地 3 月初出现历史罕见早汛。江西昌江、乐安河水位全面超警戒,新安江等多个水库创历史同期最高水位,并引发多处山洪地质灾害。

5—7 月,我国南方地区共出现 14 次强降雨天气过程,部分地区累计降雨量达 800～1200 mm。汛前降水偏多和入汛后频繁的强降水过程,使得江河湖库水位居高不下超警戒,长江上游干流、赣江、信江、抚河、渠江发生洪水,经济损失和人员伤亡较重。

7 月中旬至 9 月上旬,北方和西部地区遭受 10 轮暴雨袭击。黑、吉、辽、京、津、冀、晋、甘、陕、鲁、豫、川、滇 13 省(市)区域平均降水量 329.8 mm,较常年同期(255.1 mm)偏多 29.3%,为 1961 年以来的历史同期第二多,渭河、辽河、第二松花江等出现汛情。7 月 20—24 日,区域性大暴雨使辽宁、吉林部分地区严重受灾。

8 月 7 日 20—24 时,甘肃省甘南州出现局地短时强降水,引发舟曲县发生特大山洪泥石流灾害,造成 1700 多人死亡(含失踪)。6 月 27 日 21 时至 28 日 20 时,贵州省关岭县岗乌镇降水量达260.4 mm,引发岗乌镇重大山体滑坡,造成 42 人死亡,57 人失踪。7 月 13 日,强降水引发云南省巧家县小河镇发生特大山洪、泥石流灾害,造成 19 人死亡,26 人失踪。8 月 12—23 日,四川省多次出现区域性暴雨天气过程,导致汶川、映秀、汉源等地震灾区发生严重泥石流、滑坡等地质灾害。

10 月 1—19 日,海南平均降水量达1060.1 mm,平均暴雨日数为 6.6 天,均是常年同期的 5 倍以上,且均为历史同期最多。全省有 3 个气象观测站日降水量突破历史极值,7 个站连续降水量突破历史极值。强降水导致部分江河水库水位超过警戒水位,多个县市出现严重内涝,公路交通一度中断,旅游业受到严重影响;海口、三亚、万宁、琼海等地中小学停课。

## 2.3 热带气旋

2010 年,热带气旋生成个数异常偏少,登陆比例高、地点集中,灾情偏轻。

2010 年,在西北太平洋和南海共有 14 个热带气旋(中心附近最大风力≥8 级)生成,较常年(27 个)偏少 13 个,与 1998 年并列为 1949 年以来生成个数最少年。其中 7 个登陆中国,登陆个数接近常年(7.1 个);登陆比例高达 50%,为 1949 年以来最高。台风登陆地点集中,有 5 个在福建沿海登陆(图 12)。受登陆热带气旋影响,造成 146 人死亡(含失踪),直接经济损失 166.4 亿元,死亡人数和直接经济损失都少于 1990—2009 年平均水平。总体而言,2010 年台风灾害损失较常年偏轻。

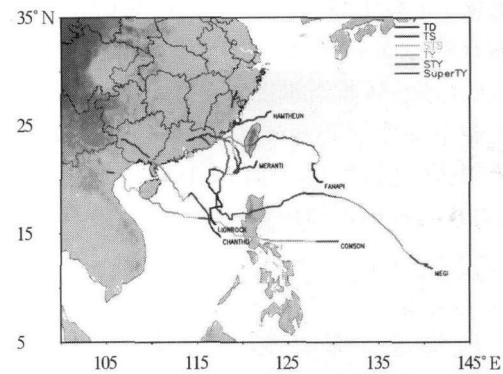


图 12　2010 年登陆中国的热带气旋路径图(中央气象台提供)

Fig. 12　The tracks of tropical cyclones landed on China during 2010 (Provided by Central Meteorological Office of CMA)

## 2.4 低温和雪灾

2010 年,中国因低温冷冻灾害和雪灾共造成农作物受灾面积 $4.121\times10^6$ $hm^2$,与常年相比,受灾面积较常年和 2009 年均偏大,为灾情偏重年份。

2009 年 11 月至 2010 年 4 月,东北、华北发生近 40 年来罕见持续低温灾害。京津冀地区(图 13)和东北三省平均气温分别为 1971 年以来历史同期最低值和次低值。1 月 1—6 日,北方遭受强寒潮袭击,东北大部及内蒙古东北部极端最低气温达 −40～−30 ℃,局部地区在 −40 ℃以下。1 月 17—23 日,中国大部地区再次遭受强寒潮袭击,渤海出现罕见海冰,海冰面积达 2000 年以来历史同期最大。低温灾害对冬小麦、油菜生长影响严重,造成冬小麦越冬期



© 1994-2011 China Academic Journal Electronic Publishing House. All rights reserved.　http://www.cnki.net

明显偏早，弱苗比例大；生长积温偏少，返青迟缓。

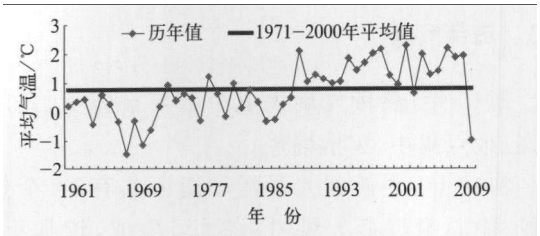


图13 1961—2010年京津冀上年11月至当年4月平均气温历年变化曲线图(单位:℃)

Fig. 13 Time series of average temperature (℃) during last November to this April in Beijing, Tianjin and Hebei from 1961 to 2010

2010年1—3月，新疆北部出现严重雪灾，平均降水量94.8 mm(较常年同期偏多3倍)、平均降水日数36天(较常年同期偏多16.7天)，均达历史同期最大值。1月上中旬，阿勒泰、塔城、富蕴等气象观测站日降雪量屡破当地1月日最大降雪量的极值，新疆北部地区积雪深度普遍在25 cm以上，阿勒泰最大积雪深度达94 cm，富蕴达88 cm，均突破冬季历史极值。强降雪导致新疆北部遭受低温冷冻和雪灾，造成人员伤亡和较重经济损失。

## 2.5 强对流

2010年，中国平均强对流日数比常年同期偏少，为1961年以来历史同期第五少。全年因风雹灾害共造成$2.18\times10^6$ $hm^2$农作物受灾，直接经济损失350.9亿元，受灾面积和经济损失都较2009年偏轻，但局部地区灾情重。

2010年，首次风雹天气出现在1月26日(云南德宏)，初雹时间较常年(平均出现在2月上旬)偏早。

5月3—8日，重庆21个县(区)遭受罕见风雹灾害，为重庆地区近20余年来最重。其中5月5—6日，重庆垫江县沙坪镇、梁平县回龙镇极大风速分别达31.2 $m\cdot s^{-1}$和30 $m\cdot s^{-1}$，均为当地有历史观测记录以来最大值。此次风雹灾害共造成157.6万人受灾，死亡33人。

5月15—16日，黑龙江省绥化市5个县(市、区)遭受雷雨大风、冰雹和龙卷风袭击，强对流造成7人死亡。

8月5—10日，江西南昌、萍乡等9市23个县(市、区)遭受风雹灾害，导致44.1万人受灾，因灾死亡11人；8月15—18日，南昌、九江、新余3市5个县(市、区)遭受风雹灾害，受灾人口3.7万人，死亡5人。

## 2.6 沙尘暴

2010年，中国春季北方沙尘天气过程较近10年同期平均值偏多，影响范围广，局地强度强。

2010年春季，中国北方地区平均沙尘日数为2.5天，比常年同期偏少3.1天，为1961年以来历史同期第八少；沙尘天气过程有16次，较常年同期(19.2次)偏少，但较2000—2009年同期平均值(12.7次)偏多。强沙尘暴过程少，仅有1次，沙尘暴过程多，有8次(图14)。沙尘天气阶段性集中多发，影响范围广，局地强度强，3月19—22日的强沙尘暴过程影响中国21个省(区、市)，是2010年影响中国范围最广的一次，给中国北方地区农业、交通以及空气质量造成不利影响。

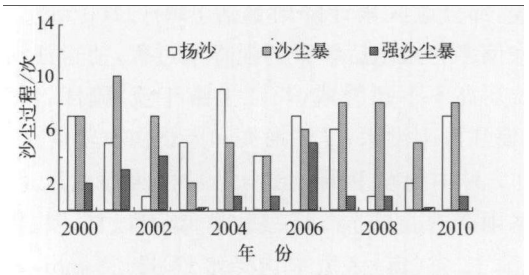


图14 2000—2010年春季中国沙尘天气过程历年变化图

Fig. 14 Number of sand and dust storm events in spring in China from 2000 to 2010

## 2.7 高温

2010年，我国夏季高温频繁、强度强、范围大；初夏东北多地最高气温破历史极值。夏季，中国平均最高气温为27.3 ℃，较常年同期偏高0.9 ℃，为1961年以来同期次高(图15)，夏季高温日数为1961年以来历史同期最多。

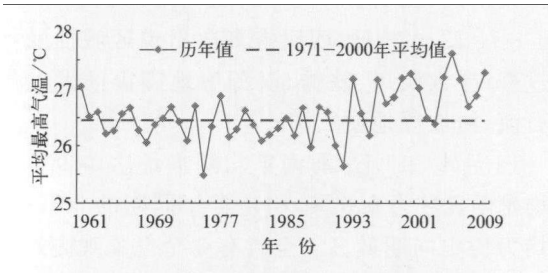


图15 1961—2010年中国夏季平均最高气温历年变化曲线图(单位:℃)

Fig. 15 Time series of summer mean maximum temperature (℃) in China from 1961 to 2010



© 1994-2011 China Academic Journal Electronic Publishing House. All rights reserved. http://www.cnki.net

6 月,黑龙江、吉林平均高温日数均为历史同期最多,6 月 23—29 日,黑龙江呼玛(40.5 ℃)、漠河(39.3 ℃)、加格达奇(39.7 ℃)、伊春(38.2 ℃),内蒙古额尔古纳 (39 ℃)、图里河(37.9 ℃),吉林松原(38.1 ℃)等 32 站日最高气温突破历史极值。少雨高温,导致黑龙江、内蒙古大兴安岭林区发生多起森林火灾。

7 月下旬至 8 月下旬,南方地区高温持续时间长,强度强,范围广。7 月 21 日至 8 月 22 日,皖、苏、沪、浙、赣、湘、渝 7 省市平均高温日数达 16.1 天,较常年同期(8.1 天)多 8 天,为 1961 年以来历史同期次大值。高温热浪造成多地电力负荷连创新高,对电力供应、电网运行安全有较大影响。

### 2.8 雾

2010 年,我国雾日偏少,但阶段性持续大雾天气对交通影响大。

2010 年,中国中东部大部地区雾日一般在 10 天以上,其中江南大部及四川东部、福建大部、黑龙江西北部、内蒙古东北部、辽宁南部、山西东北部、山东西部和东南部等地有 20～40 天,局部地区在 40 天以上。与常年相比,大部地区接近常年或偏少,其中黄淮大部、江淮东部、江汉西部、江南北部和东部及吉林东部、河北南部、山西东部、陕西南部、四川东部、重庆、贵州西部、云南中南部、福建大部等地偏少 10～30 天,云南南部、四川东南部的局部偏少 30 天以上。大雾天气主要出现在 1,2 和 10—12 月,具体为 1 月 2—4 日、1 月 17—18 日、2 月 22—25 日、10 月 8—9 日、10 月 15—17 日、11 月 5—7 日、11 月 17—20 日。

## 3 小　结

从全文分析可见,2010 年中国年平均气温偏高,尤其是夏季气温达 1961 年以来历史同期最高;年降水量偏多,为 1961 年以来第二多。年内,极端天气气候事件频发,西南罕见的秋冬春特大干旱,北方的冬春持续低温,影响全国大范围的强降水及由此引发的严重山洪、泥石流和滑坡等次生灾害,夏季全国大范围的持续性高温,台风灿都、凡亚比等,部分地区严重的风雹及强沙尘暴天气过程,均给我国的社会、经济和人民生活造成了不同程度的损失和影响。2010 年中国气象灾害是进入 21 世纪以来最为严重的年份,直接经济损失和死亡人数均为近 10 年来最多。

### 参考文献

[1] 丁一汇,张锦,徐影,等.气候系统的演变及其预测[M].北京:气象出版社,2003:25-40.

[2] 高辉,王永光.2007 年海温和大气环流异常及对中国气候的影响[J].气象,2008,34(4):107-112.

[3] 张培群,贾小龙,王永光.2008 年海洋和大气环流异常及对中国气候的影响[J].气象,2009,35(4):112-117.

[4] 艾婉秀,孙林海,宋文玲.2009 年海洋和大气环流异常及对中国气候的影响[J].气象,2010,36(4):101-105.

[5] 孔期.2010 年 6 月大气环流和天气分析[J].气象,2010,36(9):120-125.

[6] 赵伟.2010 年 8 月大气环流和天气分析[J].气象,2010,36(11):109-114.

[7] 黄奕武,赵伟.2010 年 9 月大气环流和天气分析[J].气象,2010,36(12):116-121.

[8] 钟海玲.北方旱区干旱持续　南方出现高温天气[J].气象,2009,35(12):150-151.

[9] 何文平.西南气象干旱持续　中东部地区大雾频发[J].气象,2010,36(3):140-141.



© 1994-2011 China Academic Journal Electronic Publishing House. All rights reserved.　http://www.cnki.net

第 30 卷　第 1 期
2011 年 2 月

高　原　气　象
PLATEAU METEOROLOGY

Vol. 30　No. 1
February, 2011

王遵娅，赵珊珊，张强. 我国冰冻日出现的气象条件分析及其判别模型[J]. 高原气象，2011，30(1)：158－163

# 我国冰冻日出现的气象条件分析及其判别模型

王遵娅[1]，　赵珊珊[1]，　张　强[2]

(1. 中国气象局 国家气候中心，北京　100081；2. 中国气象局，北京　100081)

**摘　要**：利用 1954－2008 年中国 700 个测站逐日气温、相对湿度、风速及 603 个测站天气现象观测资料，统计分析了出现冰冻天气(雨凇和雾凇)时的气象要素特征，研究了有利于冰冻产生的气象条件，并在此基础上研制了冰冻日判别模型。结果表明，低气温、高相对湿度和弱风速是产生冰冻的重要条件，有利于冰冻天气产生的日平均气温自北向南呈增高趋势，而相对湿度和平均风速在全国各地差别不大。利用日平均气温和天气现象资料构建的冰冻日判别模型可以较好地判断某日是否发生冰冻，该模型在冰冻频发的云南西北部、贵州、广西北部、湖南南部、江西南部等地的准确率普遍在 60%以上，漏报和空报日数较少。该模型可以将常规观测或预报产品用于冰冻监测和预警，具有一定的实用性。

**关键词**：冰冻；雨凇；雾凇；气象条件；冰冻日判别模型

**文章编号**：1000-0534(2011)01-0158-06　　**中图分类号**：P426.63　　**文献标识码**：A

## 1　引言

2008 年 1 月 10 日～2 月 2 日我国大部分(尤其是南方)地区，遭受了历史罕见的低温雨雪冰冻灾害，导致 1 亿多人受灾，直接经济损失超过 1100 亿元。在此次天气过程中，持续而大范围的冰冻天气使贵州、湖南、广西、云南等省(区)的输电线网受到严重损坏，造成部分地区停电、停水，火车停运等，对社会和人民生活造成了巨大损失[1－2]。很多学者对此次灾害性天气过程发生的原因进行了分析[3－12]，发现 2007/2008 年冬季处于 La Niña 发展的强盛期，对 2008 年中国大范围低温雨雪冰冻天气过程的产生有重要影响；而欧亚大陆异常的大气环流是大范围低温雨雪冰冻天气的直接成因。中高纬度乌拉尔地区阻塞高压和贝加尔湖－巴尔喀什湖横槽的异常发展和长时间维持及东亚大槽位置的长时间稳定有利于异常强冷空气不断沿蒙古高原东侧南下入侵我国华中、华东和华南地区；西太平洋副热带高压异常偏北使大量暖湿空气沿副热带高压西侧北上；西风带南支槽稳定维持且十分活跃，将大量水汽输送至中国大陆尤其是南方地区。

冰冻灾害主要是由于雨凇、雾凇及雨雾混合凇等造成的电线覆冰及进一步的输变线塔、通讯线塔等损坏或损毁，也包括由于雨凇、雾凇、降雨(雪)冻结等造成的道路结冰、交通受阻、农林业受灾等。考虑到气象观测数据的局限性，本文所提及的冰冻具体而言是指雨凇和雾凇。若某日出现雨凇或雾凇(天气现象)，则定义该日为一个冰冻日。实际上，我国大部分地区都有冰冻天气出现，雾凇主要发生在北方，雨凇主要发生在南方[13]。冰冻在云贵地区最为常见，广东、广西、湖南、湖北、江西等地在某些年份也会出现[14]，很多学者对云贵地区冰冻的时空分布、变化特征及形成原因等进行了详细分析[15－18]。目前，我国拥有较多的雨凇、雾凇天气现象的站点观测资料，但一方面这些站点分布不均匀，而冰冻在很大程度上受到“微地形、微气候”的影响，因而现有的站点观测资料不能满足灾害区划和风险评估工作的高精度要求；另一方面，目前针对冰冻和电线覆冰厚度的天气预报或预测技术还不成熟，不利于防灾减灾工作的进行。因而，研究产生雨凇和雾凇的气象条件，并在此基础上利用比较常规的，目前已能够预报的气象要素对其进行模拟，可以在一定程度上解决前面提出的两方面问题，具有重要的实际意义。本文拟就此进行一些初

**收稿日期**：2009-11-27；**改回日期**：2010-03-26
**基金项目**：国家科技支撑计划项目(2008BAK50B02)；国家自然科学基金项目(40905036)共同资助
**作者简介**：王遵娅(1979—)，女，四川人，高工，主要从事气候研究. E-mail：wangzy@cma.gov.cn

步的研究和探讨。

## 2　资料选取和方法介绍

本文采用的气象观测资料包括：1954－2008年中国700个测站的逐日气温、相对湿度、平均风速和1954－2008年中国603个测站的天气现象观测资料(包括雨凇、雾凇、降雨、降雪、雾和轻雾等)。

统计分析时主要采用了频率百分比分布和对比分析等方法。计算某样本的频率百分比分布，即：对某要素样本 $x_j(j=1, p)$，有 $a_1<x_j<a_{n+1}$，将 $a_1$ 至 $a_{n+1}$ 间平均分为间隔为 $aa$ 的 $n$ 等份($n$ 的值可自由选取)，若满足 $a_i-aa/2<x_j\leqslant a_i+aa/2$ 的样本值有 $m$ 个，则对应于 $a_i$ 的频率百分比为 $(m/p)\times 100$，由此可得该样本的频率百分比分布。

## 3　冰冻天气与气象要素的关系

很多研究指出[19－20]，冰冻天气的形成与气温、相对湿度和风速关系密切。下面我们利用全国603个测站的历史资料，研究出现冰冻天气时的日平均气温、日最高气温、日最低气温、日均相对湿度和日均风速，分别统计不同要素在冰冻天气发生时的频率百分比分布。这些分布反映了冰冻天气发生时相关气象要素的频率分布，由此可以确定有利于产生冰冻天气的气象条件。

如图1所示，有利于冰冻天气发生的日平均气温、日最高气温和日最低气温都集中在一定的阈值范围内，但该区间的跨度比较大，以0℃以下的温度为主。就日平均气温而言，从－26～3℃之间都有1%以上的样本发生冰冻，0℃最适宜冰冻生成，对应的频率百分比为6.94%，－3～0℃各有5%以上的样本发生冰冻。就最高气温而言，从－19～10℃之间都有1%以上的样本发生冰冻，同样是

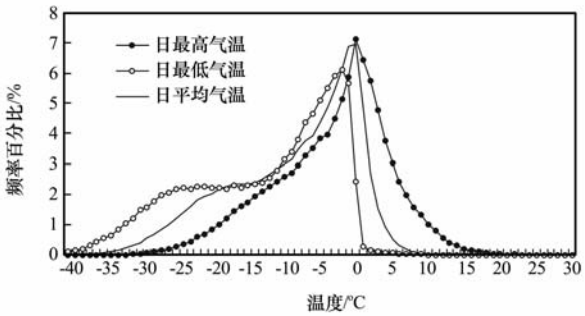


图1　中国各测站出现冰冻天气时日平均气温，日最高气温和日最低气温的频率百分比分布

Fig. 1　Distributions of frequency percentage of the daily mean, maximum and minimum temperatures at stations of China when the ice freezing occurs

0℃最适宜冰冻生成，对应的频率百分比为7.1%，－2～2℃各有5%以上的样本发生冰冻。就日最低气温而言，从－32～0℃之间都有1%以上的样本发生冰冻，－2℃最适宜冰冻生成，对应的频率百分比为6.09%，－1～－5℃各有5%以上的样本发生冰冻。

由上述分析可见，低气温适于冰冻的发生，并且气温变化范围较大，可以低至－20～－30℃，但以0℃左右最为有利。

类似地，图2是我国各站冰冻发生时日均风速和日均相对湿度的频率百分比分布图。由图可见，较小的风速和高湿条件有利于冰冻的生成。最适宜冰冻发生的平均风速是1.5 m·s$^{-1}$，其对应的频率百分比为12.5%。冰冻在≤4 m·s$^{-1}$风速条件下形成的样本数占总样本数的78%，而在≤6 m·s$^{-1}$风速条件下形成的样本数更是占到了总样本数的90%。最适宜冰冻发生的日均相对湿度为80%，对应的频率百分比为16.7%。冰冻在≥70%的相对湿度条件下形成的样本数占总样本数的

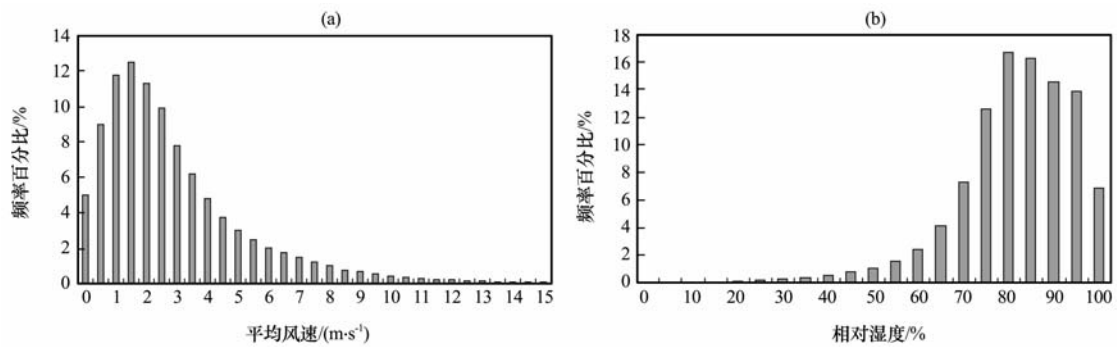


图2　中国各测站出现冰冻时日均风速(a)和日均相对湿度(b)的频率百分比分布

Fig. 2　Distributions of frequency percentage of daily mean wind speed(a) and relative humidity(b) at stations of China when the ice freezing occurs

88%。

中国地域广阔，各气象要素具有显著的地域性特征，这就决定了不同地区影响冰冻形成的气象条件存在差异。因此，我们针对每个站点，统计了历史上冰冻发生时各气象要素的频率百分比分布。结果表明，当冰冻发生时，虽然各站的气象要素值集中在一定范围内，但不同测站对应的范围和频率分布都有不同。这种地域性差异在气温的频率分布中最为显著。

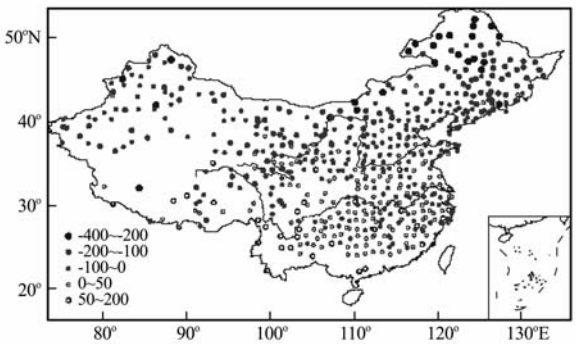


图 3 中国各测站冰冻发生时最大频率值对应的日平均气温分布(单位：0.1℃)

Fig. 3 Distribution of daily mean temperature with maximum frequency at stations of China when the ice freezing occurs. Unit：0.1℃

图 3 给出了我国各测站冰冻发生时出现频率最高的日平均气温。由图可见，日平均气温自北向南呈升高趋势。40°N 以北的东北、内蒙古、新疆等地一般在－20～－10℃之间，东北北部甚至在－20℃以下；35°～40°N 之间以－10～0℃为主；而 35°N 以南的地区大都在 0～5℃之间。也就是说，有利于冰冻产生的日平均气温越往北越低，而越往南越高。这种特征也清楚地反映在日最高气温和日最低气温中(图略)。在全国 95%以上的测站中，冰冻最大频率对应的相对湿度值都在 70%以上，北方地区相对湿度略低，黄河以南地区的相对湿度较高。冰冻最大频率对应的平均风速在全国各测站都在 4 m·$s^{-1}$以下，并且没有表现出明显的区域性特征。

上述分析表明，有利于冰冻生成的气温具有明显的区域性特征，北方低而南方高，但相对湿度和平均风速则在地域性差异不大。

## 4 冰冻日判别模型

由于冰冻观测站分布不均匀，尤其是冰冻灾害频发的高海拔地区分布更为稀疏，因此要利用常规气象要素建立冰冻日判别模型，即根据常规气象要素条件判断某日是否发生冰冻，若发生则确定该日为一个冰冻日。这对于冰冻灾害风险区划、预警和预评估是非常重要的。利用冰冻日判别模型，我们回算了中国各测站 1954－2008 年历年的冰冻日数，并将其与历史观测数据进行比较以判断模型的优良。本文主要利用以下 3 种指标来评估模型的模拟效果：

(1)模拟准确率＝$\frac{\text{模拟准确的冰冻日数}}{\text{模拟的冰冻总日数}}\times 100$；

(2)空报日数＝模拟的冰冻日数－模拟准确的冰冻日数；

(3)漏报日数＝实测的冰冻日数－模拟准确的冰冻日数。

若模拟准确率越高，空报和漏报日数越少，则模型越好；反之亦然。

### 4.1 温湿风构建的冰冻日判别模型

以往很多研究都采用气象要素来建立我国冰冻日判别模型，主要考虑气温、相对湿度和平均风速 3 种要素[19－20]，但对于每个要素的阈值选取，各研究之间存在较大差异。为了选取合适的阈值，我们采用了 2 种方法：

(1) 全国各测站确定统一的阈值。根据对图 1 和图 2 的分析，分别将冰冻发生时较高频率百分比的平均气温、相对湿度和平均风速值作为阈值，如：－5℃≤平均气温≤0℃，相对湿度≥80%，平均风速≤4 m·$s^{-1}$；并根据不同的阈值做了多组试验。结果表明，阈值的微调对冰冻日数的模拟结果影响不大。多年平均(1954—2008 年平均，下同)的模拟准确率在长江以南地区较高，一般为 40%～80%，部分地区可达到 80%以上；但在全国其余大部地区模拟准确率较低，普遍在 20%以下，仅东北

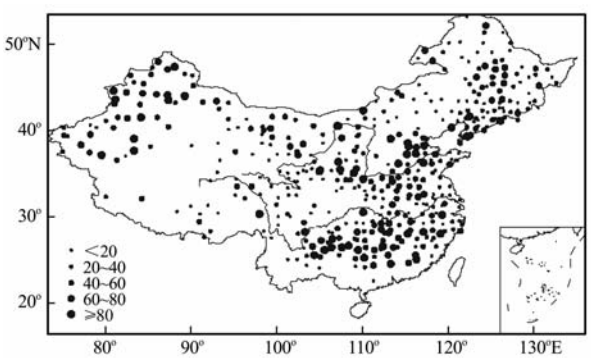


图 4 温湿风构建的冰冻日判别模型的模拟准确率(单位：%)

Fig. 4 Accuracy rates of the discriminate model of ice freezing days based on temperature, relative humidity and wind speed. Unit：%

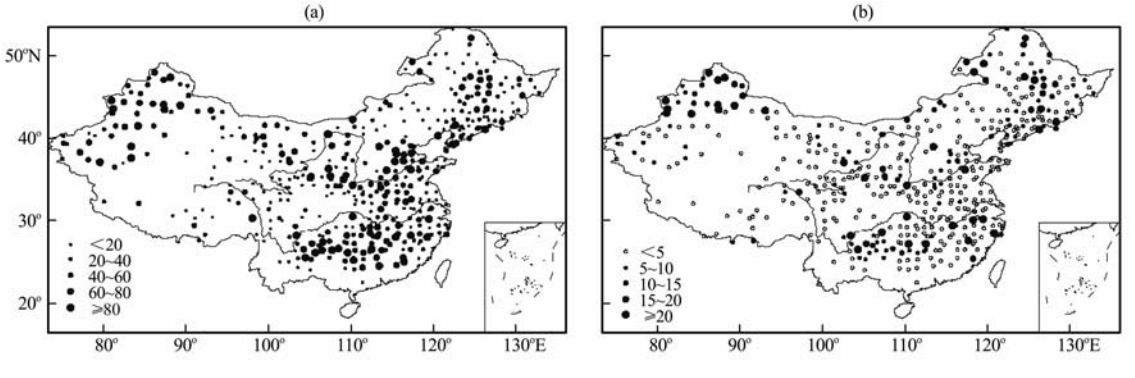


图 5　温湿风构建的冰冻日判别模型的空报日数(a)和漏报日数(b)(单位：d)

Fig. 5　The simulated false days (a) and missing days (b) of the discriminate model of ice freezing days based on temperature, relative humidity and wind speed. Unit: d

西部、华北东部、江淮西部、新疆等地可达 20%～40%。就漏报和空报日数而言，平均每年有 1～5 天，部分测站在 5 天以上。阈值范围取得越大，空报日数越多而漏报日数越少；反之亦然。

(2)　全国各测站确定不同的阈值。本文第 3 节的研究发现，全国各测站有利于冰冻发生的平均气温、相对湿度和平均风速不尽相同，尤其是气温在南北方具有较大差别。为此，以各测站冰冻发生时最高频率对应的平均气温、相对湿度和平均风速值作为阈值，以小于等于日平均气温和平均风速阈值，大于等于相对湿度阈值建立冰冻日判别模型。运用该模型对 1954 年以来冰冻日数进行模拟(图 4)，多年平均的模拟准确率在全国大部分地区都在 20%以上，其中长江以南地区、黄河中下游流域、东北、新疆和内蒙古西部等地一般在 40%以上，部分测站可达 80%～100%。全国大部分地区的空报日数在 5 天以下，但华南及四川、西藏东部、云南的部分站点空报日数较多，在 20 天以上(图 5a)。就漏报日数而言(图 5b)，一般有 1～5 天，东北西部、河北西部、贵州、湖南和新疆北部等地有 5～10 天，部分测站在 10 天以上。

从以上分析可以看到，对平均气温、相对湿度和平均风速选取适合的阈值在一定程度上可以对我国各测站某日是否发生冰冻进行模拟；且全国各测站根据当地情况分别选取阈值，其模拟准确率更高。2 种方法的漏报日数和空报日数一般为 1～5 天；模拟效果较好的区域主要分布在长江以南地区、黄淮、华北东部、东北及内蒙古西部、新疆等地。

### 4.2　日平均气温和天气现象构建的冰冻日判别模型

雨凇的发生常常伴随降水的出现，而雾凇多产生于有雾或轻雾的天气条件下，并且，雨凇和雾凇的发生都要求低气温，因而考虑采用日平均气温与天气现象相结合的方式来构建冰冻日判别模型：40°N 以北地区，某日的平均气温≤－20℃；30°～40°N 地区，平均气温≤－10℃；30°N 以南的地区，平均气温≤－2℃；并且当日当地有降雨(不包括降雪)、雾或轻雾出现，则定义该站发生冰冻，该日为一个冰冻日。利用该模型对 1954 年以来的冰冻日数进行模拟，发现就模拟准确率而言(图 6)，除华北和黄淮地区在 40%以下，全国大部地区都在 40%以上，且长江以南地区、东北西部、内蒙古和新疆等地大部分测站都在 60%以上。该模型的漏报日数和空报日数(图 7)也大都在 5 天以下，仅在东北、江南和新疆部分测站在 5 天以上。

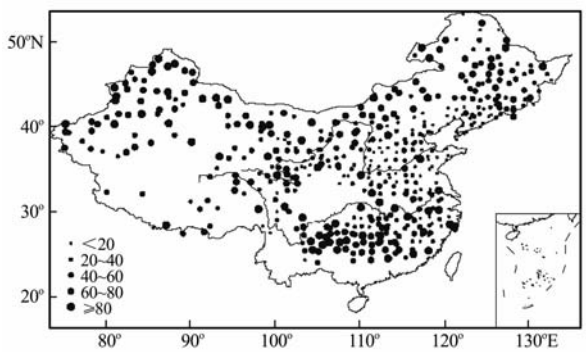


图 6　日平均气温和天气现象构建的冰冻日判别模型的模拟准确率(单位：%)

Fig. 6　Accuracy rates of the discriminate model of ice freezing days based on daily mean temperature and weather phenomena. Unit: %

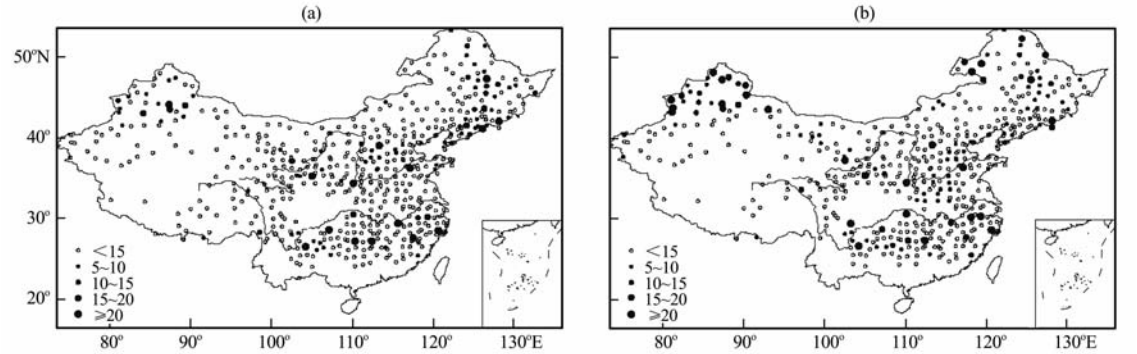


图 7 日平均气温和天气现象构建的冰冻日判别模型的空报日数(a)和漏报日数(b)(单位：d)

Fig. 7 The simulated false days (a) and missing days (b) of the discriminate model of the ice freezing days based on daily mean temperature and weather phenomena. Unit: d

另外，我们还以各站冰冻发生时最高频率的平均气温值作为阈值，若某站某日的日平均气温小于等于阈值且当日出现降水(不包括降雪)、雾或轻雾，则定义该站发生冰冻，该日为一个冰冻日。该模型的准确率较前一个由日平均气温和天气现象构建的冰冻日判别模型略高，漏报日数略少，但空报日数偏多。综合考虑，不如前一模型好。

由上述分析可以看到，采用日平均气温与降水、雾和轻雾相结合的冰冻日判别模型可以很好的对我国各站每天是否发生冰冻进行判断。模型的准确率较高，空报和漏报日数较少，总体效果比温湿风构建的冰冻日判别模型更好。这可能是由于降水、雾和轻雾这些天气现象所包含的气象要素条件较相对湿度和平均风速更丰富，且更能反映冰冻发生时的气象条件。有研究根据大量个例找出凝冻和降雪天气的环流形势和天气特征，并以此作为凝冻和降雪天气预报的参考[18]。与此相比，本文提出的模型仅需要常规的气象观测资料，可进行定量判别且准确率较高，因而具有更高的可操作性和实用性。

## 5 结论

本文主要分析了有利于中国冰冻(雨凇和雾凇)发生的气象条件，并在此基础上试验和建立冰冻日判别模型，得到以下结论：

(1) 低气温、高相对湿度和弱风速是冰冻产生的重要条件。总体而言，气温在0℃左右，相对湿度在70%以上，平均风速在4 m·s$^{-1}$以下最有利于冰冻的产生。对全国不同测站，有利于冰冻产生的气温自北向南呈增高趋势分布，而相对湿度和平均风速在全国各地区差别不大。

(2) 取某站冰冻发生时日平均气温、相对湿度和平均风速的最高频率对应值作为阈值，若某站某日平均气温和平均风速小于等于阈值，而相对湿度大于等于阈值，则定义该站发生冰冻，该日为一个冰冻日。由此构建的冰冻日判别模型可以在一定程度上模拟出中国历年各站的冰冻日数。若某站处于40°N以北地区，在某日的平均气温≤－20℃；或处于30°～40°N地区，平均气温≤－10℃；或处于30°N以南的地区，平均气温≤－2℃；并且，该站当日有降雨(不包括降雪)、雾或轻雾出现，则定义该站发生冰冻，该日为一个冰冻日。由此构建的冰冻日判别模型可以很好地模拟出中国历年各站的冰冻日数。比较而言，气温和天气现象相结合构建的模型的模拟准确率高，模拟效果更好。使用者可根据资料、需求等条件选择使用不同的模型。

(3) 由日平均气温和天气现象构建的冰冻日判别模型在东北、西北、长江以南地区及内蒙古一带的模拟准确率较高，一般在40%以上，其中云南西北部、贵州、广西北部、湖南南部、江西南部等重冰地区的准确率可达60%以上；全国各站的漏报日数和空报日数较少。该模型可以将常规观测和预报产品用于冰冻监测和预警，具有一定的实用性。

## 参考文献

[1] 王遵娅，张强，陈峪，等. 2008年初我国低温雨雪冰冻灾害的气候特征[J]. 气候变化研究进展，2008(4)：63－67.

[2] 王凌，高歌，张强，等. 2008年1月我国大范围低温雨雪冰冻灾害分析Ⅰ：气候特征与影响评估[J]. 气象，2008，34(4)：95－100.

[3] 陶诗言，卫捷. 2008年1月我国南方严重冰雪灾害过程分析[J]. 气候与环境研究，2008，13(4)：337－350.

[4] 丁一汇，王遵娅，宋亚芳. 中国南方2008年1月罕见低温雨

雪冰冻灾害发生的原因及其与气候变暖的关系[J]. 气象学报，2008，66(5)：808－825.

[5] 李崇银，杨辉，顾薇. 中国南方雨雪冰冻异常天气原因的分析[J]. 气候与环境研究，2008，13(2)：113－122.

[6] 李登文，乔琪，魏涛. 2008 年初我国南方冻雨雪天气环流及垂直结构分析[J]. 高原气象，2009，28(5)：1140－1148.

[7] 高辉，陈丽娟，贾小龙，等. 2008 年 1 月我国大范围低温雨雪冰冻灾害分析 II：成因分析[J]. 气象，2008，34(4)：101－106.

[8] 张庆云，宣守丽，彭京备. La Nina 年冬季亚洲中高纬环流与我国南方降雪异常关系[J]. 气候与环境研究，2008，13(4)：385－394.

[9] 许东蓓，张铁军，任余龙. 2008 年 1 月甘肃省连阴雪特征及成因分析[J]. 高原气象，2009，28(5)：1129－1140.

[10] 杨贵名. 2008 年初"低温雨雪冰冻"灾害天气的持续性原因分析[J]. 气象学报，2008，66(5)：836－849.

[11] 晏红明，王灵，朱勇，等. 2008 年初云南低温雨雪冰冻天气的气候成因分析[J]. 高原气象，2009，28(4)：870－879.

[12] 曾明剑，陆维松，梁信忠，等. 地形对 2008 年初中国南方持续性冰冻灾害分布影响的数值模拟[J]. 高原气象，2009，28(6)：1376－1387.

[13] 赵珊珊，高歌，张强，等. 中国冰冻天气的气候特征[J]. 气象，2010，36(3)：1－5.

[14] 谭冠日，严济远，朱瑞兆. 应用气候[M]. 上海：上海科学技术出版社，1985：3－56.

[15] 严小东，吴战平，古书鸿. 贵州冻雨时空分布变化特征及其影响因素浅析[J]. 高原气象，2009，28(3)：694－701.

[16] 许丹，罗喜平. 贵州凝冻的时空分布特征和环流成因分析[J]. 高原气象，2003，22(4)：401－404.

[17] 许丹，罗喜平. 贵州典型凝冻年及无凝冻年的环流特征分析[J]. 贵州气象，2001，25(3)：14－16.

[18] 王志云，鲁亚斌，牛法宝. 云南东部冻雨的成因分析[J]. 云南大学学报(自然科学版)，2008，30(增刊)：324－328.

[19] 王守礼主编. 云南高海拔地区电线覆冰问题研究[M]. 昆明：云南科技出版社，1993：7－44.

[20] 吉延艳，何玉龙，杜正静，等. 凝冻灾害预警系统[J]. 气象研究与应用，2007，28：140－142.

# Meteorological Conditions in Ice Freezing Day of China and Its Discriminate Model

WANG Zun-ya[1]，　ZHAO Shan-shan[1]，　ZHANG Qiang[2]

(1. *National Climate Center*，*China Meteorological Administration*，*Beijing* 100081，*China*；
2. *China Meteorological Administration*，*Beijing* 100081，*China*)

**Abstract**：Characteristics of the ice freezing weather，especially the glaze and rime in China are first analyzed，using the daily observation data of temperature，relative humidity，wind speed at 700 stations and weather phenomena at 603 stations in China from 1954 to 2008. Then the favorable meteorological conditions for the formation of the ice freezing are obtained and the discriminate model of the ice freezing days is developed. It is found that the low temperature，high relative humidity and small wind speed are the important meteorological conditions for the formation of the ice freezing. Among the three meteorological variables，the daily mean temperature appears the decreasing trend from the north to the south，while the relative humidity and wind speed present little difference in China. The discriminate model of the ice freezing days，which is established basing the daily mean temperature and the weather phenomena，can distinguish well whether the ice freezing occur or not on the certain day. The accuracy rate of the discriminate model reaches up to 60% in northwestern Yunnan，Guizhou，northern Guangxi，southern Hunan，southern Jiangxi，and so on，where the ice freezing frequently occurs. And the simulated average false days are only 1 to 5 days. Totally，the discriminate model has a relatively high practicability for the ice freezing monitoring and early warning by routine observations and prediction.

**Key words**：Ice freezing；Glaze；Rime；Meteorological condition；Discriminate model of ice freezing days

# 非球形沙尘气溶胶光学特性的分析

卫晓东[1,2] 张 华[2]

[1] 中国气象科学研究院，北京 100081

[2] 国家气候中心中国气象局气候研究开放实验室，北京 100081

**摘要** 将 T 矩阵方法与几何光学方法相结合，精确计算了从太阳短波到红外谱段具有一定形状分布和谱分布的非球形沙尘粒子的光学特性，并与等体积球形沙尘的光学特性进行了比较。结果表明：1）相比沙尘粒径大小分布对沙尘气溶胶消光效率因子，单次散射反照率以及不对称因子的影响，沙尘形状对上述参数的影响明显偏小；2）非球形与球形沙尘粒子的相函数在短波区存在显著差异，这种差异在卫星探测常用的可见光区达到最大，并且随着散射角的变化具有一定的规律；3）在短波区，雷达方程中的消光后向散射比受沙尘形状的影响比较显著，因此在利用雷达方程反演沙尘气溶胶光学厚度时应考虑非球形效应。

**关键词** 大气光学；光学特性；T 矩阵方法；几何光学方法；沙尘气溶胶；非球形粒子

**中图分类号** P415.3 **文献标识码** A **doi:** 10.3788/AOS201131.0501002

# Analysis of Optical Properties of Nonspherical Dust Aerosols

Wei Xiaodong[1,2] Zhang Hua[2]

[1] *Chinese Academy of Meteorological Sciences, Beijing* 100081, *China*

[2] *Laboratory for Climate Studies, National Climate Center, China Meteorological Administration, Beijing* 100081, *China*

**Abstract** The optical properties of nonspherical dust aerosols in the wavelength range of 0.2～40 μm are calculated by combination of T-matrix method and an improved geometric optics under the conditions of representative shape distribution and size distribution. By comparing the optical properties of dust particles between nonspherical and isochoric sphere hypothesis. It is found that 1) the shape of dust aerosols has a smaller influence on the extinction efficiencical factor, scattering albedo and asymmetry factor compared to the size distribution; 2) the difference of phase function between nonspherical and spherical dust aerosols in the short-wave region is significant, especially in the visible region, and they change with different scattering angles; 3) in short-wave region, the extinction-to-backscattering ratio in the so-called lidar equation is affected by the shape of dust aerosols greatly, therefore, the nonspherical effects should be considered in the retrieval of dust optical thickness by using the lidar equation.

**Key words** atmospheric optics; optical properties; T-matrix method; geometric optics method; dust aerosol; nonspherical particle

**OCIS codes** 010.0010; 010.1110; 010.1290; 010.3920; 290.1350

## 1 引 言

沙尘气溶胶具有特殊的光学特性，它既可以通过强烈散射太阳辐射使地面和低层大气获得的太阳辐射减少，它也可以吸收地面发射的长波辐射使对

**收稿日期：** 2010-11-08；**收到修改稿日期：** 2011-01-06

**基金项目：** 国家科技支撑计划（2008BAC40B02）、国家 973 计划（2011CB403405）和科技部公益性行业（气象）科研专项（GYHY200906020）资助课题。

**作者简介：** 卫晓东（1984—），男，硕士研究生，主要从事大气气溶胶光学特性方面的研究。
E-mail: weixiaodong007@163.com

**导师简介：** 张 华（1965—），女，研究员，博士生导师，主要从事温室气体、气溶胶和云的辐射强迫与气候效应等方面的研究。E-mail: huazhang@cma.gov.cn

本文电子版彩色效果请详见中国光学期刊网（http://www.opticsjournal.net）

流层顶出射的净辐射减少。此外，与其他气溶胶粒子不同，实验室以及观测数据表明：沙尘粒子的形状在很大程度上都是不规则的[1,2]。目前在辐射传输模式以及遥感应用中针对沙尘粒子光学特性的研究广泛采用的是洛伦兹-米氏(Lorenz-Mie)理论，但运用该方法需要满足3个条件：沙尘粒子为理想的球形，内部混合均匀，表面为镜表面。而实际存在的沙尘粒子既不是球形也不是均质，因此，采用洛伦兹-米氏散射理论来计算沙尘的光学特性，在一定程度上会影响计算结果的精度和准确性。

近年来，国外有许多研究用不同方法从不同角度证实了非球形沙尘粒子的散射与球形沙尘粒子的散射具有很大差别[3~5]。其中Yang等[4]将T矩阵与几何光学方法结合起来计算椭球沙尘粒子的光学特性，并与球形沙尘粒子对比后指出：两种计算结果在相函数，尤其是后向散射相函数，差异较大，但是文中假设沙尘粒子的形状均为纵横比为1.7的扁椭球粒子，另外文献[4]没有指出红外谱段非球形与球形沙尘光学特性的差异；Fu等[5]比较了纵横比为1.7的扁椭球沙尘粒子与等体积等表面积球形沙尘粒子光学特性的差别，指出用等体积等表面积的球形粒子代替非球形沙尘粒子的误差主要表现在相函数上，但是该结论局限于0.55 μm波长处；Mishchenko等[3]用T矩阵方法验证了用具有不同纵横比的多分散系椭球粒子模拟非球形沙尘粒子光学特性的可行性，但是该结论局限于特定的复折射指数和谱分布下。国内也有研究[6,7]用不同方法分析了非球形与球形粒子的散射差异，这些研究针对单个气溶胶粒子在单一波长下的光学特性进行对比分析，而大气气溶胶在真实大气中具有不同谱分布并且在不同波长下光学特性具有较大差别，因此对不同波长下非球形气溶胶的光学特性进行分析是十分必要的。本文在前人研究工作的基础上，将T矩阵方法与改进的几何光学方法相结合，详细计算和讨论了从太阳短波到红外谱段下椭球形沙尘气溶胶的光学特性，并与等体积球形沙尘气溶胶的光学特性进行了比较。

## 2　计算方法与物理量介绍

### 2.1　计算方法简介

T矩阵方法是由Waterman[8]于1971年引进的。目前最有效的T矩阵数值计算程序是Mishchenko和Travis[9]于1994年建立的适用于随机取向且具有对称轴粒子的算法，该数值算法已在小椭球粒子光学性质的计算中得到广泛应用[4,5,10]。当粒子尺度参数较大时，几何光学概念可以用来计算非球形粒子的光学特性。Yang和Liou[11]于1996年发展了一种改进的几何光学算法(IGOM)，可以用来准确计算具有较大尺度参数的非球形粒子光学特性。

到目前为止，没有一个单一的数值算法可以计算从瑞利到几何光学粒子尺度范围内的非球形粒子的单次散射光学特性，本文将T-matrix方法[12]与IGOM[11]方法相结合，分别用于计算粒子尺度参数小于50和大于50时的非球形粒子的单次散射特性。

球形沙尘粒子散射特性的计算是基于经典的洛伦兹-米氏散射理论，采用已经得到广泛使用的Wiscombe数值算法[13]和计算程序。

### 2.2　物理量介绍

实际沙尘粒子的形状极不规则，没有严格的几何形状，根据实际沙尘的不规则形状计算其光学性质不会导致误差，但是针对这些不规则形状的数值方法无法覆盖实际沙尘的粒径范围并且计算非常耗时[14]，因此根据实际沙尘的不规则形状计算其光学性质不具备可行性。

本文研究中用旋转对称的椭球形近似非球形沙尘粒子的形状，这种近似具有以下优点：首先该形状仅决定于两个参数即纵横比和等体积半径，因此在传统球形模型的基础上假定纵横比即可确定非球形沙尘的形状；其次根据2.1节中所述方法可以准确高效地计算椭球粒子的光学特性；最后观测结果表明：虽然各种不规则形状的沙尘粒子光学特性差别较大，但是实际沙尘粒子以多粒径分散系的形式存在，其光学特性是考虑各种形状权重后的光学特性，而这种平均后的光学特性与不同纵横比的椭球粒子平均后的光学特性差别比较接近[3]。

旋转对称的椭球形是椭圆的横轴$b$绕纵轴$a$旋转而成。纵横比$R_{a/b}<1$时旋转椭球体为扁椭球体，形状类似于圆盘形；纵横比$R_{a/b}>1$时旋转椭球体为长椭球体，形状类似于针形[3]。本文将沙尘形状划分为$R_{a/b}$的值为1.2，1.4，1.6，1.8，2.0，2.2和2.4的长椭球和横纵比$R_{b/a}$的值为1.2，1.4，1.6，1.8，2.0，2.2，2.4的扁椭球共14种，并且每种形状沙尘占的比例相等。

复折射指数是计算气溶胶光学特性的重要参数，由构成粒子的化学成分决定，随着气溶胶源区地理位置不同存在很大差异[15]。本文采用王宏等[16]总结的0.2～40 μm光谱范围内东亚沙尘的复折射指数。

由于实际气溶胶粒子大小并不均一，因此必须

考虑用一种粒径大小分布函数(即气溶胶谱分布)来代表气溶胶粒子的实际分布，从而通过积分得到整体气溶胶的光学特性。沙尘气溶胶粒子中尺度较小的粒子相对集中，因此采用对数正态分布描述沙尘粒子分布，谱分布参数采用与东亚沙尘气溶胶最接近的 OPAC 模型，该模型将沙尘气溶胶分为核膜态(MINM)，积聚态(MIAM)，粗模态(MICM)以及传输态(MITR)4 种模态[17]。

描述粒子对辐射传输影响的光学参数分别为消光效率因子 $Q_e$、单次散射反照率 $\omega$、不对称因子 $g$ 以及相函数 $P_{11}$，单个沙尘粒子的光学参数分别采用椭球和等体积球形来计算，在此基础上用 OPAC 谱分布参数计算不同谱分布下的光学特性[5]。此外，本文还分析了雷达反演气溶胶中的常用参数消光后向散射比 $R_{eb}$[18]。

## 3 计算结果及讨论

### 3.1 单分散系椭球沙尘粒子的光学特性

在分析具有一定形状分布和谱分布的椭球沙尘粒子的光学特性之前，首先通过单分散椭球沙尘粒子的光学特性来详细说明本文所采取的计算过程。图 1 给出了 T-matrix 方法与 IGOM 计算的单分散系椭球沙尘粒子在波长 0.55 μm 纵横比 $R_{a/b}=1.7$ 时光学特性随尺度参数的变化，根据 2.1 节所述两种方法的特点，T-matrix 方法和 IGOM 分别用来计算尺度参数在 0.5～50 和 20～800 的粒子。对比两种方法在尺度参数 20～50 的结果发现，该区域属于 T-matrix 方法到 IGOM 的过渡区，在该区域 T-matrix方法与 IGOM 计算的消光效率因子、单次散射反照率以及不对称因子的差别较小，由于前者的计算精度较高[14]，因此用 IGOM 计算较大尺度参数沙尘粒子的光学特性是可行的。椭球沙尘粒子在其他波长和纵横比的情况下用两种方法的计算结果与上述结果一致，因此本文在计算从太阳短波到红外谱段椭球沙尘粒子的光学特性时，分别用 T-matrix 方法和 IGOM 计算尺度参数小于或等于 50 和尺度参数大于 50 的椭球沙尘光学特性。图 1 为 T-matrix 方法与 IGOM 计算的椭球沙尘粒子在波长为 0.55 μm 纵横比 $R_{a/b}=1.7$ 时光学性质的对比，$x$ 轴是用椭球沙尘等体积半径表示的尺度参数，$x$ 值在 0.5～50 的曲线为 T-matrix 方法计算结果，$x$ 值在 20～800 的曲线为 IGOM 计算结果。

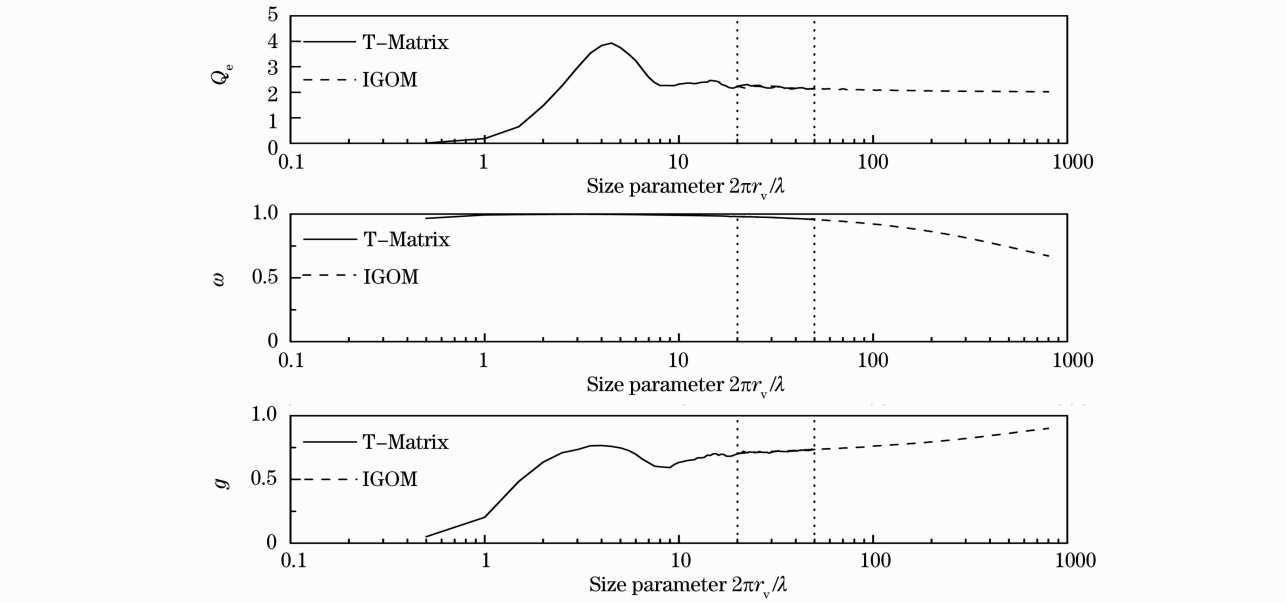


图 1 T-matrix 方法与 IGOM 方法计算结果的比较

Fig. 1 Comparison of the calculation result between the T-matrix and IGOM method

### 3.2 消光效率因子、单次散射反照率以及不对称因子的对比分析

消光效率因子是粒子从入射能中移除的总能量与粒子几何面积的比，反应了气溶胶对辐射传输的衰减作用强弱。单次散射反照率体现了气溶胶散射占辐射传输衰减的比例。沙尘气溶胶的相函数在 0°散射角普遍有尖峰，所以沙尘不对称因子表示了前向散射的相对强度[19]。上述 3 个参量是影响沙尘气溶胶辐射传输过程的重要参量，下文详细给出这 3 个参量的对比分析。

图 2 是四种模态球形沙尘粒子的消光效率因子、单次散射反照率以及不对称因子从短波到红外谱段的变化。如图 2(a)所示，四种模态沙尘气溶胶在可见光区的消光作用差别较小，长波区差异明显。在长波区 MICM 消光作用最强，尤其是在 10 μm 附近消光存在一个极大值，比 MINM 消光效率因子大 1～2 个数量级；MITR 次之，并且与 MIAM 的消光作用差别最小；MINM 的消光作用最弱，在 4～40 μm的消光接近 0。上述差别是由于所采用的谱分布差别[17]所致。

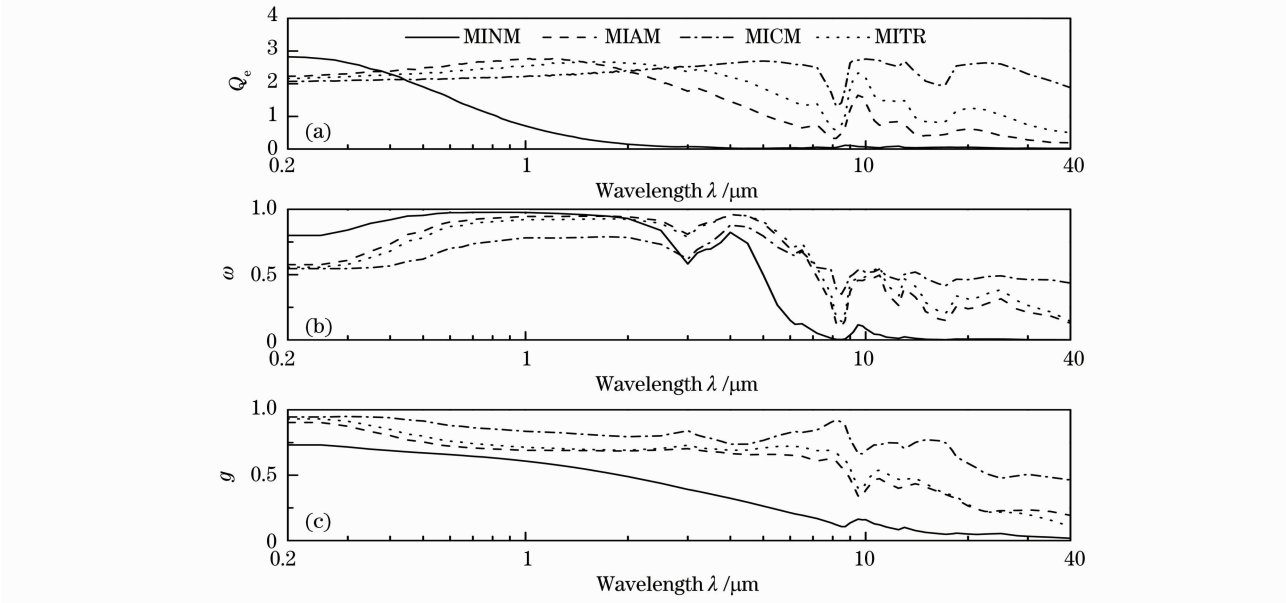


图 2　短波到红外谱段 4 种模态沙尘气溶胶的消光效率因子 $Q_e$(a)，单次散射反照率 $\omega$ (b) 以及不对称因子 $g$(c)随波长的变化

Fig. 2　Change of (a) extinction efficiency factors $Q_e$, (b) single scattering albedo $\omega$ and (c) asymmetrical factors $g$ of four types of dust aerosols with wavelength

由图 2(b)可见，四种模态气溶胶在短波区的单次散射反照率均大于 0.5，并且在可见光区单次散射反照率达到最大，MINM、MIAM、MICM 以及 MITR 的最大值依次为 0.98，0.95，0.88 和 0.93；在长波区四种模态气溶胶的单次散射反照率显著减小，而且不同模态差异明显增大，其中 MICM 与 MINM 相差 1～2 个数量级。另外由图 2(b)可见，在短波区，MINM 沙尘比其他三种模态沙尘的单次散射反照率大，说明小粒子沙尘的散射性最强，而在长波区则相反。

由图 2(c)可见不对称因子随着波长的增大而减小，这是由于随着波长的增大尺度参数在减小，而随着尺度参数的减小，散射更趋近于各向同性的瑞利散射，不对称因子也趋近于 0。另外由图 2(c)可见，从太阳短波到红外谱段范围内 MINM 沙尘粒子比其他 3 种模态的不对称因子小，在短波区 MINM 沙尘粒子与其他 3 种模态沙尘粒子的不对称因子差别较小，在长波区差异显著增大。

图 3 是分别用椭球体与等体积球体计算的沙尘粒子消光效率因子、单次散射反照率以及不对称因子的比值随波长的变化。由图 3 可见，与不同模态沙尘气溶胶光学特性的差异相比，椭球形与球形沙尘之间的光学特性差异不大。

由上述分析可知，MICM 沙尘是决定沙尘气溶胶消光强弱的主要成分，而由图 3(a)可见四种沙尘模态中，MICM 沙尘在椭球和球形两种情况下的消光差别最小，且相对误差在 ±5% 以内。对于 MIAM 和 MITR 沙尘，用椭球形与等体积球形计算的消光效率因子相对误差在 ±10% 以内。MINM 沙尘在两种形状下长波消光差别波动较大，但由上述分析可知 MINM 在长波的消光接近 0，因此，由粒子形状造成的这种消光差异可以忽略。

如图 3(b)所示，在整个波段范围内椭球形与等体积球形计算的四种模态沙尘单次散射反照率相对误差在±5%以内，在散射起主要作用的短波区二者差别最小，其相对误差在±2%之内，这种差别也小于沙尘粒径大小不同所导致的单次散射反照率差别。

如图 3(c)所示，在整个波段范围内椭球形与等体积球形计算的沙尘不对称因子相对误差在±8%以内，这个结果与 Mishchenko 等[3]对不同尺度参数的椭球形与球形沙尘在指数谱分布下的对比结果一致。

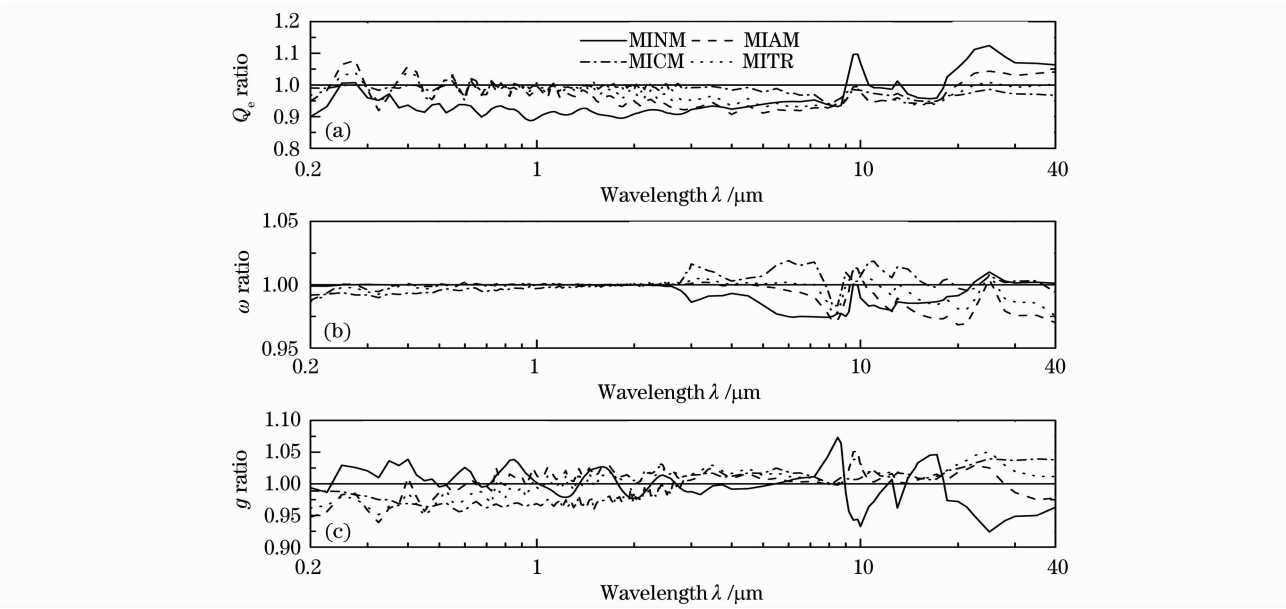


图 3 短波到红外谱段椭球与球形沙尘气溶胶消光效率因子、单次散射反照率以及不对称因子的比值随波长的变化

Fig. 3 Change of ratios of extinction efficiency factors, single scattering albedo and asymmetrical factors of spheroid to those of sphere dust aerosol with wavelength from ultraviolet to infrared band

### 3.3 相函数对比

相函数是散射角的函数，它代表散射能的角分布。在卫星探测反演气溶胶光学厚度时，气溶胶的光学厚度与双向反射比、单次散射反照率以及散射相函数有直接关系，除双向反射比由实测获得外，单次散射反照率以及散射相函数则由气溶胶的尺度分布计算得到，因此，相函数在卫星探测反演气溶胶光学厚度中起着至关重要的作用。

图 4 和图 5 分别给出 MINM 与 MICM 沙尘气溶胶从短波到红外谱段椭球沙尘与球形沙尘相函数的比值，MIAM 与 MITR 两种形状相函数的比值与 MICM 的规律相类似，此处不再赘述。综合图 4，5 可以看出，从 MINM 到 MICM，随着粒子几何平均半径的增大，椭球形与球形相函数的差异也变大，而且对于这两种模态的沙尘，相函数差异都是在短波区大于长波区，尤其是在可见光区差异达到最大。

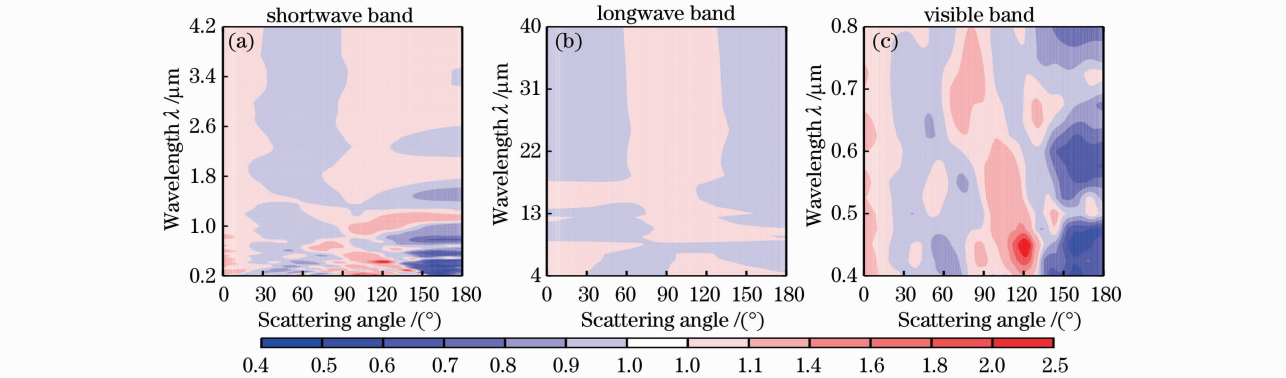


图 4 短波到红外谱段 MINM 椭球沙尘与球形沙尘相函数的比值随波长的变化

Fig. 4 Change of ratios of phase function of spheroid to that of sphere for nucleus mode dust aerosols with wavelength from ultraviolet to infrard band

由图 5 可以看出，MICM 沙尘在短波区相函数差异最明显，尤其是在可见光区，这种差别可以根据散射角分为三个区域：0°～90°，90°～150°以及 150°～180°，其中前向散射（散射角位于 0°～90°）差异较小，后向散射（散射角位于 90°～180°）差异较大。短波区散射角位于 90°～150°时，椭球沙尘比球形沙尘的相函数偏大。在可见光区散射角位于 90°～150°时，对于消光作用最强的 MICM 沙尘，椭球沙尘的相函数是球形沙尘相函数的 10 倍。短波区散射角位于 150°～180°时，椭球沙尘比球形沙尘的相函数偏小。

在可见光区散射角位于 150°～180°时，对于消光作用最强的 MICM 沙尘，椭球沙尘的相函数是球形沙尘相函数的 10%～30%。另外，虽然 MINM 沙尘相函数的差异整体偏小，但是在可见光区散射角位于 150°～180°之间时，椭球沙尘比球形沙尘的相函数明显偏小。

对于 MINM 与 MICM 沙尘，在长波区椭球形与球形相函数的比值均介于 0.9～1.1，因此这种差异相比于短波区而言可以忽略，而且长波区的相函数差异没有显著的规律。

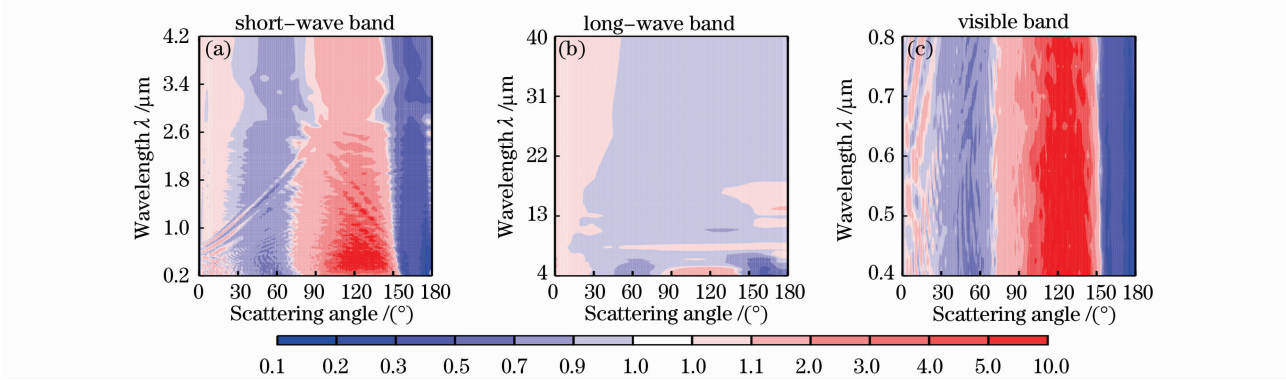


图 5　短波到红外谱段 MICM 椭球沙尘与球形沙尘相函数的比值

Fig. 5　Change of ratios of phase function of spheroid to that of sphere for coarse mode dust aerosols with wavelength from ultraviolet to infrared band

由 3.2 节可知沙尘气溶胶在可见光区的散射消光最强，卫星探测沙尘气溶胶时通常采用可见光通道，而由上述分析可知椭球形与球形沙尘在可见光区的后向散射差异最为明显，而卫星探测气溶胶时主要采用后向散射信号，因此，在卫星探测沙尘气溶胶时应该考虑非球形对沙尘相函数的影响。

由于可见光区椭球与球形相函数差别最大并且该区域对气溶胶遥感非常重要，图 6 比较了 MICM 椭球与球形沙尘在 0.532 μm 的相函数随散射角的变化。与上述分析一致，前向散射差异较小，后向散射差异较大。另外由图可见在散射角位于 90°～150°时球形沙尘相函数起伏较大，而椭球沙尘的相函数更加平滑，而实际沙尘的相函数变化趋势也十分平滑[3,14]，因此用具有一定形状分布的椭球沙尘可以更好的描述实际沙尘的相函数分布。

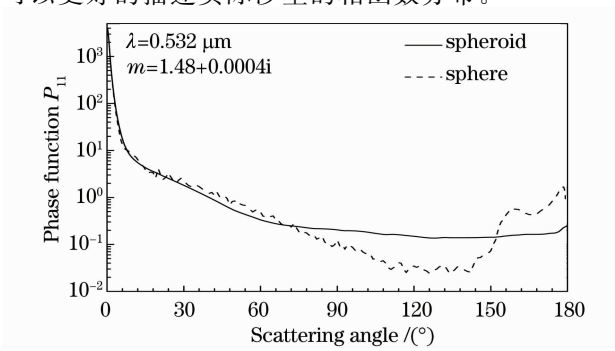


图 6　粗模态椭球与球形沙尘在 0.532 μm 的相函数

Fig. 6　Phase functions of coarse mode dust aerosol based on spheroids and spheres at the wavelength of 0.532 μm

### 3.4　消光后向散射比的对比分析

消光后向散射比在雷达方程中决定后向散射系数与消光系数的参数化关系[18]，它是激光雷达反演气溶胶光学厚度中的一个重要参数。对于洛伦兹-米氏形粒子，根据消光后向散射比的表达式可知其与粒子的复折射指数和谱分布有关。由 3.3 节可知形状对沙尘相函数的影响较大，因此根据消光后向散射比的表达式可推知沙尘气溶胶的消光后向散射比与沙尘形状有关。如图 7 所示，在短波区椭球沙尘与球形沙尘的消光后向散射比有较大差别，其中消光作用最强的粗模态沙尘在两种形状下的消光后向散射比差异最明显，因此沙尘气溶胶的消光后向

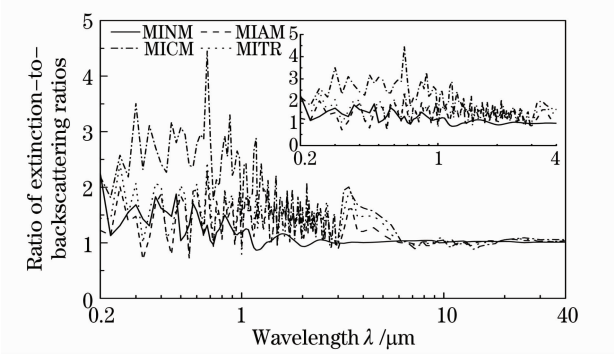


图 7　短波到红外谱段椭球沙尘与球形沙尘消光后向散射比的比值随波长的变化

Fig. 7　Change of ratios of extinction-to-backscattering ratios of spheroid to that of sphere with wavelength from ultraviolet to infrared band

散射比除了与粒子的复折射指数以及谱分布有关外，还要考虑沙尘粒子形状的影响。另外，由图 7 可见，在长波区椭球沙尘与球形沙尘的消光后向散射比没有明显的差异，由第 3.3 节分析可知，这是因为长波区二者的相函数差别较小。

由于激光雷达探测气溶胶通常采用小于 1 μm 的短波波段，如图 7 所示这个区域椭球沙尘与球形沙尘的消光后向散射比差异最为显著，因此，在用激光雷达反演沙尘气溶胶光学厚度时考虑非球形效应是非常必要的。

由于短波波段椭球与球形消光后向散射比差异明显，并且激光雷达探测气溶胶通常采用小于 1 μm 的短波波段，图 8 给出了短波波段四种模态椭球沙尘的消光后向散射比随波长的变化。由图 8 可见，在 0.2～0.5 μm 范围内不同模态椭球沙尘的消光后向散射比随波长的变化起伏较大，其中 MINM 与 MICM 的起伏最明显；在激光雷达探测常用的 0.5～0.7 μm 范围内，四种模态椭球沙尘的消光后向散射比随波长的变化起伏较小，MINM，MIAM，MITR 和 MICM 的消光后向散射比数值分别维持在 5，2，2 和 4 附近。另外由图 8 可见，除 MINM 以外，其他三种模态椭球沙尘的消光后向散射比在波长 3 μm 附近有个明显的峰值。

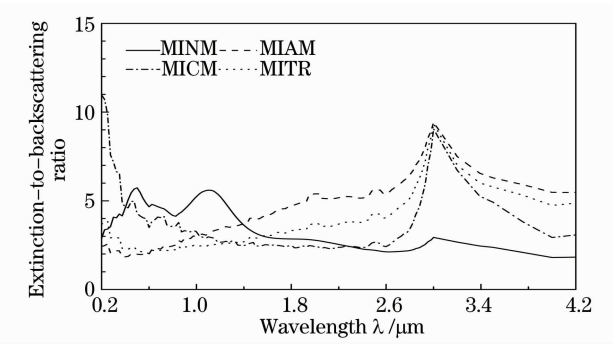


图 8 短波波段四种模态椭球沙尘的消光后向散射比随波长的变化

Fig. 8 Change of extinction-to-backscattering ratios of spheroid for four modes with wavelength in short-wave band

## 4 结 论

本文将 T 矩阵算法与几何光学方法相结合来计算椭球沙尘粒子的光学特性，并在此基础上讨论了形状对沙尘光学特性的影响。研究表明，与沙尘粒径大小分布对沙尘气溶胶消光效率因子、单次散射反照率以及不对称因子的影响相比，沙尘形状对上述参数的影响明显偏小。

椭球与球形沙尘的相函数在卫星探测常用的可见光区达到最大。在可见光区散射角位于 0°～90° 时椭球与球形相函数的差异较小；在散射角位于 90°～150°时，椭球比球形沙尘的相函数偏大，在这个区域 MICM 椭球沙尘是球形沙尘相函数的 10 倍；当散射角位于 150°～180°时，椭球比球形沙尘的相函数偏小，在这个区域 MICM 椭球沙尘是球形沙尘相函数的 10%～30%。因此，在卫星反演气溶胶光学厚度过程中必须考虑非球形对沙尘相函数的影响。

最后，对消光后向散射比的研究表明，在短波区沙尘气溶胶的消光后向散射比除了与粒子的复折射指数以及谱分布有关外，也要考虑沙尘粒子形状的影响，因此，在用激光雷达反演沙尘气溶胶光学厚度时也应该考虑沙尘的非球形效应。

**致谢** 感谢美国德克萨斯 A&M 大学大气科学系杨平教授和美国华盛顿大学大气科学系傅强教授对本文的指导和帮助。

## 参 考 文 献

1 Y. Gao, J. R. Anderson. Characteristics of Chinese aerosols determined by individual-particle analysis [J]. *J. Geophys. Res.*, 2001, **106**(D16): 18037～18045

2 K. Okada, J. Heintzenberg, K. Kai *et al.*. Shape of atmospheric mineral particles collected in three Chinese arid-egions [J]. *Geophys. Res. Lett.*, 2001, **28**(16): 3123～3126

3 M. I. Mishchenko, L. D. Travis, R. A. Kahn *et al.*. Modeling phase functions for dust tropospheric aerosols using a shape mixture of randomly oriented polydisperse spheroids [J]. *J. Geophys. Res.*, 1997, **102**(D14): 16831～16847

4 P. Yang, Q. Feng, G. Hong *et al.*. Modeling of the scattering and radiative properties of nonspherical dust aerosols [J]. *J. Aerosol Sci.*, 2007, **38**(10): 995～1014

5 Q. Fu, T. J. Thorsen, J. Su *et al.*. Test of Mie-based single-scattering properties of non-spherical dust aerosols in radiative flux calculations [J]. *J. Quant. Spectrosc. Radiat. Transfer*, 2009, **110**(14-16): 1640～1653

6 Gong Chunwen, Wei Heli, Li Xuebin *et al.*. The influence of the aspect ratio to the light scattering properties of cylinder ice particles [J]. *Acta Optica Sinica*, 2009, **29**(5): 1155～1159
宫纯文，魏合理，李学彬 等. 取向比对圆柱状冰晶粒子光散射特性的影响 [J]. 光学学报，2009，**29**(5)：1155～1159

7 Shao Shiyong, Huang Yinbo, Wei Heli *et al.*. Phase function of prolate spheroidic mono-disperse aerosol particles [J]. *Acta Optica Sinica*, 2009, **29**(1): 108～113
邵士勇，黄印博，魏合理 等. 单分散长椭球形气溶胶粒子的散射相函数研究 [J]. 光学学报，2009，**29**(1)：108～113

8 P. C. Waterman. Symmetry, unitarity, and geometry in electromagnetic scattering [J]. *Phys. Rev. D*, 1971, **3**(4): 825～839

9 M. I. Mishchenko, L. D. Travis. T-matrix computations of light scattering by large spheroidal particles [J]. *Opt. Commun.*,

1994, **109**(1-2): 16～21

10 Ping Yang, Heli Wei, Hung-Lung Huang *et al*.. Scattering and absorption property database for nonspherical ice particles in the near-through far-infrared spectral region [J]. *Appl. Opt.*, 2005, **44**(26): 5512～5523

11 P. Yang, K. N. Liou. Geometric-optics-integral-equation method for light scattering by nonspherical ice crystals [J]. *Appl. Opt.*, 1996, **35**(33): 6568～6584

12 M. I. Mishchenko, L. D. Travis, A. A. Lacis. Scattering, Absorption, and Emission of Light by Small Particles [M]. Eds. Cambridge, United Kingdom: Cambridge University Press, 2002. 445

13 W. J. Wiscombe. Improved Mie scattering algorithms [J]. *Appl. Opt.*, 1980, **19**(9): 1505～1509

14 O. Dubovik, A. Sinyuk, T. Lapyonok *et al*.. Application of spheroid models to account for aerosol particle nonsphericity in remote sensing of desert dust [J]. *J. Geophys. Res.*, 2006, **111** (D11208): 1～34

15 J. T. Houghton, Y. Ding, D. J. Griggs *et al*.. Climate Change 2001: The Scientific Basis [M]. Eds. Cambridge, United Kingdom and New York, NY, USA: Cambridge University Press, 2001. 881

16 Wang Hong, Shi Guangyu, T. Aoki *et al*.. Radiative forcings of dust aerosol over East Asia-North Pacific in 2001 spring [J]. *Chinese Science Bulletin*, 2004, **49**(19): 1993～2000
王　宏，石广玉，T. Aoki 等. 2001 年春季东亚-北太平洋地区沙尘气溶胶的辐射强迫 [J]. 科学通报, 2004, **49**(19): 1993～2000

17 M. Hess, P. Koepke, I. Schult. Optical properties of aerosols and clouds: the software package OPAC [J]. *Bull. Amer. Meteor. Soc.*, 1998, **79**(5): 863～844

18 G. L. Stephens. Remote Sensing of the Lower Atmosphere: an Introduction [M]. New York, NY, USA: Oxford University Press, 1994. 486

19 Liou Guonan. An Introduction to Atmospheric Radiation (Second Edition) [M]. Guo Caili, Zhou Shijian Transl. Beijing: China Meteorological Press, 2004. 108
廖国男. 大气辐射导论(第 2 版) [M]. 郭彩丽，周诗健译. 北京:气象出版社, 2004. 108

**文章编号**:1000-0240(2011)03-0479-09

# 新疆 21 世纪气候变化的高分辨率模拟

吴　佳[1,2,3]，　高学杰[3*]，　石　英[3]，　Filippo Giorgi[4]

(1. 中国气象科学研究院，北京　100081；2. 中国科学院 研究生院，北京　100049；3. 国家气候中心，北京　100081；
4. The Abdus Salam International Centre for Theoretical Physics，I-34151 Trieste，Italy)

**摘　要**：使用一个 25 km 高水平分辨率区域气候模式(RegCM3)，嵌套 MIROC3. 2_hires 全球气候模式结果，进行了 IPCC SRES A1B 情景下，东亚区域 21 世纪气候变化的模拟，针对新疆地区进行了分析. 首先对模式模拟的当代(1981—2000 年)气候进行检验，结果表明：模式对年平均气温、降水的空间分布和数值均具有较好的模拟能力，但与观测相比，模拟的气温一般在盆地偏高、山区偏低，降水则在盆地偏少、山区偏多. 在 IPCC SRES A1B 温室气体排放情景下，21 世纪中期(2041—2060 年)及末期(2081—2100 年)新疆地区冬、夏季气温均将升高，末期的增温幅度更大，特别是在末期的冬季. 降水除个别地区外将普遍增加，同样末期增加更多. 在不同地形条件下，气温和降水的变化特点均有所不同，其中盆地增温大、山区增温小，降水量在山区和盆地过渡地带的变化最明显，以增加为主并表现出一定的季节特征. 相对于全国平均而言，新疆地区的增温和降水量增加更显著.

**关键词**：气候变化；区域气候模式；新疆地区

**中图分类号**：P467　　**文献标识码**：A

## 0　引言

新疆地处欧亚大陆腹地，面积超过中国陆地面积的六分之一，幅员辽阔，南北跨度大，地形地貌有“三山夹两盆”之称，山脉与盆地相间排列，由南至北依次为昆仑山、塔里木盆地、天山、准噶尔盆地和阿尔泰山. 新疆远离海洋，气候特征明显，属典型的温带大陆性干旱气候. 其中天山以北的北疆为中温带，受西风带影响，降水稍多. 南疆为暖温带，降水稀少. 高山地区为高地气候，地形降水较多，所形成的积雪和冰川，是这一地区重要的水资源来源.

新疆地区气候条件较差，生态系统独特而脆弱. 多年来我国学者对这一地区的气候及环境等方面开展了广泛的研究，取得了很多成果和发现[1-8]. 研究表明，和全球一样，新疆和西北地区最近几十年来经历了以变暖为主的气候变化，而 1980 年代末以后气候又呈现自暖干向暖湿的转型[2].

IPCC 第四次评估报告指出，未来全球气候将继续增暖，到 21 世纪末，全球平均气温将升高 1.1～6.4 ℃[9]. 全球持续变暖将引起水文循环的变化，在由于大气含水能力提高降水增加的同时，会引起水资源在时空上的重新分配.

全球气候模式是气候变化模拟和预估的首要工具，一些研究使用不同全球模式的结果，给出了中国西北及新疆地区的未来气候变化[10-12]，在更高分辨率的区域气候模式的应用方面，也有了一些工作[13-14]. 为更深入了解未来新疆地区的气候变化，本文使用 RegCM3 区域气候模式，进行了东亚区域 21 世纪气候变化的模拟试验，并对试验结果中，新疆地区 21 世纪气候变化情况进行了分析.

## 1　模式、试验设计和资料

本文所使用的模式，是意大利国际理论物理中心(The Abdus Salam International Center for The-

**收稿日期**：2010-09-17；**修订日期**：2011-04-11

**基金项目**：国家重点基础研究发展规划(973 计划)项目(2009CB421407；2007CB411505)；公益性行业(气象)科研专项(GYHY200806010)；国家自然科学基金项目(40975041)资助

**作者简介**：吴佳(1984—)，女，湖南怀化人，2009 年在中国气象科学研究院获硕士学位，现为中国气象科学研究院在读博士研究生，主要从事区域气候变化及气候模拟研究. E-mail：wujia@cma. gov. cn

* 通讯作者：高学杰，E-mail：gaoxj@cma. gov. cn

oretical Physics)发展的区域气候模式 RegCM3[15]，它是在原 RegCM2 模式[16-17]基础上发展而来的. 试验中模式垂直方向分 18 层，顶层高度为 10 hPa. 模拟中的辐射采用 NCAR CCM3 方案，陆面过程使用 BATS1e(生物圈-大气圈传输方案)，行星边界层方案使用 Holtslag 方案，大尺度降水采用 SUBEX 方案. 经过模式在采用不同积云对流参数化方案情况下模拟效果的比较和检验，试验选择了基于 Fritsch-Chappell 闭合假设的 Grell 方案[18-19]，以得到中国地区的最佳模拟效果(详细结果和分析略)，这也和以往工作所报告的结果相同[20].

试验中，模式中心点取为 35° N、109° E，模式的水平分辨率取为 25 km，格点数为 288×219(东西×南北)，范围覆盖整个中国及其周边地区(图 1b)，所进行的模拟时段为 1951—2100 年，其中 2000 年之前使用观测的温室气体浓度，2000 年之后使用的是 IPCC SRES A1B 温室气体排放情景下的浓度值. A1B 是一个中等排放情景，至 2100 年的 $CO_2$ 浓度值约为 700 mL·m$^{-3}$.

模式使用的地形资料由美国地质勘探局(United States Geological Survey)制作的 10′×10′(经度×纬度)地形数据插值得到. 中国区域内植被资料使用文献[21]的实测资料，中国区域外使用 USGS 基于卫星观测反演的 GLCC(Global Land Cover Characterization)资料. 初始场和侧边界值均由日本的全球模式 CCSR/NIES/FRCGCMIROC3.2_hires(以下简称 MIROC)得到[22]，侧边界场采用指数松弛边界方案，每 6 h 输入模式 1 次，由于区域较大，模式的缓冲区设为 24 个格点(缺省值为 12 个). MIROC 模式水平分辨率为 T106(约为 100 km×100 km)，以往对气候模拟能力的分析表明，MIROC 在世界上的多个全球模式中，是对中国特别是中国东部季风区气候平均态模拟效果最好的模式[23].

本文的模拟分析集中于新疆及其中国境内相邻的周边地区，包括青藏高原北部和青海、甘肃西部等(图 1a)，图 1(a)可以看到，RegCM3 对这里的地形有较细致和精确的描述，“三山夹两盆”的独特地形得到了准确的刻画. 阿尔泰山、天山、昆仑山与准噶尔盆地、塔里木盆地之间地势高低的转变，以及如吐鲁番和哈密盆地及伊犁河谷等较小尺度的地形也得到了较好表述.

为简明起见，本文主要给出 RegCM3 模拟的结果，分析的时段为 1981—2100 年，其中 1981—2000 年做为模式对当代气候的模拟，2001—2100 年为对未来气候的预估. 检验模式对当代气候模拟能力所需的气温和降水资料，分别采用了 CN05[24]和 Xie[25]的日数据集，其水平分辨率均为 0.5°×0.5°(经纬度).

## 2 对新疆地区当代气候模拟的检验

### 2.1 年平均气温

图 2(a)，(b)分别给出观测及 RegCM3 模拟的当代(1981—2100 年)年平均气温分布. 图 2(a)观测中的气温高值中心出现在塔里木盆地、吐鲁番盆地等地，数值在 9 ℃以上，部分地区达到 12 ℃以上，阿尔泰山、天山、昆仑山和祁连山等山区附近为低值中心，中心气温值低于−9 ℃. 与观测相比，图 2(b)中 RegCM3 的模拟很好的再现了观测中盆地气温较高，山区气温较低的分布. 此外，模式对较小尺度地形引起的温度波动也有很好的描述，如天山东部巴里坤一带以及甘肃与新疆交界处的北山与邻近低地的气温冷暖对比等，都得到较好体现. 但模式模拟的塔里木盆地西部和准噶尔盆地等沙漠地区的气温值偏高，而在其他大部分地方，如昆仑山以南的青藏高原地区、祁连山及柴达木盆地等，模拟气温值偏低.

### 2.2 年平均降水

图 2(c)，(d)分别给出观测及 RegCM3 模拟的当代年平均降水. 由图 2(c)观测可见，阿尔泰山、天山、祁连山区及柴达木盆地以南地区降水在 500 mm 以上，其他地区降水量不到 250 mm，尤其盆地内部降水稀少，年平均降水量不足 50 mm. 模拟降水分布(图 2d)与观测较为一致，盆地降水少，山区降水多的分布形势得到了较好的表现.

模式所模拟的如塔里木盆地中部和准噶尔盆地的降水值较观测偏少，注意到这些盆地内部一般为沙漠地区，缺少气象台站观测，所使用的观测场在这些地区的数值，是由周边台站资料内插得来的，可能会与实际情况有所不符，有研究表明，塔里木盆地腹地的年平均降水在 25 mm 以下[26-27]，与模拟更接近(图 2d).

模式模拟的山区降水与观测值相比偏高，其原因除模式本身的误差外，一方面同样与观测台站不足有关，如在实际气候中，昆仑山北坡存在着较大的降水，是塔里木盆地南侧各河流水量的来源[28-29]，而由于这里缺乏固定的气象观测站点[25]，

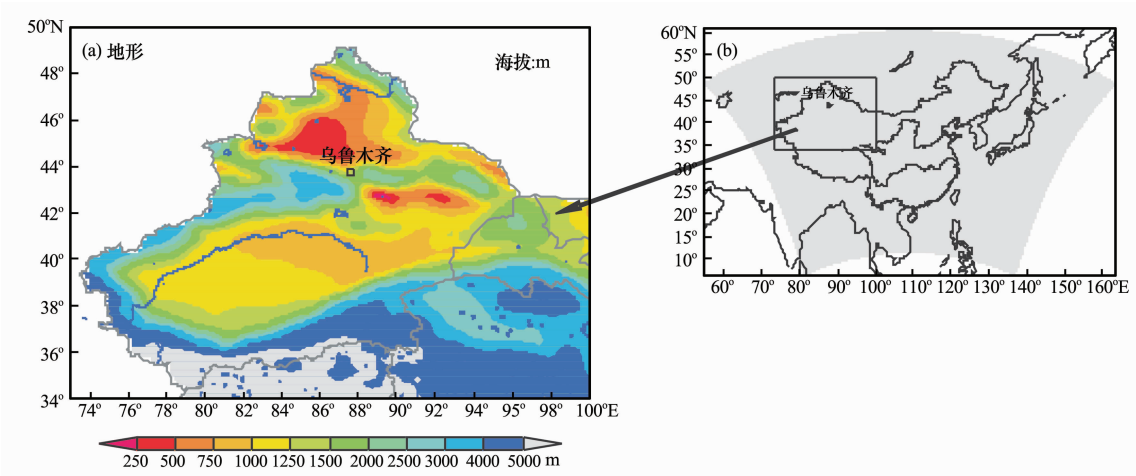


图 1　RegCM3 对关注地区地形分布的描述(a)(单位：m)及模拟区域(b 中的灰色部分)

Fig. 1　Topography over the analyzed area (a) (unit: m) and RegCM3 domain (b, shaded area)

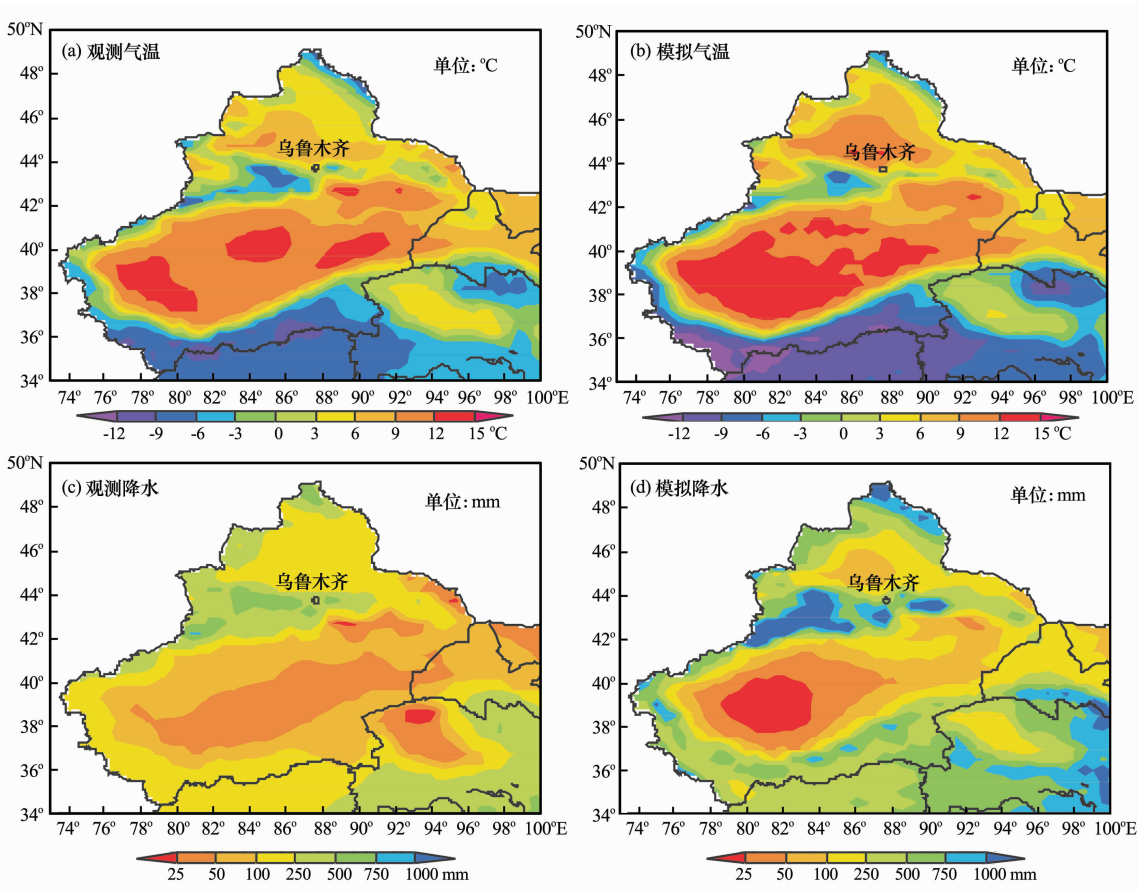


图 2　观测和 RegCM3 模拟的当代年平均气温(单位：℃)及降水(单位：mm)分布

Fig. 2　The observed and RegCM3 simulated annual mean temperatures (unit: ℃) and precipitations (unit: mm)

(a) observed temperature; (b) temperature simulated by RegCM3; (c) observed precipitation; (d) precipitation simulated by RegCM3

使得这一降水特点在使用的“观测”资料中没有出现(图 2c)，而在模拟中则有所反映(图 2d). 同时高山地区固态降水观测方面的误差[30-31]也会对此有一定影响. 以上说明了气象观测站网的分布密度及观测准确性在模式检验中的重要性.

## 3　对新疆地区未来气候变化的预估

### 3.1　21 世纪气温变化

图 3 给出 RegCM3 模拟新疆地区 21 世纪中期(2041—2060年)和末期(2081—2100年)冬、夏气

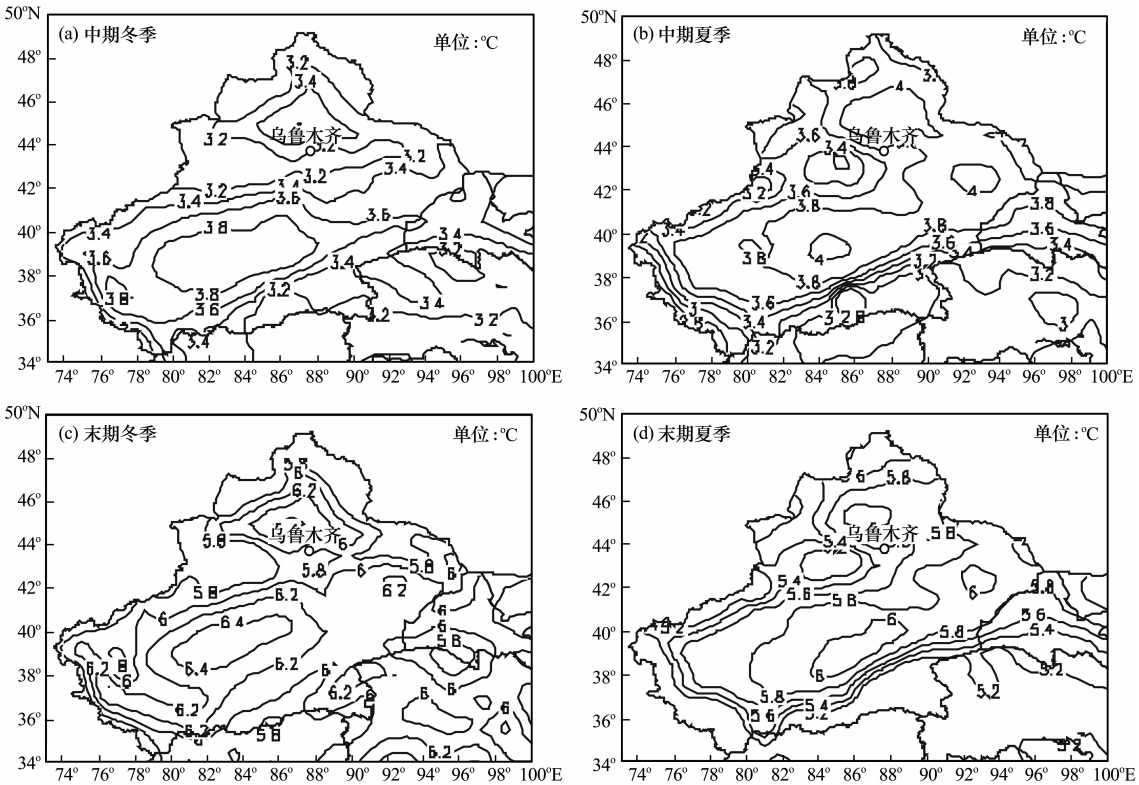


图 3 RegCM3 模拟的新疆地区 21 世纪中(2041—2060 年)、末期(2081—2100 年)冬夏气温变化(相对于 1981—2000 年)

Fig. 3 Winter and summer mean temperatures over Xinjiang Region in the middle (2041—2060) and end (2081—2100) of 21st century simulated by RegCM3 (in relative to 1981—2000, unit: ℃)

(a) winter, middle; (b) summer, middle; (c) winter, end; (d) summer, end

温的变化. 由图 3(a)可以看到，21 世纪中期新疆地区冬季气温将普遍升高，其中盆地是增温的大值区，特别是塔里木盆地，大部分地区增温值在 3.8 ℃以上，山区的增温相对较小，一般为 3.2 ℃左右. 夏季增温的分布特点和冬季类似，但数值在青藏高原稍低而其他地区偏高.

21 世纪末期新疆地区冬季气温的变化(图 3c)与中期相比分布形势基本相同，但升温幅度更明显. 如末期塔里木盆地的增温值由中期的 3.8 ℃增加到 6.2 ℃以上，天山地区等也由中期的 3.2 ℃左右增加到末期的 5.8 ℃以上. 夏季气温在末期的变化(图 3d)特征和冬季类似，但增温幅度整体较冬季要小. 一般来说由于冰雪和气温的正反馈作用[32]，全球变暖在高纬度和山地更显著，但在新疆地区出现了盆地较山地更大的升温现象，这种局地气候变化特点的机制有待进一步的研究和说明.

图 4 给出 1981—2100 年中国和新疆区域平均的年气温变化曲线，可以看到未来随着温室气体的增加，中国和新疆地区气温都呈上升趋势，2011—2100 年的增温趋势值分别为 0.53 ℃·(10a)$^{-1}$ 和 0.56 ℃·(10a)$^{-1}$，新疆地区的增温幅度较全国平均略大. 21 世纪中期新疆平均增温为 3.2 ℃左右，末期达 5.4 ℃以上.

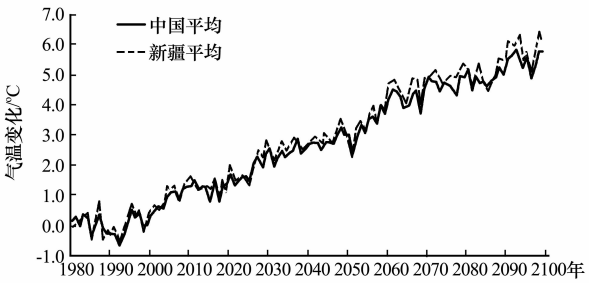


图 4 RegCM3 模拟的 1981—2100 年中国(实线)和新疆(虚线)区域年平均气温变化(相对于 1981—2000 年)(单位: ℃)

Fig. 4 Variations of regional annual mean temperatures (unit: ℃) from 1981 to 2100 (in relative to 1981—2000) over China (solid) and Xinjiang Region (dashed) simulated by RegCM3

### 3.2 21 世纪降水变化

图 5 给出 RegCM3 模拟的新疆地区未来降水变化. 从图 5(a)可以看到，21 世纪中期，新疆冬季降水在大部分地区都将增加，增加百分率基本在 5%～50%之间，其中塔里木盆地除中部外，是增加

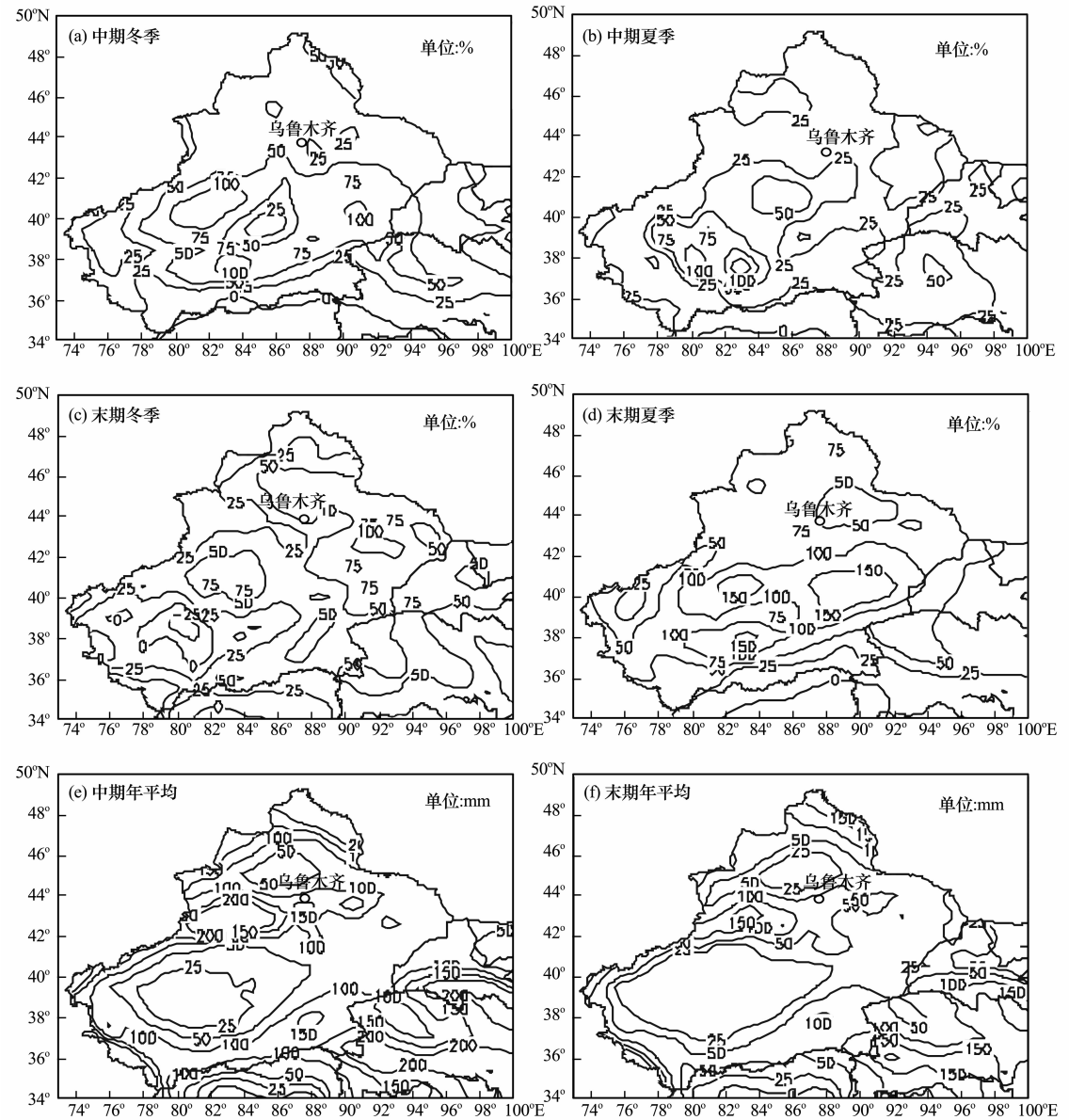


图 5　RegCM3 模拟新疆地区 21 世纪中、末期冬、夏(单位：%)及年平均(单位：mm)降水变化

Fig. 5　Winter, summer (unit: %) and annual mean precipitations (unit: mm) in the middle and end of 21st century over Xinjiang Region simulated by RegCM3

(a) winter, middle; (b) summer, middle; (c) winter, end; (d) summer, end; (e) annual, middle; (f) annual, end

的大值区，增加的数值一般在 75%以上，在盆地边缘部分地区可以达到一倍以上. 区域内仅昆仑山北坡降水有所减少.

21 世纪中期的夏季降水除个别地方外，同样将普遍增加(图 5b)，增幅与冬季相近，但具体分布上有所不同，塔里木盆地西南部降水相对增加最多，数值同样可以达到一倍以上.

21 世纪末期冬季降水变化特点和中期基本一致(图 5c)，为大范围的增加，而且数值更大，大部分地区在 50%以上，塔里木盆地部分地区增加值超过 1.5 倍. 同时存在于 21 世纪中期昆仑山北坡的降水减少区，其范围和数值在末期都有所减小. 与冬季相比，夏季降水的增加值偏小，大值区位置也有所变化(图 5d)，位于区域的东北部及塔里木盆地北部，数值在 75%以上，而塔里木盆地西部及南部地区降水则为减少，减少最多可达 25%.

新疆地区降水在各地的分布非常不均匀，为更好的了解全球变暖对这里降水的影响，图 5(e, f)分别给出新疆地区中期和末期年平均降水量的绝对变化. 可以看到，21 世纪中期年降水量增加最大的

为阿尔泰山、天山、昆仑山和祁连山区，增加值基本都在 100 mm 以上，盆地降水量增加相对较少，增加值一般在 25 mm 左右. 这与以降水百分率为单位的结果有所不同，主要是由于山区降水基数较大，盆地降水基数较小引起的(图 2d). 21 世纪末期降水量增加值在整个区域内都比中期要大(图 5f)，尤其是山区，增幅超过 150 mm.

1981—2100 年中国和新疆区域平均的年降水相对变化曲线在图 6 中给出. 可以看到，未来中国和新疆地区降水相对于当代均有增加趋势，其 2011—2100 的趋势值分别为 1.1%·$(10a)^{-1}$ 和 2.7%·$(10a)^{-1}$，新疆地区降水增加值更大. 21 世纪中期新疆区域平均降水量将增加 13%左右，到末期则将增加 26%.

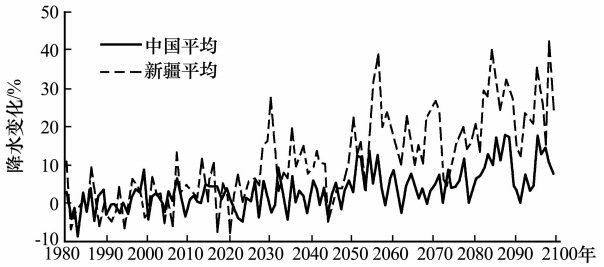


图 6 同图 4，但为降水(单位：%)

Fig. 6 Same as Fig. 4, but for precipitation (unit: %)

### 3.3 新疆地区气温、降水变化与地形的关系

为进一步了解新疆不同地形区未来气候变化的特征，图 7(a，b)分别给出 RegCM3 模拟的 21 世纪中期和末期，沿 84°～87° E 平均的气温和降水量在冬、夏季变化的剖面图.

从图 7(a)可见，总体来说，新疆不同地形下的增暖幅度有较大差别. 21 世纪中期冬、夏季的增温幅度接近，并且均在山区小，盆地大，如昆仑山地区冬季增温不到 3.0 ℃，而塔里木盆地则在 3.5 ℃以上. 昆仑山地区冬季增温较夏季大，塔里木盆地冬、夏季差别不大，而准噶尔盆地和位于中国与哈萨克斯坦交界处的塔尔巴哈台山的增温则为夏季更大.

21 世纪末期冬、夏季气温增加更显著，其特点与中期一样，增幅与地形变化之间也存在较好的对应关系，仍然是山区增幅相对较小，盆地增幅大，但与中期不同的是冬、夏季增温有较大差异，冬季增温值普遍较夏季大 0.5～1 ℃左右，其中冬季的塔里木盆地中部和准噶尔盆地中部，增温值在 6.0 ℃以上，夏季增温最少的昆仑山北部地区，数值在 4.5 ℃以下. 21 世纪末期冬季较夏季更大的增温，可能与未来冰雪覆盖减少与气温之间的正反馈过程有关[14, 32].

图 7(b)表明降水量变化与地形之间同样也有较好的对应关系. 21 世纪中期，冬季昆仑山北坡至塔里木盆地南部一带降水增加，但增加幅度较小，在 10 mm 以下. 塔里木盆地内部降水变化也不大，但天山地区降水增加显著，峰值出现在天山北坡，降水约增加 30 mm. 进入准噶尔盆地之后降水增加有较大减少，而在塔尔巴哈台山则重新达到近 40 mm.

21 世纪中期夏季降水变化随地形的分布与冬季大体类似，在盆地增加较少，山地增加明显，但昆仑山北坡到塔里木盆地南部一带，夏季降水量增加达 30 mm 以上，大于冬季. 天山地区降水增加的最大值与冬季不同，出现在天山南坡，而天山北坡降水则为有所减少，表现出一定的“雨影”效应. 天

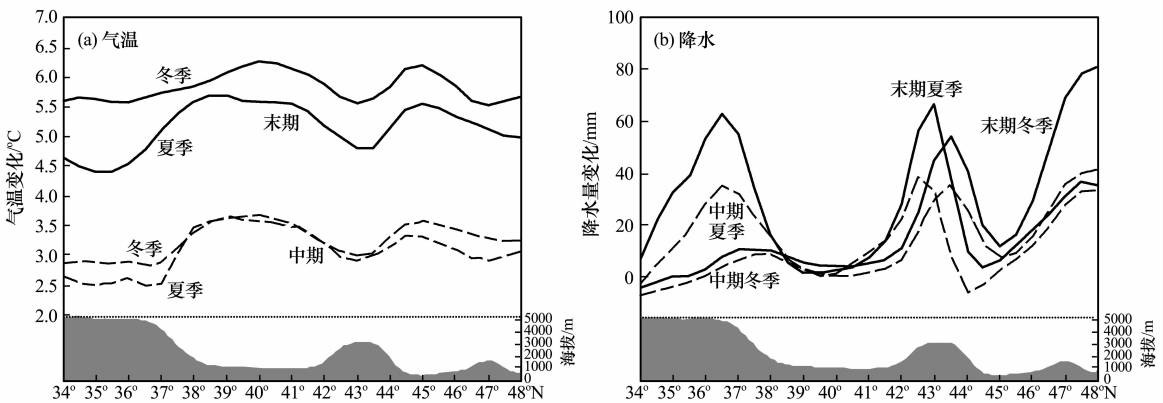


图 7 RegCM3 模拟的 21 世纪中期、末期 84°～87° E 平均冬、夏气温(单位：℃)和降水(单位：mm)的变化(相对于 1980—2000 年)

Fig. 7 Summer and winter mean temperatures (unit: ℃) and precipitations (unit: mm) over 84°～87°E in the middle and end of 21st century simulated by RegCM3 (in relative to 1980—2000)

The dashed lines are for the middle of 21st century, the solid lines are for the end of 21st century. Blue indicates winter and red indicates summer

山地区这种不同季节降水变化的不同，可能与在高分辨率模式模拟中出现的相应环流变化有关[33]. 夏季准噶尔盆地和塔尔巴哈台山地区降水的特点和大小与冬季基本一致.

21 世纪末期冬季降水的变化，在天山以南和中期相似，而在天山以北，降水增加的幅度较中期大很多，在塔尔巴哈台山的增加幅度达到中期的近一倍. 夏季降水的变化特点同样与 21 世纪中期夏季的变化较为一致，二者在塔里木、准噶尔盆地和塔尔巴哈台山的变化数值也接近，但在昆仑山和天山地区降水量的增加值较中期大很多，达到 60 mm 左右.

## 4　总结和讨论

使用区域气候模式 RegCM3，嵌套日本 MIROC3.2_hires 全球模式资料，进行了 IPCC SRES A1B 情景下，东亚地区 21 世纪气候变化的连续积分模拟，针对新疆地区，在模式检验的基础上，给出了这一地区未来的气候变化预估结果.

结果表明，在全球变暖背景下，新疆地区的气温将不断升高，区域平均的增温幅度较中国略大，增温在盆地较山区更显著，21 世纪中期冬、夏季的增温数值接近，但在末期冬季的增温更大. 在增温的同时，模式模拟得到的新疆地区冬、夏季降水也将普遍增加. 降水的相对增加在山地较盆地明显，降水量的增加则为山地更大，本世纪末天山和祁连山等地的年平均降水增加在 200 mm 以上. 21 世纪末期降水增加幅度一般来说大于中期. 相对于全国平均来说，新疆地区降水的增加更显著，21 世纪中期和末期新疆地区的年平均降水将分别增加 13% 和 26%左右.

新疆地区气温、降水变化特征与地形的对应关系，从经向平均的剖面图上得到了更好的表示，降水的变化以从山区向盆地的过渡地带最明显，同时在山脉两侧，在不同季节的降水变化也表现出一定的不同.

未来降水的增加，有利于新疆地区的社会、经济生活，以及生态环境的保护和改善，但气温升高引起的蒸发增加，会在相当程度上抵消这种正面作用，其综合效应有待进一步研究[34－35]. 此外本文和其他有限的关于新疆地区的区域气候模式模拟[13, 36]，都给出了未来这里降水会增加的结果，并与最近的观测表现出一定相似性[2]，但受诸如气候模式发展水平(如本模拟中对当代气温和降水模拟的偏差)、未来温室气体排放情景、对气候变化科学的认知以及气候模式发展水平方面等的限制，所得结果仍存在较大程度上的不确定性. 未来在改进模式基础上，进行多区域模式的集合预估，可望取得对新疆地区未来气候变化这一问题更进一步的认识.

## 参考文献(References)：


[1] Qin Dahe. Assessment of Environmental Evolution in Western China: Synthesis Report[M]. Beijing: Science Press, 2002: 1－80. [秦大河. 中国西部环境演变评估综合报告[M]. 北京：科学出版社，2002：1－80.]

[2] Shi Yafeng, Shen Yongping, Hu Ruji. Preliminary study on signal, impact and foreground of climate shift from warm-dry to warm-humid in Northwest China[J]. Journal of Glaciology and Geocryology, 2002, **24** (3): 219－226. [施雅风，沈永平，胡汝骥. 西北气候由暖干向暖湿转型的信号、影响和前景初步探讨[J]. 冰川冻土，2002，**24**(3)：219－226.]

[3] Li Dongliang, Wei Li, Cai Ying, *et al*. The present facts and the future tendency of the climate change in Northwest China [J]. Journal of Glaciology and Geocryology, 2003, **25**(2): 135－142. [李栋梁，魏丽，蔡英，等. 中国西北现代气候变化事实与未来趋势展望[J]. 冰川冻土，2003，**25**(2)：135－142.]

[4] Su Hongchao, Wei Wenshou, Han Ping. Changes in air temperature and evaporation in Xinjiang during recent 50 years [J]. Journal of Glaciology and Geocryology, 2003, **25**(2): 174－178. [苏宏超，魏文寿，韩萍. 新疆近 50 年来气温和蒸发变化[J]. 冰川冻土，2003，**25**(2)：174－178.]

[5] He Qing, Yang Qing, Li Hongjun. Variations of air temperature, precipitation and sand-dust weather in Xinjiang in past 40 years[J]. Journal of Glaciology and Geocryology, 2003, **25**(4): 423－427. [何清，杨青，李红军. 新疆 40 a 来气温、降水和沙尘天气变化[J]. 冰川冻土，2003，**25**(4)：423－427.]

[6] Liu Shiyin, Ding Yongjian, Zhang Yong, *et al*. Impact of the glacial change on water resources in the Tarim River Basin [J]. Acta Geographica Sinica, 2006, **61**(5): 482－490. [刘时银，丁永建，张勇，等. 塔里木河流域冰川变化及其对水资源影响[J]. 地理学报，2006，**61**(5)：482－490.]

[7] Su Hongchao, Shen Yongping, Han Ping, *et al*. Precipitation and its impact on water resources and ecological environment in Xinjiang region[J]. Journal of Glaciology and Geocryology, 2007, **29**(3): 343－350. [苏宏超，沈永平，韩萍，等. 新疆降水特征及其对水资源和生态环境的影响[J]. 冰川冻土，2007，**29** (3)：343－350.]

[8] Ding Yongjian, Ye Baisheng, Han Tianding, *et al*. Regional difference of annual precipitation and discharge variation over west China during the last 50 years[J]. Science in China (Series D), 2007, **50**(6): 936－945. [丁永建，叶柏生，韩添丁，等. 过去 50 年中国西部气候和径流变化的区域差异[J]. 中国科学(D 辑)，2007，**37**(2)：206－214.]

[9] Solomon S, Qin D, Manning M, *et al*. Climate Change 2007: The Physical Science Basis. Contribution of Working Group I to the Fourth Assessment Report of the Intergovernmental

Panel on Climate Change[M]. Cambridge, United Kingdom and New York, USA: Cambridge University Press, 2007: 1—996.

[10] Xu Ying, Ding Yihui, Zhao Zongci. Scenario of temperature and precipitation changes in Northwest China due to human activity in the 21st century[J]. Journal of Glaciology and Geocryology, 2003, **25** (3): 327—330. [徐影, 丁一汇, 赵宗慈. 人类活动引起的我国西北地区 21 世纪温度和降水变化情景分析[J]. 冰川冻土, 2003, **25** (3): 327—330.]

[11] Jiang Dabang, Su Mingfeng, Wei Rongqing, *et al*. Variation and projection of dought and wet conditions in Xinjiang[J]. Chinese Journal of Atmospheric Sciences, 2009, **33**(1): 90—98. [姜大膀, 苏明峰, 魏荣庆, 等. 新疆气候的干湿变化及其趋势预估[J]. 大气科学, 2009, **33**(1): 90—98.]

[12] Xu Chonghai, Xu Ying, Luo Yong. Climate change of the 21st Century in Xinjiang with SRES scenarios[J]. Desert and Oasis Meteorology, 2008, **2**(3): 1—7. [许崇海, 徐影, 罗勇. 新疆地区 21 世纪气候变化分析[J]. 沙漠与绿洲气象, 2008, **2**(3): 1—7.]

[13] Gao Xuejie, Zhao Zongci, Ding Yihui. Climate change due to greenhouse effects in Northwest China as simulated by a regional climate model[J]. Journal of Glaciology and Geocryology, 2003, **25**(2): 165—169. [高学杰, 赵宗慈, 丁一汇. 温室效应对我国西北地区气候影响的数值模拟[J]. 冰川冻土, 2003, **25**(2): 165—169.]

[14] Shi Ying, Gao Xuejie, Wu Jia, *et al*. Simulation of the changes in snow cover over China under global warming by a high resolution RCM[J]. Journal of Glaciology and Geocryology, 2010, **32**(2): 215—222. [石英, 高学杰, 吴佳, 等. 全球变暖对中国区域积雪变化影响的数值模拟[J]. 冰川冻土, 2010, **32**(2): 215—222.]

[15] Pal J S, Giorgi F, Bi Xunqiang, *et al*. Regional climate modeling for the developing world: The ICTP RegCM3 and RegCNET[J]. Bulletin of the American Meteorological Society, 2007, **88**(9): 1395—1409.

[16] Giorgi F, Marinucci M R, Bates G T. Development of a second—generation regional climate model (RegCM2). Part Ⅰ: Boundary-layer and radiative transfer processes[J]. Monthly Weather Review, 1993, **121**: 2794—2813.

[17] Giorgi F, Marinucci M R, Bates G T. Development of a second-generation regional climate model (RegCM2). Part Ⅱ: Convective processes and assimilation of lateral boundary conditions [J]. Monthly Weather Review, 1993, **121**: 2814—2832.

[18] Grell G A. Prognostic evaluation of assumptions used by cumulus parameterizations [J]. Monthly Weather Review, 1993, **121**: 764—787.

[19] Fritsch J M, Chappell C F. Numerical prediction of convectively driven mesoscale pressure systems. Part I: convective parameterization[J]. Journal of Atmospheric Sciences, 1980, **37**: 1722—1733.

[20] Li Qinghua. Comparisons of the Different Convection Parameterization Schemes in Regional Climate Simulations [D]. Lanzhou: Lanzhou University, 2006. [李清华. 区域气候模拟中对流参数化方案的比较研究[D]. 兰州: 兰州大学, 2006.]

[21] Liu Jiyuan, Liu Mingliang, Zhuang Dafang, *et al*. Study on spatial pattern of land-use change in China during 1995—2000 [J]. Science in China (Series D), 2003, **46**(4): 373—384. [刘纪远, 刘明亮, 庄大方, 等. 中国近期土地利用变化的空间格局分析[J]. 中国科学(D 辑), 2002, **32**(12): 1031—1043.]

[22] K-1 Model Developers. K-1 Coupled Model (MIROC) Description. K-1 Technical Report 1[M]. Center for Climate System Research, University of Tokyo, Tokyo, Japan, 2004: 1—34.

[23] Xu Chonghai, Shen Xinyong, Xu Ying. An analysis of climate change in East Asia by using the IPCC AR4 simulations [J]. Advances in Climate Changes Research, 2007, **3** (5): 287—292. [许崇海, 沈新勇, 徐影. IPCC AR4 模式对东亚地区气候模拟能力的分析[J]. 气候变化研究进展, 2007, **3** (5): 287—292.]

[24] Xu Ying, Gao Xuejie, Yan Shen, *et al*. A daily temperature dataset over China and its application in validation a RSM simulation[J]. Advances Atmospheric Sciences, 2009, **26** (4): 763—772.

[25] Xie Pingping, Yatagai A, Chen Mingyue, *et al*. A gauge-based analysis of daily precipitation over East Asia[J]. Journal of Hydrometeorology, 2007, **8** (3): 607—626.

[26] Editorial Board of Climatological Atlas of the People's Republic of China. Climatological Atlas of the People's Republic of China[M]. Beijing: Meteorological Press, 2002: 1—250. [《中华人民共和国气候图集》编委会. 中华人民共和国气候图集[M]. 北京: 气象出版社, 2002: 1—250.]

[27] Li Shengyu, Lei Jiaqiang, Xu Xinwen, *et al*. Features of sandstorms in hinterland of Taklimakan Desert: a case of Tazhong area[J]. Journal of Natural Disasters, 2006, **15** (2): 14—19. [李生宇, 雷加强, 徐新文, 等. 塔克拉玛干沙漠腹地沙尘暴特征——以塔中地区为例[J]. 自然灾害学报, 2006, **15**(2): 14—19.]

[28] Shi Yafeng, Liu Shiyin. Estimation on the response of glaciers in China to the global warming in the 21st century[J]. Chinese Science Bulletin, 2000, **45** (2): 434—438. [施雅风, 刘时银. 中国冰川对 21 世纪全球变暖响应的预估[J]. 科学通报, 2000, **45**(2): 434—438.]

[29] Shen Yongping, Liang Hong. High precipitation in glacial region of high mountains in High Asia: Possible cause[J]. Journal of Glaciology and Geocryology, 2004, **26**(6): 806—809. [沈永平, 梁红. 高山冰川区大降水带的成因探讨[J]. 冰川冻土, 2004, **26**(6): 806—809.]

[30] He Xiaobo, Ye Baisheng, Ding Yongjian. Bias correction for precipitation measurement in Tanggula Mountain Tibetan Plateau[J]. Advance in Water Science, 2009, **20**(3): 403—408. [何晓波, 叶柏生, 丁永建. 青藏高原唐古拉山区降水观测误差修正分析[J]. 水科学进展, 2009, **20**(3): 403—408.]

[31] Ye Baisheng, Chen Peng, Yang Daqing, *et al*. Effects of the bias—correction on changing tendency of precipitation over China[J]. Journal of Glaciology and Geocryology, 2008, **30** (5): 717—725. [叶柏生, 成鹏, 杨大庆, 等. 降水观测误差修正对降水变化趋势的影响[J]. 冰川冻土, 2008, **30**(5): 717—725.]

[32] Giorgi F, Hurrell J W, Marinucci M R, *et al*. Elevation signal in surface climate change: a model study[J]. Journal of Climate, 1997, **10**: 288—296.

[33] Gao Xuejie, Pal J S, Giorgi F. Projected changes in mean and extreme precipitation over the Mediterranean region from a

high resolution double nested RCM simulation[J]. Geophysical Research Letters, 2006, **33**: L03706.

[34] Shi Ying, Gao Xuejie, Wu Jia, *et al*. Change of future climate over North China as simulated by a high resolution regional climate model[J]. Journal of Applied Meteprological Science, 2010, **21**(5): 580－589. [石英，高学杰，吴佳，等. 华北地区未来气候变化的高分辨率数值模拟[J]. 应用气象学报，2010，**21**(5)：580－589.]

[35] Gao Xuejie, Giorgi F. Increased aridity in the Mediterranean region under greenhouse gas forcing estimated from high resolution simulations with a regional climate model[J]. Global and Planetary Change, 2008, **62**: 195－209.

[36] Gao Xuejie, Shi Ying, F Giorgi. A high resolution simulation of climate change over China[J]. Science in China (Series D), **53**, doi: 10.1007/s11430-010-4035-7. [高学杰，石英，Giorgi F. 中国区域气候变化的一个高分辨率数值模拟[J]. 中国科学（D 辑），2010，**40**（7）：911－922.]

# Climate Change over Xinjiang Region in the 21st Century Simulated by a High Resolution Regional Climate Model

WU Jia[1, 2, 3], GAO Xue-jie[3], SHI Ying[3], Filippo Giorgi[4]

(1. *Chinese Academy of Meteorological Sciences, Beijing* 100081, *China*; 2. *Graduate University of Chinese Academy of Sciences, Beijing* 100049, *China*; 3. *National Climate Center, Beijing* 100081, *China*; 4. *The Abdus Salam International Centre for Theoretical Physics* I-34151 *Trieste, Italy*)

**Abstract**: Based on a high resolution simulation of the 21st century by a regional climate model (RegCM3) nested within a global climate model (MIROC3.2_hires) over East Asia, climate changes over Xinjiang Region under the IPCC SRES A1B scenario are analyzed. Validation of the model performances in simulating annual mean temperature and precipitation of present time (1981—2000) in the region are firstly carried out. Results show that the spatial distributions and amount of them are well reproduced by the model. Compared to observations, it is found that the model exhibits a warm bias over basins and cold bias over mountainous areas. Moreover, underestimation of precipitation in the basins and overestimation of it over mountain ranges are found in the simulation. Significant warming is simulated in the middle (2041—2060) and the end of the 21st century (2081—2100) over the region, while greater warming in the end of the century, in particular in winter, are found. General increase of precipitation is found both in winter and summer, except in portions of the region. The increase is more profound in the end of the century compared to the middle of it. In addition, the magnitude of the warming and amount of the precipitation increase show strong dependency on topography. In general, the warming is greater over basins, while the increase of precipitation amount is more significant over mountain slopes with seasonal difference. As for the regional mean, greater warming and precipitation increase are found in Xinjiang Region compared to those over the whole China.

**Key words**: climate change; regional climate model; Xinjiang Region

吴佳，高学杰，张冬峰，等. 三峡水库气候效应及2006年夏季川渝高温干旱事件的区域气候模拟[J]. 热带气象学报，2011，27(1)：44-52.

**文章编号**：1004-4965(2011)01-0044-09

# 三峡水库气候效应及2006年夏季川渝高温干旱事件的区域气候模拟

吴佳[1,2,3]，高学杰[3]，张冬峰[3]，石英[3]，GIORGI F[4]

(1. 中国气象科学研究院，北京 100081； 2. 中国科学院研究生院，北京 100049；3. 国家气候中心，北京 100081；
4. International Centre for Theoretical Physics, Trieste, Italy)

**摘　　要**：针对2006年夏季川(四川)渝(重庆)地区的高温干旱事件，使用RegCM3区域气候模式，采用双重嵌套和次网格(SUB-BATS)方法，进行中国和三峡地区2005—2006年气候50 km和10 km(通过SUB-BATS方法达到2 km)分辨率数值模拟，并在此基础上进行了三峡地区下垫面改变(三峡水库建成蓄水)的气候效应模拟试验，重点分析了模式对中国和三峡地区夏季气候和气候异常的模拟能力，以及三峡水库对气温和降水的影响。结果表明，模式能较好模拟出中国和川渝地区的气候及以2006年川渝地区高温干旱为代表的气候异常，双重嵌套和SUB-BATS方法的应用，使模式能够提供局地和区域气候更详细的信息。有无三峡水库的对比试验表明，水库对周边区域气温、降水的影响很小，大部分格点上的变化达不到90%统计信度检验标准，气温变化中少数通过检验的格点基本集中于水库水体本身，邻近区域内气温和降水的变化随距库区的距离变远而变得更弱。除了库区本身降温和降水减少外，模拟结果中出现的变化更多表现为模式中出现的噪音。2006年夏季的川渝高温干旱，更多是由于大的环流场造成的，与局地强迫的关系不大，三峡水库在其中所起的作用非常微弱，可以忽略不计。

**关　键　词**：气候学；气候变化；区域气候模式；三峡水库

**中图分类号**：P461.8　　**文献标识码**：A　　**Doi**：10.3969/j.issn.1004-4965.2011.01.005

## 1 引　　言

2006年夏季，重庆和四川东部出现了持续高温、少雨天气，导致这些地区发生了近几十年以来最严重的干旱，引起人畜饮水和城市供水困难，农作物减产，造成的直接经济损失达到近200亿元人民币[1]。这一高温干旱事件引起了社会各界和媒体等的广泛关注。研究表明，这主要是由于在全球变暖大背景下大尺度环流异常造成的[1-2]，但同时在媒体和民间出现了一些是否与三峡工程和三峡水库有关的争论。

三峡工程是世界最大的水电工程。三峡水库自2003年开始蓄水，2009年将达到设计水位175 m，范围覆盖了从宜昌到重庆段的长江水域，长约660 km，水域面积1 040 km$^2$。三峡水库是一个典型的河道型水库，其平均宽度约为1.1 km。三峡地区的气候和环境研究，随着三峡工程的建设，得到了广泛的关注[3-4]。

大规模的土地利用和下垫面改变，通过地表粗糙度、反照率等的改变，会引起局地和区域气候的变化[5-7]，由陆地转为大型水体，也同样会引起地表和大气之间动量和热量交换的变化，进而影响气候。

数值模式，特别是高分辨率的区域气候模式是研究这一问题的有效工具。具体到三峡水库对周边气候的影响，国内外已有一些相关的数值模

**收稿日期**：2010-02-16；**修订日期**：2010-09-28
**资助项目**：公益性行业(气象)科研专项GYHY200806010；国家重点基础研究发展规划项目(2009CB421407、2007CB411505)共同资助
**通讯作者**：高学杰，男，河北省人，研究员，主要从事区域气候变化及气候模拟研究。E-mail: gaoxj@cma.gov.cn

拟研究。张洪涛等[8]使用一个简化模式，研究了三峡水库建成前后气象要素场的变化，认为水库对气候的水平影响范围一般不超过10 km。Miller等[9]使用MM5模式，通过多重嵌套方法，模拟得到三峡水库的蒸发会引起周边气温降低，但对降水没有明显影响。而Wu等[10]使用MM5模式所进行的模拟则表明三峡水库蓄水对气候产生的影响可能会较大，造成三峡大坝附近降水略微减少，大坝以北和以西地区的降水量增加，其作用不仅在局地，而且可以达到区域级尺度。但上述试验从严格的气候模拟角度讲，都或多或少存在不够完善之处，如模式运行时没有考虑初始化(spin-up)过程、积分时间不够长、结果缺乏统计显著性检验等。

本文使用一个区域气候模式，针对 2006 年夏季川渝地区的高温干旱事件，首先进行了2005—2006 年中国范围的模拟，以考察模式对大尺度环流和气候背景场的模拟能力，随后对三峡水库及周边地区使用双重嵌套和次网格陆面过程(SUB-BATS)方法，进行了高分辨率的数值模拟，并通过有无三峡水库的对比试验，考察了三峡水库对局地和区域气候的影响。

## 2　模式和试验设计

本研究所使用的模式为意大利国际理论物理中心(The Abdus Salam International Center for Theoretical Physics)于近年间在RegCM2 区域气候模式[11-12]的基础上，研制开发的改进版RegCM3[13]。RegCM 系列模式在中国地区有很多应用，表明模式对中国气候，特别是在夏季有较好的模拟能力[14-17]。

研究共进行了3个试验，试验的积分时间均为2005年1月1日—2006年9月1日，计1年零9个月，其中2005年1—5月作为模式初始化(spin-up)时段不做分析，重点考察模式对2006年夏季(6—8月)气候异常及三峡水库气候效应的模拟。其中气候异常以2005年的模拟为相对基础。

试验中模式使用标准的参数设置，包括辐射采用 NCAR CCM3 方案，海表通量参数化方案使用Zeng方案，行星边界层方案使用Holtslag方案，积云对流参数化方案选择基于 Arakawa-Schubert 闭合假设的 Grell 方案，海表面温度使用美国海洋大气局(NOAA)的 OISST 资料。模式在垂直方向分 18 层，顶层高度为 10 hPa。

试验 1 的模式中心点取为 36 °N，105 °E，格点数为 160×109(东西-南北，下同)，水平分辨率取 50 km，下文简称为 50 km 模式，其范围包括整个中国大陆及周边地区(图 1a)。植被覆盖采用GLCC(Global Land Cover Characterization)资料。

区域气候模式的运行，需要初始场和大尺度环流场(侧边界)的驱动，使用的是 NCEP/NCAR 再分析资料，其水平分辨率为 2.5 °× 2.5 °(经纬度)。侧边界场采用指数松弛边界方案，每 6 h 输入模式一次。

试验2中，模式中心点取为30 °N，108 °E，格点数为128×90，水平分辨率取10 km。通过SUB-BATS[18]方法，次网格点数取为5×5，分辨率达到2 km×2 km，下文简称为10-2 km模式，范围覆盖三峡地区(图1b)。

从区域气候模拟的角度讲，一般驱动场的分辨率和模式分辨率之间的差距，以3～5倍比较合适，不能过大，在试验2中我们采用双重嵌套方法，由试验1结果得到所需的初始和侧边界场。需要指出的是，试验2中三峡地区的下垫面由GLCC资料得到，其类型主要以农业用地为主(crop/mixed farming)，占95%以上，除此之外仅有少量的落叶灌木及短草等植被。

由图1b可看到10-2 km模式对地形的描述更加细致、精确，如处于山脉环绕中的四川盆地及其以西向青藏高原地势由低到高的陡峭转变，长江从宜昌出三峡后进入的洞庭湖平原，三峡北部重庆与湖北、陕西交界处大巴山及其以南重庆和湖北交界处的山脉等，都得到了较准确的刻画。

一般气候模式中的大气和陆面过程部分，使用同样的网格(如10 km)进行计算和耦合。RegCM3使用SUB-BATS方法，陆面过程在更高的次网格分辨率上进行计算(如通过5×5网格达到2 km×2 km)，这些次一级的网格都具有各自的地形和植被覆盖类型。模式的大气部分首先将其需要与陆面进行交换的热量、动量等分割在次网格上，Bats在这些次网格上进行计算，随后重新合并到

正常网格上返回大气。模拟表明，SUB-BATS方法能够进一步提供区域气候的模拟效果(详细可参见文献[18])。

将试验2中三峡水库地区的下垫面替换成内陆水(范围在图1b中以“×”表示)，成为试验3。共替换了267个格点，占模拟范围总格点数的0.1%左右。

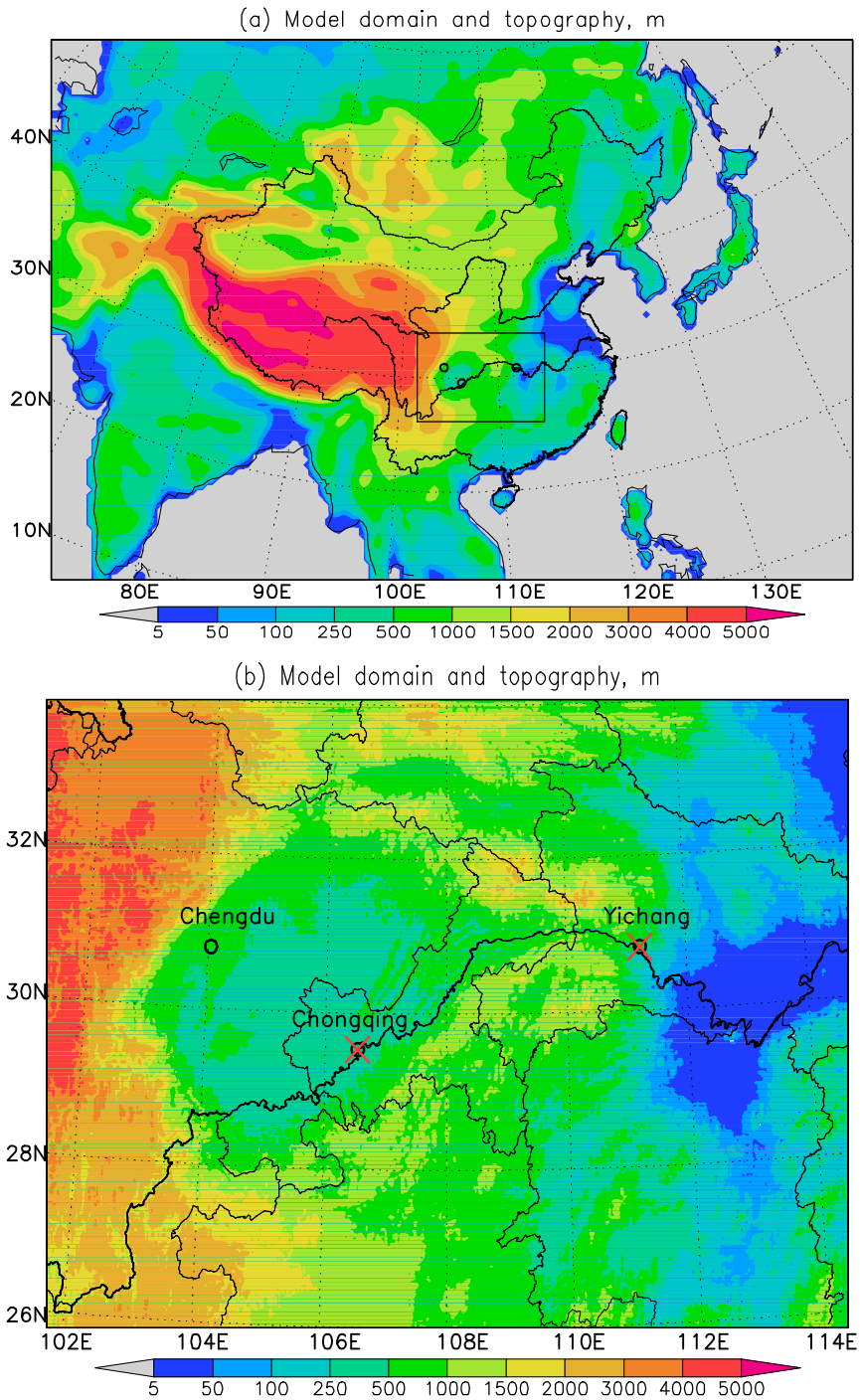


图 1 试验范围和地形分布，“×”之间区域为三峡水库 地形高度单位：m。 a. 50 km 模式；b. 10-2 km 模式。

使用国家气象信息中心提供的同期中国743个台站资料集作为用于模式检验的观测资料 去除部分存在缺测的站点后，论文所使用的站点数为662个

讨论将主要集中于2005、2006年夏季(6—8月)气温和降水两个基本气候要素上。

## 3　模式对 2006 年夏季气温和降水异常的模拟与检验

### 3.1　50 km 分辨率模式的模拟及其与观测的对比

图 2 中给出 2005 和 2006 年夏季平均的气温、降水的观测和模拟，模式对我国这两年夏季气候具有较好的模拟能力，从整体的空间分布型上，无论气温还是降水，模拟和观测都比较符合。模式对观测中一些空间分布的细节也有较好的描述，如我国西北祁连山区与其西南侧柴达木盆地气温和降水的高低、多少对比等。

模式对气温模拟存在的误差，为在中国地区存在系统性的冷偏差，模式模拟的降水在东北、华北偏大，南方偏小。这和 RegCM3 模式在 ERA40 再分析资料驱动下的模拟结果类似[15]。

以 2006 年夏季气温、降水相对于 2005 年的距平值，作为 2006 年气候异常的描述，观测和模拟的结果分别在图 3a ~ 3d 中给出。

2006 年夏季主要气温异常的分布(图 3a)，为在我国中部以四川东部和重庆地区为中心出现了一个高温区，气温的偏高最多达到 3 ℃以上。北方部分地区(华北、内蒙古和东北北部)的气温则较常年偏低。模式较好地模拟出上述特点(图 3b)，但模拟出的川渝地区高温中心数值偏大。模式模拟和观测的相关系数为 0.56，通过 95%信度的统计显著性检验标准($t$ 检验，下同)。

模式对 2006 年中国夏季降水异常的模拟也与观测相近(图 3c、3d)，如模式模拟出了四川东部至湖北北部一带幅度达到 50%以上的降水减少区(对应这里气温的偏高)，但模拟的范围较观测大。模式对东北北部、河套及其以西等地的降水偏多和西北降水的偏少等也有较好模拟，但江南地区降水的正距平区模拟出现偏差。模拟与观测的相关系数为 0.23，同样达到 95%信度标准。

总体来说，模式较好地模拟出了三峡夏季气温差的基本分布型。对高温中心的描述也比较准确，但是模拟温差较观测偏强，模拟的三峡中上游高温中心范围偏大。由观测夏季降水差(图 3c)可以看出，夏季降水的变化基本以长江为分界线，长江以南降水增加，长江以北降水减少，特别是三峡北部和中上游地区降水减少最多，超过 50%，位置与增温中心基本吻合(图 3a)，模式模拟较好地再现了这个三峡北部的降水减少区，但范围偏大(图 3d)。

由以上讨论可以看出，模式对中国地区夏季平均气温、降水和气候异常都具有较好的模拟能力，就地区而言，模式较好地模拟出 2006 年四川东部及重庆地区的高温干旱事件，与诊断结果相似[1]，川渝地区此次高温干旱事件，更多的是由大的环流背景驱动和决定，而不是在局地强迫下产生的。

### 3.2　三峡地区 50 km 和 10-2 km 模式模拟的对比

图 4 给出三峡地区 50 km 和 10-2 km 模式对气温、降水的模拟，两个模式所模拟大的分布型基本一致，如区域西部青藏高原边缘地区的气温低值和降水高值，四川盆地的气温高值等。但 10-2 km 模式提供了气温和降水两者分布更详细的特征，如在重庆与湖北、陕西交界处大巴山地区地形引起的气温相对低值和降水相对高值，在 50 km 模拟中没有出现，但在 10-2 km 模拟中得到较好体现。10-2 km 模式模拟的降水较 50 km 偏多一些。相对降水，SUB-BATS 对气温细节的描述程度更高[18]。

模式与观测场的比较表明，尽管 50 km 模式对区域级的中国气温和降水分布有较好的模拟能力(图 2a ~ 2d)，但在类似三峡地区这种局地尺度上，50 km 和 10-2 km 模式模拟都和观测表现出较大的不一致性，特别是降水(图略)。这种差别形成的原因，除模式本身需要进一步改进外，一方面是所使用的观测站点数量较少(在三峡地区为 117 个)，站点之间的距离在几十到上百 km 间，与 2 km×2 km 的模式分辨率相差较大；此外观测站点一般分布在河谷等城镇地带，由这些站点资料直接插值到格点上，会带来“观测场”一定的误差(图和进一步的分析略去)。10-2 km 模式对 2006 年气候异常的模拟结果，和 50 km 的分布基本一致，同样限于篇幅不再给出，降水和气温模拟与观测的相关系数分别为 0.73 和 0.28，较在全国范围内略高。

相对于2005年，三峡地区2006年观测、50 km和10-2 km模拟的区域平均气温差分别偏高1.28 ℃、1.73 ℃和1.84 ℃，降水差分别偏少-25.1%、-39.3%和-41.4%。

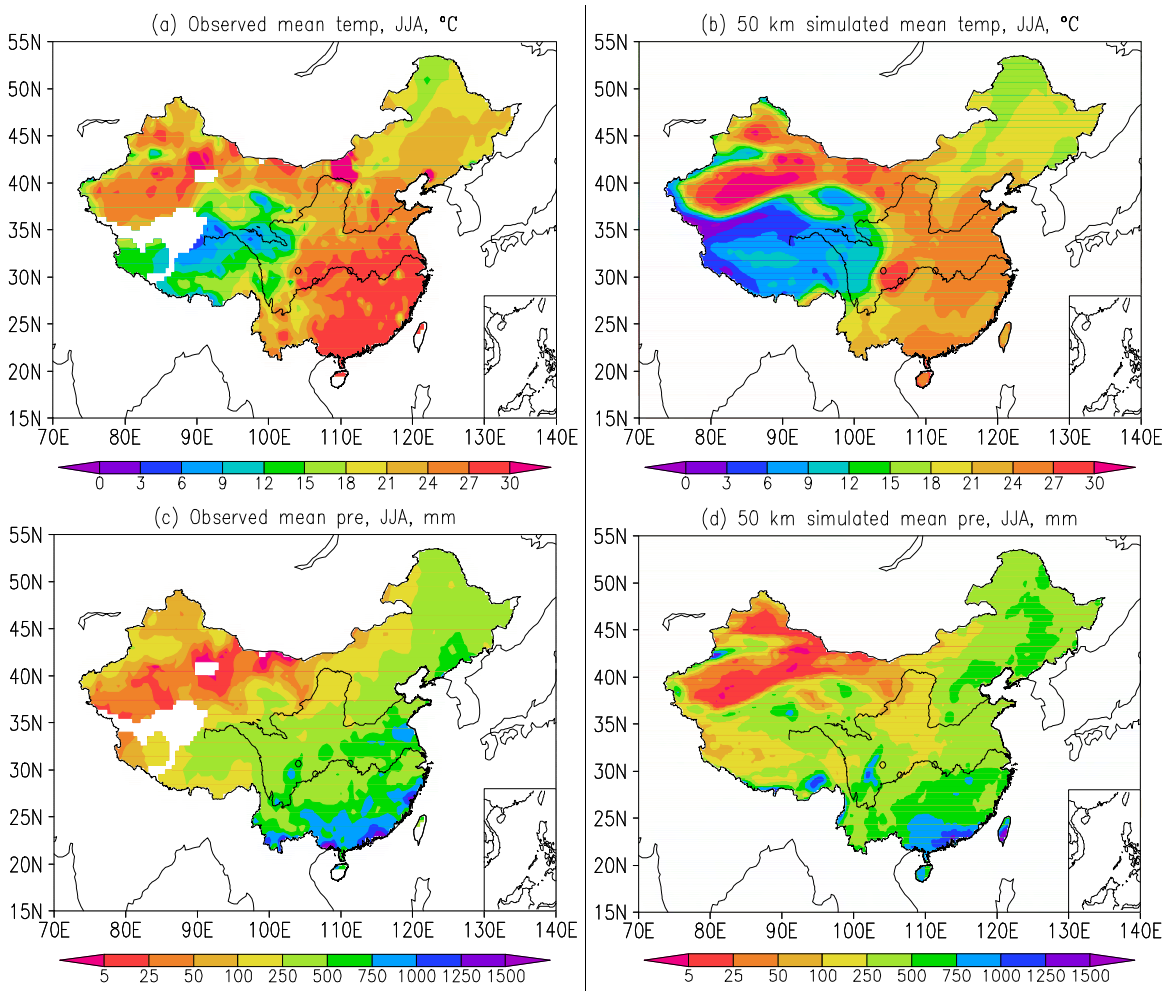


图2 2005、2006年中国夏季平均气温和降水

a. 气温观测(单位：℃)；b. 50 km气温模拟(单位：℃)； c. 降水观测(单位：mm)；d. 50 km降水模拟(单位：mm)。

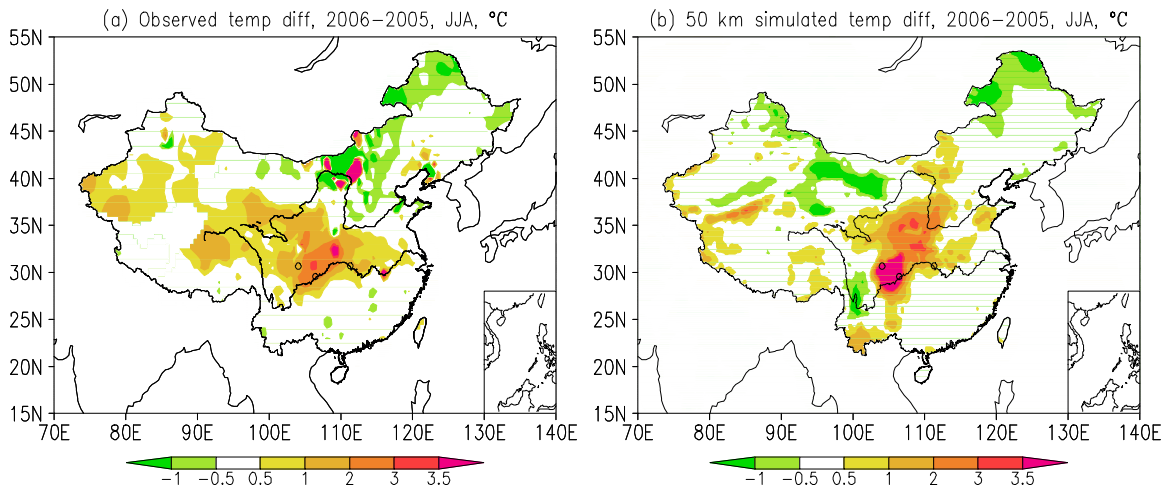

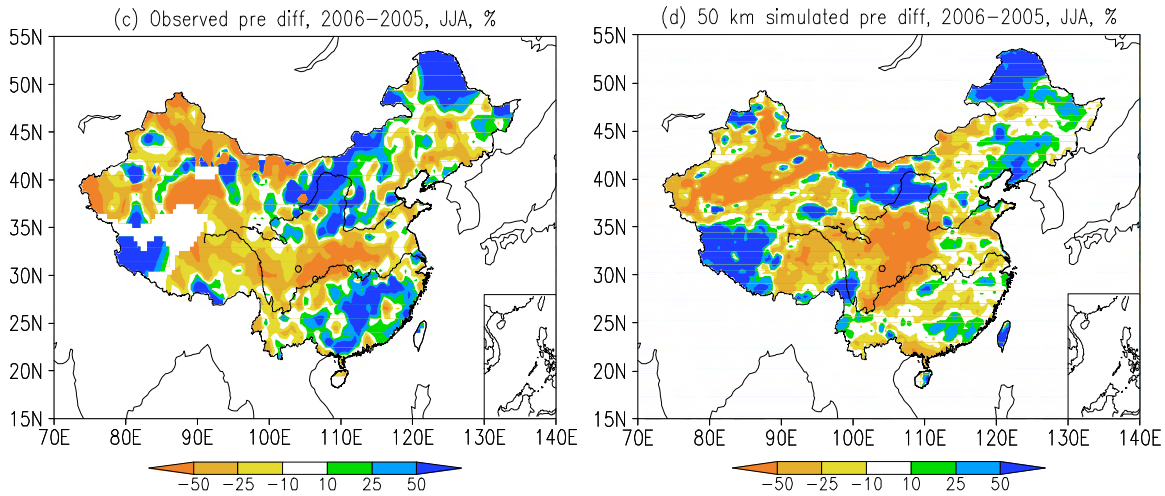


图 3　2006 年夏季中国气温和降水异常(相对于 2005 年)

a. 气温观测(单位：℃)；b. 50 km 气温模拟(单位：℃)；c. 降水观测(单位：%)；d. 50 km 降水模拟(单位：%)。

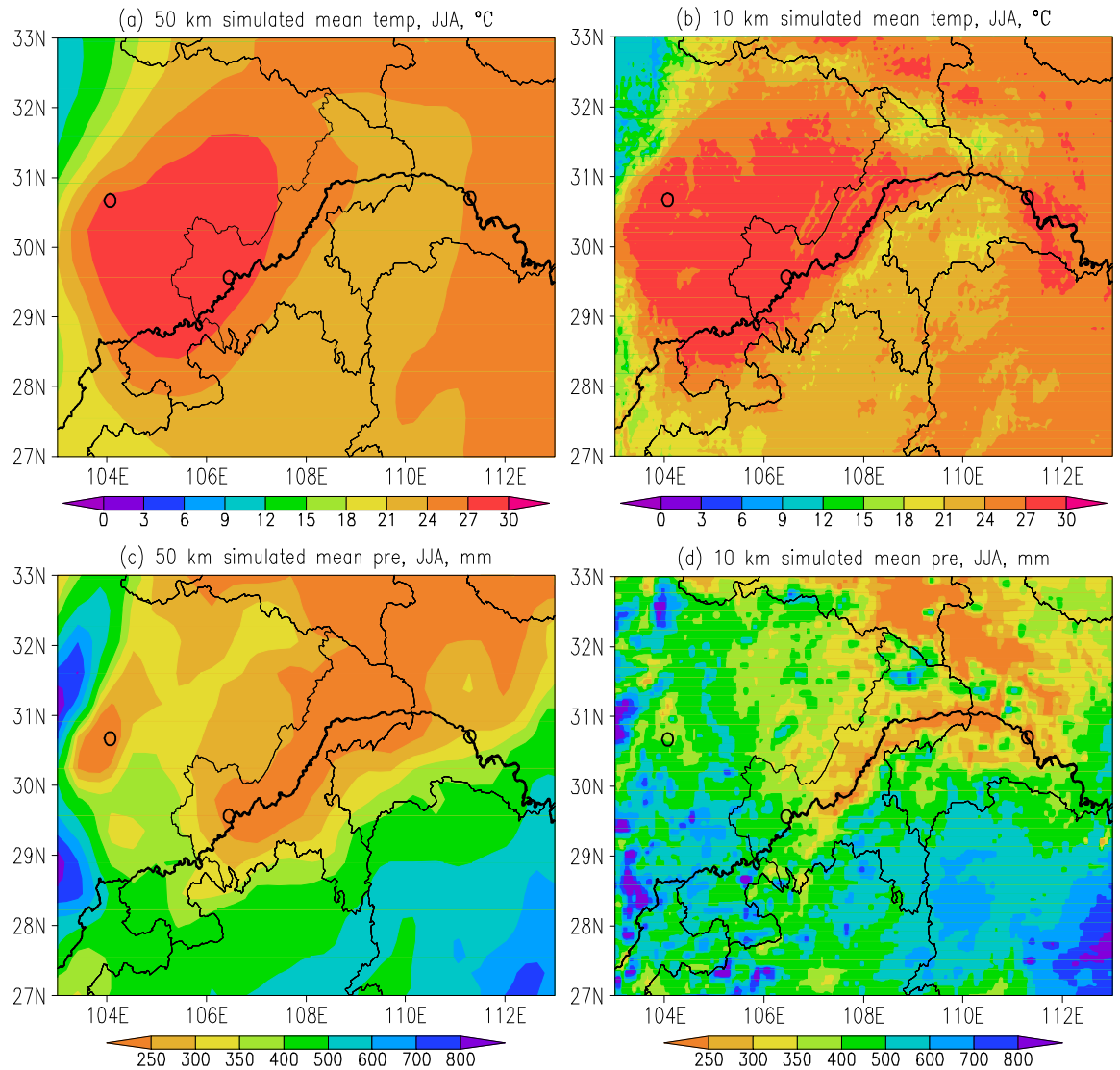


图 4　2005、2006 年三峡地区 50 km 和 10-2 km 夏季平均气温和降水的模拟

a. 50 km 气温(单位：℃)；b. 10-2 km 气温(单位：℃)；c. 50 km 降水(单位：mm)；d. 10-2 km 降水(单位：mm)。

# 4 三峡水库对区域气候的影响

## 4.1 平均气温和降水变化

下垫面大面积的由陆面转变成水面，由于水体的反照率、粗糙度及辐射性质、热容量、导热率等不同于陆地，可以改变地表与大气间的动量、热量和水分交换，进而对气温、降水的变化产生影响。下面就模式模拟出的三峡地区下垫面改变后气温、降水的相应变化(试验 3 与试验 2 之差)，即三峡水库的效应，进行简要的分析和探讨。

图 5 给出了三峡水库引起的 2005 和 2006 年两个夏季平均的气温、降水变化分布。

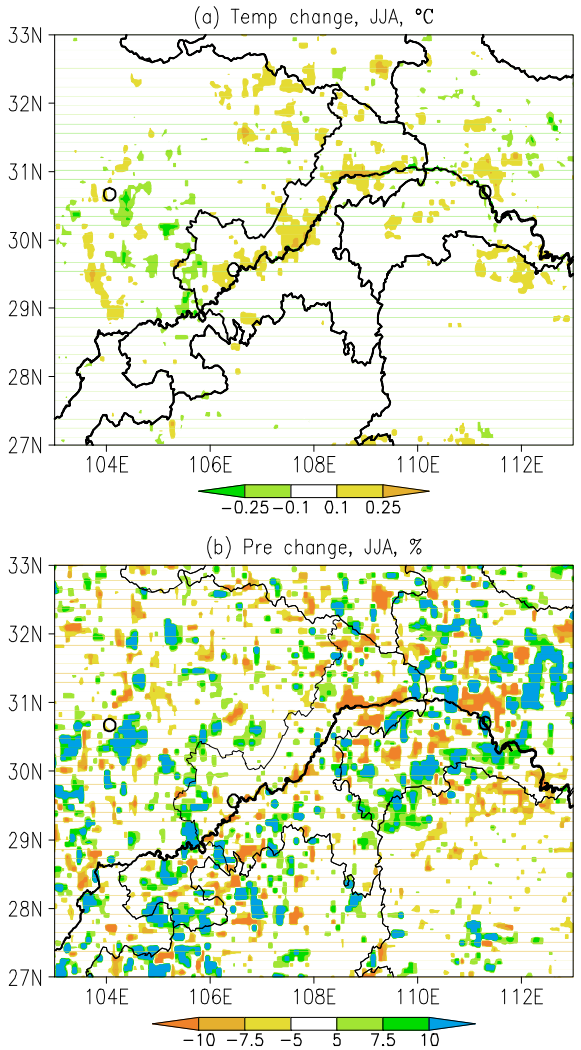


图 5 三峡水库对 2005、2006 年三峡地区夏季平均气温和降水变化 a. 气温(单位：℃)；b. 降水(单位：%)。

由图 5a 可看出，除库区外，水库引起的三峡地区气温变化分布比较零散，大致以增温的地方稍多，但总体来说变化很小，看不出有系统性，更多表现为模式由于小的改动产生噪音(模式的内部变率)，气候学上的意义不大。在狭长的库区内气温有较大的降低，一般可以达到 1 ℃以上(在图 5a 中因被所绘河流覆盖显示得不明显)。区域平均的气温变化，为一个非常微弱的正值(+0.01 ℃，表 1)。

对上述变化进行统计显著性检验，结果表明通过 95%和 90%检验的格点数占总格点数的百分率数值很小，分别为 0.09%和 0.12%，进一步的分析表明，这些格点基本都是库区本身，通过 95%和 90%检验的格点平均降温分别为 1.2 ℃和 1.1 ℃。库区降温产生的原因可能一方面是下垫面变成水后，水体比热大，吸收热量多引起的；另一方面是水体表面粗糙度小，风速增大，蒸发加强，带走更多热量造成的。

表 1 下垫面变化前后三峡地区夏季气温(单位：℃)、降水(单位：%)的变化及通过检验(90%或 95%信度检验)的格点占总格点的百分率

| | 气温变化 Temp change | 降水变化 Pre change | 气温 90%检验 Temp T90 |
|---|---|---|---|
| 夏季 JJA | +0.01 ℃ | +1.7% | 0.12% |
| | 气温 95%检验 Temp T95 | 降水 90%检验 Pre T90 | 降水 95%检验 Pre T95 |
| 夏季 JJA | 0.09% | 0.04% | 0.02% |

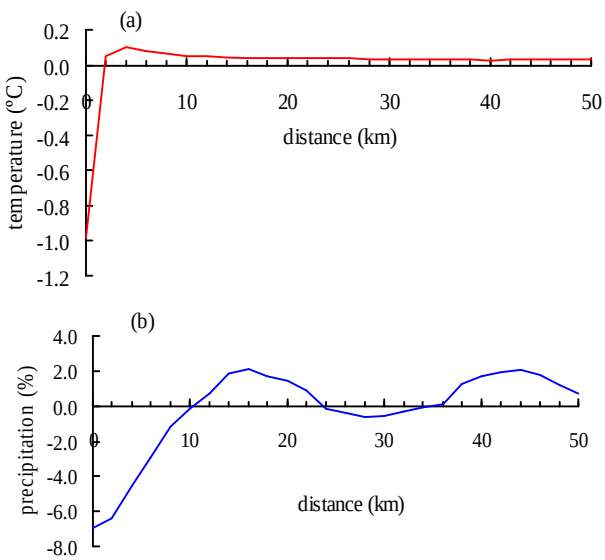


图 6 2005、2006 夏季距库区不同距离上气温和降水的变化 a. 气温(单位：℃)；b. 降水(单位：%)。

所模拟的三峡水库引起的区域降水变化相对气温，噪音成分更大(图 5b)，区域平均的变化为很小的增加(1.7%)，而这种增加通过信度检验的格点更少(表 1)，且零散分布在区域各处(图略)。这与 Miller 等[9]的模拟有一定的相似。

### 4.2　气温、降水变化与库区距离的关系

为进一步分析三峡水库对局地气候的影响以及其影响的尺度，计算了 2005、2006 年夏季，在距三峡库区(106.4 ~ 111.8 °E)南北 0 ~ 50 km 各个格点上，平均气温和降水的变化，以考察这种影响与距库区距离的关系(图 6，见上页)。

由图 6a 可以看出，三峡水库引起库区(图中的 0 km 处)气温的降低，气温的平均降低幅度为 1 ℃左右，但在库区以外第一个格点开始，变化就变得很小，数值一般都在 0.1 ℃以内，为一个微弱的增温。由库区向外，增温基本上呈现先减小，到 20 km 以后重新有所增加的趋势。

三峡水库引起的降水变化，在库区约减少 7%，库区以外数值非常小(图 6b)，基本上由在库区的减少，向外转为至 10 km 处增加，随后呈波动变化，数值在±2%之间。

作为河道型水库，三峡水库由于其宽度非常狭小，总面积也不大，仅可引起库区本身的气温和降水变化，而对库区周围地区的气温和降水产生的影响非常小。另外注意到在模式假设中的水库平均宽度为 2 km，较实际的 1.1 km 大了近一倍，模拟的效应已有所放大，实际三峡水库对气候的影响可能会更小。

## 5　结论和讨论

使用 RegCM3 区域气候模式，进行了 2005—2006 年中国及三峡地区气候变化的模拟，重点对模式模拟的夏季气候及气候异常进行了分析，并探讨了三峡水库下垫面改变对区域气候变化的可能影响。

(1) RegCM3 能够较好地模拟出中国及三峡地区夏季地面气温和降水空间分布的基本特征，对 2006 年出现的主要气候异常(川渝地区的高温干旱)有较好描述。这一方面反映了模式对气温和降水及其年际变率有较好的模拟能力，同时说明此次川渝高温干旱事件，更多的是由于大的环流场而非局地强迫造成的。

(2) SUB-BATS 方法，能够使得模式更详细地考虑下垫面强迫，从而在计算量增加不大的情况下，为局地气候特别是气温提供更多的信息。

(3) 三峡水库引起的三峡区域地面气温和降水的变化很小，区域平均夏季的气温、降水变化为微弱的上升和增加(0.01℃和 1.7%)，从其地理分布上看，除库区本身显著降温和降水略微减少外，基本看不出其它系统性的明显变化，更多表现为模拟的噪音，特别是降水。气温变化通过统计显著性检验变化的格点，大部分都在库区本身，以降温为主。三峡水库引起的气温和降水变化，与距库区远近有一定关系，但其总体效应，及对 2006 年川渝高温干旱的作用，可以忽略不计。

大范围的陆地覆盖改变，对局地和区域气候都会产生明显的影响，而作为典型的非常狭窄的河道型水库，三峡水库除引起库区本身气温降低外，对区域气候的影响非常小。

下垫面改变对气候影响的研究，仍是比较复杂的问题。未来需要使用更高分辨率(1 km 至几百米)的气候模式和进行更长时间的积分模拟，进行三峡和其他水库气候效应的研究，以得到关于这一问题的进一步结论。

**参　考　文　献：**

[1]　邹旭恺，高辉. 2006 年夏季川渝高温干旱分析[J]. 气候变化研究进展, 2007, 3(3): 149-153.

[2]　张强，罗勇，廖要明，等. 06 三峡库区夏季高温干旱及成因分析[J]. 中国三峡建设, 2007(2): 89-91.

[3]　李黄，张强. 长江三峡工程生态与环境监测系统局地气候监测评价[M]. 北京：气象出版社，2003: 191.

[4]　廖要明，张强，陈德亮. 1951—2006 年三峡库区夏季气候特征[J]. 气候变化研究进展, 2007, 3(6): 368-372.

[5] CHRISTENSEN J H, HEWITSON B, et al. 2007: Regional climate projection[M]. In: Climate Change 2007: The Physical Science Basis. Contribution of Working Group I to the Fourth Assessment Report of the Intergovernmental Panel on Climate Change [Solomon S, Qin D, Manning M, Chen Z, Marquis M, Averyt KB, Tignor M, Mille HL(eds)]. Cambridge, United Kingdom and New York, NY, USA: Cambridge University Press.

[6] GAO X J, LUO Y, LIN W T, et al. Simulation of effects of land use change on climate in China by a regional climate model[J]. Advances in Atmospheric Sciences, 2003, 20(4): 583-592.

[7] 高学杰, 张冬峰, 陈仲新, 等. 中国当代土地利用对区域气候影响的数值模拟[J]. 中国科学 D 辑, 2007, 37(3): 397-404.

[8] 张洪涛, 祝昌汉, 张强. 长江三峡水库气候效应数值模拟[J]. 长江流域资源与环境, 2004, 13(2): 133-137.

[9] MILLER N L, JIN J, TSANG Chin–Fu. Local climate sensitivity of the Three Gorges Dam[J]. Geophysical Research Letters, 2005, 32: L16704.

[10] WU L G, ZHANG Q, JIANG Z H. Three Gorges Dam affects regional precipitation[J]. Geophysical Research Letters, 2006, 33: L13806.

[11] GIORGI F, MARINUCCI M R, BATES G T. Development of a second-generation Regional Climate Model (RegCM2). Part I: Boundary-layer and radiative transfer processes[J]. Mon Wea Rev, 1993, 121(10): 2 794-2 813.

[12] GIORGI F, MARINUCCI M R, BATES G T, et al. Development of a second-generation Regional Climate Model (RegCM2). Part II: Convective processes and assimilation of lateral boundary conditions[J]. Mon Wea Rev, 1993, 121(10): 2 814-2 832.

[13] PAL J S, GIORGI F, BI X Q, et al. Regional climate modeling for the developing world: The ICTP RegCM3 and RegCNET[J]. Bulletin of the American Metrological Society, 2007, 88(9): 1 395-1 409.

[14] 高学杰, 石英, Giorgi F. 2010. 中国区域气候变化的一个高分辨率数值模拟. 中国科学, 2010, 40(7): 911-922

[15] 张冬峰, 高学杰, 赵宗慈, 等. RegCM3 对东亚环流和中国气候模拟能力的检验[J]. 热带气象学报, 2007, 23(5): 444-452.

[16] 鞠丽霞, 王会军. 用全球大气环流模式嵌套区域气候模式模拟东亚现代气候[J]. 地球物理学报, 2006, 49(1): 52-60.

[17] GAO X J, SHI Y, SONG R Y, et al. Reduction of future monsoon precipitation over China: comparison between a high resolution RCM simulation and the driving GCM[J]. Meteorology and Atmospheric Physics, 2008, 100(1): 73-86.

[18] GIORGI F, FRANCISCO R, PAL J. Efects of a subgrid-scale topography and land use scheme on the simulation of surface climate and hydrology. part 1: Effects of temperature and water vapor disaggregation[J]. Journal of Hydrometeorology, 2003, 4(2): 317-333.

# REGIONAL CLIMATE MODEL SIMULATION OF THE CLIMATE EFFECTS OF THE THREE GORGE RESERVOIR WITH SPECIFIC APPLICATION TO THE SUMMER 2006 DROUGHT OVER THE SICHUANG-CHONGQING AREA

WU Jia[1, 2, 3], GAO Xue-jie[3], ZHANG Dong-feng[3], SHI Ying[3], GIORGI Filippo[4]

(1. Chinese Academy of Meteorological Sciences, Beijing 100081, China;
2. Graduate University of Chinese Academy of Sciences, Beijing 100049, China;
3. National Climate Center, Beijing 100081, Beijing;
4. The Abdus Salam International Centre for Theoretical Physics, Trieste, Italy)

**Abstract:** High resolution multi-seasonal regional climate model experiments were conducted to simulate the effects of the Three Gorge Reservoir(TGR) on the climate of the surrounding region, with specific application to the summer of 2006 severe drought over the Sichuan-Chongqing area, or Three Gorge Area (TGA). A 50×50 km resolution simulation with the domain covering the whole China was first completed. Then two double nested simulations were carried out at a 10-km grid spacing over the TGA, one without the inland water coverage of TGR and the other with. A sub-grid method was employed in these two simulations to make the final model resolution to be 2 km×2 km(10-2 km simulations). Results show that the 50-km model reproduces the basic climatology and the anomaly of the summer temperature and precipitation over China, including the heat wave and drought over the Sichuan-Chongqing area. The 10-2 km resolution simulation provides with more detail of local climate over TGA. Sensitivity experiments with and without the TGR showed that this had little or negligible effects except right over the TGR area. The averages of the changes over the area are very small both for temperature and precipitation. Most of the changes in the grid points are not statistically significant on the 90% level while most of the significant changes in temperature are found to be located over the water body of TGR. The changes show more noise than systematic effects outside the TGR. In summary, the heat wave and drought event over the Sichuan-Chongqing area in the summer of 2006 can be more attributed to the large-scale circulation than to a local forcing. Contribution of the TGR is negligible.

**Key words:** Climatology; Climate change; Regional climate model; Three Gorges Reservoir

生物多样性 2011, **19** (4): 400–403 Doi: 10.3724/SP.J.1003.2011.04040
***Biodiversity Science*** http: //www.biodiversity-science.net

# 《生物多样性公约》下的气候变化问题: 谈判与焦点

吴 军[1] 张称意[2] 徐海根[1*]

1 (环境保护部南京环境科学研究所, 南京 210042)
2 (中国气象局国家气候中心, 北京 100081)

**摘要:** 近年来, 生物多样性与气候变化的关系逐渐成为《生物多样性公约》下的焦点议题, 各缔约方就此问题展开了激烈的多边谈判。本文梳理了《生物多样性公约》下气候变化问题谈判的发展历程, 探讨了其中的焦点问题及各方的主要立场, 指出以欧盟为代表的发达国家和以巴西、哥伦比亚、中国为代表的发展中生物多样性大国是针锋相对的两大主要谈判集团。谈判焦点问题主要包括: (1)气候变化问题的扩大化。欧盟希望将气候变化问题扩大化, 使其全面渗透到《生物多样性公约》下的各议题中, 并促进《生物多样性公约》、《联合国气候变化框架公约》和《联合国防治荒漠化公约》(简称里约三公约)之间的联合; 而发展中国家对此比较谨慎和保守。(2)地球工程(geoengineering)和海洋施肥(ocean fertilization)。欧盟提出全面禁止地球工程, 并建立全球管制框架; 而发展中国家认为可遵循“预先防范”原则。(3)减少森林砍伐和森林退化的碳排放机制。欧盟要求为该机制建立“生物多样性保障”制度, 而发展中国家表示反对。两大集团产生分歧的原因主要是发展中国家担心欧盟的快速推进会使自己将来受到制约, 这也反映了在环境领域发达国家和发展中国家之间的固有矛盾, 而这种矛盾未来还会继续深化。本文最后还就我国的应对策略和工作方向提出了建议: (1)要加强国内相关主管部门之间的沟通与协调; (2)要总结和宣传我国在气候变化领域成功的做法和经验; (3)要加强对减少森林砍伐和森林退化的碳排放机制的研究。

**关键词:** 生物多样性, 气候变化, 谈判

## Climate change issue in Convention on Biological Diversity: negotiations and focuses

Jun Wu[1], Chengyi Zhang[2], Haigen Xu[1*]

1 *Nanjing Institute of Environmental Sciences, Ministry of Environmental Protection, Nanjing* 210042
2 *National Climate Center, China Meteorological Administration, Beijing* 100081

**Abstract:** Recently, the issue of biodiversity and climate change is becoming a focus of the Convention on Biological Diversity (CBD), and parties to the convention have carried out heavy multilateral negotiations on the issue. This paper reviews the background pertaining to biodiversity and climate change, discusses the disputes and standpoints of major parties, and highlights two opposing groups: the developed countries represented by the European Union (EU), and the mega-diversity developing countries represented by Brazil, Columbia and China. The main disputes of the negotiations include: (i) Expansion of the climate change concept: EU nations hope to expand consideration of climate change and integrate it into various issues within the CBD, and to promote synergy among three Rio Conventions (Convention on Biological Diversity, United Nations Framework Convention on Climate Change, and United Nations Convention to Combat Desertification). However, the developing countries are more leery of these tendencies. (ii) Geoengineering and ocean fertilization: EU suggests forbidding geoengineering and establishing a global management framework, whereas the developing countries suggest applying the “precautionary principle” to these issues. (iii) Reducing Emissions from Deforestation and Forest Degradation (REDD): EU urges development of “Biodiversity

收稿日期: 2011-03-04; 接受日期: 2011-05-06
基金项目: 环保公益性行业科研专项(200909070)和科技支撑计划项目(2008BAC39B01, 2008BAC39B06)
* 通讯作者 Author for correspondence. E-mail: xhg@nies.org

Safeguards" for REDD, while the developing countries oppose this proposal. We surmise that the main reason for these debates is that the developing countries are afraid of being restricted by the EU and related developed countries, and that these debates will become more fierce in the future. In the end, we proposes some strategies for debate resolution: (i) strengthen communication and coordination of relevant domestic agencies; (ii) summarize and propagandize successful practices and experiences in the area of climate change in China; and (iii) improve research on REDD mechanisms.

**Key words**: biodiversity, climate change, negotiations

## 1　背景

全球气候变化已成为一个不争的事实, 20世纪全球平均气温上升了0.6℃(IPCC, 2007)。越来越多的证据表明, 气温升高、降水格局变化及其他气候极端事件会对生物多样性造成影响: 气候变化造成了物候期的改变, 导致了物种分布范围的变化, 加剧了病虫害, 加快了物种的灭绝速率, 使海洋酸化, 引起生态系统退化等(Parmesan & Yohe, 2003; Root *et al.*, 2003; IPCC, 2007)。同时, 生物多样性也能对气候变化产生反馈, 例如, 破坏森林会增加温室气体的排放, 破坏红树林会加重海岸的侵蚀等(IPCC, 2007)。随着气候变化问题的升温, 近几年来, 生物多样性与气候变化问题也逐渐成为《生物多样性公约》(Convention on Biological Diversity, CBD, 以下简称公约)下的焦点议题, 各缔约方就此问题进行了激烈的多边谈判。

## 2　公约下气候变化问题的发展脉络

2000年, 在公约第五次缔约方大会(COP-5)上首次注意到气候变化的风险, 特别是针对海水温度上升导致珊瑚礁褪色的生态风险问题展开了热烈的讨论, 并促请《联合国气候变化框架公约》采取一切可能的行动, 以减轻气候变化对水温的影响, 减少珊瑚礁褪色所造成的社会、经济影响(http://www. cbd.int/decision/cop/?id=7145)。

2001年, 公约下属的科学、技术和工艺咨询附属机构(简称科咨机构)建立了生物多样性和气候变化问题特设专家组, 旨在强化气候变化对生物多样性影响的技术评估。2003年, 该专家组发布了技术评估报告, 即《生物多样性与气候变化的联系: 将生物多样性因素整合进<联合国气候变化框架公约>及<京都议定书>的建议》, 详细阐述了气候变化对生物多样性影响的机制和可能途径, 未来情景的模拟及减缓和适应措施等(http://www.cbd.int/doc/publications/cbd-ts-10.pdf)。

2004年, 在公约第七次缔约方大会(COP-7)上, 首次正式设立了"生物多样性和气候变化"的议题, 并在特设专家组报告的基础上展开讨论。会议最终形成如下决议: (1)通过减缓和适应气候变化影响的活动, 以最佳方式保护和可持续利用生物多样性; (2)请《联合国气候变化框架公约》和《联合国防治荒漠化公约》与《生物多样性公约》进行协作, 促使缔约方在国家和地方层面同时开展支持这三项公约的活动; (3)请联合国政府间气候变化专门委员会继续就气候变化与生物多样性问题开展工作, 包括查明和确定气候变化引起的生物多样性的明显丧失(http://www.cbd.int/decision/cop/?id=7752)。

2006年, 公约第八次缔约方大会(COP-8)继续审议了上述议题。会议最终形成决议: (1)鼓励各缔约方和其他国家政府把生物多样性因素纳入应对气候变化的所有国家政策、方案和计划中, 同时致力维持和恢复生态系统的复原能力; (2)研究并制定快速评估工具, 以设计和执行旨在应对气候变化的生物多样性保护和可持续利用活动; (3)制定、支持并审查《生物多样性公约》与《联合国气候变化框架公约》、《联合国防治荒漠化公约》、《拉姆萨尔湿地公约》及其他公约采取联合行动的项目, 以更好地发挥这些公约之间的协同增效作用(http://www.cbd.int/decision/cop/?id=11044)。

2008年, 公约第九次缔约方大会(COP-9)在审议相关议题后要求: (1)在今后审查公约工作方案时, 都应适当列入气候变化的内容, 同时监测和评估气候变化及其减缓和适应活动对生物多样性产生的正面或负面影响; (2)敦促各缔约方查明本国的生态系统类型和生态脆弱区域; (3)敦促各缔约方将减缓和适应气候变化对生物多样性影响的内容纳入国家生物多样性战略与行动计划; (4)帮助发展中国家在国家层面监测气候变化对生物多样性的影响; (5)谨慎对待海洋施肥(ocean fertilization)并评估

其潜在影响(http://www.cbd.int/decision/cop/?id= 11659)。

2009年，公约科咨机构建立了生物多样性和气候变化问题第二特设专家组，并发布了题为《生物多样性和气候变化及其减缓和适应的联系》的技术报告。该报告通过文献综述，全面阐述了气候变化对生物多样性的影响、生物多样性对气候变化的反馈、生物多样性与气候变化减缓和适应活动的关系以及管理和评估的政策和技术等(http://www.cbd.int/doc/publications/cbd-ts-41-en.pdf)。

2010年，公约第十次缔约方大会(COP-10)在第二特设专家组报告的基础上展开了热烈的讨论，达成的共识如下：(1)查明、监测和处理气候变化和海洋酸化对生物多样性和生态系统功能的影响，并运用最新的评估框架及准则，评估其今后将面临的风险；(2)减轻气候变化对生物多样性和基于生物多样性的经济活动的影响；(3)应用基于生态系统综合管理的减缓和适应措施；(4)减少减缓和适应气候变化的措施对生物多样性产生的影响；(5)除了小规模的科学研究外，不得从事影响到生物多样性与气候的地球工程(geoengineering)；(6)发展中国家应减少森林砍伐和退化而降低碳排放，同时保护与可持续管理森林以增加碳储存。评估这些活动对实现公约目标作出的贡献(http://www.cbd.int/decision/cop/?id= 12299)。

## 3 焦点问题和各方主要立场

### 3.1 气候变化问题的扩大化

在“生物多样性和气候变化”议题的谈判中逐渐出现了两大针锋相对的集团，即以欧盟为代表的发达国家集团和以巴西、哥伦比亚、中国为代表的发展中生物多样性大国集团，这两大集团几乎左右了该问题的谈判历程。欧盟的立场较为激进，希望除了在本议题下讨论外，今后还应将关于气候变化的考虑扩大到各个领域的工作方案。并强调里约三公约①应采取联合行动，以达到协同增效的目的。而巴西、哥伦比亚、中国等则比较谨慎，尽量避免将生物多样性和气候变化联系得过于紧密，并指出由于里约三公约的法律地位、职责任务以及缔约方构成的不同，要想采取联合行动注定困难重重。发展中国家采取保守立场的原因主要是考虑到气候变化问题的复杂性和敏感性，担心会带来一些难以预料的不利后果。

从最近召开的公约会议来看，气候变化问题正逐渐渗透到公约下的各实质性议题中，例如在森林、农业、内陆水域、干旱和半湿润、海洋生物多样性等议题下都讨论了气候变化的影响、监测、评估、减缓和适应等问题。但是关于里约三公约的联合，目前进展不大，仅限于经验和资料的交流。

### 3.2 地球工程和海洋施肥

近年来国际上出现了地球工程的设想，即利用大尺度的环境工程来改变全球气候变化的趋势。如基于太阳辐射管理(solar radiation management)技术的平流层气溶胶(stratospheric aerosols)、对流层增云(tropospheric cloud seeding)等；基于碳捕获和碳储存(carbon capture and storage)技术的人工树(atificial trees)、生物木炭(biochar)、海洋施肥(ocean fertilization)等。虽然目前尚没有任何大尺度的地球工程实施，但是海洋施肥已经开展了多次试验。海洋施肥是通过向海洋中注入铁离子，刺激藻类爆发，从大气中吸收$CO_2$，藻类死亡后沉入海底实现碳的封存。专家估计，如果在整个南冰洋上实施铁施肥，每年可从大气层中吸收高达10亿吨的碳，这暗示了其对于减缓全球气候变化的巨大潜力。

在此问题上，欧盟的立场较为极端，要求暂停所有可能影响生物多样性的与气候变化相关的地球工程，并尽快建立全球性的管制框架。而发展中国家担忧如果由欧盟主导建立全球管制框架，会使自己受到制约。提出可对地球工程采取谨慎态度，但不必全面禁止，应遵循预先防范原则(precautionary principle)，进行科学、透明和有效的评估。对于海洋施肥，进行风险评估后，可以在沿海水域进行小规模的科学试验；但不得违背《防止倾倒废弃物及其他物质污染海洋的公约》(伦敦公约)的规定，不得使用海洋施肥制造和出售碳信用(carbon credit)，也不得用来实现其他商业目的。

### 3.3 减少森林砍伐和森林退化的碳排放机制

森林破坏是仅次于化石燃料的第二大温室气体排放源，全球约20%的温室气体来自于森林砍伐和森林退化后的碳排放(IPCC, 2007)。2005年《联合国气候变化框架公约》第十三次缔约方大会正式把“减少森林砍伐和森林退化的碳排放(Reducing

① 即《生物多样性公约》、《联合国气候变化框架公约》和《联合国防治荒漠化公约》，因同时订立于 1992 年 6 月在巴西里约热内卢召开的联合国环境与发展大会，而被国际上称为“里约三公约”。

Emissions from Deforestation and Forest Degradation, REDD)机制”列入“巴厘路线图(Bali Roadmap)”, 后来在此基础上又增加了“保护和可持续管理森林以增加森林碳汇(conservation, sustainable management of forests and enhancement of forest carbon stocks)”的内容(称为REDD+)。类似于清洁生产机制(Clean Development Mechanism, CDM), REDD/REDD+也是一种碳融资机制, 即鼓励森林温室气体高排放国家减少森林砍伐, 并允许这些国家通过碳交易市场获得相应的收入。2008年世界粮农组织(FAO)、联合国环境规划署(UNEP)和联合国开发计划署(UNDP)成立了联合国REDD项目(UN REDD Programme), 截至2010年底已融资5,140万美元, 帮助12个发展中国家设计了REDD+项目。另外, 世界银行还成立了森林碳伙伴基金(Forest Carbon Partnership Facility), 目前也在帮助一些发展中国家设计REDD+项目。专家估计, 如果REDD/REDD+机制在当前的碳交易市场获得成功, 将能以较低的碳价格对其他碳交易机制产生冲击, 而可能成为后《京都议定书》时代最主要的碳贸易形式。

许多发展中国家强调, 虽然REDD/REDD+机制能为发展中国家带来融资机会, 但不能代替公约所要求的发达国家应向发展中国家提供新的、额外的资金的义务, 并且建议REDD/REDD+机制要特别关注土著和地方社区的权益。针对REDD/REDD+机制的不确定性和风险, 欧盟要求和《联合国气候变化框架公约》协商, 为REDD/REDD+机制的实施建立“生物多样性保障(Biodiversity Safeguards)”制度。但考虑到生物多样性保障制度同样具有风险, 发展中国家表示反对。

## 4　前景与应对策略

在当前全球气候变化谈判陷入僵局的情况下, 《生物多样性公约》就成为讨论气候变化问题的一个多边外交舞台。可以预见, 未来公约下气候变化问题的谈判将会越来越白热化。最终能否达成一些实质性的目标, 还要看各方博弈的结果。另外, 气候变化是目前能争取到较多资金的领域, 例如REDD/REDD+机制把森林保护与气候变化结合在一起, 为森林生态系统和生物多样性的保护提供了资金激励机制。德国政府在《生物多样性公约》第九次缔约方大会后设立了“LifeWeb”项目, 支持发展中国家的保护区应对气候变化的活动。因此今后在该领域内的利益争夺也将会越来越激烈。

我国是全球公认的生物多样性大国, 在应对气候变化问题上也是举足轻重的国家, 《生物多样性公约》下气候变化问题的谈判会对我国产生长远影响。例如欧盟推动建立的生物多样性保障制度, 对于我国树种单一的人工林就非常不利。为积极应对, 今后应加强以下几方面的工作: (1)加强《生物多样性公约》和《联合国气候变化框架公约》相关主管部门之间的沟通与协调, 在各主要问题上统一认识与立场。参加两公约谈判的专家应对生物多样性和气候变化领域的一些复杂问题以及谈判中出现的一些新问题开展深入研究, 以积极应对谈判的新形势。(2)总结和宣传我国在气候变化领域成功的做法和经验, 如我国近几年将节能减排的目标纳入政府考核责任制, 促进产业升级和工艺革新, 种植大量的人工林以增加碳汇, 大力建设生态省(市、县), 积极推进生态文明的建设等。在公约一般性辩论中可适当介绍我国在这方面的成就, 从而赢得谈判的主动权。(3)加强对REDD/REDD+机制的研究。近几十年来我国是世界上森林资源增长最快的国家, 在植树造林、森林管理、林业资源利用等方面积累了丰富的经验, 今后应对REDD等碳交易机制的制度设计进行深入研究, 争取在标准、规则、定价权方面居世界领先地位, 为我国的森林生物多样性保护和可持续发展带来持久的动力。

### 参考文献

Intergovernmental Penal on Climate Change (IPCC) (2007) Climate change 2007: synthesis report: contribution of Working Groups I, II and III to the fourth assessment report of the Intergovernmental Panel on Climate Change (eds Pachauri RK, Reisinger A). Geneva, Switzerland.

Parmesan C, Yohe G (2003) A globally coherent fingerprint of climate change impacts across natural systems. *Nature*, **421**, 37–42.

Root TL, Price JT, Hall KR, Schneider SH, Rosenzweig C, Pounds JA (2003) Fingerprints of global warming on wild animals and plants. *Nature*, **421**, 57–60.

(责任编委: 薛达元　责任编辑: 时意专)

# 我国北方沙尘天气的气候成因分析

吴占华[1], 任国玉[2], 徐卫丽[1], 刘瑞兰[1]

(1 朔州市气象局, 山西 朔州 036001; 2 中国气象局气候研究开放实验室, 国家气候中心, 北京 100081)

摘 要: 本研究的范围在 30°N以北地区, 站点 340 个。通过采用区域平均及相关分析的方法, 将中国北方沙尘(扬沙+沙尘暴)事件的年、季特征及其关系较为密切的地面气象要素包括降水、温度、风(风速、大风日数、风速≥5 m/s的日数)、湿度、蒸发量作了详细、综合的相关、对比分析。结果表明: 春季多降水对沙尘天气的发生可以起到明显的抑制作用; 前冬至次年春季的气温突变容易诱发沙尘天气的发生; 在温度偏高、湿度较大、风力偏弱、蒸发量不大的年份, 少沙尘天气; 风要素是影响沙尘天气最为直接相关的因子。

关 键 词: 沙尘; 中国北方; 气候因子

中图分类号: P466 文献标识码: A 文章编号: 1000-6060(2011)03-0429-07(429~435)

沙尘天气可分为浮尘、扬沙和沙尘暴三类[1]。在世界范围内, 沙尘暴主要发生在沙漠及其邻近的干旱、半干旱地区, 我国西北地区即属于中亚沙尘暴高活动区之一[2]。其发生频次与环流背景异常有一定关系[3], 与各类气候因子的变化也密切相关。

迄今为止, 国内外对沙尘暴时空分布、成因与结构以及监测与对策等方面的研究很多, 其中, Thomas[4]分析了亚洲沙尘暴的频数变化与降水、气温、风速的关系。Goudie等[5]指出自然气候条件包括降水量、雪盖、风强等的变化和引水、灌溉、建筑、交通等人类活动是影响全球各个比较典型的沙尘暴多发区频数的决定性因子。McTainsh等[6]认为澳大利亚东部的沙尘暴出现的气候条件首先与下垫面的土壤湿度和植被有关, 其次与风有关。我国不少学者研究指出[7-8]沙尘天气形成要满足三个基本条件, 一是地表要有丰富的松散干燥的沙尘作为物质基础, 二是要有强冷空气作为动力条件, 即大风, 三是热力不稳定条件即要有冷暖气团的相互作用。进一步研究结果表明, 我国沙尘天气发生的频次和强度与其气候背景密切相关, 石广玉等[9]指出 20世纪 70年代及以前气候处于冷期, 是我国北方大部地区沙尘暴的频发期。李林等[10]指明大风和干燥度是造成沙尘暴天气的两个重要因素。陈洪武[11]得出在大风日数多, 年降水量少, 空气湿度低, 冬季气温低的气候背景下易导致沙尘暴日数的增多。近年来, 王式功等[12]和余林生等[13]研究了我国沙尘暴天气的时空分布特征、形成原因和发展趋势。翟盘茂等[14]指出在沙尘日数的年际变化上, 特别是西北部和中北部的夏季降水对第二年的沙尘天气影响显著。邹旭恺等[15]指出干冷(冬)、暖(春)容易诱发沙尘天气。张莉等[16]分析了我国北方境内沙尘源区的风、降水、温度、干燥度等气候要素对我国北方沙尘暴日数的影响。李彰俊等[17]指出内蒙古锡林郭勒盟中西部地区的土壤表面冻结终日与春季沙尘暴发生日数之间呈现负的相关关系, 是影响春季沙尘天气的一个因子。邱玉等[18]指出风速、相对湿度是影响沙尘天气的关键气象因子, 并得出了以此两个气象因子构建的月、季沙尘气象指数与沙尘天气频率的关系。范可等[19]讨论了 2006年春季华北地区沙尘天气频繁发生的主要原因是 2005年冬季 12月气温较多年平均偏低, 比较厚的冻土层为春季回暖后沙尘天气的发生提供了丰富的物质条件; 同时在弱南极涛动的影响下, 春季蒙古气旋活跃, 地面大风增加, 加强了沙尘发生的动力条件。

本文所讨论的沙尘天气为扬沙和沙尘暴, 研究范围为 30°N以北地区, 站点 340个。考虑到沙尘资

* 收稿日期: 2010-01-11; 修订日期: 2010-08-09
基金项目: 科技部"十五"科技攻关项目课题(2001BA611B-01)资助
作者简介: 吴占华(1974-), 女, 硕士, 高级工程师, 短期预报员. E-mail: zhanhuawu805@yahoo.com.cn



© 1994-2011 China Academic Journal Electronic Publishing House. All rights reserved. http://www.cnki.net

料序列的均一性, 资料开始统计年份选定 1961年, 因为这以后的沙尘暴记录规范、详细且日界一致, 站点密度也大, 资料截止年份为 2003年共 43 a。对与沙尘事件关系较为密切的地面气象要素包括降水、温度、风、湿度、水面蒸发量作了详细、综合的相关分析和季节性的对比分析, 揭示了控制年、季沙尘天气变化的敏感因素。

## 1 资料和方法

来源于国家气象信息中心气候资料室, 包括 1961- 2003年中国北方 340个站的扬沙、沙尘暴、大风日数、降水量、温度、风速、湿度、水面蒸发量的逐年逐月资料; 风速的逐日资料。其中, 蒸发量是用小型蒸发皿观测的, 可代表水面蒸发量或最大可能蒸发量, 特别是在干燥地区与实际蒸发量存在较大的差异。考虑到蒸发资料 1961- 1963年中月缺测值比较多, 2002年以后记录仪器型号的变动, 选出了 1964- 2001年 38 a的蒸发量资料与沙尘日数资料进行相关分析。四季划分按气象季节划分方法, 即前一年 12月 ~ 当年 2月为冬季, 3月 ~ 5月为春季, 6~ 8月为夏季, 9~ 11月为秋季。对于序列中存在缺测的部分, 根据需要进行了处理 (用平均值取代 )和剔除。

### 1.1 相关分析方法

相关分析[20]是用相关系数来表示两个变量间的相互关系。为了判定沙尘与各气象要素之间的密切程度, 文中主要采用了相关系数值的统计计算及 $t$ 检验方法。

相关系数的计算公式如下:

$$r_{12}=\frac{\sum_{i=1}^{n}(x_{1i}-\overline{x_1})(x_{2i}-\overline{x_2})}{\sqrt{\sum_{i=1}^{n}(x_{1i}-\overline{x_1})^2}\ \sqrt{\sum_{i=1}^{n}(x_{2i}-\overline{x_2})^2}}\ , \qquad (1)$$

式中: $r_{12}$为两组变量的相关系数, $n$ 为样本数, $x_1$ 为变量 1, $x_2$ 为变量 2, $\overline{x_1}$、$\overline{x_2}$分别为变量 1、2的平均值。

计算出相关系数后, 用 $t$ 检验方法来判断相关是否在某一水平下显著, 相关系数的临界值计算如下:

$$r_c=\sqrt{\frac{t_\alpha^2}{n-2+t_\alpha^2}}\ , \qquad (2)$$

式中: $r_c$ 为相关系数的临界值, $n$ 为样本数, $t_\alpha$ 为自由度 $n-2$和显著水平 下的 $t$检验值。

### 1.2 计算区域平均的方法

根据 1996年 Jones等[21]提供的用经纬度网格面积加权平均来计算某一气候要素区域平均值的方法, 建立了沙尘日数和各气象要素在研究范围内的平均值的时间序列来计算其相关性。计算公式如下:

$$\overline{X}=\frac{\sum_{i=1}^{n}\left[\cos(a_i)\times\frac{1}{k_i}\sum_{j=1}^{k_i}x_j\right]}{\sum_{i=1}^{n}\cos(a_i)}\ , \qquad (3)$$

式中: $\overline{X}$ 即为要计算的某要素 $x$ 的区域平均值, $n$ 为网格数, $a_i$ ( $i$= 1, 2, …$n$ )为每个网格的中心点纬度, $x_j$ ( $j$= 1, 2, …$k_i$ )为区域中某一网格内共参与计算的 $k_i$ 个点的气候要素值。文中使用了 1 °× 1 °经纬度的网格点。

根据沙尘的多发区及境内的主要源区取定我国北方的研究范围为: 35°N 以北地区, 站点 340个, 如图 1所示。

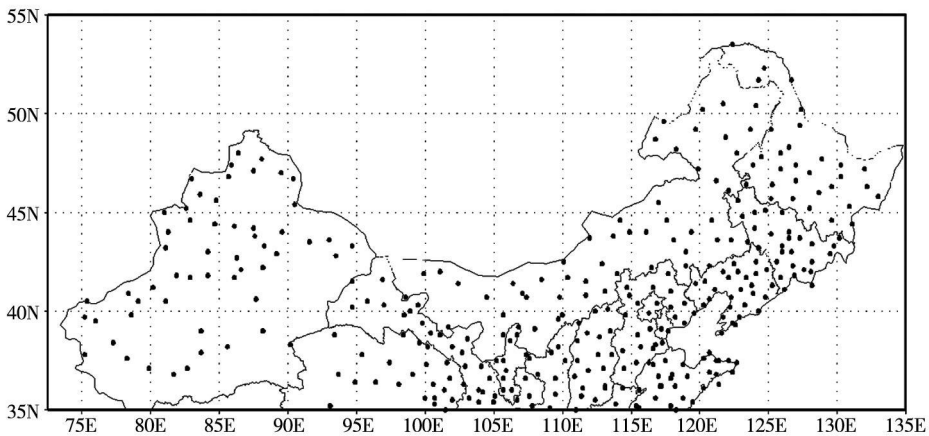


图 1 所选用的我国北方的站点分布

Fig. 1 Distribution of the researched sites in northern China

© 1994-2011 China Academic Journal Electronic Publishing House. All rights reserved. http://www.cnki.net

## 2　我国北方沙尘天气的气候成因分析

杨东贞等[22]指出我国沙尘暴的发生趋势是复杂的多因子综合作用的结果, 沙尘天气与气象要素降水、温度、风、湿度、蒸发量等的关系密切。下面就我国北方沙尘日数与相关气候因子的关系进行讨论。

### 2.1　降水

由图 2和 3可以看出, 降水的年变化呈下降趋势, 全年、春季的降水量与沙尘日数均呈反位相变化的关系。计算全年、春季平均的沙尘日数与降水的逐年序列的相关系数分别为 -0.065、-0.290, 说明降水对沙尘天气有一定的抑制作用。因为沙尘起动的物质条件是丰富、干燥、疏松的地表, 而充沛的降水量有利于改善地表条件, 因此春季 (年)降水量偏大的年份, 沙尘频次相对越低。

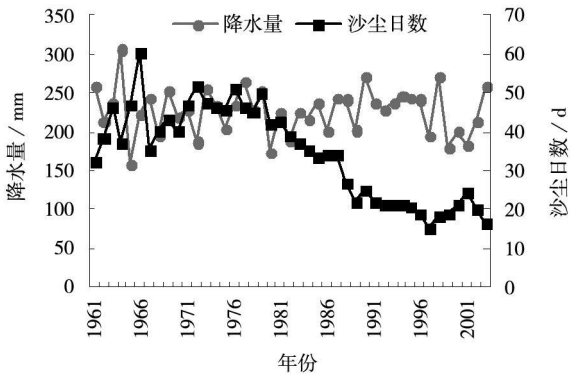


图 2　1961—2003年我国北方年降水量与年沙尘日数的平均值曲线图

Fig. 2　Annual days with dust storm weathers and precipitation in Northern China during 1961-2003

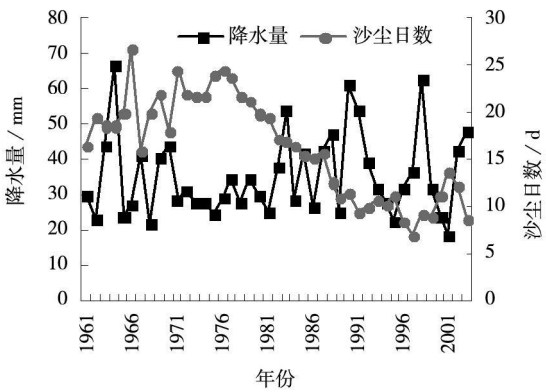


图 3　1961-2003年我国北方春季降水量与春季沙尘日数的逐年平均值曲线图

Fig. 3　Days with dust storm weathers and precipitation in spring in Northern China during 1961-2003

### 2.2　温　度

作 1961-2003年的年平均温度的平均值曲线图 4。

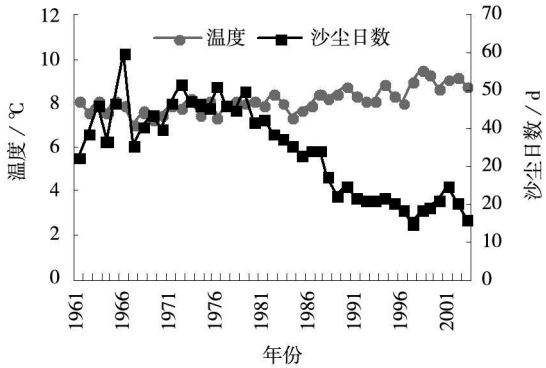


图 4　1961-2003年我国北方年平均温度与年沙尘日数的平均值曲线图

Fig. 4　Annual days with dust storm weathers and mean temperature in Northern China during 1961-2003

可以看出, 年均温度在波动中逐年上升。与相应平均的逐年扬沙+沙尘暴日数求相关, 得到相关系数为 -0.645, 信度水平均超过了 99%。说明我国北方近 43 a温度的升高可能通过大气环流间接地抑制了沙尘天气的发生。

同样, 把温度分离出前冬季和春季平均温度, 沙尘分离出春季沙尘, 发现冬春季平均气温差与年沙尘日数或春季沙尘日数呈显著正相关, 相关系数分别为 0.541、0.587, 通过了 $\alpha = 0.01$的信度检验。

从而得出:

(1) 如果出现前冬气温偏低、次年春季突然回暖的气温突变情况, 很容易诱发沙尘天气的发生, 因为在冬季低温情况下土壤冻结层比较厚, 春暖突然增温后疏松的厚地表层为沙尘天气的发生提供了丰富的物质基础。

(2) 平均温度与沙尘日数的逐年序列有显著的负相关性, 温度偏高的年份少沙尘, 反之, 则多沙尘。与钱维宏等[23]研究指出的近些年北半球中高纬度地区明显变暖导致了温带气旋锋生作用减弱、沙尘日数减少的结果是一致的。20世纪 70年代及以前处于冷期, 也是我国北方大部地区沙尘暴的频发期。冷期亚洲中高纬地区经向环流偏强, 冷空气活动频繁, 大风日数多; 同时冬季气温偏低, 土壤冻结层厚, 春季升温解冻后松土层也偏厚, 具备了丰富的沙尘源条件。可见, 温度对沙尘天气的影响是比较复杂


© 1994-2011 China Academic Journal Electronic Publishing House. All rights reserved.　http://www.cnki.net

的,年际或年代际变化中,主要是通过调整大气环流减弱了风的作用(动力条件),从而间接地影响了沙尘天气的发生;季节变化中,主要是冬季(气温低)向春季(气温高)过渡时,提供了比较丰厚的沙尘源(物质条件)。

**2.3 风速、大风日数、风速≥5 m/s的日数**

形成强沙尘天气的一个必要条件是地面大风,在以往对沙尘源的数值模拟[24]中,指出达到起沙的风速存在一定的临界值,因此以下将对风速、大风日数、风速大于等于5 m/s的日数与沙尘日数的关系进行具体分析。

比较图5、6、7发现,年扬沙+沙尘暴日数与年平均风速、年大风日数、年风速≥5 m/s的日数的逐年变化趋势相当,即先升后降,近几年又有所回升。各类风因子与沙尘日数相关系数值分别为0.928、0.959、0.931,正相关性的可信度很高。

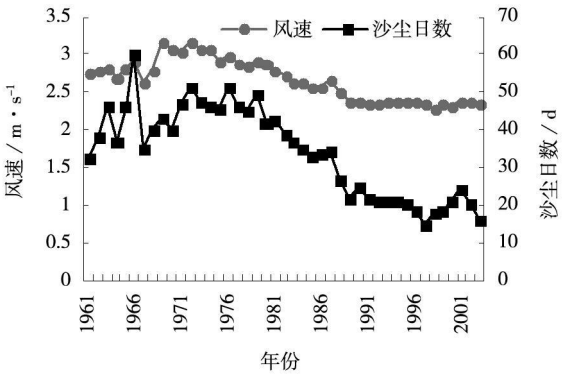


图5 1961-2003年我国北方年平均风速与年沙尘日数的平均值曲线图

Fig.5 Annual days with dust storm weathers and mean wind speed in Northern China during 1961-2003

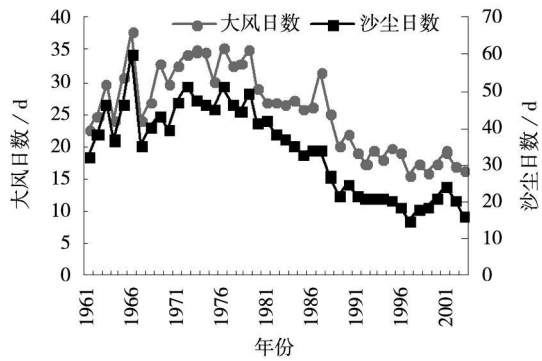


图6 1961-2003年我国北方年大风日数与年沙尘日数的平均值曲线图

Fig.6 Annual days with dust storm weathers and strong wind in Northern China during 1961-2003

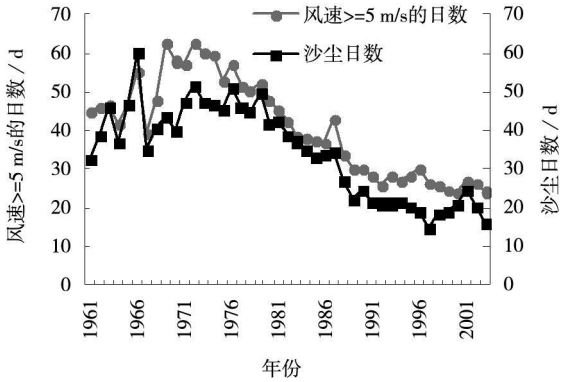


图7 1961-2003年我国北方年风速≥5 m/s的日数与年沙尘日数的平均值曲线图

Fig.7 Annual days with dust storm weathers and mean wind speed exceeding ≥5 m/s in Northern China during 1961-2003

以上分析表明,我国北方大风与扬沙+沙尘暴日数的年际振荡及多年变化趋势具有一致性。这和龚道溢等[25]、叶笃正等[26]研究指出的近些年中纬度大气温压结构的改变导致了我国北方冬春季寒潮势力的减弱,平均风速和大风日数的下降、沙尘日数减少的结果是一致的。而大风日数的增减是气候年代际和年际变化的反映,每年寒潮大风的出现与东亚季风的强度有关,东亚季风有明显的10~50 a尺度的变化。因此,从年代际的时间尺度上分析,是全球气候变暖更长时间地减弱沙尘天气的影响?还是大风日数的年代际变化导致我国北方的沙尘天气可能在经历了20世纪70年代初到现在一个长达40 a以上的减弱期后,进入新一轮的沙尘天气频发期?这一问题还有待深入探讨。但以上分析至少说明了风要素在各区沙尘日数的月、季、年际变化中,都是很重要的、决定性的影响因子。

春季是我国北方沙尘天气的多发季节,而这个季节的特点是:温度回升较快,地表开始解冻,空气变得干燥,土壤蒸发加大,植被还尚未形成。下面继续讨论沙尘天气与湿度、蒸发量的关系。

**2.4 相对湿度**

从图8可以看出,43 a来,我国北方的年平均相对湿度表现出弱的上升趋势,与相应平均的逐年扬沙+沙尘暴日数求相关,得到相关系数为-0.321,通过了95%的置信度检验。可见湿度偏高时,可以减弱沙尘天气的影响。因此,一个地区的沙尘天气是和本地的干旱程度密切相关的,同时也反映了我



© 1994-2011 China Academic Journal Electronic Publishing House. All rights reserved. http://www.cnki.net

国北方地区变湿的气候趋势对沙尘天气的减弱有一定的影响。

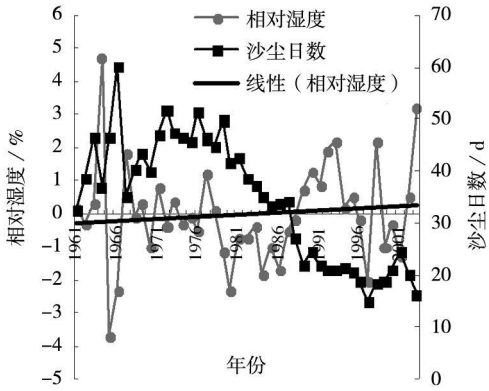


图 8 1961－2003年我国北方年平均相对湿度与年沙尘日数的平均值曲线图

Fig 8 Annual days with dust storm weathers and mean relative humidity in Northern China during 1961－2003

## 2 5 水面蒸发量

水面蒸发量和实际蒸发量有一定差距, 但可以大体反映实际蒸发量的变化趋势及在各区的量级差异。从图 9可以看出, 我国北方各区 38 a来年平均蒸发量的下降趋势是明显的, 计算逐年年平均蒸发量的距平值与沙尘日数序列的相关系数为 0. 552, 二者呈显著的正相关性。因为一个地区的蒸发量大小是和温度、风速密切相关的, 各区年平均风速显著减小是和年蒸发量也在减少的总体趋势是一致的, 而全球变暖也在影响着 1990年以后蒸发量的增加。所以水面蒸发量对沙尘天气的影响是其它气候因子的间接反映。

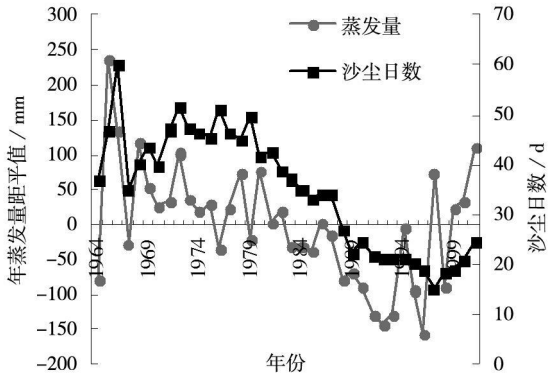


图 9 1964－2001年我国北方年蒸发量距平值与年沙尘日数的平均值曲线图

Fig 9 Annual days with dust storm weathers and evaporation anomalies in Northern China during 1961－2003

# 3 分析结果

综合以上逐年或春季的沙尘日数与气候因子的相关分析发现, 沙尘日数的逐年变化与降水、温度、风、湿度、蒸发量均存在一定的相关性, 可以归纳为:

(1) 春季降水量增多可以抑制春季的沙尘天气的发生频次。

(2) 在温度偏高、湿度较大、风力偏弱、蒸发量不大的年份, 少沙尘天气。

(3) 风要素是影响沙尘天气的最为直接、最优相关的因子, 风速的大小、大风日数的增减直接关系到沙尘天气频数的变化。

(4) 上述几个气候影响因子是区域性气候年际和年代际变化的反映, 因此沙尘天气的短期气候预测要抓住本地的敏感因子和气候异常变化的信号。

## 参考文献 (References)

〔1〕 中央气象局. 地面气象观测规范〔S〕. 北京: 气象出版社, 1979. 21－27. 〔China Meteorological Administration. Specifications for surface meteorological observation〔S〕. Beijing: China Meteorological Press, 1979. 21－27. 〕

〔2〕 王式功, 董光荣, 陈惠忠, 等. 沙尘暴研究的进展〔J〕. 中国沙漠, 2000, 20(4): 349－356. 〔WANG Shigong, DONG Guarrgrong, CHEN Huizhong, et al. Advances in studying sand-dust storms of China〔J〕. Journal of Desert Research, 2000, 20(4): 349－356. 〕

〔3〕 刘瑞兰, 吴占华, 任国玉. 大气－海洋环流异常对山西省沙尘天气的影响〔J〕. 干旱区研究, 2010, 27(2): 217－223. 〔LIU Ruilan, WU Zhanhua, REN Guoyu. Effect of atmospheric－ocean circulation fluctuation on the freguency of dust weather over Shanxi Province〔J〕. Arid Zone Research, 2010, 27(2): 217－223. 〕

〔4〕 THOMAS LITTMANN T. Dust storm freguency in Asia: climatic control and variability〔J〕. International Journal of Climatology, 1991, 11: 393－412.

〔5〕 GOUDIE A S, MIDDLETON N J. The changing frequency of dust storms through time〔J〕. Climatic Change, 1992, 20: 197－225.

〔6〕 MCTAINSH G H. Climatic controls upon dust storm occurrence in eastern Australia〔J〕. J Arid Environments, 1998: 457－466.

〔7〕 夏训诚, 杨根生. 中国西北地区沙尘暴灾害及防治〔M〕. 北京: 中国环境科学出版社, 1996. 〔XIA Xuncheng, YANG Gensheng. Sand-dust storm disaster and prevention countermeasures in Northwestern China〔M〕. Beijing: China Environmental Science Press, 1996. 〕

〔8〕 钱正安, 贺慧霞, 瞿章, 等. 我国西北地区沙尘暴的分级标准和个例谱及其统计特征〔M〕//中国沙尘暴研究. 北京: 气象出



© 1994-2011 China Academic Journal Electronic Publishing House. All rights reserved. http://www.cnki.net

版社, 1997: 1-10. [QIAN Zhengan, HE Huixia, QU Zhang, et al. The classification standard of dust-storm in northwest China and its case spectra and statistic characteristics[M]//Study of sandstorm in China. Beijing: China Meteorological Press, 1997: 1-10.]

[9] 石广玉, 赵思雄. 沙尘暴研究中的若干科学问题[J]. 大气科学, 2003, 27(4): 591-606. [SHI Guangyu, ZHAO Sixiong. Several scientific issues of studies on the dust storms[J]. Chinese Journal of Atmospheric Sciences, 2003, 27(4): 591-606.]

[10] 李林, 赵强. 青海沙尘暴天气研究[J]. 气象科技, 2002, 30(4): 218-221. [LI Lin, ZHAO Qiang. Studies on the dust storm in Qinghai[J]. Meteorological Science and Technology, 2002, 30(4): 218-221.]

[11] 陈洪武, 王旭, 马禹. 新疆沙尘暴气候背景场的分析[J]. 气象, 2003, 29(6): 37-40. [CHEN Hongwu, WANG Xu, MA Yu. Analysis of climatic background field of sandstorm in Xinjiang[J]. Meteorological Monthly, 2003, 29(6): 37-40.]

[12] 王式功, 杨德保, 金炯, 等. 我国西北地区沙尘暴时空分布及其成因分析[C]//中国科协第二届青年学术年会论文集(资源与环境科学分册). 北京: 中国科学技术出版社, 1995: 364-370. [WANG Shigong, YANG Debao, JIN Jiong, et al. Analyses of time-space distribution and formative causes of sandstorms occurred in Northwest China[C]//The Proceeding of the Second Academic Conference of Young Scientists of Chinese Association for Science and Technology. Beijing: China Science and Technology Press, 1995: 364-370.]

[13] 全林生, 时少英, 朱亚芬, 等. 中国沙尘天气变化的时空特征及其气候原因[J]. 地理学报, 2001, 56(4): 477-485. [QUAN Linsheng, SHI Shaoying, ZHU Yafen, et al. Temporal-spatial distribution characteristics and causes of dust-day in China[J]. Acta Geographica Sinica, 2001, 56(4): 477-485.]

[14] 翟盘茂, 李晓燕. 中国北方沙尘天气的气候条件[J]. 地理学报, 2003, 58: 125-131. [ZHAI Panmao, LI Xiaoye. On climate background of duststorms over northern China[J]. Acta Geographica Sinica, 2003, 58: 125-131.]

[15] 邹旭恺, 王守荣, 陆均天. 气候异常对我国北方地区沙尘暴的影响及其对策[J]. 地理学报, 2000, 55: 169-176. [ZHOU Xukai, WANG Shourong, LU Juntian. Impacts of climate abnormality on dust devil in North China and Countermeasures[J]. Acta Geographica Sinica, 2000, 55: 169-176.]

[16] 张莉, 任国玉. 中国北方沙尘暴频数演化及其气候成因分析[J]. 气象学报, 2003, 61(6): 744-750. [ZHANG Li, REN Guoyu. Change in dust storm frequency and the climatic controls in Northern China[J]. Acta Meteorologica Sinica, 2003, 61(6): 744-750.]

[17] 李彰俊, 郝璐. 地面冻结状况与春季沙尘暴发生的关系[J]. 干旱区地理, 2008, 31(2): 203-209. [LI Zhangjun, HAO Lu. Relationship between soil freezing and thawing condition and sandstorm occurrence[J]. Arid Land Geography, 2008, 31(2): 203-209.]

[18] 邱玉珺, 牛生杰, 邹学勇, 等. 沙尘天气频率与相关气象因子的关系[J]. 高原气象, 2008, 27(3): 637-643. [QIU Yujun, NIU Shengjie, ZHOU Xueyong, et al. The relationship between dust event frequency and meteorological Factors[J]. Plateau Meteorology, 2008, 27(3): 637-643.]

[19] 范可, 王会军. 异常弱的南极涛动和2006年我国春季沙尘气候趋势[J]. 气候与环境研究, 2007, 12(4): 475-480. [FAN Ke, WANG Huijun. The weakening of the antarctic oscillation and the dust climate during spring 2006 in China[J]. Climatic and Environmental Research, 2007, 12(4): 475-480.]

[20] 黄嘉佑. 气象统计分析与预报方法[M]. 北京: 气象出版社, 2004: 1-50, 121-141. [HUANG Jiayou. Meteorological Statistical Analysis and Forecasts Method[M]. Beijing: Meteorology Press, 2004: 1-50, 121-141.]

[21] JONES P D, HULME M. Calculating regional climatic time series fort temperature and precipitation: methods and illustrations[J]. Int J Climatol, 1996, 16: 361-377.

[22] 杨东贞, 房秀梅, 李兴生. 我国北方沙尘暴变化趋势的分析[J]. 应用气象学报, 1998, 9(3): 352-358. [YANG Dongzhen, FANG Xiumei, LI Xingsheng. Analysis on the variation trend of sandstorm in northern China[J]. Journal of Applied Meteorological Science, 1998, 9(3): 352-358.]

[23] QIAN Weihong, QUAN Lingshen, SHI Shaoyin. Variation of the dust storm in China and its climatic control[J]. Journal of Climate, 2002, 15: 1216-1229.

[24] 刘明义, 代全厚, 张黎辉, 等. 沙地土壤风蚀动力因子分析[J]. 中国水土保持, 2000, (7): 28-30. [LIU Mingyi, DAI Quanhou, ZHANG Lihui, et al. Analysis of factors causing wind erosion in sandy land[J]. Soil and Water Conservation in China, 2000, (7): 28-30.]

[25] 龚道溢, 王绍武. 西伯利亚高压的长期变化及全球变暖可能影响的研究[J]. 地理学报, 1999, 54(2): 125-133. [GONG Daoyi, WANG Shaowu. Long term variability of the Siberian High Pressure and the possible connection to global warming[J]. Acta Geographica Sinica, 1999, 54(2): 125-133.]

[26] 叶笃正, 丑纪范, 刘纪远, 等. 关于我国华北沙尘天气的成因与治理对策[J]. 地理学报, 2000, 55(5): 513-521. [YE Duzheng, CHOU Jifan, LIU Jiyuan, et al. Causes of sand-stormy weather in northern China and contral measures[J]. Acta Geographica Sinica, 2000, 55(5): 513-521.]



© 1994-2011 China Academic Journal Electronic Publishing House. All rights reserved. http://www.cnki.net

# Climatic controls of dust storm events in northern China

WU Zhan-hua[1], REN Guo-yu[2], XU Wei-li[1], LIU Rui-lan[1]

(1 Shuozhou Meteorological Office, Shanxi Province, Shuozhou 036001, Shanxi, China;
2 Lab for Climate Studies, National Climate Center, CMA, Beijing 100081, China)

**Abstract**: The sand-dust weather is a typical disastrous weather, which can be divided into three categories: sandstorm, blowing sand and floating dust. Sand and dust weather usually occurs in the semi-arid, arid and desert area. The formation of dust storms to be three basic conditions: First, high winds. The other is the ground bare sand material. Three are unstable air. Days with sand dust are attributed to the background of large-scale circulations. In addition to this, it is related to climatic factors. In northern China is the world's four major storms District (Central Asia, North America, Africa and Australia), sandstorm zone in Central Asia as part of modern dust storms, which are one of high incidence areas. In this paper, the author analyzed climatological variation of dust storms from 340 observation stations selected in Northern China from 1961 to 2003. By using correlation analysis and regional mean method, the relationship between the variability features on seasonal and inter-annual scales of tendency of days with dust storms and the influencial factors such as precipition, air temperature, wind, relative humidity, evaporation and so on is analyzed and discussed in detail. The results are observed, that in spring the declining of days with dust storms is obviously related to increasing precipition, dust storm events are more frequent when the temperature has an abrupt change from last winter to next spring, and this is because the spring in northern China, sparse vegetation, desert and bare surface warming rapidly warmer, the ground temperature quickly, then the event of strong cold air transit, it will be easier the formation of sandstorms. The research also shows that Dust storms are more likely to occur in the years when temperature, mean relative humidity is low, mean wind speed is high or days with strong wind are more. And mean wind speed is the most important factor influencing the frequentcy of dust storms in northern China. Once there is strong wind, dust and tiny pieces of sand will be heaved into the air, causing flying dust, flying sand and even sandstorms.

**Key Words**: dust storms; northern China; climatic factor

## 中国科学院新疆生态与地理研究所“青年人才国外培养计划”正式启动

2011年4月7日,中国科学院新疆生态与地理研究所“青年人才国外培养计划”正式启动。经过研究所“青年人才国外培养计划”管理委员会严格规范的遴选,桂东伟博士成为该项计划的首位资助获得者。他将赴美国科罗拉多州立大学水科学学院从事为期一年的土壤、水分变化及其与植物之间关系的研究工作。

“青年人才国外培养计划”是研究所为培养和储备优秀人才,以公派访问学者的形式,支持优秀青年科研人员到国外发达国家的大学和科研机构从事研究工作的一项措施。所需经费由研究所、部门、项目三方按照1∶1∶1的比例进行分摊,资助时间1年。

该计划是新疆生地所一系列加快研究所青年科技人才的培养,保证研究所的持续、快速发展的重要措施之一。旨在构筑良好的人才建设基地,为实现研究所的战略发展目标,奠定良好的人才基础。

© 1994-2011 China Academic Journal Electronic Publishing House. All rights reserved. http://www.cnki.net

科学通报 2011 年 第 56 卷 第 22 期：1828 ~ 1838
论 文 www.scichina.com csb.scichina.com
《中国科学》杂志社 SCIENCE CHINA PRESS

# 青藏高原东北部土壤冻融过程的数值模拟

夏坤[①②③], 罗勇[②④⑤*], 李伟平[②]

① 中国科学院大气物理研究所, 北京 100029;
② 中国气象局气候研究开放实验室, 北京 100081;
③ 中国科学院研究生院, 北京 100049;
④ 清华大学地球系统科学研究中心, 北京 100084;
⑤ 地球系统数值模拟教育部重点实验室, 北京 100084
* 联系人, E-mail: yluo@cma.gov.cn

2011-01-25 收稿, 2011-04-27 接受
国家重点基础研究发展计划(2007CB411505, 2010CB951902)和国家自然科学基金(40975042, 40905046)资助

**摘要** 利用青海省苏里站 2009 年 2 月 1 日~12 月 31 日的气象观测资料作为模式强迫场, 使用陆面过程模式 CLM3.0(Community Land Model), 对青藏高原东北部季节性冻土区域进行模拟. 结果表明, 模式能够较好地模拟出各层土壤的冻融变化趋势, 但在融化阶段, 模拟的土壤温度高于观测, 融化结束时间早于观测; 冻结阶段, 模拟的土壤温度略低于观测, 深层土壤冻结时间早于观测; 整体看来, 模式对冻结过程的模拟好于对融化过程的模拟, 对靠近表层的土壤模拟好于深层. CLM3.0 模式中认为冻土在土壤温度高于 0℃时发生融化, 本文根据热力学平衡方程得到土壤发生冻融的临界温度, 进而对冻土的融化条件进行调整, 融化条件的调整减缓了冻土的融化速率, 使得土壤温度模拟降低, 同时, 调整后的模式模拟结果反映了冻土融化过程中伴随有冻结过程的发生, 与真实的冻土融化过程更为接近. 此外, 通过敏感性试验发现, 融化过程和冻结过程中土壤水的冻结速率是不同的, 表明模式中用于计算土壤发生相变后温度的方案还有待进一步改进.

**关键词**
冻结过程
融化过程
临界冻融温度
冻融条件
数值模拟

冰冻圈是全球气候系统五大圈层之一, 它是对气候系统影响最直接和最敏感的圈层, 被认为是气候系统多圈层相互作用的核心纽带和关键性因素之一. 气候与冰冻圈计划(CLiC, Climate and Cryosphere)的启动是冰冻圈研究成为国际热点的标志之一[1] (http://www.climate-cryosphere.org/en/). 冻土作为我国陆地冰冻圈中一个非常重要的因子, 主要分布在青藏高原这样的气候变化敏感区, 再加上冻土独特的水热特性, 它的变化会对地气间水热交换、植被及生态系统、地气间碳循环以及天气气候系统都起着至关重要的作用. 土壤的冻结和融化过程是高原地表最显著的物理特征之一[2], 有研究表明, 与青藏高原地表相联系的冻融过程与我国夏季降水之间存在较好的相关[3], 因此, 分析研究青藏高原地区的陆气相互作用, 对提高模式的气候预测能力有着重要意义.

冻土与气候之间的相互作用研究开始较早, 但主要集中在气候变化对冻土的影响上[4~8], 而冻土变化过程对气候的影响, 特别是对我国气候变化的影响研究还相对较少. 包含复杂物理过程的冻土模式研究, 特别是与气候变化有关的模式研究, 是一项极具挑战性的工作[9]. 由于冻土过程本身的复杂性以及缺少大范围的冻土观测资料, 在一定程度上限制了冻土模型的发展. 直到 20 世纪 90 年代后期, 陆面过程模式中冻土参数化的问题才得到重视, 不少陆面过程模式中开始添加冻土参数化方案, 如 SSiB (Simplified Simple Biosphere Biosphere Model)利用简

**英文版见**: Xia K, Luo Y, Li W P. Simulation of freezing and melting of soil on the northeast Tibetan Plateau. Chinese Sci Bull, 2011, 56, doi: 10.1007/s11434-011-4542-8

单的函数关系对土壤水力传导系数、热传导系数等参数化方案进行一些修正[10]. Slater 等人[11]在 BASE 模式中考虑了冻融过程, 通过比较单位土壤中耗热或放热量与可耗热或可放热量来计算产冰率. Koren 等人[12]在中尺度模式 Eta Model 中考虑了土壤的冻融过程. Cherkauer 等人[13]在 VIC 模式中考虑了土壤水冻融时对能量以及冰对土壤有效含水量和水分输送量的影响. Niu 等人[14]在热力学平衡态基础上在 CLM 中加入了冻融方案. 国内与气候研究有关的冻土模式研发工作较少, 李倩和孙菽芬[15]发展的冻土水热传输模型是较好的一个, 该模式中选择了总焓和总土壤质量作为土壤水热运动方程的预报变量, 能有效地避免土壤发生相变时相变速率的不确定性引起的计算不稳定.

1979 和 1998 年在青藏高原进行的两次大气科学实验为高原陆气相互作用的研究提供了必要条件[16,17], 但由于观测时间集中在 5~9 月, 使得包含冻土过程的高原陆面过程模拟研究仍然是个空白. 因此, 利用较长时间序列且包含冻融过程的资料对高原冻土区域进行陆面过程模拟是一项非常有意义的工作. 国际陆面模式比较计划(PILPS)通过对 20 余个具有代表性的陆面模式的比较发现, 众多陆面模式在相同的大气强迫下, 对陆面水循环和地气通量的模拟存在显著的差别; 大多数陆面模式对湿润区、植被分布均匀区的模拟效果较好, 而对冻土、沙漠等非均匀下垫面状况的模拟能力还存在很大的缺陷[18~20]. 陆面过程模式 CLM(Community Land Model)是目前世界上发展最为完善并被广泛应用的陆面模式之一. 已有许多工作检验了该模式在不同下垫面的模拟能力, 比如季风区[21]、高原稀疏植被和水田[22]、中国典型气候区[23]、沙漠区[24]等, 相比较而言, 由于冻土观测资料的缺乏, 导致该模式对冻土区域的研究相对较少, 辛羽飞等人[25]验证了该模式在我国西北干旱区和高原西部地区的适用性, 但模拟时间较短, 而且仅对夏季进行了模拟, 王澄海等人[26]和罗斯琼等人[27]检验了该模式对我国青藏高原西部、中部的模拟能力, 然而, 该模式在高原北部的模拟能力尚未有人做过验证.

本文利用青海省苏里站 2009 年 2 月 1 日~12 月 31 日的观测资料进行单点数值模拟试验, 通过比较观测值与模拟值在土壤温度和湿度的差异, 检验该模式在高原东北部季节性冻土区域的适用性, 并针对模式中土壤冻融条件的不足对模型进行改进, 为冻土模式的发展提供了一定的依据.

## 1 模式简介及资料

### 1.1 模式说明

本文使用的陆面过程模型是由 NCAR(National Center for Atmospheric Research)发展的 CLM3.0 模式, 它是在 BATS, IAP94, LSM 等陆面模式的基础上发展起来的. 该模式主要由垂直分布不均匀的土壤层、最多 5 层积雪层和 1 层植被层构成. 考虑到水平网格内的地表特征差异或不同的植被类型下的生态学差异, 以及不同土壤类型的水力学和热力学特征差异等, 同一网格中的各下垫面类型受相同的大气强迫, 各下垫面的通量独立计算, 最后按照各下垫面类型所占权重做面积加权平均后反馈给大气.

CLM3.0 模式进行 off-line 试验时需要的大气强迫场资料有: 温度、压强、湿度、风速、降水、向下的大气长短波辐射. 关于陆面模式中土壤分层的问题至今仍无定论, 但有一点共识是, 由于浅层土壤的湿度梯度较大[28], 为了精确描述土壤湿度变化, 一般浅层土壤的分层要多于深层[29]. CLM3.0 中土壤的垂直分层采用指数形式, 各层的深度分别为 0.71, 2.79, 6.23, 11.89, 21.22, 36.61, 61.98, 103.80, 172.76, 286.46 cm, 有关该模式的详细说明可参考文献[30].

本文使用的是 CLM3.0, 它与 CLM4.0 在土壤冻融条件上的差异表现为土壤冻结条件的不同. 前者认为当土壤温度低于 0℃时, 土壤中所有的液态水均冻结成冰, 此时土壤中不含液态水; 而后者引入了过冷水的概念, 认为当土壤温度低于 0℃时, 土壤中仍含有一定的液态水, 当土壤中的液态水含量大于该温度下土壤中的最大液态水含量时, 土壤中多余的液态水才会冻结成冰. 由于后者的描述更符合观测事实, 因此, 用 CLM4.0 中的冻融条件替换 3.0 中的相应模块[31], 其冻融条件具体表现为:

$$T > T_{\mathrm{frz}} \text{ 且 } \theta_{\mathrm{ice}} > 0\text{，土壤融化，}$$

$$T < T_{\mathrm{frz}} \text{ 且 } \theta_{\mathrm{liq}} > \theta_{\mathrm{liq,max}}\text{，土壤冻结.}$$

其中, 土壤发生冻融后的温度为 $T_{\mathrm{frz}}$, $\theta_{\mathrm{liq,max}}=\theta_{\mathrm{sat}}\left\{\dfrac{10^3 L_f (T-T_{\mathrm{frz}})}{gT\psi_{\mathrm{sat}}}\right\}^{-1/b}$, 它是冰点温度下土壤中的最大液态水含量; 水的冰点温度 $T_{\mathrm{frz}}$ 为 273.16 K; $\theta_{\mathrm{sat}}$ 为

饱和土壤含水量; $\theta_{liq}$ 为土壤的体积含水量; $\theta_{ice}$ 为土壤的体积含冰量; $\psi_{sat}$ 为饱和土壤水势(mm); 融解潜热 $L_f$ 为 $0.336\times10^6$ J/kg.

### 1.2 资料介绍

本文所使用的资料为青海省苏里站(38.42°N, 98.30°E)2009 年 2 月 1 日~12 月 31 的观测资料. 该站点位于青藏高原东北部、疏勒河上游地区, 海拔3802 m, 土壤质地以砂壤土为主, 地表植被以高寒草甸为主, 具有明显的高原寒带气候特征, 年均温度较低, 降水量较少. 苏里站布有一座 10 m 高的气象观测塔, 分别在 2, 5, 7.5, 10 m 这 4 个高度上进行大气观测, 观测量有 10 min 一次的空气温度、压强、湿度、风速记录, 降水量由一个 T_200B 雨量计进行记录. 地表下的观测量有 5, 10, 30, 50, 70 cm 处的土壤温度; 20, 40, 60 cm 处的土壤湿度; 5 和 10 cm 处的土壤热通量. 另外, 气象塔上还布有一套涡动辐射仪, 每 30 分钟记录一次太阳向下长短波辐射、地面反射的短波辐射和地面向上长波辐射. 大气强迫场使用气象观测塔 2 m 高度处的观测值, 并将模式中所需要的大气底层高度取为 2 m. 对于单点 off-line 试验, 考虑到模式对初值的敏感性, 对模式进行了2 a 的 spin-up. 为了更直观地分析土壤发生冻融时的水热变化, 输出同深度上的土壤温度和土壤湿度进行比较, 因此, 将模拟的土壤温度线性插值到有土壤湿度观测的层次, 即 20, 40 和 60 cm 处.

## 2 模拟结果及分析

利用模式对青海省苏里站 2009 年 2 月 1 日~12 月 31 日的土壤水热过程进行单点 offline 试验(称该试验为控制试验, 记为 ctrl), 以检验模式对季节性冻土区域土壤水热交换过程的模拟能力. 由于冻土变化会引起土壤中冰的变化, 造成土壤水热特性的改变, 从而影响土壤温度和土壤湿度的模拟, 因此, 通过以下几项试验分别检验模式对土壤温度和土壤湿度的模拟.

### 2.1 土壤温度

陆面过程模式中土壤温度的计算准确与否关系到模式中地表与大气之间的能量和物质交换, 从而影响大气模式模拟的准确性, 因此, 土壤温度的模拟非常关键[32].

自 2009 年 2 月开始, 2 m 高度处的大气温度有小幅上升, 之后迅速降低, 3 月上旬气温降至–20℃左右. 尽管 3 月上旬~4 月初有几次小的降温过程, 但气温变化的整体趋势以上升为主, 特别是 3 月末~4 月初, 气温由–10℃迅速升至 0℃之上, 6 月之后一直维持在 0℃以上. 随着冬季的到来, 入射短波辐射减少, 2009 年 10 月上旬气温迅速下降, 在短时间内由 3℃降到 –10℃左右(图 1(a)). 靠近表层的土壤温度与气温的变化趋势较为一致, 模式模拟的 20 cm 土壤温度在 4 月初升至 0℃之上, 与观测极为接近(图 1(b)), 但中深层土壤温度的变化与浅层相比有所滞后, 观测的 40 和 60 cm 处土壤温度分别在 5 月 10 日和 6 月 5 日升至 0℃之上, 模拟的各层冻土完全融化时间均早于观测, 越深层土壤完全融化的时间与观测相比相差越大, 60 cm 处两者相差达 1 个月左右(图 1(c)和(d)). 模式模拟的20 cm 层土壤发生冻结的时间与观测很接近, 只是模拟的土壤温度在 11 月中旬之后略小于观测, 但较深层土壤发生冻结的时间早于观测, 60 cm 处土壤发生冻结的时间与观测相差 15 d 左右(图 1(d)). 整体看来, 模式对土壤冻结过程的模拟好于融化过程的模拟.

徐学祖等人[33]通过对兰州黄土、砂土、红土以及内蒙黏土、壤土等的试验发现, 各类土壤的冻结温度和融化温度均在 0℃之下, 说明冻土在土壤温度低于 0℃时就发生融化. CLM3.0 中认为当冻土温度高于冰点温度时, 土壤中的冰才发生融化. 模式模拟的 3 月上旬土壤温度低于 0℃, 土壤中的冰尚未融化, 而此时实际观测的土壤已经发生融化, 土壤未冻水含量略有增加(图 2). 冰的融化需要从土壤中吸收能量, 同时, 土壤含冰量减小也会减缓下层热量向上传导, 从而抑制土壤温度的升高, 而模拟的土壤不发生融化, 来自下层的热量使得土壤温度升高, 因此, 3~4 月土壤温度的模拟高于观测. 一旦模拟的土壤温度达到 0℃, 加上气温上升, 模拟的土壤水于 4 月中旬即全部融化, 融化时间早于观测. 当模拟的土壤温度发生融化而观测的土壤尚未发生融化时, 模拟与观测的土壤温度相差较大, 5 月初 40 cm 处土壤温度的模拟与观测相差 4℃左右(图 1(c)).

总体看来, 模式能够较好地模拟出各层土壤温度的变化趋势, 模式对冻结过程的模拟稍好于融化过程, 表层土壤温度的模拟好于深层, 但融化阶段, 模式模拟的冻土融化过程过快, 导致土壤温度的模

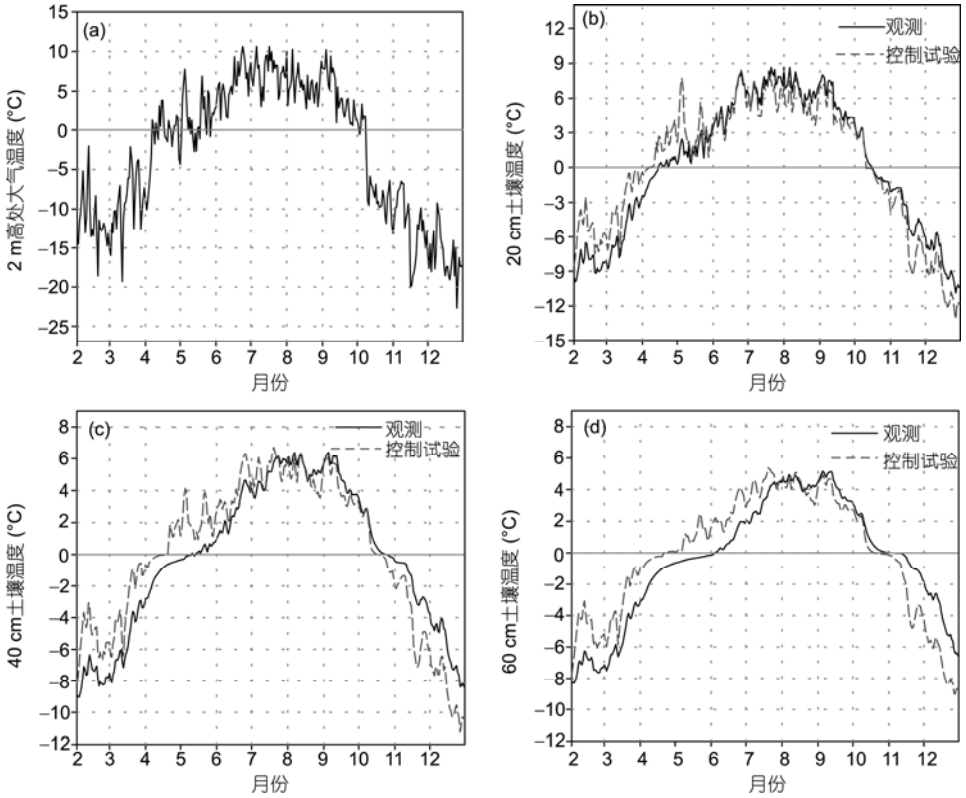


**图 1　观测的大气温度(a)和不同层次土壤温度模拟(记为 ctrl，虚线)与观测(记为 obs，实线)的对比((b)~(d))**

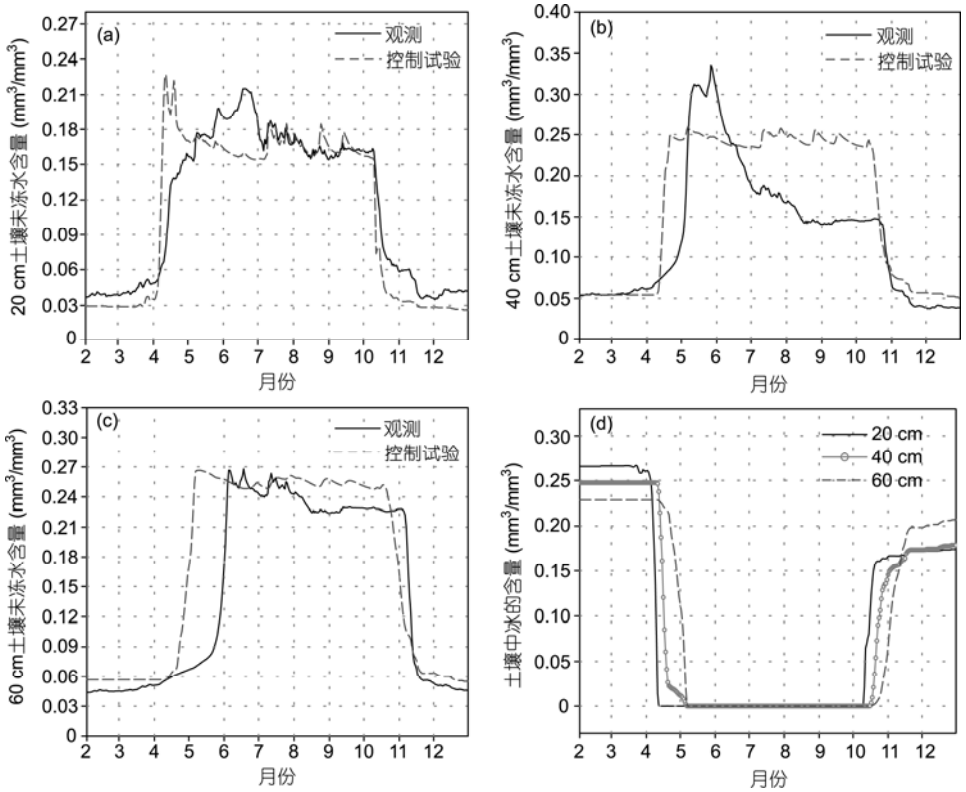


**图 2　不同层次土壤未冻水含量模拟(记为 ctrl，虚线)与观测(记为 obs，实线)的对比((a)~(c))和三层土壤含冰量的模拟(d)**

拟高于同时期的观测, 冻土融化时间早于观测; 冻结阶段, 较深层土壤冻结的时间早于观测, 模拟的土壤温度低于观测.

### 2.2 土壤湿度

土壤湿度变化可以影响径流、反照率、地表感热及潜热通量, 从而影响区域气候, 是气候变化研究中一个重要的物理量[34]. 土壤湿度模拟的好坏与否也是检验模式模拟性能的主要标准之一.

2009 年 2~4 月, 模式模拟的土壤液态水含量基本保持不变(图 2(a)~(c)), 当各层土壤依次满足融化条件时, 土壤由表层到深层逐层发生融化, 土壤中的冰在短时间内迅速减小, 以 20 cm 为例, 土壤含冰量在 4 月上旬从 0.27 迅速降至 0. 20 和 60 cm 土壤层完全融化的时间相差近 1 个月(图 2(d)), 反应了温度波向下传播的过程. 而实际观测的各层土壤液态水含量从 3 月初开始缓慢增加, 针对 60 cm 土壤层, 土壤液态水含量从 2009 年 2~3 月上旬一直保持在 0.045 附近, 至 5 月下旬, 土壤液态水含量缓慢增加到 0.08 左右(图 2(c)), 此时对应的土壤温度从–6℃升至–1℃(图 1(c)), 这一观测事实表明冻土在土壤温度低于 0℃时就已经发生融化, 而模式中认为当土壤温度超过 0℃时冻土才发生融化, 显然与观测事实不符. 虽然模式模拟的冻土开始融化时间较晚, 但融化速率较快, 融化结束的时间早于观测. 当 4 月中旬模式模拟的 60 cm 土壤中的冰全部融化时, 对应观测的冻土尚未全部融化, 因此, 模拟的土壤液态水含量大于观测(图 2(b)). 冻结阶段, 模式对土壤冻结时间以及土壤中液态水含量的模拟均与观测相当, 好于对融化阶段的模拟.

总之, 模式能够对各层土壤水分含量的季节变化进行较好地模拟, 季节变化趋势基本与观测吻合, 冻结阶段的模拟好于融化阶段, 但模式模拟的冻土融化结束时间早于观测, 融化阶段的土壤液态水含量大于观测.

## 3 模型的改进

通过 ctrl 试验的模拟结果可以看出, 尽管模式较好地模拟了土壤冻融过程的变化趋势, 但模式中认定冻土在土壤温度高于 0℃时才发生融化与观测事实不符[33], 真实的冻融过程是一个连续缓慢的变化过程, 不存在固定的冻融临界温度, 必须根据热力学平衡情况下土壤水势和温度之间的关系以及固有的土壤水力学特征本构关系来确定土壤含水量和温度之间的关系, 因此, 采用了李倩和孙菽芬[15]发展的冻土模式中计算土壤冻融临界温度的方法, 来替换 CLM 模式中土壤在 0℃发生冻融的不合理假设. 具体如下:

当土壤中有冰存在时, 土壤水势与冰表面的水汽压相平衡, 根据 Clausius-Clapeyron 方程, 可以得到冻土中土壤水势与温度的函数关系:

$$\psi(T)=\frac{10^3 L_f\left(T-T_{\mathrm{frz}}\right)}{gT}, \tag{1}$$

$\psi$为土壤水势, $T$ 和 $T_{\mathrm{frz}}$ 分别为土壤温度和凝结温度($K$), $L_f$ 为融解潜热(J/kg), $g$ 为重力加速度(m s$^{-2}$).

Spaans 和 Baker[35]证明冻融过程与干湿过程类似, 要考虑土壤水势对液态水含量的依赖关系, 土壤水势可以表示为土壤液态水含量的函数:

$$\psi(\theta_{\mathrm{liq}})=\psi_{\mathrm{sat}}\left(\frac{\theta_{\mathrm{liq}}}{\theta_{\mathrm{sat}}}\right)^{-b}, \tag{2}$$

$\psi_{\mathrm{sat}}$ 为饱和土壤水势, $\theta_{\mathrm{liq}}$ 为土壤液态水含量, $\theta_{\mathrm{sat}}$ 为饱和土壤水含量, 与含砂量有关, $b$ 为 Clapp-Hornberger 参数.

(1)和(2)式联立, 得到土壤液态水含量与临界冻融温度的函数关系为

$$T_{\mathrm{crit}}=\frac{10^3 L_f T_{\mathrm{frz}}}{10^3 L_f-\psi_{\mathrm{sat}}\left(\frac{\theta_{\mathrm{liq}}}{\theta_{\mathrm{sat}}}\right)^{-b} g}, \tag{3}$$

$T_{\mathrm{crit}}$ 即为土壤中的水发生冻融时的临界温度, 当土壤温度低于临界温度 $T_{\mathrm{crit}}$ 时, 土壤中的水开始结冰, 相反, 冻土则发生融化. 图 3 为依据(3)式计算的不同质地的土壤在不同液态水含量下临界冻融温度的变化, 可以看出, 当土壤液态水含量较少时, 砂土的临界冻融温度最高, 壤砂土次之, 其他几种类型均很小. 主要因为砂质土壤中孔隙相对较大, 在一定吸力下, 这些大孔隙容易被排空, 因而, 土壤含水量随吸力的增加而减少很快. 在黏质土壤中, 土壤孔隙大小分布均匀, 吸附的水分较多, 提高吸力使土壤含水量缓慢降低, 因此, 在同样的液态水含量下, 含砂量低的土壤的饱和土壤水势较大, 而含砂量低的土壤的饱和土壤含水量也很大, 使得在同样液态水含量下, 含砂量低的土壤水势较大[36]. 由(1)式可知, 土壤水势和土壤温度成反比关系, 因此, 当土壤液态水含量一定时,

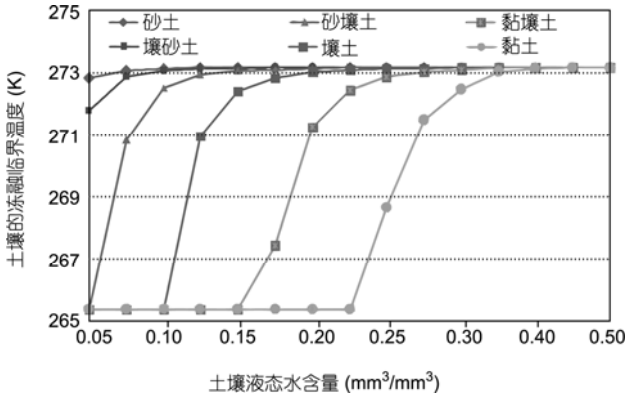


**图 3　不同土壤类型在不同液态水含量下的冻融临界温度变化**

含砂量少的土壤的冻融临界温度较低. 随着土壤液态水含量的增加, 土壤发生冻融的临界温度也逐渐升高, 但仍然略小于冰点温度.

### 3.1　冻土的融化临界温度调整后的模拟结果

用(3)式代替模式中原有冻土发生融化时的临界温度, 冻结条件保持不变, 即:

当 $T > T_{\mathrm{crit}}$ 且 $\theta_{\mathrm{ice}} > 0$ 时, 土壤发生融化, 融化后的土壤温度为 $T_{\mathrm{crit}}$.

通过一组试验(记为 test1)来检验冻土融化条件的改变对模拟结果的影响.

从图 4 可以看出, 冻土的融化临界温度改变前后

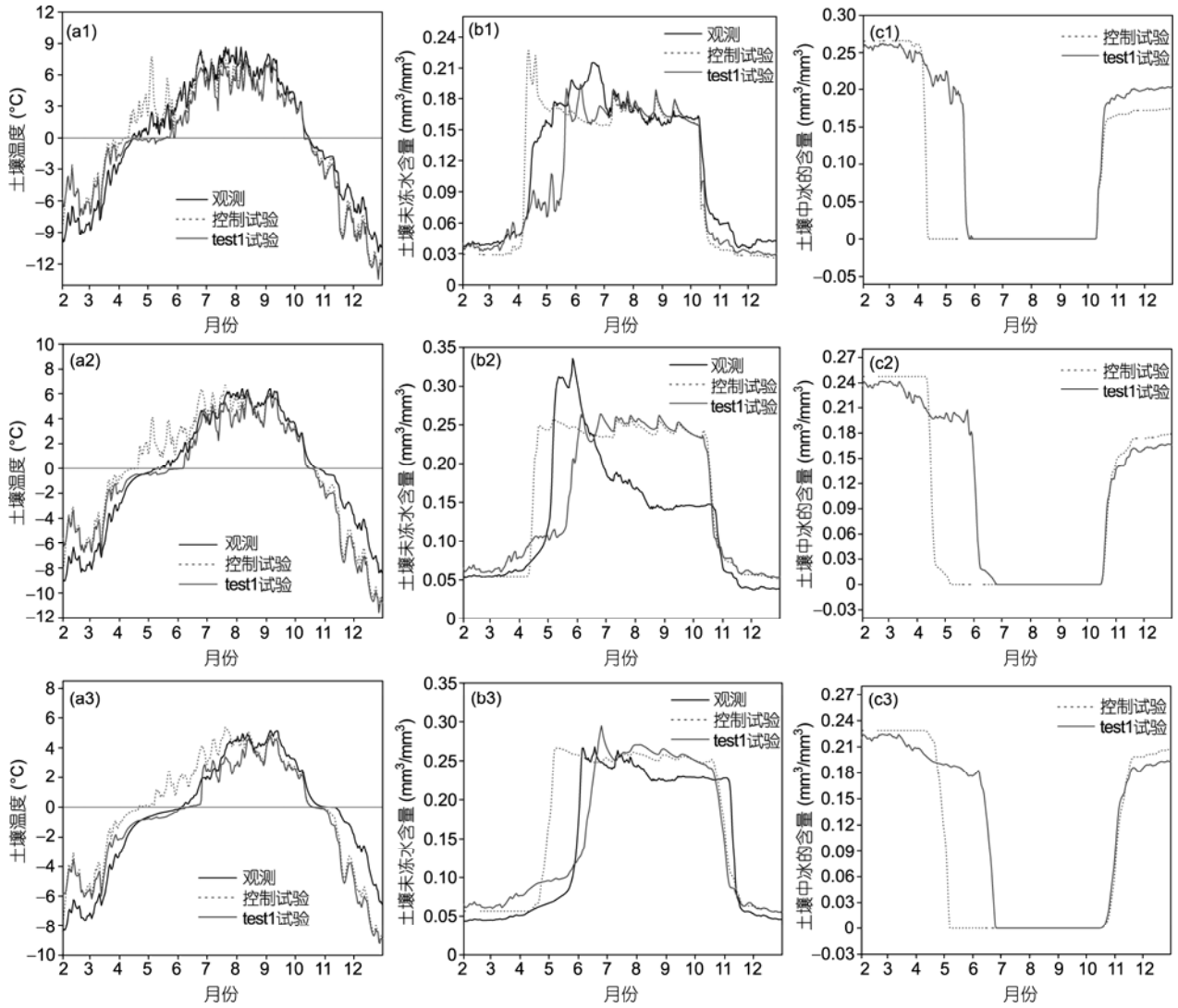


**图 4　改变冻土融化条件前(记为 ctrl, 点线)后(记为 test1, 细实线)模拟结果与观测(记为 obs, 粗实线)的对比**

a 为土壤温度; b 为土壤中未冻水含量; c 为土壤中冰的含量. 1, 2, 3 分别代表 20, 40 和 60 cm 处

对模拟结果的影响主要表现在以下 4 方面: 第一, 融化阶段土壤温度的模拟值减小, 与观测更为接近(图 4(a1)~(a3)); 第二, 融化阶段土壤未冻水含量的模拟也减小(图 4(b1)~(b3)); 第三, 冻土开始融化的时间提前(图 4(c1)~(c3)), 深层冻土完全融化的时间与观测更接近; 第四, 冻土发生融化的过程中伴随有若干小的冻结过程(图 4(c1)~(c3)), 更符合真实的土壤物理过程. 究其原因主要有以下几点:

(1) 改变冻土融化临界温度后, 冻土在 0℃之下的某一温度便开始融化, 如 test1 试验中模拟的 60 cm 处冻土在 3 月中下旬土壤温度约为–2℃时便发生融化, 由于土壤中的冰融化时需要吸收大量的能量, 从而会抑制土壤温度升高, 减缓冻土融化的速率, 使得土壤温度的模拟值小于 ctrl 试验的结果, 与观测更为接近(图 4(a3)), 同时, 也使冻土完全融化的时间有所推迟, 导致当观测的冻土完全融化时, test1 试验中模拟的冻土还未融化完毕, 因此, test1 试验中模拟的融化阶段的土壤未冻水含量小于观测(图 4(b1)~(b3) ).

(2) CLM3.0 中认为当土壤发生相变后, 土壤温度为冰点温度, 然后, 根据可用来发生相变的能量与实际消耗的相变能之差(称为能量净余)对土壤温度进行更新. 只有当土壤中的液态水全部冻结或冰全部融化, 且能量净余不为 0 时, 残余能量才用于土壤温度的变化, 当能量净余为 0 时, 土壤温度保持为冰点温度不变. 当土壤的融化临界温度改变后, 土壤发生融化后的温度为根据公式(3)得到的新融化温度, 它低于冰点温度, 与 ctrl 试验中土壤发生融化后的冰点温度相比相当于整体下移, 因此, 融化阶段土壤温度的模拟有所下降.

(3) 对不同类型的土壤而言, 当土壤温度低于 0℃时, 土壤中最大液态水含量随着土壤温度的降低而减小[37], 即土壤温度越低, 土壤中的最大液态水含量越小. 当冻土的融化临界温度改变后, 土壤中的冰在土壤温度低于 0℃时发生融化, 使得土壤中的液态水含量增加, 而此时土壤温度低于 0℃, 因此, 此时的土壤温度和土壤湿度条件易满足土壤发生冻结的条件. 由图 4(c1)~(c3)可以看出, 尽管 2~4 月期间土壤以融化为主, 但中间也伴随几次小的冻结过程的发生, 改变冻土融化临界温度后的模式对冻土融化过程的描述更符合真实的冻土融化情况.

以上分析表明, 冻土融化条件的改变减缓了冻土的融化速率, 使得模式对融化阶段土壤温度、土壤未冻水含量及冻土融化时间的模拟都与观测更为接近, 但改变冻土融化条件后模拟的浅层冻土融化过程过于缓慢, 对深层的模拟要好于浅层.

### 3.2 土壤的冻结临界温度改变后的模拟结果

在 test1 试验的基础上, 令土壤发生冻结后的温度也为新的土壤冻融临界温度, 以检验对模拟结果的影响, 该试验记为 test2.

当土壤发生冻融时, 根据土壤温度和土壤冻融临界温度的差异, 判断系统过剩或缺失的能量与土壤相变吸收或释放潜热的大小关系, 从而确定含冰量的变化速率, 净余的能量用于更新土壤温度[38]. test1 试验中认为土壤发生冻结后, 土壤的温度为 0℃, 土壤温度以 0℃为基点进行变化, test2 试验中认为土壤冻结后的温度是新的土壤冻融临界温度, 这一温度一直低于 0℃, 土壤温度更新的基点由 0℃变到了低于 0℃的某一温度, 相当于温度整体下移, 因此, test2 试验的结果对于有冰存在的土壤温度模拟呈现出整体下降的趋势, 使得 2~4 月冻土融化阶段模拟的土壤温度与观测更为接近, 但 10~12 月土壤冻结阶段的土壤温度模拟比观测更小(图 5). 10~12 月土壤温度模拟比观测更低主要是因为随着冬季短波辐射的减少, 各层土壤温度也随之降低, 当土壤温度低于冰点温度, 且土壤湿度高于此温度下的最大液态水含量时, 土壤便发生冻结, 释放凝结潜热, 从而阻碍土壤温度降的过低, 但由于模式模拟的土壤冻结过程较快, 土壤很快便处于完全冻结的状态, 此后, 土壤温度的变化主要随大气温度的变化而变化, 因此, 模式模拟的 10~12 月土壤温度低于观测. 究其原因可能是由于土壤在融化阶段和冻结阶段土壤水发生冻结的速率不同造成的.

### 3.3 冻结速率调整后的模拟结果

根据 3.2 节的分析可以推断, 土壤水在冻结阶段与融化阶段的冻结速率是不同的, 下面通过一组敏感性试验(记为 test3)进行检验. 在该试验中, 令土壤水在融化阶段(2~6 月)的冻结速率保持模式中原有速率不变, 在冻结阶段(10~12 月)的冻结速率减为原来的一半, 以检验冻结速率的变化对模拟结果的影响.

结果表明, 模式改变前后对土壤未冻水含量的模拟变化不大, 改变后的模式对 10~12 月各层土壤温度的模拟有较明显地改进, 与观测更为接近(图 6),

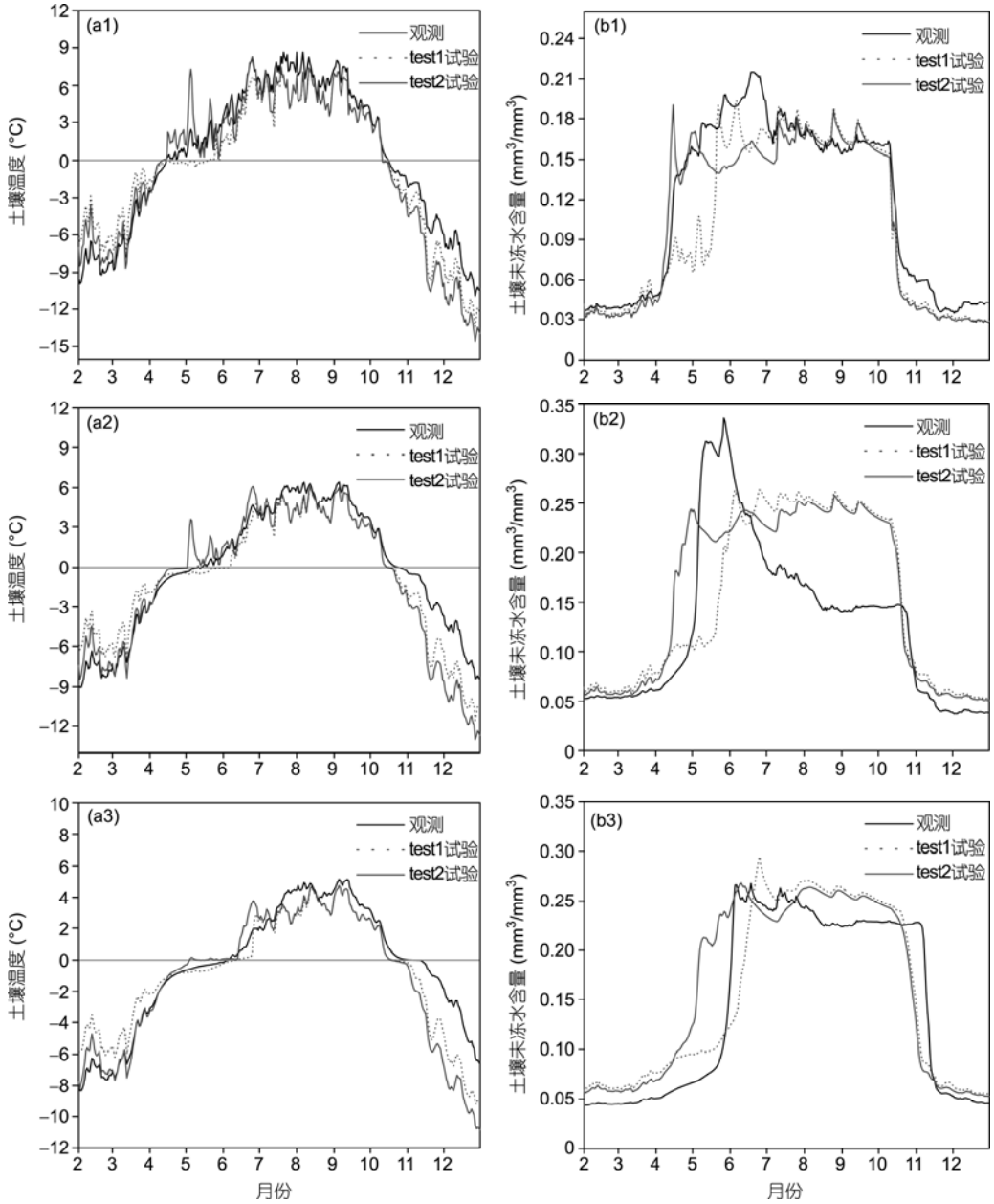


**图 5　冻土融化条件改变前提下，土壤冻结后的温度改变前(记为 test1，点线)后(记为 test2，细实线)模拟结果与观测(记为 obs，粗实线)的对比**

a 代表土壤温度; b 代表土壤未冻水含量. 1, 2, 3 分别代表 20, 40 和 60 cm 处

主要是由于 test3 试验中冻结阶段土壤水的冻结速率明显减小，即单位时间内土壤中生成的冰的含量减小，土壤中的水全部冻结成冰的时间延长，相当于减缓了土壤的冻结过程. 随着未冻水含量的缓慢减少，由于水的热容量比冰大，较大的含水量会阻碍土壤降温过快，同时，由于土壤中含冰量增加缓慢，也会阻碍表层冷却过程对深层土壤的降温影响，因此，模拟的土壤温度高于 test2 试验中的结果.

事实上，改变土壤冻结速率的最直接影响是改变了土壤中的含冰量，而冰的热传导率是水的 4 倍，水的热容量是冰的 2 倍多，因此，土壤含冰量的变化会直接影响土壤向上和向下的热通量[9]，从而影响土壤发生相变后整个系统的能量净余. 根据 CLM3.0 对相变后土壤温度的计算过程(如3.1 中介绍)可知，净

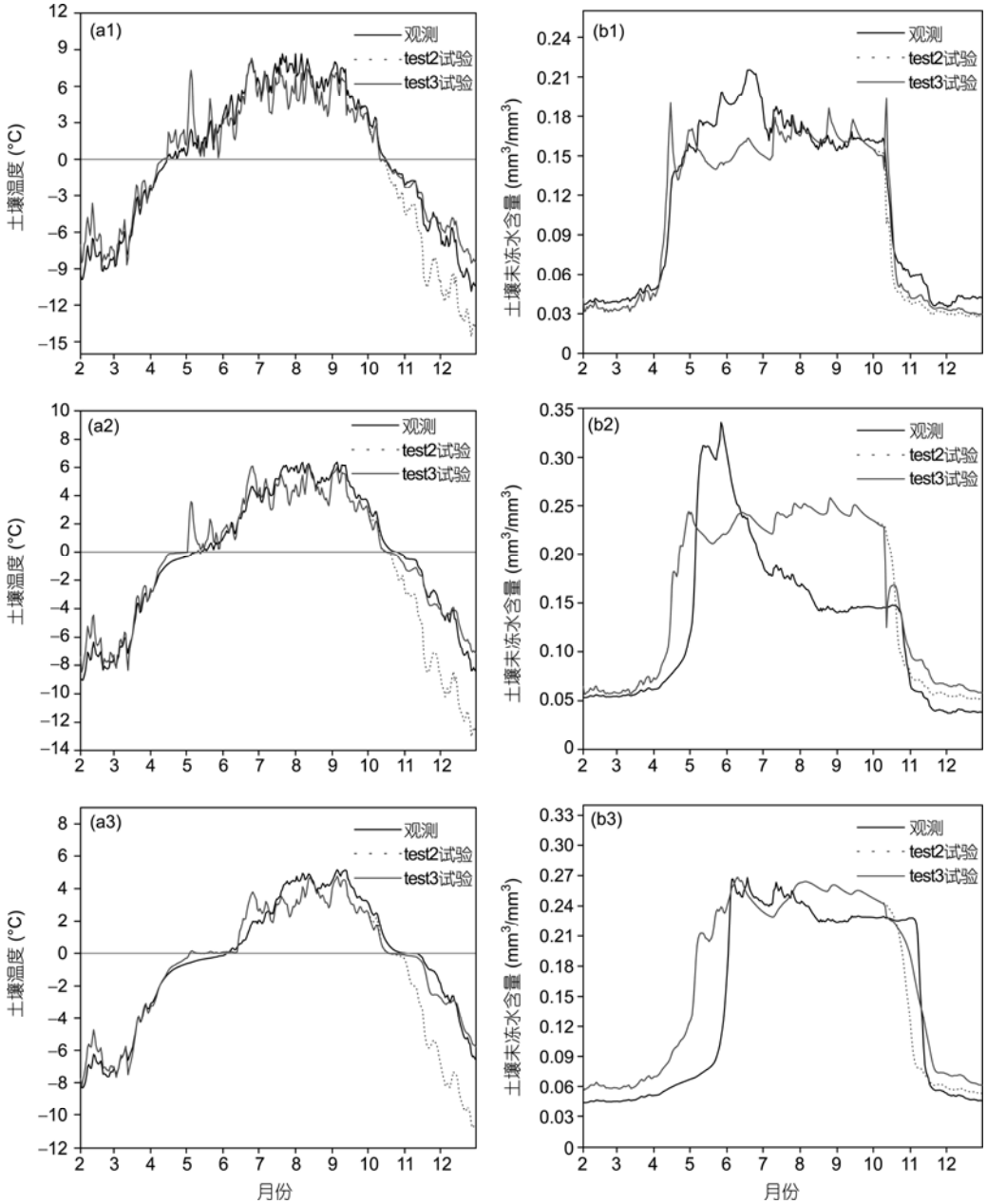


**图 6 土壤冻结阶段的冰冻结速率改变前(记为 test2, 点线)后(记为 test3, 细实线)模拟结果与观测(记为 obs, 粗实线)的对比**

a 代表土壤温度; b 代表土壤未冻水含量. 1, 2, 3 分别代表 20, 40 和 60 cm 处

余能量的多少对相变后土壤温度的计算有很大影响, 因此, 改变土壤冻结速率会影响土壤温度的变化, 同时, 也反应出模式中用于计算相变后土壤温度的算法存在不足, 由于相变项的存在, 给方程的数值求解带来很大的困难, 可以考虑用土壤总焓和土壤水总质量作为预报量, 从而避免为估计相变项的大小给数值求解带来的问题[37].

## 4 结论与讨论

利用陆面过程模式 CLM3.0 对青海省苏里站 2009 年 2 月 1 日~12 月 31 日的土壤水热过程进行模拟, 通过模拟结果与观测资料的对比分析, 检验了陆面过程模式 CLM3.0 对青藏高原东北部季节性冻土区域的模拟能力, 并根据热力学平衡方程得到土壤

发生冻融的临界温度, 对冻土融化的条件进行了调整, 结果表明:

(1) 模式能够对高原季节性冻土区域的土壤热量和水分交换过程进行较好地模拟, 但仍存在一些不足, 主要表现为: 在融化阶段, 模拟的土壤温度高于观测, 土壤中的冰全部融化的时间早于观测; 在冻结阶段, 模拟的土壤温度略低于观测, 深层土壤的冻结时间早于观测; 整体而言, 模式对冻结过程的模拟好于融化过程, 对浅层土壤的模拟好于深层.

(2) 根据热力学平衡方程可得某一液态水含量下土壤的冻融临界温度, 当土壤中液态水含量较少时, 含砂量高的土壤的冻融临界温度较高, 而含砂量低的土壤冻融临界温度较低. 随着土壤中液态水含量的增加, 土壤的冻融临界温度逐渐接近冰点温度, 但一直略低于冰点温度.

(3) 土壤的融化临界温度降低后, 模式能模拟出土壤在冰点之下某一温度开始融化的过程, 由于冻土在低于 0℃时就发生融化, 融化需要吸收能量, 同时, 水的热容量比冰大, 而导热率比冰小, 从而减缓了自下向上的热传导, 阻止土壤温度升高过快, 减缓了冻土的融化速率, 因此, 新方案对冻土融化阶段土壤温度的模拟低于原方案的结果, 与观测更为接近.

(4) 敏感性试验表明, 土壤在冻结过程和融化过程中的冻结速率不同, 冻结过程中的冻结速率大于融化过程中的冻结速率, 浅层土壤冻结较快, 而深层土壤冻结相对较慢, 为今后冻土模型的发展提供了一定的依据.

由于高原地形的复杂性, 将陆面模式应用于高原地区时存在一定的局限性. 尽管改进后的模式对融化阶段各层土壤温度和湿度的模拟有了很大改进, 但改进后的融化方案对浅层土壤融化过程的模拟与观测相比过慢, 且敏感性试验中土壤冻结速率的调节具有主观性, 反应了原模式在计算相变后土壤温度的算法上存在不足, 由于相变项的存在, 给方程的数值求解带来了很大的困难, 可以考虑用土壤总焓和土壤水总质量作为预报量, 从而避免估计相变项给数值求解带来的问题. 另外, 本文的数值试验仅仅针对单点进行, 因此, 需要在更多的高原站点和区域上开展模拟试验, 以加深对寒区土壤冻融和水热过程的认识.

**致谢** 感谢中国科学院寒区旱区环境与工程研究所叶柏生研究员在站点资料以及野外科考方面提供的帮助, (大)王杰博士在资料处理和使用方面给予的帮助, 以及吴锦奎副研究员、(小)王杰、陆胤昊博士在青海省苏里站野外观测中给予的照顾.

## 参考文献

1 秦大河, 效存德, 丁永建, 等. 国际冰冻圈研究动态和我国冰冻圈研究的现状和展望. 应用气象学报, 2006, 17: 649–656
2 王澄海, 韦志刚. 陆面模式中土壤冻融过程参数化研究进展. 地球科学进展, 2001, 17: 44–52
3 王澄海, 董文杰, 韦志刚. 青藏高原季节冻融过程与东亚大气环流关系的研究. 地球物理学报, 2003, 46: 310–312
4 金会军, 李述训, 王绍令, 等. 气候变化对中国多年冻土和寒区环境的影响. 地理学报, 2000, 55: 151–173
5 王绍令, 赵秀锋, 郭东信, 等. 青藏高原冻土对气候变化的响应. 冰川冻土, 1996, 18(增刊): 157–165
6 Jin H J, Cheng G D, Li X, et al. Permafrost on the Qinghai-Tibet Plateau under a changing climate. Chinese Sci Bull, 1999, 44(Suppl1): 152–158
7 李新, 程国栋. 高海拔多年冻土对全球变化的响应模型. 中国科学 D 辑: 地球科学, 1999, 29: 185–192
8 王绍武, 龚道溢. 中国西部环境特征及其演变. 北京: 科学出版社, 2002. 1–248
9 孙菽芬. 陆面过程的物理、生化机理和参数化模型. 北京: 气象出版社, 2005. 72–86
10 Xue Y, Zeng F J, Schlosser C A. SSiB and its sensitivity to soil properties—A case study using HAPEX-Mobilhy data. Global Planet Change, 1996, 13: 183–194
11 Slater A G, Pitman A J, Desborough C E. Simulation of freeze-thaw cycles in a circulation model land surface scheme. J Geophys Res-Atmospheres, 1998, 103: 11303–11312
12 Koren V, Schaake J, Mitchell K, et al. A parameterization of snow pack and frozen ground intended for NCEP weather and climate models. J Geophys Res-Atmospheres, 1999, 104: 19569–19585
13 Cherkauer K A, Lettenmaier D P. Hydrologic effects of frozen soils in the upper Mississippi River Basin. J Geophys Res-Atmospheres, 1999, 104: 19599–19610

14 Niu G Y, Yang Z L. Effects of frozen soil on snowmelt runoff and soil water storage at a continental scale. Amer Meteor Soc, 2006, 7: 937–952
15 李倩, 孙菽芬. 通用的土壤水热传输耦合模型的发展和改进研究. 中国科学 D 辑: 地球科学, 2007, 37: 1522–1535
16 王兰宁, 郑庆林, 宋青丽. 青藏高原中西部下垫面对东亚大气环流季节转换影响的数值模拟. 高原气象, 2003, 22: 179–184
17 李国平, 段廷扬, 巩远发. 青藏高原西部地区的总体输送系数和地面通量. 科学通报, 2000, 45: 355–356
18 Henderson-Sellers A, Yang Z L, Dickinson R E. The project for inter-comparison of land-surface parameterization schemes (PILPS). Bull Amer Meteor Soc, 1993, 74: 1335–1349
19 Henderson-Sellers A, McGuffie K, Pitman A J. The project for inter-comparison of land-surface parameterization schemes (PILPS): 1992 to 1995. Clim Dyn, 1996, 12: 849–859
20 Wood E F, Lettenmaier D, Liang X, et al. The project for inter-comparison of land-surface parameterization schemes (PILPS) Phase-2c Red-Arkansa River Basin experiment: 1. Experiment description and summary inter-comparisons. Glob Planet Change, 1998, 19: 115–135
21 黄伟, 郭振海, 宇如聪. CLM 在淮河流域数值模拟试验. 气象学报, 2004, 62: 764–775
22 刘少峰, 林朝晖. 通用陆面模式 CLM 在东亚不同典型下垫面的验证试验. 气候与环境研究, 2005, 10: 684–699
23 陆其峰. 陆面下边界对区域气候模拟的影响(LAI 为例)及区域气候模式(CWRF+CLM)陆面遥感参数预处理研究. 博士学位论文. 南京: 南京信息工程大学, 2006. 1–138
24 邹兰军. 中国区域陆面模式大气驱动数据同化及其在 CLM 中的应用. 博士学位论文. 南京: 南京信息工程大学, 2007. 42–51
25 辛羽飞, 卞林根, 张雪红. CoLM 模式在西北干旱区和青藏高原去的适用性研究. 高原气象, 2006, 25: 567–574
26 王澄海, 师锐, 左洪超. 青藏高原西部冻融期陆面过程的模拟分析. 高原气象, 2008, 27: 239–248
27 罗斯琼, 吕世华, 张宇, 等. CoLM 模式对青藏高原中部 BJ 站陆面过程的数值模拟. 高原气象, 2008, 27: 259–271
28 Deardorff J W. Efficient prediction of ground surface temperature and moisture, with inclusion of a layer of vegetation. J Geophys Res, 1978, 83: 1889–1903
29 苏凤阁, 郝振纯. 陆面水文过程研究综述. 地球科学进展, 2001, 16: 795–800
30 Oleson K W, Dai Y J, Bonan G, et al. Technical description of the Community Land Model (CLM). Technical Note NCAR/TN-461+STR, 2004
31 Oleson K W, Lawrence D M, Bonan G B, et al. Technical description of version 4.0 of the Community Land Model (CLM), NCAR Technical Note NCAR/TN-478+STR, 2010
32 周锁铨, 张翠, 王小宁, 等. 多层土壤温度模拟及其检验. 南京气象学院学报, 2004, 27: 200–209
33 徐学祖, 王家澄, 张立新. 冻土物理学. 北京: 科学出版社, 2001. 110–115
34 马柱国, 魏和林, 符淙斌. 土壤湿度与气候变化关系的研究进展与展望. 地球科学进展, 1999, 14: 290–305
35 Spaans E J, Baker J M. The soil freezing characteristic: Its measurement and similarity to the soil moisture characteristic. Soil Sci Soc Amer J, 1996, 60: 13–19
36 黄洪峰. 土壤植物大气相互作用原理及模拟研究. 北京: 气象出版社, 1997. 122–135
37 李倩. 陆面过程模型中统一土壤-雪盖水热传输耦合模型的研究. 博士学位论文. 北京: 中国科学院大气物理研究所, 2008. 33–45
38 张霞. 旱区及冻土区陆面过程研究——模式发展. 博士学位论文. 北京: 中国科学院大气物理研究所, 2004. 50–82

Article

Chinese Science Bulletin

Atmospheric Science

July 2011 Vol.56 No.20: 2145–2155
doi: 10.1007/s11434-011-4542-8

# Simulation of freezing and melting of soil on the northeast Tibetan Plateau

XIA Kun[1,2,3*], LUO Yong[2,4,5] & LI WeiPing[2]

[1] *Institute of Atmospheric Physics, Chinese Academy of Sciences, Beijing 100029, China;*
[2] *National Climate Center, China Meteorological Administration, Beijing 100081, China;*
[3] *Graduate University of Chinese Academy of Sciences, Beijing 100049, China;*
[4] *Center for Earth System Science, Tsinghua University, Beijing 100084, China;*
[5] *Key Laboratory of Earth System Numerical Simulation, Ministry of Education, Beijing 100084, China*

Received January 25, 2011; accepted April 27, 2011

Using observational data spanning the period from February to December 2009 and recorded at the Suli station in Qinghai Province, the land-surface model CLM3.0 was employed to simulate the freezing and melting of soil. The results indicate that the simulated soil temperature is higher than the observed soil temperature and the ultimate thawing date is earlier than the observed date during the melting period. During the freezing period, the simulated soil temperature is lower than the observed soil temperature and the ultimate freezing of the deep soil is earlier than that observed. Overall, the simulation of freezing is better than that of melting, and the simulation of a shallow layer is better than that of a deeper layer. In the original CLM3.0, it is assumed that frozen soil begins to melt when the soil temperature exceeds 0°C, which is inconsistent with observations. The critical freeze–thaw temperature was calculated according to thermodynamics equations and the freeze-thaw condition was modified. In this work, the melting rate for frozen soil was reduced using the modified scheme, and the simulated soil temperature was lowered. Meanwhile, the refreezing of soil during the melting season was well simulated and more closely matched observations. Additionally, it was found that the rates of melting and freezing differ, with the former being slower than the latter, but refreezing during the melting season is rather quick.

**freezing, thawing, freeze-thaw critical temperature, numerical simulation**

**Citation:** Xia K, Luo Y, Li W P. Simulation of freezing and melting of soil on the northeast Tibetan Plateau. Chinese Sci Bull, 2011, 56: 2145–2155, doi: 10.1007/s11434-011-4542-8

The cryosphere is an important component of the climate system, which consists of five components: the atmosphere, the hydrosphere, the cryosphere, the land surface and the biosphere. It is the most sensitive component and usually has the most direct influence on the climate system. Therefore, it is considered an important factor influencing the interaction between the five elements. Establishment of the Climate and Cryosphere Project (CLiC) has meant that research on the cryosphere has become a new research hotspot internationally [1] (http://www.climate-cryosphere.org/en/). Except for the poles, frozen soil is mainly distributed in high-elevation regions, such as the Qinghai-Tibetan Plateau, which are sensitive to climate change. The variation in unique hydrothermal characteristics plays an important role in the energy exchange between the land and atmosphere, and affects carbon circulation and weather-climate systems. Freezing and thawing of soil are the most remarkable physical characteristics of the plateau [2]. Research has demonstrated that freezing and thawing on the Qinghai-Tibetan Plateau have good relationships with summer precipitation [3]. Land-atmosphere interactions over the plateau need to be studied to improve the predictability of numerical models.

There have been studies on the relationship between

*Corresponding author (email: xiakun@cma.gov.cn)

© The Author(s) 2011. This article is published with open access at Springerlink.com

climate change and frozen soil [4–8], but few works about the effect of the change of frozen soil on climate change in China. It is a great challenge to study the complex physical mechanism of frozen soil, especially the parts associated with climate change [9]. The simulation of a long time sequence of land-surface processes on the Qinghai-Tibetan Plateau is meaningful work. The biggest limitation has been a lack of a wide range of observation data, which even prevents the development of the frozen soil model. Until the late 1990s, attention had been given to frozen soil parameterization in land-surface models [10–14], and a corresponding module has been added to land-surface models. In China, Li and Sun [15] developed a frozen soil hydrothermal transfer model in which total enthalpy and total soil quality are chosen as predictands, and the instability arising from uncertainty in the rate of phase change was effectively avoided. Two atmospheric experiments were carried out in 1979 and 1998 on the Qinghai-Tibetan Plateau, the data collected during the two experiments provide the necessary condition for land-atmosphere study on the plateau [16,17]. However, because the observation data were concentrated in the period from May to September, they do not contribute greatly to the simulation of freezing and thawing on the plateau.

By comparing more than 20 representative land-surface models, the Program for Inter-comparison of Land Surface Parameterization Schemes (PILPS) found that models usually have apparent distinctions for the simulation of energy and water exchange occurring at the land-atmosphere interface when forced by the same atmospheric conditions. Many models provide good results for humid areas with homogeneous vegetation, but more work is needed for areas of snow, frozen soil, desert, and inhomogeneous land surfaces to improve simulation results [18–20]. The Community Land Model (CLM) is one of the best land-surface models. Many numerical and verification experiments have been carried out for the model used in this study; i.e. adaptability of the model to Asian monsoon areas [21], plateau areas of sparse vegetation, paddy fields [22], typical climate regions of China [23], and desert [24]. However, there have been few experiments for frozen areas. Xin et al. [25] examined the applicability of the CLM to northwestern arid areas and the western Qinghai-Tibetan Plateau using short-range observation data for summer. Wang et al. [26] and Luo et al. [27] demonstrated the model's applicability to the western and central Qinghai-Tibetan Plateau, respectively. However, no work has been done for the northern Qinghai-Tibetan Plateau.

In this paper, observation data spanning the period from February 1 to December 31, 2009, and recorded at the Suli station located in northeastern Qinghai Province were adopted for a single-point numerical simulation. The performance and applicability of CLM3.0 were examined by comparing with soil temperature and moisture observations. Furthermore, the freeze-thaw condition of the model was modified.

# 1 Model and data

## 1.1 Model introduction

The CLM was developed by the National Center for Atmospheric Research and is based on the Biosphere-Atmosphere Transfer Scheme (BATS), the Institute of Atmospheric Physics Land Surface Model (IAP94) and the Land Surface Model (LSM). The CLM was constructed with uniformly distributed vertical soil layers, at most five snow layers, and one vegetation layer. The flux was calculated separately for different underlying surfaces by considering inhomogeneity on the sub-grid scale of land-surface characteristics, vegetation types, hydraulics and thermodynamic characteristics of different soil types, and the homogeneity of atmospheric forcing acting on all underlying surfaces. The flux required by the atmosphere is obtained by averaging the sub-grid quantities weighted by all vegetation types.

The atmospheric forcing data for the offline CLM3.0 experiment are data for temperature, pressure, humidity, wind speed, precipitation and downward longwave and shortwave radiation. No consensus has been reached on how to divide the soil layers in the CLM, but it is agreed that the shallow soil layer has a larger moisture gradient [28]; therefore, to precisely describe the variation in soil moisture, shallow soil has more layers than deeper soil [29]. Division of the vertical soil layers follows an exponential distribution. The depths of soil layers are 0.71, 2.79, 6.23, 11.89, 21.22, 36.61, 61.98, 103.80, 172.76 and 286.46 cm; a detailed description of the CLM is given in [30].

The version of the CLM used in this study is CLM3.0. The difference between CLM3.0 and CLM4.0 is the soil freezing condition. CLM3.0 considers that all liquid water freezes when the soil temperature is below 0°C, whereas CLM4.0 considers that liquid water and ice can coexist when the soil temperature is below 0°C. Only when the liquid-water content is greater than the maximum allowable liquid-water content does the excess freeze. Obviously the latter consideration is more realistic. Therefore, the freeze-thaw condition is replaced with the equivalent part of CLM4.0 [31]. The freeze-thaw equation can be written as

$T>T_{\mathrm{frz}}$ and $\theta_{\mathrm{ice}}>0$ for the thawing period and

$T>T_{\mathrm{frz}}$ and $\theta_{\mathrm{liq}}>\theta_{\mathrm{liq,max}}$ for the freezing period.

When the soil freezes or thaws, the soil temperature is $T_{\mathrm{frz}}$, where $\theta_{\mathrm{liq,max}}$ is the maximum liquid-water content when the soil temperature is below the freezing point; $\theta_{\mathrm{liq,max}}=\theta_{\mathrm{sat}}\left\{\frac{10^3 L_{\mathrm{f}}(T-T_{\mathrm{frz}})}{gT\psi_{\mathrm{sat}}}\right\}^{-1/b}$. The freezing point of liquid water $T_{\mathrm{frz}}$ is 273.16 K. $\theta_{\mathrm{sat}}$ is the saturated soil water content, $\theta_{\mathrm{liq}}$ is the soil volume water content, $\theta_{\mathrm{ice}}$ is the soil volume ice content, and $\psi_{\mathrm{sat}}$ is the saturated matric water potential in units of millimeters. Latent heat fusion of $L_{\mathrm{f}}$ is a constant

with a value of $0.336\times10^6$ J $kg^{-1}$.

### 1.2 Data preparation

Simulations were performed for the Suli station, which is located at 38.42°N, 98.30°E, northeast of Qinghai Province, and belongs to the upper reaches of the Shule River at an elevation of 3802 m. The data span a period from February 1 to December 31, 2009. The land surface is mainly covered by alpine meadow. The soil type is sandy loam. The area has a notable cold-plateau semi-arid climate. A meteorological observation tower with height of 10 m was built at Suli with meteorological variables (10-min air temperature, pressure, humidity, and wind speed) recorded at four heights (2, 5, 7.5 and 10 m). Precipitation was collected by a T_200B rain gauge. Soil temperature was measured at depths of 5, 10, 30, 50 and 70 cm. Soil moisture was observed at 20, 40 and 60 cm, and soil heat flux at depths of 5 and 10 cm. In addition, a vortex dynamic radiometer was set on the meteorological tower to obtain downward longwave radiation from the Sun, upward shortwave radiation reflected by the land surface and upward longwave radiation with a time interval of 30 minutes. All data were used for driving or validating the model.

The observations made at a height of 2 m were used as atmospheric forcing data and this height was set as the base of the atmosphere in the model. Considering the sensitivity of the model to initial values, a 2-year spin-up was carried out at a single point. To compare simulations and observations more conveniently, the output was linearly interpolated to depths of 20, 40 and 60 cm.

## 2 Simulations and analysis

The CLM3.0 model was employed to simulate the soil water and thermal processes at the Suli station of Qinghai Province with observation data spanning the period from February 1 to December 31, 2009. This test is referred to as the control test and is intended to validate the model's ability to simulate the exchange of soil water and heat in seasonally frozen areas. Because a change in ice content in soil affects soil water and heat properties, and influences the simulation of soil temperature and moisture, this work mainly examines simulations of soil temperature and moisture for individual layers.

### 2.1 Soil temperature

The accuracy of the calculated soil temperature in the land-surface model usually affects energy and material exchange between the land surface and atmosphere, and further affects the performance of the atmospheric model. Therefore, the simulation of soil temperature is important [32].

The air temperature at a height of 2 m rises slightly from February 2009 and then falls to about −20°C by mid-March. Afterward, although there are several insignificant temperature declines, the entire temperature tendency is to rise, especially from late March to early April during which time the air temperature increases from −10°C to above 0°C, and it remains above 0°C from June. The incident shortwave radiation reduces as winter arrives, and the air temperature decreases rapidly from 3°C to −10°C in early October (Figure 1(a)). The tendency of the temperature change for soil close to the surface is the same as that of the air temperature at a height of 2 m, and the simulated soil temperature at 20 cm depth is similar to observations (Figure 1(b)). However, for deeper soil layers, there is a lag in the temperature variation. The observed soil temperatures at 40 and 60 cm rise and exceed 0°C on May 10 and June 5, respectively. The simulated ultimate melting dates (i.e. dates on which the ice in soil completely melts) for all soil layers are earlier than those observed, and the deeper the soil, the greater the difference, which is about a month in the case of 60 cm depth (Figure 1(c), (d)). The simulated date on which the soil begins to freeze is much the same as the observed date for a depth of 20 cm, but it is further in advance for deeper soil, being about 15 days ahead for soil at 60 cm depth (Figure 1(d)).

In an experiment carried out by Xu [33], it was found that the freezing temperature and thawing temperature of loess, sandy soil, red soil, clay soil and loamy soil are all below 0°C, which means that all these soils begin to melt at temperatures lower than 0°C. In CLM3.0, it is considered that frozen soil begins to melt only when the temperature is higher than the freezing point. No melting occurs in early March when the modeled temperature is below 0°C, whereas in reality, the soil has begun to melt and the soil liquid-water content increases slightly (Figure 2). The melting of ice absorbs energy from the soil and prevents a rise in soil temperature; however, the simulated soil has not thawed, the energy from the lower soil layer increases the soil temperature, and the simulation of soil temperature from March to April is thus higher than the observed soil temperature. After the simulated soil temperature reaches 0°C, and the air temperature rises, the simulated frozen soil melts completely by mid-April, and the predicted melting date is earlier than the observed date. When the simulated soil thaws and the observed soil does not, the difference between simulation and observations is great. For example, in early May, the difference in soil temperature at 40 cm depth is about 4°C.

In summary, CLM3.0 simulates well the variations in soil temperature in all layers. Simulation of freezing is better than that of thawing, and simulations at shallower depths are better than those at deeper depths. However, the simulated thawing is too fast, which leads to a higher temperature and earlier thawing time than what is observed. During the freezing period, the simulated temperature of deeper soil is lower than the observed temperature, and the freezing

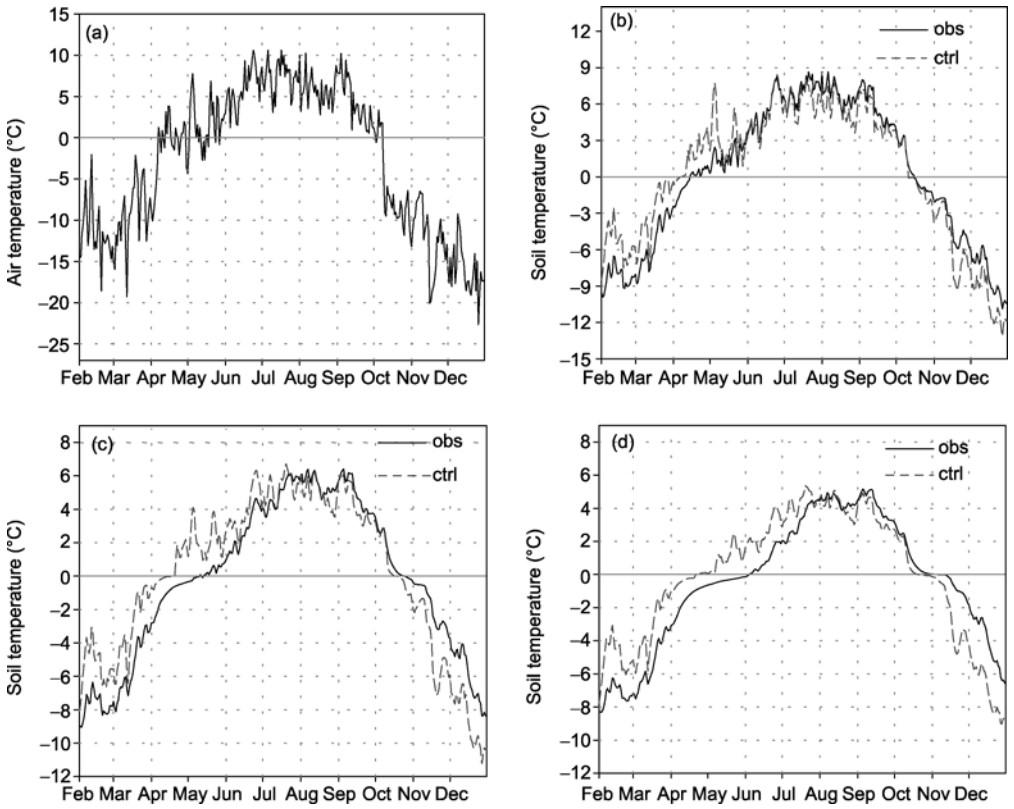


**Figure 1** Observed temperature at a height of 2 m (a) and comparison of the simulated soil temperature (dashed) with observations (solid line) at depths of 20 cm (b), 40 cm (c) and 60 cm (d).

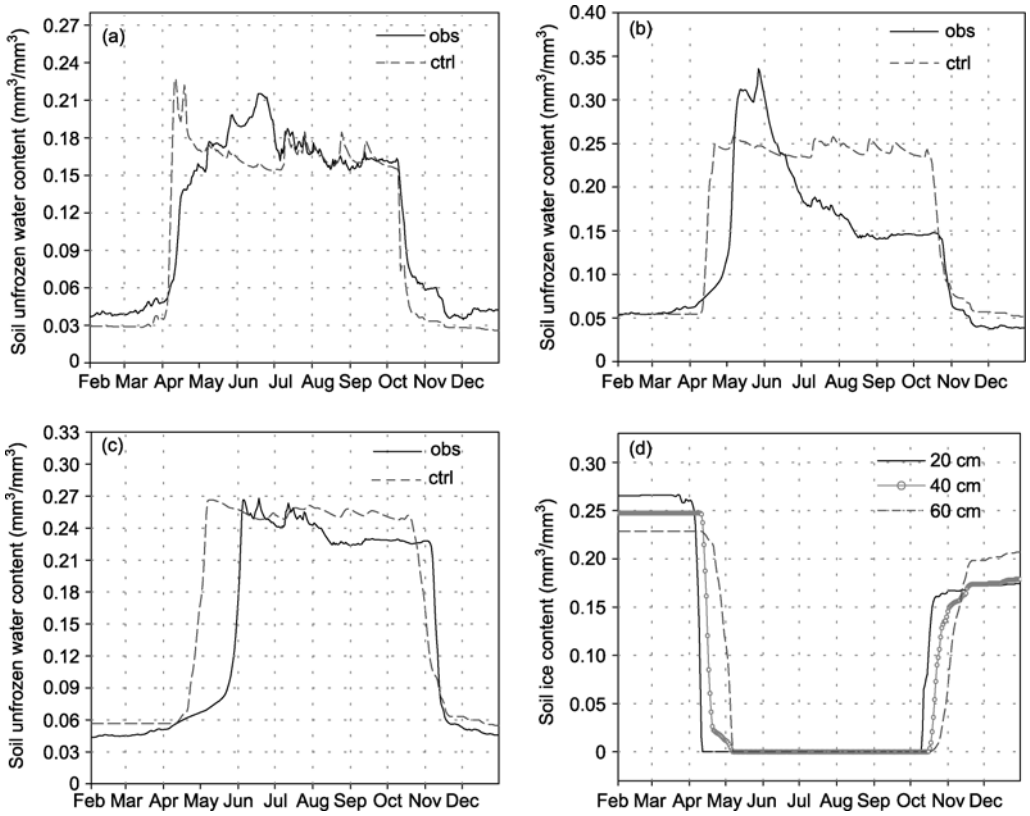


**Figure 2** Comparison of the simulated soil liquid-water content (dashed) with observations (solid line) at depths of 20 cm (a), 40 cm (b) and 60 cm (c), and simulated soil ice content (d) in the three layers.

time is earlier than the observed time.

### 2.2 Soil moisture

Soil moisture plays an important role in the interaction of land and atmosphere, affecting the regional climate by influencing runoff, albedo, surface sensible heat flux and latent heat flux [34]. It is an important variable for model estimations.

The simulated soil liquid-water content remains unchanged during February and April 2009 (Figure 2(a), (b), (c)). The soil begins to melt from the surface to deeper layers when it satisfies the frozen-soil melting condition, at which time the soil ice content decreases rapidly. For example, the ice content in soil at 20 cm depth decreases from a fractional volume of 0.27 to 0.0 over several days in early April. The ultimate melting times for 20 and 60 cm depths have lags of about 1 month, which reflects the spread of energy over time from the surface to deeper levels. In reality, the soil liquid water content begins to increase at the beginning of March; for example, the soil liquid-water content at 60 cm depth remains at 0.045 from February to early March, and gradually increases to about 0.08 by late May (Figure 2(c)). Meanwhile, the soil temperature increases from −6°C to −1°C (Figure 1(c)). This indicates that the soil began melting when the soil temperature was below 0°C. Obviously, the model setting of the thawing condition conflicts with the observation. The simulated melting starts late but has a high melting rate, and finishes earlier than what is observed. The simulation of the freezing is better than that of the thawing.

## 3 Model modifications

It was seen from the control test that the thawing and freezing tendencies are well simulated, but CLM3.0 arbitrarily specifies that the soil melts only when the soil temperature is higher than 0°C, which is not in agreement with observations [33]. An actual freezing-thawing process is a slowly and continuously changing process, and there is no fixed freeze-thaw critical temperature. The relationship between the soil water content and temperature should be determined by the thermodynamic equilibrium relationship between the soil water potential and temperature and the inherent characteristics of soil hydraulics. Therefore, the method of calculating the soil freezing-thawing critical temperature used by Sun and Li [15] was adopted in this study to replace the unreasonable hypothesis used in CLM3.0.

When ice is present, the soil water potential remains in equilibrium with the vapor pressure over pure ice. According to the Clausius-Clapeyron equation, the functional relation between the soil water matrix potential $\psi$ (mm) and soil temperature is

$$\psi(T) = \frac{10^3 L_f (T - T_{frz})}{gT}, \tag{1}$$

where $T$ and $T_{frz}$ are the soil temperature and freezing point (K), respectively, $L_f$ is the latent heat of fusion (J kg$^{-1}$), and $g$ is gravitational acceleration (m s$^{-2}$).

Spaans and Baker [35] demonstrated that freezing-thawing processes are similar to drying-wetting processes with regard to the dependence of the soil matric potential on the liquid-water content. The soil matric potential as a function of liquid-water content is

$$\psi(\theta_{liq}) = \psi_{sat}\left(\frac{\theta_{liq}}{\theta_{sat}}\right)^{-b}, \tag{2}$$

where $\psi_{sat}$ is the saturated soil matrix potential, $\theta_{sat}$ and $\theta_{liq}$ are porosity and the partial volume of liquid water, and $b$ is the Clapp-Hornberger parameter.

By equating $\psi$(T) in eq. (1) to $\psi(\theta_{liq})$ in eq. (2), we derive the expression for the functional relation between the soil liquid-water content and freeze-thaw critical temperature:

$$T_{crit} = \frac{10^3 L_f T_{frz}}{10^3 L_f - \psi_{sat}\left(\frac{\theta_{liq}}{\theta_{sat}}\right)^{-b} g}, \tag{3}$$

where $T_{crit}$ is the critical temperature at which soil water freezes or thaws. When the soil temperature is below/above $T_{crit}$, the soil water begins to freeze/thaw. Figure 3 is drawn from calculations using eq. (3). It is clearly seen that when the soil has low liquid-water content, sandy soil has the highest freeze-thaw critical temperature, loamy sand has the second highest, and the other soils have very low critical temperatures. The main reason is that sandy soil has macropores. Under certain suction conditions, a macropore can be easily drained. Therefore, the soil water content rapidly reduces as the suction increases. The pore size distribution is uniform in clayey soil and much water can be absorbed. Increasing the suction can only reduce the soil water content slowly. Thus, soil having low silt content has greater saturated soil water potential for the same liquid-water content [36]. From eq. (3), we know that the soil water matrix potential and soil temperature have an inverse relationship. Soil having lower silt content has a lower freeze-thaw critical temperature under the same liquid-water content conditions. The critical temperature rises gradually as the liquid-water content increases, but is always below the freezing temperature.

### 3.1 Results obtained using the modified critical temperature for the melting of frozen soil

The thawing critical temperature in CLM3.0 is replaced

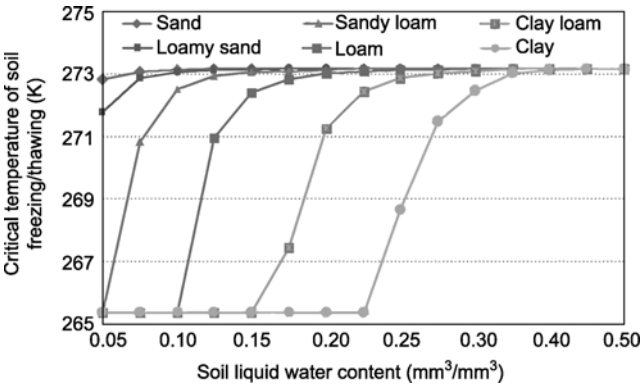


**Figure 3** Freeze-thaw critical temperature versus the soil type and liquid-water content.

with eq. (3) while the freezing conditions are kept the same:

When $T>T_{crit}$ and $\theta_{ice}>0$, soil melts and the soil temperature is $T_{crit}$ immediately after melting

This experiment is referred to as test 1 and is designed to examine the effects of the new critical temperature for thawing on the simulation.

Figure 4 shows that the new critical temperature for thawing has four main effects on the simulation. First, the simulated soil temperature during the thawing period is a little lower than it was previously, and much closer to observations (Figure 4(a)). Second, the simulated liquid-water content is reduced (Figure 4(b)). Third, the timing of the commencement of the melting of frozen soil is earlier, and the timing of ultimate melting is closer to that observed for

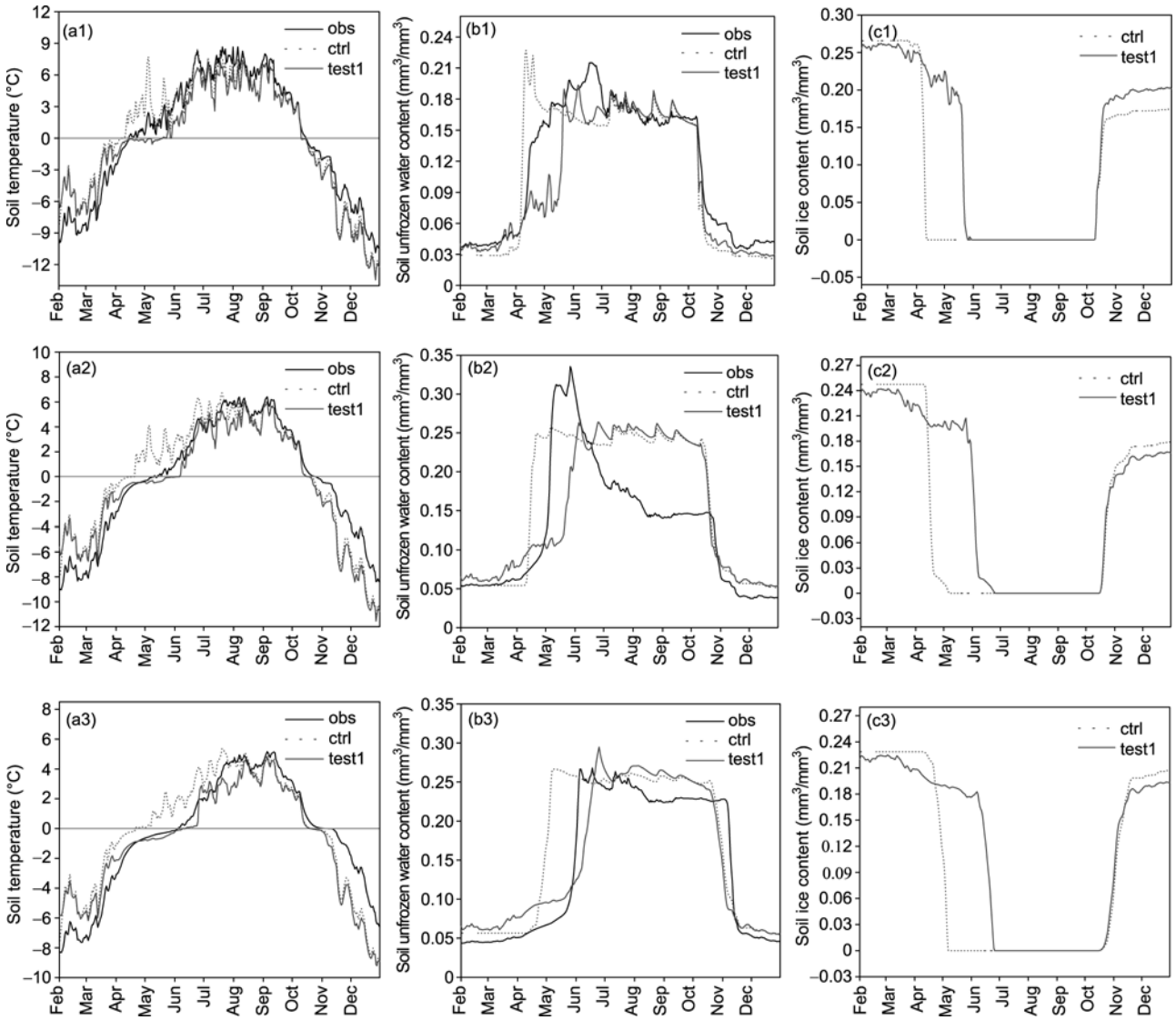


**Figure 4** Comparison of observations (obs, heavy line) with soil temperature simulated with a change in the critical temperature for thawing (ctrl, dot line) and no change (test 1, fine line). The letter "a" in each figure represents the soil temperature, "b" the soil liquid-water content, and "c" the ice content in soil. Numbers 1, 2 and 3 represent the soil depths of 20, 40 and 60 cm, respectively.

the deeper frozen soil (Figure 4(c)). Fourth, there are several insignificant freezing events during the thawing period, which is similar to the actual soil freezing-thawing process. There are three main reasons for these improvements.

First, when the critical temperature for thawing is changed, frozen soil begins to melt at certain temperatures below 0°C. Test 1 shows that frozen soil at 60 cm depth begins to melt in mid-March and the soil temperature is −2°C at that time. The soil absorbs energy as it thaws, which prevents a rise in soil temperature. Reducing the thawing rate results in the simulation of the soil temperature better matching observations (Figure 4(a3)), and delays the melting time. This means that when the observed soil has melted, the simulated frozen soil is still melting in test 1, and the simulated soil liquid-water content in test 1 is less than the observed content (Figure 4(b)).

Second, the soil temperature is equal to the freezing point after the phase change in CLM3.0, and the soil temperature is updated according to the difference in the energy cost between theory and practice (called net energy). Only when the water exists completely in liquid or solid form and the net energy does not equal zero can the energy surplus be used to change the temperature. If the net energy is zero, the soil temperature remains at the freezing point. When the critical temperature for thawing is changed, the soil temperature is replaced with eq. (3) after melting, which is lower than the freezing point and less than that in the control test. Therefore, the simulation of soil temperature during the melting phase is a little lower.

Third, for all soil types, when the soil temperature is below 0°C, the maximum liquid-water content reduces as the temperature decreases [37]. By changing the critical temperature of thawing, ice in the soil melts when the soil temperature is below 0°C, the liquid-water content increases and makes it easier for the soil temperature and moisture to meet the freezing conditions. Figure 4 shows that although the soil has a thawing tendency during February and April, there are several insignificant freezing events, indicating that the new critical temperature for thawing describes the thawing process well.

In summary, the change in the soil thawing condition reduces the thawing rate, and the simulation of soil temperature, soil liquid-water content and melting time is much closer to observations. However, the thawing of lower soil layers is slower than that observed while the performance is better for deeper layers.

### 3.2 Results obtained using the modified freezing-thawing critical temperature for soil

To examine the effect on simulation results, test 2 was carried out on the basis of test 1 but with the soil temperature after soil has frozen replaced with the new freeze–thaw critical temperature.

When there is freezing and thawing, the difference between the soil temperature and freeze-thaw critical temperature is usually used to estimate the relationships between the excess or deficiency of energy and the amount of latent heat absorbed or released, and thus to determine the rate of change in ice content. Energy surplus has typically been used to update the soil temperature [38]. In test 1, it is supposed that when soil freezes, the temperature is 0°C. Thus, 0°C was treated as the base point of the temperature update. In test 2, however, it is supposed that the frozen soil temperature is the freezing-thawing critical temperature and is lower than 0°C. The base point of the temperature update thus decreases from 0°C to a certain temperature below 0°C, which leads to the simulated temperature of soil with ice having a downward tendency. Thus, the simulated temperature during the thawing phase (February and April) is closer to observations but lower than observations during the freezing period (Figure 5). The main reason for the latter finding is that with decreasing shortwave radiation in winter, the soil temperatures of all layers decrease. When the soil temperature is below 0°C and the soil liquid-water content is greater than the maximum allowable liquid-water content, soil begins to freeze. Freezing releases latent heat, which limits the fall in soil temperature. However, as the soil freezes much faster in the model than in reality, soil is soon completely frozen. From then on, the soil temperature mainly varies with the air temperature, leading to a lower simulated soil temperature compared with the observed soil temperature during the freezing period. The root cause may be that the freezing rates for freezing and thawing periods greatly differ.

### 3.3 Results obtained using the modified freezing rate

In section 3.2, we deduced that the soil water has very different freezing rates for freezing and thawing periods. A sensitivity test (test 3) was designed to verify whether and to what degree a change in freezing rate affects the simulation results. In this test, the freezing rate remains the same during the thawing stage (February to June) while it is arbitrarily halved during the freezing stage (October to December).

Results show that the simulated soil temperatures of all layers obviously improve with the modified CLM3.0 and are closer to observations (Figure 6), while simulation of the soil liquid-water content does not vary greatly. The main reason is that the freezing rate is evidently lower during the freezing stage in test 3. In other words, the rate of increase in ice content is less, which delays the ultimate freezing of soil water. This slows down the freezing of soil. The liquid-water content of soil decreases slowly, which prevents heat loss in soil. The heat capacity of water is greater than that of ice, and more liquid water in soil prevents the soil temperature decreasing quickly. Therefore, the simulated soil temperature is higher than that obtained in test 2.

The most immediate effect of changing the soil freezing

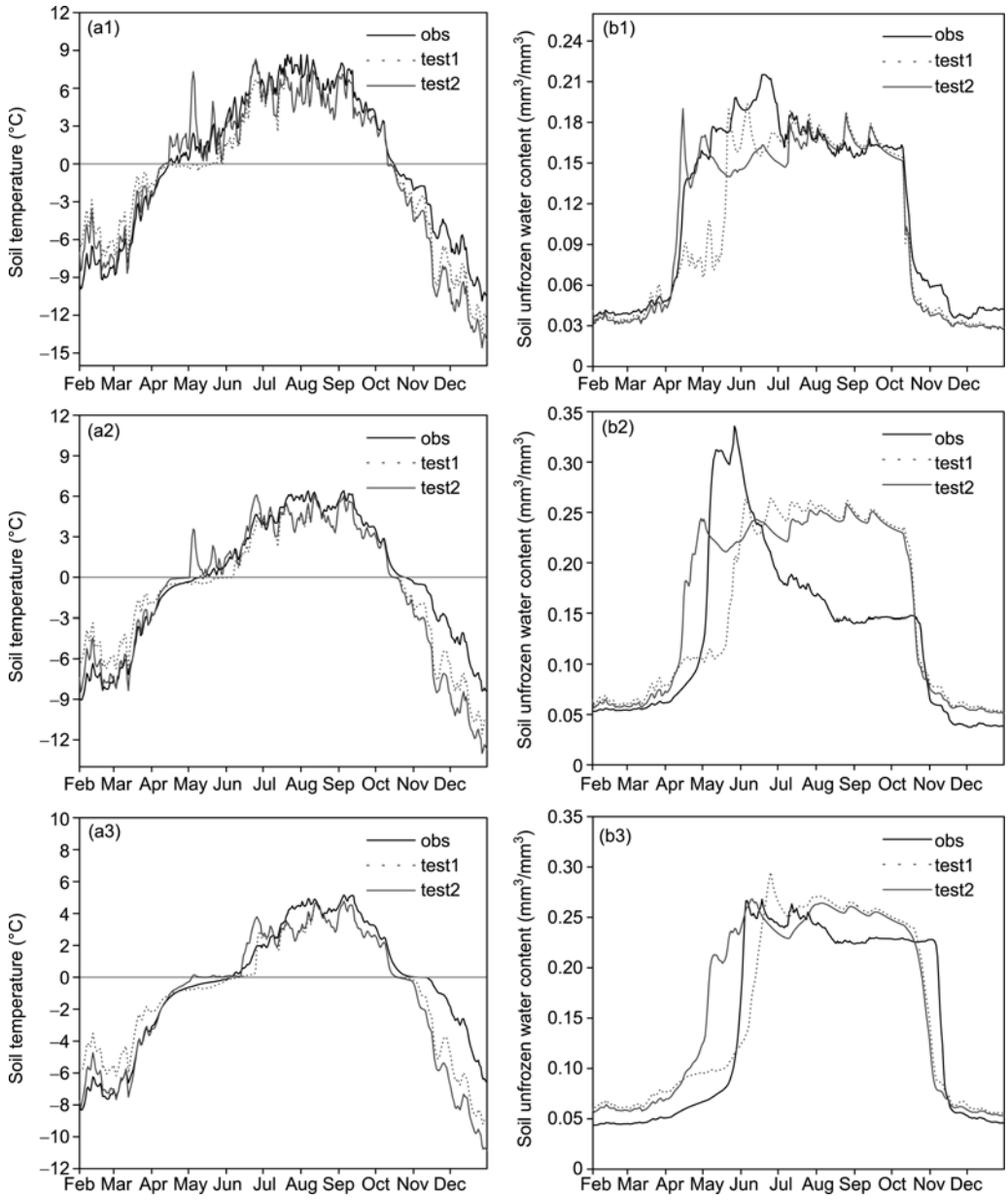


**Figure 5** Comparison of observations (obs, heavy line) with soil temperature simulated with a change in the freeze-thaw critical temperature (test 1, dot line) and no change (test 2, fine line). The letter "a" in each figure represents the soil temperature and "b" stands for the soil liquid-water content. Numbers 1, 2 and 3 represent the soil depths of 20, 40 and 60 cm, respectively.

rate is likely to be a change in the soil ice content. The heat conduction of ice is 4 times that of water, and the heat capacity of water is twice that of ice. Therefore, the change in soil ice content directly affects the upward and downward heat flux, and further affects the whole-system net energy. According to the calculation of soil temperature after phase change in CLM3.0 as introduced in section 3.1, we know that the net energy greatly affects the calculation of soil temperature. Changing the freezing rate affects the soil temperature, while it reveals the limitations of the algorithm used for the calculation of soil temperature in the case of a phase change. In the case of a phase change, it is difficult to obtain a numerical solution. We therefore suggest using the total enthalpy of soil and total quality of soil water as predictands to avoid the problem of obtaining a numerical solution.

## 4 Discussion and conclusion

The land-surface model CLM3.0 was employed to simulate the soil water and thermal processes at a site in Suli, Qinghai Province, from February 1 to December 31, 2009. The capability of the model was examined by comparing the

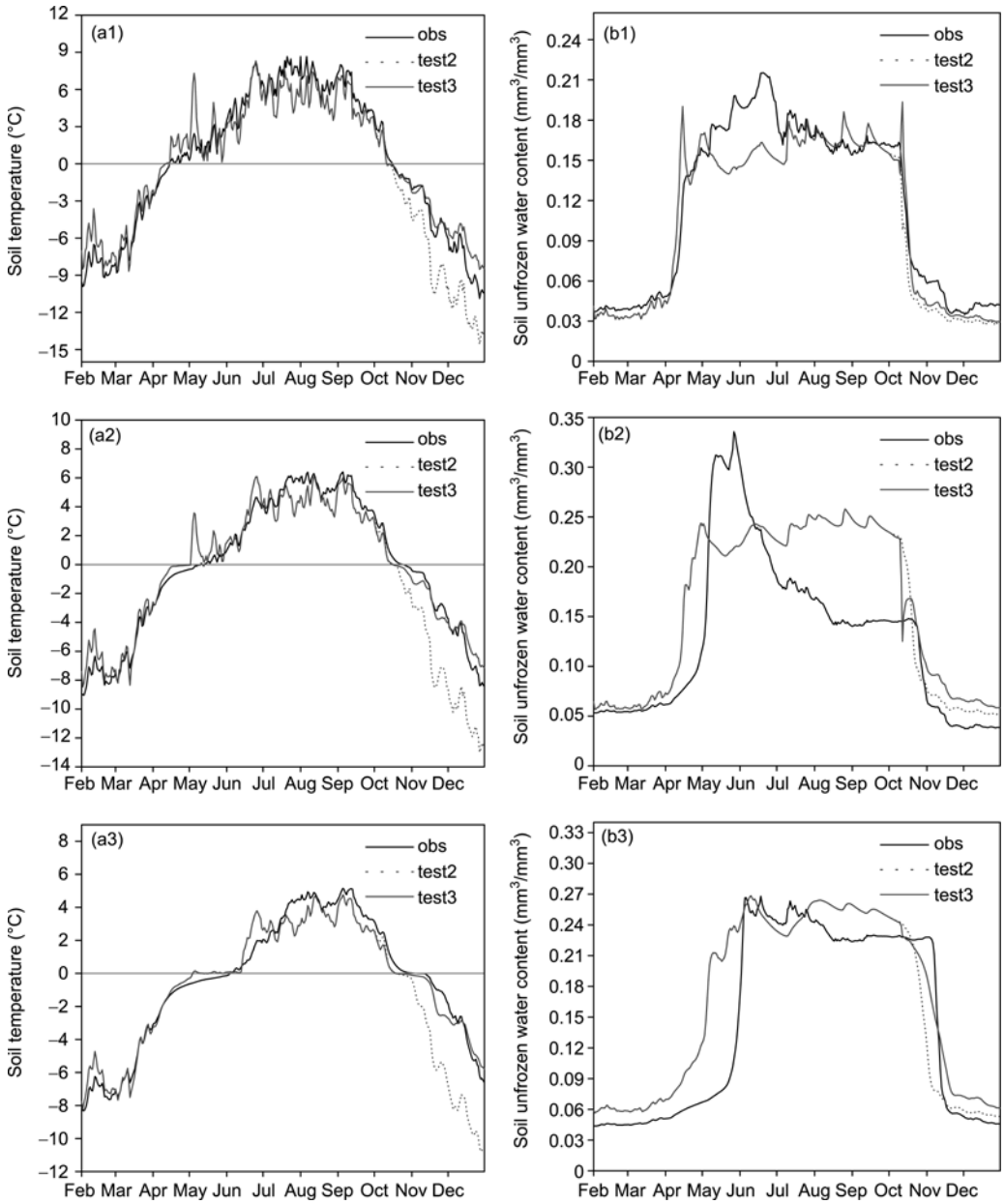


**Figure 6** Comparison of observations (obs, heavy line) with soil temperature simulated with the modified freezing rate (test 2, dot line) and without (test 3, fine line) during the freezing period. The letter "a" in each figure represents the soil temperature and "b" indicates the soil liquid-water content. Numbers 1, 2 and 3 represent soil depths of 20, 40 and 60 cm, respectively.

model results with observations. In addition, the critical freeze-thaw temperature was modified according to phase equilibrium equations. The following results were obtained.

(1) The exchange of soil water and heat was well simulated by CLM3.0. However, some limitations need to be addressed; e.g. the simulated soil temperature is higher than that observed and the ultimate thawing date is earlier than that observed during melting. The simulated soil temperature is a little lower than that observed and the ultimate freezing of deep soil is earlier than observed. Overall, the simulation of freezing is better than that of melting and the simulation of the shallow layer is better than that of deeper layers.

(2) The critical freeze-thaw temperature for certain liquid-water content can be calculated according to the phase equilibrium equation. With less liquid water content, the higher the sand content and the higher the critical freeze-thaw temperature, and *vice versa*. The critical freeze-thaw temperature approaches the freezing point as the liquid water content increases, but it is always below the freezing temperature.

(3) As the soil critical temperature for thawing decreases, the process of soil melting at a certain temperature below the freezing point is well simulated by CLM3.0. Because

the frozen soil melts when the soil temperature is below 0°C, the melting absorbs energy, and the thermal capacity of water is greater than that of ice, thus limiting the rate of increase in soil temperature and the rate of melting. The soil temperature simulated with the modified freeze-thaw scheme is thus lower than that obtained previously during the melting process, and the results are a closer match to observations.

(4) A sensitivity test shows that the freezing rate during freezing differs greatly from that during melting, with the former being lower than the latter, and the soil in the upper layers freezes more quickly than that in the lower layers. This provides a basis for improving the frozen-soil model in the future.

There are limitations to applying a land-surface model to plateau areas because of the complexity of terrain. The simulation of soil temperature and moisture has been notably improved using CLM3.0 with the modified freeze-thaw scheme. However, compared with observations, the simulated melting of shallow soil layers is slow, and the adjustment of the freezing rate is subjective, indicating that there are limitations to the calculation of soil temperature as phase change occurs. The occurrence of phase change makes it difficult to obtain a numerical solution. We therefore suggest using the total enthalpy of soil and the total quality of soil water as predictands to avoid the problem of obtaining a numerical solution. The numerical test was only carried out at a single point with the default surface dataset in this paper; therefore the observational soil properties were required and more tests should be carried out at different plateau stations and in various areas to enhance our understanding of the hydrothermal influence in cold regions.

*The authors thank Ye Baisheng (CAREERI, CAS) for helping with field exploration and data collection and processing. Thanks are also due to Dr. Wang Jie (elder), Associate Research Fellow Wu Jinkui, Wang Jie (younger), Dr. Lu Yinhao, and anonymous reviewers for their comments on an earlier version of the manuscript. This work was supported by the National Basic Research Program of China (2007CB411505), the Major National Scientific Research Project on Global Changes (2010CB951902), and the National Natural Science Foundation of China (40975042 and 40905046).*

1 Qin D H, Xiao C D, Ding Y J, et al. Progress on cryospheric studies by international and Chinese communities and perspectives (in Chinese). J Appl Meteoro Sci, 2006, 6: 649–656
2 Wang C H, Dong W J, Wei Z G. The development of study on the soil freezing-thaw progress in land surface model (in Chinese). Adv Earth Sci, 2002, 17: 44–52
3 Wang C H, Dong W J, Wei Z G. Study on relationship between the frozen-thaw progress in Qinghai-Xizang Plateau and circulation in East-Asia (in Chinese). Chinese J Geophys, 2003, 46: 310–312
4 Jin H J, Li S X, Wang S L, et al. Impacts of climatic change on permafrost and cold regions environments in China (in Chinese). Acta Geogr Sin, 2000, 55: 151–173
5 Wang S L, Zhao X F, Guo D X, et al. Response of permafrost to climate change in the Qinghai-Xizang Plateau (in Chinese). J Glaciol Geocryol, 1996, 18: 101–110
6 Jin H J, Cheng G D, Li X, et al. Permafrost on the Qinghai-Tibet Plateau under a changing climate. Chinese Sci Bull, 1999, 44(S1): 152–158
7 Li X, Cheng G D. The response model of permafrost frozen soil for global change in high altitude. Sci China Ser D-Earth Sci, 1999, 29: 185–192
8 Wang S W, Gong D Y. Western China Environmental Characteristics and Its Evolution (in Chinese). Beijing: Science Press, 2002. 1–248
9 Sun S F. The Physics, Biochemical Mechanism and Parameterization Model of Land Surface Model (in Chinese). Beijing: China Meteorological Press, 2005. 72–86
10 Xue Y, Zeng F J, Schlosser C A. SSiB and its sensitivity to soil properties—A case study using HAPEX-Mobilhy data. Glob Planet Change, 1996, 13: 183–194
11 Slater A G, Pitman A J, Desborough C E. Simulation of freeze-thaw cycles in a circulation model land surface scheme. J Geophys Res - Atmos, 1998, 103: 11303–11312
12 Koren V, Schaake J, Mitchell K, et al. A parameterization of snow pack and frozen ground intended for NCEP weather and climate models. J Geophys Res-Atmos, 1999, 104: 19569–19585
13 Cherkauer K A, Lettenmaier D P. Hydrologic effects of frozen soils in the upper Mississippi River Basin. J Geophys Res-Atmos, 1999, 104: 19599–19610
14 Niu G Y, Yang Z L. Effects of frozen soil on snowmelt runoff and soil water storage at a continental scale. Bull Amer Meteorol Soc, 2006, 7: 937–952
15 Li Q, Sun S F. Development and modification of a coupled soil-water-heat transfer common land model (in Chinese). Sci China Ser D-Earth Sci, 2007, 37: 1522–1535
16 Wang L N, Zheng Q L, Song Q L. Numerical simulation of the influences of west-central Qinghai-Xizang Plateau on East Asia seasonal transition (in Chinese). Plateau Meteorol, 2003, 22: 179–184
17 Li G P, Duan T Y, Gong Y F. The bulk transfer coefficients and surface fluxes on the western Tibetan Plateau. Chinese Sci Bull, 2000, 45: 1221–1226
18 Henderson-Sellers A, Yang Z L, Dickinson R E. The project for intercomparison of land-surface parameterization schemes (PILPS). Bull Amer Meteorol Soc, 1993, 74: 1335–1349
19 Henderson-Sellers A, McGuffie K, Pitman A J. The project for intercomparison of land-surface parameterization schemes (PILPS): 1992 to 1995. Clim Dyn, 1996, 12: 849–859
20 Wood E F, Lettenmaier D, Liang X, et al. The project for inter-comparison of land-surface parameterization schemes (PILPS) Phase-2c Red-Arkansa River Basin experiment: 1. Experiment description and summary inter-comparisons. Glob Planet Change, 1998, 19: 115–135
21 Huang W, Guo Z H, Yu R C. Numerical simulation of CLM over Huaihe basin. Acta Meteorol Sin, 2004, 62: 764–775
22 Liu S F, Lin Z H. Validation of common land model using field experiment data over typical land cover types in East Asia (in Chinese). Clim Environ Res, 2005, 10: 684–699
23 Lu Q F. Infulence of land surface boundary conditions (such as LAI) on the regional climate simulation and preparation of land surface remotely-sensed parameters for regional climate model (CWRF+CLM) (in Chinese). Dissertation for the Dotoral Degree. Nanjing: Nanjing University of Information Science & Technology, 2006. 1–138
24 Zou L J. Atmospheric forcing data assilimation for CLM and its application in China (in Chinese). Dissertation for the Doctoral Degree. Nanjing: Nanjing University of Information Science & Technology, 2007. 42–51
25 Xin Y F, Bian L G, Zhang X H. The application of CoLM to arid region of northwest China and Qinghai-Xizang Plateau (in Chinese). Plateau Meteor, 2006, 25: 567–574
26 Wang C H, Shi R, Zuo H C. Analysis on simulation of characteristic of land surface in western Qinahai-Xizang Plateau during frozen and thawing (in Chinese). Plateau Meteorol, 2008, 27: 239–248
27 Luo S Q, Lv S H, Zhang Y, et al. Simulation analysis on land surface progress of BJ site of central Tibetan Plateau using CoLM (in Chinese). Plateau Meteorol, 2008, 27: 259–271
28 Deardorff J W. Efficient prediction of ground surface temperature

and moisture, with inclusion of a layer of vegetation. J Geophys Res, 1978, 83: 1889–1903
29 Su F G, Hao Z C. Review of land-surface hydrological progress parameterization. Adv Earth Sci, 2001, 16: 795–800
30 Oleson K W, Dai Y J, Bonan G, et al. Technical description of the Community Land Model (CLM). Tech. Note NCAR/TN-461+STR, 2004
31 Oleson K W, Lawrence D M, Bonan G B, et al. Technical description of version 4.0 of the Community Land Model (CLM), NCAR Technical Note NCAR/TN-478+STR, 2010
32 Zhou S Q, Zhang C, Wang X N, et al. Simulation of soil temperature with a multi-layer model and its verification (in Chinese). J Nanjing Inst Meteor, 2004, 27: 200–209
33 Xu X Z, Wang J C, Zhang L X. Physics of Frozen Soil (in Chinese). Beijing: Science Press, 2001. 110–115
34 Ma Z G, Wei H L, Fu C B. Progress in the research on the relationship between soil moisture and climate change (in Chinese). Adv Earth Sci, 1999, 14: 290–305
35 Spaans E J, Baker J M. The soil freezing characteristic: Its measurement and similarity to the soil moisture characteristic. Soil Sci Soc Amer J, 1996, 60: 13–19
36 Huang H F. The Mechanism and Simulation of Interaction Between Soil, Vegetation and Atmosphere (in Chinese). Beijing: China Meteorological Press, 1997. 122–135
37 Li Q. Development of the universal and simplified soil model coupling heat and water transport (in Chinese). Dissertation for the Doctoral Degree. Beijing: Institute of Atmospheric Physics, Chinese Academy of Sciences, 2008. 33–45
38 Zhang X. The study of land surface model on arid and cold region-model improvement (in Chinese). Dissertation for the Doctoral Degree. Beijing: Institute of Atmospheric Physics, Chinese Academy of Sciences, 2004. 50–82

**Open Access** This article is distributed under the terms of the Creative Commons Attribution License which permits any use, distribution, and reproduction in any medium, provided the original author(s) and source are credited.

海洋水文学 http://jto.scsio.ac.cn; http://www.jto.ac.cn

# 卫星遥感海表温度资料和高度计资料的变分同化

肖贤俊[1], 何娜[2], 张祖强[1], 刘怀明[3], 王东晓[4]

1. 国家气候中心, 北京 100081; 2. 北京市气象台, 北京 100089; 3. 南京信息工程大学, 江苏 南京 210044; 4. 热带海洋环境国家重点实验室(中国科学院南海海洋研究所), 广东 广州 510301

**摘要:** 利用国家气候中心正在发展的第二代全球海洋资料同化系统(BCC_GODAS2.0), 针对多变量同化的协调性问题, 发展了一种基于三维变分框架(3DVAR)下的高度计和海表温度(SST)相互约束的同化方法。该方法使海面高度和 SST 资料在同一个动力约束关系下进行同化。在一般方法中, 海面高度和 SST 观测项是代价函数中 2 个独立的观测项, 海面高度项引入动力高度计算公式, 海表温度项用统计关系进行垂向投影。在代价函数的实际求解的计算过程中, 虽然其总体积分效应受海面高度观测的约束, 但整个水柱中各层温盐分析变量的调整是无序的。针对这个问题, 文章提出一种新的同化方案。该方案将 SST 的观测项并入海面高度观测项中, 海面高度的一部分, 确切说是上层海洋部分, 由 SST 决定, 因此至少在 SST 的统计关系能影响到深度的上层海洋, 在代价函数的求解过程中, 温盐的调整是受较强的统计关系约束的, 而这种统计关系的有效性已经在很多 SST 的同化试验中被其他学者广泛应用并证明。利用该方法, 对 1993—1997 年的 AVHRR 卫星遥感海表温度资料进行变分同化试验, 用 TAO、OISST 和 SODA 数据集进行检验证明, 通过对卫星遥感资料的同化能够有效改进对海洋温度和盐度的估计。海洋表层的月平均温、盐度的总均方根误差相对同化前分别降低了 0.67℃和 0.2‰。在混合层中, 同化效果较好。

**关键词:** 海洋资料同化; 三维变分; 海表温度; 高度计; 遥感资料; 垂向投影

**中图分类号:** P731 **文献标识码:** A **文章编号:** 1009-5470(2011)03-0001-08

## Variation assimilation using satellite data of sea surface temperature and altimeter

XIAO Xian-jun[1], HE Na[2], ZHANG Zu-qiang[1], LIU Huai-ming[3], WANG Dong-xiao[4]

1. *National Climate Center, Beijing* 100081, *China*; 2. *Beijing Meteorological Observatory, Beijing* 100089, *China*; 3. *Nanjing University of Information Science and Technology, Nanjing* 210044, *China*; 4. *State Key Laboratory of Oceanography in the Tropics* (*South China Sea Institute of Oceanology, CAS*), *Guangzhou* 510301, *China*

**Abstract:** A new method for assimilating altimeter and sea surface temperature (SST) data was developed for the second generation Global Ocean Data Assimilation System of the Beijing Climate Center. The method allows the altimeter and SST data to be assimilated under one dynamic constraint based on the three-dimensional variation (3DVAR). In the cost function, the background was temperature and salinity from the model. The analytical variables were temperature and salinity. The sea surface high and SST were from the observations. The formula of steric high was introduced in the observation term. Because the steric high formula only constrained the integral of temperature and salinity in a water column from sea level to 1000 m, it will be unprincipled for the adjustment about the temperature and salinity analytics in the calculation of iteration absenting being short of accurate describing of vertical error covariance. Unfortunately we could not obtain the accurate covariance. To resolve this problem, the authors put the SST observation into the sea surface high observation term, making one part of the steric high be determined by the SST. So at least in the upper ocean, the adjustment of temperature and salinity is constrained by the SST according to appropriately chosen vertical relationship for them, which was already shown to be possible in many methods for SST assimilation. This new method was applied in the BCC_GODAS2.0. Five years (1993–2002) of assimilation experiment was performed to test this method, with the assimilation of AVHRR SST and TOPEX/Poseidon altimeter data. The experiment showed this method was successful. The root-mean-square errors for monthly temperature and salinity were reduced 0.67℃

收稿日期: 2009-08-18; 修订日期: 2010-04-07。孙淑杰编辑

基金项目: 财政部行业专项[GYHY(QX) 20072625];中国气象局风云气象卫星遥感开发与应用项目( FiDAF22205)

作者简介: 肖贤俊(1976—), 女, 四川省宜宾市人, 副研究员, 博士, 主要从事海洋资料同化等方面研究。E-mail:xiaoxj@cma.gov.cn

and 0.2 psu, respectively compared with the results without the assimilation. All the results were evaluated with independent observations or reanalysis data, such as TAO, OISST and SODA data. The improvement was significant, particularly in the mixed layer.

**Key words:** ocean data assimilation; three dimensional variation (3DVAR); sea surface temperature (SST); altimeter; satellite data; dynamic constrain

卫星遥感技术的迅猛发展，提供了更为丰富的海洋观测数据，也为海洋资料同化开启了新的研究领域。相对于传统的浮标或潜标观测资料，卫星遥感资料具有覆盖全球、高分辨率、能及时获取的优点，因此对于业务同化应用有较高价值。然而，卫星对海洋的观测只局限于表层或者近表层。例如最广泛应用的海表温度(SST)资料，如果直接放到同化函数中，不作其他动力或统计的考虑，观测资料的效应将很快被耗散，同化难以达到预期效果[1]。在海洋卫星遥感资料的同化中，垂向投影技术一直是研究的重点问题[2−7]。

目前，单变量的卫星遥感资料的垂向投影同化技术研究较多。然而，随着卫星遥感资料种类的丰富，一个同化系统中必然涉及多种遥感资料的同化。多变量的垂向投影同化技术成为我们需要考虑的问题。

从产生平衡的初始条件的目的出发，资料同化中关注较多的是多变量的背景误差协方差矩阵设计问题。例如在集合卡曼滤波(EnKF)同化中，利用经验正交函数在一个约化的子空间计算误差协方差，可以得到较为复杂的多变量协方差结构，然而会带来秩缺乏的问题[8−9]。在实际同化应用中，最为普遍的方法还是直接引入动力约束关系，如地转关系、非线性温盐关系等的引入[10−14]。变量约束关系的引入，既有利于海洋模式的平衡，也是对资料信息的进一步挖掘，能产生更好的预报结果。对于变分同化来说，动力约束关系可以在代价函数中较为自然地引入，因此是动力约束同化方案的最好载体。

国家气候中心正在发展的第二代全球海洋资料同化系统(BCC_GODAS2.0)，是建立在三维变分(3DVAR)的框架上，因此本研究选用该系统进行高度计和 SST 资料的同化方法试验。BCC_GODAS2.0 选用的状态变量是温度和盐度，其代价函数中背景项有 2 项，分别是温度和盐度，观测项包括海面高度项和 SST 项。第 3 项观测项是 ARGO 和 GTS 上的温盐廓线观测，由于这项与本文研究内容无关，在试验中我们关掉了此项，其效应在此不作考虑。SST 的观测项是用统计关系进行垂向相关投影。海面高度的观测项中，引入了动力高度计算公式约束温盐的调整。然而我们应该注意到，动力高度公式是表示海表到约 1000m 深度的温盐的积分关系。也就是说，这个公式只能约束 0—1000m 的温盐的积分值，因此在我们求解代价函数的计算过程中，各层的温盐的调整是无序的。我们一般情况下是假定观测背景误差协方差是空间不相关的，因此它对各层温盐无法约束。而背景误差协方差虽然有垂向分量，但是它只能通过分析变量对各层关系作间接的很弱的约束。我们知道，背景误差协方差很难准确表示变量的真实相关关系。针对这个问题，我们提出一种新的同化方案。该方案将 SST 的观测项并入海面高度观测项中。海面高度的一部分，确切说是上层海洋部分，由 SST 决定。因此，至少在 SST 的统计关系能影响到的深度的上层海洋，在代价函数的求解过程中，温盐的调整是受较强的统计关系约束的，而这种统计关系的有效性已经在很多 SST 的同化试验中被其他学者广泛应用并证明。利用此方法，对 AVHRR 海表温度和 T/P 高度计两种资料进行 1993—2002 年的同化试验，通过各种独立资料的检验，验证了该方法的可行性。

本文第 1 节将对所用海洋模式和观测资料作一简单介绍，第 2 节重点介绍所用同化方法，第 3 节是同化试验结果分析，最后是结论和讨论。

## 1 模式及资料介绍

本文研究所用的 MOM4 模式使用了全球 Tripolar 格点，纬向分辨率约为 1°，经向分辨率在 29°30′S—29°30′N 间的区域从赤道(1/3)°渐变至 1°，其他区域为 1°，模式垂向分为 50 层，5—225m 以 10m 间隔等间距分层。225m 以下的层次呈不等距分布，深度越深，间隔越大，变幅从 11m 增至 366m。洋底地形数据集采用的是 72°S—72°N 之间区域的卫星数据、美国 NOAA 的 5′全球地形数据(ETOPO5)以及北冰洋世界海底地形图(IBCAO)三者的综合数据资料，模式最深处到达 5500m。动力学和热力学条件采用美国环境预报中心(NECP)的月平均再分析资料和大气的海温驱动资料[15]。

为验证高度计资料和海表温度资料的协调同化方案，本文用于同化的观测资料有 2 种：一种是海

表温度资料, 另一种是高度计资料。同化中使用的是 Altimeter Ocean Pathfinder TOPEX/Poseidon 9.2 版数据集的沿轨卫星高度计海表动力高度资料, 其空间分辨率为 6km。将资料沿轨道作 3 次五点滑动平均后插值到 60km 间隔上, 以避免资料过密使同化时矩阵条件数过大、不易收敛的问题。系统中同化的卫星海表温度观测资料是 NOAA/NASA 的 AVHRR 海表温度(SST)数据, 此数据源自 NASA 的 JPL (National Aeronautics and Space Administration Jet Propulsion Laboratory)数据中心(http://podaac.jpl.nasa.gov/), 本文所采用的数据为其 216 号产品——AVHRR Pathfinder SST 5 版本中日平均升轨的候平均数据(以下简称 AVHRR SST), 该数据的水平分辨率为 4km。根据 NASA 提供的 AVHRR 质量控制文件, 分为 0 级(最差)—7 级(最好)。本文选取质量等级为 1 级(含)以上的 SST 数据。

## 2 同化方案

本文基于 MOM4 海洋模式建立了一个全球海洋资料同化系统, 该系统采用三维变分方法[16-18], 可以同化的观测资料包括中国气象局 GTS 线路上的温盐资料、ARGO 资料、卫星遥感 SST 资料、卫星遥感高度计资料等。

同化分析过程分为两步。第一步是在沿卫星高度计轨道的剖面上同化高度计和 SST 观测资料。高度计观测垂向投影采用下面的动力高度计算的约束关系[19]:

$$h(T,S)=-\int_0^{Z_m}\frac{\rho(T,S,Z)-\rho_0(T_0,S_0,Z_0)}{\rho_0(T_0,S_0,Z_0)} \tag{1}$$

其中 $T_0$ 和 $S_0$ 是参考温度和盐度, 分别为 0℃和 35‰, $Z_0$ 是参考深度, 取为 1000m。$T$、$S$、$\rho$ 分别代表温度、盐度和密度, $Z_m$ 表示不动层深度(本文中取 1000m)。海表温度只在混合层中投影, 根据混合层中温度沿深度相关性构建投影算子, 在海表观测 SST 与模式温度相关性为 1, 相关性按温度沿深度递减率建立, 在实际计算中当相邻两层温度递减率高于 0.6 时, 认为相关为 0。SST 和海表高度如果分别作为独立的观测项进入代价函数, 需要定义各自的观测误差协方差矩阵, 定义不合适常常会引入额外的误差。因此, 我们用 SST 垂向投影得到的温度和通过温盐约束关系得到的盐度计算混合层动力高度 $h_c$。总的动力高度, 即模式长期积分得到的平均动力高度和高度计观测的海表高度异常之和, 等于混合层下的温盐计算的动力高度 $h$ 和 $h_c$ 之和。$h_c$ 的深度完全由 SST 的投影深度决定。代价函数如下, 其控制变量为 $T$、$S$:

$$\begin{aligned}J=&(\boldsymbol{T}-\boldsymbol{T}_b)^T\boldsymbol{E}_T^{-1}(\boldsymbol{T}-\boldsymbol{T}_b)+(\boldsymbol{S}-\boldsymbol{S}_b)^T\boldsymbol{E}_S^{-1}(\boldsymbol{S}-\boldsymbol{S}_b)+\\&(\boldsymbol{h}(\boldsymbol{T},\boldsymbol{S})+\boldsymbol{h}_c(\boldsymbol{T}_s,\boldsymbol{S}(\boldsymbol{T}_b))-\boldsymbol{h}_m-\boldsymbol{h}_o)^T\boldsymbol{O}^{-1}(\boldsymbol{h}(\boldsymbol{T},\boldsymbol{S})+\\&\boldsymbol{h}_c(\boldsymbol{T}_s,\boldsymbol{S}(\boldsymbol{T}_b))-\boldsymbol{h}_m-\boldsymbol{h}_o)\end{aligned} \tag{2}$$

(2)式中, $\boldsymbol{T}$、$\boldsymbol{S}$ 分别是温度、盐度向量分析场; $\boldsymbol{T}_b$、$\boldsymbol{S}_b$ 分别是由模式得到的温度、盐度背景场; $\boldsymbol{h}_m$ 是由模式得到的平均海表动力高度; $\boldsymbol{h}_o$ 是由卫星高度计资料得到的海面动力高度异常; $\boldsymbol{H}$ 表示温盐计算得到的海表动力高度; $\boldsymbol{O}$ 为观测误差协方差矩阵; $\boldsymbol{E}_T$ 和 $\boldsymbol{E}_S$ 分别为温度和盐度的背景误差协方差矩阵; $\boldsymbol{h}_c$ 为卫星遥感海表温度投影计算得到的动力高度约束; $\boldsymbol{T}_s$ 是 SST 观测值。

这个方法最显著的优点是, 卫星遥感观测的 SST 不但能通过垂向相关投影影响上层的温度, 并且能通过动力高度约束项 $\boldsymbol{h}_c$ 约束下层的温盐分析。一般 SST 的直接投影到达的影响深度只有 100m 左右, 但是本方法通过动力高度的计算, 将 SST 影响进一步向下投影, 扩大其影响深度到 1000m。其次, 该方法对于 2 种观测资料, 只需要定义一个观测误差协方差矩阵, 降低了人为因素影响的风险。

第二步, 对于每一个模式水平层, 求下面代价函数的极小值。

$$\begin{aligned}J=&(\boldsymbol{T}-\boldsymbol{T}_b)^T\boldsymbol{B}_T^{-1}(\boldsymbol{T}-\boldsymbol{T}_b)+\\&(\boldsymbol{S}-\boldsymbol{S}_b)^T\boldsymbol{B}_S^{-1}(\boldsymbol{S}-\boldsymbol{S}_b)+\\&(\mathbf{H}\boldsymbol{T}-\boldsymbol{T}_O)^T\boldsymbol{O}_T^{-1}(\mathbf{H}\boldsymbol{T}-\boldsymbol{T}_O)+\\&(\mathbf{H}\boldsymbol{S}-\boldsymbol{S}_O)\boldsymbol{O}_S^{-1}(\mathbf{H}\boldsymbol{S}-\boldsymbol{S}_O)\end{aligned} \tag{3}$$

其中 $\boldsymbol{T}$ 和 $\boldsymbol{S}$ 分别是一水平层上的温度、盐度向量分析场; $\boldsymbol{T}_b$、$\boldsymbol{S}_b$ 分别是由模式得到的一水平层上的温度、盐度向量背景场; $\boldsymbol{T}_O$ 和 $\boldsymbol{S}_O$ 分别是水平层上温度和盐度的“伪观测”向量; $\boldsymbol{B}_T$ 和 $\boldsymbol{B}_S$ 分别是该水平层上温度、盐度的背景误差协方差; $\boldsymbol{O}_T$ 和 $\boldsymbol{O}_S$ 分别是该水平层上温度、盐度的观测误差协方差; $\mathbf{H}$ 为观测算子, 是一个双线性插值算子。

背景误差协方差采用高斯型, 形式如下:

$$B=A\exp\left(-\frac{\Delta x^2}{L_x^2}-\frac{\Delta y^2}{L_y^2}\right) \tag{4}$$

其中 $A$ 为背景误差方差, 对于温度取 2.0, 盐度取 0.15‰。$\Delta x$ 和 $\Delta y$ 为两水平点在 $x$ 和 $y$ 方向上的距离; $L_x$ 和 $L_y$ 表示不相关尺度, 对于温度取 $L_x$=450km、$L_y$=650km, 对于盐度取 $L_x$=420km、$L_y$=510km。温度、盐度的观测误差方差分别取 0.1、0.05。

## 3 同化结果分析

本文选择的比较资料为 NCEP 的海表温度再分析资料 OISST_V2(简称 OISST)、TOGA/TAO (international tropical ocean and global atmosphere/tropical atmosphere ocean)阵列中的海温观测以及美国马里兰大学的 Simple Ocean Data Assimilation 海洋再分析数据集(简称 SODA)。

从 1993—1997 这 5 年平均的温盐分布(图 1)来看，同化后的 SST 与 OISST 整体分布非常相近，模拟的结果在赤道西太平洋暖池地区存在一个明显的 30℃高温区，同化后此高温区消失。同化后 27℃等温线较同化前也明显地平滑，整体分布均和 OISST 观测结果接近。盐度的改善体现在南、北副热带海域的高盐区，在这些区域模拟的盐度普遍偏高，最大能达到 37‰，同化之后盐度的分布与 SODA 资料集更加吻合。温盐的偏差分布(图 2)较明显地体现出同化系统的作用。同化温度前，在西北太平洋日本岛附近，大西洋西北部北美洲东岸，印度洋南部和太平洋南部存在温度的偏差大值区，最大的偏差值有 5℃甚至以上，经过同化后，这些偏差大值均被有效减小，全球 SST 海温与 OISST 的观测结果基本控制在±2℃之间，虽然在日本岛东部地区和北美洲东岸仍有一些偏差较大值存在，但比起模拟，该区域的偏差值减小得很多，且偏差绝对值的最大值也降到 3.5℃以内。这些局部地区(包括高纬地区)同化改善不大的原因，可能是卫星遥感资料在这些地方缺测较多或者质量不好。首先，这两种遥感资料在 60 ° 以外的较高纬度都没测量。其次，我们同化所用的 AVHRR 海表温度资料是红外资料，受云的影响，会有相当部分缺测。受潮汐影响，高度计资料在近岸效果也不好，导致我们的同化结果在这些地方提高有限。如何提高这些地方的同化效果是我们今后的工作中要重点考虑的问题。模拟与 SODA 的盐度偏差几乎大部分区域都在±1‰以上，特别是在赤道东太平洋、印度洋和大西洋，盐度的最大偏差能达到±2‰甚至以上，同化后这些偏差大值区基本控制在了±0.8‰以内，盐度有如此好的改善作用，一部分原因也是由于模式模拟盐度偏差本身就比较大。

垂向海温我们用模拟、同化和 SODA 再分析资料集进行比较，图 3a、b 分别是模拟与 SODA、同

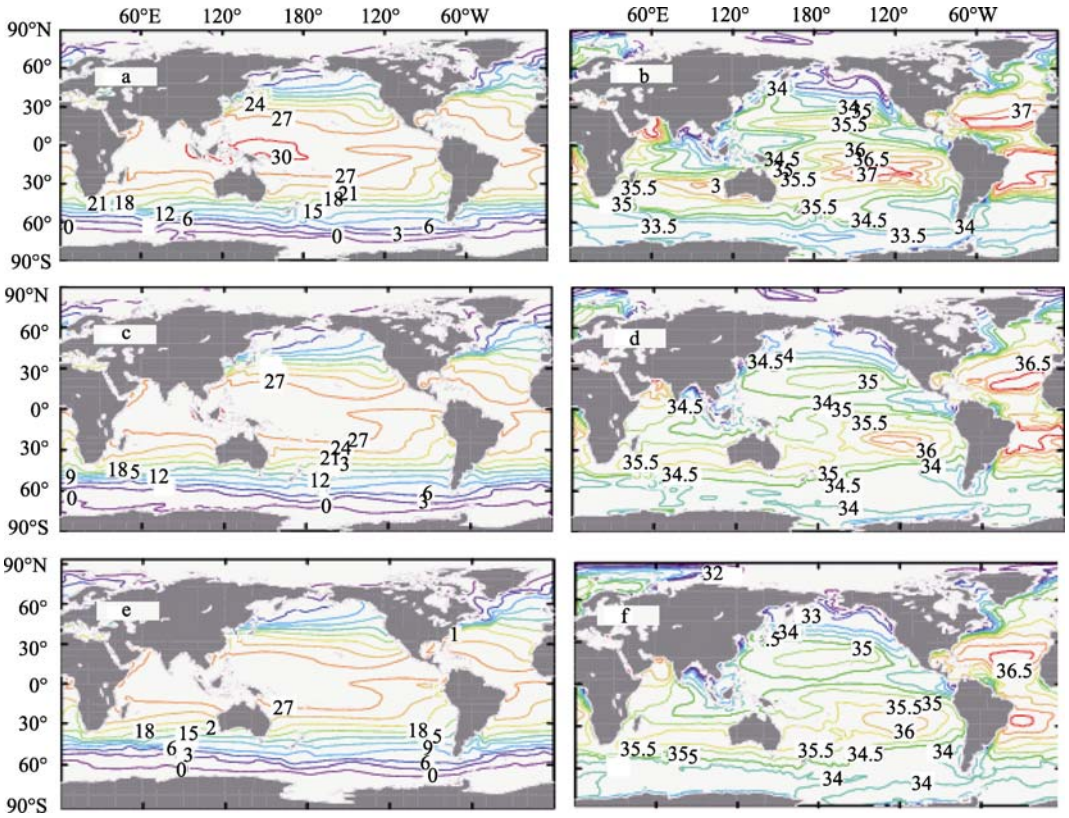


图 1 1993—1997 年平均的温度(℃)、盐度(‰)的海表分布

a.温度的模拟结果; b.盐度的模拟结果; c.温度的同化结果; d.盐度的同化结果; e. OISST; f. SODA

Fig.1 Distribution of SST (℃), sea surface salinity (SSS) (psu) averaged from 1993 to 1997, with (a) for simulation result of SST, (b) for simulation result of SSS, (c) for assimilation result of SST, (d) for assimilation result of SSS, (e) for OISST, and (f) for SODA

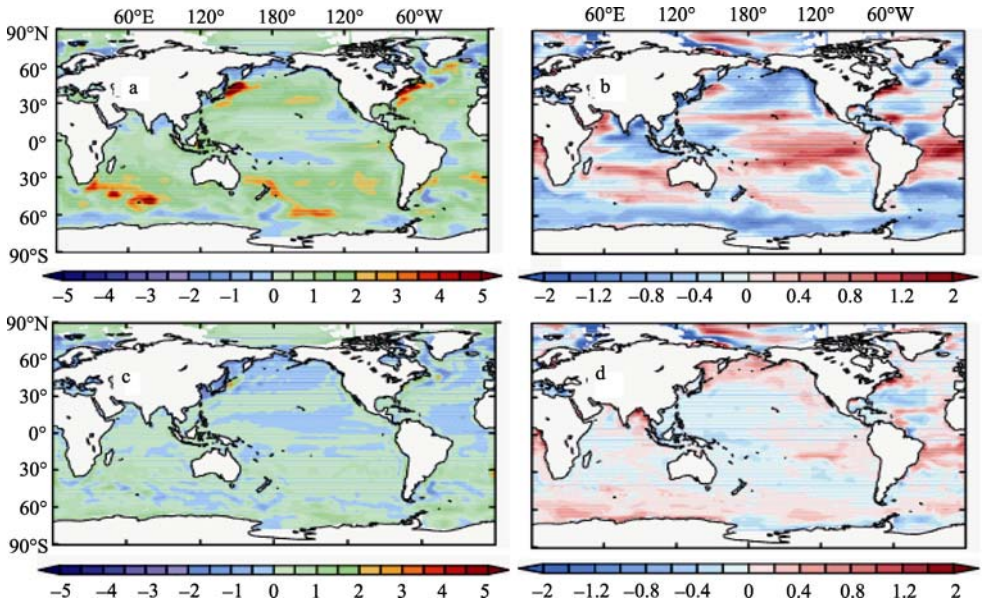


图 2 1993—1997 年平均的海表温度(℃)、海表盐度(‰)偏差分布图

a.模拟温度与 OISST; b.模拟盐度与 SODA 盐度; c.同化温度与 OISST; d.同化盐度与 SODA 盐度

Fig. 2 Distribution of SST bias (℃), SSS bias (psu) averaged from 1993 to 1997, with (a) for simulated temperature and OISST, (b) for simulated salinity and SODA salinity, (c) for assimilated temperature and OISST, and (d) for assimilated salinity and SODA salinity

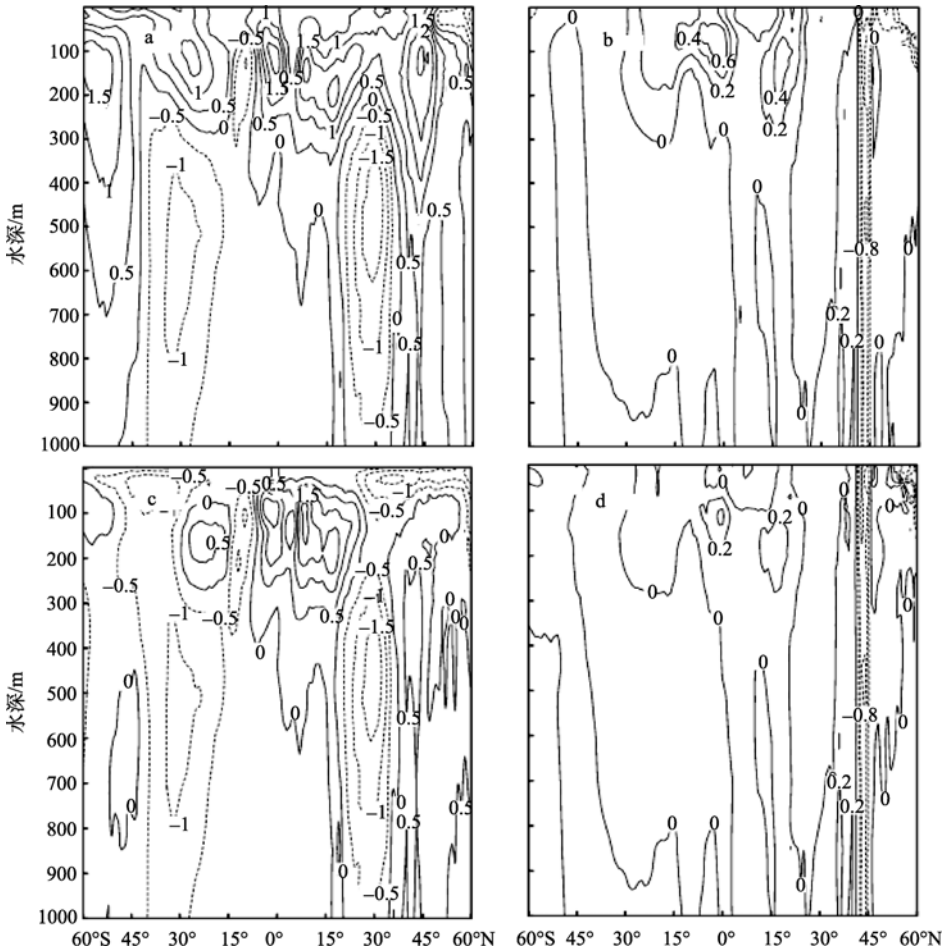


图 3 1993—1997 年平均温度(℃)、盐度(‰)沿纬向平均的垂直剖面

a. 模拟温度−SODA 温度; b. 模拟盐度−SODA 盐度; c. 同化温度−SODA 盐度; d. 同化盐度−SODA 盐度

Fig. 3 Vertical section of temperature (℃) and salinity (psu) along latitude averaged form 1993 to 1997, with (a) for simulated temperature minus SODA temperature, (b) for simulated salinity minus SODA salinity, (c) for assimilated temperature minus SODA temperature, and (d) for assimilated salinity minus SODA salinity

化与 SODA 的温度和盐度偏差图。可以看出，同化后整体的温度偏差要比模拟的平均小0.5℃，同化后盐度的整体偏差较同化前降低 0.2‰，在 300m 以上区域都有比较好的改善，在 300m 以下南北纬 30°之间的区域改善不大。尽管改进了垂向投影方法，对 100m 以下次表层的改善有所提高，但是海洋中下层的改善仍然有赖于次表层观测资料的加入，仅靠在表层观测的海洋遥感资料，难以得到海洋整层的完美调整。

为了进一步验证同化在热带太平洋地区对温度的改善情况，将模拟与同化结果插值到 TOGA-TAO 的观测点上，与其进行单点的比较。图 4 分别给出 6 个不同时次 6 个位置上的温度廓线图。可以看出，模拟的温度偏差与 TAO 观测的偏差相对较大，特别是在温跃层下方，在几个点的温度观测时间序列图(图 5)中也证实了同化对 300m 以上海域的温度场产生了正面影响，虽然在 300m 以下同化后的温度较模拟温度更接近于观测温度，但偏差还是较大，有待改进。

图 6 是 1993—1997 年平均全球海洋温、盐均方根误差(Root Mean Squared Error, RMSE)的垂向分布图。表层的温度我们仍用 OISST 作为观测数据，从第 2 层开始用 SODA 作为对比数据。从年平均来看，表层、100m 到 750m 的层次同化后对温度的改善效果比较显著，表层的 RMSE 在同化前为 1.45℃，同化后为 0.78℃，减少了 0.67℃。

## 4 小结

本文基于国家气候中心正在发展的新一代海洋资料同化系统，发展了卫星高度计资料和卫星遥感海表温度资料的协调同化方案。该方案首先考虑了卫星遥感的海洋观测资料同化中的垂向投影问题。

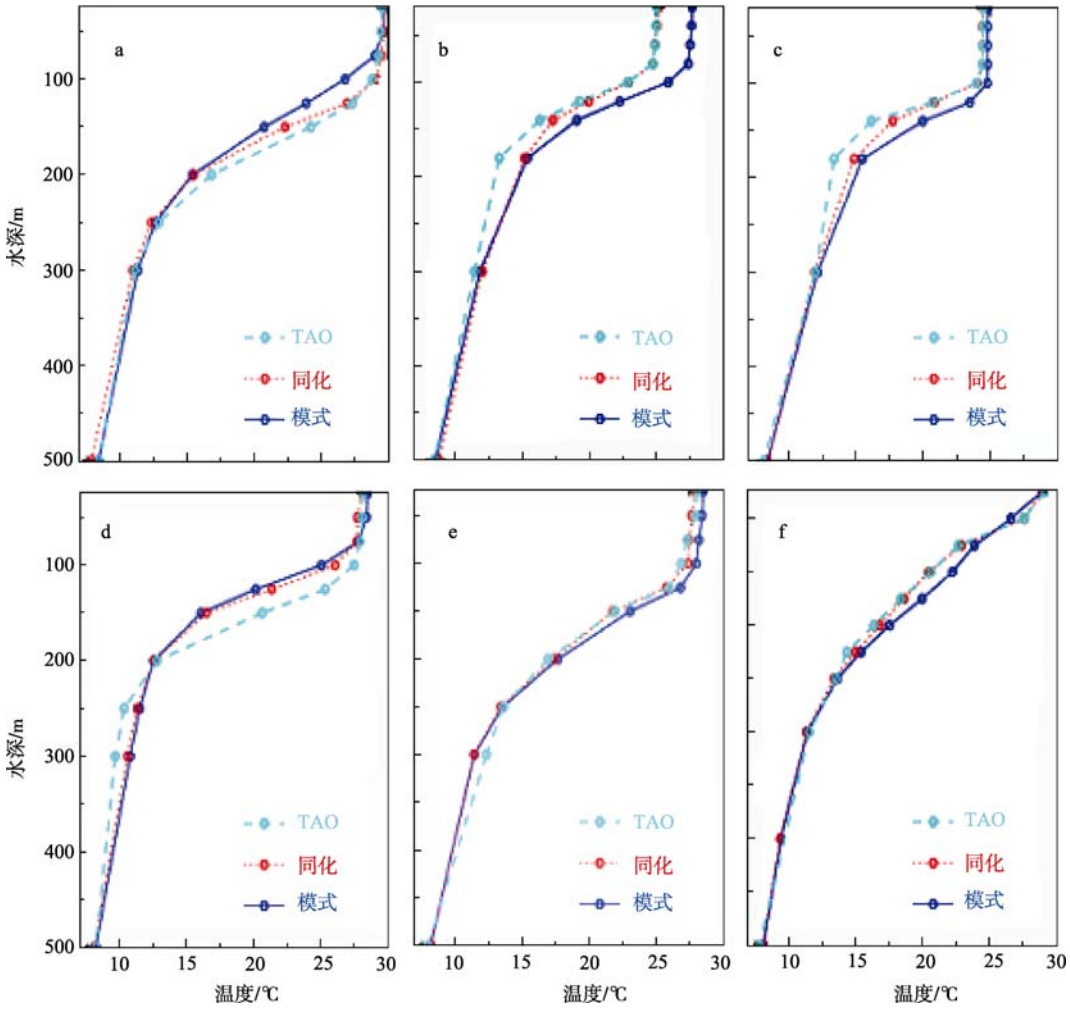


图 4 试验结果与独立的 TAO 资料的垂直温度廓线

a. 1993-10 (170°W, 5°S); b. 1994-09 (125°W, 5°S); c. 1995-11 (140°W, 2°S); d. 1996-04 (155°W, 5°N); e. 1996-05 (180°W, 0°N); f. 1997-06 (165°E, 0°N)

Fig. 4 Vertical temperature profile between test results and TAO, with short dashed lines for TAO, dotted lines for simulation, and solid lines for assimilation.

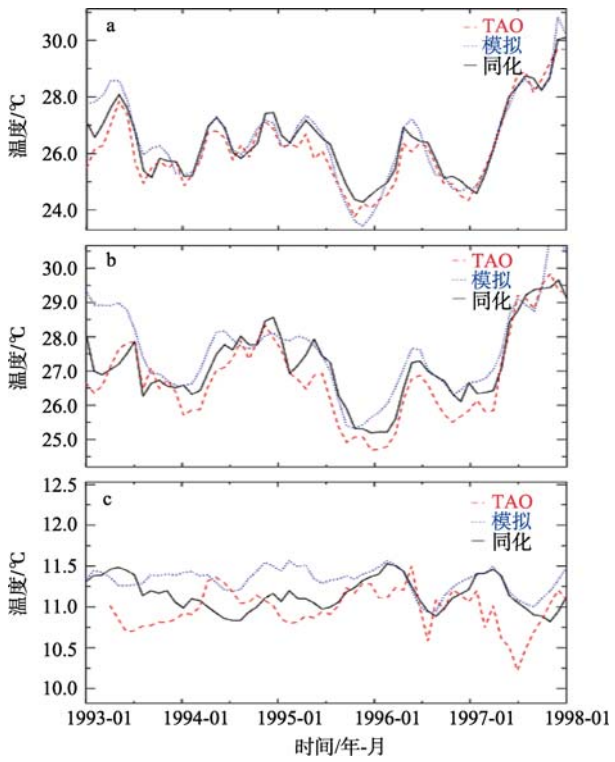


图 5 模拟、同化和 TAO 的温度

a. 点 140°W、0°N, 10m 深度; b. 点 155°W、0°N, 50m 深度; c. 点 180°W、2°S, 300m 深度。

Fig.5 Temperature of simulation, assimilation, and TAO, with (a) for 140°W, 0°N at 10 m, (b) for 155°W, 0°N, at 50 m, and (c) for 180°W, 2°S, at 300 m. Short dashed lines are for TAO, dotted lines are for simulation, and solid lines are for assimilation.

对高度计资料引入动力垂向投影方案, SST 资料采用统计相关垂向投影。方案进一步考虑两种观测资料的协调同化问题, 在动力高度计算项里, 将 SST 观测作为一个强约束引入到代价函数中。这种方案使 SST 的垂向投影深度增加, 动力上也和高度计更为协调, 并且还简化了运算, 对于两种观测资料,

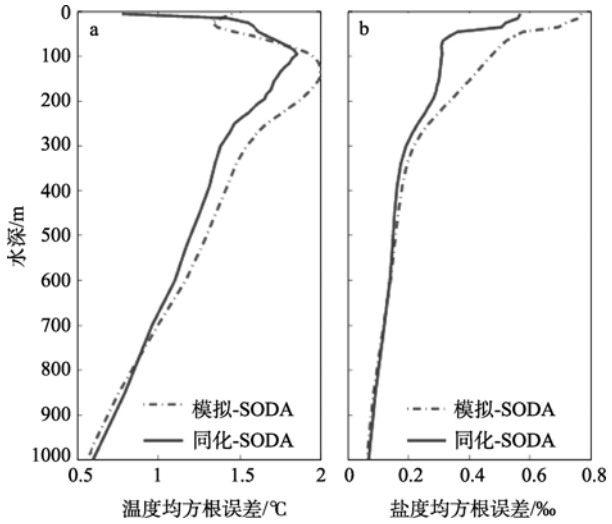


图 6 1993—1997 年平均全球海洋温度(a)、盐度(b)的均方根误差垂直分布

Fig. 5 Vertical distribution of temperature (℃) and salinity (psu) RMSE averaged from 1993 to 1997. Dot-dashed lines are for simulation minus SODA, and solid lines are for assimilation minus SODA.

只需要定义一个观测误差协方差矩阵。

利用本文发展的同化方案, 对 T/P 高度计资料和 AVHRR 海表温度产品进行了全球的 5 年资料同化试验, 分别用 TAO、OISST 和 SODA 数据集检验同化效果。试验结果证明, 通过对卫星遥感资料的同化, 能够有效改进对海洋温度和盐度的估计。海洋表层的月平均温、盐度的总均方根误差相对同化前分别降低了 0.67℃和 0.2‰, 尤其对热带太平洋暖池地区海域和东、西沿岸地带的温度、盐度场的修正比较显著。在混合层中同化效果较好。对于近岸或高纬的结果改善, 应该更多地依赖于浮标资料的同化。

## 参考文献

[1] FISCHER M, LATIF M, FLUGEL M, et al. The impact of data assimilation on ENSO simulation and prediction[J]. Mon Wea Rev, 1997, 127: 819–829.

[2] HURLBURT H E, FOX D N, METZGER J. Statistical inference of weakly correlated subthermocline fields from satellite altimeter data[J]. Geophys Res, 1990, 95: 11375–11409.

[3] HOLLAND W R. Altimeter data assimilation into ocean circulation models—Some preliminary results[C]//ANDERSON D L T, WILLEBRAND J. Oceanic Circulation Models: Combining Data and Dynamics. Netherlands: Kluwer Academic Publisher, 1989: 203–232.

[4] HAINES K. A direct method for assimilating sea surface height data into ocean models with adjustments to the deep circulation[J]. J Phys Oceanogr, 1991, 21: 843–868.

[5] TANF Y M, KIEEMAN R. A new strategy for assimilating SST data for ENSO predictions[J]. Geophys Res Lett, 2002, 29, 1841, doi: 10.1029/2002GL0148606.

[6] SHU YEQIANG, ZHU JIANG, WANG DONGXIAO, et al. Performance of four sea surface temperature assimilation schemes in the South China Sea[J]. Continental Shelf Research, 2009, 29(11/12): 1489–1501.

[7] GAO SHAN, WANG FAN, LI MINGKUI, et al. Application of altimetry data assimilation on mesoscale eddies simula-

tion[J]. Sci China Ser D-Earth Sci, 2008, 51(1): 142–151.

[8] LERMUSIAUX P F J, ANDERSON D G M, LOZANO C J. On the mapping of multivariate geophysical fields: Error and variability subspace estimates[J]. Q J R Meteorol Soc, 2000, 126: 1387–1430.

[9] KEPPENNE C L, RIENECKER M. Assimilation of temperature into an isopycnal ocean general circulation model using a parallel ensemble Kalman filter[J]. J Mar Sys, 2003, 40–41: 363–380.

[10] BURGERS G, BALMASEDA M A, VOSSEPOEL F C, et al. Balanced ocean-data assimilation near the equator[J]. J Phys Oceanogr, 2002, 32: 2509–2519.

[11] TROCCOLI A, BALMASEDA M A, SEGSCHNEIDER J, et al. Salinity adjustments in the presence of temperature data assimilation[J]. Mon Weather Rev, 2002, 130: 89–102.

[12] BALMASEDA M A. Ocean data assimilation for seasonal forecasts[C]//Proceedings of the ECMWF Seminar on recent developments in data assimilation for atmosphere and ocean. 2003: 301–325.

[13] YAN C, ZHU J, LI R. Roles of vertical correlations of background error and T-S relations in estimation of temperature and salinity profiles from sea surface dynamic height[J]. J Geophys Res, 2004, 109, C08010, 18PP, doi: 10.1029/2003JC002224

[14] ZHU J, YAN C X. Nonlinear balance constraints in 3DVAR data assimilation[J]. Science in China: D Series, 2006, 49: 331–336.

[15] KANAMITSU M, EBISUZAKI W, WOOLLEN J, et al. NCEP-DOE AMIP-Ⅱ Reanalysis (R-2)[J]. Bull Amer Meteor Soc, 2002,83: 1631–1643.

[16] 朱江 周广庆 闫长香. 一个三维变分海洋资料同化系统的设计和初步应用[J]. 中国科学: D 辑, 2007, 37 (2): 261–271.

[17] XIAO X J, WANG D X, YAN C X, et al. Evaluation of a 3dVAR system for the South China Sea[J]. Prog Nat Sci, 2008, 18: 547–554.

[18] XIAO X J, WANG D X, XU J J. The assimilation experiment in the southwestern South China Sea in summer 2000 [J]. Chinese Sci Bul, 2006, 51: 31–37.

[19] GILLA E, NIILER P P. The theory of the seasonal variability in the ocean[J]. Deep-Sea Res, 1973, 20: 141–177.

# Analogue-Dynamical Prediction of Monsoon Precipitation in Northeast China Based on Dynamic and Optimal Configuration of Multiple Predictors*

XIONG Kaiguo[1](熊开国), FENG Guolin[2,3†](封国林), HUANG Jianping[1](黄建平),

and CHOU Jifan[1](丑纪范)

1 *Key Laboratory for Semi-Arid Climate Change of the Ministry of Education, College of Atmospheric Sciences, Lanzhou University, Lanzhou* 730000

2 *Laboratory for Climate Studies, National Climate Center, China Meteorological Administration, Beijing* 100081

3 *Key Laboratory of Regional Climate–Environment Research for Temperate East Asia (RCE–TEA), Institute of Atmospheric Physics, Chinese Academy of Sciences, Beijing* 100029

(Submitted June 1, 2010; in final form March 29, 2011)

**ABSTRACT**

Based on the National Climate Center (NCC) of China operational seasonal prediction model results for the period 1983–2009 and the US National Weather Service Climate Prediction Center merged analysis of precipitation in the same period, together with the 74 circulation indices of NCC Climate System Diagnostic Division and 40 climate indices of NOAA of US during 1951–2009, an analogue-dynamical technique for objective and quantitative prediction of monsoon precipitation in Northeast China is proposed and implemented. Useful information is extracted from the historical data to estimate the model forecast errors. Dominant predictors and the predictors that exhibit evolving analogues are identified through cross validating the anomaly correlation coefficients (ACC) among single predictors, meanwhile with reference of the results from the dynamic analogue bias correction using four analogue samples. Next, an optimal configuration of multiple predictors is set up and compared with historical optimal multi-predictor configurations and then dynamically adjusted. Finally, the model errors are evaluated and utilized to correct the NCC operational seasonal prediction model results, and the forecast of monsoon precipitation is obtained at last. The independent sample validation shows that this technique has effectively improved the monsoon precipitation prediction skill during 2005–2009. This study demonstrates that the analogue-dynamical approach is feasible in operational prediction of monsoon precipitation.

**Key words:** analogue-dynamical prediction, monsoon precipitation, correction of errors, dynamic and optimal configuration

**Citation:** Xiong Kaiguo, Feng Guolin, Huang Jianping, et al., 2011: Analogue-dynamical prediction of monsoon precipitation in Northeast China based on dynamic and optimal configuration of multiple predictors. *Acta Meteor. Sinica.*, **25**(3), 316–326, doi: 10.1007/s13351-011-0307-1.

## 1. Introduction

In recent decades, due to frequent occurences of various weather disasters, short-term climate prediction becomes an important issue that has attracted increasing attention worldwide. China is located in East Asia with complicated natural conditions, where both the amount of precipitation and the distribution of the rain belt are controlled by the East Asian summer monsoon (Zhu, 1934). Monsoon precipitation anomalies can lead to large-scale droughts and floods, and thus significantly impact on the socio-economic development and people's daily life. Seasonal prediction of precipitation has been the top priority of disaster prevention and reduction in China. Under the background of global warming, increasing economic loss is

*Supported by the Special Public Welfare Research Fund for Meteorological Profession of China Meteorological Administration (GYHY200806005), National Natural Science Foundation of China (40875040 and 40930952), and National Science and Technology Support Program of China (2007BAC29B01 and 2009BAC51B04).

†Corresponding author: fenggl@cma.gov.cn.

(Chinese version to be published)

©The Chinese Meteorological Society and Springer-Verlag Berlin Heidelberg 2011



© 1994-2011 China Academic Journal Electronic Publishing House. All rights reserved. http://www.cnki.net

caused by climate anomalies and extreme weather events, so improving the accuracy of seasonal climate prediction is imperative.

Northeast China lies in the dry and warm continental monsoon climate zone. Large amounts of data reveal that the summer floods and droughts and extreme weather events are fairly active in recent years. There are signs indicating that there is an increasing trend of frequency for droughts and floods. With regard to the causes of monsoon precipitation in Northeast China, plenty of investigations have been done. The relevant studies show that geographical locality of the subtropical high ridge, the Northeast China cold vortex, and the Arctic dipole anomaly has significant correlations with summer rainfall in Northeast China (Sha and Guo, 1998; He et al., 2006; Wu et al., 2008). Liu et al. (2003) analyzed the relationship between seasonal variations of 500-hPa geopotential height in the North Pacific Oscillation (NPO) region (25°–70°N, 140°W–150°E) and precipitation in Northeast China. They found that summer precipitation over Northeast China is above normal when the 500-hPa geopotential height in the NPO region in the previous winter is in the negative phase, and vice versa. Sun and An (2003) found when the equatorial central-eastern Pacific SST has a positive (or negative) departure distribution and the SST over the west wind drift region has a negative (or positive) departure distribution from last summer to the preceding spring, then Northeast China tends to have more (or less) precipitation than normal in summer as a whole. Bai (2001) pointed out when the winter SST in North Atlantic turns warm in the south and cold in the north, it will bring about more precipitation in summer over Northeast China, and the reverse is also true. In addition to the atmospheric circulation and the SST anomalies that affect summer precipitation in Northeast China, many studies show that the snow cover over Eurasia, the Qinghai-Tibetan Plateau and East Asia in pre-winter also affects summer rainfall in Northeast China (Zhai and Zhou, 1997; Chen and Song, 2000).

On the whole, the factors and mechanisms affecting the monsoon precipitation in Northeast China have been proved to be comprehensive and complicated, especially for operational prediction. On the one hand, there are some key factors that influence monsoon precipitation of Northeast China, which have not yet been identified. On the other hand, given all the impact factors under consideration, usually for a particular region, the monsoon precipitation is the result of multi-factor co-action, and in different time periods the configuration or combination of the factors is different. Therefore, it is necessary to use available historical data to explore the formation mechanism of monsoon precipitation so as to improve the monsoon precipitation prediction level in Northeast China.

Statistical and dynamic methods are two basic methods used in short-term climate prediction. Both methods have their own advantages and shortcomings. In general, dynamical seasonal prediction has a limited skill and falls behind the high expectation. The general consensus is that statistical and dynamic methods should be combined and developed together (Chou, 2003). The problem of how to effectively integrate the two methods has been extensively researched (Thomas, 1970; Mo and Straus, 2002; Tippett et al., 2005). Gu (1958) put forward the importance and the feasibility of introducing historical data into numerical prediction. Chou (1986) discussed the principle on how to combine statistical and dynamical methods in the long-term climate prediction. Various prediction methods based on different principles have been proposed, such as utilizing multiple-instant observations in numerical weather forecast models (Zheng and Du, 1973; Chou, 1974), analogue-dynamical prediction (Qiu et al., 1989; Huang and Wang, 1991; Huang et al., 1993), and the methods based on the atmospheric self-memorization (Cao, 1993; Gu, 1998; Feng et al., 2001; Bao et al., 2004). Numerical experiments proved that these methods can improve the prediction skill.

In recent years, with increased observational data and improvement in numerical models, short-term climate prediction has rapidly developed (Ren and Chou, 2005, 2007; Zheng et al., 2009), but the current operational prediction level is not high enough, so further improvement is still needed (Wang, 2001; Barnston et al., 2005; Ren and Chou, 2007).

This study aims to conduct precipitation prediction over Northeast China (40°–55°N, 110°–135°E; total 77 grids) based on the analogue-dynamical method.



© 1994-2011 China Academic Journal Electronic Publishing House. All rights reserved. http://www.cnki.net

Through searching for analogues to the initial field in history, dynamical model errors can be estimated by the corresponding analogous errors. A new technique called changeable/dynamic and optimal configuration of multiple predictors for monsoon precipitation analogue-dynamical prediction is proposed and experimented.

## 2. Data

The National Climate Centre (NCC) of China has established an operational short-term climate prediction system (Ding et al., 2002; Li et al., 2005). The model horizontal resolution is about 1.875°×1.875°. In this study, hindcast and predicted precipitation data (after being interpolated to a 2.5°×2.5° grid) for a total of 27 yr (1983–2009) from the NCC operational seasonal prediction model are used. Note that only ensemble mean results for June–August from the integrations beginning at the end of February in each year are selected. The CPC (Climate Prediction Center, National Weather Service, U. S.) Merged Analysis of Precipitation (CMAP) data are taken as observation, and then the model errors, namely, the discrepancies between the model and the CMAP data, are obtained. Analogues are selected from the 74 circulation indices from the NCC Climate System Diagnostic Division and the 40 climate indices from NOAA of US.

## 3. Basic principle of the analogue-dynamical prediction

In essence, the numerical prediction model is an initial value problem of a set of partial differential equations, which are expressed as follows:

$$\begin{cases} \dfrac{\partial \psi}{\partial t} + L(\psi) = 0, \\ \psi(x, t_0) = \psi_0(x), \end{cases} \tag{1}$$

where $\psi(x,t)$ is the model state vector to be predicted; $x$ and $t$, respectively, are the vector in spatial coordinate and time; $L$ is the differential operator of $\psi$, which corresponds to a real numerical model; $t_0$ denotes the initial time; and $\psi_0$ is the initial value. The value $\psi$ or its function $P(\psi)$ at $t > t_0$ can be obtained by numerical integration. Then the exact model that the real atmosphere satisfies can be written as

$$\frac{\partial \psi}{\partial t} + L(\psi) = E(\psi), \tag{2}$$

where $E$ is the error operator that expresses the errors of the real numerical model. From the dynamical point of view, the historical data can be regard as a series of special solutions that satisfy Eq. (1).

Numerical model is an approximation of the behavior of the actual atmosphere. Scientists have devoted to the enhancement of climate models; however, existing models are still far from being sufficiently precise in prediction. Such efforts are generally carried out by directly improving the model's physical parameterization schemes, numerical methods, and so on, thus to reduce the model errors. Nonetheless, no matter how the model develops, the errors will remain inevitable and even substantial. In fact, although we do not know the exact solutions that control the atmospheric motion, we possess a large number of observation data that are actually a series of special solutions. Thus, we can utilize the information of historical analogues to estimate model errors, thereby to compensate the model deficiencies and reduce the model errors.

The atmosphere is a forced dissipative nonlinear system. The system adjusts to external forcing. Long-term operational prediction experiences have shown that, with alike initial and boundary conditions, the evolutions of the atmosphere are also alike. Therefore, for any initial value, we can utilize the model error information of historical analogue, assuming that the prediction field is a small perturbation superposed on the historical analogue, so the current model prediction errors can be estimated by the corresponding errors of historical analogues. In other words, the problem is transformed from improving the dynamical prediction of numerical models into the inverse problem of utilizing historical data to estimate current unknown model errors based on known historical analogical information.

## 4. Method

The mechanisms for monsoon precipitation are different in different regions, which means that each region has its own precipitation impact factors. Even



© 1994-2011 China Academic Journal Electronic Publishing House. All rights reserved. http://www.cnki.net

under the same external forcing, due to lack of knowledge of the internal physical processes, defects in physical parameterization schemes, and so on, the response pattern and model prediction errors may also vary for different regions. But for a given region, under the analogous external forcing, the model errors will be analogous on certain timescales. Thus, we can utilize the analogue error correction method to correct the model results. The current study is based on the principle of analogue-dynamical prediction, aiming at improving the monsoon precipitation prediction accuracy of the NCC operational seasonal prediction model. Figure 1 shows the flowchart of the analogue-dynamical prediction of monsoon precipitation based on dynamic and optimal multi-predictor configuration.

First, according to the 1983–2009 CMAP data and precipitation data from the NCC operational seasonal prediction model, the model errors in the recent 27 years are obtained. Subsequently, 114 climate indices are taken as 1368 predictors, and 4 cases of historical analogues are selected based on the analogue-dynamical principle. For each predictor, cross-validation is carried out. After sorting these predictors according to their cross-validation ACCs and the evolving analogous scheme, the predictors that exhibit evolving analogues are identified. With these predictors, multi-factor configuration and cross-validation are carried out again, and then the optimal multi-factor configuration is obtained. Combined with the recent historical optimal multi-factor configuration, the steady optimal multi-predictor configuration in a prediction period is eventually determined. At last, based on this final optimal multi-predictor configuration and the analogue-dynamical prediction

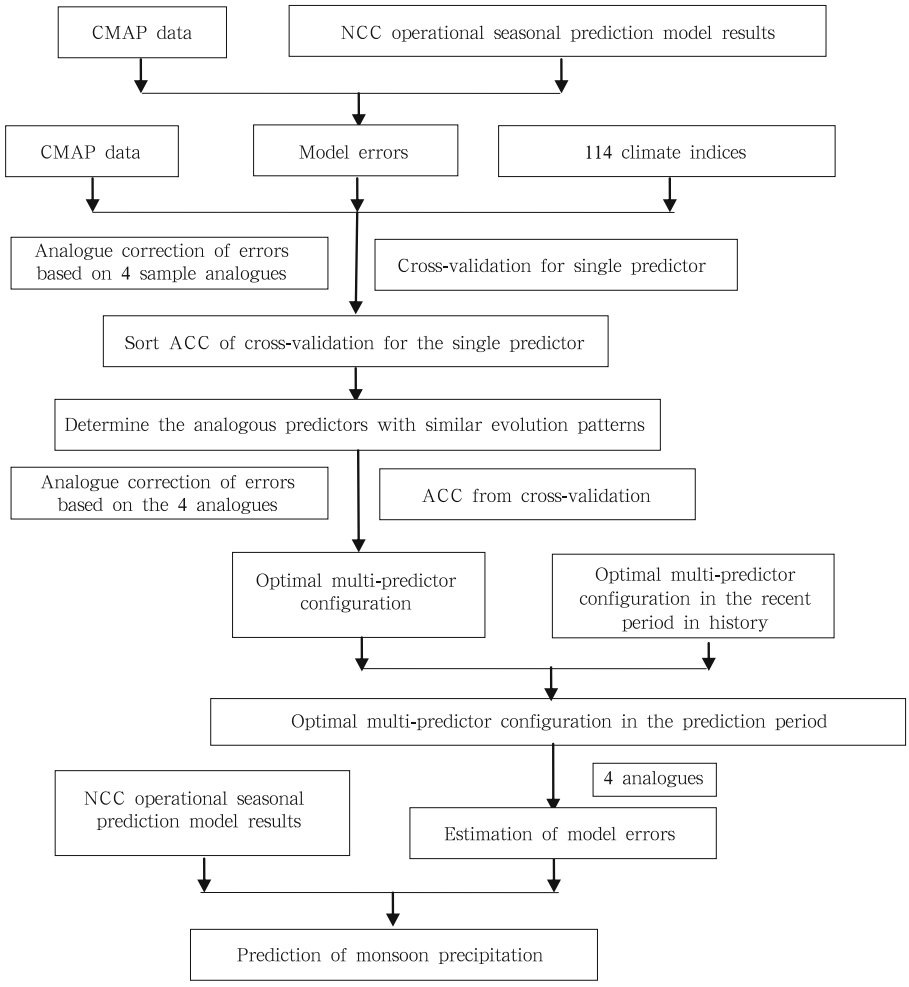


**Fig. 1.** Flowchart of the analogue-dynamical prediction of monsoon precipitation based on dynamic and optimal configuration of multiple predictors.



© 1994-2011 China Academic Journal Electronic Publishing House. All rights reserved. http://www.cnki.net

method, the model errors are estimated, by which the model prediction results are corrected and the model prediction results are obtained.

### *4.1 Analogue selection*

The analogue-dynamical prediction results are directly influenced by the selection of analogues. Appropriate selection of historical analogues and their numbers can effectively improve the prediction skill. In general, within a certain time frame, the more analogous the initial fields to history, the more closer the model climate evolution and model errors to history and past model errors. Thus, selection of the right historical analogues are very important. The Euclidean distance is taken as the historical analogue selection criterion, and historical model errors for the four most analogous cases are averaged as the prediction model errors (Bao et al., 2004; Ren and Chou, 2007). The related algorithm is shown as follows:

$$\mathrm{AI} = \left[ \frac{\sum\limits_{i=1}^{k} w_i (\varphi'_{ij} - \varphi'_{ik})^2}{\sum\limits_{i=1}^{k} w_i} \right]^{\frac{1}{2}}, \qquad (3)$$

where AI denotes the Euclidean distance, $\varphi'_{ij}$ and $\varphi'_{ik}$ represent two fields at different times ($j$ and $k$), and $w_i$ is the weight coefficient. The smaller AI is, the more analogous the initial field to the historical field. In view of the basic theory of analogue-dynamical prediction, four historical analogues are selected, and then the prediction model errors can be expressed as:

$$\hat{E}(\psi_0) = \sum_{j=1}^{4} b_j \hat{E}(\widetilde{\psi}_j) \Big/ \sum_{j=1}^{4} b_j = \sum_{j=1}^{4} a_j \hat{E}(\widetilde{\psi}_j), \qquad (4)$$

where $\hat{E}(\widetilde{\psi}_j)$ is the model error with respect to historical analogue $\widetilde{\psi}_j, a_j = b_j / \sum\limits_{j=1}^{4} b_j$ is the normalized weight coefficient, and $b_j$ is the coefficient to be determined.

### *4.2 Selection of regional predictors*

A number of previous studies have been carried out to find out predictors that impact on the monsoon precipitation in Northeast China (Zhai and Zhou, 1997; Sha and Guo, 1998; Chen and Song, 2000; Bai, 2001; Liu et al., 2003; Sun and An, 2003; He et al., 2006; Wu et al., 2008). In the current study, 74 circulation indices from NCC and 40 climate indices from NOAA are used as predictors. The distribution of circulation indices varies with months. Therefore, the response of the short-term climate prediction model is different under different circulation conditions which are supplied as the boundary or external forcing to the model. A climate index can be considered as 12 predictors following 12 months, so 114 climate indices can be viewed as 1368 predictors (impact factors).

The selection of regional monsoon precipitation predictors should follow these basic principles: 1) these factors should have clear physical meanings; 2) they should be correlated with the model errors. Predictors are often different in different periods of time, so the prediction skills of predictors in different periods of time vary. Taking into account the above considerations, the principle and process for selection of optimal multiple predictors are given as follows (taking the prediction in 2009 as an example):

1) Selecting the factors that affect regional monsoon precipitation by sorting ACC values. By processing cross-validation on single factor in the three periods: 1983–2006, 1983–2007, and 1983–2008, the factors are sorted according to cross-validation ACCs in each period. The reason why the prediction of 2009 only considers the previous three periods is that the summer rainfall in Northeast China has about 2–4-yr periodic variations (Sun et al., 2000), and a more stable forecasting skill can be achieved for the analogue-dynamical prediction based on the optimal multi-predictor configuration from the previous three periods.

2) Determining the dominant factor. Select at least one factor that can obviously improve the ACC from sorted factors in the above three periods and nominate it the dominant factor. The single factor cross-validation shows that, for a given area, the dominant climatic factor varies from time to time and its contribution to precipitation is stable, thus this factor is chosen as the dominant factor (for example, the EPO in April).

3) Determining the factors with the evolving analogues. For different periods, factors that always play an important role in the rainfall prediction should be



© 1994-2011 China Academic Journal Electronic Publishing House. All rights reserved. http://www.cnki.net

a priority. From the single factor cross-validation ACC or the correlation coefficient between the factors and observed monsoon precipitation, it can be seen that there are many factors impacting monsoon precipitation in Northeast China. The questions are: what factor is dominant and which factor only shows a false correlation? To solve these problems, the concept of "evolving analogues" is brought forth. The results show that adopting the evolving analogues to select regional predictors is one of the reliable ways in improving the precipitation prediction skill. It removes those factors that have nothing to do with the precipitation in this region. Meanwhile, the process of determining the factor with the evolving analogues is essential for selecting only one factor from a climate index. This greatly reduces the degrees of freedom of prediction factors. The process of selecting the factor with the evolving analogues is as follows: ① For a given period of time, select all the factors that have larger ACCs for predictions using the analogue error correction than those using the systematic bias correction; ② find the factors that originate from the same climate index. For a climate index, if many of the factors from it (in different months) have the ability to improve the monsoon prediction skill, then we can say this climate index has the evolving analogues. For the same climate index, only the factor corresponding to the greatest ACC is considered. For simplicity, we take the factor corresponding to the highest ACC as the evolving analogous factor.

4) Determining the optimal multi-predictor configuration. From the factors with the evolving analogues in each period, the configuration of optimal factors is identified through the cross-validation of ACC. Taking the common optimal factors in each period and establishing the regional impact factor set, then the optimal multi-predictor configuration is finalized.

For selection of multi-factor configuration, as a result of large amount of data and large degree of freedom, the calculation work load is huge. Additionally, the noise in the multiple factors and the correlation between factors will lead to nonlinear growth of errors. Mo and Straus (2002) show that, by utilizing EOF decomposition, the degree of freedom can be reduced greatly while the influence of noise can be eliminated effectively; essentially the dimension of the factors is decreased.

EOF decomposition of the multi-factor field $\psi_{m\times n}$ can be expressed as:

$$\psi_{m\times n} = V_{m\times n}T_{n\times n}, \tag{5}$$

where $m$ and $n$ are the space and time dimensions respectively. $V_{m\times n}$ is the normalized orthogonal base field, and $T_{m\times n}$ the time coefficients field for principal components (PCs). For simplicity, only the first $h$ ($h < m$) PCs that jointly explain about 80% of the total variance are used:

$$\psi_{m\times n} = V_{m\times n}T_{n\times n} \approx V_{m\times h}T_{h\times n}. \tag{6}$$

### *4.3 Sensitivity of the number of predictors*

As we know, in short-term climate prediction, for a linear system, the more historical data we use, the better the prediction is. However, for a nonlinear system, the prediction skill will not depend on data quantity but on particularity of data. The atmosphere is a nonlinear complex system and it will be an effective way to utilize the dynamic optimal multi-predictor configuration to compress the degree of freedom by extracting the component predictability so as to improve short-term prediction skill.

Figure 2 shows the sensitivity of ACC to the number of predictors in three periods: 1983–2006, 1983–2007, and 1983–2008. The multi-factor cross-validation is done in each period. It is seen that, for the analogue-dynamical monsoon precipitation prediction, it is not true that the more predictors, the better the prediction. On the whole, with the increase of number of predictors, the ACC increases at first and

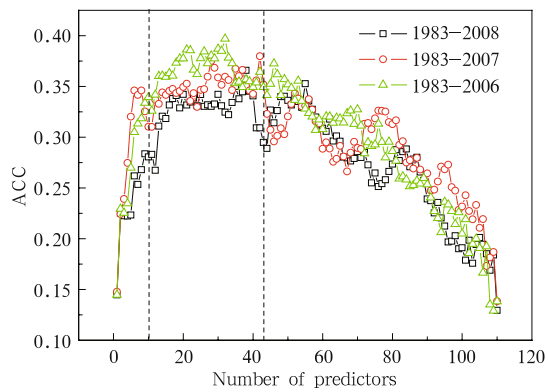


**Fig. 2.** ACC versus number of predictors for three time periods.



© 1994-2011 China Academic Journal Electronic Publishing House. All rights reserved. http://www.cnki.net

then decreases. When the number of predictors increases from 1 to about 10, the ACC in each period of time increases rapidly to a high value. When it expands to 40 or so, the ACCs for the three periods achieve relatively stable values and maintain a high prediction skill. After more impact factors are brought in, the ACC decreases rapidly. Moreover, it can be seen from Fig. 2 that the cross-validation of ACC for any single factor is below 0.2, while for the optimal multi-factor configuration it is generally above 0.35, some even reaching 0.4, implying the optimal multi-actor configuration is skillful than any single factor. Therefore, the optimal multi-factor configuration is an effective way in short-term climate prediction.

### *4.4 Physical properties of predictors*

With the analogue-dynamical prediction method and optimal multi-predictor configuration, we made a hindcast of monsoon precipitation in Northeast China in 2009. The validation results are given in Table 1. Note that only the factors in January are taken as the factors in the same year while the factors from February to November are taken as the factors of last year. The ACCs in Table 1 are cross-validation results for 1983–2008. The correlation coefficients are between the predictors and the PC1 of observed monsoon precipitation/the NCC seasonal prediction model errors in Northeast China.

For the analogue-dynamical prediction of monsoon precipitation in Northeast China, the dominant predictor is the East Pacific Oscillation (EPO) index, also known as the East Pacific-North Pacific pattern (EP-NP) (Bell and Janowiak, 1995), in last April. The cross-validation shows that for this single predictor, the average ACCs in periods 1983–2006, 1983–2007, and 1983–2008 are 0.14, 0.15, and 0.14, respectively, ranking the second highest, and the highest correlations, respectively. This well indicates the importance of this predictor in monsoon precipitation prediction in Northeast China.

Figure 3 shows the relationship between the anomaly percentages of EPO in last April and the PC1 of monsoon precipitation in Northeast China. Figure 4 gives distributions of the correlation coefficients between the EPO in last April and observed monsoon precipitation/model errors. Especially, from Fig. 4, it

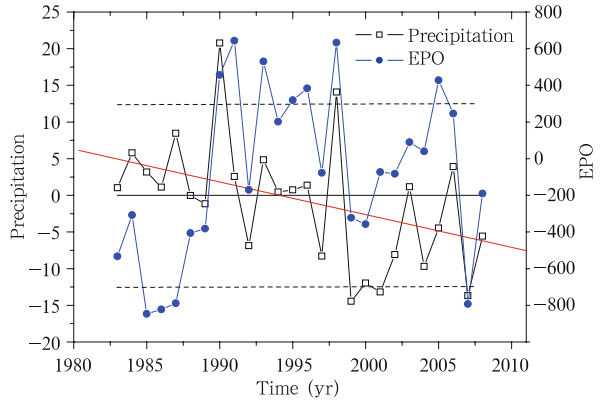


**Fig. 3.** The relationship between the EPO in April and the PC1 of monsoon precipitation in Northeast China. All values are anomaly percentage, and the climate value is the average from 1983 to 2002.

can be seen that monsoon precipitation and model errors in Northeast China have a strong correlation with the EPO in last April, especially in south of Northeast China, with values passing the 0.01 confidence test over parts of the region. Therefore, the EPO in last April is indeed a factor that impacts on the monsoon precipitation in Northeast China. Since the NCC operational seasonal prediction model has an accurate description of climate state, the distribution of the correlation coefficient between the predictor and model prediction errors is accordant with that between the predictor and observed monsoon precipitation. This is also true for other predictors (figure omitted).

Due to the complexity and nonlinear characteristics of the atmosphere, dominant predictor and evolving analogues are selected by cross-validation of ACCs instead of from the correlation coefficient between the factor and the observed precipitation or model prediction errors. In general, the regional monsoon precipitation is the result of joint effects of multiple factors, and the fact that the factors have a high correlation coefficient with observational precipitation or model prediction errors does not mean a good prediction skill. This may be the reason why the impact factors we selected are different from those of previous researchers (Zhai and Zhou, 1997; Chen and Song, 2000; He et al., 2006; Wu et al., 2008). It can be seen from Table 1, the correlation coefficient between the EPO in last April and PC1 of observed precipitation or model prediction errors in Northeast China are 0.33 and



© 1994-2011 China Academic Journal Electronic Publishing House. All rights reserved. http://www.cnki.net

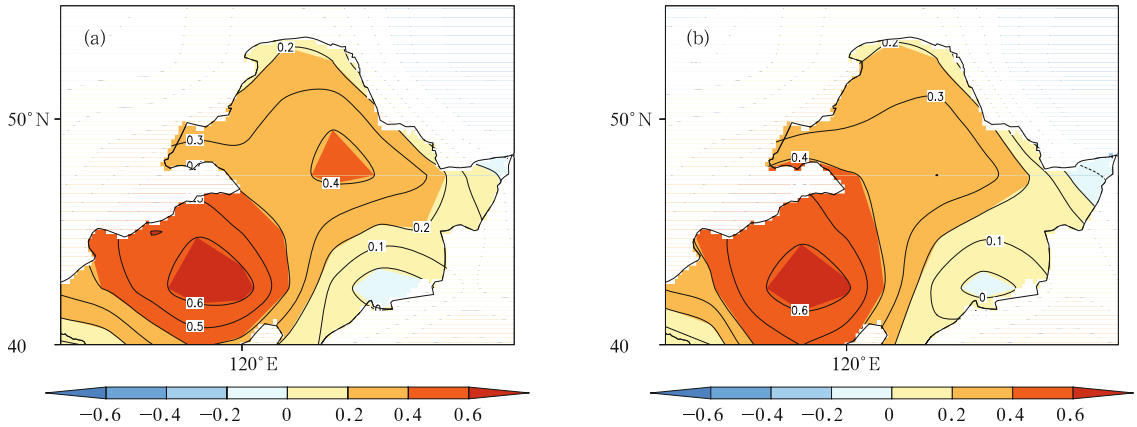


**Fig. 4.** Distributions of the correlation coefficient between the EPO in April and (a) observed monsoon precipitation, and (b) model errors in Northeast China.

**Table 1.** The optimal multi-predictor configuration for prediction of monsoon precipitation in Northeast China in 2009

| Month | Predictors | Cross-validation ACC | Correlation coefficient with PC1 of observed precipitation/model errors |
|---|---|---|---|
| 1 | Intensity of the East Asian trough | 0.08 | –0.20/–0.08 |
| 2 | Northern position of the subtropical high over the South China Sea | 0.02 | –0.18/ 0.15 |
| 4 | EPO | 0.14 | 0.33/–0.11 |
| 4 | North Tropical Atlantic SST | 0.05 | –0.38/ 0.21 |
| 6 | Pacific warm pool | 0.01 | –0.35/ 0.35 |
| 7 | India-Burma trough | –0.02 | –0.11/–0.03 |
| 10 | Ridge position of the subtropical high over India | 0.001 | –0.42/ 0.41 |
| *10 | Area-averaged precipitation for Arizona and New Mexico | –0.005 | –0.16/ 0.27 |

*http://www.esrl.noaa.gov/psd/data/climateindices/list/

–0.11, respectively. Although both of them could not pass the 0.05 confidence test, its cross-validation ACC is the largest; whereas the correlation coefficient between the ridge of the subtropical high over India in last October and PC1 of observed precipitation or model prediction errors in Northeast China passes the 0.05 confidence test, but the ACC is only 0.001. Thus, by use of the single-factor cross-validation ACC, selection of regional impact factors is more direct and effective.

In addition, the relationship between the PC1 of eight predictors in Table 1 and the monsoon precipitation in Northeast China is analyzed here (see Fig. 5). With EOF decomposition of the eight predictors, the first 5 PCs' cumulative explained variance already reaches 80%, with each accounting for 37%, 20%, 12%, 11%, and 9% of the total variance, respectively. The relationship between the PC1 of eight predictors and the monsoon precipitation in Northeast China is obviously different from that of the EPO in last April (see Fig. 3). The correlation coefficient for the former is

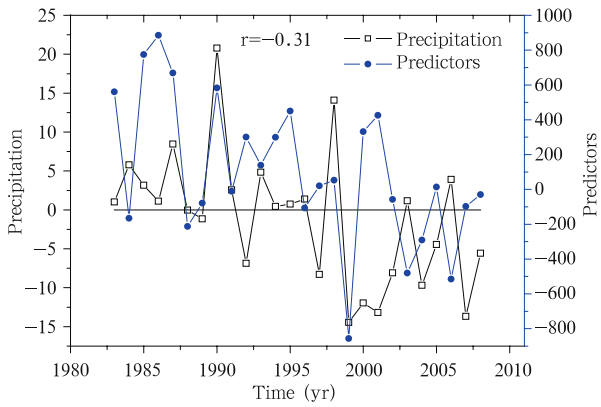


**Fig. 5.** The relationship between monsoon precipitation in Northeast China and the configuration of eight indices. All values are the anomaly percentage of PC1 after EOF, and the correlation coefficient $r = -0.31$.



© 1994-2011 China Academic Journal Electronic Publishing House. All rights reserved. http://www.cnki.net

–0.31, but for EPO is 0.31. The average cross-validation ACC from 1983 to 2008 for the 8-predictor configuration is 0.18, better than the systematic bias correction prediction and the analogue error correction prediction using the only predictor of EPO in last April, for which ACCs are –0.08 and 0.14, respectively. The improvement also shows in the correlation coefficients: for the systematic bias correction the value is –0.17, while for the analogue errors correction it reaches 0.14, showing a higher prediction skill.

## 5. Results of the independent sample validation

There are only 27-yr data that can be used in analogue-dynamical prediction experiments, so it is difficult to select a much better historical analogue that excludes the abnormal predictors in certain years. Taking the impact of the length of historical data on the selection of historical analogues into consideration, in this paper, independent sample validation experiments were only carried out in the recent 5 years from 2005 to 2009. Figure 6 shows both ACC and RMSE from the independent sample validation. Based on the principles of analogue selection, according to values of the Euclidean distance, cases for 5 yr are selected and ordered as first, second, third, and fourth analogues in Table 2 (the data in the brackets are the ACC of monsoon precipitation between analogue year and the year of hindcast).

It can be seen from the independent sample validation of ACCs in Fig. 6a that, compared with the systematic bias correction, the ACCs from the analogue error correction under the optimal multi-predictor configuration are mostly increased effectively, except for 2005 and 2006 in the hindcast of 2005–2009 in Northeast China. The ACCs in the rest 3 years are higher, changing from –0.24, –0.08, and 0.09 to 0.13, –0.06, and 0.32, respectively. In 2005, though the ACC from the analogue error correction is smaller, but it still reaches 0.18. As to RMSE, it can be seen from Fig. 6b that, compared with the systematic bias correction, the analogue error correction does not make the RMSE reduced significantly in these 5 years, except 2007. The RMSEs of the rest 4 years increase slightly; the reasons herein need to be further investigated. The ACCs between analogue years and prediction years are shown in Table 2. The ACC values between the first analogue year and prediction years are positive except for 2007. This clarifies that the analogue-dynamical prediction of monsoon precipitation based on the optimal multi-predictor configuration is reasonable and potentially useable.

**Table 2.** Analogue years of the independent sample validation

| Prediction year | First analogue | Second analogue | Third analogue | Fourth analogue |
|---|---|---|---|---|
| 2005 | 2003(0.06) | 1991(–0.08) | 2001(0.46) | 1997(–0.33) |
| 2006 | 2005(0.07) | 2002(–0.02) | 2001(–0.08) | 1990(–0.34) |
| 2007 | 1988(–0.06) | 2003(0.20) | 1984(0.50) | 1989(0.29) |
| 2008 | 1988(0.26) | 1992(–0.07) | 1989(0.05) | 1984(0.05) |
| 2009 | 2000(0.36) | 2002(0.42) | 1992(0.22) | 2004(–0.12) |

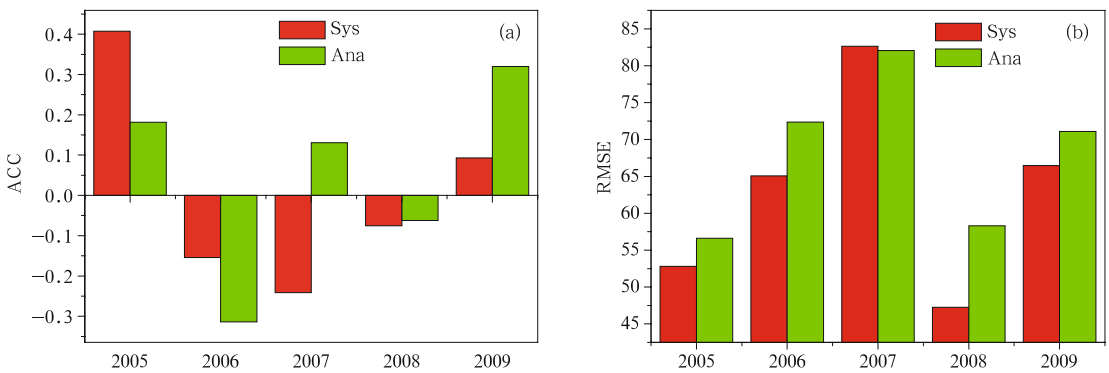


**Fig. 6.** ACC (a) and RMSE (b) of the independent sample validation. Red and green bars represent results from the systematic bias correction and the anologue error correction, respectively.



© 1994-2011 China Academic Journal Electronic Publishing House. All rights reserved. http://www.cnki.net

## 6. Conclusions and discussion

Aiming at improving the skill of the NCC seasonal prediction model that uses available historical data, and through searching for analogues to the initial field in the historical data, dynamical model prediction errors can be estimated according to the model prediction errors corresponding to historical analogues. By using the CMAP data from 1983 to 2009 and precipitation data in the same period from the NCC operational seasonal prediction model, we have identified predictors and found historical analogues based on 40 climate indices from NOAA and 74 circulation indices from NCC Climate System Diagnostic Division. Through sorting the predictors according to the cross-validation ACC, we found out the dominant factors and implemented the evolving analogue scheme, then the optimal multi-factor configuration is used, and a new technique called the analogue-dynamical prediction based on changeable/dynamic and optimal configuration of multiple predictors is proposed. Experimental monsoon prodictions were made over Northeast China. Sensitivity tests based on the cross-validation ACC were carried out, which showed that the multi-predictor configuration in monsoon precipitation prediction is feasible and practical. The results of the independent sample validation from 2005 to 2009 show that this method can effectively improve the monsoon precipitation prediction ability of the NCC operational seasonal prediction model in Northeast China. But even in these five years, the ACC average is only 0.05, at about the same level with that of the present operational short-term climate prediction. That is to say, it is not enough to improve the NCC operational seasonal prediction model by only using this method. Like other statistical prediction methods, the ACC in these five years is unstable, and it is shown that there is still a long way to go for improving the short-climate prediction skill. In addition, the impact mechanism of the identified factors on the precipitation needs to be investigated as well.

## REFERENCES


Bai Renhai, 2001: Relations between the anomaly of sea surface temperature in the Atlantic and the precipitation in summer over Northeast China. *Marine Sci. Bull.*, **20**(1), 23–29. (in Chinese)

Bao Ming, Ni Yongqi, and Chou Jifan, 2004: The experiment of monthly mean circulation prediction using the analogy-dynamical model. *Chinese Sci. Bull.*, **49**(11), 1112–1115. (in Chinese)

Barnston, A. G., A. Kumar, L. Goddard, et al., 2005: Improving seasonal prediction practices through attribution of climate variability. *Bull. Amer. Meteor. Soc.*, **86**, 59–72.

Bell, G. D., and J. E. Janowiak, 1995: Atmospheric circulation associated with the midwest floods of 1993. *Bull. Amer. Meteor. Soc.*, **76**(5), 681–695.

Cao Hongxing, 1993: Self-memorization equation in atmospheric motion. *Sci. China (Ser. B)*, **23**(1), 104–112. (in Chinese)

Chen Xingfang and Song Wenling, 2000: Analysis of relationship between snow cover on Eurasia and Qinghai Xizang Plateau in winter and summer rainfall in China and application to prediction. *Plateau Meteorology*, **19**(2), 214–223. (in Chinese)

Chou Ge-Fen, 1974: A problem of using past data in numerical weather forecasting. *Scientia Sinica*, **17**(6), 814–825.

Chou Jifan, 1986: Why to combine dynamical and statistical methods together and how to combine. *Plateau Meteorology*, **5**(4), 367–372. (in Chinese)

——, 2003: Short term climatic prediction: Present condition, problems and way out. *Bimonthly of Xinjiang Meteorology*, **26**(1), 1–4. (in Chinese)

Ding Yihui, Liu Yiming, Song Yongjia, et al., 2002: Research and experiments of the dynamical model system for short-term climate prediction. *Climatic and Environmental Research*, **7**(2), 236–246. (in Chinese)

Feng Guolin, Cao Hongxing, Gao Xinquan, et al., 2001: Prediction of precipitation during summer monsoon with self-memorial model. *Adv. Atmos. Sci.*, **18**(5), 701–709.

——, ——, Wei Fengying, et al., 2001: On area rainfall ensemble prediction and its application. *Acta Meteor. Sinica*, **59**(2), 206–212. (in Chinese)

Gu Xiangqian, 1998: A spectrum model based on self-memorization principle. *Chinese Sci. Bull.*, **43**(1), 1–9. (in Chinese)

Gu Zhenchao, 1958: On the utilization of past data in numerical weather forecasting. *Acta Meteor. Sinica*, **29**(3), 176–184. (in Chinese)

He Jinhai, Wu Zhiwei, Qi Li, et al., 2006: Relationships among the Northern Hemisphere annual mode, the Northeast cold vortex and the summer rainfall in northeast China. *Journal of Meteorology and Environment*, **22**(1), 1–5. (in Chinese)




© 1994-2011 China Academic Journal Electronic Publishing House. All rights reserved. http://www.cnki.net

Huang, J. P., Yi Y. H., Wang S. W., et al., 1993: An analogue-dynamical long-range numerical weather prediction system incorporating historical evolution. *Quart. J. Roy. Meteor. Soc.*, **119**, 547–565.

Huang Jianping and Wang Shaowu, 1991: The experiment of seasonal prediction using the analogy-dynamical model. *Sci. China (Ser. B)*, **2**, 216–224. (in Chinese)

Li Weijing, Zhang Peiqun, Li Qingquan, et al., 2005: Research and operational application of dynamical climate model prediction system. *J. Appl. Meteor. Sci.*, **16**(Suppl.), 1–11. (in Chinese)

Liu Zongxiu, Lian Yi, Shen Baizhu, et al., 2003: Seasonal variation features of 500-hPa height in north pacific oscillation region and its effect on precipitation in Northeast China. *J. Appl. Meteor. Sci.*, **14**(5), 553–56. (in Chinese)

Mo Ruping and D. M. Straus, 2002: Statistical-dynamical seasonal prediction based on principal component regression of GCM ensemble integrations. *Mon. Wea. Rev.*, **130**, 2167–2187.

Qiu Chongjian and Chou Jifan, 1989: An analogue dynamical method of weather forecasting. *Chinese J. Atmos. Sci.*, **13**(1), 22–28. (in Chinese)

Ren Hongli and Chou Jifan, 2005: Analogue correction method of errors by combining both statistical and dynamical methods together. *Acta Meteor. Sinica*, **63**(6), 988–993. (in Chinese)

—— and ——, 2007: Strategy and methodology of dynamical analogue prediction. *Sci. China (Ser. D)*, **37**(8), 1101–1109. (in Chinese)

—— and ——, 2007: Study progress in prediction strategy and methodology on numerical model. *Advances in Earth Science*, **22**(4), 376–385. (in Chinese)

Sha Wanying and Guo Qiyun, 1998: Variations of summer rainfall over China in relation to the geographical locality of subtropical high ridge over West Pacific. *J. Appl. Meteor. Sci.*, **9** (Suppl.), 31–38. (in Chinese)

Sun Li, An Gang, Ding Li, et al., 2000: A climatic analysis of summer precipitation features and anomaly in Northeast China. *Acta Meteor. Sinica*, **58**(1), 70–82. (in Chinese)

—— and ——, 2003: The effect of North Pacific sea surface temperature anomaly on the summer precipitation in Northeast China. *Acta Meteor. Sinica*, **61**(3), 346–353. (in Chinese)

Thomas, A. G., 1970: Statistical-dynamical prediction. *J. Appl. Meteor.*, **8**, 333–344.

Tippett, M. K., L. Goddard, and A. G. Barnston, 2005: Statistical-dynamical seasonal forecasts of central-southwest Asian winter precipitation. *J. Climate*, **18**, 1831–1843.

Wang Shaowu, 2001: *Progress in Climatologically Studies*. China Meteorological Press, Beijing, 306–311. (in Chinese)

Wu Bingyi, Zhang Renhe, and D'Arrigo Rosanne, 2008: Arctic dipole anomalies and summer rainfall in Northeast China. *Chinese Sci. Bull.*, **53**(12), 1422–1428. (in Chinese)

Zhai Panmao and Zhou Qinfang, 1997: The change of Northern Hemisphere snow cover and its impact on summer rainfalls in China. *J. Appl. Meteor. Sci.*, **8**(2), 230–235. (in Chinese)

Zheng Qinglin and Du Xingyuan, 1973: A new numerical weather prediction model utilizing multiple-instant observation. *Sci. China (Ser. A)*, **3**, 289–297. (in Chinese)

Zheng Zhihai, Ren Hongli, and Huang Jianping, 2009: Analogue correction of errors based on seasonal climatic predictable components and numerical experiments. *Acta Physica Sinica*, **58**(10), 7359–7367. (in Chinese)

Zhu Kezhen, 1934: Southeast monsoon and rainfall in China. *Acta Geographica Sinica*, **1**(1), 1–27. (in Chinese)



© 1994-2011 China Academic Journal Electronic Publishing House. All rights reserved. http://www.cnki.net

Hydrol. Earth Syst. Sci., 15, 333–344, 2011
www.hydrol-earth-syst-sci.net/15/333/2011/
doi:10.5194/hess-15-333-2011
© Author(s) 2011. CC Attribution 3.0 License.

Hydrology and Earth System Sciences

# Quantifying uncertainty in the impacts of climate change on river discharge in sub-catchments of the Yangtze and Yellow River Basins, China

**H. Xu[1], R. G. Taylor[2], and Y. Xu[3]**

[1]National Climate Center, Laboratory for Climate Studies of China Meteorological Administration, Beijing, 100081, China
[2]Department of Geography, University College London, Gower Street, London, WC1E 6BT, UK
[3]State Key Laboratory of Urban and Regional Ecology, Research Center for Eco-Environmental Sciences, Chinese Academy of Sciences, Beijing, 100085, China

Received: 20 August 2010 – Published in Hydrol. Earth Syst. Sci. Discuss.: 8 September 2010
Revised: 13 January 2011 – Accepted: 13 January 2011 – Published: 26 January 2011

**Abstract.** Quantitative evaluations of the impacts of climate change on water resources are primarily constrained by uncertainty in climate projections from GCMs. In this study we assess uncertainty in the impacts of climate change on river discharge in two catchments of the Yangtze and Yellow River Basins that feature contrasting climate regimes (humid and semi-arid). Specifically we quantify uncertainty associated with GCM structure from a subset of CMIP3 AR4 GCMs (HadCM3, HadGEM1, CCSM3.0, IPSL, ECHAM5, CSIRO, CGCM3.1), SRES emissions scenarios (A1B, A2, B1, B2) and prescribed increases in global mean air temperature (1 °C to 6 °C). Climate projections, applied to semi-distributed hydrological models (SWAT 2005) in both catchments, indicate trends toward warmer and wetter conditions. For prescribed warming scenarios of 1 °C to 6 °C, linear increases in mean annual river discharge, relative to baseline (1961–1990), for the River Xiangxi and River Huangfuchuan are +9% and 11% per +1 °C respectively. Intra-annual changes include increases in flood (Q05) discharges for both rivers as well as a shift in the timing of flood discharges from summer to autumn and a rise (24 to 93%) in dry season (Q95) discharge for the River Xiangxi. Differences in projections of mean annual river discharge between SRES emission scenarios using HadCM3 are comparatively minor for the River Xiangxi (13 to 17% rise from baseline) but substantial (73 to 121%) for the River Huangfuchuan. With one minor exception of a slight (−2%) decrease in river discharge projected using HadGEM1 for the River Xiangxi, mean annual river discharge is projected to increase in both catchments under both the SRES A1B emission scenario and 2° rise in global mean air temperature using all AR4 GCMs on the CMIP3 subset. For the River Xiangxi, there is substantial uncertainty associated with GCM structure in the magnitude of the rise in flood (Q05) discharges (−1 to 41% under SRES A1B and −3 to 41% under 2° global warming) and dry season (Q95) discharges (2 to 55% under SRES A1B and 2 to 39% under 2° global warming). For the River Huangfuchuan, all GCMs project a rise in the Q05 flow but there is substantial uncertainty in the magnitude of this rise (7 to 70% under SRES A1B and 2 to 57% under 2° global warming). Differences in the projected hydrological changes are associated with GCM structure in both catchments exceed uncertainty in emission scenarios. Critically, estimated uncertainty in projections of mean annual flows is less than that calculated for extreme (Q05, Q95) flows. The common approach of reporting of climate change impacts on river in terms of mean annual flows masks the magnitude of uncertainty in flows that are of most importance to water management.

*Correspondence to:* H. Xu
(xuhm@cma.gov.cn)

## 1 Introduction

Global warming induced by rising concentrations of greenhouse gases is changing global climate patterns (Bates et al., 2008). Warming of the atmosphere observed over several decades is associated with the changes in hydrological systems globally and at the basin scale. These changes include: precipitation patterns and extremes; the amount and generation of river flow; the frequency and intensity of flood and drought; and, by extension, the quantity and quality of

freshwater resources (Xu and Singh, 2004; Juen et al., 2007). The magnitude and spatial distribution of changes in climate combined with characteristics of specific basins determine which impacts are the most important at a regional scale (Menzel, 2002; Matondo et al., 2004; Wilby et al., 2006; Hagg et al., 2007).

China has experienced changes in climate that include rising air temperatures and more variable precipitation. Such changes have been linked to an increased occurrence of flood events in southern China and more frequent droughts in northern China (Wang et al., 2005). The most important and direct impact of climate change is changes to the availability of water resources. Previous research indicates that the discharge of large rivers in China has decreased since 1950 along with more frequent drought and flood events (Zhang et al., 2007; Wang et al., 2008).

The Yangtze River and Yellow River are historically, culturally, and economically of critical importance to Southern and Northern China. The Yangtze River is 6300 km long and has a basin area 1.8 million $km^2$ which primarily experiences a subtropical, monsoon climate. The Yellow River is 5464 km long and has a basin area of 0.8 million $km^2$, that mainly comprises arid and semi-arid environments. The contrasting climates and landscapes of these basins give rise to very different hydrological regimes. The inter-comparison of responses in both basins to climate change is, therefore, expected to be indicative of many regions in China.

Mean annual precipitation in the Yangtze River basin is about 1070 mm and mean annual river discharge is $\sim$976 $km^3$, equivalent to a specific discharge of 542 mm. Annual per capita water availability decreased from 2700 $m^3$ in 1980 to 2100 $m^3$ in 2005. Previous studies (Zhang et al., 2006, 2008; Jiang et al., 2007) show that there has not been a significant change in annual precipitation but an increase in the number of extreme (10th percentile) precipitation events is observed (Su et al., 2008). Greater variability in precipitation has intensified floods and prolonged droughts. Spatial and seasonal changes in precipitation have also been observed. Increased precipitation has been detected in middle and lower reaches of the Yangtze River in summer whereas a decrease in precipitation is observed in the upper reaches of the basin near the Three Gorges Dam site in autumn (Xu et al., 2008). Although no significant trend was detected for annual runoff in the Yangtze River basin during 1961–2000, a significant positive trend in flood discharges was found in the middle and lower basin over the same period.

Mean annual precipitation in the Yellow River is 470 mm and mean annual river discharge is $\sim$58 $km^3$, equivalent to a specific discharge of 73 mm. The basin can be classified as water scarce as this river discharge represents annual per capita water availability of less than 1000 $m^3$ (Pereira et al., 2007). Previous studies (Fu et al., 2004; Liu et al., 2008; Huang et al., 2009) indicate trends toward higher air temperatures in the Yellow River basin during the past 50 years. Fu et al. (2004) find no significant trend in annual precipitation from 1951 to 1998 whereas others (Xu and Zhang, 2006; Liu et al., 2008; Huang et al., 2009) indicate precipitation has decreased over slightly different time periods (1961–2006, 1957–2006, and 1951–2000). Declines are especially apparent in spring, summer and autumn as well as preferentially in the southeastern part of the basin. These decreases are calculated after allowing for human uses (Fu et al., 2004; Wang et al., 2006). Applying climate projections generated from four GCMs (HadCM3, CGCM2, CCSR and CSIRO) for one emission scenario (SRES B2), Xu et al. (2009) estimate a reduction mean annual streamflow over the period 2010 to 2099 in a headwater catchment of the Yellow River Basin.

Current understanding of impacts of climate change on water resources is complicated by uncertainty in both climate projections and the simulation of hydrological responses to climate perturbations (Prudhomme et al., 2003; Treut et al., 2008; Minvill et al., 2008). The main objective of this study is to quantify uncertainty in climate change impacts on river discharge, in two sub-catchments of the Yangtze and Yellow River basins under contrasting climate regimes (semi-arid, humid). The hydrological model used here is Soil and Water Assessment Tool (SWAT) model, which is a physically based semi-distributed hydrological model that operates on a daily time step. Baseline climate that derives from detrended monthly CRU TS3.0 datasets (Mitchell and Jones, 2005) for the period during 1961–2005, were used for calibrating and validating the SWAT model. We quantify uncertainty in projections of climate change on river discharge by applying a range of climate scenarios using different GCMs (subset of IPCC AR4 GCMs), emission scenarios (SRES A1B A2, B1, B2) and prescribed increases in global mean air temperature (1 to 6 °C), including the 2 °C threshold of 'dangerous' climate change (Todd et al., 2010). Daily climate datasets used to drive SWAT model were generated by a weather generator (Arnell, 2003).

## 2 Study area and datasets

### 2.1 Basin description

The River Xiangxi and River Huangfuchuan were selected as meso-scale catchments representative of the humid and semi-arid climates that predominate across the Yangtze and Yellow River basins, respectively. The River Xiangxi is one of the longest tributaries supplying the Three Gorges Reservoir (TGR) in Hubei Province. Eutrophication in the River Xiangxi strongly influences water quality in the TGR. The River Huangfuchuan is responsible for substantial soil erosion with annual sediment yields of $\sim$50 million tonnes to Yellow River. The location of the two sub-catchments is shown in Fig. 1; physical characteristics of both are given in Table 1. The River Xiangxi is 94 km long and originates in the Shennongjia forest region with a catchment area of 3099 $km^2$. The River Huangfuchuan is 137 km long

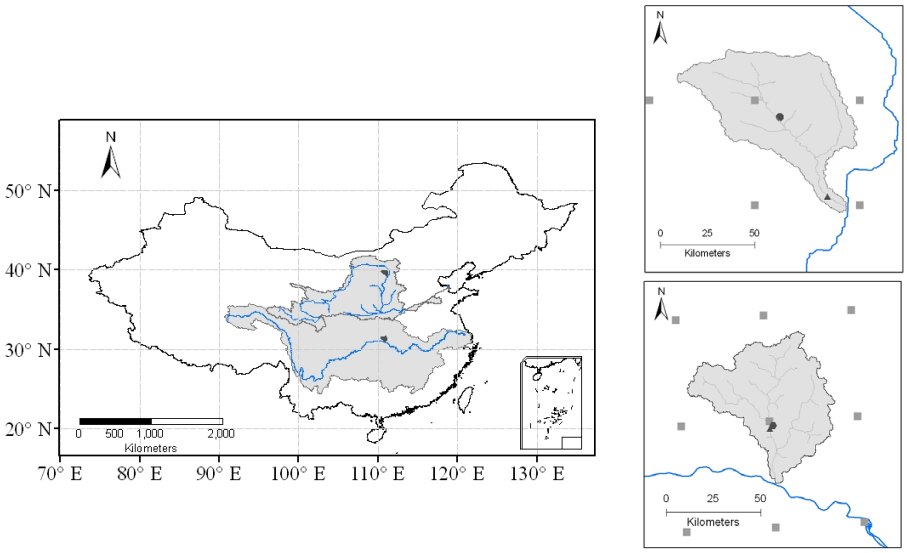


**Fig. 1.** Location of selected sub-catchments in the Yangtze and Yellow River Basins and climate stations (black circle), discharge stations (black triangle), and Climate Research Unit (CRU) grid nodes (grey square).

**Table 1.** Characteristics of the study catchments.

| | Huangfuchuan | Xiangxi |
|---|---|---|
| *Location* | | |
| River system | Yellow River | Yangtze River |
| Latitude | 39.2° ∼ 39.9° N | 31.0° ∼ 31.7° N |
| Longitude | 110.3° ∼ 111.2° E | 110.5° ∼ 111.1° E |
| *Topography* | | |
| Elevation range (m) | 836–1458 | 100–3072 |
| Catchment size ($km^2$) | 3246 | 3099 |
| *Climate* | | |
| Climate region | Semi-arid | humid |
| Mean annual precipitation (mm) | 388 | 1100 |
| Mean annual temperature (°) | 7.5 | 15.6 |
| *Runoff* | | |
| Annual mean (mm) | 53 | 688 |

that encompasses the transition from the Erdos Desert to the Loess Plateau with a catchment area of 3246 $km^2$.

The River Xiangxi catchment lies in the subtropical region and experiences a humid climate near the Three Gorges Dam. Mean annual precipitation observed from 1961 to 2004 is 1100 mm and is characterised by a dry winter and a summer monsoon from May to September. Mean annual air temperature from 1961 to 2004 is 15.6 °C and ranges from 12 °C to 20 °C. The River Xiangxi catchment is typical of northern sub-tropic landscapes with high relief. Mountainous areas are covered by forests. The main agricultural crops (rice, wheat) are grown in valleys. Terraced fields are often used for corn, potatoes and tea. Limestone soils predominate in headwater areas whereas brown and yellow-brown soils occur in the lowlands. The shallow soils with low humus content promote erosion and transport of particle-bound *P* as well as leaching of soluble N-fractions by interflow and surface runoff. To prevent soil erosion, terraces and mulching are practised but substantial nutrient fluxes to the river contribute to eutrophication.

The River Huangfuchuan has a semiarid climate and features pastoral farming in Northern China. Mean, annual precipitation observed from 1961 to 2000 is 388 mm. Mean annual air temperature from 1961 to 2000 is 7.5 °C and ranges from 6.9 °C and 9.7 °C. The River Huangfuchuan is representative of the "hill-gully" landscape of the northern Loess Plateau. The watershed is mainly covered by grassland or bush land with fragmentary woodland. The main agricultural crops, maize and millet, are grown in the sloping cultivated land. The soils are subject to considerable water and wind erosion. The River Huangfuchuan which has experienced soil erosion and land desertification, is considered to be comparatively vulnerable to climate change.

## 2.2 Available data

Spatial data used in the study include a digital elevation model (DEM), land use, soil type, and climatic data. A digital elevation model with a scale of 1: 250 000 was prepared by the China Fundamental Geographic Information Center. Spatial soil data with a scale of 1:1 000 000 derive from Environment and Ecology Scientific Data Center of western China, National Natural Science Foundation of China. Soil properties were generated from the Soil Attribute Data Set which based on "Soil Species of China" and other sources with total information includes 7300 soil profiles collected

**Table 2.** Mean and stand deviation (SD) of the posterior distribution resulting from application of the ParaSol technique.

| Parameters | Canmx | Esco | Ch_K2 | Surglag | CN2 | Biomix | Alpha_BF |
|---|---|---|---|---|---|---|---|
| Mean | 0.46 | 0.83 | 141.77 | 4.24 | 43.71 | 0.11 | 0.89 |
| SD | 0.60 | 0.19 | 8.49 | 1.98 | 8.02 | 0.14 | 0.09 |

For description of the parameters see Xu et al. (2010).

from all over China. Land use is an important input parameter to SWAT as it influences runoff generation (Wu and Johnston, 2007). There is, however, limited land-use data for both catchments. Modelling of baseline and projected river discharge consequently do not consider changes in land-use and it as acknowledged that some disparities between simulated and observed discharge may be attributable to land-use change during the simulation period. The most recent land-use maps for the River Xiangxi compiled by the Hubei Land Management Bureau in the 1990s, were used to represent catchment land use. In the River Huangfuchuan, natural vegetative cover of grassland and woodland was converted to farmland from the 1950s to 1970s; restoration of artifical grassland and bush land has occurred since the late 1990s. Land-use records from the Inner Mongolia Autonomous Region Department of Land and Resource in the 1980s were used to represent catchment land use.

Monthly streamflow records for the Xiangshan gauging station of River Xiangxi and Huangfu gauging station of River Huangfuchuan were obtained from Water Year Books and are available for periods 1961–1994 and 1954–1997 respectively. Climate data used in this study during 1961–2005 are gridded ($0.5° \times 0.5°$) CRU TS3.0 monthly datasets (Mitchell and Jones, 2005), which included monthly precipitation total and monthly average as well as maximum and minimum air temperatures.

## 3 Methodology

### 3.1 Hydrological model: SWAT

The Soil and Water Assessment Tool (SWAT) model is a physically based, semi-distributed, basin scale, continuous-time hydrological model that operates on a daily time step. In SWAT, basins are divided into multiple subwatersheds which are further subdivided into hydrologic response units (HRUs) that consist of homogeneous land use, management, and soil characteristics. The overall hydrological balance is simulated for each HRU including precipitation, irrigation water, infiltration, soil water redistribution, evapotranspiration, lateral subsurface flow, and return flow (Gassman et al., 2007). Applications of SWAT occur worldwide and include direct assessments of anthropogenic, climate change and other influences on a wide range of water resources. In China, SWAT has been used to simulate river discharge and sediment transport in sub-catchments of the Yellow River such as the Lushi and Heihe rivers for sediment simulation (Hao et al., 2004; Cheng et al., 2007), and in sub-catchments of Yangtze River such as Poyang Lake and small watershed in the TGR area for streamflow and soil erosion simulation (Guo et al., 2008; Shen et al., 2009).

### 3.2 Calibration and validation of hydrological model

Model parameterization was specified using the Arcview GIS interface for SWAT. The Xiangxi and Huangfuchuan catchments were divided respectively into 10 and 13 subwatersheds based on the DEM and the location of river gauging stations. After considering land use and soil characteristics, the River Xiangxi catchment was divided into 195 HRUs and River Huangfuchuan was divided into 314 HRUs. Potential evapotranspiration was calculated using the Hargreaves function (Hargreaves et al., 1985); surface runoff was estimated by a modification of the SCS curve number method (USDA-NRCS, 2004), and routing processes were estimated by the Muskingum method (Neitsch et al., 2005).

The employed SWAT model had recently been calibrated and validated for the River Xiangxi using monthly river discharge observations for the periods 1970–1974 and 1976–1986 (Xu et al., 2010). The ParaSol autocalibration routine (van Griensven and Meixner, 2007) embedded in AVSWAT2005 was used to improve the fit between simulated and observed discharge and to assess parameter uncertainty. Autocalibration considered the seven most sensitive parameters in the hydrological model. Summary statistics are reported in Table 2. Each parameter solutions shows very similarly good values of the Nash-Sutcliffe efficiency ($E_{ns}$) (not shown) and small standard deviations of the estimated model parameters (Table 2). In this study, the SWAT models were re-calibrated for 1961–1990 baseline period using monthly river discharge from Xiangshan gauging station of River Xiangxi and Huangfu gauging station of River Huangfuchuan, and validated with recent monthly river discharge data (1991–1994 Xiangxi; 1991–1997 Huangfuchuan). The performance of the SWAT2005 model was evaluated using statistical analyses to compare the quality and reliability of the predicted discharge with observed records. Summary statistics included the mean discharge ($Q$), coefficient of determination ($R^2$), and Nash-Sutcliffe efficiency ($E_{ns}$). The

**Table 3.** Goodness of fit for SWAT simulations in River Xiangxi and River Huangfuchuan ($Q_{obs}$and $Q_{sim}$ are observed and simulated mean monthly discharge in $m^3\,s^{-1}$).

| | Huangfuchuan | | | | Xiangxi | | | |
|---|---|---|---|---|---|---|---|---|
| | $Q_{obs}$ | $Q_{sim}$ | $E_{ns}$ | $R^2$ | $Q_{obs}$ | $Q_{sim}$ | $E_{ns}$ | $R^2$ |
| Calibration | 3.2 | 4.4 | 0.64 | 0.61 | 34.1 | 32.2 | 0.43 | 0.44 |
| Validation | 4.8 | 5.1 | 0.66 | 0.66 | 40.1 | 37.1 | 0.56 | 0.57 |

observed and modelled flow duration curve and monthly discharge for the 1961–1994 period for River Xiangxi and 1961–1997 period for River Huangfuchuan are presented in Fig. 2. The calibrated SWAT model was used in the climate scenarios modeling for the two sub-catchments.

Model performance over the calibration and validation periods is generally acceptable, with efficiencies ranging from 0.61 to 0.66 for River Huangfuchuan and 0.43 to 0.56 for River Xiangxi (Table 3). The performance statics $E_{ns}$ and $R^2$ are poorest for River Xiangxi in the calibration period with 0.43 and 0.44 respectively. Simulated mean monthly river discharge is overestimated (37% and 6%) for the River Huangfuchuan and underestimated (6% and 7%) for the River Xiangxi over both calibration and validation periods. The frequency distributions of simulated river discharge in both sub-catchments closely approximates those of the observed discharge records as indicated by flow duration curves. Peak flows of the River Xiangxi are very slightly underestimated (Fig. 2a and b). The model is capable of reproducing the observed flow for River Xiangxi (1961–1994) and Huangfuchuan (1961–1997) as showed in Fig. 2c and d.

### 3.3 Climate change scenarios

The generally good performance over the calibration and validation periods, suggest that the model can be used to simulate the impact of climate change scenarios. In addition to assessing projected changes in mean annual river discharge, we also changes in high and low monthly runoff, expressed as Q05 and Q95 respectively, where for example, Q05 is the runoff exceeded only 5% of the time.

Climate projections for temperature and precipitation were generated using the ClimGen pattern-scaling technique described in Osborn (2009) and Todd et al. (2010). Scenarios were generated for (1) greenhouse-gas emission scenarios (A1B, A2, B1, B2) and (2) prescribed increases in global mean temperature of 1, 2, 3, 4, 5, and °C using the UKMO HadCM3 GCM as well as (3) A1B emission scenario and prescribed warming of 2 °C ("dangerous" climate change) using six additional GCMs from the World Climate Research Programme (WCRP) Coupled Model Intercomparison Project phase 3 (CMIP3) multi-model dataset: CCCMA CGCM3.1, CSIRO Mk30, IPSL CM4, MPI ECHAM5, NCAR CCSM3.0, and UKMO HadGEM1.

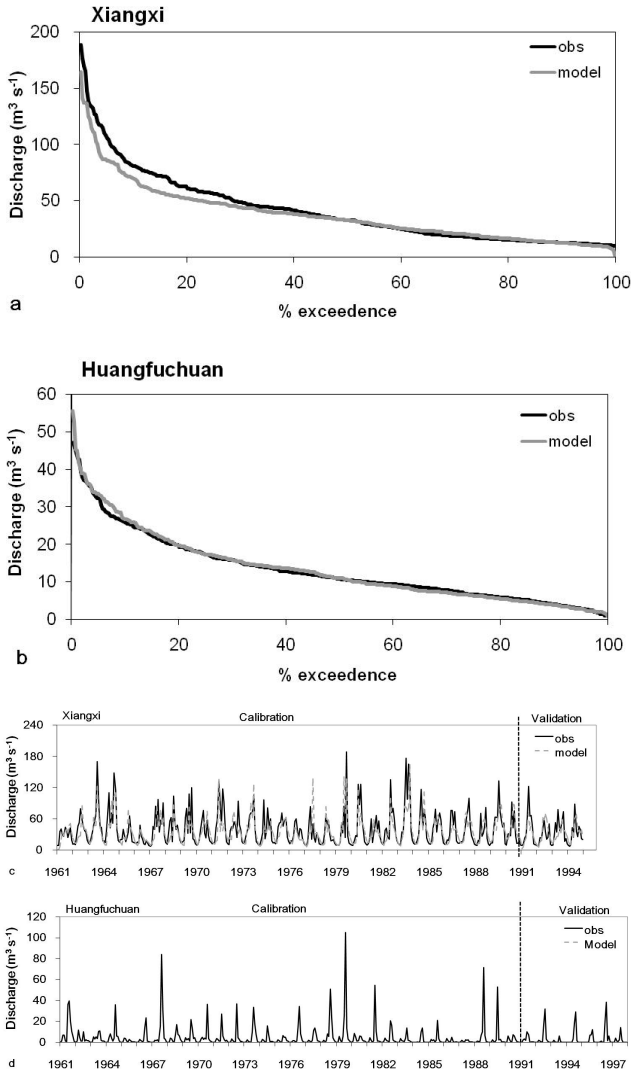


**Fig. 2.** Observed and simulated river discharge in River Xiangxi – 1961–1994, **(a)** flow duration curve; **(c)** monthly discharge – and River Huangfuchuan for 1961–1997, **(b)** flow duration curve, **(d)** monthly discharge.

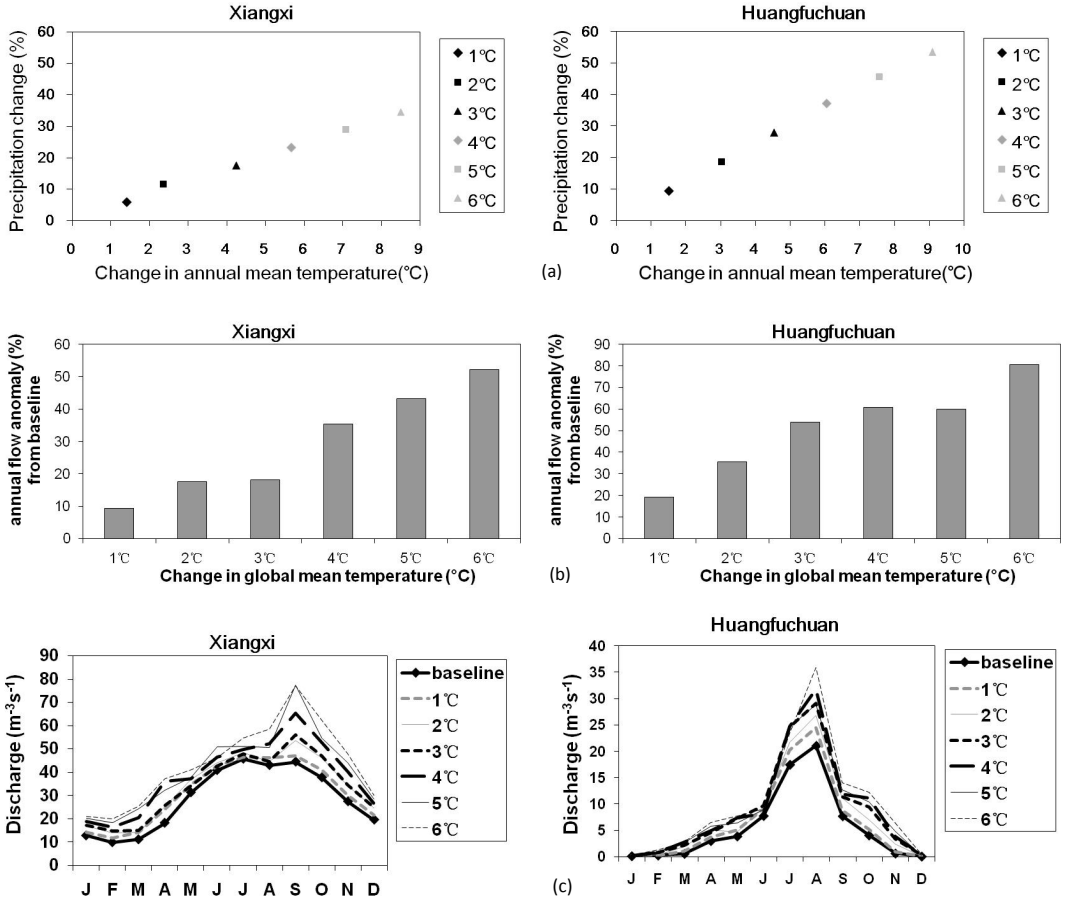


**Fig. 3. (a)** Projected changes in annual mean temperature (°) and annual precipitation (%), **(b)** annual and **(c)** monthly discharge for HadCM3 prescribed warming scenarios.

## 4 Results

### 4.1 Uncertainty in the magnitude of prescribed increases in global mean air temperature

Figure 3a indicates that for the chosen sub-basins precipitation is projected by HadCM3 to increase at a near-linear rate with a rise in global mean air temperature of 1 °C to 6 °C. Annual precipitation is projected to increase, relative to baseline, by 6% to 35% for the River Xiangxi and 9% to 53% for the River Huangfuchuan. Along with linear increases in precipitation, preferential increases in air temperature relative to global mean are also projected (e.g. 8.5 °C in River Xiangxi and 9.1 °C in River Huangfuchuan for a 6 °C rise in global mean air temperature (Fig. 3a).

Mean annual river discharge is estimated to increase in both the Xiangxi and Huangfuchuan catchments under prescribed increases in global mean air temperature projected by HadCM3 (Fig. 3b). Increases in mean annual river discharge with rising air temperatures are, however, non-linear (Fig. 3b). Under rises of 1 °C to 3 °C, the trend in rising river discharge for the River Xiangxi is lower than that estimated for warming of 4 °C to 6 °C; the reverse is observed for the River Huangfuchuan. Substantial changes in intra-annual river discharge are associated with the non-linear response in annual river discharge to increasing global mean air temperature (Fig. 3c). Monthly flow is projected to increase in all months and there is a shift in flood season (high flows) from summer to autumn for the River Xiangxi. The low (Q95) flow increases dramatically (24% to 93%) for the River Xiangxi and the high (Q05) flow increases substantially (13% to 64%) but in a non-linear fashion for the River Huangfuchuan.

### 4.2 Uncertainty associated with different SRES emissions scenarios

Figure 4a shows the changes in mean climate projected by HadCM3 for each of the four SRES scenarios (A1B, B1, B2, A2) in both study catchments. Increases in mean annual temperature range from 2.5° to 3.4° for the River Xiangxi and from 2.7° to 3.6° for the River Huangfuchuan. The highest increases occur under the A1B emission scenario for both basins. Projected precipitation increases by ∼10% with little variance between emission scenarios for the River Xiangxi.

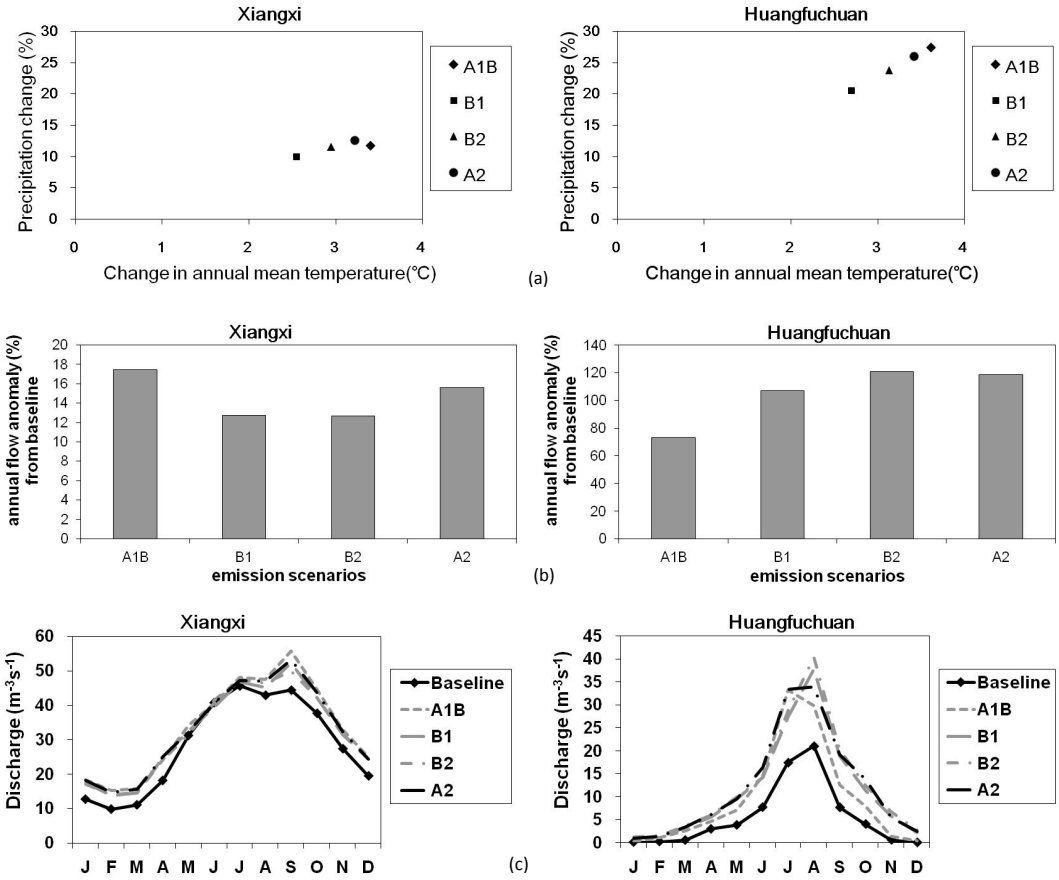


**Fig. 4. (a)** Projected changes in annual mean temperature (°) and annual precipitation (%), **(b)** annual and **(c)** monthly discharge for HadCM3 different emission scenarios.

For the River Huangfuchuan, precipitation is projected to increases by 20 to 28% relative to baseline with slightly greater differences between the four emission scenarios. These projected changes in climate give rise to substantially different increases in river discharge (Fig. 4b). The magnitude of changes for annual discharge varies from 13 to 17% for the River Xiangxi and from 73 to 121% for the River Huangfuchuan. The projected monthly discharge for River Huangfuchuan under different SRES emission scenarios increases throughout the year (Fig. 4c). There is only minor uncertainty in the magnitude for the rise in the Q05 flow (10 to 17%) and the Q95 flow (45 to 55%) for the River Xiangxi whereas high (Q05) flows increase considerably (70 to 90%) for the River Huangfuchuan.

### 4.3 Uncertainty in GCM structure for SRES A1B emission scenario

Figure 5a shows the projected changes in climate under the A1B emission scenario for the priority subset of seven AR4 GCMs. The projected annual mean temperature increases for all GCMs under SRES A1B but ranges from approximately 2° (CSIRO, HadGEM1 and CCSM3.0 GCM) to 3.4° (HadCM3, IPSL and ECHAM5 GCM) for the River Xiangxi and from ∼2.2° (CSIRO and CCSM3.0 GCM) to 3.8° (HadCM3 and ECHAM5 GCM) for the River Huangfuchuan. Projected changes in mean annual precipitation for the River Xiangxi are minor ($< \pm 2\%$ from baseline) for three GCMs (CCSM3.0, CSIRO, ECHAM5) but show moderate increases of 7 to 12% for four GCMs (HadCM3, CGCM31, HadGEM1, IPSL). Projected changes in mean annual precipitation for the River Huangfuchuan are minor ($< 5\%$ from baseline) for two GCMs (CSIRO, ECHAM5), moderate (12 to 17% from baseline) for four GCMs (CCSM3.0, HadGEM1, CGCM3.1, IPSL) and substantial (27%) for HadCM3. In contrast, there is considerably less variation in projected increases in annual mean temperature for both basins. Projected changes in precipitation between basins reveal large differences. For example, the CCSM3.0 GCM projects a decrease in precipitation of −2% for River Xiangxi and an increase in precipitation of +17% for the River Huangfuchuan. Indeed, this trend is robust as all GCMs project greater increases in precipitation for the River Huangfuchuan than the River Xiangxi.

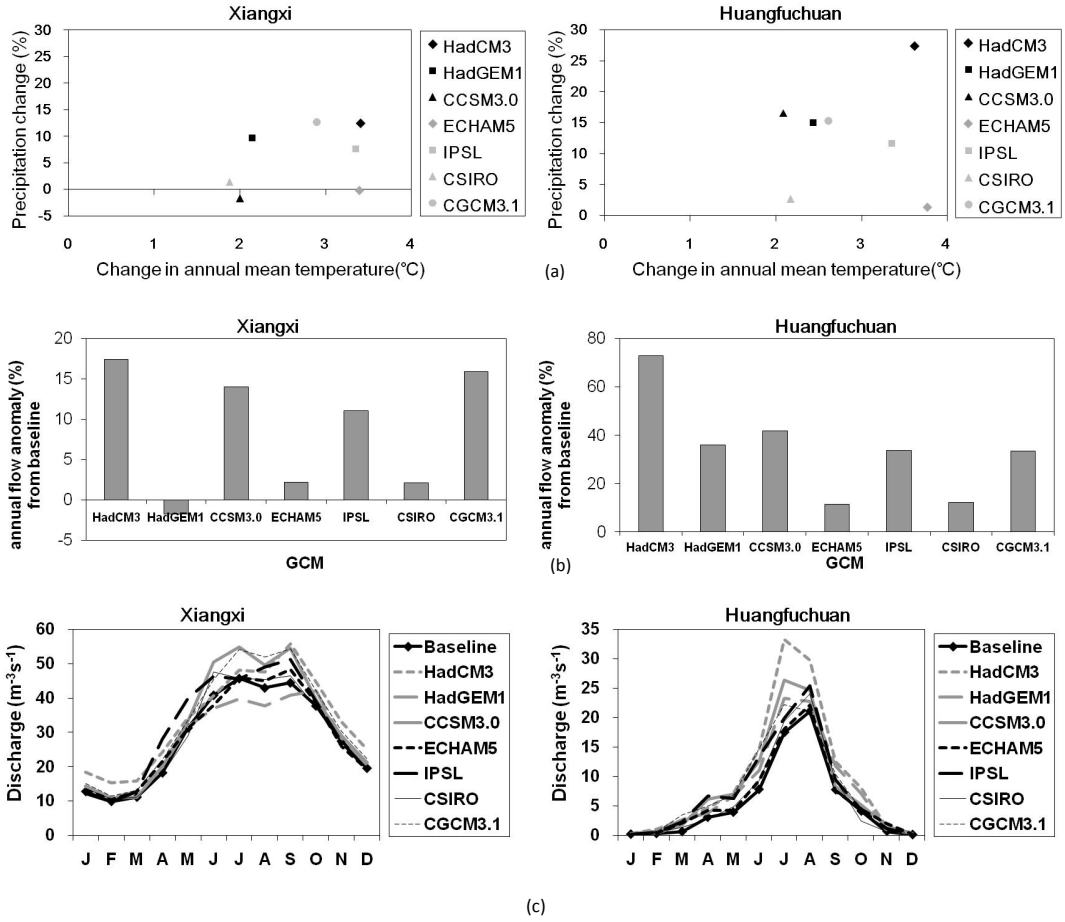


**Fig. 5. (a)** Projected changes in annual mean temperature (°) and annual precipitation (%), **(b)** annual and **(c)** monthly discharge under SRES A1B across 7 GCMs.

Following precipitation projections, hydrological modelling shows a consistent increase in river discharge for the two sub-basins though with substantial disparities between GCMs. HadGEM1 is the only GCM to project a decrease in annual mean discharge (Fig. 5b). For the River Xiangxi, the ensemble mean (of GCMs) is an increase of 9% in mean annual river discharge; HadGEM1 projects a decrease of −2% in annual discharge whereas the other GCMs project increases ranging from 2 to 17%. For the River Huangfuchuan, the ensemble mean is an increase of 34% in mean annual river discharge; HadCM3 projects the largest increase in mean annual discharge (73%) whereas the other GCMs project increases ranging from 11 to 42%.

Relative to projected changes in mean annual river discharge, there is less consistency in projections of intra-annual river discharge in both catchments (Fig. 5c). For the River Xiangxi, all GCMs project a rise in the low (Q95) flow but they range from 2 to 55%. There is also a near-uniform rise (HadGEM1 excepted) in projections of high (Q05) flows but there is substantial uncertainty in the magnitude of these rises for the River Xiangxi (−1 to 41%) and River Huangfuchuan (7 to 70%).

### 4.4 Uncertainty in GCM structure for 2° rise in global mean air temperature

Uncertainty in projected changes in climate under a 2° rise in global mean air temperature associated with the priority subset of AR4 GCMs is shown in Fig. 6a. Preferential increases in mean, annual temperature are evident in both the River Xiangxi and River Huangfuchuan. The rise ranges from 2.2° for the HadGEM1 GCM to 2.8° for the IPSL GCM in River Xiangxi. For the River Huangfuchuan, the rise ranges from 2.3° for CGCM31 GCM to 3.0° for HadCM3 GCM. Differences between GCMs in projections of mean annual precipitation are greater than that for temperature. Projected changes in mean annual precipitation, relative to baseline, vary from a −2% decrease for HadGEM1 to a 12% increase for HadCM3 in River Xiangxi and from a 1 to 19% increases for ECHAM5 and CCSM3.0 GCMs respectively for the River Huangfuchuan.

An increase in mean annual river discharge in both basins under a 2 °C rise in global mean air temperature is a robust projection using all GCMs (Fig. 6b) except HadGEM1 (slight decrease). For the River Xiangxi, the ensemble mean

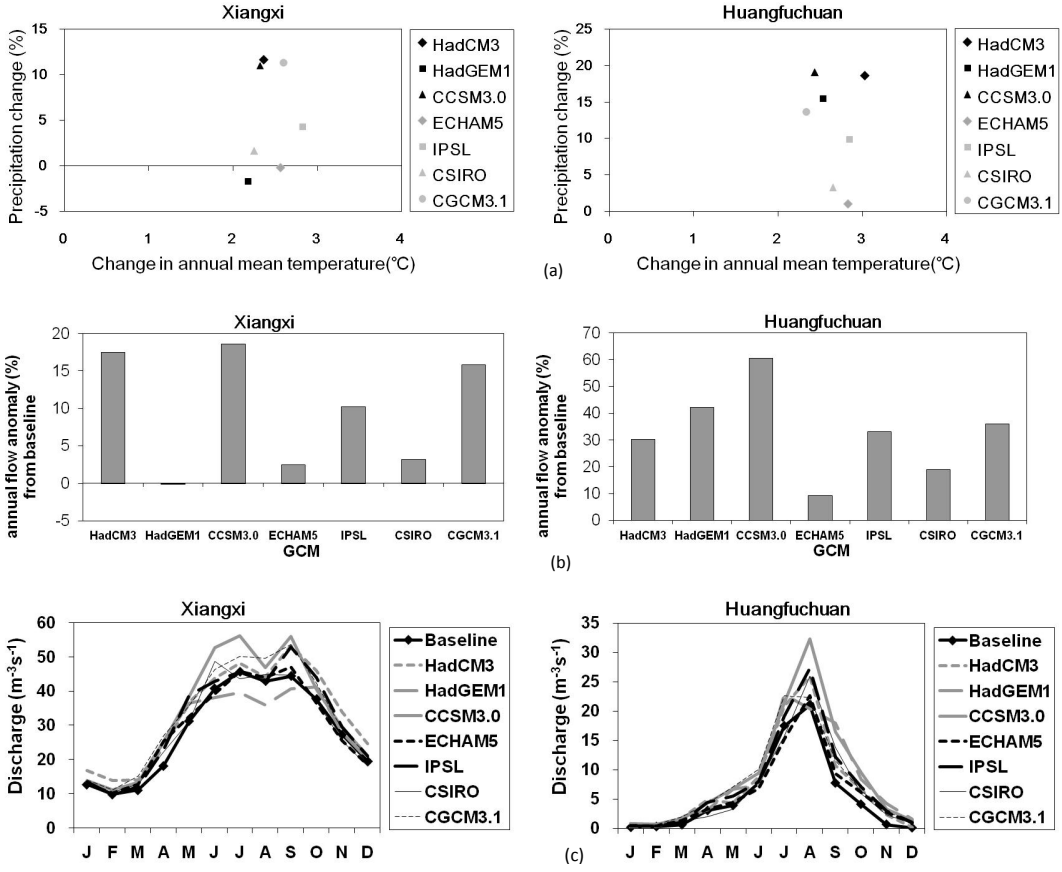


**Fig. 6. (a)** Projected changes in annual mean temperature (°) and annual precipitation (%), **(b)** annual and **(c)** monthly discharge under 2° warming scenarios across 7 GCMs.

projection (of GCMs) is an increase in mean annual discharge of 10% relative to baseline and ranges from 2.5% for ECHAM5 to 19% for CCSM3.0. For the River Huangfuchuan, the ensemble mean projection is a 33% increase in mean annual river discharge which ranges from 9% for ECHAM5 to 60% for CCSM3.0. Projected intra-annual (seasonal) changes in river discharge for the River Huangfuchuan indicate an earlier (July) peak flow relative to baseline (August) for CGCM31 and HadCM3 and an increase in peak discharges in July for the other GCMs (Fig. 6c). All GCMs project a rise in the Q05 flow but there is uncertainty in the magnitude of this rise (2 to 57%) for River Huangfuchuan. For the River Xiangxi, all GCMs with one exception (HadGEM1) project a rise in the Q05 flow (Fig. 6c); uncertainty ranges from −3 to 41%. Uncertainty in the magnitude of the rise in the Q95 flow ranges from 2 to 39%.

## 5 Discussion

The assessment of the impacts of climate change on river discharge in a humid subtropical sub-basin of the Yangtze River and a semi-arid temperate sub-basin of the Yellow River reveals near-uniformity in projections of greater mean annual river discharge. There is, however, substantial uncertainty in the magnitude of projected increases in river discharge that is primarily associated with GCM structure, magnitude of global warming, and emission scenarios. The greatest uncertainty in the projected changes in river discharge stems from the choice of GCM from the priority subset of seven AR4 GCMs. With the exception of projections of a slight (−2%) decrease in river discharge from HadGEM1, mean annual river discharge increases under both the SRES A1B emission scenario and 2° rise in global mean air temperature irrespective of the applied GCM. This finding is unique among the catchments examined on five continents reported in this special issue (Arnell, 2010; Hughes et al., 2010; Kingston and Taylor, 2010; Kingston et al., 2010; Nobrega et al., 2010; Singh et al., 2010; Thorne, 2010). Differences in hydrological projections between the SRES emission scenarios projected by HadCM3 are comparatively minor (13 to 17% increase relative to baseline) for the River Xiangxi but substantial for the River Huangfuchuan (73 to 121% increase relative to baseline). The differences result primarily from differences in projections of precipitation in both basins.

Warmer and wetter scenarios for the River Huangfuchuan are projected to increase river discharge substantially which, if properly managed, could serve to alleviate current water scarcity. The projected increase in peak flows (Q05) in the River Huangfuchuan serves to exacerbate soil erosion. The general increase in peak flow (Q05) and low flow (Q95) in River Xiangxi is expected to increase the fluxes of non-point source pollution and sediment to river channel by runoff. Increased river discharge could serve to dilute point-source pollution and increase the likelihood that environmental flows are realized (Shao et al., 2008; Li et al., 2009). Increasing river discharge has important implications for the management of water resources in both catchments. Increases in mean flow expand available water resources but the rise in peak flows (Q05) in both basins will increase flood frequency and flood risk. Adaption measures need to consider projected changes in both mean and extreme (Q05, Q95) flows and uncertainties therein.

## 6 Conclusions

Uncertainty in the impact of climate change on river discharge in two representative catchments in the Yangtze River (Xiangxi) and the Yellow River (Huangfuchuan) basins associated with GCM structure, emissions scenarios and prescribed increases in global mean temperature has been quantified. The first notable conclusion from this work is the near-uniform consistency in the direction of the climate change signal of increased river discharge observed in both basins associated with seven CMIP3/IPCC-AR4 GCMs, four SRES emissions scenarios (A1B, A2, B1, B2), and prescribed increases of 1 °C to 6 °C in global mean air temperature. Substantially greater increases in river discharge relative to baseline are consistently projected for the semi-arid, River Huangfuchuan catchment in north China compared to the sub-tropical humid, River Xiangxi catchment in south China. There is, however, substantial uncertainty in the magnitude of projected increases in river discharge resulting from climate change. The greatest source of uncertainty in hydrological projections in both catchments is GCM structure (choice of GCMs). Our results provide an indication of the relative magnitude of uncertainty in current projections of hydrological change in sub-basins of the Yangtze River and the Yellow River, and highlight the importance of using multi-model (GCM) evaluations of climate change impacts on water resources. Although the priority subset of senven GCMs was specifically selected to represent the expected range of uncertainty in GCM projections, uncertainty would be expected to increase if a larger number of GCMs had been employed. Similar to other studies in this issue (Arnell, 2010; Kingston and Taylor, 2010; Thorne, 2010), noted differences in projections of mean river discharge and intra-annual (seasonal) flows question the representivity of using mean flows to represent hydrological change to water managers as changes in extreme flows (e.g. Q05, Q95) are far more critical.

*Acknowledgements.* This work was made possible by grants from the UK Natural Environment Research Council under the Quantifying and Understanding the Earth System (QUEST) programme (Ref. NE/E001890/1), Natural Science Foundation of China (NSFC, Ref. 40971022) and National Basic Research Program of China (973, Ref. 2010CB428401). The climate change scenarios were created with the ClimGen package, which was developed by Tim Osborn at the Climatic Research Unit (CRU) at the University of East Anglia (UEA), UK. Discussions and helpful insights of quantify uncertainties provided by participants of QUEST-GSI in study are also appreciated.

Edited by: J. Thompson

## References

Arnell, N. W.: Effects of IPCC SRES* emissions scenarios on river runoff: a global perspective, Hydrol. Earth Syst. Sci., 7, 619–641, doi:10.5194/hess-7-619-2003, 2003.

Arnell, N. W.: The relationship between climate forcing and hydrological response in UK catchments, Hydrol. Earth Syst. Sci. Discuss., 7, 7633–7667, doi:10.5194/hessd-7-7633-2010, 2010.

Bates, B. C., Kundzewicz, Z. W., Wu, S., and Palutikof, J. P.: Climate Change and Water, Technical Paper of the Intergovernmental Panel for Climate Change, IPCC Secretariat, Geneva, Switzerland, 2008.

Cheng, H., Ouyang, W., Hao, F., Ren, X., and Yang, S.: The nonpoint-source pollution in livestock-breeding areas of the Heihe River basin in Yellow River. Stoch. Environ. Res. Risk Assess., 21, 213–221, doi:10.1007/s00477-006-0057-2, 2007.

Fu, G. B., Chen, S. L., Liu, C. M., and Shepard, D.: Hydro-climatic trends of the Yellow River Basin for the last 50 years, Climatic Change, 65, 149–178, 2004.

Gassman, P. W., Reyes, M. R., Green, C. H., and Arnold, J. G.: The soil and water assessment tool: Historical development, applications and future research directions, T. ASABE, 50, 1211–1250, 2007.

Guo, H., Hu, Q., and Jiang, T.: Annual and seasonal streamflow responses to climate and land-cover changes in the Poyang Lake basin, China, J. Hydrol., 355, 106–122, 2008.

Hagg, W., Braun, L. N., Kuhn, M., and Nesgaard, T. I.: Modelling of hydrological response to climate change in glacierized central Asian catchments, J. Hydrol., 332, 40–53, 2007.

Hao, F. H., Zhang, X. S., and Yang, Z. F.: A distributed nonpoint-source pollution model: Calibration and validation in the Yellow River basin, J. Environ. Sci., 16(4), 646–650, 2004.

Hargreaves, G. L., Hargreaves, G. H., and Riley, J. P.: Agricultural benefits for Senegal River basin, J. Irrig. Drain. E.-ASCE, 108(3), 225–230, 1985.

Huang, Y., Cai, J., Yin, H., and Cai, M.: Correlation of precipitation to temperature variation in the Huanghe River (Yellow River) basin during 1957–2006, J. Hydrol., 372, 1–8, 2009.

Hughes, D. A., Kingston, D. G., and Todd, M. C.: Uncertainty in water resources availability in the Okavango River Basin as a result of climate change, Hydrol. Earth Syst. Sci. Discuss., 7, 5737–5768, doi:10.5194/hessd-7-5737-2010, 2010.

Jiang, T., Su, B., and Hartmann, H.: Temporal and spatial trends of precipitation and river flow in the Yangtze River basin, 1961–2000, Geomorphology, 85, 143–154, 2007.

Juen, I., Kaser, G., and Georges, C.: Modelling observed and future runoff from a glacierized tropical catchment (Cordillera Balanca, Peru), Global. Planet. Change, 59, 37–48, 2007.

Kingston, D. G. and Taylor, R. G.: Sources of uncertainty in climate change impacts on river discharge and groundwater in a headwater catchment of the Upper Nile Basin, Uganda, Hydrol. Earth Syst. Sci., 14, 1297–1308, doi:10.5194/hess-14-1297-2010, 2010.

Kingston, D. G., Thompson, J. R., and Kite, G.: Uncertainty in climate change projections of discharge for the Mekong River Basin, Hydrol. Earth Syst. Sci. Discuss., 7, 5991-6024, doi:10.5194/hessd-7-5991-2010, 2010.

Li, F., Cai, Q., Fu, X., and Liu, J.: Construction of habitat suitability odels (HSMs) for benthic macroinvertebrate and their applications to instream environmental flows: A case study in Xiangxi River of Three Gorges Reservoir region, China, Prog. Nat. Sci., 19, 359–367, 2009.

Liu, Q., Yang, Z., and Cui, B.: Spatial and temporal variability of annual precipitation during 1961–2006 in Yellow River Basin, China, J. Hydrol., 361, 330–338, 2008.

Matondo, J. I., Peter, G., and Msibi, K. M.: Evaluation of the impact of climate change on hydrology and water resources in Swaziland: Part II, Phys. Chem. Earth., 29, 1193–1202, 2004.

Menzel, L. and Bürger, G.: Climate change scenarios and runoff response in the mulde catchment (Southern Elbe, Germany), J. Hydrol., 267, 53–64, 2002.

Minville, M., Brissette, F., and Lecontem, R.: Uncertainty of the impact of climate change on the hydrology of a Nordic watershed, J. Hydrol., 358, 70–83, 2008.

Mitchell, T. and Jones, P.: An improved method of constructing a database of monthly climate observations and associated high-resolution grids, Int. J. Climatol., 25, 693–712, 2005.

Neitsch, S. L., Arnold, J. G., Kiniry, J. R., and Williams, J. R.: Soil and Water Assessment Tool Theoretical Documentation, Version 2005, Temple, Tex.: USDA-ARS Grassland, Soil and Water Research Laboratory, available at: swatmodel.tamu.edu/media/1292/swat2005theory.pdf, last access: 1 November 2006, 2005.

Nóbrega, M. T., Collischonn, W., Tucci, C. E. M., and Paz, A. R.: Uncertainty in climate change impacts on water resources in the Rio Grande Basin, Brazil, Hydrol. Earth Syst. Sci. Discuss., 7, 6099–6128, doi:10.5194/hessd-7-6099-2010, 2010.

Osborn, T. J.: A user guide for ClimGen: a flexible tool for generating monthly climate data sets and scenarios, Climatic Research Unit, University of East Anglia, Norwich, 17 pp., 2009.

Pereira, L. S., Goncalves, J. M., Dong, B., Mao, Z., and Fang, S. X.: Assessing basin irrigation and scheduling strategies for saving irrigation water and controlling salinity in the upper Yellow River Basin, China, Agr. Water Manage., 93, 109–122, 2007.

Prudhomme, C., Jakob, D., and Svensson, C.: Uncertanity and climate impact on flood regime of small UK catchments, J. Hydrol., 277, 1–23, 2003.

Shao, M., He, L., Han, X., Xie, Z., Li, D., and Cai, Q.: Seasonal patterns of sedimentation and their associations with benthis communities in Xiangxi Bay of the Three Gorges Reservoir, China, J. Freshwater. Ecol., 23, 151–160, 2008.

Shen, Z. Y., Gong, Y. W., Li, Y. H., Hong, Q., Xu, L., and Liu, R. M.: A comparison of WEPP and SWAT for modeling erosion of the Zhangjiachong watershed in the Three Gorges Reservoir Area, Agr. Water. Manage., 96, 1435–1442, 2009.

Singh, C. R., Thompson, J. R., French, J. R., Kingston, D. G., and Mackay, A. W.: Modelling the impact of prescribed global warming on runoff from headwater catchments of the Irrawaddy River and their implications for the water level regime of Loktak Lake, northeast India, Hydrol. Earth Syst. Sci., 14, 1745–1765, doi:10.5194/hess-14-1745-2010, 2010.

Su, B., Gemmer, M., and Jiang, T.: Spatial and temporal variation of extreme precipitation over the Yangtze River Basin, Quatern. Int., 186, 22–31, 2008.

Thorne, R.: Uncertainty in the impacts of projected climate change on the hydrology of a subarctic environment: Liard River Basin, Hydrol. Earth Syst. Sci. Discuss., 7, 3129–3157, doi:10.5194/hessd-7-3129-2010, 2010.

Todd, M. C., Taylor, R. G., Osborne, T., Kingston, D., Arnell, N. W., and Gosling, S. N.: Quantifying the impact of climate change on water resources at the basin scale on five continents a unified approach, Hydrol. Earth Syst. Sci. Discuss., 7, 7485–7519, doi:10.5194/hessd-7-7485-2010, 2010.

Treut, H. L., Gastineau, G., and Li, L.: Uncertainties attached to global and local climate changes, C. R. Geosci., 340, 584–590, 2008.

USDA – NRCS: Part 630: Hydrology, Chapter 10: Estimation of direct runoff from storm rainfall: Technical references, in: NRCS National Engineering Handbook, Washington, DC, USDA National Resources Conservation Service, available at: www.wcc.nrcs.usda.gov/hydro/hydro-techref-neh-630.html, last access: 14 February 2007, 2004.

Van Griensven, A. and Meixner, T.: A global and efficient multi-objective auto-calibration and uncertainty estimation method for water quality catchment models, J. Hydroinform., 9, 277–291, 2007.

Wang, J. X., Zhang, J. Y., Li, Y., and Zhang, S. L.: Variation trends of runoffs seasonal distribution of the six large basins in China over past 50 years (in Chinese), Adv. Water. Sci., 19(5), 656–661, 2008.

Wang, S. W., Wu, R. S., and Yang, X. Q.: Chapter 2: climate change in China, in: Climate and Environment change in China (in Chinese), edited by: Qing, D. H., Ding, Y. H., Su, J. L., and Wang, S. M., Science Press, Beijing, China, 63–103, 2005.

Wilby, R. L., Whithhead, P. G., Wade, A. J., Butterfield, D., Davis, R. J., and Watts, G.: Integrated modeling of climate change impacts on water resources and quality in a lowland catchment: River Kennet, UK, J. Hydrol., 330, 204–220, 2006.

Wu, K. and Johnston, C. A.: Hydrologic response to climatic variability in a Great Lake Watershed: A case study with the SWAT model, J. Hydrol., 337, 187–199, 2007.

Xu, C.-Y. and Singh, V. P.: Review on regional water resources assessment models under stationary and changing climate, Water. Resour. Manag., 18, 591–612, 2004.

Xu, H., Taylor, R., Kingston, D., Jiang, T., Thompson, J., and Todd, M.: Hydrological modeling of River Xiangxi using SWAT2005: a comparison of model parameterizations using station and gridded meteorological observations, Quatern. Int., 226, 54–59, doi:10.1016/j.quaint.2009.11.037, 2010.

Xu, J., Yang, D., Yi, Y., Lei, Z., Chen, J., and Yang, W.: Spatial and temporal variation of runoff in the Yangtze River basin during the past 40 years, Quatern. Int., 186, 32–42, 2008.

Xu, Z. X. and Zhang, N.: Long-term trend of precipitation in the Yellow River Basin during the past 50 years (in Chinese), Geogr. Res., 25(1), 27–34, 2006.

Xu, Z. X., Zhao, F. F., and Li, J. Y.: Response of streamflow to climate change in the head water catchment of the Yellow River basin, Quatern. Int., 208, 62–75, doi:10.1016/j.quaint.2008.09.001, 2009.

Zhang, J. Y., Zhang, S. L., Wang, J. X., and Li, Y.: Study on runoff trends of the six larger basins in China over the past 50 years (in Chinese), Adv. Water Sci., 18(2), 230–234, 2007.

Zhang, Q., Xu, C.-Y., Becker, S., and Jiang, T.: Sediment and runoff changes in the Yangtze River basin during past 50 years, J. Hydrol., 331, 511–523, 2006.

Zhang, Q., Xu, C.-Y., Zhang, Z. X., Chen, Y. D., Liu, C.-L., and Lin, H.: Spatial and temporal variability of precipitation maxima during 1960–2005 in the Yangtze River basin and possible association with large-scale circulation, J. Hydrol., 353, 215–227, 2008.

# 33 年来中国铁路运输行业的大气污染物排放

徐雨晴[1], 何吉成[2*], 王长科[1]
(1. 中国气象局国家气候中心, 北京 100081; 2. 交通运输部规划研究院环境资源所, 北京 100028)

**摘要**: 铁路是中国重要的交通运输方式,但中国至今尚无铁路运输行业大气污染物排放的报道. 根据中国铁路部门逐年统计数据,采用基于燃料消耗量的排放因子法,估算了 1975 ~ 2007 年中国铁路机车大气污染物排放量,并分析了大气污染物排放强度及其变化. 结果表明,33 年来中国铁路机车烟尘、$SO_2$、CO 和 $C_nH_m$ 排放量逐年降低,分别由 1975 年的 351.06、39.97、84.60 和 84.53 万 t 降至 2007 年的 7.87、1.14、3.67 和 2.64 万 t,年均减排量分别为 10.70、1.21、2.53 和 2.56 万 t. 但 $NO_x$ 排放量呈上升趋势,由 1975 年的 3.48 万 t 增至 2007 年的 9.83 万 t,年均增加 0.20 万 t. 烟尘、$SO_2$、CO 和 $C_nH_m$ 的排放强度呈现明显的降低趋势,其值分别由 1975 年的 68.62、7.81、16.54 和 $16.52 \times 10^{-4}$ kg·(t·km)$^{-1}$ 降至 2007 年的 0.54、0.08、0.25 和 $0.18 \times 10^{-4}$ kg·(t·km)$^{-1}$,$NO_x$ 的排放强度在 $0.5 \sim 0.8 \times 10^{-4}$ kg·(t·km)$^{-1}$ 范围内波动. 中国铁路运输行业大气污染物排放量占全国总排放量的比重较低,加上其排放强度还逐年降低,因此可以说铁路运输是中国交通运输领域中理想的节能减排运输方式.

**关键词**: 中国铁路; 机车; 大气污染物; 烟尘; $SO_2$; CO; $C_nH_m$; $NO_x$
**中图分类号**: X511 **文献标识码**: A **文章编号**: 0250-3301(2011)05-1217-07

# Air Pollutants Emissions of Locomotives in China Railways in Recent 33 Years

XU Yu-qing[1], HE Ji-cheng[2], WANG Chang-ke[1]
(1. National Climate Center, China Meteorological Administration, Beijing 100081, China; 2. Division of Environment and Resources Research, Transport Planning and Research Institute, Ministry of Transport, Beijing 100028, China)

**Abstract**: Although railway has played a great role in transportation in china, there has been no any study on air pollutants emissions of locomotives until now. Based on the annual statistical data collected by the Chinese Railway Statistic Center, using the emission factor method derived from fuel consumption, the air pollutants emissions of locomotives during 1975-2007 were calculated, and their emission intensities and dynamic characteristics were analyzed. The results show that the emissions of soot, $SO_2$, CO and $C_nH_m$ from steam and diesel locomotives in china decreased from 3510.6 thousand, 399.7 thousand, 846.0 thousand and 845.3 thousand ton in 1975 to 78.7 thousand, 11.4 thousand, 36.7 thousand and 26.4 thousand ton in 2007, indicating a decrease of 107.0 thousand, 12.1 thousand, 25.3 thousand and 25.6 thousand ton per year, respectively. However, the emissions of $NO_x$ showed an increase trend from 34.8 thousand ton in 1975 to 98.3 thousand ton in 2007 with an increase rate of 2.0 thousand ton per year. The emission intensities of soot, $SO_2$, CO and $C_nH_m$ decreased significantly from 686.2, 78.1, 165.4 and 165.2 g/(hundred converted ton-km) in 1975 to 5.4, 0.8, 2.5 and 1.8 g/(hundred converted ton-km) in 2007, respectively. The emission intensity of $NO_x$ fluctuated in the range of 5.0-8.0 g/(hundred converted ton-km). Air pollutants emissions of locomotives accounted for very little of the total emissions in China, and the emission intensities decreased persistently. It shows that railway transportation is a perfect way of saving energy and reducing emission in the sector of transportation.

**Key words**: China railways; locomotive; air pollutant; soot; $SO_2$; CO; $C_nH_m$; $NO_x$

交通运输工具会排放多种大气污染物,$SO_2$ 和 $NO_x$ 等气体是影响大气环境质量的重要污染物,受到科学家和公众的普遍关注[1~5]. $SO_2$ 可对呼吸系统造成伤害,还可导致硫酸型烟雾[6,7],$NO_x$ 和 CO 可以引发城市光化学烟雾污染[8,9]. 在我国交通运输行业的大气污染物排放研究方面,主要关注城市机动车的排放问题[10~14],而对包括火车、飞机、船舶在内的非道路移动源的排放问题研究较少[15]. 在铁路运输中,蒸汽机车燃烧原煤、内燃机车耗用柴油均会直接排放 CO、$NO_x$、$SO_2$、$C_nH_m$(碳氢化合物)和烟尘等大气污染物. 虽然目前已有一些内燃机车气态污染物排放测定工作[16,17],但对我国整个铁路运输行业的大气污染物排放量及排放强度变化的研究工作还未见报道, 30 多年来,我国铁路运输密度、组织方式、能源消费结构不断变化,本研究针对我国铁路运输行业的自身特点,基于我国铁路行业逐年的统计数据来估算大气污染物排放量,探讨了 30 多年来我国铁路运输行业的大气污染物排放规律及其强度变化,讨论了铁路运输行业大气污染物排放占全

**收稿日期**: 2010-05-25; **修订日期**: 2010-07-28
**基金项目**: 国家自然科学基金项目(40775070); 国家重点基础研究发展规划(973)项目(2010CB955703); 中国气象局 2011 年气候变化专项(CCSF2011-14)
**作者简介**: 徐雨晴(1977 ~ ),女,博士,高级工程师,主要研究方向为气候变化及生态环境,E-mail: xuyq@cma.gov.cn
* 通讯联系人, E-mail: jichenghe@gmail.com

国排放总量的比重及其变化,以期为估算我国交通行业大气污染物排放清单提供依据.

## 1 数据来源与计算方法

### 1.1 数据来源及说明

本研究中 1975 ~ 2005 年的原始数据来自铁路统计部门逐年的《全国铁路统计资料汇编》资料,2006 ~ 2007 年的数据来自文献[18].数据内容主要有机车运用指标、机车工作量等统计数据以及每年的货物周转量和旅客周转量.我国铁路机车分为 3 种类型:蒸汽机车、内燃机车和电力机车.蒸汽机车燃煤、内燃机车燃烧柴油会直接排放 CO、$NO_x$、$SO_2$、$C_nH_m$和烟尘等大气污染物,电力机车因使用电力而达到了大气污染物的"零排放",所以本研究只考虑蒸汽机车和内燃机车排放量及其强度.

### 1.2 机车大气污染物排放量计算方法

机车大气污染物排放量的估算采用基于燃料消耗量的排放因子法,我国铁路的蒸汽机车和内燃机车有多种型号,但在年度统计上,只有整个蒸汽机车或内燃机车的燃料消耗总量,没有对不同型号机车的燃料消耗状况进行分门别类地统计.若要获得不同型号机车的燃料消耗状况和污染物排放水平,不仅十分困难,而且意义不大,采用燃料消耗总量和平均排放因子来定量分析我国铁路机车污染物排放状况更实际一些.同时,适当的排放因子对获得可靠的估算结果较为重要,从我国已有的研究工作来看[15,19~21],在分行业和分燃料的污染物排放因子选择上,铁路行业的排放因子均引用国外 20 世纪 70 年代中期的数据,事实上我国铁路运输的组织方式、燃料结构与国外相差较大,因此造成一定的误差和不确定性.在本研究中,采用我国铁路行业自己通过试验测定获得的排放因子来估算大气污染物排放量将较为合理,从而可获得较为可靠的估算结果.蒸汽机车的 CO、$NO_x$、$SO_2$、$C_nH_m$和烟尘年排放量计算公式为:

$$Z_{ij} = \frac{M_i \times K_j}{10^3} \tag{1}$$

式中,$Z_{ij}$为蒸汽机车 $i$ 年所排放的 $j$ 种大气污染物数量(万 t),$M_i$ 为蒸汽机车 $i$ 年的原煤消耗量(万 t),$K_j$ 为蒸汽机车 $j$ 种大气污染物的排放因子.烟尘的排放因子采用大连机车厂的试验数据,为 187 g/kg,CO、$SO_2$、$NO_x$ 和 $C_nH_m$ 的排放因子分别为[22]:45 g/kg、19 × $S$ g/kg、1.5 g/kg和 45 g/kg,其中 $S$ 为燃煤的含硫量(%),有研究表明我国原煤平均含硫量为 1.12%[19],因此 $S$ 取 1.12%.

内燃机车的 CO、$NO_x$、$SO_2$、$C_nH_m$和烟尘年排放量计算公式为:

$$N_{ij} = \frac{Y_i \times W_j}{10^3} \tag{2}$$

式中,$N_{ij}$为内燃机车 $i$ 年所排放的 $j$ 种大气污染物数量(万 t),$Y_i$ 为内燃机车 $i$ 年的燃油消耗量(万 t),$W_j$ 为内燃机车 $j$ 种大气污染物的排放因子.内燃机车 CO、$NO_x$、$SO_2$ 的排放因子采用蔡惟瑾等[16]对 3 种内燃机车试验测试的平均值,其值分别为 7.1 g/kg、50.3 g/kg、2.2 g/kg.内燃机车的烟尘和 $C_nH_m$排放因子采用铁道部劳动卫生研究所及铁道机车车辆研究所的试验数据[22],其排放因子分别为 15.2 g/kg和 5.1 g/kg.

我国铁路机车的大气污染物年排放量为蒸汽机车和内燃机车的年排放量之和,即为:

$$P_{ij} = Z_{ij} + N_{ij} \tag{3}$$

式中,$P_{ij}$为我国铁路机车 $i$ 年所排放的 $j$ 种大气污染物数量(万 t),$Z_{ij}$和 $N_{ij}$的含义见公式(1)和(2).

### 1.3 机车大气污染物排放强度的计算方法

在铁路运输统计中,通常采用换算t·km作为计量全部周转量的单位(简称:t·km),并规定全部周转量(换算t·km) = 货物周转量(t·km) + 旅客周转量(人·km)[23].由于铁路燃料消耗统计没有将货运消耗和客运消耗分开进行统计,针对我国铁路运输行业特点,本研究设定机车某种大气污染物排放强度为单位全部周转量的排放量,具体为每万换算t·km的污染物排放量.根据每年蒸汽机车和内燃机车承担的牵引工作量比例,估算出这 2 类机车承担的全部周转量,然后求得我国铁路机车的大气污染物排放强度.

## 2 我国铁路机车大气污染物排放量及排放强度

### 2.1 排放量

1975 ~ 2007 年我国铁路机车的烟尘、$SO_2$、CO 和 $C_nH_m$ 的排放量变化基本相似,均呈降低态势;1975 ~ 1984 年的排放量较高,并呈小幅上下波动,其中 1984 年的排放量最大,1985 年以后排放量逐年大幅跌落.具体而言,烟尘由 1975 年的 351.06 万 t 降至 2007 年的 7.87 万 t,年均减排量达 10.70 万 t. 1975 ~ 1984 年烟尘的年均排放量达 351.88 万 t,1984 年高达 367.01 万 t;1985 ~ 2007 年年均降低 16.12 万 t(降幅为 4.4%),其中 1997 年降至 100 万 t 以下,2002 年以后降至 10 万 t 以下[图 1(a)].就 $SO_2$ 来说,其排放量由 1975 年的 39.97 万 t 降至

2007 年的 1.14 万 t，年均减排 1.21 万 t. 1975 ~ 1984 年 $SO_2$ 的年均排放量达 40.1 万 t，1984 年高达 41.81 万 t；1985 ~ 2007 年年均降低 1.83 万 t，其中 1994 年降至 20 万 t 以下，1999 年以后降至 5 万 t 以下，2002 ~ 2007 年年均排放量维持在 1.1 万 t 左右[图 1(b)]. 就 CO 而言，其排放量由 1975 年的 84.60 万 t 降至 2007 年的 3.67 万 t，年均减排 2.53 万 t. 1975 ~ 1984 年 CO 的年均排放量达 84.90 万 t，1984 年高达 88.68 万 t；1985 ~ 2007 年年均降低 3.82 万 t，其中 1993 年降至 50 万 t 以下，1999 年以后降至 10 万 t 以下，2002 ~ 2007 年年均排放量维持在 3.54 万 t 左右[图 1(c)]. $C_nH_m$ 排放量则由 1975 年的 84.53 万 t 降至 2007 年的 2.64 万 t，年均减排 2.56 万 t. 1975 ~ 1984 年 $C_nH_m$ 的年均排放量达 84.77 万 t，1984 年高达 88.47 万 t；1985 ~ 2007 年年均降低 3.85 万 t，其中 1993 年降至 50 万 t 以下，1999 年以后降至 10 万 t 以下，2002 ~ 2007 年年均排放量维持在 2.55 万 t 左右[图 1(e)]. 33 年来，由于大规模地淘汰能效低、排放强度大的蒸汽机车，同时大量运用能效高、排放强度相对较低的内燃机车和“零排放”的电力机车，使得我国铁路运输行业的烟尘、$SO_2$、CO 和 $C_nH_m$ 排放量逐年下降，也使我国铁路行业在客货运输量不断增大的情形下取得了“运输量增加，排放量降低”的好成绩，为减少我国交通运输行业的大气污染物排放做出了贡献.

与烟尘、$SO_2$、CO 和 $C_nH_m$ 这 4 种大气污染物排放量变化不同，1975 ~ 2007 年我国铁路机车 $NO_x$ 排放量逐年上升，其值由 1975 年的 3.48 万 t 升至 2007 年的 9.83 万 t，年均增长量达到 0.20 万 t(增幅为 5.7%). 其中，1978 年的排放量超过 4 万 t，1985 年超过 5 万 t，1987 年超过 6 万 t，1991 年超过 7 万 t，1995 年超过 8 万 t，2004 年超过 9 万 t，2007 年接近 10 万 t [图 1(d)].

## 2.2　排放强度

就大气污染物排放强度而言(图 1)，1975 ~ 2007 年我国铁路机车烟尘、$SO_2$、CO 和 $C_nH_m$ 这 4 种污染物的排放强度逐年降低，变化趋势也基本相似. 烟尘的排放强度由 1975 年的 $68.62 \times 10^{-4}$ kg·(t·km)$^{-1}$ 降至 2007 年的 $0.54 \times 10^{-4}$ kg·(t·km)$^{-1}$，年均降低 $2.13 \times 10^{-4}$ kg·(t·km)$^{-1}$，其中 1981 年降至 $50 \times 10^{-4}$ kg·(t·km)$^{-1}$ 以下，1997 年降至 $10 \times 10^{-4}$ kg·(t·km)$^{-1}$ 以下，2002 年以后降至 $1 \times 10^{-4}$ kg·(t·km)$^{-1}$ 以下[图 1(a)]. $SO_2$ 的排放强度由 1975 年的 $7.81 \times 10^{-4}$ kg·(t·km)$^{-1}$ 降至 2007 年的 $0.08 \times 10^{-4}$ kg·(t·km)$^{-1}$，年均降低 $0.24 \times 10^{-4}$ kg·(t·km)$^{-1}$，其中 1984 年降至 $5 \times 10^{-4}$ kg·(t·km)$^{-1}$ 以下，1997 年以后降至 $1 \times 10^{-4}$ kg·(t·km)$^{-1}$ 以下，2002 ~ 2007 年年均排放强度维持在 $0.08 \times 10^{-4}$ kg·(t·km)$^{-1}$ 左右[图 1(b)]. 就 CO 而言，其排放强度由 1975 年的 $16.54 \times 10^{-4}$ kg·(t·km)$^{-1}$ 降至 2007 年的 $0.25 \times 10^{-4}$ kg·(t·km)$^{-1}$，年均降低 $0.51 \times 10^{-4}$ kg·(t·km)$^{-1}$，其中 1985 年降至 $10 \times 10^{-4}$ kg·(t·km)$^{-1}$ 以下，1992 年降至 $5 \times 10^{-4}$ kg·(t·km)$^{-1}$ 以下，1999 年以后降至 $1 \times 10^{-4}$ kg·(t·km)$^{-1}$ 以下，2002 ~ 2007 年年均排放强度在 $0.26 \times 10^{-4}$ kg·(t·km)$^{-1}$ 左右[图 1(c)]. $C_nH_m$ 排放强度则由 1975 年的 $16.52 \times 10^{-4}$ kg·(t·km)$^{-1}$ 降至 2007 年的 $0.18 \times 10^{-4}$ kg·(t·km)$^{-1}$，年均降低 $0.51 \times 10^{-4}$ kg·(t·km)$^{-1}$，其中 1985 年降至 $10 \times 10^{-4}$ kg·(t·km)$^{-1}$ 以下，1992 年降至 $5 \times 10^{-4}$ kg·(t·km)$^{-1}$ 以下，1999 年以后降至 $1 \times 10^{-4}$ kg·(t·km)$^{-1}$ 以下，2002 ~ 2007 年年均排放强度只有 $0.19 \times 10^{-4}$ kg·(t·km)$^{-1}$ 左右[图 1(e)].

1975 ~ 2007 年我国铁路机车 $NO_x$ 的排放强度

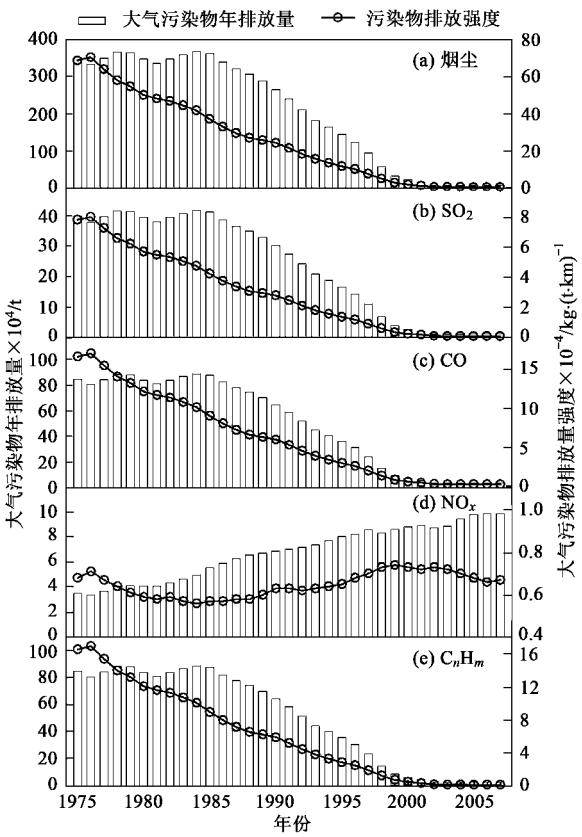


**图 1　我国铁路机车的烟尘、$SO_2$、CO、$NO_x$ 和 $C_nH_m$ 逐年排放量及强度**

Fig. 1　Annual soot, $SO_2$, CO, $NO_x$ and $C_nH_m$ emissions and their intensities of the locomotives in China

在 0.50 ~ 0.80 × $10^{-4}$ kg·(t·km)$^{-1}$范围内波动,平均排放强度为 0.65 × $10^{-4}$ kg·(t·km)$^{-1}$[图 1(d)]. 1975 ~ 2007 年 $NO_x$ 的排放强度与烟尘、$SO_2$、CO 和 $C_nH_m$ 这 4 种大气污染物变化不同,其变化可分为 3 个阶段: 1975 ~ 1983 年属于下降阶段,其值由 1975 年的 0.68 × $10^{-4}$ kg·(t·km)$^{-1}$降低到 1983 年的 0.57 × $10^{-4}$ kg·(t·km)$^{-1}$, 年均降低 0.014 × $10^{-4}$ kg·(t·km)$^{-1}$; 1984 ~ 1999 年属于缓慢上升阶段,其值由 1984 年的 0.56 × $10^{-4}$ kg·(t·km)$^{-1}$升至 1999 年的 0.74 × $10^{-4}$ kg·(t·km)$^{-1}$,年均增加 0.012 × $10^{-4}$ kg·(t·km)$^{-1}$; 2000 ~ 2007 年属于缓慢下降阶段,其值由 2000 年的 0.73 × $10^{-4}$ kg·(t·km)$^{-1}$降至 2007 年的 0.67 × $10^{-4}$ kg·(t·km)$^{-1}$.

## 3 讨论

在我国环境状况逐年统计资料中,大气污染物中只有 $SO_2$ 和烟尘的全国逐年排放量数据较为连续和完整. 根据文献[24 ~ 27]中对我国 1985 ~ 2007 年 $SO_2$ 和烟尘排放量的统计数据,结合本研究的计算结果可看出,我国铁路机车 $SO_2$ 排放量占全国 $SO_2$ 排放量的比重很小: 1985 ~ 2007 年平均比重只有 1.03%,并且还逐年降低,由 1985 年的 3.12% 降至 2007 年的 0.05%,年均降低 0.14%[图 2(a)]. 就烟尘排放量比重来看[图 2(b)], 1985 ~ 2007 年我国铁路机车烟尘排放量占全国排放量比重也不大,平均为 10.1%,由 1985 年的 28% 降至 2007 年的 0.8%,年均降低 1.24%. 其中, 1985 ~ 1990 年平均比重较大,达 23%,但 1995 年降至 10% 以下, 2002 年降到不足 1%,综合上述结果可以看出,我国铁路运输行业所排放的 $SO_2$ 和烟尘占全国总排放量的比重较低,加上其排放强度还逐年降低[图 1(a)和 1(b)],因此,可以说铁路运输是我国交通运输领域中理想的节能减排运输方式.

据田贺忠等[28]的研究,1991、1998 和 1999 年我国生物质燃料燃烧排放的 $SO_2$ 分别为 38.1、31.2 和 33.2 万 t,上述年份我国铁路机车 $SO_2$ 排放量均低于生物质燃烧的排放量,分别只有前者的 72%、22% 和 12%. 水泥工业是多种大气污染物的重要排放源, 1995 和 2005 年我国水泥工业 $SO_2$ 排放量分别为 46.70 万 t 和 86.09 万 t[29],对应年份我国铁路机车 $SO_2$ 排放量分别只有水泥工业排放量的 35.7% 和 1.3%.

我国 $NO_x$ 排放量统计上十分薄弱,直到 2006 年才纳入国家环境统计范围中,因此全国及行业的

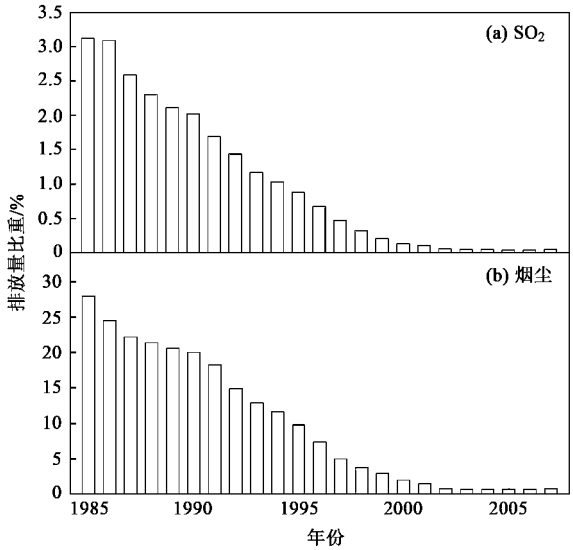


**图 2 铁路机车 $SO_2$ 和烟尘排放量占全国排放量的比重**

Fig. 2 Percentages of $SO_2$ and soot emissions of the locomotives to the total emissions in China

$NO_x$ 排放量数据只能在部分研究工作中获得(表 1). 通过比较发现,我国铁路机车 $NO_x$ 年排放量占全国总排放量比重很小,不到 1%(平均值仅为 0.73%). 1991、1998 和 1999 年我国生物质燃料燃烧排放的 $NO_x$ 分别为 54.9、45.5 和 45.3 万 t[28],上述年份我国铁路机车 $NO_x$ 排放量分别只有前者的 13%、18% 和 19%. 1995 和 2005 年我国水泥工业 $NO_x$ 排放量分别为 95.20 万 t 和 286.67 万 t[29],对应年份我国铁路机车 $NO_x$ 排放量只有水泥工业的 8% 和 3%. 田贺忠等[20]研究表明 1997 年我国交通运输行业排放了 130.86 万 t $NO_x$, 1997 年我国铁路机车共排放了 8.57 万 t $NO_x$,只占交通运输行业排放总量的 6.5%.

**表 1 铁路机车 $NO_x$ 排放量占全国排放量比重**

Table 1 Percentages of $NO_x$ emission of the locomotives to the total emissions in China

| 年份 | 全国排放量数据及来源/万 t | 全国排放量均值/万 t | 占全国排放量比重/% |
|---|---|---|---|
| 1980 | 476[21] | 476 | 0.86 |
| 1988 | 784.9[19] | 784.9 | 0.83 |
| 1990 | 840[20]; 842.2[19]; 827.3[30]; 954[31] | 865.9 | 0.79 |
| 1995 | 1 130[21];1 199.1[31] | 1 164.6 | 0.69 |
| 1996 | 1 203[21] | 1 203 | 0.68 |
| 1997 | 1 167[21] | 1 167 | 0.73 |
| 1998 | 1 118[21] | 1 118 | 0.74 |
| 2000 | 1 371.9[30];1 112.1[32]; 1 135[33] | 1 206.3 | 0.73 |
| 2006 | 1 524[27] | 1 524 | 0.65 |
| 2007 | 1 643[27] | 1 643 | 0.60 |

就 CO 而言，Tonooka 等[34]估计我国 1990 年的 CO 排放量为8 740 万 t，Streets 等[31]的估算值为 9 795万 t，取平均值为9 268万 t，Streets 等[31]估算的我国 1995 年 CO 排放量为11 267万 t，王丽涛等[35]通过 CO 排放清单估算我国 2001 年 CO 排放量为 1.5 $\times 10^4$ 万 t，即我国铁路机车 1990、1995 和 2001 年的 CO 排放量分别只占全国总排放量的 0.7%、0.3% 和 0.04%. 1995 年和 2005 年我国水泥工业 CO 排放量分别为 864.33 万 t 和1 987.97万 t[29]，对应年份我国铁路机车 CO 排放量只有水泥工业的 4.2% 和 0.2%. Streets 等[31]认为 1995 年我国交通运输行业排放的 CO 占全国总排量的 22%，为2 478.7万 t，按此数估算的话，1995 年我国铁路机车 CO 排放量仅占全国交通运输行业排放量的 1.5%.

在 20 世纪 80 年代中期以后，内燃机车和电力机车逐渐大幅度取代蒸汽机车，90 年代末期至今，进入电力机车取代内燃机车的阶段. 由于电力机车使用电力本身不会直接排放大气污染物，即减少了铁路运输行业的大气污染物排放，其减排量可采用替代算法来估算，即采用内燃机车承担电力机车的牵引工作量而直接排放的大气污染物的数量. 1975～2007 年，我国铁路电气化率逐步升高，铁路电气化率与蒸汽和内燃机车承担的工作量比例呈线性负相关[图 3(a)]，电气化率与污染物减排量之间呈线性正相关关系[图 3]，今后几年里随着一批客运专线的建成，我国电气化铁路规模会更高，因此我国铁路运输行业的大气污染物排放量还会不断降低. 根据我国中长期铁路网调整规划，到 2020 年我

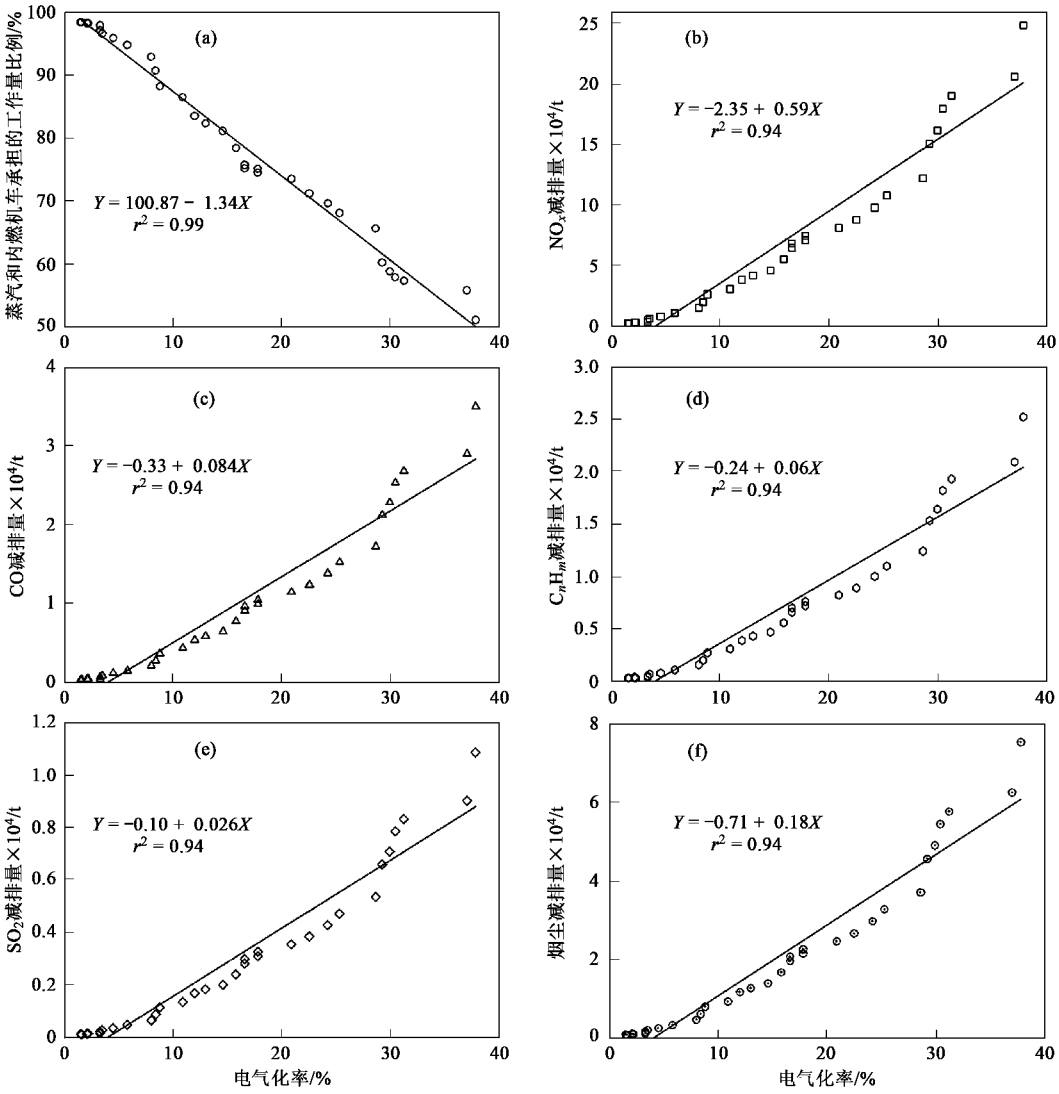


701

**图 3　铁路电气化率与蒸汽和内燃机车承担的工作量比例及污染物减排量间的关系**

Fig. 3　Correlations of electrification rate with the traction proportion of steam and diesel locomotives, and with air pollutants emission reduction

国铁路电气化率要达到 60% 以上[36],可以推算到 2020 年,我国铁路运输行业的烟尘、$SO_2$、CO、$NO_x$ 和 $C_nH_m$ 的排放量将分别减少 10.1、1.46、4.71、33.1 和 3.4 万 t.

为了保障铁路运输的安全,我国铁路运营组织实行"全国一盘棋",通过 18 个铁路局来对运营工作进行管理,没有分地区或省市进行管理. 张礼俊等[15]基于客货周转量、我国内燃机车平均燃油消耗量和国外的排放因子,估算了珠三角地区铁路机车 2006 年 $SO_2$、$NO_x$ 和 CO 排放量,其值分别为 759.4 t、2 760.9 t 和 209.7 t,结合本研究 2006 年的排放量数据可知,其值占全国的比例分别只有 6.7%、2.8% 和 0.6%. 本研究是对中国铁路运输行业大气污染物排放总体状况的初步核算,由于我国不同地区铁路的线路条件、列车运行速度、电化率等因素的不同,导致不同铁路局的燃料消耗和污染物排放也有较大差异,但限于统计资料的缺乏和多数列车跨局运行的事实,目前要实现分不同铁路局甚至不同地区或省市来对我国铁路运输行业的污染物排放进行分解还较为困难,这也是下一步研究的重点.

## 4 结论

(1)1975 ~ 2007 年,我国铁路机车的烟尘、$SO_2$、CO 和 $C_nH_m$ 的排放量均呈降低态势. 烟尘由 1975 年的 351.06 万 t 降至 2007 年的 7.87 万 t,年均减排 10.70 万 t; $SO_2$ 由 1975 年的 39.97 万 t 降至 2007 年的 1.14 万 t,年均减排 1.21 万; CO 由 1975 年的 84.60 万 t 降至 2007 年的 3.67 万 t,年均减排 2.53 万 t; $C_nH_m$ 则由 1975 年的 84.53 万 t 降至 2007 年的 2.64 万 t,年均减排 2.56 万 t. 但 $NO_x$ 排放量逐年上升,其值由 1975 年的 3.48 万 t 升至 2007 年的 9.83 万 t,年均增长 0.20 万 t.

(2)就大气污染物排放强度来说, 1975 ~ 2007 年我国铁路机车烟尘、$SO_2$、CO 和 $C_nH_m$ 这 4 种污染物的排放强度逐年降低. 烟尘由 1975 年的 $68.62 \times 10^{-4}$ kg·(t·km)$^{-1}$ 降至 2007 年的 $0.54 \times 10^{-4}$ kg·(t·km)$^{-1}$, $SO_2$ 由 1975 年的 $7.81 \times 10^{-4}$ kg·(t·km)$^{-1}$ 降至 2007 年的 $0.08 \times 10^{-4}$ kg·(t·km)$^{-1}$, CO 由 1975 年的 $16.54 \times 10^{-4}$ kg·(t·km)$^{-1}$ 降至 2007 年的 $0.25 \times 10^{-4}$ kg·(t·km)$^{-1}$, $C_nH_m$ 排放强度则由 1975 年的 $16.52 \times 10^{-4}$ kg·(t·km)$^{-1}$ 降至 2007 年的 $0.18 \times 10^{-4}$ kg·(t·km)$^{-1}$, $NO_x$ 的排放强度则在 $0.65 \times 10^{-4}$ kg·(t·km)$^{-1}$ 上下波动.

(3)我国铁路运输行业所排放的 $SO_2$、烟尘、$NO_x$ 和 CO 量占全国总排放量的比重很低,且所占比重还呈降低态势,与其他行业排放量相比,我国铁路运输行业所排放的大气污染物量也较小.

**参考文献:**


[1] Wang W X, Chai F H, Zhang K, *et al*. Study on ambient air quality in Beijing for the summer 2008 Olympic Games[J]. Air Quality, Atmosphere & Health, 2008, **1**(1): 31-36.

[2] Streets D G, Fu J S, Jang C J, *et al*. Air quality during 2008 Beijing Olympic Games[J]. Atmospheric Environment, 2007, **41**(3): 480-492.

[3] Sun Y, Wang Y S, Zhang C C. Measurement of the vertical profile of atmospheric $SO_2$ during the heating period in Beijing on days of high air pollution[J]. Atmospheric Environment, 2009, **43**(2): 468-472.

[4] Shao M, Zhang Y H, Zeng L M, *et al*. Ground-level ozone in the Pearl River Delta and the roles of VOC and $NO_x$ in its production [J]. Journal of Environmental Management, 2009, **90**(1): 512-518.

[5] 潘月鹏, 王跃思, 胡波, 等. 北京奥运时段河北香河大气污染观测研究[J]. 环境科学, 2010, **31**(1): 1-9.

[6] 吴小玲, 张斌, 艾南山, 等. 基于小波变换的上海市近 10 年 $SO_2$ 污染指数的变化[J]. 环境科学, 2009, **30**(8): 2193-2198.

[7] 刘洁, 张小玲, 徐晓峰, 等. 北京地区 $SO_2$、$NO_x$、$O_3$ 和 $PM_{2.5}$ 变化特征的城郊对比分析[J]. 环境科学, 2008, **29**(4): 1059-1065.

[8] 安俊琳, 李昕, 王跃思, 等. 北京气象塔夏季大气 $O_3$、$NO_x$ 和 CO 浓度变化的观测实验[J]. 环境科学, 2003, **24**(6): 43-47.

[9] 薛敏, 王跃思, 孙扬, 等. 北京市大气中 CO 的浓度变化监测分析[J]. 环境科学, 2006, **27**(2): 200-206.

[10] 邓顺熙, 董小林. 我国山岭公路汽车 CO, $HC_s$ 和 $NO_x$ 排放系数[J]. 环境科学, 2000, **21**(1): 109-112.

[11] Cai H, Xie S D. Estimation of vehicular emission inventories in China from 1980 to 2005[J]. Atmospheric Environment, 2007, **41**(39): 8963-8979.

[12] 汪婷, 谢绍东. 北京奥运交通限行前后街道机动车污染的模拟[J]. 环境科学, 2010, **31**(3): 566-572.

[13] 傅立新, 郝吉明, 何东全, 等. 北京市机动车污染物排放特征[J]. 环境科学, 2000, **21**(3): 68-70.

[14] 谢绍东, 宋翔宇, 申新华. 应用 COPERT Ⅲ模型计算中国机动车排放因子[J]. 环境科学, 2006, **27**(3): 415-419.

[15] 张礼俊, 郑君瑜, 尹沙沙, 等. 珠江三角洲非道路移动源排放清单开发[J]. 环境科学, 2010, **31**(4): 886-891.

[16] 蔡惟瑾, 赵春亭, 杨玉森. 内燃机车用柴油机排放气态污染物的试验研究[J]. 铁道劳动安全卫生与环保, 1996, **23**(2): 136-138.

[17] 任富民, 牛牧晨, 周玉松, 等. 铁路内燃机车不同工况下废气排放的影响研究[J]. 铁道学报, 2008, **30**(2): 94-97.

[18] 铁道部统计中心. 铁路简明统计资料[M]. 北京: 中国铁道

出版社，2009. 10-35.

[19] 王文兴，王玮，张婉华，等. 我国 $SO_2$ 和 $NO_x$ 排放强度地理分布和历史趋势[J]. 中国环境科学，1996，**16**(3)：161-167.

[20] 田贺忠，郝吉明，陆永琪. 中国商品能源消耗导致的氮氧化物排放量[J]. 环境科学，2001，**22**(6)：24-28.

[21] 田贺忠，郝吉明，陆永琪，等. 中国氮氧化物排放清单及分布特征[J]. 中国环境科学，2001，**21**(6)：493-497.

[22] 铁道部劳动卫生研究所. 陇海线郑州—宝鸡段铁路电气化改造工程环境影响报告书(大气环境影响评价)[R]. 北京：铁道部劳动卫生研究所，1988. 3-4.

[23] 佟立本. 铁道概论[M]. 北京：中国铁道出版社，2008. 225.

[24] 《中国环境年鉴》编辑委员会. 中国环境年鉴(1985-1993 年)[M]. 北京：中国环境科学出版社，1986-1994.

[25] 《中国环境年鉴》编辑委员会. 中国环境年鉴(1994-2001 年)[M]. 北京：中国环境年鉴社，1995-2002.

[26] 国家环保总局. 中国环境统计年报(2006)[M]. 北京：中国环境科学出版社，2007. 1-15.

[27] 中华人民共和国环境保护部. 中国环境统计年报(2007)[M]. 北京：中国环境科学出版社，2008. 3-16.

[28] 田贺忠，郝吉明，陆永琪，等. 中国生物质燃烧排放 $SO_2$、$NO_x$ 量的估算[J]. 环境科学学报，2002，**22**(2)：204-208.

[29] 王永红，薛志刚，柴发合，等. 我国水泥工业大气污染物排放量估算[J]. 环境科学研究，2008，**21**(2)：207-212.

[30] Aardenne J A, Carmichael G R, Levy H, *et al*. Anthropogenic $NO_x$ emissions in Asian in the period 1990- 2020 [J]. Atmospheric Environment, 1999, **33**(4): 633-646.

[31] Streets D G, Waldhoff S T. Present and future emissions of air pollutants in China: $SO_2$, $NO_x$, and CO [J]. Atmospheric Environment, 2000, **34**(3): 363-374.

[32] 孙庆贺，陆永琪，傅立新，等. 我国氮氧化物排放因子的修正和排放量计算：2000 年[J]. 环境污染治理技术与设备，2004，**5**(2)：90-94.

[33] Streets D G, Bond T C, Carmichael G R, *et al*. An inventory of gaseous and primary aerosol emissions in Asia in the year 2000 [J]. Journal of Geographical Research, 2003, **108** (D21): 8809-8831.

[34] Tonooka Y, Kannari A, Higashino H, *et al*. NMVOCs and CO emission inventory in East Asia [J]. Water, Air, and Soil Pollution, 2001, **130**: 199-204.

[35] 王丽涛，张强，郝吉明，等. 中国大陆 CO 人为源排放清单[J]. 环境科学学报，2005，**25**(12)：1580-1585.

[36] 李军. 中国铁路新读[M]. 北京：中国铁道出版社，2009. 75.

文章编号: 1674-7070(2011)01-0036-11

# 不同温室气体排放情景下未来中国地面气温变化特征

闫冠华[1,2]　李巧萍[3]　邢超[2]

**摘要**

采用20多个参与政府间气候变化委员会第4次评估报告(IPCC AR4)的全球气候模式,在20世纪气候模拟试验和SRES B1、A1B和A2 3种排放情景下进行数值集合分析,结果表明未来中国大陆的气温变化有着明显的时间和空间差异. 21世纪,中国大陆年平均气温呈显著升高趋势,至2099年平均增温范围为2.5~4.9 ℃,高于全球平均值. 冬季升温明显高于其他季节,年较差呈减小趋势. 21世纪前期,变暖预估值受排放情景假设或模式敏感性的影响较小,不同排放情景和不同模式之间的预估结果一致,中国大陆平均增温范围为0.88~0.92 ℃,21世纪中期以后这种差异逐渐增大,增暖范围为2.44~4.28 ℃. 相对于1980—1999年平均气候场,中国大陆平均升温值在20世纪50年代前后达到2 ℃,此后,A1B及A2情景下中国大陆气温快速升高,在21世纪60年代末达到或超过3 ℃,但区域差异明显,升温值达2 ℃的时间由北至南在不同排放情景下相差10~30 a,东北、西北地区将成为未来受气温升高影响最为敏感的地区.

**关键词**

温室气体排放情景; 地面气温; 变化特征

**中图分类号** P467
**文献标志码** A

**收稿日期** 2010-08-31
**资助项目** 公益性行业(气象)科研专项(GYHY-200906020); 国家自然科学基金(40871095); 国家科技支撑计划(2007BAC29B01)

**作者简介**

闫冠华,男,博士生,主要从事数值预报及区域气候变化研究. yangh@cma.gov.cn

1 南京信息工程大学 大气科学学院,南京,210044
2 中国气象局 培训中心,北京,100081
3 中国气象局 国家气候中心,北京,100081

## 0 引言

最近的观测事实表明,1906—2005年全球平均气温上升了0.74 ℃[1],期间我国气候变化也呈现出显著的变暖特征,与全球气候变暖的趋势一致. 根据1905—2001年以我国东部台站为主观测到的最高和最低温度,得到的我国平均气温增加率为0.81 ℃/(100 a),比全球同期增温略高. 近50 a我国平均气温升高以北方为主,最高升温速率达0.8 ℃/(10 a),最大升温出现于东北北部、内蒙古、塔里木盆地,从全球范围看,这里也是增温最显著的地区之一[2-4],且无论是季节变化还是年变化,都具有一定的复杂性[5].

政府间气候变化专门委员会(IPCC)2007年发布的第4次评估报告(IPCC AR4)[1]指出,全球平均地面气温升高超过90%的可能性是由于人为温室气体排放引起的. 根据国际上20余个气候模式对未来气候的预估结果,在6种SRES排放情景下,到21世纪末,全球地表的平均增温将为1.1~6.4 ℃,海平面上升0.18~0.59 m(与1980—1999年相比). 在未来20 a中,气温大约以0.2 ℃/(10 a)的速度升高,即使所有温室气体和气溶胶的浓度稳定在2000年的水平上不变,气温也要以约0.1 ℃/(10 a)的速度继续升高[1,6].

全球气候变暖对自然生态和人类生存环境产生了显著的影响. 例如: 冰川湖泊范围扩大,数量增加; 许多由冰川和积雪供水的河流的径流量和早春最大溢流量增大; 许多地区湖水和河水温度升高,并影响到水质; 永冻区地表不稳定性增加; 动植物的地理分布向高纬度和高海拔地区推移; 生物的物候期提前. 气候变化甚至还威胁到人类健康,如热浪造成的死亡率和一些传染病的发病率有所上升[7-8].

2004年欧盟一些科学家率先提出了"2 ℃升温阈值"的概念,认为2 ℃是人类社会可以容忍的最高升温. 2005年,国际气候变化特别工作组发表了一份名为《应对气候挑战》建议书,建议书中指出: 如果升温幅度超过2 ℃界限,气候突变的可能性和危险性会大大增加,如农业严重歉收,粮食安全的风险加大; 水资源将严重短缺等. 为此,必须控制温室气体质量分数不超过$4\times10^{-4}$,由此将2 ℃升温阈值与"气候变化危险水平"直接联系起来. 这一切都为中国的减排带来了巨大的压力. IPCC AR4第2工作组的报告指出: 增温从1.5 ℃到2.0~2.5 ℃的过程中,遭受水资源短缺威胁的人口将会从目前的近6



© 1994-2011 China Academic Journal Electronic Publishing House. All rights reserved. http://www.cnki.net

亿增加到24~31亿,这其中包括中国和印度的一些大城市;温度超过2 ℃,全球遭遇沿海洪涝、饥饿、疟疾、水短缺的人数将大大增加[7]. 熊伟等[9-10]的研究也指出,从温度来看,如果不考虑肥效和相应的适应措施,平均温度升高2.0~2.5 ℃左右将导致我国3大作物的单产水平持续下降,影响到我国未来的粮食安全. 如果气温升高3 ℃,在降水不变的情况下,长度不足4 km的青藏高原冰川将消融[11].

尽管欧盟等提出的2 ℃升温阈值的科学性还有待进一步研究证实,但全球地面气温的升高确实已经并将继续影响人们赖以生存的地球环境,特别是对中国这样的发展中国家来说,在应对气候变化挑战的同时,还要承受来自国际社会的减排压力. 因此,未来百年,中国大陆地面气温变化及区域特征如何,所谓的温度阈值出现的时间和空间,是否存在特别脆弱的地区或区域,这些变化特征与全球平均状况有何异同,是目前需要回答的科学问题. 本文借助国家气候中心整编发布的IPCC AR4多模式集合的全球气温资料,分析21世纪中国平均地面气温变化的时空特征,分析未来中国大陆及各气候分区升温幅度分别达到2、2.5、3 ℃出现的时间和区域特征,为气候变化影响评估提供科学基础,为国家制定可持续发展计划提供决策依据.

## 1 资料、方法及区域划分

本文分析采用参与政府间气候变化委员会第4次评估报告(IPCC AR4)的全球20多个气候模式提供的20世纪气候模拟结果(1901—2000年)及21世纪(2001—2099年)在SRES B1、A1B、A2 3种排放情景下的预估结果(由国家气候中心整编和发布). 参加IPCC第4次评估报告的模式代表了当前国际上主要先进气候模式的最新版本,较之参与IPCC第3次评估报告的模式均有较大的改进,相应的情景试验设计也更加合理. 这些模式精度高,参数化方案更合理,采用了更新的数值方法,模式的更多详细信息可参见http://www-pcmdi.llnl.gov/ipcc/about_ipcc.php. 文中所用20世纪气候场的模拟及21世纪不同情景下的预估结果是将这些单模式结果统一插值到同一分辨率下(1.0°×1.0°),并采用多模式集合的方法,即仅通过算术平均得到的多模式集合结果. 不同SRES情景下,月平均资料模式集合平均值所用的模式数量如下:SRES A1B共17个模式,SRES A2共16个模式,SRES B1共17个模式,这些模式的基本特征及集合资料说明参见http://ncc.cma.gov.cn. 为便于与IPCC AR4中的全球平均变化相比较,文中采用了多模式集合的1980—1999年平均场作为20世纪基准气候场.

文中也使用了中国743站同期地面气温的观测资料,以检验模式对平均气候场的模拟性能. 在将模式结果与观测进行比较时,将台站的观测资料插值在与模式结果相同的格点上.

为了考察模式和观测结果之间的差距,计算了模式的均方根偏差:

$$D_{\mathrm{RMS}} = \sqrt{\frac{1}{n}\sum_{i=1}^{n}\left(x_{i,\mathrm{m}} - x_{i,\mathrm{obs}}\right)^2}. \qquad (1)$$

式(1)中:$x_{i,\mathrm{m}}$为模式的气候平均第$i$个月的物理量;$x_{i,\mathrm{obs}}$为观测的气候平均第$i$个月的物理量;$n$为资料长度;$D_{\mathrm{RMS}}$为模式结果与观测结果之间的均方根偏差.

本研究所选区域覆盖了包括青藏高原在内的整个中国大陆及周边地区,范围为70~140°E,15~55°N. 此外,为了全面考察中国地面气温变化的区域特性,将中国大陆分为6个主要气候区(图1):A区为东北区,主要包括东北三省和内蒙古北部;B区为华北区,主要为华北平原;C区为华东区,主要指长江中下游地区;D区为华南区,包括广东、广西、湖南等地;E区为西北区,包括内蒙古东部、陕西、宁夏、甘肃、青海和新疆等地;F区为西南区,包括西藏、四川、云南和贵州等地.

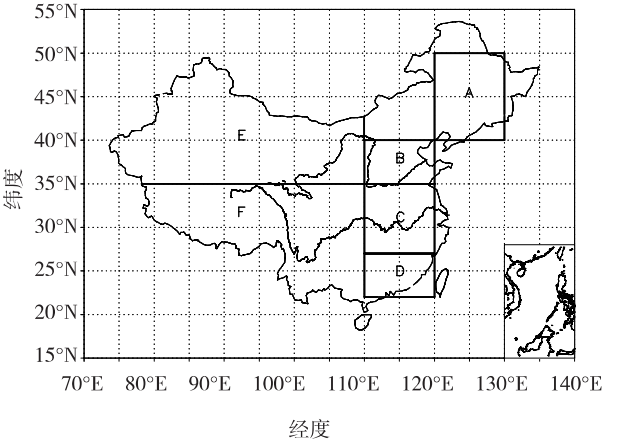


图1 研究区域及分区

Fig. 1 Distribution of the researched regions and sub-regions

## 2 中国地面气温的模拟检验

关于IPCC AR4中采用的全球模式对中国降水、



© 1994-2011 China Academic Journal Electronic Publishing House. All rights reserved. http://www.cnki.net

东亚季风等的模拟性能已有较多的检验和分析[12-15],认为大部分模式基本上能够模拟出中国东部地区降水的季节进退,但不同模式对东亚季风降水的空间分布模拟差异较大,多模式集合一般优于大部分单个模式的结果.

此处仅对模拟的地面气温进行检验. 图 2 给出了 1980—1999 年中国台站实测及 IPCC AR4 多模式集合的中国冬季、夏季平均地面气温及模式的均方根偏差. 由图 2 可见: 冬季我国大陆温度梯度较大,南部平均温度可达 15 ℃,而我国最北方地区平均温度可低至 -27 ℃,除青藏高原外,等温线基本上与纬圈平行; 比较模拟场和实测场可见,模式较好地模拟出了我国冬季平均气温随纬度的阶梯分布,但模拟的温度比观测值偏冷,这也是目前模式在东亚地区模拟中普遍存在的偏差[16-17]; 长江以南地区温度偏高、塔里木盆地温度偏高以及青藏高原地区温度偏低是夏季中国地表气温的几个主要特征,模式较好地模拟了夏季气温的主要区域特征. 从图 2 中给出的模式均方根误差也可看到( 图 2e—f) : 模式对东部地区的模拟性能较好,在华北、长江中下游及华南地区的模拟偏

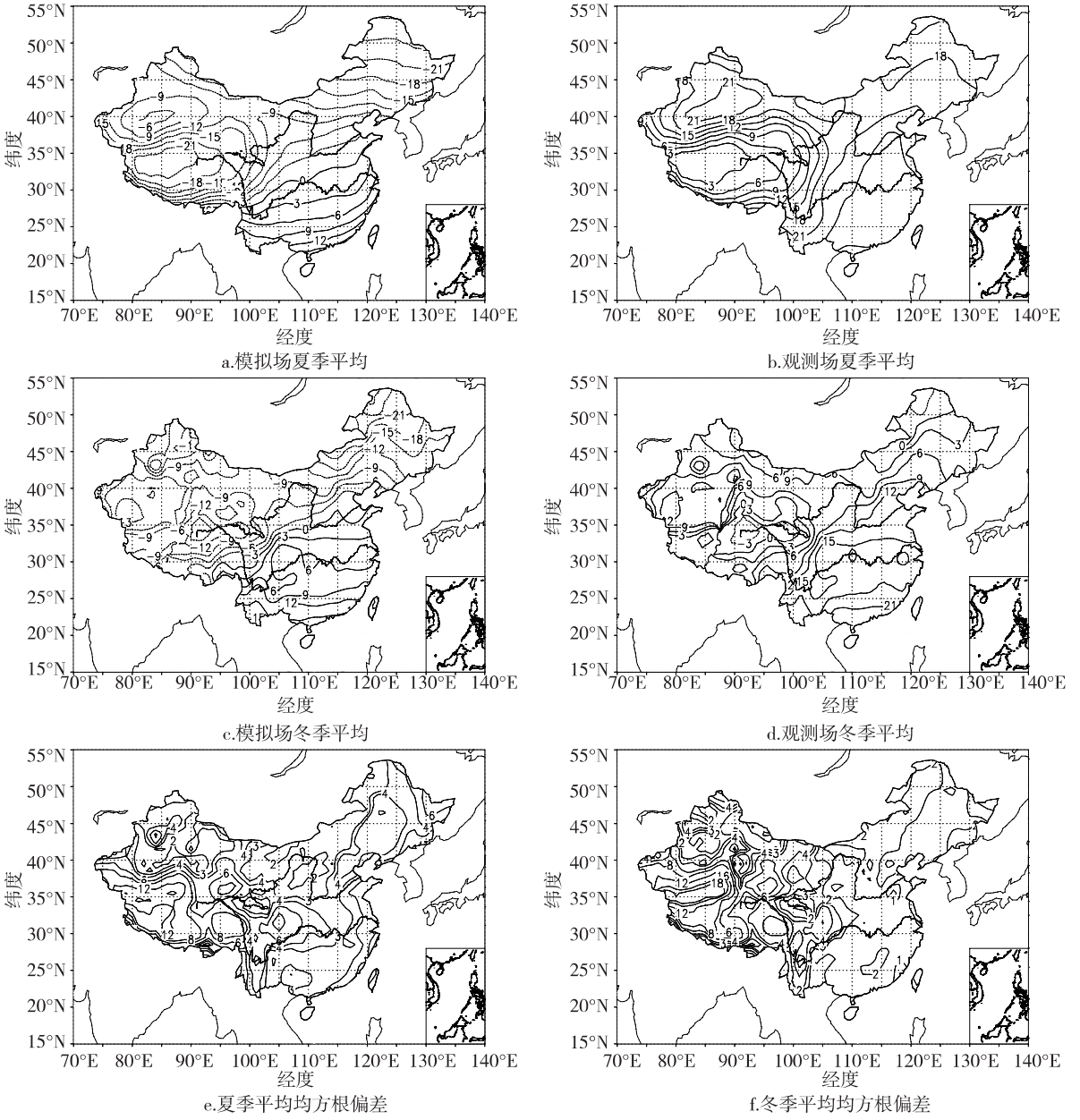


**图 2　模拟和观测的 1980—1999 年地面气温及模式的均方根偏差( 单位: ℃)**

Fig. 2　Mean surface air temperature during 1981—1999 from observation and simulation and model's root-mean-square error ( units: ℃)



© 1994-2011 China Academic Journal Electronic Publishing House. All rights reserved.　http://www.cnki.net

差较小;对西部地区模拟偏差较大,特别是青藏高原地区;夏季的模拟偏差小于冬季. 姜大膀等[18]计算了17个模式及其集合结果与CRU观测资料之间的空间相关系数,最小为0.948,最高可达0.992,可见,模式对地面气温场模拟的空间差异很小,均能较好地反映模式的空间分布特征. 大部分模式对地面气温年际变率及线性趋势也有一定模拟能力[19].

## 3 未来中国地面气温变化特征

图3给出了中国大陆及6个分区域2001—2099年在3个主要排放情景下多模式集合的地面气温变化情况. 需要说明的是,为了消除年变化的影响,本文在给出未来温度变化的时间序列演变图时对资料进行了9 a滑动平均处理. 由图3可见,未来各区域平均地面气温在3种排放情景下均呈显著升温趋势. 东北地区的升温幅度最大,西北地区次之,华南地区最小. 相对于模式气候场,B1排放情景下各区域平均升温速率范围为0.20~0.24 ℃/(10 a),区域之间的差异不明显,到2099年升温幅度为2.03~2.68 ℃;A1B排放情景下各区域平均升温速率范围为0.33~0.44 ℃/(10 a),东北地区升温速率最大,到2099年升温幅度为3.12~4.26 ℃;A2排放情景下各区域平均升温速率范围为0.36~0.51 ℃/(10 a),区域之间的差异明显增大,到2099年升温幅度为3.68~5.26 ℃,与江志红等[20]的分析结果基本一致. 从图3中还可以看出,A1B作为中等排放情景,尽管该情景下$CO_2$排放浓度仅在2030年前高于A2情景,但可能是由于气温变化对$CO_2$浓度具有持续或是滞后的响应,因此,该情景下中国大部分区域升温幅度在2050年前比A2情景略偏高.

从季节变化特征来看(图4给出21世纪3种排放情景下各区域月平均气温的变化曲线),东北、西

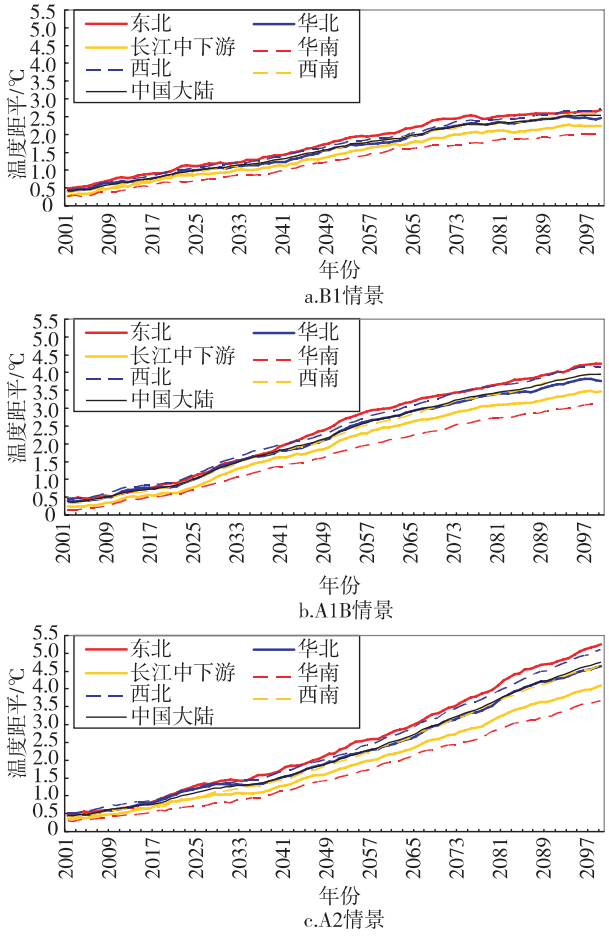


图3 21世纪区域年平均地面气温距平变化曲线(相对于1980—1999年)

Fig. 3 Time series of regional surface air temperature departure(relative to 1980—1999)

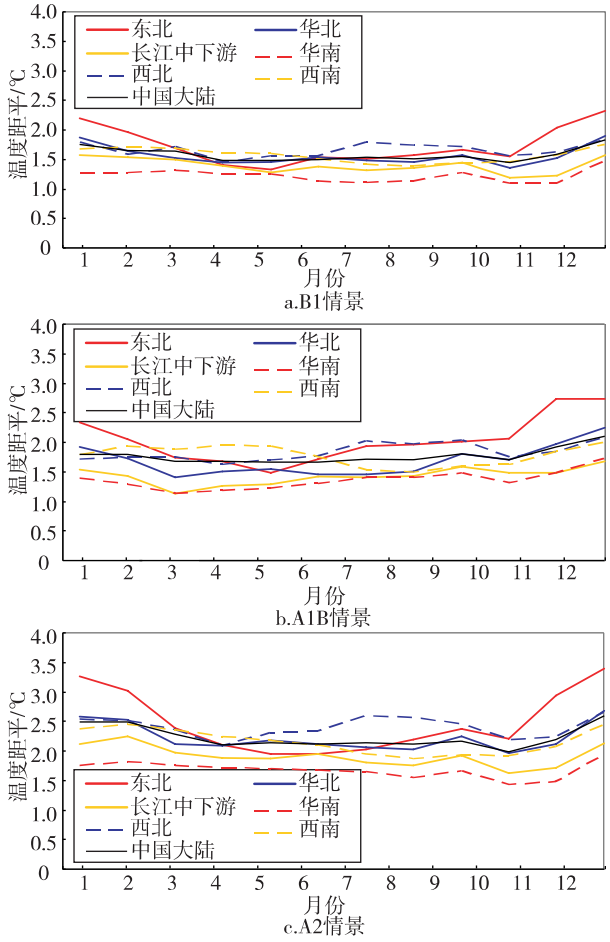


图4 21世纪区域月平均地面气温距平变化曲线(相对于1980—1999年)

Fig. 4 Monthly mean surface air temperature departure in sub-regions(relative to 1980—1999)



© 1994-2011 China Academic Journal Electronic Publishing House. All rights reserved. http://www.cnki.net

北升温的季节变化较其他地区明显，华南地区升温的季节差异较小. 大部分区域冬季升温幅度明显高于其他季节，个别区域例外，如西北地区在 3 种排放情景下 6—9 月的升温幅度均高于其他月份. 需要指出的是，考察 21 世纪前期、中期、后期各区域平均气温变化的季节变化（图略）发现，冬季、夏季增温幅度的差异逐渐增大，即冬季增温越来越明显于夏季，因此，未来气温的年较差将呈减小趋势.

图 5、6 分别给出了 21 世纪 20 年代和 40 年代东亚地区年平均地面气温的空间变化图. 可见，3 种排放情景下地面气温距平场等值线呈经向分布，高纬度地区增温幅度明显高于低纬度地区，这一特征

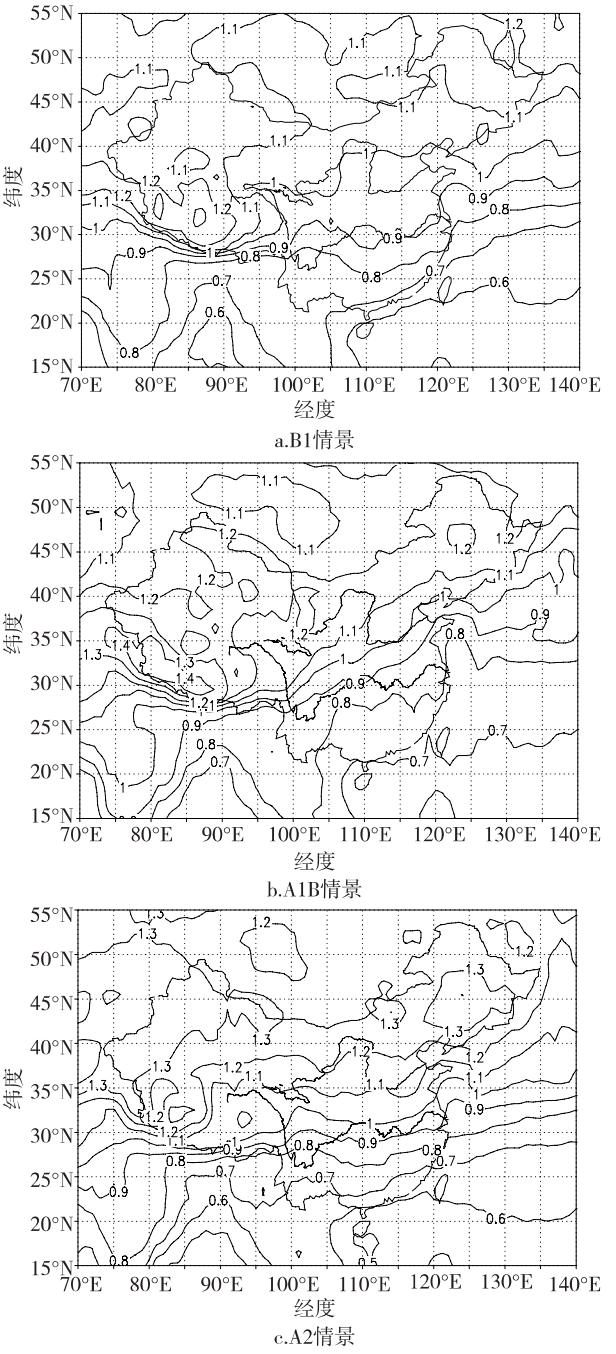


a.B1情景

b.A1B情景

c.A2情景

**图 5　21 世纪 20 年代年平均地面气温变化**
**（相对于 1980—1999 年；单位：℃）**

Fig. 5　Surface air temperature changes in 2020s
(relative to 1980—1999; unit: ℃)

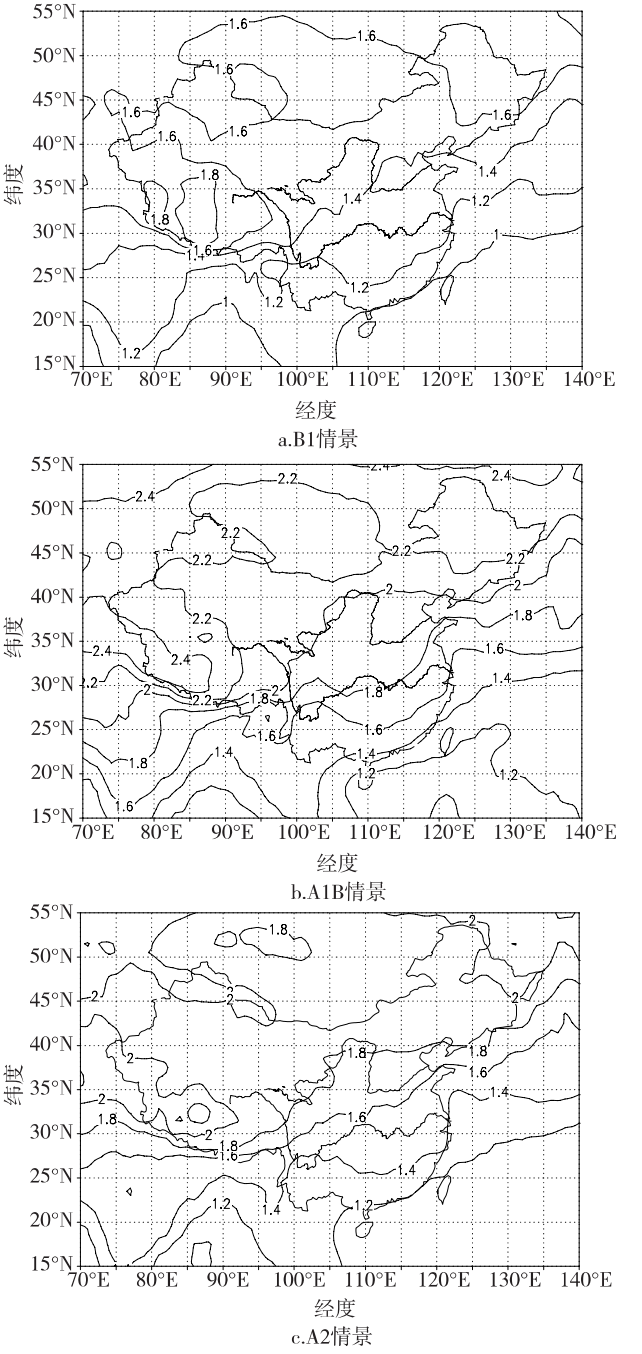


a.B1情景

b.A1B情景

c.A2情景

**图 6　21 世纪 40 年代年平均地面气温变化**
**（相对于 1980—1999 年；单位：℃）**

Fig. 6　Surface air temperature changes in 2040s
(relative to 1980—1999; units: ℃)



© 1994-2011 China Academic Journal Electronic Publishing House. All rights reserved.　http://www.cnki.net

与 IPCC AR4 的结论相一致. 21 世纪前期(2020 年前)不同情景之间升温值差别较小,黄河流域升温范围约 1.0~1.2 ℃,长江流域地区约为 0.8~1.0 ℃,华南地区略低,青藏高原地区升温较显著,新疆天山以北地区升温幅度高达 1.3 ℃. 不同季节之间温度变化存在较明显差异(图略). 冬季 3 种情景下较普遍的特征是:除黄河以南地区温度变化与年平均一致外,东北地区、华北北部地区升温幅度较年平均偏高,东北地区最高升温值可达 1.8 ℃,西部地区较年平均偏低,但夏季则表现为西部地区升温较为明显. 21 世纪 40 年代 3 种排放情景下中国大陆地面气温增值普遍在 1 ℃以上,高、低纬之间升温差异可高达 1 ℃,显著升温区主要位于东北、西北、西南地区,且不同情景下升温差异较大,B1 情景下升温幅度最小,A1B 和 A2 情景下升温幅度明显增大,高、低排放情景下黄河以北的大部分地区升温幅度达到 2 ℃. 冬季在 A1B 和 A2 情景下黄河流域及其以北地区升温值均达到 2 ℃以上,东北地区最高值可达 2.8 ℃. 夏季升温最明显的地区仍位于高原西北部及新疆地区,最高升温值可达2.4 ℃. 与以往研究相比[21-22],这两个阶段大陆的升温值比 IPCC 第 3 次评估报告(IPCC TAR)中多模式或单模式的结果略偏低. 参加 IPCC AR4 的模式和参加 IPCC TAR 的模式相比在物理过程参数化方案、模式空间分辨率等方面均有较大的改进,相应的情景试验设计也更加合理,因此预估结果的不确定性在一定程度上有所减小.

表 1 给出了 21 世纪前期、中期、末期全球和中国平均地面气温增暖的预估结果. 表 1 中结果为各时段年平均地面气温相对于 1980—1999 年平均的变化值,其中全球预估结果引自 IPCC AR4[1]. 可见,所考察的 3 种排放情景下,中国平均地表增暖幅度均高于 IPCC AR4 给出的最佳估算值. 此处对中国大陆的分析结果与 IPCC AR4 给出的全球结果中一致性的特点是:21 世纪前期,变暖预估受不同排放情景假设或不同模式的敏感性的影响较小,3 种排放情景之间的升温幅度相差较小,全球平均增温范围在 0.64~0.69 ℃,中国为 0.88~0.92 ℃,但是到 21 世纪中、后期,不同排放情景下各区域升温差异逐渐明显,如 2088—2099 年,全球增温范围为 1.79~3.13 ℃,中国为 2.44~4.28 ℃,A2 高排放情景下,气温变化对二氧化碳浓度增加的响应更加显著. 由此可见,中国未来不同时期的升温幅度均高于全球平均. 中国大陆气温变化特征存在较大区域差异,至 2099 年,在 B1、A1B 和 A2 这 3 种排放情景下,各区域平均的温度增幅分别为:东北地区 2.68~5.26 ℃,华北地区 2.46~4.65 ℃,长江中下游地区 2.23~4.10 ℃,华南地区 2.03~3.68 ℃,西北地区 2.70~5.10 ℃,西南地区为 2.56~4.67 ℃. 可见,东北、西北地区与其他区域相比,未来面临地面气温大幅度增加带来的压力更大,可能成为气候变化影响更加脆弱的地区. 以往的研究也对西北地区未来气候变化较为关注[23-24],这些研究结果均揭示了未来西北地区显著的增温趋势,尽管研究中也指出未来西北地区降水量可能增加,但在较大幅度的增温背景下未来该区仍可能面临干旱的威胁.

**表 1 21 世纪全球和中国平均地表增暖预估结果**

Table 1 Projected global and China averaged surface warming in the 21st century

| 时期 | SRES | 全球增暖/℃ | 中国增暖/℃ |
|---|---|---|---|
| 2011—2030 年 | B1 | 0.66 | 0.88 |
| | A1B | 0.69 | 0.90 |
| | A2 | 0.64 | 0.92 |
| 2046—2065 年 | B1 | 1.29 | 1.76 |
| | A1B | 1.75 | 2.52 |
| | A2 | 1.65 | 2.25 |
| 2080—2099 年 | B1 | 1.79 | 2.44 |
| | A1B | 2.65 | 3.71 |
| | A2 | 3.13 | 4.28 |

图 7 给出的单个模式对东北地区 21 世纪前期和后期地面气温的预估结果(其他地区图略)进一步说明:21 世纪前期,不同模式、不同排放情景之间的预估结果差异较小,气温变暖受温室气体排放假设及模式设计的敏感性较小;但随着时间的推移,21 世纪中期(图略)各情景及各单个模式之间的差别开始逐渐增大;到 21 世纪后期(图 7b),B1、A1B、A2 3 种排放情景的升温差异明显增大,不同模式之间最大升温差异也可高达 5 ℃. 这不仅体现了 21 世纪中后期地面气温对温室气体浓度值的响应差异,也揭示了预估结果不确定性的存在. 模式的个体性能及其对温室气体的敏感程度各不相同,其中,GFDL_CM2_1 的预估结果偏高,CSIRO_MK3_0 的预估结果偏低. 为了考察模式之间的差异,本文计算了不同模式结果之间的标准差,以 2011—2030 年为例,东北地区模式间的标准差在 B1、A1B 和 A2 情景下分别为 0.582、0.825 和 0.591 ℃. 由此可见,尽管多模式集合在一定程度可以减小预估结果的不确定性,



© 1994-2011 China Academic Journal Electronic Publishing House. All rights reserved. http://www.cnki.net

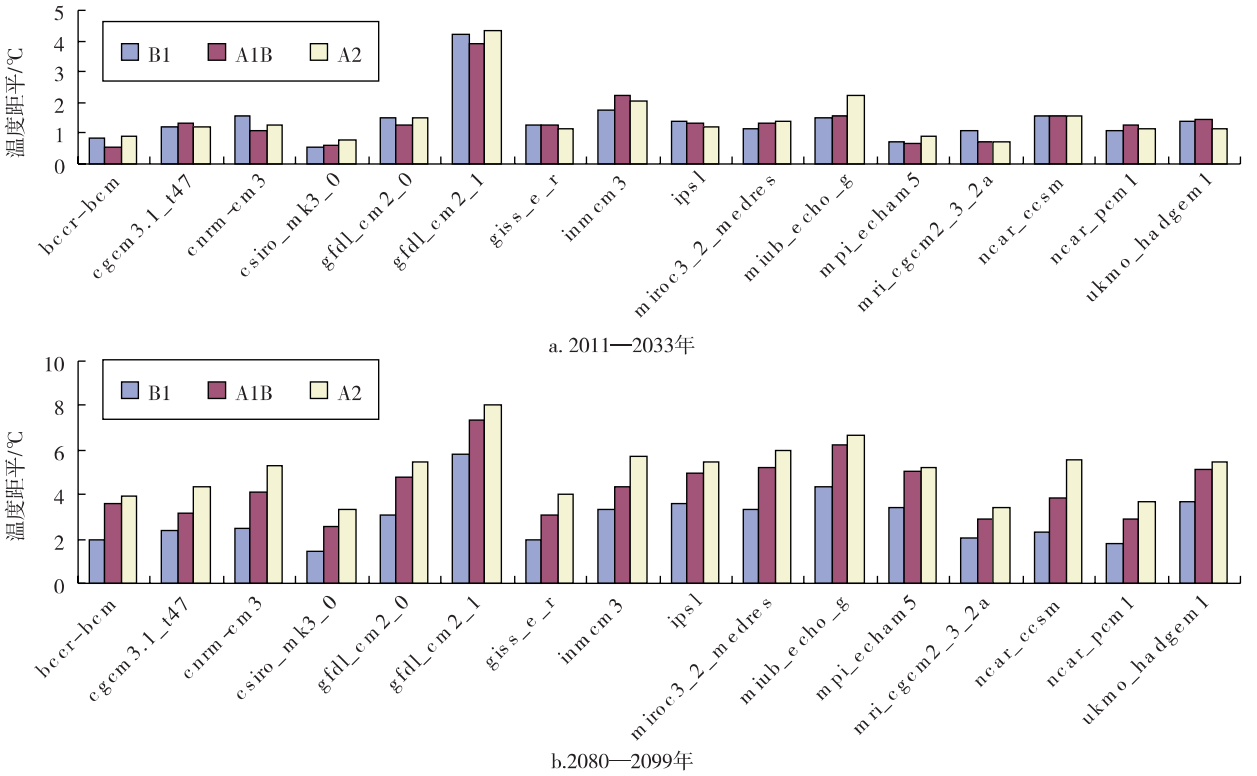


**图 7　单个模式对未来东北地区地面气温的预估结果**

Fig. 7　Projected future temperature departure relative to 1980—1999 from each single model

但单个模式的模拟性能对集合结果的影响仍值得考虑.

## 4　21 世纪不同升温幅度出现的时间分析

IPCC AR4 第 2 工作组报告指出[4],未来全球地表平均气温的持续升高将可能引发全球气候系统的许多变化. 主要表现在淡水资源、生态系统、粮食生产、工业、人居环境、社会、健康等诸多领域. 例如,未来气候变化对亚洲的影响主要包括: 到 2050 年,中亚、南亚、东亚和东南亚地区的淡水供应将趋于紧张,特别在大河流域; 沿海地区,特别是人口密集的南亚、东亚和东南亚三角洲地区,发生洪涝的风险将极大地增加; 伴随着城市化、工业化和经济发展的加速,气候变化将增加对自然资源和环境的压力; 在东亚、南亚和东南亚地区,洪涝和干旱所引发的腹泻的发病率和死亡率将增加. 因此,本节主要分析未来中国大陆平均气温升幅达 2、2.5 和 3 ℃的时间和区域,为气候变化影响研究提供依据.

图 8 给出了 3 种排放情景下未来中国年平均地面气温升温值达 2 ℃的时空分布. 由图 8 可见: B1 情景下,长江以北大部分地区升温值达 2 ℃的时间出现在 2070 年前后,东北、西部地区略偏早,青藏高原地区最早,约在 2055 年升温值达到 2 ℃,华南地区升温最为缓慢,至 2090 年以后达到 2 ℃; A1B 情景下,各区升温值达 2 ℃的时间较 B1 情景明显偏早,中国大陆在 2060 年之前全部达到 2 ℃,西部地区最早,在 2040 年前后即可达到 2 ℃; A2 情景下升温速率在 21 世纪中前期略缓于 A1B 情景,大部分区域升温值到 2 ℃的时间与 A1B 情景相比滞后 5 a,但整个大陆地区升温值仍然在 2065 年前达到 2 ℃. 本文也考察了不同排放情景下地面气温升高 2.5 ℃和 3.0 ℃的时间(图 9 仅给出升温值达 2.5 ℃的情况). 可见,B1 情景下,长江以北地区在未来百年升温值可达到或超过 2.5 ℃,东北地区和高原地区偏早,其余大部分地区在 21 世纪末可超过 2.5 ℃,且 A1B 情景下在 21 世纪不会出现升温幅度超过 3 ℃的情况. A1B 情景下各区升温值达 2.5 ℃的时间与 A2 情景相近,大部分地区出现 2.5 ℃的时间比 A2 情景提前 5 a 左右. 从 3 ℃升温阈值出现时间来看,A1B 情景和 A2 情景下约在 2090 年前整个大陆升温值均达到或超过 3 ℃,A1B 情景下东北地区和青藏高原南部地区更是在 2055 年前后就达到 3 ℃.



© 1994-2011 China Academic Journal Electronic Publishing House. All rights reserved.　http://www.cnki.net

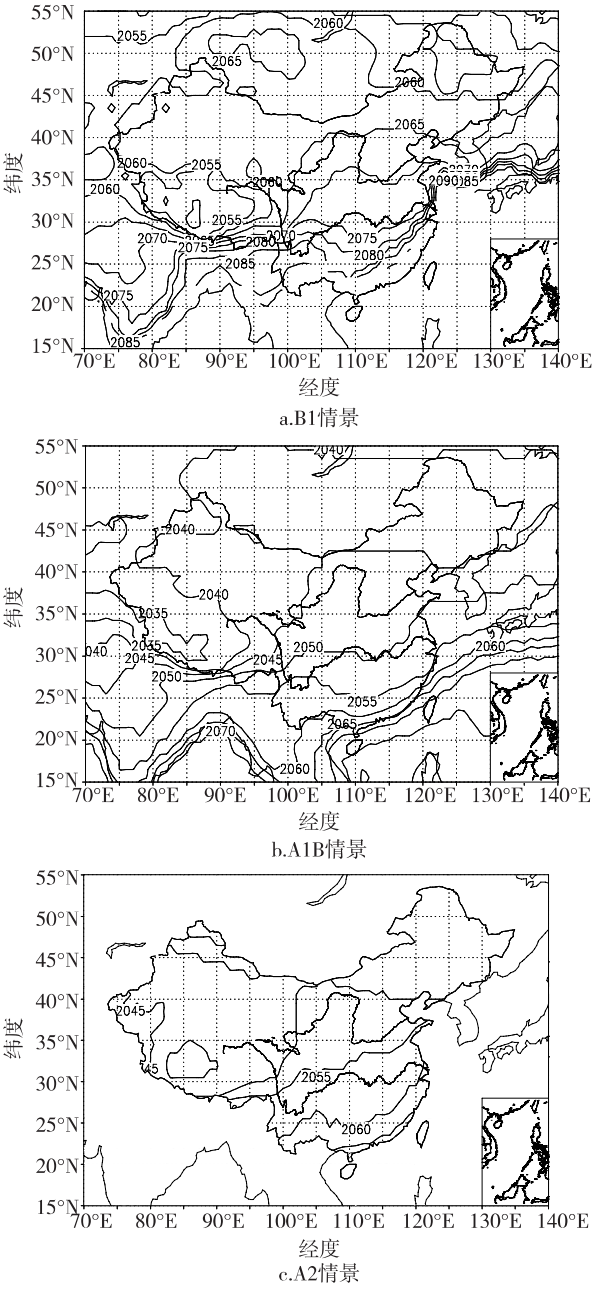


图8 平均地面气温增温值达2 ℃的年份

Fig. 8 The year when mean surface temperature rise by 2 ℃

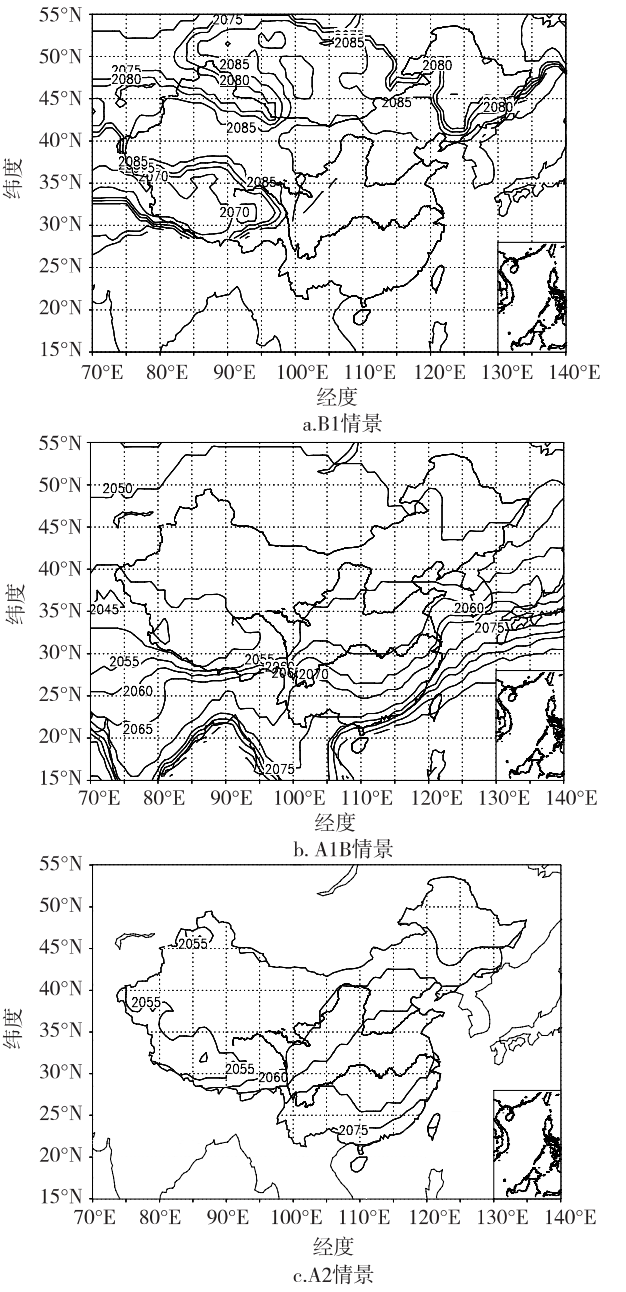


图9 平均地面气温增温值达2.5 ℃的年份

Fig. 9 The year when mean surface temperature rise by 2.5 ℃

表2进一步统计了各区域未来百年升温值分别达到2、2.5、3 ℃的时间,表中符号"—"表示在所研究的时段尚未出现.可见,B1、A1B、A2 3种排放情景下中国大陆平均地面气温升温值达2 ℃的时间分别在2065年、2046年、2051年,东北和西北地区偏早,华北地区、西南地区居中,华南地区最晚,由北至南相差10 a左右,特别是B1情景下,南北差异更明显.B1情景下21世纪中国大陆平均气温升幅不超过3 ℃,但在另2种排放情景下均在21世纪60年代末开始先后达到或超过3 ℃.特别是东北、西北、华北地区在21世纪中期开始面临地面气温的显著增加,成为未来受气温升高影响最敏感的地区.虽然气温增加在一定程度上可能延长这些地区农作物的播种期或生长期,但同时干旱、热浪及农作物害虫等方面的负面影响可能会更大,这些地区未来将可能面临气候变化引发的更加严峻的影响,需要研究未来气候变化影响与区域持续发展之间的联系,提高环境决策水平[25].



© 1994-2011 China Academic Journal Electronic Publishing House. All rights reserved. http://www.cnki.net

表 2　不同排放情景下区域平均地面气温增温值分别达到 2、2.5 和 3 ℃的年份

Table 2　The year of mean surface temperature rise separately by 2, 2.5 and 3 ℃ under 3 emission scenarios

| 情景 | 区域 | 年份 | | |
|---|---|---|---|---|
| | | 增温达到 2.0 ℃ | 增温达到 2.5 ℃ | 增温达到 3.0 ℃ |
| B1 | 东北地区 | 2059 | 2074 | — |
| | 华北地区 | 2067 | 2092 | — |
| | 长江中下游地区 | 2073 | — | — |
| | 华南地区 | 2093 | — | — |
| | 西北地区 | 2064 | 2087 | — |
| | 西南地区 | 2066 | 2091 | — |
| | 中国大陆 | 2065 | 2092 | — |
| A1B | 东北地区 | 2042 | 2050 | 2060 |
| | 华北地区 | 2046 | 2054 | 2069 |
| | 长江中下游地区 | 2051 | 2061 | 2076 |
| | 华南地区 | 2058 | 2072 | 2093 |
| | 西北地区 | 2041 | 2052 | 2063 |
| | 西南地区 | 2047 | 2055 | 2068 |
| | 中国大陆 | 2046 | 2054 | 2067 |
| A2 | 东北地区 | 2047 | 2054 | 2065 |
| | 华北地区 | 2051 | 2062 | 2070 |
| | 长江中下游地区 | 2058 | 2067 | 2078 |
| | 华南地区 | 2063 | 2075 | 2083 |
| | 西北地区 | 2048 | 2058 | 2066 |
| | 西南地区 | 2052 | 2062 | 2070 |
| | 中国大陆 | 2051 | 2061 | 2069 |

## 5　小结

未来中国大陆气温升高对农业、经济、水资源、生态、人体健康等诸多方面有着重要的影响. 文中采用参与政府间气候变化委员会第 4 次评估报告(IPCC AR4)的全球 20 多个气候模式在 20 世纪气候模拟试验和 SRES B1、A1B 和 A2 3 种排放情景下数值模拟结果的集合分析表明，未来中国大陆的气温变化有着明显的时间和空间差异. 主要结论如下.

1) 21 世纪，中国大陆年平均气温呈显著升高趋势，3 种排放情景下至 2099 年平均增温范围为 2.5 ~4.9 ℃，高于全球平均. 东北、西北地区增温幅度较大，华南地区最小. 从季节尺度来看，大部分地区增温幅度都表现为冬季升温明显高于其他季节，年较差呈减小趋势.

2) 21 世纪前期，变暖预估受排放情景假设或模式敏感性的影响较小，不同排放情景和不同模式之间的预估结果一致，中国大陆增温范围为 0.88 ~ 0.92 ℃，但从 21 世纪中期以后这种差异逐渐增大，21 世纪后期增暖范围为 2.44 ~4.28 ℃.

3) 中国大陆平均升温值在 20 世纪 50 年代前后达到 2 ℃，随后，A1B 及 A2 情景下中国大陆气温快速升高，在 21 世纪 60 年代末达到或超过 3 ℃，但区域差异明显，升温值达 2 ℃的时间由北至南在不同排放情景下可相差 10 ~30 a，东北、西北地区将成为未来受气温升高影响最为敏感的地区.

IPCC AR4 中采用的气候模式较第 3 次评估报告已经有较大的发展，但从目前的分析仍可以看到，不同排放情景、不同模式之间的预估结果仍有较大差异，特别是对于 21 世纪中、后期的预估结果，这种差异更加明显. 未来气候变化预估的不确定性问题极其复杂，主要包括来自模式的不确定性(如气候模式对云反馈、海洋热吸收、碳循环反馈等过程的描述差别及模式模拟性能导致的不确定性)以及来自未来温室气体排放情景的不确定性(如对化石燃料排放、固定源排放、流动源排放等温室气体排放量估算的不确定性以及对与温室气体相关的各种政策影响、未来人口增长、经济增长、技术进步、新型能源开发及管理结构变化等影响估算的不确定性)，由此可见，预估问题中不确定性的研究仍需要进一步加强. 另外，由于全球气候模式的空间分辨率还普遍较低，针对中国区域气候的分析还需要考虑使用各种降尺度方法得到更加详细的区域特征.

致谢: 本研究所使用的全球气候模式气候变化预估数据，由国家气候中心研究人员对数据进行整理、分析和惠许使用. 原始数据由各模式组提供，PCMDI (Program for Climate Model Diagnosis and Intercomparison) 负责搜集归类，由 WGCM (JSC/CLIVAR Working Group on Coupled Modelling) 组织下进行，多模式数据集的维护由美国能源部科学办公室提供资助. 在此一并表示衷心感谢!

## 参考文献
References

[1] IPCC. Summary for policymakers of climate change 2007: The physical science basis [M] // Contribution of Working Group Ⅰ to the Fourth Assessment Report of the Intergovernmental Panel on Climate Change. Cambridge: Cambridge University Press, 2007

[2] 秦大河，丁一汇，苏纪兰，等. 中国气候与环境演变: 上卷: 气候与环境的演变与预测 [M]. 北京: 科学出版



© 1994-2011 China Academic Journal Electronic Publishing House. All rights reserved.　http://www.cnki.net

社,2005:507-555
QIN Dahe,DING Yihui,SU Jilan,et al. Climate and environment changes in China: Vol. I: Climate and environment changes in China and their projections [M]. Beijing: Science Press,2005:507-555

[3] Ding Y H,Ren G Y,Zhao Z C,et al. Detection,causes and projection of climate change over China: An overview of recent progress [J]. Advances in Atmospheric Sciences,2007,24(6):954-971

[4] 左洪超,吕世华,胡隐樵. 中国近50年气温及降水量的变化趋势分析 [J]. 高原气象,2004,23(2):238-244
ZUO Hongchao,LÜ Shihua,HU Yinqiao. Variations trend of yearly mean air temperature and precipitation in China in the last 50 years [J]. Plateau Meteorology,2004,23(2):238-244

[5] 邓自旺,闵锦忠,张勇. 中国近50 a气候变化复杂性分析 [J]. 南京气象学院学报,2001,24(2):186-193
DENG Ziwang,MIN Jinzhong,ZHANG Yong. Complexity of climatic change in China in the last 50 years [J]. Journal of Nanjing Institute of Meteorology,2001,24(2):186-193

[6] 秦大河,陈振林,罗勇,等. 气候变化科学的最新认知 [J]. 气候变化研究进展,2007,3(2):63-73
QIN Dahe,CHEN Zhenlin,LUO Yong,et al. Updated understanding of climate change sciences [J]. Advances in Climate Change Research,2007,3(2):63-73

[7] IPCC. Climate change 2007: Impacts,adaptation and vulnerability [M] //Contribution of Working Group Ⅱ to the Fouth Report of the Intergovernmental Panel on Climate Change. Cambridge: Cambridge University Press,2007

[8] 林而达,吴绍洪,戴晓苏,等. 气候变化影响的最新认知 [J]. 气候变化研究进展,2007,3(3):126-131
LIN Erda,WU Shaohong,DAI Xiaosu,et al. Updated understanding of climate change impacts [J]. Advances in Climate Change Research,2007,3(3):126-131

[9] 熊伟,林而达,居辉,等. 气候变化的影响阈值与中国的粮食安全 [J]. 气候变化研究进展,2005,1(2):84-87
XIONG Wei,LIN Erda,JU Hui,et al. A study of the threshold of climate change impact on food production in China [J]. Advances in Climate Change Research,2005,1(2):84-87

[10] 熊伟,居辉,许吟隆,等. 气候变化对中国农业温度阈值影响研究及其不确定性分析 [J]. 地球科学进展,2006,21(1):70-76
XIONG Wei,JU Hui,XU Yinlong,et al. The threshold of temperature increase due to climate change for Chinese agriculture and its uncertainties [J]. Advances in Earth Science,2006,21(1):70-76

[11] 刘奇勇,郑景云,葛全胜. IPCC关于水资源风险的评估综述 [J]. 安徽农业科学,2008,26(32):14267-14270
LIU Qiyong,ZHENG Jingyun,GE Quansheng. IPCC assessment on the risk of water resource [J]. Journal of Anhui Agricultural Sciences,2008,26(32):14267-14270

[12] Sun Y,Solomon S,Dai A,et al. How often does it rain [J]. Journal of Climate,2006,19:916-934

[13] 张莉,丁一汇,孙颖. 全球海气耦合模式对东亚季风降水模拟的检验 [J]. 大气科学,2008,32(2):261-276
ZHANG Li,DING Yihui,SUN Ying. Evaluation of precipitation simulation in east Asian monsoon areas by coupled ocean-atmosphere general circulation models [J]. Chinese Journal of Atmospheric Sciences,2008,32(2):261-276

[14] 孙颖,丁一汇. IPCC AR4气候模式对东亚夏季风年代际变化的模拟性能评估 [J]. 气象学报,2008,66(5):765-780
SUN Ying,DING Yihui. Validation of IPCC AR4 climate models in simulating interdecadal change of East Asian summer monsoon [J]. Acta Meteorologica Sinica,2008,66(5):765-780

[15] 江志红,陈威霖,宋洁,等. 7个IPCC AR4模式对中国地区极端降水指数模拟能力的评估及其未来情景预估 [J]. 大气科学,2009,33(1):109-120
JIANG Zhihong,CHEN Weilin,SONG Jie,et al. Projection and evaluation of the precipitation extremes indices over China based on seven IPCC AR4 coupled climate models [J]. Chinese Journal of Atmospheric Sciences,2009,33(1):109-120

[16] Jiang D B,Wang H J,Lang X M. Evaluation of East Asian climatology as simulated by seven coupled models [J]. Advances in Atmospheric Sciences,2005,22(4):479-495

[17] Zhou T J,Yu R C. Twentieth-century surface air temperature over China and the global simulated by coupled climate models [J]. Journal of Climate,2006,19(22):5843-5858

[18] 姜大膀,张颖,孙建奇. 中国地区1~3 ℃变暖的集合预估分析 [J]. 科学通报,2009,54(24):3870-3877
JIANG Dabang,ZHANG Ying,SUN Jianqi. Ensemble projection of 1-3 ℃ warming in China [J]. Chinese Science Bulletion,2009,54(24):3870-3877

[19] 刘敏,江志红. 13个IPCC AR4模式对中国区域近40 a气候模拟能力的评估 [J]. 南京气象学院学报,2009,32(2):256-268
LIU Min,JIANG Zhihong. Simulation ability evaluation of surface temperature and precipitation by thirteen IPCC AR 4 coupled climate models in China during 1961—2000 [J]. Journal of Nanjing Institute of Meteorology,2009,32(2):256-268

[20] 江志红,张霞,王冀. IPCC-AR4模式对中国21世纪气候变化的情景预估 [J]. 地理研究,2008,27(4):787-799
JIANG Zhihong,ZHANG Xia,WANG Ji. Projection of climate change in China in the 21st century by IPCC-AR4 Models [J]. Geographical Research,2008,27(4):787-799

[21] 姜大膀,王会军,郎咸梅. SRES A2情景下中国气候未来变化的多模式集合预测结果 [J]. 地球物理学报,2004,47(5):776-784



© 1994-2011 China Academic Journal Electronic Publishing House. All rights reserved. http://www.cnki.net

JIANG Dabang, WANG Huijun, LANG Xianmei. Mutimodel ensemble prediction for climate change trend of China under SRES A2 scenario [J]. Chinese Journal of Geophysics, 2004, 47(5): 776-784

[22] 许吟隆. 中国 21 世纪气候变化的情景模拟分析 [J]. 南京气象学院学报, 2005, 28(3): 323-329
XU Yinlong. Analyses on scenario simulations of the 21st century climate change in China [J]. Journal of Nanjing Institute of Meteorology, 2005, 28(3): 323-329

[23] 徐影, 丁一汇, 赵宗慈, 等. 我国西北地区 21 世纪季节气候变化情景分析 [J]. 气候与环境研究, 2003, 8(1): 19-25
XU Ying, DING Yihui, ZHAO Zongci, et al. A scenario of seasonal climate change of the 21st century in Northwest China [J]. Climatic and Environmental Research, 2003, 8(1): 19-25

[24] 徐影, 丁一汇, 李栋梁. 青藏地区未来百年气候变化 [J]. 高原气象, 2003, 22(5): 451-457
XU Ying, DING Yihui, LI Dongliang. Climatic change over Qinghai and Xizang in 21st century [J]. Plateau Meteorology, 2003, 22(5): 451-457

[25] 殷永元. 全球气候变化对区域持续发展的影响: 研究方法探讨 [J]. 南京气象学院学报, 1999, 22(增刊 1): 465-471
YIN Yongyuan. Impact of global climate change on regional sustainable development: Discussion of research method [J]. Journal of Nanjing Institute of Meteorology, 1999, 22(sup1): 465-471

# Future surface air temperature changes in China under different greenhouse gas emission scenarios

YAN Guanhua[1,2] LI Qiaoping[3] XING Chao[2]

1 School of Atmospheric Sciences, Nanjing University of Information Science & Technology, Nanjing 210044

2 China Meteorological Administration Training Center, Beijing 100081

3 National Climate Center, China Meteorological Administration, Beijing 100081

**Abstract** Based on IPCC AR4 outputs simulated by multi-model for 20th century and future projection under SRES B1, A1B and A2 green emission scenarios, the surface air temperature changes in the 21st century are analyzed. It is revealed that the surface temperature presents different spatial and temporal features over China. Annual mean temperature will rise by 2.5-4.9 ℃ at the end of the 21st century under 3 Scenarios, and the enhancement magnitude is larger than global mean. In addition, the warming magnitude in winter will be larger than in the other seasons, the annual range of temperature is expected to decrease in the future. The projection results are consistent between the different emission scenarios and models in the first half of the 21st century, with the warming magnitude being 0.88-0.92 ℃. However, the projected temperature becomes more sensitive to the scenarios and models since mid of the 21st century. By the end of the 21st century, the temperature will increase by about 2.44-4.28 ℃. Relative to 1980—1999, annual mean temperature over China will rise by 2 ℃ around 2050, then the temperature will increase more quickly under SRES A1B and A2 scenarios and reach or exceed 3 ℃ at the end of 2060s. The temperature changes differently with regions, and the year of temperature rise above 2 ℃ in Southern regions will be later for about 10-30 years than that in Northern regions over China. Affected by the rising temperature, Northeast China and Northwest China will be the most sensitive regions in the future.

**Key words** greenhouse gases emission; surface air temperature; change features



© 1994-2011 China Academic Journal Electronic Publishing House. All rights reserved. http://www.cnki.net

# 动态最优多因子组合的华北汛期降水模式误差估计及预报*

杨 杰[1)2)] 王启光[1)] 支 蓉[3)] 封国林[2)3)†]

1)(兰州大学大气科学学院,兰州 730000)

2)(中国科学院大气物理研究所东亚区域气候-环境重点实验室,北京 100029)

3)(国家气候中心,中国气象局气候研究开放实验室,北京 100081)

(2010 年 6 月 22 日收到;2010 年 7 月 15 日收到修改稿)

利用国家气候中心季节预报 1983—2009 年 27 年模式预报结果,结合 74 项环流指数及美国国家海洋局和大气管理局提供的 40 个气候指数和美国气候预报中心实际降水分析资料,采用资料诊断分析和数值模拟实验相结合的方法,通过多因子的历史相似信息提取预报相似年,获得预报场的误差订正项. 在这一订正思路的基础上,考虑前期关键影响因子的选取、多因子组合的优化配置,构建适用于不同预报年的区域动力-统计模式预报误差订正方案. 以华北为例,探索多因子最优组合的多元客观相似判据,发展基于多因子动力-统计模式预报误差的动态订正新技术,改善华北夏季降水预报效果,提高预报技巧. 通过 2005—2009 年独立样本回报结果表明,动态最优多因子组合相似订正方法距平相关系数评分相对于系统订正方法有着显著的提高,该订正方案对华北地区的夏季降水预测有着很好的业务前景,具有重要的应用价值,即将投入业务运行.

**关键词:** 关键因子集, 模式误差估计, 汛期降水, 预测

**PACS:** 92.60.Wc

## 1. 引 言

洪涝和干旱是影响我国最大的两种主要气候灾害,50% 以上的自然灾害都是由旱、涝引起[1—3]. 随着气候系统的不确定性演变,包括异常干旱、破纪录洪灾、超低温雨雪冰冻等极端气候事件发生的频率和强度不断加剧,对国民经济影响巨大[4—7]. 如 2006,2007 年夏季我国重庆地区分别遭受大旱和大涝,2009 年东北夏季低温,2009—2010 年西南五省夏冬春三季持续干旱,造成了前所未有的损失. 因此,提高短期气候预测、预警以及应急决策能力是保障国家安全、发展经济和防灾减灾的现实需要[8—10]. 近代以来华北地区水资源贫乏问题变得越来越严重,如何有效利用和规划该地区的有限的水资源是目前十分迫切的一个科学问题[11—13]. 华北地区旱涝时空分布的不均匀性带来的水资源利用的不确定性严重制约了华北地区社会和经济发展,自然生态系统和环境也在不断恶化. 解决这些问题的前提仍然是如何准确预测夏季旱涝的分布趋势,只有掌握了空中水资源活动规律,才能从根本上缓解华北地区的水资源匮乏,确保该地区的可持续发展,这也是气象科技工作者历来关注的科学问题[14,15].

主导华北地区夏季降水的气候背景十分复杂,一方面由于华北处于季风活动的北缘,汛期降水主要受夏季风活动等影响;另一方面,该地区还受中高纬西风环流系统影响,这些复杂因素导致预测每年华北夏季的旱涝趋势难度很大[16,17]. 因此,单纯的统计学方法和动力学方法都不能有效开展该地区的短期气候预测. 丑纪范[18,19]认为,统计学方法虽善于利用大量历史资料,但其自身局限性使它并不能成为主要的预测工具;而动力学方法虽然善于运用物理规律,但同样面临着模式物理过程不够准

* 公益性行业(气象)科研专项基金(批准号:GYHY200806005)、国家自然科学基金(批准号:40875040,40930952)和国家科技支撑计划(批准号:2007BAC29B01,2009BAC51B04)资助的课题.

† 通讯联系人. E-mail:fenggl@cma.gov.cn

©2011 中国物理学会 Chinese Physical Society 

确和初值不精确的问题. 解决的关键是将两者有机结合,取长补短,通过充分利用历史统计信息达到修正动力学方法积分过程中的系统性误差. 如此一来,可以从很大程度上避免直接进行数值模式动力框架的大幅修改,减少对初值同化方案和物理参数的复杂处理,以相对较小的代价达到相同的模式预测效果. 这种思想的核心是在动力模式预报基础上结合物理统计方法充分利用历史资料对模式预报结果加以修正,目前已成为备受关注的研究方向. 在国内外该研究已取得了一定的进展[20—23],包括相似动力方法[24—27]、预报误差订正以及模式后处理[28]、基于大气自记忆原理的方法[29—31]等, 使得短期气候预测发展很快并已初步建立了适合中国条件的短期气候预测业务动力模式系统[32,33],但业务应用水平仍然不高,仍需进一步提升[34—36].

本文从动力和统计相结合角度出发,利用1983—2009 年美国气候预报中心组合降雨分析资料(Climale Prediction Center Mergod Analysis of Precipitation, CMAP)和国家气候中心(National Climate Center, NCC)季节/年际预测业务系统模式回报的资料挖掘历史相似信息,以单因子交叉检验的距平相关系数(anomaly correlation coefficient, ACC)确定关键影响因子集,建立适用于华北夏季降水的动态相似因子库,通过数值模拟与 ACC 检验获取相似因子配置方案. 由于影响因子具有周期性动态变化,不同因子影响季节不同,为了兼顾不同预报时段动态因子的最优组合,以 4 个历史最相似年的信息为主订正预报结果,形成最终的动力-相似预报修正方案,达到改善华北地区夏季降水预报效果的目的.

## 2. 资料和方法

### 2.1. 资料

本文的研究资料来自三个方面:

1)美国气候预报中心组合降雨分析资料的1983—2009 年夏季总降水量, 水平分辨率为 2.5°×2.5°;

2)国家气候中心提供的季节/年际预测业务系统模式预报的历史回报产品中的逐月降水场资料,经纬度格点 2.5°×2.5°,共 144×73 个格点;

3)国家气候中心气候系统诊断预测室提供的74 项环流特征量和美国国家海洋局和大气管理局(National Oceanic and Atmospheric Administration, NOAA)提供的 40 项气候指数.

### 2.2. 模式预报误差估计原理[37,38]

实际大气的准确数值模式表示为

$$\frac{\partial\psi}{\partial t} + L(\psi) = E(\psi),$$
$$\psi(\boldsymbol{x}, t_0) = \psi_0(\boldsymbol{x}), \tag{1}$$

其中 $\psi(x,t)$ 为模式预报变量, $\boldsymbol{x}, t$ 分别表示空间坐标向量和时间, $L$ 是 $\psi$ 的微分算子. $t_0$ 为初始时刻, $\psi_0$ 为初值. $t > t_0$ 时刻的值可由初值进行数值积分得到 $\psi$ 或者其泛函 $M(\psi)$. $E$ 为模式的误差算子,反映模式中未知的总误差项, 即模式预报误差. 将预报场 $\psi$ 看作历史相似场 $\tilde{\psi}$ 与叠加在相似场上的小扰动 $\psi'$ 之和,即 $\psi = \tilde{\psi} + \psi'$,并且将上述方程进行积分推导可得到一个动力相似预报方程

$$\hat{M}(\psi_0) = M(\psi_0) + \check{M}(\tilde{\psi}_j) - M(\tilde{\psi}_j), \tag{2}$$

该方程引入历史相似对应的预报误差信息估计当前的模式预报误差,即在模式预报结果的基础上添加了一个历史相似误差订正项

$$\hat{E}(\tilde{\psi}_j) \xrightarrow{\text{估计}} \hat{E}(\psi_0), \tag{3}$$

该式将动力模式预报改进问题转化为模式误差的估计问题,模式的预报即包含误差预报.

## 3. 模式误差订正方法

### 3.1. 华北地区气候背景及系统误差订正方法

华北地区属于半湿润、半干旱大陆性季风气候区,受东亚季风的影响,降水量年内分配很不均匀,多年平均的逐月降水量呈单峰型分布,1—7 月份呈逐步递增趋势,8 月以后逐渐减少,80% 左右集中在6—9 月,且往往集中在几次强降雨过程,降雨相对集中使流域洪水具有峰值高、峰型陡、一次性洪量大的特点[39]. 华北雨季主要集中在 7 月和 8 月,所以夏季降水的多寡程度将直接影响着华北地区全年的旱涝分布. 降水量年际变化很大,丰水年可达1000 mm 以上,枯水年仅 200 mm 左右. 1951 年以来,1979 年以前为多雨时段,1979 年以后处于少雨的时段. 总体来说,目前仍处于少雨的气候背景. 图1 给出了 1983—2009 年华北地区夏季降水量的年际变化,对这 27 年的实际降水量进行聚类分析,结

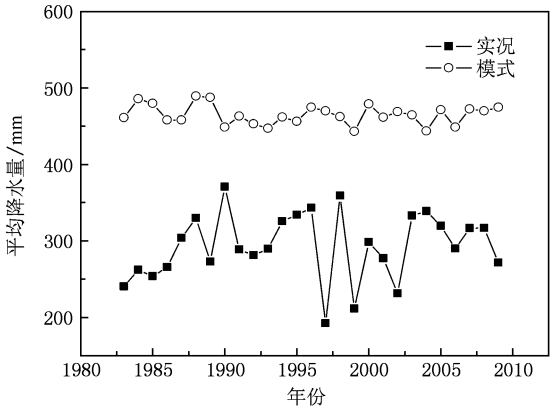


图 1 华北近 27 年夏季平均降水量变化及模式原始预报结果

果显示,相对 27 年夏季降水情况而言,降水偏少年为 1983,1985,2002 年;降水偏多年为 1988,1995,1996,1998,2003,2004 年;降水异常偏少年为 1997,1999 年;降水异常偏多年为 1990 年. 对比 1983—2009 年华北地区的夏季降水量变化趋势与模式预报结果,可以发现在整个华北地区处于少雨的气候背景下,该地区每年的实际降水量都要比模式原始的预报结果小很多,且实际降水量的年际变化很明显,最大的年降水量为 370 mm,最小的年降水量为 192 mm,二者之间相差达到约 180 mm,而模式预报结果年际变化很小,基本上结果都是在 470 mm 上下波动. 可见模式的原始预报结果与实况之间的误差较大,若无适当订正,将失去应有的参考价值.

模式原始结果订正最直接的是预报误差订正,如能够通过统计方法较为准确地得到模式在预报年的预报误差场,将预报误差场与模式原始结果进行叠加即可对预报结果有很好的改进. 如前所述,降水预报问题就转换成模式预报误差的估计问题. 最简单的预报误差订正方法是对统计历史资料中已知的历年模式预报误差取平均,以多年预报误差的平均值作为预报年的模式原始预测结果与实际降水的误差来对预测结果进行订正,即系统误差订正方法. 图 2(a),(b)分别给出了 1983—2009 年交叉检验的系统误差订正后的夏季降水的预报结果以及相应的 ACC 评分情况,可以看出经过系统订正后的预报结果较模式原始结果有了较大的提高,预报误差也有很大的改进,交叉检验系统订正后预报结果的所有年份的距平相关系数平均值为 0.15. 结合图 1 可以看出,系统误差订正结果与实际观测误差异常大的年份为:1985,1992,1997,1999,2002 年,而其中 1992,1997,1999,2002 年都对应了华北地区的降水偏少或异常偏少. 我们可以看出系统订正后的预报效果仍然不是十分理想,特别是对于一些夏季降水关键的异常年份,例如 1997,1999 这两个降水异常偏少年,其预报结果的 ACC 都只有 −0.7左右,几乎是给出了完全相反的预报结果. 因此,模式的系统订正结果对于降水偏少年的预报效果较差,对降水偏多的预报效果则相对较好. 综上所述,系统订正模式预报结果的方法是比较简单、粗糙的,对每个预报年份缺乏一定的针对性,使得预报准确率仍处于较低的水平;提高预报准确率,需要用具有一定技巧性的统计方法结合模式,来对预报年的预报误差进行有针对性的、较准确的订正.

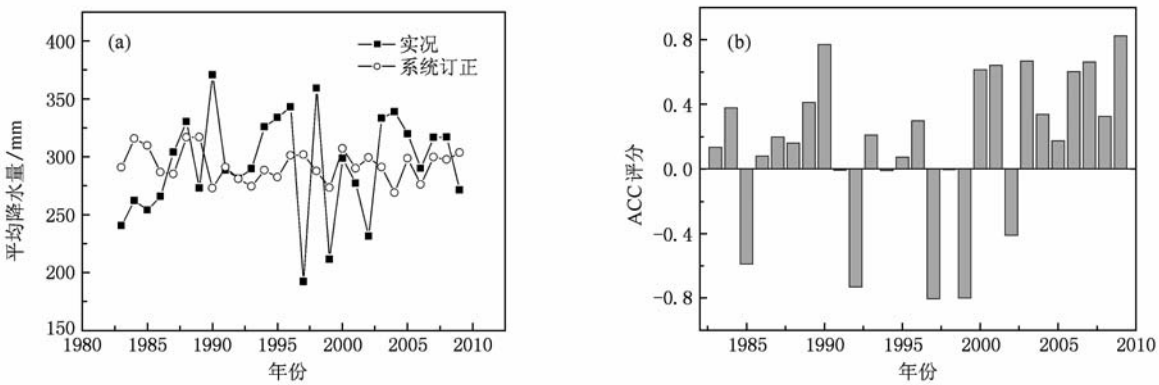


图 2 华北近 27 年夏季降水 (a)系统订正预报结果,(b)ACC 评分

### 3.2. 动力-相似订正

短期气候预测中应用相似的概念由来已久,这是由于继天气过程的相似发展之后,未来一段时间内也往往继续出现相似的天气过程. 早在 20 世纪 40 年代,前苏联就在长期天气预报方面提出过两个

自然天气季节的相似条件,这些相似条件在理论上是严谨的,但在实际工作中很难完全满足[40]. 相似预报的成效在很大程度上取决于相似条件选取得是否客观合理,因此相似预报的关键问题在于历史相似的选取. 由于数值模式的初值条件的自由度非常大,要在历史资料中找到与其合适的相似,在现有资料条件下几乎是不可能的,但对某一特定区域而言,并不是所有前期环境变量都有同等重要的作用,都存在着前期关键变量,但是要想通过统计方法从初始时刻场中确定关键变量也是不太现实的. 由于大气是不断地向外强迫适应的,所以前期外强迫的异常信号会导致数值模式初边值的异常. 统计预报方法正是通过历史资料建立起前期外强迫异常与未来异常的联系,那么就可用统计预报中前期的环境变量选取历史相似,在缩小了自由度的同时又抓住了关键的历史相似信息.

### 3.3. 区域关键因子的选取

汛期降水是由多种影响因子综合作用的结果,对中国各个区域都存在各自占主导作用并直接影响区域夏季降水多寡的前期关键因子. 例如,副高是直接影响中国夏季降水的天气系统. 研究表明,在副高、海温、积雪、阻高、季风等影响长江流域夏季降水的因子中,副高与降雨的对应关系最好,作用最为显著. 姚愚和严华生[41]研究了副高的5种指数对中国降雨的影响,发现副高北界和脊线位置主要影响汛期雨带南北位置的变化,副高加强西伸时则有利于中国大部分地区的降水,强度指数和面积指数与局部地区降水的多寡有关. 其他研究也表明,副高的形状、强弱和位置变动与我国大部地区主汛期旱涝趋势有密切联系. 西太平洋副热带高压和阻塞高压形势、西风急流、大陆副热带高压等因子对于华北夏季降水量的多少具有很好的指示意义,也为选择关键的前期相似因子提供了可靠的依据.

大量研究表明,前冬海温对夏季副高的形状、位置和强弱等特征有显著影响,是具有前兆意义的预测信号,可以为相似预报方法提供参考,检验在影响区域降水的海温关键区域是否真的存在相似之处. 我们给出了华北夏季降水与前冬平均海温的相关,如图3所示. 从图3中可以看出,华北的夏季降水与前冬印度洋、赤道中东太平洋海温以及加勒比海域的海温呈现出显著的正相关,即前期赤道印度洋及阿拉伯海域和孟加拉湾的海温如果处于异常偏冷状态,而印度洋南部是偏暖分布时,则华北地区夏季降水具有整体上偏少的倾向,反之亦然. 冬季印度洋海温异常对预测未来华北地区降水具有较明确的指示意义,所以可以用海温场来检验利用关键因子选择的历史相似年与预报年之间在特定的关键区域是否真的相似.

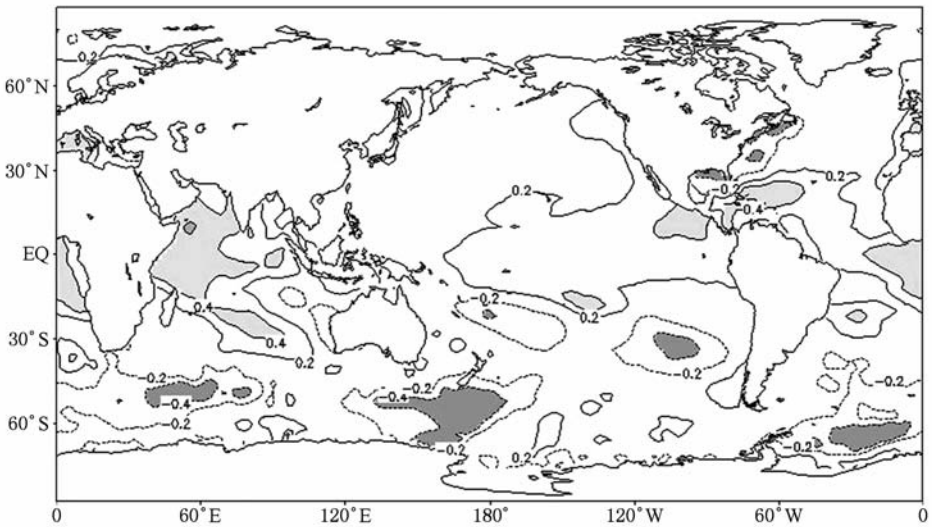


图3 华北地区夏季降水与前冬平均海温的相关

利用相似预报方法对预报年选取相似误差场时,从国家气候中心气候系统诊断预测室提供的74项环流特征量以及NOAA提供的40项气候指数(由于环流特征量是逐月数据,对于同一个指数12个月的数值看作12个独立的前期影响因子,因此我们一共可以得到1368个前期因子)中筛选出一部

分对华北地区有物理意义并且可以对模式的预报误差做很好订正的因子作为关键因子. 首先,对前期的预报因子与华北汛期降水量进行相关性检验,初步提取出对华北夏季降水影响较大的因子,在相关系数都通过95%可信度检验的环流特征量中寻找前期关键因子,对相关性高的因子还需进行进一步的筛选,因为有的因子虽然与华北地区的夏季降水有很好的相关,但模式结果对其没有很好的响应,从而不能对预报误差进行估计. 因此,还要通过预报误差订正回报结果的评分,提取出评分较高的因子,将这些因子作为模式预报的前期关键因子,在进行相关性检验之后,对通过相关性检验的因子进行单因子相似误差订正交叉检验回报评分,即以每个因子作为选相似的依据,将欧氏距离作为选取相似年的条件,计算预报年中因子强度与之前每年强度的欧氏距离选取相似,距离越短则越相似,为了保证相似质量,选取最接近的4个相似年进行误差线性估计,以此确定预报年的相似误差,通过该方法可筛选出能够提高模式预报结果准确率的关键因子.

选择合适的因子进行相似误差的订正对于提高预报水平的效果是比较明显的. 我们这里以交叉检验平均ACC最高的东太平洋涛动指数为例,给出了预报年前期8月东太平洋涛动指数进行华北汛期降水相似误差订正的27年ACC及均方根误差,如图4所示. 由图4可得,总体而言单因子(8月东太平洋涛动指数)相似订正的方法较系统订正方法有一定的改进,提高较为明显的年份是1992,2001—2005年,其中2002年为降水偏少年,2003,2004年为降水偏多年,其他为降水正常年,这几个年份中的8月东太平洋涛动指数都是处于偏小的状态,通过对ACC有一定提高的年份以及图4(c)中8月东太平洋涛动指数的年际变化进行分析研究,可以发现当8月东太平洋涛动指数偏小时,利用该因子相似订正的方法效果较好,对于8月东太平洋涛动指数强度较大时订正效果则并不明显,反而会起到相反的作用. 可以看到,由于近几年该因子变小的趋势,所以近几年的相似订正效果相对系统订正基本都有一定的提高,对于降水异常年的预报结果仍然不理想,对关键的降水年份例如1997和1999年两个异常年,订正结果相对系统订正提高非常有限,没有给出很好的预报结果. 此外,由于其他环境要素的影响以及因子对于区域降水影响的年际变化,单个因子不能保持每年都和区域的降水有着很好的对应关系,不能保证预报结果都要优于系统订正的结果,且从图4(b)均方根误差的改进也是非常有

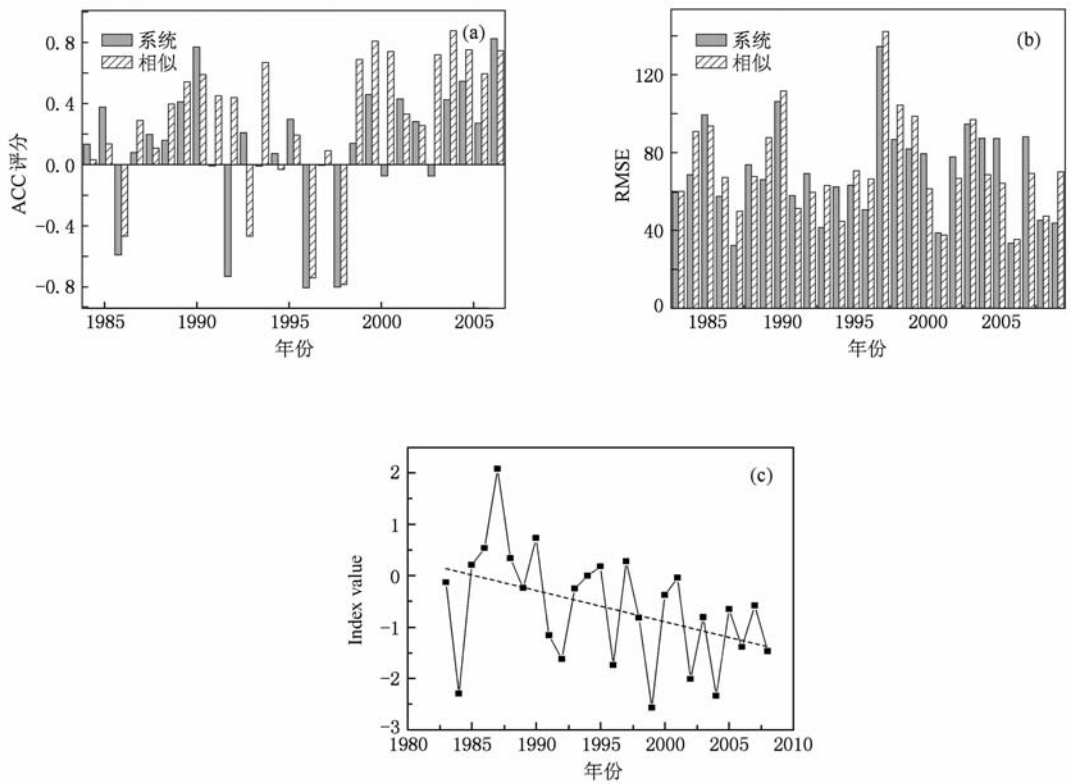


图4 系统订正与单因子(8月东太平洋涛动)相似订正的近27年变化趋势 (a)ACC评分,(b)均方根误差,(c)8月东太平洋涛动指数

限的,在部分年份的预报结果还要低于系统订正方法的结果. 综上所述,单因子相似误差订正也存在着一定的局限性:由于汛期降水是多种因素综合作用的结果,只用单因子选择相似就忽略了其他因子对于华北地区的影响,单个因子不可能完全反映出预报年前期环境变量场的整体信息,因此利用单个影响因子的前期信号作为相似年选取依据有时候会比较片面,在因子对华北地区降水影响较强的年份选取的相似年与预报年的相似度较好,但在该因子作用较弱时,选取的相似年可能会出现较大的偏差.

由此可见,单因子选取相似历史的方法对预报效果的订正和提高仍是非常有限的,且因子对于华北地区的降水影响可能存在着年代际的变化,使得单因子相似订正不能够保证对每年的预报效果都有提高,只对该因子信号影响较大的年份有着较好的订正,对于因子影响较弱的年份则效果并不理想. 因此,在利用影响因子的前期信号选取历史相似年时,必须同时考虑多个影响因子的作用,将这些因子进行组合以后得到的前期综合作用信号作为选取相似年的最佳判据.

### 3.4. 最优多因子组合相似判据的配置

对于多因子组合相似判据的配置,由于前期环境场变量的自由度很大,导致计算量非常大,另外,多因子进行组合配置时的噪声问题以及因子间可能存在的自相关会使得相似订正误差出现非线性增长. 研究表明,通过正交经验函数(empirical orthogonal function, EOF)分解方法能有效压缩自由度同时消除部分噪声影响,从而降低前期环境场的自由度. 因此,对多因子组合构成的变量场 $\boldsymbol{X}_{m\times n}$ 进行 EOF 分解,即

$$\boldsymbol{X}_{m\times n} = \boldsymbol{V}_{m\times n}\boldsymbol{T}_{m\times n}, \tag{4}$$

其中, $\boldsymbol{V}_{m\times n}$ 空间函数矩阵, $\boldsymbol{T}_{m\times n}$ 为时间系数矩阵.

通过计算得到每个特征向量 $\boldsymbol{\lambda}_k$ 的方差贡献,即

$$\boldsymbol{R}_k = \boldsymbol{\lambda}_k \Big/ \sum_{i=1}^{m}\boldsymbol{\lambda}_i$$
$$[k = 1,2,3,\cdots,p\ (p < m)], \tag{5}$$

由于前几个主分量的方差贡献已经包含了原变量场的大部分信息,为了进一步压缩相似判据的自由度,我们取累积方差贡献达到 80%,即

$$\boldsymbol{G} = \sum_{i=1}^{p}\boldsymbol{\lambda}_i \Big/ \sum_{i=1}^{m}\boldsymbol{\lambda}_i > 0.8, \tag{6}$$

此时,将得到的主分量时间系数作为相似年的选取依据,进行交叉检验以及多因子独立样本检验的双重检验,以此得到最优的多因子组合配置.

多因子组合中元素个数的变化以及不同因子间的搭配对预报效果也会有很大的影响. 为得到最佳的组合个数以及最佳的因子搭配,首先研究组合中因子个数的变化对于 ACC 的影响,如图 5 所示. 图 5 给出了 1983—2006, 1983—2007, 1983—2008, 1983—2009 年 4 个时段内交叉检验的平均 ACC 随影响因子个数的变化趋势. 图中 1983—2006 指的是对 1983—2006 年时段进行多因子组合交叉检验, 1983—2007 以此类推. 这里分不同时段进行多因子组合交叉检验是因为考虑到影响因子的实测数据是不断更新的,并且部分影响因子对于华北地区汛期降水的影响作用可能存在着年代际的变化,会导致对不同时段进行交叉检验筛选出最佳的因子组合搭配有所差别,因此,有必要考虑多因子组合的配置关系随不同时段的变化,从而可对不同的预报时期因子影响作用的变化进行有针对性的动态最优多因子组合配置.

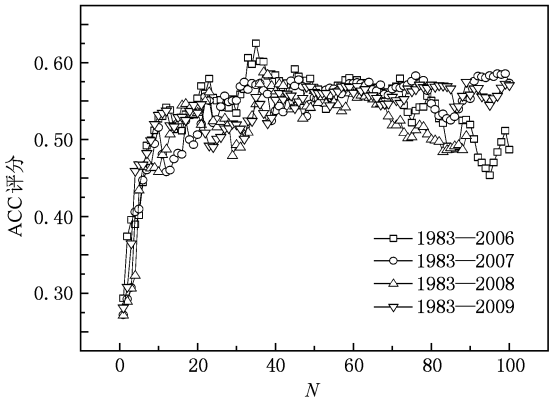


图 5 空间 ACC 评分随影响因子个数变化的敏感性实验结果

从图 5 中可以看出,4 个时段的多因子配置交叉检验 ACC 评分随影响因子个数的变化规律是非常一致的:当组合影响因子个数从 1 个增加至 10 个的过程中,ACC 的提高非常明显,当增加到 10 个以上时,ACC 增幅逐渐减小并趋于稳定,当因子个数进一步增大至 60 个以上时,平均 ACC 都出现了不同程度的减小,但减幅较小. 同时我们也可看到,不同时段内交叉检验得到最终平均 ACC 稳定值之间差别不大,基本在 0.5—0.6 之间,说明在现有的资料条件下,通过相似误差订正后的华北地区模式预报结果可以达到的平均 ACC 上限为 0.6 左右. 因

此,采用多因子组合配置是提高汛期降水预测水平的一个有效途径. 通过上述变化我们也可得到,因子组合个数在增加至 15 个以上时对于 ACC 的提高已经很小,此时 ACC 已经基本达到了上限值,同时考虑到计算量的问题,因此在最优因子组合筛选的时候因子个数在 15 个左右是最优化的. 表 1 分别给出了 1983—2004, 1983—2005, 1983—2006, 1983—2007, 1983—2008 年 5 个时段配置出的 15 个因子的动态最优组合. 考虑到业务应用以及影响因子更新等问题,配置的最优组合中 1 月份因子视为预报年当年前期因子,而 2—12 月份的因子则采用预报年前年因子.

表 1 不同时段配置出的动态最优多因子组合

| 组合 a (1983—2004) | 组合 b (1983—2005) | 组合 c (1983—2006) | 组合 d (1983—2007) | 组合 e (1983—2008) |
|---|---|---|---|---|
| 9 月东太平洋副高面积 | 4 月东太平洋涛动 | 4 月东太平洋涛动 | 7 月西太平洋指数 | 1 月大西洋三极 SST |
| 3 月北大西洋涛动(nao) | 4 月东亚槽位置 | 4 月东亚槽位置 | 3 月亚洲纬向环流指数 | 7 月大西洋欧洲区极涡面积 |
| 3 月加勒比海 SST | 4 月太平洋区极涡强度 | 10 月亚洲经向环流指数 | 7 月大西洋欧洲区极涡面积 | 5 月印度副高面积强度 |
| 3 月太平洋暖池 | 9 月大西洋副高北界 | 5 月太平洋副高强度 | 8 月亚洲区极涡面积 | 6 月东太平洋副高北界 |
| 7 月大西洋欧洲区极涡面积 | 7 月大西洋欧洲区极涡面积 | 11 月南海副高北界 | 4 月北半球极涡强度 | 12 月欧亚经向环流指数 |
| 4 月北非副高强度 | 3 月北半球极涡面积 | 8 月太平洋副高面积 | 5 月印度副高面积 | 1 月青藏高原 |
| 6 月北方涛动指数 | 8 月全球平均陆地海洋温度 | 4 月太平洋区极涡强度 | 10 月北大西洋涛动 | 9 月太平洋暖池 |
| 11 月太平洋区极涡面积 | 9 月东太平洋副高强度 | 12 月欧亚经向环流指数 | 3 月北半球极涡强度 | 2 月加勒比海 SST |
| 5 月太平洋副高面积 | 8 月大西洋副高强度 | 2 月南海副高北界 | 5 月太平洋暖池 | 1 月东亚季风指数 |
| 6 月北太平洋型 | 5 月印度副高面积 | 4 月加勒比海 SST | 2 月印度副高面积 | 6 月北方涛动指数 |
| 4 月东太平洋涛动 | 11 月东亚槽强度 | 9 月北非副高北界 | 4 月加勒比海 SST | 9 月东太平洋副高面积 |
| 3 月北半球极涡面积 | 5 月北美大西洋副高脊线 | 5 月印度副高面积 | 7 月北非副高强度 | 2 月青藏高原 |
| 8 月北半球副高面积 | 4 月加勒比海 SST 指数 (CAR) | 8 月北半球副高面积 | 9 月欧亚经向环流指数 | 1 月东太平洋涛动 |
| 5 月北美大西洋副高面积 | 2 月大西洋欧洲区极涡强度 | 5 月北非大西洋北美副高面积 | 4 月太平洋区极涡强度 | 10 月太平洋副高北界 |
| 2 月太平洋暖池 | 3 月北大西洋涛动 | 5 月热带南大西洋指数 | 7 月北非大西洋北美副高强度 | 8 月全球平均陆地海洋温度 |

从表 1 中可看出,在最优因子组合配置的因子中,表示极涡和副高的因子占了绝大部分,这是因为副高与极涡是影响我国天气气候变化的两个主要的大气环流实体,并且二者对气候的影响并不是孤立的,而是相互作用、相互配合. 极涡主要体现的是中高纬环流特征,而副高很大程度上反映了中低纬大气环流的变化. 东亚大气环流的年际和年代际变化对华北气候异常具有重要的影响. 气候系统中大气环流因子对大气中水分的输送起到了非常重要的作用,大气中的水汽含量不仅与大气环流关系密切,而且作为能量和水循环过程的主要因子对区域水分平衡有很大的影响[42]. 从前面的相关计算可知,副高脊线、极涡指数与华北汛期降水之间以正相关为主,而副高面积、强度与华北降水基本呈负相关. 当亚洲和欧洲区极涡异常南扩,北非、大西洋、北美副高显著收缩减弱,西太平洋和南海副高明显北抬时,华北降水易偏多. 除此之外,可以看到在动态最优多因子组合中出现较为频繁、起到主导作用的影响因子还有太平洋暖池、加勒比海的海表温度(sea surface temperature, SST)等. 太平洋暖池是全球空气对流最强烈的地区,且活动持久,是气候异常的源地之一,太平洋暖池的变化制约着亚洲、太平洋区域,甚至全球气候变化和某些重大自然灾害的形成与变化. 而对于加勒比海 SST,在前面图 3

我们已经得到加勒比海 SST 与华北地区的汛期降水具有非常好的正相关,该海域的海温对于华北地区的汛期降水具有很好的指示意义.

图 6 给出了 1983—2009 年 27 年的模式误差组合 a 与组合 e 的 EOF 分解第一主分量时间系数与之间的相关关系,对比图 6(a)和(b)我们可以发现,组合 a 的 EOF 第一主分量的时间系数在前面大部分年份里与模式误差保持着较好的正相关关系,而从 2004 年往后则表现为负相关关系,而组合 e EOF 第一主分量时间系数在前半段时期内与模式误差的相关关系并不非常明显,但在后期特别是近 10 年里与模式误差之间表现出了较强的正相关关系,正是由于两个组合对于模式误差的相关关系的年代际变化使得两个多因子组合对于不同时段的相似预报能力也不一致,因此,随着时段的推移以及观测资料的不断更新,最优多因子组合配置也是动态的、不断更新的,应针对各时段内具体情况配置最优多因子组合.

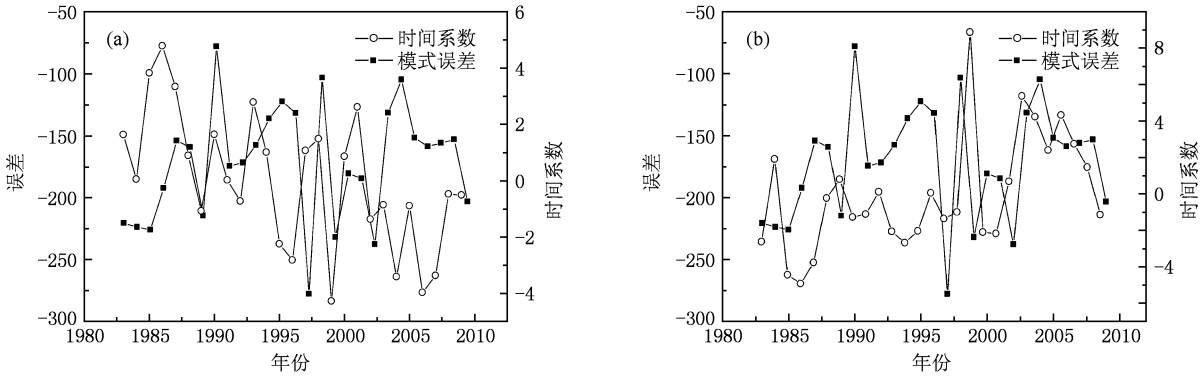


图 6 模式误差与多因子组合 EOF 分解第一主分量时间系数(pci)的相关关系 (a)组合 a,(b)组合 e

综合表 1 中的多因子组合配置以及图 6 中多因子组合 EOF 主分量时间系数与模式误差的相关关系可知,影响因子对于华北地区汛期降水的影响作用存在着年际或年代际的变化,导致对不同时段内进行交叉检验配置出的多因子组合有所差别,多因子组合是动态变化的. 由于我们的最终目的是利用多因子组合相似判据对未来的汛期降水情况进行较准确的订正预报,有必要研究多因子组合的配置关系随时间的变化对比其实际预报效果的变化,从而找到适合近阶段内汛期降水的最优多因子组合配置. 因此,为了对比检验多因子组合的真正预报能力,对不同时段配置出的最优多因子组合进行 2005—2009 年 5 年的独立样本回报检验,如图 7 所示. 图 7(a),(b)分别给出了 5 个不同时段交叉检验配置的最优多因子组合的 5 年回报的 ACC 和均方根误差结果. 图中组合 a 至组合 e 分别代表了利用 1983—2004 年,1983—2005 年,1983—2006 年,1983—2007 年,1983—2008 年 5 个时段配置的最优多因子组合.

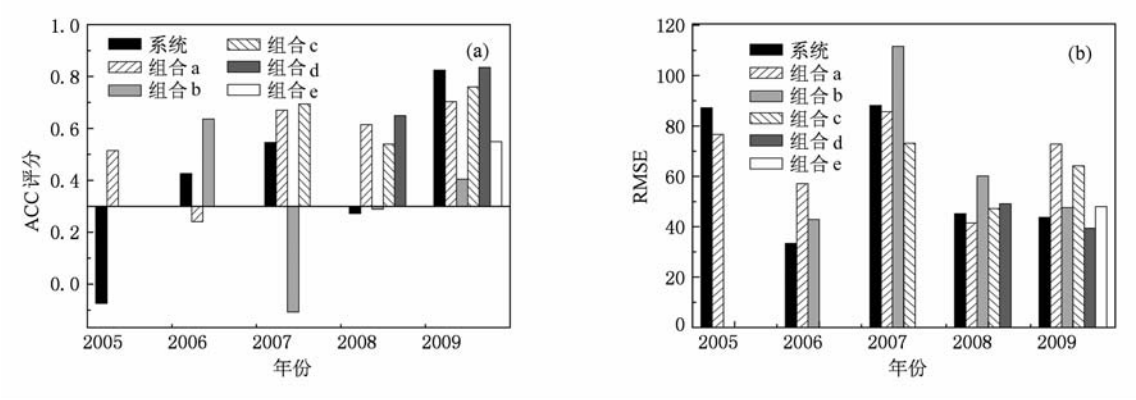


图 7 多因子组合相似 2005—2009 年独立回报的对比 (a)ACC 评分,(b)均方根误差

由于独立样本回报不能用到预报年当年的降水数据,因此1983—2004时段配置的最优多因子组合,即组合a可以对2005年以后的年份进行独立样本回报,而1983—2005时段资料配置的最优组合则只能对2006年以后的年份进行回报,以此类推.从图7中可以看出,利用1983—2004年资料配置出的组合a可以对2005年汛期降水进行很好的预测,相较系统订正提高非常明显,而对于2006的汛期降水组合a的相似订正预报结果则不太理想,订正结果要低于系统订正,但1983—2005时段配置的组合b的相似订正结果则对2006年的汛期降水则显示出良好的预报能力,预报效果要明显高于组合a与系统订正,类似地,对于2007年汛期独立样本回报,组合c的相似订正要好于组合a与组合b.因此,通过对比各个组合对每个预报年的独立样本回报结果分析可以看出,交叉检验时段越长配置出来的最优多因子组合对于该预报年汛期的预报效果相对较好,一方面因为时段越长对应的相似年的样本量也就越多,另一方面,汛期降水有2—4年周期变化,时段越长配置的因子所包含的预报年的历史关键相似信息也越多,配置出来的最优多因子组合也就越有针对性,能够对该预报年的模式误差进行较好的订正.由于样本量较少使得以上结论仍然存在一定的不确定性,但从近5年回报结果可以看出,该方法是现阶段样本量较少的情况下提高汛期预测能力较为有效的方法.因此,对不同预报年采用不同的最优多因子组合即动态最优多因子组合可以有效地提高预报结果.

综上所述,不同组合在不同时间段内显示出的预报能力也是不一样的,并且一般来说,交叉检验所选取的时段越长其相应配置出的多因子组合对预测年的效果越好.因此,随着资料的不断更新,在不同年份进行实际的汛期降水预报时,由于可使用的样本量长度不同以及前期因子对降水影响的年际或年代际变化,配置出最优多因子组合也应当是动态变化的.

### 3.5. 预报个例分析

为了较直观地了解最优因子组合的相似选取方法对于夏季降水预报的改进能力,选择了2005—2009年夏季降水作为独立样本进行研究,限于篇幅,以2007年为典型预报个例,给出了实况与预报图,其他年份只给出了相应的评分结果.之所以选择2007年,一方面为了采用尽可能多的资料选取较为准确的历史相似,另一方面,华北的北部地区在2007年出现较强的负异常,同时在华北南部靠近淮河流域的地区则是呈现很强的降水正异常,以此可以检验该动力-相似方法对降水异常的区域是否有异常信号的预报能力,能否针对其给出降水异常的预测.

图8(a)—(c)分别给出了2007年汛期降水的实况、系统订正和相似订正的预报结果.总体来说,2007年汛期西太平洋副热带高压持续偏强,亚洲地区西风带以纬向环流为主,北半球极涡偏西,7,8月份极涡龟缩于极地,导致入侵我国的冷空气势力偏弱,主要雨带在黄河和长江之间,而其中淮河流域汛期出现了仅次于1954年的大洪水.从2007年华北汛期降水实况图可以看出,华北2007年降水量分布呈现较明显的纬向分布,北部地区整体呈现降水偏少的态势,其中北京、河北中部以及山西北部有较强的降水负异常,西太平洋副高持续偏强以及北方冷空气势力偏弱是造成华北北部地区汛期降水量偏少的重要原因之一;而华北南部地区则呈现不同程度的降水偏多,其中山东南部地区降水偏多达到5成左右.从图8(b)中可以看到系统误差订正给出的结果是整个华北都是降水偏多,对于南部地区降水预报较为准确,而对整个华北北部地区的预报效果并不理想,没有预报出北部地区的降水偏少,系统误差订正ACC为0.54.图8(c)的相似误差订正结果则相对系统订正结果有了一定的提高,虽然相似误差订正也没有很好地给出华北北部的降水偏少,但对华北南部地区的降水偏多则给出了较准确的预报,并且给出了非常强的降水正异常预报,强度与实况大致相当,范围略小于实况,相似误差订正ACC为0.69,较系统误差订正ACC提高了0.15,相似订正方法具有很好的可行性.由此也可看出,多因子优化组合的相似选取方法对前期的异常信号会有很好的响应并且能够将该异常信号反映到异常降水区域的预报中.

表2给出了各个预报年进行相似订正时所选取的相似年以及预报年的实况与相似年实况之间的距平相关系数,通过计算距平相关系数可以判断预报年与相似年之间的相似度的大小,进行判断选取的相似年的准确性.结果显示,各预报年的实际降水与所选取相似年降水之间具有较好的相似性,只有2006和2009年选取的4个相似年中有一个相似

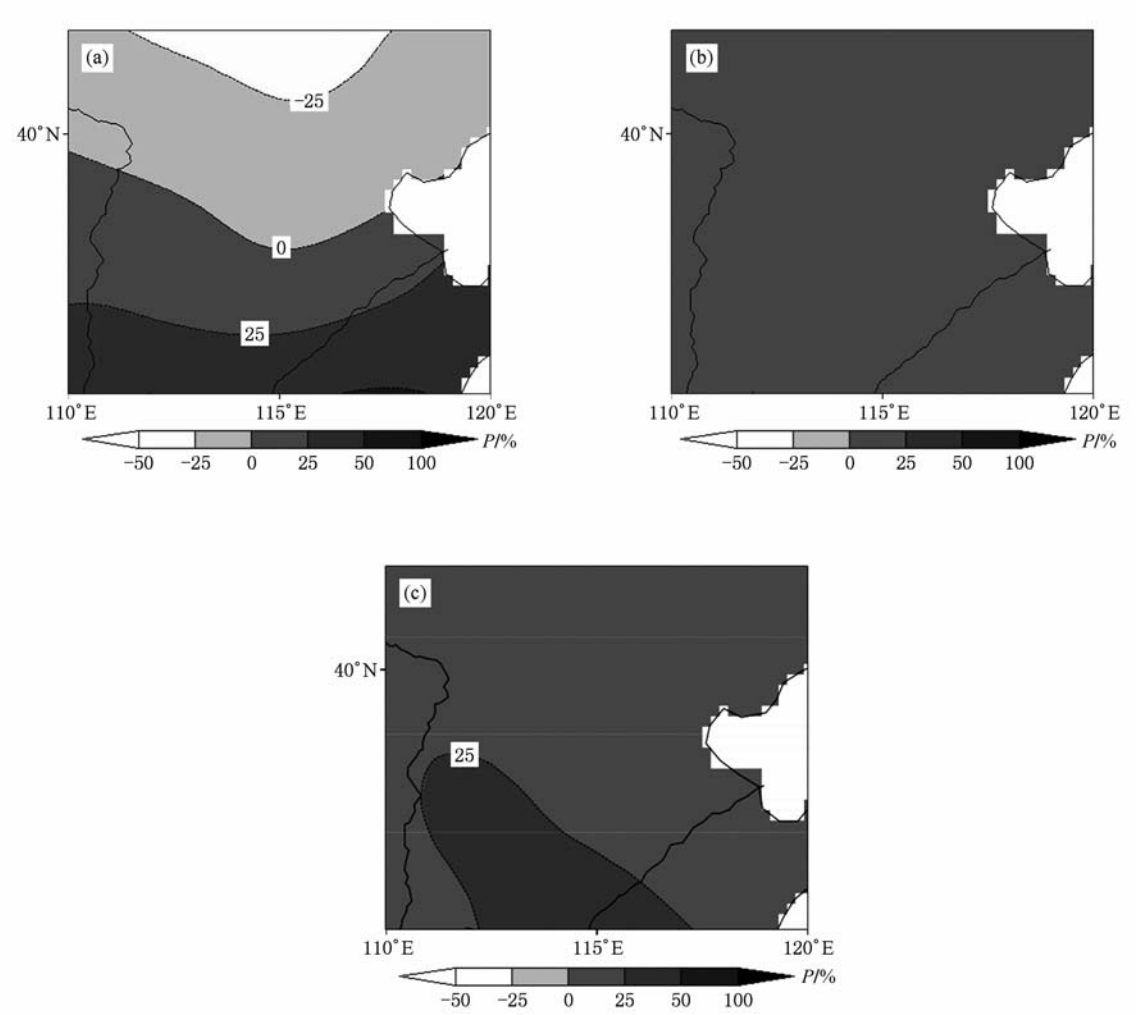


图 8 2007 年独立样本回报 色标为距平百分率 $P$ (a)实况,(b)系统订正,(c)相似订正

表 2 独立样本回报 2005—2009 年选取的相似年及预报年与相似年的距平相关系数

| 预报年 | 第 1 相似年 | 第 2 相似年 | 第 3 相似年 | 第 4 相似年 | ACC |
|---|---|---|---|---|---|
| 2005 | 2003(0.75) | 2004(0.38) | 1998(0.65) | 1996(0.06) | 0.51 |
| 2006 | 1989(0.32) | 1992(-0.55) | 1984(0.52) | 2005(0.74) | 0.64 |
| 2007 | 2003(0.93) | 1989(0.41) | 1996(0.01) | 2004(0.47) | 0.69 |
| 2008 | 2005(0.56) | 2007(0.73) | 1984(0.43) | 2006(0.80) | 0.65 |
| 2009 | 2004(0.53) | 2003(0.79) | 1997(-0.69) | 1989(0.38) | 0.55 |

年选的不够准确,差异较大,距平相关系数达到了负值,对最终的预报结果造成了一定的影响,使得订正效果有一定下降,但由于预报年选取的其他相似年都较为准确,对最终的结果影响并不大,预报年的实况与选取的相似年实况相似度较高,最终的相似订正结果也较为理想,预报结果与实况比较接近,基本预报出了预报年的降水主要分布形式.

为了直观地了解动态最优多因子组合相似误差订正对于模式误差的订正效果,图 9(a),(b)分别给出了独立样本回报的 2005—2009 年汛期降水系统误差订正和相似误差订正的距平相关系数以及均方根误差对比. 从图中可以看出,相似误差订正的结果都要优于系统误差订正结果,将系统订正较差的年份的预报 ACC 评分提高到较高的水平,近 5 年独立样本的系统订正平均 ACC 为 0.40,而相似订正的平均 ACC 约为 0.61,相比提高了 0.21,并且始终保持较高的准确率. 对于图 9(b)中的均方根误差而言,相似订正效果较系统订正也有一定的提高,但并不十分明显,对于系统订正的均方根误差较大的 2005 和 2007 年都有明显的减小,显示出明显的优越性. 因此,相似订正结果能够稳定地提高模式预报的准确率,由此可见,基于动态最优多因

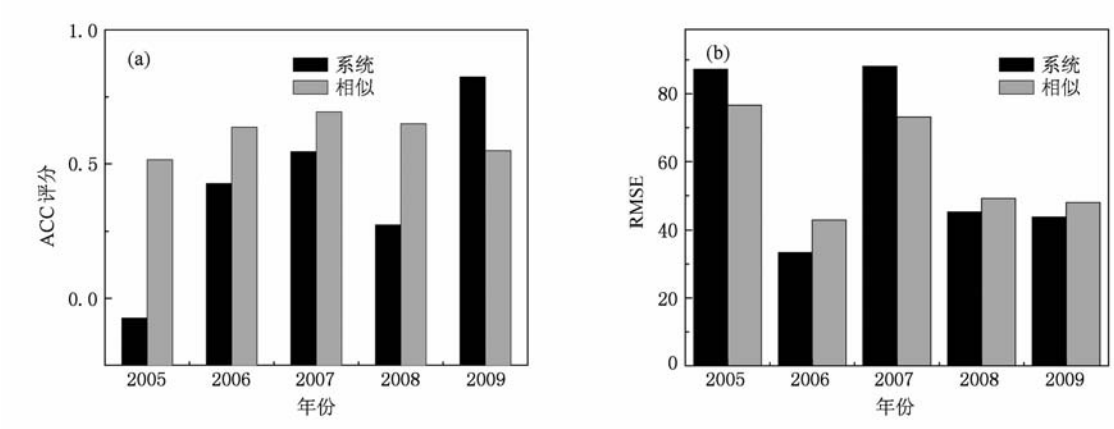


图 9 2005—2009 年独立样本回报系统订正与相似订正 ACC 评分和均方根误差 (a) ACC 评分,(b) 均方根误差

子集组合的相似误差订正方法能有效提高模式的预报技巧.

## 4. 动态最优多因子组合相似预报方案

通过前面的研究可知,多因子组合相似预报方法可以有效地改善华北地区汛期预报效果,提高预报水平,具有很好的应用前景. 为了与业务应用相结合,给出了最终的动态最优多因子组合的相似预报方案,如图 10 所示. 从图 10 中可以得到该预报方案的框架流程:首先,利用汛期降水 CMAP 资料和国家气候中心季节预报模式对每年汛期降水预报结果得到汛期降水模式预报误差集,将 114 项指数作为影响因子,对所有影响因子进行单因子交叉检验预报实验,通过交叉检验的 ACC 排序筛选出对华北地区模式误差订正较好的前期关键因子,建立关键因子集;针对关键因子集中的各项因子,对其进行组合配置实验,通过交叉检验 ACC 敏感性实验确定最优的多因子组合成员个数,通过得到区域预报年前期最优多因子组合,并针对影响因子对区域汛期降水的年际或年代际变化导致不同时段内最优多因子配置的变化,结合历史近期最优多因子组合得到适合不同预报时段的动态最优多因子配置,最后进行模式误差预报并对模式预报结果进行订正并给出订正后模式预报结果.

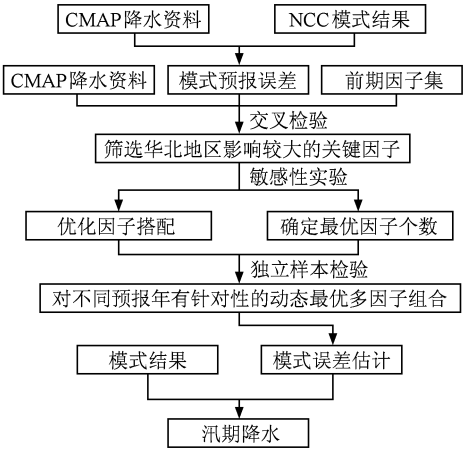


图 10 动态最优多因子组合预报方案流程图

## 5. 结 论

基于动力-相似的基本原理,利用已有的物理统计气候学方面的研究成果,通过对前期因子进行单因子交叉检验筛选,建立适用于华北夏季降水的区域特点的普适性固定关键相似因子集,对关键因子集中的影响因子进行单因子交叉检验回报实验,给出单因子交叉检验 ACC 排序;针对单因子交叉检验 ACC 排序,筛选出能反映模式预报误差分布特征的关键预报因子;对关键预报因子进行配置试验,通过独立样本检验 ACC 得到区域最优多因子配置,考虑到影响因子对区域汛期降水的年际或年代际变化导致在不同的研究时段内的最优多因子配置的动态变化,结合历史近期最优多因子组合得到适合不同预报时段的动态最优多因子配置,结合历史近期最优因子配置得到预报时段内稳定的最优关键因子组合;针对预报年,通过最优多因子组合分别选取最优的 4 个相似年估计当前的预报误差,利用计算出的预报误差订正模式的预报结果,改善华北地区夏季降水预报效果. 经独立样本回报检验显示,动态最优关键因子组合的相似误差订正方法可以显著提高华北地区汛期降水的预报技巧,对华北地区夏季降水具有很好的预报可行性,并最终形成了动态最优多因子组合的相似预报方案.

[1] Feng G L, Gong Z Q, Zhi R, Zhang D Q 2008 *Chin. Phys.* B **17** 2745

[2] Feng G L, Dong W J, Li J P 2004 *Chin. Phys.* **13** 1582

[3] Zhao S R, Song Z S 1999 *Plateau Meteorol.* **18** 535 (in Chinese) [赵声蓉、宋正山 1999 高原气象 **18** 535]

[4] Hou W, Yang P, Feng G L 2008 *Acta Phys. Sin.* **57** 3932 (in Chinese) [侯 威、杨 萍、封国林 2008 物理学报 **57** 3932]

[5] Barnett T P 1990 *Nature* **343** 743

[6] Feng G L, Dong W J, Jia X J, Cao H X 2002 *Acta Phys. Sin.* **51** 1181 (in Chinese) [封国林、董文杰、贾晓静、曹鸿兴 2002 物理学报 **51** 1181]

[7] Hou W, Yang P, Zheng Z H, Gong Z Q 2009 *Acta Phys. Sin.* **58** 2106 (in Chinese) [侯 威、杨 萍、郑志海、龚志强 2009 物理学报 **58** 2106]

[8] Gong Z Q, Feng G L, Wan S Q, Li J P 2006 *Acta Phys. Sin.* **55** 477 (in Chinese) [龚志强、封国林、万仕全、李建平 2006 物理学报 **55** 477]

[9] Zhang D Q, Zhang L, Yang J, Feng G L 2010 *Acta Phys. Sin.* **59** 655 (in Chinese) [章大全、张 璐、杨 杰、封国林 2010 物理学报 **59** 655]

[10] Yang J, Hou W, Feng G L 2010 *Acta Phys. Sin.* **59** 664 (in Chinese) [杨 杰、侯 威、封国林 2010 物理学报 **59** 664]

[11] Zhi R, Lian Y, Feng G L 2007 *Acta Phys. Sin.* **56** 1837 (in Chinese) [支 蓉、廉 毅、封国林 2007 物理学报 **56** 1837]

[12] Xie K, Ren X J 2008 *Sci. Meteorol. Sin.* **28** 508 (in Chinese) [谢 坤、任雪娟 2008 气象科学 **28** 508]

[13] Zhang L J, Xia J, Hu Z F 2008 *Adv. Clim. Chang. Res.* **4** 140 (in Chinese) [张利平、夏 军、胡志芳 2008 气候变化研究 **4** 140]

[14] Lu R Y 2005 *Chin. Sci. Bull.* **50** 1131 (in Chinese) [陆日宇 2005 科学通报 **50** 1131]

[15] Gong Z Q, Feng G L 2008 *Acta Phys. Sin.* **57** 3920 (in Chinese) [龚志强、封国林 2008 物理学报 **57** 3920]

[16] Fan K, Lin M J, Gao Y Z 2008 *Sci. Chin.* **38** 1452 (in Chinese) [范 可、林美静、高煜中 2008 中国科学 **38** 1452]

[17] Feng G L, Dai X G, Wang A H, Chou J F 2001 *Acta Phys. Sin.* **50** 606 (in Chinese) [封国林、戴新刚、王爱慧、丑纪范 2001 物理学报 **50** 606]

[18] Chou J F 2003 *Bimonth. Xinjiang Meteorol.* **26** 1 (in Chinese) [丑纪范 2003 新疆气象 **26** 1]

[19] Chou J F 1986 *Plateau Meteorol.* **5** 367 (in Chinese) [丑纪范 1986 高原气象 **5** 367]

[20] Thomas A G 1970 *J. Appl. Meteorol.* **8** 333

[21] Michael K T, Lisa G, Anthony G B 2005 *Notes Corresp.* **18** 1831

[22] Gu Z C 1958 *Acta Meteorol. Sin.* **29** 176 (in Chinese) [顾震潮 1958 气象学报 **29** 176]

[23] Chou J F 1974 *Sci. Chin. Ser.* A **6** 635 (in Chinese) [丑纪范 1974 中国科学 A 辑 **6** 635]

[24] Qiu C J, Chou J F 1989 *Chin. J. Atmos. Sci.* **13** 22 (in Chinese) [邱崇践、丑纪范 1989 大气科学 **13** 22]

[25] Huang J P, Wang S W 1991 *Sci. Chin. Ser.* B **2** 216 (in Chinese) [黄建平、王绍武 1991 中国科学 B 辑 **2** 216]

[26] Huang J P, Yi Y H, Wang S W, Chou J F 1993 *Quart J. Roy. Meteor. Soc.* **119** 547

[27] Ren H L, Zhang P Q, Li W J, Chou J F 2006 *Acta Phys. Sin.* **55** 4388 (in Chinese) [任宏利、张培群、李维京、丑纪范 2006 物理学报 **55** 4388]

[28] Chen H, Lin ZH 2006 *Adv. Atmos. Sci.* **23** 425

[29] Gu X Q 1998 *Chin. Sci. Bull.* **43** 1 (in Chinese) [谷湘潜 1998 科学通报 **43** 1]

[30] Cao H X 1993 *Sci. Chin. Ser.* B **23** 104 (in Chinese) [曹鸿兴 1993 中国科学 B 辑 **23** 104]

[31] Feng G L, Cao H X, Wei F Y, Chou J F 2001 *Acta Meteorol. Sin.* **59** 206 (in Chinese) [封国林、曹鸿兴、魏凤英、丑纪范 2001 气象学报 **59** 206]

[32] Ding Y H, Liu Y M, Song Y J, Li Q Q 2002 *Clim. Envir.* **7** 236 (in Chinese) [丁一汇、刘一鸣、宋永加、李清泉 2002 气候与环境研究 **7** 236]

[33] Li W J, Zhang P Q, Li Q Q, Wang L N, Liu Y M, Shi X L, Zhang Z Q, Liu Y M, Hu G Q, Dang H Y, Zhang F, Chen L J, Sun C R, Zhao Q G, Dong M 2005 *Quart. J. Appl. Meteorol.* **16** 1 (in Chinese) [李维京、张培群、李清泉、王兰宁、刘益民、史学丽、张祖强、刘一鸣、胡国权、党鸿雁、张 芳、陈丽娟、孙除荣、赵其庆、董 敏 2005 应用气象学报 **16** 1]

[34] Ren H L, Chou J F 2007 *Sci. Chin. Ser.* D **37** 988 (in Chinese) [任宏利、丑纪范 2007 中国科学 D 辑 **37** 988]

[35] Ren H L, Chou J F 2007 *Adv. Earth Sci.* **22** 376 (in Chinese) [任宏利、丑纪范 2007 地球科学进展 **22** 376]

[36] Feng G L, Dong W J 2003 *Acta Phys. Sin.* **52** 2347 (in Chinese) [封国林、董文杰 2003 物理学报 **52** 2347]

[37] Zheng Z H, Ren H L, Huang J P 2009 *Acta Phys. Sin.* **58** 7359 (in Chinese) [郑志海、任宏利、黄建平 2009 物理学报 **58** 7359]

[38] Bao M, Ni Y Q, Chou J F 2004 *Chin. Sci. Bull.* **49** 1112 (in Chinese) [鲍 名、倪允琪、丑纪范 2004 科学通报 **49** 1112]

[39] Shi Y S, Yao X X, Yang X L, Li Z T 2008 *Sci. Meteorol. Sin.* **28** 377 (in Chinese) [史印山、姚学祥、杨晓亮、李宗涛 2008 气象科学 **28** 377]

[40] Mao Y J 2005 *Bull. Sci. Tech.* **5** 533 (in Chinese) [毛燕军 2005 科技通报 **5** 533]

[41] Yao Y, Yan H S 2008 *J. Trop. Meteorol.* **24** 483 (in Chinese) [姚 愚、严华生 2008 热带气象学报 **24** 483]

[42] Zhang H D, Jin R H, Zhang Y S 2008 *J. Trop. Meteorol.* **24** 417 (in Chinese) [张恒德、金荣花、张友姝 2008 热带气象学报 **24** 417]

# Dynamic optimal multi-indexes configuration for estimating the prediction errors of dynamical climate model in North China*

Yang Jie[1)2)] Wang Qi-Guang[1)] Zhi Rong[3)] Feng Guo-Lin[2)3)†]

1) (*College of Atmospheric Scicences, Lanzhou University, Lanzhou 730000, China*)

2) (*Key Laboratory of Regional Climate-Environment Research for Temperate East Asia of the Institute of Atmospheric Physics, Chinese Academy of Sciences, Beijing 100029, China*)

3) (*Laboratory for Climate Studies of China Meteorological Administration, National Climate Center, Beijing 100081, China*)

(Received 22 June 2010; revised manuscript received 15 July 2010)

Abstract

Based on the idea of using the historical-analogue information to revise the prediction errors of National Climate Centre numerical business model, for North China, based on analysis data of the CMAP from 1983 to 2009, 40 pieces of climate indices from NOAA, 27 years of the season prediction model results from 1983 to 2009 and 74 pieces of circulation characteristics materials provided by Weather Diagnostic Forecasting Room of National Climate Center, using the method of combining data analysis and numerical simulation of diagnostic tests, taking the advantage of the prediction error of the key information of similar model from the historical data, by identifying key factors, optimizing allocation of the different factors of different forecasting years, we established specific multi-factor dynamic optimal portfolios to revise prediction errors in different periods of the power-statistical model in North China, and constructed early environmental factors similar to field multiple objective criteria, to develop new technology of revising prediction errors from the power-statistical model based on dynamic optimal combination of multi-factor, and improved the prediction effect in the summer precipitation in North China and the forecasting skills. Results of independent sample return of 2005—2009 shows that, the score of similarity revised method has improved significantly compared with the score of systematic revised method. The method has a good prospect for summer precipitation forecast in North China, and is going to be put into operation.

**Keywords**: set of key factors, estimation of model errors, precipitation, prediction

**PACS**: 92.60.Wc

* Project supported by the Special Scientific Research Fund of Meteorological Public Welfare Profession of China (Grant No. GYHY200806005), the National Natural Science Foundation of China (Grant Nos. 40875040, 40930952) and the National Key Technology Research and Development Program of the Ministry of Science and Technology of China (Grant Nos. 2007BAC29B01, 2009BAC51B04).

† Corresponding author. E-mail: ferggl@cma.gov.cn

# 北京地区极端温度事件的变化趋势和年代际演变特征*

杨 萍[1]，刘伟东[1]，侯 威[2]

（1. 中国气象局北京城市气象研究所，北京 100089；2. 国家气候中心，北京 100081）

**摘 要**：利用北京地区 20 个气象观测站 1978 – 2007 年逐日平均温度资料，分析了近 30 年北京地区极端温度事件的变化趋势以及年代际空间演变特征。研究结果显示，北京观象台近 30 年的两次迁站对研究极端温度事件并无太大影响；近 10 年夏季显著的热岛效应，是城区极端高温事件发生频次明显高于其他地区的重要原因；尽管北京地区冬季平均温度的空间分布形态变化甚微，并始终存在着明显的热岛效应，但城区极端低温事件的发生频次有可能发生了与热岛效应无关的突变过程。

**关键词**：北京地区；极端高温事件；极端低温事件；年代际演变；热岛效应

**中图分类号**：P423.3 **文献标识码**：A **文章编号**：1000 – 811X(2011)01 – 0060 – 05

## 0 引言

关于城市气候的诸多研究中，城市热岛效应研究得最多[1-3]。不同时段、不同国家的不同城市都或多或少地受到城市热岛效应的影响[4-5]。若从对城市发展的影响以及城市对极端事件的承载能力来看，城市中极端气候事件的研究显得更为迫切和重要[6-8]。分析极端事件在城市中的长期变化趋势、空间演变特征具有非常重要的现实意义。

北京城区是典型的“热岛”，其热岛强度比中国沿海城市明显，城市热岛增强的结果是造成冬季寒冷期缩短和夏季炎热期增强，城市高温热浪等灾害更加频繁[9]。对于北京地区温度的已有研究侧重于对热岛效应的探讨以及城郊温度的对比分析，对城市中极端事件气候特征的研究较少。本文以北京地区极端温度事件为研究对象，讨论了近 30 年北京地区极端温度事件的变化趋势及年代际的空间演变特征。

## 1 资料

1978 年后，北京地区 20 个常规气象站具有较为完整的观测资料。本文使用的资料为国家信息中心提供的 1978 – 2007 年北京地区 20 个常规站（图 1）逐日平均温度资料。为尽可能消除测站海拔高度上存在的差异对温度造成的影响，对北京地区 20 站的日平均温度资料按照 0.6℃/100 m 的垂直递减率统一订正到海平面高度。

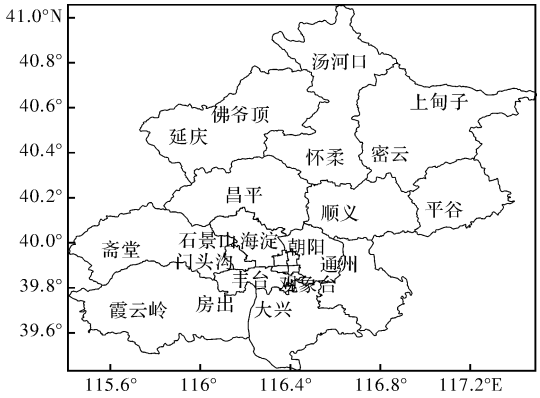


图 1 研究选用的北京地区 20 个台站分布示意图

本文基于日平均温度资料定义极端温度事件[10]，采用国际上通用的百分位阈值法[11]。具体定义为：将 1978 – 2007 年夏季（冬季）日平均温度资料按从小到大（从大到小）排序，取第 90 百分位作为极端高（低）温事件的上（下）阈值，超过上（下）阈值的定义为极端高（低）温事件。

## 2 1978 年以来北京地区极端温度事件的变化趋势

北京观象台（54511）为国家基准站，通常使用

* 收稿日期：2010 – 6 – 23
基金项目：北京市气象局“北京优秀人才项目”（20061D0200800060）；国家自然科学基金项目（40975006，41005043）
作者简介：杨萍（1981 – ），女，汉族，江苏兴化人，博士，主要从事城市气候和极端气候事件的研究. E-mail：pyang@ium.cn

该台站的气象数据代表北京地区。1978 年以来北京观象台发生过两次较大的迁站，不少研究表明北京观象台数据包含了明显的城市效应[12]，迁站因素是否会对该地区极端事件的气候特征造成影响，值得进行对比和分析。

有研究表明北京地区 20 个常规气象站属于同一气候区，其气象要素统计平均值可代表北京地区接近于真实状态的气候特征[13]。基于此，采用北京地区 20 个常规站极端温度事件年频次的平均值作为参考序列，对比分析基于观象台资料的极端温度事件的发生频次。具体结果如图 2 所示，其中实线为参考序列，虚线为北京观象台的结果。

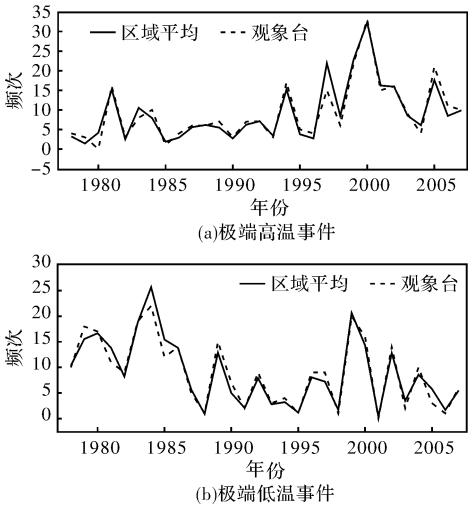


图 2　极端温度事件发生频次的变化趋势

图 2 显示，1990 年代中期以后，极端高温事件的频次呈现明显的上升趋势，1980 年代末以前极端低温事件频次呈现较为明显的下降趋势，之后以震荡波动为主。对比观象台时间序列与参考序列的结果发现，尽管北京观象台发生过两次迁站，但利用观象台资料研究近 30 年极端温度事件的发生频次，无论从逐年结果还是从线性倾向率来看，基于观象台的时间序列与基于全区平均的参考序列基本一致，可见迁站对极端温度事件发生频次的影响甚微。

## 3　极端温度事件的年代际演变特征

大量统计事实表明，北京地区具有明显的城市热岛效应[14]，那么在此气候背景下的极端温度事件发生频次空间分布形态及其年代际演变特征如何？基于此，本文分别统计了 1978 – 1987 年、1988 – 1997 年、1998 – 2007 年这三个时段北京地区 20 个站极端温度事件发生频次的年代际空间分布图，并分析了其年代际演变特征。

### 3.1　极端高温事件发生频次的年代际演变特征

图 3 为北京地区极端高温事件年代际演变的空间分布图。图 3 中大于等于所处时段全区平均发生频次的等值线用实线标识，反之则为虚线。观象台的位置用“★”标出。

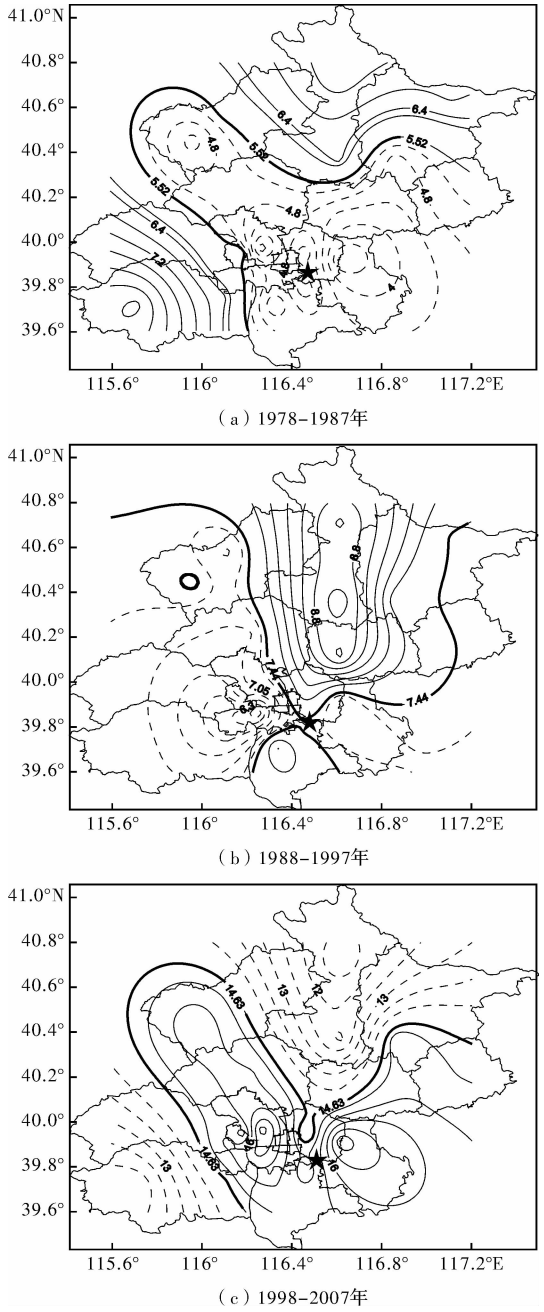


图 3　北京地区极端高温事件发生频次空间分布

图 3 显示，近 30 年北京地区极端高温事件发生频次的高值中心具有明显的年代际差异。1978 – 1987 年，极端高温事件发生频次的高值区主要位于北京北部的汤河口、上甸子、佛爷顶以及北京

西南部的霞云岭和斋堂；1988 – 1997 年，高值区为以怀柔为中心的广大北方地区，西部尤其是西部偏南的大部分地区为低值区；1998 – 2007 年的分布格局与 1978 – 1987 年具有较对称的反相关系，在 1978 – 1987 年时段中的高值区成为了 1998 – 2007 年的低值区域，该时段的高温中心之一位于石景山工业密集区，这与郑祚芳等人得到的夏季高温日的高值中心较为吻合[14]。

有文献根据与观象台距离的远近区别城区和郊区[15]，按此定义，丰台、大兴等均可纳入城区范围。通过比较不同年代际之间城区极端高温事件发生频次的空间分布特征发现，1978 – 1987 年，城区极端高温事件的发生频次均低于北京全区的平均水平，1988 – 1997 年，其中与平均水平相当，1998 – 2007 年，其值明显高于北京全区的平均态。这种年代际演变特征说明在最近的十年中，北京城区极端高温事件的发生频次呈现明显增大的趋势。已有研究指出，气候平均值及变率的改变有可能造成异常温度频次的改变[10]，北京地区夏季气温平均态与极端高温事件的空间演变是否有联系，针对此问题我们给出了 1978 – 2007 年每 10 年夏季平均温度空间距平分布图，如图 4 所示，其中实线为正距平，虚线为负距平。

图 4 显示，图 4a 和图 4b 空间分布格局非常相似，东部以负距平为主，西北以正距平为主。1998 – 2007 年夏季平均温度正距平的区域更加集中，集中在城区周围，这与图 3c 的结果存在较好的对应关系，这可能说明了近 10 年城区热岛效应更加明显，热岛效应很可能是导致该时段内极端高温事件发生频次明显高于其他地区的主要原因。

### 3.2 极端低温事件的年代际演变特征

类似地，图 5 给出了北京地区极端低温事件年代际演变的空间分布。

图 5 显示，1978 – 1987 年，城区的朝阳和城郊平谷形成两个高值中心，高值区主要覆盖于东北部东南部一带；1988 – 1997 年，高值中心移至西南位置的霞云岭站附近；1998 – 2007 年，西南地区的霞云岭等地的发生频次保持了前一个年代际的高值状态，而以怀柔为中心的北方大部从上个年代际的低值中心转变为高值中心，城区的发生频次与全区平均发生频次相当。对比不同年代际之间城区极端低温事件发生频次的空间分布特征发现，1978 – 1987 年，城区的发生频次均高于北京全区的平均水平；1988 – 1997 年，其发生频次均低于北京全区的平均水平；1998 – 2007 年，发生频次又有上升的趋势，其值接近于北京全区的平均态。这种年代际变化表明，与 1970、1980 年代相比，1990 年代以后北京城区极端低温事件的发生频次经历了先减小后增加的变化过程。与极端高温事件的讨论类似，图 6 给出了 1978 – 2007 年冬季平均温度年代际空间距平分布图。

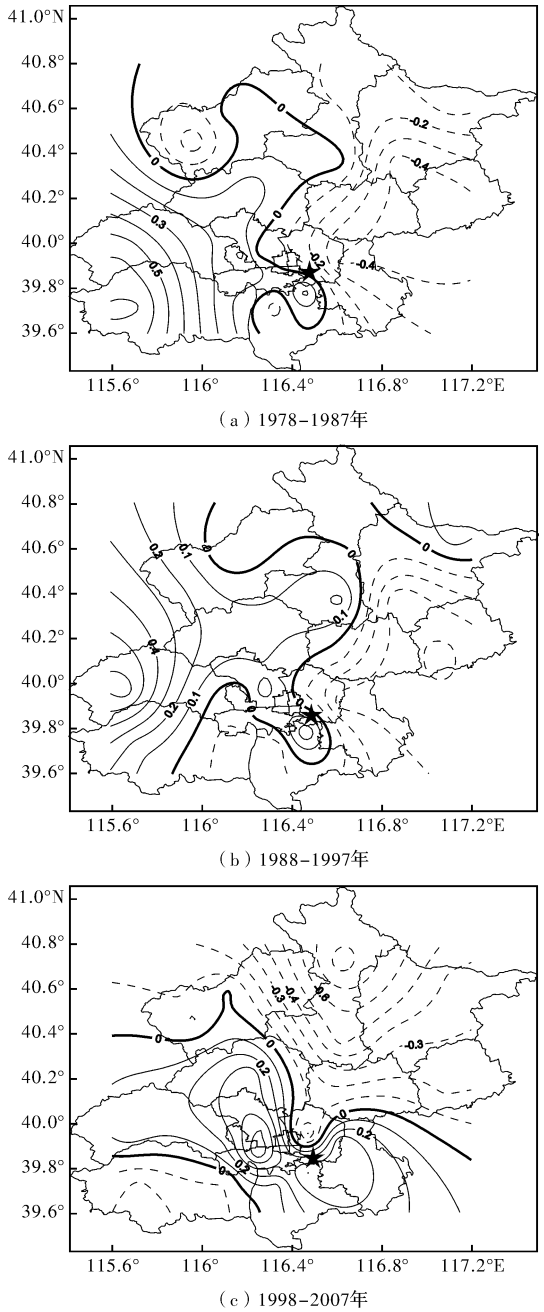


（a）1978–1987年

（b）1988–1997年

（c）1998–2007年

图 4 北京地区夏季平均温度空间距平分布

图 6 显示，冬季平均温度距平的年代际空间分布差异很小，北部山区为气温的小值区域，包含城区在内的西部和南部在内均为气温偏暖区。1998 – 2007 年，城区热岛中心有增强的趋势，但整体而言没有明显的年代际差异。而冬季极端低温事

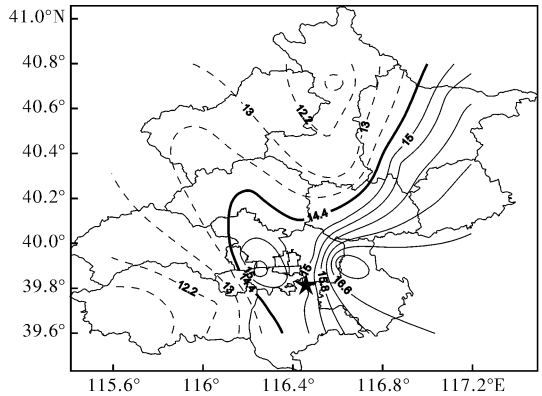


（a）1978-1987年

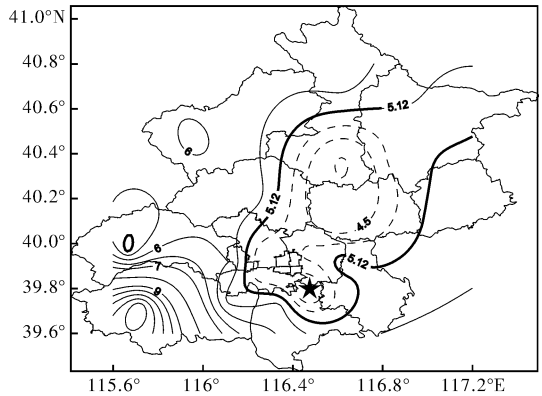


（b）1988-1997年

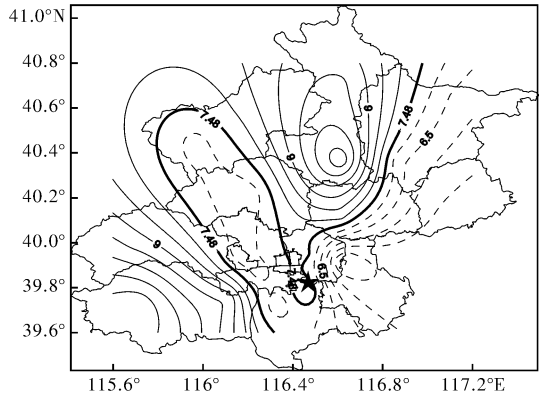


（c）1998-2007年

图 5　北京地区冬季极端低温事件发生频次空间分布

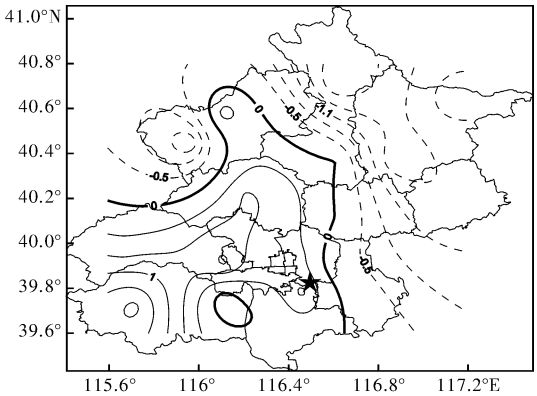


（a）1978-1987年

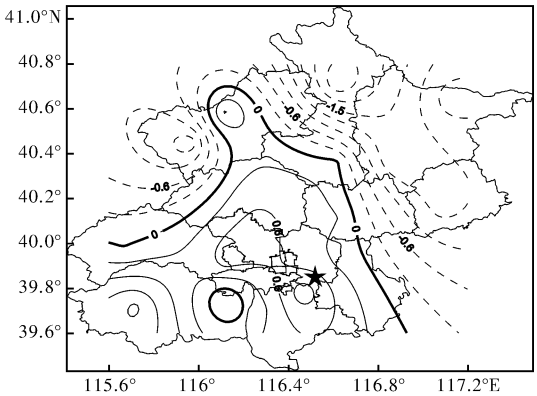


（b）1988-1997年

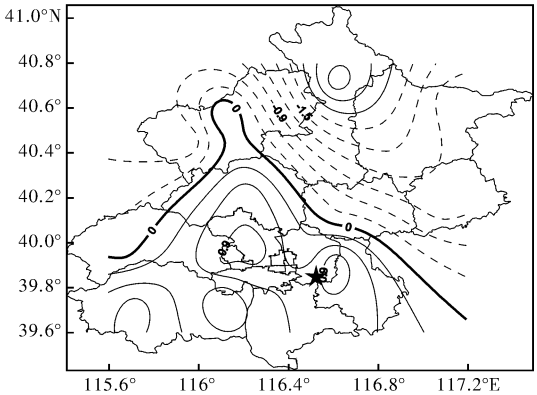


（c）1998-2007年

图 6　北京地区冬季平均温度距平空间分布图

件在不同年代际之间的空间分布差异非常明显，从 SE－NW 走向（1978－1987 年）过渡到 SW－NE 走向（1988－1997 年）再过渡到 SW－NE 中心的走向（1998－2007 年）。这种年代际空间演变特征和冬季平均温度空间分布特征没有明显的联系，可能说明了冬季城市热岛效应对极端低温事件的影响不明显，即局地城市热岛效应对北京地区极端低温事件的影响不明显，城区的极端低温事件发生频次存在着与热岛效应相互独立的突变过程。这可能是因为冬季北京地区主要在大陆西伯利亚季风的控制之下，城市气候的小尺度变化并没有影响大尺度的气候变化。

## 4　结论

本文以北京地区极端温度事件为重点，讨论了近 30 年北京地区极端温度事件的变化趋势以及年代际的空间演变特征，具体结论如下：

（1）北京观象台极端温度事件发生频次与北京全区平均发生频次的差别不大，这可能说明观象台近 30 年两次迁站对研究极端温度事件并没有直接显著的影响；

（2）近 10 年北京城市热岛效应更加明显，热岛效应很可能是导致了该时段内极端高温事件发

生频次明显高于其他地区的主要原因；

(3)极端低温事件年代际空间演变特征和冬季平均温度空间分布特征没有明显的联系，说明尽管近几十年北京地区冬季热岛效应明显，但城区的极端低温事件发生频次仍旧存在突变的可能性，且与热岛效应的增强无关。

## 参考文献：


[1] Karl T R, Diaz H F, Kukla G. Urbanization: its detection and effect in the United States climate record [J]. Journal of Climate, 1988, 11: 1099 – 1123.

[2] 刘小宁. 我国暴雨极端事件的气候变化特征[J]. 灾害学, 1999, 14(1): 54 – 59.

[3] 董文杰，江静. 人类对北方干旱化的有序适应—观测、虚拟试验和实验研究[M]. 北京：气象出版社，2004：103 – 110.

[4] Kalnay E, Cai M. Impact of urbanization and land – use change on climate [J]. Nature, 2003, 423: 528 – 531.

[5] Karl T R, P D Jones. Urban bias in area – averaged surface air temperature trends [J]. Bulletin American Meteorological Society, 1989, 70: 265 – 270.

[6] 封国林，龚志强，支蓉. 气候变化检测与诊断技术的若干新进展[J]. 气象学报，2008，66(6)：892 – 905.

[7] 李青春，曹晓彦，郑祚芳，等. 极端气温对城市人群死亡的影响评估[J]. 灾害学，2006，21(1)：13 – 17.

[8] 封国林，王启光，侯威，等. 气象领域极端事件的长程相关性[J]. 物理学报，2009，58(4)：2853 – 2861.

[9] 张金峰，张丽娟，李文亮，等. 哈尔滨市高空气候变暖变化分析[J]. 灾害学，2010，25(2)：41 – 44.

[10] 龚道溢，韩晖，华北农牧交错带夏季极端气候的趋势分析[J]. 地理学报，2004，59(3)：230 – 238.

[11] Jones P D, Horton E B, Folland C K, et al. The use of indices to identify changes in climatic extremes [J]. Climatic Changes, 1999, 42: 131 – 149.

[12] Liu W D, You H L, Dou J X. Urban – rural humidity and temperature differences in the Beijing area [J]. Theoretical and Applied Climatology, 2009, 96: 201 – 207.

[13] 林学椿，于淑秋. 北京地区气温的年代际变化和热岛效应[J]. 地球物理学报，2005，48(1)：39 – 45.

[14] 郑祚芳，范水勇，王迎春. 城市热岛效应对北京夏季高温的影响[J]. 应用气象学报，2006，17(S1)：48 – 53.

[15] 王喜全，王自发，齐彦斌，等. 城市化进程对于北京地区冬季降水分布的影响[J]. 中国科学 D 辑，2008，38(11)：1438 – 1443.


# The Trend and Inter-decadal Evolution of Extreme Temperature Events in Beijing Area


Yang Ping[1], Liu Weidong[1] and Hou Wei[2]

(1. *Institute of Urban Meteorology of Beijing*, *China Metrology Adminstration*, *Beijing* 100089, *China*; 2. *Laboratory for Climate Studies of China Meteorological Administration*, *National Climate Center*, *Beijing* 100081, *China*)



**Abstract**: The trend and inter-decadal evolution of extreme temperature events in Beijing area have been investigated by using daily mean temperature data from 20 meteorological stations in recent 30 years (1978 ~ 2007). The results indicate that the trend is almost similar between Beijing observatory and the average of all stations in Beijing region. The result of inter-decadal evolution shows that the frequency of maximum temperature in the urban areas increase obviously, which is inseparably close to urban heat island. Adversely, the spatial distribution of winter minimum temperature has no obvious relation with the mean temperature in winter.



**Key words**: Beijing region; extreme high-temperature; extreme low-temperature; inter-decadal evolution; heat island effect

杨小波,陈丽娟,刘芸芸. 我国降水和气温的分级概率时空分布特征. 应用气象学报,2011,22(5):513-524.

# 我国降水和气温的分级概率时空分布特征

杨小波[1)2)3)] 陈丽娟[2)*] 刘芸芸[2)]

[1)](中国气象局成都高原气象研究所,成都 610072)

[2)](国家气候中心 中国气象局气候研究开放实验室,北京 100081)

[3)](四川省气候中心,成都 610072)

**摘 要**

采用全国 160 站 1951—2009 年月降水和气温资料,分析了短期气候预测业务评分办法中六级要素概率时空分布特征,并以 1 月、7 月为代表获得了不同地区、不同级别降水和气温异常发生频率。结果表明:降水和气温的六级异常分布存在显著空间不均匀性和年代际变化特征,1980—2009 年,北方降水在 1 月出现特少、特多等级和 7 月出现特少、偏少等级的概率较大,南方降水出现 6 个等级的概率基本相同;全国气温在 1 月和 7 月出现正常略低、正常略高和偏高等级的概率较大。1980—2009 年与 1951—1979 年相比,全国 1 月降水为特多、偏多等级和 7 月降水为偏少等级的站数明显增加,全国 1 月气温为正常略高、偏高和特高等级的站数明显增加,呈明显的年代际变化特征。

**关键词**:降水;气温;分级概率;时空分布;气候预测

## 引 言

随着国民经济的迅速发展,社会更加迫切需要准确和丰富的短期气候预测服务产品[1]。而分析降水和气温的分级概率时空分布特征,可以获得不同地区、不同量级降水和气温的异常发生频率,这可以作为一种背景性信息为气候预测评估和预测产品制作提供非常有用的参考,也为极端气候的预测提供了基础信息,有利于短期气候预测服务水平的提高。

在全球气候变暖背景下[2],关于多种气象要素极端特性变化的研究有很多[3-10]。Easterling 等指出[11-12],全球最低气温、最高气温有明显的上升趋势,而我国气温的变化趋势与全球基本一致[13-15]。唐红玉等[16]研究表明,我国年平均最高气温的变化特征呈现北方增暖明显、南方变化不明显的特征,各地年平均最低气温呈明显的变暖趋势。与此同时,许多研究也分析了极端降水的变化情况。Zhai 等研究指出[17],我国南方极端降水事件增加趋势明显,我国北方极端降水事件减少趋势明显,蔡敏等[18]研究也有类似结论。王小玲等[19]发现,降水量的趋势变化主要由强降水量的变化引起,降水频率变化对降水量趋势的贡献远大于强度变化,趋势变化主要由频率的趋势产生。此外,全球气候存在明显的年代际变化特征[20],在我国则表现为长江、淮河流域 20 世纪 70 年代末后降水明显增多,而华北地区降水明显减少[21],我国东部季风区中的"北涝南旱"型在 20 世纪 70 年代末后转为"南涝北旱"型[22]。这些研究成果提示预报员在气候预测业务和服务中要以发展的眼光看待预报因子和预报对象。

多数研究成果[23-27]主要集中于极端气温、降水的分析,实际上在气候预测业务中面对的是从正常到异常的多级情况,如何为决策者提供丰富的预测信息具有实际应用价值。本文采用中国气象局预报与网络司下发的《短期气候预测质量分级检验办法》① 中对降水、气温的六级分级定义和评分办法,分析各月各要素的六级概率时空分布特征,以期为预报员进行气候预测时综合考虑年代际变化、年际变化和季节内变化特征提供重要参考信息,同时也对气候预测质量检验方法的特点和合理性提出建议。

2010-11-18 收到,2011-06-07 收到再改稿。

资助项目:国家科技部科技支撑项目(2007BAC29B04 和 2009BAC51B05),公益性行业(气象)科研专项(GYHY200906015)

* 通信作者,E-mail: chenlj@cma.gov.cn

① 关于下发《短期气候预测质量分级检验办法》的通知. 气预函〔2009〕141 号. 2009.

## 1 资料与方法

本文采用国家气候中心常规业务中使用的1951—2009年我国160站月降水、气温资料，根据《短期气候预测质量分级检验办法》中对降水、气温等级划分标准(表1)，以20%和50%的阈值将降水划分为特少、偏少、正常略少、正常略多、偏多、特多共6个等级，以1℃和2℃的阈值将气温划分为特低、偏低、正常略低、正常略高、偏高、特高共6个等级。针对6个等级的评分办法如表2所示。可以看到，预报等级与实况相符时，单站评分为100分；预报等级与实况不符时，如果预报为正常等级，而实况与预报相差1个等级，则得分在100分基础上减20分，相差两个等级减40分；但如果预报为异常等级而实况也为异常等级，但预报与实况相差1个等级，则单站评分为80分基础上再加10分的加权奖励分。六级异常是针对0呈对称分布，得分对应分级预测与实况的关系也呈对称分布。表2的评分办法强调了级别预测正确的重要性，且对异常级别预报正确的情况有加权奖励。在这种评分思路下，如何清楚地了解降水、气温在不同级别下的时间和空间分布特征对预测和服务非常必要。

**表1 降水和气温趋势预测六级评分制用语及等级划分标准**

**Table 1 The terminology of six-level scoring method and the classification standards of each level for precipitation and temperature prediction**

| 预测用语 | $\Delta R$/% | $\Delta T$/℃ |
|---|---|---|
| 特少(特低) | $\Delta R \leqslant -50$ | $\Delta T \leqslant -2.0$ |
| 偏少(偏低) | $-50 < \Delta R \leqslant -20$ | $-2.0 < \Delta T \leqslant -1.0$ |
| 正常略少(正常略低) | $-20 < \Delta R < 0$ | $-1.0 < \Delta T < 0$ |
| 正常略多(正常略高) | $0 \leqslant \Delta R < 20$ | $0 \leqslant \Delta T < 1.0$ |
| 偏多(偏高) | $20 \leqslant \Delta R < 50$ | $1.0 \leqslant \Delta T < 2.0$ |
| 特多(特高) | $50 \leqslant \Delta R$ | $2.0 \leqslant \Delta T$ |

注：$\Delta R$ 为降水距平百分率；$\Delta T$ 为气温距平。

**表2 单站降水和气温趋势预测六级评分制评分表**

**Table 2 The six-level scoring method for precipitation and temperature predictions at one station**

| 实况 | 预测 | | | | | |
|---|---|---|---|---|---|---|
| | 特少(特低) | 偏少(偏低) | 正常略少(正常略低) | 正常略多(正常略高) | 偏多(偏高) | 特多(特高) |
| 特少(特低) | 100 | 80+10 | 60 | 20 | 0 | 0 |
| 偏少(偏低) | 80+10 | 100 | 80 | 40 | 20 | 0 |
| 正常略少(正常略低) | 60 | 80+10 | 100 | 60 | 40 | 20 |
| 正常略多(正常略高) | 20 | 40 | 60 | 100 | 80+10 | 60 |
| 偏多(偏高) | 0 | 20 | 40 | 80 | 100 | 80+10 |
| 特多(特高) | 0 | 0 | 20 | 60 | 80+10 | 100 |

限于篇幅，本文以1月和7月作为代表进行重点分析。这里主要采用了概率统计方法，分析了气候发生年代际转折后1980—2009年1月和7月降水和气温的六级概率空间分布特征，并在此基础上对比了1951—1979年和1980—2009年气温和降水不同等级概率的年代际变化。这里采用的概率统计原理为 $P(A)=m/n$，其中 $P(A)$ 为事件 $A$ 出现的频率值，$n$ 是总事件发生的总数，$m$ 表示事件 $A$ 发生的总次数。具体到本文，$P(A)$ 为某一等级出现的频率值，$n$ 为资料长度，$m$ 是该等级在 $n$ 年内出现该等级的总次数。本研究可为预报员做分级预报提供重要的背景信息。

## 2 降水和气温分级概率时空分布特征

### 2.1 1980—2009年1月和7月降水分级概率空间分布特征

均方差能够反映出气候要素值的波动振幅大小，均方差高值区域易出现异常等级气候事件，均方差低值区域易出现正常等级气候事件。因此，这里首先给出了我国1月和7月降水距平百分率的均方差图(图1)。由于我国目前的短期气候预测业务是

以距平百分率作为预报对象（表 1），因此这里计算的是降水距平百分率均方差。图 1 表明，1 月降水距平百分率均方差高值区主要分布于我国西藏及北方大部地区，低值区主要分布于我国南方地区；7 月均方差高值区主要分布于我国西藏及西北地区，低值区主要分布于我国东部地区。对比 1 月和 7 月均方差分布后发现，1 月均方差要明显大于 7 月，且北方要明显大于南方。这说明 1 月易发生异常等级降水事件，且北方发生异常等级降水事件的概率要明显大于南方。

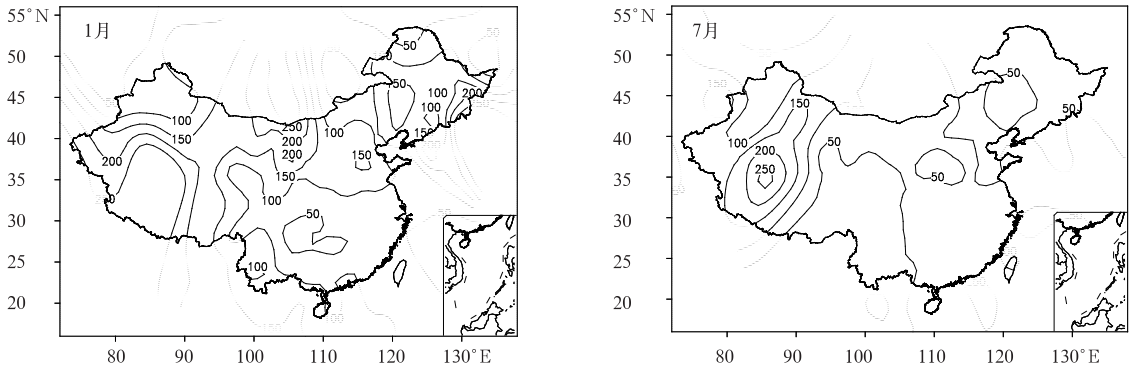


图 1　1980—2009 年 1 月和 7 月我国降水距平百分率的均方差（单位：%）

Fig. 1　The standard deviation of precipitation percentage anomalies in China in January and July from 1980 to 2009（unit：%）

不同等级降水出现概率对预报降水趋势的量级具有重要参考价值。这里参照表 1 的降水等级划分标准，给出了 1980—2009 年 1 月降水六级概率分布图（图 2）。图 2 表明，1 月降水出现特少、特多等级概率大于 20% 的高值区主要分布于东北、内蒙古、华北、黄淮、西北、西南地区西部以及华南沿海，部分地区出现概率超过 50%。1 月我国降水出现偏少、正常略少、正常略多、偏多等级的概率相对较小。对比图 1a 也可以看出，特多和特少等级的高概率区域对应均方差高值区，而低概率区则对应均方差低值区。综合以上分析可知，1 月我国北方降水出现特多、特少等级的概率较大，出现偏少、正常略少、正常略多、偏多等级的概率较小，而我国南方大部分地区出现 6 个等级的概率接近。

1980—2009 年 7 月降水的六级概率分布（图 3）表明，7 月降水出现特少等级概率大于 20% 的高概率区主要分布于西北地区、内蒙古、江南大部；偏少等级的高概率区主要分布于东北、华北、黄淮、内蒙古、西北地区中东部、西南地区以及江南地区；特多等级概率大于 20% 的高概率区主要分布于新疆、西藏西部、江淮以及华南沿海地区。7 月降水基本未出现正常略少、正常略多、偏多等级的高概率区域。对比图 1b 也可以看出，特多和特少级的高概率区域对应了均方差高值区。综合以上分析可知，7 月北方降水出现特少、偏少等级的概率较大，而南方地区出现偏少、特多的概率略占优势。

综合上面分析可知，1980—2009 年 1 月北方降水出现特少、特多等级的概率较大，且部分地区出现特少等级概率接近 50%；7 月北方降水出现特少、偏少等级的概率较大。1 月和 7 月南方降水出现 6 个等级的概率比较接近。对比 1 月和 7 月降水概率空间分布特征后还可以发现，1 月出现异常等级概率要明显高于 7 月。以往短期气候预测业务人员倾向于正常等级的趋势预报，几乎不考虑预报异常等级。然而在全球气候变暖的大背景下，降水异常事件频发，而预报员发布的预测信息多数为正常等级，直接影响到降水预测准确率的提高，同时也大大降低了预测服务的效果。现行的短期气候预测评分标准更着重强调等级预报的正确性，并在此基础上增加了对预报异常等级的加权奖励。因此，针对现行短期气候预测业务评分标准和服务需求，并综合考虑年代际气候变化背景，在有利的年际、季节内变化特征和预测因子、预测方法的支持下，对于一些出现异常等级降水概率比较高的区域（如北方部分地区），给出异常等级趋势预报的把握比较大。

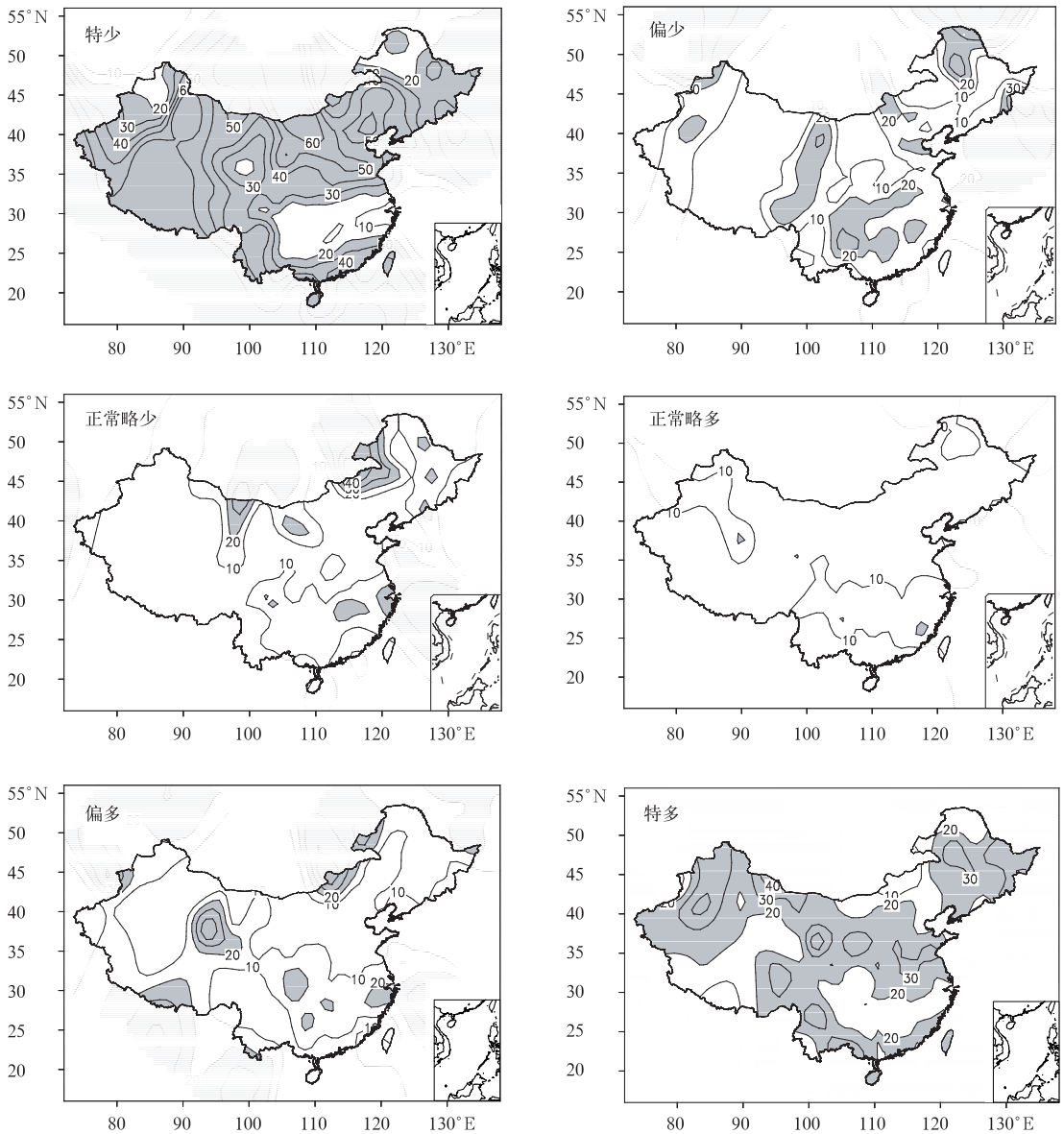


图2 1980—2009年1月我国降水六级概率分布(单位:%)
(阴影区表示概率分布超过20%的区域)
Fig. 2 Distributions of the six-level probability of precipitation anomalies in January from 1980 to 2009(unit:%)
(the shaded area denotes the probability over 20%)

## 2.2 1980—2009年1月和7月气温分级概率空间分布特征

1980—2009年1月和7月我国气温的均方差分布(图4)表明,1月气温均方差异常高值区主要集中于我国北方及西藏地区,均方差低值区主要分布于我国南方地区。相比于1月,7月气温的均方差明显减小,且北方地区气温的均方差也要明显大于南方。以上分析说明,1月北方大部地区气温变化剧烈,容易出现极端气温事件,而南方气温波动相对较小;7月全国气温波动都较小。

参照表1中气温等级划分标准,本文绘制出了1980—2009年1月我国气温的六级概率分布图(图5)。图5表明,1月出现正常略低等级概率大于20%的高概率区主要分布于华北、黄淮、江淮、江汉、华南、西藏东部、西南地区东部;正常略高等级的高概率区主要位于华北、西北、西南、江南、华南、江淮、黄淮及

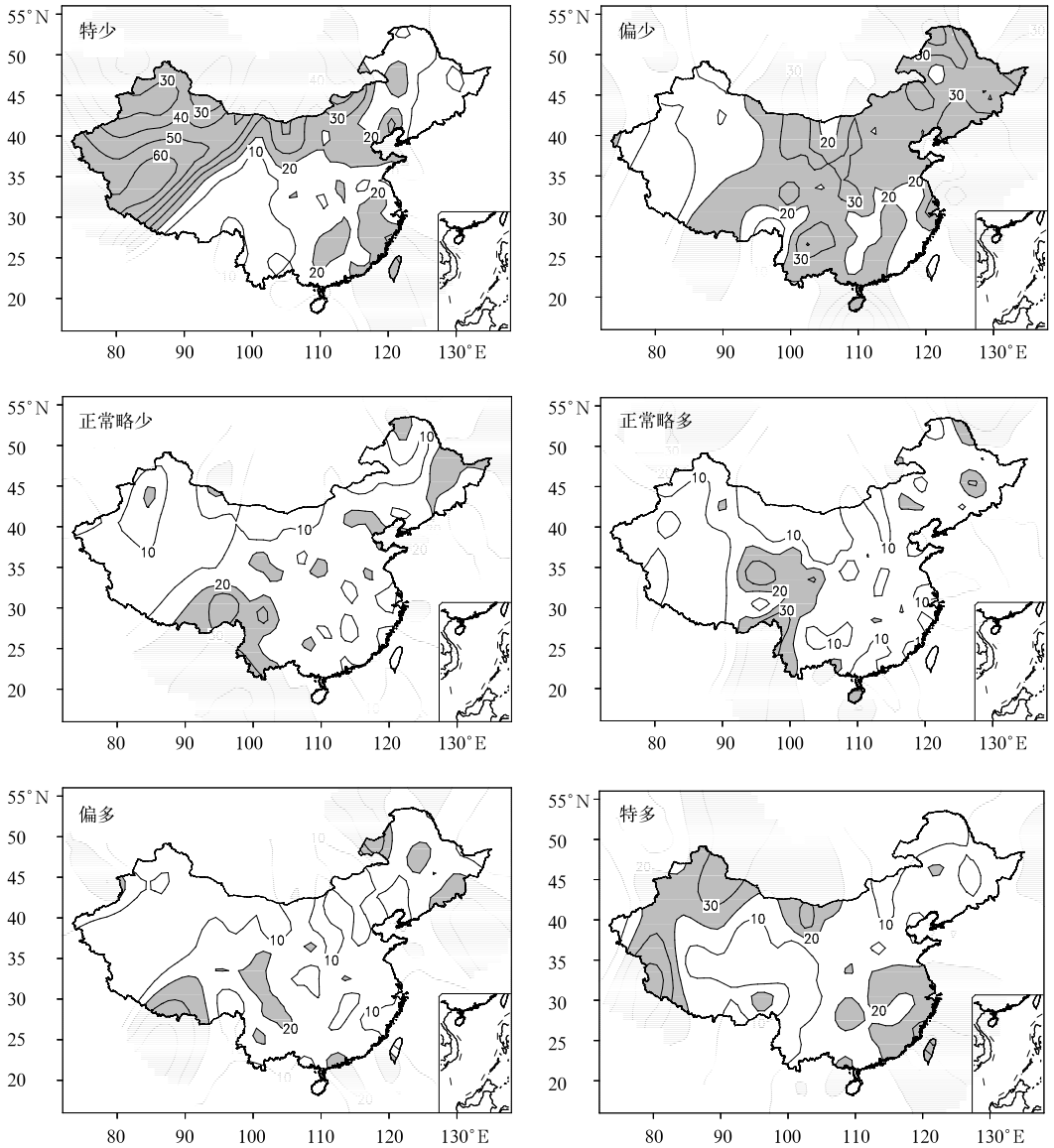


图 3　1980—2009 年 7 月我国降水六级概率分布(单位：%；其他说明同图 2)

Fig. 3　Distributions of the six-level probability of precipitation anomalies in July from 1980 to 2009(unit：%；others same as in Fig. 2)

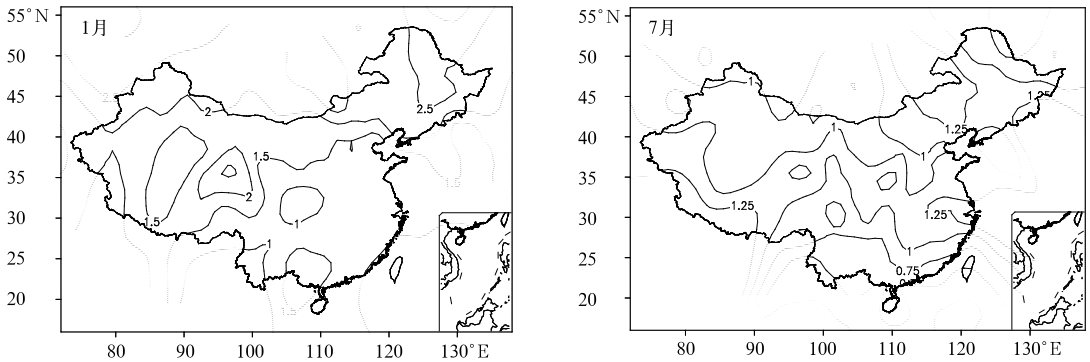


图 4　1980—2009 年 1 月和 7 月全国气温均方差(单位：℃)

Fig. 4　The standard deviation of temperature in China in January and July from 1980 to 2009(unit：℃)

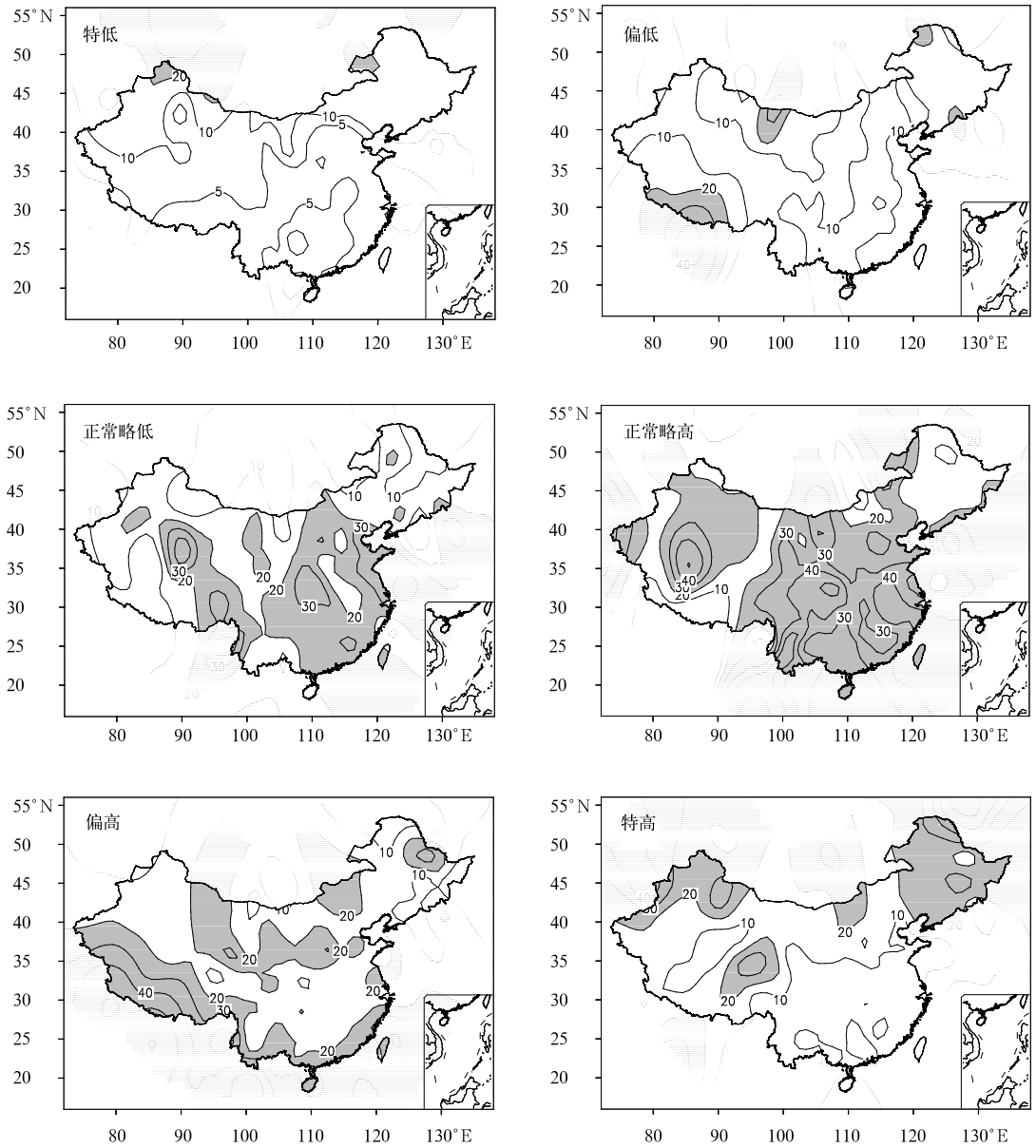


图 5 1980—2009 年 1 月全国气温六级概率分布(单位:%;其他说明同图 2)
Fig. 5 Distributions of the six-level probability of temperature anomalies in January from 1980 to 2009(unit:%; others same as in Fig. 2)

江汉地区,其中长江流域地区的正常略高等级出现概率达到 40%左右;偏高等级的高概率区主要位于西藏、西北地区中东部及华南沿海地区;特高等级的高概率区主要位于新疆北部、东北大部地区。1 月气温出现特低、偏低等级的高概率区在全国都较少。综合上面分析可知,1 月全国气温出现正常略低、正常略高的概率较大,出现偏高等级的概率次之,而出现特低、偏低、特高等级的概率相对较小。

图 6 为 1980—2009 年 7 月我国气温的六级概率分布。图 6 表明,7 月气温基本以正常略低、正常略高等级为主,其中大部地区出现正常略低、正常略高的概率大于 30%,尤其是南方部分地区正常略高等级出现概率大于 40%以上。与之相反,7 月我国气温基本未出现特低、偏低和特高等级的高概率区。7 月气温出现偏高等级的高概率区主要位于西北地区中东部、西藏、内蒙古和江南北部地区。从以上分析可知,7 月全国气温主要集中于正常略低、正常略高和偏高 3 个等级,而特低、偏低和特高气温等级出现的概率很小。同时,对比图 4 与图 5、图 6 后发现,1 月和 7 月气温均方差高值中心都主要分布于我国北方地区,然而全国大部地区气温都集中于正常略低、正常略高和偏高 3 个等级,因此评分办法中的六级气温得到的均方差分布特征与六级的概率分布特征有较大的差异。气温的六级分布特征在时间

和空间上表现出明显的不对称。

综合上面分析可知，1980—2009 年 1 月和 7 月降水距平百分率均方差能较好反映出降水六级概率分布特征，而 1 月和 7 月气温均方差不能很好反映出气温六级概率分布特征。从气温六级概率空间分布特征看到，1 月和 7 月出现正常略低、正常略高和偏高等级的概率较大，而出现特低、偏低、特高等级的概率较小。虽然现行预报评分标准对异常等级气温预报也有额外加权奖励，但是从 1 月和 7 月全国气温六级概率空间分布特征来看，我国大部地区气温基本都处于正常等级之中，基本不会出现异常等级情况。因此，结合现行的气温评分标准和气温六级概率分布特点，并同时考虑年代际、年际尺度的气候背景，1 月、7 月全国大部地区气温出现正常略低、正常略高和偏高等级的概率较高，而特低、偏低和特高等级出现概率低，呈现明显的偏态分布。业务人员在进行气候预测服务时应充分考虑这种气候特征。

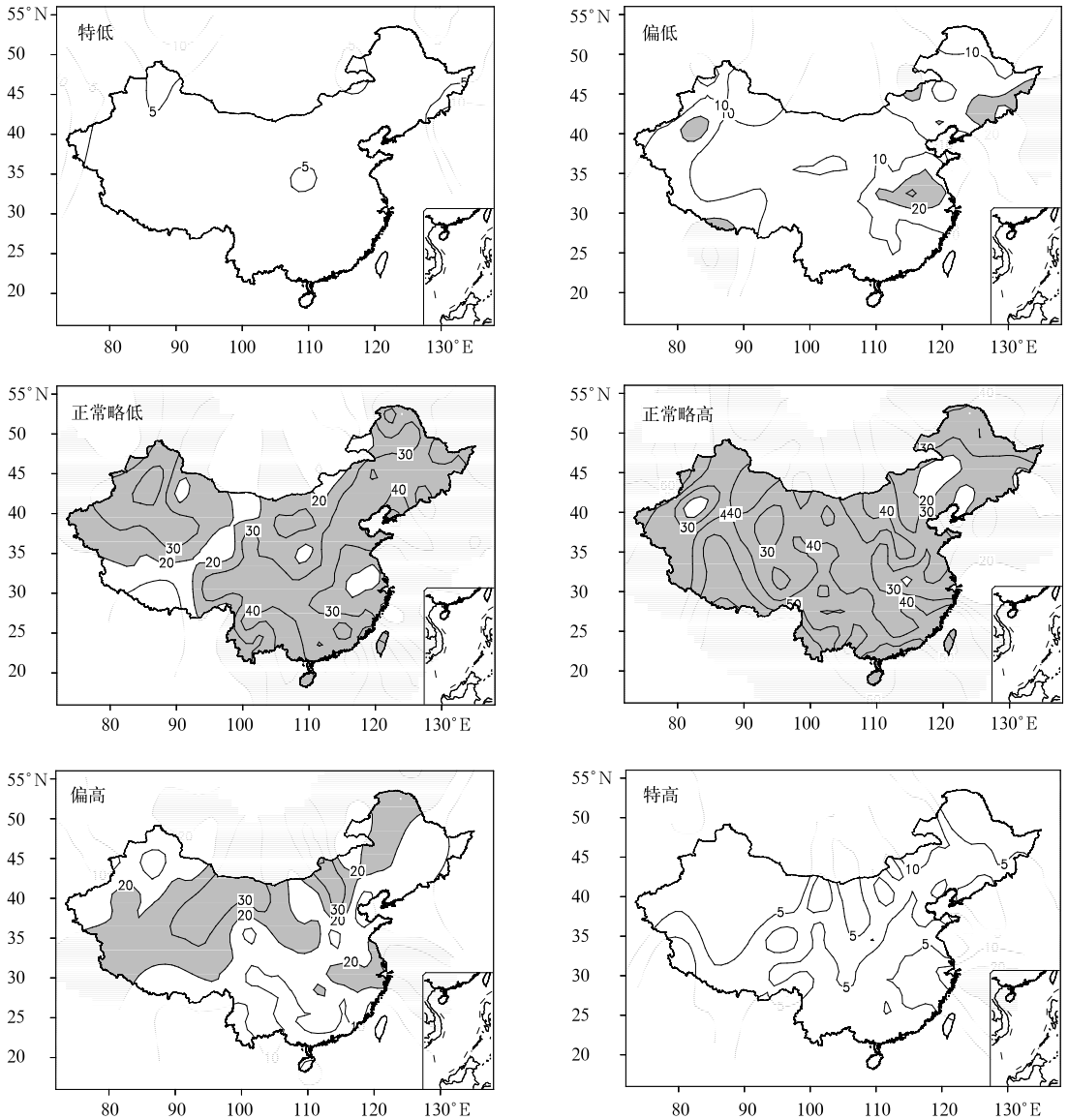


图 6　1980—2009 年 7 月全国气温六级概率分布（单位：%；其他说明同图 2）

Fig. 6　Distributions of the six-level probability of temperature anomalies in July from 1980 to 2009 (unit: %; others same as in Fig. 2)

## 2.3　气温和降水概率年代际变化特征

全球气候在 20 世纪 70 年代末期发生了显著的年代际变化。为了揭示气候年代际变化对气温、降水概率分布的影响，本文还对比了 1951—1979 年和 1980—2009 年两个时间段中降水和气温的差别，分别计算出这两个时段降水和气温 6 个等级概率大于

25%的站数(如图7所示)。由图7可知,1980—2009年,1月降水特多、偏多等级和7月降水偏少等级的站数要明显多于1951—1979年,1月降水特少等级和7月降水特少、正常略少等级的站数要明显少于1951—1979年,而1月降水偏少、正常略少、正常略多等级和7月偏多、特多等级的站数变化不大。1980—2009年1月气温特低、偏低、正常略低等级的站数明显少于1951—1979年,而正常略高、偏高和特高等级的站数明显多于1951—1979年。两个时段7月气温6个等级的站数都没有太大变化。以上分析同时表明,全球变暖引起降水、气温等级分布的改变在冬季最显著,需要引起预报员关注。

降水特少、特多等级和气温特低、特高等级的概率分布在很大程度上反映了气温、降水极端事件发生的频率。1980—2009年与1951—1979年全国降水特少、特多等级的概率差值分布可以很好地表现不同年代降水异常等级的变化特征(图8)。图8表明,1月和7月降水特少等级概率的显著负值区域

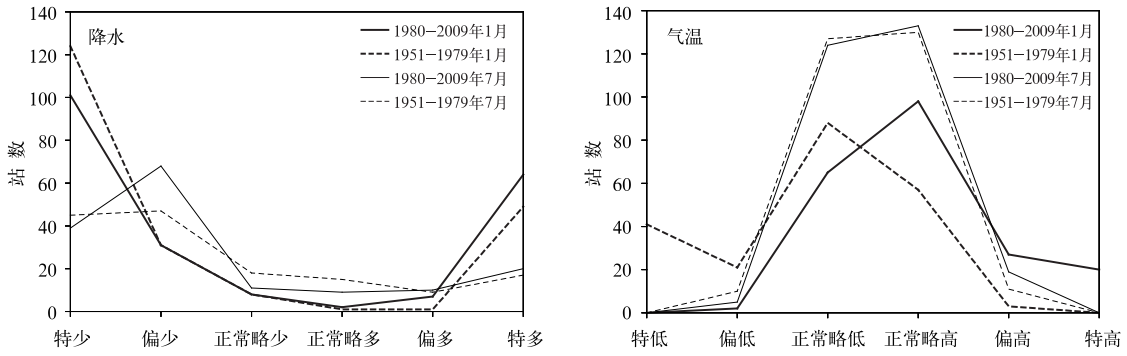


图7 1月和7月的降水与气温六级概率大于25%的站数

Fig. 7 The number of stations where the six-level probability of precipitation and temperature anomalies greater than 25% in January and July

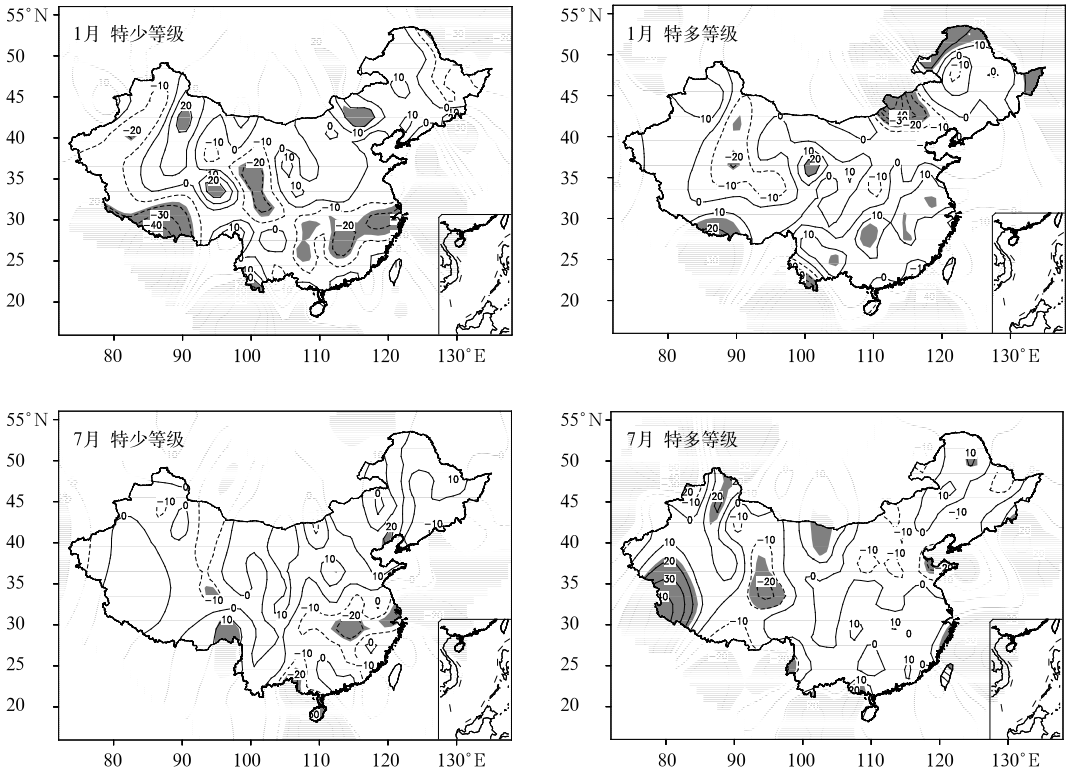


图8 1980—2009年与1951—1979年全国降水概率的差值分布(单位:%)

(阴影区表示达到0.1显著性水平)

Fig. 8 Precipitation probability anomalies between the periods of 1980—2009 and 1951—1979(unit:%)(the shaded area denotes passing the test of 0.1 level)

主要分布于西南东部、江南等地区，其出现概率下降了 20%左右；而北方大部为未通过显著性检验的正值区域，其出现概率上升了 10%左右。1 月和 7 月降水特多等级概率的显著性负值区主要分布于内蒙古、西北部分地区等地；正值区主要分布于江淮、江南等地区。综合以上分析可知，1 月和 7 月降水特少等级概率在我国南方地区有下降趋势，在北方地区有上升趋势，而降水特多等级概率在我国南方地区有上升趋势，在北方地区有下降趋势。以上结论与文献[23-27]结果一致。

1980—2009 年与 1951—1979 年的气温特低、特高等级的概率差值分布(图 9)表明，1 月气温特低等级概率为全国一致的负距平区，且显著性负值区主要分布于北方地区，即气温特低、特高等级出现概率下降了 10%以上。与之相反，1 月气温特高等级概率表现为全国一致的正距平区，且显著性正值区也主要分布于北方地区，其出现概率上升了 10%以上。7 月气温出现特低、特高等级概率基本没有明显的变化。从上面分析可知，1 月我国大部地区出现气温特低等级的概率在降低，而出现气温特高等级的概率在上升，这一年代际变化趋势在北方尤为显著。7 月全国气温特低、特高等级的概率基本维持不变。同时，这也说明我国夏季气温增暖不显著，而冬季气温增暖显著，并且北方地区异常增暖幅度要明显大于南方。以上结论与文献[13-16]结果较一致。

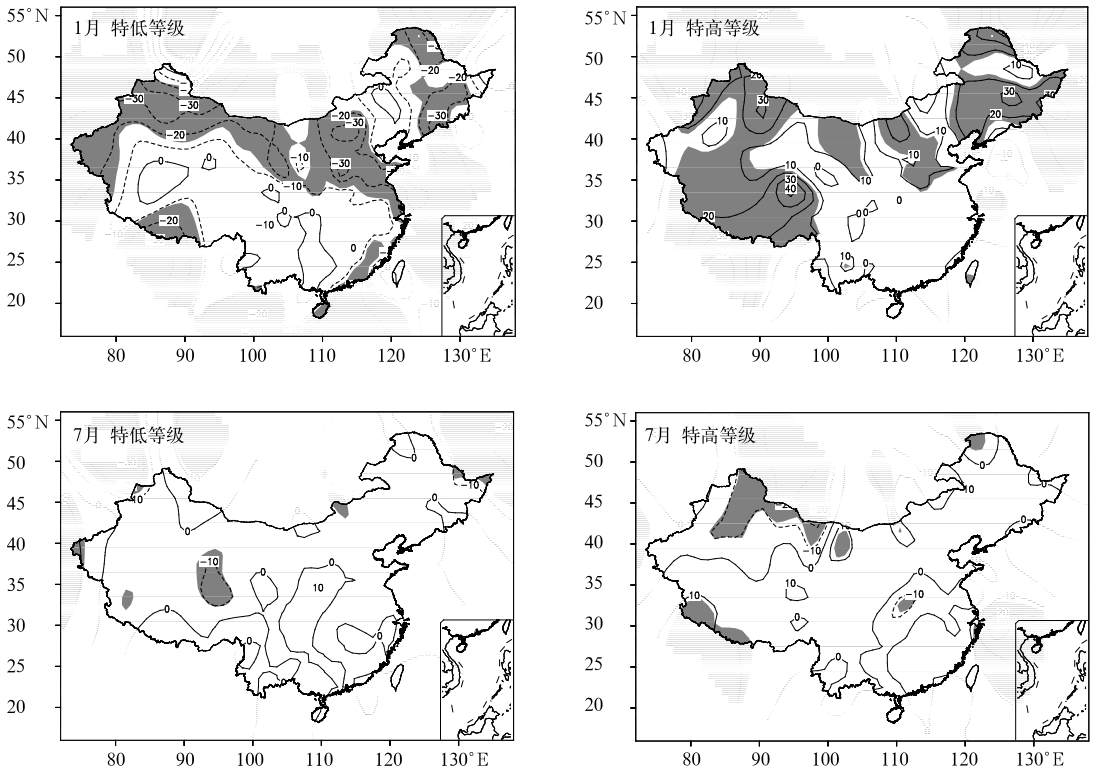


图 9　1980—2009 年与 1951—1979 年全国气温概率的差值分布(单位：%)

(阴影区表示达到 0.1 显著性水平)

Fig. 9　Temperature probability differences between the periods of 1980—2009 and 1951—1979(unit：%)

(the shaded area shows passing the test of 0.1 level)

综上所述，与 1951—1979 年相比，1980—2009 年 1 月降水特多、偏多等级和 7 月降水偏少等级的站数增加明显，1 月降水特少等级和 7 月降水特少、正常略少等级的站数减少明显；1980—2009 年时段 1 月气温特低、偏低、正常略低等级的站数明显减少，1 月气温正常略高、偏高和特高等级的站数明显增加，而 7 月气温 6 个等级的站数基本无变化。同时，1 月和 7 月降水特少等级概率在我国南方地区有年代际下降趋势，在北方地区有上升趋势，而降水特多等级概率在我国南方地区有年代际上升趋势，在北方地区有下降趋势。1 月我国大部地区出现气温特低等级的概率在降低，而出现气温特高等级的

概率在上升，这一变化趋势在北方尤为显著。7月我国气温特低、特高等级的概率基本维持不变。这也说明我国夏季气温增暖不显著，而冬季气温增暖显著，并且北方地区增暖幅度要明显大于南方。

降水和气温分级概率特征在时间上表现出显著的年代际变化，从侧面反映出气候背景的变化对降水和气温预报趋势的影响，预测因子的选择也要随年代际变化特征而更新。因此在短期气候预测业务中，除了要考虑月、季尺度和年际尺度的变化外，还需要结合降水和气温的六级概率分布特征，考虑年代际变化对降水和气温趋势的影响，通过多时间尺度综合集成来提高气候预测、评估及服务水平。

## 3 结论和讨论

本文利用中国气象局预报与网络司下发的《短期气候预测质量分级检验办法》中对降水、气温的分级定义和评分办法，采用国家气候中心常规业务中使用的1951—2009年全国160站月降水、气温资料，分析了各月降水、温度在不同年代际背景下的六级概率时空分布特征，并以1月和7月作为代表进行了重点分析，得到了如下结论：

1)下发的短期气候预测质量分级标准和评估办法是针对正负异常对称分布要素设置的，而实际降水和气温的六级异常分布存在显著的空间不均匀性和年代际变化特征。

2)1980—2009年，北方1月降水特少、特多等级和7月降水特少、偏少等级出现的概率较大。南方降水在1月和7月出现6个等级的概率比较接近。1月和7月我国气温出现正常略低、正常略高和偏高等级的概率较大。这种概率分布特征提示预报员要慎重分析小概率事件出现的原因及其影响。

3)1980—2009年与1951—1979年相比，1月降水特多、偏多等级和7月降水偏少等级的站数明显增加。1月气温正常略高、偏高和特高等级站数也明显增加，而7月气温六级等级站数基本无变化。以上结果说明六级概率分布的年代际变化特征在全球变暖背景下引起降水、气温等级分布的改变在冬季最显著。

4)1980—2009年与1951—1979年相比，1月和7月降水特少(特多)等级概率在我国南方(北方)地区有下降趋势，在北方(南方)地区有上升趋势。1月我国大部地区出现气温特低(特高)等级的概率在降低(上升)；7月气温特低、特高等级的概率基本维持不变。这种气候变化的年代际背景提示预报员在集成预测结果时要考虑年代际信号变化的影响。

5)针对现行短期气候预测业务评分标准，结合年代际气候变化背景，在有利的年际和季节内变化特征支持下，北方地区降水趋势应给出异常量级的预报信息，而南方地区预报指示意义相对不明显。全国气温出现正常略低、正常略高和偏高3个等级的概率较高。

现行气候预测评分标准侧重于分级预报的准确率，尤其支持异常等级降水和气温的预测。因此该评分方法鼓励提升气候预测的服务效果。降水六级概率时空分布特征基本符合正负异常对称分布，其六级评分制比较合理。但气温六级概率时空分布特征呈现出明显的偏态分布，六级评分不能很好反映出实际情况，应适当改进。

此外，现行评分方法未考虑到降水和气温的空间不均匀性和年代际变化特征，忽视了不同地区出现不同等级要素异常的概率不同所造成的预测难度的差异。近年来已经有研究将概率权重引入天气预报评估方法之中[28-29]，另外对比无技巧预报(如气候预报、持续性预报)的技巧评分[30]，也可以不同程度地解决区域差异的问题，因此现行气候预测评分可以引入其他评估方法的优点并进一步合理化。

## 参 考 文 献

[1] Kunkel K E, Pielke J R A, Changnon S A. Temporal fluctuations in weather and climate extremes that cause economic and human health impacts: A review. *Bull Amer Meteor Soc*, 1999, 80 (6): 1077-1098.

[2] Solomon S, Qin D, Manning M, et al. Climate Change 2007: The Physical Science Basis. Cambridge: Cambridge University Press, 2007.

[3] Klein Tank A M G, Konnen G P. Trends in indices of daily temperature and precipitation extremes in Europe, 1946—99. *J Climate*, 2003, 16: 3665-3680.

[4] 张耀存，张录军. 东北气候和生态过渡区近50年来降水和气温概率分布特征变化. 地理科学，2005，25(5)：561-566.

[5] 孙凤华，杨素英，任国玉. 东北地区降水日数、强度和持续时间的年代际变化. 应用气象学报，2007，18(5)：610-618.

[6] Choi G, Collins D, Ren G, et al. Changes in means and extreme events of temperature and precipitation in the Asian-Pacific Network region, 1955—2007. *International Journal of Climatology*, 2009, Published online in Wiley InterScience, doi: 10.1002/joc.1979.

[7] Alexander L V, Zhang X, Peterson T C, et al. Global ob-

served changes in daily climate extremes of temperature and precipitation. *J Geophys Res*, 2006, 111, D05109, doi:10.1029/2005JD006290.

[8] Jiang Y, Luo Y, Zhao Z, et al. Changes in wind speed over China during 1956-2004. *Theor Appl Climatol*, 2010, 99(3): 421-430.

[9] DeGaetano A T, Allen R J. Trends in twentieth century temperature extremes across the United States. *J Climate*, 2002, 15: 3188-3205.

[10] Ren G, Zhou Y, Chu Z, et al. Urbanization effect on observed surface air temperature trend in North China. *J Climate*, 2008, 21(6): 1333-1348.

[11] Easterling D R, Horton B, Jones P D, et al. Maximum and minimum temperature trends for the globe. *Science*, 1997, 277: 364-367.

[12] Vose R S, Easterling D R, Gleason B. Maximum and minimum temperature trends for the globe: An update through 2004. *Geophys Res Lett*, 2005, 32, L23822, doi:10.1029/2005GL024379.

[13] 屠其璞，邓自旺，周晓兰. 中国近 117 年年平均气温变化的区域特征研究. 应用气象学报，1999，10(增刊)：34-42.

[14] 丁一汇，戴晓苏. 中国近百年气温的变化. 气象，1994，20(12)：19-26.

[15] 张明庆，刘桂莲. 我国近 40 年气温变化地域类型的研究. 气象，1999，25(4)：10-14.

[16] 唐红玉，翟盘茂，王振宇. 1951—2002 年中国平均最高、最低气温及日较差变化. 气候与环境研究，2005，10(4)：728-735.

[17] Zhai P M, Zhang X B, Wan H, et al. Trends in total precipitation and frequency of daily precipitation extremes over China. *J Climate*, 2005, 18: 1096-1108.

[18] 蔡敏，丁裕国，江志红. 我国东部极端降水时空分布及其概率特征. 高原气象，2007，26(2)：309-317.

[19] 王小玲，翟盘茂. 1957—2004 年中国不同强度级别降水的变化趋势特征. 热带气象学报，2008，24(5)：459-466.

[20] 王绍武. 近百年气候变化与变率的诊断研究. 气象学报，1994，52(3)：261-273.

[21] 黄荣辉，徐予红，周连童. 我国夏季降水的年代际变化及华北干旱化趋势. 高原气象，1999，18(4)：465-476.

[22] 钱维宏，符娇兰，张玮玮，等. 近 40 年中国平均气候与极值气候变化的概述. 地球科学进展，2007，22(7)：673-684.

[23] 杨萍，刘伟东，王启光，等. 近 40 年我国极端温度变化趋势和季节特征. 应用气象学报，2010，21(1)：29-36.

[24] 苏布达，姜彤，任国玉，等. 长江流域 1960—2004 年极端强降水时空变化趋势. 气候变化研究进展，2006，2(1)：9-14.

[25] 杨金虎，江志红，王鹏祥，等. 中国年极端降水事件的时空分布特征. 气候与环境研究，2008，13(1)：75-83.

[26] 翟盘茂，任福民，张强. 中国降水极值变化趋势检测. 气象学报，1999，57(2)：208-216.

[27] 翟盘茂，王志伟，周旭凯. 全国及主要流域极端气候事件变化//气候变化与中国水资源. 北京：气象出版社，2007：91-112.

[28] 罗阳，赵伟，翟景秋. 两类天气预报评分问题研究及一种新评分方法. 应用气象学报，2009，20(2)：129-136.

[29] 张强，熊安元，张金艳，等. 晴雨(雪)和气温预报评分方法的初步研究. 应用气象学报，2009，20(6)：692-698.

[30] 陈桂英，赵振国. 短期气候预测评估方法和业务初估. 应用气象学报，1998，9(2)：178-185.

# Spatial and Temporal Distributions of Probability Classification of Precipitation and Temperature Anomalies over China

Yang Xiaobo[1)2)3)] Chen Lijuan[2)] Liu Yunyun[2)]

[1)] (*Institute of Plateau Meteorology*, *CMA*, *Chengdu* 610072)

[2)] (*National Climate Center*, *Laboratory for Climate Studies of China Meteorological Administration*, *Beijing* 100081)

[3)] (*Sichuan Provincial Climate Center*, *Chengdu* 610072)

**Abstract**

Based on the standard of the probability classification definition and scoring method in short term climate prediction operation, analysis is conducted on six-level probability classification of monthly precipitation and temperature anomalies in January and July. Spatial and temporal distributions are obtained through the monthly precipitation and temperature data at 160 stations in China, which are operationally used by National Climate Center of CMA. The six levels are defined as much more than normal (L1), moderately more than normal (L2), slightly more than normal (L3), slightly less than normal (L4), moderately less than normal (L5), much less than normal (L6).

The results indicate that the issued six-level probability classification is suitable for symmetrical distribution cases for positive and negative anomalies but neglecting spatial inhomogeneous distributions and inter-decadal variations of monthly temperature and precipitation. During the period of 1980—2009, the probability of L1 and L6 for precipitation in North China is high in January whereas that of L6 and L5 is elevated in South China in July. The six-level probability for precipitation in January and July is generally similar in South China. The probability of L4, L3, and L2 temperature is high whereas that of L6, L5, and L1 is low for temperature in China in both January and July. Compared to those in the period of 1951—1979, the station numbers of L1 and L2 in January and L5 for precipitation in July have significantly increased but those of L6 precipitation in January and L6 and L4 for precipitation in July have remarkably decreased in the period of 1980—2009. Meanwhile, the station numbers of L4, L5, L6 for temperature in January have substantially decreased but those of L1, L2, L3 for temperature in January increases significantly and the six-level temperature probability in July shows no variability since 1980.

The above results could provide an important reference for climate forecasters to fully consider inter-decadal, inter-annual and inter-seasonal variability. The standard of the scoring method for the climate prediction focuses on the accurate rate of classification prediction, and especially emphasizes the abnormal level of precipitation and temperature. Therefore, the scoring method will help promote climate prediction services. The six-level scoring method for precipitation is more reasonable, while for temperature the method needs appropriate improvements.

**Key words**: precipitation; temperature; probability classification; spatial and temporal distribution; climate prediction

杨小波，王永光，梁潇云. 11 月气候异常型及前期环流信号. 应用气象学报，2011，22(3)：275-282.

# 11 月气候异常型及前期环流信号

杨小波[1)2)3)]　王永光[2)*]　梁潇云[2)]

[1)]（中国气象局成都高原气象研究所，成都 610072）

[2)]（国家气候中心，北京 100081）　[3)]（四川省气候中心，成都 610072）

**摘　　要**

利用全国 160 站 1951—2008 年 11 月温度、降水资料和同期秋季 NCEP/NCAR 500 hPa 高度场再分析资料，分析了我国东部季风区 11 月暖湿、暖干、冷湿、冷干年同期环流特征，并对同期、前期环流特征进行了差异 $t$ 检验。结果表明：暖型（冷型）同期环流对应乌拉尔山阻塞高压不明显（明显），欧亚中高纬度地区盛行纬向（经向）环流；干型（湿型）同期环流对应西太平洋副热带高压偏弱（强）、偏东（西）。差异 $t$ 检验分布特征表明：在亚洲中高纬度地区，暖干、冷湿型（暖湿、冷干型）同期环流主要表现为南北（东西）气压场的差异；暖干、冷湿型的前期和同期环流特征分别具有 EU（Eurasia）和反 EU 遥相关距平结构，而暖湿、冷干型前期和同期环流特征分别具有反 PNA（Pacific/North American）和 PNA 遥相关距平结构。

**关键词**：冷暖；干湿；环流型；EU；PNA

## 引　言

20 世纪 80 年代后期以来，在我国冬季变暖的年代际背景下，也出现过 1995/1996，1999/2000，2004/2005，2007/2008 年 4 个冷冬的年际异常，低温雨雪灾害异常事件也时有发生。如 2008 年 1 月 10 日—2 月 2 日，我国南方发生了 4 次大范围的低温雨雪冰冻灾害；2009 年 11 月我国出现了秋末以来大范围的雨雪天气，此次过程降水量之大、持续时间之长均为历史同期罕见，给我国经济、社会造成了重大影响。近 60 年来，典型的冷湿年曾发生过 5 次（1962，1967，1981，1993，2000 年），华北平原、黄淮、江淮、江南、西北地区东部和内蒙古西部降水偏多 5 成至 1.5 倍，内蒙古西部更是偏多 2～3 倍。与此同时，长江中游以北地区气温普遍偏低 1～2℃，华北南部、汉水中下游、江南西部、内蒙古西部偏低超过 2℃。

近年来许多研究也开始关注我国冷冬和暖冬的异常变化[1-6]，分析了我国异常冷、暖冬年的大气、海洋等影响因子[7-10]。东亚强冬季风时，我国冬季为冷、干气候，大气环流具有强 WP（Western Pacific）型、弱 EU 遥相关型的特征[11]。纪立人等[12]进一步分析了厄尔尼诺事件与北太平洋/北美区的 PNA 型密切，拉尼娜事件与 EAWM（东亚冬季风）流型的强东亚冬季风环流型相联系。陈见等[13]分析春季广西凝冻时指出东亚经向环流和南支槽活跃的影响；杨素英等[14]分析东北冬季气温时指出强西伯利亚高压对应东北冷冬；黄露菁等[15]分析广东春季冷暖环流特征时指出，特暖年西风指数偏强，副热带高压偏强。不过以往的研究多侧重于暖冬或冷冬的变化，并未涉及到冷冬或暖冬年东部季风区温度和降水的整体配置情况，对冷暖、干湿年的月温度、降水趋势前期环流特征的探讨较少，尤其是对前期年际信号影响大范围冷暖、干湿的研究更少。因此，针对以上问题，本文在综合考虑温度、降水的配置下，得到 11 月暖湿、暖干、冷湿、冷干年的同期500 hPa高度场的分布特征，并在此基础上分析了同期和前期 500 hPa 高度场的显著性差异。

2010-03-10 收到，2011-02-28 收到再改稿。

资助项目：国家科技支撑计划项目（2009BAC51B04）

* 通信作者，E-mail：ygwang@cma.gov.cn

## 1 资料和方法

本文采用的资料包括：① 全国160站1951—2008年11月温度、降水资料；② NCEP/NCAR 1951—2008年9月、10月、11月逐日500 hPa高度场再分析资料。

本文选取我国东部季风区64站11月温度、降水资料，去除其9年以上长期趋势变化，得到仅含9年以下时间尺度变化的温度、降水新序列。在此基础上，分别计算我国东部季风区64站温度和降水的正距平站数，并对其进行标准化处理，得到1955—2004年温度、降水正距平站数序列，分别记为 $S_1$ 和 $S_2$，来代表全国温度、降水的年际变化。$S_1+S_2$ 大值定为暖湿年，小值定为冷干年；$S_1-S_2$ 大值定为暖干年，小值定为冷湿年。同时，本文也对高度场滤去9年以上的年代际趋势变化。需要特别指出的是，本文所用资料仅保留9年以内尺度的年际变化部分，这样可以最大限度消除气候变暖对 $S_1+S_2$，$S_1-S_2$ 的影响，获得较准确的冷暖干湿年份。同时，这也突出了气候要素年际变化部分，对月、季气候预测有更好的指示意义。

以标准化处理后的 $S_1+S_2$ 和 $S_1-S_2$ 大于1.5倍标准差和小于−1.5倍标准差为标准，确定出具体的暖干、冷湿、暖湿、冷干年，得到4种不同温度、降水配置型的同期500 hPa高度距平场特征。同时，通过差异显著性 $t$ 检验方法可以获得不同典型年前期和同期500 hPa高度距平场显著性差异区域。

## 2 环流分型

本文首先参照第1章的方法，计算去除9年以上年代际变化的全国160站11月温度、降水的正距平站数序列，分别记为 $S'_1$ 和 $S'_2$，并据此计算了 $S'_1$（$S'_2$）和去除9年以上年代际变化的全国160站11月温度（降水）的相关系数（图1），以此来检验选取研究区域的合理性。从图1a看到，$S'_2$ 与降水未通过信度检验的相关区主要分布于西南地区东部、东北大部、内蒙古中东部以及新疆部分地区，$S'_2$ 与降水的显著正相关区主要分布于我国华南、华中、华东、华北以及西北地区大部。从图1b可知，$S'_1$ 与温度的负相关区主要分布于青藏高原南部部分地区，而我国其余大部地区为显著正相关区。图1还表明，温度整体的代表性要明显高于降水，这说明降水的分布特征远比温度复杂。综合以上分析，$S'_1$ 和 $S'_2$ 能较好地反映出我国东部季风区温度、降水演变特征，但不能反映我国西部地区和东北地区的变化，因此，以下分析都以我国东部季风区64站（图中方框内区域）计算的 $S_1$ 和 $S_2$ 进行讨论。

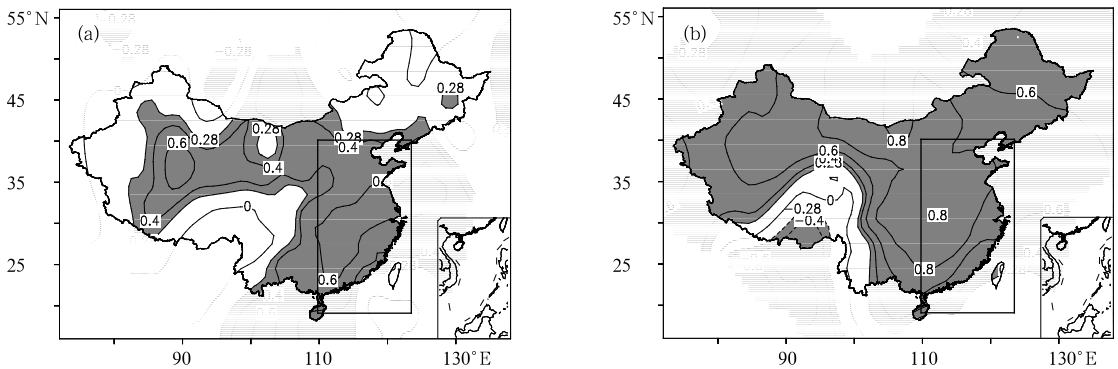


图1 1955—2004年 $S'_2$ 与全国160站11月降水的相关系数(a)和 $S'_1$ 与全国160站11月温度的相关系数(b)（阴影区为信度超过95%的区域）

Fig. 1 The correlation of $S'_2$ to precipitation of 160 stations in November(a) and $S'_1$ to temperature of 160 stations in November(b) during 1955—2004 (the area passing the test of 95% level is shaded)

$S_1+S_2$ 和 $S_1-S_2$ 的序列如图2所示。根据 $S_1+S_2$（图2中实线）大小，定义典型暖湿年为1961，1965，1972，1982，1990年；典型冷干年为1969，1979年。同理，根据 $S_1-S_2$（图2中虚线）大小，定义典型暖干年为1980，1998年；典型冷湿年为1962，1967，1981，1993，2000年。普查历年温度、降水配置情况后发现，这里所选典型年份都能较好地反映出实况分布特征。

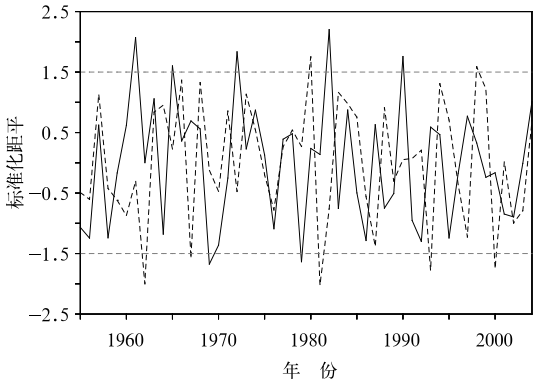


图 2　近 50 年来 $S_1+S_2$(实线)和 $S_1-S_2$(虚线)的时间演变序列

Fig. 2　The time series of $S_1+S_2$(solid line) and $S_1-S_2$(dashed line) in recent 50 years

## 3　同期环流特征

为了揭示同期大气环流异常对温度和降水的影响，图 3 分别给出了暖干年平均和冷湿年平均的 11 月 500 hPa 高度距平场。当出现暖干型环流时(图 3a)，欧洲、西伯利亚、北太平洋地区为负距平区，中亚至日本纬向带以及低纬大部为正距平区。这表明乌拉尔山地区未出现阻塞高压，欧亚中高纬地区为“南高北低”的环流形势，盛行纬向环流，不利于北方强冷空气活动。此类型环流分布易导致我国大部地区温度偏高、降水偏少。与之相反，当出现冷湿型环流时(图 3b)，我国北方大部地区、鄂霍次克海、贝加尔湖地区以及整个低纬度地区为负距平区，我国东部至日本地区、东北太平洋以及乌拉尔山为正距平区。这表明乌拉尔山地区出现阻塞高压，欧亚中高纬度地区自西向东为“正-负-正”的环流形势，经向环流发展，有利于北方强冷空气的活动，负距平区南扩，锋区南压。此类型环流分布导致我国大部地区温度偏低、降水偏多。

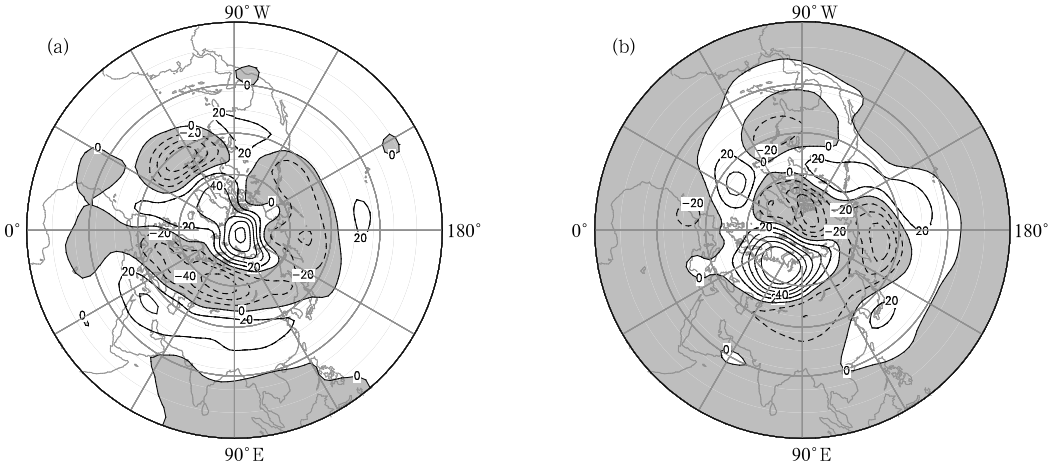


图 3　暖干年平均(a)和冷湿年平均(b)的 11 月 500 hPa 高度距平场(单位：gpm；阴影区为负值区)

Fig. 3　The mean geopotential height anomaly of warm and dry years(a), cold and wet years(b) at 500 hPa in November(unit: gpm; the negative is shaded)

图 4 分别给出了暖湿年平均与冷干年平均的 11 月 500 hPa 高度距平场。当出现暖湿型环流时(图 4a)，欧洲至乌拉尔山地区、鄂霍次克海以北、中国西部地区为负距平区，东亚地区为正距平区。这表明：乌拉尔山地区未出现阻塞高压，东亚大槽偏弱，欧亚中高纬度地区为“东高西低”的环流形势，不利于强冷空气的活动；同时，西太平洋副热带高压偏强、偏西，有利于引导水汽北上进入我国，此类型环流分布导致我国温度偏高、降水偏多。当出现冷干型环流时(图 4b)，东亚地区为负距平区，乌拉尔山至我国西部地区、鄂霍次克海地区为正距平区。这表明：乌拉尔山和鄂霍次克海地区有阻塞高压，东亚槽偏强、偏西，欧亚中高纬度地区为“西高东低”的环流形势，盛行经向环流，有利于北方强冷空气南下活动，此类型环流分布导致我国温度偏低、降水偏少。

为了进一步认清图 3、图 4 中典型环流场的显著差异区，本文利用 $t$ 检验方法，分别给出了 11 月暖干型与冷湿型和暖湿型与冷干型的 500 hPa 高度场的差值分布(如图 5 所示)。图 5a 表明，暖干型与冷湿型的显著差异区主要分布于东亚槽区、乌拉尔

山、欧洲西岸及北大西洋副热带地区，为 EU 遥相关型。这种分布说明暖干型与冷湿型在亚洲地区主要表现为中高纬度地区南北气压场的异常。图 5b 表明，暖湿型与冷干型的显著差异区主要位于乌拉尔山、东亚、西北太平洋、东北太平洋、北美西部、墨西哥湾附近地区，表现出反 PNA 的遥相关特征。这种分布说明在亚洲中纬度地区主要表现为东西气压场的差异。

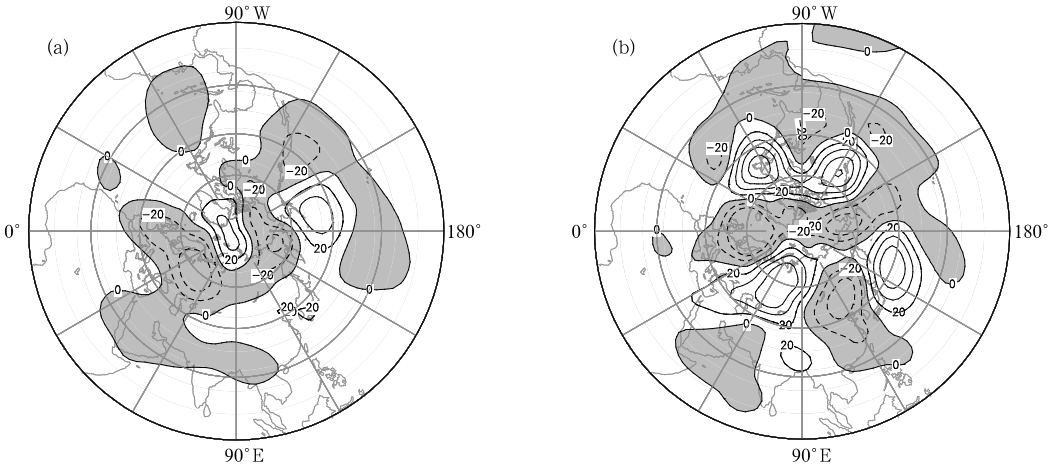


图 4 暖湿年平均(a)和冷干年平均(b)的 11 月 500 hPa 高度距平场(单位：gpm；阴影区为负值区)

Fig. 4 The mean geopotential height anomaly of warm and wet years (a), cold and dry years (b) at 500 hPa in November (unit: gpm; the negative is shaded)

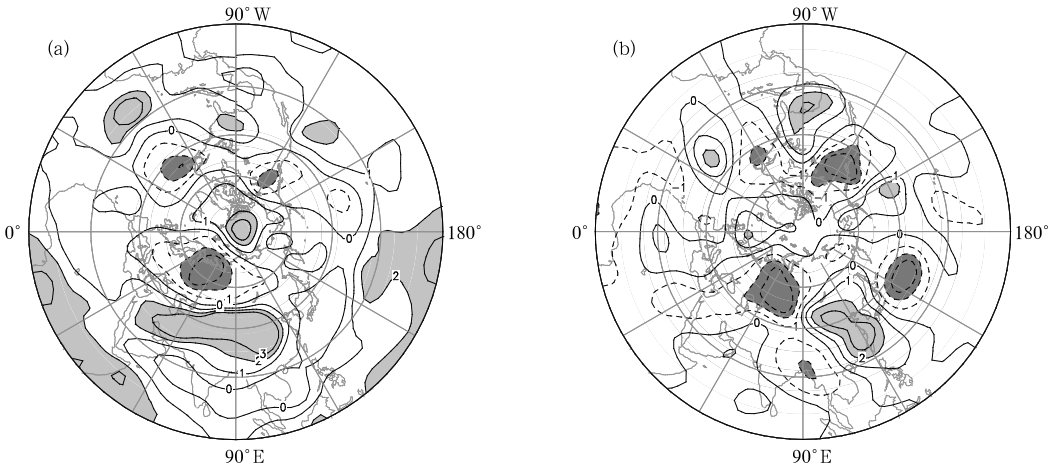


图 5 11 月 500 hPa 高度场的 $t$ 检验值分布(阴影区为信度超过 90%的显著差异区)

(a)暖干年平均与冷湿年平均偏差，(b)暖湿年平均与冷干年平均偏差

Fig. 5 The $t$-test of geopotential height anomaly of warm and dry years to cold and wet years (a), warm and wet years to cold and dry years (b) at 500 hPa in November (the area passing the test of 90% level is shaded)

综上所述，暖型(冷型)环流对应乌拉尔山阻塞高压不明显(明显)，欧亚中高纬度地区盛行纬向(经向)环流；干型(湿型)环流对应西太平洋副热带高压偏弱(强)、偏东(西)。这一结论与文献[15-16]得到的结果相符。同时，$t$ 检验值分布特征表明，暖干、冷湿型在亚洲地区主要表现为南北气压场的差异，暖湿、冷干型在亚洲地区主要表现为东西气压场的差异。$t$ 检验结果还表明用 $S_1$，$S_2$ 方法计算得到的 4 个典型环流型具有一定的代表性，各个特征环流型之间存在明显的差异。

## 4　前期环流特征

前期大气环流演变发展会造成后期环流的异常,因此,为了揭示出前期环流有预报指示意义的关键区,利用不同滑动时段 500 hPa 逐日高度场资料(仅保留了 9 年以下年际变化),计算了暖干型与冷湿型的前期高度场偏差 $t$ 检验分布值。从图 6 可以看到,当超前时段为 9 月 6 日—10 月 5 日时,欧洲、贝加尔湖以北地区高度场为负值显著性差异区,欧洲西岸、北非、乌拉尔山以东、日本海以东地区以及北大西洋副热带地区为正值显著性差异区。即乌拉尔山高压脊、欧洲上空低压槽偏强,东亚沿岸的低压槽偏弱,鄂霍次克海上空无阻塞高压发展,表现出近似 EU 的遥相关波列特征;当超前时段为 9 月 11 日—10 月 10 日时,$t$ 检验值基本维持 9 月 6 日—10 月 5 日的分布特征;当超前时段为 9 月 16 日—10 月 15 日和 9 月 21 日—10 月 20 日时,EU 遥相关波列特征更加明显,北非至乌拉尔山地区正高度距平向东伸展,即将与鄂霍次克海上空的正距平连成一片,欧洲和西西伯利亚地区负高度距平也将连成一片,中高纬度地区表现出“南高北低”的环流型。从以上分析可知,超前时段为 9 月 16 日—10 月 15 日和 9 月 21 日—10 月 20 日的高度距平场具有较好的显著性差异区,差异区主要分布于欧洲西岸、北非、欧洲、乌拉尔山以南地区,表现出显著的 EU 遥相关波列特征。

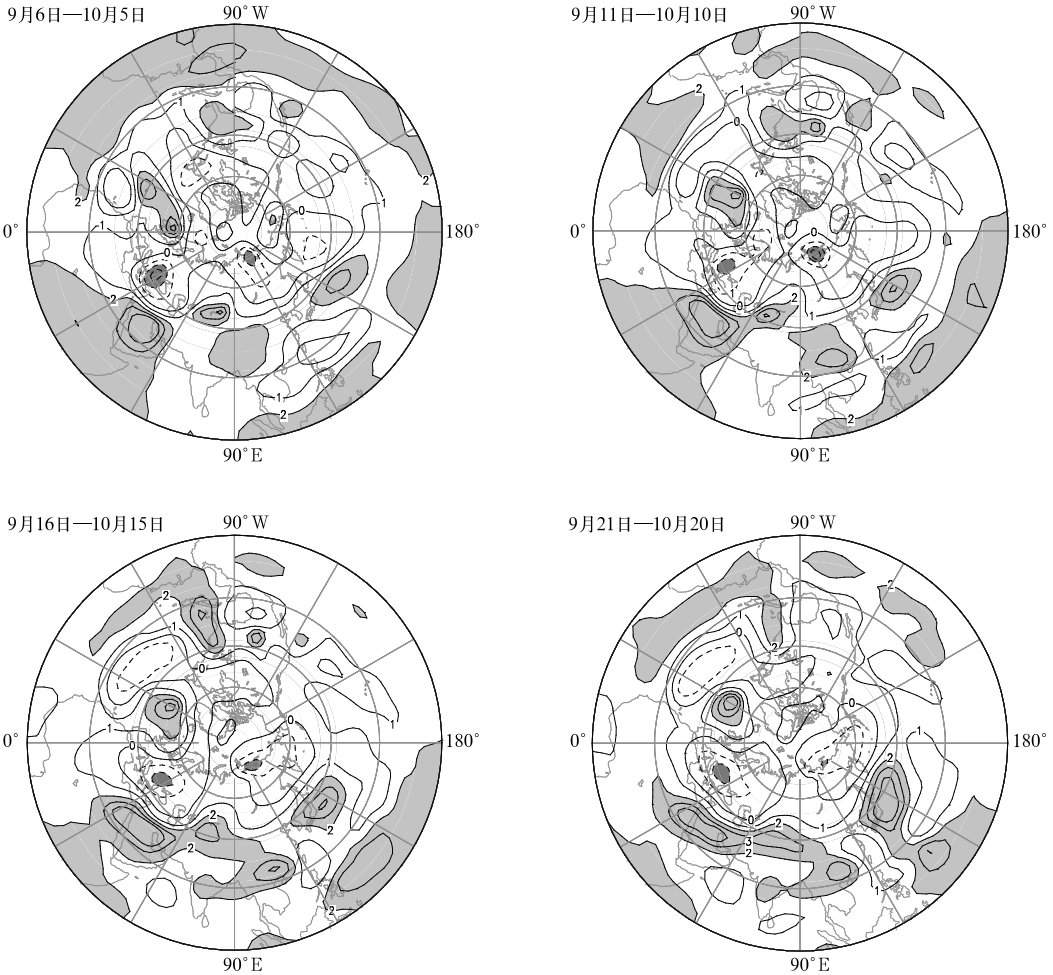


图 6　不同时段暖干年平均与冷湿年平均的前期 500 hPa 高度场偏差 $t$ 检验值分布

(阴影区为信度超过 90%的显著差异区)

Fig. 6　The $t$-test of geopotential height anomaly of warm and dry years to cold and wet years at 500 hPa in different lead-time(the area passing the test of 90% level is shaded)

图7为暖湿型与冷干型的前期高度场偏差 $t$ 检验分布值。当超前时段为9月6日—10月5日时，乌拉尔山、北美西部、夏威夷群岛附近高度场为负值显著性差异区，鄂霍次克海、东北太平洋以及墨西哥湾附近高度场为正值显著性差异区，表现出近似反PNA的遥相关波列特征；当超前时段为9月11日—10月10日和9月16日—10月15日时，显著差异区基本维持9月6日—10月5日的分布特征，北美南部的正距平北移，北太平洋的正距平增强，表现出近似反PNA的遥相关波列特征；当超前时段为9月21日—10月20日时，东亚槽区的正值显著性差异区明显增强，欧亚地区从西到东为“负-正-负”的环流型。对比图5b可以看出，超前时段为9月6日—10月5日、9月11日—10月10日、9月16日—10月15日和9月21日—10月20日的高度场显著差异区与图5b中东亚至太平洋、北美地区的分布特征非常类似。

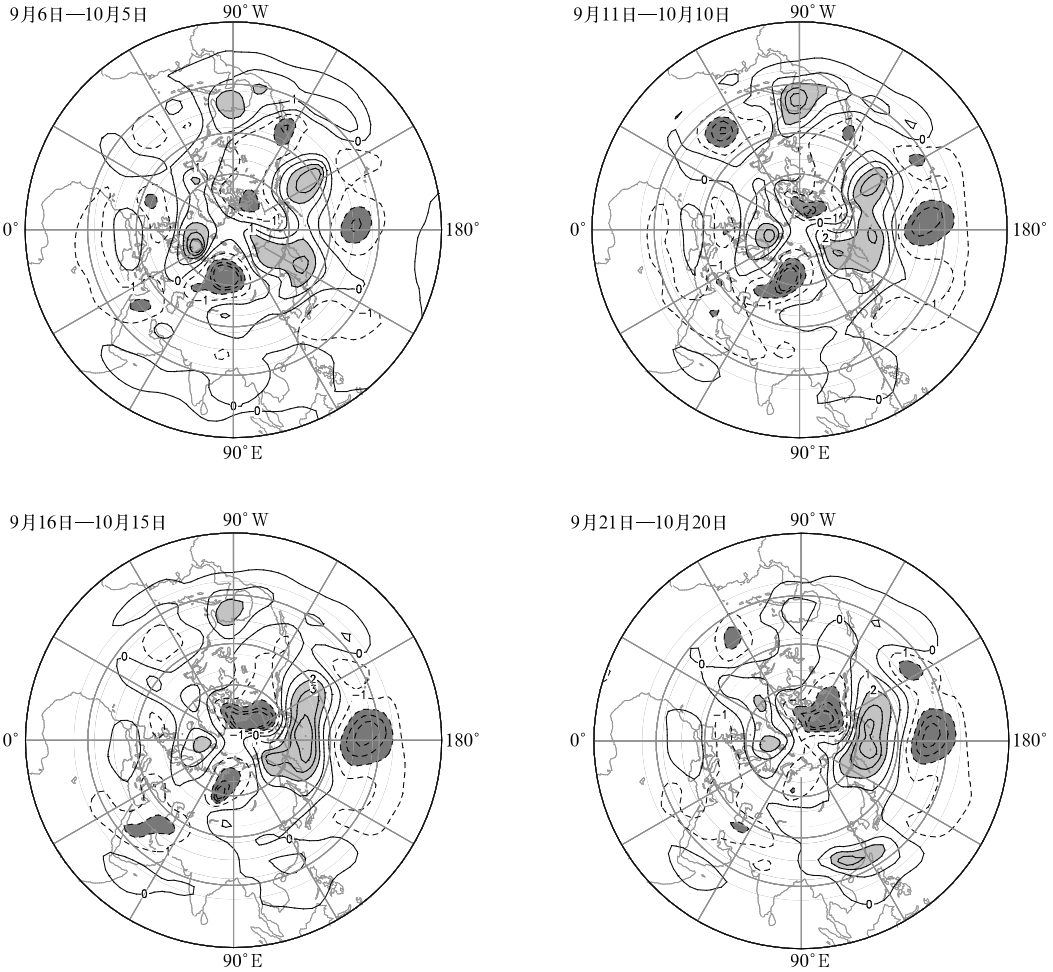


图7 不同时段暖湿年平均与冷干年平均的前期500 hPa高度场偏差 $t$ 检验值分布

（阴影区为信度超过90%的显著差异区）

Fig. 7 The $t$-test of geopotential height anomaly of warm and wet years to cold and dry years at 500 hPa in different lead-time (the area passing the test of 90% level is shaded)

## 5 小 结

本文利用全国160站温度、降水资料和NCEP/NCAR 500 hPa高度场再分析资料，分析了东部季风区11月暖湿、暖干、冷湿、冷干年同期环流特征，并对同期、前期环流特征进行了差异 $t$ 检验，得到如下结论：

1）温度正距平站数（$S'_1$）代表了除青藏高原南部部分地区以外的全国大部地区温度，降水正距平

站数($S_2'$)代表了除西南地区东部、东北、内蒙古中东部以及新疆部分地区以外的全国大部季风区降水。

2) 暖型(冷型)环流对应乌山阻塞高压不明显(明显),欧亚中高纬度地区盛行纬向(经向)环流;干型(湿型)环流对应西太平洋副热带高压偏弱(强)、偏东(西)。

3) $t$ 检验值分布特征表明:暖干(冷湿)型在亚洲地区主要表现为中高纬度南北气压场的差异,具有 EU(反 EU)遥相关距平结构;暖湿(冷干)型在亚洲主要表现为中高纬度地区东西气压场的差异,具有反 PNA(PNA)遥相关距平结构。

4) 超前时段为 9 月 6 日—10 月 5 日、9 月 11 日—10 月 10 日和 9 月 16 日—10 月 15 日的暖干(冷湿)型具有显著差异区,表现出显著的 EU(反 EU)遥相关波列特征;超前时段为 9 月 11 日—10 月 10 日、9 月 16 日—10 月 15 日和 9 月 21 日—10 月 20 日的暖湿(冷干)型具有显著差异区,表现出近似反 PNA(PNA)的遥相关波列特征。

对于暖湿型、冷干型在亚洲主要表现为中高纬度地区东西气压场的差异,即欧亚经向环流对应冷干、纬向环流对应暖湿,过去研究较多;但对于冷湿(暖干)型环流的差异,则在分析前兆信号时,一方面表现为高纬度高度场偏高(低)、中低纬度高度场偏低(高),处于 AO 的负(正)位相,导致大范围气温偏低(高);同时,乌拉尔山高度场也偏低(高);另一方面,青藏高原高度场偏低(高),南支槽偏强(弱),致使暖湿气流偏强(弱),东部大范围降水偏多(少)。

## 参 考 文 献


[1] 龚道溢,王绍武. 近百年我国的异常暖冬与冷冬. 灾害学,1999,14(2):63-68.

[2] 王绍武. 中国冷冬的气候特征. 气候变化研究进展,2008,4(2):68-72.

[3] 缪启龙,许遐祯,潘文卓. 南京 56 年来冬季气温变化特征. 应用气象学报,2008,19(5):620-626.

[4] 王凌,张强,陈峪,等. 1956—2005 年中国暖冬和冬季温度变化. 气候变化研究进展,2007,3(1):26-30.

[5] 陈少勇,郭忠祥,高蓉,等. 我国东部季风区冬季气温的气候变暖特征. 应用气象学报,2009,20(4):478-485.

[6] 赵汉光,张桂森. 我国异常冬暖的时空变化及其环流特征的分析. 气象,1989,15(11): 16-20.

[7] 李春晖,管兆勇,何金海,等. 西太平洋海温和南方涛动与中国冬季气候异常关系年代际变化的对比分析. 应用气象学报,2005,16(1):105-113.

[8] 沈爱华,王成友,任广成. 北京冷暖冬年环流特征及其与前期北太平洋海温的关系. 气象科技,2008,36(2):185-189.

[9] 毛睿,龚道溢,房巧敏. 冬季东亚中纬度西风急流对我国气候的影响. 应用气象学报,2007,18(2):137-146.

[10] 孙林海,赵振国. 我国暖冬气候及其成因分析. 气象,2004,30(12):57-60.

[11] 施能. 近 40 年东亚冬季风强度的多时间尺度变化特征及其与气候的关系. 应用气象学报, 1996, 7(2):175-182.

[12] 纪立人,布和朝鲁,孙淑清. EAWM 流型域——一种与东亚冬季风异常相联的海-气耦合流型域. 大气科学,1998,22(4):491-502.

[13] 陈见,黄明策,赵金彪,等. 2008 广西罕见凝冻灾害成因分析. 热带地理,2008,28(4):297-301.

[14] 杨素英,王谦谦,孙凤华. 中国东北南部冬季气温异常及其大气环流特征变化. 应用气象学报,2005,16(3):334-344.

[15] 黄露菁,陈志芳,陈创买,等. 广东冬末春初冷暖变化时空分布特征及类型. 中山大学学报(自然科学版),2004,43(1):102-106.

[16] 王永光,赵振国,赵汉光. 中国温度、降水的长期气候趋势及其相关因子分析//短期气候监测、预测、服务综合业务系统的研制. 北京:气象出版社,2000.

# The Patterns of Anomalous Climate and Their Pre-circulation Signals in November

Yang Xiaobo[1)2)3)] Wang Yongguang[2)] Liang Xiaoyun[2)]

[1)] (*Institute of Plateau Meteorology*, *China Meteorological Administration*, *Chengdu* 610072)

[2)] (*National Climate Center*, *Beijing* 100081) [3)] (*Sichuan Provincial Climate Center*, *Chengdu* 610072)

**Abstract**

Based on the stationery data of temperature and precipitation of 160 stations in China in November, the reanalysis data of 500 hPa geopotential height (GPH) of NCEP/NCAR, the four circulation patterns corresponding to the warm and wet, warm and dry, cold and wet, cold and dry in the monsoon regions over eastern China are analysed, and the previous and corresponding circulations are inspected with *t*-test method. The time series of positive station numbers about the temperature and precipitation are labeled as $S_1$ and $S_2$ respectively after removing long-term trend more than 9 years. Then the typical years according to the cold, warm, dry and wet patterns could be acquired by using the values of $S_1+S_2$ and $S_1-S_2$. In detail, the larger values of $S_1+S_2$ are defined as the warm and wet years, and the smaller values are defined as the cold and dry years. Meanwhile, the larger values of $S_1-S_2$ are represented as the warm and dry years, and the smaller values are represented as the cold and wet years. The results are as follows: The warm (cold) pattern takes on the inactive (active) blocking high over Ural Mountain and zonal (meridional) circulation prevails at middle and high latitudes. The dry (wet) type is corresponding to the weak (strong) and eastward (westward) of subtropical high in western North Pacific. The circulation difference of warm and dry pattern minus cold and wet pattern in *t*-test is in meridional direction, similar to the EU pattern. The circulation difference of warm and wet pattern minus cold and dry pattern in *t*-test is in zonal direction, similar to the anti-PNA pattern. The pentad running-mean of monthly circulation has significant differences for the warm and dry (cold and wet) type in the beginning time on 6, 11, 16 September and warm and wet (cold and dry) type in the beginning time on 11, 16 and 21 September which indicate that the previous circulation has significant implication for climate prediction. The characteristics of cold and wet (warm and dry) type are as below: On one hand, the GPH is high (low) at high latitude and low (high) at middle and low latitudes, and meanwhile AO is negative (positive), leading to low (high) temperature over northern China; on the other hand, the GPH is low (high) at the Qinghai-Tibet Plateau, and the active (inactive) southern branch trough induces the more (less) precipitation.

**Key words**: cold and warm; dry and wet; circulation type; EU; PNA

尹红, 王靖, 刘洪滨, 黄磊, 朱海峰. 小兴安岭红松径向生长对未来气候变化的响应. 生态学报, 2011, 31(24): 7343-7350.
Yin H, Wang J, Liu H B, Huang L, Zhu H F. A research on the response of the radial growth of *Pinus koraiensis* to future climate change in the XiaoXing′AnLing. Acta Ecologica Sinica, 2011, 31(24): 7343-7350.

# 小兴安岭红松径向生长对未来气候变化的响应

尹 红[1,*], 王 靖[2], 刘洪滨[1], 黄 磊[1], 朱海峰[3]

(1. 中国气象局国家气候中心, 北京 100081; 2. 中国农业大学资源与环境学院, 北京 100193;
3. 中国科学院青藏高原研究所, 北京 100085)

**摘要**: 基于 SRES A1B 温室气体排放情景, 由全球气候模式 (MPI_ECHAM5) 产生的逐日气候模拟数据驱动 TREE-RING 树轮生态机理模型, 模拟了小兴安岭红松(*Pinus koraiensis*)树木径向生长变化。结果表明: 在 A1B 情景下, 随着大气 $CO_2$浓度的不断增加以及局地气温的不断升高, 红松树木生长开始和结束时间显著提前, 2011—2060 年比 1961—2010 年径向生长开始时间平均提前约 5d 左右, 生长结束时间平均提前约 3d 左右。红松树木的径向生长量不断增加, 2011—2060 年比 1961—2010 年径向生长量平均增加约 35%, 径向生长量的增加主要是 $CO_2$施肥作用的结果, 在不考虑 $CO_2$施肥效应下, 只考虑降水量变化使树木径向生长量增加约 2%, 而未来 50a 的气温变化使树木径向生长量相对于 1961—2010 年减少约 23%。

**关键词**: 小兴安岭; 红松; 树轮生态机理模型; 气候变化

# A research on the response of the radial growth of *Pinus koraiensis* to future climate change in the XiaoXing′AnLing

YIN Hong[1,*], WANG Jing[2], LIU Hongbin[1], HUANG Lei[1], ZHU Haifeng[3]

1 *National Climate Center, China Meteorological Administration, Beijing* 100081, *China*

2 *College of Resources and Environmental Sciences, China Agricultural University, Beijing* 100193, *China*

3 *Institute of Tibetan Plateau Research, Chinese Academy of Sciences, Beijing* 100085, *China*

**Abstract**: Climate change has had a significant impact on forest ecosystem. *Pinus koraiensis* is one of precious tree species in Northeast China. The coniferous and broadleaved mixed forest dominated by pine is the representative vegetation type in XiaoXing′AnLing of China. Under the climate change background, studying the response of the growth of *Pinus koraiensis* to climate change is important to understand the climate change impact on forest ecosystem. Simulation models as effective tools for assessing the climate change impact have been applied widely in different regions over the world. A process-based ecological mechanism model (TREE-RING) had been verified for simulating the radial growth of *Pinus koraiensis* in XiaoXing′AnLing of China. The results showed that simulated phenology was well coincident with observed phenology. There was a high correlation between simulated and observed cell series of *Pinus koraiensis*. Based on the validated TREE-RING model, the study simulated the growth trend of *Pinus koraiensis* in XiaoXing′AnLing under future climate scenarios and explored the response mechanism of tree growth to climate change, which is helpful to understand climate change impact, alleviate the negative effects of climate changes on tree growth and provide references for policy-making related to addressing the climate change.

For this study, we intend to use TREE-RING model to simulate the growth of *Pinus koraiensis* in the XiaoXing′AnLing based on a middle medium emissions climate change scenario (SRES A1B) generated by global climate model (MPI_

**基金项目**: 全球变化研究国家重大科学研究计划(2010CB950104); 国家气象公益性行业科研专项(GYHY201106013); 国家林业公益性行业科研专项(200804001)共同资助

**收稿日期**: 2011-07-22; **修订日期**: 2011-10-27

* 通讯作者 Corresponding author. E-mail: yinh@cma.gov.cn

ECHAM5) from 1961 to 2060. The meteorological data including daily maximum temperature, daily minimum temperature and daily precipitation with the resolution of 1°×1° was interpolated to Yichun meteorological station (47°73′N,128°92′E, 240.9 m. a. s. l) with the method of Bilinear interpolation. The analysis on the variation characteristics of climate factors from 1961 to 2060 showed that atmospheric $CO_2$ concentration will continue to increase and reach 563 mg/L in 2060. Maximum and minimum temperature will have a fluctuating rising tendency while precipitation will change slightly.

TREE-RING droved by climate data model was run for 100 years from 1961 to 2060. The simulated results showed that under the SRES A1B emission scenarios, with the increase in atmospheric $CO_2$ concentration and air temperature, the beginning and end dates of *Pinus koraiensis* growth will advance significantly in the XiaoXing′AnLing from 2011 to 2060 with a mean advance of 5 days in the beginning date and 3 days in the end date compared with 1961—2010. Annual radial growth period will prolong by about 2 days in the future fifty years. The radial growth rate will be increased by 35% in 2011—2060 compared with 1961—2010, which is mainly due to the effect of $CO_2$ fertilization. The individual change in precipitation will increase tree radial growth by about 2% while the individual change in air temperature will decrease tree radial growth by 23%. Sensitivity analyses were performed to see the response of the model under variable climatic environmental conditions. The results show that rising air temperature in spring (March and April) increases tree growth rate significantly, however, rising air temperature in summer (June-August) decreases tree growth rate when air temperature was increased by 1℃ and $CO_2$ concentration and precipitation were not changed.

**Key Words**: XiaoXing′AnLing; *Pinus koraiensis*; REE-RING Eco-physiological model; Climate change

2007 年政府间气候变化专门委员会(IPCC)发布的第四次评估报告指出,全球变暖已经是不争的事实。在不同的 SRES 温室气体排放情景下,到 21 世纪末,全球地表平均气温可能上升 1.8℃—4.0℃[1]。全球气候变暖趋势加剧使得我国极端天气气候事件发生频率可能增加;降水分布不均现象更加明显,强降水事件发生频率增加;干旱区范围可能扩大;海平面上升趋势进一步加剧[2]。气候变化潜在地影响我国的农牧业、森林与自然生态系统、水资源和海岸带等。已观测的气候变化对森林生态系统的影响现象表现为,气候变暖促使植物物候期提前[3-5],生长期延长,加上大气 $CO_2$浓度增加形成的“施肥效应”,使得森林生态系统的生产力增加[6],如 Zhou 等基于卫星数据研究表明,1981—1999 年欧亚大陆北部和北美洲北部植被活力显著增长,生长期延长[7]。基于生态系统模型的模拟研究表明气候变暖下中国东部亚热带、温带北界普遍北移[8];中国东北主要森林类型发生显著变化[9-10];$CO_2$浓度倍增后, 中国森林生产力将有所增加,增加的幅度因地区不同而异[11]。

红松是东北地区的珍贵树种,以红松为主的针阔叶混交林是我国小兴安岭地区最具代表性植被类型。森林在应对气候变化中扮演着重要角色,既可以作为温室气体的储藏库和吸收源,又可能因毁林、森林退化、火灾等,成为温室气体的排放源。同时,森林本身也会受到气候变化的显著影响。在未来气候变化情景下,小兴安岭地区红松树木的生长状况如何变化,对于加深理解气候变化的影响具有重要的意义。模型模拟是进行气候变化影响定量评价的方法之一,已有研究基于 TREE-RING 树轮生态机理模型对采自小兴安岭红松树轮样本建立时间序列的统计量子样本信号强度 SSS(Subsample Signal Strength)大于 0.9 时随机选取的 9 棵树,18 个样芯进行了模拟,模拟的生育期和物候观测比较一致,红松树木细胞模拟序列和实测序列具有较好的相关性[12]。本研究在此基础上,模拟了未来气候情景下小兴安岭红松树木的生长趋势,从树木生长的物候、径向生长、气候因子对树木生长的影响方面探讨了树木生长对气候变化的响应机制,对于理解和认识气候变化,减缓气候变化带来的负面效应,以及应对气候变化政策的制定提供参考依据。

## 1 研究地区与研究方法

### 1.1 自然概况

小兴安岭森林资源丰富,树种较多。其中红松为主的针阔叶混交林是小兴安岭主要森林资源。本文的研

究区在丰林国家级自然保护区(48°02′—48°12′N,128°58′—129°15′E),位于我国小兴安岭南部北坡,黑龙江省伊春市五营区五营林业局境内,地带性植被为温带针阔叶混交林,总面积 18400 $hm^2$,是中国目前保存最完整、最典型的原始红松林保护区(图 1)。全区地形平缓,海拔 280—683 m,夏季湿润多雨,冬季严寒少雪。分析伊春气象站 1958—1998 年资料显示该地区平均年降水量在 450—1000 mm 之间,6—8 月份降水在 230—700 mm 之间,约占全年降水量的 65%。年平均气温在 1℃左右,其中 1—3 月、11 月和 12 月份平均气温都在 0℃以下,5 月到 9 月份平均气温一般大于 10℃以上[12]。

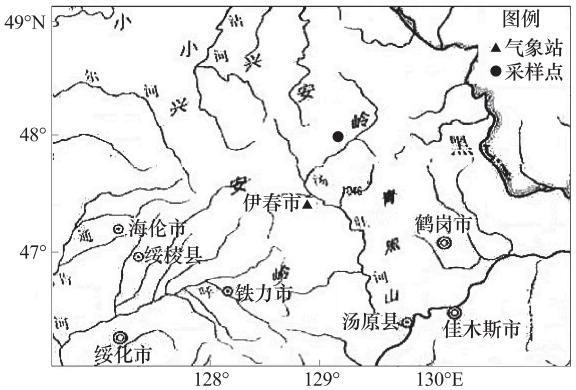


**图 1　采样点和气象站示意图**

**Fig. 1　Schematic diagram of sampling site and meteorological station**

### 1.2　数据与方法

#### 1.2.1　数据资料

2000 年 IPCC《排放情景特别报告》发布了一系列新的排放情景,即 SRES 情景,SRES 设计了 4 种世界发展模式,其中 A1B 是各种能源平衡发展下的未来温室气体排放情景[2]。本文利用全球气候模式 MPI_ECHAM5 输出的 A1B 排放情景下 1961—2060 年,空间分辨率是1°×1°的逐日最高气温、最低气温、逐日降水量资料,利用双线性插值到各气象站点,由于伊春气象站(47°73′N,128°92′E,海拔 240.9m)是距离采样点最近的气象基准站,因此本文利用伊春气象站的逐日预估资料对小兴安岭红松树木径向生长对未来气候变化的响应进行模拟研究。

#### 1.2.2　模型描述

本文所使用的 TREE-RING 模型是描述树木形成层生长过程的模型[13]。模型描述的外部环境对树木的影响主要是在形成层区域具有生命活动的细胞,影响细胞的线性生长率和细胞的分裂周期。树木的光合产物含量 $f(S)$、温度 $f(T)$ 和树木的水分平衡 $f(W)$ 状态 3 个因素控制相对生长速率[12,14-15]。其中 $CO_2$浓度变化对树木光合作用的影响表示为:

$$\begin{cases} p = P_m \dfrac{C_a - a}{b - a + P_m R^c}, & P_m R^c \geqslant C_a - a \\ p = P_m, & P_m R^c \leqslant C_a - a \end{cases} \tag{1}$$

公式(1)中 a 和 b 分别为胞间 $CO_2$补偿点和饱和点,模型取值分别为 1.5 mmol/$m^3$ 和 10.5 mmol/$m^3$。$C_a$为空气中 $CO_2$浓度。$R^c$为叶片中 $CO_2$扩散阻力,$R^c = \lambda R$,$\lambda$ 为 $CO_2$扩散阻力 $R^c$与水汽扩散阻力 $R$ 的比率:

$$P_m = P_{\max} f(T) f(I) \tag{2}$$

式中,$P_{max}$为潜在的最大光合速率,$f(I)$为光照 $I$ 对光合速率的影响,满足 Michaelis-Menten 方程:

$$f(I) = \frac{I}{I + I^*} \tag{3}$$

式中,$I^*$ 为 Michaelis-Menten 常数。

## 2　结果与分析

### 2.1　小兴安岭地区未来气候变化状况

在 A1B 情景下 2011—2060 年该地区气候因子以及 $CO_2$浓度变化趋势如图 2 所示,从图 2 中可见,未来 50a 小兴安岭地区 $CO_2$浓度持续增加,2060 年达到 563mg/L,年最高和最低气温都呈波动上升趋势,而降水量的变化较小。进一步对春季(3、4 月和 5 月)、夏季(6、7 月和 8 月)、秋季(9、10 月和 11 月)和冬季(12、1 月和 2 月)的气温和降水每 10a 的变化进行深入分析显示(表 1):最高和最低气温在春、夏、秋和冬季也持续升高,

其中最高气温年代际变化显示秋季升温最大,之后依次是春季、冬季和夏季。春季最高气温 21 世纪 30 年代温度比 20 年代要略微偏低。夏季最高气温 21 世纪 20 年代比 10 年代略有降低。秋季和冬季最高气温都是 40 年代比 30 年代略有降低。最低气温年代际变化显示秋季气温升温最高,之后依次是冬季、春季和夏季。其中夏季最低气温 21 世纪 20 年代比 10 年代略有偏低,冬季 21 世纪 40 年代比 30 年略有偏低。降水的年代际变化分析显示,秋季、春季和夏季降水略有降低,其中秋季降低最大,春季和夏季次之,冬季降水略有增加,总体上看各季节降水变化的幅度较小。

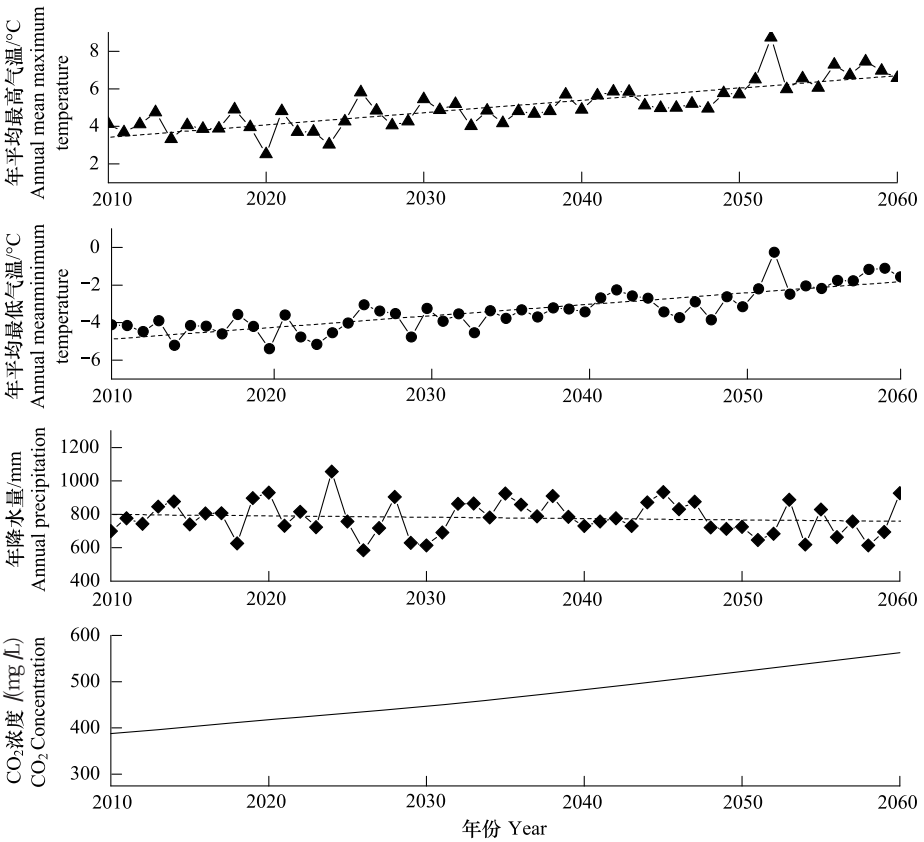


**图 2 A1B 情景下各气候因子及 $CO_2$ 浓度的变化趋势**

**Fig. 2 Changes in climatic factors and $CO_2$ concentration under SRES A1B climate scenario**

**表 1 A1B 情景下伊春气象站 2011—2060 年的每 10a 尺度气候要素变化**

**Table 1 Decadal change of climate factors under SRES A1B scenario in Yichun from 2011 to 2060**

| 要素 Elements | 季节 Season | 年份 Year | | | | |
|---|---|---|---|---|---|---|
| | | 2011—2020 | 2021—2030 | 2031—2040 | 2041—2050 | 2051—2060 |
| 最高气温/℃ | 春 Spring | 4.20 | 5.11 | 4.79 | 6.36 | 7.23 |
| Maximum temperature | 夏 Summer | 22.28 | 21.86 | 22.36 | 23.33 | 24.14 |
| | 秋 Autumn | 6.38 | 7.02 | 7.63 | 7.51 | 10.03 |
| | 冬 Winter | -17.27 | -16.89 | -15.63 | -15.93 | -14.32 |
| 最低气温/℃ | 春 | -5.30 | -4.61 | -4.59 | -3.58 | -2.41 |
| Minimum temperature | 夏 | 14.50 | 14.43 | 14.55 | 15.51 | 16.01 |
| | 秋 | -1.49 | -1.23 | -0.69 | -0.41 | 1.70 |
| | 冬 | -24.96 | -24.58 | -23.42 | -23.46 | -21.93 |
| 降水量/mm | 春 | 2.43 | 2.26 | 2.49 | 2.13 | 2.14 |
| Precipitation | 夏 | 4.07 | 4.24 | 4.32 | 4.52 | 3.79 |
| | 秋 | 1.79 | 1.18 | 1.56 | 1.53 | 1.44 |
| | 冬 | 0.49 | 0.53 | 0.57 | 0.47 | 0.62 |


http://www.ecologica.cn

## 2.2　未来气候情景下小兴安岭红松树木径向生长物候期变化

模型中径向生长开始定义为形成层区域细胞被激活,形成层细胞体积开始增大的日期(从 1 月 1 日开始算起),生长结束的日期为最后一个细胞原生质消逝,进入休眠状态的日期。利用 A1B 排放情景下全球气候模拟资料输出 1961—2060 年气候资料计算得到的,1961—2010 年小兴安岭红松树木径向生长开始期平均为第 126 天,生长结束期平均为第 284 天,2011—2060 年红松树木径向生长开始期平均为第 121 天,生长结束期平均为第 281 天。从红松树木径向生长开始和结束日期 1961—2060 年变化趋势的线性回归统计检验来看(图略),红松树木径向生长开始和结束时间显著提前,2011—2060 年比 1961—2010 年径向生长开始时间平均提前约 5d 左右,径向生长结束时间平均提前约 3d 左右,未来 50a 径向生长期约延长 2d 左右。树木径向生长形成的树木年轮是树木形成层周期活动的结果,形成层活动受到多种因素影响,其中在温带地区,温度是影响树木生长开始时期最重要的因素,当春季气温达到一定高度时,形成层细胞才能开始活动[16]。前期的研究结果也显示,该地区的红松树木生长开始时期主要受到气温变化控制[12]。从未来气候变化情景数据来看,春季气温不断升高,如 21 世纪 50 年代比 10 年代春季气温升高约 3℃ 的情况下,树木的生长开始时间约提前 6.5d(表 2)。很多研究表明,春季物候变化与气温变化密切相关,徐雨晴等[17]分析了北京近 50a 春季物候变化及其对气候变化的响应,近 10a 来北京春季物候持续偏早,北京春温升高开花期提前,春温每升高 1℃,开花期平均提前 3.6d,春季树木开花物候与春季气温的年际、年代际的波动基本对应。郑景云等[18]根据中国科学院物候观测网络 26 个观测点的物候资料,分析显示我国木本植物的物候变化提前与春季增温有关。本文所用的树轮年轮宽度资料与气象站点的相关分析,也表明了生长初期的气温变化对树木生长影响很大[12]。而树木径向生长结束时间,也就是形成层休眠期从整体来看与气温升高没有直接关系。研究显示,树木的径向生长的时间主要由形成层开始日期决定[19]。由于春季气温升高,使得树木形成层生长开始时间提前,由形成层生长自身的遗传因素决定,因此树木开花、结果以及形成层生长的结束日期也会提前。观测研究显示,只有气温达到一定的高度时树木径向生长才开始,而生长达到一定时间,尽管温度较高,树木的径向生长仍然会停止[20]。当然秋季气温较高,对于延迟树木叶的脱落,增加光合累积具有重要的作用。而光合累积将有利于树木下一年的生长。从该地区树木生长情况可见,生长结束日期在 10 月上旬,而 10 月份气温与下一年的树轮宽度相关显著[12]。

**表 2　A1B 情景下小兴安岭红松 10a 平均径向生长期变化**

**Table 2　Decadal average change in radial growth period of *Pinus koraiensis* in Xiao Xing′AnLing under SRES A1B climate scenario**

| 生长阶段 Growth stages | 年份 Year | | | | |
|---|---|---|---|---|---|
| | 2011—2020 | 2021—2030 | 2031—2040 | 2041—2050 | 2051—2060 |
| 生长开始 Growth start | 124.8 | 122.7 | 123.4 | 117.8 | 118.3 |
| 生长结束 Growth end | 283.1 | 283.3 | 276.8 | 283.7 | 277.6 |
| 生长期 Growth periods/d | 158.3 | 160.6 | 153.4 | 165.9 | 159.3 |

## 2.3　未来气候情景下小兴安岭红松树木径向生长状况

模型模拟如图 3a 显示在 A1B 排放情景下,小兴安岭红松树木的径向生长量在明显增加,2011—2060 年比 1961—2010 年的径向生长量平均增加约 35%。径向生长量不断增加的趋势,也说明了小兴安岭红松在未来气候变化情景下材积量的不断增加,树木固碳能力在显著提高,这对降低大气中 $CO_2$ 含量,缓解由于温室气体引起的气候变暖能够起到一定作用。赵俊芳等[21]模拟显示未来平衡发展(A1B)气候变化情景下,2003—2049 年东北森林生态系统净初级生产力呈波动上升趋势,东北森林的吸碳总量在不断增加。杨书运等[22]的研究结果也表明,从 2005—2044 年中国森林的碳储存能力在提高。吴祥定等[23]根据树木年轮指数与气象记录之间的相关性,建立回归方程,推算在未来全球气候变暖情景下树木的径向生长量和材积量显示,年平均气温升高分别达到 1、2、3℃,吉林长白落叶松径向生长量分别增加 9.2%、15.7%、22.3%,材积量则分别增加 24.4%、44.7%、66.3%,在贡嘎山区径向增加量则分别为 5.3%、10.1%、14.7%,材积量分别为 13.9%、

27.3% 和 41.6%，也与本文的研究结果基本一致。

从很多研究结果中，都可以看出一个共同点，就是气候变化使树木的生长量增加。树木生长对不同气候因子的响应是怎样的，可以借助模型进行深入研究。本文假定 2011—2060 年的 $CO_2$ 浓度值与 1961—2010 年相同，代入模型进行模拟结果如图 3b 所示，通过图 3a 和 3b 对比，可以看出 $CO_2$ 对树木生长的助长作用，在 2011—2060 年 $CO_2$ 浓度与 1961—2010 年相等的情况下，2011—2060 年比 1961—2010 年树木径向生长量减少了 21%，说明未来 50a 的气温或降水变化使树木的生长速率降低，当 $CO_2$ 浓度在 1961—2010 年的基础上增加 33 μmol/mol，可以弥补由 2011—2060 年气温或降水变化引起的树木径向生长速率降低。通过模拟进一步显示，在 2011—2060 气温和 $CO_2$ 浓度与与 1961—2010 年保持不变的情况下，只降水发生变化的情况下使树木径向生长量比 1961—2010 年平均增加约 2%。而在 2011—2060 年的降水和 $CO_2$ 浓度与 1961—2010 年保持不变的情况下，气温变化使树木的径向生长量比 1961—2010 年平均减少约 23%，说明温度过高会抑制树木生长。

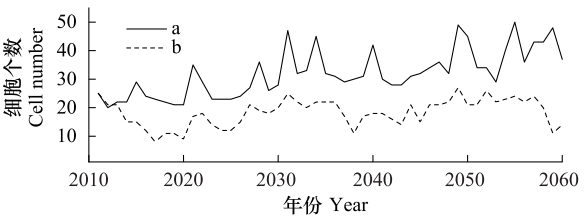


**图 3 A1B 情景下小兴安岭红松树木的径向生长趋势（a），2011—2060 年与 1961—2010 年 $CO_2$ 值相等的树木径向生长趋势（b）**

**Fig. 3 Radial growth trend of *Pinus koraiensis* under SRES A1B climate scenario (a), Radial growth trend with the equality $CO_2$ of 2011—2060 year and 1961—2010 year (b)**

由于该地区未来 50a 降水变化趋势较小，而气温升高趋势明显，因此本文对树木生长对气温变化的响应的敏感性进一步模拟分析，利用模型对 1961—2010 年在降水和 $CO_2$ 浓度不变的情况下，对每月的平均温度分别增加 1℃ 进行模拟，结果与 1961—2060 年气温不变时模拟的红松树木径向生长量比较发现（表 3），3 月和 4 月温度升高树木径向生长量分别增加约 2.5% 和 3.7%，而 6、7 月和 8 月份气温升高树木生长量分别降低了约 5.3%、6.8% 和 5.5%，其它月份的生长量变化不大，说明该地区在各月份升温相同的情况下，树木径向生长速率的降低主要由夏季 6、7 月和 8 月份的气温升高引起。分析显示这主要与光合作用对气温变化的响应有关，光合过程中的暗反应是由酶所催化的化学反应，因而受温度影响[24]，Peng 等[25]模拟研究了几种树种生物量随温度的变化曲线可以看出，树木的总生物量在一定的温度范围内，随温度的升高而增加，但是斜率逐渐变小，生物量达到最大值之后，随温度的增加而降低，斜率逐渐变大。在一定的温度范围内，生物量的值变化较小且接近最大值，这个温度范围为光合最适温度，模型设定的最适温度范围为 15—25℃。其中 3、4 月份温度在光合作用最低温度到最适温度下限之间，光合速率随温度的增加线形增加，因此这几个月份温度增加，树木的径向生长速率增大。而 6、7、8 月份温度在最适温度上下限范围内，随着温度的增加，光合速率变化较小，而随着气温升高，呼吸消耗却在加剧，树木的径向生长速率降低。

**表 3 1961—2010 年的逐月气温增加 1℃ 时模型模拟的红松径向生长变化**

**Table 3 Simulated radial growth change rate under rising monthly temperature by 1 ℃ from 1961 to 2010**

| 月份 Month | 1 | 2 | 3 | 4 | 5 | 6 | 7 | 8 | 9 | 10 | 11 | 12 |
|---|---|---|---|---|---|---|---|---|---|---|---|---|
| 树木径向生长变化/%<br>The change rate in radial growth | -1.0 | -0.4 | 2.5 | 3.7 | 0.4 | -5.3 | -6.8 | -5.5 | -1.8 | 1.4 | -1.5 | -0.1 |

“-”表示减少

## 3 结论与讨论

本文应用 TREE-RING 树轮生态机理模型对我国小兴安岭红松在未来气候变化 A1B 情景下的树木径向生长状况进行了模拟，探讨了气候变化对红松树木生长的影响机制。通过模拟研究得出以下结论：在各种能源平衡发展（A1B）的未来气候变化情景下，小兴安岭红松树木生长开始和结束时间不断提前，2011—2060 年比 1961—2010 年生长开始时间平均提前约 5d 左右，生长结束时间平均提前约 3d 左右。红松树木的径向生

长量不断增加,2011—2060 年比 1961—2010 年径向生长量平均增加 35%,径向生长量的增加主要是 $CO_2$施肥作用的结果,2011—2060 年气温和 $CO_2$ 浓度与 1961—2010 年保持不变的情况下,只考虑降水变化使树木生长量增加约 2%,而未来 50a 的气温变化使树木径向生长量相对于 1961—2010 年减少约 23%。在 1961—2010 年降水和 $CO_2$浓度保持不变,逐月气温升高 1℃的情况下,主要是春季 3、4 月气温升高使树木生长量增加明显,而夏季 6、7、8 月气温升高使树木相对生长量降低。

在本研究中也值得注意这样一个问题即本文假设的情景是考虑 $CO_2$对树木生长的施肥作用存在长期效应下未来气候变化对树木生长的影响,是对未来气候变化的一种情景预估。$CO_2$施肥作用是否具有长期效应是一个存在争议的问题,一些文献已经证实了 $CO_2$施肥作用的长期效应,如 Ainsworth 和 Long 基于大量的 FACE 试验观测数据分析发现,$CO_2$浓度增加会提高植物的光合能力[26];Liberloo 等对杨树连续 6a 的 $CO_2$增加试验显示,$CO_2$施肥作用具有长期效应[27]。许多研究已经对 $CO_2$对树木生长施肥作用的缺乏长期效应现象进行了解释,树木生长的立地条件限制根系生长[28]和土壤氮肥的缺乏都会限制 $CO_2$ 的施肥作用[29-30],根据采样点的实际考察,红松树木生长立地条件好,生长季树木生长茂盛,叶片颜色不存在黄叶现象,模型认为土壤氮素养分充足,该地区树木生长不会受到土壤氮肥的限制。

**致谢**:国家气候中心对全球气候模式气候变化预估数据进行整理、分析和惠许使用。原始数据由各模式组提供,由 WGCM(JSC/CLIVAR Working Group on Coupled Modelling)组织 PCMDI (Program for Climate Model Diagnosis and Intercomparison)搜集归类。多模式数据集的维护由美国能源部科学办公室提供资助

**References:**

[1] IPCC. Summary for Policymakers//Climate Change 2007: The Physical Science Basis: Contribution of Working Group I to the Fourth Assessment Report of the Intergovernmental Panel on Climate Change. Cambridge, England: Cambridge University Press, 2007.

[2] The Compilation Committee of National Assessment Report of Climate Change. China's National Assessment Report on Climate Change. Beijing: Science Press, 2007, 1-422.

[3] Chen X Q, Zhang F C. Spring phonological change in Beijing in the last 50 years and its response to the climatic changes. Chinese Journal of Agrometeorology, 2001, 22 (1): 1-5.

[4] Zheng J Y, Ge Q S, Hao Z X. Impacts of climate warming on plants phenophases in China for the last 40 years. Chinese Science Bulletin, 2002, 47(20): 1582-1587.

[5] Xu W D, He X Y, Chen W, Hu J B, Wen H. Responses of Shenyang urban tree phenology to climate warming. Chinese Journal of Applied Ecology, 2006, 17(10): 1777-1781.

[6] Zhu J H, Hou Z H, Zhang Z J, Luo Y J, Zhang X Q. Climate change and forest ecosystem: impacts, vulnerability and adaptation. Scientia Silvae Sinicae. 2007, 43(11):138-145.

[7] Zhou L M, Tucker C J, Kaufmann R K, Slayback D, Shabanov N V, Myneni R B. Variations in northern vegetation activity inferred from satellite data of vegetation index during 1981 to 1999. Journal of Geophysical Research-Atmospheres. 2001, 106:20069-20083.

[8] Sha W Y, Shao X M, Huang M. Climate warming and its impact on natural regional boundaries in China in 1980s. Science in China (Series D). 2002, 32(4): 317-326.

[9] Leng W F, He H S, Bu R C, Hu Y M. The spatial distribution of constructive species of Northeast forest under the climate chaing. Acta Ecologica Sinica, 2006, 26(12): 4257-4266.

[10] Cheng X X, Yan X D. Effects of climate change on typical forest in the northeast of China. Acta Ecologica Sinica. 2008, 28(2):534-543.

[11] Fang J Y. Forest productivity in China and its response to global climate change. Acta Phytoecologica Sinica. 2000, 24(5):513-517.

[12] Yin H, Liu H B, Guo P W, Hans Linderholm. An analysis on the climatic response mechanism of the growth of Pinus koraiensis in the lower mountains of XiaoXing'AnLing. Acta Ecologica Sinica. 2009, 29(12):6333-6341.

[13] Vaganov E A, Hughes M K, Shashkin A V. Growth dynamics of conifer tree rings: images of past and future environments. Berlin: Springer, xiv, 2006, 1-354.

[14] Fritts H C, Vaganov E A, Sviderskaya I V, Shashkin A V. Climatic variation and tree-ring structure in conifers: Empirical and mechanistic models of tree-ring width, number of cells, cell size, cell-wall thickness and wood density. Climate Research. 1991, 1(2): 97-116.

[15] Fritts H C, Shashkin A V, Downes G M. A simulation model of conifer ring growth and cell structure. In Tree-Ring Analysis, edited by R. Wimmer

and R. E. Vetter, Cambridge University Press, Cambridge. Gates D M. Biophysical Ecology. New York: Springer, 1999, 3-32.

[16] Cannell M G R, Smith R L. Climatic warming, spring bud burst, and frost damage on trees. Journal of Applied Ecology, 1986, 23:177-191.

[17] Xu Y Q, Lu P L, Yu Q. Response of tree phenology to climate change for recent 50 years in Beijing. Geographical Research, 2005, 24(3): 412-420.

[18] Zheng J Y, Ge Q S, Zhao H X. Changes of plant phenological period and its response to climate change for the last 40 years in China. Chinese Journal of Agrometeorology, 2003, 24 (1): 28-32.

[19] Mikola P. Temperature and tree growth near the northern timberline. In: Kozlowski TT(ed). Tree growth. Ronald Press, New York, 1962, 1-442.

[20] Denne M P. Temperature and tracheid development in Pinus sylvestris seedlings. Journal of Experimental Bonaty. 1971, 22(2): 362-370.

[21] Zhao J F, Yan X D, Jia G S. Changes in carbon budget of Northeast China forest ecosystems under future climatic scenario. Chinese Journal of Ecology, 2009, 28(5): 781-787.

[22] Yang S Y, Jiang Y L, Zhang Q G, Yang C L. The Research of carbon's storage capacity of China forest systems in the future. Journal of Fujian Forestry Science and Technology, 2006, 33 (1): 118-120.

[23] Wu X D, Shao X M. A preliminary study on impact of climate change on tree growth using tree ring width data. Acta Geographica Sinica, 1996, 51 (suppl.): 92-101.

[24] Wang Z. Plant physiology. Beijing, China Agricultural Press. 1999, 1-492.

[25] Peng Y Y, Dang Q L. Effects of soil temperature on biomass production and allocation in seedlings of four boreal tree species. Forest Ecology and Management, 2003, 180, 1-9.

[26] Ainsworth E A, Long S P. What have we learned from 15 years of free-air $CO_2$ enrichment (FACE)? A meta-analytic review of the responses of photosynthesis, canopy properties and plant production to rising $CO_2$. New Phytologist, 2005, 165, 351-372.

[27] Liberloo M, Tulva I, Raim O, Kull O, Ceulemans R. Photosynthetic stimulation under long-term $CO_2$ enrichment and fertilization is sustained across a closed Populus canopy profile (EUROFACE). New Phytologist, 2007, 173, 537-549.

[28] Drake B G, Gonzalez-Meler M A, Long S P. More efficient plants: a consequence of rising atmospheric $CO_2$?. Annual Review of Plant Physiology and Plant Molecular Biology 1997, 48, 609-639.

[29] Curtis P S, Wang X Z. A meta-analysis of elevated $CO_2$ effects on woody plant mass, form, and physiology. Oecologia, 1998, 113, 299-313.

[30] Rey A, Jarvis P G. Long-term photosynthetic acclimation to increased atmospheric $CO_2$ concentration in young birch (Betula pendula) trees. Tree Physiology 1998, 18, 441-450.

**参考文献:**

[2] 气候变化国家评估报告编写委员会. 气候变化国家评估报告. 北京:科学出版社,2007,1-422.

[3] 陈效逑,张福春. 近50年北京春季物候的变化及其对气候变化的响应. 中国农业气象,2001, 22(1): 1-5.

[4] 郑景云,葛全胜,郝志新. 气候增暖对我国近40年植物物候变化的影响. 科学通报, 2002, 47(20): 1582-1587.

[5] 徐文铎,何兴元,陈玮,胡健波,闻华. 沈阳城市森林主要树种物候对气候变暖的响应. 应用生态学报, 2006, 17(10): 1777-1781.

[6] 朱建华, 侯振宏, 张治军, 罗云建, 张小全. 气候变化与森林生态系统:影响、脆弱性与适应性. 林业科学, 2007, 43(11):138-145.

[8] 沙万英,邵雪梅,黄玫. 20世纪80年代以来中国的气候变暖及其对自然区域界线的影响. 中国科学(D辑),2002, 32(4): 317-326.

[9] 冷文芳, 贺红士, 布仁仓, 胡远满. 气候变化条件下东北森林主要建群种的空间分布. 生态学报, 2006, 26(12):4257-4266.

[10] 程肖侠, 延晓冬. 气候变化对中国东北主要森林类型的影响. 生态学报, 2008, 28(2):534-543.

[11] 方精云. 中国森林生产力及其对全球气候变化的响应. 植物生态学报, 2000, 24(5):513-517.

[12] 尹红, 刘洪滨, 郭品文, Hans Linderholm. 小兴安岭低山区红松生长的气候响应机制. 生态学报, 2009, 29(12):6333-6341.

[17] 徐雨晴, 陆佩玲, 于强. 近50年北京树木物候对气候变化的响应. 地理研究, 2005, 24(3): 412-420.

[18] 郑景云, 葛全胜, 赵会霞. 近40年中国植物物候对气候变化的响应的研究. 中国农业气象, 2003, 24 (1): 28-32.

[21] 赵俊芳,延晓冬,贾根锁. 未来气候情景下中国东北森林生态系统碳收支变化. 生态学杂志, 2009, 28(5): 781-787.

[22] 杨书运,蒋跃林,张庆国, 杨春雷. 未来中国森林碳蓄积预估初步研究. 福建林业科技, 2006, 33 (1): 118-120.

[23] 吴祥定,邵雪梅. 采用树轮宽度资料分析气候变化对树木生长量影响的尝试. 地理学报, 1996,51,增刊,92-101.

[24] 王忠. 植物生理学. 北京: 中国农业出版社, 1999,1-492.

第 6 卷 第 1 期 大 气 与 环 境 光 学 学 报 Vol.6 No.1
2011 年 1 月 JOURNAL OF ATMOSPHERIC AND ENVIRONMENTAL OPTICS Jan. 2011

DOI: 10.3969/j.issn.1673-6141.2011.01.006

# 近 48 年华东地区地面太阳总辐射变化特征和影响因子分析

尹 青[1,2,3], 张 华[2*], 何金海[3]

( 1 北京军区空军气象中心, 北京 100061 ;
2 中国家气候中心, 国气象局气候研究开放实验室, 北京 100081 ;
3 南京信息工程大学, 江苏省气象灾害重点实验室, 江苏 南京 210044 )

**摘 要:** 利用中国最新公布的截至 2008 年华东地区 13 个站点资料, 对华东地区平均的地面太阳总辐射长期变化趋势进行了分析, 并讨论了该地区云、气溶胶和水汽对地面太阳总辐射变化的影响. 研究表明, 1961~2008 年华东地区平均总辐射呈现减少趋势, 减少速率为 2.05 $W\cdot m^{-2}\cdot(10yr)^{-1}$; 1990 年前该地区总辐射呈现出显著的下降趋势, 1990~1995 年呈现快速增加趋势, 但是 1995~2000 年再次呈下降趋势, 2000 年后在平均线上下波动略有增加。气溶胶、云和水汽对华东地区地面太阳总辐射的长期变化都有一定的影响, 但是在不同的时段影响程度不同, 在 1961~1989 年总辐射的减少主要归因为气溶胶的增加; 而在 1990~1999 年和 2000~2008 年则是以云量的影响为主, 而且低云量对地面总辐射的影响要大于总云量的影响。

**关键词:** 华东地区; 总辐射; 相关气象要素; 影响因子

**中图分类号:** TN012, P422.1 **文献标识码:** A **文献编号:** 1673-6141(2011)01-0037-010

# Long-Term Change of Surface Total Solar Radiation and Influencing Factors over East China in Recent 48 years

YIN Qing[1,2,3], ZHANG Hua[2], HE Jin-hai[3]

( 1 Meteorological Center of Air Force in Beijing Military Area, Beijing 100061 ;
2 Laboratory for Climate Studies, China Meteorological Administration, Beijing 100081 ;
3 Key Laboratory of Meteorological Disaster of Ministry of Education, Nanjing University of Information Science Technology, Nanjing 210044, China )

**Abstract:** Based on updated daily surface solar radiation and associated meteorological elements data from 13 observational stations over East China, the long term trend of surface total solar radiation was analyzed, and the influence of cloud, aerosol and water vapor on total solar radiation were explored. The total solar

**收稿日期:** 2010-11-17; **修改日期:** 2010-11-30

**基金项目:** 科技基础性工作专项重点项目 (2007FY110700) 资助

**E-mail:** yinqing800@sohu.com



© 1994-2011 China Academic Journal Electronic Publishing House. All rights reserved. http://www.cnki.net

radiation decreased from 1961~2008 at a rate of 2.05 $W\cdot m^{-2}\cdot(10yr)^{-1}$; it decreased obviously from 1961 to 1989, and increased from 1990 to 1995, but decreased again since 1995, after 2000 fluctuated in the average line and slightly increased. The change of aerosol, cloud and water vapor contribute much to the variation of total radiation, from 1961 to 1989, the results imply that the atmospheric aerosols burden enhancement is the major reason for global radiation reduction, while cloud cover's contribution is relatively larger from 1990 to 2008, and the influence on total solar radiation of the low cloud is greater than that of the total cloud.

Key words: East China; total solar radiation; associated meteorological elements; influencing factor

# 1 引 言

到达地表的太阳辐射是地球生命的最终能量来源，是决定气候形成的重要因子，同时也是地表能量平衡的重要成分，支配着很多地表过程，例如：蒸发及相关的水循环、冰雪融化、植物光合作用以及地面气温的变化等[1]。在地球上界某一点接收到的太阳辐射中长期变化非常小，而到达地面的太阳辐射量的变化则相对较大，造成这种差别的主要原因是某一地区在不同时段大气对太阳辐射的吸收和散射不同，它与该地区的大气成分、云量、大气中的水汽含量以及大气悬浮物含量的变化密切相关。研究到达地面的太阳辐射的中长期变化，不但具有直接的气候意义，还有助于了解该地区的其他一些大气状况，如大气中气溶胶粒子的消光系数等的变化趋势，同时还可以指导太阳能资源的开发利用[2]。因此，关于地面太阳辐射特征的研究一直是国内外的一个研究热点。国际上对到达地面太阳辐射进行广泛观测始于 20 世纪国际地球物理年 (1957~1958 年)，普遍认为近 50 年来亚洲、非洲、北美洲、欧洲等全球大部分区域的地面太阳辐射都经历了由减少到增加的逆转，即由 "变暗" 到 "变亮" 的变化[3-7]。中国的学者也对中国不同地区地面太阳辐射变化特征进行了研究，得出相似的结论。Che 等[8]、Shi 等[9] 分别利用 64 个站和 72 个站 1960~2000 年的资料分别给出了总辐射、直接辐射、散射辐射的年际变化，发现总辐射和直接辐射在 1990 年前后发生了由减少到增加的转折。此外，还有学者对我国海河流域、黄河流域、华南、新疆、鄂尔多斯、长江三角洲、黄土高原等地区的辐射时空变化情况及原因给出了分析[10-16]。但是对于地面太阳辐射发生变化的原因，目前还存在很大的不确定性，这一问题还需要进一步深入的研究。

本文研究的华东地区包括江苏省、安徽省、江西省、浙江省、福建省和上海市。关于华东地区太阳辐射的变化特征和影响因子分析还不多见，本文试图利用华东地区部分气象站的观测资料，分析该地区的地面太阳总辐射和相关气象因素的长期变化趋势，以研究影响地面太阳总辐射变化的可能因子。

# 2 资 料

## 2.1 数据介绍

本文所使用的地面太阳辐射和有关气象因素的资料均来自中国气象局气象信息中心气象资料室。辐射资料包括华东地区 13 个观测站 (见图 1) 1960~2008 年的逐日曝辐量地面观测资料，包括总辐射量、直接辐射量和散射辐射量，单位转换为 $W\cdot m^{-2}$。为了与之对应，其他气象因素，包括云量、地面水汽压和能见度均使用相同 13 个站 1960~2008 年的逐日数据。以上数据经过计算转化为月平均、年平均值。图 1 是华东地区 13 个辐射台站的分布图。由图 1 可以看出，13 个站分布比较均匀，基本能代表华东地区的整体状况。

## 2.2 数据处理方法

### 2.2.1 数据的质量控制

为达到更加准确的目的，本文采用 Shi 等[8] 的质量控制方法对所使用地面太阳辐射资料进行



© 1994-2011 China Academic Journal Electronic Publishing House. All rights reserved. http://www.cnki.net

检验。该方法利用的是物理阀值检验、日照百分率检验和标准偏差检验，关于该方法的详细介绍见文献 [8]。

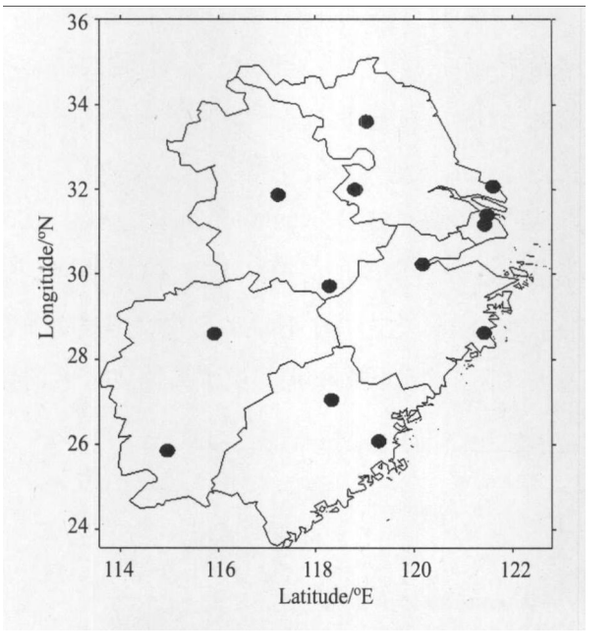


图 1　华东地区辐射台站分布图

Fig.1　Locations of the 13 stations in East China

2.2.2 有关参数的定义

总辐射比 (又可以称为晴空指数) 定义为

$$K_t = G/G_0, \tag{1}$$

$$G_0 = \frac{24I_{sc}}{\pi\rho^2}(\omega_0 \sin\varphi \sin\delta + \cos\varphi \sin\omega_0), \tag{2}$$

其中，$G$ 为到达地面的太阳总辐射，$G_0$ 为到达大气层顶的太阳总辐射，$I_{sc}$ 是太阳常数 (1367 $W\cdot m^{-2}$),$\varphi$ 是纬度，$\delta$ 是太阳赤纬，$\rho$ 是日地距离，$\omega_0$ 是日出 (日落) 太阳时角，可以由以下公式求出

$$\cos\omega_0 = -\tan\varphi\tan\delta. \tag{3}$$

2.2.3 使用方法

本文使用的分析方法包括相关分析、5 年滑动平均、线性倾向估计和回归分析，方法的详细介绍见文献 [17]。

## 3　地面太阳辐射的年际变化特征

图 2 给出了华东地区平均地面太阳总辐射的长期变化趋势，由于全国的平均总辐射变化趋势在 1990 年前后和 2000 年前后都有转折 [18]，为了方便与全国平均总辐射进行对比，本文也将总辐射分为三个时段进行分析，即 1961~1989 年、1990~1999 年和 2000~2008 年。就整个时段而言华东地区平均总辐射呈现出减少趋势，减少速率为 2.05 $W\cdot m^{-2}\cdot(10yr)^{-1}$。1990 年前该地区总辐射呈现出显著的下降趋势，这一时段最高值出现在 1963 年，最低值出现在 1989 年，两年相差 42 $W\cdot m^{-2}$，1990~1995 年呈现快速增加趋势，而且在 1995 年已经达到 20 世纪 70 年代初的水平，但是 1995~2000 年再次呈下降趋势，2000 年后在平均线上下波动略有增加。为了方便与其它文献进行对比，将总辐射的变化分为三个时段进行分析，即 1961~1989 年、1990~1999 年和 2000~2008 年，三个阶段总辐射变化速率分别为：$-11.7\ W\cdot m^{-2}\cdot(10yr)^{-1}$、$8.0\ W\cdot m^{-2}\cdot(10yr)^{-1}$ 和 $5.6\ W\cdot m^{-2}\cdot(10yr)^{-1}$。

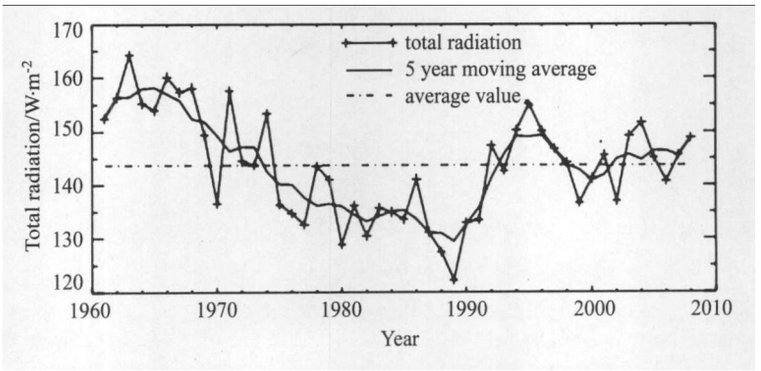


图 2　华东地区地面太阳总辐射长期变化趋势

Fig.2　Time series of annual mean total solar radiation of the above 13 stations in East China



© 1994-2011 China Academic Journal Electronic Publishing House. All rights reserved.　http://www.cnki.net

# 4 相关气象要素的年际变化特征

## 4.1 云量的变化

云量的变化是影响到达地面太阳总辐射的重要因素之一，云对总辐射的影响具有两重性，一是会造成直接辐射减小，同时会造成反射、散射辐射增大。但是在一般情况下，太阳直接辐射在总辐射中所占比例比较大，因此一般来说云量减少(增加)会使得到达地面的总辐射增加(减少)。

图 3 是 1961~2008 年华东地区平均总云量的变化趋势图。多年平均的总云量为 66% 。相对总辐射而言，总云量的变化较为平缓，由图 3 可以看出，两者在整个时段都呈现出很好的反相关关系。 1961~2008 年总云量的变化速率为 $-0.6\%\cdot(10\text{yr})^{-1}$(表 1)，与总辐射的变化并不相符，但是两者的相关系数为 −0.45(表 2)，通过了 95% 的显著性检验。如果从各个时段分别看两者的变化趋势可以发现，两者在每个时段的变化都很相符，即在 1961~1989 年、1990~1999 年、2000~2008 年总云量分别呈现出增加、减少、减少的变化趋势，虽然总云量在各个时段的变化均不显著，但是两者在各个时段的相关系数都通过了 95% 的显

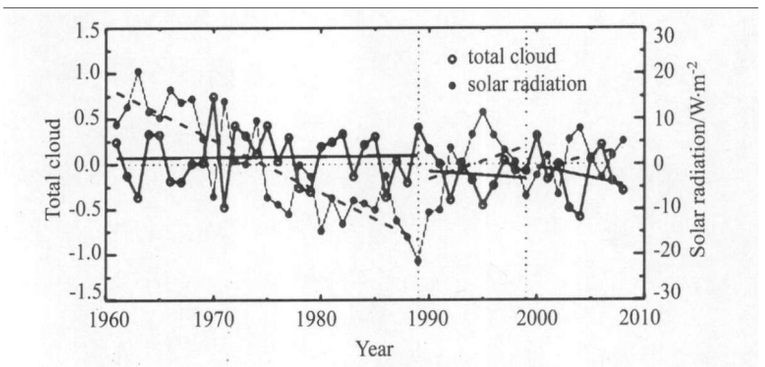


图 3 华东地区平均总云量的长期变化趋势，其中直线表示总云量在各个时段的变化趋势，虚线表示总辐射在各个时段的变化趋势

Fig.3 Time series of annual mean total solar radiation and total cloud amount of the above 13 stations in East China, the solid line is the linear trend of total cloud amount in each time, and the dashed line is the linear trend of total solar radiation in each time

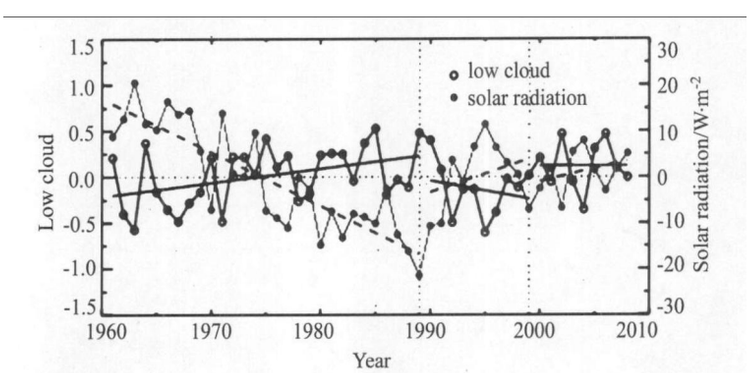


图 4 华东地区平均低云量长期变化趋势，其中直线表示低云量在各个时段的变化趋势，虚线表示总辐射在各个时段的变化趋势

Fig.4 Time series of annual mean total solar radiation and low cloud amount of the above 13 stations in East China, the solid line is the linear trend of low cloud amount in each time, and the dashed line is the linear trend of total solar radiation in each time



© 1994-2011 China Academic Journal Electronic Publishing House. All rights reserved. http://www.cnki.net

著性检验，说明在华东地区，云量可以比较好地解释总辐射的变化。

图 4 是 1961~2008 年华东地区平均低云量的变化趋势图。多年平均的低云量为 39%。相对总云量而言，低云量的变化更为明显。无论是对于整个时段，还是将三个时段分开看，低云量的变化趋势与总辐射的变化总是相符，即低云量呈减少趋势时，总辐射增加，而低云量呈增加趋势时，总辐射减少，而且在每个时段低云量与总辐射都呈现出显著的负相关，且所有相关系数绝对值都大于总云量与总辐射之间的相关系数绝对值，说明低云量比总云量能更好地解释总辐射的这种变化趋势，换言之，低云量在各个时段都是影响总辐射变化的重要因子。

表 1　华东地区地面太阳总辐射和有关气象要素变化趋势 (/10 年)

Table 1　Trend coefficient of annual mean total solar radiation and associated meteorological elements over East China (/10 yr.)

| 要　素 | 1961~2008 | 1961~1989 | 1990~1999 | 2000~2008 |
|---|---|---|---|---|
| 总辐射 | **−2.05** | **−11.7** | 8.0 | 5.6 |
| 总云量 | **−0.06** | 0.008 | −0.09 | 0.26 |
| 低云量 | 0.036 | **0.15** | −0.22 | 0.005 |
| 能见度 | **−1.91** | **−2.62** | **−2.1** | **−2.08** |
| 大于 20 km 能见度 | **−8.76** | **−13.65** | **−7.38** | **−7.65** |
| 地面水汽压 | 0.018 | −0.14 | 0.56 | −0.93 |

注：粗体加下划线表示通过 95% 的显著性检验 (下同)

表 2　华东地区地面太阳总辐射与有关气象要素的相关系数

Table 2　Correlation coefficient of annual mean total solar radiation and associated meteorological elements over East China (/10 yr.)

| 要　素 | 1961~2008 | 1961~1989 | 1990~1999 | 2000~2008 |
|---|---|---|---|---|
| 总云量 | **−0.45** | **−0.39** | **−0.76** | **−0.83** |
| 低云量 | **−0.66** | **−0.67** | **−0.85** | **−0.90** |
| 能见度 | **0.49** | **0.90** | −0.04 | 0.09 |
| 大于 20 km 能见度 | **0.54** | **0.90** | −0.11 | 0.01 |
| 地面水汽压 | −0.06 | −0.08 | −0.35 | −0.61 |

图 5 和图 6 分别给出了全年所有天平均和晴天情况下平均的晴空指数 ($K_t$) 变化趋势，之所以用晴空指数代替总辐射，是为了消去总辐射本身的季节变化。对比两个图可以看出，两种情况下 $K_t$ 在 1990~1999 年和 2000~2008 年间的变化趋势发生了很大的变化，晴天情况下两个时段的 $K_t$ 变化速率很小，只有 $0.19\%\cdot(10\text{yr})^{-1}$ 和 $0.26\%\cdot(10\text{yr})^{-1}$，仅为全年所有天平均情况下 $K_t$ 变化趋势的 10% 左右，这说明云量在这两个阶段对总辐射的影响很大。但是在第一时段这种变化并不明显，$K_t$ 的下降趋势在晴天情况反而加大，但是对比两者的年际变化可以发现两者还是有很大的区别，而且在晴天情况下，$K_t$ 的减少主要集中在 20 世纪 70 年代中期，其它时间变化比较缓慢，而在全年所



© 1994-2011 China Academic Journal Electronic Publishing House. All rights reserved.　http://www.cnki.net

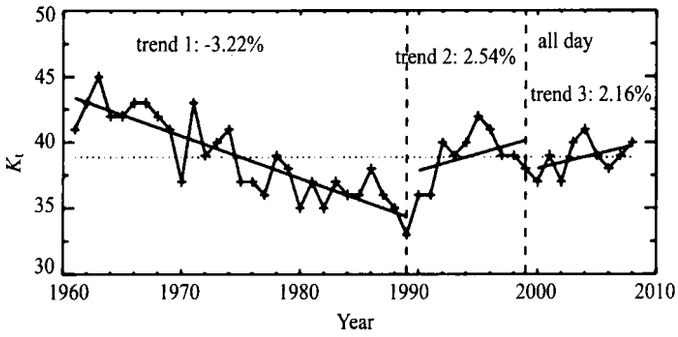


图 5 华东地区晴空指数长期变化趋势

Fig.5 Time series of annual mean $K_t$ of the above 13 stations in East China in all-day

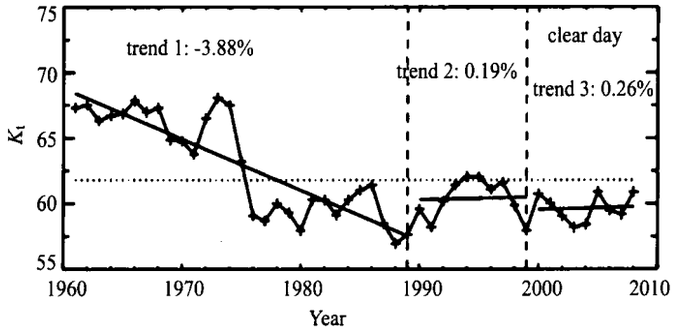


图 6 华东地区晴天情况下平均晴空指数长期变化趋势

Fig.6 Time series of annual mean $K_t$ of the above 13 stations in East China in clear-day

有天平均的情况下，$K_t$ 一直呈现出波动下降趋势，因此云量在这一时段对总辐射还是有一定的影响。

### 4.2 能见度的变化

气溶胶是影响到达地面太阳辐射的另一个重要因子，它不仅可以通过散射或吸收太阳辐射来直接改变太阳辐射 (直接气候效应); 也可以作为云凝结核改变云的光学性质以及云的寿命 (第一和第二间接气候效应); 此外，吸收性气溶胶在高污染地区还可以加热和稳定大气，从而阻止云的形成或者溶解已经存在的云 (半直接气候效应)。一般情况下，大气中气溶胶含量增加 (减少) 会使得到达地面的太阳总辐射减少 (增加)。但是由于在目前的地面观测中，还没有长时间序列的气溶胶观测资料，而能见度资料被认为能够在一定程度上反映观测时大气的污染程度和气溶胶的水平，已有研究表明水平能见度与气溶胶光学厚度之间有很好的负相关性 [19−21], 因此本文用能见度资料来反映气溶胶的变化情况。由于我国水平能见度观测方法在 1980 年前后的不同，导致能见度资料存在格式上的不统一，在分析中会造成比较大的影响，因此本文采用秦世广 [22] 给出的能见度转换方法，先将 1980 年前的等级资料估算为实际距离资料，具体转换方法和转换前后的对比详见文献 [22]。

图 7 和图 8 分别给出的是华东地区平均能见度和能见度大于 20 km 出现频率的长期变化趋势，1961~2008 年平均能见度为 19.97 km, 而能见度大于 20 km 平均出现频率只有 49%, 。可以看出能见度除了在 20 世纪 80 年代初期到中期变化相对平缓外，其余时间均呈现出比较明显的下降趋势。而好能见度出现频率在整个时段都呈现出快



© 1994-2011 China Academic Journal Electronic Publishing House. All rights reserved. http://www.cnki.net

速下降趋势。对于整个时段，能见度与总辐射的变化相符，而且呈现出正相关，相关系数通过了95% 的显著性检验，说明就整个时段而言气溶胶对总辐射的变化趋势有明显的贡献；如果分时段研究气溶胶的作用可以发现，1961~1989 年与整个时段的情况类似，气溶胶与总辐射变化相符，而且相关系数达到 0.9，远大于云量与总辐射之间的相关系数，说明在第一时段，气溶胶是造成总辐射减少的主要因素，这与华北地区的结果是一致的；但是在第二时段和第三时段气溶胶与总辐射的变化趋势不再相符，而且在第二时段两者呈现出负相关，这说明在这两个阶段气溶胶不再是影响总辐射变化的主要因素，尤其是在第二时段这种影响几乎可以忽略。

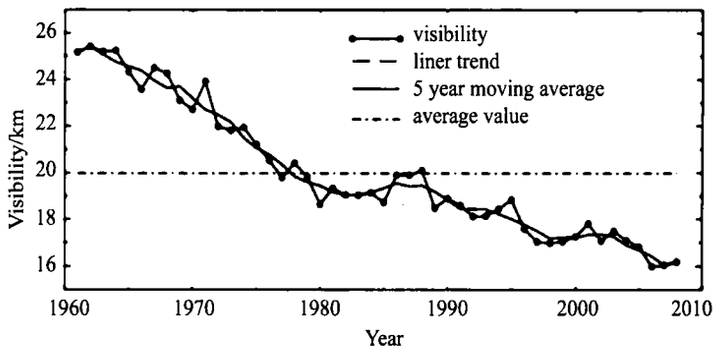


图 7　华东地区平均能见度长期变化趋势

Fig.7　Time series of annual mean visbility of the above 13 stations in East China

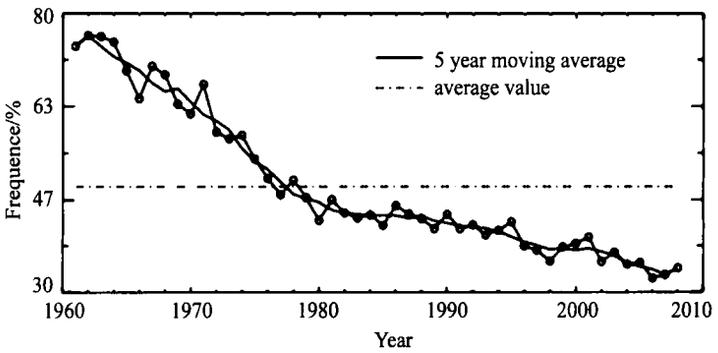


图 8　华东地区能见度大于 20 km 出现频率的长期变化趋势

Fig.8　Time series of annual mean frequence of good visbility (visibility greater than 20 km) of the above 13 stations in East China

但是由于能见度反映的只是水平方向的大气浑浊度，并不能完全代表气溶胶含量，因此这些结果还需要积累更长时间的气溶胶光学厚度资料后再来检验。

### 4.3 水汽的变化

水汽对太阳辐射有较强的吸收作用，因此水汽的增加 (减少) 会使得到达地面的总辐射减少 (增加)。实际工作中，通常用可降水量来表示单位截面大气柱中的水汽含量，但由于计算整层大气可降水量比较麻烦，通常需要有探空资料 [22]，但有研究表明我国整层大气可降水量同地面水汽压之间存在很好的线性关系 [23]，因此本文使用水汽压代表水汽含量来研究其与地面太阳辐射之间的关系。



© 1994-2011 China Academic Journal Electronic Publishing House. All rights reserved.　http://www.cnki.net

图 9 给出的是华东地区平均地面水汽压的长期变化趋势， 48 年来平均地面水汽压为 16.9 hPa。地面水汽压在 20 世纪 60 年代末期前呈现出下降趋势，此后一直到 90 年代初期均为波动状态，没有明显变化趋势， 20 世纪 90 年代开始上升，但是进入 21 世纪又开始呈现下降趋势。从整个时段看，地面水汽压的变化趋势与地面太阳总辐射的变化趋势是相符的，地面水汽压略有增加，而地面太阳总辐射在整个时段略有减少，同时两者在整个时段也呈现出显著的负相关，但是相关系数小于总辐射与能见度之间的相关系数，说明就整个时段而言，水汽是华北地区影响到达地面太阳辐射的因子之一，但是影响小于气溶胶的影响。如果分时段看水汽的影响，可以发现只有在第三时段 2000~2008 年地面水汽压的变化与地面总辐射的变化相符，但是两者在所有时段均呈现出负相关，这种相关并不显著，这表明，水汽对到达地面的太阳辐射在每个时段都有贡献，但是影响比较弱。

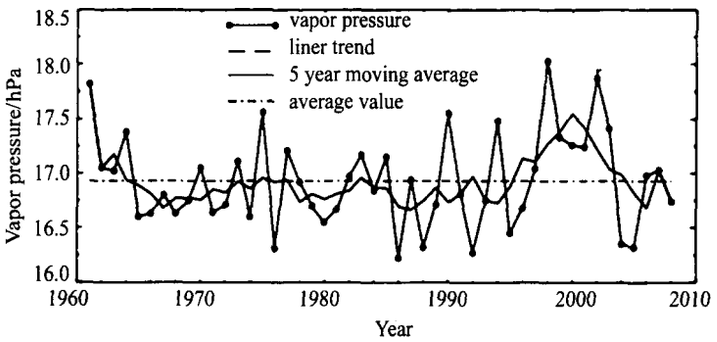


图 9 华东地区平均水汽压长期变化趋势

Fig.9 Time series of annual mean vapor pressure of the above 13 stations in East China

## 5 小 结

本文利用华东地区 13 个观测站的地面太阳总辐射和云量、地面水汽压、能见度资料分析和讨论了华东地区地面太阳总辐射的长期变化趋势和原因。主要结论有：

1) 就整个时段而言华东地区平均总辐射呈现出减少趋势，减少速率为 2.05 $W\cdot m^{-2}\cdot(10yr)^{-1}$。1990 年前该地区总辐射呈现出显著的下降趋势，1990~1995 年呈现快速增加趋势，而且在 1995 年已经达到 20 世纪 70 年代初的水平，但是 1995~2000 年再次呈下降趋势， 2000 年后在平均线上下波动略有增加。

2) 气溶胶、云和水汽对华东地区地面太阳总辐射的长期变化都有一定的影响，但是在不同的时段影响程度不同，在 1961~1989 年总辐射的减少主要归因为气溶胶的增加，云和水汽也有一定的影响；而在 1990~1999 年和 2000~2008 年则是以云量的影响为主，而且低云量对地面总辐射的影响要大于总云量的影响，水汽也有一定的贡献，而气溶胶的影响较小。

**参考文献：**

[1] Wild M. Global dimming and brightening: A review [J]. *J. Geophys. Res.*, 2009, **114**(21): D00D16.1-D00D16.31.

[2] Li Xiaowen, Li Weiliang, Zhou Xiuji. Analysis of the solar radiation variation of China in recent 30 years [J]. *Quarterly Journal of Applied Meterology*, 1998, **9**(1): 24-31(in Chinese).

李晓文，李维亮，周秀骥. 中国近 30 年太阳辐射状况研究 [J]. 应用气象学报， 1998, **9**(1): 24-31.



© 1994-2011 China Academic Journal Electronic Publishing House. All rights reserved. http://www.cnki.net

[3] Long C N, Dutt on E G, Augustine J A, *et al.* Significant decadal brightening of downwelling shortwave in the continental United States [J]. *J. Geophys. Res.*, **114**(10): D00D06.

[4] Norris J R, Wild M. Trends in aerosol radiative effects over Europe inferred from observed cloud cover, solar 'dimming' and solar 'brightening' [J]. *J. Geophys. Res.*, 2007, **112**(D8): D08214.1-D08214.13.

[5] Ohmura A. Observed long-term variations of solar irradiances at the Earth's surface [J]. *Space Sci. Rev.*, 2006, **125**(1-4): 111-128.

[6] Liley J B. New Zealand dimming and brightening [J]. *J. Geophys. Res.*, 2009, **114**(10): D00D10.

[7] Wild M, Trüssel B, Ohmura A, *et al.* Global dimming and brightening: An update beyond 2000 [J]. *J. Geophys. Res.*, 2009, **114**(10): D00D13.

[8] Che H Z, Shi G Y, Zhang X Y, *et al.* Analysis of 40 years of solar radiation data from China, 1961-2000 [J]. *Geophys. Res. Lett.*, 2005, **32**(6): L06803.1-L06803.5.

[9] Shi G Y, Hayasaka T, Ohmura A, *et al.* Data quality assessment and the long-term trend of ground solar radiation in China [J]. *J. Appl. Meteorol. and Climatol.*, 2008, **47**(4): 1006-1016.

[10] Liu Changming, Liu Xiaomang, Zheng Hongxing, *et al.* The change of solar radiation and its cause in Haihe River basin and surrounding areas [J]. *Acta Geographica Sinica*, 2009, **64**(11): 1283-1291(in Chinese).

刘昌明，刘小莽，郑红星，等. 海河流域他阳辐射变化及其原因分析 [J]. 地理学报， 2009, **64**(11): 1283-1291.

[11] Yang Xianmin, Zeng Yan, Qiu Xinfa, *et al.* The climatic change of global solar radiation over the Yellow River basin during 1960-2000 [J]. *Quarterly Journal of Applied Meterorology*, 2005, **16**(2): 243-248(in Chinese).

杨羡敏，曾燕，邱新法，等. 1960-2000 年黄河流域太阳辐射气候变化规律研究 [J]. 应用气象学报，2005, **16**(2): 243-248.

[12] Shi Hong, Xu Jianming, Li Chengcai. Analysis on variation and transition of surface solar radiation in south China area [J]. *Journal of Tropical Meteorology*, 2009, **25**(2): 209-215(in Chinese).

施红，徐建明，李成才. 华南地面太阳辐射状况及其转折特征分析 [J]. 热带气象学报， 2009, **25**(2): 209-215.

[13] Liu Bo, Feng Jinming, Ma Zhuguo, *et al.* Characteristics of climate changes in Xinjiang f rom 1960 to 2005 [J]. *Climatic and Environmental Research*, 2009, **14**(4): 414-426(in Chinese).

刘波，冯锦明，马柱国，等. 1960-2005 年新疆气候变化的基本特征 [J]. 气候与环境研究， 2009, **14**(4): 414-426.

[14] Shen Yanbo, Zhao Dong, Zhu Changhan, *et al.* Variational characteristics of surface solar radition and associated meteorological elements over Ordos plateau in recent 50 years [J]. *Plateau Meteorology*, 2009, **28**(4): 786-794(in Chinese).

申彦波，赵东，祝昌汉，等. 近 50 年来鄂尔多斯地面太阳辐射的变化及与相关气象要素的联系 [J]. 高原气象， 2009, 28(4): 786-794.

[15] Cai Ziying, Zheng Youfei, Liu Jianjun, *et al.* Analysis of solar radiation and relative factors in Yangtze River delta of China [J]. *Scientia Meteorologica Sinica*, 2009, **29**(4): 447-453(in Chinese).

蔡子颖，郑有飞，刘建军，等. 长江三角洲地面太阳辐射变化和相关因素分析 [J]. 气象科学， 2009, **29**(4): 447-453.

[16] Han Hong, Ren Guoyu, Wang Wen, *et al.* Temporal and spatial variation characteristic of total solar radiation over the Loess Platean region [J]. *Climatic and Environmental Research*, 2008, **13**(1): 61-66(in Chinese).



© 1994-2011 China Academic Journal Electronic Publishing House. All rights reserved.　http://www.cnki.net

韩红，任国玉，王文，等. 黄土高原地区太阳辐射时空演变特征 [J]. 气候与环境研究， 2008, **13**(1): 61-66.

[17] Wei Fengying. *Modern Climatic Statistical Diagnosis and Prediction* [M]. 2nd ed., Beijing: China Meteorological Press, 2007(in Chinese).

魏凤英. 现代气候统计诊断与预测技术 [M]. 第二版，北京：气象出版社， 2007.

[18] Yin Qing. *Study on the Dimming and Brightening Problem over China* [D]. Nanjing: Master's Thesis of Nanjing University of Information Science & Technology, 2010(in Chinese).

尹青. 中国地区变暗变亮问题的研究 [D]. 南京信息工程大学硕士学位论文， 2010.

[19] Zong Xuemei, Qiu Jinhuan, Wang Pucai. Charactertics of atmospheric aerosol optical depth over 16 radiation stations in the last 10 years [J]. *Climatic and Environmental Research*, 2005, **10**(2): 202-208(in Chinese).

宗雪梅，邱金桓，王普才. 近 10 年中国 16 个台站大气气溶胶光学厚度的变化特征分析 [J]. 气候与环境研究， 2005, **10**(2): 202-208.

[20] Zhao Xiujuan, Chen Changhe, Yuan Yi, *et al.* Lanzhou aerosol optical depth in winter and their relation with visibility [J]. *Plateau Meteorology*, 2005, **24**(4): 617-622(in Chinese).

赵秀娟，陈长和，袁铁，等. 兰州冬季大气气溶胶光学厚度及其与能见度的关系 [J]. 高原气象， 2005, 24(4): 617-622.

[21] Luo Yunfeng, Lu Daren, He Qing, *et al.* An analysis of direct solar radiation, visibility and aerosol optical depth in South China coastal area [J]. *Climatic and Environmental Research*, 2000, **5**(1): 36-44(in Chinese).

罗云峰，吕达仁，何晴，等. 华南沿海地区太阳直接辐射、能见度及大气气溶胶变化特征分析 [J]. 气候与环境研究， 2000, **5**(1): 36-44.

[22] Qin Shiguang. *Long-Term Variation Characteristics of Surface Radiation over China, Its Cause and Climatic Effects* [D]. Beijing: Doctorial Dissertation of Institute of Atmospheric Physics, Chinese Academy of Sciences, 2009(in Chinese).

秦世广. 中国地面太阳辐射长期变化特征、原因及其气候效应 [D]. 中国科学院大气物理研究所博士学位论文， 2009.

[23] Yang Jingmei, Qiu Jinhuan. The empirical expressions of the relation between precipitable water and ground water vapor pressure for some areas in China [J]. *Science Atmospherica Sinica*, 1996, **20**(5): 620-626(in Chineses).

杨景梅，邱金桓. 我国可降水量同地面水汽压关系的经验表达式 [J]. 大气科学， 1996, **20**(5): 620-626.

**作者简介：** 尹 青 (1983–), 女，河北南宫人，硕士研究生，主要从事太阳辐射、激光雷达的研究.

**导师简介：** 张 华 (1965 - ), 女，吉林磐石人，博士，研究员，主要从事大气辐射传输模式，云 - 辐射相互作用的研究.



© 1994-2011 China Academic Journal Electronic Publishing House. All rights reserved. http://www.cnki.net

ADVANCES IN ATMOSPHERIC SCIENCES, VOL. 28, NO. 4, 2011, 725–734

# Diurnal Variations of Summer Precipitation in the Beijing Area and the Possible Effect of Topography and Urbanization

YIN Shuiqing*[1,2,3] (殷水清), LI Weijing[3] (李维京), Deliang CHEN[4], Jee-Hoon JEONG[4], and GUO Wenli[5] (郭文利)

[1] *State Key Laboratory of Earth Surface Processes and Resource Ecology, Beijing Normal University, Beijing* 100875

[2] *School of Geography, Beijing Normal University, Beijing* 100875

[3] *Beijing Climate Center, China Meteorological Administration, Beijing* 100081

[4] *Department of Earth Sciences, University of Gothenburg, Gothenburg,* 40530*, Sweden*

[5] *Beijing Regional Climate Center, Beijing Meteorological Bureau, Beijing* 100089

(Received 17 March 2010; revised 24 July 2010)

**ABSTRACT**

The present study examined the diurnal variations of summer precipitation in the Beijing area by using subdaily precipitation and wind observations. A combined effect of topography and urbanization on the characteristics of diurnal variations was suggested. It was shown that stations located in the plain area exhibited typical night rain peaks, whereas those in the mountainous area exhibited clear afternoon peaks of precipitation diurnal variations. The precipitation peaks were associated with wind fields around the Beijing area, which were found to be highly modulated by mountain-valley circulation and urban-country circulation. The lower-tropospheric wind exhibited a clear diurnal shift in its direction from north at 0800 LST to south at 2000 LST, which reflected mountain-valley circulation. The transitions from valley to mountain wind and the opposite generally happened after sunset and sunrise, respectively, and both occurred earlier for the stations located closer to mountains. By comparing the diurnal variations of precipitation at stations in a northeast suburb, an urban area, and a southwest suburb, it was revealed that the northeast suburb group had the highest normalized rainfall frequency, but the southwest group had the lowest from late afternoon to late evening. On the contrary, in the early morning from about 0200 to 1000 LST, the southwest group and urban group had the highest normalized rainfall frequency. This pattern might originate from the combined effects of mountain-valley topography and urbanization.

**Key words**: diurnal variations, precipitation, mountain-valley circulation, urban effect, Beijing area

**Citation**: Yin, S. Q., W. J. Li, D. L. Chen, J.-H. Jeong, and W. L. Guo, 2011: Diurnal variations of summer precipitation in the Beijing area and the possible effect of topography and urbanization. *Adv. Atmos. Sci.*, **28**(4), 725–734, doi: 10.1007/s00376-010-9240-y.

## 1. Introduction

The diurnal variation of precipitation is one of the fundamental characteristics of weather and the climate system. Basically arising from diurnal variation of solar radiation and affected by dynamical backgrounds from very local to large-scale, a precipitation event tends to happen during a specific period of time in a day. In spite of the fact that much research has been done in recent decades, the ability of climate models to simulate diurnal variations of precipitation still needs to be improved. Therefore, more and more research focuses on the diurnal variations of precipitation, because it is acknowledged as one of the representative

*Corresponding author: YIN Shuiqing, yinshuiqing@bnu.edu.cn

© China National Committee for International Association of Meteorology and Atmospheric Sciences (IAMAS), Institute of Atmospheric Physics (IAP) and Science Press and Springer-Verlag Berlin Heidelberg 2011



© 1994-2011 China Academic Journal Electronic Publishing House. All rights reserved. http://www.cnki.net

features required to diagnose local climate systems and to verify the performance of climate models (Zhou et al., 2008).

Previous research showed that for the warm season (May to September), nocturnal (2000–0800 LST) precipitation predominated over the Tibetan Plateau, Southwest China, and Northwest China, whereas daytime (0800–2000 LST) precipitation predominated over Northeast China and Southeast China (Yu et al., 2007a; Yin et al., 2009). An early morning peak is distinct in central eastern China, which is mainly caused by frequent precipitation occurrences of relatively long duration (Yu et al., 2007b). This morning peak tends to be strengthened (weakened) along with the advancement (retreat) of the East Asian monsoon trough (Yin et al., 2009). Research on the diurnal variations of precipitation over southeastern China further revealed the mechanism of an enhanced early morning peak associated with the diurnal variation of monsoon activity (Chen et al., 2009a, 2009b). Additionally, cloud radiative forcing was suggested as one of the primary factors in modulating the diurnal cycle of rainfall when the diurnal cycle in the southwestern and southeastern parts of southern contiguous China were compared (Li et al., 2008a). Diurnal variations of surface flow over central eastern China were also revealed, and the contribution of the diurnal surface wind to the diurnal feature of precipitation was previously discussed (Yu et al., 2009; Chen et al., 2010). Furthermore, it was found that diurnal variations exhibited long-term change (Fujibe et al., 2006). For example, hourly precipitation records during 1961–2004 from the Beijing Nanjiao observatory station indicated that convective rainfall events of relatively short duration in the afternoon and early evening increased while relatively long duration events during the night and early morning decreased remarkably in forty recent years (Li et al., 2008b). The afternoon peak caused by convective precipitation was believed to be enhanced by the intensification of the urban heat island (Fujibe et al., 2006).

Beijing is situated at the northwestern part of the North China Plain, surrounded by mountains to the north, northwest, and west of the area (see Fig. 1). Therefore, it has been recognized that mountain-valley circulation significantly influences the local climate in the region around Beijing (Hu et al., 2005; Sun, 2005; Li and Shu, 2008; Wang et al., 2008a). Associated with the diurnal variation of precipitation, Wu (1993) suggested that the precipitation in the mountainous area of Beijing, Tianjin, and Hebei Province exhibited a clear afternoon peak from convective precipitation, whereas that in the plain area exhibited a nighttime peak (Wu, 1993). Lin (1995) made a general conclusion that stations in convex topography were prone to have more precipitation in the daytime, whereas those with concave topography have more nocturnal precipitation. The mountain-valley circulation around Beijing and its mechanism have been well described. In addition, Beijing is one of the most urbanized regions in the world, and more than 15 million people reside in the urban plain area, so it has been suggested that the urban heat island effect is also likely to have an influence on the diurnal variations of precipitation around the Beijing area. Sun and Yang (2008) showed that most mesoscale torrential rain processes induced by the combined influence of topography and urban circulation easily occurred in front of mountains in the evening or in the early morning. The amount and frequency of rainfall tends to be larger in urban centers and downwind areas than in the surrounding areas, especially for relatively intense convective rainfall in summer (Collier, 2006; Zheng and Liu, 2008) This effect, however, is not confirmed in the Beijing area in the existing literature by Sun and Shu (2007) and Wang et al. (2008b). One possibility is that the indicators for seasonal rainfall amount and rainfall days used in these two studies may be not sensitive indices for convective rainfall processes.

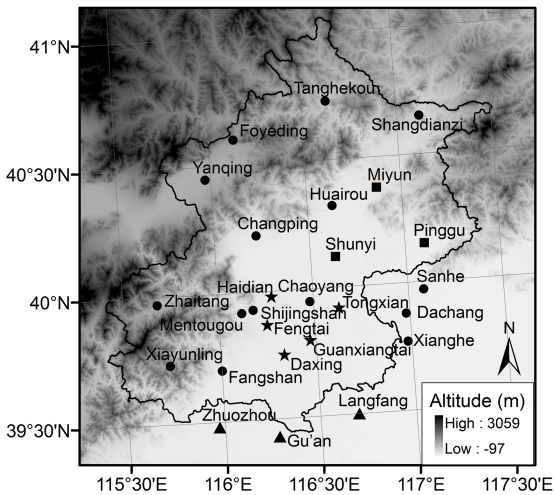


**Fig. 1.** Stations with hourly precipitation and six-hourly surface wind data in this study. Squares stand for the stations in Northeast group, stars for those in Urban area and triangles for those in Southwest group.

The objectives of this research were to investigate: (1) diurnal variations of precipitation in Beijing and its adjacent area based on hourly precipitation data in summer from 26 stations; (2) mountain-valley circulation using lower- and upper-level National Centers for Environmental Prediction (NCEP) final analysis wind



© 1994-2011 China Academic Journal Electronic Publishing House. All rights reserved. http://www.cnki.net

data and *in situ* surface observation wind data; (3) urban effects on rainfall using hourly precipitation as the indicator; and (4) possible effects of mountain-valley topography and urban effects on diurnal variations of precipitation.

## 2. Data and method

Hourly precipitation data from 1990 to 2007 from 26 automatic weather stations, of which 20 stations were located in the Beijing municipality and the other six belonged to neighboring Hebei Province (Fig. 1, Tables 1 and 2), were utilized. About 72.5% of annual precipitation occurs in summer (June-July-August, JJA in short) in the Beijing area due to the East Asian monsoon (Wang et al., 2008c), so only data in summer were analyzed in this study. The data loss rate, which was defined as percent of hours without observation dividing by total hours during 1990–2007, ranged from 0.5% to 24.5% with an average of 9.4%. Diurnal variations of precipitation can be characterized by the frequency, amount, and intensity of precipitation (Zhou et al., 2008). Present study utilized the diurnal variation of precipitation frequency. Our previous study (Yin et al., 2009) suggested that diurnal patterns of precipitation frequency and amount were quite similar except that the afternoon maximum of precipitation amount was relatively higher due to intense convective precipitation in the afternoon. The frequency of hourly precipitation was defined as the number of rainfall hours divided by the total observation hours by using Eqs. (1) and (2). To facilitate the comparisons among stations in suburban and urban areas, the hourly occurrences were normalized by dividing them by the 24-h means following Yin et al. (2009) [Eq. (3)].

$$f_n = \frac{\sum_{d=1}^{D} c_{d,n}}{D} \tag{1}$$

$$c_{d,n} = \begin{cases} 0, & p_{d,n} < 0.1 \\ 1, & p_{d,n} \geqslant 0.1 \end{cases} \tag{2}$$

$$F_{\mathrm{N},n} = \frac{24 f_n}{\sum_{n=1}^{24} f_n} \tag{3}$$

**Table 1.** Information on the stations analyzed in the study.

| Station No. | Station Name | Latitude (°N) | Longitude (°E) | Altitude (m) | Percent of hours without observation (%) | Annual average during 1971–2000 (mm) | Percentage of night rain (%) |
|---|---|---|---|---|---|---|---|
| 54399 | Haidian | 39.98 | 116.28 | 46.3 | 12.6 | 582.3 | 53.3 |
| 54433 | Chaoyang | 39.95 | 116.48 | 36.5 | 9.7 | 581.7 | 55.7 |
| 54511 | Guanxiangtai | 39.80 | 116.47 | 32 | 14.7 | 571.9 | 57.2 |
| 54514 | Fengtai | 39.87 | 116.25 | 56.3 | 6.9 | 567.0 | 53.9 |
| 54398 | Shunyi | 40.12 | 116.63 | 39.5 | 15.8 | 603.2 | 54.8 |
| 54412 | Tanghekou | 40.73 | 116.63 | 333.7 | 24.0 | 485.1 | 44.9 |
| 54416 | Miyun | 40.38 | 116.87 | 73.1 | 24.5 | 638.7 | 55.7 |
| 54419 | Huairou | 40.32 | 116.63 | 60.6 | 7.5 | 670.2 | 51.9 |
| 54421 | Shangdianzi | 40.65 | 117.12 | 286.5 | 22.1 | 627.6 | 54.2 |
| 54424 | Pinggu | 40.15 | 117.10 | 29.4 | 11.6 | 641.1 | 54.3 |
| 54431 | Tongxian | 39.92 | 116.63 | 26.9 | 9.2 | 562.0 | 57.5 |
| 54594 | Daxing | 39.75 | 116.33 | 41.3 | 7.4 | 552.6 | 55.8 |
| 54501 | Zhaitang | 39.97 | 115.68 | 441.1 | 4.5 | 464.2 | 43.6 |
| 54505 | Mentougou | 39.92 | 116.12 | 93.6 | 9.5 | 601.4 | 54.9 |
| 54596 | Fangshan | 39.70 | 116.00 | 48.9 | 1.9 | 582.8 | 56.0 |
| 54597 | Xiayunling | 39.73 | 115.73 | 409.1 | 24.2 | 640.6 | 54.7 |
| 54406 | Yanqing | 40.45 | 115.97 | 489 | 8.6 | 441.8 | 45.0 |
| 54499 | Changping | 40.22 | 116.22 | 79.7 | 6.2 | 542.9 | 49.5 |
| 54410 | Foyeding | 40.60 | 116.13 | 1216.9 | 3.8 | 535.5 | 45.9 |
| 54513 | Shijingshan | 39.93 | 116.18 | 70.8 | 11.1 | 558.0 | 54.1 |
| 54502 | Zhuozhou | 39.48 | 115.97 | 36.5 | 0.5 | 563.8 | 56.1 |
| 54510 | Dachang | 39.88 | 116.98 | 16.5 | 1.6 | 590.6 | 50.9 |
| 54512 | Gu'an | 39.43 | 116.28 | 23.8 | 0.8 | 548.2 | 54.9 |
| 54515 | Langfang | 39.50 | 116.70 | 14.3 | 2.0 | 555.3 | 55.2 |
| 54520 | Sanhe | 39.97 | 117.08 | 19.4 | 1.5 | 607.2 | 53.0 |
| 54521 | Xianghe | 39.77 | 116.98 | 13.5 | 2.4 | 580.8 | 50.7 |



© 1994-2011 China Academic Journal Electronic Publishing House. All rights reserved. http://www.cnki.net

**Table 2.** Information on precipitation and wind data used in the study.

| Data type | Number of stations | Length of series |
|---|---|---|
| Hourly precipitation data | 26 | JJA, 1990–2007 |
| Six-hourly wind data | 26 | JJA, 1990–2007 |
| Hourly wind data | 20 | JJA, 2005–2007 |
| NCEP final analysis data | 38°–43°N, 113°–119°E | JJA, 2000–2007 |

In Eqs. (1)–(3), $n$ is the LST expressed in hours, $d$ is the number of observation days, $f_n$ is the frequency of precipitation, $c_{d,n}$ is a counter (units: mm h$^{-1}$), $p_{d,n}$ is the hourly precipitation amount, and $F_{\mathrm{N},n}$ is the normalized precipitation frequency.

Six-hourly zonal and meridional wind, from the NCEP final analysis of $1° \times 1°$ spatial resolution data, in summer (June to August) from 2000 to 2007 were analyzed to show the characteristics of lower- and upper-level wind profiles (Table 2). Six-hourly *in situ* observations of wind speed and wind direction from 1990 to 2007 for 26 stations were also analyzed to reveal surface wind fields (Table 2). Hourly wind data from 2005 to 2007 for 20 stations (selected by the criteria with data loss less than 1%) were also collected to detect diurnal variations of wind (Table 2).

## 3. Results and Discussion

### 3.1 *Diurnal variations of precipitation*

First, the general feature of diurnal variations of precipitation in the regions around the Beijing area was examined in Fig. 2. Overall, most stations had more precipitation in the nighttime (2000–0800 LST) than in the daytime (0800–2000 LST) except for several stations located in the foot of the western and northwestern mountainous areas: Zhaitang, Tanghekou, Yanqing, Foyeding (the percentages of night rain for these stations were 43.6%, 44.9%, 45%, 45.9% and 49.5%, respectively, see Table 1). In particular, diurnal patterns of precipitation frequency at Zhaitang, Tanghekou, and Yanqing showed clear afternoon and early morning peaks (Fig. 2a). These three

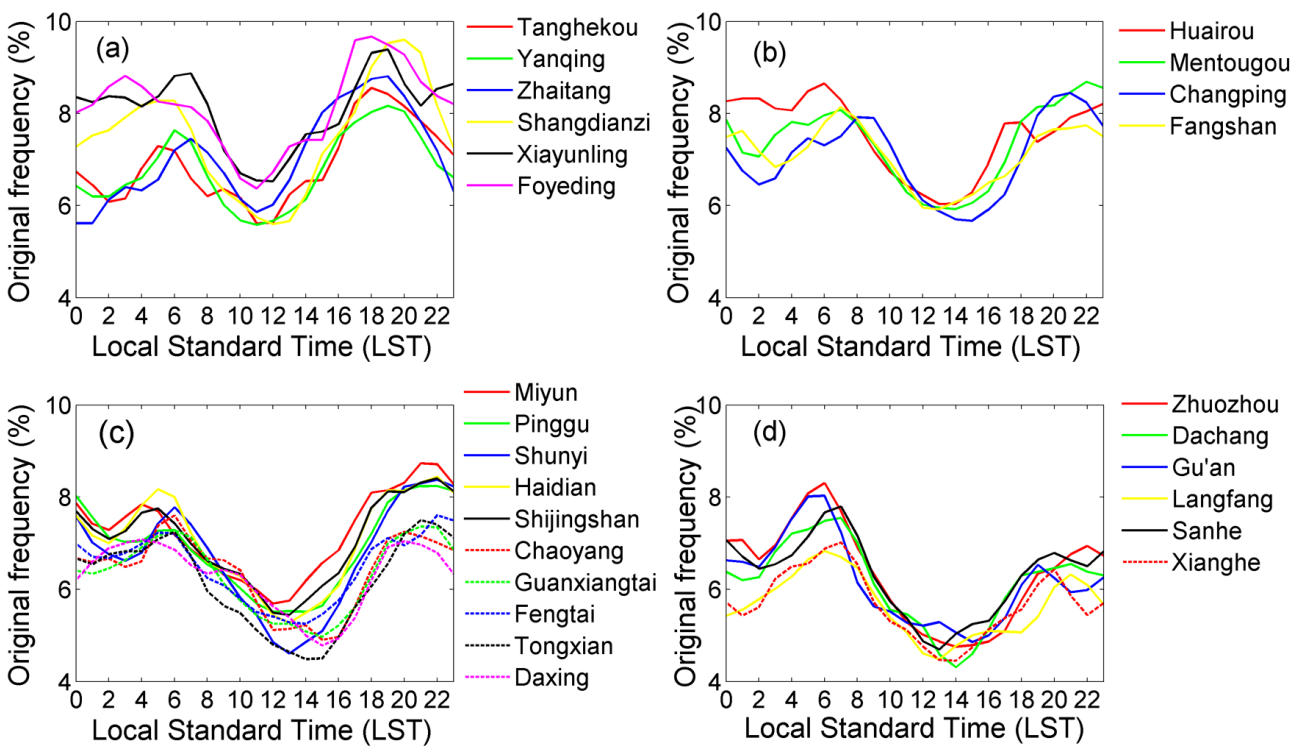


**Fig. 2.** Diurnal variations of precipitation frequency in summer for 26 stations in Beijing and its surrounding area: (a) six stations in the mountainous area; (b) four stations close to mountainous area; (c) ten stations in the plain in Beijing municipality; (d) six stations in the plain in Hebei province close to southeastern part of Beijing municipality.



© 1994-2011 China Academic Journal Electronic Publishing House. All rights reserved. http://www.cnki.net

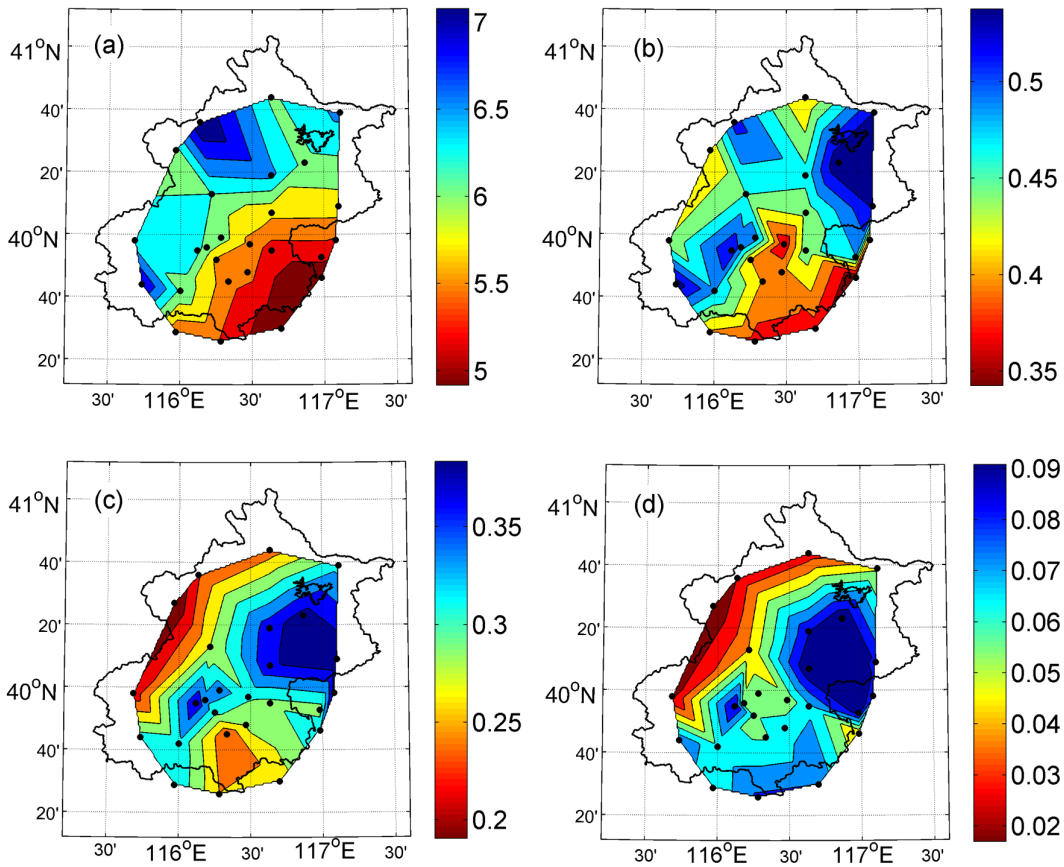


**Fig. 3.** Spatial distribution of hourly precipitation occurring frequency (%) grouped by intensity: (a) 0–5 mm $h^{-1}$; (b) 5–10 mm $h^{-1}$; (c) 10–25 mm $h^{-1}$; (d) over 25 mm $h^{-1}$.

stations were located on the lee slope of the western and northern mountainous areas where the annual precipitation was relatively lower compared with other stations (Table 1). The other three stations in Fig. 2a, Shangdianzi, Xiayunling, and Foyeding, were also located in the western and northern mountainous areas, but their precipitation frequencies were generally higher, especially for the period from late night to early morning. The diurnal patterns of these six stations seem to be attributed to their local topography. They are located in the mountainous areas, where the surface is easily heated by incoming solar radiation during the daytime, and this may induce convective precipitation in the afternoon more frequently.

Diurnal patterns of precipitation frequency for the remaining 20 stations located in the plain area (Figs. 2b, c, and d) exhibited high probability from 1800 LST to 0600 LST. Most of these 20 stations in Beijing and its adjacent area also exhibited an afternoon peak at about 1800–1900 LST and an early morning peak at 0600 LST. However, neither peak was very obvious due to relatively continuous higher rainfall probability during the nighttime. There were still some small differences among the stations in the plain area. First, the stations close to the piedmont windward slopes tend to have relatively higher precipitation frequency in the daytime. Second, for stations in the northeastern part of the Beijing Plain, the frequency from 1800 to 0200 LST tends to be higher (Fig. 2c), which is more clearly seen in the spatial distribution of hourly precipitation frequency (Fig. 3). The frequency distribution of hourly precipitation less than 5 mm $h^{-1}$, which is defined as the rainfall hours with intensity less than 5 mm $h^{-1}$ dividing by total hours with observations, exhibits a high value in the areas close to piedmont windward slopes from southwest to northeast (Fig. 3a), while the high probability values of hourly precipitation over 5 mm $h^{-1}$ tends to move to the northeastern part of the Beijing Plain (Figs. 3b, c, and d). The possible reason for this pattern will be discussed in the next section.

### 3.2 *Related circulation*

From the wind profile based on the NCEP final analysis data, it was demonstrated that the tropospheric circulation around Beijing exhibits a diurnal



© 1994-2011 China Academic Journal Electronic Publishing House. All rights reserved. http://www.cnki.net

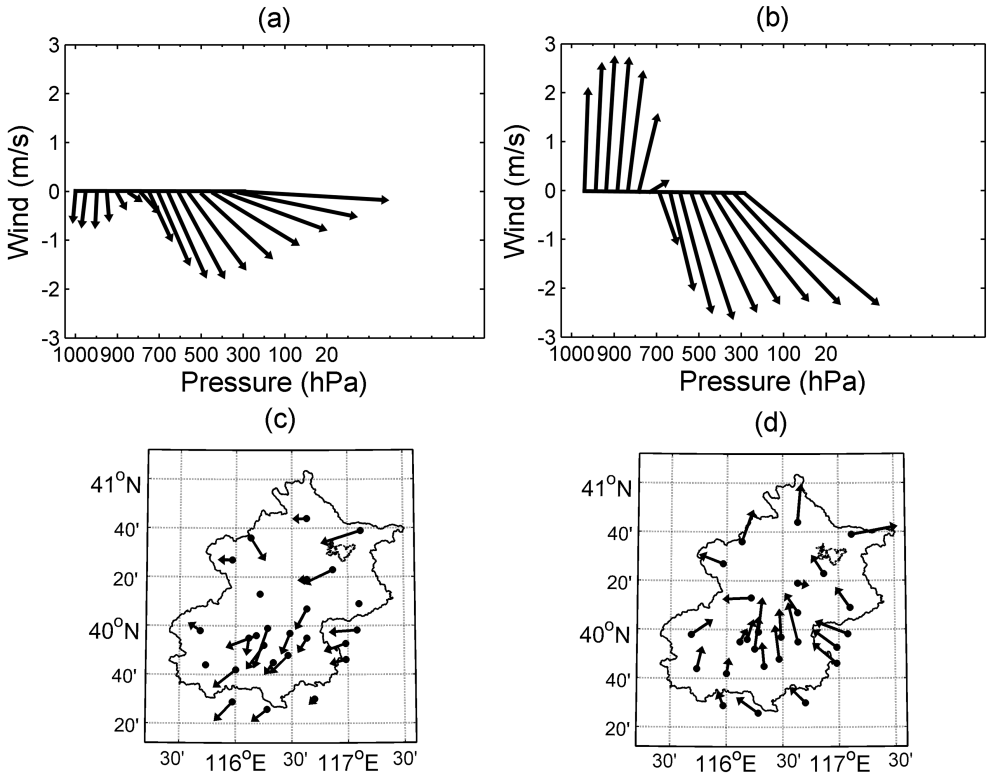


**Fig. 4.** Wind profile using NCEP final analysis data averaged over grids (40°N, 116°E) and (40°N, 117°E) and surface wind field using six-hourly in situ observation wind data in JJA: (a) wind profile at 0800 LST; (b) wind profile at 2000 LST; (c) surface wind field at 0800 LST; (d) surface wind field at 2000 LST. The heights are 1000 hPa, 975 hPa, 950 hPa, 925 hPa, 900 hPa, 850 hPa, 800 hPa, 750 hPa, 700 hPa, 650 hPa, 600 hPa, 550 hPa, 500 hPa, 450 hPa, 400 hPa, 350 hPa, 300 hPa for horizonal axes for (a) and (b). The length of lines denotes vector wind speed and the arrows denote the direction which the wind blowing to.

reversal of wind direction, which may be related to the mountain-valley circulation (Figs. 4a, b). At 0800 LST, wind in the lower troposphere was northerly (Fig. 4a), while it was strongly southerly at 2000 LST (Fig. 4b). Recalling that the mountainous regions are located to the north and northwest of Beijing, the northerly wind at 0800 LST and southerly wind at 2000 LST seem to represent the so-called down-valley and up-valley wind, respectively. The reversal of wind direction is confined in the lower troposphere, from the surface up to the 800 hPa level. In the upper level, strong westerly or northwesterly wind prevails both at 0800 LST and at 2000 LST.

This reversal of wind direction is also confirmed by the *in situ* surface wind observation for the 26 stations during 1990–2007. The wind directions for most stations are opposite between 0800 LST and 2000 LST (Figs. 4c, d). At 0800 LST, surface wind tends to be from the northern and western mountainous areas, while at 2000 LST, surface wind is from the southern valley area. At 0200 LST and 1400 LST, wind directions are not so homogeneous, but it seems that wind directions point to the city center, which may be attributed to urban-country circulation (figures not shown). Furthermore, additional details of diurnal variations of surface wind are examined based on hourly wind data. It is found that the transition time from the up-valley wind to down-valley wind after sunset is quite different among stations, as is that from down-valley wind to up-valley wind after sunrise. The transition time is earlier for the stations closer to mountains as shown in Fig. 5. For Shangdianzi, Miyun, Shunyi, Zhuozhou, and Gu'an (Figs. 5a, b, c, e, f), the transition time from southerly wind to northerly wind is about 1900, 2000, 2300, 0100, and 0200 LST respectively; that from northerly wind to southerly wind is about 0800, 1100, 1100, 1100, and 1200 LST, respectively. The wind direction does not change until 0700 LST for Daxing (Fig. 5d), which is possibly attributed to urban-country circulation. Daxing is located to the south of the urban area, where the country wind in the night points to the city center from



© 1994-2011 China Academic Journal Electronic Publishing House. All rights reserved. http://www.cnki.net

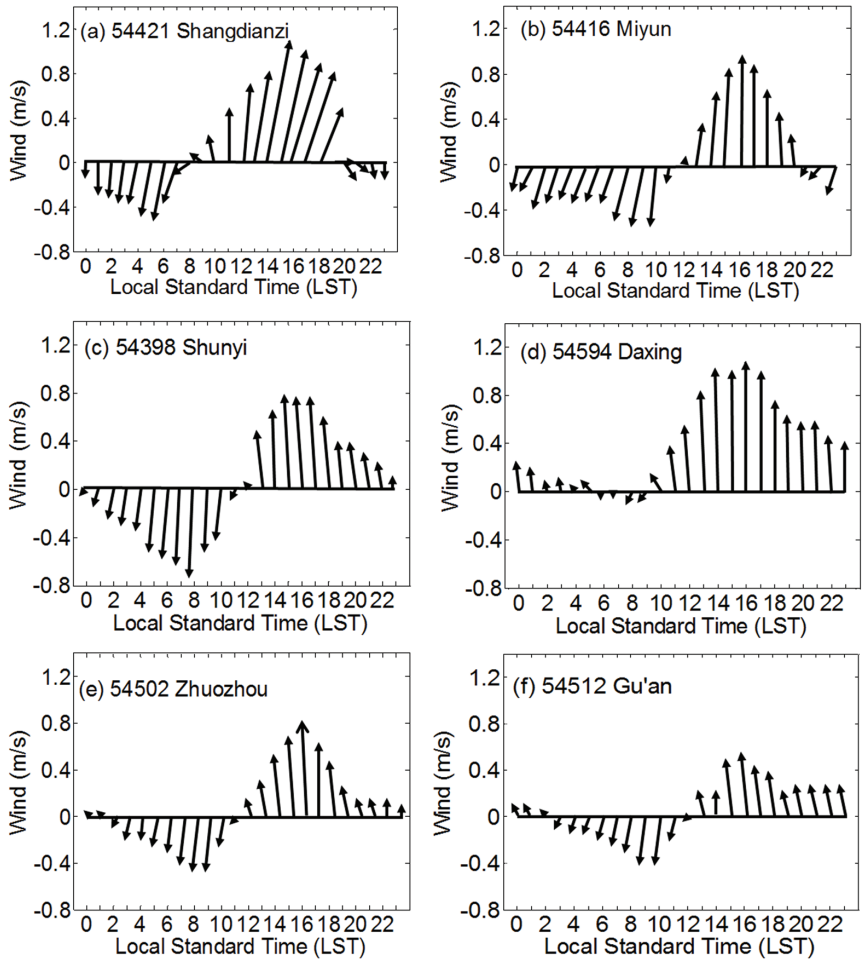


**Fig. 5.** Diurnal variations of wind for 6 stations: (a) Shangdianzi; (b) Miyun; (c) Shunyi; (d) Daxing; (e) Zhuozhou and (f) Gu'an. The length of lines denotes vector wind speed and the arrows denote the direction which the wind blowing to.

the south.

### 3.3 *Possible effects of mountain-valley circulation and urbanization*

As suggested by the diurnal variations of surface wind around the Beijing area, the urban and country winds may affect diurnal changes in local circulation and further affect precipitation. To detect the urban effect on diurnal variations of precipitation in Beijing, eleven representative stations in the plain area are grouped into three regions which represent the southwest suburbs, the urban area, and the northeast suburbs (Fig. 1). The southwest suburb group includes Zhuozhou, Gu'an, and Langfang; the urban group includes Haidian, Fengtai, Tongxian, Guanxiangtai, and Daxing; and the northeast suburb group includes Miyun, Pinggu, and Shunyi (see Fig. 1). These stations are selected because they are relatively far from mountainous areas. Note that Chaoyang station is not selected because it is surrounded by trees and cannot represent the urban climate anymore (Wang and Hu, 2006). Huairou station is not selected because its location has been changed since 1996 and the temperature shows a decreasing trend since 1990, which is not consistent with the increasing trend of other stations in the Beijing Plain. Overall, from late afternoon to late evening, the normalized frequency for the northeast group exhibits the highest probability and that for the southwest group exhibits the lowest. On the contrary, in the morning from about 0200 to 1000 LST, the southwest group and urban group show higher normalized probability than the northeast group (Fig. 6). Figure 6 supports that the differences among three groups are quite obvious during 1900–2300 LST and 0400–0800 LST.

The higher occurrence of nighttime rain in Beijing is presumed to be mainly attributed to mountain-valley circulation. In summer, southerly and southeast-



© 1994-2011 China Academic Journal Electronic Publishing House. All rights reserved. http://www.cnki.net

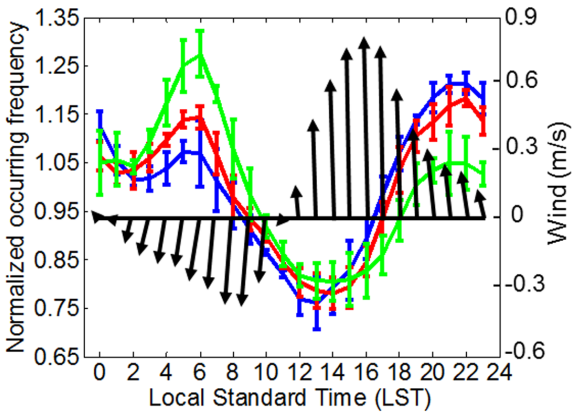


**Fig. 6.** Diurnal variations of normalized precipitation occurring frequency for three groups of station in the northeast (blue line), urban area (red line) and southwest (green line) respectively and diurnal variation of wind for these stations (black line). The solid blue, red and green lines stand for the values averaged over stations in the same group; The error bars stand for the standard deviation among stations in the same group; The length of black lines denotes vector wind speed and the arrows denote the direction which the wind blowing to. Northeast group includes Miyun, Pinggu, and Shunyi; urban group includes Haidian, Fengtai, Tongxian, Guanxiangtai and Daxing; and southwest group includes Zhuozhou, Gu'an and Langfang.

erly winds originating from the prevailing East Asian monsoon circulation supply a lot of moisture for precipitation, which seems to be one of the prerequisites. In the afternoon, the divergence at the 950 hPa level is negative in the western and northern mountainous areas, which indicates that upward motions are developing and coincident with the afternoon peak of diurnal precipitation variations in this area. At the same time, the downward motion leads to a low probability of precipitation over the plain (Figs. 7a, b). After sunset, wind becomes mountainous, and, thus, relatively cool air from mountainous rural areas converges in the warmer plain urban areas (Fig. 7c), possibly causing the nocturnal precipitation maximum in the plain, similarly suggested by Jiang and Liu (2007). At 0800 LST, the convergence remains over the plain but is substantially weakened (Fig. 7d).

Also, diurnal variations of precipitation in the Beijing area show some modulation from the urbanization effect. The urban heat island is known to increase the thermal difference between mountains and plains (Lin and Yu, 2005), which may further enhance the so-called Mountain-Plains Solenoid (MPS). From 1400 LST to 0200 LST, the northeast group shows the highest normalized precipitation probability, while the southwest group shows the lowest, but the opposite situation is found from 0200 LST to 1400 LST (Fig. 6). This pattern may be attributed to the combined effects of mountain-valley topography and urbanization. Namely, in the afternoon, when the surface wind is from south, the probability of rainfall in the urban center and downwind area (northeast suburbs now) increase (Fig. 6). On the contrary, in the early evening around 2000 LST, when valley wind begins to change to mountainous wind for stations in the northeastern part of the Beijing Plain, resulting winds from the west, northwest, and northeast begin to converge in the plain. Thus the northeastern area, where Miyun, Shunyi, and Pinggu are located, can likely be the convergence point, where it is easily to trigger precipitation. The convective rain triggered by the convergence of cool mountainous winds and the warm urban atmosphere seems to induce heavy rain intensity in the northeastern part of the Beijing Plain, where the hourly precipitation with an intensity higher than 5 mm $h^{-1}$ exhibits highest frequency. As the wind direction begins to change in the urban area and southwest suburb after 0100 LST, the corresponding precipitation probabilities in these areas also increase rapidly. Therefore, the normalized frequency of rainfall in the urban and downwind area (southwest suburbs now) is found to be higher than that in the northeast area in the early morning during 0400–0800 LST. This transition of the highest normalized precipitation probability within a day (from the northeast area in the afternoon and evening to the southwest area in the morning) may induce insignificant differences between upwind and downwind areas if the indicator is daily or seasonal precipitation as shown in studies by Sun and Shu (2007) and Wang et al. (2008b).

## 4. Conclusion

The present study has investigated detailed characteristics of the diurnal variation of precipitation in Beijing and suggested possible influences from localized circulation characteristics induced by mountain-valley topography and urbanization effects. The spatial variations of precipitation are generally influenced by large-scale systems, local topography, and LUCC (land-use and land-cover change). The effect of large-scale systems on precipitation distribution could be generally regarded as the same within a city scope. The difficulty is how to distinguish and separate the effect of topography from urban effects on diurnal variations of precipitation, which is necessary when the effects of human activities on climate change are to be evaluated. We will further explore this by using a longer series of hourly data and utilizing mesoscale



© 1994-2011 China Academic Journal Electronic Publishing House. All rights reserved. http://www.cnki.net

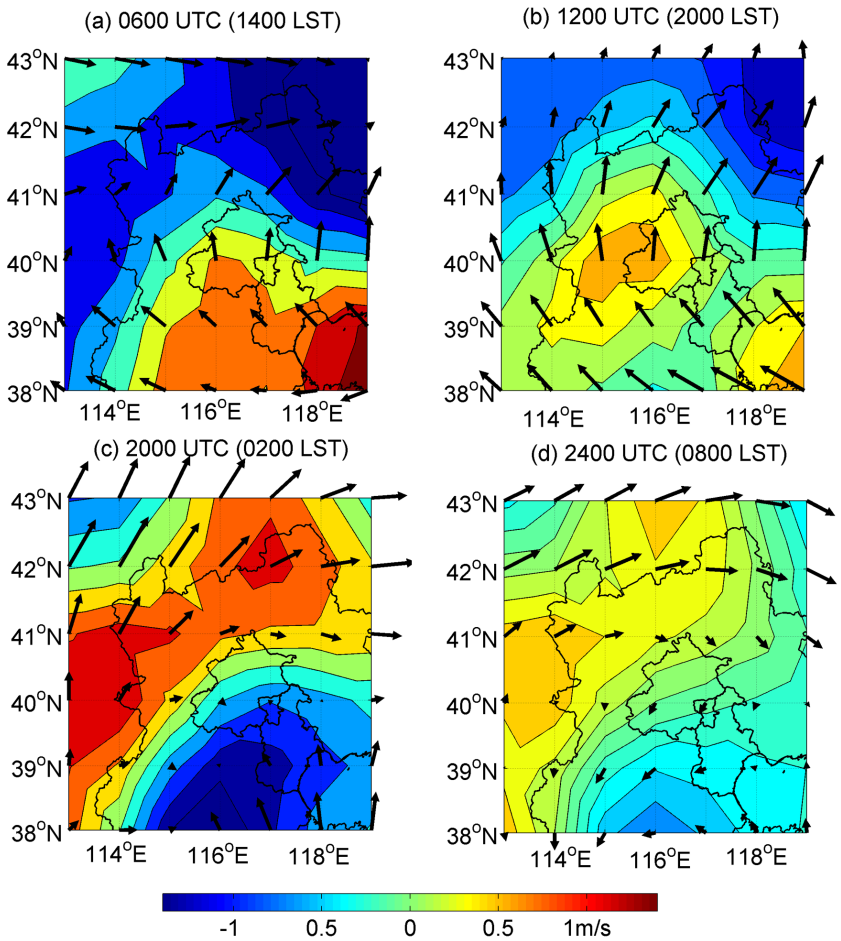


**Fig. 7.** Spatial distribution of the 950 hPa divergence (colored) and wind vectors based on the NCEP final analysis data in JJA during 2000–2007 at (a) 1400 LST, (b) 2000 LST, (c) 0200 LST and (d) 0800 LST.

model experiments. The study may be useful for refining short-range precipitation forecasts and, further, be a benefit for urban drainage system planning and water resources protection in the Beijing area.

***Acknowledgements.*** The authors would like to thank the Hebei Meteorological Bureau for supplying surface wind and precipitation data and two anonymous reviewers for their valuable comments. NCEP final analysis data for this study are from the Research Data Archive (RDA), which is maintained by the Computational and Information Systems Laboratory (CISL) at the National Center for Atmospheric Research (NCAR). NCAR is sponsored by the National Science Foundation (NSF). The original data are available from the RDA (http://dss.ucar.edu) in dataset number ds083.2. This research is supported by grants from the National Basic Key Research Program (973) under Grant No. 2006CB403606, the National Key Technology R&D Program under Grant No. 2007BAC29B04, and the National Science Foundation Project for Post-doctoral Scientists of China under Grant No. 20080440343.

## REFERENCES

Chen, G., W. M. Sha, and T. Iwasaki, 2009a: Diurnal variation of precipitation over southeastern China: Spatial distribution and its seasonality. *J. Geophys. Res.*, **114**, D13103, doi: 10.1029/2008JD011103.

Chen, G., W. M. Sha, and T. Iwasaki, 2009b: Diurnal variation of precipitation over southeastern China: 2. Impact of the diurnal monsoon variability. *J. Geophys. Res.*, **114**, D21105, doi: 10.1029/2009JD012181.

Chen, H. M., R. C. Yu, J. Li, W. H. Yuan, and T. J. Zhou, 2010: Why nocturnal long-duration rainfall presents an eastward delayed diurnal phase along the Yangtze River. *J. Climate*, **23**(4), 905–917, doi: 10.1175/2009JCLI3187.1.

Collier, C. G., 2006: The impact of urban areas on weather. *Quart. J. Roy. Meteor. Soc.*, **132**(614), 1–25.



© 1994-2011 China Academic Journal Electronic Publishing House. All rights reserved. http://www.cnki.net

Fujibe, F., N. Yamazaki, and K. Kobayashi, 2006: Long-term changes in the diurnal precipitation cycles in Japan for 106 years (1898–2003). *J. Meteor. Soc. Japan*, **84**(2), 311–317.

Hu, X. M., S. H. Liu, F. M. Liang, J. H. Wang, H. P. Liu, Y. C. Wang, and J. Li., 2005: Observational study of wind fields, temperature fields over Beijing area in summer and winter. *Acta Scientiarum Naturalium, Universitatis Pekinensis*, **41**(3), 399–407.

Jiang, X. Y., and W. D. Liu, 2007: Numerical simulation on impacts of urbanization on heavy rain in Beijing using different land use data. *Acta Meteorologica Sinica*, **21**(2), 245–255.

Li, J., and W. J. Shu, 2008: Observation and analysis of nocturnal low-level jet characteristics over Beijing in summer. *Chinese Journal of Geophysics*, **51**(2), 360–368. (in Chinese)

Li, J., R. C. Yu, and T. J. Zhou, 2008a: Seasonal variation of the diurnal cycle of rainfall in the southern contiguous China. *J. Climate*, **21**, 6036–6043.

Li, J., R. C. Yu, and J. J. Wang, 2008b: Diurnal variations of summer precipitation in Beijing. *Chinese Science Bulletin*, **53**(12), 1933–1936.

Lin, X. C., and S. Q. Yu, 2005: Interdecadal changes of temperature in the Beijing region and its heat island effect. *Chinese Journal of Geophysics*, **48**(1), 39–45. (in Chinese)

Lin, Z. G., 1995: *Topography-Induced Precipitation Climatology*. Science Press, Beijing, 407pp. (in Chinese)

Sun, J. S., 2005: A study of the basic features and mechanism of boundary layer Jet in Beijing area. *Chinese J. Atmos. Sci.*, **29**(3), 445–451. (in Chinese)

Sun, J. S., and W. J. Shu, 2007: The effect of urban heat island on winter and summer precipitation in Beijing region. *Chinese J. Atmos. Sci.*, **31**(2), 311–320. (in Chinese)

Sun, J. S., and B. Yang, 2008: Meso-$\beta$ scale torrential rain affected by topography and the urban circulation. *Chinese J. Atmos. Sci.*, **32**(6), 1352–1364. (in Chinese)

Wang, X. Q., Z. F. Wang, Y. B. Gong, and H. Guo, 2008a: Modulation of urban heat island circulation on mountain-plain wind in the Beijing area. *Climatic and Environmental Research*, **13**(5), 639–644. (in Chinese)

Wang, X. Q., Z. F. Wang, Y. B. Qi, and H. Guo, 2008b: The effect of urban heat island on the distribution of winter precipitation in Beijing region. *Science in China* (*D*), **38**(11), 1438–1442. (in Chinese)

Wang, X. R., W. G. Wang, H. Z. Liu, and H. Wang, 2008c: Beijing region precipitation feature and some statistics of relationship between it and SHWP. *Plateau Meteorology*, **27**(4), 822–829. (in Chinese)

Wang, Y., and F. Hu, 2006: Variations of the urban heat island in summer of the recent 10 years over Beijing and its environment effect. *Chinese Journal of Geophysics*, **49**(1), 61–68. (in Chinese)

Wu, Z. H., 1993: Climate analysis of summer short-period precipitation in Beijing-Tianjin-Hebei area. *Scientia Atmospherica Sinica*, **17**(3), 268–273. (in Chinese)

Yin, S. Q., D. Chen, and Y. Xie, 2009: Diurnal variations of precipitation during the warm season over China. *Int. J. Climatol.*, **29**(8), 1154–1170, doi: 10.1002/joc.1758.

Yu, R. C., J. Li, and H. M. Chen, 2009: Diurnal variation of surface wind over central eastern China. *Climate Dyn.*, **33**, 1089–1097, doi: 10.1007/s00382-008-0478-3.

Yu, R. C., T. J. Zhou, A. Y. Xiong, Y. J. Zhu, and J. Li, 2007a: Diurnal variations of summer precipitation over contiguous China. *Geophys. Res. Lett.*, **34**, L01704, doi: 10.1029/2006GL028129.

Yu, R. C., Y. P. Xu, T. J. Zhou, and J. Li, 2007b: Relation between rainfall duration and diurnal variation in the warm season precipitation over central eastern China. *Geophys. Res. Lett.*, **34**, L13703, doi: 10.1029/2007GL030315.

Zheng, S. Y., and S. H. Liu, 2008: Urbanization effect on climate in Beijing. *Climatic and Environmental Research*, **13**(2), 123–133. (in Chinese)

Zhou, T. J., R. C. Yu, H. M. Chen, A. G. Dai, and Y. Pan, 2008: Summer precipitation frequency, intensity, and diurnal cycle over China: A comparison of satellite data with rain gauge observations. *J. Climate*, **21**(16), 3997–4010.



© 1994-2011 China Academic Journal Electronic Publishing House. All rights reserved. http://www.cnki.net

第66卷 第3期 地 理 学 报 Vol.66, No.3
2011年3月 ACTA GEOGRAPHICA SINICA Mar., 2011

# 我国热带气旋潜在影响力指数分析

尹宜舟[1,2], 肖风劲[1], 罗 勇[1], 赵珊珊[1]
(1. 中国气象局国家气候中心, 北京 100081;
2. 中国科学院大气物理研究所, 北京 100029)

**摘要:** 利用热带气旋路径资料和灾情资料,综合考虑热带气旋的频数、强度、范围以及持续时间,建立热带气旋潜在影响力指数,分析了1949-2009年我国热带气旋的潜在影响力的空间格局和年际变化特征,并以0608号超强台风"桑美"为例分析了该指数与灾害损失、过程极大风速、过程雨量的关系。研究结果表明:1949-2009年间,我国的热带气旋的潜在影响力呈现出弱减少的趋势,这种趋势并不显著,但各阶段性的趋势比较明显;近20年来,我国海南、广东、广西等华南沿海受热带气旋潜在影响力在下降,而浙江、福建、台湾等东南沿海省份受热带气旋潜在影响力在上升;潜在影响力指数最高的区域主要分布在台湾、海南、广东沿海、福建沿海以及浙江南部沿海等地;TCPI与灾害损失、过程极大风速、过程降水量等有较好的相关性,并都通过了0.01的显著性检验。

**关键词:** 热带气旋;潜在影响力指数;桑美;中国;西北太平洋

## 1 引言

热带气旋 (Tropical Cyclone, TC) 是一种发生在热带或副热带海洋上的气旋性涡旋,常伴有狂风、暴雨和风暴潮,是一种破坏性很强的天气系统,具有发生频次高、影响范围广、突发性强、成灾强度大等特征。主要影响我国的东南沿海地区,这些地区人口稠密、经济发达、社会财富高度密集,是我国的最严重的自然灾害之一。TC灾害带来的影响十分巨大[1-4],如2006年强热带风暴"碧利斯"在福建省霞浦县登陆,共造成843人死亡,直接经济损失达348.3亿元[5]。根据我国最新的热带气旋等级标准,将热带气旋划划分为6个等级:热带低压 (10.8~17.1 m/s),热带风暴 (17.2~24.4 m/s),强热带风暴 (24.5~32.6 m/s),台风 (32.7~41.4 m/s),强台风 (41.5~50.9 m/s) 和超强台风 (≥ 51.0 m/s)[6]。

为了研究大西洋TC活动特征,Gray提出了飓风破坏潜力指数 (Hurricane Destruction Potential,HDP,又称为台风破坏潜力Typhoon Destruction Potential,TDP),HDP被定义为某时期内所有每6小时强度达到飓风级别 (即最大风速达32.7m/s) 的TC中心附近最大风速的平方之和[7-8];Bell等指出,HDP指数仅局限于强度较大的TC系统,没有考虑较弱的TC系统,在HDP的基础上,Bell等将热带风暴级别的TC系统也加入了计算,并将改进过的指数定义为累积气旋能量指数 Accumulated Cyclone Energy (ACE)[9]; Emanuel在能量耗散 (Dissipation of Power) 的概念基础上提出了潜在破坏力指数 (Index of Potential destructiveness,PDI)[10],该指数是TC中心附近最大风速的立方在整个TC生命史期间的积分。这些指数综合考虑了TC强度、频数以及持续时间,克服了以往的研究单独分析TC强度及频数的限制。但是这些均是针对TC自身而言,无法判断TC对某一地区的潜在影响状

**收稿日期:** 2010-10-17; **修订日期:** 2010-12-27
**基金项目:** 国家"十一五"科技支撑项目 (2008BAK50B02),( 2007BAC29B05) [**Foundation:** National Science & Technology Pillar Program during the Eleventh Five-Year Plan Period (2008BAK50B02), (2007BAC29B05)]
**作者简介:** 尹宜舟 (1984-), 男, 博士研究生, 主要从事热带气旋气候及风险等方面研究。Email: ship2001691@sohu.com
**通讯作者:** 肖风劲 (1973-), 男, 博士, 副研究员, 主要从事台风及气象灾害影响及风险评估研究。
Email: xiaofj@cma.gov.cn



© 1994-2011 China Academic Journal Electronic Publishing House. All rights reserved. http://www.cnki.net

况。对于TC对某地区影响的基本气候特征,在目前研究中[11-14],仅仅是分析登陆或影响频数、强度等,这无法综合表达TC对该地区的影响。由于TC的影响范围广,有可能出现TC中心未经过该区域但同样能够对该区域造成较大影响的情况。因此在研究TC对区域的影响时,只考虑有TC中心经过的情形显然是不够全面。本文综合考虑了热带气旋的频数、强度、范围以及持续时间等因素,建立热带气旋潜在影响力指数 (Tropical Cyclone Potential Impact, TCPI),分析了1949-2009年我国热带气旋的潜在影响力的空间格局和年际变化特征,并以2006年超强台风"桑美"为例分析了该指数与灾害损失、过程极大风速、过程雨量的关系。

## 2 数据来源与研究方法

### 2.1 资料来源

本文所用的热带气旋最佳路径资料来自中国气象局主编的《热带气旋年鉴》或《台风年鉴》[15],该年鉴收集了每年西北太平洋和我国南海每次热带气旋路径资料,包括每6小时的TC中心位置以及中心附近最大平均风速、中心气压等。热带气旋的灾害损失资料来自于中国气象局《年气候影响评价》和《中国气象灾害年鉴》[5],这两类文献收集了每次热带气旋导致的灾害影响,包括受灾人口、死亡人口、直接经济损失、倒塌房屋、损毁房屋、受灾面积等。

### 2.2 指数的定义

为了解某地区受TC潜在影响的特征,定义基于地区分析的热带气旋潜在影响力指数:

$$TCPI=\sum_{i=1}^{N}\sum_{j=1}^{M}b_j(a_j\bar{v}_i)^2 \tag{1}$$

式中:$i=1,\cdots,N$,表示某次TC过程对某地区 (面状) 影响的次数 (以每6小时作一次统计),$j=1,\cdots,M$,表示TC不同的影响区域,即在不同的区域TC的影响强度有差别,以系数$a$为权重;$\bar{v}_i$为该次平均的TC中心附近最大平均风速;$b$表示某地区受TC影响的面积权重,若该地区完全在TC某影响区域内,则$b$为1,若部分在,则依影响范围,$b$取值在0至1之间,若不在,则$b$取值为0。若将该地区各年TC过程中的TCPI进行累加,得到年TCPI指数,利用此指数可以分析该地区受热带气旋潜在影响的年际变化特征。

### 2.3 分析方法

TCPI计算的关键在于$a$、$b$权重系数的确定,本文以0608号超强台风"桑美"登陆时的6小时路径线段为例,取1°×1°网格为研究区域,来具体地介绍TCPI的计算过程。

参考文献[16],依据平均的TC中心附近最大平均风速$\bar{v}$,定义如下扫描半径d (因参加范围计算所涉及到的点的位置均为经纬度,所以d的单位取为度),具体的取值半径见表1。

**表1 我国热带气旋中心附近最大风速所影响的半径距离**

**Tab. 1 The affected radius distances from the center of TC by their maximum wind speed in China**

| 速度 $\bar{V}$ (m/s) | 半径 d (°) |
|---|---|
| $\bar{V}<17.2$ | d = 2° |
| $17.2\leqslant\bar{V}<24.5$ | d = 3° |
| $24.5\leqslant\bar{V}<32.7$ | d = 4° |
| $\bar{V}\geqslant 32.7$ | d = 5° |

确定TC的影响范围是以TC路径点为圆心,以确定的长度为半径进行扫描,所得到的圆即为该点对应的影响范围。那么,6小时路径线段所构成的影响范围则是以线段上各点所对应的影响范围的叠加,则最终得到的图形是由以线段长度为长,2倍扫描半径为宽的长方形和分别以两个端点为圆心的半圆构成。

图1给出了"桑美"登陆时的6小时路径线段,此段$\bar{v}$的数值为52.5m/s,则相应的d为5度。按照上述方法得到此6小时"桑美"的影响范围,即图1中最外围的点圈。考虑到TC对不同地区的影响程度不同,分别以1至4度为扫描半径,再建立4个大小不一的点圈,定义最内层点圈的TC影响强度权重$a$为1,次内层除去最内层区域的$a$为4/5,依次类推,则最外层除去次外层的区域,$a$取值为1/5。其他时段依据d的值划定相应的d个影响区域,再按照上述方法确定$a$值。



© 1994-2011 China Academic Journal Electronic Publishing House. All rights reserved. http://www.cnki.net

为了得到权重b的值,在1°×1°的单元格内,以0.1度为间隔取81个点,若经过统计,该单元格在权重系数为$a_1$的TC影响区域有$k_1$个点,则定义该单元格在该TC影响区域的面积权重系数$b_1$为$k_1/81$;若$k_1 = 0$,则$b_1 = 0$;若$k_1 = 81$,即表示该单元格完全在此影响区域内,$b_1 = 1$,此时在其他的影响区域b取值就为0。

已知a、b值后,就可以求出这一时段TC对相关区域的影响状况,再将其他时段的影响进行累加,则可得到相关区域的TCPI数值。当然在实际的计算中,可以根据精度要求调整单元格的大小以及单元格内点的设置。若研究的区域是一个不规则的地区,则以合适的间隔取点,所得点数即相当于上文单元格内得到的总点数,然后采用上述方法计算在TC影响过程中该不规则地区的TCPI数值。

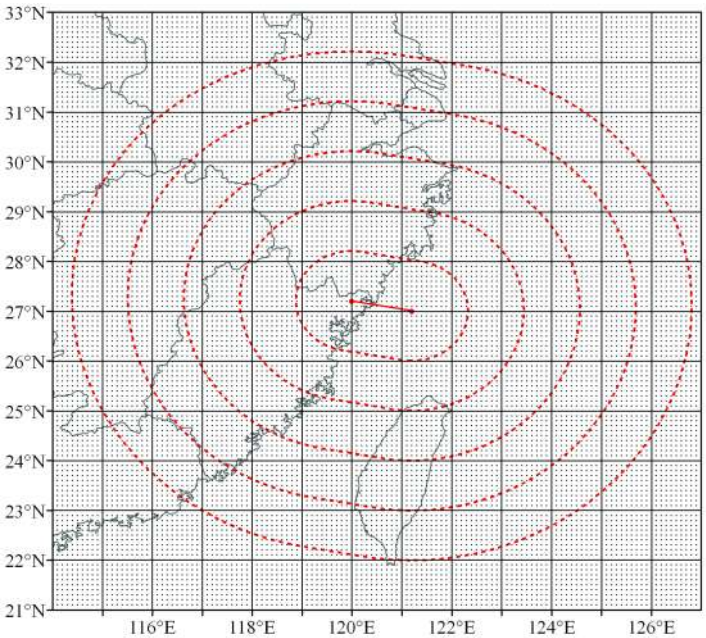


图1　TCPI计算方法示意图(中央实线段为"桑美"登陆时的6小时线段,点圈为不同的影响区域,方格为1×1°,方格内以0.1度取点)

Fig. 1　Calculation scheme for TCPI (The central real line is the 6 hours' track when Saomai made landfall. Dashed circles are for different impacted regions. The cell is 1°×1° and get points in the cell with an interval of 0.1°)

下文分析中,若研究区域为单元格,则其大小为0.5°×0.5°,以每隔0.05°取点,每单元格内共81个点;若为县级研究区域,以每隔0.05°取点,若以我国陆地为研究区域,以每隔0.1°取点,得到相应范围内的点。

## 3　结果分析与讨论

### 3.1　我国热带气旋潜在影响力指数的年际变化

为了研究我国年TCPI指数的年际变化特征,我们以0.1度为单位在我国行政区域(不包括海洋)内取点,共得到95950个点。利用上文提到的方法,对我国的TCPI指数进行逐次逐年累加,以1971-2000年平均值为气候基准值来分析年TCPI的年际变化特征。

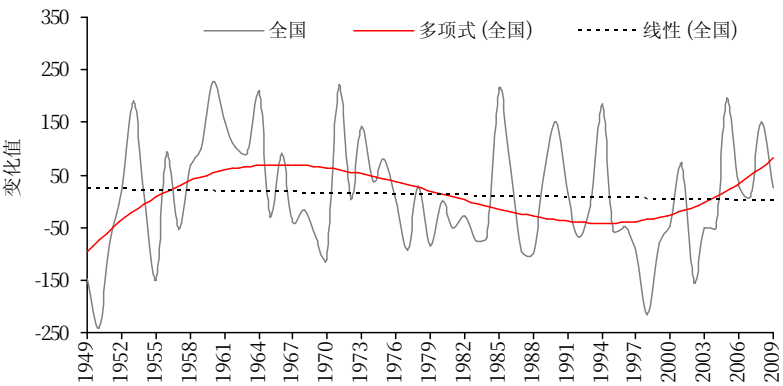


图2　1949-2009年我国年TCPI指数年际变化图(相对于1971-2000年)

Fig. 2　Variety of yearly TCPI from 1949 to 2009 for China (relative to the average from 1971 to 2000)

图2给出了我国逐年TCPI指数的变化趋势,



© 1994-2011 China Academic Journal Electronic Publishing House. All rights reserved.　http://www.cnki.net

从1949-2009年，我国的台风潜在破坏力呈现出弱减少的趋势，这种趋势并不显著。但各阶段性的趋势比较明显，从1949年至1960年代中后期，我国年TCPI指数呈现的是上升的趋势，1960年代末期至1990年代中期则为下降趋势，从1990年代中期开始为上升趋势。这与登陆中国的热带气旋略有减少，但减少趋势不明显基本一致。

**表2 1949–2009年各省对我国61年TCPI指数之和的贡献值及比率**

**Tab. 2 Contributions and ratios in various provinces of the sum of TCPI from 1949 to 2009 for Chinese TCPI**

| 省份 | 相对贡献值 | 比率(%) | 省份 | 相对贡献值 | 比率(%) | 省份 | 相对贡献值 | 比率(%) |
|---|---|---|---|---|---|---|---|---|
| 山西 | 1.85 | 0.01 | 吉林 | 88.53 | 0.44 | 浙江 | 1881.20 | 9.44 |
| 北京 | 2.30 | 0.01 | 上海 | 92.85 | 0.47 | 海南 | 1954.46 | 9.81 |
| 天津 | 3.65 | 0.02 | 辽宁 | 99.29 | 0.50 | 广西 | 2050.01 | 10.29 |
| 贵州 | 21.60 | 0.11 | 黑龙江 | 145.54 | 0.73 | 福建 | 2996.03 | 15.03 |
| 河北 | 27.57 | 0.14 | 山东 | 168.27 | 0.84 | 台湾 | 3192.55 | 16.02 |
| 内蒙古 | 29.66 | 0.15 | 湖南 | 182.66 | 0.92 | 广东 | 5214.48 | 26.17 |
| 河南 | 37.89 | 0.19 | 安徽 | 332.25 | 1.67 | | | |
| 云南 | 51.74 | 0.26 | 江苏 | 482.61 | 2.42 | | | |
| 湖北 | 56.65 | 0.28 | 江西 | 813.22 | 4.08 | **总计** | **19927.79** | **100** |

注：香港、澳门并入广东省计算，贡献值和比率保留两位小数。

我们进一步计算了各省行政区域对我国61年来TCPI的贡献值及所占比率(表2)。从表2可以看出，广东省的贡献最大，达到26.2%，这可能与热带气旋在广东登陆的比例有关系，在广东省登陆的热带气旋占我国登陆热带气旋总数的36.8%，在沿海省份中占第一位[17]，而台湾、福建、广西、海南、浙江各省的贡献率依次为16%、15%、10.3%、9.8%、9.4%。以上省份贡献值之和占全国的87%。

图3分别给出了浙江、福建、台湾、广西、广东、海南6个省从1949-2009年TCPI逐年贡献

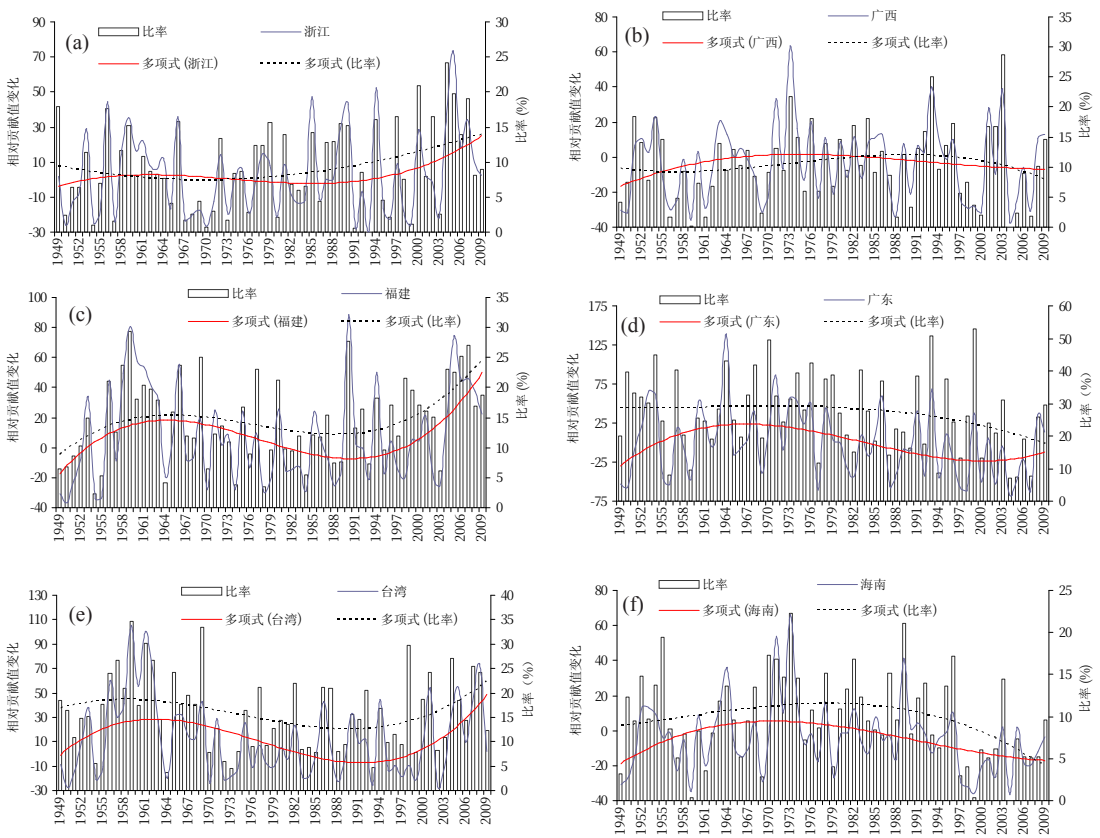


图3 主要省份1949-2009年TCPI逐年贡献值(相对于1971-2000年)及比率(相对于全国)变化图

Fig. 3 Contributions (relative to the average from 1971 to 2000) and ratios of the TCPI of China in some provinces



© 1994-2011 China Academic Journal Electronic Publishing House. All rights reserved. http://www.cnki.net

值 (相对于1971-2000年) 及比率 (相对于全国)。福建、台湾两省贡献值的变化曲线与全国的相似,从1949年至1960年代中后期,贡献率呈上升的趋势,1960年代末期至1990年代初则为下降趋势,从1990年代则表现为上升趋势;浙江省贡献值变化从1949年至1990年代初比较平缓,1990年代中期以来为上升趋势;从1949年至1960年代中后期,海南、广西、广东三省贡献值变化均为上升趋势,1970年代初以来海南表现为下降趋势,广西则在1960年代末之后为略下降趋势,广东省则从1960年代末期至1990年代中期为下降趋势,之后变化平缓。总体来讲,海南、广西、广东三省的比率近20年来表现为下降的趋势,而浙江、福建、台湾表现为上升的趋势。这反映了我国海南、广东、广西等华南沿海受热带气旋潜在的影响在下降,而浙江、福建、台湾等东南沿海受热带气旋潜在的影响在上升,这可能与近20年来,我国北抬热带气旋增加、西进热带气旋减少有关。相关方面的研究也证明了这一点,随着全球气候变暖,台风登陆位置有向中部移动的趋势,西北太平洋台风在生命史中强度达最强时的位置有向北移动的趋势[18-19]。

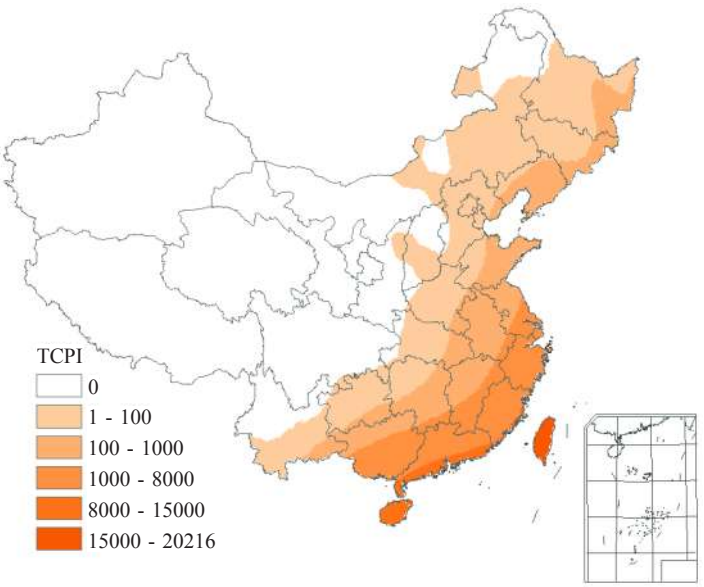


图4　1949-2009年我国年平均TCPI分布

Fig. 4　The spatial pattern for average regional typhoon potential impacts from 1949-2009

### 3.2 我国热带气旋潜在影响力区域分布

我们计算了1949-2009年逐年、逐个台风的TCPI,并将每个单元格的TCPI进行累加求后,再进行平均,得到1949-2009年61年间我国平均TCPI的分布 (图4)。从图4可以看出,我国东南沿海和中部多数省份都能够受到TC的影响,主要影响区域在我国的东南沿海地区。我们根据TCPI指数对全国受TC影响的区域划分为5个等级,年平均TCPI指数最高为15000以上属于一级

**表3　2000–2008年间65个TCs TCPI值和直接经济损失**

**Tab. 3　The relationship between direct economic losses and TCPI for 65 TCs during 2000–2008 in China**

| TC编号 | LOSS | TCPI | TC编号 | LOSS | TCPI | TC编号 | LOSS | TCPI |
|---|---|---|---|---|---|---|---|---|
| 0004 | 190 | 11.65 | 0308 | 56 | 6.65 | 0604 | 9597 | 34.97 |
| 0008 | 75 | 21.77 | 0309 | 69 | 6.14 | 0605 | 1585 | 32.59 |
| 0010 | 1305 | 61.18 | 0311 | 20 | 5.29 | 0606 | 2167 | 50.65 |
| 0012 | 1337 | 17.68 | 0312 | 918 | 67.43 | 0608 | 5417 | 89.51 |
| 0013 | 742 | 16.89 | 0313 | 718 | 32.16 | 0703 | 23 | 7.70 |
| 0014 | 936 | 9.07 | 0320 | 470 | 13.72 | 0707 | 608 | 18.87 |
| 0016 | 394 | 15.26 | 0407 | 114 | 11.38 | 0709 | 2295 | 56.28 |
| 0102 | 1311 | 35.10 | 0411 | 9 | 2.23 | 0713 | 2214 | 75.57 |
| 0103 | 1869 | 50.62 | 0414 | 5694 | 67.53 | 0714 | 55 | 3.42 |
| 0104 | 4825 | 39.99 | 0418 | 907 | 45.45 | 0715 | 137 | 10.22 |
| 0105 | 12 | 0.42 | 0421 | 84 | 5.35 | 0716 | 2570 | 51.80 |
| 0107 | 251 | 47.16 | 0505 | 3000 | 54.58 | 0801 | 198 | 22.88 |
| 0108 | 985 | 24.33 | 0508 | 11 | 8.11 | 0806 | 669 | 20.94 |
| 0114 | 561 | 25.42 | 0509 | 5021 | 84.27 | 0807 | 326 | 23.29 |
| 0116 | 17 | 8.35 | 0510 | 838 | 24.79 | 0808 | 1954 | 63.62 |
| 0205 | 425 | 9.57 | 0513 | 4275 | 49.79 | 0809 | 497 | 18.23 |
| 0212 | 1644 | 24.17 | 0515 | 3927 | 64.75 | 0812 | 1075 | 30.23 |
| 0214 | 838 | 24.44 | 0516 | 31 | 1.16 | 0813 | 35 | 12.35 |
| 0216 | 2342 | 39.07 | 0518 | 3398 | 56.41 | 0814 | 3342 | 92.10 |
| 0218 | 100 | 8.69 | 0519 | 2174 | 30.12 | 0815 | 49 | 7.99 |
| 0220 | 319 | 11.53 | 0601 | 2311 | 52.37 | 0817 | 22 | 7.07 |
| 0307 | 950 | 63.79 | 0602 | 8 | 0.62 | | | |



© 1994-2011 China Academic Journal Electronic Publishing House. All rights reserved.　http://www.cnki.net

的区域，主要分布在我国的台湾省，热带气旋潜在影响力最高，热带气旋的影响最严重，是我国热带气旋危险性最高的地区；其次为海南、广东沿海、福建沿海、浙江南部沿海地区，TCPI指数在8000~15000之间，是我国遭受热带气旋仅次于台湾的地区，也是中国大陆遭受热带气旋影响最严重的区域，这些地区热带气旋强度强、频率高，是我国大陆热带气旋危险性最高的地区；TCPI指数在1000~8000之间属于第三级，主要分布在广西东南部、广东北部、福建中西部、浙江、上海等地，这些地区热带气旋强度强、频率高，热带气旋的影响也较为严重，属于热带气旋危险性较高的地区；第四级的TCPI指数在100~1000之间，主要分布在广西北部、湖南南部、江西、安徽、江苏、山东半岛、辽东半岛等地，热带气旋破坏潜力指数低，热带气旋强度小，频率较低，热带气旋能够产生一定的影响，但影响的程度远小于第三级区域，属于热带气旋危险性较低的地区；第五级的TCPI指数在1~100之间，主要包括云南东南部、贵州、湖南北部、古北河南、山东西部、河北、北京、天津、内蒙古东部、辽宁中北部、吉林、黑龙江中南部等地，热带气旋破坏潜力指数极低，热带气旋强度小，频率也低，属于热带气旋危险性低的地区。

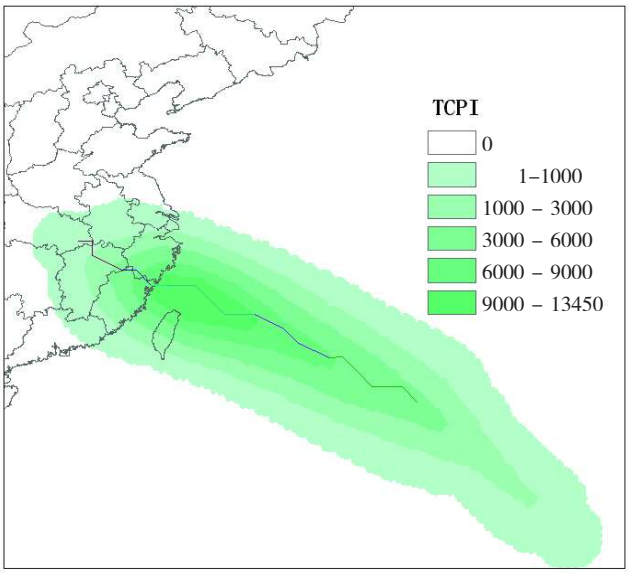


图5 “桑美”影响我国期间的TCPI分布

Fig. 5 TCPI distribution during the impacted period of Saomai in China

### 3.3 TCPI指数与我国热带气旋灾害损失的关系

为了进一步分析TCPI与灾害损失之间的关系，我们选取2000-2008年间有直接经济损失 (LOSS) 的65个TC，这65个TC基本上都是登陆我国。灾害损失经过价格指数的修订，TCPI指数和灾害损失都是每次台风过程产生的，并且是影响区域的累计之和。表3给出了65个TC影响我国期间的LOSS记录以及相应的TCPI值，经过统计发现两者的相关系数达0.67，通过了99.9%的信度检验，两者高度相关，表明TCPI指数在一定程度上能够反映热带气旋的直接经济损失。

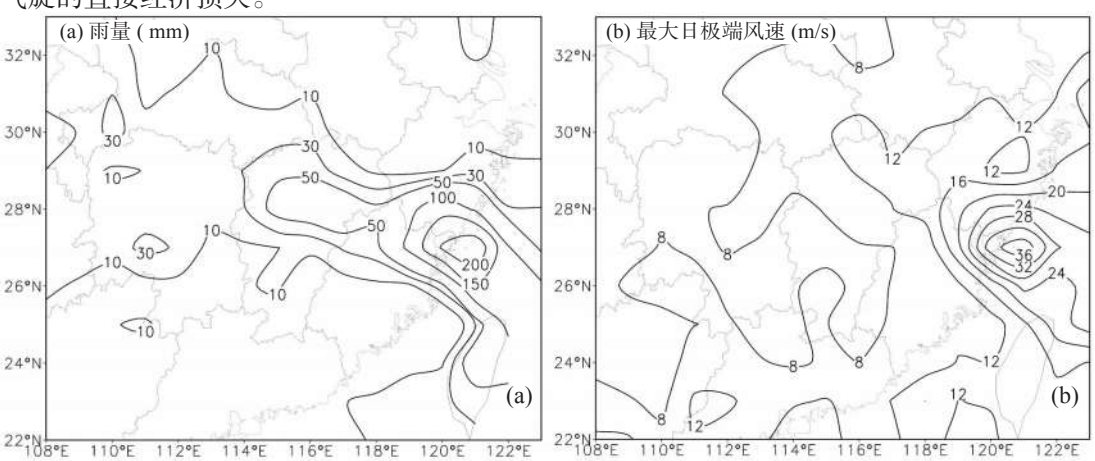


图6 “桑美”过程雨量 (a ) 及过程最大日极端风速 (b )

Fig. 6 Accumulated precipitation (a) and maximum daily extreme wind speed (b) during the process of "Saomai"



© 1994-2011 China Academic Journal Electronic Publishing House. All rights reserved. http://www.cnki.net

### 3.4 2006年"桑美"台风的潜在影响力分析

2006年8月10日0608号台风"桑美"在浙江省苍南县沿海登陆,登陆时中心附近最大风速达60 m/s,中心气压为920 hPa,其破坏性极大,超出了人们的承受能力,因灾死亡483人,直接经济损失达到196.58亿元,其中浙江、福建、江西、湖北的损失分别127.3、63.55、5.5、0.23亿元[5]。根据本文的计算方法,我们计算了"桑美"台风过程的潜在影响力分布(图5),从图中可以看出,台风中心经过的地方,其潜在影响力比较大,随着台风的强度增加,台风的潜在破坏力也明显增加,在登陆点浙江省苍南县的破坏潜力达到10373,破坏力极强,登陆后强度迅速减弱,其潜在的影响力也相应减小。"桑美"对台湾、浙江、福建三省的潜在影响较大,江西、安徽、上海、江苏、湖北等地处于其潜在的影响范围之内,也造成了一定影响。

图6给出了根据气象台站监测到的台风"桑美"降水和大风的分布[20],通过研究发现,此次TC过程中,过程雨量带以及主要极大风速带均处于潜在影响区内,同时两者的大值中心与TCPI的大值中心分布较为一致。因此TCPI对于单个"桑美"过程来说,可以给出受其潜在影响的范围及相对程度。

我们收集了"桑美"台风过程中32个县的直接经济损失情况,进一步分析了有直接经济损失(LOSS)记录的县市的LOSS与过程雨量(RAIN)、过程极大风速(WIND)的相互关系(表4)。通过分析发现:LOSS与TCPI、过程雨量、过程极大风速相关系数分别为0.636、0.717、0.704,而TCPI与过程雨量及过程极大风速相关系数分别为0.566、0.881,都达到了0.01的显著性水平(表5)。因此,TCPI在一定程度上能反映出LOSS的状况。

**表4 "桑美"台风县级直接经济损失与TCPI、过程降水量(RAIN)、过程极大风速(WIND)的关系**

**Tab. 4 The relationship between direct economic losses and TCPI, the precipitation, and maximum extreme wind speed during the period of Typhoon Saomai**

| 编号 | 县区市 | 直接经济损失(万元) | TCPI | 过程雨量(mm) | 过程极大风速(m/s) |
|---|---|---|---|---|---|
| 1 | 邵武市 | 77 | 2816 | 63 | 9.5 |
| 2 | 罗源县 | 80 | 7048 | * | 23.2 |
| 3 | 建瓯市 | 1167 | 4884 | 95 | 11.8 |
| 4 | 武夷山市 | 1360 | 3817 | 92 | 12.0 |
| 5 | 屏南县 | 2050 | 5706 | 81 | 16.4 |
| 6 | 政和县 | 4667 | 5804 | 63 | 15.9 |
| 7 | 柘荣县 | 13670 | 8028 | 261 | 40.2 |
| 8 | 宁德市 | 17660 | 7272 | 69 | 21.0 |
| 9 | 霞浦县 | 42728 | 8283 | 161 | * |
| 10 | 福安市 | 61000 | 7735 | 189 | 28.3 |
| 11 | 寿宁县 | 61500 | 7408 | 233 | 29.1 |
| 12 | 周宁县 | 110000 | 7190 | 181 | 26.4 |
| 13 | 福鼎市 | 327230 | 8764 | 262 | 43.2 |
| 14 | 铅山县 | 2310 | 3167 | 48 | 10.2 |
| 15 | 南昌市市辖区 | 2850 | 1027 | 78 | 11.7 |
| 16 | 高安市 | 3100 | 513 | 130 | 10.1 |
| 17 | 金溪县 | 5933 | 1894 | * | 13.5 |
| 18 | 临海市 | 500 | 6359 | 26 | 8.8 |
| 19 | 云和县 | 714 | 6117 | 68 | 15.8 |
| 20 | 青田县 | 1141 | 6879 | 93 | 20.3 |
| 21 | 丽水市 | 1223 | 5395 | 34 | 12.0 |
| 22 | 洞头县 | 2688 | 9640 | 80 | 28.3 |
| 23 | 玉环县 | 4720 | 6915 | 40 | 30.0 |
| 24 | 龙泉市 | 5635 | 5289 | 45 | 19.0 |
| 25 | 乐清市 | 6400 | 6878 | 85 | 18.5 |
| 26 | 温州市市辖区 | 6793 | 8140 | 93 | 26.5 |
| 27 | 景宁畲族自治县 | 12400 | 7166 | - | - |
| 28 | 瑞安市 | 17271 | 8525 | - | 33.0 |
| 29 | 文成县 | 37240 | 7920 | 175 | 23.9 |
| 30 | 庆元县 | 71000 | 6123 | 103 | 20.0 |
| 31 | 泰顺县 | 94500 | 7833 | 132 | 35.7 |
| 32 | 平阳县 | 95340 | 8842 | 265 | 30.0 |

-表示数值缺失，不参加相关系数的计算

**表5 "桑美"台风灾情损失与TCPI、过程降水量、过程极大风速的相互系数**

**Tab. 5 The matrix of correlations coefficient between LOSS and TCPI, RAIN and WIND**

| | LOSS | TCPI | RAIN | WIND |
|---|---|---|---|---|
| LOSS | 1 | 0.636** | 0.717** | 0.704** |
| TCPI | 0.636** | 1 | 0.566** | 0.881** |
| RAIN | 0.717** | 0.566** | 1 | 0.615** |
| WIND | 0.704** | 0.881** | 0.615** | 1 |

**表示在0.01水平上达到显著相关，Correlation is significant at the 0.01 level (2-tailed)



© 1994-2011 China Academic Journal Electronic Publishing House. All rights reserved.　http://www.cnki.net

## 4 结论

本文通过综合考虑热带气旋的影响频数、强度、范围以及持续时间等因素，建立热带气旋潜在影响力指数，分析了1949年以来我国热带气旋的潜在影响力的空间格局和年际变化特征，并以0608号超强台风“桑美”为例分析了该指数与灾害损失、过程极大风速、过程雨量的关系，得到出如下结论：

(1) 从1949-2009年，我国的热带气旋的潜在影响力呈现出弱减少的趋势，这种趋势并不显著。但各阶段性的趋势比较明显，从1949年至1960年代中后期，我国年TCPI指数呈现的是上升的趋势，1960年代末期至1990年代中期则为下降趋势，之后为上升趋势。

(2) 广东省对我国累计TCPI贡献最大，达到26.2%，台湾、福建、广西、海南、浙江各省的贡献率依次为16%、15%、10.3%、9.8%、9.4%。近20年来，我国海南、广东、广西等华南沿海受热带气旋潜在影响力在下降，而浙江、福建、台湾等东南沿海省份受热带气旋潜在影响力在上升。

(3) 热带气旋对我国东南沿海和中部多数省份都有潜在的影响，但主要影响区域在我国的东南沿海地区。潜在影响力指数最高的区域主要分布在台湾、海南、广东沿海、福建沿海以及浙江南部沿海等地。

(4) 通过热带气旋潜在影响力指数与直接经济损失之间的关系，两者的相关系数达0.67，具有高度的相关性，表明TCPI指数能够在一定程度上反映热带气旋的经济损失。

(5) “桑美”台风对台湾、浙江、福建三省的潜在影响力大，江西、安徽、江苏、上海、湖北等地也处在其潜在影响的范围内；TCPI与灾害损失、过程极大风速、过程降水量等有较好的相关性，并都通过了0.01的显著性检验。

本文依据路径资料分析了热带气旋的潜在影响力，其中所利用的资料也是风的速度，尚未考虑到热带气旋的降水特征，在今后的研究中要结合其他资料来修订该指数，以便更好地反映热带气旋对我国的潜在影响力；同时要通过更多热带气旋个例的分析，在TCPI与灾害损失程度、TCPI造成灾害的阈值等方面做进一步深入分析研究。

### 参考文献 (References)

[1] Chen Lianshou, Xu Xiangde, Luo Zhexian et al. Introduction to Tropical Cyclone Dynamics. Beijing: China Meteorological Press, 2002: 17-21. [陈联寿, 徐祥德, 罗哲贤 等. 热带气旋动力学引论. 北京: 气象出版社, 2002: 17-21.]

[2] Wu Rongsheng. Preface: Some problems of typhoon study. Journal of Nanjing University: Natural Sciences, 2007, 43(6): 567-571. [伍荣生. 前言: 台风研究中的一些科学问题. 南京大学学报: 自然科学, 2007, 43(6): 567-571.]

[3] Xu Shiyuan, Wang Jun, Shi Chun et al. Research of the natural disaster risk on coastal cities. Acta Geographica Sinica, 2006, 61(2): 127-138. [许世远, 王军, 石纯 等. 沿海城市自然灾害风险研究. 地理学报, 2006, 61(2): 127-138.]

[4] Fan Qi, Liang Biqi. The evaluation of disastrous losses caused by tropical cyclones. Acta Geographica Sinica, 2000, 55 (suppl.): 52-55. [樊琦, 梁必骐. 热带气旋灾情的预测及评估. 地理学报, 2000, 55(增刊): 52-55.]

[5] China Meteorological Administration. Yearbook of Meteorological Disaster in China (2005-2009). Beijing: China Meteorological Press, 2005-2009. [中国气象局. 中国气象灾害年鉴(2005-2009). 北京: 气象出版社, 2005-2009.]

[6] Chinese Standardization Administration Committee. Classification of tropical cyclones (GB/T19201-2006). Beijing: Standard Press of China, 2006. [中国标准化管理委员会. 热带气旋等级国家标准(GB/T 19201-2006). 北京: 中国标准出版社, 2006.]

[7] Gray W M. Summary of 1990 Atlantic tropical activity and seasonal forecast verification. Colorado State University, Department of Atmospheric Science. Paper issued on 28 November 1990, Fort Collins, Colorado, 29pp.

[8] Gray W M. Predicting Atlantic seasonal hurricane activity 6-11 months in advance. Wea. Forecasting, 1992, 7: 440-455.

[9] Bell G D, Halpert M S, Schnell R C et al. Climate assessment for 1999. Bull. Amer. Meteor. Soc., 2000, 81(6): S1-S50.

[10] Emanuel K. Increasing destructiveness of tropical cyclones over the past 30 years. Nature, 2005, 436(4): 686-688.

[11] Lei Xiaotu, Xu Ming. A review on the impacts of global warming on tropical cyclone activities. Acta Meteorologica



© 1994-2011 China Academic Journal Electronic Publishing House. All rights reserved. http://www.cnki.net

Sinica, 2009, 67(5): 679-688. [雷小途, 徐明. 全球变暖对台风活动影响的研究进展. 气象学报, 2009, 67(5): 679-688.]
[12] Li Ying, Chen Lianshou. Statistical characteristics of tropical cyclone making landfalls on China. Journal of Tropical Meteorology, 2004, 20(1): 14-23. [李英, 陈联寿. 登陆我国热带气旋的统计特征.热带气象学报, 2004, 20(1): 14-23.]
[13] Yang Yuhua, Ying Ming, Chen Baode. The climatic changes of landfall tropical cyclones in China over the past 58 years. Acta Meteorologica Sinica, 2009, 67(5): 689-696. [杨玉华, 应明, 陈葆德. 近58年来登陆中国热带气旋气候变化特征. 气象学报, 2009, 67(5): 689-696.]
[14] Wang Xiaoling, Wu Liguang, Ren Fumin et al. Influences of tropical cyclones on china during 1965-2004. Advances in Atmospheric Sciences, 2008, 25(3): 417-426.
[15] China Meteorological Administration. Yearbook of Tropical Cyclone (Typhoon) in China (1951-2009). Beijing: China Meteorological Press, 1951-2009. [中国气象局. 中国热带气旋(台风)年鉴(1951-2009). 北京: 气象出版社, 1951-2009.]
[16] Ren Fumin, Wang Yongmei, Wang Xiaoling et al. Estimating tropical cyclone precipitation from station observations. Advances in Atmospheric Sciences, 2007, 24(4): 700-711.
[17] Xiao Fengjin. Characteristics of tropical cyclones in China and their impacts analysis. Natural Hazards, 2010, 54: 827-837.
[18] Cao Chu, Peng Jiayi, Yu Jinhua. An analysis on the characteristics of landfalling typhoons in China under global climate warming. Journal of Nanjing Institute of Meteorology, 2006, 29(4): 455-461. [曹楚, 彭加毅, 余锦华.全球气候变化背景下登陆我国台风特征分析. 南京气象学院学报, 2006, 29(4): 455-461.]
[19] Hu Yamin, Song Lili, Liu Aijun et al. Analysis of the climatic features of landfall tropical cyclones in China during the past 58 years. Acta Scientiarum Naturalium Universitatis Sunyatseni, 2008, 47(5): 115-121. [胡雅敏, 宋丽莉, 刘爱君 等. 近58年登陆我国热带气旋的气候特征分析. 中山大学学报, 2008, 47(5): 115-121.]
[20] Chen Lifang. Numerical simulation and comparative analysis of typhoons talim and saomei. Meteorological Science and Technology, 2008, 36(3): 262-267. [陈丽芳. 相似台风泰利和桑美的数值模拟和对比分析. 气象科技, 2008, 36(3): 262-267.]

# Study on Tropical Cyclone Potential Impact Index in China

YIN Yizhou[1, 2], XIAO Fengjin[1], LUO Yong[1], ZHAO Shanshan[1]
(1. *National Climate Center*, *CMA*, *Beijing* 100081, *China*;
2. *Institute of Atmospheric Physics*, *CAS*, *Beijing* 100029, *China*)

**Abstract:** Based on tropical cyclone traces and disasters information, considering the tropical cyclone frequency, intensity, scope and duration, the study established the Tropical Cyclone Potential Impact Index (TCPI). It also analyzed the spatial pattern and interannual variations of TCPI for China during 1949-2009. As an example, the Super Typhoon "Saomai" (No.0608) was selected to analyze the relationship between TCPI and the direct economic losses, total rainfall, and maximum wind speed. The research had the following results: China's TCPI presented a weak decreasing trend during 1949-2009 and this trend was not significant, but in different phases the decreasing or increasing trend was more significant. The tropical cyclones potential impact decreased in coastal provinces of southern China such as Hainan, Guangdong and Guangxi while it increased in southeastern coastal provinces such as Zhejiang, Fujian and Taiwan in recent 20 years. Highest TCPI is mainly observed in Taiwan, Hainan, Guangdong coast, Fujian coast and southern Zhejiang coast. TCPI has good correlation with the direct economic losses, rainfall and maximum wind speed, and the correlation is significant at the 0.01 level.

**Key words:** tropical cyclone; potential impact index; Saomai; China; Northwest Pacific



© 1994-2011 China Academic Journal Electronic Publishing House. All rights reserved. http://www.cnki.net

云南大学学报（自然科学版），2011，33（2）：172～178　　CN 53－1045/N　ISSN 0258－7971
Journal of Yunnan University　　http://www.yndxxb.ynu.edu.cn

# 2008年“2.28”低纬高原强对流成因诊断与数值模拟*

尤　红[1,2]，肖子牛[3]，艾永智[1]
（1.云南省玉溪市气象局，云南 玉溪　653100；2.云南大学 大气科学系，云南 昆明　650091；
3.中国气象局 国家气候中心，北京　100081）

**摘要：**利用常规观测、NCEP1°×1°再分析资料和中尺度WRF模式，对低纬高原云南2008年“2.28”强对流进行成因诊断和数值模拟研究，结果表明：此次复杂强对流在春季低温冷冻灾害和位势稳定背景下，由强垂直风切变、低层潮湿和足够水汽供应以及强抬升机制共同作用造成.过程中，强对流由强斜压不稳定释放诱发在低层湿舌附近；冰雹、雷雪上空－20 ℃温度层在450 hPa层上少动，0～－20 ℃温度梯度是冰雹大于雷雪的；降雹的饱和水汽团高度比雷雪高；垂直干位涡反映了对流层高层强位涡高值的强干冷西北气流向低层、低纬传送和中低层小位涡西南暖湿急流交汇特征.WRF模拟结果佐证了位势稳定条件下存在强垂直风切变会发生剧烈对流的事实，水平风、抬升凝结高度和最大对流有效位能等可为判断云南有无强对流及其种类提供参考依据.

**关键词：**强对流天气；冰雹；雷雪；垂直风切变；对流有效位能；抬升凝结高度；数值模拟
**中图分类号：**P 425　　**文献标识码：**A　　**文章编号：**0258－7971(2011)02－0172－07

2008年2月27日夜间至29日凌晨，云南大部交替出现强雷暴局地强冰雹和雷雪复杂强对流天气，其中北部、东部有强降温和降雪.为云南有气象观测以来所罕见.雷电、大风和冰雹等是云南最常见气象灾害，这些空间尺度小、生命期短、对流强烈的气象灾害发生时，常常会造成重大人员伤亡和重大经济损失.对于雷暴、雹暴等强对流天气的研究和模拟，已有许多气象工作者进行了探讨[1-5]，对出现概率极少的雷雪天气，以前研究少且侧重环流背景和物理机制[6-7]方面.目前云南学者许美玲[8]、尤红[9]等的数值模拟研究多是基于云南暴雨的，段旭等[10]应用湿位涡理论对云南冰雹做了诊断分析，郭荣芬等[11]利用加密自动站、雷达等多种探测资料综合分析了2008年“2.28”云南罕见“雷打雪”过程中雷达回波和地面温、压、湿的中尺度特征，而用WRF对云南冰雹、雷暴等强对流过程同时进行模拟和成因诊断未见报道.本文利用常规观测、NCEP1°×1°再分析资料和WRFV3.0.1诊断、模拟2008年2月28日云南强对流过程，深入探讨其成因和WRF模拟能力，丰富预报员对此类复杂天气的认识.

## 1　大环流形势影响背景

“2.28”强对流过程开始前500 hPa上（图略）N－S向南支低槽在85°E附近，中高纬95°E有N－S向北支西风槽，其后有强冷温度槽，温度槽后等温线与西风槽后等高线交角近90°；强对流天气期间，强冷平流作用致使南支低槽和北支西风槽经向度增大，两槽线转为NE－SW向并连为一体，槽后盛行携有强冷平流的14 m·s$^{-1}$以上西北风，云南上空为南支槽前20 m·s$^{-1}$以上的西偏南暖湿急流控制；700 hPa上93°E附近有南支槽，云贵高原处于槽前12 m·s$^{-1}$以上低空西南急流区中，高层强冷平流推动作用下川滇切变增强、南移到重庆、西昌至巴塘一线，西昌有低涡中心.700 hPa低涡切变、地面西路冷空气南下和500 hPa低槽东南移诱发“2.28”复杂强对流过程.

## 2　“2.28”冰雹、雷雪强对流成因

### 2.1　强垂直风切变特征　垂直风切变增强有利于

* 收稿日期：2010－03－15
基金项目：国家重点基础研究发展规划项目（2009CB421504）资助；国家自然科学基金资助项目（40975032）.
作者简介：尤　红（1971－），女，云南人，硕士，高级工程师，主要从事短期天气预报和预测方法研究.E－mail：youhyn71@sina.com.



© 1994-2011 China Academic Journal Electronic Publishing House. All rights reserved.　http://www.cnki.net

上升、下沉气流在相当长的时间内共存，在造成上升气流倾斜的同时增强中层干冷空气的吸入，使得对流风暴进一步加强和发展[12]. 分析昆明雷雪(图 1a)和玉溪冰雹上空(图 1b)水平风时间高度剖面发现，27～29 日两站自低层到高层均为西南或西偏南风，28 日 20:00～29 日 02:00 昆明雷雪间，地面有冷空气南下影响昆明，700 hPa 以下低层的风向出现逆时针旋转为东南风，而 700 hPa 以上层仍为西南气流，表明低层存在较大的风向曲率和利于加强风暴旋转潜势的垂直风切变，到 29 日 02:00 昆明近地层转为偏北气流控制这直接导致 03:00 时后天气迅速转晴. 28 日 08:00 玉溪降雹前不仅低层风向曲率增大且对流层高层西南风风速迅速增大，这种水平风垂直分布使得低层暖湿气流源源不断地输送到发展中的上升气流中并加强移过风暴的旋转，是有利于组织完好对流风暴发展的强垂直风切变的典型分布[12]，28 日 14:00 后玉溪上空中高层偏南风分量减小、逐渐转为偏西风，天气也相应好转，可见冰雹是发生在中低层西南急流影响区中且存在强垂直风切变环境.

**2.2　不稳定特征**　过程中昆明探空站 $T-\ln p$ 图(图略)上，$E_k$ 为负稳定能量，大气呈对流性稳定状态即低层有冷空气活动和垂直方向上对流受到抑制. 过程中 800 hPa $\theta_{se}$ 沿 24°N 的时间变化图 2a 上，槽前西南暖湿急流高能区和冷高控制的低能气团间的 $\theta_{se}$ 等值线密集区(能量锋)一直在 102°～103°E 间少动，过程中冰雹、雷雪发生在能量锋附近.

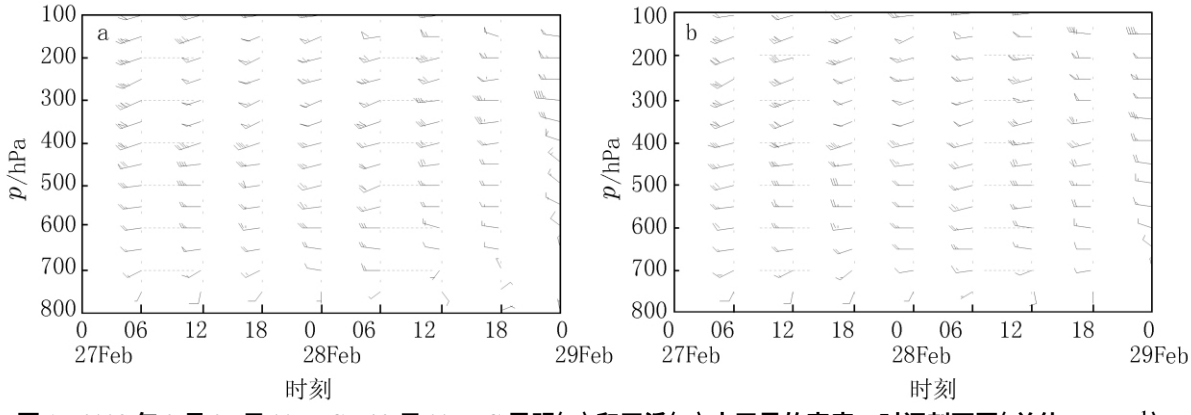


**图 1　2008 年 2 月 27 日 00UTC～29 日 00UTC 昆明(a)和玉溪(b)水平风的高度－时间剖面图(单位: m·s$^{-1}$)**

Fig. 1 The time－height cross－section of wind field over Kunming(a) and Yuxi(b) (unit: m·s$^{-1}$) from 27 to 29 February 2008

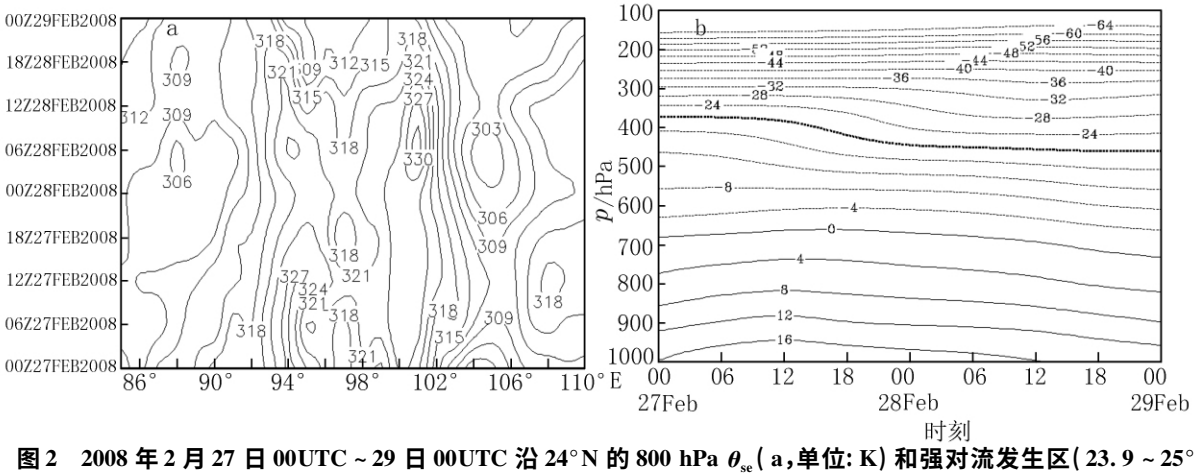


**图 2　2008 年 2 月 27 日 00UTC～29 日 00UTC 沿 24°N 的 800 hPa $\theta_{se}$(a，单位: K)和强对流发生区(23.9～25°N、101.9～103°E)平均温度(b，单位℃)的时间高度剖面**

Fig. 2 The $\theta_{se}$ on 800 hPa along 24°N(a，unit: K) and the time－height cross－section of temperature above the severe convection area(b，unit: ℃) from 00UTC February 27 to 00UTC February 29，2008



© 1994-2011 China Academic Journal Electronic Publishing House. All rights reserved.　http://www.cnki.net

前人研究认为，-20℃温度层高度在400 hPa等压面高度附近或以下时有利于成雹[13]. 分析过程中冰雹、雷雪强对流发生区(23.9°~25°N，101.9°~103°E，下同)平均温度的时间变化图2b发现，28日00:00前-20℃温度层高度在400~350 hPa间，之后迅速下降到400 hPa层下并一直维持在450 hPa层上少动. 表明了本区域处于强不稳定区，有产生冰雹对流天气可能，冰雹发生时段相应0℃线在675 hPa，而雷雪时0℃线下降到725 hPa，0℃层到-20℃层温度梯度是冰雹大于雷雪的.

**2.3 潮湿环境和强水汽输送特征** 这次特殊强对流天气与潮湿环境场和充足水汽供应密切相关. 过程中比湿沿25°N的时间垂直剖面图上(图略)，100°~103°E间的近地层为9~12×$10^{-3}$ g/g比湿大值区并向上层伸展形成一个明显的湿舌，该湿舌向东移动时，其上部逐渐向东北方向倾斜，28日08:00和20:00湿舌在102°~103°E间活动，滇中正是处于湿舌线附近.

雷雪发生地昆明相对湿度变化(图3a)充分反映出了地面冷锋和中低空的西南急流的活动特征，27日20:00开始中低空的西南暖湿急流影响强对流发生区域，昆明站相对湿度迅速增大于28日02:00接近饱和，80%线伸展到400 hPa层附近，分别在450，600，750 hPa层附近有饱和中心；之后到16:00对流层中层出现小的相对湿度区；20:00冷空气自东向西入侵，昆明一带地面东北风达6~8 m·$s^{-1}$，600 hPa以下层相对湿度再次于28日20:00~29日02:00间在700 hPa出现大饱和中心，昆明上空的0℃线从720 hPa下降到800 hPa层，期间近地层饱和水汽和东移的湿舌在锋面动力抬升作用下以及近地层0℃气温，为昆明雷雪强对流天气产生创造了有利条件. 而冰雹发生地玉溪(图3b)相对湿度表现是28日02:00~12:00间中低层为水汽大值，冰雹发生时段中，600 hPa层附近为饱和中心，400~550 hPa层间有相对湿度小值向下层入侵，出现相对湿度梯度大值区，即冰雹是由低槽前干、湿气流交汇引发的. 这与前面垂直风切变环境分析结论一致. 相应强对流区800 hPa附近有最强的小于-30×$10^{-6}$ g·$cm^{-2}$·$hPa^{-1}$·$s^{-1}$水汽辐合中心，中低层西太平洋到孟加拉湾南部到云南为大水汽通量带，强对流过程中低层存在大水汽输送和强水汽辐合，西太平洋和孟加拉湾为此次强对流过程的水汽源地.

**2.4 抬升条件**

2.4.1 垂直螺旋度特征 分析强对流区域平均垂直螺旋度时间剖面图4可见：27日20:00~28日12:00强雷暴、冰雹发生时段，650~400 hPa的对流层中层间为强负螺旋度区，550 hPa上有小于-1.8×$10^{-6}$ Pa·$s^{-2}$的强负中心，相应对流层上层和800~650 hPa间分别为2个弱正值区，垂直区间较小的对流层中低层800~400 hPa间为低正上负配置，下正值远小于上负值中心即旋转与沿旋转轴方向运动剧烈造成强冰雹、雷暴天气；之后低层正值增大并向中高层伸展，对流层中层的强负区减弱消失，28日14:00后800~250 hPa间全部转为

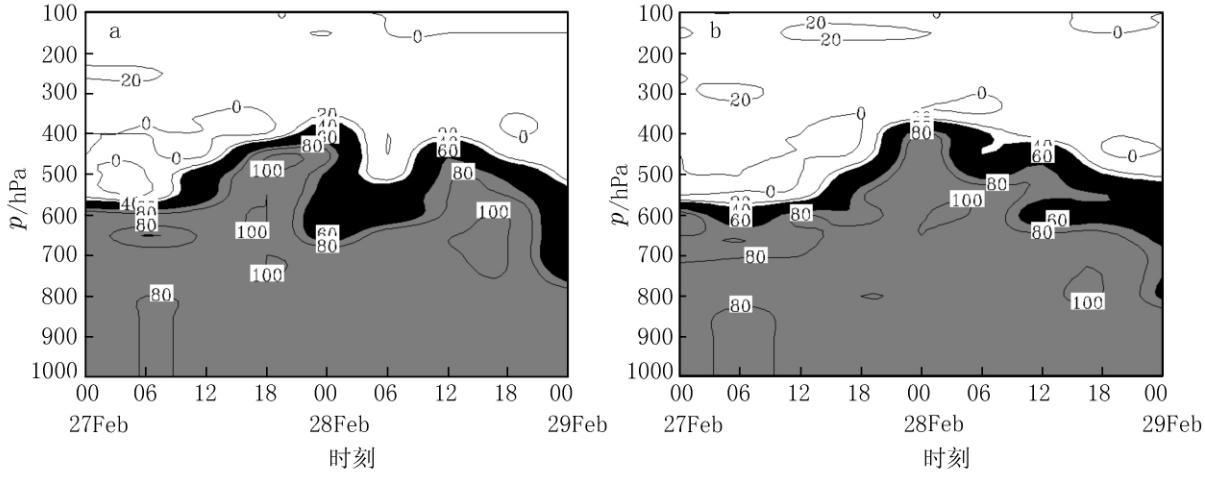


**图3 2008年2月27日00UTC~29日00UTC昆明(a)和玉溪(b)相对湿度时间-垂直剖面(单位：%)**

Fig. 3 The time-height cross-section of Kunming(a) and Yuxi(b) relative humidity(unit: %) from 00UTC February 27 to 00UTC February 29, 2008



© 1994-2011 China Academic Journal Electronic Publishing House. All rights reserved. http://www.cnki.net

正螺旋度控制区，对流层高层为弱负值区，700 hPa 和 450 hPa 上分别有 2 个强正值中心，在低层正值中心迅速增大和向上层伸展期间，昆明市出现罕见雷雪天气. 对应弱垂直上升运动首先出现在 400 hPa 层以下，27 日 20:00 ~ 28 日 08:00 间中低层的垂直速度迅速增强并向高层伸展到 250 hPa，$-0.7$ Pa · $s^{-1}$最强上升中心在 600 hPa 上，之后垂直速度缓慢减弱，表明影响系统活动为此次强对流过程提供了强的动力抬升机制.

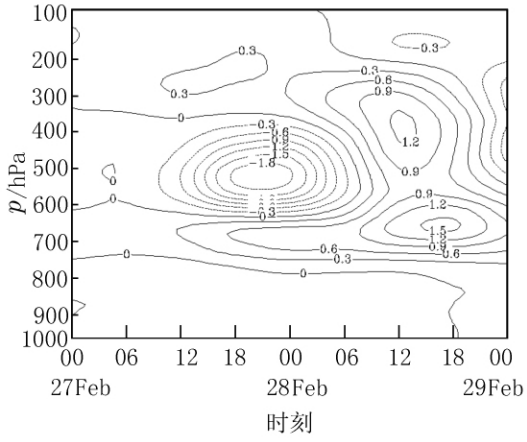


**图 4　2008 年 2 月 28 日雷雪、冰雹区域的平均垂直螺旋度(单位: $10^{-6}$Pa · $s^{-2}$) 的时间 - 垂直剖面**

Fig. 4 The time - height cross - section of average vertical helicity (unit: $10^{-6}$hPa · $s^{-2}$) in the thunderstorm snow and hailstorm field on 28 February 2008

2.4.2　**干位涡垂直分布特征**　沿 102.5°E 的干位涡垂直剖面图(图 5) 上可见: 过程前北部的 27° ~ 32°N 间的对流高层为强位涡高值区，强对流区上空 500 hPa 以上层为 5 ~ 15 × $10^{-1}$ PVU 的位涡相对小值区，700 ~ 500 hPa 间为小负位涡中心; 强对流发生期间，中高纬对流层高层强高位涡中心向低纬、低层输送，强对流区整层位涡值迅速增大到 5 ~ 30 × $10^{-1}$ PVU，大增值幅度在 400 hPa 以上层. 以上变化表征了对流层高层到低层的气流活动特征，强位涡高值中心对应的对流层高层强干冷西北气流向低层和低纬传送，和中低层小位涡的西南暖湿急流交汇导致了此次冷环境下的罕见强对流过程.

## 3　数值模拟和分析

**3.1　数值模拟方案设计**　用 WRFV3.0.1 版本采用 3 重双向嵌套方案模拟此次过程，第 1 重水平分辨率 90 km，格点数为 70 × 60，覆盖了 5° ~ 50°N，60° ~ 140°E 区域; 第 2 重水平分辨率 30 km，格点数为 61 × 61，覆盖了 18° ~ 33°N，94 ~ 114°E 区域; 第 3 重水平分辨率 10 km，格点数为 97 × 97，覆盖了 20° ~ 30°N，97° ~ 107°E 的“2.28”强对流天气发生区. 第 1 重采用 Thompson 微物理过程方案、Betts - Willer - Janjic 积云参数化方案; 第 2 重采用 Thompson 微物理过程方案、Kain - Fritsch (new Eta) 积云参数化方案; 第 3 重采用 WSN 6 - class graupel 微物理过程方案、Grell - Devenyi ensemble 积云参数化方案. 其余的辐射、近地面和边界层均采用: Rrtm 长波辐射方案、Dudhia 短波辐射方案、Monin - Obukhov 地面层物理过程方案、Thermal diffusion 陆面参数过程和 YSU 边界层方案. 初始场选取 NCEP 1° × 1°再分析资料，起始时间 2008 年 2 月 27 日 08 时，积分 48 h，3 重嵌套均是每隔 6 h 更换侧边界条件. 使用 RIP 和 ARWpost 软件对模式输出结果进行后处理. 由于此次强对流过程中冰雹和雷雪空间尺度小，以下重点分析第 3 重水平分辨率 10 km 模拟结果来佐证其模拟能力.

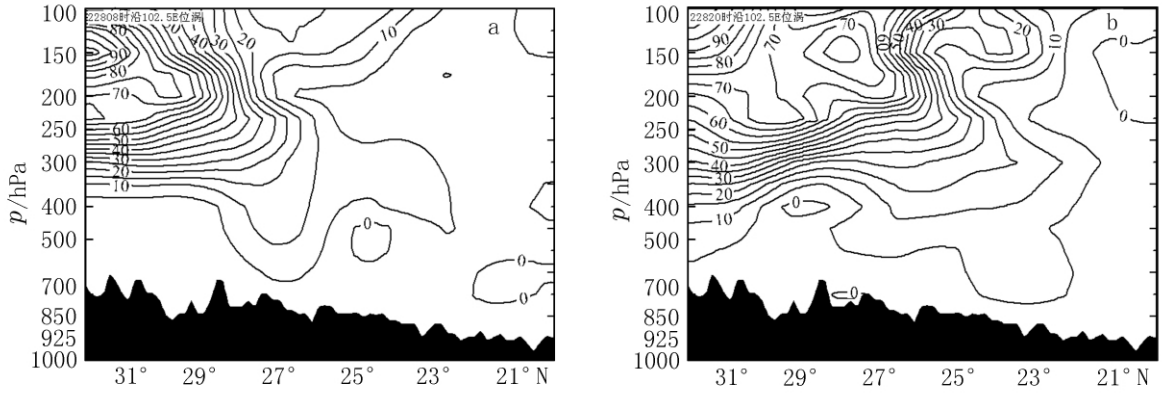


**图 5　2008 年 2 月 28 日 08:00(a)，20:00(b) 两个时次的沿 102.5°E 的位势涡度垂直剖面(单位: $10^{-1}$PVU)**

Fig. 5 The vertical cross sections of PV (unit: $10^{-1}$PVU) along 102.5°E at 08BJT(a) and 20BJT(b) February, 2008



© 1994-2011 China Academic Journal Electronic Publishing House. All rights reserved.　http://www.cnki.net

**3.2 垂直风场和抬升凝结高度模拟结果** 图6a,b是第3重每3 h强对流发生地玉溪和昆明的垂直风时间变化模拟结果. 图中可见过程中昆明、玉溪上空全部为西南气流区,风速随高度明显增大,低层风向曲率明显比对流层中高层大,这种水平风垂直分布特征预示未来环境风场有利于组织完好的对流风暴发展. 对比实况图1,表明该方案模拟出了强对流发生期间的强垂直风切变环境.

由两地抬升凝结高度随时间变化模拟结果图6c,d发现,强对流时段内两地抬升凝结高度处于相对偏低的高度,其中玉溪冰雹发生前6 h内先迅速抬升后降低,高度从玉溪站(海拔高度1 716.9 m)地面层以上1 500 m上升到2 400 m再下降到1 500 m,高度平均每小时变化幅度达到300 m;冰雹期间抬升凝结高度在1 500~1 600 m即在700 hPa层附近少动;而昆明雷雪开始前抬升凝结高度则先缓慢抬升后降低,高度从2 500 m下降到800 m用了近9 h,高度平均每小时变化幅度为189 m,昆明雷雪时抬升凝结高度相对更低在其地面以上1 100~1 400 m间,可见冰雹发生时其饱和水汽团所在高度比雷雪时高,水汽饱和中心所在位置高度变化幅度是冰雹比雷雪更剧烈. 对比实况图3发现模拟抬升凝结高度结果能较好地预示强对流上空饱和空气团所在位置和强对流天气类型.

**3.3 最大对流有效位能模拟结果** 从冰雹、雷雪发生地最大对流有效位能时间变化分布图7可见,2月28日08:00前玉溪和昆明上空的最大CAPE变化剧烈,时而迅速上升,时而迅速降低,期间地面实况是间歇性晴好天气和强雷暴;玉溪强冰雹发生期间有16 J·kg$^{-1}$的能量释放,这与实况上冰雹是发生在中低层西南暖湿急流影响时对应,而昆明雷雪期间几乎没有能量释放过程,表征了地面冷空气活动和位势稳定的实况. 过程中模拟结果虽没有强最大CAPE释放,但模拟出了强垂直风切变环境,强垂直风切变环境下动力效应可加强上升气流强度,强烈上升运动常常能够在较小的CAPE中得以

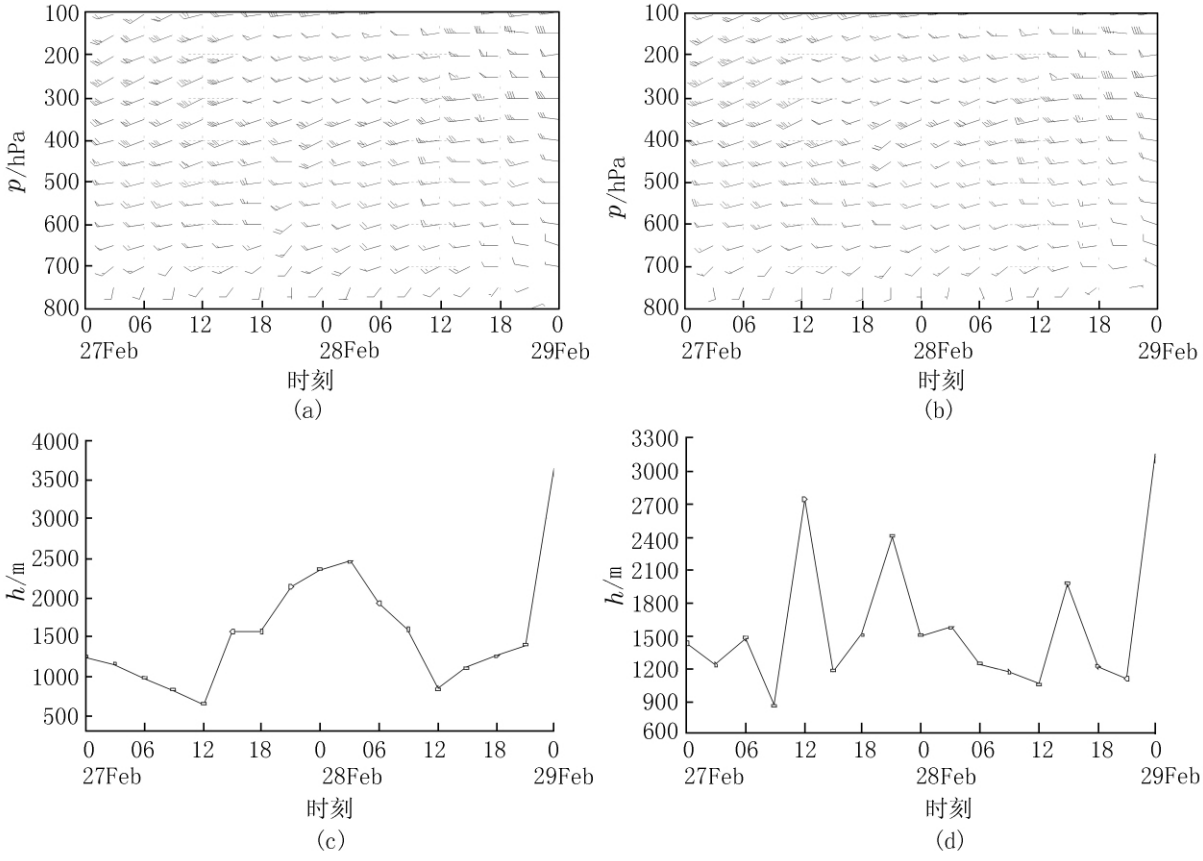


**图6 第3重嵌套模拟的水平风场(昆明a,玉溪b;单位:m·s$^{-1}$)和抬升凝结高度(昆明c,玉溪d;单位:meters AGL)的时间演变图**

Fig. 6 The time - height cross - section of horizontal wind (Kunming: a, Yuxi: b; unit: m·s$^{-1}$) and lifted condensation level (Kunming: c, Yuxi: d; unit: meters AGL) of the third doman



© 1994-2011 China Academic Journal Electronic Publishing House. All rights reserved. http://www.cnki.net

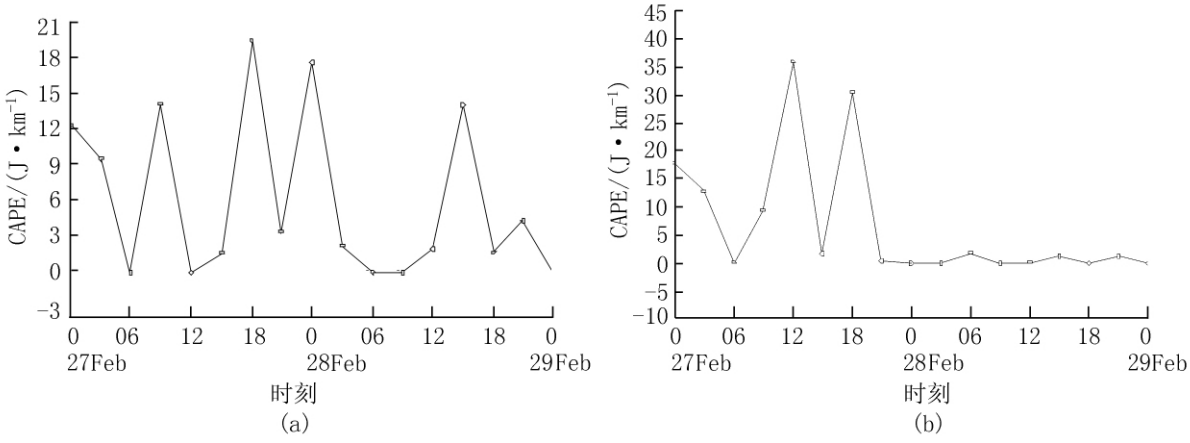


**图 7　第 3 重嵌套模拟的玉溪(a)和昆明站(b)的最大对流有效位能时间变化图(单位: J·kg$^{-1}$)**

Fig. 7 The time section of maximum convective available potential energy of Yuxi(a) and Kunming(b) (unit: J·kg$^{-1}$)

发展并产生强对流天气. 即 WRF 模拟结果佐证了此次强冰雹、雷雪过程是在小的最大 CAPE 和强垂直风切变环境下发生剧烈对流的事实.

## 4　小　结

对 2008 年“2.28”春季罕见冰雹、雷雪复杂强对流天气成因诊断和 WRF 数值模拟研究后,得到以下几点结论.

(1) “2.28”春季罕见冰雹、雷雪复杂强对流是由 500 hPa 南支槽与高原西风槽合并成的强 NE-SW 向低槽、700 hPa 上低涡切变、强西南低空急流和地面冷空气共同造成.

(2) 此次复杂强对流发生在强垂直风切变、低层潮湿和足够的水汽供应以及强抬升机制条件下. 强垂直风切变促使倾斜对流发展,使低空上升运动加强,不断输送水汽和不稳定能量. 锋面与急流相互作用促使强斜压不稳定强烈释放,导致罕见雷雪、冰雹天气. 强对流大多发生在低层湿舌附近,西太平洋和孟加拉湾是过程的水汽源地.

(3) 冰雹、雷雪发生地上空的 -20℃温度层高度在 450 hPa 层上少动,0℃层到 -20℃层的温度梯度是冰雹大于雷雪的,降雹时的饱和水汽团所在高度比雷雪的高. 该过程是 1 次典型的无对流有效位能条件支撑下,由强垂直风切变动力效应引发的局地强对流风暴个例.

(4) 过程中垂直干位涡表征了对流层高层位涡高中心的强干冷西北气流向低层和低纬传送,和中低层小位涡西南暖湿急流交汇的特征. 强冰雹发生期间,对流层中低层 800 ~ 400 hPa 间相对较小的垂直区间存在低正上负的经典垂直螺旋度配置.

(5) 文中 WRF 模拟方案输出的强垂直风切变环境和相对湿度饱和中心低层所在位置与实况分布基本一致,表征出冰雹发生地上空饱和水汽团高度比雷雪高,抬升凝结高度变化幅度冰雹更剧烈的特征. WRF 数值模拟佐证了位势稳定条件下存在强垂直风切变会发生剧烈对流的事实.

## 参考文献:

[1] 郭荣芬,鲁亚斌,高敏琪. 低涡引发的盛夏持续性暴雨机理及中尺度特征分析[J]. 云南大学学报: 自然科学版,2007,29(S2):434-441.

[2] 张腾飞,邓勇,谢屹然,等. “20060717”低纬高原强雷暴天气过程分析[J]. 云南大学学报: 自然科学版,2008,30(2):166-174.

[3] 罗娅,刘开宇,张云瑾. 一次强对流天气的诊断分析[J]. 云南大学学报: 自然科学版,2006,28(S1):189-193.

[4] 隋东,沈桐立,张涛. 沈阳地区一次冰雹天气过程形成机制的数值模拟[J]. 气象,2005,31(7):20-23.

[5] 朱莉,闵颖,许美玲,等. 低纬高原地区 2008 年“7.02”特大暴雨 M_βCS 结构特征的数值模拟分析[J]. 云南大学学报: 自然科学版,2009,31(S1):265-273.

[6] 王仁乔,宋清翠. “雷打雪”现象发生机制初探[J]. 气象,16(3):45-48.

[7] 丁栋生,李树林. 一次“雷打雪”天气的初步分析[J]. 气象,19(4):52-53.

[8] 许美玲,段旭,张腾飞,等. 低纬高原地区一次罕见大暴雨的中尺度数值模拟[J]. 高原气象,2006,25(2):268-276.

[9] 尤红,肖子牛,王曼,等. 2008 年“7.02”滇中大暴雨的



© 1994-2011 China Academic Journal Electronic Publishing House. All rights reserved.　http://www.cnki.net

成因诊断和数值模拟[J].气象,2010,36(1):7-16.
[10] 段旭,李英,周毅.春季滇南大风冰雹天气的大尺度环境特征[J].气象,2002,24(6):39-43.
[11] 郭荣芬,鲁亚斌、高安生,等,低纬高原罕见"雷打雪"中尺度特征分析[J].气象,2009,35(2):49-56.
[12] 俞小鼎,姚秀萍,熊廷南,等.多普勒天气雷达原理与业务应用[M].北京:气象出版社,2005:90-169.
[13] 刘贵萍.两次强对流天气过程的对比分析[J].四川气象,2001(4):12.

# Diagnotistic analysis and numerical simulation of severe convection on February 28, 2008 in low - latitude plateau

YOU Hong[1,2], XIAO Zi-niu[3], AI Yong-zi[1]
(1. Department of Atmosphereic Science, Yunnan University, Kunming 650091, China;
2. Meteorological Abservatory of Yuxi, Yuxi 653100, China;
3. National Climate Center, China Meteorological Administration, Beijing 100081, China)

**Abstract:** Using the convention observed data, the NCEP1°×1° grid point material, the mesoscale numerical model WRF, the severe convection in low - latitude plateau on February 28, 2008 has been diagnotistic analysed and numerical simulated. The result shows that the severe convection, which occurred under the Spring low temperature, freezing calamity and potential stability condition, cause include strong vertical wind shear, wet low level, adequate vapor served and severe lift movement. In this extremely convection process, severe convection result in the rapid release of strong absolute baroclinic instability, which happen about the wet lingua of low level. The negative twenty degree celsius layer over hailstorm, thunderstorm snow region on 450 hPa level, the temperature gradient between zero and negative twenty degree celsius of hailstorm is bigger than the thunderstorm snow's, the saturated vapor location of hailstorm is higher. Vertical dry potential vorticity (PV) takes on the characteristic of the upper troposphere high PV of strong dry and cold northwest air tends downwards to the low - level and low - latitude, which join with the worm, wet southwest jet on middle and low - level. The WRF simulation scheme in the test has good simulated capability, the case that strong vertical wind shear can cause sever convection under potential stability condition are well validated, the simulation results by WRF meso - scale numerical model such as horizontal wind, lifted condensation level and max convective available potential energy can well indicate the occurrence and kind of strong convection in Yunnan.

**Key words:** severe convection; hailstorm; thunderstorm snow; vertical wind shear; convective available potential energy; lifted condensation level; numerical simulation



© 1994-2011 China Academic Journal Electronic Publishing House. All rights reserved. http://www.cnki.net

# 中国旱涝格局演变（1961－2050 年）及其对水资源的影响

翟建青[1]，曾小凡[2]，姜　彤[1]

（1．中国气象局国家气候中心，气候变化中心，北京 100081；2．华中科技大学 水电学院，武汉 430074）

摘　要：利用中国气象局提供的 483 个气象站 1961－2000 年月降水数据以及 ECHAM5/MPI-OM 气候模式输出的 1961－2050 年月降水数据，分别计算其月 SPI 值，分析中国过去 40 年来及未来 3 种排放情景（A2：温室气体高排放情景；A1B：温室气体中排放情景；B1：温室气体低排放情景）下旱涝格局的演变；同时分析了 8 个水文站径流变化百分率与对应流域 SPI 平均值的相关关系。结果显示：过去 40 年来中国有一条由东北向西南延伸的干旱趋势带，A2 情景下，这条干旱带将持续存在，A1B 情景下，贯穿中国中部及南部沿海区域呈湿润化趋势，B1 情景下，中国东部将出现“北涝南旱”的旱涝格局。研究认为：SPI 指数与径流量变化百分率有较好的相关关系，可以对中国未来水资源的研究提供一定的参考。

关键词：ECHAM5/MPI-OM；SPI 旱涝指数；旱涝格局；未来情景

中图分类号：P467　　文献标识码：A　　文章编号：1001-5221(2011)03-0237-06

伴随着人口的增长和经济的发展，水资源越来越成为制约全球经济和社会发展的主要因素。中国是水资源相对短缺的国家，人均水资源占有量只有世界人均水平的 1/4，而且由于水资源时空分布不均，经济社会高速发展及水环境恶化，中国水资源短缺的矛盾十分突出[1]。气候变化及其对水资源的影响已引起国内学者和有关部门的高度重视[2]。已有研究表明：在过去的 100 年，中国大陆地区的平均温度呈明显上升趋势，降水变化的空间特征比较明显[3]。气温和降水的变化必将影响到旱涝事件,我国学者对此进行了许多相关研究：马柱国等利用 1951－2006 年中国区域 160 个站的月降水及月平均气温资料,对中国区域近 56 年来区域干旱化特征进行了研究[4]；翟盘茂等的研究表明，1951－2003 年，中国干旱化面积总体上趋于增加，但趋势不显著，区域差异比较大，并且分析得出降水量是我国干旱变化的最主要因素[5]。

本文利用已有的月降水观测数据及 ECHAM5 全球气候模式输出的未来 3 种排放情景下月降水数据，对比分析了 1961－2000 年及 2001－2050 年中国旱涝格局的演变及旱涝指数与径流量变化的相关关系，以期为中国水资源的管理利用和研究提供一定的参考。

## 1　数据和方法

### 1.1　数据来源

研究从全国气象站中选取了 483 个气象站的月降水数据（1961-01－2000-12），这主要是考虑到数据时间序列的一致性，并对所选气象站的实测数据进行了均一性检验，气象站点位置如图 1 所示。

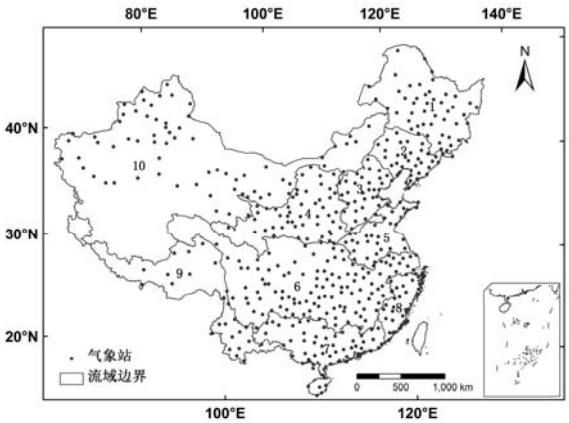


1．松花江流域；2．辽河流域；3．海河流域；4．黄河流域；5．淮河流域；6．长江流域；7．珠江流域；8．东南诸河流域；9．西南诸河流域；10．西北内陆河流域

图 1　中国十大流域及气象站示意图

Fig.1　Ten large river basins and meteorological stations in China

收稿日期：2010-11-18；修订日期：2011-02-22

基金项目：国家自然科学基金项目（NSFC 41001021）；山东省水资源与水环境重点实验室开放基金项目（WRISD0901）

作者简介：翟建青（1980－），男，山西省祁县人，博士后，主要从事气候变化与旱涝灾害研究，（E-mail）zhaijianqing1980@gmail.com。

未来情景研究则采用德国马普气象研究所提供的大气海洋环流模式（ECHAM5/MPI-OM）输出的降水量月数据（1961-01－2050-12）。

ECHAM5/MPI-OM模式同时耦合海冰和陆面过程模式，采用较高的模式分辨率对地球系统的未来气候进行预测，其中大气模式采用T63 的网格，水平网格分辨率为 1.875°×1.875°，垂直分 31 层。新模式更新了可预报的气溶胶模块，对云覆盖重新进行了参数化过程，同时对云里面的冰和水进行了不同的过程处理，大大提高了对降水过程的模拟[6]。中国水利部水文局提供了八大流域 8 个水文站的年径流数据（表 1）。

表 1 流域及水文站信息

Tab.1 Information of river basins and hydrologic stations

| 流域名称 | 流域面积/$10^4$km$^2$ | 水文站名称 | 水文站集水面积/$10^4$km$^2$ |
|---|---|---|---|
| 松花江流域 | 93.48 | 佳木斯 | 52.8 |
| 辽河流域 | 31.42 | 铁岭 | 12.1 |
| 海河流域 | 32.01 | 雁翅 | 4.4 |
| 黄河流域 | 79.51 | 花园口 | 73 |
| 淮河流域 | 33 | 吴家渡 | 12.1 |
| 长江流域 | 180 | 大通 | 170.5 |
| 珠江流域 | 57.9 | 高要 | 35.2 |
| 东南诸河流域 | 24.46 | 竹岐 | 5.5 |

### 1.2 研究方法

由于干旱成因及其影响的复杂性，很难找到一种普遍适用各种用途的干旱指数，因此应用于不同需求的各种干旱指数得到了发展[7]。本文主要采用McKee等发展的标准降水指数（SPI），该指数的优点是计算简单，可反映不同时间尺度的干旱[8]，详细计算方法见参考文献[8-9]。SPI通过计算给定时间尺度的累积概率，能够在多个时间尺度上进行计算，从而不仅可以监测短期的水分变化，也可以监测长期的水分动态，SPI各级旱涝指标见表 2[9]。本文计算的SPI时间尺度为 12 个月。

表 2 SPI 指数旱涝等级

Tab. 2 Classification of drought based on SPI

| 旱涝等级 | SPI 指数值 | 旱涝等级 | SPI 指数值 |
|---|---|---|---|
| 极端旱 | ≤-2.0 | 中等涝 | 1.0~1.49 |
| 严重旱 | -1.99~-1.5 | 极端涝 | 1.5~1.99 |
| 中等旱 | -1.49~-1.0 | 严重涝 | ≥2.0 |
| 正常 | -0.99~0.99 | | |

根据观测和 ECHAM5 模式输出的月降水数据计算其月 SPI 指数值，利用线性倾向率计算其变化趋势，并分析了 8 个水文站径流量变化百分率与水文站汇水区平均 SPI 指数的相关关系。旱涝格局空间图采用反距离加权插值法（Inverse Distance Weighted，简称 IDW）插值成图。径流量变化百分率（$A$）计算公式如下：

$$A=\frac{x_i-\overline{x}}{\overline{x}} \tag{1}$$

式中，$x_i$为第$i$年径流量，$\overline{x}$ 为多年平均径流量。

## 2 模型验证

通过对比实验期（1961－2000 年）ECHAM5 模式与 483 站同期观测年降雨量空间分布格局，验证模型对中国降雨量空间分布特征的模拟能力，结果如图 2。

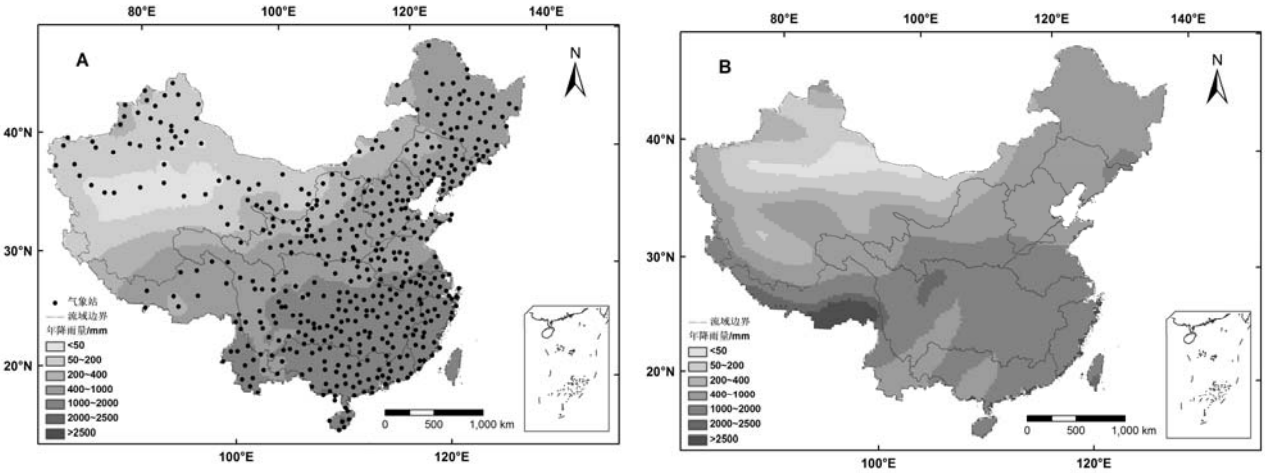


图 2 年降雨量空间分布图（A. 气象站观测值；B. ECHAM5 模拟值）

Fig.2 Spatial distribution of annual precipitation in China（A. observed data；B. simulated data）

由图 2 可知，ECHAM5 模式较好地反映了中国年降雨量由东南向西北逐渐减少的空间分布特征；

但各等级降雨量空间区域分布范围有一定差别，如年降水量低于 50 mm的区域不同；此外，ECHAM5 模式模拟的最大降雨量位于中国西南地区，与观测事实不符。这可能是由于该模式过高地估计了陡峭山坡一线的降水以及亚洲夏季风所导致的降水[10]。

将中国年平均降雨量与ECHAM5模式模拟值进行比较（图 3），可以看出：ECHAM5 模式模拟的中国年平均降水量变化同实测值有一定的相似性，特别是在 1980 年以后趋势更趋一致。这种变化的原因可能是由于在 1979－1980 年，北半球的大气和海洋环流经历了一次较明显的突变，而ECHAM5 模式对东亚夏季风降水变化的主要动力和热力学机制把握不够造成的[11]。

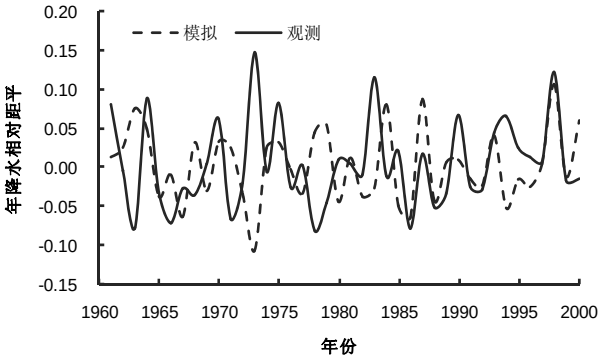


图 3　中国降水量变化（相对于 1961－1990 年）

Fig.3　Precipitation change in China during 1960-2000（Compared with averaged during 1961-1990）

可见，ECHAM5 全球气候海洋耦合模式对中国降雨量的模拟虽存在一定的不足,但仍具有一定的模拟能力。

## 3　旱涝格局趋势演变及其对水资源的影响

### 3.1　旱涝格局趋势演变

在计算 483 个气象站 1961－2000 年月 SPI 指数的基础上,计算每个站点月 SPI 指数的线性趋势,并插值成图(图 4-a)；同样地,在对 ECHAM5 模式提供的 3 种情景下 2001－2050 年格点月降水量计算 SPI 指数的基础上，得出每个格点月 SPI 指数的线性趋势，插值得到 SPI 指数趋势空间分布图(图 4-b、c、d)。趋势负值代表趋于干旱，正值表示趋于湿润。

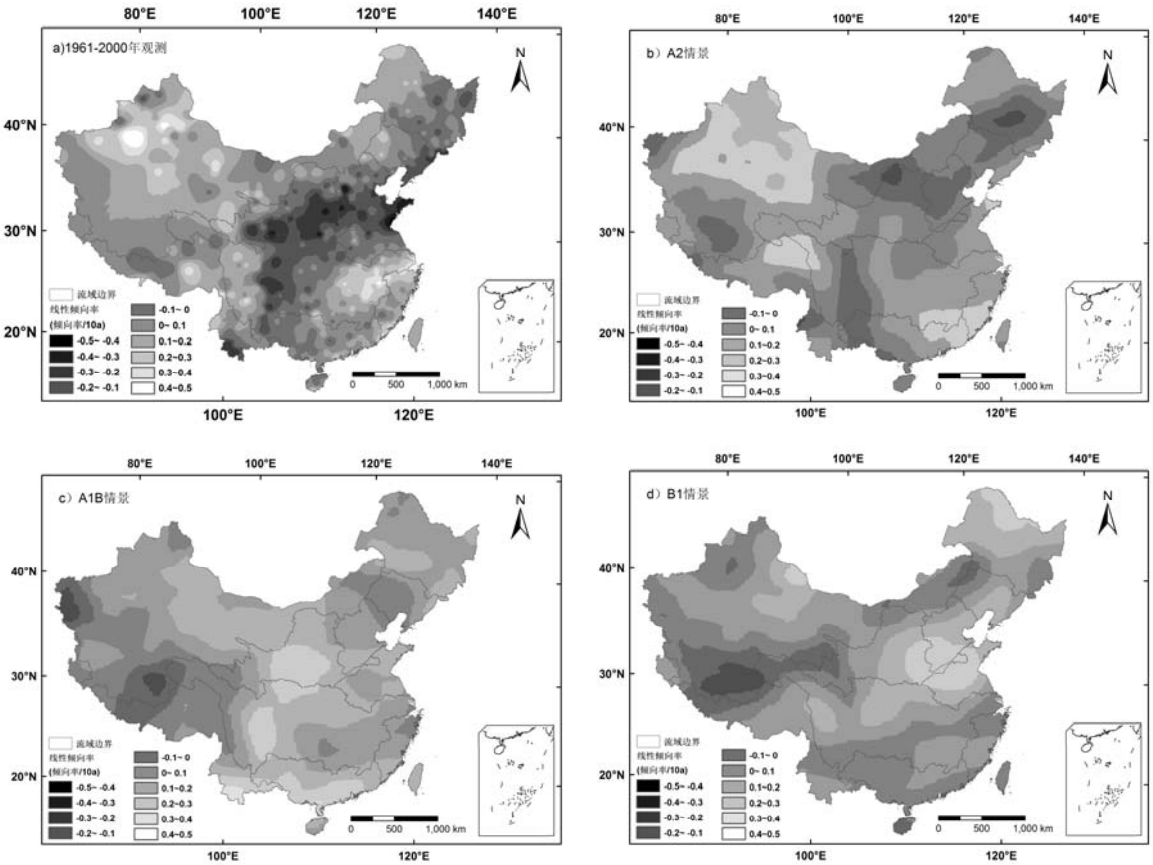


图 4　1961－2000 年观测到旱涝趋势及模式模拟 2001－2050 年 3 种情景下旱涝趋势

Fig.4　Trend of drought and flood observation during 1961-2000 and three scenarios from 2001 to 2050

由图 4-a可知，1961－2000 年中国存在一条由东北向西南方向的干旱趋势带，包括松花江、辽河、海河和黄河流域的南部，淮河流域北部，通过长江流域中部到达珠江流域西部；西北诸河流域的西北部及长江流域中下游则趋于湿润。这同施雅风等关于我国西北由暖干向暖湿转变的研究结果一致[12]。

由图 4-b 可知，A2 情景下，2001－2050 年中国也存在一条由东北向西南方向过渡的干旱带，主要包括松花江流域南部、辽河流域大部、海河流域及黄河流域北部，并穿过长江流域中部到达珠江流域；而中国西北及长江流域的鄱阳湖流域及东南诸河流域则趋于湿润。

由图 4-c 可知，A1B 情景下，湿润化区域集中于中国中部地区，主要包括黄河流域南部，穿过长江流域中部接南部沿海。

由图 4-d 可知，B1 情景下，松花江流域北部，辽河、海河流域南部，黄河流域东部及淮河流域北部出现湿润化趋势；出现了“北涝南旱”的空间格局。

### 3.2 干旱指数与水资源

截取水文站集水面积内格点并计算其平均 SPI 指数，与对应水文站年径流量变化百分率作比较，结果如图 5。张建云等对我国十大河流的径流量研

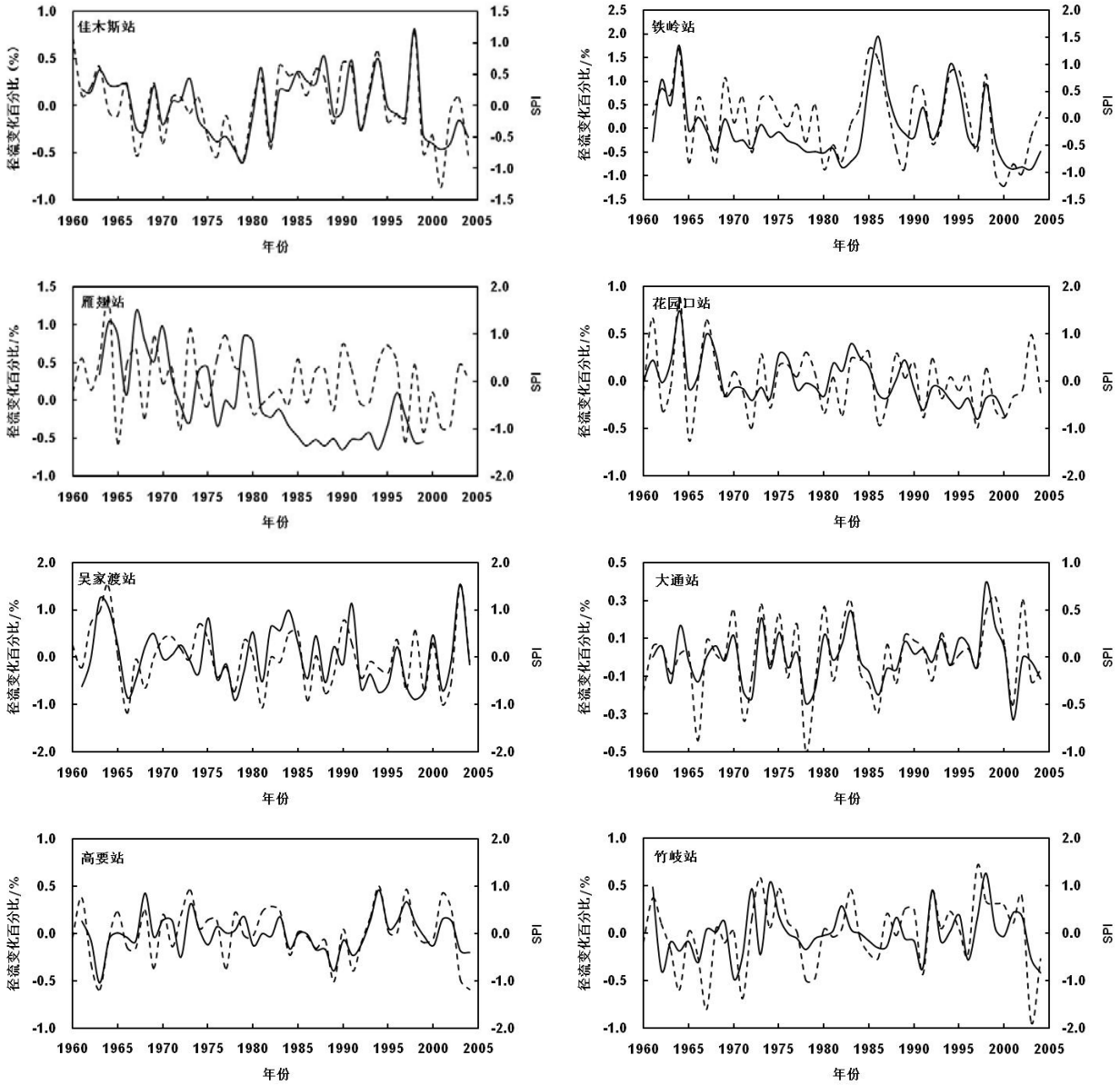


图 5 径流变化百分率（实线）同流域平均 SPI（虚线）关系

Fig.5 Relations between percentage of runoff variation (solid line) and averaged SPI (dotted line)

究表明：近 50 年中国主要江河的实测径流量均呈下降趋势，其中海河、黄河、辽河、松花江实测径流量下降明显[13]。由图 5 可以看出：8 个水文站中位于北方流域的 4 个水文站径流量有明显的下降趋势，而除海河流域雁翅站外其它 7 个水文站径流变化百分率与相应汇水区内平均SPI值有相似的变化趋势，说明SPI平均值对径流变化有很好的指示作用。

计算径流变化百分率与平均SPI值的相关系数（表 3），可以看出，除雁翅站的相关系数没有达到置信水平外，其它所有站点的径流变化百分率与平均SPI值的相关系数均达到 99%的置信水平。海河流域雁翅站相关系数低可能是由于该站处于海河流域人类活动最为严重的子流域，水利工程建设、水土保持、种植结构变化等改变了流域的自然形态，引起流域调蓄能力增强，植物蒸散发强度增大，从而使得地表径流量减少[14]。

表 3　水文站径流变化百分率与汇水区内平均 SPI 值相关系数

Tab. 3　Correlation coefficients between the percentage of runoff variation and annual averaged SPI

| 水文站 | 相关系数 | 水文站 | 相关系数 |
|---|---|---|---|
| 佳木斯 | 0.85** | 吴家渡 | 0.79** |
| 铁岭 | 0.75** | 大通 | 0.76** |
| 雁翅 | 0.04 | 高要 | 0.82** |
| 花园口 | 0.72** | 竹岐 | 0.47** |

注：**表示达到 99%置信度水平（双尾检验）。

由上述分析可知，8 个水文站径流变化百分率与流域平均 SPI 指数有较好的相关关系，分别计算此 8 个水文站所在流域未来三种情景下 SPI 指数序列 MK 趋势，可从一定程度上反映 8 个流域未来径流变化趋势特征（表 4）。

表 4　水文站所在流域平均 SPI 值 2001－2050 年序列 Mann-Kendall 趋势检验

Tab.4　MK-test for averaged SPI of river basins during 2001-2050

| 排放情景 | 松花江 | 辽河 | 海河 | 黄河 | 淮河 | 长江 | 珠江 | 东南诸河 |
|---|---|---|---|---|---|---|---|---|
| A2 | -0.33 | -0.84 | -1.83** | -0.45 | 0.12 | 0.24 | -0.2 | 0.69 |
| A1B | 1.06 | 0.98 | 0.36 | 2.6*** | 1.29* | 1.84** | 2.6*** | 0.78 |
| B1 | 1.50* | 0.53 | 1.79** | 1.29* | 2.64*** | 0.36 | -0.59 | -0.55 |

注：*表示通过 90%置信度检验；**表示通过 95%置信度检验；***表示通过 99%置信度检验。

由表 4 可知，地处北方的松花江流域、辽河流域、海河流域和黄河流域径流变化表现为：在 A2 情景下，径流量呈下降趋势；在 A1B 和 B1 情景下则表现为上升趋势。其中松花江流域在 B1 情景下通过了 90%显著性检验，海河流域在 A2 情景和 B1 情景下都通过了 95%显著性检验，黄河流域则在 A1B 情景下通过 99%显著性检验、B1 情景下通过了 90%显著性检验；淮河流域和长江流域在 3 种情景下都呈径流增加趋势，其中淮河流域在 A1B 情景下通过 90%显著性检验，B1 情景下通过 99%显著性检验，而长江流域则仅在 A1B 情景下通过 95%显著性检验；珠江流域在 A2 和 B1 情景下呈径流微弱减少趋势，且没有通过显著性检验，而在 A1B 情景下则表现为径流量明显增加，且通过了 99%显著性检验；东南诸河流域在 A2 和 A1B 情景下表现为微弱增加趋势，B1 情景下则为微弱减少趋势，且 3 种情景下都没有通过显著性检验。

### 3.3　不确定性分析

未来气候变化预估存在一定的不确定性。这主要是因为用于预估未来气候变化的大气环流模式存在局限性，如模式计算稳定性、参数化的有效性、物理过程描述的合理性等[15]；此外，由于大气环流模型输出的分辨率相对于局部地区比较低也导致预估存在一定的不确定性；最后，目前还没有很好的办法能够区分人类活动或自然进程对气候变化的贡献，使得预估有更大的难度。

SPI指数作为众多旱涝指数之一，其优点是计算所需的输入量——降水资料较易获取，也避免了机理模型复杂的计算和大量经验性参数输入；但该指数不涉及干旱机理，也没有考虑气温、蒸发对干旱的影响[9]，所以该指数用于分析未来水资源量的变化趋势时存在一定的不确定性。

## 4　结语及讨论

综上研究，得出如下主要结论：

1）在 A2 情景下，中国旱涝格局继续延续现有格局，同样存在由东北延伸到西南的干旱带，但分布区域略有差异。A1B 情景下，中国贯穿中部地区及南部沿海出现湿润化趋势，其余地区有干旱化倾向。B1 情景下，中国东部地区将有可能从过去的“北旱南涝”格局转变为“北涝南旱”。

2）对 8 个流域的研究表明，SPI 旱涝指数与径流量变化百分率相关关系良好，可从一定程度上反映出中国未来水资源的变化特征，对中国未来水资源的合理利用及管理有一定参考意义，但其仍存在一定的不确定性。

为进一步研究未来中国水资源变化趋势特征，

利用 IPCC 第五次评估报告提出的多种全球气候模式预估结果，通过计算流域 SPI 干旱指数的方法，可充分考虑到未来各流域水资源变化的多种可能性；同时，由于 SPI 指数的局限性，可开展利用水文模型模拟未来水资源变化特征的研究工作。

致谢：中国气象局国家气象信息中心及德国马普气象研究所提供了计算所需数据，德国波茨坦气候影响研究所提供 SPI 计算程序，在此一并感谢！

参考文献：

[1] 夏军，Thomas T，任国玉，等．气候变化对中国水资源影响的适应性评估与管理框架[J].气候变化研究进展,2008,4(4)215-219.

[2] 任国玉，姜彤，李维京，等．气候变化对中国水资源情势影响综合分析[J]．水科学进展，2008，19（6）：772-779.

[3] 任国玉．气候变化与中国水资源[M]．北京：气象出版社，2007：11-18.

[4] 马柱国，任小波．1951－2006 年中国区域干旱化特征[J]．气候变化研究进展，2007，3（4）：195-201.

[5] 翟盘茂，邹旭恺．1951－2003 年中国气温和降水变化及其对干旱的影响[J]．气候变化研究进展，2005，1（1）：16-18.

[6] 牟林，吴德星，陈学恩，等．温室气体浓度增加情景下全球海洋变化主要特征分析[J]．科学通报，2006，51（19）：2304-2308.

[7] 宫德吉．干旱监测预警指数研究[J]．气象，1998，24（8）：14-18.

[8] Mckee T B，Doesken N J，Kleist J．The relationship of drought frequency and duration to time scales[J]．Eighth Conference on Applied Climatology，1993：17-22.

[9] 袁文平，周广胜．标准化降水指标与 z 指数在我国应用的对比分析[J]．植物生态学报，2004，28（4）：523-529.

[10] Stefan H，Klaus A，Erich R．Evaluation of the hydrological cycle in the ECHAM5 model[J]．Journal of Climate，2006，19（16）：3810-3827.

[11] 孙颖，丁一汇．IPCC AR4 气候模式对东亚夏季风年代际变化的模拟性能评估[J]．气象学报，2008，66（5）：765-780.

[12] 施雅风，沈永平，李栋梁，等．中国西北气候由暖干向暖湿转型的特征和趋势探讨[J]．第四纪研究，2003，23（2）：152-164.

[13] 张建云，王金星，李岩，等．近 50 年我国主要江河径流变化[J]．中国水利，2008（2）：31-34.

[14] 刘春蓁，刘志雨，谢正辉．近 50 年海河流域径流的变化趋势研究[J]．应用气象学报，2004，15（4）：385-393.

[15] 秦大河，丁一汇，苏纪兰，等．中国气候与环境演变(上卷)——气候与环境的演变及预测[M]．北京：科学出版社，2005：507-555.

## Evolution of Drought and Flood Pattern and Its Effect on Water Resources in China from 1961 to 2050

ZHAI Jianqing[1]，ZENG Xiaofan[2]，JIANG Tong[1]

（1．*National Climate Center*，*China Meteorological Administration*，*Beijing* 100081，*China*；

2．*Huazhong University of Science and Technology*，*Wuhan* 430074，*China*）

**Abstract:** With the monthly data of 483 weather stations during 1961-2000 and the precipition data derived from ECHAM5/MPI- OM climate model for 1961-2050, the monthly SPI (Standard Precipitation Index) are caculated, and evolution of drought and flood pattern in last 40 years and that for three kinds of future greenhouse gas emission scenarios(A2: high emission scenario; A1B: medium emission scenario; B1: low emission scenario) are analyzed, as well as the correlation between the runoff percentage in 8 hydrologic stations and corresponding SPI. The results show that: there was a drought trend zone which extended from northeast to southwest in the past 40 years in China, Under scenario A2, this drought zone would still exist; Under scenario A1B, a wet zone would spread in middle part of China; Under scenario B1, flood might occur in northern part while drought in southern part in east China. It is concluded that there is a good correlation between SPI and the percentage of runoff change.

**Key words**：ECHAM5/MPI-OM；Standardized Precipitation Index；drought and flood pattern；future scenarios

第 31 卷 第 1 期
2011 年 1 月

第 四 纪 研 究
QUATERNARY SCIENCES

Vol. 31, No. 1
January, 2011

doi:10.3969/j.issn.1001-7410.2011.01.05 文章编号 1001-7410(2011)01-29-07

# 历史极端雨涝事件研究*
## ——1823 年我国东部大范围雨涝

张德二① 陆龙骅②

(①国家气候中心,北京 100081;②中国气象科学研究院,北京 100081)

**摘要** 1823 年(清道光三年)我国发生大范围、多流域的严重雨涝,这是在小冰期寒冷气候背景下的重大气象灾害和极端气候事件。文章依据历史文献记载复原了 1823 年的气候实况并绘图显示,指出该年我国华北夏季雨期长、多大雨,北京 6~8 月雨日 53 天、降水量 663mm 超过现代(1971~2000 年)平均值 5 成;长江中下游全年多雨,梅雨期长、低地积涝 4 个多月,比 1804 年的水灾更严重;华南夏秋多雨。各地主要降雨时段由南向北的递次推迟,显示我国雨带的季节性移动特点。海河、黄河、长江、珠江诸流域发生雨涝灾害、粮棉减产甚至失收,还有疫疾流行,政府实施赈济。该年的天气气候特点与大范围持续多雨的 1954 年极为相似,且二者都发生在太阳活动周的极小值年和中等强度的厄尔尼诺结束之后。

**主题词** 极端气候事件 雨涝 气候灾害 1823 年 历史气候

**中图分类号** P426.6, P468~322.4 **文献标识码** A

当今,关于极端气候事件的问题备受关注,但极端事件的认定标准尚无定论,一致的看法只是将之归于"发生概率很低的事件"。而极端降水事件的认定要复杂些,它不仅仅由年、季雨量的多少来决定,还可由降水强度、降水持续时间以及发生季节的异常而被认定。我们固然可以采用年、季降水量负距平低于某界限值(例如$-2\sigma$ 或 $\sigma$ 为方差)来确定极端干旱事件,但却不宜仅仅由降水量高于同一界限值(如$+2\sigma$)的正距平值来确定极端降水事件,因为如罕见的暴雨强度、次数、雨期的起讫日期等也属于低发生概率,也应引为判据。至于极端的雨涝灾害事件的认定又更为复杂,它与降水量、地形、河道状况有密切关系,只是降水量过多仍是产生雨涝灾害的主要原因。笔者根据历史气候记载,和我国东部的千年干湿指数区域序列,选出若干历史上的重大雨涝事件,它们皆是由异常的、持续强降水而酿成流域性的或跨流域的严重雨涝灾害。尽管对这些事件尚不能像现代降水事件那样按其雨量和降雨强度来进行排序,但以这些事件在历史上的罕见程度,可认为这些事件符合"发生概率很低"的要求,可以归入极端气候事件之列,本文所论的 1823 年的雨涝事件即其中之一。1823 年在我国大范围多雨的特点在《中国近五百年旱涝分布图集》[1]中已清楚显示,本文依据多种科学资料对此个例的气候实况、社会影响、外界因子等细作剖析。

1823 年(清道光三年)我国东部大范围持续多雨,造成严重的雨涝灾害和粮棉减产失收。这极端雨涝事件出现在小冰期寒冷气候的背景下,对该个例的剖析正好可以为当代温暖气候背景下的极端雨涝事件提供对比。此事件具有代表性,有助于全面认识我国极端灾害事件的特点。

## 1 1823 年雨涝实况

依据我国历史文献中有关 1823 年天气气候和灾害状况的记载 277 条(出自 268 种古籍),对该年的天气实况作复原推断。这些历史气候记录引自《中国三千年气象记录总集》[2],是经系统采集和勘校的,文中用引号标示。它们出自 39 种古籍,其书名和版本详见文献[2],本文中不再标注。

1823 年的雨涝特点概括为:华北夏季雨期长、多大雨,长江中下游自春至秋持续多雨,华南夏秋多雨。历史记载的 1823 年夏-秋出现大雨和持续多

第一作者简介:张德二 女 67 岁 研究员 气象学专业 E-mail:derzhang@cma.gov.cn

* 国家重点基础研究发展规划项目(973 项目)(批准号:2010CB950903)和"十一五"国家科技支撑计划重点项目"极端天气气候事件的检测和可预测性关键技术研究"(批准号:2007BAC29B01)共同资助

2010-10-08 收稿,2010-11-20 收修改稿

图 1 1823 年历史记载的夏-秋大雨发生地域(深蓝色所示)

Fig. 1 Distributions of persistent precipitation areas(blue)in 1823 over East China

雨的地域如图 1 所示,其空间绘图单元为县。

华北夏季多雨。北京、天津、河北各地夏季持续大雨,河北东部和中部雨期较长,如卢龙、新城等地皆"霪雨四十余日",河北南部雨期稍短,如内丘"自五月二十七日起至六月二十七日(7 月 5 日 ~8 月 3 日)大雨三十日"。华北的持续降雨区还包括河南北部,但这些地方至 8 月 9 ~10 日还有暴雨,如武陟县"至七月初四、五等日又复大雨滂沱,连宵达旦"。据北京的逐日天气记录——清代宫庭文档北京"晴雨录"资料判读,1823 年北京的主要雨期是 6 月 4 日至8 月 24 日。由北京"晴雨录"的逐月雨量推算和雨日研究[2]知,该年 6 ~8 月降水量 633mm,比多年(1724 ~2000 年)平均值 447mm 高出 186mm,也比现代(1971 ~ 2000 年)平均值 423mm 高出 210mm; 雨日达 53 天,比多年平均值多 10 天、比现代(1971 ~2000 年)平均值 35.3 天多 17.7 天; 降雨时数 356 小时,比多年(1724 ~1903 年)平均值多 131 小时。

长江中下游自春至秋持续多雨。上海附近地区的历史记述如"春二月苦雨至夏五月始略止,七月又苦雨,禾稼尽淹,九月亦如之"(历史记载的月份为农历,用汉字表示,以下同)、"夏四月阴雨至八月止,晴止数日,五月二十日大雨平地水高三、四尺"等。由历史记载推知太湖流域的降雨有两个集中时段: 第一降雨时段为 4 月 5 日 ~7 月 6 日,这期间多次出现强降水"大雨如注",其发生日期分别是 4 月 5 日(二月二十四日)、6 月 24 ~27 日(五月十六至十九日)、6 月 29 ~30 日(五月二十一和二十二日)。江苏靖江—南通一线以南、浙江北部、安徽沿长江地区皆在同一雨区内,大雨时段大致相近,如安徽旌德"四月中旬至五月二十日大雨如注,日夜不绝,七月复大雨",大雨集中发生在 5 月 21 日 ~6 月 28 日; 偏西地点的大雨时段开始稍迟,如江西波阳"自五月初八日雨至二十六日止",其大雨集中发生在 6 月 16 日 ~7 月 4 日。第二降雨时段为 8 月 7 日 ~9 月 9 日(七月初二至八月初五),其间有台风带来的多次暴雨,如 8 月 7 日(七月初二日)夜,台风登陆嘉兴"暴雨如注、平地水深数尺",次日暴风雨即肆虐江苏之吴江、青浦、靖江、泰县等地。其他的台风暴雨还出现在 8 月 14 日(七月初九)、9 月 3 日(七月二十九日)和 9 月 9 日(八月初五)。历史记载如嘉善"七月初二、初九大风雨,水骤涨,较五月增尺余"、吴江"七月甲戌又大风雨,水骤涨二尺余,圩岸尽圮",这表明第二个降水时段的天气过程雨量更大。图 2 列示南、北方 8 个地点的部分降雨集中时段,从中可见各地降雨时段的开始和结束时间由南

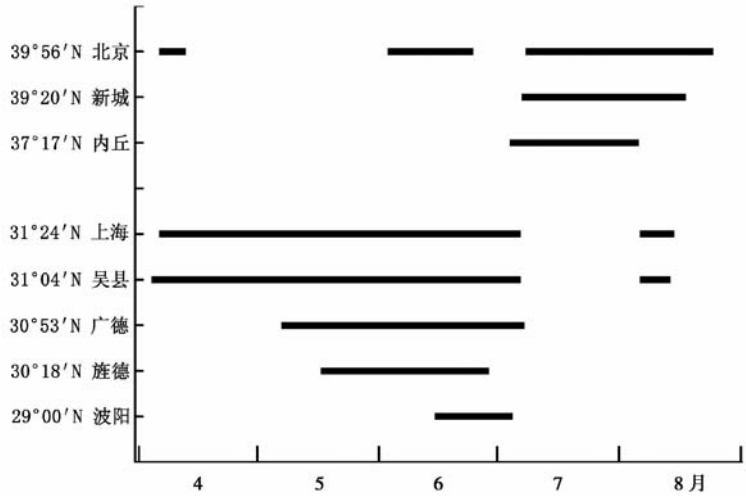


图 2　1823 年各地春夏主要降雨时段由南向北的递次推迟

Fig. 2　The main rainy spell of spring-summer for 8 places in 1823

向北的递次推迟,显示我国雨带由春到夏的季节性向北移动的特点。

华南各地夏秋多雨。广东多处地方有夏秋多雨的记载,如广宁“夏四月至秋七月连雨”、肇庆、郁南“夏五月至秋七月大雨水”、四会“秋七月大雨”等等;福建政和“五月大雨”、罗源等地“八月淫雨”;而海南省的多雨特点并不突出,仅有“秋八月雨颇透地,九月风雨淋漓”的记载。

## 2　雨涝和伴生灾害

### 2.1　涝灾

1823 年久雨和降雨过多、过猛引起海河、黄河、长江和珠江干流、支流水位急速上涨或决溢,以致漂屋害稼、沙压田亩等灾害多多发生。夏-秋季,华北发生决溢的河流计有滹沱河、滏河、浑河、漳河、滦河、卫河、大清河、子牙河、永定河等,“直隶百余州县皆成巨浸”,天津“田禾尽没,南城外行舟”,迁安县“大水入城”,河南境内沁河漫溢。长江下游各地主要是大雨水涨、圩岸圮毁、低地淹没成灾,扬州、靖江等地 6 月 11 日(五月十五日)后的大雨又遇江潮泛溢,故加剧水患的危害。长江中游的湖北、湖南发生大水、堤溃河溢、淹没农田庐舍的地点很多,仅江西省即有“夏五月南昌等十三县大水”的记载。该年遭受涝灾的地域如图 3 所示

1823 年涝灾的一个特点是积水长久不退,这加剧了水患之危害。华北平原因土地长时浸泡以致唐县、元氏县等地“平地生泉,水流皆月余”。长江下游积水最严重,如松江府“水溢不退计四月余”,青浦县“水大于嘉庆九年(1804 年)三尺,而退更迟”;江苏太仓“至初冬四乡犹巨浸,农不得耕”,吴江县等地“乾隆三十四年(1769 年)、嘉庆九年(1804 年)皆被水患,旋即退减,未有积水至五十日久如今日者”,吴县“浸霪汨没越九旬”;浙江嘉兴府“潦水骤涨泛溢,堤岸低处田庐尽没,数月不退,禾苗三次被淹”,直到“八月间江苏开刘家河泄水,九月始渐消去”;安徽宿松县“大水经冬始退”。江西余干县竟然也“禾稼淹没殆尽,水浸月余”。

值得注意的是 1823 年的灾情因其前期 1822 年的水灾而加重。1822 年夏秋河北和黄河中下游地区即已多雨酿成大范围水灾,河北 1822 年“大雨时行、田禾被淹,被水者八十州县之多”。连绵大雨等也引起河南“沁河决”、“各地川渠尽溢”等灾害。

### 2.2　疫病

1823 年大范围雨涝灾害伴有疫疾流行是这次雨洪灾害引人关注之点。疫区大致有两片(图 3 红色区),北方的瘟疫出现在河北、山西、辽宁,南方的福建、湖南、广东、广西、云南有“绞肠痧”等疫病流行。至于这瘟疫与雨涝灾害的关联尚不清楚,因为早在 1822 年,山东、河南、陕西、四川、广东、广西多处地方已有瘟疫发生,1823 年雨灾发生之前,河北卢龙、文安等地即已有“四月瘟疫盛行,死者相继,吊唁不通”的记载。

### 2.3　粮、棉歉收和赈济

1823 年久雨和水灾致使农作受损严重。华北各地多有诸如淫雨害稼、禾稼荡尽,以及米价增倍、

图 3 1823 年水灾发生地域(浅蓝)和疫病发生区(红色)

Fig. 3 Distributions of areas suffering flash floods(light blue) and pestilence(red) in 1823 over East China

斗米千钱、民扫草实为食之类的记载。长江下游夏季的久雨和气温偏低,因此时正值水稻和棉花的生长期,故减产甚至失收,松江府"禾豆、木棉、瓜果皆不熟",浙江嘉兴"潦水数月不退,禾苗三次被淹,秋禾大半无收",其他如早禾歉收、秋谷大半无收、木棉尽坏、禾稼不实、民多饥死的记载也为江浙各地多见,更有棉花的"尽偃于泥淖"而失收,以致"木棉荒而花价贵昂,百斤之值八千余文"。

1823 年的大范围雨灾、水灾危害深重,江苏、浙江的水灾被称为"百年未有之灾也",对此,中央和地方政府采取了一系列的赈灾措施。例如九月二十二日的圣谕"免直隶通州二十七州县水灾额赋。赈直隶通州等四十州县、山东临清等五州县水灾。加赈江西德化县、湖北黄梅县、河南武陟等五县水灾。给江苏仪征等四县、湖北江陵等三县水灾口粮。蠲缓山东临清等十六州县卫、直隶蓟州五十州县水灾新旧额赋,河南武陟县、湖北黄梅县水灾额赋及屯坐各卫应征新旧额赋,并给修屋费"。又如对北京"降旨令于五城分设厂座,发给仓贮米五万石,平价粜卖,下诏各地给予赈济或减免田赋";又如对河北玉田县"诏成灾七、八分村庄极贫者给赈二个月,次贫者给赈一个月";再如河北任丘"自十月至十二月共赈米二万七千二百三十九石,银六万一千五百七十二两"等;再如六月安徽"奉上谕铜陵、无为、繁昌、芜湖、当涂等五州县,因本年雨水过多,著加恩将被水军民一体给予抚恤"、七月"给江苏太仓等 17 厅州县水灾一月口粮";八月嘉兴府"奉恩旨地丁漕米分别蠲缓,发帑赈给农民三月口粮";八月"奉上谕:安徽省滨江各州县被水较重,米价渐昂,前赴四川、湖广、江西等省采作购买米十万石,分运灾区减价平粜",十月,奉上谕:本年安徽省夏雨连旬,江潮涨发,其无为等三十二州县并屯坐各卫被淹,盱眙等六州县高田被旱、低田被淹,又凤阳县被旱,经该抚查勘,灾分轻重,分别和恳恩施,著照所请,加恩将被水被旱成灾六、七、八、九之分之无为、铜陵、当涂、宣城、南陵、芜湖、繁昌、望江、桐城、和州、怀宁、宿松、贵池、青阳、东流、庐江、巢县、含山、全椒等十九州县,及屯坐各卫灾民灾军均按成灾分数照例分别给赈。"等等不一一列举。此外,各地方政府也采取一些赈济措施,如江苏"自院司以下均各捐廉助赈。是冬,人情尚得安静,凡有田之家,大小粒米无收,粮亦停征。"等等

## 3 气候概况和可能的影响因子

806

### 3.1 气候概况

1823 年多雨且低温寒冷。该年我国东部地区

春夏秋持续多雨,仅黄淮地区有局地短时干旱。华北北部的雨期较南部长约 10 天。据清代宫廷“晴雨录”资料的推算结果[3],北京夏季(6 ~ 8 月)的降雨日数和雨量分别较近 30 年(1971 ~ 2000 年)平均值多出 5 成和接近 5 成,而降雨时数则高于多年平均值 6 成以上。长江流域梅雨期长,梅雨开始早,可由苏州等地的记述“三月三日(4 月 13 日)至五月二十日连雨(6 月 28 日)”认为有异常的早梅雨提早于 4 月 13 日就开始了,综合其他记载可认为常梅雨期止于 7 月 6 日,还可能有所谓“二度梅雨”始于 8 月上旬持续 1 个月之久。当年的台风活动虽无完整的记录,但沿海地带的一些强降水显然是台风活动的影响所致,如 8 月 7 日、8 月 14 日、9 月 3 日和 9 月 9 日的暴雨等等。

1823 年全年气温偏低。春季多雪和寒冷的记载表明气温偏低:早春山东、河南、江西“大雪连月”,春三月河北、山西有霜灾;夏季长江下游地区阴雨低温、上海地区“七月天气如冬”江西余干县“八月,风冻愈加”表明 8 月、9 月份即有强冷空气活动;秋季山西早霜,冬季湖北、湖南“大雪寒甚”且降雪时间长、持续月余,还有四川大雪、上海冻雨危害等。

值得注意的是上述的 1823 年的气候概况与现代全国大范围多雨的 1954 年很类似:1954 年海河流域 6 ~ 8 月总雨量>700mm,出现夏涝;长江中下游及其以南的广大地区雨季开始早、持续时间长、雨量大,长江流域的梅雨期长达 50 天、梅雨量为常年的 3 倍[4];长江中下游和华南秋季冷空气活跃,9 ~ 10 月先后遭遇寒露风天气[4]。

### 3.2　可能的外界影响因子

1823 年气候如此异常,其成因必然备受关注,但是 1823 年尚没有大气环流场、海温场的资料,所以,那些用于现代气候异常成因分析的天气动力学方法本文不可能采用。故以下仅对其可能的外界影响因子——太阳活动、火山活动、海温状况等试作些讨论,并将这些外部条件与雨涝事件的对应关系,和已有的研究结论作些对照。

太阳活动 :据太阳活动记录[5]知,1823 年正值太阳活动周第 7 周的极小年(m),太阳黑子相对数仅为 1.8。这是自 1749 年以来 200 多年间的次极低值。

火山活动:由世界火山活动记录[6]知,1822 年 3 月日本 Usu 火山爆发(喷发强度指数 VEI = 4)和 10 月爪洼 Galunggung 火山爆发(VEI = 5),这是中、低纬度重大火山喷发事件。至于这些火山喷发物与 1823 年我国大范围多雨事件的关联尚难轻易断言。

海温条件:由厄尔尼诺事件历史年表[7]知,1823 年正处于两个中等强度的厄尔尼诺事件之间,这两次厄尔尼诺事件分别出现在 1821 年和 1824 年,因此可被视为厄尔尼诺事件的前一年或事件结束之后,即非厄尔尼诺年。尽管近些年已有许多关于厄尔尼诺与我国降水关系的研讨,指出厄尔尼诺的不同发展阶段和中国降水的季节分布特征等[8,9],认为厄尔尼诺现象对中国降水有重要影响,但主要不在发生的当年,而是次年[10]等等。然而,笔者由厄尔尼诺历史记录[7]获知的信息却仅限于 1823 年为非厄尔尼诺年而已,不过值得注意的是,这个非厄尔尼诺年与我国大范围多雨的对应关系正和现有的关于我国降水与厄尔尼诺事件的研究结论一致,如陈菊英等的研究[11]指出 1951 ~ 1985 年的 9 例厄尔尼诺年次年的我国 6 ~ 8 月降水量距平合成图显示出我国大范围多雨的特点;另外,笔者[12]得出的 1500 ~ 1990 年的 101 例中等以上强度的厄尔尼诺事件结束后的“非厄尔尼诺年”的旱涝等级合成图,也同样显示出全国大范围多雨的特点,认为在厄尔尼诺结束之后较多地对应于我国大范围多雨。

有趣的是,上述可能影响 1823 年气候的外界因子和 20 世纪最严重的大范围多雨年 1954 年的外界因子作对比,二者竟然很相似:1)1954 年也是太阳活动极小年,处于太阳活动周第 19 周的 m 位相,年平均太阳黑子相对数仅为 4.4,1 月太阳黑子数仅 0.2[5],是 1823 年以来的最小值;2)1954 年处于中等强度的厄尔尼诺事件(1953 年 M+级)之后和强厄尔尼诺事件(1957 ~ 1958 年 S 级)之前[7],正是“非厄尔尼诺年”。

## 4　结语

我国 1823 年的大范围、多流域严重雨涝是在小冰期寒冷气候背景下的重大气象灾害和极端气候事件。利用历史文献记载复原当年雨涝实况,讨论了当年的天气特点、伴生灾害、社会影响。还对其可能的外部影响因子作初步探讨,并与 20 世纪我国最严重的雨涝年份 1954 年作了对比,以期有助于增进我们对极端气候事件的认识。研究指出:

(1)1823 年我国华北雨期长、多大雨,长江中下游自春至秋持续多雨,华南夏秋多雨,海河、黄河、长江、珠江诸流域发生雨涝灾害,南、北方主要降雨时

段由南向北的递次推迟,显示我国雨带的季节性移动的特点。

(2)1823 年北京、天津、河北各地夏季持续大雨 40 余天。北京 6 ~ 8 月降水量 633mm,高出现代(1971 ~ 2000 年)平均值 210mm、超过近 5 成; 6 ~ 8 月雨日 53 天,比现代平均值多 17.7 天,超过 5 成。长江下游多处低地积水长达 4 个多月,比 1804 年的水灾更严重。

(3)1823 年大范围粮食歉收,长江下游因久雨、低温和积涝,水稻大半无收、棉花绝收、粮棉价格飞涨。政府对各地饥荒采取赈济措施。

(4)1823 年在河北等 8 省伴有疫疾流行。但疫疾流行与雨涝是否有关联的问题尚未作探讨。

(5)1823 年气温偏低、冷气团活跃: 春季多雪、寒冷,夏季阴雨低温,秋季早霜,冬季大雪、冻雨严寒,梅雨开始早、持续时间长、雨量大,这些特点与 20 世纪最严重的多雨年 1954 年极为相似。

(6)从外界影响因子看,1823 年位于太阳活动周的极小值位相,该年又是厄尔尼诺现象结束后的非厄尔尼诺年,这些特点与异常多雨的 1954 年相似。

**致谢** 感谢审稿专家对文章提出的修改意见。

## 参考文献(References)

1 中国气象科学研究院. 中国近 500 年旱涝分布图集. 北京: 地图出版社,1981. 182
Chinese Academy of Meteorological Sciences, CMA. Yearly Charts of Dryness/Wetness in China for the Last 500-year Period. Beijing: Cartographic Publishing House, 1981. 182

2 张德二主编. 中国三千年气象记录总集. 南京:凤凰出版社,江苏教育出版社,2004. 2863 ~ 2875
Zhang De'er ed. A Compendium of Chinese Meteorological Records of the Last 3,000 years. Nanjing: Phoenix Publishing, Jiangsu Education Press, 2004. 2863 ~ 2875

3 张德二,刘月巍. 北京清代"晴雨录"降水记录的再研究——应用多因子回归方法重建北京 1724 ~ 1904 年降水量序列. 第四纪研究,2002,**22**(3):199 ~ 208
Zhang De'er, Liu Yuewei. A new approach to the reconstruction of temporal rainfall sequences from 1724 ~ 1904 Qing-Dynasty weather records for Beijing. *Quaternary Sciences*, 2002, **22**(3):199 ~ 208

4 冯佩芝,李翠金,李小泉等编著. 中国主要气象灾害分析 1951 ~ 1980. 北京: 气象出版社,1985. 138 ~ 139
Feng Peizhi, Li Cuijin, Li Xiaoqun eds. Analysis on the Major Meteorological Disaster in China 1951 ~ 1980. Beijing: Meteorological Press, 1985. 138 ~ 139

5 Waldmeier M. The sunspot activity in the years 1610 ~ 1960. *Planetary and Space Science*, 1961, **9**(10):768

6 Simkin T, Siebert L. Volcanoes of the world(2nd edition). Tucson, Arizona: Geoscience Press, INC, 1994. 205 ~ 206

7 Quinn W H, Neal V T. The historical record of El Niño events. In: Bradley R S, Jones P D eds. Climate since A. D. 1500. London and New York: Routedge, 1992. 623 ~ 648

8 赵振国. 厄尔尼诺现象对北半球大气环流和中国降水的影响. 大气科学,1996,**20**(4):422 ~ 428
Zhao Zhenguo. Impact of El Niño events on atmospheric circulations in the Northern Hemisphere and precipitation in China. *Chinese Journal of Atmospheric Sciences*, 1996, **20**(4):422 ~ 428

9 Zhang Renhe, Akimasa S, Masahide K. A diagnostic study of the impact of El-Niño on the precipitation in China. *Advaces in Atmospheric Sciences*, 1999, **16**(2):229 ~ 241

10 丁一汇. 我国短期气候预测业务系统. 气象,2004,**30**(12):12
Ding Yihui. China operational short range climate prediction system. *Meteorological Monthly*, 2004, **30**(12):12

11 陈菊英等. 中国旱涝的分析和长期预报研究. 北京: 农业出版社,1992. 154 ~ 159
Chen Juying *et al*. A Study of Long-Rang Forecasting and Analysis on Floods and Droughts of China. Beijing: China Agricultural Press, 1992. 154 ~ 159

12 张德二,薛朝晖. 公元 1500 年以来El Niño事件与中国降水分布型的关系. 应用气象学报,1994,**5**(2):168 ~ 175
Zhang De'er, Xue Zhaohui. Relationship between the El Niño and precipitation patterns in China since 1500 AD. *Quaterly Journal of Applied Meteorology*, 1994, **5**(2):168 ~ 175

# STUDY OF THE LARGE EXTENT FLOODING OVER EASTERN CHINA IN 1823 AS ONE OF THE EXTREME CLIMATIC EVENTS IN HISTORY

Zhang De'er[①]　Lu Longhua[②]

(①*National Climate Center*, *Beijing* 100081; ②*Chinese Academy of Meteorological Sciences*, *Beijing* 100081)

**Abstract**

Disastrous floods happened in 1823 to more than one river valley over Eastern China and they were serious meteorological and extreme climatic event in the cold background of Little Ice Age. In this paper the rainy and flood situation in 1823 is reproduced by means of historical literature records, and the weather character, accompanied disasters, societal impact and the external affecting factors in this year are discussed.

In 1823 the North China had suffered prolonged rainy season with multiple torrential rains; over the mid to lower basin of the Yangtze by persistent precipitation in spring to autumn; in South China by abundance in rains in summer-autumn, leading to rainstorms-caused calamities in the drainage areas of the Haihe, Huanghe, Yangtze, Pearl River etc, with these regions suffering heavy rains and flash floods and the beginning/ending dates of rainy spell for 8 places drawn on maps, indicative of the rain belt be progressively moving from south to north comply with seasonal change. It is discovered that >40-day heavy rains in the summer of 1823 were recorded in Beijing, Tianjin and part of the Hebei Province. June ~ August rainfall in Beijing was 633mm, 210mm higher compared to the mean over 1971 ~ 2000, equivalent to nearly 50% increase, and the number of rainy days of 53 d. was 17. 7 d. more than the mean over 1971 ~ 2000 at the same interval, the figure being bigger in excess of 50%. Floods over the North China plains in 1832 were produced by burst banks of Rivers Hutuo, Zi, Hun, Zhang, Luo, Luan, Wei and Ziya, to name but a few. For the lower Yangtze Basin, burst banks of rivers and damaged coasts of lakes caused low-land to be flooded for 4months or more, a situation that was more serious in comparison to the 1804 case.

The 1823 precipitation and floods gave rise to large-scale crop production drop and even entire harvest failure. As a result of the rainfall and floods, temperature was low enough in the lower basin of the Yangtze to give poor harvest of paddy rice and absolute failure of cotton, leading to their soaring prices to result in famine in many regions, and corresponding relief was carried out by the governments. And epidemic occurred over provinces of Hebei, Shanxi, Liaoning (in the north), Hunan, Fujian, Guangdong, Guangxi and Yunnan (in the south of the country) in this year.

The year of 1823 was characterized by low temperature and actively cold air masses, heavy snowfalls in the spring, long spells of rainy weather and cool temperature in the summer, early frost in the autumn and heavy snowfall and freezing rains in the winter, with the rainy season starting earlier, persisting long enough and marked by high intensity. These synoptic and climatic aspects of 1823 were extremely similar to those of 1954 the severest flood year of 20th century. As for the external affecting factors, both cases taking place in the minimum-value phase of the solar activity period and 1 ~ 2 years after ending the moderate-intensity El Niño event.

**Key words**　extreme climatic event, floods, meteorological disaster, 1823 A. D., historical climate

# 天山乌鲁木齐河源 1号冰川致冷效应的小气候观测

张东启[1,2], 明 镜[3], 魏文寿[2]

(1 中国气象科学研究院, 北京 100081; 2 中国气象局 乌鲁木齐沙漠气象研究所, 新疆 乌鲁木齐 830002;
3 国家气候中心, 北京 100081)

摘 要: 高山冰川以其下垫面的致冷效应形成独特的冰川小气候。为研究冰川小气候特征, 2007年 7月在天山乌鲁木齐河源 1号冰川表面及末端冰碛上架设 5台自动气象站, 并进行了为期一个月的基本气象要素的观测。以观测数据为基础, 描述和分析了与冰川致冷效应有关的冰川区温度与湿度变化特征、冰面逆温、温跃现象、冰川风现象, 并就冰川致冷效应对局地对流性降水的可能影响进行了初步分析。

关 键 词: 天山乌鲁木齐河源 1号冰川; 小气候观测; 致冷效应
中图分类号: P463.25 文献标识码: A 文章编号: 1000-6060(2011)03-0449-09(449~457)

山地冰川与周围裸露山坡、冰碛物、草原草甸等相比, 具有热传导率低、反射率大、热发射率高、表面水汽含量低等特点, 使冰川表面产生致冷效应, 并由此引发了冰川下垫面不同于周围其它性质下垫面的局地小气候效应[1-7]。理论上讲, 正是这些小气候效应使得冰川改变了大气下垫面的温度和湿度状况, 并通过影响上层大气的温湿场和风场而对高山区的降水产生了一定程度的影响[6-9]。对山地冰川小气候的研究工作主要集中在冰面微气象观测[10-16]、冰川区降水观测与校正[17-19]、冰面能量平衡观测[20-23]等方面。但是山地冰川作为气候系统的一部分, 对山区气候的作用, 尤其是对高山区降水量的影响却较少有人涉及。本文主要侧重于对高山区降水可能产生影响的冰川小气候效应方面的观测与研究, 如冰川与非冰川之间的温跃现象、逆温现象、冰川风以及冰川区的温度和湿度特征和降水量的变化等。

## 1 资 料

2007年 7月 15日~7月 17日, 先后在天山乌鲁木齐河源 1号冰川表面和冰川周围架设了 5台相同型号的自动气象站(图 1)。自动气象站的编号分别为 S1-S5, 其中, 自动气象站 S1位于 1号冰川东支末端前缘的冰碛上, 距离 1号冰川东支末端 50 m, 海拔高度 3 740 m, 下垫面为岩石和砂土。S2位于距离 1号冰川东支末端约 500 m的冰碛垅上, 海拔高度 3 733 m, 下垫面为高山草甸。S3和 S4安装在 1号冰川东支中部海拔 3 881 m处的冰面上的同一个支架上, 距冰川末端约 500 m, 下垫面为裸露的冰面。两个自动气象站的传感器上下垂直排列, S3位于上层, S4位于下层。S5位于冰川平衡线附近, 距冰川末端约 800 m, 海拔高度为 3 980 m, 下垫面为积雪。S1、S2和 S3自动气象站具有温度、湿度、

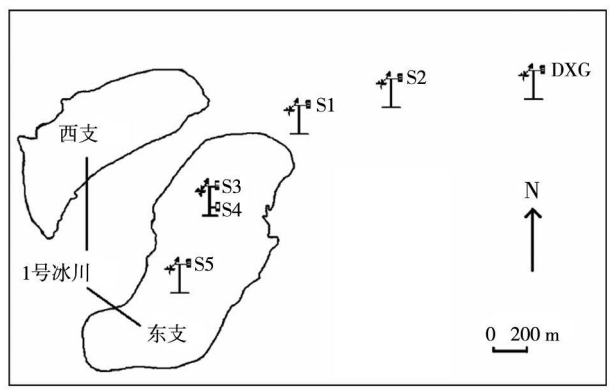


图 1 自动气象站位置示意图

Fig.1 The sketch map of AWS sites

* 收稿日期: 2010-09-24; 修订日期: 2010-12-14
基金项目: 中国沙漠气象科学研究基金(Sqj2006008); 中国气象科学研究院基本科研业务费专项基金(2007Y005)资助
作者简介: 张东启(1971-), 男, 山东昌邑人, 副研究员, 主要从事冰冻圈变化的观测研究. E-mail: zhangdq@cams.cma.gov.cn



© 1994-2011 China Academic Journal Electronic Publishing House. All rights reserved. http://www.cnki.net

气压、太阳辐射、风向、风速等传感器, S5自动气象站与前三个自动站相比, 缺少太阳辐射传感器, 而S4自动气象站仅具有温度、湿度传感器。除 S4外, 其它各个自动气象站的各种气象传感器安装在距离地面 (或者冰雪面) 1.5 m的高度上, 而 S4的温度、湿度传感器安装在距离冰面 0.5 m的高度上。

自动气象站每 5 min采集一组数据, 包括 5 min平均值和极值以及极值出现的时间等信息。5个自动气象站的数据采集时间从 7月 15日 16:00(北京时间, 下同)到 7月 17日 17:00不等, 而结束时间也在 8月 16日和 8月 17日的不同时间, 为了便于统一计算和比较, 本文中使用的气象数据全部统一到从 7月 18日 0:00起, 到 8月 16日 23:55止, 共 30 d的观测资料, 其中每台自动气象站采集到 8 640组 5 min平均值数据。另外本文中还引用了新疆气象局大西沟气象站 (以 DXG表示, 海拔 3 539 m) 2007年 7~8月份部分自动气象站的数据, 尽管两种自动气象站类型不同, 但经过 24 h的对比观测 (8月 16日 17:38~17日 17:38, 每分钟采集一组数据), 1 440组数据的比较显示, 与大西沟自动气象站数据相比, 本项目所采用的自动气象站温度平均读数偏高 0.17 ℃, 相对湿度读数平均偏低 0.64%, 24 h记录的降水量分别为 2.03 mm和 2.2 mm, 上述偏差不影响本文所涉及数据的分析结果, 因此对引用的大西沟自动气象站的数据未做任何订正。

## 2 结果与讨论

### 2.1 温度

从 7月 18日~8月 16日共 30 d的观测期间 (这段时间冰川正处于消融期内), 所有自动气象站观测到的气温在绝大多数情况下都在 0 ℃以上, 其中非冰川下垫面上的三个站 0 ℃以上的气温比例超过 90%, 而冰川下垫面上的三个站则在 85%~90%之间 (表 1)。从高山草甸到接近冰川平衡线处离地面高度都为 1.5 m的五个气象站平均气温 DXG>S2>S1>S3>S5, 表明从冰川谷地到冰川上部平均温度逐渐降低。从温度的波动幅度看, 非冰面下垫面上自动气象站的温度波动要大于冰川下垫面上自动气象站温度的波动幅度。如 DXG、S2和 S1三个自动气象站一个月的温度标准偏差分别为 4.01、3.74和 3.76, 而 S3、S5两站的标准偏差分别为 3.06和 2.73, 说明越接近冰川上部温度波动越小。为了更深入了解不同下垫面的温度变化特征, 按照当地日出和日落的时间划分白天和夜间, 即以 8:00~20:00为白天, 以 20:00~次日 8:00为夜间, 对各个自动气象站之间的温度进行统计, 可以看到: 非冰川表面各站点的白天、夜晚和昼夜温差接近冰川表面各站点的 1.5~2倍, 昼夜温差基本上随海拔的升高而降低, 最高值是位于高山草甸上的 DXG站, 昼夜温差达 3.82 ℃, 最低值是位于冰川平衡线附近的 S5, 昼夜温差仅 1.52 ℃。而处于同一地点的两个自动站则位置低的比位置高的昼夜温差更大。这些都表明不同性质下垫面辐射特征存在较大的差异。而基本位于同一海拔高度的 S1比 S2昼夜温差要大一些则可能是受到所处位置和地形的影响。

### 2.2 冰面逆温现象

逆温现象是指近冰面空气层中温度的垂直分布随高度而递增的现象。这种逆温现象是由冰雪下垫面较强的反射率、长波辐射能力以及冰面蒸发耗热等因素引起的[3,5]。逆温现象的强弱与云量、风速

表 1 自动气象站描述及温度统计

Tab.1 Description of AWSs and their temperature statistics

| 自动站编号 | DXG | S2 | S1 | S3 | S4 | S5 |
|---|---|---|---|---|---|---|
| 海拔高度 /m | 3 539 | 3 733 | 3 740 | 3 881 | 3 881 | 3 980 |
| 下垫面特征 | 高山草甸 | | 岩石和砂土 | 裸露的冰面 | | 积雪 |
| 传感器距地面高度 /m | 1.50 | 1.50 | 1.50 | 1.50 | 0.50 | 1.50 |
| 白天平均温度 /℃ | 8.86 | 7.23 | 7.11 | 4.81 | 4.17 | 3.89 |
| 夜间平均温度℃ | 5.04 | 4.38 | 4.12 | 2.57 | 1.86 | 2.37 |
| 观测期间平均温度 /℃ | 6.96 | 5.81 | 5.62 | 3.69 | 3.02 | 3.13 |
| 观测期间昼夜温差 /℃ | 3.82 | 2.84 | 2.98 | 2.25 | 2.32 | 1.52 |
| 大于 0 ℃数据比例 /% | 96.20 | 94.60 | 92.40 | 87.20 | 85.40 | 87.90 |
| 标准偏差 | 4.01 | 3.74 | 3.76 | 3.06 | 3.00 | 2.73 |



© 1994-2011 China Academic Journal Electronic Publishing House. All rights reserved. http://www.cnki.net

等天气因素有关。云量多、风速大, 则温度梯度减小, 反之增大。逆温现象是冰川致冷效应的反映, 以前的研究指出, 夏季 1号冰川冰面附近 (1.5 m以下) 的温度梯度相当于一般自由大气的 200倍以上[4]。

为了研究冰川表面不同高度上的气温差异, 在 1号冰川东支海拔 3 881 m处的冰面上的同一个支架上安装 S3和 S4两个自动气象站, S3和 S4的各种气象传感器分别安装在距离冰面 1.5 m和 0.5 m的高度上。从图 2可以看到, 上下层气温差异非常明显。统计结果显示, 绝大部分时间 (98.03%) 上层气温高于下层气温, 即从冰面到冰面上空至少 1.5 m处几乎整个观测时段都存在非常明显的逆温现象。30 d的观测数据表明, 上下层之间平均温差为 0.67 ℃。上下层之间日平均气温之差最小为 0.11 ℃, 最大为 1.61 ℃, 而 5 min平均气温数据显示上下层之间的温度差异最大达到 4.6 ℃。逆温现象受云量的影响很大, 晴天冰面上逆温现象明显, 如 7月 20日和 8月 14日上下层之间日平均温差为 1.03 ℃和 1.61 ℃; 而降雪天或者阴天冰面上逆温现象减弱, 如 7月 28日和 8月 12日上下层之间日平均温差分别仅为 0.25 ℃和 0.49 ℃ (图 3), 反映无水汽影响时冰面蒸发耗热对逆温现象贡献较明显。

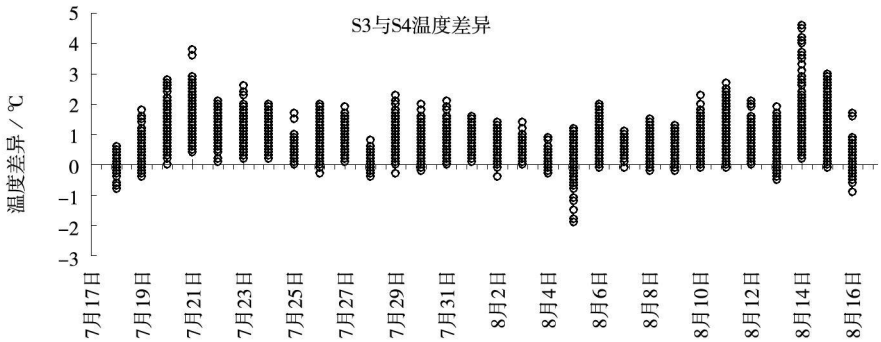


图 2　冰面逆温现象

Fig. 2　Temperature inversion on glacier surface

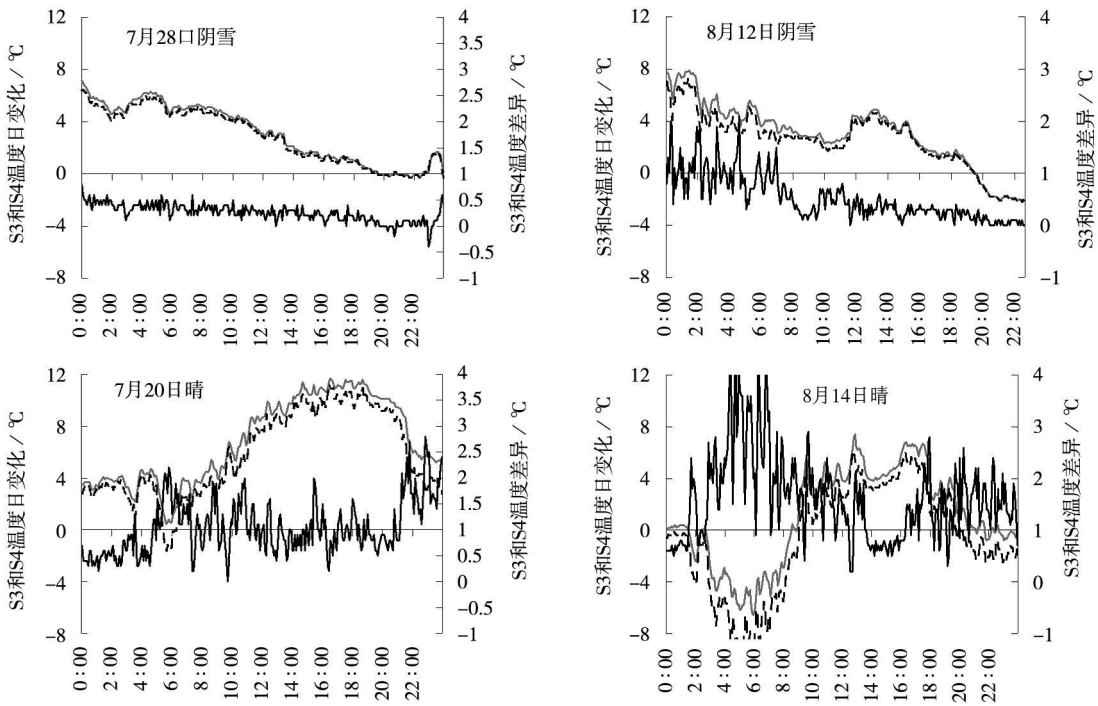


图 3　不同天气状况下的冰面逆温现象

(蓝色和红色虚线分别表示 S3和 S4站的日温度变化, 黑色实线表示 S3－S4温度之差)

Fig. 3　Temperature inversions at different weather condition

(Blue and red dased line denote temperature variation of AWS S3 and S4 respectively; solid black line denotes the temperature difference between AWS S3 and S4)

© 1994-2011 China Academic Journal Electronic Publishing House. All rights reserved.　http://www.cnki.net

晴朗的天气, 逆温现象在夜间 (主要是后半夜至早晨太阳升起之前这段时间 )最为显著, 白天随着太阳高度角的上升, 冰面逆温现象逐渐减弱, 到当地时间的中午以后上下层温度差异达到最小, 然后再随着太阳的落山逆温现象又逐渐明显起来。而在阴天或者下雪的天气, 冰面逆温现象随时间的变化规律不太明显, 但总的看来也是夜间逆温比白天明显 (图略 )。夜间冰面逆温更加显著的现象也可以从表 1中昼夜温差数据中反映出来, 整个观测期间夜间的上下层平均温差 0. 71 ℃, 大于白天的平均温差 0. 64 ℃。

**2. 3** 温跃现象

温跃现象即温度“跃动”, 指温度随平面空间或随高度的突变现象。特别是在由非冰川表面过渡到冰川表面时, 温度梯度突然增大, 甚至接近或超过干绝热梯度的现象[16]。这种温跃现象, 主要是由于冰川的冷却作用加大了气温差异所致[23]。从本次观测 5个自动气象站的资料来看 (图 4), 处于同一性质的下垫面上的自动站之间的温度垂直递减率差异不大, 如 DXG站与 S2和 S1之间的温度垂直递减率分别是 - 0. 59 ℃ /100 m和 - 0. 66 ℃ /100 m, 而同处于冰川表面的 S5与 S3之间的温度垂直递减率仅为 - 0. 57 ℃ /100 m, 比自由大气的温度垂直递减率还要小一些。不同性质的下垫面上的自动站之间的温度垂直递减率比自由大气的温度垂直递减率要大得多。例如, 位于冰舌上部的 S3与位于冰舌前端的 S1之间的温度垂直递减率 30 d的平均值为 - 1. 37 ℃ /100 m, 这个结果比白重瑗根据 1983年 7月 5日 ~ 20日观测资料求得的冰舌中上部的温度垂直递减率 - 1. 176 ℃ /100 m还要大[3]。位于冰川上部的 S5与 S1之间为 - 1. 04 ℃ /100 m, 也大于自由大气中 - 0. 67 ℃ /100 m的温度垂直递减率。位于冰川表面的 S5、S3与距离冰川末端约 500 m处草垫上的 S2之间的温度垂直递减率则更大, 分别为 - 1. 08 ℃ /100 m和 - 1. 43 ℃ /100 m。如此大的温度垂直递减率表明, 对于同一对流云团来说, 不管它以干绝热还是湿绝热方式从非冰川下垫面上空上升到冰川下垫面上空, 冰川下垫面始终是一个冷源, 较大的温度差异很可能会加速暖湿气团从非冰川下垫面向冰川下垫面的流动, 对暖湿气团起到了一种类似“吸拉”的作用, 也为冰川上空成云致雨 (雪 )创造了条件。

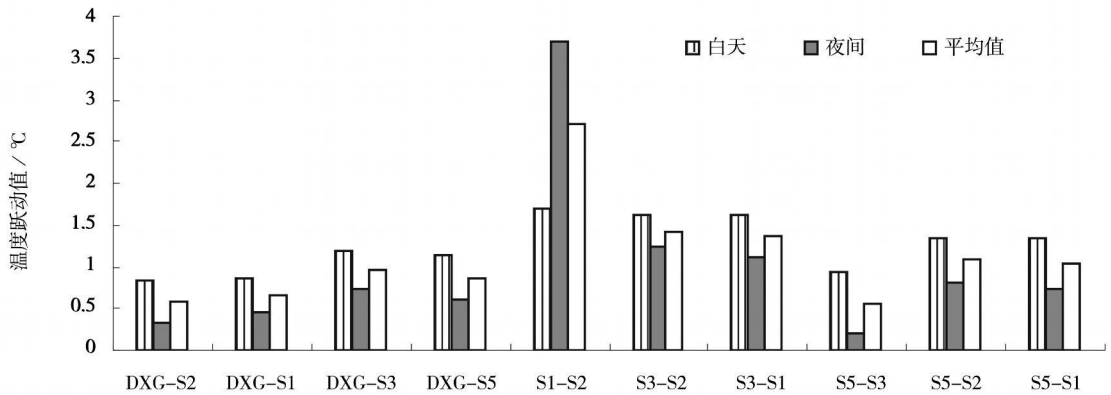


图 4 不同站点之间的温度跃动值

Fig. 4 Temperature jump values between different AWSs

按照白天和黑夜对各个自动气象站之间的温度垂直递减率进行统计计算, 从结果可以看到, 除 S2和 S1之间外, 其他各个自动气象站之间的温度垂直递减率都遵循基本相同的规律, 即白天大、夜间小, 这与本地区的局地对流天气的发展过程是一致的[24]。比较特殊的是, 均位于非冰川表面的 S2和 S1之间的相对高度差仅有 7 m, 但它们之间的温度差异却非常大, 如平均垂直递减率高达 - 2. 69 ℃ / 100 m, 说明处于冰川前端的 S1受到沿冰川表面下沉流动的冷空气 (冰川风, 后面的 2. 5节还要详细论述 )的影响非常明显, 尤其是在夜间, 冰川表面的下沉气流聚集在冰舌前缘的冰川与冰碛物包围形成的小盆地之中, 使得 S1处的夜间平均温度比 S2处低 0. 26 ℃, 导致 S2与 S1之间的夜间温度垂直递减率高达 - 3. 71 ℃ /100 m。

**2. 4** 相对湿度

位于冰面和非冰面上空 1. 5 m处的 5个自动气象站的相对湿度记录没有表现出很明显的差异, 观



© 1994-2011 China Academic Journal Electronic Publishing House. All rights reserved. http://www.cnki.net

测期间的相对湿度平均值在 64% ~ 69% 之间, 且它们的变化趋势也非常一致。总的来说各站相对湿度在晴天小, 而阴雪天气大。但位于冰川表面上同一位置但不同高度上的自动站记录显示, 冰川表面上下层之间存在明显的相对湿度的差异。如图 5显示, S3和 S4的湿度传感器分别位于冰面上 1. 5 m处和 0. 5 m处, 在大部分时间 (76. 53% ), 1. 5 m处的相对湿度 < 0. 5 m处的相对湿度, 即冰川表面上干下湿, 这段时间内上层平均相对湿度要比下层低 4%; 有 13. 38% 的时间上下层相对湿度一致, 仅有 10. 08% 的时间上层相对湿度大于下层相对湿度, 而这段时间内上层平均相对湿度要比下层高 1%。在晴朗的天气, 冰面上相对湿度小但波动幅度较大, 如 7月 30日和 8月 14日冰面相对湿度日平均值分别为 37% 和 35%, 在 10% ~ 80% 之间波动, 而上下层之间的差值波动也较大, 在 - 20% ~ 5% 之间波动, 日差异平均值分别 - 5. 3% 和 - 7. 7%; 而阴雪天气, 冰面上相对湿度大但波动幅度较小, 如 7月 28日和 8月 12日冰面相对湿度日平均值均为 84%, 在 60% ~ 100% 之间波动, 而上下层之间的差值波动也很小, 波动幅度基本上不超过 5%, 日差异平均值分别为 - 0. 3% 和 - 1. 3%。

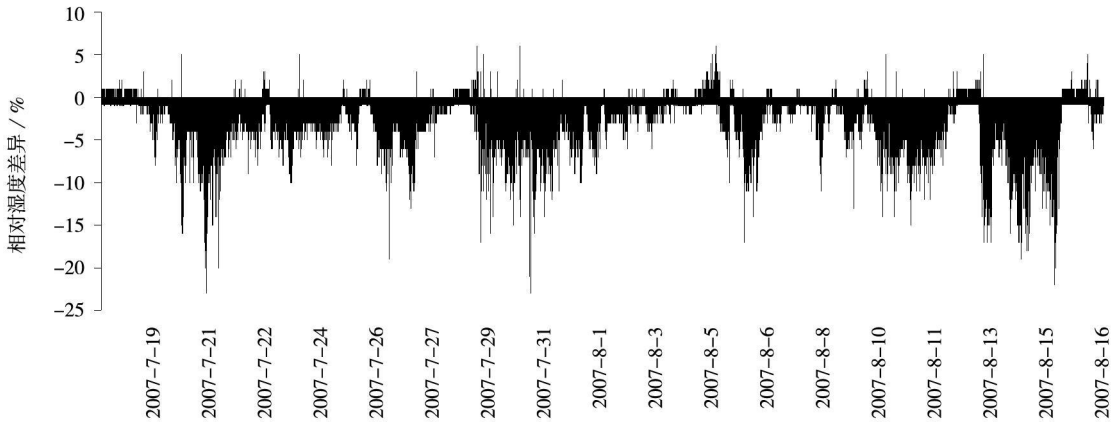


图 5　冰川表面 1. 5 m处和 0. 5 m处相对湿度的差异 (S3 - S4)

Fig 5　Relative humidity differences between AWS S3 (1. 5 m) and S4 (0. 5 m)

**2. 5　冰川风**

冰川风也是由于冰川的致冷作用形成的一种气流现象。由于冰川的致冷作用, 使近冰面空气冷却下沉, 密度较大的冷空气沿冰川表面向下流动就形成了冰川风。冰川风的大小与冰川规模、天气状况有关[11-12]。

沿冰川流动方向从下而上, 四个自动气象站的风向玫瑰图如图 6所示。总的看来观测期间冰川上各站自始至终受到冰川风和地形的影响。S5位于冰川最上部接近冰川积累区, 这里的风向以南北向为主, 而自冰川积累区沿冰面向下的偏南风 (这里指 SW、SSW、S、SSE和 SE风向总和, 下同 ) 与沿冰面向上吹的偏北风 (这里指 NW、NNW、N、NNE和 NE风向的总合, 下同 ) 占全部风向总频率的比例分别为 45. 3% 和 25. 5%, 显然偏南风更占主导优势; 位于冰川中下部的 S3风向也是以偏南风为主导风向, 偏南风和偏北风分别占全部风向总频率的 48. 3% 和 25. 7%。与 S5相比, 这里风向主导 (SSW) 与冰川流动方向更加一致; 与 1号冰川末端流动方向和冰川谷地方向一致, 位于冰川末端 S1自动气象站的风向转为东西向为主导风向, 而偏西风 (这里指 WSW、W和 WNW风向总和, 下同 ) 的比重 (42. 6% ) 比偏东风 (这里指 ENE、E和 ESE风向总和, 下同 ) 的比重 (35. 6% ) 稍大, 表明观测时段内该处的风向是从冰面向下吹向冰川谷地的冰川风稍占优势; 距离冰川末端稍远一些的 S2处的风向与 S1一样, 仍然以东西向为主, 但与 S1相比, 沿谷地向上的偏东风的比重稍微增加, S2处偏东风和偏西风的风向频率分别占全部风向总频率的 37. 5% 和 43. 8%。

通过分析 4个自动气象站风向的日变化, 可以看到在不同的位置上风向的日夜变化规律是不一致的。按照白天和黑夜对各个自动气象站的风向进行划分和统计。结果显示位于冰川中上部的 S3和 S5站不论白天还是夜间, 主导风向均是沿冰川表面向下吹的冰川风 (偏南风 )。其中, S3白天偏南风和偏北风的比例分别是 45. 4% 和 27. 5%, 夜间偏南风和偏北风的比例分别是 43. 4% 和 24. 7%; S5白天偏南风和偏北风的比例分别是 40. 3% 和 30. 5%, 夜间



© 1994-2011 China Academic Journal Electronic Publishing House. All rights reserved.　http://www.cnki.net

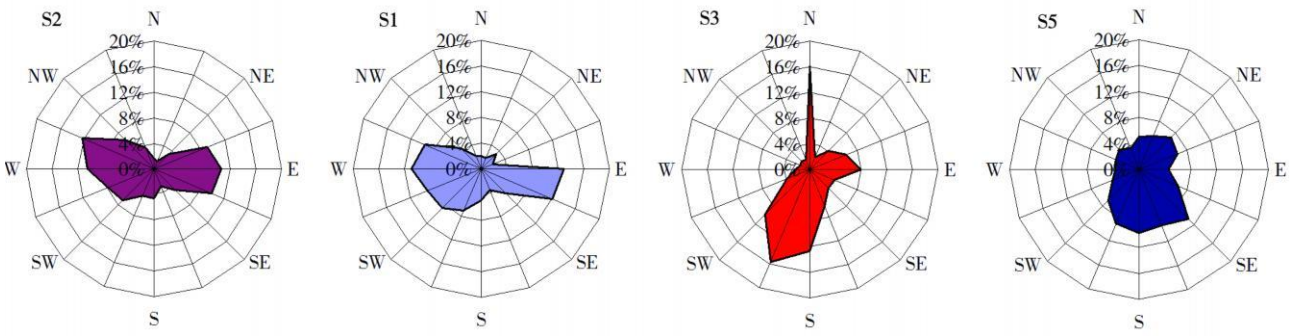


图 6 四个自动气象站的风向玫瑰图

Fig 6 Wind rose Chart at four AWSs

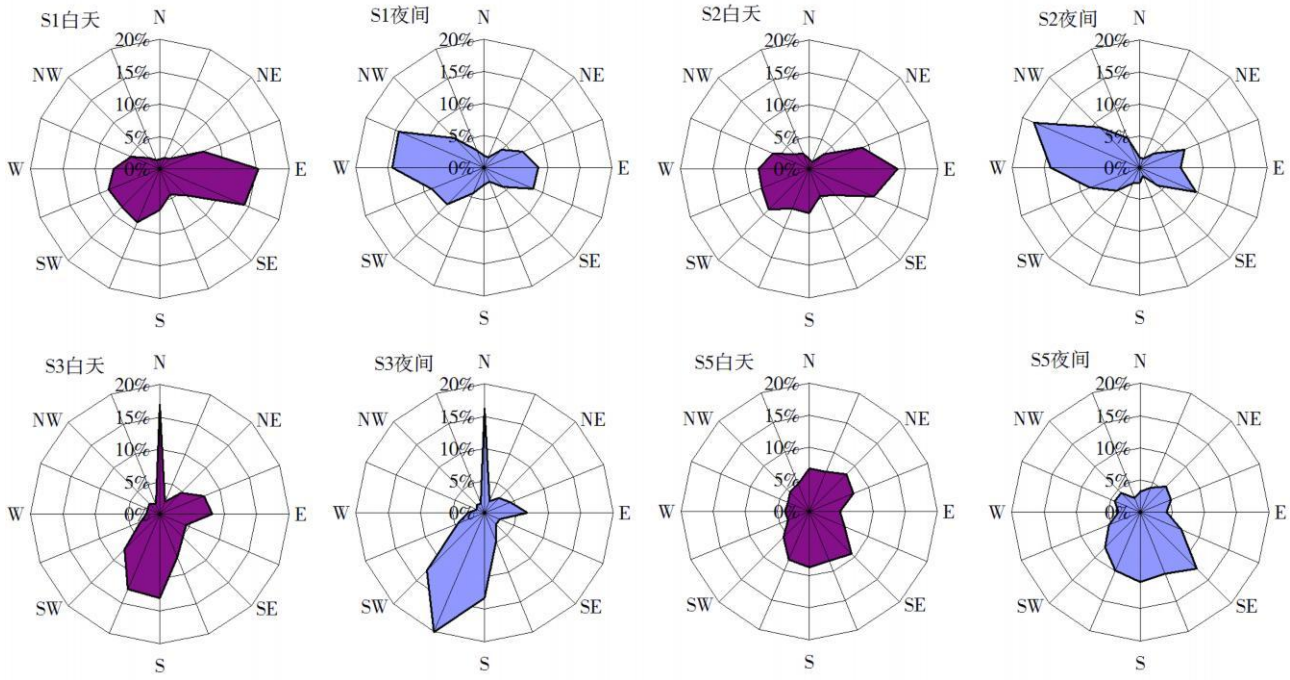


图 7 4个自动气象站的白天和夜间的风向玫瑰图

Fig 7 Wind rose chart at four AWSs in day and night

偏南风和偏北风的比例分别是 51.1% 和 19.7%。显然, 在夜间这两个站点以下降的冰川风 (偏南风) 占绝对优势, 相对于夜间, 这两个站点白天沿冰面上升的风向比例比夜间稍微大一点, 但下降的冰川风仍然是占优势的。而位于冰川末端的 S1 和冰川谷内的 S2 自动气象站, 相反的风向频率在白天和夜间互占优势, 即白天这两个站以沿谷地向冰川表面吹的谷风 (偏东风) 稍占优势, 而夜间则以与白天相反的沿冰川表面吹向冰川谷地的冰川风 (偏西风) 占绝对优势 (图 7)。在白天, S1站偏东风与偏西风的比例分别是 44.6% 和 31.5%, S2站偏东风与偏西风的比例分别是 42.6% 和 33.9%; 而到了夜间, S1站偏东风与偏西风的比例分别是 31.9% 和 52.2%, S2站偏东风与偏西风的比例分别是 31.0% 和 54.5%。

从风速统计结果来看, S1、S2、S3、S5, 4个站的平均风速基本在 2 m/s左右, 非冰川下垫面上的风速稍大于冰川下垫面上的风速, 风速有从冰川末端向冰川中上部逐渐减小的趋势。在不同方向上的主导风速、日平均风速等变化都不大, 没有明显规律性, 这里就不再详细描述。

### 2.6 降水

造成天山乌鲁木齐河源区降水的天气过程可以分为三类: 高空槽前, 地面冷锋入侵; 高空西风带小波动和地面闭合小高压掠过; 高空脊控制下的天气[24]。这里笼统地把前两类天气过程归为系统性天气过程, 把后一类归为局地对流性天气。冰川下垫面的致冷作用对系统性天气过程带来的降水基本起不到影响作用 (这里不讨论地形对降水的影响),



© 1994-2011 China Academic Journal Electronic Publishing House. All rights reserved. http://www.cnki.net

而只对局地对流性天气过程的降水产生影响。本文在上述基础上分析河源区不同地点的降水情况。

对河源区 DXG、S2、S1、S3, 4个站 7月 18日 8: 00~ 8月 16日 20: 00的降水量按照白天 ( 8: 00~ 20: 00)和夜间 ( 20: 00~次日 8: 00)进行了整理和计算 (表 2), 从该时段的降水总量看, 上述 4个气象站记录到的降水总量有随高度逐渐减少的趋势。但考虑到本地区在降雪的情况下降水量观测误差增大[17-18], 首先把负温情形下的降水量去除, 即如果各个观测时段内 ( 12 h)有一个以上的自动站平均温度低于 0 ℃, 那么四个自动站在该时段的降水量均不列入计算范围; 然后在冰川下垫面的致冷作用对系统性天气过程带来的降水不起影响作用的假定条件下, 把系统性天气过程带来的降水量去除 (这里把四个自动站 12 h记录同时超过 10 mm 的降水量作为系统性天气过程带来的降水 )。最终结果显示, 局地对流性降水并没有出现随海拔高度的升高而降低的现象, 而是随海拔升高而逐渐增大, 到冰川末端 ( S1)处达到最大, 而这里正是冰川致冷作用导致的温跃值最大之处, 然后从冰舌前缘沿冰川表面向上降水量又有所减少, 但冰面上 S3处的局地对流性降水降水量仍然比 DXG 要大。这里值得指出的是, 随着海拔高度的升高, 降水中以雪的形式出现的比重逐渐加大, 如作者几次观测到尽管气温高于 0 ℃, 冰川表面的降水仍然以降雪的形式出现, 这就增大了该处降水量的观测误差, 因此不排除冰川表面的实际降水量比本文给出的观测值要更大一些的可能性。上述数据表明冰川下垫面的致冷效应对局地对流性降水产生了一定的影响, 使降水量似乎随着与冰川距离的接近而增大, 但更确切的结论还需要用其他更为准确的观测方式和观测值来得出[17-19]。

表 2　乌鲁木齐河源区不同站点的降水量
( 2007年 7月 18日 ~ 8月 16日 )

Tab. 2　Precipitation of different AWSs at the Headwater of Urumqi River( Jul. 18– Aug. 16, 2007)

| 自动站编号 | DXG | S2 | S1 | S3 |
|---|---|---|---|---|
| 降水总量 /mm | 141. 1 | 134. 2 | 134. 4 | 100 |
| 去除负温天气后降水量 /mm | 109. 4 | 115 | 123 | 99. 2 |
| 去除系统性天气过程降水量 /mm | 53. 8 | 69. 2 | 77. 2 | 61. 6 |
| 白天降水量 /mm | 35. 4 | 53. 6 | 61. 4 | 53. 2 |
| 夜间降水量 /mm | 18. 4 | 15. 6 | 15. 8 | 8. 4 |
| 日: 夜降水量比率 /% | 192. 3 | 343. 6 | 388. 6 | 633. 3 |

从表 2中还可以看到, 局地对流性降水主要发生在白天, 白天与夜间降水量的比率随海拔高度的上升迅速增大, 到冰川中部其比率更高达 6. 3: 1, 这与河源区对流性天气的发展过程一致[24], 也表明冰川下垫面的致冷效应对局地对流性降水产生的影响是白天大于夜间。

## 3　结 论

通过对天山乌鲁木齐河源区 1个月的气象观测的计算分析, 结果表明冰川下垫面的存在对该区域的小气候产生了比较明显的影响。如冰川的致冷效应使冰面与非冰面之间存在明显的温跃现象, 从冰川谷地到冰舌末端的气温垂直递减率最大, 可达 – 2. 69 ℃ /100 m, 是自由大气中的平均气温垂直递减率的 3倍多, 冰舌末端到冰川中部的气温垂直递减率也高达 – 1. 37 ℃ /100 m。冰雪的高辐射特征使得冰川表面 1. 5 m 以下存在非常显著的逆温现象, 1. 5 m 处比 0. 5 m 处的气温 (取 30 d平均) 高 0. 67 ℃。观测期间各自动站风向主要受到冰川风和地形的影响。冰面上两个站点始终以沿冰面下降的风 (冰川风 )为主, 而非冰川下垫面上两个自动气象站的风向除受到冰川风和地形的双重影响而改变主导方向外, 白天和夜间的主要风向频率也发生变化, 在白天以沿谷地向冰川表面吹的谷风稍占优势, 而夜间则以沿冰川表面吹向冰川谷地的冰川风占更大优势。

冰川下垫面的致冷效应导致的温跃现象、冰面逆温以及冰川风等很可能对局地对流性降水产生了一定程度的影响。几个自动气象站的降水数据分析表明, 局地对流性降水量并没有出现随海拔高度的升高而降低, 而是逐渐升高, 到冰川末端达到最大, 似乎出现随着与冰川距离的接近而增大的现象。对这一问题的深入探讨还需要大量更为细致和准确的观测和研究工作。

致谢: 感谢中国科学院天山冰川观测试验站全体人员在野外考察和观测期间的无私帮助; 感谢新疆气象局大西沟气象站观测人员提供 2007年 7~ 8月份部分自动气象站资料。金爽同学、中国科学院冰冻圈科学国家重点实验室的刘宇硕和杜文涛同学在自动气象站维护和数据采集方面做了大量的工作, 在此深表谢意。



© 1994-2011 China Academic Journal Electronic Publishing House. All rights reserved.　http://www.cnki.net

## 参考文献(References)


〔1〕 BARRY R G. 安顺清,王长根译. 山地天气和气候〔M〕. 北京:气象出版社, 1988. 165-245. 〔BARRY R G. Mountain weather and climate〔M〕. Methuen & Co. Ltd, 1981.〕

〔2〕 KUKLA G. Snow covers and climate〔C〕//KUKLA G, HECHT A, WIESNET D, eds. Snow watch 1980. World Data Center A - Glaciology, University of Colorado, Boulder, 1981.

〔3〕 白重瑗. 冰川与气候关系的研究〔J〕. 冰川冻土, 1989, 11(4): 287-309. 〔BAI Chongyuan. A study of relationship between climate and mountain glaciers〔J〕. Journal of Glaciology and Geocryology, 1989, 11(4): 287-309.〕

〔4〕 陈恩久. 天山冰川小气候特征〔J〕. 地理, 1963, 5: 193-200. 〔CHEN Enjiu. The microclimate characteristics of Tianshan glaciers〔J〕. Geography, 1963, 5: 193-200.〕

〔5〕 陈金玺,肖鈖. 天山胜利达坂 1号冰川夏季小气候〔C〕//新疆维吾尔自治区科学技术委员会, 新疆冰川积雪研究文集, 1964: 137-145. 〔CHEN Jinxi, XIAO Shu. The summer microclimate of glacier No. 1, Shengli Daban, Tianshan〔C〕//Science and Technology committee of Xinjiang Uygur Autonomous Region. Collections of glacier and snow study in Xinjiang, 1964: 137-145.〕

〔6〕 张东启,周尚哲. 天山乌鲁木齐河源 1号冰川对降水影响的定量分析〔J〕. 冰川冻土, 2000, 22(3): 243-249. 〔ZHANG Dongqi, ZHOU Shangzhe. Quantitative analysis of the glacial effect on precipitation of Glacier No. 1 at the headwaters of the Urumqi River, Tianshan Mountains〔J〕. Journal of Glaciology and Geocryology, 2000, 22(3): 243-249.〕

〔7〕 李跃清,刘辉志,冯健武,等. 高山草甸下垫面夏季近地层能量输送及微气象特征〔J〕. 大气科学, 2009, 33(5): 1003-1014. 〔LI Yueqing, LIU Huizhi, FENG Jianwu, et al. Characteristics of energy transfer and micrometeorology in the surface layer of the atmosphere in summer over the alpine meadow of the Tibetan Plateau〔J〕. Chinese Journal of Atmospheric Sciences, 2009, 33(5): 1003-1014.〕

〔8〕 林之光. 地形降水气候学〔M〕. 北京:科学出版社, 1995. 〔LIN Zhiguang. Climatology of topographic precipitation〔M〕. Beijing: Science Press, 1995.〕

〔9〕 沈永平,梁红. 高山冰川区大降水带的成因探讨〔J〕. 冰川冻土, 2004, 26(6): 806-809. 〔SHEN Yongping, LIANG Hong. High precipitation in glacial region of high mountains in High Asia: possible cause〔J〕. Journal of Glaciology and Geocryology, 2004, 26(6): 806-809.〕

〔10〕 韩海东,刘时银,丁永健,等. 科其喀尔巴西冰川的近地层基本气象特征〔J〕. 冰川冻土, 2008, 30(6): 967-975. 〔HAN Haidong, LIU Shiyin, DING Yongjian, et al. Near surface meteorological characteristics on the Koxkar Baxi Glacier, Tianshan〔J〕. Journal of Glaciology and Geocryology, 2008, 30(6): 967-975.〕

〔11〕 OERLEMANS J, BJÖRNSSON H, KUHN M, et al. Glacio-meteorological investigations on Vatnajökull, Iceland, summer 1996: an overview〔J〕. Boundary-Layer Meteorology, 1999, 92: 3-26.

〔12〕 SODERBERG S, PARMHED O. Numerical modeling of Katabatic flow over a melting outflow glacier〔J〕. Boundary-Layer Meteorology, 2006, 120: 509-534.

〔13〕 DING Yongjian. Some glacio-micrometeorological features on the north side of Mount Qogir (K2), Karakoram Mountain〔J〕. Annals of Glaciology, 1992, 16: 67-72.

〔14〕 KONYA K, MATSUMOTO T. Influence of weather conditions and spatial variability on glacier surface melt in Chilean Patagonia〔J〕. Theor Appl Climatol, Published online: 02, Feb, 2010, DOI: 10.1007/s00704-009-0248-0.

〔15〕 GREUELL W, KNAP W H, SMEETS P C. Elevational changes in meteorological variables along a mid-latitude glacier during summer〔J〕. Journal of Geophysical Research, 1997, 102: 25941-25954.

〔16〕 刘潮海. 祁连山冰面气温的推算和温度跃动值的确定〔C〕//中科院兰州冰川冻土研究所集刊(7). 北京:科学出版社, 1992: 34-39. 〔LIU Chaohai. Calculation of ice surface temperature and determination of temperature jump value in Qilian Mountain〔C〕//Memoirs of Lanzhou Institute of Glaciology and Geocryology, Chinese Academy of Seicnces, No. 7. Beijing: Science Press, 1992: 34-39.〕

〔17〕 杨大庆,姜彤,张寅生,等. 天山乌鲁木齐河源降水观测误差分析及其改正〔J〕. 冰川冻土, 1988, 10(4): 384-399. 〔YANG Daqing, JIANG Tong, ZHANG Yinsheng, et al. Analysis and correction of errors in precipitation measurement at the head of Urümqi River, Tianshan〔J〕. Journal of Glaciology and Geocryology, 1988, 10(4): 384-399.〕

〔18〕 杨大庆,施雅风,康尔泗,等. 天山乌鲁木齐河流域降水观测系统误差分析和修正〔C〕//乌鲁木齐河山区水资源形成和估算. 北京:科学出版社, 1992: 14-40. 〔YANG Daqing, SHI Yafeng, KANG Ersi, et al. Analysis and correction of systematic errors in precipitation measurement in the Urümqi River Basin, Tianshan〔C〕//Formation and estimation of mountain water resources in the Urümqi River Basin. Beijing: Science Press, 1992: 14-40.〕

〔19〕 张寅生,康尔泗,杨大庆. 乌鲁木齐河流域高寒区蒸发量观测试验研究〔C〕//乌鲁木齐河山区水资源形成和估算. 北京:科学出版社, 1992: 79-89. 〔ZHANG Yinsheng, KANG Ersi, YANG Daqing. Experimental study on the evaporation in the high-altitude area of the Urümqi River Basin〔C〕//Formation and estimation of mountain water resources in the Urümqi River Basin. Beijing: Science Press, 1992: 79-89.〕

〔20〕 BAI Chongyuan, YU Xinzhi. Energy exchange and its influence factors on mountain glaciers in West china〔J〕. Annals of Glaciology, 1986, 6: 154-157.

〔21〕 OHATA T, BAI Chongyuan, DING Liangfu. Heat balance study on glacier No. 1 at head of Urumqi River, Tianshan Mountains, China〔J〕. Journal of Glaciology and Geocryology, 1989, 11(4): 298-323.

〔22〕 BROEKE Van den, MOMENTUM M R. Heat and moisture budgets




© 1994-2011 China Academic Journal Electronic Publishing House. All rights reserved. http://www.cnki.net

of the Katabatic Wind Layer over a mid-latitude glacier in summer〔J〕. J Appl Meteorol, 1997, 36(6): 763-774

〔23〕施雅风, 黄茂桓, 任炳辉. 中国冰川概论〔M〕. 北京: 科学出版社, 1988: 21. 〔SHI Yafeng, HUANG Maohuan, REN Binghui. An introduction to the glaciers in China〔M〕. Beijing: Science Press, 1988: 21.〕

〔24〕王德辉, 张丕远. 天山乌鲁木齐河谷气候特征〔J〕. 冰川冻土, 1985, 7(3): 239-248. 〔WANG Dehui, ZHANG Peiyuan. On the valley climate of Urumqi River in the Tianshan Mountains〔J〕. Journal of Glaciology and Geocryology, 1985, 7(3): 239-248.〕

# Microclimate measurements related to glacier cooling effect at No. 1 glacier, headwater of Urumqi River, Tianshan Mountains

ZHANG Dong-qi[1,2], MING Jing[3], WEI Wen-shou[2]

(1. Chinese Academy of Meteorological Sciences, Beijing 100081, China; 2. Institute of Desert Meteorology, China Meteorological Administration, Urumqi 830002, Xinjiang, China; 3. National Climate Center, Beijing 100081, China)

**Abstract**: Glacier microclimate comes into being when there exist mountain glaciers in temperate latitudes and they interact with surrounding environment through the glacier cooling effect. Little studies focused on the glacier cooling effect. To study the characteristics of glacier microclimates related to glacier cooling effect, especially effects on local precipitation, five Automatic Weather Stations (AWS) were established at the surface of No. 1 glacier, the headwater of the Urumqi River, the Tianshan Mountains in July, 2007, and basic meteorological data were collected for 30 days. The temperature and humidity characteristics and glacier cooling effect related phenomena are described and analyzed based on these data. One month observation data indicate that the existence of glacier surface has a distinct impact on local microclimate of the surrounding region, including local temperature, humidity, wind direction and convective precipitation. Temperature jump exists between glacier and non-glacier surface and the vertical temperature descending rate is -1.37 ℃/100 m from the glacial valley to the glacier tongue, which is much larger than that in free atmosphere (about 0.67 ℃/100 m). The temperature jump graduates away on the connatural surface such as glacier surface and alpine meadow. There is a distinct inversion layer between the heights of 1.5 m and 0.5 m on the glacier surface at most observation times, the average temperate at 0.5 m height is 0.67 ℃ lower than that at 1.5 m height. The inversion layer was influenced strongly by cloud covers and wind speed. Generally, it is more distinct on clear days than on cloudy or snowing days and so forth on nighttime than on daytime. The relative humidity at 1.5 m height is smaller than that at 0.5 m height above the glacier surface and it varies in different weather conditions. Wind direction statistical analyses indicate that all AWS's wind directions were influenced by glacier breeze and topography during the observation period, and the glacier breeze dominates on the glacier surface with two-AWS for whole day. In the glacial valley with two-AWS, the valley wind and glacier breeze dominate alternately in the daytime and nighttime. The glacier cooling effect has a potential influences on local convective precipitation. A cursory partition method was applied to the precipitation data of the research region and the result indicates that the more closer to the glacier, the more convective precipitation occurs. But it's a complicated phenomenon, and the influence of topography is not excluded. More meticulous and precise observation and research work is necessary to discuss this topic in depth.

**Key Words**: No. 1 glacier; Headwater of Urumqi River; Tianshan Mountains; microclimate obversation; glacier cooling effect



© 1994-2011 China Academic Journal Electronic Publishing House. All rights reserved. http://www.cnki.net

# 一种处理漫射因子的新方法*

张 峰[1)2)] 张 华[2)†] 沈钟平[3)] 卫晓东[1)]

1)(中国气象科学研究院, 北京 100081)

2)(中国气象局国家气候中心, 北京 100081)

3)(上海市气候中心, 上海 200030)

(2010 年 2 月 6 日收到;2010 年 3 月 18 日收到修改稿)

提出了一种新的处理漫射因子的拟合方案,通过与前人提出的方案相比,具有较高的拟合精度;然后,将该拟合方案和前人提出的方案同时放入辐射传输模式中来计算大气加热率,结果表明:新方案的结果总体上优于前人的结果,尤其是对 45 km 以上的中间层大气.

**关键词:** 漫射因子, 指数积分, 加热率

**PACS:** 07.57.Hm, 42.68.Ay, 42.68.Ca

## 1. 引 言

大气中的辐射传输过程包括大气吸收、散射和热辐射过程[1—3]. 它在气溶胶遥感反演中起着非常重要的作用[4—6]. 在辐射传输过程中,辐射通量和大气冷却率(加热率)的计算必须要进行四重积分,即除了进行沿光学路径、光学厚度的垂直积分以及频率积分外,还必须对天顶角进行角度积分[7]. 在实际计算过程中,很难对以上积分进行精确计算,常常对以上积分进行简化和近似处理,其中漫射因子近似便是对天顶角进行角度积分的一种简化处理方法. Elsasser 在 1942 年提出了漫射率因子近似为 1.66,该结果已经广泛应用于大气辐射传输计算过程中[7], Rodgers 和 Walshaw[8] 表示漫射因子 1.66 近似所带来的水汽转动带的最大冷却率相对误差不应该超过 1.5%, Goody 和 Yung[7] 对此问题也进行过详细的讨论,认为这种近似可以满足大气辐射计算的需要,并指出该近似所产生的加热率误差不应该超过 2%. 然而,以上结论均局限于压力加宽的 Lorentz 线型的范围内, Shi[9] 及 Xu 和 Shi[10] 的研究发现:在平流层的中上部,1.66 近似所带来的误差有可能高达 5%—10%. 为了克服 1.66 常数漫射率因子所带来得误差, Shi 和 Qu[11] 最先提出了一个漫射率因子随光学厚度变化的近似表达式;随后, Zhang 和 Shi[12] 提出了一个精度更高的拟合公式. 但 Zhang 和 Shi[12] 提出的公式在光学厚度为 5 附近和光学厚度大于 15 时仍较大误差.

本文在前人工作的基础上,提出了一个在更宽广的光学厚度范围内拟合精度更高的新的公式;然后,将该拟合公式和前人提出的公式同时放入到辐射传输模式中,计算大气加热率并进行比较.

## 2. 理论分析

在长/短波辐射通量和大气加热率的计算过程中,从高度 $z$ 到 $z'$ 的通量通过率 $T_r(z,z')$ 是一个重要的物理量,其定义如下:

$$T_r(z,z') \equiv 2\int_0^1 \exp[\tau_v(z,z')]\mu \mathrm{d}\mu = 2E_3(\tau_v(z,z')). \quad (1)$$

其中 $\mu$ 为天顶角的余弦; $\tau_v(z,z')$ 为光学厚度,定义为

$$\tau_v(z,z') = \int_z^{z'} K_v(z'')\rho_a(z'')\mathrm{d}z'', \quad (2)$$

其中 $\rho_a(z'')$ 和 $K_v(z'')$ 分别代表质量吸收系数和吸收物质的密度. 由于指数积分 $2E_3(x)$ 的特性与指数函数 $\exp(-rx)$ 的特性相似($r$ 为数值因子),因此有许多作者试图用指数函数来表示通量透过率,取

$$T_r(z,z') \cong \exp(-r\tau_v(z,z')), \quad (3)$$

* 国家自然科学基金(批准号:40775006)和国家重点基础研究发展计划(批准号:2011CB403405)资助的课题.

† 通讯联系人. E-mail: huazhang@cma.gov.cn

©2011 中国物理学会 Chinese Physical Society 

上式中 $r$ 则被称作为漫射率因子,由(1)和(3)式可以得一个 $r$ 的精确表达式

$$r = \frac{-\ln[2E_3(\tau_v(z,z'))]}{\tau_v(z,z')}. \tag{4}$$

Elsasser 提出了 $r$ 的最好近似取值是 1.66[7],显然 $r$ 不应该是一个常数,而是随着光学厚度变化的. $r$ 随 $\tau_v$ 的变化可以如图 1 曲线 $A$ 所示. 从理论上可以证明 $r$ 应当在 1 到 2 之间变化:当 $\tau_v \to 0$ 时,$r \to 2$;当 $\tau_v \to \infty$ 时,$r \to 1$[11]. 只有当 $\tau_v = 0.4$,$r$ 才等于 1.66. 因此用常数漫射因子(1.66)来处理任意光学厚度的天顶角角度积分,必然会给辐射通量和加热率的计算带来误差.

为了克服 1.66 的常数漫射因子所带来的误差,我们提出一种新的简单的数学表达式来描述 $r$ 随光学厚度 $\tau_v$ 的变化,表达式为

$$r = 2 - \frac{a\tau_v^b}{(c\tau_v^d + e)^f}, \tag{5}$$

该表达式满足 $\tau_v \to 0$ 时 $r \to 2$. 对上式中的含六参数($a$, $b$, $c$, $d$, $e$, $f$)的表达式,在实际大气中光学厚度最有可能的区间 $0 \leqslant \tau_v \leqslant 30$ 进行非线形拟合得到 $a = 0.8637$, $b = 0.8434$, $c = 0.7832$, $d = 0.4864$, $e = 0.5915$ 及 $f = 1.8257$. 并把该六参数代入(5)式得到

$$r = 2 - \frac{0.8637\tau_v^{0.8434}}{(0.7832\tau_v^{0.4864} + 0.5915)^{1.8257}}. \tag{6}$$

上述拟合公式虽然是在 $0 \leqslant \tau_v \leqslant 30$ 范围上得到的,但是已经足以满足实际大气的计算范围,因为当 $\tau_v \geqslant 30$ 之前,透过率函数 $T_r(z,z')$ 实际上早已经变为零.

Shi 和 Qu[11] 的拟合方案是在 $\tau_v \to 0$ 时 $r \to 2$;$\tau_v \to \infty$ 时 $r \to 1$ 的限制下用双曲线进行拟合得到的(如图 1 中的曲线 $F$ 所示). Shi 和 Qu 的拟合结果和由(4)式给出精确结果存在较大的误差,他们的拟合结果在光学厚度 $\tau_v \geqslant 0.01$ 时,相对误差几乎都超过 1%,最大相对误差高达 10%. 鉴于此,Zhang 和 Shi[12] 放弃 $\tau_v \to 0$ 时 $r \to 2$ 及 $\tau_v \to \infty$ 时 $r \to 1$ 的限制条件,并选用实际大气中最有可能出现的光学厚度范围进行拟合,结果如图 1 中的曲线 $C$ 所示,该结果较 Shi 和 Qu 的拟合结果有较大改进,但是,他们的结果在光学厚度非常小时,即 $\tau_v \to 0$ 时,相对误差超过了 Shi 和 Qu 的拟合结果(如图 2 中曲线 $C$ 所示). Zhang 和 Shi 的拟合结果在光学厚度为 1 到 7 范围之间的相对误差约为 10%,并且当光学厚度大于 15 时,相对误差增加较快. 因此,有必要提出一个新的拟合公式对此加以改进. 如图 1 中曲线 $B$ 所示,本文的拟合结果和精确值符合得非常好;当 $\tau_v \leqslant 20$ 时,该拟合结果的相对误差都在 0.01% 以内(见图 2 曲线 $B$),并在实际大气中光学厚度最有可能的区间 $0 \leqslant \tau_v \leqslant 30$ 内,最大相对误差不超过 0.03%. 综上所述,本文构造的公式更符合漫射率因子随光学厚度的变化特征,该结果与精确结果相比,比前人提出的公式具有更高的精度.

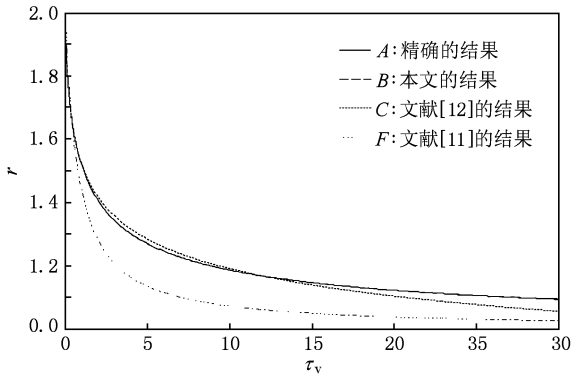


图 1 漫射因子 $r$ 随光学厚度 $\tau_v$ 的变化

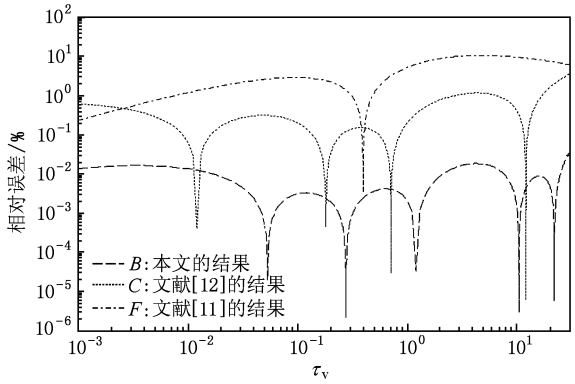


图 2 漫射因子拟合公式的相对误差随光学厚度 $\tau_v$ 的变化

## 3. 结果比较

本文在计算中采用 McClatchey[13] 的热带大气,所用的模式为改进的 BSTAR5C/CCSR/NCC 辐射传输模式[14—16],将其中的高光谱分辨率的 998 带方案应用于下面的研究中. 998 带方案是一个高精度的 $k$ 分布辐射传输模式,其精度几乎与精确的逐线积分模式相当. 但其计算速度大大提高,可以替代逐线积分模式应用于大气遥感和地面太阳辐射谱分布[17]等精度要求比较高的辐射传输计算中. 该模式

的长波区间10—2680 $cm^{-1}$被划分为534个带,平均谱分辨率宽度为5 $cm^{-1}$;短波2680—50000 $cm^{-1}$区间被划分为464个带,平均谱分辨率为0.076 μm[16],并考虑了水汽、二氧化碳、臭氧、氧化亚氮、甲烷和氧气等主要温室气体的吸收,以及云和气溶胶的吸收和散射过程.其中云和气溶胶散射辐射采用Nakajima等[18]的算法,温室气体吸收算法采用Zhang等[14—16]的算法.

图3是大气加热率的精确结果,其中的漫射因子采用方程(4)进行精确处理.图4给出用不同的漫射因子的近似方案计算的大气加热率结果的绝对误差.从图上可以看出,总体上,Shi和Qu的结果误差比较大,而Zhang和Shi的结果及本文的结果误差比较小,都在±0.05 K/d内.本文的结果在30 km以下与Zhang和Shi的结果基本一致;在30 km到45 km之间的平流层大气,Zhang和Shi的结果略优于本文;而在45 km到60 km之间的中间层大气,本文的结果优于Zhang和Shi.这是因为,本文提出的漫射因子公式虽然在总体上优于Zhang和Shi的拟合方案,但是,长波区间总的加热率结果不仅取决于漫射因子,还取决于在各个波段加热率结果在相加过程中的误差抵消,这个可能导致Zhang和Shi的结果在30 km到45 km之间精度略优于本文的结果.总的来说,用本文提出的新方法能得到高精度的大气加热率结果,特别是对45 km以上的中间层大气.

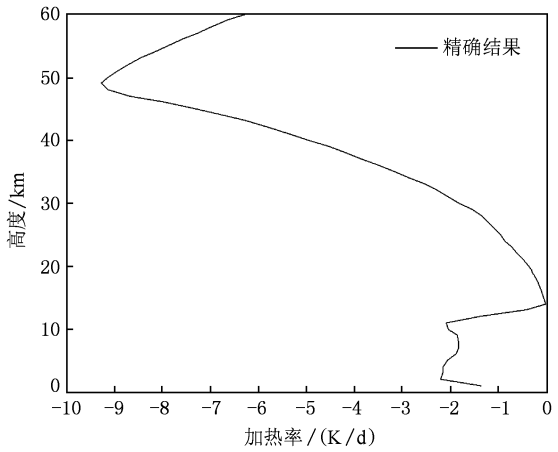


图3 大气加热率随高度的变化

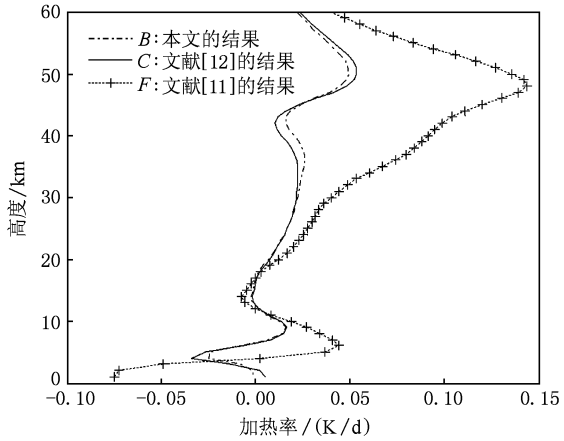


图4 加热率误差比较

## 4. 结 论

本文在前人工作的基础上,提出了一个新的漫射因子拟合公式.研究表明,本文的拟合公式在更宽广的光学厚度范围内比前人提出的公式具有更高的精度.在实际大气中光学厚度最有可能的区间$0 \leqslant \tau_v \leqslant 30$内,本文提出漫射因子拟合方案的最大相对误差不超过0.03%.然后,我们将本文和前人提出的漫射因子拟合方案同时放入辐射传输模式对大气加热率结果进行比较发现:本文的方案能获得较高精度的大气冷却率,特别是在45 km以上的中间层大气,利用本方案计算得到的大气加热率的精度最高.

[1] Liang Z C, Jin Y Q 2002 *Acta Phys. Sin.* **51** 2239 (in Chinese) [梁子长、金亚秋 2002 物理学报 **51** 2239]

[2] Liang Z C, Jin Y Q 2003 *Acta Phys. Sin.* **52** 247 (in Chinese) [梁子长、金亚秋 2002 物理学报 **52** 247]

[3] Duan M Z, Guo X 2009 *Acta Phys. Sin.* **58** 1353 (in Chinese) [段民征、郭霞 2009 物理学报 **58** 1353]

[4] Han Y, Wang T J, Rao R Z, Wang Y J 2008 *Acta Phys. Sin.* **57** 7396 (in Chinese) [韩永、王体健、饶瑞中、王英俭 2008 物理学报 **57** 7396]

[5] Zuo H Y, Yang J G 2007 *Acta Phys. Sin.* **56** 6132 (in Chinese) [左浩毅 杨经国 2007 物理学报 **56** 6132]

[6] Du H D, Huang S X, Shi H Q 2008 *Acta Phys. Sin.* **57** 7685 (in Chinese) [杜华栋、黄思训、石汉青 2008 物理学报 **57** 7685]

[7] Goody R M, Yung Y L 1989 *Atmospheric radiation: theoretical basis* (Oxford: Oxford University Press) p49

[8] Rodgers C D, Walshaw C D 1966 *Quart. J. Roy. Met. Soc.* **92** 67

[9] Shi G Y 1984 *Sci. China Ser.* B **24** 378 (in Chinese) [石广玉 1984 中国科学 B **24** 378]

[10] Xu L, Shi G Y 1985 *Adv. Atoms. Sci.* **2** 531

[11] Shi G Y, Qu Y N 1985 *Chin. Sci. Bull.* **24** 1887 (in Chinese) [石广玉、曲燕妮 1985 科学通报 **24** 1887]

[12] Zhang H, Shi G Y 2001 *J. Quant. Spectro. Radia. Trans.* **70** 367

[13] McClatchey R A, Fenn R W, Selby J E A, Volz F E, Garing J S 1972 *Optical Properties of the Atmosphere* 3rd edn (AFCRL-72-0497, Air Force Geophysics Laboratory, Hanscom AFB, Massachusetts).

[14] Zhang H, Nakajima T, Shi G Y, Suzuki T, Imasu R 2003 *J. Geophys. Res.* **108** 4641

[15] Zhang H, Shi G Y, Nakajima T, Suzuki T 2006 *J. Quant. Spectro. Radia. Trans.* **98** 31

[16] Zhang H, Suzuki T, Nakajima T, Shi G Y, Zhang X Y, Liu Y 2006 *Opt. Eng.* **45** 016002

[17] Shen Z P, Zhang H 2009 *Acta Energiae Sol. Sin.* 30 1389 (in Chinese) [沈钟平、张 华 2009 太阳能学报 **30** 1389 ]

[18] Nakajima T, Tsukamoto M, Tsushima Y, Numaguti A, Kimura T 2000 *Appl. Opt.* **39** 4869

# A new approach to deal with diffusivity factor*

Zhang Feng[1)2)] Zhang Hua[2)†] Shen Zhong-Ping[3)] Wei Xiao-Dong[1)]

1) (*Chinese Academy of Meteorological Sciences, Beijing* 100081, *China*)

2) (*National Climate Center, China Meteorological Administration, Beijing* 100081, *China*)

3) (*Shanghai Climate Center, Shanghai* 200030, *China*)

(Received 6 February 2010; revised manuscript received 18 March 2010)

Abstract

In this paper, a new scheme, which is more precise in comparison with the previous ones in dealing with diffusivity factor is presented. The new scheme and the previous ones are applied to a radiative transfer model to calculate the atmospheric heating rate. The results show that the new scheme is generally better than previous ones, especially in the upper atmosphere al a height of more than 45 km.

**Keywords**: diffusivity factor, exponential integral, heating rate

**PACS**: 07.57.Hm, 42.68.Ay, 42.68.Ca

* Project supported by the National Natural Science Foundation of China (Grant No. 40775006) and the National Basic Research Program of China (Grant No. 2011CB403405)..

† Corresponding author. E-mail: huazhang@cma.gov.cn

中国科学: 地球科学 2011 年 第 41 卷 第 2 期: 225 ~ 233
www.scichina.com earth.scichina.com
《中国科学》杂志社
SCIENCE CHINA PRESS

论 文

# PFCs 和 $SF_6$ 的辐射强迫与全球增温潜能

张华[①*], 吴金秀[②①], 沈钟平[③①]

① 中国气象局气候研究开放实验室, 国家气候中心, 北京 100081;
② 上海市气象信息传媒中心, 上海 200030;
③ 上海市气候中心, 上海 200030
* E-mail: huazhang@cma.gov.cn

收稿日期: 2010-08-23; 接受日期: 2010-10-29
国家自然科学基金(批准号: 40775006)、国家重点基础研究发展计划(编号: 2010CB955703)和中国气象局气候变化专项课题(编号: 2010-2200509)资助

**摘要** PFCs 和 $SF_6$ 作为臭氧消耗物质(ODSs)的部分替代物质, 近年来排放量大大增加, 作为控制排放的人造长寿命温室气体已经被列入《京都议定书》. 本文采用最新的分子吸收数据库 HITRAN2004 中 PFCs 最主要的两种化合物 $C_2F_6$ 和 $CF_4$ 的吸收截面和 $SF_6$ 的吸收截面数据, 利用吸收系数重排法, 建立了它们的不同谱带精度(998-带和 17-带)的相关 k-分布计算方案, 比较了不同方案对计算结果的影响. 在此基础上, 采用高精度的 998-带辐射计算方案研究了它们晴空大气和有云大气下的瞬时辐射效率和平流层调整的辐射效率, 以及它们的全球增温潜能(GWP)和全球温变潜能(GTP). 本文的研究表明: $C_2F_6$, $CF_4$ 和 $SF_6$ 在有云大气下的平流层调整的辐射效率分别为 0.346, 0.098 和 0.680 W $m^{-2}$ $ppbv^{-1}$(ppbv 表示体积比为十亿分之一); 自工业革命到 2005 年的辐射强迫分别为 0.001, 0.007 和 0.004 W $m^{-2}$; 根据 IPCC(2007)给出的排放情景, 到 2100 年的辐射强迫分别为 0.008, 0.036 和 0.037 W $m^{-2}$. $C_2F_6$, $CF_4$ 和 $SF_6$ 相对于 $CO_2$ 的 100 a 的全球增温潜能 GWP 分别为 17035, 7597 和 31298; 100 a 的脉冲排放的全球温变潜能 $GTP^P$ 分别为 22468, 10052 和 40935; 持续排放的全球温变潜能 $GTP^S$ 分别为 16498, 355 和 30341. 与其他长寿命人造温室气体一道, 它们对全球变暖的长期影响不容忽视.

**关键词**
PFCs $SF_6$ 辐射强迫
全球增温潜能(GWPs)
全球温变潜能(GTPs)
相关 k-分布

由于臭氧消耗物质(ODSs)会导致平流层臭氧损耗, 《蒙特利尔协议》控制了这类化合物的生产和排放. 作为 ODSs 的替代品, PFCs 和 $SF_6$ 等化合物由于不含溴原子或氯原子, 对平流层臭氧没有威胁, 因此在过去的几十年中, 排放量大大增加. 同时, 由于它们也是非常强的温室气体, 作为控制排放的人造长寿命温室气体已经被列入《京都议定书》. PFCs 和 $SF_6$ 以下两个特性使它们成为有效的温室气体. 首先, 它们具有相当长的大气寿命, 例如 $CF_4$ 的大气寿命长达 50000 a, 一旦排放, 将在大气中停留 50000 a 之久. 工业革命前, $CF_4$ 的自然背景浓度约为 40 pptv(pptv 表示体积比为万亿分之一), $C_2F_6$ 和 $SF_6$ 在大气中并不存在. 工业革命以来, 这些气体在大气中的含量迅速增加. 最新的观测数据表明[1], $CF_4$ 的大气含量为 74

英文引用格式: Zhang H, Wu J X, Shen Z P. Radiative forcing and global warming potential of perfluorocarbons and sulfur hexafluoride. Sci China Earth Sci, 2011, doi: 10.1007/s11430-010-4155-0



© 1994-2011 China Academic Journal Electronic Publishing House. All rights reserved. http://www.cnki.net

pptv; $C_2F_6$ 的大气含量为 2.9 pptv; $SF_6$ 的大气含量为 5.6 pptv. 其次, PFCs 和 $SF_6$ 的吸收光谱主要位于"大气窗区"内, 对地面长波辐射有很强的吸收, 因而改变了这一光谱区域大气的吸收性质, 对地气系统向外空的辐射冷却产生了很大的影响[2]. 单个 PFCs 和 $SF_6$ 的分子吸收地球辐射能量的效率比单个 $CO_2$ 分子高出数千倍. 因此, 即使少量的这类气体排放就可能对温室气体总的辐射强迫做出较大贡献, 并由此对地球辐射平衡和气候产生持续的影响[2].

为了研究人造长寿命温室气体浓度增加对全球变暖的贡献, 很多学者研究了 PFCs 和 $SF_6$ 的辐射强迫. 这些研究使用了不同的分子吸收数据库, 包括 Spectroscopy and Warming Potentials of Atmospheric Greenhouse Gases (SWAGG)[3], High-resolution Transmission Molecular Absorption (HITRAN)[4,5]和 Ford Motor Company[6,7]等. 所采用的辐射方案主要是带宽 5 或 10 $cm^{-1}$ 的窄带模式[3,4,6,7]. 为了得到更加准确的结果, 在更新的谱吸收资料基础上, 本文利用高精度 998-带辐射方案[8,9]和相关 k-分布方法[10]建立了 PFCs 和 $SF_6$ 的新的辐射传输方案.

## 1 谱吸收资料和模式介绍

HITRAN 分子吸收资料集是国际科学界公认和被广泛应用于大气辐射传输计算的基础资料. 该数据库每 4 a 左右更新一次, 经 HITRAN1986, HITRAN1992 和 HITRAN2000 发展到目前的 HITRAN2004 版本. 本文采用 HITRAN2004 中在严格的实验室条件下测得的不同温度和压强下 $C_2F_6$, $CF_4$ 和 $SF_6$ 的红外吸收截面资料. 首先, 通过分析吸收系数对压力和温度的依赖关系, 分别对已知温度和压力下的吸收系数进行线性插值, 得到 22 个压力和 3 个温度下的吸收截面. 22 个压力分别是 0.01, 0.0158, 0.0215, 0.0251, 0.0464, 0.1, 0.158, 0.215, 0.398, 0.464, 1.0, 2.15, 4.64, 10.0, 21.5, 46.4, 100.0, 220.0, 340.0, 460.0, 700.0 和 1013.25 hPa; 三个温度分别为 160 , 260 和 320 K, 它们基本上覆盖了实际地球大气能出现的范围. 以压强为例, 在同一个温度下, 对于待插压强的上下两个已知压强上的吸收系数进行线性插值, 得到该温度, 该压强下的吸收系数. 与以前研究中普遍使用的某一温度和压强下的积分吸收截面[3,6,11]相比, 更准确地考虑了温度和压强的影响. 随着 HITRAN 资料的进一步完善, 温度和压强组合增加, 使用该处理方法能够得到更准确的结果.

图 1 给出了 HITRAN2004 中 $C_2F_6$, $CF_4$ 和 $SF_6$ 的典型吸收截面图(温度为 296 K, 压强为 1013.25 hPa). 由图 1 可见, $C_2F_6$ 在 1220~1285 $cm^{-1}$ 区间有一个较强的吸收带, 在 1061~1165 $cm^{-1}$ 区间有一个较弱的吸收带; $CF_4$ 在 1250~1290 $cm^{-1}$ 区间有一个很强的吸收带; $SF_6$ 在 925~955 $cm^{-1}$ 区间有一个变化剧烈的吸收带. 它们共同的吸收特点是在较窄的谱带中有较强的吸收.

Zhang 等[8] 的 17 带辐射方案将长波区间 10~2680 $cm^{-1}$(3.7~1000 μm)分为 8 个带, 每个带上的 k-间隔数量不等, 见表 1. Zhang 等[9]的 998 带辐射方案将长波区间 10~2680 $cm^{-1}$ 平均分为间隔为 5 $cm^{-1}$ 的 534 个窄带, 每个带上的 k-间隔数量 2~16 不等, 谱带划分和 k-间隔数量详见 Zhang 等[9]. 模式中包括了 5 种主要温室气体: $H_2O$, $CO_2$, $O_3$, $N_2O$ 和 $CH_4$, 还考虑了 4 种 CFCs 化合物: $CCL_4$, CFC-11, CFC-12 和 CFC-13, 并假设这些 CFCs 在大气中混合均匀. 由表 1 可见, 17 带辐射方案中, $C_2F_6$, $CF_4$ 和 $SF_6$ 主要吸收位于第 4 到第 6 带. 在 998 带辐射方案中, $C_2F_6$ 在第 211~231 带和第 243~255 带共 34 个带上均有吸收, $CF_4$ 在 249~256 带上有吸收, $SF_6$ 在 184~190 带上有吸收. 因此, 高光谱精度的 998 带辐射方案几乎考虑了

**表 1 17-带结构**

| 带 | 区间($cm^{-1}$) | k-间隔数量 | 吸收气体 |
|---|---|---|---|
| 1 | 10~250 | 4 | $H_2O$ |
| 2 | 250~550 | 4 | $H_2O$ |
| 3 | 550~780 | 11 | $H_2O$, $CO_2$ |
| 4 | 780~990 | 5 | $H_2O$, $CCl_4$, CFC-11, CFC-12, CFC-13, $SF_6$ |
| 5 | 990~1200 | 5 | $H_2O$, $O_3$, CFC-11, CFC-12, CFC-13, $C_2F_6$ |
| 6 | 1200~1430 | 5 | $H_2O$, $N_2O$, $CH_4$, CFC-13, $C_2F_6$, $CF_4$ |
| 7 | 1430~2110 | 5 | $H_2O$ |
| 8 | 2110~2680 | 2 | $H_2O$, $CO_2$, $N_2O$ |



© 1994-2011 China Academic Journal Electronic Publishing House. All rights reserved. http://www.cnki.net

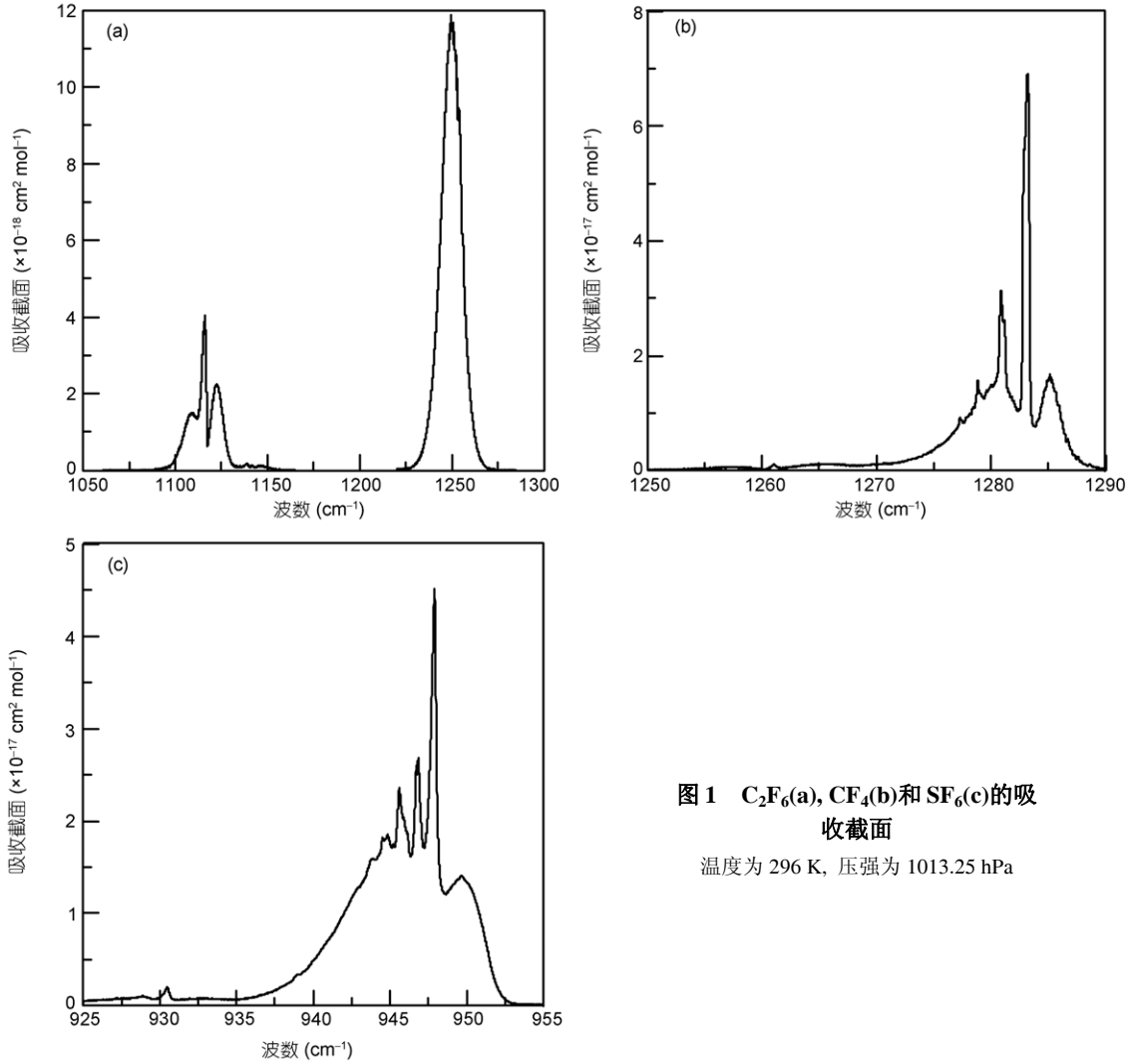


**图 1　$C_2F_6$(a), $CF_4$(b)和 $SF_6$(c)的吸收截面**

温度为 296 K, 压强为 1013.25 hPa

这些气体所有的强弱带吸收, 计算结果比 17 带的结果更加精确, 可以作为 17 带辐射方案计算结果的参考[9]. 本文首先计算了 17 带和 998 带辐射方案中, 22 个压力和 3 个温度下所有 k-分布间隔点上的有效吸收系数[10,12], 作为辐射模式的输入. 对辐射通量和加热率的计算, 采用六种模式大气: 热带大气(TRO),中纬度夏季大气(MLS), 中纬度冬季大气(MLW),亚极夏季大气(SAS), 亚极冬季大气(SAW)和美国标准大气(USS). 整层大气分为 100 层, 垂直分辨率为 1 km, 地面高度设为 0 km, 大气顶为 100 km. 模式中热辐射传输采用二流近似算法[13].

为了计算平流层调整的辐射强迫, 本文利用迭代法对 998 带辐射传输模式进行了改进. 图 2 给出了迭代法的流程图, 图中$\xi$为收敛值, $\Delta t$ 为迭代的时间步长, 单位为 d, 本文取为 1 d. 如果满足收敛条件, 即可认为平流层经过调整达到了新的辐射平衡. 0 到 0.1 ppbv 的扰动是为了保留 PFCs 的弱吸收特性, 然后再通过线性比例计算得到 1 ppbv 扰动引起的全球平均的辐射强迫[14], 即全球平均的辐射效率, 用这种方法计算大气含量明显小于 1 ppbv 的痕量气体的辐射强迫更加合适.

## 2　$C_2F_6$, $CF_4$ 和 $SF_6$ 的辐射强迫

瞬时辐射强迫的定义为: 由于某种温室气体浓度或其他因子的变化造成的对流层顶净辐射通量的变化[1]. 调整的辐射强迫的定义为: 在保持地表和对流层温度不变的情况下, 通过调整平流层的温度结





© 1994-2011 China Academic Journal Electronic Publishing House. All rights reserved.　http://www.cnki.net

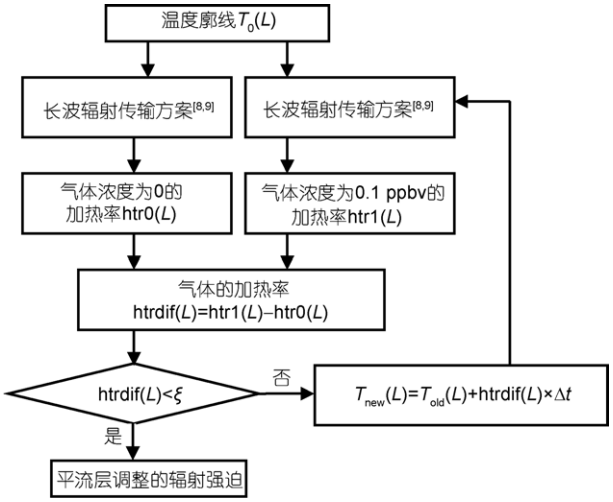


**图 2　计算流程图**

构, 使平流层达到辐射平衡时, 对流层顶的净辐射通量的变化[1]. 根据温室气体辐射强迫的定义, 正的辐射强迫将使对流层和地面系统变暖, 引起地表平均温度升高; 负的辐射强迫使对流层和地面系统变冷, 引起地表平均温度降低. 因此, $C_2F_6$, $CF_4$ 和 $SF_6$ 大气含量的变化对全球气候系统的影响可以通过计算它们的辐射强迫来估计.

云是影响气体辐射强迫的一个重要因子. 本文根据国际卫星云气候计划(ISCCP)D2 数据, 其时间范围为 1983~2007 年, 全球网格分辨率为 2.5°×2.5°[15], 得到不同云态, 云顶压力和光学厚度的 15 类云的云量和云水含量等资料. 热带,中纬度和亚极大气的云量,云水含量分别是 0°~30°, 30°~60°和 60°~90°N 的纬向平均, 见表 2. 其中低云的高度为 1~2 km, 中云的高度为 4~5 km, 高云的高度为 10~12 km. 低云 Cu, Sc, St 和中云 Ac, As, Ns 等 6 种云的云粒子相态有水云和冰云两种, 冰云的平均有效半径为 30 μm, 水云为 10 μm[16]. 模式利用了这些云参数输入辐射传输模式来考虑云的影响, 计算中, 地表发射率设为 1.0.

通过以上三种大气得到有云大气下的平流层调整的辐射效率, 所采用的计算方法与[16]相似, 只是用辐射效率代替了辐射加热率:

$$RE=\sum_{i=1}^{15}C_i RE_i+(1-C)RE_{\text{clear}}, \tag{1}$$

其中 $C_i$ 为每类云的云量, $C=\Sigma C_i$ 是总云量, $RE_{\text{clear}}$ 和 $RE_i$ 分别表示晴空和有云(云类型为 $i$)大气下的辐射效率. 然后, 通过公式(2)计算全球平均的有云大气下调整的辐射效率[3]:

$$RE_{\text{mean}}=\frac{1}{2}\times RE_{\text{tro}}+\left(\frac{\sqrt{3}}{2}-\frac{1}{2}\right)\times RE_{\text{mid}}+\left(1-\frac{\sqrt{3}}{2}\right)\times RE_{\text{sub}}, \tag{2}$$

其中, $RE_{\text{mean}}$ 是全球平均辐射效率, $RE_{\text{tro}}$, $RE_{\text{mid}}$ 和 $RE_{\text{sub}}$ 分别表示热带、中纬度和亚极大气的辐射效率.

表 3 列出了 998 带辐射方案计算的 $C_2F_6$, $CF_4$ 和

**表 2　云参数**

| 云类 | 热带大气 | | | 中纬度大气 | | | 亚极大气 | | |
|---|---|---|---|---|---|---|---|---|---|
| | 云量(%) | 水/冰含量 (g m$^{-3}$) | 有效半径 (μm) | 云量(%) | 水/冰含量 (g m$^{-3}$) | 有效半径 (μm) | 云量(%) | 水/冰含量 (g m$^{-3}$) | 有效半径 (μm) |
| 积云(水云) | 11.43 | 0.03 | 10 | 9.50 | 0.03 | 10 | 2.43 | 0.03 | 10 |
| 层积云(水云) | 9.38 | 0.07 | 10 | 10.48 | 0.09 | 10 | 5.36 | 0.11 | 10 |
| 层云(水云) | 0.75 | 2.47 | 10 | 2.26 | 2.79 | 10 | 5.17 | 4.11 | 10 |
| 积云(冰云) | 0.00 | 0.01 | 30 | 2.03 | 0.03 | 30 | 3.42 | 0.04 | 30 |
| 层积云(冰云) | 0.00 | 0.20 | 30 | 1.12 | 0.17 | 30 | 5.76 | 0.22 | 30 |
| 层云(冰云) | 0.00 | 5.90 | 30 | 0.30 | 4.26 | 30 | 2.85 | 3.76 | 30 |
| 高积云(水云) | 5.55 | 0.05 | 10 | 2.55 | 0.05 | 10 | 0.38 | 0.06 | 10 |
| 高层云(水云) | 4.43 | 0.09 | 10 | 3.67 | 0.10 | 10 | 0.82 | 0.13 | 10 |
| 雨层云(水云) | 1.14 | 0.07 | 10 | 1.66 | 0.08 | 10 | 1.03 | 0.10 | 10 |
| 高积云(冰云) | 0.95 | 0.06 | 30 | 9.02 | 0.09 | 30 | 9.48 | 0.10 | 30 |
| 高层云(冰云) | 0.18 | 0.14 | 30 | 6.43 | 0.18 | 30 | 12.99 | 0.22 | 30 |
| 雨层云(冰云) | 0.06 | 0.11 | 30 | 2.20 | 0.11 | 30 | 4.93 | 0.10 | 30 |
| 卷云(冰云) | 15.36 | 0.01 | 30 | 13.27 | 0.01 | 30 | 6.49 | 0.01 | 30 |
| 卷层云(冰云) | 5.25 | 0.06 | 30 | 6.89 | 0.08 | 30 | 1.59 | 0.09 | 30 |
| 卷积云(冰云) | 2.49 | 0.27 | 30 | 3.54 | 0.25 | 30 | 0.64 | 0.24 | 30 |





© 1994-2011 China Academic Journal Electronic Publishing House. All rights reserved.　http://www.cnki.net

$SF_6$ 晴空大气下的瞬时辐射效率和平流层调整的辐射效率以及有云大气下的平流层调整的辐射效率, 其中, 晴空大气下的结果是六种模式大气结果的算术平均值, 有云大气的结果是上面三种大气的区域加权平均值. 同时, 表 3 还列出了 IPCC 的结果[1]作为参考. 通过对比表 3 中晴空大气下瞬时辐射效率和平流层调整后的辐射效率, 可以看出, 经过平流层调整, $C_2F_6$, $CF_4$ 和 $SF_6$ 的辐射效率分别增加了 5%, 3%和 5%. 平流层温度调整对辐射强迫的作用是增大或是减小, 取决于平流层温度调整后, 温度廓线对对流层顶净辐射通量的影响[4]. 以 $C_2F_6$ 为例, 图 3 给出 17 带和 998 带辐射方案在六种模式大气下, 气体 0.1 ppbv 的扰动在长波区间引起的辐射加热率. 加热率随着模式大气的不同而变化, 但同一个辐射传输方案(17 带或 998 带)下的加热率量级一致, 并且有相似的垂直分布. 同时也可以看出, 两种辐射方案下, USS 的结果都接近其他结果的平均值. 对比图 3 中两种辐射方案的结果, 17 带辐射方案计算的加热率明显小于 998 带的计算结果, 这是因为 998 带辐射方案能够全面考虑气体的强弱吸收, 而 17 带辐射方案由于谱带划分宽, k-间隔数量少, 对 $C_2F_6$ 这类吸收带较窄的气体的计算精度较低. 同时, 由于 USS 的结果接近其他结果的平均值, 以下就以 USS 的结果为例进行分析. 因此, 本文对 998 带辐射方案下 USS 的加热率进行分析得出, $C_2F_6$ 的加热率从地面到 5 hPa 左右的平流层下部都是正值, 在这些大气层上起加热作用. 当平流层经过调整达到新的平衡后, 平流层下部向对流层的向下辐射通量增加, 引起对流层顶的辐射强迫增加. 同理, 表 3 中 $CF_4$ 和 $SF_6$ 的平流层调整的辐射效率也比相应的瞬时辐射效率大.

表 3 中 $C_2F_6$, $CF_4$ 和 $SF_6$ 区域平均的有云大气下平流层调整的辐射效率分别比晴空下的结果小 24%, 18%和 25%. 这是因为这类气体的光学厚度较小, 云引起的向上辐射通量的减少对它们的辐射强迫有较大的影响[4].

本文 $C_2F_6$, $CF_4$ 和 $SF_6$ 有云大气下的平流层调整

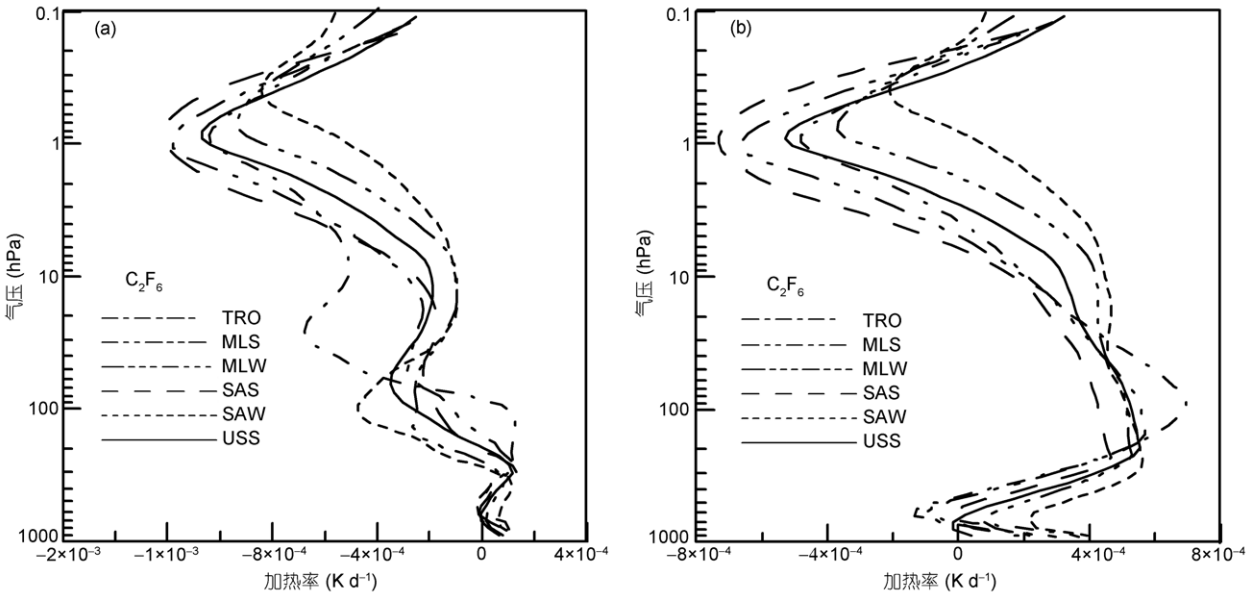


**图 3　17 带(a)和 998 带(b)辐射方案中六种模式大气下 0.1 ppbv $C_2F_6$ 扰动的加热率**

**表 3　$C_2F_6$, $CF_4$ 和 $SF_6$ 的辐射效率**

| 气体 | 晴空瞬时辐射效率 ($W\ m^{-2}\ ppbv^{-1}$) | 晴空调整的辐射效率 ($W\ m^{-2}\ ppbv^{-1}$) | 有云调整的辐射效率 ($W\ m^{-2}\ ppbv^{-1}$) | IPCC[1] ($W\ m^{-2}\ ppbv^{-1}$) |
|---|---|---|---|---|
| $C_2F_6$ | 0.433 | 0.453 | 0.346 | 0.26 |
| $CF_4$ | 0.116 | 0.119 | 0.098 | 0.1 |
| $SF_6$ | 0.869 | 0.909 | 0.680 | 0.52 |





© 1994-2011 China Academic Journal Electronic Publishing House. All rights reserved.　http://www.cnki.net

的辐射效率分别为 0.346, 0.098 和 0.680 W $m^{-2}$ $ppbv^{-1}$, 与 IPCC 的结果[1]相比, 差别分别为 33%, –2%和 31%. 分子谱吸收资料, 辐射模式和云方案的不同都是引起这些差别的原因. 首先, 本文采用了 HITRAN2004 数据库中 $C_2F_6$, $CF_4$ 和 $SF_6$ 的分子吸收截面资料, 其中, $C_2F_6$ 的积分吸收截面与 Sihra 等[6]的结果差别为 1%, $CF_4$ 的积分吸收截面与 Hurley 等[7]的结果差别同样为 1%, $SF_6$ 的红外吸收截面资料则与黄兴友[5]的结果完全相同, 对辐射效率结果的影响不会太大. 本文采用的基于相关 k-分布法的 998 带辐射方案与先前研究较为普遍使用的窄带模式相比, 998 带辐射方案更全面地考虑了这些气体的强弱吸收带, 因此, 本文的计算的辐射效率偏大. 此外, 由于云对辐射效率的影响较大, 不同作者采用了不同的云方案也会引起辐射效率计算的差别.

自工业革命以来, $C_2F_6$, $CF_4$ 和 $SF_6$ 的大气含量持续增加, IPCC 给出 $C_2F_6$, $CF_4$ 和 $SF_6$ 最新的大气含量值分别为 2.9, 76 和 5.6 pptv[1], 其中, $CF_4$ 的大气含量中有 40 pptv 是自然源产生的. 根据 $C_2F_6$, $CF_4$ 和 $SF_6$ 的大气含量和本文计算的辐射效率, 它们引起的辐射强迫为分别约为 0.001, 0.007 和 0.004 W $m^{-2}$. IPCC 排放情景特别报告 SRES 给出了它们在十种不同排放情景下的大气含量[2], 本文计算了它们在十种不同排放情景下的大气含量的平均值, 以此计算 $C_2F_6$, $CF_4$ 和 $SF_6$ 在未来 100 a 的辐射强迫的变化, 如图 4 所示. 图 4 中, 随着大气含量的增加, $C_2F_6$, $CF_4$ 和 $SF_6$ 引起的辐射强迫迅速增加, 到 2100 年, 它们的辐射强迫分别约为 0.008, 0.036 和 0.037 W $m^{-2}$, 分别是它们当前辐射强迫的 8 倍, 5 倍和 9 倍左右.

## 3 $C_2F_6$, $CF_4$ 和 $SF_6$ 的全球增温潜能 GWP 和全球温变潜能 GTP

在上文给出的辐射效率的基础上, 本文根据 GWP 和 GTP 的定义, 建立了计算 $C_2F_6$, $CF_4$ 和 $SF_6$ 的 GWP 和 GTP 模型, 用该模型计算了它们未来 20, 100 和 500 a 的 GWPs 和 GTPs.

GWP 的定义是瞬时脉冲排放 1 kg 化合物 $x$, 在一定的时间范围内引起的辐射强迫的积分相对于脉冲排放等量参考气体(一般为 $CO_2$)在同一时间范围内的辐射强迫的积分. 公式如下[1]:

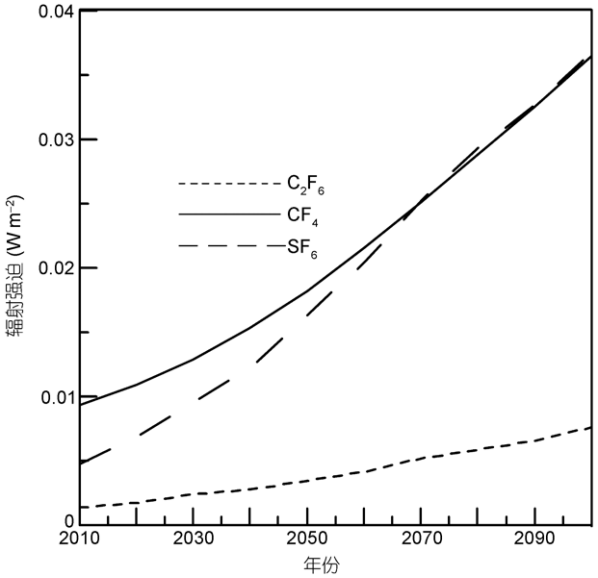


**图 4 $C_2F_6$, $CF_4$ 和 $SF_6$ 从 2010 年到 2100 年的辐射强迫**

$$\mathrm{GWP}_x = \frac{\int_0^{TH} RF_x(t)\mathrm{d}t}{\int_0^{TH} RF_r(t)\mathrm{d}t} = \frac{\int_0^{TH} a_x[x(t)]\mathrm{d}t}{\int_0^{TH} a_r[r(t)]\mathrm{d}t}, \tag{3}$$

$$x(t) = \mathrm{e}^{-t/\tau}, \tag{4}$$

$$r(t) = a_0 + \sum_i a_i \exp\left(-\frac{t}{\alpha_i}\right), \tag{5}$$

其中, $TH$ 是时间范围(本文为 20, 100 和 500 a), $t$ 表示时间, $RF_x$ 和 $RF_r$ 分别表示化合物 $x$ 和参考气体 $CO_2$ 的辐射强迫, $a_x$ 和 $a_r$ 分别表示相应的辐射效率, $x(t)$和 $r(t)$分别表示化合物 $x$ 和参考气体 $CO_2$ 的时间响应函数, 公式(4)中的$\tau$表示大气寿命, 单位为 a, 公式(5)中采用的 $CO_2$ 时间响应函数是 IPCC 给出的最新版本公式, 其中 $a_0$, $a_i$ 和$\alpha_i$ 均为给定计算参数, 详见文献[1].

GWP 概念[17]自提出以来, 研究者就对它提出了质疑. 首先, GWP 不能简单地用在所有对气候有影响的化合物上, 相对于寿命较长的气体而言, 全球平均的 GWP 不能很好地体现寿命较短的气体对气候的影响. 其次, 它也不能区分气体不同大气寿命的影响. 再者, GWP 只表现了不同气体脉冲排放在一个给定时间范围内的辐射强迫的积分的比值, 不能给出气体对地表温度变化的直接影响, 即, GWP 不能指示地表温度变化随时间的变化[18,19]. Shine 等[20]提出了一





© 1994-2011 China Academic Journal Electronic Publishing House. All rights reserved. http://www.cnki.net

个新的评估概念: 全球温变潜能(GTP), 并被 IPCC 采用[1]. 它的定义为: 在脉冲排放 1 kg 化合物 $x$ 或者以 1 kg $a^{-1}$ 递增的持续排放化合物 $x$, 在给定的一段时间 $TH$ 内造成的全球平均地表温度的变化与参考气体 $r$(这里指二氧化碳)所造成的相应变化之比. 脉冲排放和持续排放的 GTP 分别表示为 $GTP^P$ 和 $GTP^S$[20]. 公式如下:

$$GTP_x^{TH} = \frac{\Delta T_x^{TH}}{\Delta T_r^{TH}}, \tag{6}$$

其中, $TH$ 表示时间范围(这里为 20, 100 和 500 a); $\Delta T_x$ 和 $\Delta T_r$ 分别表示化合物 $x$ 和 $CO_2$ 引起的全球平均地表温度变化, 它们可以通过求解全球平均地表温度变化 $\Delta T$ 与辐射强迫 $\Delta F$ 之间的公式[20]得到:

$$C\frac{\mathrm{d}\Delta T(t)}{\mathrm{d}t} = \Delta F(t) - \frac{\Delta T(t)}{\lambda}, \tag{7}$$

其中, $t$ 表示时间, $C$ 是系统的热容量, $\lambda$ 是气候灵敏度参数.

脉冲排放和持续排放的绝对全球温变潜能分别记为 $AGTP^P$ 和 $AGTP^S$, 表示在初始时刻排放的气体在时间 $t$ 时刻引起的地表温度的变化, 单位为 K $kg^{-1}$ 和 K (kg $a^{-1}$)$^{-1}$. 故脉冲排放和持续排放的 GTP 也可以分别表示为[20],

$$GTP^P = \frac{AGTP_x^P}{AGTP_{CO_2}^P}, \tag{8}$$

$$GTP^S = \frac{AGTP_x^S}{AGTP_{CO_2}^S}. \tag{9}$$

计算 GWP 和 GTP 所需要的参数为气体 $x$ 和 $CO_2$ 的辐射效率和时间响应函数. 这里采用前文计算 $C_2F_6$, $CF_4$ 和 $SF_6$ 的辐射效率, $C_2F_6$, $CF_4$ 和 $SF_6$ 和 $CO_2$ 的时间响应函数以及 $CO_2$ 的辐射效率都取自 IPCC[1], 气候灵敏度参数, 热容量等参数取值与 Shine 等[20]相同. 表 4 列出了 $C_2F_6$, $CF_4$ 和 $SF_6$ 的 20, 100 和 500 a 的 GWP, 脉冲排放的 $GTP^P$ 和持续排放的 $GTP^S$, 同时还列出了 IPCC 的 GWP 值[1]作为比较.

由表 4 的 GWP 值可以看出, 对于脉冲排放等量的气体, $C_2F_6$, $CF_4$ 和 $SF_6$ 对气候变化的贡献是 $CO_2$ 的上万倍. 对 100 a 的时间范围, 本文计算的 $C_2F_6$, $CF_4$ 和 $SF_6$ 结果分别比 IPCC 的结果[1]大 40%, 3%和 37%. 通过对公式(3)的分析得出, GWP 计算主要与四个参数直接相关, 即气体的辐射效率和时间响应函数以及参考气体 $CO_2$ 的辐射效率和时间响应函数, 它们共同作用造成 GWP 值的计算差别. 本文经分析可以得出, GWP 的差别主要是因为 $C_2F_6$, $CF_4$ 和 $SF_6$ 辐射效率的不同造成的.

$GTP^P$ 的主要物理意义与 GWP 相同, 最大的区别在于, $GTP^P$ 给出的结果是在一定时间范围内, 等量排放 $C_2F_6$, $CF_4$, $SF_6$ 这些气体和 $CO_2$ 分别引起的地表温度变化的比值, 而 GWP 给出的是在一定时间范围内, 等量排放这些气体和 $CO_2$ 分别引起的辐射强迫时间积分的比值. 前者直接表示了在相同的时间内, 1 kg 的这些气体排放相对于 1 kg $CO_2$ 排放引起的地表温度变化. 由于 $C_2F_6$, $CF_4$ 和 $SF_6$ 在工业生产中广泛适用, 其实际排放量持续增加, $GTP^S$ 恰恰考虑了气体持续排放对地表温度的变化产生的相对影响, 所以, $GTP^S$ 可以为国家针对目前持续排放这类温室气体的特定工业和农业进行政策和产业调整提供很好的评价方法. Shine 等[20]通过数学推导说明了在时间跨度较大的情况下, $GTP^S$ 和 GWP 有相似的数学表达式, 因而得到的结果也相近, 本文的结果也验证了这个结论, 如表 4. 同时, Shine 等[20]也指出, 同样采用公式(7)计算的 $GTP^P$ 和 $GTP^S$, 后者的结果要比前者准确. 因此, $GTP^S$ 的概念清晰, 计算所需参数较少, 结果准确, 同时排放条件也更符合实际大气情况, 是目前最佳的评价方法.

本文计算了 $C_2F_6$, $CF_4$, $SF_6$ 在未来 500 a 内的绝对全球温变潜能 $AGTP^P$ 和 $AGTP^S$, 表示这些气体脉冲排放或者持续排放在未来 500 a 内引起的地表温度变化, 见图 5. 由图 5(a)可见, 脉冲排放的气体在排放初期会迅速引起地表温度持续增加, 并且在排放后 50 a 左右达到一个最大值, 然后地表温度开始缓慢恢

**表 4　本文计算的 $C_2F_6$, $CF_4$ 和 $SF_6$ 的 20, 100 和 500 a GWP, $GTP^P$, $GTP^S$ 和 GWP[1]**

| 气体 | 在大气中寿命 a) | GWP 20/100/500 a | GWP[1] 20/100/500 a | $GTP^P$ 20/100/500 a | $GTP^S$ 20/100/500 a |
|---|---|---|---|---|---|
| $C_2F_6$ | 10000 | 11614/17035/25955 | 8630/12200/18200 | 12530/22468/34975 | 10909/16498/25732 |
| $CF_4$ | 50000 | 5163/7597/11761 | 5210/7390/11200 | 5572/10052/15694 | 4849/7355/11655 |
| $SF_6$ | 3200 | 21520/31298/45744 | 16300/22800/32600 | 23202/40935/56856 | 20224/30341/45399 |





© 1994-2011 China Academic Journal Electronic Publishing House. All rights reserved.　http://www.cnki.net

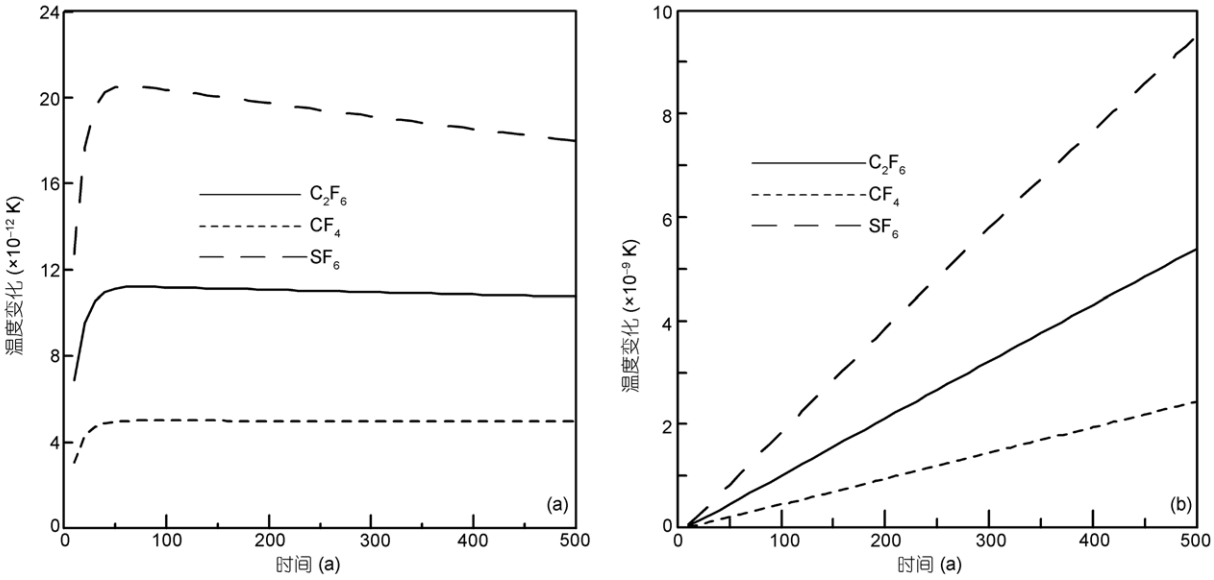


**图 5　$C_2F_6$, $CF_4$ 和 $SF_6$ 脉冲排放(a)和持续排放(b)引起的温度变化**

复; 图 5(b)显示, 持续排放的气体自排放时刻起, 它们引起的地表温度的变化基本呈直线上升, 这是因为 $C_2F_6$, $CF_4$ 和 $SF_6$ 能够在大气中停留相当长的时间, 持续排放会导致大气累积含量持续增加, 引起的地表温度变化也持续增加. 通过图 5 可以看出, 气体持续排放引起的地表温度变化要比其脉冲排放引起的相应值大三个数量级, 对地表温度变化的影响要大得多. 如果对目前工业中 $C_2F_6$, $CF_4$ 和 $SF_6$ 的生产, 使用和排放不加以控制, 它们的持续排放对地表温度变化的影响将持续增大, 并且很难得到恢复.

## 4　结论

本文采用 HITRAN2004 资料计算了基于相关 k-分布法的 17 带和 998 带长波辐射方案中 $C_2F_6$, $CF_4$ 和 $SF_6$ 的有效吸收系数. 讨论了不同辐射方案对 $C_2F_6$, $CF_4$ 和 $SF_6$ 的辐射强迫计算的影响. 工业革命前到 2005 年, $C_2F_6$, $CF_4$ 和 $SF_6$ 总的辐射强迫约为 0.012 W $m^{-2}$, 到 2100 年, 将达到 0.081 W $m^{-2}$, 与其他长寿命温室气体一道, 它们会对未来的全球变暖做出贡献. 利用高光谱的 998 带长波辐射方案得出, 有云大气下 $C_2F_6$, $CF_4$ 和 $SF_6$ 的平流层调整的辐射效率分别为 0.346, 0.098 和 0.680 W $m^{-2}$ $ppbv^{-1}$, 与 IPCC 的结果[1] 相比, 差别分别为 33%, –2%和 31%.

本文还基于 $C_2F_6$, $CF_4$ 和 $SF_6$ 更新的辐射效率计算了 20, 100 和 500 a 的 GWPs 和 GTPs, 然后, 分别计算了它们脉冲排放和持续排放在未来 500 a 内引起的地表温度变化. 结果表明, $C_2F_6$, $CF_4$ 和 $SF_6$ 的 20, 100 和 500 a GWP 和 GTP 分别是等量排放 $CO_2$ 的成千上万倍, 对全球变暖有长期和持续的影响. 通过比较和分析指出, $GTP^S$ 是评价人造长寿命温室气体排放对全球气候变暖的最佳方法.

**致谢**　感谢美国华盛顿大学大气科学系傅强教授对本文平流层调整的辐射强迫计算方案给予的十分有益的建议和帮助, 同时感谢审稿专家提出的宝贵意见.

**参考文献**

1　Solomon S, Qin D, Manning M, et al., eds. Climate Change 2007: The Physical Science Basis. Contribution of Working Group I to the Fourth Assessment Report of the Intergovernmental Panel on Climate Change. Cambridge and New York: Cambridge University Press, 2007

2　Metz B, Kuijpers L, Solomon S, et al., eds. Safeguarding the Ozone Layer and the Global Climate System: Issues Related to



© 1994-2011 China Academic Journal Electronic Publishing House. All rights reserved.　http://www.cnki.net

Hydrofluorocarbons and Perfluorocarbons. Cambridge: Cambridge University Press, 2004
3 Highwood E J, Shine K P. Radiative forcing and global warming potentials of 11 halogenated compounds. J Quant Spectrosc Radiat Transf, 2000, 66: 169–183
4 Jain A K, Briegleb B P, Minschwaner K, et al. Radiative forcings and global warming potentials of 39 greenhouse gases. J Geophys Res, 2000, 105(D16): 20773–20790
5 黄兴友. 温室气体全球增温潜能的研究. 博士学位论文. 北京: 中国科学院大气物理研究所, 2001
6 Sihra K, Hurley M D, Shine K P, et al. Updated radiative forcing estimates of 65 halocarbons and onomethane hydrocarbons. J Geophys Res, 2001, 106(D17): 20493–20505
7 Hurley M D, Wallington T J, Buchanan G A, et al. IR spectrum and radiative forcing of $CF_4$ revisted. J Geophys Res, 2005, 110: D02102
8 Zhang H, Shi G Y, Nakajima T, et al. The effects of the choice of the k-interval number on radiative calculations. J Quant Spectrosc Radiat Transf, 2006, 98: 31–43
9 Zhang H, Suzuki T, Nakajima T, et al. Effects of band division on radiative calculations. Opt Eng, 2006, 45: 016002–016010
10 Shi G Y. An accurate calculation and representation of the infrared transmission function of the atmospheric constituents. Doctoral Desertation. Tohoku: Tohoku University of Japan, 1981
11 Gohar L K, Myhre G, Shine K P. Updated radiative forcing estimates of four halocarbons. J Geophys Res, 2004, 109: D01107, doi: 10.1029/2003JD004320
12 Zhang H, Nakajima T, Shi G Y, et al. An optimal approach to overlapping bands with correlated k distribution method and its application to radiative calculations. J Geophys Res, 2003, 108(D20): 4641
13 Nakajima T, Tsukamoto M, Tsushima Y, et al. Modeling of the radiative process in an atmospheric general circulation model. Appl Opt, 2000, 39: 4869–4878
14 Freckleton R S, Pinnock S, Shine K P. Radiative forcing of halocarbons: A comparison of line-by-line and narrow-band models using CF4 as an example. J Quant Spectrosc Radiat Transf, 1996, 55: 763–769
15 Rossow W B, Schiffer R A. Advances in understanding clouds from ISCCP. Bull Amer Meteorol Soc, 1999, 80: 2261–2288
16 Yang Q, Fu Q, Austin J, et al. Observationally derived and general circulation model simulated tropical stratospheric upward mass fluxes. J Geophys Res, 2008, 113: D00B07, doi: 10.1029/2008JD009945
17 Houghton J T, Jenkins G J, Ephraums J J, eds. Climate Change 1990: The IPCC Scientific Assessment. Cambridge: Cambridge University Press, 1990
18 Fuglestvedt J S, Berntsen T, Godal O, et al. Metrics of climate change: Assessing radiative forcing and emission indices. Clim Change, 2003, 58: 267–331
19 Steven J S, Wigley T M L. Global warming potentials: 1. Climatic implications of emissions reductions. Clim Change, 2000, 44: 445–457
20 Shine K P, Fulestvedt J S, Hailemariam K, et al. Alternatives to the global warming potential for comparing climate impacts of emissions of greenhouse gases. Clim Change, 2005, 68: 281–302





© 1994-2011 China Academic Journal Electronic Publishing House. All rights reserved.　http://www.cnki.net

Clim Dyn
DOI 10.1007/s00382-011-1131-0

# Simulation of direct radiative forcing of aerosols and their effects on East Asian climate using an interactive AGCM-aerosol coupled system

**Hua Zhang · Zhili Wang · Zaizhi Wang · Qianxia Liu · Sunling Gong · Xiaoye Zhang · Zhongping Shen · Peng Lu · Xiaodong Wei · Huizheng Che · Laurent Li**

Received: 23 November 2010 / Accepted: 20 June 2011
© Springer-Verlag 2011

**Abstract** An interactive system coupling the Beijing Climate Center atmospheric general circulation model (BCC_AGCM2.0.1) and the Canadian Aerosol Module (CAM) with updated aerosol emission sources was developed to investigate the global distributions of optical properties and direct radiative forcing (DRF) of typical aerosols and their impacts on East Asian climate. The simulated total aerosol optical depth (AOD), single scattering albedo, and asymmetry parameter were generally consistent with the ground-based measurements. Under all-sky conditions, the simulated global annual mean DRF at the top of the atmosphere was $-2.03$ W m$^{-2}$ for all aerosols including sulfate, organic carbon (OC), black carbon (BC), dust, and sea salt; the global annual mean DRF was $-0.23$ W m$^{-2}$ for sulfate, BC, and OC aerosols. The sulfate, BC, and OC aerosols led to decreases of 0.58° and 0.14 mm day$^{-1}$ in the JJA means of surface temperature and precipitation rate in East Asia. The differences of land-sea surface temperature and surface pressure were reduced in East Asian monsoon region due to these aerosols, thus leading to the weakening of East Asian summer monsoon. Atmospheric dynamic and thermodynamic were affected due to the three types of aerosol, and the southward motion between 15°N and 30°N in lower troposphere was increased, which slowed down the northward transport of moist air carried by the East Asian summer monsoon, and moreover decreased the summer monsoon precipitation in south and east China.

**Keywords** AGCM · Aerosol · Radiative forcing · Climate effects · East Asian monsoon

H. Zhang (✉)
Laboratory for Climate Studies, National Climate Center,
China Meteorological Administration,
46 Zhongguancun Nandajie, Beijing 100081, China
e-mail: huazhang@cma.gov.cn

Z. Wang
Chinese Academy of Meteorological Sciences,
Beijing 100081, China

Z. Wang
National Climate Center, China Meteorological Administration,
Beijing 100081, China

Q. Liu · P. Lu · X. Wei
National Climate Center, China Meteorological Administration,
46 Zhongguancun Nandajie, Beijing 100081, China

S. Gong
Air Quality Research Branch, Meteorological Service of Canada,
Toronto, ON, Canada

X. Zhang · H. Che
Center for Atmosphere Watch and Services,
Chinese Academy of Meteorological Sciences,
China Meteorological Administration, Beijing, China

Z. Shen
Shanghai Climate Center, Shanghai, China

L. Li
Laboratoire de Météorologie Dynamique,
CNRS/UPMC, Paris, France

## 1 Introduction

Both natural processes and anthropogenic activities contribute to global climate changes. The latter has played an important role in the significant changes in atmospheric components since the beginning of industrialization. Currently, the aerosol climate effects (especially the interactions among aerosols, radiation, and clouds) remain one of the largest uncertainties in model simulation and climate

Published online: 09 July 2011

change assessment (IPCC 2007). Aerosols can affect climate in several ways. Firstly, aerosol particles can directly scatter or absorb infrared and solar radiation, thereby disturbing the energy budget of the earth-atmosphere system (Houghton et al. 1996; Haywood and Ramaswamy 1998). Secondly, aerosol particles acting as cloud condensation or ice nuclei can change cloud microphysical and radiative properties and cloud lifetimes, and hence indirectly affect the climate (Twomey 1977; Albrecht 1989; Ramaswamy et al. 2001; Lohmann and Feichter 2005; IPCC 2007). Thirdly, the absorbing aerosol particles located in cloud layers can strengthen evaporation processes in clouds and thus decrease cloud cover through strongly absorbing solar radiation and heating the atmosphere. This is referred to as the semi-direct effect of aerosols (Hansen et al. 1997; Ackerman et al. 2000). Additionally, absorbing aerosols can be transported over long distances by atmospheric circulation and be deposited onto remote snow/ice surfaces where they may reduce the snow/ice surface albedo and hence increase melting (Warren and Wiscombe 1980; Hansen and Nazarenko 2004; Jacobson 2004; Flanner et al. 2007).

Atmospheric aerosols include sulfate, black carbon (BC), organic carbon (OC), and nitrate, which are mostly produced by human activities, and sea salt and soil dust, which mostly emit naturally. There are five dominant source regions of anthropogenic aerosols: East and South Asia, Western Europe, eastern U.S., South America, and central Africa (Streets et al. 2003; IPCC 2007). The sources of soil dust aerosol mainly locate in deserts and semi-desert regions, such as the Sahara in Africa and deserts of Central and West Asia. Anthropogenic dust sources have been increasing since industrialization because of desertification in some areas (Zhang et al. 2008). Sea salt aerosols are mostly distributed over oceans. Some field studies, such as the Cloud Indirect Forcing Experiment (CIFEX; Wilcox et al. 2006), the Aerosols over China and their Climate Effect (Zhang 2007), the East Asian Regional Experiment (EAREX; Nakajima et al. 2007), have investigated aerosol properties and radiative effects. Satellite data have also been used to estimate the global direct radiative forcing (DRF) of aerosols. Using the latest version of MODIS products, Bellouin et al. (2008) estimated the global annual mean DRF at the TOA with respect to present-day natural aerosols was $-1.30$ and $-0.65$ W m$^{-2}$ in clear-sky and all-sky conditions, respectively. Myhre (2009) estimated the anthropogenic aerosol DRF of $-0.3$ W m$^{-2}$, with an uncertainty of $-0.2$ W m$^{-2}$, by combining a global aerosol model and satellite observations.

Quantitatively understanding the different aerosol effects on climate through observation is very difficult due to the large spatial variations in aerosol concentrations. An atmospheric general circulation model (AGCM) coupled with an aerosol chemical and transport model is therefore a useful tool with which to study aerosol climate effects. The feedback between climate and aerosols can be considered using an interactively coupled system. Liao et al. (2004) simulated the global annual mean forcing due to all aerosols as $-0.72$ W m$^{-2}$ at the top of the atmosphere (TOA) and $-4.04$ W m$^{-2}$ at the surface. The Laboratoire de Météorologie Dynamique GCM coupled with a multi-component aerosol module was used to estimate the global annual average DRF and got a value of $-1.04$ W m$^{-2}$ at the TOA due to total aerosols in all-sky condition (Reddy et al. 2005). The GISS climate model embedded with a detailed aerosol microphysical scheme, called MATRIX, was used to estimate the net aerosol direct effect of $-1.78$ W m$^{-2}$ at the TOA (Bauer et al. 2010). Posselt and Lohmann (2009) found that the total anthropogenic aerosol effect decreased by 0.5–0.9 W m$^{-2}$ when employing a prognostic rain scheme in the global climate model ECHAM5 which represented a more physical treatment of the warm rain precipitation process. AGCMs coupled with ocean models have also been used to study the effects of aerosols on climate. Allen and Sherwood (2010) showed a large-scale land-sea contrast, with general increases in ocean clouds, and decreases in land clouds due to anthropogenic aerosol. They also indicated that the net solar radiation at the surface would increase if absorbing aerosols decrease mid-level clouds, and this is the dominant effect. Several studies showed that aerosols could decrease the solar flux arriving at the surface, causing surface cooling through direct and indirect effects (Takemura et al. 2005; Kristjansson et al. 2005; Ming and Ramaswamy 2009). Koch et al. (2009) found that the global cooling from aerosol direct and indirect effects was $-0.2$ and $-1.0$°C, respectively. The net aerosol cooling effect was about half as large as the greenhouse gas warming. The obvious local characteristics of aerosol emissions have a significant effect on regional climate (Li et al. 2010). The advection of warmer air heated by BC from South and East Asia over the Himalayas contributes to a warming of about 0.6°C (annual mean) in the lower and mid-troposphere of the Himalayan region (Ramanathan et al. 2007). Vertical redistribution of energy caused by aerosols may change the atmospheric thermodynamics and atmospheric circulation significantly. In monsoon regions, aerosols have an important influence on the monsoon circulation and precipitation (Lau and Kim 2006; Wang et al. 2009a, b). Menon et al. (2002) studied the climate effects of BC aerosols in the Asian monsoon region, and showed that the phenomenon of "northern drought/southern flooding'' that has often occurred in summer during the past 50 years in China may be related to BC aerosols. However, some studies also indicated the BC or carbonaceous aerosols didn't produce the aforementioned precipitation pattern (Gu et al. 2006; Zhang et al. 2009). Liu et al. (2009) simulated the effect of aerosol on monsoon using an aerosol-climate offline GCM, and demonstrated that the

direct effects of sulfate and BC aerosols in China both weakened the East Asian winter and summer monsoons. Ji et al. (2011) also found that the anthropogenic aerosols over South Asia had an impact on the Indian summer monsoon onset and precipitation. Observation showed that increased dust and BC loading from local sources in northern India during late spring may lead to an advance of the rainy periods and subsequently an intensification of the Indian summer monsoon (Lau et al. 2006). Using CALIPSO lidar satellite data, Kuhlmann and Quaas (2010) found that aerosol plumes reduced the pre-monsoon seasonal (March–April–May) average shortwave radiation throughout the Asian monsoon region by between 20 and 30 W $m^{-2}$.

To more accurately estimate the DRF due to aerosols and understand their climatic response, we coupled an AGCM developed by the National Climate Center of the China Meteorological Administration [NCC/CMA; the Beijing Climate Center (BCC) BCC_AGCM2.0.1; Wu et al. 2008] to a size-segregated multi-component aerosol module [the Canadian Aerosol Module (CAM)] developed by Gong et al. (2002, 2003). We simulated the optical properties of typical aerosols and compared the results to Aerosol Robotic Network (AERONET) and China Aerosol Robot Sunphotometer NETwork (CARSNET) observations. The DRF of aerosols and their effects on East Asian climate are discussed based on the above coupled model. Both of sea surface temperature (SST) changes and aerosols have important effects on the Asian monsoon (Lestari and Iwasaki 2006; Randles and Ramaswamy 2008). The advantage of this work is that the coupling AGCM is used with an interactive aerosol model and a slab ocean model, which allow the responses of aerosol to climate changes and responses of SSTs to aerosol forcing comparing with the previous studies by Lau et al. (2006), Gu et al. (2006), Chung and Ramanathan (2006), Randles and Ramaswamy (2008), and Liu et al. (2009) who used either the prescribed aerosol masses or AODs or SSTs.

Section 2 introduces the BCC_AGCM2.0.1, the CAM, and our numerical experimental design. Section 3 shows the global distributions of different species of aerosol column burden and optical properties simulated by the coupled model and compares them to observations. The DRF of aerosols and their effects on East Asian summer climate are also described. Finally, the discussion and summary are given in Sect. 4.

## 2 Model description and experimental design

### 2.1 Atmospheric general circulation model

The BCC_AGCM2.0.1 was developed by the NCC/CMA based on the Community Atmosphere Model Version 3 (CAM3) developed by the National Center for Atmospheric Research (NCAR). In this study BCC_AGCM2.0.1 was coupled with a slab ocean model which is from Hansen et al. (1984). The model uses horizontal triangular truncation at wavenumber 42 (T42, approximating 2.8° × 2.8°) and vertical hybrid $\sigma$-pressure coordinates similar to CAM3, which includes 26 vertical layers with the top layer at a pressure of 2.9 hPa. The shortwave radiation is parameterized by a 19-spectral-band scheme that uses a two-stream $\delta$-Eddington approximation (Briegleb 1992). The cloud fraction was derived from diagnostic relationships introduced by Slingo (1987), with variations described by Hack et al. (1993), Kiehl et al. (1998), and Rasch and Kristjansson (1998). The parameterization of non-convective cloud processes has been described by Rasch and Kristjansson (1998), with updates by Zhang et al. (2003). The shallow and upper-level convection used the parameterization from Hack (1994). The radiation parameterization of liquid water clouds was taken from the scheme given by Slingo (1989). Monthly mean climatological data from 1971 to 2000 on a Gaussian grid, obtained from the National Centers for Environmental Prediction (NCEP) reanalysis products, were used as the initial model state. The geographical distribution of sea surface temperature was prescribed based on the 21-year (1981–2001) climatology (available online from http://www/ccsm.ucar.edu/models/atmcam/docs/description).

Compared to CAM3, a few improvements have been implemented in BCC_AGCM2.0.1. The dynamics in the model differs significantly from the Eulerian spectral formulation of the CAM3, and reference stratified atmospheric temperature and surface pressure were introduced into the governing equations to improve calculation of the pressure gradient force and the gradients of surface pressure and temperature (Wu et al. 2008). The major modifications to the model physics included a new convection scheme (Zhang and Mu 2005), a dry adiabatic adjustment scheme in which potential temperature is conserved (Yan 1987), a modified scheme to calculate sensible heat and moisture fluxes over open ocean that considers the effect of ocean waves on latent and sensible heat fluxes (Wu et al. 2010), and an empirical equation to compute the snow cover fraction (Wu and Wu 2004). The model provides overall improvements to climate simulations in comparison to CAM3, especially for simulating the tropical maxima/subtropical minima of precipitation, wind stress, and sensible and latent heat fluxes at the ocean surface (Wu et al. 2010).

### 2.2 Aerosol module

The Canadian Aerosol Module (CAM), a size-segregated multi-component aerosol algorithm, was developed by Gong et al. (2002, 2003). It includes processes for the

emission, transport, chemical transformation, cloud interaction, and deposition of atmospheric aerosols. Five aerosol species were taken into account, including sulfate, BC, OC, soil dust, and sea salt. We used updated source emissions that were derived primarily from AeroCom data. These included the surface emission rate of both natural and anthropogenic aerosols: BC and OC (Van der Werf et al. 2004; Bond et al. 2004), $SO_2$ and sulfate (Van der Werf et al. 2004; Cofala et al. 2005), and dimethyl sulfide (DMS; Kettle and Andreae 2000 for ocean data; Nightingale et al. 2000 for air-sea transfer). Additional emission data were obtained from the Emission Database for Global Atmospheric Research (EDGAR) version 3.2, 1995, database (Olivier et al. 2002; http://www.mnp.nl/edgar). The sea salt module was developed by Gong et al. (2002), and the soil dust scheme was from Marticorena and Bergametti (1995). The model included an online sulfur chemistry module, in which $H_2S$, DMS, $SO_2$, and $H_2SO_4$ are prognostic variables, but the concentrations of OH, $O_3$, $H_2O_2$, and $NO_3$ are prescribed offline from the MOZART/NCAR model (Brasseur et al. 1998; Hauglustaine et al. 1998).

There are two common methods for representing particle size distributions in models: the modal and sectional representations. In the modal representation, each aerosol is represented by an analytical modal distribution function (e.g., Binkowski and Shankar 1995; Ghan et al. 2001). In the sectional representation, the aerosol size distribution is generally approximated by a set of contiguous, non-overlapping, and discrete size bins (e.g., Gong et al. 1997; Jacobson 1997; Meng et al. 1998). This representation of aerosol size distribution is used for its flexibility in treating processes including multi-component interactions such as coagulation, condensation, and chemistry (Gong et al. 2003). The concentrations and optical properties of aerosols can be calculated more accurately according to the given size bins. In our model, the aerosol size spectrum was divided into 12 bins with radii between 0.005–0.01, 0.01–0.02, 0.02–0.04, 0.04–0.08, 0.08–0.16, 0.16–0.32, 0.32–0.64, 0.64–1.28, 1.28–2.56, 2.56–5.12, 5.12–10.24, and 10.24–20.48 μm. The effective radius of the aerosols was taken as the average value in each bin. The hygroscopic growth of soluble aerosol particles was also taken into account. The aerodynamic size of the particles was taken from Kohler theory to be in equilibrium with the ambient relative humidity. A cloud module with explicit microphysical processes was incorporated to simulate cloud droplet activation and subsequent aerosol-cloud-raindrop interaction, as well as cloud chemistry. Within a size bin, internally mixed aerosols were assumed for all aerosol types except the freshly emitted (at the source grid) insoluble components (BC and soil dust). These were assumed to be externally mixed for one integration time step in each grid cell. The number densities of externally mixed components were calculated at every time step in the source grid and then used to obtain the externally mixed aerosol activation and radiative forcing (Ayash 2007).

### 2.3 Optical properties of aerosol

The aerosol optical properties (extinction coefficient, single scattering albedo, and asymmetry parameter) were calculated using Mie scattering theory. The refractive indices of dry aerosols were adopted from D'Almeida (1991), and the Mie scattering code of Wiscombe (1980) was used. Table 1 lists the refractive indices and densities of dry aerosols.

Sulfate, OC, and sea salt particles are hygroscopic, and therefore their size distribution and particle shape may change when they are mixed with water vapor in the ambient air. This can lead to alterations of their refractive indices and corresponding radiative properties. Figure 1 shows the radius growth of the three species of hygroscopic aerosol particles with increasing relative humidity calculated according to Kohler theory. In this calculation, the relative humidity is first divided into 10 bins: 0.0, 0.45, 0.5, 0.6, 0.7, 0.8, 0.9, 0.95, 0.98, and 0.99. Then the radii of wet aerosol particles in each size bin are obtained for these relative humidity bins. The wet particle densities and refractive indices consisting of real and imaginary parts are obtained according to volume-weighted method, respectively. New size-segregated aerosol optical properties, namely the extinction coefficient, single scattering albedo, and asymmetry parameter, were calculated for all 19 spectral bands and each of the 10 relative humidity bins using Mie scattering theory (Wiscombe 1980). These were then incorporated into the BCC_AGCM2.0.1 instead of the original bulk scheme. Therefore, the aerosol optical properties for any relative humidity at each time step could be obtained through linear interpolation. Finally, the optical depth of each aerosol type for each spectral band was calculated according to formula by Liou (2004).

### 2.4 Experimental design

Our aim was to explore the effects of three types of aerosols mainly produced by human activities including sulfate, BC, and OC on East Asian summer climate, including both

**Table 1** The refractive index and densities of dry aerosols

| Component | Refractive index ($\lambda = 0.55$ μm) | Density (kg m$^{-3}$) |
|---|---|---|
| Sulfate | $1.43–1.0 \times 10^{-8}\, i$ | 1,769.0 |
| BC | $1.75–0.44\, i$ | 1,500.0 |
| OC | $1.53–0.0059\, i$ | 1,300.0 |
| Dust | $1.53–0.008\, i$ | 2,650.0 |
| Sea salt | $1.5–9.7 \times 10^{-9}\, i$ | 2,170.0 |

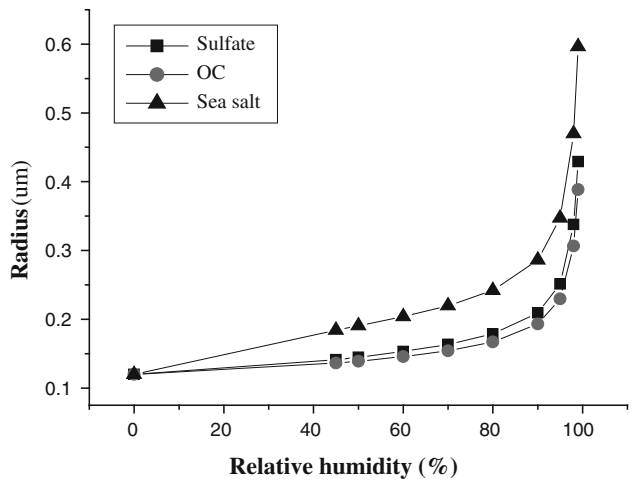


**Fig. 1** The radius growth of the three species of hygroscopic aerosol particles with increasing relative humidity

direct and semi-direct effects. To this end, two experiments were conducted: (*i*) all five species of aerosol were considered (EXP1); (*ii*) only soil dust and sea salt aerosols were included (EXP2). The differences between the results of EXP1 and EXP2 (EXP1 minus EXP2) were regarded as the effects of sulfate, BC and OC aerosols on the climate. In each experiment, the interactive system coupling the BCC_AGCM2.0.1 and CAM has run for 60 years. There was a spin-up period covering the first 30 years, during this period the climate gradually changes. But after that, the simulated climatology had reached a new equilibrium, and we consequently analyzed the last 30 years of each 60-year simulation. The instantaneous DRFs due to total aerosols and individual species were calculated in an additional experiment. Only radiative forcing is estimated with the prescribed SSTs and sea ice according to the general method of calculating the radiative forcing with AGCMs (Hansen et al. 2002; Takemura et al. 2005).

## 3 Results

### 3.1 Global distribution of simulated aerosol column burden

Figure 2 shows the global distributions of annual mean column burden of simulated sulfate, BC, OC, soil dust, and sea salt compared with AEROCOM_MEDIAN (Textor et al. 2006; Schulz et al. 2006; Kinne et al. 2006). The main precursors of sulfate aerosol were $SO_2$, volcanic eruptions, and biological sources, especially the DMS oxidation of marine plankton. The maximum values of sulfate aerosol column burden were mainly located in East Asia, especially south, east, and north China, as well as southeastern U.S., Europe, and India. The maximum burden value was about 10 mg $m^{-2}$ (Fig. 2a). The high sulfate aerosol column burden in these continental areas is attributable to their large industrial $SO_2$ emissions. Over oceans, there was an extended distribution of sulfate aerosols due to long-distance transport of terrestrial sulfate and marine DMS oxidation. The simulated global annual mean sulfate column burden was 1.74 mg $m^{-2}$.

BC is produced from the incomplete combustion of hydrocarbons, including fossil fuels, biofuels, and biomass. Maximum BC column burdens appeared over Asia and central Africa with a maximum value of approximately 1.4 mg $m^{-2}$ (Fig. 2b). These regions have recently experienced rapid urbanization and industrialization, which have triggered soaring carbon consumption by increasing populations and intense traffic emissions. Secondary high values of 0.8 mg $m^{-2}$ were located in parts of India-Bengal and central South America. In contrast, there was comparatively little BC column burden in southeastern U.S., western Europe, and Australia. The simulated global annual mean of BC column burden was 0.14 mg $m^{-2}$.

OC is produced during the complete combustion of biomass or fossil fuels. The highest column burdens of OC occurred in the central regions of South America and Africa, with a maximum burden exceeding 18 mg $m^{-2}$ in Africa (Fig. 2c). This may be caused by the full combustion of carbonaceous material due to the dry conditions in the tropics. There were also obvious OC concentrations over Southeast Asia, India, Australia, and southeastern U.S. The simulated OC concentrations were low in Europe, mainly because secondary organic aerosols, the primary components of OCs, were not taken into account in our model. The simulated global annual mean of OC column burden was 1.31 mg $m^{-2}$.

The dust column burdens were mainly located in the North African Sahara region and West Asia, with a maximum value as high as 1,000 mg $m^{-2}$ (Fig. 2d). The secondary value of more than 100 mg $m^{-2}$ was located in Inner Mongolia and the Xinjiang region of China. The simulated global annual mean dust column burden was 40.8 mg $m^{-2}$.

The distributions of sea salt aerosol covered almost the entire ocean (Fig. 2e). Large column burdens mainly occurred over the oceans between 30° and 60° in both the Southern Hemisphere (SH) and Northern Hemisphere (NH) with values exceeding 20 mg $m^{-2}$. The simulated global annual mean sea salt column burden was 14.7 mg $m^{-2}$.

Figures 2f–j show the corresponding global distributions of annual mean column burden in AEROCOM_MEDIAN. As can be seen from these figures, the magnitude and distribution of the simulated sulfate, sea salt and dust column burdens generally agreed with those of AEROCOM_MEDIAN, but the simulated dust burdens in Sahara and West Asia and sea salt burdens between 30° and 60°S

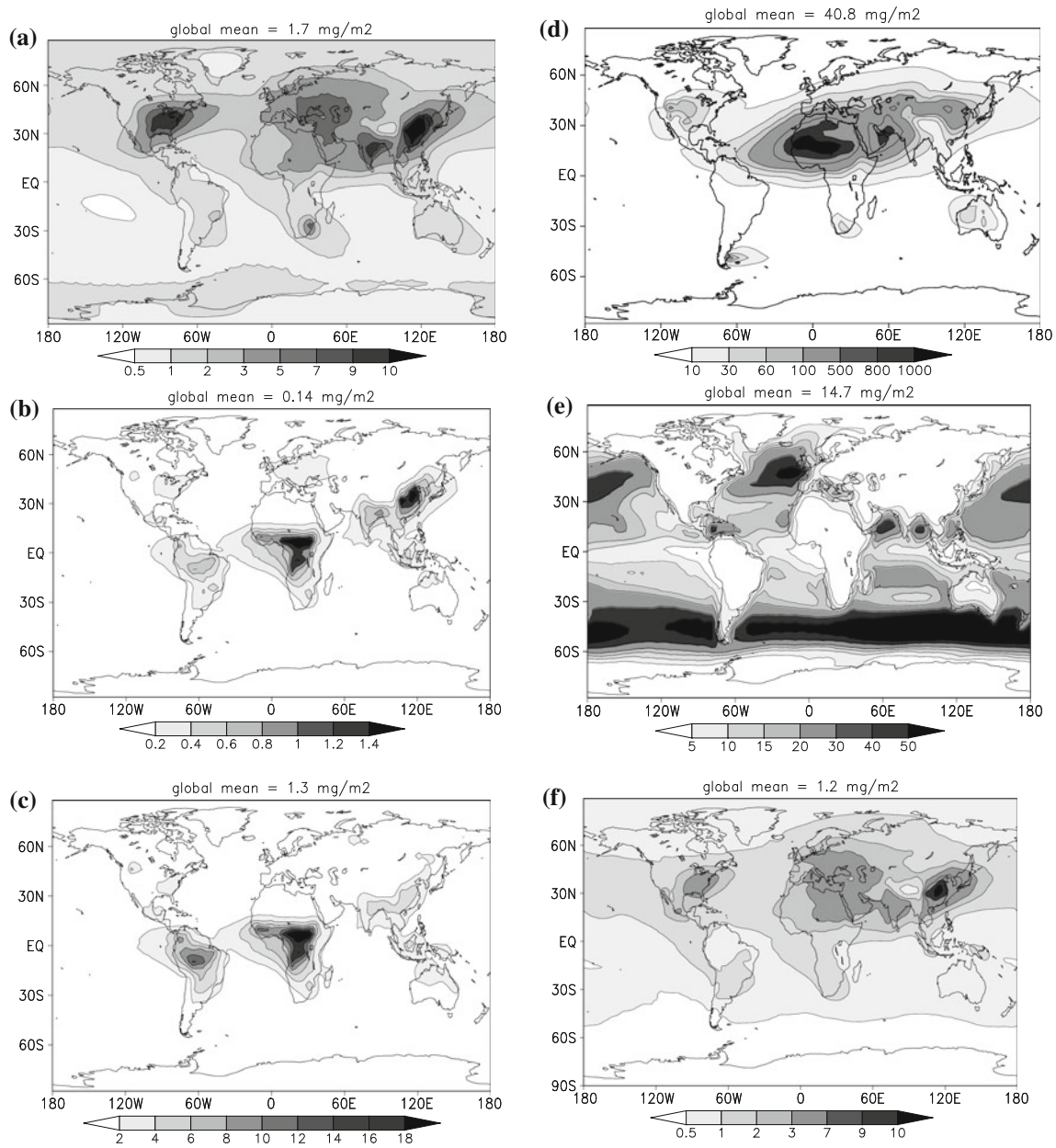


**Fig. 2** The global distributions of annual mean column burden of simulated **a** sulfate, **b** BC, **c** OC, **d** soil dust and **e** sea salt. The **f–j** are the corresponding distributions of AEROCOM_MEDIAN (mg $m^{-2}$)

were larger than the corresponding AEROCOM_MEDIANs. The values and ranges of simulated BC and OC column burdens were smaller than those of AEROCOM_MEDIAN, especially in West Europe, North America and East Asia. Compared with observations and other modeling results (i.e. AEROCOM), the simulated BC and OC concentrations from this model are low and the ratio of dry to wet depositions is different from other models. We have done a series of model experiment to examine the performance of the model. Firstly, we checked the budget information of the model in terms of emission and atmospheric burden. Table 2 is a summary of the budget information for a number of reference models. For example, the emission of BC in our model is just a little over half of GISS model (Koch 2001), and the atmospheric burden of BC from our model is also about half of that for GISS model. And compared with the IPCC-TAR, the BC emission in AEROCOM is lower (Dentener et al. 2006). It seems that the BC and OC bias from our model is largely from the emission underestimation compared with other models. Furthermore, all types of aerosols are treated as the internal mixture in this model and their wet depositions are calculated with the same parameterization scheme. In reality, due to its hydrophobic nature, BC should be less

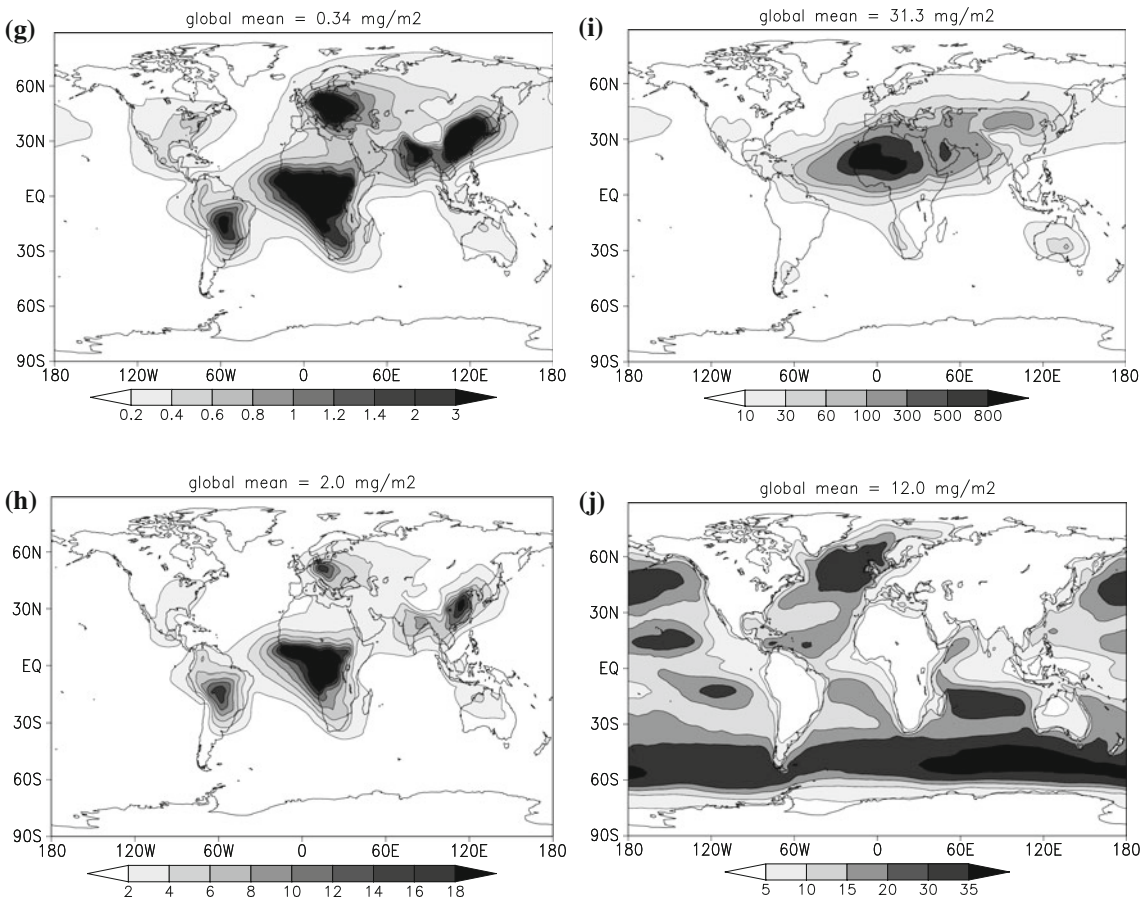


**Fig. 2** continued

**Table 2** Summary of the global emission and burden of BC

| Model | Emission (Tg year$^{-1}$) | Burden (Tg) | References |
|---|---|---|---|
| Our study | 7.7 | 0.07 | Dentener et al. (2006) |
| GISS | 12.41 | 0.14 | Koch (2001) |
| MIRAGE | 14.0 | 0.22 | Easter et al. (2004) |
| LMDZT | 10.5 | 0.19 | Reddy et al. (2005) |
| GOCART | 13.7 | 0.27 | AEROCOM |
| PNNL | 11.4 | 0.19 | AEROCOM |
| IPCC-TAR | 12.3 | | Dentener et al. (2006) |

The results of AEROCOM are from the website http://nansen.ipsl.jussieu.fr/AEROCOM/data.html

removed by wet deposition than hydrophilic aerosols (i.e. sulfate). This also results in under-estimate of BC concentrations. Additionally, the secondary organic aerosols (SOAs) are not included in our model which can lead to underestimation of simulated OC concentration. As to the dry to wet deposition ratios, we found that the difference was from the size distributions of primary emissions of BC and OC. The change of the primary BC size distribution can change the dry and wet deposition ratios. In this paper, the model uses a sectional representation to simulate the aerosol size distributions with 12 size bins and uses a mass mean diameter (MMD) "0.1 um" as the size distribution of primary BC emissions. After we changed the MMD to 0.24 um, the ration of dry to wet deposition has been changed to the value similar to most of other models (Table 3).

### 3.2 Simulated aerosol optical properties

Figure 3a shows the global annual mean distribution of the simulated total AOD at 550 nm. The highest AOD values (0.4–0.7) were found over the Sahara Desert, followed by

**Table 3** The global budget of BC for different mass mean diameter (MMD)

| MMD (um) | Burden (Tg) | Emission (Tg year$^{-1}$) | Dry deposition (%) | Wet deposition (%) |
|---|---|---|---|---|
| 0.1 | 0.07 | 7.7 | 59 | 41 |
| 0.24 | 0.071 | 7.7 | 29 | 71 |

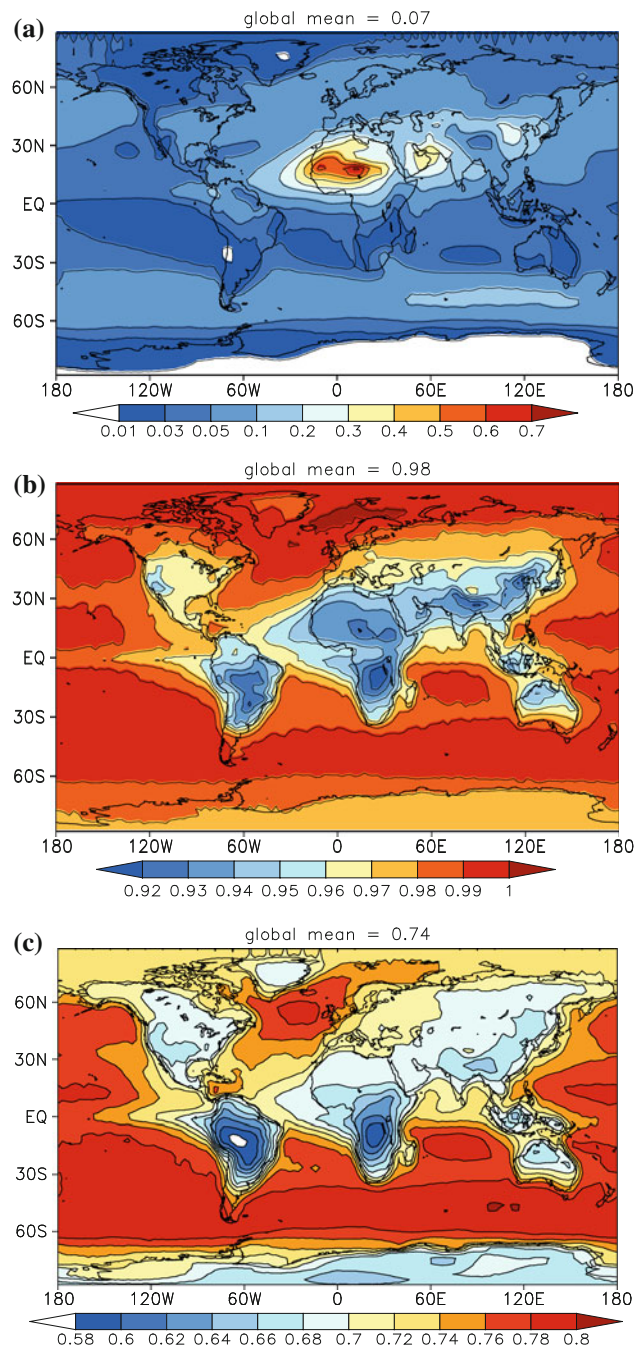


**Fig. 3** The global annual mean distributions of simulated **a** total AOD, **b** single scattering albedo and **c** asymmetry parameter at 550 nm

Arabia in West Asia (0.2–0.4). These were both due to the large contribution from soil dust. The AODs in east China were usually more than 0.1. They reached a maximum value of more than 0.2 in north China, which was larger than that for most other continental areas, except for those mentioned above. The AOD values were around 0.1 in developed countries such as those in North America and west Europe and ranged from 0.05 to 0.1 over the oceans between 30° and 60° in both hemispheres, due to the contributions from sea salt and sulfate. In terms of the global mean, soil dust aerosols had the largest optical depth (0.028), followed by sea salt (0.026), sulfate (0.01), OC (0.005), and BC (0.0006). Figure 3b, c represent the global annual mean distributions of simulated single scattering albedo and the asymmetry parameter at 550 nm for all aerosols, respectively. The single scattering albedos were around 0.92 and the asymmetry parameters were in the range of 0.58–0.66 in East Asia, South Asia, and South America, where carbonaceous aerosols are a major aerosol component, and in North Africa and West Asia, where the soil dust is dominant. However, in North America, where the sulfate burden is high, the single scattering albedo and asymmetry parameter were around 0.96 and 0.68, respectively. This was also the case in Europe, where the two variables were around 0.97 and 0.7, respectively. Over oceans, the single scattering albedo approached 1.0, and the asymmetry parameters ranged from 0.74 to 0.9 due to the scattering effect of sea salt aerosols.

Figure 4 compares the monthly mean AODs between the simulation and measurement from CARSNET at six sites: Beijing (116.5°E, 39.8°N), Lin'an (119.73°E, 30.3°N), Pudong (121.5°E, 31.3°N), Dunhuang (94.7°E, 40.15°N), Ejinaqi (101.1°E, 42°N), and Lasa (91.1°E, 29.7°N). The simulated values were close to the minimum limit of observations at Beijing and Dunhuang, and the magnitude and seasonal variation of simulated AODs agreed closely with the observations at Ejinaqi. However, the simulated values were lower than the observed values at Lin'an, Pudong, and Lasa, which can partially be attributed to the lack of nitrate and ammonium aerosols.

The simulated total AODs were compared with the ground-based sun photometer measurements from AERONET in Fig. 5. Figure 5a–c show comparisons at sites in

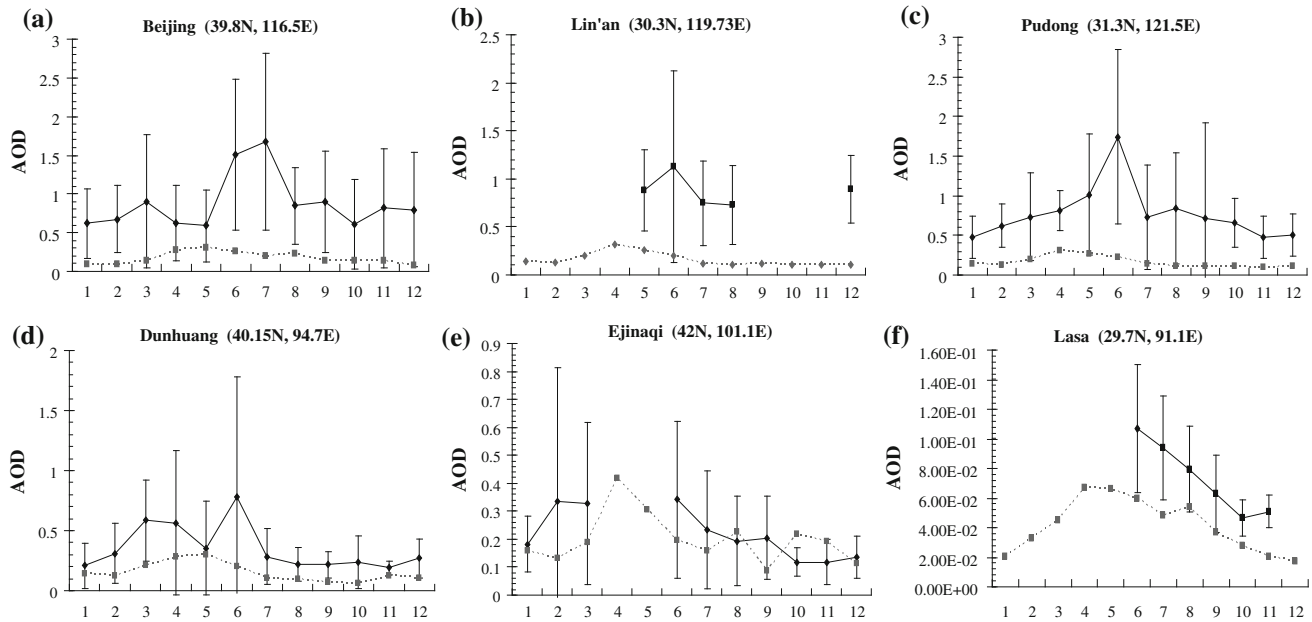


**Fig. 4** Comparisons of simulated total AOD (*dashed line*) with those measured (*solid line*) at 6 CARSNET sites at 550 nm. The *error bar* indicates the standard deviation of observed optical depth. The CARSNET data are from China Meteorological Administration Aerosol Remote Sensing NETwork

East Asia. The modeled total AODs over Beijing (116.3°E, 40°N) and Gosan (126.2°E, 33.3°N) agreed reasonably with measurements of seasonal variation. Both showed higher magnitudes in spring and summer, which were slightly higher than the minimum limit of the observed values at these sites. The simulated values in Osaka (135.6°E, 34.7°N) were lower than the observations in spring and summer, most likely because of the weaker transport of aerosols from China and omission of nitrate and ammonium aerosols in the model.

Figure 5d–h compare the modeled and measured AODs at the sites that were mainly influenced by soil dust aerosols. As can be seen from the comparison of the Hamin (54.3°E, 23°N) site in West Asia, the model could capture the seasonal variations fairly well, including a peak from June to August. However, the simulated values were higher in summer (July) and lower in winter than those of AERONET. The magnitude and seasonal variation of the simulated AODs agreed closely with those observed at Dalanzadgad (104.4°E, 43.6°N) in Mongolia and at the IER_Cinzana (5.9°W, 13.3°N), Saada (8.2°W, 31.6°N), and La_laguna (16.3°W, 28.5°N) sites in Africa. However, the values were slightly higher than the maximum limit of observations at La_laguna in spring.

Figure 5i–k exhibited similar properties at three sites in Europe that were mostly affected by sulfate: Venice (12.5°E, 45.3°N), Davos (9.8°E, 46.8°N), and Laegeren (8.4°E, 47.5°N). The magnitude and seasonal variation of simulated AODs agreed well with the observations at Davos, and the simulated values were close to the minimum limit of observations at Venice and Laegeren. The deviations of simulations from observed values in Europe were also partially due to SOAs being ignored in the model.

Figure 5l–n show comparisons at sites in North America where sulfate and dust aerosols dominate. As can be seen for Ames (93.8°W, 42°N), Bondville (88.4°W, 40°N), and Sevilleta (106.9°W, 34.4°N), the simulated AODs agreed reasonably with measurements from November to March, but approached the minimum limit of the observations in other months. At the same time, the model tended to underestimate AODs in South America (Fig. 6o, p), likely because of the low carbonaceous aerosol emissions shown by the model in that region.

Finally, Fig. 5q, r give AODs for remote oceanic sites: Dunedin (170.5°E, 45.9°S) and Lanai (156.9°W, 20.7°N). The model system reproduced the seasonal variations of AODs well, but it obviously overestimated the AOD at Dunedin during May and September and underestimated the values at Lanai between April and June. The AODs of other months were in the range of the measurements.

Figure 6 summarizes the comparisons of the single scattering albedo and asymmetry parameter between the simulations and observations at 52 AERONET sites at 550 nm. The biases of the simulated single scattering albedos were less than 0.04 at most sites, with overestimation in general (Fig. 6a). The mean difference between simulated and observed single scattering albedos was 4%, but extreme deviations exceeded 7% at some sites in western Europe, North and South America and northern

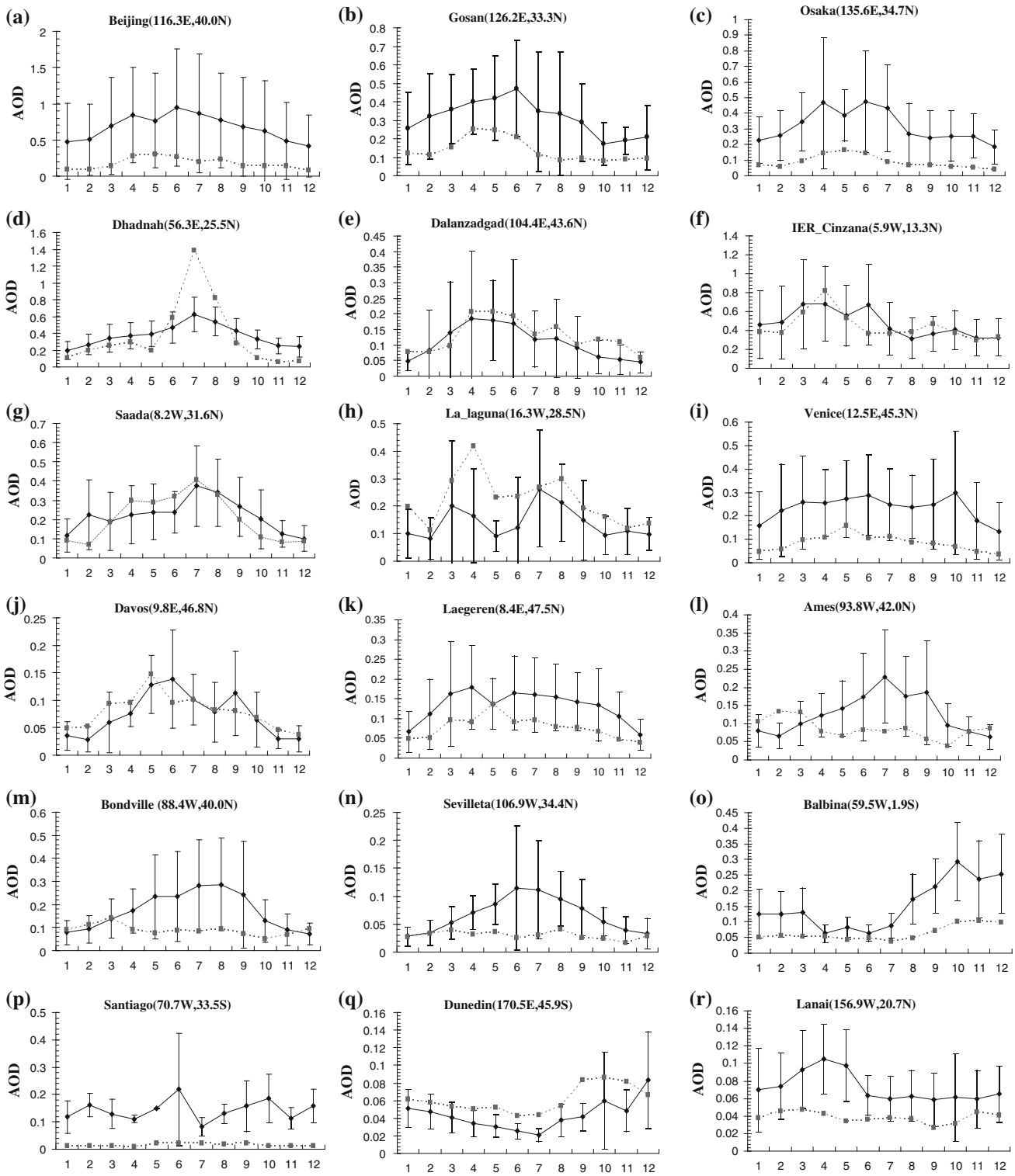


**Fig. 5** Same as in Fig. 5 but for AERONET observations

Africa due to the underestimation of the BC concentration. The model simulated the asymmetry parameters well, with reasonable agreement with measurements (Fig. 6b). The mean difference between the simulated and observed asymmetry parameters was 5%, with the largest biases around 10% at some sites in Africa.

The errors in the above comparison were caused by various factors, including errors in the source emissions,

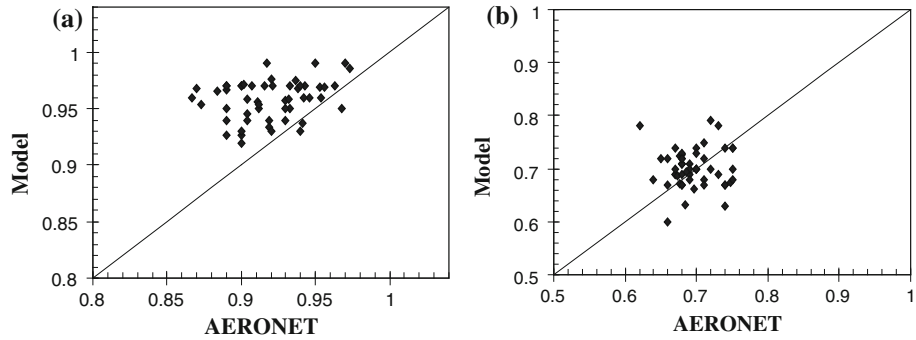


**Fig. 6** Scatterplots of the simulated **a** single scattering albedo and **b** asymmetry parameter versus AERONET at 52 sites at 550 nm

observational instruments, limitations in the model resolution and the implementation of physical processes in the model. In addition, nitrate and ammonium aerosols and SOAs were not included.

### 3.3 Direct radiative forcing of aerosols

Instantaneous radiative forcing calculations were performed online with the AGCM-aerosol coupled system. Figure 7 shows the annual mean distributions of the simulated DRF of each aerosol species at the TOA under all-sky and clear-sky conditions. Generally, sulfate aerosols caused negative radiative forcing at the TOA due to their strong scattering under all-sky conditions (Fig. 7a). The highest DRFs of sulfate, with a maximum value exceeding $-1.0$ W m$^{-2}$, occurred in East Asia and North America due to large industrial emissions of $SO_2$ and sulfate particles. The second strongest DRFs were about $-0.5$ W m$^{-2}$ in India and western Europe. Long-distance transport of sulfate aerosols from the continent and the oxidation of DMS in the ocean caused negative forcing over the ocean. The simulated global annual mean of sulfate DRF at the TOA was $-0.19$ W m$^{-2}$, which was consistent with the estimations of $-0.19$ W m$^{-2}$ by Koch (2001) and $-0.21$ W m$^{-2}$ by Takemura et al. (2005).

BC can absorb solar radiation, generating positive radiative forcing at the TOA under all-sky conditions (Fig. 7b). The region with the largest DRF was East Asia, especially south and east China, where the maximum value reached approximately $+1.0$ W m$^{-2}$. The large DRF of BC in that region was mainly caused by local fossil fuel and biomass burning. The DRFs exceeded $+0.5$ W m$^{-2}$ in most of central Africa and were attributable to the natural burning of carbonaceous materials. BC DRFs were mainly above $+0.1$ W m$^{-2}$ in western Europe, eastern U.S., and South America. There was also positive forcing at the high latitudes of more than 60°N, resulting from long-distance transport of BC emitted at lower latitudes. The simulated global annual mean of BC DRF at the TOA was $+0.1$ W m$^{-2}$, close to the results of $+0.08$ W m$^{-2}$ estimated by Pitari et al. (2002) but much smaller than the $+0.32$ W m$^{-2}$ reported by Takemura et al. (2005) and $+0.61$ W m$^{-2}$ estimated by Hansen et al. (2005). In this study, the assuming external mixing states of black carbon aerosols could potentially lead to an underestimate of BC forcing (Bond and Bergstrom 2006).

The main optical property of OC is its scattering of solar radiation. This results in negative DRF at the TOA under all-sky conditions (Fig. 7c). The distributions of the DRF of OC were basically consistent with those of BC but with negative values. The largest DRFs of OC occurred in central Africa, where maximum values exceeded $-1.0$ W m$^{-2}$. Other regions with large OC DRF included South America, Southeast Asia, North America, and Europe. DRFs in these regions were generally between $-0.2$ and $-1.0$ W m$^{-2}$. The transport distance of OC is generally much farther than that of BC because of the strongly hydrophilic properties of OC. This implies that the spatial extent of the forcing due to OC is larger than that of BC. The simulated global annual mean of OC DRF at the TOA was $-0.15$ W m$^{-2}$, which agreed closely with the results of $-0.18$ W m$^{-2}$ estimated by Chung and Seinfeld (2002), $-0.14$ W m$^{-2}$ by Koch (2001), and $-0.1$ W m$^{-2}$ by Takemura et al. (2005).

Soil dust is another kind of aerosol that scatters solar radiation. It usually causes negative DRF at the TOA under all-sky conditions (Fig. 7d). However, the absorbing effect of dust on longwave radiation was not considered in this work. The largest forcing mainly occurred over West Asia, north China, and especially northern and western Africa. In those regions, maximum forcing exceeded $-10$ W m$^{-2}$ because of the large dust loading, high surface albedo, and abundance of large-scale stratus clouds that cause multiple scattering of solar radiation (Schumacher and Houze 2006). The simulated global annual mean DRF of dust at the TOA was $-0.9$ W m$^{-2}$, which was smaller than those of AEROCOM models (e.g. $-0.75$ W m$^{-2}$ by GISS, $-0.6$ by LSCE, and $-0.54$ by UMI; IPCC 2007).

Sea salt aerosols produced negative forcing globally at the TOA under all-sky conditions because of their scattering properties (Fig. 7e). The largest forcing by sea salt occurred over the oceans between 30° and 60° in both

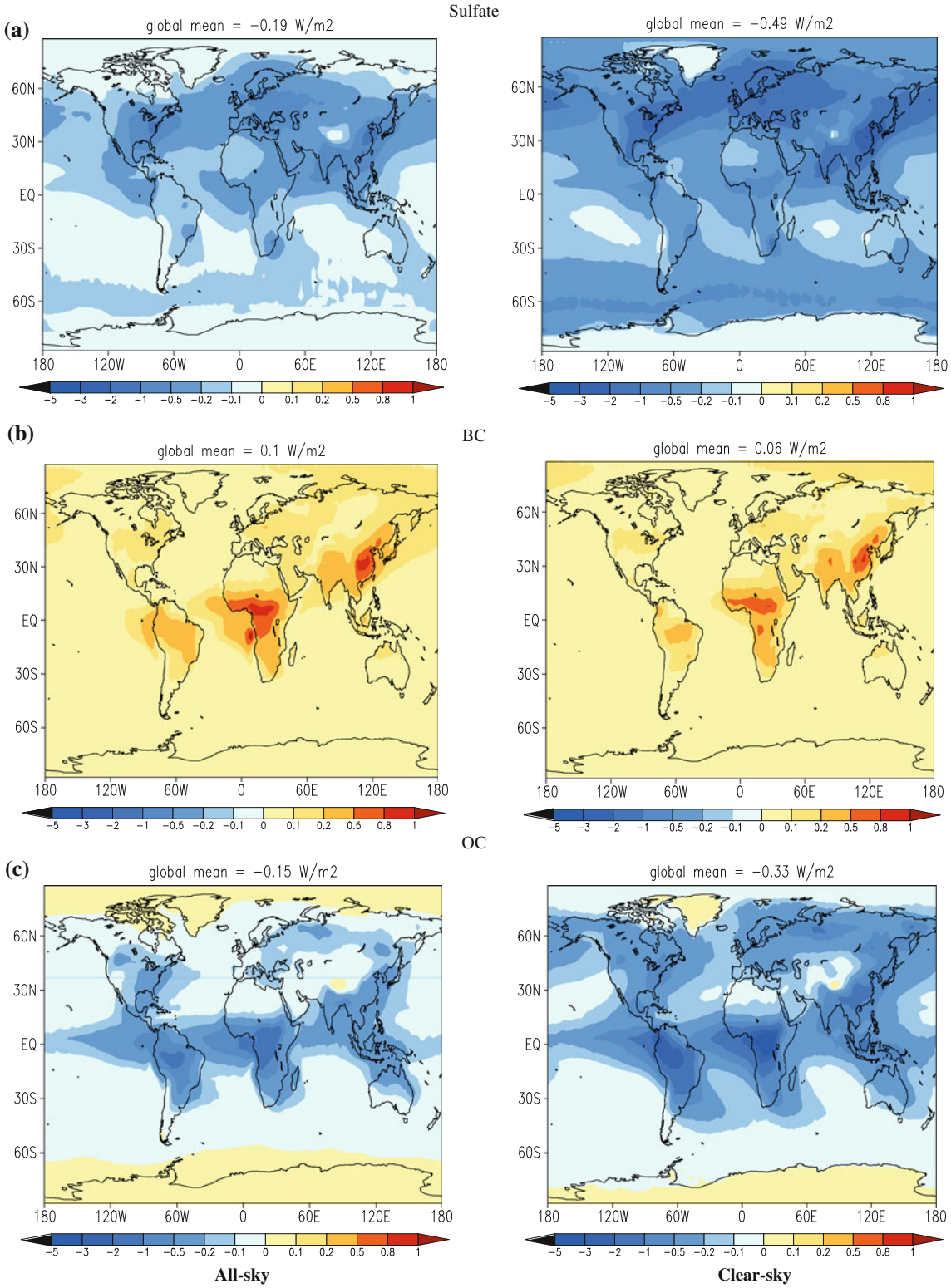


**Fig. 7** Annual mean distributions of the simulated DRF (W $m^{-2}$) due to **a** sulfate, **b** BC, **c** OC, **d** soil dust and **e** sea salt at the TOA under all-sky (*left*) and clear-sky (*right*) conditions

hemispheres. The maximum cooling of −2.0 W $m^{-2}$ in the model was very similar to the results obtained by Liao et al. (2004). The simulated global annual mean DRF of sea salt at the TOA was −0.83 W $m^{-2}$. However, there are still large uncertainties in sea salt forcing, and previous estimates of the global annual mean of this forcing range from

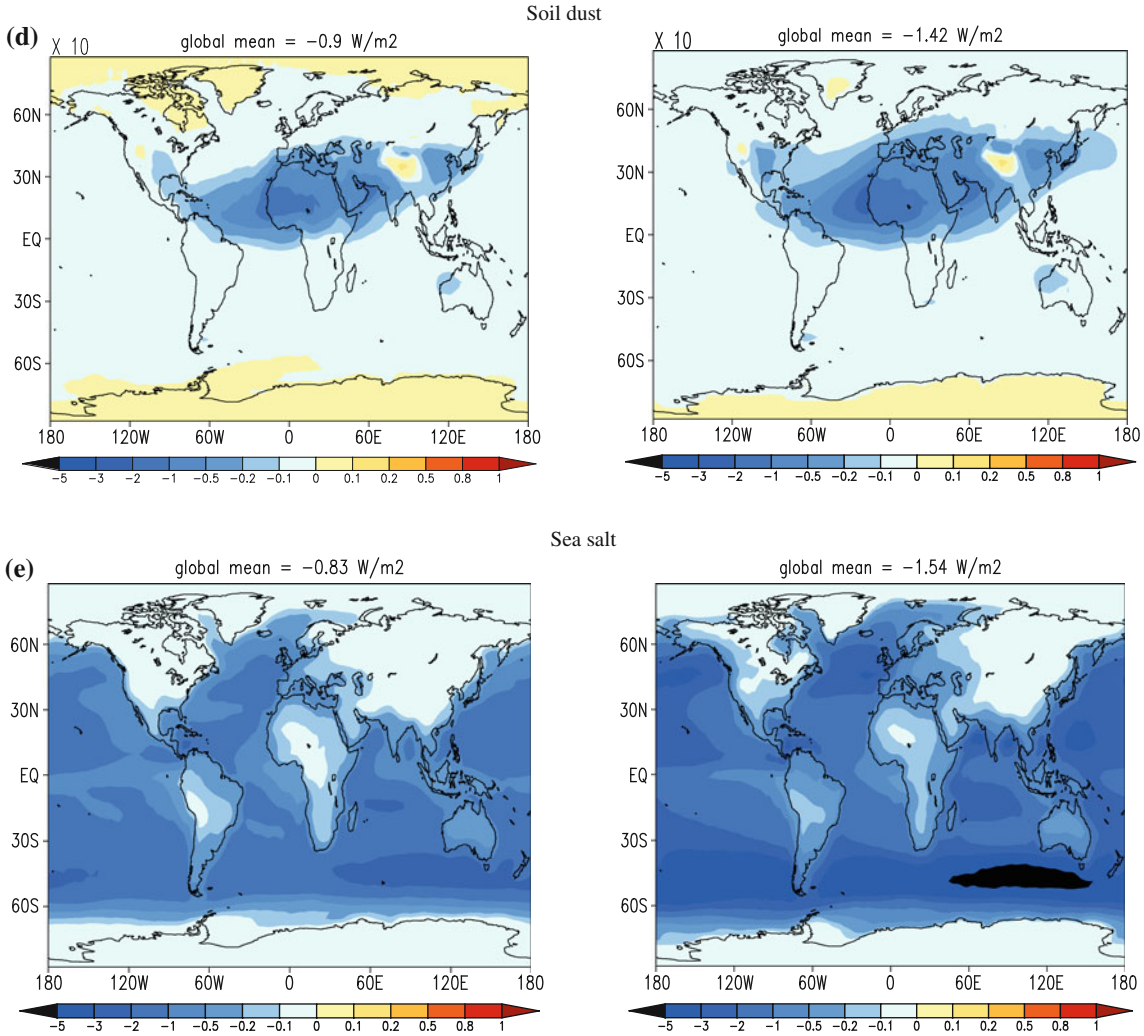


**Fig. 7** continued

−0.31 (Takemura et al. 2002) to −1.1 W $m^{-2}$ (Grini et al. 2002).

The strength and extension of the DRF due to various scattering aerosols may be less under all-sky conditions than under clear-sky conditions, as seen in Fig. 7. However, the sign of the forcing becomes opposite for absorbing aerosols such as BC. Therefore, it is concluded that the presence of clouds can enhance positive forcing and weaken negative forcing at the TOA, which is consistent with the results of Zhang et al. (2009). Table 4 lists the simulated annual hemispherical and global mean DRF by each species of aerosol components at the TOA and surface under all-sky and clear-sky conditions. The annual mean DRFs for three types of aerosol mainly produced by human activities including sulfate, BC, and OC were obviously higher in the NH than in the SH, and the DRFs were higher at the surface than at the TOA due to the multiple scattering and absorption of solar radiation by aerosols in the atmosphere. The simulated global annual means of the DRFs at the TOA due to all aerosols and three types of aerosol (sulfate, BC and OC) were −2.03 and −0.23 W $m^{-2}$ under all-sky conditions, respectively.

### 3.4 Effect of sulfate, BC and OC aerosols on the East Asian summer monsoon

The East Asian summer monsoon plays a controlling role in the summer climate in East Asia, where the emissions of sulfate, BC and OC aerosols are the highest in the world. The large aerosol burden inevitably affects the temperature structure and atmospheric circulation by changing the radiation fields and thereby also affects the East Asian summer monsoon and regional climate. The results obtained in this work showed that the summer season (June, July, August: JJA) average DRFs due to the aforementioned three types of aerosol in East Asia (20°–40°N,

**Table 4** Simulated annual hemispherical and global mean DRF due to different aerosol components at the TOA and surface under all-sky and clear-sky conditions (W $m^{-2}$)

| | All sky | | | Clear sky | | |
|---|---|---|---|---|---|---|
| | NH | SH | Global | NH | SH | Global |
| Sulfate | −0.28 (−0.3) | −0.1 (−0.11) | −0.19 (−0.21) | −0.68 (−0.71) | −0.26 (−0.27) | −0.47 (−0.49) |
| BC | +0.12 (−0.24) | +0.06 (−0.15) | +0.1 (−0.19) | +0.09 (−0.32) | +0.03 (−0.18) | +0.06 (−0.25) |
| OC | −0.16 (−0.27) | −0.13 (−0.21) | −0.15 (−0.24) | −0.39 (−0.52) | −0.27 (−0.36) | −0.33 (−0.44) |
| Dust | −1.7 (−3.8) | −0.13 (−0.21) | −0.9 (−1.98) | −2.6 (−4.8) | −0.2 (−0.29) | −1.42 (−2.55) |
| Sea salt | −0.61 (−0.71) | −1.0 (−1.2) | −0.83 (−0.94) | −1.1 (−1.3) | −2.0 (−2.2) | −1.54 (−1.72) |
| Sulfate + BC + OC | | | −0.23 (−0.59) | | | −0.73 (−1.13) |
| All aerosols | | | −2.03 (−3.63) | | | −3.84 (−5.61) |

The values in parentheses represent the corresponding surface forcing

*NH* northern hemisphere, *SH* southern hemisphere

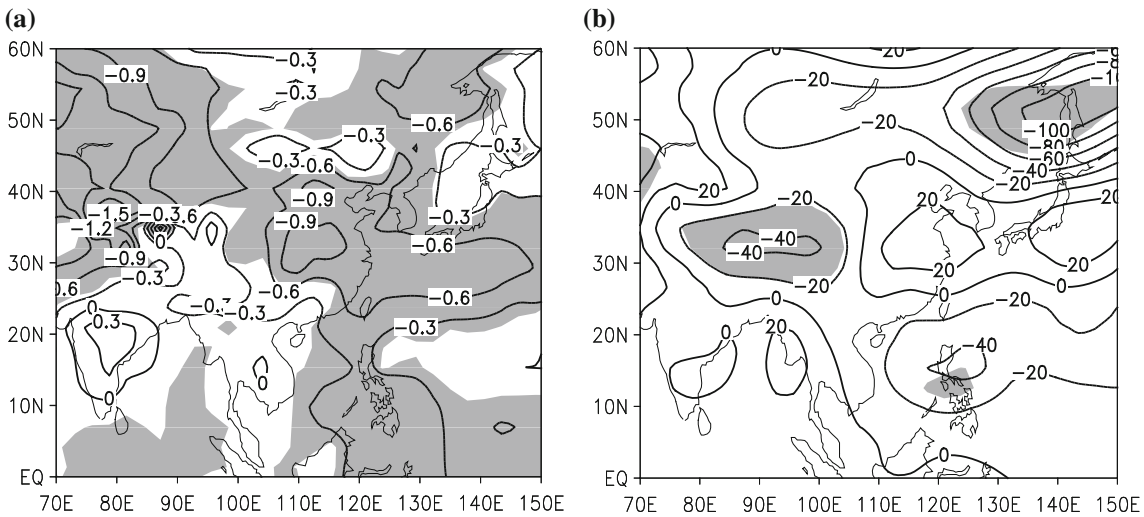


**Fig. 8** The differences of JJA mean **a** surface temperature (°C) and **b** surface pressure (Pa) between EXP1 and EXP2. The *shade* indicates a confidence level of 90% from the *T*-test

100°–140°E) at the TOA and surface were −1.4 and −3.3 W $m^{-2}$, respectively, leading to decreases of 0.58°C and 0.14 mm $day^{-1}$ in the JJA means of surface temperature and precipitation rate in this area, respectively.

Figure 8 shows the changes of the JJA mean surface temperature and surface pressure in East Asian monsoon region due to sulfate, BC and OC aerosols. Any species of aerosol, whether absorbing or scattering, will decrease the solar radiative flux arriving at the surface and hence the surface temperature. A decrease of surface temperature was seen almost everywhere in East Asian monsoon region, but the decrease of surface temperature over land was obviously stronger than that over sea (Fig. 8a). The cooling over land at most areas of East Asia exceeded −0.6°C, especially in north China and central and east China with a magnitude of −0.9°C or so due to the huge loading of aerosols. The cooling in the west Pacific was below −0.6°C. The distribution of surface temperature changes over land basically agreed with the results reported by Liu et al. (2009) which considered the sulfate and BC aerosols in a GCM, whereas the changes over oceans is contrary to the results by Liu et al. (2009) because they used the prescribed SST in their GCM. As can be seen from the change of surface pressure in JJA (Fig. 8b), surface pressure was increased dramatically in the central and east China due to cooling over land, whereas surface pressure over the ocean on the south of China was reduced which could be relative to the changes of wind field and local circulation (Figs. 9, 11). The formation of East Asian summer monsoon is mainly due to contrast of land-sea temperature and pressure. Figure 8 showed that the differences of land-sea surface temperature and pressure were weakened in East Asian monsoon region due to the effect of aerosols, thus leading to the weakening of East Asian

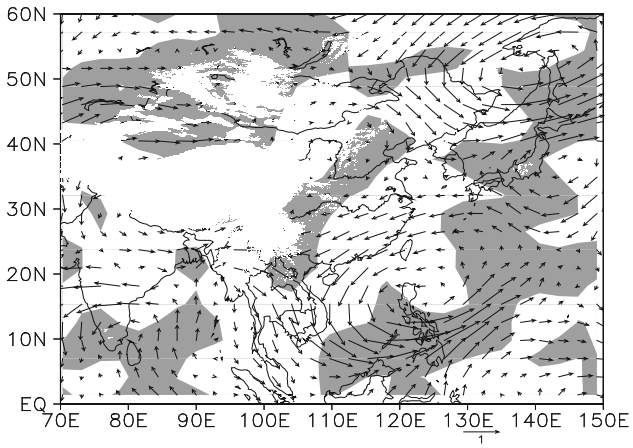


**Fig. 9** The differences of JJA mean wind field at 850 hPa (*vector*) between EXP1 and EXP2. The *shade* shows the differences of moisture flux divergence between EXP1 and EXP2 are negative integrated from 850 to 700 hPa

summer monsoon. The temperature changes are significant at a 90% confidence level in most areas of East Asian monsoon region, whereas the confidence level of pressure changes was not significant here.

East Asian summer monsoon has a typical feature on summer wind field at 850 hPa. The southwest and south winds prevail in south and east China in summer, which carries warm and moist air into China from ocean and induces precipitation. As can be seen from the change of wind field at 850 hPa in JJA (Fig. 9), the enhanced northeasterly flow in south and east China due to sulfate, BC and OC aerosols distinctly weakened the intensity of the southwest summer monsoon, and moreover the moisture flux divergence in lower atmosphere was strengthened. Thus, the monsoon precipitation is suppressed in most areas of south and east China and over the nearby oceans (Fig. 10b). Generally, the increase (or decrease) of surface latent heat flux corresponds to the increase (or decrease) of precipitation. The decrease of surface temperature led to the reducing of surface evaporation and latent heat flux in south and east China (Fig. 10a), which caused less moist air into atmosphere and reduced the precipitation. However, the change of precipitation wasn't consistent with that of surface latent heat flux over the South China Sea, which could mainly caused by the changes of wind field and circulation. A cyclonic circulation formed over the west Pacific and South China Sea at 850 hPa and the moisture flux convergence in lower atmosphere in the south of the cyclonic was obviously strengthened (Fig. 9), which increased the vertical transport of water vapor and precipitation. This indicated that the effect of dynamic on precipitation was predominant over ocean. The changes of precipitation in East Asian monsoon region in this paper were consistent with the results by Lau et al. (2006) due to the effect of five aerosol species including sulfate, BC, OC, soil dust, and sea salt.

Figure 11 shows the changes of JJA mean temperature and vertical meridional circulation zonally averaged between 105°E and 120°E due to the aerosols. The figure clearly indicated the responses of atmospheric dynamic and thermodynamic on the aerosol effects. As can be seen from Fig. 11a, aforementioned three species of aerosol led to the decrease of temperature in whole troposphere, which indicated the total feature of these aerosols was scattering over China. The reduce of temperature in the lower atmosphere was smaller than that in mid and high atmosphere to the south of 15°N which was beneficial to the

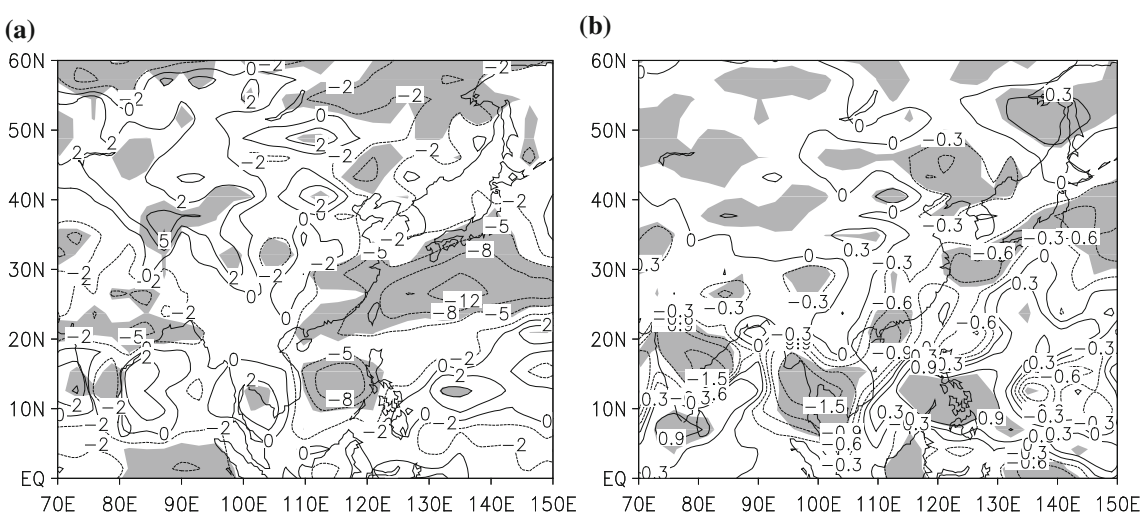


**Fig. 10** The differences of JJA mean **a** surface latent heat flux (W m$^{-2}$) and **b** precipitation (mm day$^{-1}$) between EXP1 and EXP2. The *shade* indicates a confidence level of 90% from the *T*-test

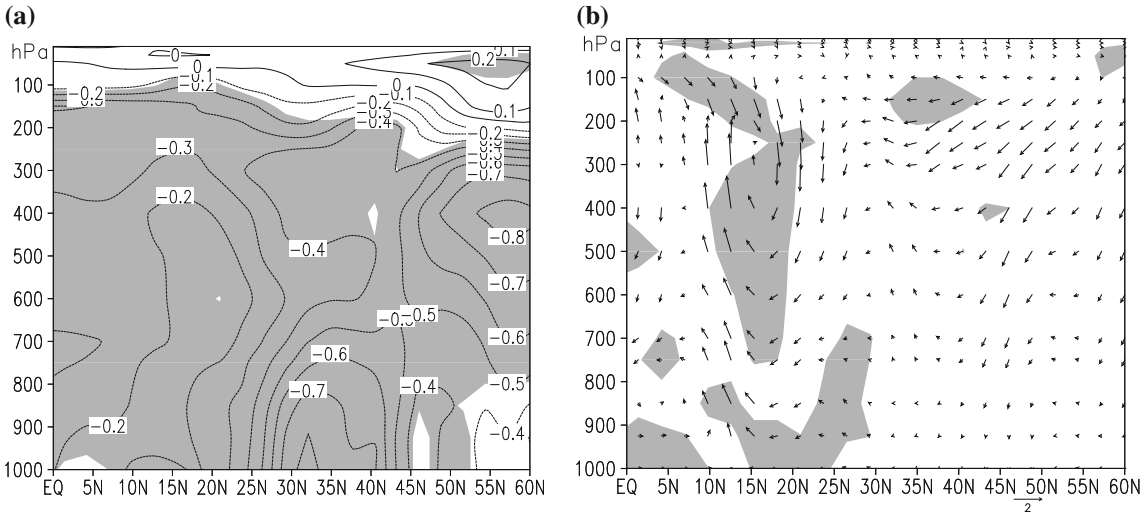


**Fig. 11** The differences of JJA mean **a** temperature (°C) and **b** vertical meridional circulation zonally averaged between 105°E and 120°E between EXP1 and EXP2. The *shade* indicates a confidence level of 90% from the *T*-test

enhancing of vertical ascending motion, whereas the contrary changes occurred between 15°N and 30°N which enhanced the atmospheric stability and suppressed convective motions. The local meridional circulation was changed with the atmospheric temperature changes (Fig. 11b). A clockwise rotation appeared between 10°N and 30°N in which ascending motion developed between 10°N and 15°N and subsidence motion developed between 15°N and 30°N, leading to the weakening of the normal summer meridional circulation here which poses as a counter-clockwise rotation (Liu et al. 2009). The increased subsidence between 15°N and 30°N strengthened the southward motion in lower troposphere, which weakened the northward transport of warm and moist air carried by the East Asian summer monsoon. This result accorded with the changes induced by sulfate reported by Liu et al. (2009). Ultimately, the decrease of moist air and increase of subsidence led to the decrease of monsoon precipitation between 15°N and 30°N in south and east China.

It should be noted that the absorbing BC and scattering OC masses were underestimated obviously in East Asia by this model, which will necessarily affect simulated climatic effect of aerosols over Asia. Menon et al. (2002) showed that absorbing BC aerosol could increase precipitation over southern China and decrease precipitation over northern China. Chung and Ramanathan (2006) indicated that BC aerosol could heat the troposphere and enhance vertical convection over the North Indian Ocean and Indian subcontinent, causing an increase in monsoon precipitation. Randles and Ramaswamy (2008) also found that an enhanced monsoon circulation associated with increased higher absorption aerosol optical depth resulted in the increase of low-level convergence, upward motion, and precipitation, whereas increase of only scattering aerosols weakened the monsoonal circulation and inhibited precipitation. Both of the underestimation of scattering OC and absorbing BC aerosols will have more complicated effects on the local climate of China.

## 4 Conclusions

An interactive coupled climate-aerosol model consisting of the BCC_AGCM2.0.1 and the Canadian Aerosol Module (CAM) was developed at the NCC/CMA. The magnitude and distribution of the simulated sulfate, sea salt and dust column burdens generally agreed with those of AEROCOM_MEDIAN, but the simulated values and ranges of simulated BC and OC column burdens were obviously smaller than those of AEROCOM_MEDIAN, especially in West Europe, North America and East Asia. These biases can be largely from the emission underestimation in our model compared with other models, and moreover the SOAs are not included in our model.

The simulated optical depth, single scattering albedo, and asymmetry parameter of total aerosols (including sulfate, BC, OC, dust, and sea salt) at 550 nm were basically consistent with AERONET observations, except for an obvious underestimation over South America. The mean relative errors of the simulated single scattering albedo and asymmetry parameter against observations were 4% and 5%, respectively. The magnitude and seasonal variation of the simulated AODs agreed closely with CARSNET observations at Ejinaqi, Dunhuang, and Beijing, but the simulated values were slightly lower than observations at Lin'an, Pudong, and Lasa. Ammonium and nitrate aerosols were not included in the present model, which led to lower simulated AODs in some regions and seasons.

The simulated global annual means of DRF due to total aerosols and three types of aerosol including sulfate, BC, and OC at the TOA were −2.06 and −0.23 W $m^{-2}$, respectively, under all-sky conditions. The global annual means of sulfate, BC, and OC DRF at the TOA were −0.19, +0.1, and −0.15 W $m^{-2}$, respectively. Clouds can decrease the extension and strength of the DRF for scattering aerosols, but increase them for absorbing aerosols such as BC.

The summer seasonal average DRFs due to three types of aerosol (sulfate, BC, and OC) in East Asia at the TOA and surface were −1.4 and −3.3 W $m^{-2}$, respectively, leading to decreases of 0.58°C and 0.14 mm $day^{-1}$ in the JJA means of surface temperature and precipitation rate in this area, respectively. The differences of land-sea surface temperature and surface pressure were reduced in East Asian monsoon region due to the effect of these aerosols, thus leading to the weakening of East Asian summer monsoon. The enhanced northeasterly flow in south and east China at 850 hPa due to sulfate, BC and OC aerosols distinctly weakened the intensity of the southwest summer monsoon, and suppressed the monsoon precipitation in most areas of south and east China and over the nearby oceans. The local meridional circulation was also affected due to these aerosols, and a clockwise rotation appeared between 10°N and 30°N. The increased subsidence between 15°N and 30°N strengthened the southward motion in lower troposphere, which weakened the northward transport of warm and moist air carried by the East Asian summer monsoon, and moreover decreased the summer monsoon precipitation in south and east China.

In addition, the model also does not simulate nitrate and SOA, both of which are the important components of aerosols in some parts of Asia. The decrease of land surface temperature in some areas may be larger if taking account these scattering aerosols into in this model, which could more significantly weaken East Asian summer monsoon. But it needs further investigations in the next.

**Acknowledgments** This work is financially supported by National Basic Research Program of China (Grants No. 2011CB403405 and 2006CB403707), the Public Meteorology Special Foundation of MOST (Grant No. GYHY200906020), and the National Key Technology R&D Program (Grant No. 2007BAC03A01&2008-BAC40B02). The authors would like to give thanks to Prof. Q. Fu of Department of Atmospheric Science, University of Washington and Mr. X. W. Jing of NCC/CMA for his helps to the text of this paper.

## References

Ackerman AS et al (2000) Reduction of tropical cloudiness by soot. Science 288:1042–1047

Albrecht B (1989) Aerosols, cloud microphysics, and fractional cloudiness. Science 245:1227–1230

Allen RJ, Sherwood SC (2010) Aerosol-cloud semi-direct effect and land-sea temperature contrast in a GCM. Geophys Res Lett 37. doi:10.1029/2010GL042759

Ayash (2007) Development of an interactive model for studying aerosol-climate interactions using the Canadian aerosol module-Canadian climate center general circulation model modeling framework. Ph D Thesis, p 207

Bauer SE, Menon S, Koch D et al (2010) A global modeling study on carbonaceous aerosol microphysical characteristics and radiative effects. Atmos Chem Phys 10:7439–7456

Bellouin N, Jones A, Haywood J, Christopher SA (2008) Updated estimate of aerosol direct radiative forcing from satellite observations and comparison against the Hadley Centre climate model. J Geophys Res 113. doi:10.1029/2007JD009385

Binkowski FS, Shankar U (1995) The Regional Particulate Matter Model 1. Model description and preliminary results. J Geophys Res 100:26191–26209

Bond T, Bergstrom R (2006) Light absorption by carbonaceous particles: an investigative review. Aerosol Sci Technol 40:27–67

Bond T, Streets D, Yarber K, Nelson S, Wo JH, Klimont Z (2004) A technology-based global inventory of black and organic carbon emissions from combustion. J Geophys Res 109. doi:10.1029/2003JD003697

Brasseur GP, Hauglustaine DA, Walters S, Rasch PJ, Muller JF, Granier C, Tie XX (1998) MOZART, a global chemical transport model for ozone and related chemical tracers 1. Model description. J Geophys Res 103:28265–28289

Briegleb BP (1992) Delta-Eddington approximation for solar radiation in the NCAR Community Climate Model. J Geophys Res 97:7603–7612

Chung C, Ramanathan V (2006) Weakening of North Indian SST Gradients and the Monsoon Rainfall in India and the Sahel. J Climate 19:2036–2045

Chung SH, Seinfeld JH (2002) Global distribution and climate forcing of carbonaceous aerosols. J Geophys Res 107. doi:10.1029/2001JD001397

Cofala J, Amann M, Klimont Z, Schopp W (2005) Scenarios of world anthropogenic emissions of $SO_2$, NOx, and CO up to 2030, internal report of the transboundary air pollution programme, international institute for applied systems analysis. Laxenburg, Austria, p 17

D'Almeida GA, Koepke P, Shettle EP (1991) Atmospheric aerosols: global climatology and radiative characteristics. A. Deepak Publishing, Virginia, p 561

Dentener F, Kinne S, Bond T et al (2006) Emissions of primary aerosol and precursor gases in the years 2000 and 1750 prescribed datasets for AeroCom. Atmos Chem Phys 6:4321–4344

Easter RC (2004) MIRAGE: model description and evaluation of aerosols and trace gases. J Geophys Res 109. doi:10.1029/2004JD004571

Flanner MG, Zender CS, Randerson JT, Rasch PJ (2007) Present-day climate forcing and response from lack carbon in snow. J Geophys Res 112. doi:10.1029/2006JD008003

Ghan SJ, Easter RC, Chapman EG, Abdul-Razzak H, Zhang Y, Leung LR, Laulainen NS, Saylor RD, Zaveri RA (2001) A physically based estimate of radiative forcing by anthropogenic sulfate aerosol. J Geophys Res 106:5279–5293

Gong SL, Barrie LA, Blanchet JP (1997) Modeling sea-salt aerosols in the atmosphere 1. Model development. J Geophys Res 102:3805–3818

Gong SL, Barrie LA, Lazare M (2002) Canadian aerosol module: a size-segregated simulation of atmospheric aerosol processes for climate and air quality models 2. Global sea-salt aerosol and its budgets. J Geophys Res 107. doi:10.1029/2001JD002004

Gong SL et al (2003) Canadian aerosol module: a size-segregated simulation of atmospheric aerosol processes for climate and air

quality models 1. Module development. J Geophys Res 108. doi:10.1029/2001JD002002

Grini A, Myhre G, Sundet JK, Isaksen ISA (2002) Modeling the annual cycle of sea salt in the global 3D model Oslo CTM2: concentrations, fluxes, and radiative impact. J Climate 15:1717–1730

Gu Y, Liou KN, Xue Y, Mechoso CR, Li W, Luo Y (2006) Climatic effects of different aerosol types in China simulated by the UCLA general circulation model. J Geophys Res 111. doi:10.1029/2005JD006312

Hack JJ (1994) Parameterization of moist convection in the NCAR community climate model, CCM2. J Geophys Res 99:5551–5568

Hack JJ, Boville BA, Briegleb BP, Kiehl JT, Rasch PJ, Williamson DL (1993) Description of the NCAR community climate model (CCM2). Technical Report NCAR/TN-382 + STR, National Center for Atmospheric Research, p 120

Hansen J, Nazarenko L (2004) Soot climate forcing via snow and ice albedos. Proc Natl Acad Sci 101:423–428

Hansen J et al (1984) Climate sensitivity: analysis of feedback mechanisms, in climate processes and climate sensitivity. Geophys Monogr Ser 29:130–163

Hansen J, Sato M, Ruedy R (1997) Radiative forcing and climate response. J Geophys Res 102:6831–6864

Hansen J et al (2002) Climate forcings in Goddard Institute for Space Studies SI2000 simulations. J Geophys Res 107(D18). doi:10.1029/2001JD001143

Hansen J et al (2005) Efficacy of climate forcings. J Geophys Res 110. doi:10.1029/2005JD005776

Hauglustaine DA, Brasseur GP, Walters S, Rasch PJ, Muller J-F, Emmons LK, Carroll MA (1998) MOZART, a global chemical transport model for ozone and related chemical tracers 2. Model results and evaluation. J Geophys Res 103:28291–28335

Haywood JM, Ramaswamy V (1998) Global sensitivity studies of the direct radiative forcing due to anthropogenic sulfate and black carbon aerosols. J Geophys Res 103:6043–6058

Houghton JT, Meira Filho LG, Callander BA, Harris N, Kattenberg A, Maskell K (1996) Climate change 1995: the science of climate change. Cambridge University Press, Cambridge, p 572

IPCC (2007) Climate change 2007: the physical science basis. In: Solomon S, Qin D, Manning M, Chen Z, Marquis M, Averyt KB, Tignor M, Miller HL (eds) Contribution of working group I to the fourth assessment report of the intergovernmental panel on climate Change. Cambridge University Press, Cambridge, pp 131–217

Jacobson MZ (1997) Development and application of a new air pollution modeling system, part II, aerosol module structure and design. Atmos Environ 31:131–144

Jacobson MZ (2004) Climate response of fossil fuel and biofuel soot, accounting for soot's feedback to snow and sea ice albedo and emissivity. J Geophys Res 109. doi:10.1029/2004JD004945

Ji ZM et al (2011) Simulation of the anthropogenic aerosols over South Asia and their effects on Indian summer monsoon. Clim Dyn. doi:10.1007/s00382-010-0982-0

Kettle AJ, Andreae MO (2000) Flux of dimethylsulfide from the oceans: a comparison of updated data sets and flux models. J Geophys Res 105:26793–26808

Kiehl JT, Hack JJ, Bonan GB, Boville BB, Williamson DL, Rasch PJ (1998) The national center for atmospheric research community climate model: CCM3. J Climate 11:1131–1149

Kinne S et al (2006) An AeroCom initial assessment optical properties in aerosol component modules of global models. Atmos Chem Phys 6:1815–1834

Koch D (2001) Transport and direct radiative forcing of carbonaceous and sulfate aerosols in the GISS GCM. J Geophys Res 106:20311–20332

Koch D, Menon S, Genio AD (2009) Distinguishing aerosol impacts on climate over the past century. J Climate 22:2659–2677

Kristjansson JE, Iversen T, Kirkevag A, Seland Ø, Debernard J (2005) Response of the climate system to aerosol direct and indirect forcing: role of cloud feedbacks. J Geophys Res 110. doi:10.1029/2005JD006299

Kuhlmann J, Quaas J (2010) How can aerosols affect the Asian summer monsoon? Assessment during three consecutive pre-monsoon seasons from CALIPSO satellite data. Atmos Chem Phys 10:4887–4926

Lau KM, Kim KM (2006) Observational relationships between aerosol and Asian monsoon rainfall, and circulation. Geophys Res Lett 33. doi:10.1029/2006GL027546

Lau KM et al (2006) Asian summer monsoon anomalies induced by aerosol direct forcing: the role of the Tibetan Plateau. Clim Dyn 26:855–864. doi:10.1007/s00382-006-0114-z

Lestari R, Iwasaki T (2006) A GCM study on the roles of the seasonal marches of the SST and land-sea thermal contrast in the onset of the Asian summer monsoon. J Meteorol Soc Jpn 84(1):69–83

Li Z, Lee KH, Wang Y, Xin J, Hao WM (2010) First Observation-based Estimates of Cloud-free Aerosol Radiative Forcing across China. J Geophys Res 115. doi:10.1029/2009JD013306

Liao H, Seinfeld JH, Adams PJ, Mickley LJ (2004) Global radiative forcing of coupled tropospheric ozone and aerosols in a unified general circulation model. J Geophys Res 109. doi:10.1029/2003JD004456

Liou KN (2004) Introduction to atmospheric radiation version 2. China Meteorological Press, p 614

Liu Y, Sun J, Yang B (2009) The effects of black carbon and sulfate aerosols in China regions on East Asia monsoons. Tellus(B) 61:642–656

Lohmann U, Feichter J (2005) Global indirect aerosol effects: a review. Atmos Chem Phys 5:715–737

Marticorena B, Bergametti G (1995) Modeling the atmospheric dust cycle. 1: design of a soil-derived dust emission scheme. J Geophys Res 100:16415–16430

Meng Z, Dabdub D, Seinfeld JH (1998) Size-resolved and chemically resolved model of atmospheric aerosol dynamics. J Geophys Res 103:3419–3435

Menon S, Hansen J, Nazarenko L, Luo YF (2002) Climate effects of black carbon aerosols in China and India. Science 297:2250–2253

Ming Y, Ramaswamy V (2009) Nonlinear climate and hydrological responses to aerosol effects. J Climate 22:1329–1339

Myhre G (2009) Consistency between satellite-derived and modeled estimates of the direct aerosol effect. Science 325:187–190

Nakajima T, Yoon S-C, Ramanathan V et al (2007) Overview of the atmospheric Brown Cloud East Asian regional experiment 2005 and a study of the aerosol direct radiative forcing in East Asia. J Geophys Res 112. doi:10.1029/2007JD009009

Nightingale P, Malin G, Law C, Watson A, Liss P, Liddicoat M, Boutin J, Upstill-Goddard RC (2000) In situ evaluation of airsea gas exchange parameterizations using novel conservative and volatile tracers. Glob Biogeochem Cycles 14:373–387

Olivier J, Berdowski J, Peters J, Bakker J, Visschedijk A, Bloos J (2002) Applications of EDGAR including a description of EDGAR V3.0: reference database with trend data for 1970–1995. NRP Report, 410200 051. RIVM, Bilthoven

Pitari G, Mancini E, Rizi V, Shindell DT (2002) Impact of future climate and emissions changes on stratospheric aerosols and ozone. J Atmos Sci 59:414–440

Posselt R, Lohmann U (2009) Sensitivity of the total anthropogenic aerosol effect to the treatment of rain in a global climate model. Geophys Res Lett 36. doi:10.1029/2008GL035796

Ramanathan V, Ramana MV, Roberts G, Kim D, Corrigan C, Chung C, Winker D (2007) Warming trends in Asia amplified by brown cloud solar absorption. Nature 448:575–578

Ramaswamy V et al (2001) Radiative forcing of climate change. In: Climate change 2001: the scientific basis. In: Houghton M et al (eds) Contribution of working group I to the third assessment report of the intergovernmental panel on climate change. Cambridge University Press, pp 349–416

Randles CA, Ramaswamy V (2008) Absorbing aerosols over Asia: a geophysical fluid dynamics laboratory general circulation model sensitivity study of model response to aerosol optical depth and aerosol absorption. J Geophys Res 113. doi:10.1029/2008JD010140

Rasch PJ, Kristjansson JE (1998) A comparison of the CCM3 model climate using diagnosed and predicted condensate parameterizations. J Climate 11:1587–1614

Reddy MS et al (2005) Estimates of global multicomponent aerosol optical depth and direct radiative perturbation in the Laboratoire de Meteorologie Dynamique general circulation model. J Geophys Res 110. doi:10.1029/2004JD004757

Schulz M et al (2006) Radiative forcing by aerosols as derived from the AeroCom present-day and pre-industrial simulations. Atmos Chem Phys 6:5225–5246

Schumacher C, Houze RA (2006) Stratiform precipitation production over sub-Saharan Africa and the tropical East Atlantic as observed by TRMM. Q J R Meteor Soc 132:2235–2255

Slingo JM (1987) The development and verification of a cloud prediction scheme for the ECMWF model. Quart J Roy Meteor Soc 113:899–927

Slingo A (1989) A GCM parameterization for the shortwave radiative properties of clouds. J Atmos Sci 46:1419–1427

Streets DG et al (2003) An inventory of gaseous and primary aerosol emissions in Asia in the year 2000. J Geophys Res 108. doi:10.1029/2002JD003093

Takemura T, Nozawa T, Emori S, Nakajima TY, Nakajima T (2005) Simulation of climate response to aerosol direct and indirect effects with aerosol transport-radiation model. J Geophys Res 110. doi:10.1029/2004JD005029

Textor C et al (2006) Analysis and quantification of the diversities of aerosol life cycles within AeroCom. Atmos Chem Phys 6:1777–1813

Twomey SA (1977) The influence of pollution on the shortwave albedo of clouds. J Atmos Sci 34:1149–1152

Van der Werf GR, Randerson JT, Collatz GJ, Giglio L, Kasibhatla PS, Arellano AF, Olsen SC, Kasischke ES (2004) Continental-scale partitioning of fire emissions during the 1997 to 2001 El Nino/La Nina period. Science 303:73–76

Wang ZL, Guo PW, Zhang H (2009a) A numerical study of direct radiative forcing due to black carbon and its effects on the summer precipitation in China. Clim Environ Res 14:161–171 (in Chinese)

Wang ZL, Zhang H, Guo PW (2009b) Effects of black carbon aerosol in south Asia on Asian summer monsoon. Plat Meteorol 28:419–424 (in Chinese)

Warren S, Wiscombe W (1980) A model for the spectral albedo of snow. II: snow containing atmospheric aerosols. J Atmos Sci 37:2734–2745

Wilcox EM, Roberts G, Ramanathan V (2006) Influence of aerosols on the shortwave cloud radiative forcing from North Pacific oceanic clouds: results from the Cloud Indirect Forcing Experiment (CIFEX). Geophys Res Lett 33. doi:10.1029/2006GL027150

Wiscombe WJ (1980) Improved mie scattering algorithms. Appl Opt 19:1505–1509

Wu T, Wu G (2004) An empirical formula to compute snow cover fraction in GCMs. Adv Atmos Sci 21:529–535

Wu T, Yu R, Zhang F (2008) A modified dynamic framework for the atmospheric spectral model and its application. J Atmos Sci 65:2235–2253

Wu TW et al (2010) The Beijing Climate Center atmospheric general circulation model: description and its performance for the present-day. Climate Dyn 34:123–147. doi:10.1007/s00382-008-0487-2

Yan H (1987) Design of a nested fine-mesh model over the complex topograph, Part two: parameterization of the subgrid physical processes. Plat Meteorol 6(suppl):64–139

Zhang XY (2007) Aerosol over China and their climate effects. Adv Earth Sci 22(1):12–16

Zhang GJ, Mu M (2005) Effects of modifications to the Zhang-McFarlane convection parameterization on the simulation of the tropical precipitation in the National Center for Atmospheric Research Community Climate Model, version 3. J Geophys Res 110. doi:10.1029/2004JD005617

Zhang M, Lin W, Bretherton CS, Hack JJ, Rasch PJ (2003) A modified formulation of fractional stratiform condensation rate in the NCAR community atmospheric model CAM2. J Geophys Res 108. doi:10.1029/2002JD002523

Zhang X, Wang X, Yan P (2008) Re-evaluating the impacts of human activity and environmental change on desertification in the Minqin Oasis, China. Environ Geol 55:705–715

Zhang H, Wang ZL, Guo PW et al (2009) A modeling study of the effects of direct radiative forcing due to carbonaceous aerosol on the climate in East Asia. Adv Atmos Sci 26:57–66

Journal of Quantitative Spectroscopy & Radiative Transfer 112 (2011) 220–229

Contents lists available at ScienceDirect

Journal of Quantitative Spectroscopy & Radiative Transfer

journal homepage: www.elsevier.com/locate/jqsrt

# A study of the radiative forcing and global warming potentials of hydrofluorocarbons

Hua Zhang [a,*], Jinxiu Wu [b], Peng Lu [c,a]

[a] Laboratory for Climate Studies, National Climate Center, China Meteorological Administration, Beijing 100081, China
[b] Shanghai Meteorological Media Center, Shanghai 200030, China
[c] Chinese Academy of Meteorological Sciences, Beijing 100081, China

ARTICLE INFO

*Keywords:*
HFCs
Correlated *k*-distribution
Radiative forcing
Global warming potential (GWPs)
Global temperature potential (GTPs)

ABSTRACT

We developed a new radiation parameterization of hydrofluorocarbons (HFCs), using the correlated *k*-distribution method and the high-resolution transmission molecular absorption (HITRAN) 2004 database. We examined the instantaneous and stratospheric adjusted radiative efficiencies of HFCs for clear-sky and all-sky conditions. We also calculated the radiative forcing of HFCs from preindustrial times to the present and for future scenarios given by the Intergovernmental Panel on Climate Change Special Report on Emission Scenarios (SRES, in short). Global warming potential and global temperature potential were then examined and compared on the basis of the calculated radiative efficiencies. Finally, we discuss surface temperature changes due to various HFC emissions.

© 2010 Elsevier Ltd. All rights reserved.

## 1. Introduction

Hydrofluorocarbons (HFCs) have been widely used in industry since 1990 as part of efforts to replace ozone-depleting substances (ODSs) such as chlorofluorocarbons (CFCs), and emissions of HFCs have increased greatly in recent years. However, HFCs are potent greenhouse gases associated with global warming and are included in the Kyoto Protocol of the United Nations' Framework Convention on Climate Change (http://www.unfccc.int). Two main properties of HFCs make them potent greenhouse gases: they have relatively long lifetimes, and their absorption region is located in the 8–12 μm atmospheric window. HFCs of industrial importance have lifetimes ranging from 1.4 to 270 years [1] and can remain in the atmosphere long after being emitted. Hence, HFCs have accumulated in the atmosphere, and increasing concentrations may significantly alter the climate. The observed mixing ratios of HFCs can be explained by anthropogenic emissions, such as those associated with refrigerants and detergents [2]. Observational data show that HFC concentrations have increased rapidly since preindustrial times, with especially rapid rates of increase since the 1990 s [1–3]. The atmospheric abundances of HFC-134a and HFC-152a increased from 0.015 and 0.09 pptv in the 1990s to 35 and 3.9 pptv in 2005, respectively. Similarly, observed concentrations of HFC-32, HFC-125, and HFC-143a were 3 pptv in 2005, 3.7 pptv in 2005, and 3.3 pptv in 2003 [1]. The atmospheric window is not only in a transparent region for the major greenhouse gases (e.g., $CO_2$, $H_2O$, and $O_3$) but also in the large Earth's terrestrial emission region. Absorption of terrestrial radiation by HFCs located in the window can change the atmospheric properties of this spectral region and significantly affect the "cooling to space" of the earth-atmosphere system [2]. The absorptive efficiency of a single HFC molecule is many thousands of times greater than that of carbon dioxide ($CO_2$). Therefore, even very small amounts of these gases emitted to the atmosphere

* Corresponding author. Tel.: +86 10 6840 0070; fax: +86 10 6840 8508.
*E-mail address:* huazhang@cma.gov.cn (H. Zhang).

0022-4073/$ - see front matter © 2010 Elsevier Ltd. All rights reserved.
doi:10.1016/j.jqsrt.2010.05.012

can make large contributions to the total radiative forcing of the climate system and thus produce long-lasting effects on the radiative energy balance of the earth-atmosphere and global climate change [2]. Radiative forcing has been used to denote an externally imposed perturbation in the radiative energy budget of the Earth's climate system, while the global warming potential (GWP) is one type of simplified index based on the climate system in a relative sense. Both have been employed in the Kyoto Protocol as metrics for quantitative comparison.

To investigate the effects of increasing contributions of human-made long-lived greenhouse gases on global warming, many researchers have studied the radiative forcing of HFCs and other replacements for ODSs [4–11]. Recent studies have used various databases of absorption cross-sections, including the spectroscopy and warming potentials of atmospheric greenhouse gases (SWAGG) [7–9], high-resolution transmission molecular absorption (HITRAN) [8–10], and Ford Motor Company [9–11] databases. The radiation models employed have included the broadband model [8] and narrowband model [5–7,10,11]. However, because previous studies have used different absorption cross-section datasets and radiation models, large uncertainties exist in the final results of the calculated radiative forcing. For HFC-134a, which has the highest atmospheric abundance of HFCs, calculated radiative forcing has differed by as much as 37% [4,8], whereas HFC-152a, HFC-125, HFC-143a, HFC-32, and HFC-134 results have shown differences of 47%, 49%, 49%, 72%, and 17%, respectively [7–11]. The spectral absorption cross-sections of HFCs have been updated in HITRAN 2004 [12]. This study builds on those new parameterizations with a correlated *k*-distribution method according to a high-accuracy band-dividing method (998-band) [13,14], with the aim of reducing the uncertainties noted above.

Section 2 provides a brief description of the dataset and radiative transfer model; in Section 3, the global mean radiative efficiencies of HFCs for all-sky conditions are calculated with the 998-band method. Finally, the radiative forcings due to concentration changes of HFCs since preindustrial to present times and for the future 100 years are calculated. Section 4 discusses the GWPs and global temperature potentials (GTPs) of HFCs and analyzes surface temperature changes due to pulse and sustained HFC emissions. Conclusions are summarized in Section 5.

## 2. Introduction to the dataset and radiative transfer model

The molecular absorption database HITRAN is generally accepted by the international scientific community and is widely used to provide inputs to radiative transfer models. The database is updated approximately every 4 years, and has developed from the previous HITRAN 1986, HITRAN 1992, HITRAN 1996, and HITRAN 2000 versions to the present HITRAN 2004 version. The infrared absorption cross-sections of HFCs from HITRAN 2004 used in this paper were measured under different combinations of temperatures and pressures. First, we analyzed the dependence of the absorption cross-sections on different temperatures and pressures; the absorption cross-sections under 22 pressures and three temperatures were then obtained by linearly interpolating the cross-sections at known temperatures and pressures. The following 22 pressures were obtained from the interpolation of mid-latitude atmospheric profiles provided by the US Air Force Geophysics Laboratory: 0.01, 0.0158, 0.0215, 0.0251, 0.0464, 0.1, 0.158, 0.215, 0.398, 0.464, 1.0, 2.15, 4.64, 10.0, 21.5, 46.4, 100.0, 220.0, 340.0, 460.0, 700.0, and 1013.25 hPa. The three temperatures were 160, 260, and 300 K. These values were intended to cover the range of the Earth's atmosphere. For example, for the pressure, the absorption coefficients to be obtained at the above-prescribed pressures were calculated by linearly interpolating the two absorption coefficients at the two known neighboring pressures under the same temperature. The effects of different temperatures and pressures on absorption cross-sections can be better considered by this method than by using integrated absorption cross-sections of HFCs obtained under one given temperature and pressure condition, as has been widely used in previous studies [7,9,11]. In the future, we will be able to more accurately calculate absorption cross-sections of halocarbons under more temperatures and pressures as the HITRAN database is further improved and more temperature and pressure conditions are provided.

To show how different input data affect the modeled radiative transfer results, Table 1 lists integrated absorption cross-sections of HFCs obtained using the HITRAN 2004 data and corresponding values from the Intergovernmental Panel on Climate Change [1]. Using HITRAN 2004, the reference temperature was 296 K and wavenumber regions of each of HFC were all obtained from HITRAN 2004. For the IPCC [1] dataset, HFC-32, HFC-134, HFC-134a, and HFC-152a were measured at 296 K and were from the Ford Motor Company dataset; wavenumber regions were 200–2000 $cm^{-1}$ for HFC-32 and HFC-134a, 450–2000 $cm^{-1}$ for HFC-134, and 700–2000 $cm^{-1}$ for HFC-152a. Further, HFC-125 and HFC-143a were measured at 253 K and were obtained from SWAGG; their wavenumber regions were 0–3000 $cm^{-1}$. As shown in Table 1, the integrated absorption cross-sections of HFC-32, HFC-125, and HFC-134a in HITRAN 2004 were

**Table 1**
Comparison between integrated absorption cross-sections of this work and IPCC (2007).

| Gases | Integrated cross-section ($10^{-17}$ $cm^2$ $molecule^{-1}$ $cm^{-1}$) | |
|---|---|---|
| | This work | Adopted in IPCC (2007) |
| HFC-32 | 5.24 | 5.77 |
| HFC-125 | 16.12 | 16.73 |
| HFC-134 | 11.37 | 10.57 |
| HFC-134a | 12.38 | 13.07 |
| HFC-143a | 14.0 | 12.01 |
| HFC-152a | 6.89 | 6.87 |

smaller than those of the IPCC [1], whereas the HFC-134, HFC-143a, and HFC-152a values were larger than those given by the IPCC [1]. Additionally, comparing this work and previous studies, the differences in the integrated absorption cross-sections of HFCs among past studies have generally been within 10% except for HFC-143a. For HFC-134a, the integrated absorption cross-sections in this work were 2%, 9%, and 5% less than those reported by Pinnock et al. [5], Highwood and Shine [7], and Gohar et al. [11], respectively. For HFC-143a, the values used here were 14% and 17% higher than those of Pinnock et al. [5] and Highwood and Shine [7], respectively.

The 998-band method was designed as an algorithm for atmospheric remote sensing (see http://www.ccsr.u-tokyo.ac.jp/~clastr/index.html, Open-CLASTR) and has been discussed in detail by Zhang et al. [14]. By this method, bands are divided as follows. The longwave region of 10–2680 $cm^{-1}$ is divided into 534 narrow bands regularly spaced with an average interval of 5 $cm^{-1}$, and the *k*-intervals in each band are optimized with a minimum of 2 and a maximum of 16. According to Goody and Yung [15] and Peixoto and Oort [16], each narrow band contains almost all observed absorptive gases, as much as possible so as to include the weakest band in the 998-band method [14]. In this study, we first calculated the effective absorption coefficients of HFCs at all *k*-intervals in the 998-band division by the correlated *k*-distribution method [17,18] at 22 pressures and three temperatures; these values were then used as inputs in our radiation model. Radiative flux and heating rate were calculated under six model atmospheres: tropical (TRO), mid-latitude summer (MLS), mid-latitude winter (MLW), subarctic summer (SAS), subarctic winter (SAW), and US Standard (USS) atmospheres. Each atmosphere was divided into 100 layers with a vertical resolution of 1 km, the surface at 0 km, and the top of the atmosphere (TOA) at 100 km. The thermal radiation transfer was solved using a two-stream algorithm developed by Nakajima et al. [19]. The global mean radiative efficiency was obtained by averaging the results of the six model atmospheres arithmetically.

To calculate the stratospheric adjusted radiative forcings of HFCs, the 998-band method was improved in this work using an iterative method. Fig. 1 provides a schematic illustration of the iterative method, where $\xi$ is convergence value, and $\Delta t$ is the time-step iteration with a unit of days (here, we used 1 day). If the convergence condition is satisfied, then the new radiative equilibrium in the stratosphere is assumed to be reached after the adjustment. Perturbation of HFCs from 0 to 0.1 ppbv is used to maintain their weak limit and then to obtain their radiative forcing due to 1 ppbv perturbation [20], i.e., the radiative efficiency by linear scaling. This method is suited for calculating radiative forcing due to trace gases having concentrations significantly less than 1 ppbv [9].

## 3. Radiative forcing due to HFCs

The World Meteorological Organization (WMO [21]) has defined instantaneous radiative forcing as the change of net radiative flux at the tropopause due to a variation in the concentration of greenhouse gases or other factors. Adjusted radiative forcing has been defined by the IPCC [22] as the change of net radiative flux at the tropopause after allowing stratospheric temperatures to readjust to radiative equilibrium, but with surface and tropospheric temperatures held fixed. According to the definition of radiative forcing, positive radiative forcing makes the troposphere and surface system warmer, leading to an increase in the surface temperature; in contrast, negative radiative forcing makes the troposphere-surface system cooler, leading to a decrease in the surface temperature. Therefore, the radiative forcing of HFCs can be used to estimate their effects on the global climate system due to their concentration changes.

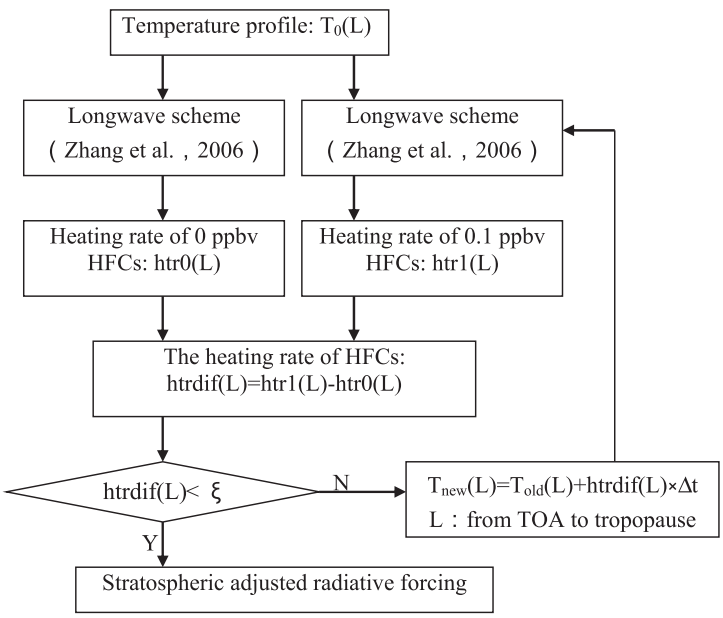


**Fig. 1.** Schematic for stratospheric adjusted radiative forcing.

In model atmospheres, HFCs are assumed to be well mixed; however, in reality, their concentrations could vary with height due to their varying lifetimes of 1.4–270 years in the atmosphere [1]. Sihra et al. [9] noted that the vertical distributions of HFCs concentrations have some effects on their radiative forcing and proposed an empirical coefficient called the lifetime correction factor for lifetimes greater than 0.25 years to include such effects: $1-0.241\times t^{-0.358}$, where $t$ is lifetime (in years). Although there are still some errors in the radiative forcing calculation after such corrections, the errors after these corrections should become smaller than before [9]. Thus, we conducted lifetime corrections of HFCs after calculating the stratospheric adjusted radiative efficiencies.

Clouds can have a great effect on the radiative forcing due to gases. We used annually varying monthly mean cloud fields constructed from the International Satellite Cloud Climatology Project (ISCCP) D2 dataset [23], which contains cloud fractions and cloud water content for 15 cloud types according to cloud phase states, cloud top pressures, and cloud optical depths with a spatial resolution of $2.5^\circ\times 2.5^\circ$ from July 1983 to June 2007. The cloud fractions and cloud water content for tropical, mid-latitude, and subarctic atmospheres are zonal mean values between 0°N and 30°N, 30°N and 60°N, and 60°N and 90°N, respectively, as listed in Table 2. The mean effective radius is assumed to be 30 μm for ice clouds, but 10 μm for liquid clouds [24]. We added these cloud parameters into our radiation transfer model to consider cloud effects. The thermal surface emissivity was set to 1.0 in our radiative transfer calculations.

For the above three atmospheres, we derived the stratospheric adjusted radiative efficiency in all-sky conditions; our formula was similar to that given by Yang et al. [24] but instead of the radiative heating rate,

$$RE=\sum_{i=1}^{15} C_i RE_i+(1-C)RE_{clear} \tag{1}$$

where $C_i$ is the cloud amount for each cloud type, $C=\sum C_i$ is the total cloud amount, and $RE_{clear}$ and $RE_i$ are the radiative efficiencies for clear sky and cloudy sky, respectively (with cloud type $i$). Next, we calculated the area-averaged stratospheric adjusted radiative efficiencies [7] due to HFCs for the all-sky condition, using the formula

$$RE_{mean}=\frac{1}{2}\times RE_{tro}+\left(\frac{\sqrt{3}}{2}-\frac{1}{2}\right)\times RE_{mid}+\left(1-\frac{\sqrt{3}}{2}\right)\times RE_{sub} \tag{2}$$

where $RE_{mean}$ is the global mean radiative efficiency, and $RE_{tro}$, $RE_{mid}$, and $RE_{sub}$ are the radiative efficiencies for tropical, mid-latitude, and subarctic atmosphere, respectively.

Table 3 lists the global mean instantaneous radiative efficiencies for clear sky, the stratospheric adjusted radiative efficiencies for clear-sky and all-sky conditions, and the lifetime adjusted radiative efficiencies of HFCs for all sky, where the values for clear sky are averaged from the results of six model atmospheres and the values for all sky are area-averaged as above. The IPCC [1] values are also included in Table 3 for comparison; and the HFC lifetimes are from the IPCC [1]. As indicated in Table 3, the calculated stratospheric adjusted radiative forcing of HFCs are up to 8% larger than the corresponding instantaneous radiative forcing for the same 0.1 ppbv perturbation in clear sky. The effect of stratospheric adjustment on radiative forcing depends on whether the adjustment induces a heating or a cooling of the lower stratosphere, which can produce an increase or a decrease in thermal infrared emissions from the lower stratosphere to the troposphere, respectively [8]. Taking HFC-134a as an example, the integrated heating rates for the whole longwave region caused by 0.1 ppbv perturbations for six model atmospheres are shown in Fig. 2. The heating rates vary with different model atmospheres, but their magnitudes are almost the same and their vertical distributions are similar for the six atmospheres. The calculated heating rate profile of HFC-134a for USS was near the middle of the results for other atmospheres, and we thus chose the USS results as an example in the

**Table 2**
Cloud conditions derived from ISCCP D2 dataset.

| Types | Tropical atmosphere | | | Mid-latitude atmosphere | | | Subarctic atmosphere | | |
|---|---|---|---|---|---|---|---|---|---|
| | Cloud amount (%) | Water or ice content (g/m$^3$) | Effective radius (μm) | Cloud amount (%) | Water or ice content (g/m$^3$) | Effective radius (μm) | Cloud amount (%) | Water or ice content (g/m$^3$) | Effective radius (μm) |
| Cu(water) | 11.43 | 0.03 | 10 | 9.50 | 0.03 | 10 | 2.43 | 0.03 | 10 |
| Sc(water) | 9.38 | 0.07 | 10 | 10.48 | 0.09 | 10 | 5.36 | 0.11 | 10 |
| St(water) | 0.75 | 2.47 | 10 | 2.26 | 2.79 | 10 | 5.17 | 4.11 | 10 |
| Cu(ice) | 0.00 | 0.01 | 30 | 2.03 | 0.03 | 30 | 3.42 | 0.04 | 30 |
| Sc(ice) | 0.00 | 0.20 | 30 | 1.12 | 0.17 | 30 | 5.76 | 0.22 | 30 |
| St(ice) | 0.00 | 5.90 | 30 | 0.30 | 4.26 | 30 | 2.85 | 3.76 | 30 |
| Ac(water) | 5.55 | 0.05 | 10 | 2.55 | 0.05 | 10 | 0.38 | 0.06 | 10 |
| As(water) | 4.43 | 0.09 | 10 | 3.67 | 0.10 | 10 | 0.82 | 0.13 | 10 |
| Ns(water) | 1.14 | 0.07 | 10 | 1.66 | 0.08 | 10 | 1.03 | 0.10 | 10 |
| Ac(ice) | 0.95 | 0.06 | 30 | 9.02 | 0.09 | 30 | 9.48 | 0.10 | 30 |
| As(ice) | 0.18 | 0.14 | 30 | 6.43 | 0.18 | 30 | 12.99 | 0.22 | 30 |
| Ns(ice) | 0.06 | 0.11 | 30 | 2.20 | 0.11 | 30 | 4.93 | 0.10 | 30 |
| Ci(ice) | 15.36 | 0.01 | 30 | 13.27 | 0.01 | 30 | 6.49 | 0.01 | 30 |
| Cs(ice) | 5.25 | 0.06 | 30 | 6.89 | 0.08 | 30 | 1.59 | 0.09 | 30 |
| Dc(ice) | 2.49 | 0.27 | 30 | 3.54 | 0.25 | 30 | 0.64 | 0.24 | 30 |

**Table 3**
A comparison of instantaneous radiative efficiency, stratospheric adjusted radiative efficiency, lifetime adjusted radiative efficiency, and the radiative efficiency in IPCC (2007) for HFCs.

| Gases | Instantaneous radiative efficiency for clear sky/ $W\,m^{-2}\,ppbv^{-1}$ | Stratospheric adjusted radiative efficiency for clear sky/$W\,m^{-2}\,ppbv^{-1}$ | Stratospheric adjusted radiative efficiency for all-sky/ $W\,m^{-2}\,ppbv^{-1}$ | Lifetime adjusted radiative efficiency for all-sky/ $W\,m^{-2}\,pbv^{-1}$ | Radiative efficiency in IPCC (2007)/ $W\,m^{-2}\,ppbv^{-1}$ |
|---|---|---|---|---|---|
| HFC-32 | 0.189 | 0.195 | 0.147 | 0.127 | 0.11 |
| HFC-125 | 0.401 | 0.421 | 0.318 | 0.295 | 0.23 |
| HFC-134 | 0.329 | 0.356 | 0.304 | 0.272 | 0.45 |
| HFC-134a | 0.294 | 0.307 | 0.232 | 0.210 | 0.16 |
| HFC-143a | 0.291 | 0.304 | 0.231 | 0.217 | 0.13 |
| HFC-152a | 0.214 | 0.223 | 0.168 | 0.132 | 0.09 |

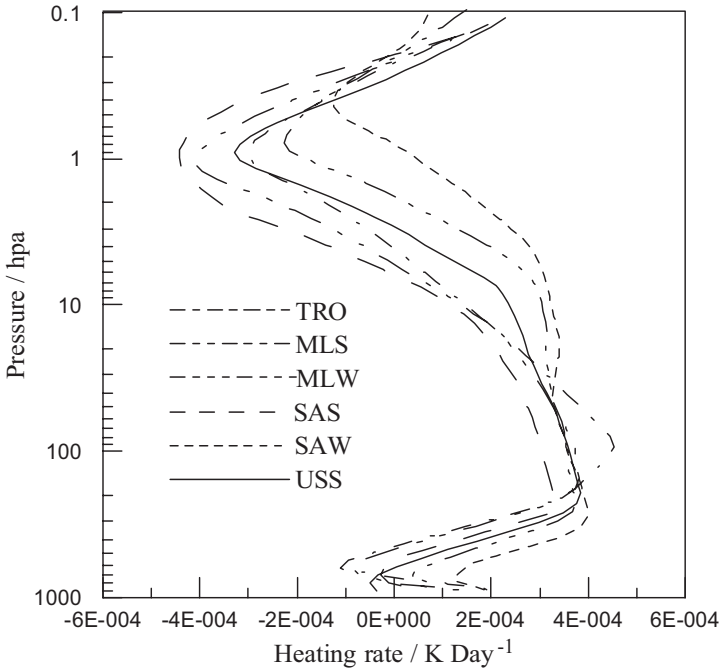


**Fig. 2.** Heating rates of 0.1 ppbv perturbation of HFC-134a for six model atmospheres.

following analysis. As shown in Fig. 2, the heating rates of HFC-134a for USS are positive from the surface to the lower stratosphere at a height of approximately 3 hPa, which could cause a warming effect on these levels. Therefore, the down-radiative flux from the lower stratosphere to the troposphere would be increased when the stratospheric temperatures reach a new equilibrium, resulting in an increase in the radiative forcing. Therefore, the stratospheric adjusted radiative forcing of HFC-134a due to 0.1 ppbv perturbation is 4% larger than its instantaneous forcing (see Table 3). For the same reason, the stratospheric adjusted radiative forcings of other HFCs in Table 3 are all larger than their corresponding instantaneous forcings.

The area-averaged stratospheric adjusted radiative efficiencies of HFCs for the all-sky condition in Table 3 show that clouds could reduce the adjusted clear-sky radiative forcing for the same perturbation by as much as 25%. HFCs absorb in the weak line limit [20]; therefore, their optical depths are small, and the impact of clouds on their radiative forcing is large due to smaller upward irradiance during all-sky conditions, in agreement with the results of Jain et al. [8].

Table 3 also gives the final global mean radiative efficiencies of HFCs after lifetime corrections on the basis of the stratospheric adjusted radiative efficiencies for the all-sky case. The differences in the radiative efficiencies brought about by the lifetime correction are closely related to the lifetime; that is, the shorter the lifetime, the larger the difference becomes. Thus, HFC-152a with the shortest lifetime shows the largest difference ($-21\%$), whereas HFC-143a with the longest lifetime has the smallest difference (approximately $-5\%$). This result indicates that lifetime corrections should be considered in HFC radiative forcing calculations. We know that the lifetimes of most HFCs are less than 52 years, with the exception of HFC-23. Therefore, the effect of lifetime on the forcing of HFCs cannot be ignored, especially for very short-lived HFCs. The differences between our input data and IPCC [1] values are less than 10%, except

for HFC-143a, as shown in Table 1. Cloud effects could produce a maximum difference in radiative forcing due to HFCs of −25%. The differences in the radiative efficiencies of HFCs between the final results in this work and those of the IPCC [1] range from −40% to approximately +67%. These differences likely arose from differences in the spectral input data for HFCs, cloud effects, lifetime corrections, etc.

For comparison, Table 4 presents the radiative forcing from preindustrial times to 2005 as calculated in this work and as given by IPCC [1], and from preindustrial times to 2000 as given by IPCC/TEAP [2]. Present-day concentrations of HFCs [1] are also listed in Table 4 for reference. It should be noted that the concentration of HFC-143a in 2005 was based on observational data of about 3.3 pptv with an increasing rate of 0.5 pptv $yr^{-1}$ in 2003 [2]. As shown in Table 4, the total radiative forcing due to the five kinds of HFCs considered in this work from preindustrial times to 2005 was about 0.0103 W $m^{-2}$, which is 37% larger than the value of 0.0075 W $m^{-2}$ given by the IPCC [1] and 232% larger than the value of 0.0031 W $m^{-2}$ from preindustrial times to 2000 reported by the IPCC/TEAP [2].

The SRES has given ten scenarios for changes in HFC concentrations. We used the average value of these ten scenarios to calculate HFC radiative forcings in the future 90 years. Fig. 3 shows the calculated average value of the concentration and corresponding radiative forcings of HFCs. In Fig. 3(a), the concentration of HFCs from 2010 to 2100 increases significantly. The largest abundance and highest rate of increase are shown for HFC-134a, which is projected to reach approximately 900 pptv by 2100. Fig. 3(b) indicates that the corresponding radiative forcings of HFCs will increase rapidly in the next 90 years due to increases in their concentrations. The total radiative forcing will increase by approximately 1500%, from about 0.015 W $m^{-2}$ in 2010 to about 0.23 W $m^{-2}$ in 2100. The greatest contribution (~80%) to total radiative forcing will be from HFC-134a.

## 4. GWPs and GTPs of HFCs

On the basis of the updated radiation efficiencies given above, we developed GWP and GTP models for HFCs. We then used these models to calculate the GWPs and GTPs of HFCs in the future 20, 100, and 500 years.

According to GWP's definition, its formula is given as [1]

$$GWP_x = \frac{\int_0^{TH} RF_x(t)dt}{\int_0^{TH} RF_r(t)dt} = \frac{\int_0^{TH} a_x[x(t)]dt}{\int_0^{TH} a_r[x(t)]dt} \tag{3}$$

$$x(t) = e^{-t/\tau} \tag{4}$$

$$r(t) = a_0 + \sum_i a_i \exp\left(-\frac{t}{\alpha_i}\right) \tag{5}$$

**Table 4**
Radiative forcing of HFCs since 1750.

| Gases | Abundance IPCC (2007)/pptv | Radiative forcing in this work (1750–2005)/W $m^{-2}$ | Radiative forcing in IPCC (2007) (1750–2005)/W $m^{-2}$ | Radiative forcing in IPCC/TEAP (1750–2000)/W $m^{-2}$ |
|---|---|---|---|---|
| HFC-32 | 3 | 0.0004 | 0.0003 | 0.0000 |
| HFC-125 | 3.7 | 0.0011 | 0.0009 | 0.0003 |
| HFC-134a | 35 | 0.0074 | 0.0055 | 0.0024 |
| HFC-143a | 4.3 | 0.0009 | 0.0004 | 0.0002 |
| HFC-152a | 3.9 | 0.0005 | 0.0004 | 0.0002 |

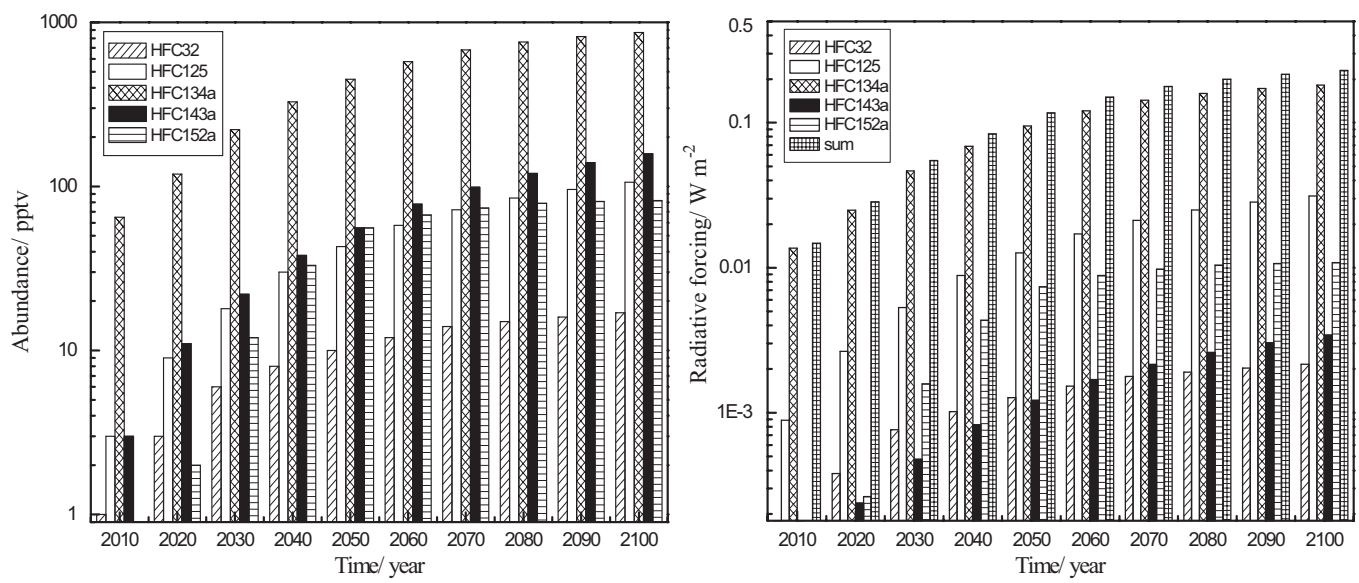


**Fig. 3.** Changes in HFCs abundances (a) and corresponding radiative forcings (b) from 2010 to 2100.

where TH is the considered time horizon (i.e., 20, 100, and 500 years in this study), and $t$ is the time. The terms $RF_x$ and $RF_r$ are the radiative forcings due to agent $x$ and $CO_2$, respectively. The terms $a_x$ and $a_r$ are the radiative efficiencies due to an one-unit increase in the atmospheric concentration of gas $x$ and $CO_2$, respectively. $x(t)$ and $r(t)$ are the respective time-decaying functions of pulses of the injected gas $x$ and $CO_2$, where $\tau$ is the lifetime of gas $x$ in formula (4). The $CO_2$ time-decaying function, as used in formula (5), was adopted from the IPCC [1]; in the function, $a_0$, $a_i$, and $\alpha_i$ are parameters for the calculation (detailed values have been reported by the IPCC [1]).

Researchers (e.g., [25,26]) have widely debated the concept of GWP since its introduction in the first IPCC Assessment Report [27]. First, GWP values cannot be easily developed for all substances that have an impact on climate; there are also serious limitations in using global mean GWPs to assess the possible climate impacts of short-lived species and in comparing those impacts to those of the long-lived greenhouse gases; further, the effects of the different lifetimes of gases cannot be distinguished [1]. Second, GWPs only express equivalence, in terms of the integrated radiative forcing over a chosen time horizon, of pulse emissions of different gases; GWPs do not give the contribution of different gases to increasing temperatures [26]. This implies that GWPs are not necessarily equivalent in terms of the temporal evolution of temperature change [25,26,28,29]. The concept of GTP was proposed by Shine et al. [30] and adopted by the IPCC [1]. Following the convention of the IPCC to quote GWP relative to $CO_2$, GTP is defined as the ratio of the global temperature changes over the time horizon of a gas $x$ and the reference gas $CO_2$ for a pulse emission (1 kg at $t$=0) and sustained emission (1 kg yr$^{-1}$). The GTP from a pulse emission and sustained emission are expressed here as GTP$^P$ and GTP$^S$, respectively. GTP was given by Shine et al. [30] as

$$GTP_x^{TH} = \frac{\Delta T_x^{TH}}{\Delta T_r^{TH}} \tag{6}$$

where TH is the considered time horizon (here, 20, 100, and 500 years), and $\Delta T_x$ and $\Delta T_r$ are the global mean surface temperature changes caused by gas $x$ and $CO_2$, respectively, which can be obtained from the following formula, as a simple relationship between the global mean surface temperature change, $\Delta T$, and the global mean radiative forcing $\Delta F$, as follows [30]:

$$C\frac{d\Delta T(t)}{dt} = \Delta F(t) - \frac{\Delta T(t)}{\lambda} \tag{7}$$

In the above equation, $t$ is time, $C$ is the heat capacity of the system, and $\lambda$ is a climate sensitivity parameter, which indicates the change in equilibrium surface temperature per unit radiative forcing.

The absolute global temperature potentials for pulse and sustained emissions are expressed as AGTP$^P$ and AGTP$^S$, respectively, indicating the temperature changes at time $t$ due to 1 kg emission at $t$=0 with units K kg$^{-1}$ and constant 1 kg yr$^{-1}$ increase in emissions between $t$=0 and $t$ in units of K (kg yr$^{-1}$)$^{-1}$, respectively. The GTPs for pulse and sustained emissions can also be expressed by the following equations, respectively [30]:

$$GTP^P = \frac{AGTP_X^P}{AGTP_C^P} \tag{8}$$

$$GTP^S = \frac{AGTP_X^S}{AGTP_C^S} \tag{9}$$

The parameters required for calculating GWP and GTP are radiative efficiencies and time-decaying functions of HFCs and $CO_2$. Here, we used our calculated radiative efficiencies of HFCs; the time-decaying function of HFCs and $CO_2$ and the radiative efficiency of $CO_2$ data were obtained from the IPCC [1]. The heat capacity of the system and climate sensitivity parameter required for the calculation of GTP were the same as those used by Shine et al. [30]. Table 5 lists the GWPs, GTP$^P$s for pulse emissions, and GTP$^S$s for sustained emissions of HFCs with time horizons of 20, 100, and 500 years, respectively; GWPs given by the IPCC [1] are also listed for comparison.

The GWPs of HFCs given in Table 5 indicate that their contributions to climate change are hundreds to thousands of times larger than that of the same emission of $CO_2$. Further, in general, for the same time horizon, longer lifetimes of HFCs correspond to greater GWPs. Note that by the GWP metric, the HFCs shown in Table 5 seem to still have effects on the climate system beyond their lifetime scopes. For example, the GWP value for HFC-143a with a lifetime of 52 years is 2850 for the 500-year horizon, indicating that the GWP metric may largely overestimate the long-term effects of HFCs on climate change. In contrast, the new metric of GTP has been significantly improved in this aspect. The GWP values of HFCs found in this study and those of the IPCC [1] over the 100-year time horizon differ in the range +21 to 75%. Here, special attention should be given to the fact that the IPCC [1] listed the values of radiative efficiencies and GWPs of HFCs from IPCC/TEAP [2], but renewed the radiative

**Table 5**
Comparisons between GWPs, GTP$^P$s, and GTP$^S$s of HFCs in this work and the GWPs of HFCs in IPCC (2007) with time horizons of 20, 100, and 500 years, respectively. Here, the lifetime in the calculation is given for reference.

| Gases | Lifetime/yr | GWP 20/100/500 (yr) | GWP in IPCC (2007) 20/100/500 (yr) | GTP$^P$ 20/100/500 (yr) | GTP$^S$ 20/100/500 (yr) |
|---|---|---|---|---|---|
| HFC-32 | 4.9 | 2727/817/254 | 2330/675/205 | 1670/2/0 | 3469/885/257 |
| HFC-125 | 29 | 8235/4713/1513 | 6350/3500/1100 | 8004/1113/0 | 8362/5008/1532 |
| HFC-134 | 10 | 5345/1820/566 | 3200/1100/330 | 4007/10/0 | 6098/1791/573 |
| HFC-134a | 14 | 5080/1966/612 | 3830/1430/435 | 4406/55/0 | 5538/2125/619 |
| HFC-143a | 52 | 9940/7829/2850 | 5890/4470/1590 | 10124/4288/3 | 9764/8107/2885 |
| HFC-152a | 1.4 | 649/191/59 | 437/124/38 | 273/0/0 | 914/207/60 |

efficiencies of $CO_2$ at the same time. Thus, our calculations used the radiative efficiencies of $CO_2$ with the updated background concentration listed in the IPCC [1]. We used a different time-decaying function of $CO_2$ from that listed in the IPCC [1] (i.e., [2]) but adopted its renewed function [1] and the same time-decaying functions of HFCs as before (i.e., [2]). Therefore, the radiative efficiencies for both HFCs and $CO_2$ and the time-decaying function of $CO_2$ together are the main causes for the difference in GWP calculations. The background concentration of $CO_2$ increased from 365 ppmv in 1998 to 378 ppmv in 2005, leading to a difference of −9% in the radiative efficiency of $CO_2$. With the improvement of the time-decaying function of $CO_2$ from IPCC/TEAP [2] to IPCC [1], the differences of GWPs over time horizons of 20, 100, and 500 years between the old and new time-decaying function of $CO_2$ are 0%, 1%, and −1%, respectively. The differences of the radiative efficiencies of HFCs between this work and the IPCC [1] are in the range −40% to approximately +67%. Therefore, we can conclude from the above analyses that the GWP differences are mainly attributable to the computation of radiative efficiencies of HFCs.

The physical meaning of $GTP^P$ is almost the same as that of GWP; the most significant difference between them is that GWP is the ratio of the integrated radiative forcing caused by 1 kg HFCs to that caused by 1 kg $CO_2$ over a given time horizon, whereas $GTP^P$ is the ratio of the surface temperature change caused by 1 kg HFCs to that caused by 1 kg $CO_2$ over a given time horizon, which directly reflects the surface temperature change caused by HFCs relative to $CO_2$ over the same time horizon. In Table 5, for the 20-year time horizon, the $GTP^P$s of HFCs are all less than their corresponding GWPs except for HFC-143a, which has a relatively long lifetime; the shorter the lifetime of a gas is, the greater is the difference between its $GTP^P$ and GWP. For the 100-year and 500-year time horizons, the $GTP^P$s of all HFCs are much less than their corresponding GWPs, and all of the 500-year $GTP^P$s are nearly zero. This result matches that found by Shine et al. [30] and implies that the GTP metric is a good measure for short-lived species, whereas GWP usually significantly overestimates the effect of pulse-emitted short-lived species on long-term climate change. The 100-year $GTP^P$ of HFCs in Table 5 indicates that the emitted substances will have been broken down in the atmosphere beyond their lifetimes during the integrated time horizon, which will reduce their accumulated concentration and thus decrease their effects on the surface temperature changes. Therefore, the $GTP^P$s for the 100-year time horizon are much smaller than those for the 20-year time horizon. Taking HFC-152a, which has a short lifetime of 1.4 years, as an example, its 100-year $GTP^P$ is approximately zero, showing that the surface temperature change caused by the pulse emission of 1 kg HFC-152a at the initial time is zero, i.e., it has no effect on surface temperature over the 100-year period. For the same reason, because 500 years is much longer than the atmospheric lifetime of all HFCs, all 500-year $GTP^P$s of HFCs are nearly zero. Therefore, $GTP^P$ not only directly reflects the surface temperature change due to pulse emission of a substance, but also expresses more clearly the effect of atmospheric lifetime on the surface temperature change.

HFCs are widely used in industrial production, and emissions of HFCs have increased nearly constantly in recent years. $GTP^S$ considers the effect of the sustained emission of gases on the surface temperature change; thus, $GTP^S$ could provide a good metric for assessing regulatory policies for some special industries and agricultural activities that produce sustained emissions of these gases. Table 5 also gives the $GTP^S$ values calculated in this study. Shine et al. [30] experimentally verified that $GTP^S$s calculated from formula (7) are more accurate than $GTP^P$s from the same formula. Although $GTP^S$ and GWP are based on quite different concepts, as can be seen in Table 5, the differences between GWP and $GTP^S$ values are less than those between GWPs and $GTP^P$s for the same gas over the same time horizon, and the difference between $GTP^S$ and GWP decreases as the time horizon increases. The difference between the 500-year $GTP^S$ and GWP of HFCs is only about 1%. Shine et al. [30] explained that $GTP^S$ and GWP have a similar mathematical expression if the time horizon is long enough, so that their results are similar to each other. Because GTPs measure surface temperature change more directly than do GWPs, the sustained emission condition is more suitable to the actual situation. Further, because it is convenient to obtain $GTP^S$ with almost the same parameters (e.g., radiative efficiency, lifetime) as GWP, $GTP^S$ is a much better metric for evaluating the effect of gas emissions on climate change compared to GWP and $GTP^P$.

We calculated the 500-year $AGTP^P$ and $AGTP^S$ of HFCs by formula (7) to estimate the surface temperature change caused by pulse and sustained emissions of HFCs during the future 500 years. Fig. 4 shows the results. Fig. 4(a) illustrates that the surface temperature change caused by pulse emission of HFCs reaches a peak value rapidly at the initial stage of emission and then recovers to zero over time. The recovery rate is related to the atmospheric lifetime of HFCs; for example, HFC-152a with the shortest lifetime recovers most rapidly, whereas HFC-143a with the longest lifetime has the slowest recovery rate. Fig. 4(b) shows that the surface temperature change caused by sustained emission of HFCs increases over the whole emission process, but increases greatly at the initial stage of emission; the large initial increasing rate is then followed by slow and smooth increase. Additionally, Fig. 4(b) indicates that the time required from the initial time of emission to a nearly zero rate of surface temperature change is also related to atmospheric lifetime. The required time increases with the increase of lifetime. This means that sustained emission of HFCs can cause a rapid increase in their concentrations in the atmosphere at the initial stage. Then, because the emitting and breakdown of HFCs occurs simultaneously beyond their lifetimes, their production and decomposition rates tend to balance each other, making their accumulated atmospheric concentration stable. Thus the induced surface temperature change will eventually arrive at a new stable level.

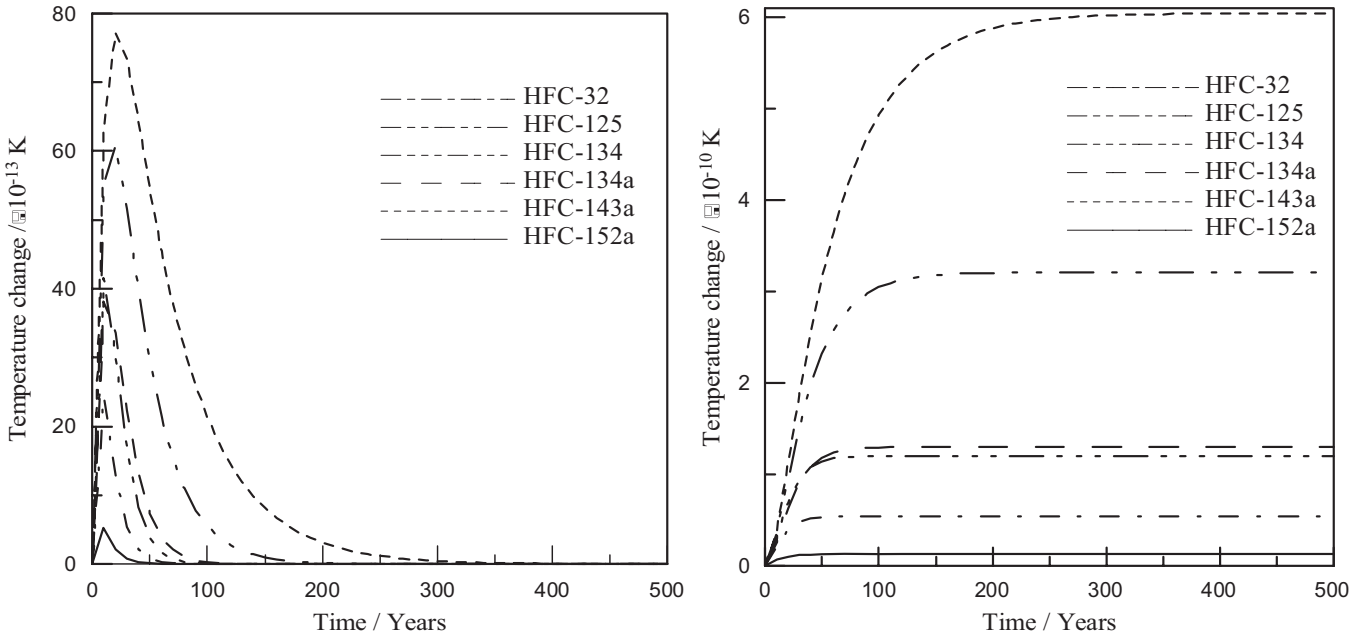


**Fig. 4.** Temperature changes due to a pulse emission of 1 kg of HFCs (a) and sustain emission of 1 kg $yr^{-1}$ of HFCs (b).

## 5. Conclusions

The effective absorptive coefficients of HFCs were calculated with HITRAN 2004 using the correlated *k*-distribution method and the 998-band division method. The total radiative forcing due to HFCs (except HFC-134) calculated by the 998-band method was approximately 0.0103 W $m^{-2}$ from preindustrial time to 2005 and will become 0.23 W $m^{-2}$ by 2100. This result indicates that HFCs will affect climate change significantly in the future. The global mean stratospheric adjusted radiative efficiencies of HFCs for all-sky conditions were calculated based on their radiative forcing after lifetime corrections; values ranged from 0.127–0.295 W $m^{-2}$ $ppbv^{-1}$.

The GWPs and GTPs of HFCs for 20-, 100-, and 500-year time horizons were then each calculated on the basis of the updated radiative efficiencies calculated in this study. Next, we conducted detailed comparisons among the GWPs and $GTP^P$s of pulse emissions, and the $GTP^S$s of sustained emissions, of HFCs. The surface temperature changes were calculated with AGTPs caused by pulse and sustained emissions of HFCs during the future 500 years. The results show that the contributions of HFCs to future climate change are hundreds to thousands of times greater than the contributions of the same emission of $CO_2$; thus HFCs will have a long-term impact on global warming. Finally, this paper also shows that $GTP^S$ is an optimal metric for assessing the long-term effects of HFC emissions on global climate change.

## Acknowledgements

The authors would like to thank Prof. Qiang Fu, Department of Atmospheric Science, University of Washington for his suggestion to the stratospheric adjusted radiative forcing scheme used in this work and Miss Zhongping Shen and Miss Ruoyu Zhang, National Climate Center for their calculations of the cloud method used in this work and edit to the text and figures of this manuscript. This work is supported by the National Natural Science Foundation of China (Grant no. 40775006) and the Special Foundation for Climate Change (Grant no. 2010-2200509).

## References

[1] IPCC. In: Climate change 2007: the physical science basis. Contribution of working group I to the fourth assessment report of the intergovernmental panel on climate change. Cambridge, UK and New York, NY, USA: Cambridge University Press; 2007. Available from: 〈http://www.ipcc.ch/ipccreports/ar4-syr.htm〉.
[2] IPCC/TEAP. In: Safeguarding the ozone layer and the global climate system: issues related to hydrofluorocarbons and perfluorocarbons. Cambridge: Cambridge University Press; 2005. Available from: 〈http://www.ipcc.ch〉.
[3] IPCC. In: Climate change 2001: the scientific basis. Contribution of working group I to the third assessment report of the intergovernmental panel on climate change. Cambridge, UK: Cambridge University Press; 2001.
[4] Shi GY. Global warming potential due to CFCs and their substitutes. Chin J Atmos Sci 1992;16(3):345–52.
[5] Pinnock S, Hurley MD, Shine KP, Wallington TJ, Smyth TJ. Radiative forcing of climate by hydrochlorofluorocarbons and hydrofluorocarbons. J Geophys Res 1995;100(23):227–38.
[6] Christidis N, Hurley MD, Pinnock S, Shine KP, Wallington TJ. Radiative forcing of climate change by CFC-11 and possible CFC replacements. J Geophys Res 1997;D16(19):597–609102 1997;D16(19):597–609.
[7] Highwood EJ, Shine KP. Radiative forcing and global warming potentials of 11 halogenated compounds. J Quant Spectrosc Radiat Transfer 2000;66:169–83.
[8] Jain AK, Briegleb BP, Minschwaner K, Wuebbles DJ. Radiative forcings and global warming potentials of 39 greenhouse gases. J Geophys Res 2000;105(D16):20,773–90.
[9] Sihra K, Hurley MD, Shine KP, Wallington TJ. Updated radiative forcing estimates of 65 halocarbons and nonmethane hydrocarbons. J Geophys Res 2001;D17(20):493–505106 2001;D17(20): 493–505.
[10] Huang XY. Study on global warming potential of greenhouse gas. Ph.D. Thesis. Institute of Atmospheric Physics, Chinese Academy of Sciences. 2001. Chinese.

[11] Gohar LK, Myhre G, Shine KP. Updated radiative forcing estimates of four halocarbons. J Geophys Res 2004;109:D01107, doi:10.1029/2003JD004320.
[12] Rothman LS, Jacquemart D, Barbe A, Benner DC, Birkd M, Brown LR, et al. The HITRAN 2004 molecular spectroscopic database. J Quant Spectrosc Radiat Transfer 2005;96:139–204. Available from: 〈http://www.cfa.harvard.edu/HITRAN/〉.
[13] Zhang H, Shi GY, Nakajima T, Suzuki T. The effects of the choice of the k-interval number on radiative calculations. J Quant Spectrosc Radiat Transfer 2006;98(1):31–43.
[14] Zhang H, Suzuki T, Nakajima T, Shi GY, Zhang XY, Liu Y. Effects of band division on radiative calculations. Opt Eng 2006;45(1) 016002-10.
[15] Goody RM, Yung YL. In: Atmospheric radiation. New York: Oxford University Press; 1989.
[16] Peixoto JP, Ooert AH. In: Physics of climate. New York: Am. Inst. of Phys.; 1992.
[17] Shi GY. An accurate calculation and representation of the infrared transmission function of the atmospheric constituents. Ph.D. Thesis. Tohoku University of Japan. 1981.
[18] Zhang H, Nakajima T, Shi GY, Suzuki T, Imasu R. An optimal approach to overlapping bands with correlated k distribution method and its application to radiative calculations. J Geophy. Res 200310.1029/2002JD003358.
[19] Nakajima T, Tsukamoto M, Tsushima Y, Numaguti A, Kimura T. Modeling of the radiative process in an atmospheric general circulation model. Appl Opt 2000;39(4):869–78.
[20] Freckleton RS, Pinnock S, Shine KP. Radiative forcing of halocarbons: a comparison of line-by-line and narrow-band models using $CF_4$ as an example. J Quant Spectrosc Radiat Transfer 1996;55:763–9.
[21] WMO. Atmospheric Ozone 1985, Assessment of our understanding of the processes controlling its present distribution and change, vol. I, WMO Global Ozone Research and Monitoring Project, Report no.16. 1986.
[22] IPCC. In: Climate change 1995: the science of climate change (the SAR). Cambridge, United Kingdom and New York, NY, USA: Cambridge University Press; 1996.
[23] Rossow WB, Schiffer RA. Advances in understanding clouds from ISCCP. Bull Am Meteorol Soc 1999;80(2):261–87.
[24] Yang Q, Fu Q, Austin J, Gettelman A, Li F, Vömel H. Observed and simulated tropical stratospheric upward mass fluxes. J Geophys Res 113, D00B07, doi:10.1029/2008JD009945.
[25] O'Neil BC. The jury is still out on global warming potentials. Climatic Change 2000;44:427–43.
[26] Fuglestvedt JS, Berntsen TK, Godal O, Sausen R, Shine KP, Skodvin T. Metrics of climate change: assessing radiative forcing and emission indices. Climatic Change 2003;58:267–331.
[27] IPCC. In: Climate change: the IPCC scientific assessment. Cambridge, UK: Cambridge University Press; 1990.
[28] Smith SJ, Wigley TML. Global warming potentials: 1. Climatic implications of emissions reductions. Climatic Change 2000;44: 445–57.
[29] Smith SJ, Wigley TML. Global warming potentials: 2. Accuracy. Climatic Change. 2000;44:459–69.
[30] Shine KP, Fuglestvedt JS, Hailemariam K, Stuber N. Alternatives to the global warming potential for comparing climate impacts of emissions of greenhouse gases. Climatic Change 2005;68(3): 281–302.

SCIENCE CHINA
Earth Sciences

• RESEARCH PAPER •

May 2011 Vol.54 No.5: 764–772
doi: 10.1007/s11430-010-4155-0

# Radiative forcing and global warming potential of perfluorocarbons and sulfur hexafluoride

ZHANG Hua[1*], WU JinXiu[2,1] & SHEN ZhongPing[3,1]

[1] *Laboratory for Climate Studies, National Climate Center, China Meteorological Administration, Beijing 100081, China;*
[2] *Shanghai Meteorological Media Center, Shanghai 200030, China;*
[3] *Shanghai Climate Center, Shanghai 200030, China*

Received August 23, 2010; accepted October 29, 2010; published online January 10, 2011

We developed two radiation parameterizations with different resolutions (17-band and 998-band) for perfluorocarbons (PFCs) and sulfur hexafluoride ($SF_6$) using the updated High-resolution Transmission Molecular Absorption (HITRAN) 2004 database and the correlated k-distribution method. We analyzed the impacts of the two radiation schemes on heating rates. Then we studied their instantaneous radiative efficiency, stratospheric adjusted radiative efficiency, global warming potential (GWP), and global temperature potential (GTP), for both clear- and all-sky conditions using a high-resolution radiation scheme. We found that the stratosphere-adjusted radiative efficiencies of $C_2F_6$, $CF_4$, and $SF_6$ for the whole sky were 0.346, 0.098, and 0.680 W $m^{-2}$ $ppbv^{-1}$, respectively. Radiative forcing from the industrial revolution to 2005 was 0.001, 0.007, and 0.004 W $m^{-2}$, respectively; and was predicted to rise to 0.008, 0.036, and 0.037 W $m^{-2}$, respectively, by 2100, according to emission scenarios provided by the IPCC. The GWPs of $C_2F_6$, $CF_4$, and $SF_6$ are 17035, 7597, and 31298, respectively, for a time horizon of 100 years relative to $CO_2$. Their GTPs of pulse and sustained emissions, $GTP^P$ and $GTP^S$, are 22468, 10052, and 40935 and 16498, 7355, and 30341, respectively, for a 100-year time horizon.

**PFCs, $SF_6$, radiative forcing, global warming potential (GWP), global temperature potential (GTP), correlated k-distribution**

**Citation:** Zhang H, Wu J X, Shen Z P. Radiative forcing and global warming potential of perfluorocarbons and sulfur hexafluoride. Sci China Earth Sci, 2011, 54: 764–772, doi: 10.1007/s11430-010-4155-0

Because ozone-depleting substances (ODSs) can decrease ozone concentration in the stratosphere, their production and emission has been controlled by the *Montreal Protocol*. The replacements of ODSs, perfluorocarbons (PFCs) and sulfur hexafluoride ($SF_6$), do not contain Br or Cl atoms and thus pose no threat to stratospheric ozone. However, PFC and $SF_6$ concentrations in the atmosphere have increased greatly over the past few decades, and they have been listed as controlled greenhouse gases in the *Kyoto Protocol* because they strongly absorb radiation. Several characteristics of PFCs and $SF_6$ explain their classification as strong greenhouse gases. First, they have a considerably long lifetime. For example, the lifetime of $CF_4$ in the atmosphere is 50,000 years. Before the industrial revolution, the background concentration of $CF_4$ was about 40 pptv, and there was no $C_2F_6$ or $SF_6$. However, these gases have increased rapidly since the industrial revolution, especially recently. The latest observational data show atmospheric concentrations of $CF_4$, $C_2F_6$, and $SF_6$ of 74, 2.9, and 5.6 pptv, respectively [1]. Second, the absorption spectra of PFCs and $SF_6$ are located mainly within an "atmospheric window". Thus, they strongly absorb terrestrial longwave radiation. Consequently, atmospheric absorption in this spectral region has

*Corresponding author (email: huazhang@cma.gov.cn)

© Science China Press and Springer-Verlag Berlin Heidelberg 2011

changed and the outward longwave radiation (OLR) of the surface-atmosphere system may have been influenced significantly [2]. Because the absorption efficiency of single PFC and SF molecules is thousands of times greater than that of $CO_2$ molecules, they could make significant contributions to the total radiative forcing of the Earth system, even if their concentration in the atmosphere is not so large. Hence, they may have a strong effect on the terrestrial radiation balance and global climate change [2].

To evaluate the contribution of long-lived human-made greenhouse gases to global warming, many studies of the radiative forcing due to PFCs and $SF_6$ have been performed. Of these, different absorption cross-section databases have been used, including the Spectroscopy and Warming Potentials of Atmospheric Greenhouse Gases (SWAGG) [3], the High-resolution Transmission Molecular Absorption (HITRAN) database [4, 5], and the Ford Motor Company database [6, 7]. The radiation schemes used are mainly 5 or 10 $cm^{-1}$ narrowband models [3, 4, 6, 7]. To obtain more accurate results, new PFCs and $SF_6$ radiation schemes have been developed in this work on the basis of the high-accuracy 998-band scheme [8, 9] with the updated HITRAN 2004 database using the correlated k-distribution method [10].

## 1 Introduction to spectral absorption data and models

The HITRAN molecular absorption database is widely used as basic input for radiative transfer models. It has been updated periodically from HITRAN 1986, HITRAN 1992, and HITRAN 2000 to the present HITRAN 2004. In this paper, the infrared absorption cross-section data of $C_2F_6$, $CF_4$, and $SF_6$ from HITRAN 2004, which were measured under different temperatures and pressures under strict conditions in laboratories, are used. We used linear interpolation to produce absorption coefficients at 22 pressures and 3 temperatures from the database. The 22 pressures were 0.01, 0.0158, 0.0215, 0.0251, 0.0464, 0.1, 0.158, 0.215, 0.398, 0.464, 1.0, 2.15, 4.64, 10.0, 21.5, 46.4, 100.0, 220.0, 340.0, 460.0, 700.0, and 1013.25 hPa. The three temperatures were 160, 260, and 320 K. This covers the entire range of possible atmosphere conditions. Compared with the integrated absorption cross-sections for one temperature and pressure that were commonly used in previous studies [3, 6, 11] this approach allowed us to account for the effect of temperature and pressure on a cross-section more accurately.

Figure 1 shows the typical absorption cross-sections of $C_2F_6$, $CF_4$, and $SF_6$ vs. wavenumber at 296 K and 1013.25 hPa. There are two absorption bands of $C_2F_6$ with the strongest located in the 1220–1285 $cm^{-1}$ region, another is in the 1061–1165 $cm^{-1}$ region. There is a very strong absorption band for $CF_4$ in the 1250–1290 $cm^{-1}$ region. $SF_6$ has broad absorption over the whole longwave region that varies significantly with wavenumber.

According to the 17-band scheme of Zhang et al. [8], the longwave region of 10–2680 $cm^{-1}$ (3.7–1000 μm) is divided into eight bands with different k-intervals (Table 1). In the 998-band scheme of Zhang et al. [9], the longwave region of 10–2680 $cm^{-1}$ is divided into 534 narrow bands at a mean interval of 5 $cm^{-1}$, on each of which the k-intervals vary from 2 to 16. The spectral band division and k-intervals were described by Zhang et al. [9] in detail. This scheme includes the major greenhouse gases, $CO_2$, $H_2O$, $N_2O$, $O_3$, and $CH_4$, and four CFCs, i.e., $CCL_4$, CFC-11, CFC-12, and CFC-13, are also considered. These CFCs are assumed to be evenly mixed in the atmosphere. Table 1 shows that the absorption of $C_2F_6$, $CF_4$, and $SF_6$ is located mainly in bands 4–6 in the 17-band scheme. In the 998-band scheme, there are a total of 34 absorption bands for $C_2F_6$ (bands 211–231 and 243–255). For $CF_4$ the absorption is in bands 249–256, and for $SF_6$ the absorption is in bands 184–190. Therefore, almost all the weak absorption bands have been considered in the high-accuracy 998-band scheme. The 998-band scheme is more accurate than the 17-band scheme and hence can be used as a reference for intercomparison [9]. First, we calculated the effective absorption coefficients [10, 12] for 22 pressures and 3 temperatures at all the k-intervals in the 17- and 998-band schemes. We then incorporated them into our radiative transfer model as inputs. Radiative fluxes and heating rates were calculated using six model atmospheres: tropical (TRO), mid-latitude summer (MLS), mid-latitude winter (MLW), sub-arctic summer (SAS), sub-arctic winter (SAW), and United States standard (USS). The whole atmosphere was divided into 100 layers with a

**Table 1** Band limits for the 17-band scheme

| Band | Region ($cm^{-1}$) | k-interval number | Gase |
|---|---|---|---|
| 1 | 10–250 | 4 | $H_2O$ |
| 2 | 250–550 | 4 | $H_2O$ |
| 3 | 550–780 | 11 | $H_2O$, $CO_2$ |
| 4 | 780–990 | 5 | $H_2O$, $CCl_4$, CFC-11, CFC-12, CFC-13, $SF_6$ |
| 5 | 990–1200 | 5 | $H_2O$, $O_3$, CFC-11, CFC-12, CFC-13, $C_2F_6$ |
| 6 | 1200–1430 | 5 | $H_2O$, $N_2O$, $CH_4$, CFC-13, $C_2F_6$, $CF_4$ |
| 7 | 1430–2110 | 5 | $H_2O$ |
| 8 | 2110–2680 | 2 | $H_2O$, $CO_2$, $N_2O$ |

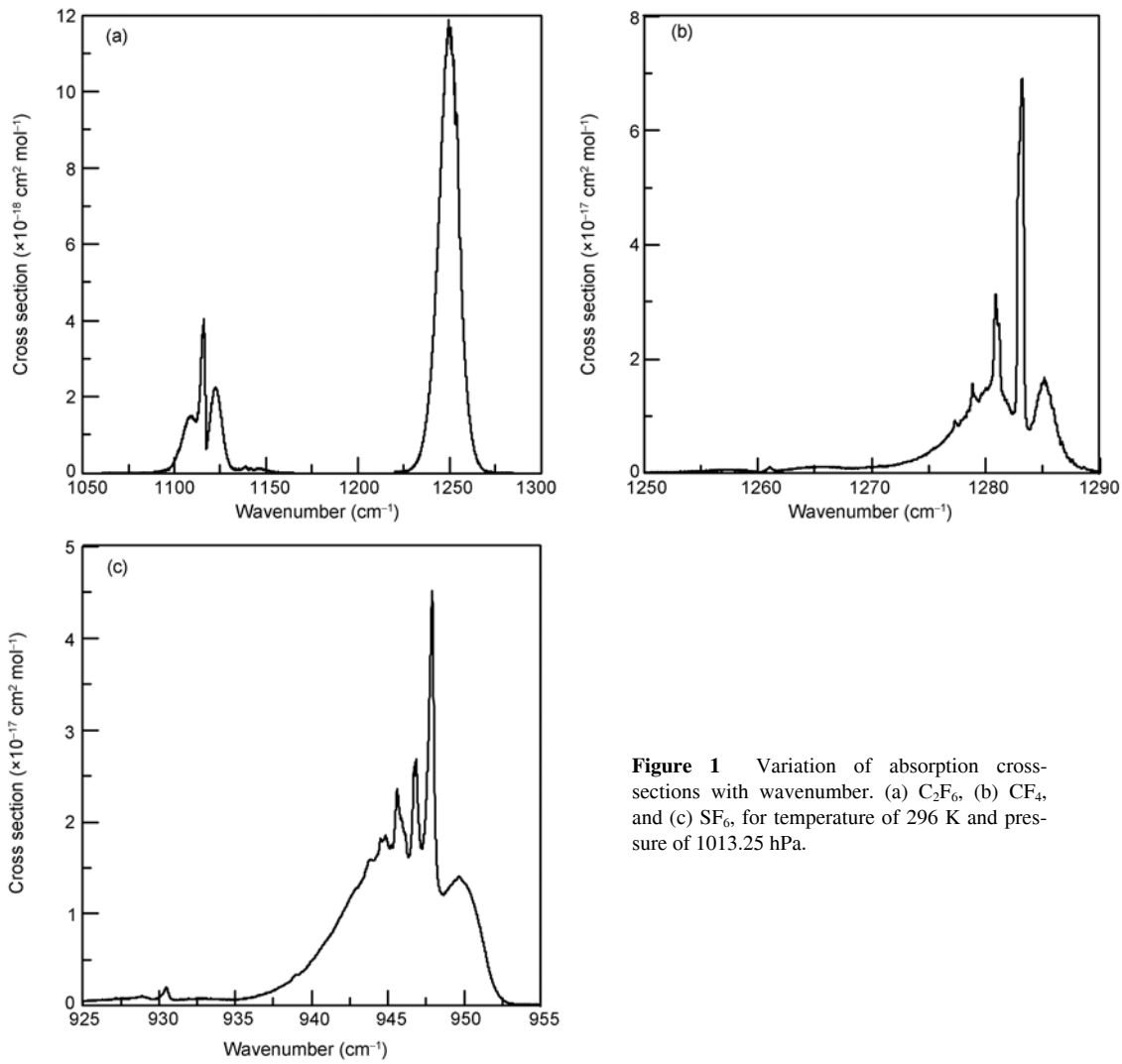


**Figure 1** Variation of absorption cross-sections with wavenumber. (a) $C_2F_6$, (b) $CF_4$, and (c) $SF_6$, for temperature of 296 K and pressure of 1013.25 hPa.

vertical resolution of 1 km. The surface height was set at 0 km and the top of atmosphere (TOA) was set at 100 km. The two-stream approximation [13] was used in our radiative transfer model.

To calculate the stratospheric adjusted radiative forcing for the 998-band scheme, we used an iterative method. The calculation schematic is shown in Figure 2, in which $\xi$ is the convergence value and $\Delta t$ is the time step iteration (we used 1 day here). If the convergence condition is satisfied, the new radiative equilibrium of the stratosphere is reached after adjustment. The disturbance of 0–0.1 ppbv was used to keep the weak absorption properties of PFCs and $SF_6$. The global mean radiative forcing due to 1 ppbv disturbance was then calculated by linear scaling [14], i.e., the global mean radiative efficiency. This method is more suitable for the calculation of radiative forcing due to trace gases with concentrations less than 1 ppbv.

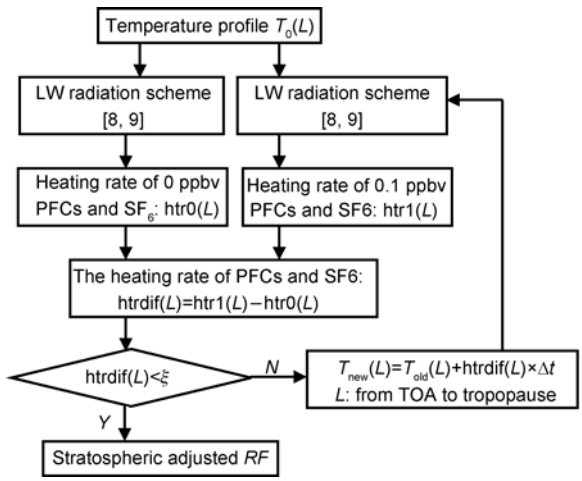


**Figure 2** Schematic of the stratospheric adjusted radiative forcing method.

## 2 Radiative forcing of $C_2F_6$, $CF_4$, and $SF_6$

The instantaneous radiative forcing was defined as the change of net radiation flux at the tropopause due to the variation of a greenhouse gas or other factors [1]. The stratospheric adjusted radiative forcing was defined as the

change of net radiation flux at the tropopause through adjustment of the thermal structure of the stratosphere to radiative equilibrium when the temperature at the surface and in the troposphere remains constant [1]. According to the definition of radiative forcing of greenhouse gases, positive radiative forcing will make the surface-troposphere system warmer, leading to an increase in the mean surface temperature. In contrast, negative radiative forcing will make the surface-troposphere system cooler, leading to a decrease in the mean surface temperature. Therefore, the effect of the change of atmospheric concentration of $C_2F_6$, $CF_4$, and $SF_6$ on the global climate system can be estimated by calculating their radiative forcing.

Clouds have an important influence on the radiative forcing due to gases. In this paper, the cloud cover and cloud water content for 15 cloud categories at different cloud phases, cloud top pressures, and cloud optical depths were obtained from the International Satellite Cloud Climate Project (ISCCP) D2 dataset during 1983–2007, with a global grid resolution of 2.5°×2.5° [15]. The values of cloud cover and cloud water content in the tropical, mid-latitude, and sub-arctic zones are the corresponding latitudinal means of 0°–30°, 30°–60°, ad 60°–90°N, respectively (Table 2). The heights of low, middle, and high clouds were put between 1–2, 4–5, and 10–12 km, respectively. Low clouds included Cu, Sc, and St, whereas middle clouds included Ac, As, and Ns. There are two kinds of phases of water and ice for these low and middle clouds. The mean effective radii of ice and water clouds are 30 and 10 μm, respectively [16]. In our radiative transfer model, these cloud parameters were used as inputs for cloudy and all-sky cases, so as to consider the effect of clouds in our calculation. We set the surface emissivity to 1.0.

Given the three atmospheres described above, the stratospheric adjusted radiative efficiency for the all-sky case was calculated using a method similar to that proposed by Yang et al. [16]. Here, the radiative efficiency replaced the heating rate in the formula:

$$RE = \sum_{i=1}^{15} C_i RE_i + (1-C)RE_{\text{clear}}, \tag{1}$$

where $C_i$ is cloud cover for each cloud category, $C=\Sigma C_i$ is the total cloud cover, and $RE_{\text{clear}}$ and $RE_i$ are the radiative efficiencies for clear and cloudy atmospheres, respectively (cloud category: $i$). Then, the global mean adjusted radiative efficiency for the all-sky case was calculated by eq. (2) [3]:

$$RE_{\text{mean}} = \frac{1}{2}\times RE_{\text{tro}} + \left(\frac{\sqrt{3}}{2}-\frac{1}{2}\right)\times RE_{\text{mid}} + \left(1-\frac{\sqrt{3}}{2}\right)\times RE_{\text{sub}}, \tag{2}$$

where $RE_{\text{mean}}$ is the global mean adjusted radiative efficiency and $RE_{\text{tro}}$, $RE_{\text{mid}}$, and $RE_{\text{sub}}$ are the adjusted radiative efficiencies in the tropical, mid-latitude, and sub-arctic zones, respectively.

In Table 3, the instantaneous and adjusted radiative efficiency of $C_2F_6$, $CF_4$, and $SF_6$ for clear sky and their adjusted radiative efficiency for all-sky are shown using the 998-band scheme. Of these, the result for clear sky is the arithmetic mean of the values of the six model atmospheres, whereas that for all-sky is the zonal area weighted average of the above three model atmospheres. Additionally, the corresponding values from the IPCC [1] are also listed as a reference in Table 3. The radiative efficiencies of $C_2F_6$, $CF_4$, and $SF_6$ are shown to have increased by 5%, 3%, and 5%, respectively, after stratospheric adjustment, by comparison

**Table 2** Cloud parameters

| Type | Tropical atmosphere | | | Midlatitude atmosphere | | | Subarctic atmosphere | | |
|---|---|---|---|---|---|---|---|---|---|
| | Cloud amount (%) | Water or ice content (g m$^{-3}$) | Effective radius (μm) | Cloud amount (%) | Water or ice content (g m$^{-3}$) | Effective radius (μm) | Cloud amount (%) | Water or ice content (g m$^{-3}$) | Effective radius (μm) |
| Cu (water) | 11.43 | 0.03 | 10 | 9.50 | 0.03 | 10 | 2.43 | 0.03 | 10 |
| Sc (water) | 9.38 | 0.07 | 10 | 10.48 | 0.09 | 10 | 5.36 | 0.11 | 10 |
| St (water) | 0.75 | 2.47 | 10 | 2.26 | 2.79 | 10 | 5.17 | 4.11 | 10 |
| Cu (ice) | 0.00 | 0.01 | 30 | 2.03 | 0.03 | 30 | 3.42 | 0.04 | 30 |
| Sc (ice) | 0.00 | 0.20 | 30 | 1.12 | 0.17 | 30 | 5.76 | 0.22 | 30 |
| St (ice) | 0.00 | 5.90 | 30 | 0.30 | 4.26 | 30 | 2.85 | 3.76 | 30 |
| Ac (water) | 5.55 | 0.05 | 10 | 2.55 | 0.05 | 10 | 0.38 | 0.06 | 10 |
| As (water) | 4.43 | 0.09 | 10 | 3.67 | 0.10 | 10 | 0.82 | 0.13 | 10 |
| Ns (water) | 1.14 | 0.07 | 10 | 1.66 | 0.08 | 10 | 1.03 | 0.10 | 10 |
| Ac (ice) | 0.95 | 0.06 | 30 | 9.02 | 0.09 | 30 | 9.48 | 0.10 | 30 |
| As (ice) | 0.18 | 0.14 | 30 | 6.43 | 0.18 | 30 | 12.99 | 0.22 | 30 |
| Ns (ice) | 0.06 | 0.11 | 30 | 2.20 | 0.11 | 30 | 4.93 | 0.10 | 30 |
| Ci (ice) | 15.36 | 0.01 | 30 | 13.27 | 0.01 | 30 | 6.49 | 0.01 | 30 |
| Cs (ice) | 5.25 | 0.06 | 30 | 6.89 | 0.08 | 30 | 1.59 | 0.09 | 30 |
| Cc (ice) | 2.49 | 0.27 | 30 | 3.54 | 0.25 | 30 | 0.64 | 0.24 | 30 |

between the instantaneous radiative efficiency and the adjusted radiative efficiency for clear sky in Table 3. The change of radiative forcing after stratospheric temperature adjustment depends on the effect of the temperature profile after the net radiation flux at the tropopause has been adjusted [4]. Taking $C_2F_6$ as an example, the heating rates caused by a disturbance of 0.1 ppbv in the longwave region for the six model atmospheres calculated by both the 17-band and 998-band schemes are listed in Figure 3. The heating rate profiles varied with the model atmospheres, but the magnitudes of these heating rates are consistent with each other in the same radiation scheme (17-band or 998-band) and show a similar vertical distribution. Figure 3 shows that the heating rates of the 17-band scheme were significantly less than those of the 998-band scheme. This was because the strong and weak absorptions were all included in the 998-band scheme, whereas the band division was too broad and the k-intervals too few in the 17-band scheme, reducing the calculation accuracy. The USS results were close to the average of all results for the six model atmospheres and are thus further analyzed here as an example. The heating rate of $C_2F_6$ in the USS atmosphere with the 998-band scheme was positive from the surface to the lower stratosphere (about 5 hPa). When a new thermal balance was reached after stratospheric adjustment, the downward radiation flux from the lower stratosphere to the troposphere increased. This caused an increase in the radiative forcing at the tropopause. In a similar way, the stratospheric-adjusted radiative efficiencies of $CF_4$ and $SF_6$ were also greater than their corresponding instantaneous radiative efficiencies (see Table 3).

As shown in Table 3, the regional means of the stratosphere-adjusted radiative efficiencies of $C_2F_6$, $CF_4$, and $SF_6$ for all-sky were 24%, 18%, and 25% less than the corresponding values for clear sky, respectively. This was because the optical thickness of these greenhouse gases is very thin, and thus the decrease in the upward radiative flux caused by clouds has a significant effect on their radiative forcing [4].

We found that the stratosphere-adjusted radiative efficiencies of $C_2F_6$, $CF_4$, and $SF_6$ for the all-sky case were 0.346, 0.098, and 0.680 W $m^{-2}$ $ppbv^{-1}$, respectively, with corresponding differences of 33%, −2%, and 31% from those reported by the IPCC [1]. The different input spectral absorption data, radiation schemes, and cloud schemes were the main causes of these differences. First, the absorption cross-section data of $C_2F_6$, $CF_4$, and $SF_6$ from HITRAN 2004 were used in this work. The calculated integrated absorption cross-section of $C_2F_6$ was different from that used by Sihra et al. [6] by 1%. There was also a difference of 1% between the integrated absorption cross-section of $CF_4$ and that used by Hurley et al. [7]. The absorption cross-section

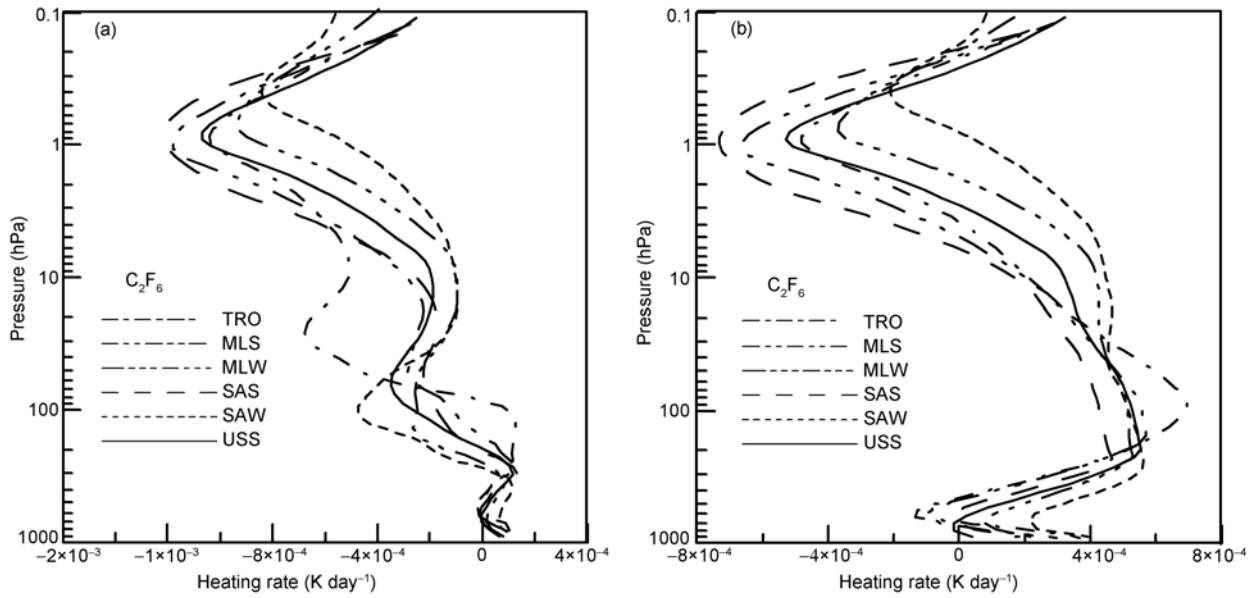


**Figure 3** Heating rates of a 0.1 ppbv $C_2F_6$ perturbation for six model atmospheres using the 17-band (a) and 998-band (b) schemes.

**Table 3** Radiative efficiencies of $C_2F_6$, $CF_4$ and $SF_6$

| Gase | Instantaneous radiative efficiency for clear sky (W $m^{-2}$ $ppbv^{-1}$) | Stratospheric adjusted radiative efficiency for clear sky (W $m^{-2}$ $ppbv^{-1}$) | Stratospheric adjusted radiative efficiency for all-sky (W $m^{-2}$ $ppbv^{-1}$) | Radiative efficiency in IPCC [1] (W $m^{-2}$ $ppbv^{-1}$) |
|---|---|---|---|---|
| $C_2F_6$ | 0.433 | 0.453 | 0.346 | 0.26 |
| $CF_4$ | 0.116 | 0.119 | 0.098 | 0.1 |
| $SF_6$ | 0.869 | 0.909 | 0.680 | 0.52 |

data of $SF_6$ were the same as those given by Huang [5], showing that the input absorption cross-section data have no significant influence on the radiative forcing results. The 998-band scheme used in this work considered the strong or weak absorption bands more accurately than previous generally used narrow-band models, and thus the calculated radiative efficiencies in this work were larger. Moreover, clouds had a significant effect on the radiative efficiency; the difference in the radiative efficiency could be caused by different cloud schemes used by different researchers.

Since the industrial revolution, the atmospheric concentrations of $C_2F_6$, $CF_4$, and $SF_6$ have been gradually increased. According to the IPCC [1], the new concentrations of $C_2F_6$, $CF_4$, and $SF_6$ are 2.9, 74, and 5.6 pptv, respectively. Of these, the atmospheric concentration of 40 pptv for $CF_4$ comes from natural sources. According to the concentrations of $C_2F_6$, $CF_4$, and $SF_6$ and the radiative efficiencies calculated in this paper, $C_2F_6$, $CF_4$, and $SF_6$ have caused radiative forcing of 0.001, 0.007, and 0.004 W $m^{-2}$, respectively, since 1750. Ten kinds of atmospheric scenarios for $C_2F_6$, $CF_4$, and $SF_6$ were given in the IPCC's Special Report on Emissions Scenarios (SRES) [2]. The mean atmospheric concentrations of $C_2F_6$, $CF_4$, and $SF_6$ for these 10 scenarios are calculated here. On this basis, the changes in the radiative forcing of $C_2F_6$, $CF_4$, and $SF_6$ for the next 100 years were calculated (see Figure 4). By 2100, the radiative forcing values for $C_2F_6$, $CF_4$, and $SF_6$ were predicted to become 0.008, 0.036, and 0.037 W $m^{-2}$, respectively; or about 8, 5, and 9 times as much as at present.

## 3 GWP and GTP of $C_2F_6$, $CF_4$, and $SF_6$

The GWP and GTP calculation models for $C_2F_6$, $CF_4$, and $SF_6$ were built according to the definitions of GWP and GTP in this work, based on the radiative efficiencies given above. The models predicted the GWPs and GTPs of these gases in the next 20, 100, and 500 years.

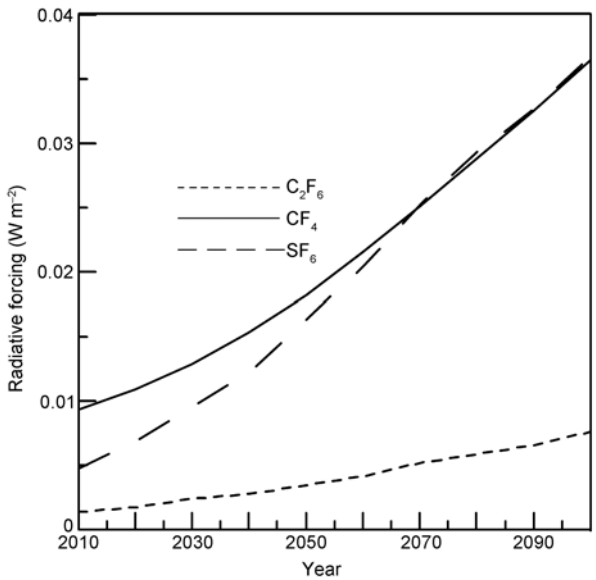


**Figure 4** Radiative forcing of $C_2F_6$, $CF_4$, and $SF_6$ from 2010 to 2100.

The GWP is a measure of the relative radiative effect of a given substance compared to another, integrated over a chosen time horizon. It is defined as the ratio of the time-integrated radiative forcing from the instantaneous release of 1 kg of a trace substance $x$ relative to that of 1 kg of a reference gas ($CO_2$). The eq. (1) is

$$\mathrm{GWP}_x = \frac{\int_0^{TH} RF_x(t)\mathrm{d}t}{\int_0^{TH} RF_r(t)\mathrm{d}t} = \frac{\int_0^{TH} a_x[x(t)]\mathrm{d}t}{\int_0^{TH} a_r[r(t)]\mathrm{d}t}, \tag{3}$$

where

$$x(t) = \mathrm{e}^{-t/\tau},\ x(t) = \mathrm{e}^{-t/\tau}, \tag{4}$$

$$r(t) = a_0 + \sum_i a_i \exp\left(-\frac{t}{\alpha_i}\right), \tag{5}$$

$TH$ is the considered time horizon (i.e., 20, 100, and 500 years in this study), and $t$ is the time. $RF_x$ and $RF_r$ are the radiative forcing due to agent $x$ and $CO_2$, respectively. $a_x$ and $a_r$ are the radiative efficiencies due to a one-unit increase in the atmospheric concentration of gas $x$ and $CO_2$, respectively. $x(t)$ and $r(t)$ are the respective time-decaying functions of pulses of the injected gas $x$ and $CO_2$, where $\tau$ is the lifetime of gas $x$ in eq. (4). The $CO_2$ time-decaying function, as used in eq. (5), was adopted from the IPCC [1]. In the function, $a_0$, $a_i$, and $\alpha_i$ are parameters for the calculation (detailed values have been reported by ref. [1]).

Ever since the concept of the GWP was first proposed [17], it has been questioned by researchers. First, the GWP cannot be used simply for all compounds that affect climate. Relative to long-lived gases, the mean global GWP cannot show the influence of short-lived gases on climate well. Second, it cannot differentiate the influence of different gases in a lifetime. The GWP simply shows the ratio of the integrated radiative forcing of different gas pulse emissions within a given time horizon. It cannot show the direct influence of gases on the surface temperature, i.e., it cannot show how the surface temperature varies with time [18, 19]. Shine et al. [20] proposed the GTP as a new metric, and it was adopted by the IPCC [1]. The GTP is defined as the ratio of the global temperature change over the time horizon of a gas $x$ and the reference gas $CO_2$ for a pulse emission (1 kg at $t$=0) and sustained emission (1 kg $year^{-1}$). The GTPs from a pulse emission and sustained emission are expressed here as $GTP^P$ and $GTP^S$, respectively. The GTP was given by Shine et al. [20] as

$$\mathrm{GTP}_x^{TH} = \frac{\Delta T_x^{TH}}{\Delta T_r^{TH}}, \tag{6}$$

where *TH* is the time horizon considered (here, 20, 100, and 500 years), and $\Delta T_x$ and $\Delta T_r$ are the global mean surface temperature changes caused by gas *x* and $CO_2$, respectively. These can be obtained from the following formula as a simple relationship between the global mean surface temperature change $\Delta T$ and the global mean radiative forcing $\Delta F$ [19]:

$$C\frac{\mathrm{d}\Delta T(t)}{\mathrm{d}t} = \Delta F(t) - \frac{\Delta T(t)}{\lambda}, \tag{7}$$

where, *t* is time, *C* is the heat capacity of the system, and $\lambda$ is a climate sensitivity parameter, which indicates the change in equilibrium surface temperature per unit radiative forcing.

The absolute global temperature potentials for pulse and sustained emissions are expressed as $\mathrm{AGTP^P}$ and $\mathrm{AGTP^S}$, respectively, indicating the temperature changes at time *t* due to 1 kg emission at $t = 0$ with units K $\mathrm{kg^{-1}}$ and constant 1 kg $\mathrm{year^{-1}}$ increase in emissions between $t$=0 and *t* in units of K (kg $\mathrm{year^{-1}})^{-1}$, respectively. The GTPs for pulse and sustained emissions can also be expressed by the following equations, respectively [20]:

$$\mathrm{GTP^P} = \frac{\mathrm{AGTP}_x^{\mathrm{P}}}{\mathrm{AGTP}_{\mathrm{CO_2}}^{\mathrm{P}}}, \tag{8}$$

$$\mathrm{GTP^S} = \frac{\mathrm{AGTP}_x^{\mathrm{S}}}{\mathrm{AGTP}_{\mathrm{CO_2}}^{\mathrm{S}}}. \tag{9}$$

The calculation of GWP and GTP requires the radiative efficiency of gas *x* and $CO_2$ and the time-decaying function. Here, the radiative efficiencies of $C_2F_6$, $CF_4$, and $SF_6$ are from our work as calculated above. The time-decaying functions of $C_2F_6$, $CF_4$, $SF_6$, and $CO_2$ and the radiative efficiency of $CO_2$ are obtained from the IPCC [1], with the same values of such parameters as climate sensitivity and heat capacity as used by Shine et al. [20]. In Table 4, the GWP of $C_2F_6$, $CF_4$, and $SF_6$ for the next 20, 100, and 500 years, the $\mathrm{GTP^P}$ of the pulse emission, and the $\mathrm{GTP^S}$ of the sustaining emission are listed. The GWP values reported by the IPCC [1] are also listed for comparison.

The GWP values in Table 4 show that the contributions of $C_2F_6$, $CF_4$, and $SF_6$ to climate change are thousands of times larger than that of $CO_2$. On the 100-year time horizon, the values for $C_2F_6$, $CF_4$, and $SF_6$ increased by 40%, 3%, and 37%, respectively, compared with those of the IPCC [1]. From the analysis of eq. (3), the calculation of the GWP was mainly and directly related to the four parameters, i.e., the radiative efficiency and time-decaying function of the considered gases and those of the reference gas $CO_2$, the combined effect of which leads to the difference in the GWP calculation. Our analysis shows that the GWP difference is caused mainly by the different radiative efficiencies of $C_2F_6$, $CF_4$, and $SF_6$.

The main physical meaning of $\mathrm{GTP^P}$ is almost the same as that of GWP. $\mathrm{GTP^P}$ is the ratio of the change in the surface temperature caused by the emissions of $C_2F_6$, $CF_4$, and $SF_6$ to that caused by the equal emission of $CO_2$ in a given time horizon. It clearly shows the change of surface temperature caused by $C_2F_6$, $CF_4$, and $SF_6$ relative to $CO_2$ in the same time horizon. GWP is the ratio of the integrated radiative forcing due to these gases to that due to the equal emission of $CO_2$ in a given time horizon. $C_2F_6$, $CF_4$ and $SF_6$ are widely used in industrial processes and their cumulated concentration in the atmosphere has increased rapidly in recent years. $\mathrm{GTP^S}$ does consider the relative effect of sustaining the emission of these gases on the surface temperature change, and could therefore be a good metric to estimate greenhouse gas emission. $\mathrm{GTP^S}$ can provide a good reference for adjusting policies for certain industries to limit the emission of these kinds of greenhouse gases. Shine et al. [20] demonstrated that $\mathrm{GTP^S}$ and GWP can be expressed by a similar equation over a relatively long time horizon, with similar calculated results. We came to the same conclusion in this work (see Table 4). Shine et al. [20] also noted that both $\mathrm{GTP^P}$ and $\mathrm{GTP^S}$ are calculated from eq. (7), and that the results for the latter are more accurate than those for the former. Therefore, $\mathrm{GTP^S}$ is based on a clear concept, fewer parameters are needed for its calculation, it is more accurate than other metrics, and the emission is consistent with that in the real atmosphere case. Therefore, this metric is optimal for estimating the emission of human-made long-lived greenhouse gases.

Here the absolute GTP ($\mathrm{AGTP^P}$ and $\mathrm{AGTP^S}$) of $C_2F_6$, $CF_4$, and $SF_6$ has been calculated to estimate the surface temperature change caused by pulse and sustaining emissions over the next 500 years (see Figure 5). As shown in Figure 5(a), pulse emission can result in the continuous increase of surface temperature rapidly in the initial stage, reaching a peak after 50 years of emission. Thereafter, the

**Table 4** 20-, 100- and 500-year GWP, $\mathrm{GTP^P}$, $\mathrm{GTP^S}$ of $C_2F_6$, $CF_4$ and $SF_6$ in this work and their GWP in IPCC [1]

| Gas | Lifetime (yr) | GWP 20/100/500 yr | GWP IPCC [1] 20/100/500 yr | $\mathrm{GTP^P}$ 20/100/500 yr | $\mathrm{GTP^S}$ 20/100/500 yr |
|---|---|---|---|---|---|
| $C_2F_6$ | 10000 | 11614/17035/25955 | 8630/12200/18200 | 12530/22468/34975 | 10909/16498/25732 |
| $CF_4$ | 50000 | 5163/7597/11761 | 5210/7390/11200 | 5572/10052/15694 | 4849/7355/11655 |
| $SF_6$ | 3200 | 21520/31298/45744 | 16300/22800/32600 | 23202/40935/56856 | 20224/30341/45399 |

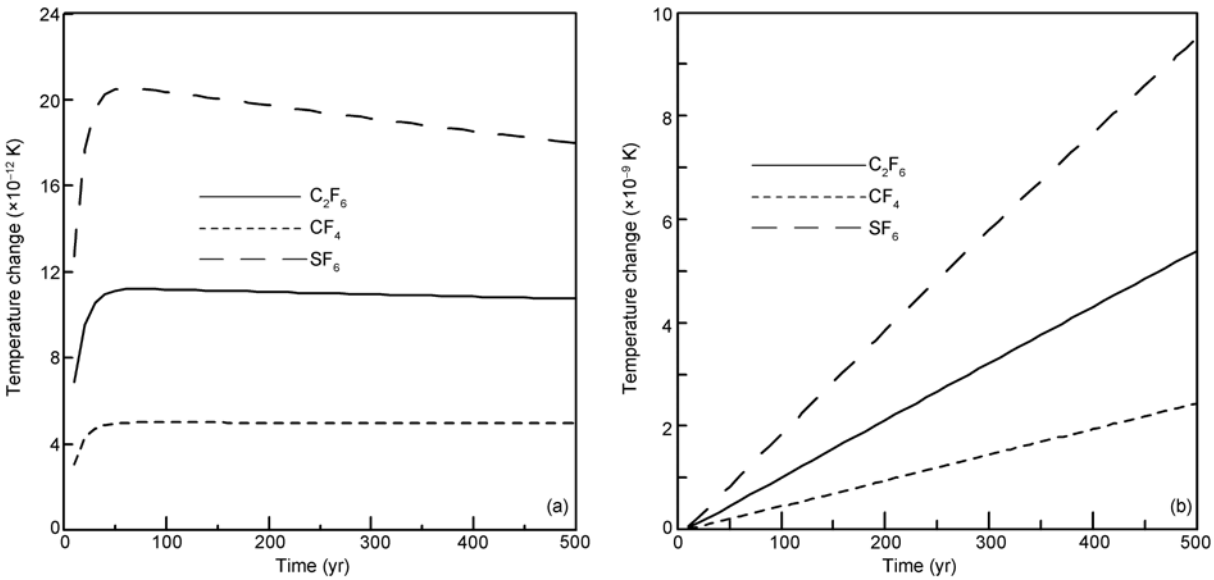


**Figure 5** Temperature changes caused by pulse emission (a) and sustained emission (b) due to $C_2F_6$, $CF_4$, and $SF_6$.

surface temperature begins to decrease slowly or remains constant. Figure 5(b) shows that the surface temperature change caused by sustained emission increases linearly after the initial time. This is because $C_2F_6$, $CF_4$, and $SF_6$ can stay in the atmosphere for a long time. Hence, sustained emissions increase their concentration and thus cause continuous surface temperature increases. Figure 5 shows that the surface temperature change caused by sustained emission is two orders of magnitude larger than the corresponding values caused by pulse emission, with a significant effect on the surface temperature change. If the production, consumption, and emission of $C_2F_6$, $CF_4$, and $SF_6$ in current industries are not controlled, the changes in surface temperature caused by sustained emission will increase constantly.

## 4 Summary

In this paper, the effective absorption coefficients of $C_2F_6$, $CF_4$, and $SF_6$ were calculated from the HITRAN 2004 database using both 17-band and 998-band schemes based on the correlated k-distribution method. We also discussed the effect of different radiation schemes on the radiative forcing calculation of $C_2F_6$, $CF_4$, and $SF_6$. From the industrial revolution to 2005, the total radiative forcing of $C_2F_6$, $CF_4$, and $SF_6$ has been about 0.012 W $m^{-2}$. However, total radiative forcing was predicted to reach 0.081 W $m^{-2}$ by 2100, indicating that these gases will contribute to global warming in the future, together with other long-lived greenhouse gases. Using the accurate 998-band scheme, we calculated the stratosphere-adjusted all-sky radiative efficiencies of $C_2F_6$, $CF_4$, and $SF_6$ as 0.346, 0.098, and 0.680 W $m^{-2}$ $ppbv^{-1}$, respectively, with corresponding differences of 33%, –2%, and 31%, compared with those in the IPCC [1].

Based on the updated radiative efficiencies of $C_2F_6$, $CF_4$, and $SF_6$, we calculated the GWP and GTP in the next 20, 100, and 500 years to be thousands of times greater than those of the equal emission of $CO_2$. We also calculated the surface temperature change caused by their pulse and sustained emissions over the next 500 years. These gases will have a long-term sustained effect on global warming in the future. Our results show that $GTP^S$ is a better metric to estimate the effect of human-made long-lived greenhouse gases on the global climate.

*The authors would like to thank Prof. Qiang Fu, Department of Atmospheric Science, University of Washington for his suggestion to the stratospheric adjusted radiative forcing scheme used in this work and Mr. Peng Lu, National Climate Center for his calculations in the cloud scheme used in this work. This work was supported by National Natural Science Foundation of China (Grant No. 40775006), National Basic Research Program of Chnia (Grant No. 2010CB955703) and the Special Foundation for Climate Change (Grant No. 2010-2200509).*

1 Solomon S, Qin D, Manning M, et al., eds. Climate Change 2007: The Physical Science Basis. Contribution of Working Group I to the Fourth Assessment Report of the Intergovernmental Panel on Climate Change. Cambridge and New York: Cambridge University Press, 2007
2 Metz B, Kuijpers L, Solomon S, et al., eds. Safeguarding the Ozone Layer and the Global Climate System: Issues Related to Hydrofluorocarbons and Perfluorocarbons. Cambridge: Cambridge University Press, 2004
3 Highwood E J, Shine K P. Radiative forcing and global warming potentials of 11 halogenated compounds. J Quant Spectrosc Radiat Transf, 2000, 66: 169–183
4 Jain A K, Briegleb B P, Minschwaner K, et al. Radiative forcings and global warming potentials of 39 greenhouse gases. J Geophys Res, 2000, 105(D16): 20773–20790
5 Huang X Y. Global Warming Potential of Greenhouse Gases. Doctoral Dissertation. Beijing: Institute of Atmospheric Physics, Chinese Academy of Sciences, 2001

6 Sihra K, Hurley M D, Shine K P, et al. Updated radiative forcing estimates of 65 halocarbons and onomethane hydrocarbons. J Geophys Res, 2001, 106(D17): 20493–20505

7 Hurley M D, Wallington T J, Buchanan G A, et al. IR spectrum and radiative forcing of $CF_4$ revisted. J Geophys Res, 2005, 110: D02102

8 Zhang H, Shi G Y, Nakajima T, et al. The effects of the choice of the k-interval number on radiative calculations. J Quant Spectrosc Radiat Transfer, 2006, 98: 31–43

9 Zhang H, Suzuki T, Nakajima T, et al. Effects of band division on radiative calculations. Opt Eng, 2006, 45: 016002–016010

10 Shi G Y. An Accurate calculation and representation of the infrared transmission function of the atmospheric constituents. Doctoral Dissertation. Tohoku: Tohoku University of Japan, 1981

11 Gohar L K, Myhre G, Shine K P. Updated radiative forcing estimates of four halocarbons. J Geophys Res, 2004, 109: D01107, doi: 10.1029/2003JD004320

12 Zhang H, Nakajima T, Shi G Y, et al. An optimal approach to overlapping bands with correlated k distribution method and its application to radiative calculations. J Geophys Res, 2003, 108(D20): 4641

13 Nakajima T, Tsukamoto M, Tsushima Y, et al. Modeling of the radiative process in an atmospheric general circulation model. Appl Opt, 2000, 39: 4869–4878

14 Freckleton R S, Pinnock S, Shine K P. Radiative forcing of halocarbons: A comparison of line-by-line and narrow-band models using $CF_4$ as an example. J Quant Spectrosc Radiat Transfer, 1996, 55: 763–769

15 Rossow W B, Schiffer R A. Advances in understanding clouds from ISCCP. Bull Amer Meteorol Soc, 1999, 80: 2261–2288

16 Yang Q, Fu Q, Austin J, et al. Observationally derived and general circulation model simulated tropical stratospheric upward mass fluxes. J Geophys Res, 2008, 113: D00B07, doi: 10.1029/2008JD009945

17 Houghton J T, Jenkins G J, Ephraums J J, eds. Climate Change 1990: The IPCC Scientific Assessment. Cambridge: Cambridge University Press, 1990

18 Fuglestvedt J S, Berntsen T, Godal O, et al. Metrics of climate change: Assessing radiative forcing and emission indices. Clim Change, 2003, 58: 267–331

19 Steven J S, Wigley T M L. Global Warming Potentials: 1. Climatic implications of emissions reductions. Clim Change, 2000, 44: 445–457

20 Shine K P, Fulestvedt J S, Hailemariam K, et al. Alternatives to the global warming potential for comparing climate impacts of emissions of greenhouse gases. Clim Change, 2005, 68: 281–302

张 雷,任国玉,刘 江等. 城市化对北京气象站极端气温指数趋势变化的影响. 地球物理学报,2011,**54**(5):1150～1159,DOI:10.3969/j.issn.0001-5733.2011.05.002

Zhang L, Ren G Y, Liu J, et al. Urban effect on trends of extreme temperature indices at Beijing Meteorological Station. *Chinese J. Geophys.* (in Chinese), 2011, **54**(5):1150～1159,DOI:10.3969/j.issn.0001-5733.2011.05.002

# 城市化对北京气象站极端气温指数趋势变化的影响

张 雷[1,2],任国玉[2*],刘 江[1],周雅清[3,2],任玉玉[2],张爱英[4],冯亚文[2]

1 沈阳农业大学,沈阳 110161

2 中国气象局气候研究开放实验室,国家气候中心,北京 100081

3 山西省晋中市气象局,山西晋中 030600

4 北京市气象局,北京 100081

**摘 要** 利用 5 个乡村气象站和北京气象站(简称北京站)1960～2008 年日最高、最低气温资料,比较分析了北京地区城市和乡村极端气温指数年、季节的时间变化以及城市化对北京站各极端气温指数趋势变化的影响. 结果表明:1960～2008 年北京站霜冻日数、冷夜日数、冷昼日数和平均日较差均显著减少,暖夜日数、暖昼日数、平均最高气温和平均最低气温均显著上升,这些指数的趋势变化全部通过了 0.01 显著性水平检验,其中霜冻日数、冷夜日数、暖夜日数、平均最低气温、平均气温日较差等与最低气温有关的极端气温指数比冷昼日数、暖昼日数、平均最高气温等基于最高气温记录的极端气温指数变化趋势更明显;城市化因素已致使北京站 1960～2008 年期间霜冻日数、冷夜日数和平均气温日较差显著减少,暖夜日数和平均最低气温显著增加,这些与最低气温有关的极端气温指数序列,其城市化影响都通过了 0.01 显著性水平检验. 在北京站的霜冻日数、冷夜日数和平均气温日较差长期减少趋势中,城市化影响分别达到－5.78 d/10a、－17.83 d/10a 和－0.73 ℃/10a,而在北京站暖夜日数和平均最低气温增加趋势中,城市化影响分别为 14.76 d/10a 和 0.70 ℃/10a. 在所有与最低气温有关的年平均极端气温指数的趋势变化中,城市化影响贡献率均达到 100%,即观测到的趋势变化完全是由城市化因素造成的. 城市化致使四季北京站冷夜日数、平均气温日较差均显著减少,暖夜日数、平均最低气温均显著增加,其中平均最低气温和平均气温日较差序列中的城市化影响在冬季最大,暖夜日数序列中的城市化影响在夏季最显著.

**关键词** 极端气候事件,极端气温指数,气候变化,城市化影响,北京站

DOI:10.3969/j.issn.0001-5733.2011.05.002 **中图分类号** P423 **收稿日期** 2010-08-09,2011-01-17 收修定稿

# Urban effect on trends of extreme temperature indices at Beijing Meteorological Station

ZHANG Lei[1,2], REN Guo-Yu[2*], LIU Jiang[1], ZHOU Ya-Qing[3,2], REN Yu-Yu[2], ZHANG Ai-Ying[4], FENG Ya-Wen[2]

1 *Shenyang Agricultural University, Shenyang* 110161, *China*

2 *Laboratory for Climate Studies, National Climate Center, China Meteorological Administration, Beijing* 100081, *China*

3 *Jinzhong Meteorological Bureau of Shanxi Province, Shanxi Jinzhong* 030600, *China*

4 *Beijing Meteorological Bureau, Beijing* 100089, *China*

**Abstract** This research analyzes the urban effect on annual and seasonal trends and the extreme temperature indices at Beijing Meteorological Station, using daily maximum and minimum temperature data of 6 meteorological stations from 1960 to 2008. The results show that the warm

**基金项目** 国家"十一五"科技支撑项目(2007BAC29B02 和 2007BAC03A01)资助.

**作者简介** 张 雷,男,1980 年 7 月生,从事气候变化研究. E-mail:zhanglei3505962@126.com

* **通讯作者** 任国玉,研究员,从事气候变化和古气候研究. E-mail: guoyoo@cma.gov.cn

nights, warm days, mean maximum temperature and mean minimum temperature increase, the frost days, cold days, cold nights and mean diurnal temperature range decrease at Beijing Observatory during the time period, and these changes are significant statistically. The extreme temperature indices based on daily minimum temperature including frost days, cold nights, warm nights, mean minimum temperature and mean diurnal temperature range undergo more significant changes than those indices based on daily maximum temperature such as cold days, warm days and the mean maximum temperature. The effects of urbanization causes a significant decrease of frosts days (−5.78 d/10a), cold nights (−17.83 d/10a) and the average daily temperature range or DTR (−0.73 ℃/10a), and a significant increase of warm nights (14.76 d/10a) and the average minimum temperature (0.70 ℃/10a) in Beijing Station. Urban effects on the trends of the indices series of Beijing Station relative to daily minimum temperature are significant at the 0.01 confidence level, and the contributions of the urban effect to the overall changes of the annual mean extreme indices series all reach 100%, indicating that the changes observed are overwhelmingly caused by the urban effect. Due to the urban effect, cold nights and DTR significantly decrease, and warm nights and mean minimum temperature significantly increase for all seasons (significant at the 0.01 confidence level). The urban effects on trends of the indices series of mean minimum temperature and mean DTR are the largest in wintertime, and the urban effects on trends of the indices series of warm nights are mainly in summertime. It is essential to pay more attention to the urban effects on extreme temperature indices trends of China meteorological stations near big cities like Beijing.

**Keywords**　Extreme climate, Extreme temperature indices, Climate change, Urban effect, Beijing Station

## 1　引　言

极端天气气候事件频率和强度的变化受到科学界、政府部门和公众的极大关注. Karl 等人[1]的研究表明,美国和前苏联地区的平均最低气温在过去几十年有明显的上升趋势,平均高温气温的变化区域性较强,大范围看无明显的变化趋势;Plummer[2]指出,澳大利亚平均最低气温呈上升趋势,而平均最高气温的变化趋势则很弱;Frich 等人[3]和 Alexander 等人[4]对极端气候事件指标进行了研究,结果表明在近 50 年全球陆地区域夏季暖夜频次显著增加,冬季冷夜频次和霜冻日数显著减少.

对中国地区的研究表明,近几十年全国平均最高气温略有增加,而最低气温显著升高,气温日较差显著减小[5,6],且在各个季节中冬季最低气温上升最明显[7,8];中国北方夜间气温极端偏低的日数显著趋于变少,白天气温极端偏高的日数有所增多,日最低气温小于 0 ℃的日数显著减少[9,10];谢庄等人[11]指出,1940～1990 年北京地区最低气温明显上升,最高气温反而下降,结果导致日较差减少;Yan 等人[12]发现 1940～1970 年北京地区极端冷事件频率在减少,极端暖事件频率在增加.

早先的研究还发现,城市热岛效应等因素对于城市附近气象台站观测到的地面平均气温趋势变化具有明显的影响[13～18]. 在华北地区,由于受城市化影响国家基准气候站和基本气象站网观测的年平均地面气温上升幅度非常明显,城市化对全部增温趋势的贡献率达到了 37.9%[18]. 城市化因素对北京地区国家基准气候站和基本气象站年平均气温变化的影响更加显著[17].

由于迄今大多数研究中所用各类极端气温指数均由日最高和最低气温记录导出,上述研究结果暗示,城市化对全球陆地区域地面极端气温指数变化趋势可能具有明显的影响[19]. 但到目前为止,这个问题还没有引起足够重视,对于单站和区域尺度极端气温变化序列中的城市化影响分析还很少,尤其没有对国家基准气候站和基本气象站观测的极端气温事件频率变化趋势进行过系统评价. 最近,周雅清等人[20]利用华北地区 255 个气象站资料,分析了 1961～2000 年城市化对各类气象台站平均最高和最低气温变化趋势的影响,发现国家基本、基准站观测的年平均最低气温上升趋势中,城市化造成的增温为 0.20 ℃/10a,对全部增温的贡献率达 52.6%,

从一个较大区域尺度上证明了最低气温观测记录中存在着十分明显的城市化影响.此外,季崇萍等人[21]发现北京市夜间热岛强度明显大于日间,暗示北京站记录到的夜间最低气温上升可能在一定程度上是城市热岛强度增加的结果.因此,有必要在早先研究的基础上,进一步分析评价城市化因素对单站和区域平均的极端气温指数变化趋势可能产生的影响.

本文根据北京地区5个乡村气象站和北京站最近49年日最高、最低气温资料,计算分析北京站和乡村站平均的年、季极端气温指数的变化趋势,并对北京站各极端气温指数的城市化影响及城市化影响贡献率进行定量估计.

## 2 资料和方法

采用北京地区共6个气象站的逐日最高、最低气温资料,资料来源于国家气象信息中心.其中,北京、上甸子和霞云岭站资料选用时段为1960～2008年,佛爷顶、斋堂和汤河口气象站由于开始观测时间较晚,仅有30～34年不等的记录.此外,一些站还存在少量缺测现象,但缺测数据仅占总数据量的0.27%,不影响资料的可靠性.台站分布情况见图1,其基本信息列于表1.人口信息来自中国统计局[22].

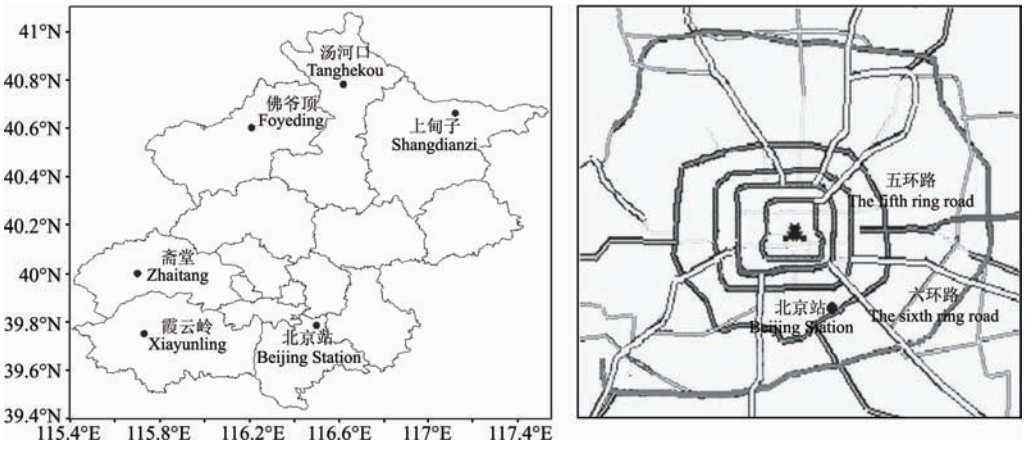


图1 (a)北京站和北京地区乡村站的分布;(b)北京站在市区的位置

Fig.1 (a)The distribution of Beijing station and Beijing area rural stations; (b) Location of Beijing station in the city

**表1 北京地区气象台站信息**

**Table 1 Information about meteorological stations in Beijing area**

| 台站号 | 站名 | 经度(°E) | 纬度(°N) | 海拔(m) | 开始记录年份 | 1960年以来迁站情况 | 台站类型 | 常住人口($10^3$)[22] |
|---|---|---|---|---|---|---|---|---|
| 54511 | 北京 | 116.47 | 39.80 | 31 | 1913 | 1965年1月 | 基本站 | 7122.7 |
| | | | | | | 1969年1月 | | |
| | | | | | | 1970年7月 | | |
| | | | | | | 1981年1月 | | |
| | | | | | | 1997年4月 | | |
| 54597 | 霞云岭 | 115.72 | 39.72 | 408 | 1959 | | 一般站 | 山区 |
| 54501 | 斋堂 | 115.67 | 39.97 | 440 | 1974 | | 一般站 | 6.8 |
| 54410 | 佛爷顶 | 116.13 | 40.60 | 1225 | 1978 | | 一般站 | 山区 |
| 54412 | 汤河口 | 116.62 | 40.72 | 332 | 1974 | | 一般站 | 6.5 |
| 54421 | 上甸子 | 117.12 | 40.65 | 293 | 1958 | 1988年1月 | 一般站 | 山区 |

为进一步保证气温资料的质量,对观测数据再次进行了质量控制.质量控制按以下步骤进行:(1) 最高气温减去最低气温为负值则标记为错误值,且最高气温和最低气温均按照缺测值处理.经检验本数据集中不存在此类错误值;(2)超出平均值4倍标准差的记录被标记可疑值,根据邻近台站的对应记

录进行人工判断,合理的记录保留,不合理的记录按缺测值处理.在此数据集中出现了 9 个可疑值,与周围台站资料进行对比,确定存在 1 个不合理值,并按缺测值处理;(3)所有缺测值取本站 1971～2000 年的平均值,资料序列不足 30 年的,取 1971～2000 年期间记录存在年份的平均值.

北京和上甸子站发生过迁移.上甸子站 1988 年 1 月迁移 1 次,经纬度略有改变,高度增加约 20 m.本文采用滑动 $t$ 检验方法分别对上甸子站最高、最低气温和气温日较差序列进行了均一性检测,但在上述迁站时间附近未发现有跃变点,因此决定不做订正.由于已经对作为国家基本站的北京站进行了均一性检验和订正[23],因此未对其进行检验和处理.

本文选取 1971～2000 年为气候参考期,资料序列不足 30 年的取参考期内所有年份的平均值.表 2 列出了本文所分析的极端气温指数[4],其中高温日数的阈值鉴于研究区域的差异确定为 35 ℃.

百分位指数定义的方法:将某站 1971～2000 年中同日的最高(低)气温资料按升序排列,得到该日第 90(10)个最高(低)气温的百分位值,照此方法可得到 365 个最高(低)气温的第 90(10)个百分位值.百分位值在一年内的分布情况可能不连续,因此采用 5 日滑动平均对其进行处理,将滑动平均后的百分位值作为极端高(低)温事件的上(下)阈值.如果某日的最高气温超过了该日极端气温事件的上阈值,则认为该日出现了极端高温事件;同理,如果某日的最低温度低于该日极端气温事件的下阈值,则认为该日出现了极端低温事件.

乡村站的选取综合参考初子莹等人[17]和周雅清等人[18]的方法.初子莹等人[17]对 1979～2000 年北京地区 20 个台站年和季节平均气温做经验正交函数分解(EOF),认为空间函数第二特征向量指示城市热岛效应或土地利用等局地因素对地面气温的影响,并将年和季节平均气温 EOF 第二特征向量均为负值的站作为“乡村”站;周雅清等人[18]根据台站记录和人口数据,要求台站附近居民点的常住人口数量最多不能超过 8 万.最后从 20 个台站中筛选出霞云岭、斋堂、佛爷顶、汤河口和上甸子等 5 个乡村站.首先建立各单站月极端气温指数的距平序列,在此基础上计算北京站和乡村站季节、年平均极端气温指数距平序列的线性趋势;然后将北京站和乡村站平均的趋势进行比较,得到城市化影响和城市化影响贡献率.对极端气温指数序列变化趋势的估计采用最小二乘法计算.季节划分的方法是:1,2 月和上年 12 月为冬季,3～5 月为春季,6～8 月为夏季,9～11月为秋季.

为了定量评价城市化对极端气温指数变化趋势的影响,参照周雅清等人[20]定义如下术语:

城市化影响:指由于城市热岛效应加强等因素引起的城市附近台站极端气温指数线性趋势的变化,用 $\Delta X_{ur}$ 表示.设 $X_u$ 为城市站极端气温指数的变化趋势,$X_r$ 为乡村站极端气温指数的变化趋势.城市化影响($\Delta X_{ur}$)的表达式为

$$\Delta X_{ur} = X_u - X_r, \tag{1}$$

当 $\Delta X_{ur} > 0$ 时,表示城市化影响使极端气温指数上升或增加;当 $\Delta X_{ur} = 0$ 时,表示城市化影响为 0;当 $\Delta X_{ur} < 0$ 时,表示城市化影响使极端气温指数下降或减少.

**表 2　极端气温指数[4]的定义**

**Table 2　The definition of indices for extreme temperature[4]**

| 指数名称 | 代码 | 定义 | 单位 |
|---|---|---|---|
| 1.霜冻日数 | FD0 | 第 $j$ 时期内日最低气温 $Tn_{ij}<0$ ℃(其中下标为第 $j$ 时期第 $i$ 日)的日数 | d |
| 2.结冰日数 | ID0 | 第 $j$ 时期内日最高气温 $Tx_{ij}<0$ ℃(其中下标为第 $j$ 时期第 $i$ 日)的日数 | d |
| 3.高温日数 | SU35 | 第 $j$ 时期内日最高气温 $Tx_{ij}>35$ ℃(其中下标为第 $j$ 时期第 $i$ 日)的日数 | d |
| 4.冷夜日数 | TN10P | 第 $j$ 时期内第 $i$ 日的最低气温 $Tn_{ij}$ 小于 10%分位数(以每滑动 5 日为中心)的日数 | d |
| 5.暖夜日数 | TN90P | 第 $j$ 时期内第 $i$ 日的最低气温 $Tn_{ij}$ 大于 90%分位数(以每滑动 5 日为中心)的日数 | d |
| 6.冷昼日数 | TX10P | 第 $j$ 时期内第 $i$ 日的最高气温 $Tx_{ij}$ 小于 10%分位数(以每滑动 5 日为中心)的日数 | d |
| 7.暖昼日数 | TX90P | 第 $j$ 时期内第 $i$ 日的最高气温 $Tx_{ij}$ 大于 90%分位数(以每滑动 5 日为中心)的日数 | d |
| 8.平均最高气温 | MAT | 第 $j$ 时期内日最高气温 $Tx_{ij}$ 的平均值 | ℃ |
| 9.平均最低气温 | MIT | 第 $j$ 时期内日最低气温 $Tn_{ij}$ 的平均值 | ℃ |
| 10.平均日较差 | DTR | 第 $j$ 时期内日最高气温 $Tx_{ij}$ 与最低温度 $Tn_{ij}$ 之差的平均值 | ℃ |

城市化影响贡献率:指城市化影响对城市附近台站极端气温指数趋势变化的贡献率,即城市化影响在城市附近台站极端气温指数趋势变化中所占的比率,用 $E_u$ 表示. 城市化影响贡献率($E_u$)的表达式为

$$E_u = |\Delta X_{ur}/X_u| \times 100\% = |(X_u - X_r)/X_u| \times 100\%, \quad (2)$$

考虑到使城市化影响贡献率 $0 \leqslant E_u \leqslant 100\%$,所以取了绝对值. 当 $E_u = 0$ 时,表示城市化对城市站极端气温指数的变化趋势没有贡献;当 $E_u = 100\%$时,表示城市站极端气温指数的变化完全是由城市化影响造成的. 实际计算当中,少数情况下 $E_u$ 可能超过100%,说明可能存在某种尚未认清的局地因子影响,但这种情况均按100%处理.

## 3 结果分析

### 3.1 城市和乡村站极端气温指数变化趋势

表3给出了1960~2008年5个乡村站平均和北京站极端气温指数变化趋势. 图2为1960~2008年5个乡村站和北京站年极端气温指数距平值及变化趋势. 年结冰日数、高温日数、冷昼日数、暖昼日数、平均最高气温等极端气温指数在北京站和在乡村站变化趋势相似,均表现为极端低温事件减少,极端高温事件增多. 北京站的年霜冻日数和冷夜日数显著减少,趋势分别为-5.45 d/10a和-15.9 d/10a,而暖夜日数和平均最低气温显著增加,趋势分别为13.79 d/10a和0.67 ℃/10a,所有变化趋势均通过了0.01水平的显著性检验;但乡村站年霜冻日数、冷夜日数、暖夜日数和平均最低气温等极端气温指数均无显著性变化. 因此,平均最高气温和基于最高气温的极端气温指数在城市和乡村具有相似的变化,但不是所有变化趋势都通过了显著性检验;而平均最低气温和基于最低气温的夜间极端气温指数在城市发生了显著的变化,但在乡村没有经历明显变化. 尽管平均最高气温都表现为增加,但由于北京站平均最低气温大幅下降,乡村站平均最低气温没有明显变化,因此北京站气温日较差显著减小,而乡村站气温日较差显著增大.

由于霜冻日数、结冰日数和高温日数等极端事件季节性强,故本文只分析其年变化情况. 其他极端气温指数在各个季节与年平均变化趋势相近(表3和图2). 各个季节冷昼日数、暖昼日数、平均最高气温等极端气温指数在北京站和在乡村站变化趋势方向相同,且均表现为极端低温事件减少,极端高温事件增多. 冷昼日数和平均最高气温在冬季变化最明显,暖昼日数在冬、秋季变化最显著. 北京站冷夜日数四季均显著下降,暖夜日数、平均最低气温四季均显著上升,变化趋势均通过了0.01显著性水平检验,其中冷夜日数、平均最低气温在冬季变化最明显,暖夜日数在夏季变化最显著. 乡村站四季冷夜日数、暖夜日数、平均最低气温的变化都不显著,但气温日较差四季均出现显著性增大.

### 3.2 城市化影响分析

表4和图3给出了北京站年极端气温指数趋势变化中的城市化影响和城市化影响贡献率. 1960~2008年,城市化造成北京站年霜冻日数、冷夜日数显著减少,暖夜日数和平均最低气温显著增加,城市

**表3 1960~2008年北京地区乡村站和北京站极端气温指数变化趋势(单位:d/10a或℃/10a)**

**Table 3 Trends of extreme temperature indices of rural stations and Beijing Station for 1960~2008 (unit: d/10a or ℃/10a)**

| | 年 | | 春 | | 夏 | | 秋 | | 冬 | |
|---|---|---|---|---|---|---|---|---|---|---|
| | 乡村 | 北京 | 乡村 | 北京 | 乡村 | 北京 | 乡村 | 北京 | 乡村 | 北京 |
| 霜冻日数 | 0.32 | -5.45** | | | | | | | | |
| 结冰日数 | -2.96** | -2.16* | | | | | | | | |
| 高温日数 | 0.53 | 0.27 | | | | | | | | |
| 冷夜日数 | 1.94 | -15.90** | 0.32 | -4.40** | 1.54** | -2.99** | 0.67 | -3.53** | -0.64 | -5.32** |
| 暖夜日数 | -0.97 | 13.79** | -0.31 | 3.66** | -0.67 | 4.02** | -0.35 | 2.84** | 0.42 | 3.42** |
| 冷昼日数 | -3.18* | -4.03** | -0.85 | -1.23* | -0.18 | -0.48 | -0.46 | -0.64 | -1.68* | -1.60* |
| 暖昼日数 | 6.77** | 5.74** | 1.49** | 1.34* | 1.82* | 1.14 | 1.89** | 1.64** | 1.75** | 1.89** |
| 平均最高气温 | 0.28** | 0.23** | 0.31** | 0.29* | 0.16 | 0.11 | 0.23* | 0.19 | 0.44** | 0.38** |
| 平均最低气温 | -0.04 | 0.67** | -0.03 | 0.73** | -0.10 | 0.45** | -0.11 | 0.58** | 0.13 | 0.96** |
| 平均日较差 | 0.30** | -0.43** | 0.32** | -0.44** | 0.24** | -0.34** | 0.34** | -0.39** | 0.29** | -0.58** |

注:* 表示通过0.05水平的显著性检验,** 表示通过0.01水平的显著性检验.

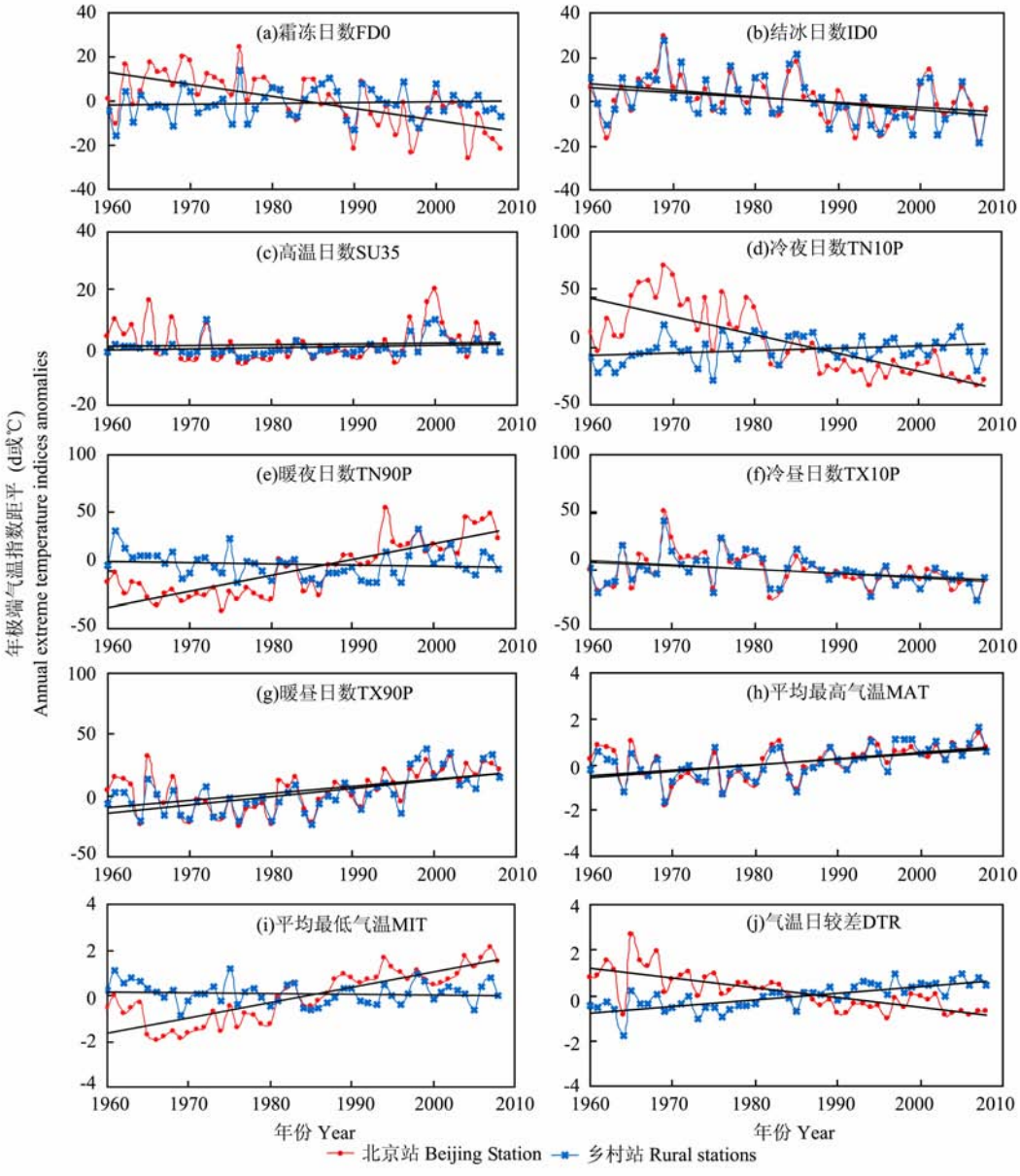


图 2　1960～2008 年北京站(红)和北京地区乡村站(蓝)年平均极端气温指数距平，黑实线为趋势线

Fig. 2　Anomalies of annual mean extreme temperature indices of rural stations (blue) and Beijing Station (red) for 1960～2008. The black solid lines show the linear trends

化对这些极端气温指数趋势变化的影响都通过了 0.01 显著性水平检验. 其中，霜冻日数和冷夜日数序列中的城市化影响分别为－5.78 d/10a 和－17.83 d/10a，暖夜日数和平均最低气温序列中的城市化影响分别是 14.76 d/10a 和 0.70 ℃/10a，城市化影响贡献率均达到 100%. 近 49 年北京站结冰日数、高温日数、冷昼日数、暖昼日数和平均最高气温等极端气温指数趋势变化中的城市化影响很小，均未通过显著性检验，分别为 0.80 d/10a、－0.26 d/10a、－0.85 d/10a、－1.04 d/10a和－0.04 ℃/10a，对应的城市化影响贡献率分别为 37.23%、98.15%、21.08%、18.10% 和 17.71%. 由于平均最低气温受城市化影响显著上升，因此平均日较差受城市化影响显著减小，且城市化影响贡献率为 100%.

因此，北京站基于日最低气温的年极端气温指数变化趋势受城市化影响均很显著，但基于日最高气温的极端气温指数变化趋势受城市化影响很弱. 由于最高气温指数趋势变化中的城市化影响为弱的负值，城市化对各相关极端气温指数变化趋势的影响也是负值，说明城市化因素可能造成北京站白天最高气温相对乡村站下降了.

从各季节来看，由城市化造成的北京站冷夜日

数四季均显著减少,暖夜日数、平均最低气温四季均显著增加,城市化影响都通过了0.01显著性水平检验(表4和图3).平均最低气温的城市化影响在冬季最大为0.83 ℃/10a,城市化影响贡献率为86.42%;而暖夜日数的城市化影响在夏季最显著,达到4.69 d/10a,城市化影响贡献率为100%.由于城市化影响造成四季平均最低气温均显著上升,从而使平均气温日较差受城市化影响在四季都明显减小,且均通过了0.01显著性水平检验,城市化影响贡献率均达到100%.冷昼日数、暖昼日数、平均最高气温等极端气温指数趋势变化中的城市化影响在各季节均未达到显著性水平.

**表4 1960～2008年北京站极端气温指数序列中的城市化影响和城市化影响贡献率**

**Table 4 Effects of urbanization on extreme temperature indices trends and contribution of urbanization effect to extreme temperature indices trends for Beijing Station for period 1960～2008**

| | 年 | | 春 | | 夏 | | 秋 | | 冬 | |
|---|---|---|---|---|---|---|---|---|---|---|
| | A | B | A | B | A | B | A | B | A | B |
| 霜冻日数 | −5.78** | 100.00 | | | | | | | | |
| 结冰日数 | 0.80 | 37.23 | | | | | | | | |
| 高温日数 | −0.26 | 98.15 | | | | | | | | |
| 冷夜日数 | −17.83** | 100.00 | −4.72** | 100.00 | −4.53** | 100.00 | −4.20** | 100.00 | −4.68** | 88.05 |
| 暖夜日数 | 14.76** | 100.00 | 3.96** | 100.00 | 4.69** | 100.00 | 3.19** | 100.00 | 3.00** | 87.69 |
| 冷昼日数 | −0.85 | 21.08 | −0.38 | 31.19 | −0.30 | 62.32 | −0.18 | 28.70 | 0.08 | 4.99 |
| 暖昼日数 | −1.04 | 18.10 | −0.15 | 11.37 | −0.68 | 59.63 | −0.25 | 15.07 | 0.15 | 7.84 |
| 平均最高气温 | −0.04 | 17.71 | −0.02 | 7.55 | −0.05 | 45.33 | −0.04 | 20.15 | −0.06 | 15.43 |
| 平均最低气温 | 0.70** | 100.00 | 0.76** | 100.00 | 0.55** | 100.00 | 0.69** | 100.00 | 0.83** | 86.42 |
| 平均日较差 | −0.73** | 100.00 | −0.76** | 100.00 | −0.59** | 100.00 | −0.73** | 100.00 | −0.87** | 100.00 |

注:A:城市化影响(单位:d/10a或℃/10a);B:城市化影响贡献率(单位:%).** 表示通过0.01水平的显著性检验.

## 4 讨 论

目前分析城市化对单站或区域平均极端气温事件影响的工作还很少.有不少研究对陆地区域平均最高、最低气温和气温日较差的变化进行了分析,发现地面气温的上升是不对称的,最低气温上升很明显,而最高气温上升趋势较弱,气温日较差明显变小[1,11,24～28].地面气温长期趋势变化的这种"非对称性"现象在国内外的大量研究中得到证实.谢庄等人[11]较早指出北京站最低气温明显上升、而最高气温反而下降的非对称性变化,这种变化导致气温日较差显著减少.

陈正洪等[29]在研究湖北省城市化对平均气温变化趋势影响的同时,分析了城市热岛效应对平均最高和最低气温变化趋势的影响及其热岛增温贡献率,发现1961～2000年城市热岛效应导致城市台站的年平均最低气温增加速率比最高气温增加速率快接近1倍,热岛增温贡献率均在70%以上,但平均最高气温的热岛增温贡献率更大.周雅清等[20]分析了1961～2000年城市化对华北地区各类城市台站和国家基准气候/基本气象站平均最高和最低气温变化趋势的影响,发现城市化对平均最高气温变化趋势的影响微弱,个别台站和季节甚至可能造成降温,而对平均最低气温变化趋势的影响非常明显,国家基准气候/基本气象站观测的年平均最低气温上升趋势中,城市化影响贡献率达到52.6%,城市化影响也是乡村站以外的各类气象台站气温日较差明显减小的唯一因子.

本文对北京站的分析结果印证了谢庄等[11]和陈正洪等[29]的研究,并且表明城市化对北京站平均最低气温变化的影响比最高气温变化的影响大得多;本文研究结果与周雅清等[20]针对华北地区的分析结论非常相似,两项研究均指出,1960年以来平均最高气温序列中的城市化影响很弱,而平均最低气温序列中的城市化影响则十分明显,气温日较差明显减小趋势完全由城市化因素造成.本文和周雅清等[20]的研究说明,长期以来国内外研究者反复证实的"气温非对称性变化"现象,主要与城市化对常用观测站网地面最低气温的明显增加效应有关.

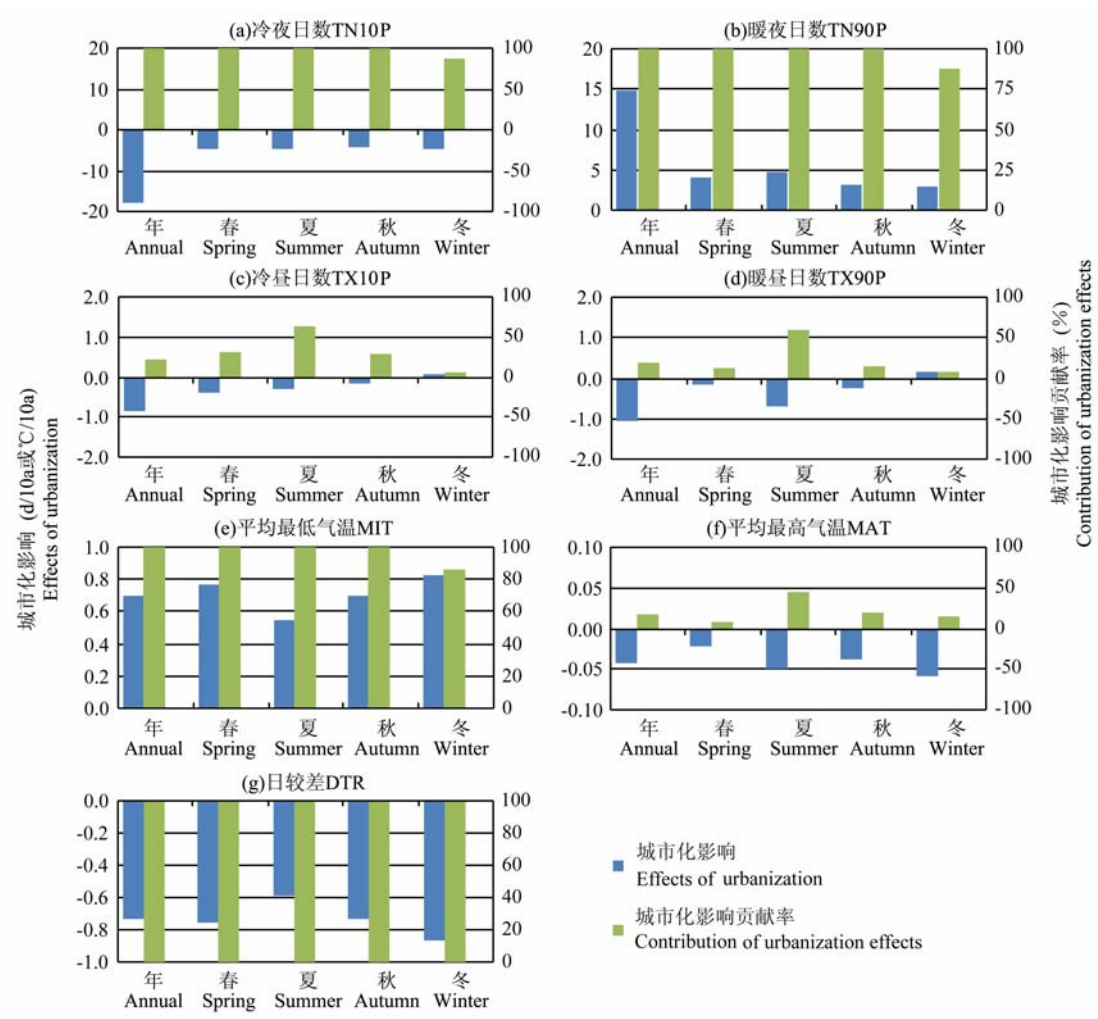


图 3　1960～2008 年北京站极端温度指数的城市化影响和城市化影响的贡献率

Fig. 3　Effects of urbanization on extreme temperature indices trend and the contribution of the effects of urbanization to the overall changes for Beijing Station for period 1960～2008

司鹏等[30]对北京站 1960～2006 年地面气温序列中的城市化影响进行了分析,发现年平均最高气温、平均最低气温和平均气温日较差序列中的城市化影响分别为 0.108 ℃/10a、0.299 ℃/10a 和－0.191 ℃/10a,对应的城市化影响贡献率分别为 31.6%、46.4%和 57.4%;平均最高气温在春季的城市化影响最明显,平均最低气温、平均日较差在冬季的城市化影响最显著.这些分析结果与本文部分一致,但也存在明显差异.本文分析表明,城市化对北京站平均最低气温和气温日较差趋势变化的影响更大些,而城市化对平均最高气温变化的影响则弱得多.造成这种差异的原因主要在乡村站或参考站点的选取上,也可能与资料处理方法及线性趋势计算方法不同有一定关系.

除了分析城市化对平均最高、最低气温和气温日较差变化趋势的影响外,本文还进一步分析了城市化因素对基于日最高、最低气温资料的主要极端气温指数变化趋势的影响.这种分析是迄今国内外研究中未见报道的.本文的分析表明,城市化对北京站霜冻日数、冷夜日数和暖夜日数等基于日最低气温的极端气温指数趋势变化均产生了明显的影响,而对结冰日数、冷昼日数和暖昼日数等基于日最高气温的极端气温指数趋势变化影响很小.造成这种现象的一个原因是白天的城市热岛强度要小于夜间[21],城市热岛强度的这种非对称性致使北京站最低气温上升迅速,而最高气温上升缓慢,基于日最低气温的极端气温指数趋势变化显著,而基于日最高气温的极端气温指数趋势变化较小.另一个可能影响因子是城乡站上空气溶胶的差异.白天城市内和近郊区更高浓度的气溶胶减弱了太阳直接辐射和总辐射,可能在一定程度上消弱甚至抵消了城市热岛效应的增温作用,致使由于城市热岛效应加强因素

引起的相对不明显的最高气温上升幅度进一步减小,相关的极端气温指数变化也很小;夜间城市上空的气溶胶则减弱了北京站附近的外逸地面长波辐射和冷却效应,在增强的城市热岛效应基础上,进一步增强了平均最低气温的上升速率,增强了基于日最低气温的极端气温指数变化趋势.因此,城市化对城市站平均气温以及最高、最低气温的影响,至少包含了城市热岛强度和气溶胶浓度增加两个因素的作用.

城市化因素不仅对北京站等具有长序列观测资料的台站地面平均气温变化趋势造成显著影响,也对基于日最低气温计算的各种极端气候指数序列的趋势变化具有明显的影响,而且这种影响甚至更突出.今后在开展与气温有关的极端气候事件频率变化研究时,要充分注意这个问题.

## 5 结 论

采用北京地区6个气象站1960~2008年逐日最高、最低气温资料,分析了北京站和5个乡村站平均的极端气温指数变化趋势,并检验了城市化因素对北京站极端气温指数变化趋势的影响及贡献率,得到以下结论:

(1)北京站年极端气温指数序列中,霜冻日数、冷夜日数、冷昼日数和平均气温日较差均显著减少,暖夜日数、暖昼日数、平均最高气温和平均最低气温均显著上升,这些指数的趋势变化均通过了0.01显著性水平检验,其中霜冻日数、冷夜日数、暖夜日数、平均最低气温、平均气温日较差的变化趋势比冷昼日数、暖昼日数、平均最高气温的变化趋势更明显,说明基于日最低气温的极端气温指数比基于日最高气温的极端气温指数的变化趋势更显著.这些结果与过去多数研究结论是一致的.

北京地区5个乡村站各极端气温指数虽也发生了一定变化,但这种变化主要与平均最高气温的明显上升有关,表现为结冰日数减少、冷昼日数减少、暖昼日数增加、气温日较差增大,而与最低气温有关的各项极端气温指数变化趋势均不明显.

(2)北京站年霜冻日数、冷夜日数、暖夜日数和平均最低气温等极端气温指数序列中的城市化影响非常显著,分别为-5.78 d/10a、-17.83 d/10a、14.76 d/10a和0.70 ℃/10a,对应的城市化影响贡献率均为100%;而年结冰日数、高温日数、冷昼日数、暖昼日数和平均最高气温等极端气温指数序列中的城市化影响一般很弱,分别仅为0.80 d/10a、-0.26 d/10a、-0.85 d/10a、-1.04 d/10a和-0.04 ℃/10a,对应的城市化影响贡献率为37.23%、98.15%、21.08%、18.10%和17.71%;由于平均最低气温序列中的城市化影响显著,因此北京站平均气温日较差受城市化影响显著减小,减少幅度达到-0.73 ℃/10a,其城市化影响贡献率为100%.

(3)城市化致使北京站的冷夜日数、平均气温日较差四季均显著减少,暖夜日数、平均最低气温四季均显著增加,其中冬季的平均最低气温和气温日较差趋势变化中的城市化影响最明显,而夏季的暖夜日数趋势变化中的城市化影响最显著;冷昼日数、暖昼日数和平均最高气温等极端气温指数的城市化影响在各季节均未达到显著性水平.

因此,北京站基于日最低气温的极端气温指数变化趋势受城市化影响十分显著,而基于日最高气温的极端气温指数受城市化影响很小,早先研究发现的"气温非对称性变化"现象[11]主要是由于城市化造成夜间最低气温显著上升所引起的.造成夜间和白天极端气温指数序列中城市化影响性质与程度明显差异的原因,可能同城市热岛效应的非对称性以及城市上空更高浓度的气溶胶影响有关.

## 参考文献(References)

[1] Karl T R, Kukla G, Razuvayev V N, et al. Global warming: Evidence for asymmetric diurnal temperature changes. *Geophy Res Lett*, 1991, **18**: 2253~2256

[2] Plummer N. Temperature variability and extreme over Australia: Part 1—recent observed changes. *Aust Meteorol Mag*, 1996, **45**: 233~250

[3] Frich P, Alexander L V, Della-Marta P, et al. Observed coherent changes in climatic extremes during the second half of the 20th Century. *Climate Res*, 2002, **19**: 193~212

[4] Alexander L V, Zhang X, Pererson T C, et al. Global observed changes in daily climate extremes of temperature and precipitation. *J Geophys Res*, 2006, **111**, D05109, doi: 10.1029/2005JD006290

[5] 翟盘茂,潘晓华.中国北方近50年温度和降水极端事件变化.地理学报,2003,**58**(增刊):1~10
Zhai P M, Pan X H. Change in extreme temperature and precipitation over northern China during the second half of the 20th century. *Acta Geographica Sinica* (in Chinese), 2003, **58**(Suppl.): 1~10

[6] Zhai P M, Pan X H. Trends in temperature extreme during 1951~1999 in China. *Geophy Res Lett*, 2003, **30**(17): 1~4

[7] 王翠花,李 雄,缪启龙.中国近50年来日最低气温变化特征研究.地理科学,2003,**23**(4):441~447
Wang C H, Li X, Miao Q L. Study of characteristics of daily minimum temperature change in China. *Scientia Geographica Sinica* (in Chinese), 2003, **23**(4): 441~447

[8] 张　宁，孙照渤，曾　刚. 1955～2005 年中国极端气温的变化. 南京气象学院学报，2008，**31**(1)：123～128
Zhang N, Sun Z B, Zeng G. Change of extreme temperatures in China during 1955～2005. *Journal of Nanjing Institute of Meteorology* (in Chinese), 2008, **31**(1): 123～128

[9] 丁一汇，任国玉，翟盘茂等. 气候变化国家评估报告. 北京：科学出版社，2007. 30～37
Ding Y H, Ren G Y, Zhai P M, et al. National Assessment Report of Climate Change (in Chinese). Beijing: Science Press, 2007. 30～37

[10] 丁一汇，任国玉. 中国气候变化科学概论. 北京：气象出版社，2008. 87～99
Ding Y H, Ren G Y. Introduction to Climate Change Science of China (in Chinese). Beijing: Meteorological Press, 2008. 87～99

[11] 谢　庄，曹鸿兴. 北京最高和最低气温的非对称变化. 气象学报，1996，**54**(4)：501～507
Xie Z, Cao H X. The asymmetric trend of change in maximum and minimum temperature in Beijing. *Acta Meteor Sinica* (in Chinese), 1996, **54**(4): 501～507

[12] Yan Z W, Yang C. Influence of inhomogeneity on the estimation of mean and extreme temperature trends in Beijing and Shanghai. *Adv Atmos Sci*, 2001, **18**(3): 309～322

[13] Karl T R, Jones P D. Urban bias in area-averaged surface air temperature trends. *B Am Meteorol Soc*, 1989, **70**(3): 265～270

[14] 赵宗慈. 近 39 年中国气温变化与城市化影响. 气象，1991，**17**(4)：14～16
Zhao Z C. Surface temperature variability and urbanization effect on it over the past 39 years in China. *Meteor Mon* (in Chinese), 1991, **17**(4): 14～16

[15] 林学椿，于淑秋. 北京地区气温的年代际变化和热岛效应. 地球物理学报，2005，**48**(1)：39～45
Lin X C, Yu S Q. Interdecadal changes of temperature in the Beijing region and its heat island effect. *Chinese J Geophys* (in Chinese), 2005, **48**(1): 39～45

[16] 林学椿，于淑秋，唐国利. 北京城市化进程与热岛强度关系的研究. 自然科学进展，2005，**15**(7)：882～886
Lin X C, Yu S Q, Tang G L. Research on the relationship between urbanization and urban heat island in Beijing City. *Progress of Natural Sciences* (in Chinese), 2005, **15**(7): 882～886

[17] 初子莹，任国玉. 北京地区城市热岛强度变化对区域温度序列的影响. 气象学报，2005，**63**(4)：534～540
Chu Z Y, Ren G Y. Effect of enhanced urban heat island magnitude on average surface air temperature series in Beijing region. *Acta Meteor Sinica* (in Chinese), 2005, **63**(4): 534～540

[18] 周雅清，任国玉. 华北地区地表气温观测中城镇化影响的检测和订正. 气候与环境研究，2005，**10**(4)：743～753
Zhou Y Q, Ren G Y. Identifying and correcting urban bias for regional surface air temperature series North China over period of 1961～2000. *Climatic and Environmental Research* (in Chinese), 2005, **10**(4): 743～753

[19] 任国玉. 关于极端气温变化研究的几个问题. 见：刘燕华. 气候变化与科技创新. 北京：科学出版社，2009. 85～86
Ren G Y. On issues of extreme temperature change researches. In: Liu Y H. Climate Change and Scientific Innovation (in Chinese). Beijing: Science Press, 2009. 85～86

[20] 周雅清，任国玉. 城市化对华北地区最高、最低气温和日较差变化趋势的影响. 高原气象，2009，**28**(5)：1158～1166
Zhou Y Q, Ren G Y. Urbanization effect on trends of mean maximum temperature, minimum temperature and daily temperature range in North China. *Plateau Meteorology* (in Chinese), 2009, **28**(5): 1158～1166

[21] 季崇萍，刘伟东，轩春怡. 北京城市化进程对城市热岛的影响研究. 地球物理学报，2006，**49**(1)：69～77
Ji C P, Liu W D, Xuan C Y. Impact of urban growth on the heat island in Beijing. *Chinese J Geophys* (in Chinese), 2006, **49**(1): 69～77

[22] 中国统计局. 中国乡、镇、街道人口资料. 北京：中国统计出版社，2002. 1～6
China Statistic Bureau. Population Data of China Towns and City Districts (in Chinese). Beijing: China Statistic Press, 2002. 1～6

[23] Li Q X, Liu X N, Zhang H Z, et al. Detecting and adjusting temporal inhomogeneity in Chinese mean surface air temperature data. *Adv Atmos Sci*, 2004, **21**(2): 260～268

[24] Easterling D R, Horton B, Jones P D, et al. Maximum and minimum temperature trends for the globe. *Science*, 1997, **277**: 364～367

[25] 翟盘茂，任福民. 中国近四十年最高最低温度变化. 气象学报，1997，**55**(4)：418～429
Zhai P M, Ren F M. Maximum and minimum temperature change of China over the past 40 years. *Acta Meteorologica Sinica* (in Chinese), 1997, **55**(4): 418～429

[26] Qian W H, Lin X. Regional trends in recent temperature and indices in China. *Climate Res*, 2004, **27**: 119～134

[27] 华丽娟，马柱国，罗德海. 1961～2000 年中国区域气温较差分析. 地理学报，2004，**59**(5)：680～688
Hua L J, Ma Z G, Luo D H. Analysis of temperature range from 1961 through 2000 across China. *Acta Geographica Sinica* (in Chinese), 2004, **59**(5): 680～688

[28] 陈正洪，王海军，任国玉. 武汉市城市热岛强度非对称性变化. 气候变化研究进展，2007，**3**(5)：282～286
Chen Z H, Wang H J, Ren G Y. Asymmetrical change of urban heat island intensity in Wuhan, China. *Advances in Climate Change Research* (in Chinese), 2007, **3**(5): 282～286

[29] 陈正洪，王海军，任国玉等. 湖北省城市热岛强度变化对区域气温序列的影响. 气候与环境研究，2005，**10**(4)：771～779
Chen Z H, Wang H J, Ren G Y, et al. Change of urban heat island intensity and its effect on regional temperature series: A case study in Hubei Province. *Climatic and Environmental Research* (in Chinese), 2005, **10**(4): 771～779

[30] 司　鹏，李庆祥，轩春怡等. 城市化对北京气温变化的贡献分析. 自然灾害学报，2009，**18**(4)：138～144
Si P, Li Q X, Xuan C Y, et al. Contribution of urbanization to change of air temperature in Beijing. *Journal of Natural Disasters* (in Chinese), 2009, **18**(4): 138～144



（本文编辑　何　燕）

Vol. 50: 227–245, 2011
doi: 10.3354/cr01066

CLIMATE RESEARCH
Clim Res

Published December 22

*Contribution to CR Special 28 'Changes in climatic extremes over mainland China'*

# Changes in precipitation extremes over Eastern China simulated by the Beijing Climate Center Climate System Model (BCC_CSM1.0)

**Li Zhang*, Min Dong, Tongwen Wu**

**Beijing Climate Center, China Meteorological Administration, Beijing, PR China**

ABSTRACT: Performance of the Beijing Climate Center Climate System Model (BCC_CSM1.0) in simulating the regional extreme precipitation change over eastern China east of 105°E was evaluated. Daily observed precipitation data for 1956–2009 at 349 rain gauge stations in China were used for comparison. The 20th century simulation forced by observed greenhouse gases, aerosols, solar irradiance and volcanic aerosols shows that (1) BCC_CSM1.0 can reproduce the basic feature of observed climatology of annual total precipitation and extreme precipitation over the 95th percentile, with spatial correlation of 0.77 for both of them. (2) BCC_CSM1.0 is also able to capture the main change patterns of yearly accumulated extreme precipitation above the 95th percentile, although there are some model biases in the spatial extension and strength. Some model biases are also noted: (1) Annual total and extreme precipitation south of Yangtze River are underestimated. (2) Frequency of heavy precipitation (≥25.0 mm $d^{-1}$) over eastern China is underestimated, but the frequency of light rain (0.1 to 9.9 mm $d^{-1}$) is overestimated. (3) Simulated long-term trends of annual extreme precipitation amount and frequency in the last 50 yr are the opposite of the observations in North and South China.

KEY WORDS: Extreme precipitation · Eastern China · BCC_CSM1.0 · Evaluation

*Resale or republication not permitted without written consent of the publisher*

## 1. INTRODUCTION

Under the background of global warming, frequencies and intensities of extreme climate events may either increase or decrease, with obvious regional differences (IPCC 2007). More and more attention has been paid to the variations and trends in extreme precipitation (Easterling et al. 2000, Karl & Easterling 1999). Both frequencies and intensities of extreme precipitation over mid- and high-latitude land regions of the North Hemisphere have increased in recent decades (Alexander et al. 2006) and might be a response to the anthropogenic global warming (e.g. IPCC 2007, Zhang et al. 2007).

It seems that flood disasters in China, especially in the eastern part, occurred more frequently in the late 1990s than during other periods, which brought enormous economic losses (Wu 2002). In the last decade, there have been many studies focusing on extreme precipitation events over China (Zhai et al. 1999a,b, 2005, Yan & Yang 2000, Zhai & Pan 2003, Qian et al. 2007, You et al. 2010, Dong et al. 2011, Gemmer et al. 2011). Extreme precipitation exhibits increasing trends over northwest and southwest China, the Yangtze River Basin, and southeastern and southern coast regions of China (Zhai et al. 2005, Yang et al. 2008, You et al. 2010). There are decreasing trends over Sichuan Basin (You et al. 2010) and northern China (Zhai et al. 2005, Yang et al. 2008, You et al. 2010), such as the mid-lower reaches of the Yellow River Basin and the Huaihe River Basin (Dong et al. 2011). Regional analysis

*Email: zhangli@cma.gov.cn

© Inter-Research 2011 · www.int-res.com

shows that abrupt changes occurred in Northeast and North China (Yang et al. 2008). At the same time, there were no significant trends for extreme maximum daily precipitation in most of the 60 stations analyzed during 1951–1997 over China (Yan & Yang 2000). Monthly data analysis shows that the positive and negative trends of precipitation are significant in all months except December, and nearly 90% of the driest October months can be explained by wind directions typical of the East Asian winter monsoon (Gemmer et al. 2011). The frequencies of extreme precipitation events in different seasons on a regional scale exhibit significant interannual and interdecadal variabilities (Chen et al. 2009, Ning & Qian 2009). The latent heat flux over the South China Sea and the sensible heat flux over the Indochina Peninsula influence extreme precipitation in different calendar months. These effects are achieved by the interdecadal increase of the strengthening convection over South China through the South China Sea summer monsoon (Ning & Qian 2009). The annual and interannual trends of the 500 hPa geopotential height and 850 hPa horizontal winds over the Eurasian continent affect Chinese summer extreme wet and dry events (Weng et al. 2004).

Rapid advances in climate modeling improved the estimation of climate change during the past decades. Although several climate models reasonably capture the main characteristics of the spatial distribution and linear trends of precipitation extremes (Jiang et al. 2009), the coupled climate system models often lack skill for simulating extreme precipitation (Sun et al. 2006, Kiktev et al. 2003). The projections of future changes in extreme events, however, still depend on the climate model. Increases in extreme precipitation greater than the mean under increased greenhouse gases have been reported in many climate models both on global and regional scales (Pall et al. 2007). The projection of extreme precipitation over China has also been analyzed based on the output from the Fourth Assessment Report (AR4) of the Intergovernmental Panel on Climate Change (IPCC) (Jiang et al. 2009).

Beijing Climate Center Climate System Model version 1.0 (BCC-CSM1.0) is a fully-coupled climate model developed by the Beijing Climate Center. Several studies (e.g. Chen 2008, Zhang et al. in press) show that BCC_CSM1.0 can capture the basic climate feature of summer atmospheric circulation and precipitation over East Asia. This study will focus on the model performance in simulating extreme precipitation in the last 50 yr.

## 2. MODEL, DATA AND METHODS

### 2.1. Model and experiment design

The BCC-CSM1.0 is a global fully-coupled climate model. It is originated from the Community Climate System Model version 2 (CCSM2; Kiehl & Gent 2004). The main differences between the BCC-CSM1.0 and CCSM2 are their atmospheric and land surface model components. For the atmosphere, the BCC-CSM1.0 uses an atmospheric general circulation model BCC-AGCM2.0.1 developed by the BCC (for details see Wu et al. 2008, 2010). It is a spectral model with horizontal T42 truncation (~2.8125° horizontal resolution) and 26 layers in the vertical direction. It performs well in simulating the basic climate of precipitation, temperature, thermal structure and atmospheric circulation (Wu et al. 2010), intraseasonal oscillations of zonal wind and precipitation (Dong et al. 2009), and the Asian–Australian Monsoon (Wang et al. 2009). The land surface model component in BCC-CSM1.0 is the Community Land Model (CLM) v. 3, which displaced CLM v. 2 used in CCSM2 (Dickinson et al. 2006). The ocean model (Parallel Ocean Program [POP]) and ice model (Community Sea Ice Model version 4 [CSIM4]) are the same as those in CCSM2. The ocean model POP has 40 vertical levels and tripolar grids in the horizontal. The longitudinal resolution is ~1° and the latitudinal resolution is variable with finer resolution (~0.3°) near the equator.

In order to evaluate the capability of BCC_CSM1.0 for historical climate simulation, the 20th century historical experiment (20C3M) is carried out. In the simulation of 20C3M, BCC-CSM1.0 was forced by observed greenhouse gases, aerosols, solar irradiance, and volcanic aerosols used in IPCC AR4 experiments. A pre-industrial control experiment was carried out first with the external forcing fixed to the values of 1870, initialized from a present-day control run of 500 yr. With ~100 yr of spin-up, the global mean sea surface temperature (SST) and sea ice fraction became stable, then the 20C3M run was branched from the pre-industrial control run with year-to-year changed external forcing from 1870 to 1999, and then continuously run with the corresponding external forcing according to SRESB1 (IPCC 2000) until 2010.

### 2.2. Data

The observed precipitation data from 1956 to 2009 at 349 rain gauge stations over the eastern part of China east of 105° E (Fig. 1) are used in this study.

They were selected from a new dataset with a higher spatial density, and the quality control has been done by the National Meteorological Information Center of China Meteorological Administration (CMA) using climatic extreme value check, extreme value check, and internal consistency examination. This dataset has not been used in extreme precipitation research before. In order for inter-comparison, the model data are linearly interpolated into 0.5 × 0.5° gridded points, and the station observations are interpolated to the same gridded points using 'oacres' function in the meteorological software Grads.

The National Center for Environmental Prediction/ National Center for Atmospheric Research (NCEP/ NCAR) reanalysis dataset v. 1 (Kalnay et al. 1996) is used to analyze the atmospheric circulation background over East Asia. The horizontal resolution of the data is 2.5 × 2.5°. The monthly precipitation data from Climate Prediction Center (CPC) Merged Analysis of Precipitation (CMAP) dataset (Xie & Arkin 1997) is also used in this study. For inter-comparison, the model output data are linearly interpolated into the same grid points as the reanalysis data.

### 2.3. Extreme precipitation indices and analysis methods

Daily precipitation intensity was classified into 5 categories: light rain (0.1–9.9 mm $d^{-1}$), moderate rain (10.0–24.9 mm $d^{-1}$), heavy rain (25.0–49.9 mm $d^{-1}$), rainstorm (50.0–99.9 mm $d^{-1}$), and heavy rainstorm (≥100.0 mm $d^{-1}$). To consider large-scale differences in precipitation, we used percentiles to analyse the precipitation extremes.

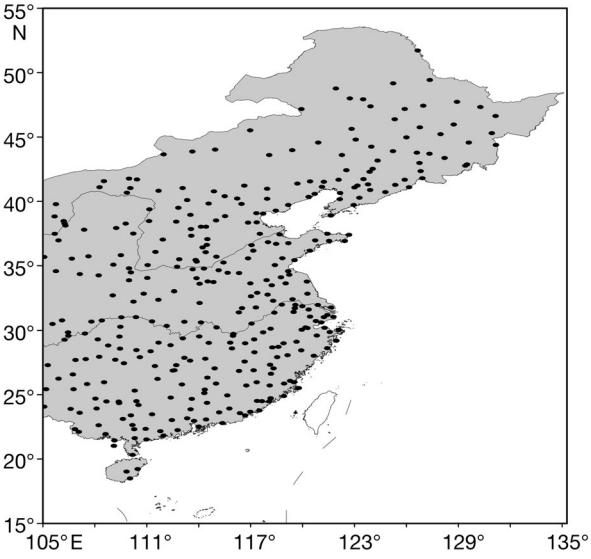


Fig. 1. Distribution of stations

The thresholds of extreme precipitation are estimated on the basis of percentiles. First, the time series of the 95th percentile of daily precipitation amounts for all rainy days (precipitation ≥1.0 mm $d^{-1}$) of each year from 1971 to 2000 are calculated. Then the 30 yr (1971–2000) mean is regarded as the extreme precipitation threshold. The thresholds for separate stations are different. The nonparametric method is used to determine the threshold (for details refer to Bonsal et al. 2001). As for each station, the amount of daily precipitation (≥1.0 mm $d^{-1}$) was ranked in ascending order: $X_1, X_2, \ldots, X_N$. The probability $P_m$ for each rank $m$ ($m = 1, 2, \ldots, N$; where $N$ is the length of the record) can be estimated by:

$$P_m = (m - 0.31) / (N + 0.38) \quad (1)$$

Here, $P_m$ is an ascending series. Then the precipitation amount at the 95th percentile (hereafter R95) can be linearly interpolated from the $P_m$ series. This method to estimate the percentiles is simple and avoids any other assumptions of the underlying distributions (Bonsal et al. 2001).

Then, the number of days with rainfall above R95 (R95p), the total precipitation above R95 (R95pTOT), and the intensity index of the extreme precipitation (R95pI) defined as: R95pI = R95pTOT / R95p, can be calculated. The daily precipitation intensity index (SDII) is also used in this work. It is defined as the rate of total precipitation (PRCPTOT) over total precipitation days above 1.0 mm $d^{-1}$ in a year.

The non-parametric Mann-Kendall method (M-K method) is utilized to test the trend of extreme precipitation (Mann 1945, Kendall 1948, 1975). It has been widely used to evaluate statistically significant trends in hydrological and climatological time series (e.g. Xu et al. 2004, Zheng et al. 2007). As for the given time series of $x_i$ ($i = 1$, n), its statistic variable $Z_c$ is introduced as:

$$Z_c = \begin{cases} \dfrac{S-1}{\sqrt{\mathrm{var}(S)}}, & S > 0 \\ 0, & S = 0 \\ \dfrac{S+1}{\sqrt{\mathrm{var}(S)}}, & S < 0 \end{cases} \quad (2)$$

in which:

$$S = \sum_{i=1}^{n-1} \sum_{k=i+1}^{n} \mathrm{sgn}(x_k - x_i) \quad (3)$$

$$\mathrm{var}(s) = \left[ n(n-1)(2n+5) - \sum_{t=1}^{n} t(t-1)(2t+5) \right] / 18 \quad (4)$$

where:

$$\mathrm{sgn}(x_k - x_i) = \begin{cases} +1\ , & x_k > x_i \\ 0\ , & x_k = x_i \\ -1\ , & x_k < x_i \end{cases} \quad (5)$$

$Z_c > 0$ indicates the increase trend and $Z_c < 0$ the decrease trend, respectively. The magnitude of the trend (β) is expressed as:

$$\beta = \mathrm{Median}\left(\frac{x_i - x_j}{i - j}\right),\ 1 < j < i < n \quad (6)$$

where Median () is the value in the median location of a series. A positive value of β indicates an increase or upward trend; a negative value of β indicates a decrease or downward trend.

Empirical Orthogonal Function (EOF) analysis (Chelton et al. 1990, North et al. 1995) is used to extract the spatial modes of extreme precipitation change. We use the sub-regions according to Li et al. (2011), where rotating EOF (hereafter REOF) analysis is used in partitioning sub-areas. First, the annual precipitation data series of each station is normalized. Principal components analysis is used to extract factors. The REOF method is to rotate the 20 leading factors (with >85% accumulative variance contribution) by using varimax orthogonal rotation to make the maximum load in the least variables. Then Euclidean distance and Pearson's correlation coefficient are both used as the measurements of similarity between one station and another in cluster analysis. The results by 2 different measurements are similar in spatial distribution. Given the consistency in one region and differences among regions, as well as the size of each area and the climatic zones used in previous studies (e.g. Wang et al. 2004, Ding et al. 2008, Huang et al. 2011), mainland China is divided into 8 sub-regions. In this study, we selected 5 sub-regions in the eastern part of China, with minor adjustments to the boundaries of each area. The 5 sub-regions are Northeast China (NE) (115–135° E, 42–52° N), North China (NC) (105–125° E, 35–42° N), Jianghuai Region (JH) (105–122° E, 28–35° N), South China I (SCI) (105–110° E, 20–28° N) and South China II (SCII) (110–122° E, 20–28° N). The sub-regions are generally consistent with previous divisions for the eastern part of China. South China was divided into 2 regions, which is different from previous studies.

Power spectrum analysis and linear trend analysis (Wei 1999) are also used in this study.

## 3. RESULTS

### 3.1. Climatology of precipitation

Simulated precipitation gradually decreases with the increment of latitude, especially north of 30° N, which is similar to the observation (Fig. 2). The spatial correlation coefficient between simulation and observation over Eastern China is 0.77, while the root-mean-square error (RMSE) is 336 mm, a large value. The precipitation in the southern part of eastern China is underestimated, whereas in the northern part it is slightly overestimated. The large RMSE value mainly results from the large negative biases of the southern part of eastern China. The model fails to capture the high value area on the South China coast and sub-high value center in the middle and lower reaches of the Yangtze River Basin. The position of PRCPTOT maximum center is shifted to the east of the Qinghai–Tibet Plateau, which is similar to some models in CMIP3 (Zhang 2008). The result may be due to the resolution, treatment of topography or other reasons (Gao et al. 2006).

The evaluation for summer precipitation simulation based on CMAP monthly precipitation over East Asia shows similar results (Fig. 3). The spatial correlation coefficients between simulated and CMAP summer precipitation over East Asia (105–140° E, 20–45° N) and most of East China (105–125° E, 20–50° N) are 0.71 and 0.79 respectively, and the RMSEs are 1.69 and 1.63 mm $d^{-1}$ respectively. The precipitation north of 30° N is underestimated. In order to explore the attribution of precipitation biases, several circulation fields were analyzed. The analyses show that the simulated local drier air, weaker water vapor transportation, weaker convergence and weaker upward motion contribute to underestimating precipitation over this area.

Fig. 3a shows that the local integrated water vapor in summer in most of Eastern China is underestimated by BCC_CSM1.0, with minimum values below −12 kg $m^{-2}$. Over East Asia, the correlation coefficient between simulation and NCEP reanalysis is 0.94 and the RMSE is 4.12 kg $m^{-2}$; 51% of the grids have consistent signs between precipitation biases and precipitable water biases.

Fig. 3b shows that the vertical integrated water vapor flux over most of the 105–140° E, 20–32° N area is underestimated with southward transportation bias. The consistency of signs between precipitation biases and vertical integrated water vapor flux biases is 75%, which indicates the contribution of water vapor transportation to precipitation biases. Thus the capability of the model in simulating water vapor flux is more important for precipitation simulation in summer over East Asia.

The dynamic factor is also important for precipitation formation. Fig. 4 shows the longitude–height section for divergence in summer over 20–30° N.

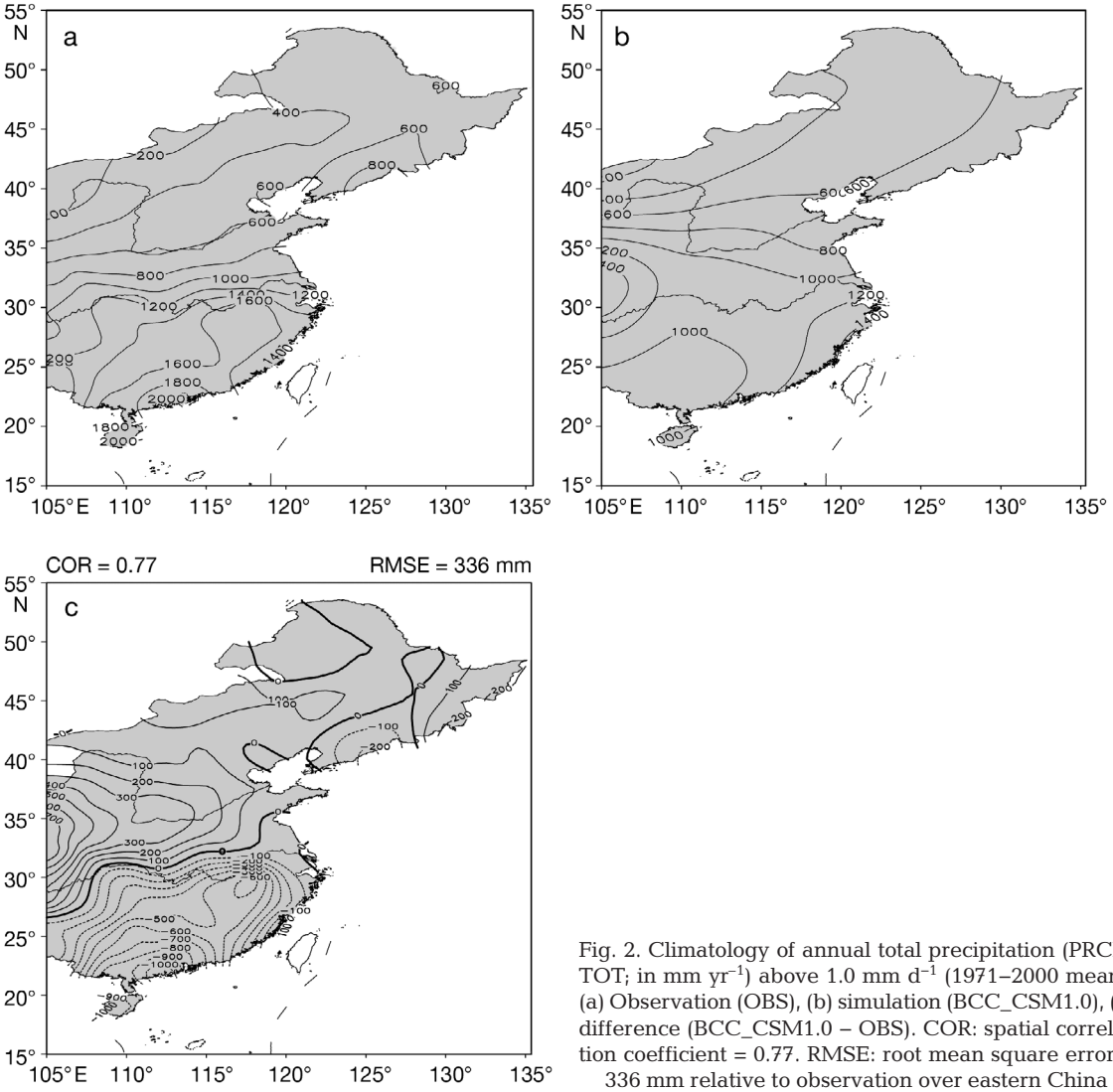


Fig. 2. Climatology of annual total precipitation (PRCPTOT; in mm $yr^{-1}$) above 1.0 mm $d^{-1}$ (1971–2000 mean). (a) Observation (OBS), (b) simulation (BCC_CSM1.0), (c) difference (BCC_CSM1.0 – OBS). COR: spatial correlation coefficient = 0.77. RMSE: root mean square error = 336 mm relative to observation over eastern China

Negative values denote convergence and positive values denote divergence. The height of convergence can be up to 400 hPa in NCEP reanalysis, while it is only up to 500 hPa in the BCC_CSM1.0 simulation (Fig. 4). The specific values at the lower levels are greater in the simulation than in the reanalysis field, which implies that the simulated convective activity is weaker over this area. The simulated upward vertical velocities over this area are less than the observed ones, which implies that the upward motion is weaker and the deep convection may be underestimated in BCC_CSM1.0 (data not shown). The analysis for outgoing longwave radiation supports this point to some extent (data not shown).

Fig. 5 shows the bias in frequency of rain for the 1971–2000 mean simulated by BCC_CSM1.0. Fig. 5a indicates that rainy days with light precipitation are overestimated over eastern China. The biases are >90 d over most of eastern China and even up to 180 d in the coastal area of South China. Fig. 5b shows that moderate rainy days are underestimated south of the Yangtze River and in the northeast, but overestimated over the other regions. The maximum positive bias is >20 d, which is located at the eastern side of the Qinghai–Tibet Plateau. There is a positive bias in the mid-lower reaches of the Yellow River Basin, with the maximum >10 d. The negative bias center is located in South China, and the value is less than –10 d.

For heavy rain (Fig. 5c), the rainy days are underestimated over most areas of eastern China except some regions in the Yellow River Basin. There are maximum biases (below –10 d) in the South China coastal area. A negative bias center lies in the south of the Yangtze River Basin, with the center values below –8 d. The maximum deviation in the northeast is below –2 d. For rainstorm and heavy rainstorm, the

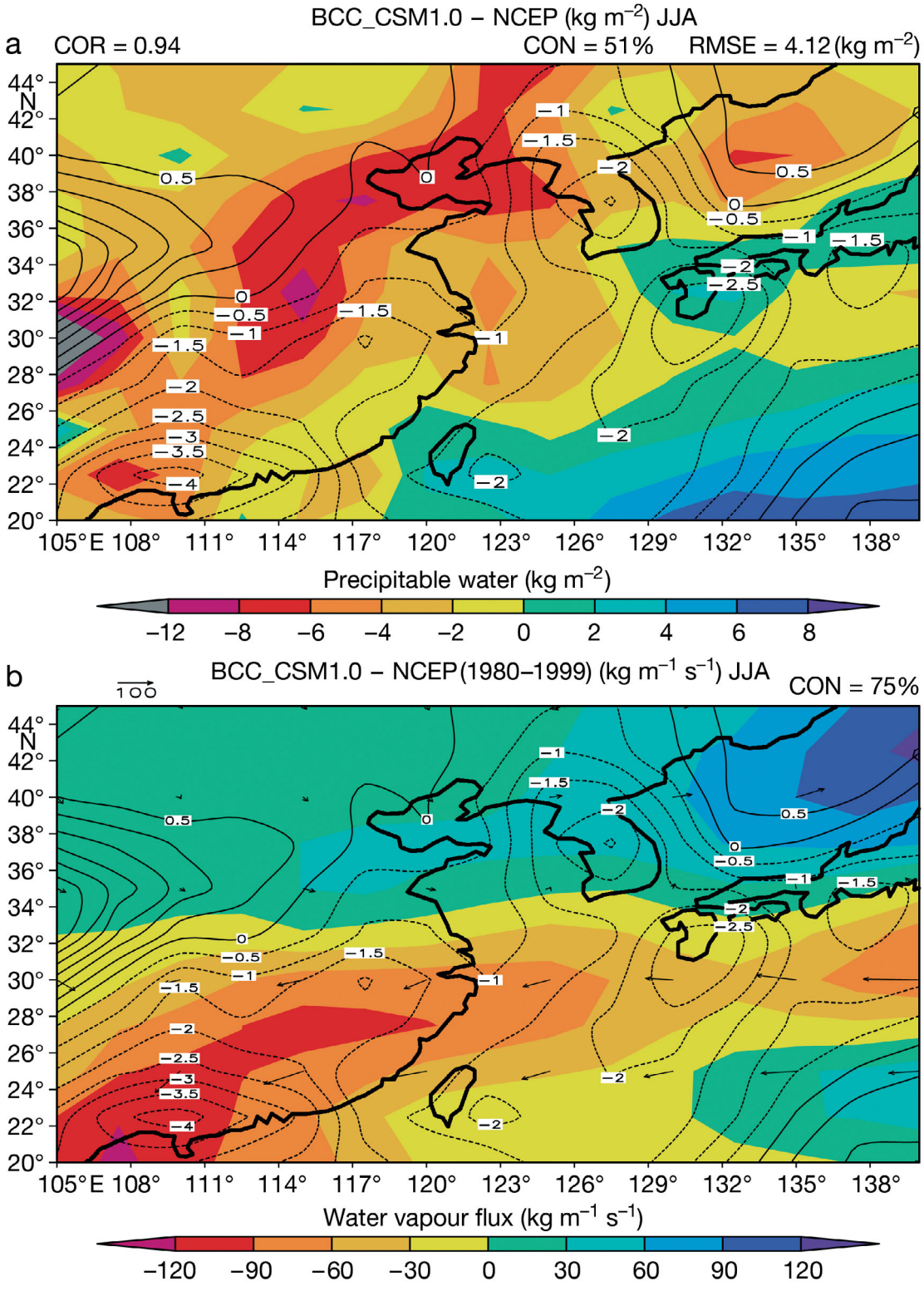


Fig. 3. Biases of simulated precipitation (BCC_CSM1.0 data – CMAP data; contours in mm d$^{-1}$), and (a) atmospheric total precipitable water (in color; kg m$^{-2}$) and (b) vertical integrated water vapor flux (in color and vectors; kg m$^{-1}$ s$^{-1}$) in Jun–Aug (JJA) of 1980–1999 (BCC_CSM1.1 data – NCEP reanalysis data). COR: correlation coefficient between simulated and NCEP reanalysis data (colored areas). RMSE: root mean square error of simulated precipitable water relative to reanalysis data. CON: consistent rates of the biases fields between precipitation and precipitable water or water vapor flux. Precipitation is calculated based on the CMAP monthly precipitation data; circulation fields are calculated based on monthly NCEP I reanalysis data by NCAR

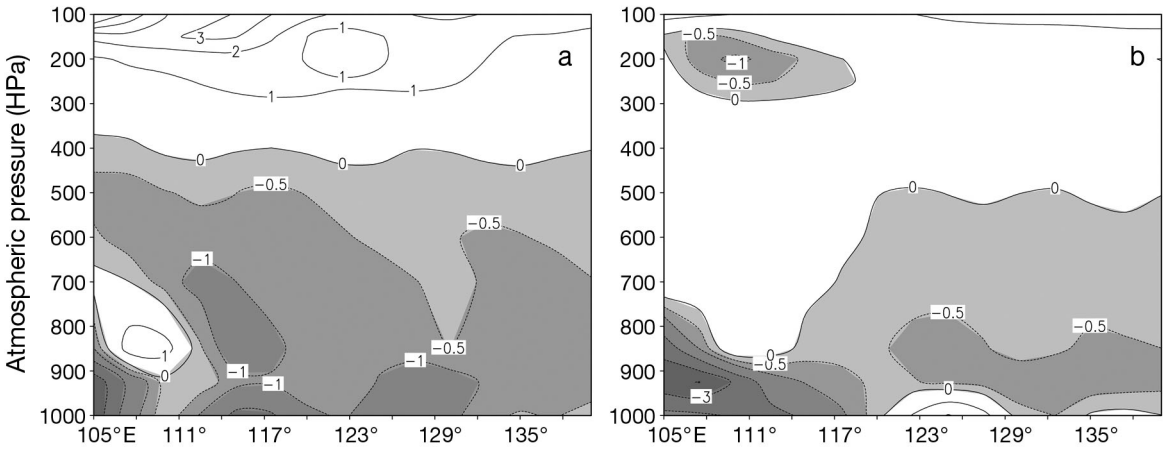


Fig. 4. Zonal averaged (a) observed and (b) simulated divergence ($10^{-6}$ $s^{-1}$) over 20–30° N in Jun–Aug for 1971–2000

rainy days are all underestimated over almost the whole of eastern China (Fig. 5d,e).

The result is similar to the evaluation of models under CMIP3 by Sun et al. (2006). The models under CMIP3 also underestimated the frequency of heavy or even stronger precipitation events. The precipitation event with a much larger precipitation amount is often related to the stronger or deep convection activity. The weaker circulation may have an important contribution to the negative biases of heavy precipitation frequency in BCC_CSM1.0.

### 3.2. Climatology of thresholds, frequency and amount of extreme precipitation

Considering the large spatial difference of precipitation and also the bias of BCC_CSM1.0 in simulating the absolute rainfall, we use the percentile method to define the extreme precipitation event. Here we select the 95th percentile to calculate the threshold and related statistics.

Fig. 6 shows the observed and simulated thresholds of extreme precipitation events at the 95th percentile for 1971–2000. The observation shows that there are 3 high-value areas in the South China coast, the middle and lower reaches of the Yangtze River Basin and North China. The maximum in South China is >40 mm $d^{-1}$, and those in North China and the middle and lower reaches of the Yangtze River Basin are up to 28 mm $d^{-1}$ (Fig. 6a).

A comparison between simulation and observation reveals that the spatial correlation coefficient is 0.74. The model reproduces the high value areas of thresholds located in the South China coastal area and North China, but the maximum values are underestimated, up to 18 and 16 mm $d^{-1}$, respectively, and the biases are −28 and −12 mm $d^{-1}$, respectively. The simulation fails to capture the observed high value center in the middle and lower reaches of the Yangtze River Basin, as well as a little westward deflection from Bohai Coast to central North China for the second high value center (Fig. 6b). The RMSE of the simulation over eastern China is 10.5 mm $d^{-1}$. Generally, the model reproduces the high–low value distribution of the threshold, although there are negative biases in the whole of eastern China.

Fig. 7 shows the observed and simulated climatology of R95p, as well as the biases of simulated R95p. The spatial correlation coefficient between simulation and observation is 0.65. In observation, the high frequency area is located in South China with the maximum >10 d. In simulation, however, the high frequency center is shifted northward to the middle and lower reaches of the Yangtze River Basin, with maxima >12 d. Moreover, there is another higher frequency area in the east side of the Qinghai–Tibetan Plateau due to the large bias in precipitation simulation. The simulated R95p are greater than the observation in most of eastern China except in local areas in South China. The area with largest biases is located in the east side of the Qinghai–Tibetan Plateau and the biases are also much larger in some local areas between the Yellow River and Yangtze River.

Based on the above analysis, the annual total extreme precipitation above the 95th percentile is calculated. Fig. 8a,b shows the observed climatology (1971–2000 mean) of R95pTOT and its proportion in PRCPTOT. The spatial distribution of R95pTOT is similar to PRCPTOT (Fig. 2) over Eastern China, with the characteristic of gradual decrease from south to north. The annual R95pTOT is >1000 mm in the South China coast and <100 mm in central Inner Mongolia. The percentages of R95pTOT in PRCPTOT are >45 %

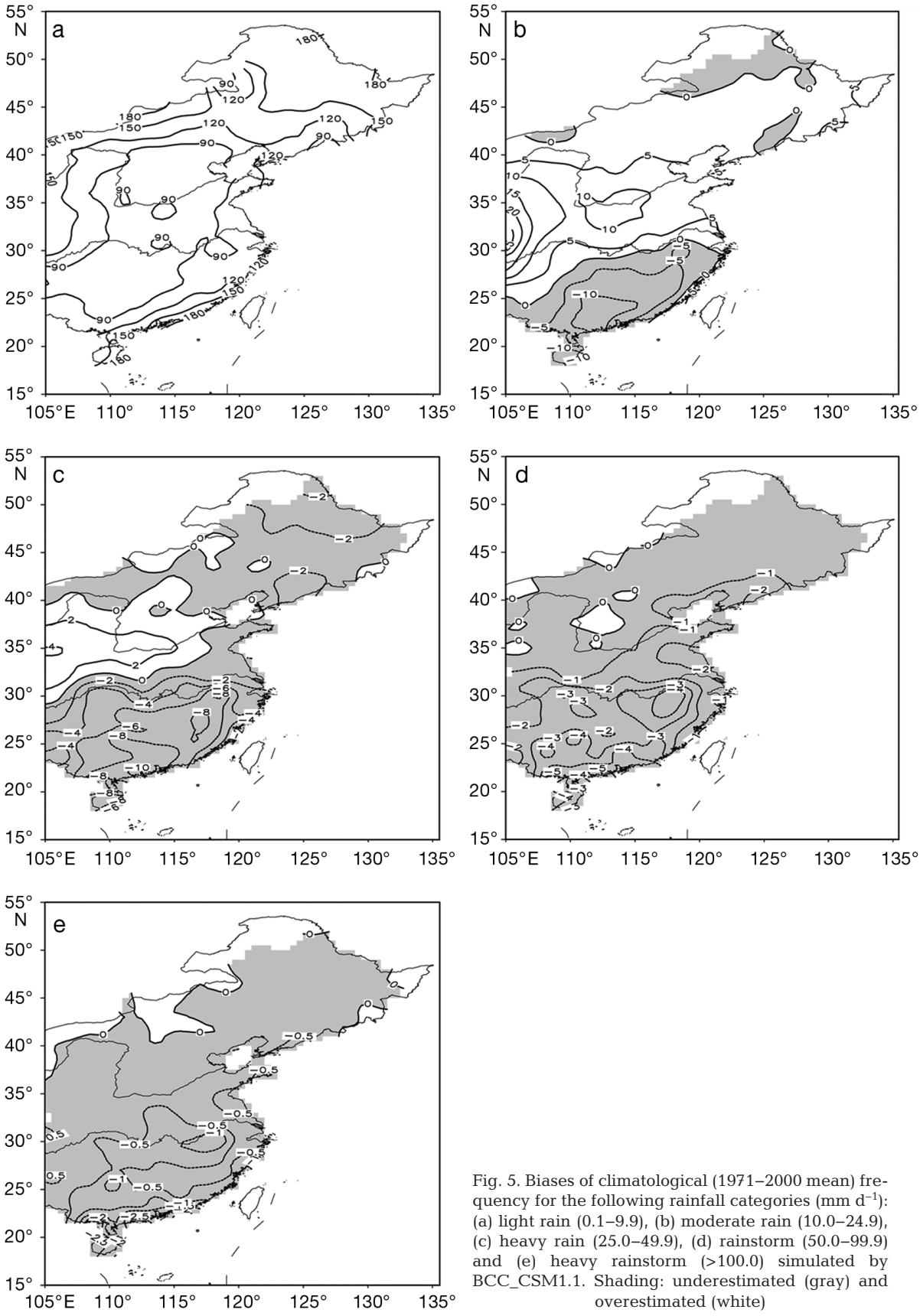


Fig. 5. Biases of climatological (1971–2000 mean) frequency for the following rainfall categories (mm $d^{-1}$): (a) light rain (0.1–9.9), (b) moderate rain (10.0–24.9), (c) heavy rain (25.0–49.9), (d) rainstorm (50.0–99.9) and (e) heavy rainstorm (>100.0) simulated by BCC_CSM1.1. Shading: underestimated (gray) and overestimated (white)

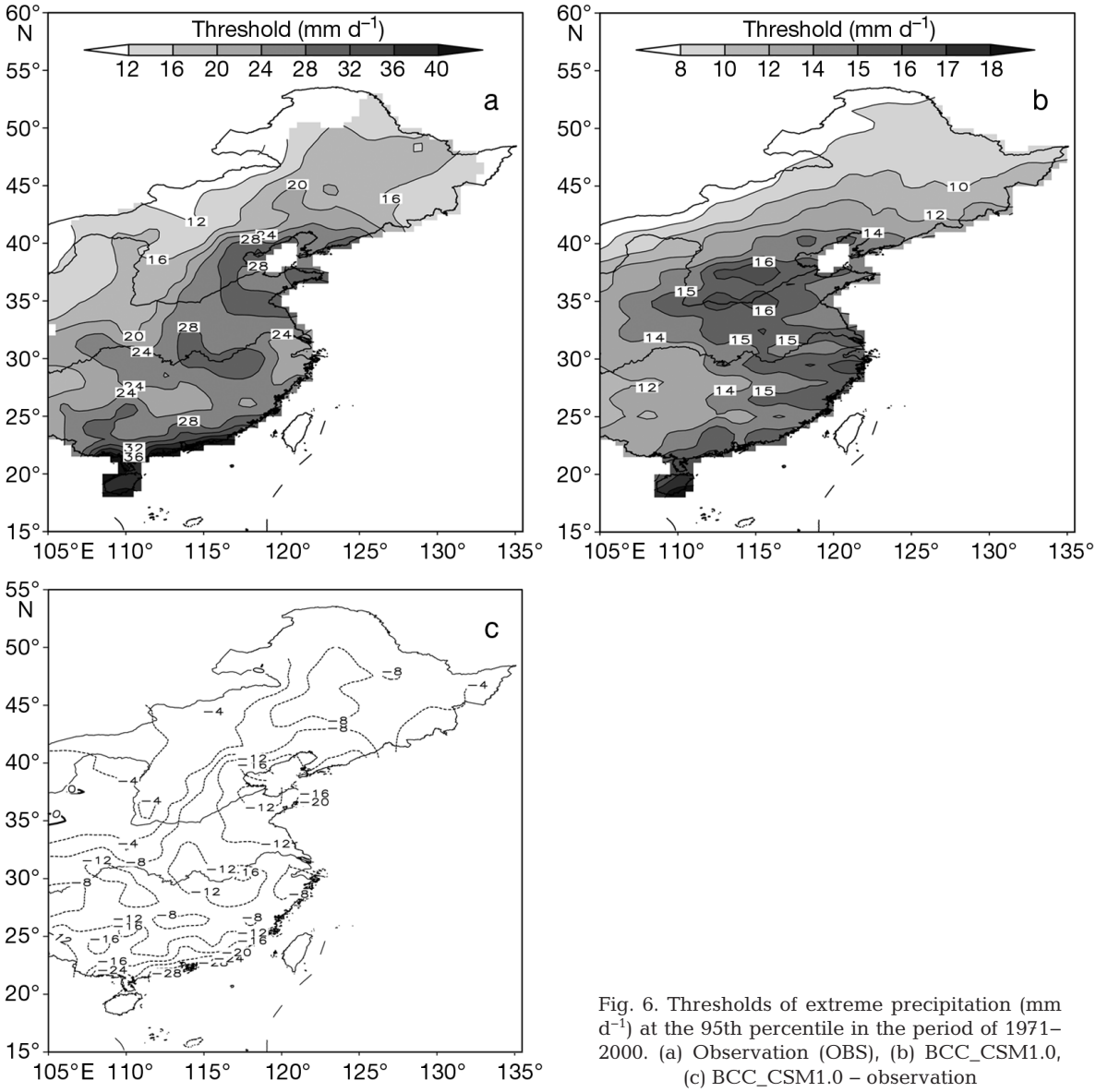


Fig. 6. Thresholds of extreme precipitation (mm d$^{-1}$) at the 95th percentile in the period of 1971–2000. (a) Observation (OBS), (b) BCC_CSM1.0, (c) BCC_CSM1.0 – observation

in most of eastern China, except for Inner Mongolia (<36%), with the higher value area in South China (up to 50%) and gradually decreasing from south to north. The high portion of extreme precipitation is determined by the method to calculate the threshold.

Fig. 8c shows the simulated climatology of R95pTOT by BCC_CSM1.0. The simulated R95pTOT north of 32.5° N is greater than the observation, especially in the central area between the mid–upper reaches of the Yellow River and Yangtze River. The simulation south of the Yangtze River, however, is lower than the observation, especially in the South China coastal area, with the negative biases (<–500 mm) in the center (Fig. 8e). Fig. 8d shows the percentage of R95pTOT in PRCPTOT simulated by BCC_CSM1.0. The simulated percentages of R95pTOT in PRCPTOT are similar to observation in magnitude. There is a high value center in the middle and lower reaches of the Yellow River Basin, which is larger than the observation. The simulated percentage values in South China, middle reaches of Yangtze River Basin and the north part of Northeast are slightly lower than the observation, and most of the bias values are <4% (Fig. 8f).

### 3.3. Spatial feature of extreme precipitation amount change

Observed (Fig. 9a–c) and simulated (Fig. 9d–f) EOF modes for R95pTOT change were calculated for 1956–2009.

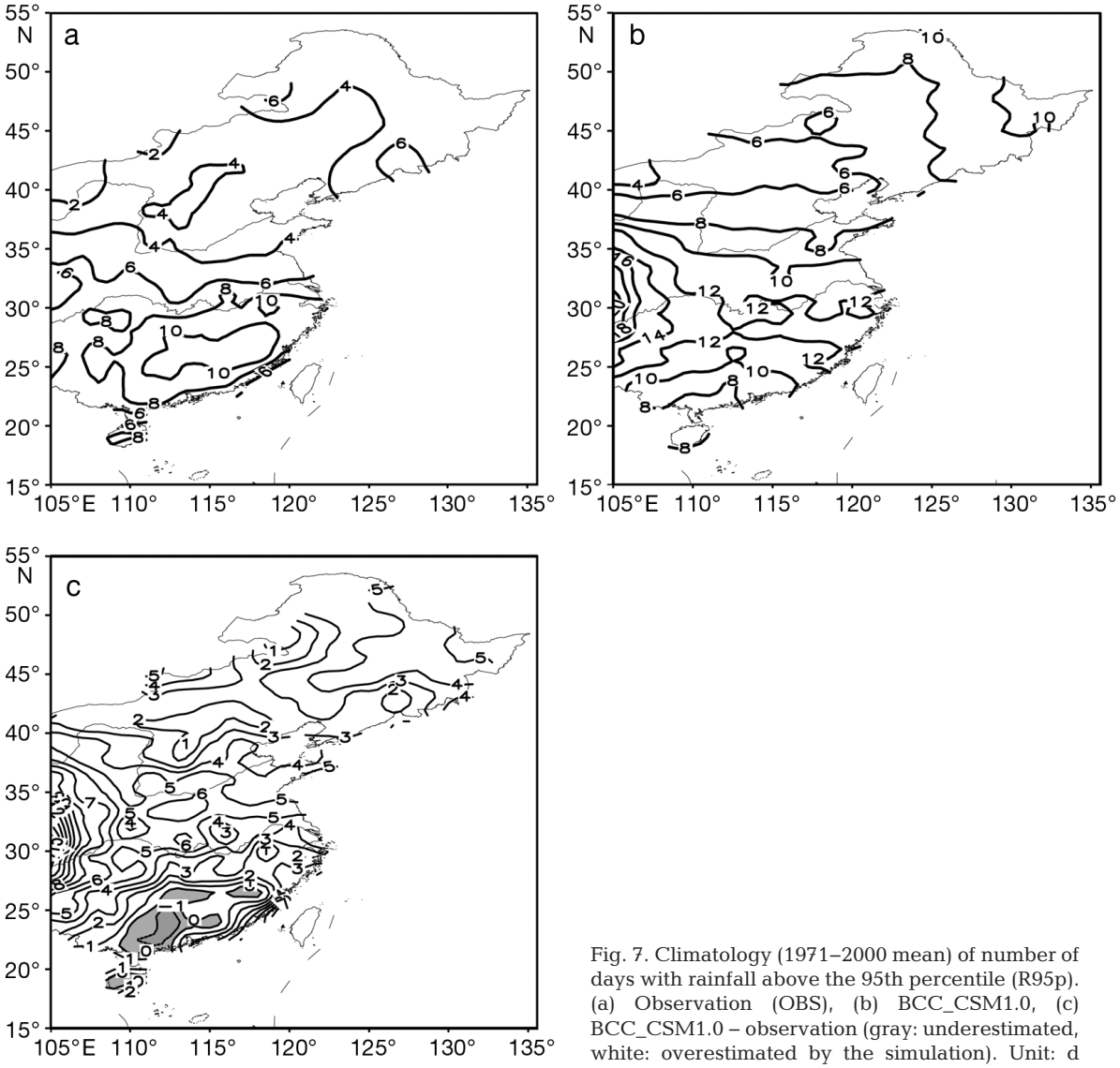


Fig. 7. Climatology (1971–2000 mean) of number of days with rainfall above the 95th percentile (R95p). (a) Observation (OBS), (b) BCC_CSM1.0, (c) BCC_CSM1.0 – observation (gray: underestimated, white: overestimated by the simulation). Unit: d

EOF1 of observed R95pTOT (Fig. 9a) shows that the change of R95pTOT south of the Yangtze River has the same tendency as that over the middle part of Inner Mongolia and the local area of the northeast, and opposite to that north of the Yangtze River. EOF1's variance contribution is 9.4%. The first EOF mode of T95pTOT simulated by BCC_CSM1.0 captures the main spatial pattern for observed R95pTOT change (Fig. 9d), although parts of the negative area in the southern part of the Yangtze River expands northwards to the Huaihe River Basin. The variance contribution of EOF1 is 11.8%, which is greater than observations.

EOF2 of observed R95pTOT (Fig. 9b) shows that the change tendency over most of the Yellow River Basin area is similar to that in the South China coast. However, the northeast and the area between 25 and 35° N in eastern China show the opposite trend. The variance contribution is 7.5%. The EOF2 of R95pTOT simulated by BCC_CSM1.0 also captures the general observed characteristics, although there is some difference in spatial extension (Fig. 9e). The variance contribution is 8.5%.

EOF3 mode of observed R95pTOT (Fig. 9c) is characterized by the opposite change tendency between the Jianghuai area and other areas of eastern China. Its variance contribution is 7.4%. The EOF3 mode of simulated R95pTOT (Fig. 9f) is characterized by an opposite change trend between the local area in the mid–lower reaches of the Yangtze River Basin and most other areas in eastern China, which is generally similar to the observation. There is a difference be-

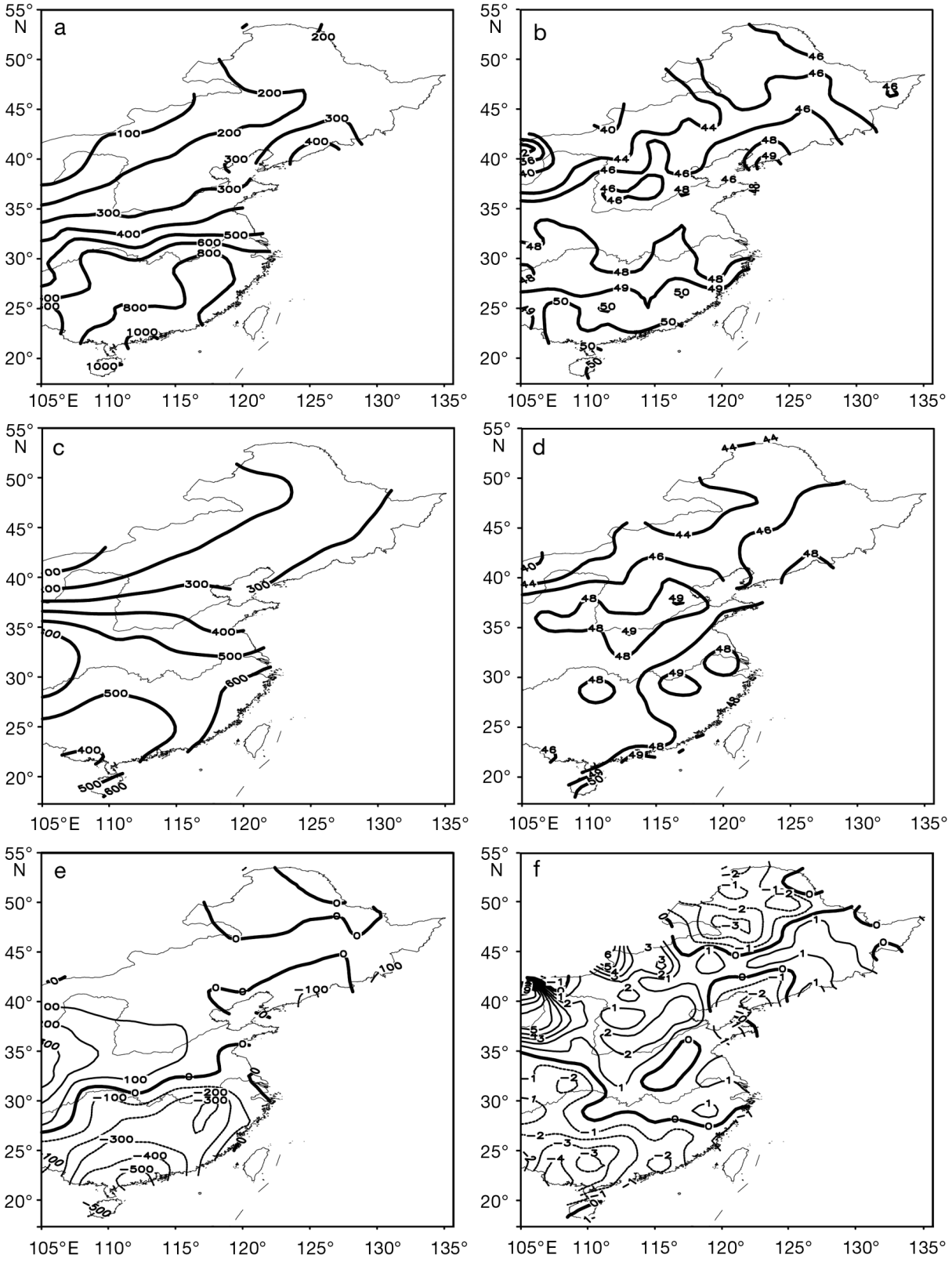


Fig. 8. Distribution of climatology (1971–2000 mean) for (a,c) total rainfall above the 95th percentile (R95pTOT; mm), (b,d) R95pTOT as a percentage of total precipitation (PRCPTOT) and (e,f) the biases fields. (a,b) Observation (OBS), (c,d) BCC_CSM1.0

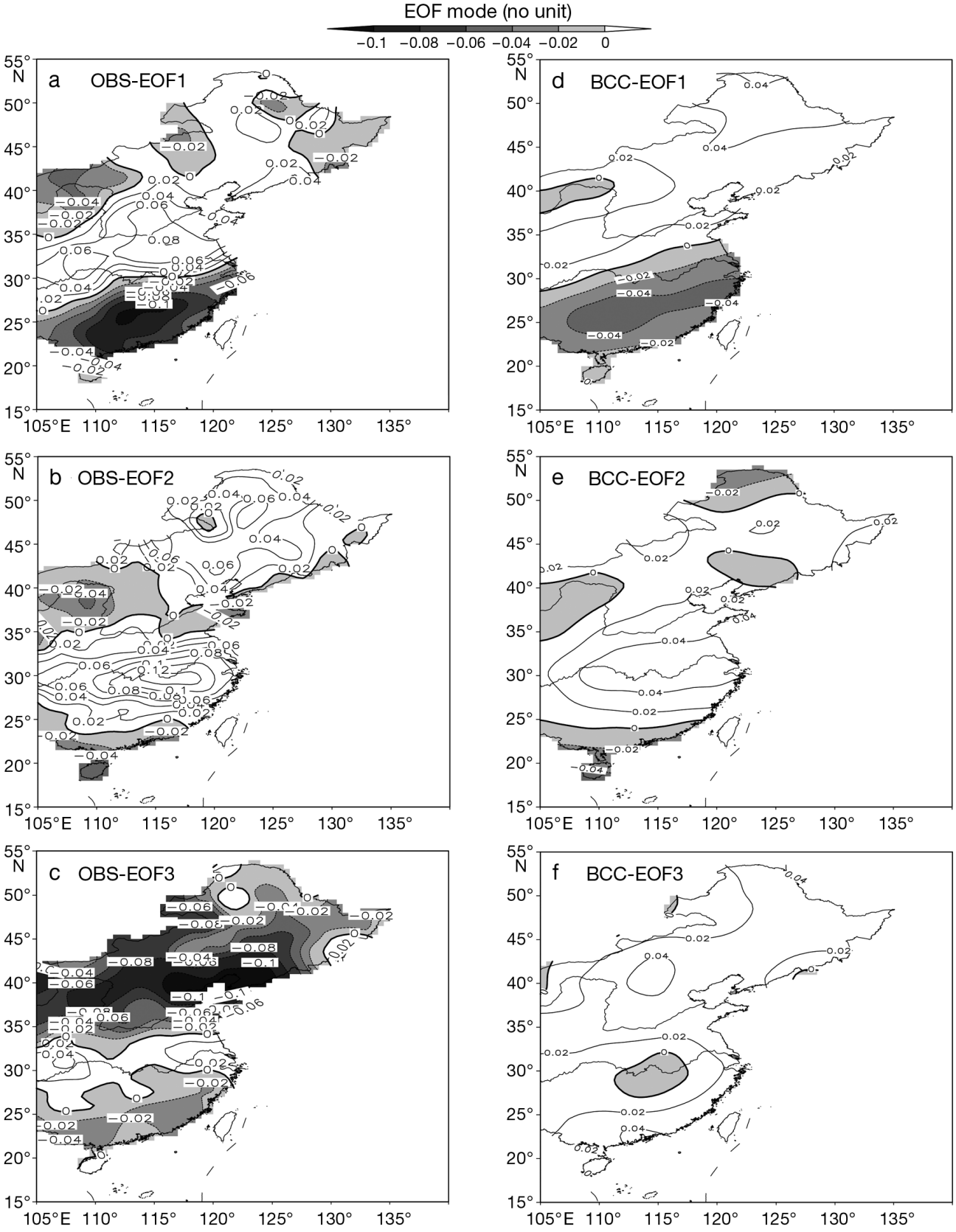


Fig. 9. The first 3 leading Empirical Orthogonal Function (EOF) modes for annual total rainfall above the 95th percentile (R95pTOT) during 1956–2009. (a–c) Observation, (d–f) BCC_CSM1.0. (a,d) EOF1, (b,e), EOF2, (c,f) EOF3

tween simulation and observation along the middle and lower Yangtze River Basin and weaker change signals in North China. The variance contribution of EOF3 is 8.0%, which is greater than observations.

Generally speaking, although BCC_CSM1.0 has obvious systematical biases in extreme precipitation indices, the model can reasonably capture the general long term change patterns of R95pTOT.

### 3.4. Long term trend of extreme precipitation

To analyze the performance of BCC_CSM1.0 in simulating the long term trend of extreme precipitation events, linear trend analysis and the nonparametric Mann-Kendall test were used.

Fig. 10 shows the linear trend coefficient of R95pTOT, R95p, R95pI, and SDII during 1956–2009. The spatial distributions of linear trends of R95pTOT, R95p, R95pI, and SDII are similar, with opposite linear trend coefficients between the north (–) and south (+) of ~33°N, but with more positives in northern areas for R95pI and SDII. The results are similar to previous research (Pan 2002, Zhai et al. 2005, Dong et al. 2011).

BCC_CSM1.0 captures the negative trends of R95pTOT, R95p, and SDII in the northeast, as well as the positive trends for R95pTOT, R95p, R95pI, and SDII in the mid-lower reaches of the Yangtze River Basin (Table 1). But the model fails to capture the negative trend of R95pI in the northern area. The opposite linear trends of the 4 indices over most or part of southern China indicate that the model has poor performance in simulating the long term linear trend of extreme precipitation over this area. The regional averaged anomalies of proportion of R95pTOT and R95p during the period of 1956–2009 were calculated. As for R95pTOT, there is a significant 36-yr period in NE China and a 2.8 yr period in North China. No significant period is detected in Jianghuai, South China I, and South China II. The simulation shows a significant 12 yr period in NE China, which is shorter than observed, and no significant period in the other 4 sub-regions. As for observed R95p, there is a significant 36 yr period in NE China and 2.8 and 2.6 yr periods in North China. No significant period is detected in Jianghuai, South China I and South China II. The result reveals that there is a significant 12 yr period in NE China, which is shorter than observation. A significant 2.8 yr period is detected in South China I. No significant period is detected in the other 3 sub-regions.

The Mann-Kendall test for observed regional averaged percentage of R95pTOT (Table 1) shows that there are significantly decreasing trends at the 0.1 significance level in NE China and North China, and increasing trends in Jianghuai, South China I and South China II, but the increasing trends are not significant. BCC_CSM1.0 captures the decreasing and increasing trends in NE China and Jianghuai respectively for R95TOT, although the tendencies are weaker. The trends, however, are opposite in North China, South China I, and South China II for both of simulated R95TOT and R95p.

As for observation, the regional averaged R95p in North China has a significant decreasing trend at the 0.05 significance level. The R95p in NE China decreased but the tendency is not significant. Those in Jianghuai, South China I and South China II have increased in some extent. The result in North China is similar to previous studies (Zhai et al. 2005, Dong et al. 2011), and that in southern China is similar to that shown in Zhai et al. (2005). BCC_CSM1.0 captures the decreasing and increasing trends in NE China and Jianghuai for R95p, with weaker tendencies. The trends, however, are opposite in North China, South China I and South China II for R95p in the simulation.

### 3.5. Interdecadal change of extreme precipitation frequency

Observation analysis showed interdecadal change in the summer climate in East Asia at the end of the 1970s (Hu 1997), and an abrupt change for summer precipitation in South China (Ding et al. 2008). Probability density analysis was used to explore the regional interdecadal change of extreme precipitation frequency in the 5 sub-regions, which has not been analyzed in previous work. Here we selected 1956–1979 and 1980–2009 as 2 periods for interdecadal analysis in NE China, North China and Jianghuai. In addition, we selected 1956–1979, 1980–1992, and 1993–2009 as 3 periods for interdecadal analysis in South China I and South China II. Probability density of R95p was calculated for each period in each subregion (Fig. 11), and the spatio-temporal mean during the 2 or 3 periods for the 5 sub-regions are listed in Table 2. Generally, the frequency of extreme precipitation above the 95th percentile in simulation is higher than that in observation in each sub-region.

In NE China, the model is able to capture the increment of the regional averaged decadal mean of R95p. The observed spatio-temporal averaged frequency

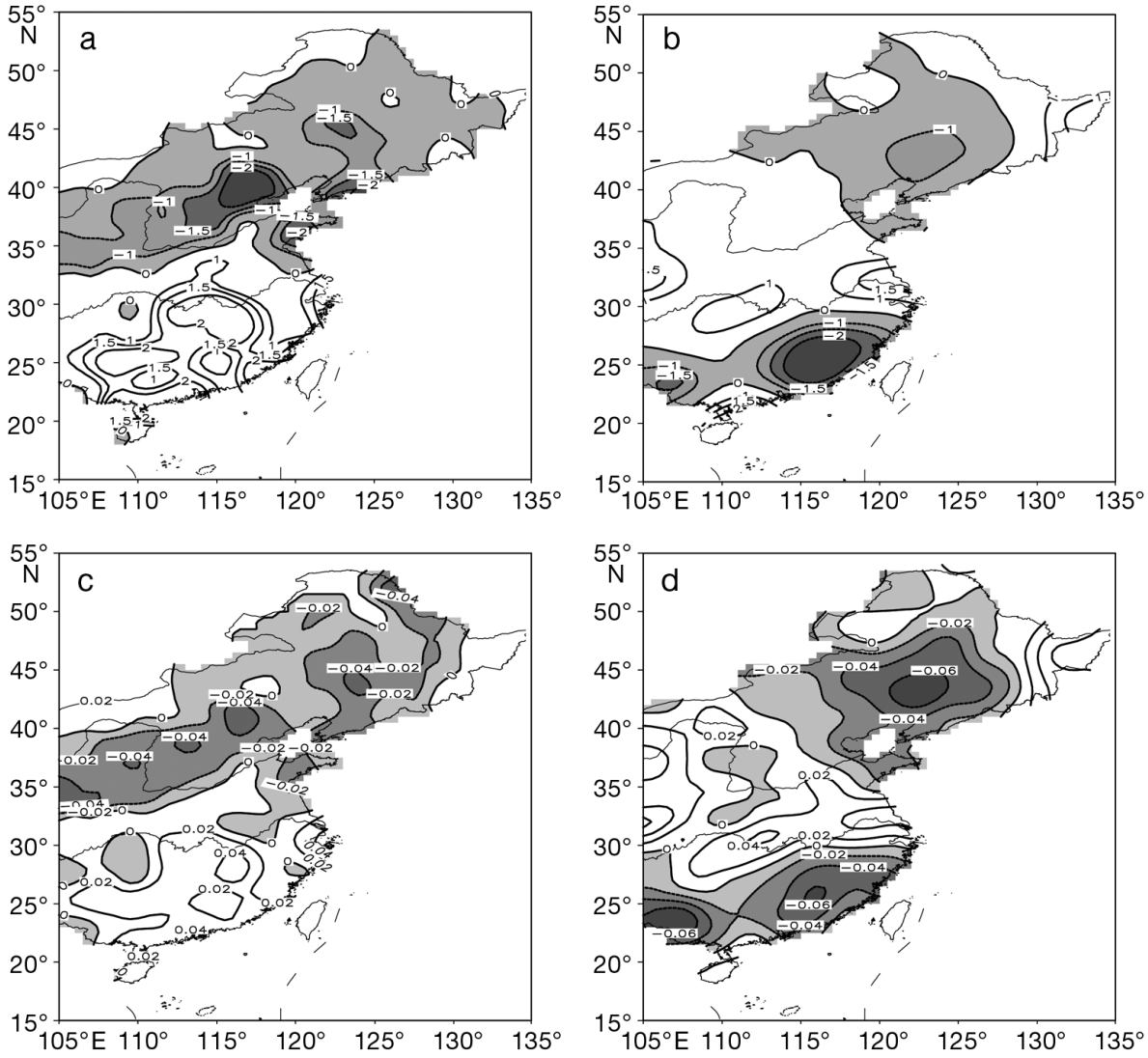


Fig. 10. Linear trends for (a,b) total rainfall above the 95th percentile (R95pTOT; mm decade$^{-1}$), (c,d) number of days with rainfall above the 95th percentile (R95p; d decade$^{-1}$), (e,f) intensity index of the extreme precipitation (R95pI; mm d$^{-1}$ decade$^{-1}$), and (g,h) daily precipitation intensity index (SDII; mm d$^{-1}$ decade$^{-1}$) over eastern China during 1956–2009. (a,c,e,g) Observation (OBS), (b,d,f,h) BCC_CSM1.0

increases from 7.41 to 7.64 and the simulated results change from 20.36 to 21.18. The model also captures the increment in higher frequency range and decrement in mid frequency range but it fails to capture the decrement in the lower frequency range.

In North China, the model shows inability in simulating the interdecadal change of R95p. Fig. 10b shows that the observed probability density curve of R95p shifts to a lower frequency and the spatio-temporal mean value decreases from 6.62 to 6.08. However, there is no obvious change in the simulation (Fig. 11g), with similar values in both time periods.

In the Jianghuai area, BCC_CSM1.0 reproduces the general shift of the probability density curve from a lower frequency range to a higher one. The spatio-temporal mean increases in observations and in simulation, but the simulated spatio-temporal mean frequencies are higher than observations.

In South China I, the probability density curve has a slight shift from a higher frequency range to the lower one from 1956–1979 to 1980–1992 in the simulation, with the regional R95p mean decreasing. The change is similar to the observations. The model generally fails to reproduce the observed shift from a lower to a higher frequency range from 1980–1992 to 1993–2009. The regional averaged R95p value in observations increases, while that in simulation just has a slight increase.

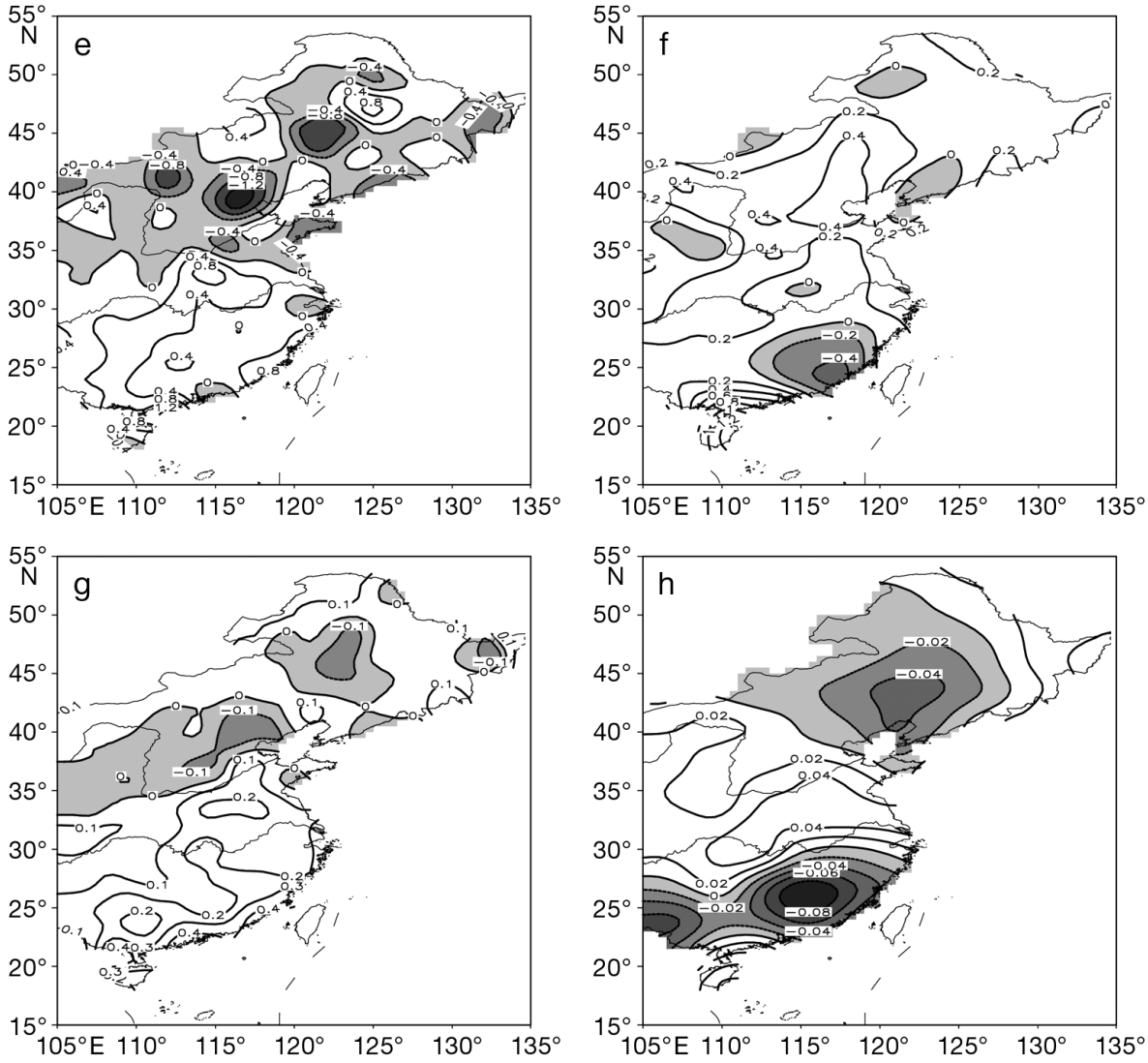


Fig. 10 (continued)

Table 1. Mann-Kendall trend testing for observed (OBS) and simulated (BCC) total rainfall above the 95th percentile (R95pTOT) and number of days with rainfall above the 95th percentile (R95p) for the 5 sub-regions. β: magnitude of the trend (Eq. 6); $Z_c$: test of significance (Eq. 2); $|Z_{0.1}| = 1.64$, $|Z_{0.05}| = 1.96$

| Region | OBS | | BCC | |
|---|---|---|---|---|
| | β | $Z_c$ | β | $Z_c$ |
| **R95pTOT (% yr$^{-1}$)** | | | | |
| NE China | −0.300 | −1.69 | −0.074 | −0.33 |
| North China | −0.405 | −1.75 | 0.128 | 0.60 |
| Jianghuai | 0.075 | 0.66 | 0.195 | 1.15 |
| South China I | 0.138 | 1.28 | −0.036 | −0.18 |
| South China II | 0.250 | 1.45 | −0.229 | −1.13 |
| **R95p (d yr$^{-1}$)** | | | | |
| NE China | −0.018 | −1.46 | −0.016 | −0.57 |
| North China | −0.019 | −1.98 | 0.003 | 0.10 |
| Jianghuai | 0.003 | 0.16 | 0.035 | 1.12 |
| South China I | 0.006 | 0.37 | −0.033 | −0.84 |
| South China II | 0.024 | 1.0 | −0.039 | −0.98 |

In South China II, the observed extreme precipitation events above the 95th percentile become more frequent from 1956–1979 to 1980–1992 and 1993–2009. However, the simulated spatio-temporal averaged value of R95p tends to decrease. The change is opposite to the observations. The interdecadal tendency is similar to the observations. Generally, the BCC_CSM1.0 does not reproduce the interdecadal change feature of R95p in South China II.

The observed increment of extreme precipitation over South China since 1993 is similar to the work of Ning & Qian (2009). Here South China is divided into 2 sub-regions and one can find the differences between South China I and South China II. The R95p decreased in South China I, but increased in South China II from 1956–1979 to 1980–1992. The mechanism which causes the difference needs to be studied in future work.

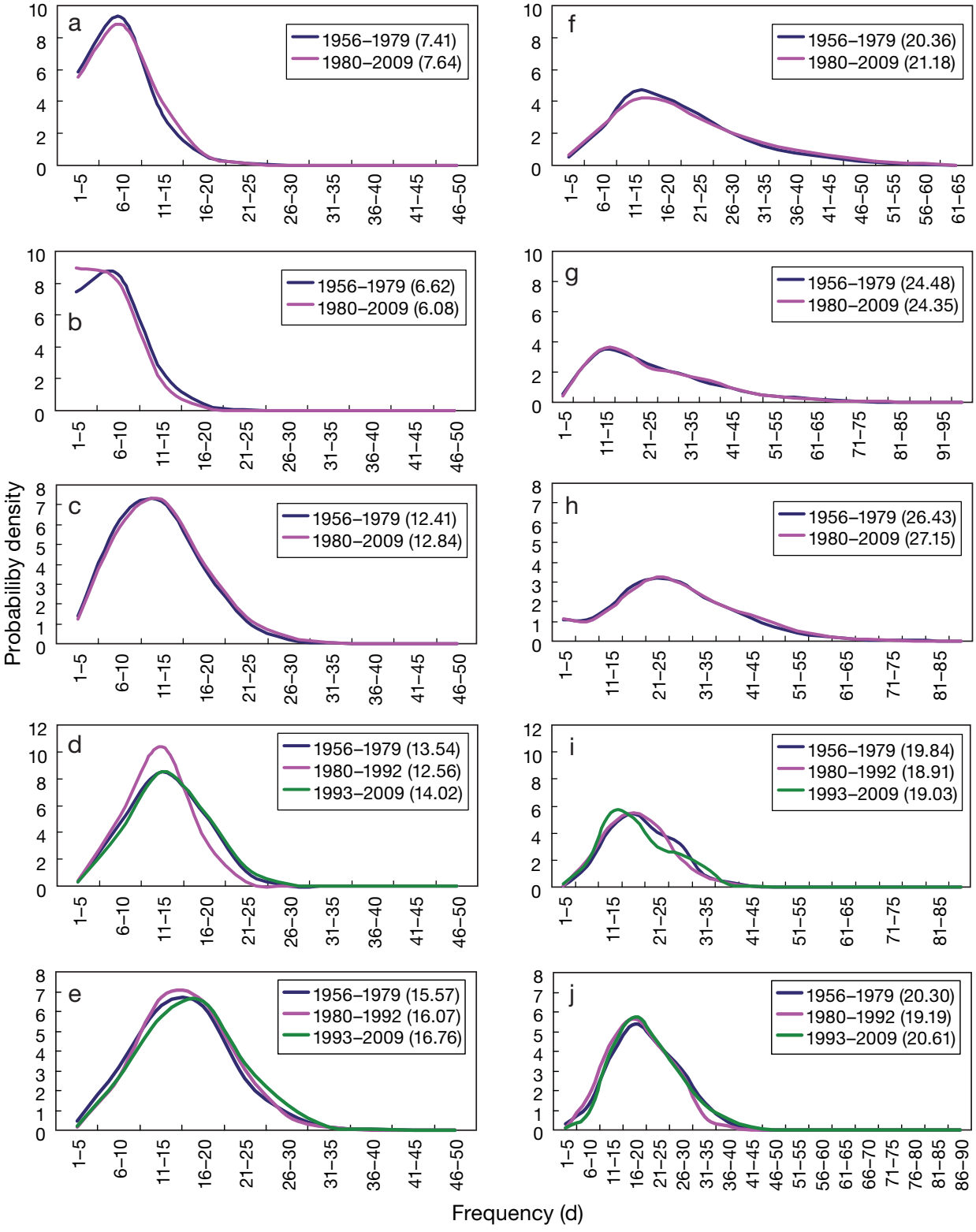


Fig. 11. Probability density curves for number of days with rainfall above the 95th percentile (R95p) in 5 sub-regions: (a,f) NE China (115–135° E, 42–52° N), (b,g) North China (105–125° E, 35–42° N), (c,h) Jianghuai Region (105–122° E, 28–35° N), (d,i) South China I (105–110° E, 20–28° N), (e,j) South China II (110–122° E, 20–28° N). (a–e) Observation, (f–j) BCC_CSM1.0. Numbers inside parentheses: spatio-temporal averaged values

Table 2. Spatio-temporal averaged number of days with rainfall above the 95th percentile (R95p). OBS: observed, BCC: simulation by BCC_CSM1.0

| Region | 1956–1979 | | 1980–2009 | | 1980–1992 | | 1993–2009 | |
|---|---|---|---|---|---|---|---|---|
| | OBS | BCC | OBS | BCC | OBS | BCC | OBS | BCC |
| NE China | 7.41 | 20.36 | 7.64 | 21.18 | – | – | – | – |
| North China | 6.62 | 24.48 | 6.08 | 24.35 | – | – | – | – |
| Jianghuai | 12.41 | 26.43 | 12.84 | 27.15 | – | – | – | – |
| South China I | 13.54 | 19.84 | 13.39 | 18.98 | 12.53 | 18.91 | 14.02 | 19.03 |
| South China II | 15.57 | 20.30 | 16.46 | 19.99 | 16.07 | 19.19 | 16.76 | 20.61 |

## 4. DISCUSSION

Based on daily precipitation during 1956–2009 from 349 rain gauge stations in eastern China, the performance of the BCC_CSM1.0 in simulating the regional extreme precipitation change over eastern China (east of 105° E) is evaluated. We also obtain similar results as previous research about the observation (e.g. Pan 2002, Zhai et al. 2005, Dong et al. 2011), such as the frequency and amount of extreme precipitation decreased in Northeast and North China, and increased in South China during the period of 1956 to 2009.

The 20th century simulation forced by observed greenhouse gases, aerosols, solar irradiance and volcanic aerosols shows that (1) BCC_CSM1.0 reproduces the basic feature of observed climatology of annual total and extreme precipitation over the 95th percentile, with spatial correlation of 0.77 for both of them, and (2) BCC_CSM1.0 captures the main change patterns of yearly accumulated extreme precipitations above the 95th percentile, although there are some model biases in the spatial extension and strength.

There are also some model biases: (1) the annual total and extreme precipitation south of Yangtze River are underestimated. (2) The frequency of heavy precipitation (≥25.0 mm $d^{-1}$) over eastern China is underestimated, but the frequency of light rain (0.1–10 mm $d^{-1}$) is overestimated. (3) The long-term trends of annual extreme precipitation amount and frequency in the recent 50 yr are opposite to those from observations in North and South China. The model also has poor performance in simulating their interdecadal variations in North and South China.

The regional differences for extreme precipitation change is considerable and there are interdecadal variation signals for extreme heavy precipitation. Although some encouraging results for extreme precipitation simulation are obtained, the performance of BCC_CSM1.0 needs to be improved. IPCC AR4 models also have large biases in simulation of precipitation resulting from the East Asian summer monsoon (EASM) (Sun & Ding 2008). It is therefore a common task for current climate system models to improve their performance in simulating the precipitation over East Asia.

A good simulation of the EASM is very important for precipitation simulation in East Asia. The probability of climate extremes is also strongly affected by atmospheric circulation and climate variability, such as Madden–Julian Oscillation, El Niño–Southern Oscillation, and Pacific interdecadal variability, in the global and/or regional scale (Jones et al. 2004, Curtis et al. 2007, Kenyon & Hegerl 2010).

The climate system model working group in BCC are devoting themselves to improve the capability of BCC_CSM.

*Acknowledgements.* The authors thank the National Meteorological Information Center, China Meteorological Administration (CMA) for providing the daily station precipitation data, and they also thank the climate system model working group of National Climate Center, CMA, for their efforts in the development of the climate system model. This work is supported by the National Key Project of Scientific and Technical Supporting Programs of China (2007BAC29B02, 2007BAC29B03 and 2007BAC03A01) and National Basic Research Program of China (2010CB 951902), which are all from the Ministry of Science and Technology. This study is also supported by National Science Foundation of China (41175074). We also thank all reviewers and editors for their constructive suggestions. We thank Dr. Y. Cheng who made helpful suggestions on the content, syntax, and expressions.

LITERATURE CITED

Alexander LV, Zhang X, Peterson TC, Caesar J and others (2006) Global observed changes in daily climate extremes of temperature and precipitation. J Geophys Res 111:D05109, doi:10.1029/2005JD006290

Bonsal BR, Zhang XB, Vincent LA, Hogg WD (2001) Characteristics of daily and extreme temperature over Canada. J Clim 14:1959–1976

Chelton DB, Schlax M, Witter D, Richman J and others (1990) GEOSAT altimeter observations of the surface circulation of the Southern Ocean. J Geophys Res 95: 17877–17903

Chen HS, Fu SD, Zhang XH (2009) Seasonal differences of variation characteristics of extreme precipitation events over China in the last 50 years. Transactions of Atmospheric Sciences 32:744–751 (in Chinese)

Chen XY (2008) Inter-annual change of East Asian Summer Monsoon and simulating analysis of BCC_CSM. MSc thesis, Nanjing University of Information Science & Technology (in Chinese)

Curtis S, Salahuddin A, Adler RF, Huffman GJ, Gu G, Hong Y (2007) Precipitation extremes estimated by GPCP and TRMM: ENSO relationships. J Hydrometeor 8(4):679–689

Dickinson RE, Oleson KW, Bonan G, Hoffman F and others (2006) The Community Land Model and its climate statistics as a component of the Community Climate System Model. J Clim 19:2302–2324

Ding YH, Wang ZY, Sun Y (2008) Inter-decadal variation of the summer precipitation in China and its association with decreasing Asian summer monsoon. Int J Climatol 28:1139–1161

Dong M, Wu TW, Wang ZZ, Zhang F (2009) Simulations of the tropical intra-seasonal oscillations by the AGCM of the Beijing Climate Center. Acta Meteorol Sin 67: 912–922 (in Chinese)

Dong Q, Chen X, Chen T (2011) Characteristics and changes of extreme precipitation in Yellow–Huaihe and Yangtze–Huaihe River Basins, China. J Clim 24:3781–3795

Easterling DR, Evans JL, Groisman PY, Karl TR, Kunkel KE, Ambenje P (2000) Observed variability and trends in extreme climate events: a brief review. Bull Am Meteorol Soc 81:417–425

Gao XJ, Xu Y, Zhao ZC, Pal JS, Giorgi F (2006) Impacts of horizontal resolution and topography on the numerical simulation of East Asian precipitation. Chin J Atmos Sci 30:185–192 (in Chinese)

Gemmer M, Fischer T, Jiang T, Su BD, Liu LL (2011) Trends in precipitation extremes in the Zhujiang River Basin, South China. J Clim 24:750–761

Hu ZZ (1997) Interdecadal variability of summer climate over East Asia and its association with 500 hPa height and global sea surface temperature. J Geophys Res 102: 19403–19412

Huang Y, Feng GL, Dong WJ (2011) Temporal changes in the patterns of extreme air temperature and precipitation in the various regions of China in recent 50 years. Acta Meteorol Sin 69:125–136 (in Chinese)

IPCC (2000) Emissions Scenarios. Nakicenovic N, Swart R (eds) Special Report of the Intergovernmental Panel on Climate Change (IPCC). Cambridge University Press, Cambridge

IPCC (2007) Climate change 2007: the physical science basis. Contribution of Working Group I to the Fourth Assessment Report of the Intergovernmental Panel on Climate Change. Solomon S, Qin D, Manning M, Chen Z, Marquis M, Averyt KB, Tignor M, Miller HL (eds). Cambridge University Press, Cambridge

Jiang ZH, Chen WL, Song J, Wang J (2009) Projection and evaluation of the precipitation extremes indices over China based on seven IPCC AR4 coupled climate models. Chin J Atmos Sci 33:109–120 (in Chinese)

Jones C, Waliser DE, Lau KM, Stern W (2004) Global occurrences of extreme precipitation and the Madden–Julian Oscillation: observations and predictability. J Clim 17: 4575–4589

Kalnay E, Kanamitsu M, Kistler R, Collins W and others (1996) The NCEP/NCAR 40-year reanalysis project. Bull Am Meteorol Soc 77:437–471

Karl TR, Easterling DR (1999) Climate extremes: selected review and future research directions. Clim Change 42: 309–325

Kendall MG (1948) Rank correlation methods. Hafner, New York, NY

Kendall MG (1975) Rank correlation measures. Charles Griffin, London

Kenyon J, Hegerl G (2010) Influence of modes of climate variability on global precipitation extremes. J Clim 23: 6248–6262

Kiehl JT, Gent PR (2004) The Community Climate System Model, version 2. J Clim 17:3666–3682

Kiktev D, Sexton DMH, Alexander L, Folland CK (2003) Comparison of modeled and observed trends in indices of daily climate extremes. J Clim 16:3560–3571

Li QX, Tang GL, Chen Y, Ren YY (2011) Summing-up report on monitoring and detection of precipitation over China during the last one hundred years. Department of Science & Technology and Climate Change, China Meteorological Administration (in Chinese)

Mann HB (1945) Non-parametric tests against trend. Econometrica 13:245–259

Ning L, Qian YF (2009) Interdecadal change in extreme precipitation over South China and its mechanism. Adv Atmos Sci 26:109–118

North GR, Kim KY, Shen SSP, Hardin JW (1995) Detection of forced climatic signals. Part I: theory. J Clim 8:401–408

Pall P, Allen MR, Stone DA (2007) Testing the Clausius–Clapeyron constraint on changes in extreme precipitation under $CO_2$ warming. Clim Dyn 28:351–363

Pan XH (2002) The spatial and temporal characteristics of change of temperature and precipitation extremes over China during the second half of the 20th century. MSc thesis. Chinese Academy of Meteorological Sciences, Beijing (in Chinese)

Qian WH, Fu JL, Zhang WW, Xiang LN (2007) Changes in mean climate and extreme climate in China during the last 40 years. Adv Earth Sci 22:673–684 (in Chinese)

Sun Y, Ding YH (2008) Validation of IPCC AR4 climate models in simulating interdecadal change of East Asian summer monsoon. Acta Meteorol Sin 66:765–780

Sun Y, Solomon S, Dai AG, Portmann R (2006) How often does it rain? J Clim 19:916–934

Wang L, Zhou TJ, Wu TW and others (2009) Simulation of the leading mode of Asian–Australian monsoon interannual variability with Beijing Climate Center atmospheric general circulation model. Acta Meteorol Sin 67:973–982 (in Chinese)

Wang ZY, Ding YH, He JH, Yu J (2004) An updating analysis of the climate change in China in recent 50 years. Acta Meteorol Sin 62:228–236 (in Chinese)

Wei FY (1999) Technology of modern climate statistic diagnosis and prediction. China Meteorological Press, Beijing (in Chinese)

Weng HY, Sumi A, Takayabu YN, Minoto M, Li CY (2004) Interannual– interdecadal variation in large-scale atmospheric circulation and extremely wet and dry summers in China/Japan during 1951–2000. Part II: dominant timescales. J Meteorol Soc Jpn 82:789–804

Wu QZ (2002) A review of flood disasters in China in the

20th century. J Catastrophol 17:62–69 (in Chinese)
Wu TW, Yu RC, Zhang F (2008) A modified dynamic framework for atmospheric spectral model and its application. J Atmos Sci 65:2235–2253
Wu TW, Yu RC, Zhang F, Wang Z, and others (2010) The Beijing Climate Center atmospheric general circulation model (BCC-AGCM2.0.1): description and its performance for the present-day climate. Clim Dyn 34:123–147
Xie P, Arkin PA (1997) Global precipitation: a 172 year monthly analysis based on gauge observations, satellite estimates, and numerical model outputs. Bull Am Meteorol Soc 78:2539–2558
Xu ZX, Chen YN, Li JY (2004) Impact of climate change on water resources in the Tarim River Basin. Water Resour Manage 18:439–458
Yan ZW, Yang C (2000) Geographic patterns of extreme climate changes in China during 1951–1997. Clim Environ Res 5:265–270 (in Chinese)
Yang JH, Jiang ZH, Wang PX, Chen YS (2008) Temporal and spatial characteristics of extreme precipitation events in China. Clim Environ Res 13:75–83 (in Chinese)
You QL, Kang SC, Aguilar E, Pepin N and others (2010) Changes in daily climate extremes in China and their connection to the large scale atmospheric circulation during 1961–2003. Clim Dyn 36:2399–2417
Zhai PM, Pan XH (2003) Change in extreme temperature and precipitation over northern China during the second half of the 20th century. Acta Geogr Sin 58:1–10 (in Chinese)
Zhai PM, Ren FM, Zhang Q (1999a) Detection of trends in China's precipitation extremes. Acta Meteorol Sin 57: 208–216 (in Chinese)
Zhai PM, Sun AJ, Ren FM, Liu XN, Gao B, Zhang Q (1999b) Changes of climate extremes in China. Clim Change 42:203–218
Zhai PM, Zhang XB, Wang H, Pan XH (2005) Trends in total precipitation and frequency of daily precipitation extremes over China. J Clim 18:1096–1108
Zhang L (2008) Evaluation of AOCGCMs for precipitation in East Asia. PhD thesis, Graduate University of the Chinese Academy of Sciences, Beijing (in Chinese)
Zhang L, Wu TW, Xin XG, Dong M, Wang ZZ (in press) Projected annual air temperature and precipitation over the Globe and China during the 21st century by BCC_CSM1.0. Acta Meteorol Sin
Zhang X, Zwiers FW, Hegerl GC, Lambert FH and others (2007) Detection of human influence on twentieth-century precipitation trends. Nature 448:461–465
Zheng H, Zhang L, Liu C, Shao Q, Yoshihiro F (2007) Changes in stream flow regime headwater catchments of the Yellow River basin since the 1950s. Hydrol Process 21:886–893

*Submitted: February 28, 2011; Accepted: October 24, 2011*

*Proofs received from author(s): December 4, 2011*

张灵,李维京,陈丽娟. 北半球平流层大气环流转型的基本气候特征. 应用气象学报,2011,22(4):411-420.

# 北半球平流层大气环流转型的基本气候特征

张 灵[1)2)] 李维京[2)] 陈丽娟[2)*]

[1)](兰州大学大气科学学院,兰州 730000)

[2)](国家气候中心 中国气象局气候研究开放实验室,北京 100081)

**摘 要**

利用 1948—2009 年 NCEP/NCAR 逐日高度场和风场再分析资料探讨了平流层各主要层次上环流转型的年际、年代际时空演变特征。结果表明:北半球平流层冬季环流转为夏季环流的过程是高层环流转型早,低层环流转型晚,但在各层次上环流转型早晚存在着区域性差异。自新地岛到西伯利亚北部地区的环流转型最早,且该区域与北半球环流平均转型时间的年际以及年代际特征最相近。北半球平流层环流转型的气候平均时间早于东亚热带季风爆发时间,从而可能成为季风预测的前兆信号。分析还得到平流层各主要层次环流转型时间具有明显的年代际特征,环流转型时间呈现由偏晚到偏早、又从偏早到偏晚的变化特征,只是年代际转折年份在不同区域、不同层次存在差异。此外,平流层环流转型时间普遍存在准 2 年、准 3～6 年、准 9～12 年以及准 21～24 年的周期,可能与气候系统其他成员有密切联系。

**关键词**:平流层大气环流;环流转型时间;气候特征

## 引 言

平流层对于整个大气环流具有重要作用,平流层变化通常具有维持时间长、异常出现的时间早于对流层异常发生的时间等特征。已有许多研究证明:平流层环流的异常对于对流层天气、气候异常有一定先兆作用[1-6],从而可为短期气候预测提供前兆信号。

平流层大气环流的季节变化和环流转型的迟早及其与对流层的关系一直被人们所关注。平流层冬夏季节的转换主要体现在极地冷低压与暖高压的转换以及绕极的西风转为弱东风[7]。依据冬夏环流形势的显著差异,瞿章等[8-9]采用 1965—1984 年共 20 年的逐月高度场资料计算了北半球 50 hPa 上不同经度 3 个纬度带间(60°～90°N,30°～60°N,0°～30°N)的高度梯度反转的日期,以此确定各经度上在此纬度带的转换日期,研究了 50 hPa 上环流特征与 500 hPa 的关联,指出了平流层环流的季节变化具有在高纬度和低纬度地区出现早、中纬度地区出现晚的趋势。葛玲等[10]利用 1965—1986 年的高度场和臭氧资料,计算了 30 hPa 上 50°N 以北地区高度场涡动方差,给出了 30 hPa 春季开始的日期及季节转变早、晚情况下臭氧的异常分布。田荣湘等[11]采用 1979 年的全球大气研究计划第 1 次试验期间的全球气象资料(FGGEIII$_b$),研究了 1979 年平流层大气环流在季节变化期间,南北半球不同区域的演变特征。许多研究都表明:平流层环流及环流转型异常与对流层气候及对流层大气环流系统有联系[12-14],因此有关平流层季节性的环流转换及转换异常的研究对短期气候预测有重要意义。由于受平流层观测资料匮乏的限制以及平流层季节转变定义方法差异的影响,早期对于平流层环流转型的研究较难从气候及其异常角度清晰地给出平流层各层次环流转型的时空变化特征及其与对流层的关系,为此,本文通过对 1948—2009 年共 62 年的 NCEP/NCAR 逐日再分析资料,利用高度梯度反转和风向转向相结合的方法来确定各层次的环流转型日期,

2010-10-28 收到,2011-04-22 收到再改稿。

资助项目:科技部科技支撑项目(2007BAC29B04,2009BAC51B05),973 项目(2010CB950501)

* 通信作者,E-mail:chenlj@cma.gov.cn

分析转型日期的年际、年代际变化特征，研究平流层环流转型在气候学上的时空变化特点，为分析平流层环流转型的时空变化特征及其异常与对流层内重要的天气、气候的具体关系奠定基础。

## 1 资料和方法

本文所用的资料来自 NCEP/NCAR 逐日再分析资料[15]，该资料序列时间长度为 1948 年 1 月 1 日—2009 年 12 月 31 日，垂直方向共 17 层(1000，925，850，700，600，500，400，300，250，200，150，100，70，50，30，20，10 hPa)，水平分辨率为 2.5°×2.5°，要素为位势高度场和纬向风场。

平流层环流在冬夏有显著差异，冬季高度场呈现南高北低的形势，极地为冷低涡，中高纬度地区主要盛行绕极西风；而夏季高度场则呈现南低北高形势，主要盛行东风。根据冬夏的环流差异，本文定义北半球位势高度场南北每隔 5°的梯度差为高度梯度：

$$\Delta H_{\lambda,\phi} = H_{\lambda,\phi} - H_{\lambda,\phi+5^\circ}。\qquad (1)$$

式(1)中，$\lambda$，$\phi$ 分别为经度、纬度，$H_{\lambda,\phi}$ 为格点($\lambda$，$\phi$)处对应的位势高度值。

由于北半球平流层气象要素场(温度场、风场、高度场等)在 55°N 以北地区的方差都较大，因此选取(55°～85°N，0～177.5°E，180～2.5°W)的中高纬度地区作为研究区域。在该区域内，如果高度场呈南低北高型，即 $\Delta H_{\lambda,\phi}<0$，则计数器 $N_{\lambda,\phi}=1$；若 $\Delta H_{\lambda,\phi}\geqslant 0$，则 $N_{\lambda,\phi}=0$。此外，如果该区域内某格点风场为东风，即 $U_{\lambda,\phi}<0$，则计数器 $M_{\lambda,\phi}=1$；若 $U_{\lambda,\phi}\geqslant 0$，则 $M_{\lambda,\phi}=0$。

当研究区域内的负高度梯度($N_{\lambda,\phi}$)的格点数和东风($M_{\lambda,\phi}$)的格点数占研究区域内总格点数的百分率(式(2)中 $R_H$ 和 $R_U$)连续 5 d 都达到 80%(经验值)以上时，即定义满足以上条件的第 1 天为平流层冬季环流转为夏季环流的日期。

$$R_H = \frac{\sum N_{\lambda,\phi}}{\text{总格点数}} \times 100\%,$$

$$R_U = \frac{\sum M_{\lambda,\phi}}{\text{总格点数}} \times 100\%。\qquad (2)$$

式(2)中，$R_H$ 和 $R_U$ 分别为研究区域内的负高度梯度、东风的格点数占研究区域总格点数的百分率。

文中环流转换时间一般指某年的日序，如 1 月 1 日对应的数值是 1，1 月 31 日对应的数值是 31，2 月 1 日对应的数值是 32，依次类推。

对北半球平流层高度梯度场的均方差分析显示，北半球存在 3 个均方差极大值中心(图 1 为 10 hPa上冬季环流转为夏季环流过渡月份的高度梯度的均方差分布，其他层次以及 1—12 月的均方差分布图略)，这 3 个极值中心为季节变化、气候异常的敏感区域，因此，除计算北半球环流转型的日期外，还依据极值中心选定 3 个代表性区域：1 区是从新地岛到西伯利亚北部地区(55°～85°N，50°～120°E)，简称为西伯利亚区；2 区是以白令海为中心，从东西伯利亚到加拿大西北部地区(55°～85°N，120°E～120°W)，简称为白令海区；3 区是位于大西洋北部的格陵兰岛地区(55°～85°N，2.5°～60°W)，简称为格陵兰区。采用上述同样方法计算出这 3 个区域的环流转型日期。

本文采用经验小波分析[16]研究 62 年来环流转型日期的时频结构，此外还用曼-肯德尔法(M-K)[17]对于多年来的转型时间变化趋势进行突变年份的检测。

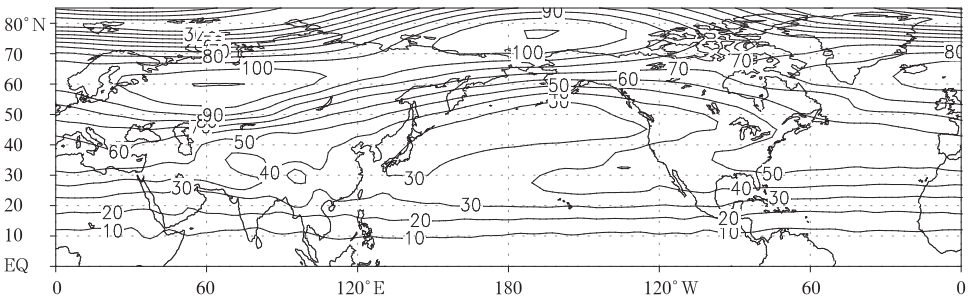


图 1 3 月 1 日—6 月 30 日 10 hPa 高度梯度的均方差分布(单位：gpm)

Fig. 1 The mean square deviation of the geopotential height gradient from 1 March to 30 June at 10 hPa(unit: gpm)

## 2　结果分析

### 2.1　平流层环流转型时间的平均气候特征

图 2 是 10 hPa 的高度梯度和风速气候平均态的时间-经度分布图,可以看出:同层次的高度场梯度与风速的转换时间相近。其中 10 hPa 和 20 hPa(图略)的冬季环流转为夏季环流的转型日期相近,平均出现在 4 月上旬和中旬,30 hPa(图略)环流转型时间出现在 4 月下旬,50 hPa(图略)环流转型时间则出现在 5 月上旬。而夏季环流转为冬季环流的平均日期则是 50 hPa 最早,转型时间为 8 月初,30 hPa转型时间出现在 8 月中下旬,20 hPa 和 10 hPa 均出现在 8 月底,但 10 hPa 稍晚于 20 hPa。各层夏季环流维持的时间长度:10 hPa 约为 5 个月,20 hPa 超过 4 个月,30 hPa 为近 4 个月,维持时间最短的是 50 hPa,为近 3 个月(表 1)。即层次越高,夏季环流维持的时间越长;层次越低,夏季环流维持的时间越短。同时可以看出,在不同的区域,冬季环流向夏季环流转型的时间也存在差异。西伯利亚区和格陵兰区所在的经度范围内,环流转型时间明显较其他区域偏早,且高度梯度和风速的变化相对于白令海区来说要小很多。白令海区所在的经度范围内环流转型的时间较其他区域稍晚。

根据已有季风领域的研究,孟加拉湾、中南半岛和南海是亚洲热带夏季风最早爆发的地区[18],其中南海夏季风平均的爆发时间为 5 月中下旬[19]。而根据本文的分析,平流层夏季环流转为冬季环流的平均时间出现在 4 月上中旬至 5 月上旬(表 1、图 2)。即从气候平均状态上来看,平流层的冬季环流转为夏季环流的转型时间明显早于东亚热带季风爆发时间,从而可能成为一个研究东亚季风气候监测、预测的先兆信号。季风活动与我国夏季降水关系密切[20],因此,平流层环流转型对于汛期气候趋势也有指示意义。

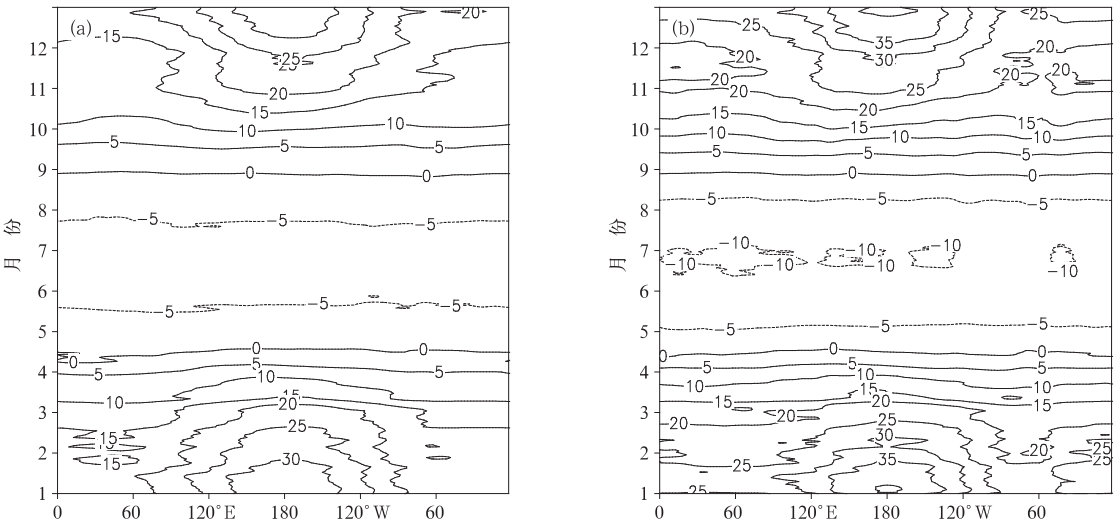


图 2　10 hPa 位势高度梯度(单位:dagpm)(a)以及纬向风(单位:m·s$^{-1}$)(b)的时间-经度分布图

Fig. 2　Time-longitude evolution of geopotential height gradient (unit:dagpm)(a) and zonal wind (unit:m·s$^{-1}$)(b) at 10 hPa

**表 1　北半球平流层环流转型时间**

**Table 1　Transition date of stratospheric circulation in Northern Hemisphere**

| 高度/hPa | 冬季环流转为夏季环流时间 | 夏季环流转为冬季环流时间 |
|---|---|---|
| 10 | 4 月上中旬 | 8 月底 |
| 20 | 4 月上中旬 | 8 月底 |
| 30 | 4 月下旬 | 8 月中下旬 |
| 50 | 5 月上旬 | 8 月初 |

### 2.2　平流层环流转型日期的年际和年代际特征

#### 2.2.1　平流层环流不同区域和不同层次的平均转型时间

由表 1 和表 2 可知,北半球平流层高层(10 hPa 与 20 hPa)高度场以及风场最先发生环流反转,并逐渐向下传播至 50 hPa,前后经历约 1 个月左右。表 2 是北半球以及 3 个区域不同层次的平均环流转

型时间，在西伯利亚区内的环流转换明显早于白令海区。结合3个区域的地理分布可知，东半球环流转型早于西半球，而西伯利亚区是北半球最先开始环流转型的地区。对比10 hPa与20 hPa上北半球环流转型时间与不同区域环流转型时间可知，这两个层次的环流转型时间较为接近，相差约为1～2 d，与30 hPa环流转型时间相差可达4～6 d，而50 hPa环流转型的发生时间明显落后于其以上层次环流转型时间。

**表2 不同区域、不同层次的平均环流转型时间**

**Table 2 Average transition dates at all levels of the regions**

| 高度/hPa | 北半球 | 西伯利亚区 | 白令海区 | 格陵兰区 |
|---|---|---|---|---|
| 10 | 第112天 | 第111.7天 | 第139.9天 | 第139.6天 |
| 20 | 第113.5天 | 第112.7天 | 第138.7天 | 第137.9天 |
| 30 | 第118.3天 | 第116.6天 | 第143.4天 | 第140.5天 |
| 50 | 第145天 | 第141.4天 | 第173.6天 | 第154.4天 |

### 2.2.2 不同区域环流转型时间的年际变化

北半球不同层次环流转型时间的年际变率较显著(图3)。在10 hPa上环流转型早的年份与转型晚的年份时间相差可达80 d(表3)，其中1989年环流在第70天(即3月11日)转型，是62年中环流转换最早的一年，比平均时间(第112天)早42天，次早年为1964年和1961年，比平均早37天；最晚是2001年，比平均时间晚38天，次晚年为1951年和1949年。20 hPa环流转型早晚差异最大达81 d(表3)，其中转型最早年为1999年(第70天)，次早年为1989年(第71天)和1984年(第73天)；最晚年为2001年，比平均时间晚38天，次晚年为1955年和1951年。在30 hPa上环流转型最早与最晚年时间差达85 d(表3)，转型最早年为1999年(第70天)，次早年为1984年(第74天)、1961(第84天)年和1964年(第84天)；转型最晚年为2001年(第155天)，次晚年为1955年(第148天)。而在50 hPa上环流转型早晚年相差85 d(表3)，1974年转型最早，转型时间为该年第96天，次早年为1996年和1978年(第106天)，最晚年为1983年(第181天)，次晚年为2006年(第179天)。在10～30 hPa上环流转型早晚的年份一致，转型早的年份分别为1989年、1984年、1961年，转型晚的年份为2001年，但50 hPa与其他3个层次的早晚年份存在较大差异，其中的原因值得进一步分析。由逐年变化曲线也可以看出，10～30 hPa环流转型时间较为接近，只是高层转型时间略早于低层，极少数年份例外。此外，50 hPa以上各层次转型时间都早于50 hPa环流转型时间。

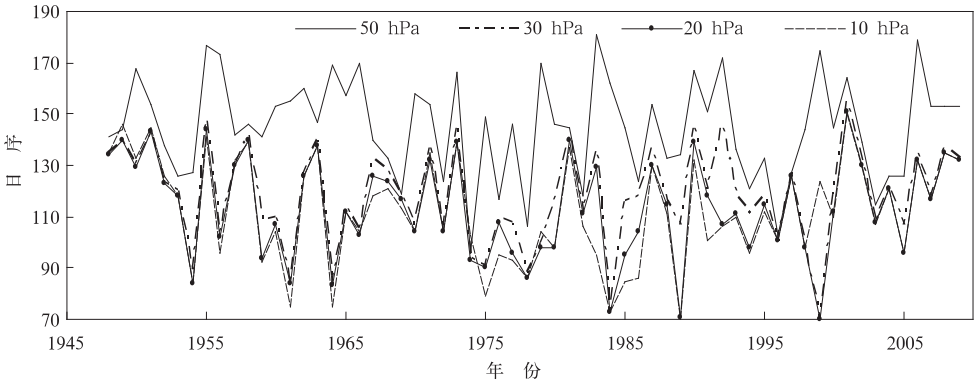


图3 北半球平流层不同层次环流转型时间的逐年变化

Fig. 3 Annual transition dates at different levels in North Hemisphere

**表3 北半球不同层次的最早、最晚转型时间**

**Table 3 Extreme transition dates at all levels in Northern Hemisphere**

| 高度/hPa | 最早转型时间 | 最晚转型时间 |
|---|---|---|
| 10 | 第70天 | 第150天 |
| 20 | 第70天 | 第151.5天 |
| 30 | 第70天 | 第155天 |
| 50 | 第96天 | 第181天 |

由于环流转型具有明显的区域性差异，因此在北半球不同区域环流转型早晚并不一致。图4为北半球以及3个不同区域在10 hPa上环流转型时间逐年变化的对比(其他层次对比图略)。10 hPa上西伯利亚区的转型时间平均是第111.7天，相对北半球平均转型时间稍早，最早为1989年和1999年，均为第70天；其次为1984年、1961年以及1964年；转型最晚年

份为 2001 年,为第 150 天;其次偏晚年分别是 1971,1949,1981,1990 年以及 1998 年。即西伯利亚区转型偏早年和偏晚年与北半球的环流转型早晚年较为一致。白令海区 10 hPa 上的环流转型时间平均是第 139.6 天,明显晚于北半球,转型偏早年为 1964,1976,1959 年以及 1961 年,转型最晚的年份为 1951 年,次晚的年份有 1950,1963,1960,1987,2000,2001 年。格陵兰区环流转型最早年份为 1964 年,次早年份分别为 1951 和 1961 年;最晚年份为 1951 年,次晚年份分别为 2002 和 1950 年。

对比图 4 中北半球与 3 个区域的环流转型时间可见,各区转型日期的年际变化显著。自 1948 年以来的 62 年中,北半球与西伯利亚区环流转型时间较为相近,白令海区与格陵兰区的环流转型时间较为接近,且明显晚于北半球和西伯利亚区的环流转型时间。此外,北半球以及西伯利亚区的环流转型时间早晚的振幅明显大于另外两个区域转型时间的早晚振幅。

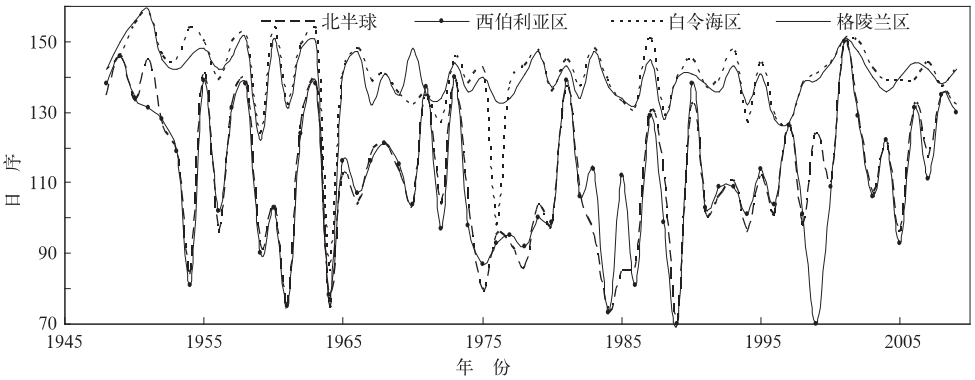


图 4　10 hPa 不同区域环流转型时间的逐年变化

Fig. 4　Annual transition dates of different regions at 10 hPa

2.2.3　不同区域环流转型时间的年代际变化

环流转型时间的年代际变化特征也较显著,这在图 5 环流转型时间逐年变化的线性趋势、二阶多项式回归趋势以及高斯九点平滑的结果中可得到较好反映。图 5 中的二阶回归趋势线以及高斯九点平滑线反映出北半球 10 hPa 上环流转型在近 62 年中经历了季节转换时间由偏晚转为偏早,又转为偏晚的过程,只是在不同区域转折年份不同。北半球从 20 世纪 40 年代末到 70 年代中期环流转型逐渐变早,期间有波动,转型时间的标准化距平在 1974 年为 1.33,在 1975 年降为 −1.62,两者差值达 2.95;而在 20 世纪 70 年代中期至 21 世纪初,环流转型时间逐渐由偏早转为偏晚。当然在此期间也存在一些小的周期变化,尤其是在 2005—2006 年转型时间的标准化距平相差达 1.7。北半球 10 hPa 环流转型时间的 M-K 检验结果图(图 6a)也显示出在 20 世纪 70 年代中期存在突变。在北半球 20 hPa(图 6b)以及 30 hPa 环流转型时间的 M-K 检验(图略)同样显示,在 20 世纪 70 年代中期发生了转折。

对平流层环流转型时间的小波分析(图 7)显示了几个明显的周期特征。北半球 10 hPa 上周期为 2 年处,等值线较为密集,对应的准 2 年周期较为明显。而在周期为 10～12 年的 1975 年处,小波系数出现了最大值,表明在 1975 年前后环流转型早晚出现了明显的变化。另外,小波系数图像的周期呈现出明显的阶段性特征,1948—1975 年准 6 年、准 22 年的周期显著,而在 1975—2009 年,9～12 年周期相对稳定。

西伯利亚区(图 5b)、白令海区(图 5c)以及格陵兰区(图 5d)的环流转型时间与北半球环流转型时间(图 5a)的年代际变化特征相似,即 20 世纪 70 年代中期之前环流转型逐渐变早,而 70 年代中期之后环流转型呈现逐渐变晚趋势,但在主要变化特征下不同区域的环流转型时间又存在阶段性差异。其中西伯利亚区环流转型时间与北半球的环流转型时间的年代际变化极为相似,但在 20 世纪 90 年代以后,西伯利亚区环流逐渐偏晚的这种趋势弱于北半球变化趋势。白令海区和格陵兰区除个别年份外,环流转型的时间早晚变化波动较北半球小很多。

西伯利亚区环流转型时间的小波分析图(图 7b)与北半球的环流转型时间的小波分析图很相似(图 7a),并且突变年份也接近。白令海区和格陵兰

区的环流转型时间的小波分析图(图 7c 和图 7d)与北半球环流转型时间小波分析图(图 7a)存在较大的差异。整体来看,白令海区与格陵兰区都是在1965 年以前存在准 3～6 年的周期,1965 年以后存在准 2 年、准 9～12 年以及准 21～24 年左右的周期。

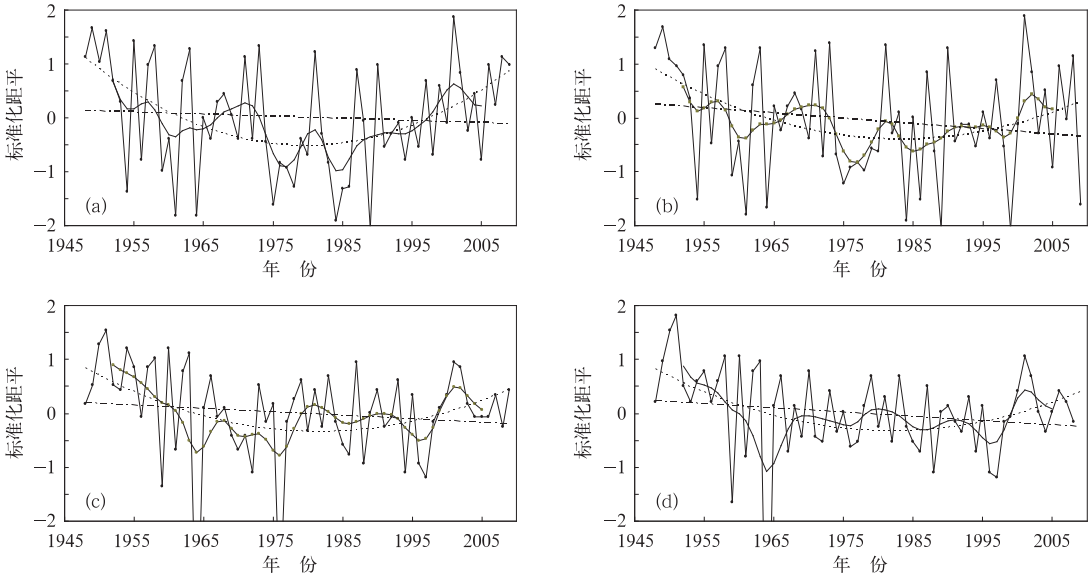


图 5 不同区域 10 hPa 环流转型时间的标准化距平(带标记的实折线)、线性趋势(点划线)、二阶多项式回归趋势(虚线)、高斯九点平滑(实折线)
(a)北半球,(b)西伯利亚区,(c)白令海区,(d)格陵兰区

Fig. 5 Standard deviation of annual transition dates at 10 hPa geopotential height of all regions (labeled solid line), the corresponding to linear trend (chain dotted line), second order polynomial regression line (dotted line), Gaussian 9-year running averages (solid line)
(a)North Hemisphere,(b)Siberia,(c)Bering Sea,(d)Greenland

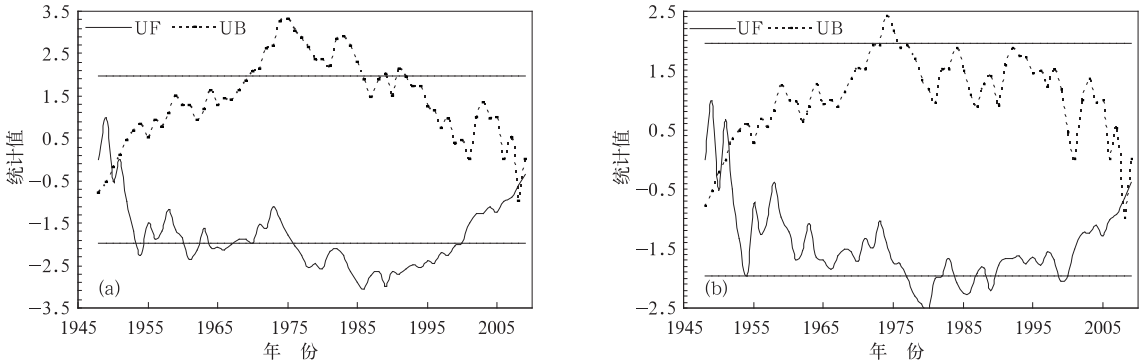


图 6 不同层次环流转型日期的 M-K 统计量曲线 (a)10 hPa,(b)20 hPa
(UF 为顺序时间序列的统计量,UB 为逆序时间序列的统计量)

Fig. 6 Mann-Kendall statistic curves of standard deviation of annual transition date at 10 hPa(a) and 20 hPa(b) geopotential heights
(UF: statistic value of ordinal data; UB: statistic value of reverse data)

可以发现,在平流层各层次(10～50 hPa)不同区域都存在着显著的准 2 年、准 3～6 年、准 9～12 年以及准 21～24 年周期。而这些周期可能与赤道平流层纬向风的准两年振荡[21]、海气相互作用[22]、太阳活动周期[23]具有一定联系,值得进一步分析。

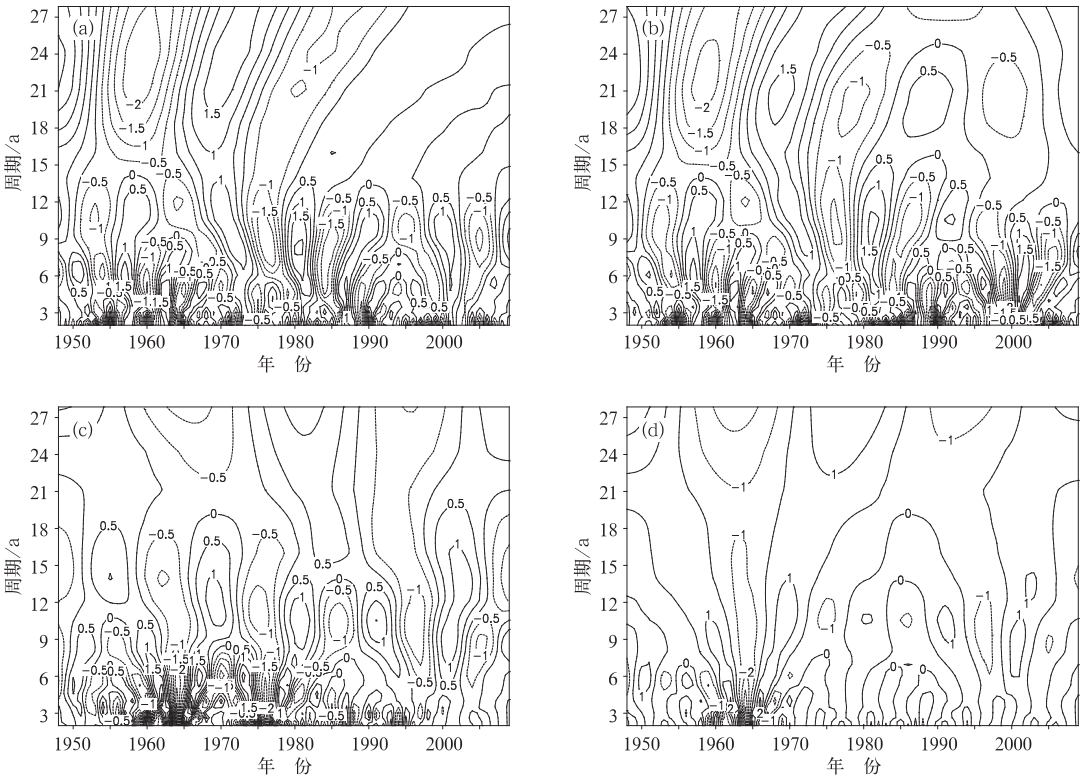


图 7　不同区域 10 hPa 环流转型时间标准化距平的小波分析
(a)北半球,(b)西伯利亚区,(c)白令海区,(d)格陵兰区
Fig. 7　Wavelet analysis statistic curves of standard deviation of annual transition dates at 10 hPa geopotential height of different regions in North Hemisphere(a), Siberia(b), Bering Sea(c), Greenland(d)

## 2.3　平流层环流转型日期的频次统计

图 8 是不同区域、不同层次环流转型日期在候时间尺度上发生的频次(以百分率表示)。由北半球统计结果可以看出,不同层次环流转型时间的频次分布有显著差异。10 hPa 上环流转型时间分布呈现双峰型特征,分别在第 21 候和第 27 候,出现的频次为 13%。20 hPa 上环流转型时间分布表现为多峰型特征,其中最高概率出现在第 26 候,为 13%,其次为第 28 候,占 10%。30 hPa 上环流转型时间分布表现为三峰型特征,16%的年份在第 24 候转型,13%的年份在第 22 候转型,9.7%的年份在第 28 候转型。而 50 hPa 上环流转型时间为单峰型特征,高概率时段主要出现在第 29 候至第 34 候。

西伯利亚区 10 hPa 环流转型时间概率分布呈现双峰型特征,接近于北半球平均分布特征,主要出现在第 21 候和第 28 候; 20 hPa 环流转型时间分布呈现三峰型,主要在第 21 候; 30 hPa 环流转型时间呈多峰型分布,主要集中在第 20 候到第 29 候; 50 hPa在第 28 候,其次是第 31 候和第 26 候。在 10 hPa, 20 hPa 以及 50 hPa 上,此区相对于北半球环流转型时间的高概率时段要早。

白令海区和格陵兰区环流转型时间概率分布特征与北半球平均特征差异较大,一般都表现出单峰型特征,只是环流转型时间的高概率时段相对北半球以及西伯利亚区偏晚,且概率高。白令海区 10～30 hPa 上的环流转型时间主要出现在第 28 候和第 29 候,只是高层次偏早; 50 hPa上环流转型主要出现在第 35 候,达 24%。格陵兰区 10～30 hPa主要出现在第 29 候,频次达到 25%以上; 50 hPa 环流转型主要出现在第 36 候。

以上分析表明,北半球 10～50 hPa 环流转型日期出现的高概率时段依次为第 21 候、第 26 候、第 22 候、第 29 候,而西伯利亚区依次为第 21 候、第 22 候和第 26 候。白令海区和格陵兰区在 10～30 hPa 都为第 28 候和第 29 候;而 50 hPa 分别为第 35 候和第 36 候。各层转型时间的高概率时段分布特征及其可能的影响值得进一步分析。

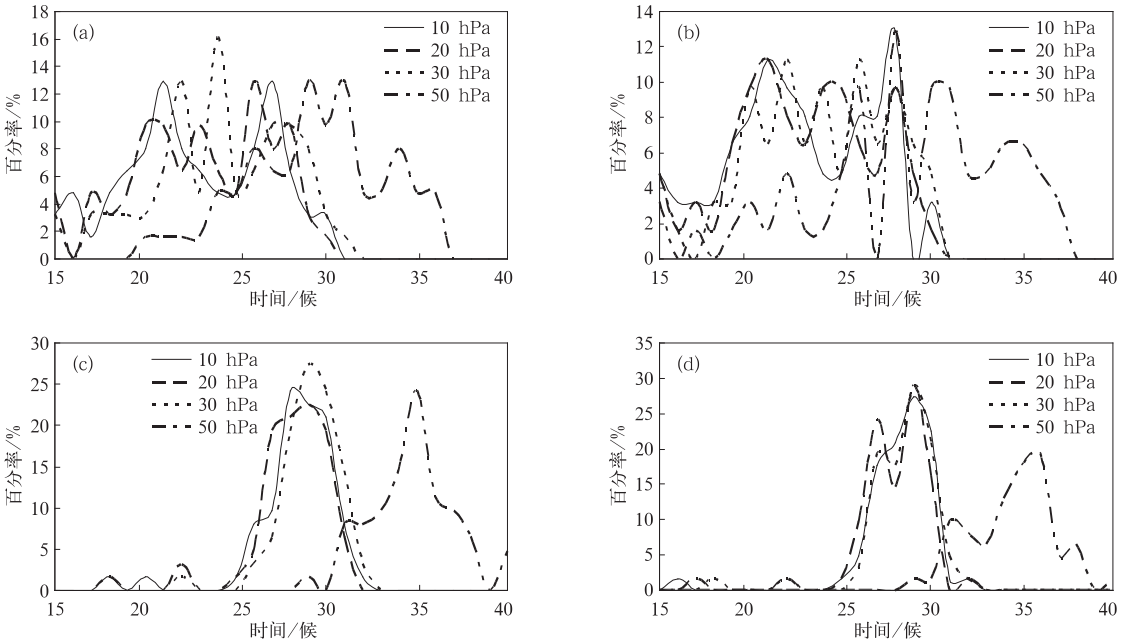


图 8 不同区域、不同层次环流转型日期出现频次

(a)北半球,(b)西伯利亚,(c)白令海区,(d)格陵兰区

Fig. 8 Percentage of annual transition dates at all levels of different regions in North Hemisphere(a), Siberia(b), Bering Sea(c), Greenland(d)

## 3 结论与讨论

利用 NCEP/NCAR 逐日高度场和风场再分析资料,定义并计算了平流层各主要层次和代表性区域环流转型日期,采用小波分析、高斯九点平滑以及 M-K 检验等统计方法分析了北半球平流层各主要层次自冬季环流到夏季环流转型日期的年际、年代际变化特征,得到以下主要结论:

1) 北半球平流层中环流转型最早出现在 10 hPa 和 20 hPa,然后经历较短的时间传至 30 hPa。环流平均转型时间在 4 月下旬之前。南海夏季风是亚洲热带夏季风建立最早的地区之一,平均爆发时间(5 月中下旬)相对于平流层环流转型的平均时间晚,因而平流层环流转型时间可能成为一个研究东亚季风气候监测、预测的先兆信号。

2) 环流转型存在着区域性差异,其中以西伯利亚区各层次环流转型时间最早,北半球平均环流转型时间次之,白令海区和格陵兰区的环流转型时间相对较晚,且白令海区略早于格陵兰区。

3) 北半球以及 3 个不同区域的环流转型时间的年际、年代际变化特征显著,62 年以来的转型时间均表现出偏晚转为偏早,又由偏早转为偏晚的过程。其中西伯利亚区与北半球环流转型时间的年际以及年代际特征相似,而另外两个区域的转型时间变化特征相似。

4) 不同区域、不同层次环流转型时间的周期有差异,但是都存在着准 2 年、准 3～6 年、准 9～12 年以及准 21～24 年的周期。

在平流层中环流的变化以及平流层内有重要作用的臭氧浓度发生改变,都可能引起高低纬度辐射的变化,最终导致温度梯度和风场的变化[24-27]。温度梯度、风场等的变化与冬夏环流的转型紧密联系。这说明,臭氧浓度的分布以及变化、太阳辐射的强弱对于环流转型都有重要影响。太阳活动存在 11 年的变化周期,那么环流转型中的准 10～12 年的周期是否受太阳活动周期的影响还值得进一步研究。此外,研究表明[28],赤道纬向风的准两年振荡(QBO)对北半球冬季大气环流的影响主要表现在平流层和对流层上层的中高纬度地区。QBO 的变化对于平流层环流转型早晚的影响有待于深入探讨。当然平流层爆发性增温可以导致温度急剧的增加,造成高度梯度迅速反转和纬向风转向,成为夏季环流型,尤其是最后一次爆发性增温对于环流转型早晚有较为重要的作用[29-31]。总体说来,平流层环流转型可能受到太阳活动、臭氧分布、QBO 以及平流层最后一

次爆发性增温等因子的影响,这些因子各自对于平流层环流转型的贡献及影响机制值得深入研究。

## 参 考 文 献


[1] 艾祝秀,陈兴芳.北半球 50 hPa 平均环流场的气候特征及其与我国夏季降水关系的初步分析.高原气象,2000,19(1):66-74.

[2] Baldwin M P,Dunkerton T J. Stratospheric harbingers of anomalous weather regimes. *Science*,2001,294:581-584.

[3] Baldwin M P,Cheng X H,Dunkerton T J. Observed correlations between winter-mean troposphere and stratospheric circulation anomalies. *Geophys Res Lett*,1994,21(12):1141-1144.

[4] 陈文,魏科.大气准定常行星波异常传播及其在平流层影响东亚冬季气候中的作用.地球科学进展,2009,24(3):272-285.

[5] 廖荃荪,王永光.赤道平流层 QBO 与我国 7 月雨型的关联.应用气象学报,1998,9(1):104-108.

[6] 陈兴芳,艾祝秀.1997 年中国夏季旱涝和北半球平流层平均环流分析. 应用气象学报,1998,10(3):340-346.

[7] 李崇银,李琳,谭言科,等. 平流层气候. 北京:气象出版社,2008:43-67.

[8] 瞿章,陈芳,张海俊,等. 北半球 50 hPa 多年月平均经向剖面上的季节变化. 高原气象,1989, 8(4):345-350.

[9] 瞿章,张海俊,贺慧霞. 北半球 50 hPa 平均环流的若干特征及其与 500 hPa 的某些关联. 高原气象,1990,9(4):424-431.

[10] 葛玲,郭树军. 北半球 30 hPa 环流春季转变过程的诊断研究. 应用气象学报,1992,3(3):306-313.

[11] 田荣湘,高由禧,瞿章. 1979 年平流层大气环流季节变化的研究. 高原气象,1992,11(2):170-177.

[12] 刘晓东,瞿章. 北半球平流层环流与亚洲夏季风的关系的初步分析.气象学报,1991,49(2):244-248.

[13] 陶诗言,朱福康. 夏季亚洲南部 100 毫巴流型的变化及其与西太平洋副热带高压进退的关系.气象学报,1964,34(4):385-396.

[14] 李崇银,顾薇,潘静. 梅雨与北极涛动及平流层环流异常的关联.地球物理学报,2008,51(6):1632-1641.

[15] Kalnay E,Kanamitsu M,Kistler R, et al. The NCEP/NCAR 40-year reanalysis project. *Bull Amer Meteor Soc*,1996,77:437-471.

[16] 魏凤英.现代气候统计诊断与预测技术. 北京:气象出版社,2007:99-104.

[17] 魏凤英. 气候统计诊断与预测方法研究进展——纪念中国气象科学研究院成立 50 周年. 应用气象学报,2007,17(6):736-742.

[18] 钱永甫,江静,张艳,等. 亚洲热带夏季风的首发地区和机理研究. 气象学报,2004,62(2):129-139.

[19] 柳艳菊,丁一汇. 南海季风爆发前后大气层结和混合层的演变特征. 气象与环境研究,2000,5(4):459-468.

[20] 王启祎,丁一汇,江滢. 亚洲季风活动及其与中国大陆降水关系. 应用气象学报,1998,9(1):83-89.

[21] James R H, Tan H C. The influence of the equatorial Quasi-Biennial oscillation on the global circulation at 50 mb. *J Atmos Sci*,1980,37:2200-2208.

[22] 李双林. 热带印度洋增暖对南极平流层极涡的影响. 中国科学(D 辑),2009,39(6):813-822.

[23] Baldwin M P,Dunkerton T J. Observations and statistical simulations of a proposed solar cycle/QBO/weather relationship. *Geophys Res Lett*,1989,16(8):863-866.

[24] 胡永云,丁峰,夏炎. 全球变化条件下的平流层大气长期变化趋势. 地球科学进展,2009,24(3):242-251.

[25] 郑彬,施春华. 全球平流层下部降温及其对纬向风的影响.气象科技,2006,34(5):538-541.

[26] 魏科,陈文,黄荣辉.北半球平流层极涡崩溃过程的动力诊断分析.中国科学(D 辑),2007,37(8):1110-1119.

[27] 朱乾根,郭品文. 北半球春季大气臭氧变化特征及其对大气温度和环流场的影响. 应用气象学报,2001,11(1): 448-454.

[28] 陈文,杨蕾,黄荣辉,等. 热带准两年振荡影响北半球冬季大气环流的诊断分析.大气科学,2004,28(2):161-173.

[29] Black R X, McDaniel B A,Robinson W A. Stratosphere-troposphere coupling during spring onset. *J Climate*,2006,19:4891-4901.

[30] Black R X, McDaniel B A. Interannual variability in the southern hemisphere circulation organized by stratospheric final warming events. *J Atmos Sci*,2006,64:2968-2974.

[31] Black R X, McDaniel B A. The dynamics of Northern Hemisphere stratospheric final warming events. *J Atmos Sci*,2006,64:2932-2946.

# The Basic Climatic Features of Stratospheric Circulation Transition in Northern Hemisphere

Zhang Ling[1)2)] Li Weijing[2)] Chen Lijuan[2)]

[1)] (*College of Atmospheric Sciences*, *Lanzhou University*, *Lanzhou* 730000)

[2)] (*Laboratory for Climate Studies*, *National Climate Center*, *CMA*, *Beijing* 100081)

**Abstract**

The basic climatic features of stratospheric circulation in Northern Hemisphere demonstrate different forms in winter and summer. In winter, the cold cyclone system and westerly winds prevail in high latitudes, while in summer the situation is the opposite. In terms of inversion of geopotential height gradient and zonal wind direction, a transition date index (TDI) indicating the change dates from summer to winter circulations in the stratosphere in Northern Hemisphere is defined by using NCEP/NCAR reanalysis daily data. Some statistic methods such as linear tendency, wavelet analysis, binomial coefficient smooth and Mann-Kendall are applied to analyze the inter-annual and inter-decadal features of the transition dates at all main levels in the stratosphere. Results indicate that in the stratosphere, with the height rising, the transition date becomes earlier and the summer circulation lasts longer. For instance, the earliest circulation transition in the stratosphere occurs at the height of 10 hPa and 20 hPa, and it shifts to 30 hPa in a short period. However, it takes longer for the transition to shift from 30 hPa to 50 hPa than that from 10 hPa to 30 hPa, which takes almost one month. The average onset date of the South China Sea Summer Monsoon (SCSSM) is one of the earliest dates in Asia Summer Monsoon (ASM) system and it is much later than the transition dates in stratosphere. Therefore, TDI can be used as a pre-signal for monitoring and predicting ASM. Furthermore, there exists an obvious regional difference in the circulation transition, among which the transition dates at each level in Siberia is the earliest and that is relatively later in Bering Sea and Greenland. The inter-annual and inter-decadal features of the circulation transition dates in Northern Hemisphere and the aforementioned three different regions are quite apparent, turning from late to early and then to late again in the past 62 years. Particularly the circulation transition date in Northern Hemisphere and in Siberia shares some similarities in inter-annual and inter-decadal variations, for example, the time variation shows significant fluctuations, and both have a transition peak in 1975. The transition dates in Bering Sea and Greenland also have the similar features, for example, the time fluctuation is relatively small. Moreover, circulation transition dates vary with the height and region, but they all have a quasi-2-year, a quasi-3-to-6-year, a quasi-9-to-12-year or a quasi-21-to-24-year cycle which may have close connections with other members of the climate system.

**Key words**: stratosphere circulation; circulation transition date; climatic features

# Interdecadal Change of the Relationship Between the Tropical Indian Ocean Dipole Mode and the Summer Climate Anomaly in China*

ZHAO Shanshan[1†] (赵珊珊), ZHOU Tianjun[2](周天军), YANG Xiuqun[3](杨修群), ZHU Yimin[4](朱益民), TAN Yanke[4](谭言科), and SUN Xuguang[3](孙旭光)

1 *Division of Climate Impact Assessment, National Climate Center, Beijing* 100081

2 *State Key Laboratory of Numerical Modeling for Atmospheric Sciences and Geophysical Fluid Dynamics, Institute of Atmospheric Physics, Chinese Academy of Sciences, Beijing* 100029

3 *School of Atmospheric Sciences, Nanjing University, Nanjing* 210093

4 *Institute of Meteorology, PLA University of Science and Technology, Nanjing* 211101

(Received July 26, 2010)

**ABSTRACT**

The interdecadal change of the relationship between the tropical Indian Ocean dipole (IOD) mode and the summer climate anomaly in China is investigated by using monthly precipitation and temperature records at 210 stations in China and the NCEP/NCAR reanalysis data for 1957–2005. The results indicate that along with the interdecadal shift in the large-scale general circulation around the late 1970s, the relationship between the IOD mode and the summer climate anomaly in some regions of China has significantly changed. Before the late 1970s, a developing IOD event is associated with an enhanced East Asian summer monsoon, which tends to decrease summer precipitation and increase summer temperature in South China; while after the late 1970s, it is associated with a weakened East Asian summer monsoon, which tends to increase (decrease) precipitation and decrease (increase) temperature in the south (north) of the Yangtze River. During the next summer, following a positive IOD event, precipitation is increased in most of China before the late 1970s, while it is decreased (increased) south (north) of the Yangtze River after the late 1970s. There is no significant correlation between the IOD and surface air temperature anomaly in most of China in the next summer before the late 1970s; however, the IOD tends to increase the next summer temperature south of the Yellow River after the late 1970s.

**Key words:** tropical Indian Ocean dipole (IOD), summer climate anomaly in China, interannual variability, interdecadal change

**Citation:** Zhao Shanshan, Zhou Tianjun, Yang Xiuqun, et al., 2011: Interdecadal change of the relationship between the tropical Indian Ocean dipole mode and the summer climate anomaly in China. *Acta Meteor. Sinica*, **25**(2), 129–141, doi: 10.1007/s13351-011-0021-z.

## 1. Introduction

It is widely recognized that sea surface temperature (SST) in the tropical Indian Ocean features considerable variabilities. Observational analyses have identified two dominant modes in the SST variabilities in the tropical Indian Ocean. One is the uniform basin-wide mode closely associated with the El Niño/Southern Oscillation (ENSO) (Lanzante, 1996; Klein et al., 1999; Zhou et al., 2004; Tan et al., 2003), and the other is the so-called Indian Ocean dipole (IOD) mode (Saji et al., 1999; Webster et al., 1999). Like the ENSO cycle, the IOD mode is phase-locked to seasonal cycle, maturing in boreal autumn and decaying in winter and next spring (Saji and Yamagata, 2003). The relationship between the IOD mode and ENSO is quite complicated. Some scientists believed that the IOD mode is influenced by the ENSO (Allan

*Supported by the National Natural Science Foundation of China under Grant Nos. 40730953, 40523001, and 40905036, and National Public Welfare Research Fund of China under Grant Nos. GYHY200706005 and GYHY200806004.

†Corresponding author: zhaoss@cma.gov.cn.

(Chinese version published in Vol. 67, No. 4, 549–560, 2009)

©The Chinese Meteorological Society and Springer-Verlag Berlin Heidelberg 2011

et al., 2001; Xie et al., 2002; Krishnamurthy and Kirtman, 2003; Tan et al., 2004; Zhong et al., 2005), while others pointed out that it is independent of the ENSO (Yamagata et al., 2003; Qian et al., 2003). The IOD-related SST anomalies in the tropical Indian Ocean can exert significant impacts on the East Asian summer monsoon and associated summer climate anomaly in China. Numerical simulations have shown that the positive SST anomalies in the eastern tropical Pacific and Indian Ocean tend to weaken the East Asian and Indian summer monsoons (Zou and Liu, 2002). However, considering the possible independence of the IOD mode, we speculate that the impact of the IOD mode on the East Asian summer climate may be different from that of the ENSO. Therefore, it is of interest to probe into the role of the IOD mode in the East Asian climate variability.

Some observational analyses have revealed a significant relationship between the IOD mode and the summer precipitation anomaly in China. Xiao et al. (2002) documented that the East Asian trough appears to be weaker and the western Pacific subtropical high extends more southward, leading to more precipitation in South China but less in North China, when the IOD is in its positive phase. Li and Mu (2001) pointed out that, during a positive IOD phase, the anticyclone over the Tibet and the western Pacific subtropical high are weaker, while the South China Sea and Indian summer monsoons are enhanced, which can significantly influence the summer precipitation in South China. Tang and Sun (2005) showed that during a positive IOD phase, the convective activity over the Philippines is weakened and the East Asian summer monsoon is stronger with more precipitation in South China; while during a negative IOD phase, the atmospheric circulation is characterized by an opposite anomaly pattern with more precipitation between the Yellow and Yangtze River valleys. Numerical experiments have confirmed the observed impact of the IOD mode on the climate variability of China (Xiao et al., 2000; Yan and Zhang, 2004).

The global climate system experienced a remarkable interdecadal shift in the late 1970s. For example, the ENSO features different characteristics during the pre- and post–1970s (Wang, 1995; An and Wang, 2000), and the relationship between the ENSO and the summer climate variability in China has also changed (Torrence and Webster, 1999; Wang, 2002; Xu and Wang, 2000; Zhu and Yang, 2003). Under such a background interdecadal shift, the East Asian summer monsoon also exhibits significant interdecadal variations with a clear three-dimensional structure over East Asia (Yu and Zhou, 2007; Yu et al., 2004). An interdecadal cooling in the upper troposphere over East Asia is found, which tends to strengthen the westerlies south of the East Asian jet through an anomalous upper-level cyclone and to weaken the East Asian summer monsoon through an anomalous lower-level anticyclone (Yu et al., 2004; Li et al., 2005; Xin et al., 2006). The tropical Indian Ocean SST variability also experienced an interdecadal change in the late 1970s. The first Empirical Orthogonal Function (EOF) of the tropical Indian Ocean SST anomaly during autumn displays a uniform basin-wide mode during the pre-1970s, while a dipole mode during the post-1970s (Annamalai et al., 2005). It is therefore interesting to examine the relationship between the IOD mode and the summer climate anomaly in China under different decadal backgrounds.

## 2. Data and method

Monthly precipitation and surface air temperature records at 210 stations in China and the NCEP/NCAR monthly reanalysis data (Kalnay et al., 1996) are used in this study. All the data are taken for the common period 1957–2005 and band-filtered to retain interannual variability (from 12 mon to 8 yr). Following Saji et al. (1999), a so-called IOD index is defined as the area-averaged SST anomaly in the tropical western Indian Ocean (10°S–10°N, 50°–70°E) and in which the SST anomaly in the tropical southeastern Indian Ocean (10°S–0°, 90°–110°E) is subtracted. The IOD index is calculated for September–November

(autumn), and the precipitation and temperature anomalies are computed for June–August (summer). The sliding correlation in a moving window with a 21-yr width is used to reveal the relationship between the IOD mode and the summer climate interannual variability in China. The composite analysis is used to examine typical summer atmospheric circulation anomalies over East Asia for positive and negative IOD events under different interdecadal backgrounds, respectively.

## 3. Relationship between IOD and summer climate anomaly in China

### *3.1 Summer climate anomaly and autumn IOD index*

Figure 1 shows the spatial distributions of the sliding correlations between the summer precipitation anomalies in China and the autumn IOD index on the interannual timescale. During 1957–1977 (Fig. 1a), a striking feature is that the summer precipitation

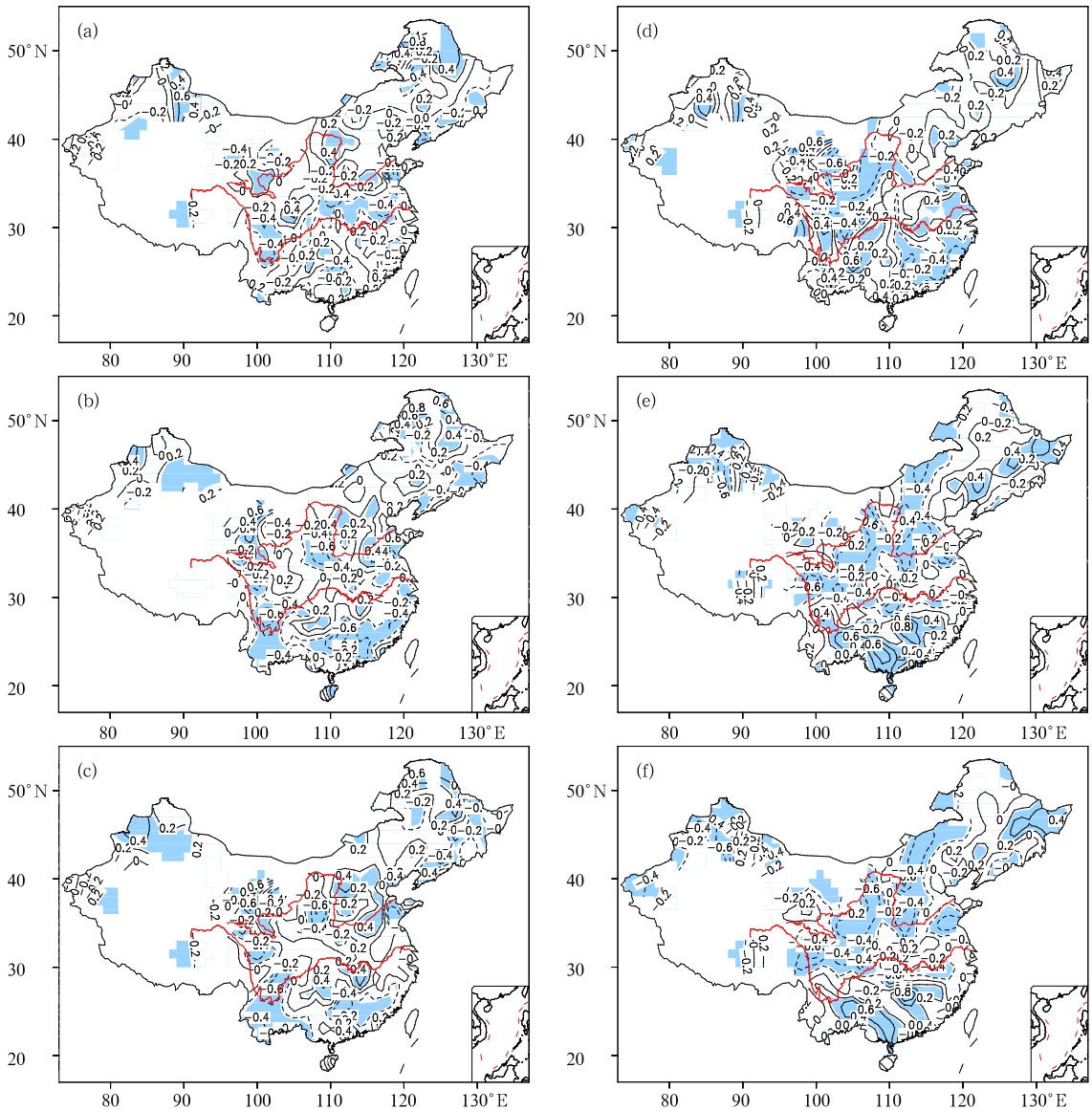


**Fig. 1.** The sliding correlation coefficients between the summer precipitation anomalies in China and the autumn IOD index for (a) 1957–1977, (b) 1962–1982, (c) 1967–1987, (d) 1972–1992, (e) 1977–1997, and (f) 1982–2002. Shadings indicate areas with the confidence level larger than 95%.

anomalies in most of China are negatively correlated with the IOD index, while the precipitation anomalies in northern Xinjiang Autonomous Region and northwestern Heilongjiang Province are positively correlated with the IOD index. During 1982–2002 (Fig. 1f), significant negative correlations are located in the north of the Yangtze River valley, especially in North China and the eastern part of Northwest China, while positive correlations are found in South China and eastern part of Northeast China. This is consistent with the result of Xiao et al. (2002). It can be seen from Figs. 1a–f that the summer precipitation anomalies between the Yangtze River and Huanghe valley are consistently negatively correlated with the IOD index. There is an obvious interdecadal change from the significant negative to positive correlation in South China. The spatial pattern of the interannual correlation changed significantly in the late 1970s (Fig. 1e).

In order to further investigate the inderdecadal change in the sliding correlations shown above, the regions with significantly changing correlations are selected and the sliding correlations between the summer precipitation anomalies averaged over these regions

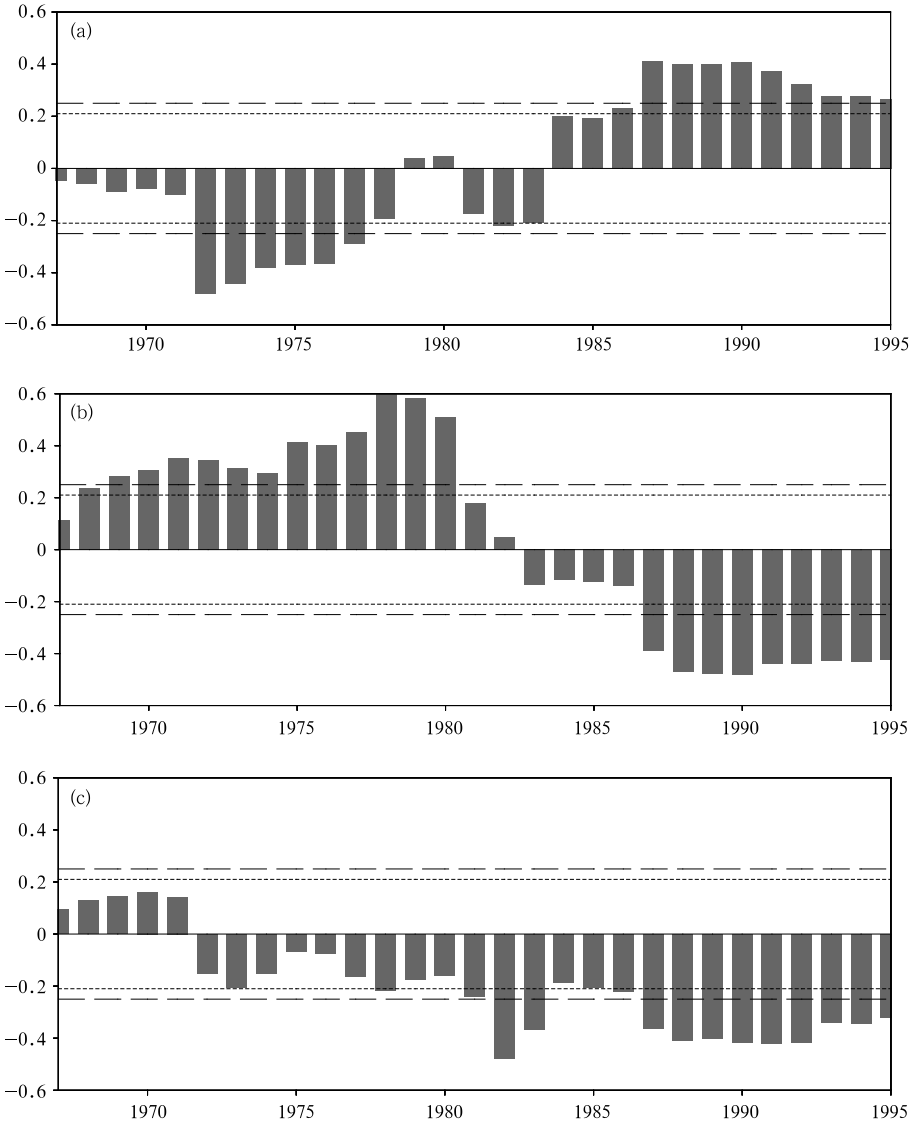


**Fig. 2.** The time series of the sliding correlation between the autumn IOD index and the summer precipitation anomalies averaged over (a) South China, (b) northern Xinjiang, and (c) Hetao. The dotted and dashed lines indicate confidence levels more than 90% and 95%, respectively.

and the autumn IOD index are calculated. Three regions are selected to denote South China (21 stations within 20°–27°N, 105°–120°E), northern Xinjiang (9 stations), and Hetao (10 stations within 35°–42°N, 104°–110°E), respectively. Figure 2 shows the time series of the sliding correlations for the three selected regions. It can be seen that the correlations between the IOD index and summer precipitation anomalies in South China changed significantly from negative values to positive ones around the end of 1970s (Fig. 2a), while those in northern Xinjiang changed in an opposite way (Fig. 2b). The IOD index exhibits significant negative correlations with summer precipitation anomalies in the Hetao area since the 1980s (Fig. 2c). Overall, the relationships between IOD index and summer precipitations in China changed significantly around the end of 1970s. Afterwards, the correlations tends to strengthen.

Similarly, the sliding correlations between the summer air temperature anomalies and the autumn IOD index are calculated to examine the impact of the IOD on the summer air temperature anomalies in China under different interdecadal backgrounds (Fig. 3). The IOD mode exhibits little impact on the sum-

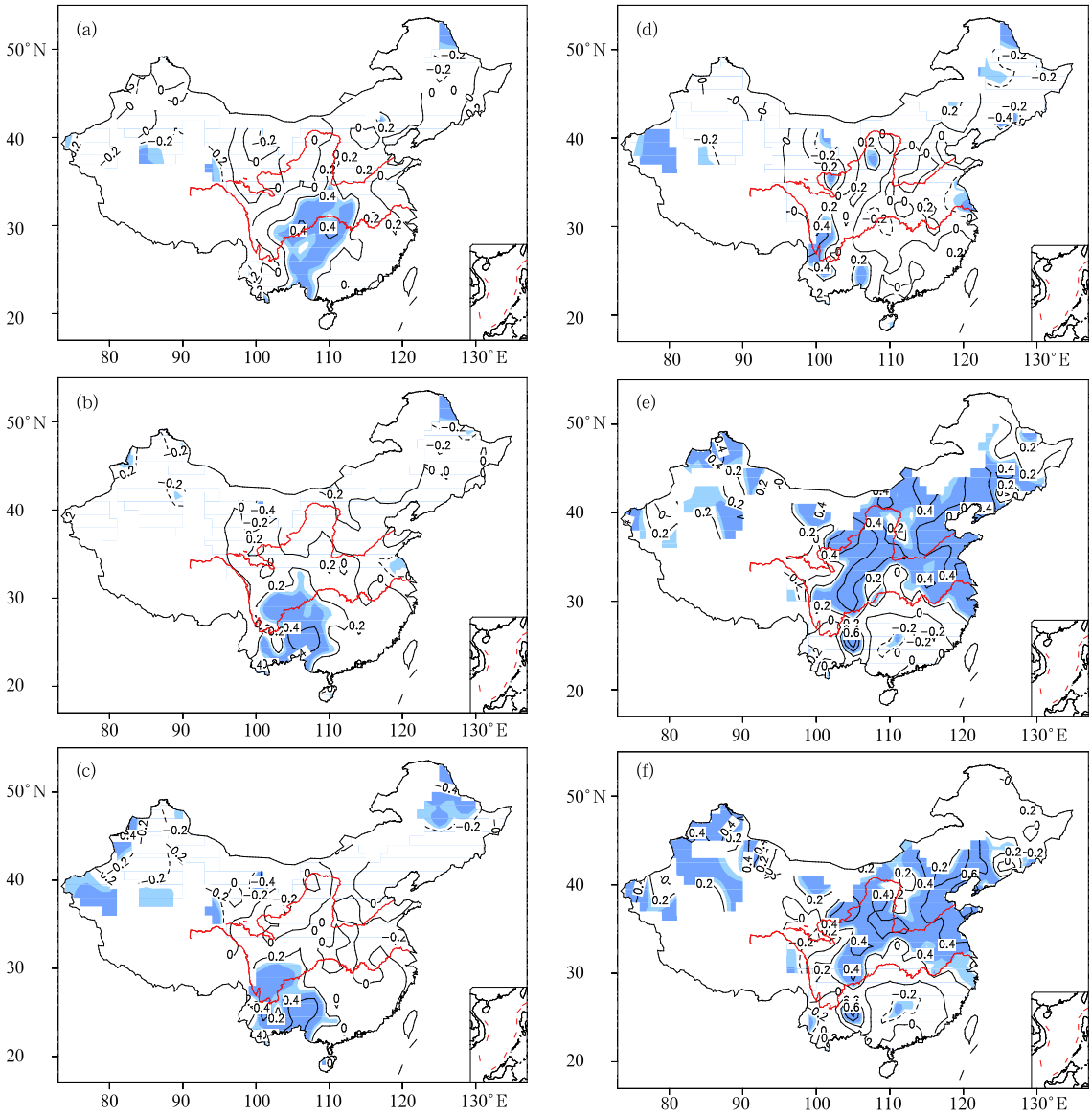


**Fig. 3.** As in Fig. 1, but for temperature anomalies.

mer temperature anomalies in most of China except the eastern part of Southwest China during 1957–1977 (Fig. 3a). During 1982–2002 (Fig. 3f), the IOD is positively correlated with the summer temperature anomalies north of the Yangtze River valley while negatively correlated with those south of the Yangtze River valley. The summer temperature anomalies in Sichuan Province have robust positive correlations with the IOD (Figs. 3a–f). However, there is a change from significant negative to positive correlations in the northern Xinjiang Autonomous Region, while there is a significant change from positive correlations to negative ones in South China. The relationships between the IOD and the summer temperature anomalies are significantly changed in the 1970s (Fig. 3e). Yan and Zhang (2004) also found that the summer air temperature anomalies in northwestern China are higher than normal, especially in Xinjiang, while lower in South China during a positive IOD phase.

Similar to Fig. 2, we select two representative regions: Sichuan basin (17 stations within 28°–34°N, 99°–110°E) and northern Xinjiang. It can be seen that the IOD index has persistent positive correlations with the summer temperature anomalies in Sichuan basin (Fig. 4a), except during a period of early 1980s when correlations are not significant. The correlations in northern Xinjiang changed from negative values to positive ones at the beginning of 1980s and the correlations tend to be significant since 1987 (Fig. 4b). Overall, the correlations between the IOD index and the summer temperature anomalies in both Sichuan basin and northern Xinjiang changed significantly at the end of 1970s.

### *3.2 Autumn IOD index and next-summer climate anomaly*

The sliding correlations between the autumn IOD index and the next summer precipitation anomalies in China are shown in Fig. 5. During 1957–1977, the precipitation anomalies in most parts of China (mainly South China and northern Southwest China) are positively correlated with the IOD, while negatively correlated in Northeast China and northern Xinjiang

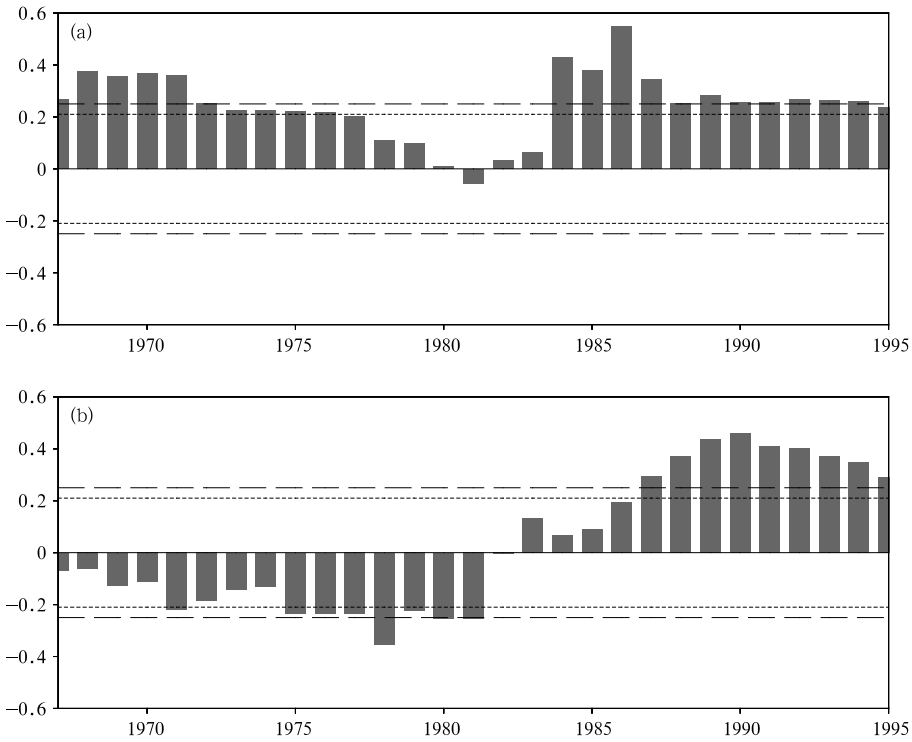


**Fig. 4.** As in Fig. 2, but for summer temperature anomalies over (a) Sichuan basin and (b) northern Xinjiang.

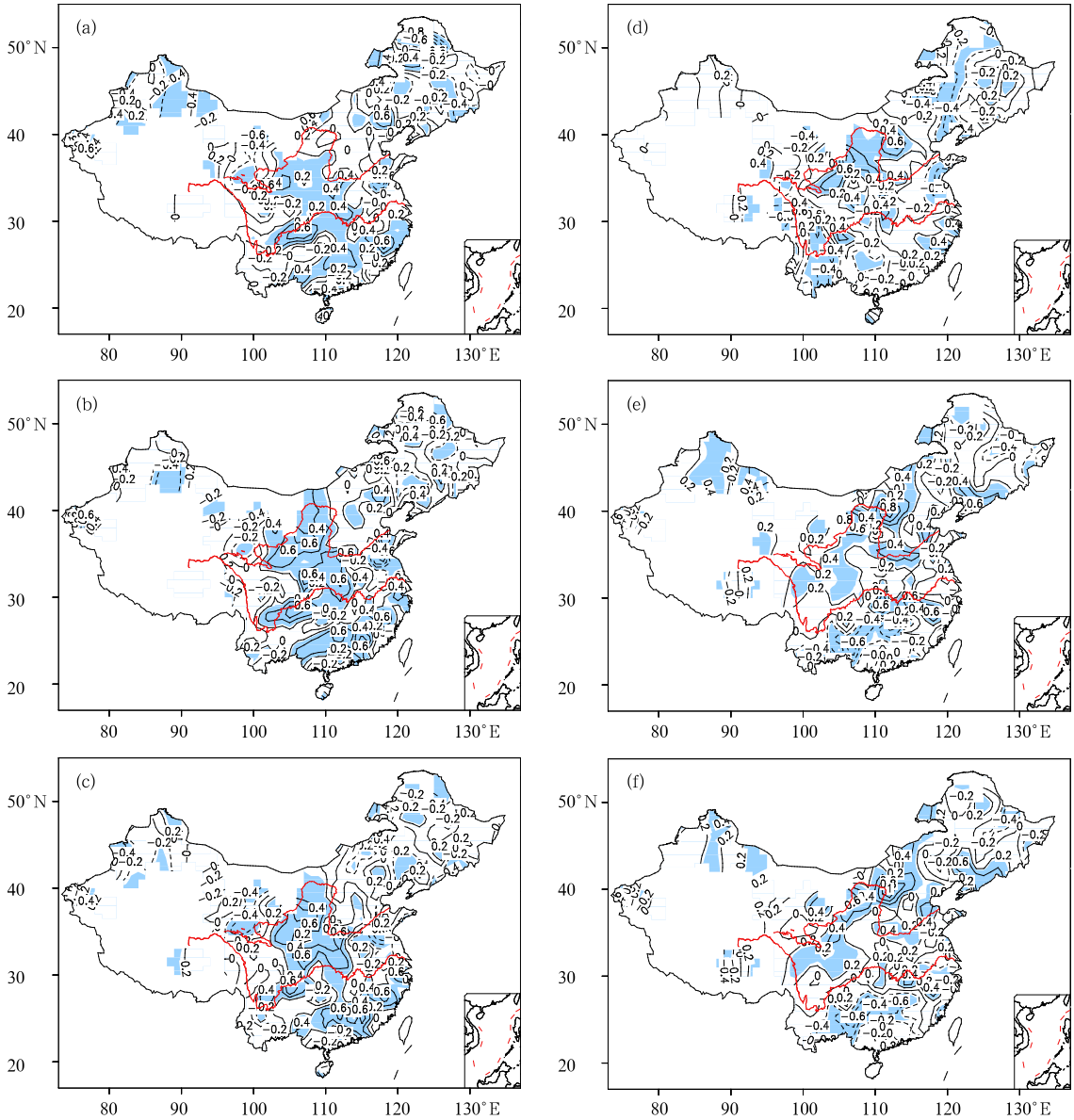


**Fig. 5.** The sliding correlation coefficients between the autumn IOD index and the next summer precipitation anomalies in China for (a) 1957–1977, (b) 1962–1982, (c) 1967–1987, (d) 1972–1992, (e) 1977–1997, and (f) 1982–2002. Shadings indicate areas with the confidence level larger than 95%.

(Fig. 5a). During 1982–2002, the precipitation anomalies are positively correlated with the IOD in the north of the Yangtze River valley while negatively correlated in the south (Fig. 5f). This pattern is opposite to that shown in Fig. 1f. The sliding correlations (Figs. 5a–f) show that the positive correlations are interdecadally weakened in eastern Northwest China and northeastern Southwest China. There is a significant interdecadal change from positive to negative correlation in South China while an opposite change in northern Xinjiang. Therefore, the relationship between the IOD and the next summer precipitation anomalies had a significant change from the late 1970s to the early 1980s (Figs. 5b and 5e).

During 1957–1977, the correlations between the IOD index and the next summer air temperature

anomalies are negative in the Hetao area and Sichuan Province while positive in northern Xinjiang. However, there is no significant correlation in other regions of China (Fig. 6a). The summer air temperature anomalies south of the Yellow River valley are positively correlated with the IOD during 1982–2002 (Fig. 6f). During 1957–2002, there is no persistent significant correlation in most parts of China. The correlations are weakened from the late 1970s to the early 1980s (Fig. 6d). Consequently, the relationship between the IOD and the next summer air temperature anomalies in China is not robust. The IOD mainly exerts its impact on those in South China since the late 1970s.

Hence, the above analyses suggest that the IOD exerts more impacts on the next summer precipitation than on air temperature anomalies. Since the early 1980s, a positive IOD event has been related to less precipitation and higher air temperature in the next summer in South China.

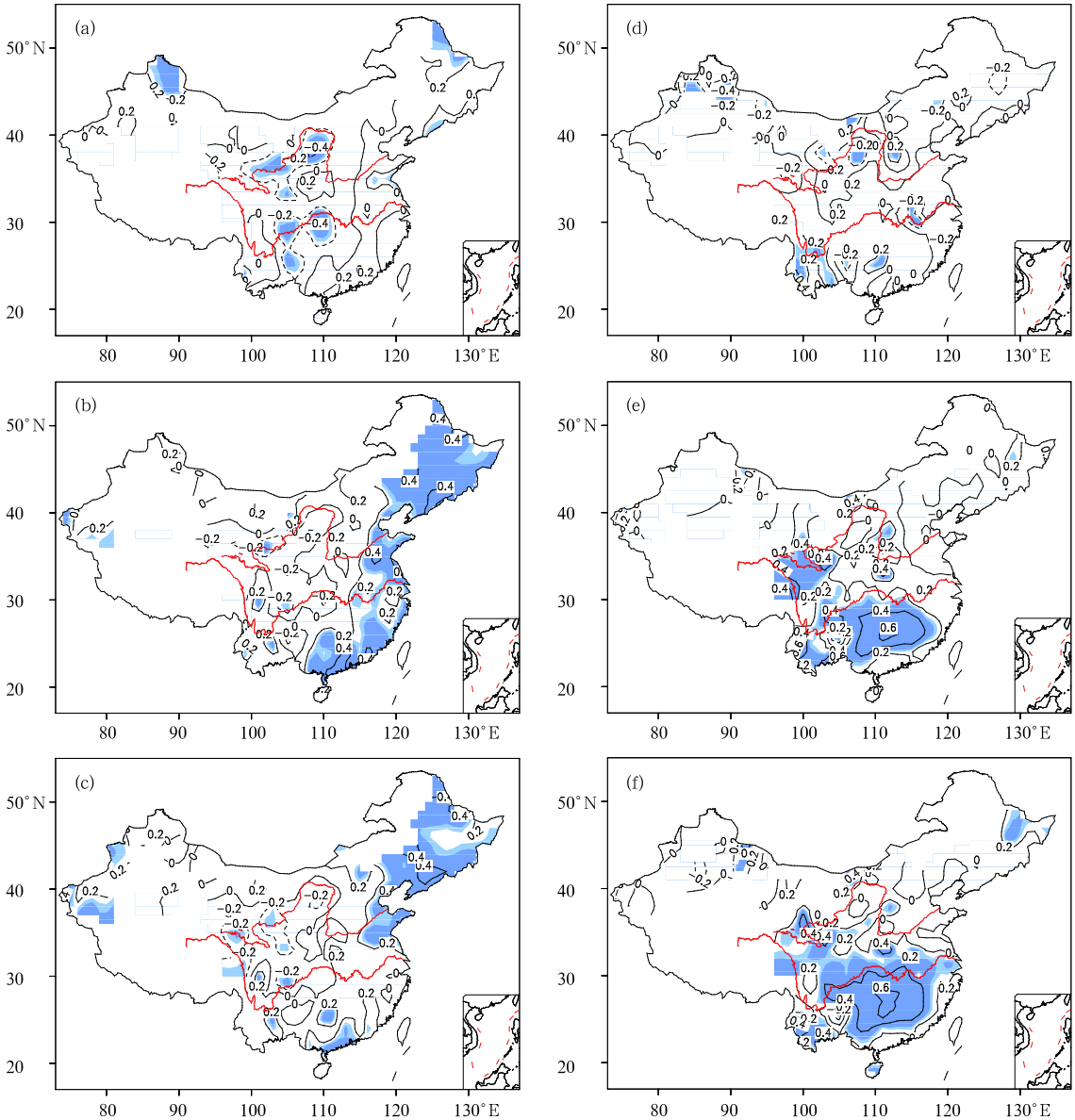


**Fig. 6.** As in Fig. 5, but for temperature anomalies.

## 4. IOD-related summer atmospheric circulation anomaly over East Asia

### *4.1 During the same year*

In order to understand the possible physical mechanism responsible for the IOD-related atmospheric circulation anomalies for different interdecadal epoches, composites in terms of 9 positive IOD events (1961, 1963, 1967, 1972, 1977, 1982, 1994, 1997, and 2003; Saji et al., 2003; Yamagata et al., 2003) during the pre- and post-1970s are made, respectively.

The summer atmospheric circulation anomalies over East Asia for positive IOD events during the pre- and post-1970s are shown in Fig. 7. During the pre-1970s, the composite 200-hPa geopotential height is anomalously positive over the tropical Indian Ocean and negative over the Tibetan Plateau (Fig. 7a). This indicates that the South Asian high is weakened when the geopotential height over North China, Northeast China, and Inner Mongolia is strengthened. The pos-

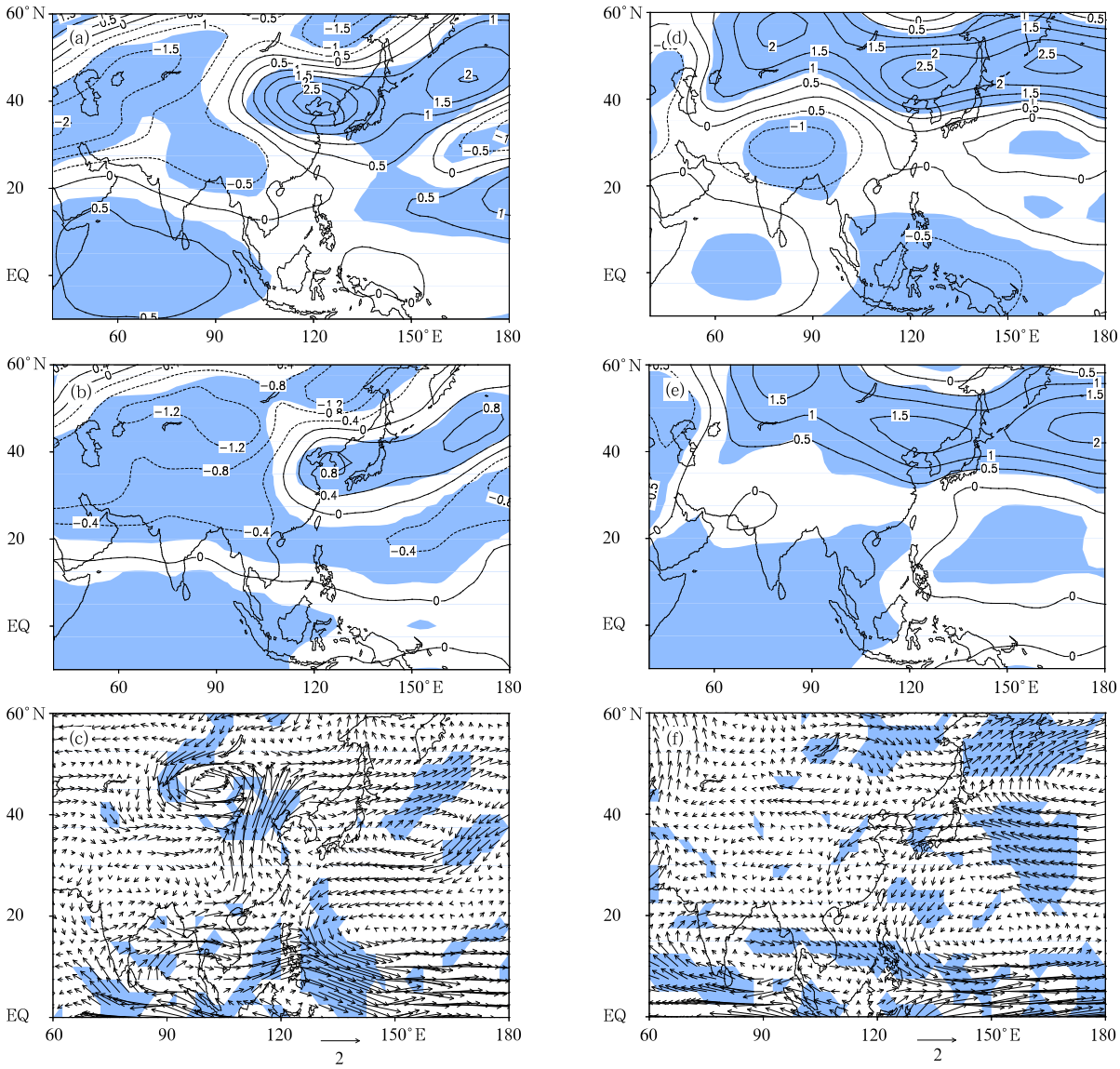


**Fig. 7.** Composite anomalies of summer 200- (a, d; gpm) and 500-hPa (b, e; gpm) geopotential height, and 850-hPa wind (c, f; m $s^{-1}$) over East Asia in the developing phase of a positive IOD event during (a–c) 1957–1977 and (d–f) 1978–2005. Shadings indicate areas with the 95% confidence level.

itive 500-hPa geopotential height anomalies (Fig. 7b) are found over the region from North China to Japan and over the tropical Indian Ocean. There are southeasterly anomalies over the equatorial Indian Ocean, westerly anomalies over the region from South Asia to Southeast Asia, and southerly anomalies over entire eastern China (Fig. 7c). An anomalous anticyclonic circulation stretches from the Bay of Bengal to Indochina Peninsula, an anomalous anticyclonic circulation occupies east of Japan, an anomalous cyclonic circulation resides over the tropical western Pacific, and an anomalous cyclonic circulation appears over Mongolia. The Indian monsoon, South China Sea monsoon, and East Asian monsoon are all strengthened.

Compared to the period 1957–1977, the summer atmospheric circulation anomalies related to the positive IOD events during 1978–2005 exhibit an obvious change over East Asia. As shown in Fig. 7d, at 200 hPa, there are positive geopotential height anomalies extending from North China to Japan and over the tropical Indian Ocean, while an anomalous cyclonic circulation exists over the Tibetan Plateau. At 500 hPa (Fig. 7e), positive geopotential height anomalies exist from the Lake of Balkhash to Sea of Okhotsk and negative anomalies exist over the tropical western Pacific. The South Asian high is much more weakened (Fig. 7d) than during the previous epoch (Fig. 7a). At 850 hPa (Fig. 7f), the wind anomalies in the tropical regions are similar to those in Fig. 7c. The tropical monsoon is enhanced. However, the distinction of Fig. 7f from Fig. 7c is that there are northerly anomalies over eastern China, which is indicative of weakening of the East Asian summer monsoon. This is why there is increase of summer precipitation in South China during the post-1970s (Figs. 1e and 1f).

The above analyses suggest that during the developing phase of an IOD event, summer atmospheric circulation anomalies over East Asia are considerably different during the pre- and post-1970s. During the epoch before 1977, a developing IOD event is associated with an enhanced East Asian summer monsoon, inducing southerly anomalies in eastern China and more precipitation in North China and high temperature in eastern Southwest China. During the epoch after 1977, a developing IOD event is associated with a weakened East Asian summer monsoon, inducing northerly anomalies in eastern China, more precipitation in South China and high temperature in North China.

### *4.2 During the next summer*

During 1958–1978, the connections between the IOD events and the next summer atmospheric circulation anomalies are overall weak. The 200-hPa geopotential height (Fig. 8a) is anomalously high over the region from eastern Lake Baikal to western Japan, and over the tropical western Pacific. There exists an anomalous anticyclonic circulation over the region from eastern Lake Baikal to western Japan. The 500-hPa geopotential height (Fig. 8b) anomalies are positive from Northeast China to eastern Japan, and the northwestern Pacific subtropical high is strengthened. At 850 hPa (Fig. 8c), the southeasterly anomalies from the tropical western Pacific affect China. During 1977–2005, the relationship between the IOD and the atmospheric circulation anomaly in the next summer is relatively strong. At 200 hPa (Fig. 8d), the South Asian high is stronger and located more westward. An anomalous cyclonic circulation is dominant over South China, and an anomalous anticyclonic circulation extends from North China to Japan. The western Pacific subtropical high is stronger and shifts westward (Fig. 8e). At 850 hPa (Fig. 8f), the easterly anomalies are found to stretch from the tropical western Pacific to east of India. The tropical summer monsoon is weakened. The northwestern Pacific subtropical high is strengthened and located more westward, which favors less precipitation in South China.

The above analyses indicate that the IOD impacts the next summer climate anomaly in China through changing the atmospheric circulations over East Asia. During 1957–1976, a positive IOD event causes southerly anomalies over South China, Hetao area, and Sichuan Province, inducing more precipitation in those regions in the next summer. During 1977–2005, a positive IOD event leads to an enhanced South Asian high and an enhanced western Pacific subtropical high, resulting in less precipitation in

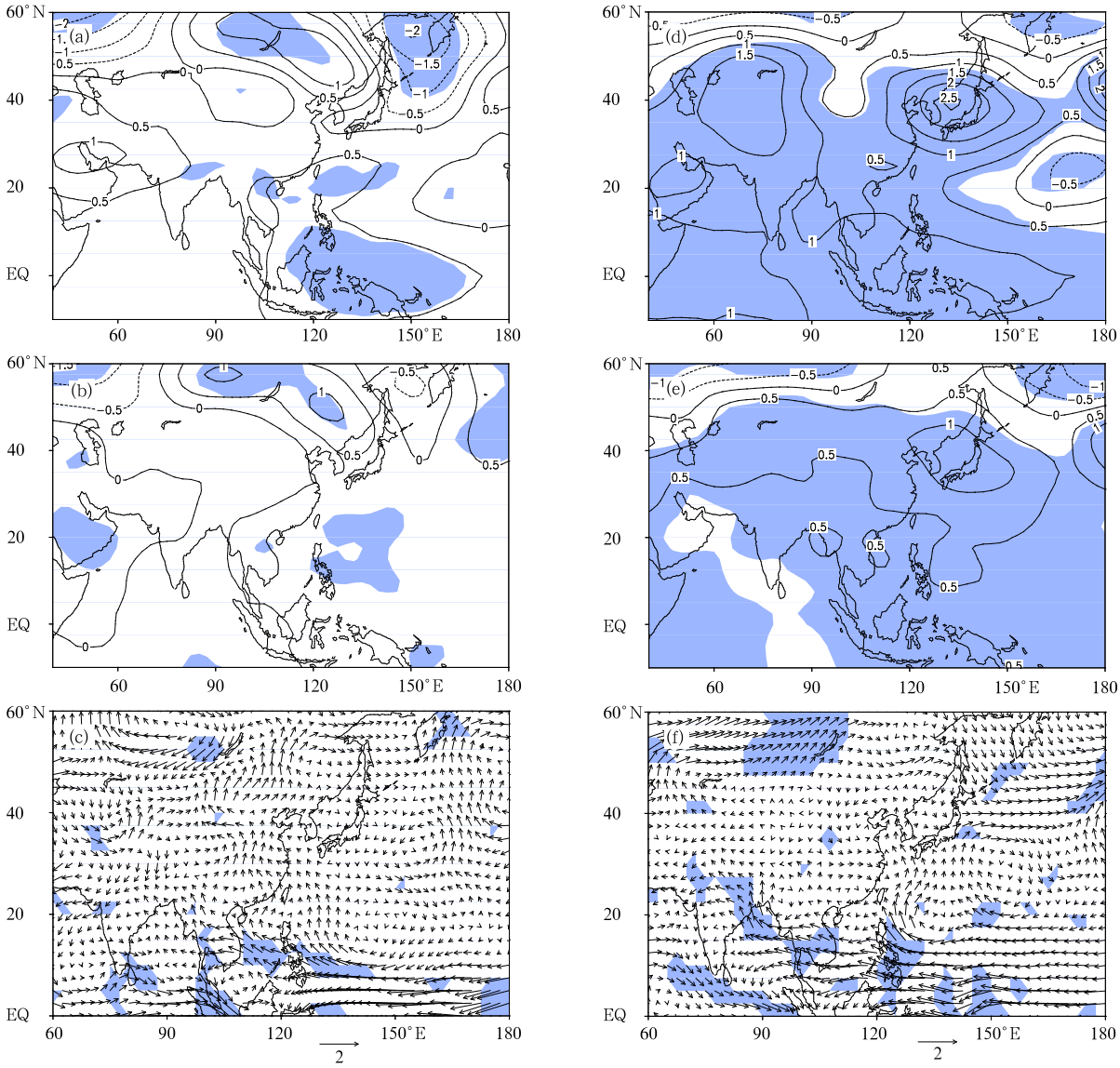


**Fig. 8.** Composite anomalies of summer 200- (a, d; gpm) and 500-hPa (b, e; gpm) geopotential height, and 850-hPa wind (c, f; m $s^{-1}$) over East Asia in the following summer of a positive IOD event during (a–c) 1957–1977 and (d–f) 1978–2005. Shadings indicate areas with the 95% confidence level.

South China.

## 5. Summary

The interdecadal change of the relationship between the IOD mode and the summer climate anomaly in China is documented by using sliding correlation and composite analysis methods based on the monthly precipitation and temperature records at 210 stations in China and the NCEP/NCAR reanalysis data during 1957–2005. The results reveal that such a relationship is robust in some regions, but features interdecadal changes in other regions. The robust relationship manifests mainly in the significant negative correlations between the IOD and the summer precipitation anomaly in the Yangtze River and Yellow River valleys, positive correlations between the IOD and the summer air temperature anomaly in Sichuan, and positive correlations between the IOD and the next summer precipitation anomaly in Sichuan. However, under the interdecadal shift of the large-scale general circulation in the late

1970s, the relationship between the IOD and the summer climate anomaly of China is changed. Before the late 1970s, a developing IOD event tends to decrease summer precipitation in most parts of China and increase temperature in Southwest China, while after the late 1970s, it tends to increase (decrease) precipitation and decrease (increase) temperature in the south (north) of the Yangtze River. During the next summer following a positive IOD event, the precipitation increases in most of China before the late 1970s, while it decreases (increases) in the south (north) of the Yangtze River after the late 1970s. There is no significant correlation between the IOD and the surface air temperature anomaly in most of China in the next summer before the late 1970s. However, the IOD tends to increase the next summer air temperature south of the Yellow River after the late 1970s.

The significant difference in the IOD-related atmospheric circulation anomalies in East Asia between the two interdecadal epoches is responsible for the change of the interannual relationship between the IOD and the summer climate anomaly in China. Before the late 1970s, a developing IOD event tends to enhance the Indian summer monsoon, South China Sea summer monsoon, and East Asian summer monsoon, which leads to less precipitation in South China but more precipitation in western North China. After the late 1970s, a developing IOD event is associated with an enhanced tropical summer monsoon but a weakened East Asian summer monsoon, which results in more precipitation in South China. During the next summer following a positive IOD event, before the late 1970s, southerlies prevail over South China, Hetao area, and Sichuan Province, inducing more precipitation, while after the late 1970s, the South Asian high and the northwestern Pacific subtropical high are stronger and extend westward, causing deficient precipitation in South China.

The interdecadal change of the relationship between the IOD and the summer climate anomaly in China may be influenced by the interdecadal variations of the IOD itself and the East Asian summer monsoon. The global climate system, especially in the Indo-Pacific sector, has experienced a significant interdecadal shift in the late 1970s (Wang, 1995; An and Wang, 2000; Torrence and Webster, 1999; Wang, 2002). Therefore, the interdecadal change of the relationship between the IOD and the summer climate anomaly in China may be closely related to the interdecadal climate variation of the global climate system. The detailed mechanism responsible for these facts revealed in this study needs to be further investigated by using full air-sea coupled general circulation model in the future.

## REFERENCES

Allan, R. J., D. Chambers, W. Drosdowsky, et al., 2001: Is there an Indian Ocean dipole independent of the El Niño-Southern Oscillations? CLIVAR exchanges, International CLIVAR Project Office, Southampton, United Kingdom, **6**, 18–22.

An, S. I., and B. Wang, 2000: Interdecadal change of the structure of the ENSO mode and its impacts on the ENSO frequency. *J. Climate*, **13**, 2044–2055.

Annamalai, H., S. P. Xie, and J. P. McCreary, 2005: Impact of Indian Ocean sea surface temperature on developing El Niño. *J. Climate*, **18**, 302–319.

Kalnay, E., M. Kanamitsu, R. Kistler, et al., 1996: The NCEP/NCAR 40-year reanalysis project. *Bull. Amer. Meteor. Soc.*, **77**, 437–472.

Klein, S. A., B. J. Soden, and N. C. Lau, 1999: Remote sea surface variations during ENSO: Evidence for a tropical atmospheric bridge. *J. Climate*, **12**, 917–932.

Krishnamurthy, V., and B. P. Kirtman, 2003: Variability of the Indian Ocean: Relation to monsoon and ENSO. *Quart. J. Roy. Meteor. Soc.*, **129**, 1623–1646.

Lanzante, J., 1996: Lag relationships involving tropical sea surface temperatures. *J. Climate*, **9**, 2568–2578.

Li, C. Y., and M. Q. Mu, 2001: The influence of the Indian Ocean dipole on atmospheric circulation and climate. *Adv. Atmos. Sci.*, **18**, 831–843.

Li, J., R. C. Yu., T. J. Zhou, et al., 2005: Why is there an early spring cooling shift downstream of the Tibetan Plateau. *J. Climate*, **18**, 4660–4668.

Qian Haifeng, Yin Yonghong, and Ni Yunqi, 2003: Tropical Indian Ocean subsurface dipole mode and diagnostic analysis of the dipole event in 1997/1998. *J. Appl. Meteor. Sci.*, **14**, 129–139. (in Chinese)

Saji, N. H., B. N. Goswami, P. N. Vinayachandran, et al., 1999: A dipole mode in the tropical Indian Ocean. *Nature*, **401**, 360–363.

——, and T. Yamagata, 2003: Structure of SST and surface wind variability during Indian Ocean dipole mode events: COADS observations. *J. Climate*, **16**, 2735–2751.

Tan Yanke, Zhang Renhe, and He Jinhai, 2003: Features of the interannual variation of sea surface temperature anomalies and the air-sea interaction in tropical Indian Ocean. *Chinese J. Atmos. Sci.*, **27**, 53–66.

——, Zhang Renhe, He Jinhai, et al., 2004: Relationship of the interannual variations of sea surface temperature in tropical Indian Ocean to ENSO. *Acta Meteor. Sinica*, **62**, 831–840. (in Chinese)

Tang Weidong and Sun Zhaobo, 2005: Effect of IOD on East Asian circulation and precipitation. *Journal of Nanjing Institute of Meteorology*, **28**, 316–322.

Torrence, P., and J. Webster, 1999: Interdecadal changes in the ENSO–monsoon system. *J. Climate*, **12**, 2679–2690.

Wang, B., 1995: Interdecadal changes in El Niño onset in the last four decades. *J. Climate*, **8**, 267–285.

Wang, H. J., 2002: The instability of the East Asian summer monsoon–ENSO relations. *Adv. Atmos. Sci.*, **19**, 1–11.

Webster, P. J., A. M. Moore, J. P. Loschnig, et al., 1999: Coupled ocean-atmosphere dynamics in the Indian Ocean during 1997-1998. *Nature*, **401**, 356–360.

Xiao Ziniu, Sun Jihua, and Li Congyin, 2000: A numerical simulation of the Indian Ocean SSTA influence on the early summer precipitation of the southern China during an El Niño year. *Chinese J. Atmos. Sci.*, **24**, 461–469.

——, Yan Hongming, and Li Congyin, 2002: The relationship between Indian Ocean SSTA dipole index and the precipitation and temperature over China. *Journal of Tropical Meteorology*, **18**, 335–344.

Xie, S. P., H. Annamalai, F. A. Schott, et al., 2002: Structure and mechanisms of south Indian Ocean climate variability. *J. Climate*, **15**, 867–878.

Xin, X. G., R. C. Yu, T. J. Zhou, and B. Wang, 2006: Drought in late spring of South China in recent decades. *J. Climate*, **19**, 3197–3206.

Xu Jianjun and Wang Dongxiao, 2000: Diagnosis of interannual and interdecadal variations in SST over Indian-Pacific Ocean and numerical simulation of their effect on Asian summer monsoon. *Acta Oceanologica Sinica*, **22**, 34–43.

Yamagata, T., S. Behera, S. A. Rao, et al., 2003: Comments on "Dipoles, temperature gradients, and tropical climate anomalies". *Bull. Amer. Meteor. Soc.*, **84**, 1418–1422.

Yan Xiaoyong and Zhang Ming, 2004: A study of the Indian Ocean dipole influence on climate variations over East Asian monsoon region. *Climatic and Environmental Research*, **9**, 435–444.

Yu, R. C., and T. J. Zhou, 2007: Seasonality and three-dimensional structure of the interdecadal change in East Asian monsoon. *J. Climate*, **20**, 5344–5355.

——, B. Wang, and T. J. Zhou, 2004: Tropospheric cooling and summer monsoon weakening trend over East Asia. *Geophysical Research Letters*, **31**, L22212, doi: 10.1029/2004GL021270.

Zhong, A., H. H. Hendon, and O. Alives, 2005: Indian Ocean variability and its association with ENSO in a global coupled model. *J. Climate*, **18**, 3634–3649.

Zhu Yimin and Yang Xiuqun, 2003: Relationships between Pacific decadal oscillation (PDO) and climate variabilities in China. *Acta Meteor. Sinica*, **61**, 641–654. (in Chinese)

Zhou Tianjun, Yu Yongqiang, Yu Rucong, et al., 2004: Indian Ocean response to ENSO: Observation and air-sea coupled model simulation. *Chinese J. Atmos. Sci.*, **28**, 357–373.

Zou Liyao and Liu Xuanfei, 2002: Numerical study on the effect of SSTA in the tropical Indian Ocean and Pacific on Asian summer monsoon. *Journal of Nanjing Institute of Meteorology*, **25**, 166–172.

第7卷 第2期 气候变化研究进展 Vol. 7 No. 2
2011年3月 ADVANCES IN CLIMATE CHANGE RESEARCH March 2011

文章编号：1673-1719 (2011) 02-0149-03

# 全球大风在减少吗?

# Is global Strong Wind Declining?

赵宗慈[1,2]，罗 勇[1,2]，江 滢[3]

(1 中国气象局国家气候中心，北京 100081；2 清华大学地球系统科学研究中心，北京 100084；3 中国气象局公共气象服务中心，北京 100081)

为了减缓全球变暖，使用清洁能源、发展低碳经济以及倡导绿色环保的呼声越来越高，其中风能资源的开发和利用成为各国关注的热点问题之一。与此同时，一些科学家对气候变化的研究着眼于与风能利用有关的全球风速和大风的变化，归结为以下几个问题。

## 1 全球近地面平均风速在减小吗?

总结大量研究文献，根据近50余年气象台站观测资料，计算全球、北半球或某个地区（或国家）年（或季）平均风速变化趋势，注意到中低纬度陆地风速有减小的趋势，高纬度及一些海洋区域风速有增大的趋势。表1给出最新的全球研究例证，其中前5行选择全球822个地面观测台站1979—2008年连续无间断的资料[1]，注意到风速明显减小的地区有中亚、东亚、东南亚－南亚、欧洲和北美，地面风速近30年已经下降了5%～15%，达到高显著性水平（$\alpha=0.05$）。这些计算结果与许多分区（或国家）的研究结果一致。为了提供更多的个例，表中还给出中国和澳大利亚的结果。大约7个关于中国近地面平均风速变化的研究表明，近50余年中国年和季近地面平均风速有明显减弱的趋势，尤以春季和西北地区减弱更明显[2-4]。

需要指出的是，一些基于再分析资料NCEP/NCAR近30年和ERA40近20年的计算表明，NCEP/NCAR资料并没有显示出上述地区近地层（10 m）年平均风速有任何明显减小趋势，ERA40资料只显示出近20年北美地区风速减小10%，欧洲减小50%，其他地区则没有明显趋势[1]。中国的研究注意到

表1 全球一些地区年平均风速减小例证（前5行资料长度为1979—2008年）

Table 1 Exemplifications on annual mean wind speeds decreased trends in some regions of the world (Length of the data for the first five rows is 1979–2008)

| 地区 | 站点数 | 风速变化 /((m/s)/10a) | 风速变化率 /(%/10a) |
|---|---|---|---|
| 欧洲（20°W～40°E，30°～75°N） | 276 | −0.09 | −2.9 |
| 中亚（40°～100°E，30°～75°N） | 96 | −0.16 | −5.9 |
| 东亚（100°～160°E，30°～75°N） | 190 | −0.12 | −4.2 |
| 东南亚－南亚（40°～160°E，0°～30°N） | 40 | −0.08 | −5.0 |
| 北美（170°～50°W，30°～75°N） | 170 | −0.07 | −1.8 |
| 中国（1956—2004年） | ＞500 | −0.12 | −5～−9 |
| 澳大利亚（1975—2006年） | 160 | −0.09 | −5 |

第一作者：赵宗慈（1940—），女，研究员，主要从事气候变化研究。E-mail: zhaozc@cma.gov.cn

NCEP/NCAR和ERA40资料（1956—2004年）显示出中国区域近地面年平均风速也有减小的趋势，分别是−0.12和−0.05 (m/s)/10a[2]。两套再分析资料和台站观测资料计算的全球年平均风速变化趋势的分布有如此大的差异，所得结论如此不同，这是因为地面观测资料受城市化影响，还是因为全球气候模式具有不确定性，或是什么其他原因，值得重视和进一步研究。

## 2　全球近地面大风强度在减弱且大风日数在减少吗？

有些研究表明，大多数地区近地面年平均风速的减小主要是由大风强度减弱和日数减少所致。注意到东亚、中亚、欧洲和北美风速超过 5 m/s的频数减小明显，即强风比弱风减小更明显，尤以东亚最突出[1]（见表2）。中国的研究验证了这一点，近50余年中国年和季的大风日数均呈减少趋势，尤以春季明显，最大风速和大风强度也有减弱趋势。另一方面还注意到，小风强度和日数有所增加。其他中低纬度国家和地区的研究也得到类似的结论[2]。

表2　1979—2008 年全球几个地区近地层风速超过某阈值的年频数变化（单位：%）

Table 2　Changes of annual frequency of wind exceeding a given threshold in some regions of the world for 1979−2008 (unit: %)

| 风速 /(m/s) | 欧洲 | 中亚 | 东亚 | 北美 |
|---|---|---|---|---|
| ≥ 1 | 0 | 0 | 2 | −1 |
| ≥ 3 | −1 | −6 | −4 | −2 |
| ≥ 5 | −5 | −13 | −10 | −4 |
| ≥ 7 | −7 | −18 | −15 | −5 |
| ≥ 9 | −11 | −23 | −19 | −3 |
| ≥ 11 | −12 | −24 | −23 | −3 |
| ≥ 13 | −11 | −22 | −30 | −3 |
| ≥ 15 | −12 | −23 | −37 | −11 |

注：风速≥ 1 m/s的年频数即指某年出现风速≥ 1 m/s的日数，以此类推。

## 3　全球大气整层的风速在减小吗？

全球许多地区近地面风速特别是大风在减小，全球大气整层风速是如何变化的呢？表3给出根据台站探空资料计算的全球几个区域各层风速变化趋势[1,5]，由表3可见，欧洲和北美除1000 hPa风速减小外，向上各层风速均呈明显增加的趋势。中亚和东亚则表现为500 hPa以下各层风速呈减小的趋势，其上呈增加趋势。中国则从地表到200 hPa风速都呈减小的趋势。近几十年大气整层风速的变化趋势在各个地区的差异如此之大，其原因何在？目前研究较少，需要进行更深入的研究。

表3　全球几个地区（国家）大气整层风速变化趋势（单位：(m/s)/10a）

Table 3　Linear trends of wind changes for troposphere and stratosphere in several regions of the world (unit: m/s per decade)

| 高度场 /hPa | 欧洲 | 中亚 | 东亚 | 北美 | 中国 |
|---|---|---|---|---|---|
| 1000 | −0.07 | −0.13 | −0.08 | −0.12 | −0.16 |
| 850 | 0.14 | −0.05 | −0.01 | 0.19 | −0.04 |
| 700 | 0.14 | −0.07 | −0.02 | 0.17 | −0.04 |
| 500 | 0.10 | −0.08 | −0.07 | 0.16 | −0.12 |
| 400 | 0.20 | −0.02 | 0.00 | 0.20 | −0.18 |
| 300 | 0.35 | 0.05 | 0.09 | 0.25 | −0.17 |
| 200 | 0.45 | 0.12 | 0.16 | 0.30 | −0.17 |

注：所用资料为台站探空资料。

## 4　全球风速变化的原因？

观测台站的风速资料显示，全球中低纬度陆地近几十年近地面平均风速和大风强度呈减小趋势，大风日数亦呈减少趋势，是什么原因造成全球中低纬度陆地风速减小？

(1) 与风速有关的大气环流的变化。计算表明近50年北半球温带气旋路径向高纬度方向移动，造成高纬度气旋增加和温带地区气旋减少的趋势，因此平均风速和大风日数在中纬度有减小、高纬度有增加的趋势，这是主因。一些针对东亚地区的研究还表明，近50年来年和冬、夏季亚洲经向环流指数有减弱的趋势，纬向环流指数有增强的趋势，东亚冬季风和夏季风都有减弱趋势，相应冬半年寒潮日数和沙尘暴日数明显减少，这些都引起年和各季平均风速和大风日数有减小的趋势。此外，近几十年西

www.climatechange.cn



北太平洋热带气旋和台风数减少也可能造成沿海平均风速有减小趋势[2,5]。持这种观点的研究给出，大气环流的变化能够解释风速减小的 10%～50%[6]。

(2) 下垫面变化。多数研究针对城市化影响，近几十年城区建筑增加很快，与此同时，高楼越来越多、越来越高[2−3,5]；同时，研究者也注意到土地利用的变化，如大面积植被森林生长和造林以及农业活动的变化[1]；另一方面是近些年全球大范围风电场的建立和运行发电对下游风速产生明显影响[6]。有些研究利用数值模式进行了定量计算模拟，由卫星与遥感观测记录得到北半球春季和夏季植被增加及森林覆盖增加和增高，利用中尺度模式MM5分别考虑北半球各个地区表面粗糙度增加，模拟的近地面风速有明显减小趋势，其数量级与观测值相当。另有一些研究集中于风电场对风速变化的定量影响，考虑 2100 年全球风能利用将占总能源的 10% 或更多，相应的全球风电场所占面积陆地为$58\times10^6$ km$^2$，沿岸海洋为$10\times10^6$ km$^2$。在此基础上设计几种试验，考虑风电场涡轮机不同的高度和旋转叶片不同的直径，相应表面摩擦力、粗糙度和拖曳系数的增加不同，利用 NCAR CCM3 模式计算得到，风电场对风速的影响是明显的，其大小取决于风电场的规模、发电能力以及高度。持这种观点的研究指出，近几十年下垫面粗糙度的增加能够解释风速减小的 25%～60%[6]。

(3) 人类排放增加导致的全球变暖对风速的影响。利用IPCC第四次评估报告的多模式，考虑人类排放增加情景（SRES A1B，中等排放），21 世纪未来全球继续变暖，相应海平面气压场两半球冬、夏季高纬度、极区、北美和欧亚大陆大部分地区气压减小，温带气旋路径向高纬度移动，中纬度海洋上气压增加，多数大气活动中心减弱，冬季风减弱，因此冬半年全球中纬度地区风速继续减弱。夏季风是增强还是减弱，不同模式结果差异较大[2]。因此，人类排放增加导致的全球变暖对全球风速变化的贡献尚需更深入的研究。

此外，风速变化是否存在准周期振荡或多年代际变率的研究尚未见到，但这也是需要考虑的问题。

对造成全球中低纬度陆地风速减小的原因的研究，关系到对未来全球风速变化的预测和预估以及风能的应用，因而成为国际研究的热点问题，需要引起我国的重视。■

## 参考文献


[1] Vautard R,Cattiaux J, Yiou P, *et al*. Northern Hemisphere atmospheric stilling partly attributed to an increase in surface roughness [J]. Nature Geoscience, 2010, 3: 17, doi: 10.1038/NGEO979

[2] Jiang Ying, Luo Yong, Zhao Zongci, *et al*. Changes in wind speed over China during 1956−2004 [J]. Theor Appl Climatol, 2010, 99: 421−430, doi 10.1007/s00704−009−0152−7

[3] Guo H, Xu M, Qi H. Changes in near-surface wind speed in China: 1969−2005 [J]. Int J Climatol, 2010, 30, doi:10.1002/joc.2091

[4] McVicar T R, van Niel T G, Li L T, *et al*. Wind speed climatology and trends for Australia, 1975−2006 [J]. Geophy Res Lett, 2008, 35, L20403, doi: 10.1029/2008GL035627

[5] 张爱英，任国玉，郭军，等. 1980 — 2006 年我国高空风速变化趋势分析 [J]. 高原气象，2009, 28 (3): 680−687

[6] Wang C, Prinn R G. Potential climate impacts and reliability of very large-scale wind farms [R]. MIT Joint Program on the Science and Policy of Global Change, 2009, 175: 1−21

科学通报 2011 年 第 56 卷 第 16 期：1301 ~ 1307
论 文 www.scichina.com csb.scichina.com
《中国科学》杂志社 SCIENCE CHINA PRESS

# 冬季澳大利亚东侧海温与长江流域夏季降水的联系及可能物理机制

周波涛

国家气候中心, 北京 100081
E-mail: zhoubt@cma.gov.cn

2011-01-04 收稿, 2011-03-23 接受
公益性行业(气象)科研专项(GYHY200906018)、国家自然科学基金(40805029)和国家重点基础研究发展计划(2009CB421407, 2010CB950304)资助

**摘要** 通过对观测资料的分析, 初步探讨了冬季澳大利亚东侧海温和夏季长江流域降水的关系及可能物理机制. 研究表明, 澳大利亚东侧冬季海温与我国长江流域夏季降水之间具有同位相变化关系. 当冬季澳大利亚东侧海温变暖时, 随后夏季西太平洋副热带高压和东亚西风急流位置往往偏南, 我国大陆沿岸低层盛行异常的西南风, 有利于长江流域降水增多, 反之亦然. 冬季澳大利亚东侧海温对后期夏季东亚大气环流的影响通过两种途径来实现: (ⅰ) 冬季澳大利亚东侧海温异常信号由于自身的持续性可维持到夏季, 并通过南北半球遥相关影响东亚夏季大气环流的变化; (ⅱ) 冬季澳大利亚东侧海温偏高时, 同期西南印度洋海温也易于偏高. 在海气相互作用下, 这种异常信号逐渐向东发展, 并造成夏季海洋大陆附近海温升高. 海洋大陆海温的升高反过来影响对流活动进而导致东亚夏季大气环流异常.

**关键词**
澳大利亚东侧海温
夏季降水
长江流域
遥相关
物理机制

我国地处东亚季风区, 受东亚夏季风活动的影响, 我国长江流域经常出现干旱或洪涝灾害, 给国民经济和人民生命财产造成严重损失. 因此, 开展夏季重大旱涝过程的成因分析和预测理论研究非常重要. 通过这方面的研究, 可以深入认识长江流域夏季降水的变化机理, 并为短期气候预测提供科学依据.

近 10 多年来, 气象工作者在影响长江流域夏季降水的前期信号及变化机理方面作了不少研究. 如, 龚道溢等人[1,2]分析了春季北极涛动变化对随后夏季长江流域降水的影响, 发现春季北极涛动偏强(弱)时, 夏季急流位置偏北(南), 长江流域降水偏少(多), 呈一种反位相变化关系. 王会军等人[3,4]的工作揭示, 春季欧亚中高纬大气环流异常在夏季东亚大气环流和降水变化中起着重要作用. 另外, 春季青藏高原积雪也与长江流域夏季降水具有密切联系. 春季青藏高原积雪增多可通过改变土壤湿度影响东亚夏季大气环流, 最终导致长江流域降水偏多[5]. Zhao 等人[6]还指出, 春季白令海和鄂霍茨克海海冰面积减少(增多)可使中国东部夏季降水量增加(减少). 周波涛等人[7,8]基于观测资料分析和数值模拟研究, 提出春季 Hadley 环流强度与夏季长江流域降水之间存在显著的正相关. 春季 Hadley 环流主要是通过影响印度洋-南海区域海温进而影响长江流域夏季降水异常. 此外, 一些研究还揭示, 北半球冬季 WA 遥相关型[9]、东亚冬季风[10,11]等的年际变化对夏季长江流域降水异常也具有明显的影响.

以上研究从不同角度揭示了影响长江流域夏季降水的北半球前期信号. 南半球作为季风发源地之

**英文版见**: Zhou B T. Linkage between winter sea surface temperature east of Australia and summer precipitation in the Yangtze River valley and a possible physical mechanism. Chinese Sci Bull, 2011, 56, doi: 10.1007/s11434-011-4497-9

一和全球气候系统变化的关键区，其大气环流异常也必然会导致东亚夏季风异常并影响长江流域旱涝. 研究表明，南极涛动作为南半球环流的主要模态，它的变动对东亚夏季风年际变化以及中国夏季降水变化具有重要影响[12~15]. 春季南极涛动增强时，长江流域夏季降水偏多，反之，春季南极涛动减弱时，长江流域夏季降水则偏少. 高辉等人[16]的研究还表明，5 月南极涛动加强会导致江淮出梅晚和梅雨期加长. 范可等人[17]将南极涛动作为一个显著的预测因子，建立了一个长江中下游夏季降水的物理统计预测模型. 此外，薛峰等人[12,18]还从年际尺度分析了春季南半球副热带高压(马斯克林高压和澳大利亚高压)的变化对长江流域夏季降水的影响，发现它们之间为显著的正相关，并且指出这种影响是通过改变西太平洋副热带高压等来实现的.

可见，南半球大气环流异常对东亚夏季风环流有显著影响，而海温的变化又会对南半球大气环流产生直接影响[19,20]. 例如，刘舸等人[20]的研究揭示澳大利亚东侧海温异常可以影响澳大利亚高压的变化. 当夏季澳大利亚东侧海温升高(降低)时，澳大利亚高压东移或东扩(西缩). 由于南北半球的相互作用主要是冬半球影响夏半球为主，那么，冬季澳大利亚东侧海温的变化是否对夏季东亚大气环流特别是长江流域降水存在影响？如存在，其中的物理过程又是什么？为此，基于前人工作，本文重点研究冬季澳大利亚东侧海温与长江流域夏季降水的关系，并探讨其中联系的物理机制.

## 1 资料

所用资料包括: (1) 美国国家环境预报中心/大气研究中心(NCEP/NCAR)的再分析资料[21]，水平分辨率为 2.5°×2.5°; (2) 美国国家海洋和大气局(NOAA)提供的海表温度(SST)[22]，水平分辨率为 2°×2°; (3) 中国 160 站的月降水总量资料. 研究所用的时间长度为 1951~2002 年. 文中冬季(DJF)指的是前一年 12 月和当年的 1 与 2 月，春季(MAM)和夏季(JJA)分别为当年 3~5 月和 6~8 月，季节划分均相对于北半球而言. 本文选取 6~8 月长江中下游的 17 站(南京、合肥、上海、杭州、安庆、屯溪、九江、汉口、钟祥、岳阳、宜昌、常德、宁波、衢县、贵溪、南昌、长沙)平均降水量作为长江流域夏季降水指数(YRRI)，以此表征长江流域夏季降水量的旱涝变化.

## 2 澳大利亚东侧冬季海温与长江流域夏季降水

图 1(a)是长江流域夏季降水与冬季 SST 的相关分布. 可见，澳大利亚东侧海区为显著的正相关，最大相关系数超过 0.4，揭示冬季澳大利亚东侧 SST 异常偏暖时，夏季长江流域降水往往偏多. 反之，冬季澳大利亚东侧 SST 异常偏冷时，夏季长江流域降水往往偏少. 为衡量澳大利亚东侧海区 SST 的变化，选取图 1(a)中显著相关区域平均的 SST 作为海温指数(EASST). 图 1(b)给出了冬季 EASST 与夏季 YRRI 的时间变化曲线. 如图所示，两者之间具有同位相变化特征(相关系数为 0.40，超过 99%的信度). 从图 1(b)还可以看到，冬季 EASST 和夏季 YRRI 在研究时段内都呈现线性增长的趋势. 扣除线性趋势后，冬季 EASST 和夏季 YRRI 之间的相关系数为 0.35，仍高于 95%的信度. 因此，冬季澳大利亚东侧 SST 与长江流域夏季降水在年际时间尺度上存在显著联系. 本文重点研究两者在年际时间尺度上的联系，所以在随后的分析中均扣除了线性趋势.

为了阐述澳大利亚东侧冬季 SST 和长江流域夏

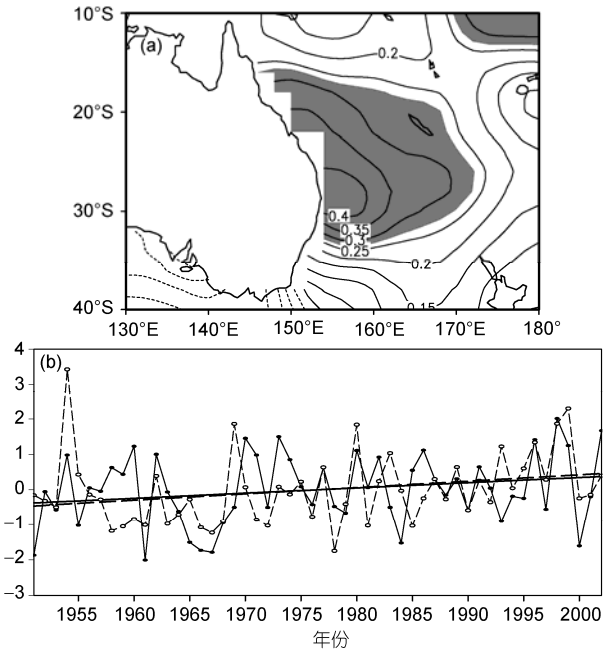


**图 1 长江流域夏季降水指数(YRRI)与冬季 SST 的相关(a)及夏季 YRRI(虚线)和冬季 EASST(实线)的标准化时间序列以及各自的趋势(b)**

阴影区表示通过 95%信度

季降水正相关关系背后的大尺度环流背景，分析了夏季低层水平风场分别与冬季 EASST 和夏季 YRRI 的回归分布(图 2). 图 2(a)显示，与 YRRI 相关联的 700 hPa 水平风场的变化特征为: 30°N 以南的西太平洋地区为异常的反气旋型环流，东亚热带季风槽区为东风异常，梅雨锋区为西风异常，指示夏季西太平洋副热带高压偏南. 另外，在我国东部沿岸盛行异常的西南风，有利于水汽从热带向中纬地区输送. 这种分布特征与张庆云等人[23]所得的结论相吻合. 他们的研究指出，西太平洋上 30°N 以南出现异常反气旋距平环流时，长江流域夏季降水偏多. 与冬季 EASST 相联系的低层风场的变化(图 2(b))与图 2(a)揭示的特征相类似. 即在西太平洋 30°N 以南地区同样存在异常的反气旋型环流，而且我国东部沿岸盛行异常的西南风气流. 这种分布型态说明，当澳大利亚东侧冬季 SST 异常升高(降低)时，随后夏季 30°N 以南的西太平洋地区会出现异常的反气旋型(气旋型)环流，西太平洋副热带高压偏南(北). 这种环流背景有(不)利于长江流域降水的发生，长江流域夏季降水因而增加(减少).

东亚西风急流的变化，尤其是急流位置的变化对长江流域夏季降水同样具有重要的影响. 当急流位置偏南(北)时，长江流域降水偏多(偏少)[24,25]. 这点可从夏季 200 hPa 纬向风与 YRRI 的回归分布图(图 3(a))上得到证实. 图 3(a)清楚地显示，与长江流域降水偏多相联系的高空大气环流特征表现为: 40°N 南北两侧分别为西风异常和东风异常，昭示西风急流位置偏南(西风急流中心的平均位置位于 40°N). 冬季 EASST 与夏季 200 hPa 纬向风的回归分布(图 3(b))表现出与图 3(a)相一致的特点. 即，当冬季 EASST 偏高时，40°N 以北区域为负值，高空西风减弱，40°N 以南区域为正值，高空西风加强. 因此，东亚西风急流位置较常年偏南，与这种环流特征相对应的正是我国长江流域降水偏多，再次印证了冬季澳大利亚东侧 SST 与夏季长江流域降水的正相关变化关系.

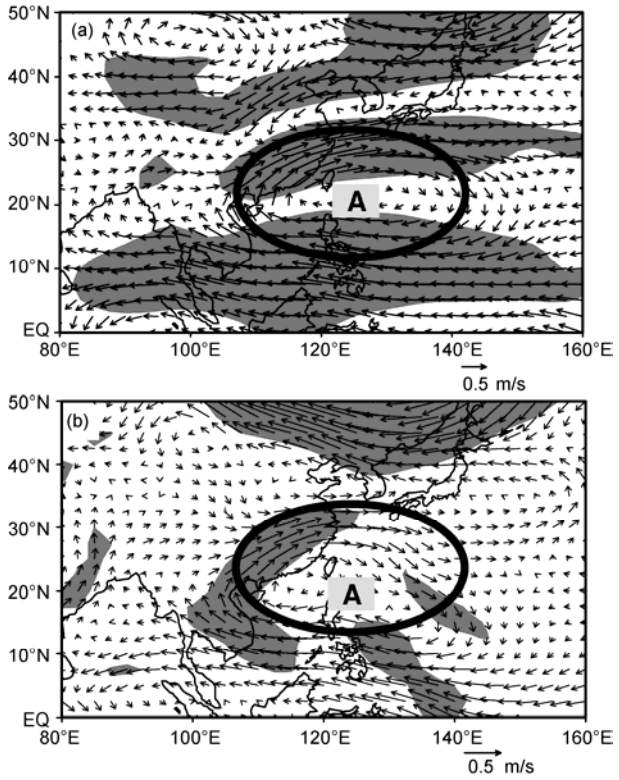


**图 2　夏季 700 hPa 水平风场与同期 YRRI (a)和冬季 EASST (b)的回归分布**

阴影区表示通过 95%信度; A 代表反气旋环流系统

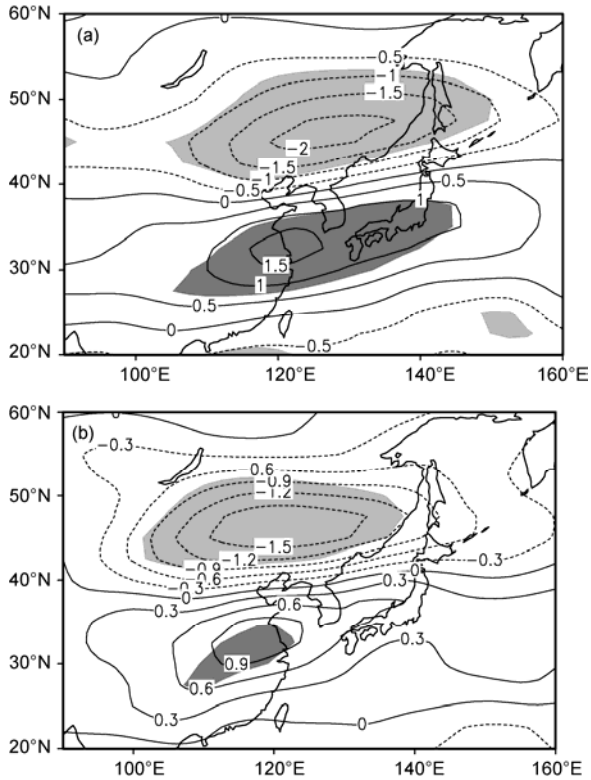


**图 3　夏季 200 hPa 纬向风(m/s)与同期 YRRI (a)和冬季 EASST (b)的回归分布**

阴影区表示通过 95%信度

## 3 可能的物理机制

从以上分析可知, 澳大利亚东侧冬季 SST 的变化可以影响后期夏季东亚大气环流系统, 从而导致我国长江流域夏季降水出现显著的年际波动. 那么, 冬季澳大利亚东侧 SST 是通过何种途径影响夏季东亚大气环流系统的? 其中具体的物理过程又是什么? 为回答这一问题, 分别计算了冬季 EASST 与同期以及后期春季和夏季 SST 的相关分布, 结果如图 4 所示. 从该图上可以看到两个明显的特征. 一个是澳大利亚东侧海温信号自身的持续性. 在澳大利亚东侧海域, 相关系数从冬季到夏季都为显著的正值, 而且是逐渐减小的. 另一个是南印度洋海温的发展和东传. 冬季, EASST 与西南印度洋 SST 具有显著的正相关, 随后, 正相关区域逐渐向东移动并在夏季位于海洋大陆上.

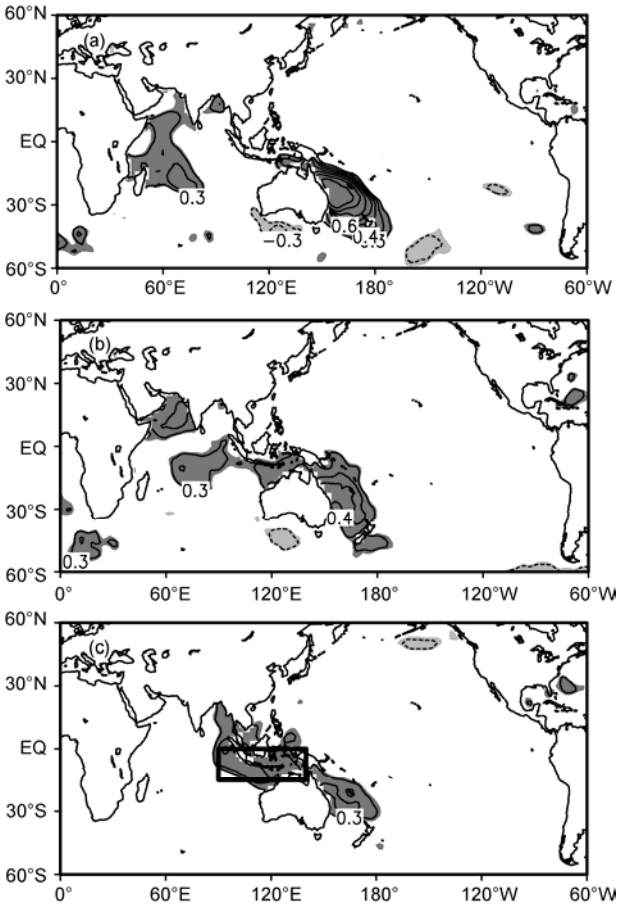


**图 4 冬季 EASST 与冬季(a)、春季(b)和夏季(c) SST 相关的空间分布**

阴影区表示通过 95%信度

因此, 澳大利亚东侧 SST 变化可能通过如下两种途径影响夏季大气环流和降水的变化. 当冬季澳大利亚东侧 SST 出现异常时, 一方面由于海温自身的记忆能力, 这种异常信号可以维持到夏季, 而夏季澳大利亚东侧的局地 SST 异常可以激发南北半球遥相关[26], 进而影响长江流域降水. 当夏季澳大利亚东侧 SST 偏高(低)时, 该区域位势高度偏高(低), 这种气压异常扰动通过 Rossby 波列传播到北半球副热带地区, 致使西太平洋副热带高压偏强(偏弱)并偏南偏西(偏北偏东), 结果造成长江中下游地区降水偏多(少)[20,26]. 另一方面, 当冬季澳大利亚东侧 SST 偏暖(冷)时, 同期西南印度洋 SST 也异常偏暖(冷). 该异常信号随后逐渐发展和向东移动, 并造成夏季海洋大陆区域 SST 异常, 最终影响夏季大气环流的变化. 夏季海洋大陆 SST 异常对同期大气环流的影响可由(90°~140°E, 0°~15°S)(如图 4(c)中矩形框所示)区域平均的 SST 与散度场的相关分布(图 5)得到佐证. 高层 150 hPa(图 5(a)), 海洋大陆基本上为显著的正相关, 而在西太平洋地区为显著的负相关. 低层 1000 hPa 的相关分布则相反, 在海洋大陆为显著的负相关, 在西太平洋地区为显著的正相关(图 5(b)). 这种相关分

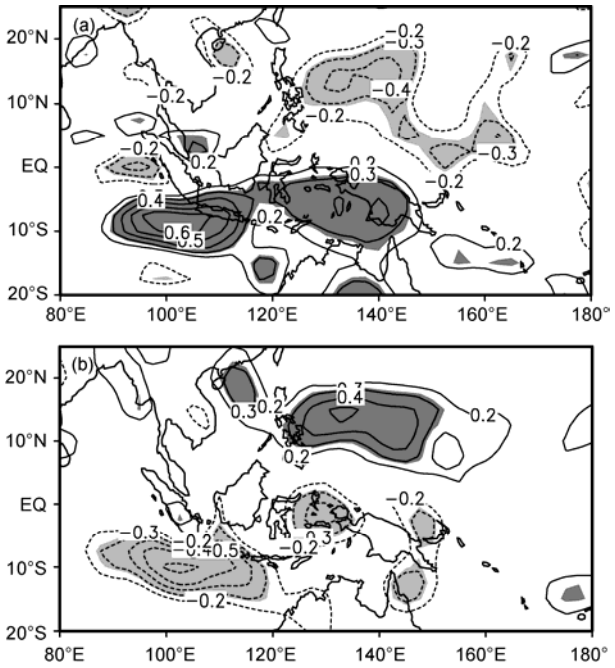


**图 5 夏季(90°~140°E, 15°S~0°)平均 SST 与 150 hPa (a)和 1000 hPa (b)散度场相关的空间分布**

阴影区表示通过 95%信度; 图中仅给出大(小)于 0.2(−0.2)的相关系数值

布型态表明，当海洋大陆夏季SST偏暖时，该地区高层为异常辐散，低层为异常辐合，对流活动旺盛；而在西太平洋地区特别是菲律宾以东洋面，高层为异常辐合，低层为异常辐散，对流活动减弱，减弱的对流活动可以通过 PJ 遥相关波列影响夏季东亚大气环流和长江流域降水[27,28].

为进一步探讨澳大利亚东侧 SST 与西南印度洋 SST 的关联，选取扣除线性趋势后的标准化冬季 EASST 值大于(小于)1(−1)的年份作为正(负)异常组合进行合成分析. 这样选取的正负 EASST 异常组合分别有 11 和 8 年. 图 6 是强弱 EASST 年冬季 200 hPa 纬向风的合成差异. 可见，在澳大利亚东侧和南非-西南印度洋之间存在一个明显的遥相关分布型(如图 6 中粗虚线所示)，这个遥相关型将两个区域的大气环流变化联系在一起. 当冬季澳大利亚东侧 SST 偏高时，该区域高层出现反气旋型环流异常，而在南非-西南印度洋区域则出现气旋型环流异常，反之亦然.

相应于高空大气环流的变化，西南印度洋区域的低层大气环流也将作出调整. 从图 7(a)可以看到，在马达加斯加东侧的西南印度洋出现气旋型环流异常，其东北侧为反气旋型环流异常，两者之间盛行异常的西北气流. 研究表明，由风驱动的海洋动力过程(海水上翻/下沉和温跃层变化)是导致西南印度洋 SST 变化的主要原因[29~31]. 因此，图 7(a)揭示的异常表层风将会对局地 SST 的变化产生重要影响. 位于西南印度洋上的气旋型环流北侧的风旋度可驱动向下的 Ekman 抽吸，结果使海水潜沉. 同时，近赤道地区的东风异常可以激发下沉的海洋 Rossby 波并造成温跃层加深[30,32]. 这些均有利于西南印度洋 SST 增暖. 因此，相应于图 7(a)中的异常表层风分布，西南印度洋冬季会出现正的 SST 异常.

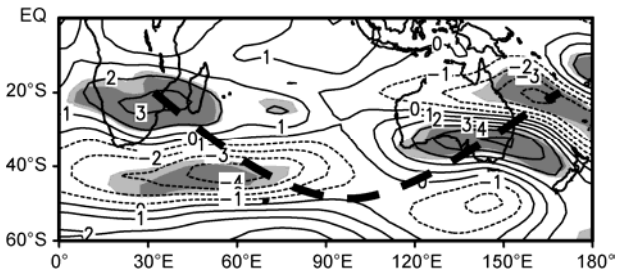


**图 6　强弱 EASST 年冬季 200 hPa 纬向风(m/s)的合成差值**
深(浅)阴影区表示通过 95% (90%)的信度

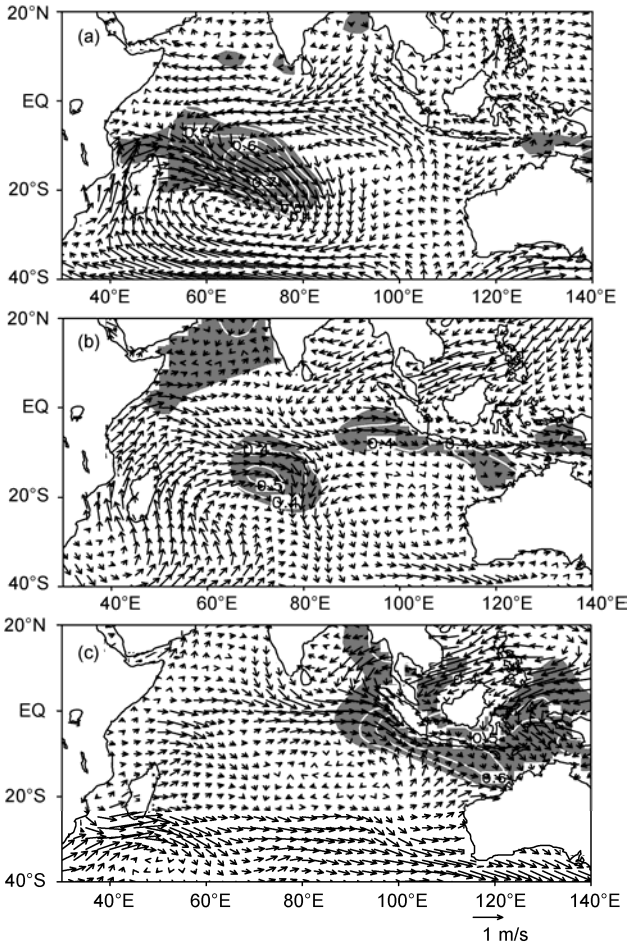


**图 7　强弱 EASST 年表层风和 SST(等直线，℃)的合成差值**
(a) 冬季; (b) 春季; (c) 夏季. 阴影区表示 SST 差异通过 95%的信度. 为清晰起见，图中仅给出通过显著性检验的 SST 差值

西南印度洋 SST 增暖后又会影响春季表层风的变化. 春季(图 7(b))，在海温变暖区域将出现异常的气旋型环流，在其东北侧则出现异常的反气旋型环流. 表层风的这种异常分布是大气环流对不对称加热响应的一种体现[33]. 另一方面，表层风的异常反过来又可影响到局地 SST 的变化. 与异常气旋型环流相联系的 Ekman 上升流抑制下沉的海洋 Rossby 波，从而减弱西南印度洋 SST 增暖，呈现负反馈关系[34,35]. 在苏门答腊和爪哇岛一带为异常的西北气流. 气候意义下，该区域盛行东南风，所以西北风异常意味着该区域东南风减弱，减弱的东南风可以通过蒸发减少和海流下沉造成海岸带 SST 升高[36,37].

夏季，海岸带 SST 异常在风-蒸发-SST 反馈机制(WES feedback)[38,39]下进一步发展. 也就是，春季

SST 异常的南北差异(赤道以南增温幅度大于赤道以北的增温幅度)可在表层强迫出向南的气压梯度力并产生异常北风. 在科氏力的作用下, 赤道以南(北)的北风向东(西)偏转形成西北风(东北风)(图 7(c)). 赤道以南的西北风异常通过减少蒸发和引起海水下沉促使海洋大陆附近 SST 进一步增暖.

## 4 结论

本文研究了冬季澳大利亚东侧 SST 与我国长江流域夏季降水的关系. 结果表明, 澳大利亚东侧冬季 SST 与长江流域夏季降水之间存在显著的正相关. 与澳大利亚东侧冬季 SST 相关联的东亚大气环流条件为这一关系的存在提供了背景场. 当前期冬季澳大利亚东侧 SST 偏暖时, 夏季西太平洋副热带高压和东亚西风急流位置偏南, 我国东部沿岸低层盛行西南风异常. 这种环流背景有利于长江流域降水的发生, 我国长江流域夏季降水因而偏多. 冬季澳大利亚东侧 SST 偏冷时的情况则相反, 不利于长江流域降水的发生, 长江流域夏季降水因而减少.

本文还进一步探讨了前期冬季澳大利亚东侧 SST 与后期夏季东亚大气环流联系的可能物理机制. 研究揭示, 澳大利亚东侧冬季 SST 异常可能通过其自身的持续性和南印度洋海温的调制作用影响东亚夏季大气环流. 当冬季澳大利亚东侧 SST 出现正异常时, 由于 SST 本身的记忆能力, 这种异常信号一直维持到夏季, 并通过南北半球遥相关影响到西太平洋副热带高压强度和位置的变化, 进而导致长江流域夏季降水偏多. 同时, 冬季澳大利亚东侧 SST 增暖时, 西南印度洋同期 SST 也易于增暖. 两区域的海温变化可通过大气遥相关波列联系在一起. 随后, 在海气相互作用下, 西南印度洋 SST 异常增暖信号逐渐向东发展, 并造成夏季海洋大陆附近 SST 升高, 而海洋大陆附近 SST 的升高可以通过影响对流活动进而影响东亚夏季大气环流和降水. 当然, 这只是一个初步解释. 海气相互作用是一个比较复杂的问题, 冬季澳大利亚东侧 SST 还可能通过其他途径影响后期大气环流的变化. 这有待于今后作更多的分析和采用先进的气候模式作深入的研究.

## 参考文献


1 龚道溢, 朱锦红, 王绍武. 长江流域夏季降水与前期北极涛动的显著相关. 科学通报, 2002, 47: 546–549

2 Gong D Y, Ho C H. Arctic Oscillation signals in the East Asian summer monsoon. J Geophys Res, 2003, 108: 4066, doi: 10.1029/2002JD002193

3 王会军. 关于我国几个大水年大气环流特征的几点思考. 应用气象学报, 2000, 11: 79–86

4 Wang H J, Matsuno T, Kurihara Y. Ensemble hindcast experiments for the flood period over china in 1998 by use of the CCSR/NIES atmospheric general circulation model. J Meteorol Soc Jpn, 2000, 78: 357–365

5 Zhao P, Zhou Z J, Liu J P. Variability of Tibetan spring snow and its associations with the hemispheric extratropical circulation and East Asian summer monsoon rainfall: A observational investigation. J Clim, 2007, 20: 3942–3955

6 Zhao P, Zhang X D, Zhou X J, et al. Sea-ice extent anomaly in the North Pacific and its impact on the East Asian summer monsoon rainfall. J Clim, 2004, 17: 3434–3447

7 Zhou B T, Wang H J. Relationship between the boreal spring Hadley circulation and the summer precipitation in the Yangtze River valley. J Geophys Res, 2006, 111: D16109, doi: 10.1029/2005JD007006

8 周波涛, 崔绚. 春季 Hadley 环流与长江流域夏季降水关系的数值模拟. 气候与环境研究, 2008, 13: 182–188

9 徐海明, 何金海, 管兆勇, 等. 北半球 WA 遥相关型影响东亚初夏季风的可能途径. 南京气象学院学报, 2000, 23: 361–369

10 孙淑清, 孙柏民. 东亚冬季风环流异常与中国江淮流域夏季旱涝天气的关系. 气象学报, 1995, 53: 438–450

11 Chen W, Graf H F, Huang R H. The interannual variability of East Asian winter monsoon and its relation to the summer monsoon. Adv Atmos Sci, 2000, 17: 48–60

12 Xue F, Wang H J, He J H. Interannual variability of Mascarene high and Australian high and their influences on East Asian summer monsoon. J Meteorol Soc Jpn, 2004, 82: 1173–1186

13 Wang H J, Fan K. Central-north China precipitation as reconstructed from the Qing dynasty: Signal of the Antarctic Atmospheric Oscillation. Geophys Res Lett, 2005, 32: L24705, doi: 10.1029/2005GL024562

14 范可. 南半球环流异常与长江中下游夏季旱涝的关系. 地球物理学报, 2006, 49: 672–679

15 Sun J Q, Wang H J, Yuan W. A possible mechanism for the co-variability of the boreal spring Antarctic Oscillation and the Yangtze River valley summer rainfall. Int J Climatol, 2009, 29: 1276–1284

16 高辉, 薛峰, 王会军. 南极涛动年际变化对江淮梅雨的影响及预测意义. 科学通报, 2003, 48(增刊Ⅱ): 87–92

17 范可, 王会军, Choi Y J. 一个长江中下游夏季降水的物理统计预测模型. 科学通报, 2007, 52: 2900–2905
18 薛峰, 王会军, 何金海. 马斯克林高压和澳大利亚高压的年际变化及其对东亚夏季降水的影响. 科学通报, 2003, 48: 287–291
19 周波涛, 崔绚. 澳大利亚东侧海温: 西北太平洋热带气旋生成频数的预测信号? 科学通报, 2010, 55: 3053–3059
20 刘舸, 张庆云, 孙淑清. 澳大利亚东侧环流及海温异常与长江中下游夏季旱涝的关系. 大气科学, 2008, 32: 231–241
21 Kalnay E, Kanamistu M, Kistler R, et al. NCEP/NCAR 40-year reanalysis project. Bull Am Meteorol Soc, 1996, 77: 437–471
22 Smith T M, Reynolds R W. Improved extended reconstruction of SST (1854–1997). J Clim, 2004, 17: 2466–2477
23 张庆云, 陶诗言, 陈烈庭. 东亚夏季风指数的年际变化与东亚大气环流. 气象学报, 2003, 61: 559–568
24 Liang X Z, Wang W C. Association between China monsoon rainfall and tropospheric jets. Q J R Meteorol Soc, 1998, 124: 2597–2623
25 Lau K M, Kim K M, Yang S. Dynamical and boundary forcing characteristics of regional components of the Asian summer monsoon. J Clim, 2000, 13: 2461–2482
26 Liu G, Ji L R, Sun S Q, et al. An inter-hemispheric teleconnection and a possible mechanism for its formation. Adv Atmos Sci, 2010, 27: 629–638
27 Nitta T. Convective activities in the tropical western Pacific and their impact on Northern Hemisphere summer circulation. J Meteorol Soc Jpn, 1987, 65: 373–390
28 Huang R H, Sun F Y. Impact of the tropical western Pacific on the East Asian summer monsoon. J Meteorol Soc Jpn, 1992, 70: 243–256
29 Klein S A, Soden B, Lau N C. Remote sea surface temperature variations during ENSO: Evidence for a tropical atmospheric bridge. J Clim, 1999, 12: 917–932
30 Xie S P, Annanalai H, Schott F A, et al. Structure and mechanisms of South Indian Ocean climate variability. J Clim, 2002, 15: 864–878
31 Yu L, Jin X Z, Weller R A. Annual, seasonal, and interannual variability of air-sea heat fluxes in the Indian Ocean. J Clim, 2007, 20: 3190–3209
32 Huang B, Kinter III J L. Interannual variability in the tropical Indian Ocean. J Geophys Res, 2002, 107: 3199, doi: 10.1029/2001JC001278
33 Wu R G, Kirtman B P, Krishnamurthy V. An asymmetric mode of tropical Indian Ocean rainfall variability in boreal spring. J Geophys Res, 2008, 113: D05104, doi: 10.1029/2007JD009316
34 Philander S G H, Yamagata T, Pacanowski R C. Unstable air-sea interactions in the Tropics. J Atmos Sci, 1984, 41: 604–613
35 Hirst A C. Unstable and damped equatorial modes in simple coupled ocean–atmosphere models. J Atmos Sci, 1986, 43: 606–630
36 Saji N H, Goswami B N, Vinayachandran P N, et al. A dipole mode in the tropical Indian Ocean. Nature, 1999, 401: 360–363
37 Murtugudde R, McCreary J P, Busalacchi A J. Oceanic processes associated with anomalous events in the Indian Ocean with relevance to 1997–1998. J Geophys Res, 2000, 105: 3295–3306
38 Xie S P, Philander S G H. A coupled ocean-atmosphere model of relevance to the ITCZ in the eastern Pacific. Tellus, 1994, 46A: 340–350
39 Chang P, Ji L, Li H. A decadal climate variation in the tropical Atlantic Ocean from thermodynamics air-sea interactions. Nature, 1997, 385: 516–518

Vol. 50: 125–139, 2011
doi: 10.3354/cr01053

CLIMATE RESEARCH
Clim Res

Published December 22

*Contribution to CR Special 28 'Changes in climatic extremes over mainland China'*

# Change in extreme temperature event frequency over mainland China, 1961–2008

**Yaqing Zhou[1,2], Guoyu Ren[2,*]**

[1]Jinzhong Meteorological Bureau of Shanxi Province, Jinzhong 030600, PR China
[2]Laboratory for Climate Studies, National Climate Center, China Meteorological Administration (CMA), Beijing 100081, PR China

ABSTRACT: Based on homogeneity-adjusted daily temperature data from national stations, the spatial and temporal change in extreme temperature events in mainland China have been analyzed for the period 1961–2008. The analysis shows that the numbers of frost days and ice days were significantly reduced, with the most significant reduction generally in northern China for ice days but more extensively across the country for frost days. Summer days and tropical nights significantly increased along the middle and lower reaches of the Yangtze River and in southern Southwest China. The maximum values of $T_{max}$ (TXx) and $T_{min}$ (TNx) and the minimum values of $T_{max}$ (TXn) and $T_{min}$ (TNn) generally rose, and TXx and TNx significantly increased in northern China, while TXn and TNn significantly increased across the whole country. A significant reduction at a rate of –8.23 d decade$^{-1}$ (–3.26 d decade$^{-1}$) occurred for cool nights (days), and a significant increase at a rate of 8.16 d decade$^{-1}$ (5.22 d decade$^{-1}$) occurred for warm nights (days). The reduction of cool nights and cool days occurred mainly in winter, but the increase of warm days and warm nights occurred mostly in autumn and summer. Extreme cold indices were reduced, mainly after the mid-1980s, while extreme warm indices increased remarkably after the mid-1990s. The analysis also shows that, for North China, the urbanization effect on the series of extreme temperature indices was statistically significant for the negative trends of frost days, diurnal temperature range, cool nights and cool days, and for the positive trends of summer days, tropical nights, TNx, TNn, and warm nights.

KEY WORDS: Extreme temperature index · Maximum temperature · Minimum temperature · Climate change · Urbanization effect · Mainland China

*Resale or republication not permitted without written consent of the publisher*

## 1. INTRODUCTION

Extreme climate has recently received more attention due to its huge impacts on economic and social development. In the past decade, many analyses have been conducted on long-term change in extreme climate events, and a number of scientific conclusions have been reached (e.g. Easterling et al. 2000, IPCC 2007, Ding et al. 2006). Based on 27 extreme temperature and precipitation indices defined by the Expert Team of Climate Change Detection, Monitoring and Index (ETCCDMI), the global variations in extreme climate have been analyzed by Alexander et al. (2006). Results showed widespread significant changes in temperature extremes associated with warming from 1951 to 2003. More than 70% of the Earth's land area underwent a significant reduction in the number of cool nights and a significant increase in the number of warm nights. Positive trends occurred in daily minimum and maximum temperatures over the entire globe, while the minimum temperature change was greater. In the analysis of daily temperature and precipitation indices in Europe from 1946 to 1999, conducted by Klein Tank & Konnen (2003), cool days (nights) were shown to be significantly reduced, while warm days (nights) were significantly increased. Similar conclusions have also been drawn from studies of, e.g. SE Asia, the South Pacific, South America, and the Asian Pacific region (Manton et al.

*Corresponding author. Email: guoyoo@cma.gov.cn

© Inter-Research 2011 · www.int-res.com

2001, Brabson & Palutikof 2002, Vincent et al. 2005, Choi et al. 2009).

Chinese studies (Tang et al. 2005, Ding et al. 2006) show that, in recent decades, increasing trends in mean maximum temperatures have occurred in northern China, while weak decreasing or insignificant trends have occurred in southern China. Mean minimum temperatures have increased all over China. Due to the asymmetry of the maximum and minimum temperature variations, the diurnal temperature range (DTR) showed a downward trend (Zhou & Ren 2009). Nation-wide cold waves gradually weakened, frost days were significantly reduced, warm days (nights) increased, cool days (nights) decreased, and cool nights showed a more significant decreasing trend (Zhai & Pan 2003, Ren et al. 2005, 2010a, Liu et al. 2006, Hu et al. 2007). The annual average number of extreme high temperature events has increased, while the extreme low temperature events have decreased (Zhang & Qian 2008). Extreme cold indices varied prominently in winter, and trends in the temperature indices have strong regional characteristics and seasonal variations in China (Yan et al. 2002, Qian & Lin 2004, Ding et al. 2009, Yang et al. 2010). According to research results for North China, East China, and some other regions (Gong & Han 2004, Ye et al. 2008, You et al. 2008, Cui et al. 2009, Shi et al. 2009), the variation trends in cold indices and the warm indices based on percentile thresholds for different regions were generally similar, with certain differences in magnitude. However, the variation trends for extreme high temperature indices were spatially quite different.

Differences among the studies of long-term variations in extreme climate events in China resulted primarily from the different periods and areas analyzed and from the different index criteria used. The adoption of common definitions for such indices could prove to be beneficial for the comparison of research results. Further attention should also be given to the procedure used in dealing with daily temperature data. The use of inhomogeneous data in previous studies (e.g. Tang et al. 2005, You et al. 2008, Zhou & Ren 2009) on changes in extreme temperature events in China might have contributed to the inconsistencies in their research results.

Applying the homogeneity-adjusted daily maximum and minimum temperature data from 1961 to 2008 and the internationally comparable extreme temperature indices recommended by the ETCCDMI (Zhang & Yang 2004; and also at http://cccma.seos.uvic.ca/etccdmi/index.shtml), we have updated analyses of the spatial and temporal variations over the past 48 yr in the extreme temperature indices for mainland China, with a focus on the trends in the series of indices. In order to understand the possible biases induced by local human activities in the country, an urbanization effect on the trends of the extreme temperature indices was preliminarily evaluated for North China.

## 2. DATA AND METHODS

### 2.1. Data and quality control

Daily temperature records were chosen from the China Homogenized Historical Temperature Datasets (CHHTD) compiled by the National Meteorological Information Center of the China Meteorological Administration (CMA), including the daily maximum and minimum temperature data from 1951 to 2008, which was recorded at national-level ground weather stations, or national basic meteorological stations and reference climatic stations (hereinafter referred to as national stations). The data sets were quality controlled and homogeneity adjusted. The homogeneity adjustment method was described by Liu & Li (2003) and Li et al. (2004). In short, it involved selecting time series from 5 stations that were highly positively correlated with the candidate stations, and combining the 5 temperature series into a reference series. Subsequently, they checked whether significant discontinuous points existed in different candidate series by comparison with the reference series. The reasonableness of the discontinuous points was determined according to station metadata. Once all the significant discontinuities were detected and proved, the correction value could be obtained from the offsets derived from the difference series (based on differences between candidate and reference data).

By investigating metadata of weather stations, it was found that 328 of 526 stations had relocation records; 155 stations had been moved once and 173 stations had been moved more than once. Homogeneity detection showed that significant discontinuous points existed in the maximum temperatures of 177 stations and in the minimum temperatures of 213 stations. Correction was carried out for the discontinuous points, and the corrected stations then accounted for 34 and 40% of the total, respectively (Li et al. 2004).

The large-scale establishment of stations in China was started in the mid- to late 1950s, accompanied by standardized and improved meteorological records, and thus the data period 1961–2008 was selected for the present study. According to the criteria that the

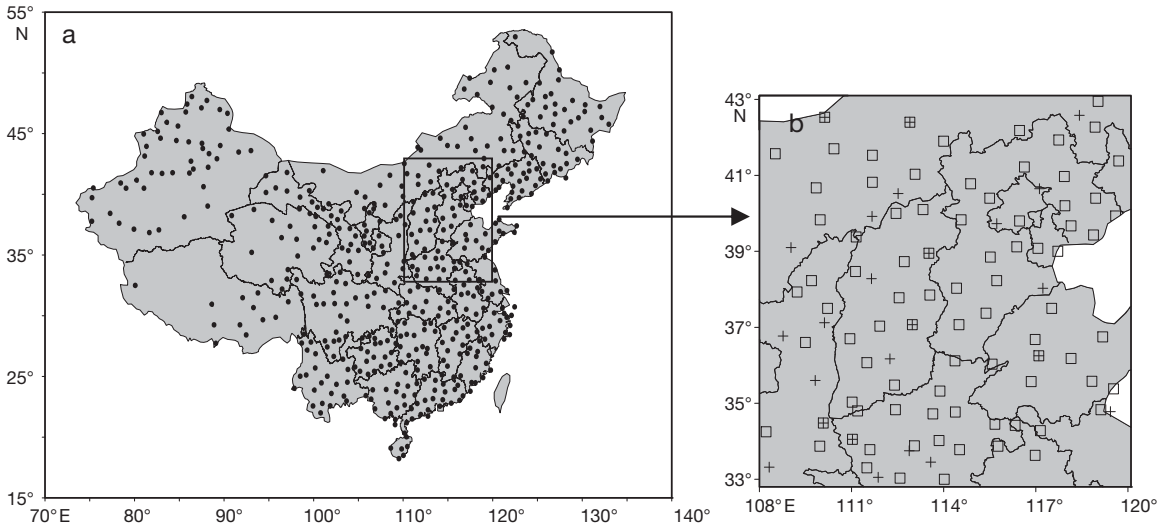


Fig. 1. Distribution of the weather stations used in the present study: (a) the 526 stations in mainland China and (b) stations in North China, with squares indicating the national stations and crosses indicating the rural stations

series length is no less than 48 yr and no more than 2% of the data are missing, the data of 526 stations were finally selected for analysis (Fig. 1).

Quality control was repeated for the homogenized daily temperature data with Rclimdex software (Zhang & Yang 2004). Quality control was performed in 2 steps: (1) if the maximum temperature minus minimum temperature was negative, the record was marked as unreasonable and dealt with as a missing value, and (2) records with standard deviations 4-fold greater than the average were marked as outliers. Artificial determination was carried out according to the corresponding records of neighboring stations, and reasonable records were retained, while unreasonable ones were dealt with as missing values. After the check, outliers were detected in 358 stations, of which 10 daily temperature values of 6 stations were determined as unreasonable, accounting for 5 per million of the total records.

### 2.2. Definition of extreme temperature indices

If the weather status shows a large deviation from the mean state it can be termed an extreme event in a statistical sense. We used 15 extreme temperature indices (see Table 1), of which 13 are based on definitions by the ETCCDMI and 2 additional indices involved monthly average maximum and minimum temperatures. With the period 1971–2000 taken as a reference period, Rclimdex software was used to calculate the time series and linear trends of the extreme temperature indices for each station, and the statistical significance of the trends were evaluated.

The extreme temperature indices were divided into 3 types. The first type was based on original observation data and fixed thresholds, and was considered 'absolute'. The 4 absolute indices include frost days, summer days, ice days, as well as tropical nights. Due to the vast area and complex climate in China, the following considerations were also taken into account. For the 4 absolute indices, if no record of an extreme event occurred at a certain station within a period of two-thirds of the 48 yr, the estimated linear trend was considered unreliable, and thus the station was not included in the statistics of index time series. The second index type utilized the means and extremes of daily maximum and minimum temperatures, termed extreme value indices, including mean maximum (minimum) temperature, maximum $T_{max}$ (TXx) and $T_{min}$ (TNx), minimum $T_{max}$ (TXn) and $T_{min}$ (TNn), and DTR. The third type of indices was based on relative or floating thresholds, termed the relative indices, including cool days (nights) and warm days (nights). In the calculation of these indices, the 90th (10th) percentile of the daily maximum (minimum) temperature data at a certain station in the period 1971–2000 was taken as the upper (lower) threshold. If a daily maximum temperature was greater (less) than the upper (lower) threshold, then it was considered a warm (cool) day event. Similarly, if a daily minimum temperature was greater (less) than the upper (lower) threshold, then it was considered a warm (cool) night event. The specific definitions of the indices are listed in Table 1. In order to facilitate comparisons with other research results, the percentages of days were converted to the days with daily maximum (minimum) temperatures greater (less) than the upper (lower) thresholds.

Table 1. Extreme temperature indices used in the present study (modified according to Zhang & Yang 2004) and their linear trends in mainland China, 1961–2008. All trends in the table are statistically significant at the 0.05 confidence level. Data given as d decade$^{-1}$ for absolute and relative indices, and °C decade$^{-1}$ for extreme value indices. TN: daily minimum temperature; TX: daily maximum temperature

| Index abbreviation | Term | Definition | Linear trend |
|---|---|---|---|
| **Absolute indices** | | | |
| FD0 | Frost days | Annual count when TN < 0°C | –3.48 |
| SU25 | Summer days | Annual count when TX > 25°C | 2.69 |
| ID0 | Ice days | Annual count when TX < 0°C | –2.32 |
| TR20 | Tropical nights | Annual count when TN > 20°C | 2.47 |
| **Extreme value indices** | | | |
| TXa | Average TX | Monthly mean value of TX | 0.26 |
| TNa | Average TN | Monthly mean value of TN | 0.40 |
| DTR | Diurnal temperature range | Monthly mean value of difference between TX and TN | –0.15 |
| TXx | Maximum TX | Monthly maximum value of TX | 0.15 |
| TNx | Maximum TN | Monthly minimum value of TX | 0.25 |
| TXn | Minimum TX | Monthly maximum value of TN | 0.35 |
| TNn | Minimum TN | Monthly minimum value of TN | 0.58 |
| **Relative indices** | | | |
| TN10p | Cool nights | Percentage of days when TN < 10th percentile | –8.23 |
| TX10p | Cool days | Percentage of days when TX < 10th percentile | –3.26 |
| TN90p | Warm nights | Percentage of days when TN > 90th percentile | 8.16 |
| TX90p | Warm days | Percentage of days when TX > 90th percentile | 5.22 |

### 2.3. Statistical analysis

The least squares method was used for calculation of the linear trend, and the Kendall-tau non-parametric test method was adopted for testing the statistical significance of the linear trend (Kendall & Gibbons 1981). The average time series for China was obtained according to the grid area weighted average method (Jones & Hulme 1996), with a grid size of 2.5° × 2.5°. Seasons were divided into spring (March–May), summer (June–August), autumn (September–November) and winter (December–February of the following year), and annual mean (total) values were those from January to December.

### 2.4. Urbanization effect analysis

In order to quantitatively evaluate the urbanization effect on the linear trend of the extreme temperature indices, we used a subset of data from 142 surface temperature reference stations (rural stations) in China (Ren et al. 2010b, Zhang et al. 2010) to analyze the difference in index trends between national and rural stations, with North China as a case study. The 142 rural stations were selected from 2400 stations, including all of the national stations and 1700 ordinary stations. A number of indicators were considered, such as the settlement population near a station, the distance of the observational grounds from city centers, and the ratio of built-up area to total area within a radius of 2 km from the observational grounds (Ren et al. 2010b, Ren & Ren 2011). North China was defined as the area between 33–43°N and 108–120°E, where 84 national stations and 24 rural stations are located.

The following terms were defined with reference to Ren et al. (2008), Zhou & Ren (2009) and Zhang et al. (2011). The urbanization effect refers to the linear trends in extreme temperature indices recorded at urban or national stations and caused by the strengthening of the urban heat island (UHI) effect and other local anthropogenic factors, expressed as $\Delta X_{ur}$. $X_u$ is the linear trend of an extreme temperature index at an urban or national station, and $X_r$ is the linear trend of an extreme temperature index at a rural station. The urbanization effect ($\Delta X_{ur}$) is expressed as:

$$\Delta X_{ur} = X_u - X_r \quad (1)$$

If $\Delta X_{ur} > 0$, the extreme temperature index series rises relatively or increases due to the urbanization effect; if $\Delta X_{ur} = 0$, no urbanization effect exists; and if $\Delta X_{ur} < 0$, the extreme temperature index series declines relatively or is reduced due to the urbanization effect.

Contribution of the urbanization effect refers to the proportion of the urbanization effect to the overall trend of an extreme temperature index series at an urban or national station, expressed as $E_u$ (in%):

$$E_u = |\Delta X_{ur}/X_u| \times 100 = |(X_u - X_r)/X_u| \times 100 \quad (2)$$

If $E_u = 0$, the urbanization effect shows no contribution to the overall trend of the extreme temperature index series at the urban or national station; if $E_u$ = 100%, the linear trend of the extreme temperature index series at the urban or national station is entirely caused by the urbanization effect. In practical calculations, $E_u$ may exceed 100% in a few cases, indicating that unknown local factors might have had an effect; we adjusted the $E_u$ of such cases to 100%.

## 3. TRENDS OF EXTREME TEMPERATURE INDICES

### 3.1. Absolute indices

The extreme index with a fixed threshold is called the absolute index. Table 1 shows the linear trends in extreme temperature indices for mainland China, and Fig. 2 shows the anomaly time series curves of absolute indices. Frost days underwent a slight decrease prior to the mid-1980s, and a rapid decline after 1987, leading to a reduction of almost 17 d in the last 48 yr. Similarly, ice days also showed a decreasing trend with significant reduction occurring after the mid-1980s. However, the variations in ice days were more moderate than those in frost days. Summer days showed negative anomalies, mostly prior to the mid-1990s, but a turning point occurred in 1994, and positive anomalies prevailed after 1997, with the maximum being reached in 2006 and 2007. Similar to summer days, the variations in tropical nights have also accelerated considerably since 1994, reaching a maximum in 2005.

Frost days were significantly reduced across the country (Fig. 3a). This is consistent with the conclusions reached by Zhai & Pan (2003) as well as Qian & Lin (2004). Ice days occurred in the areas north of 32°N, mainly with a deceasing trend. The areas with significant reduction were primarily concentrated in northern China, with scope and degree smaller than those of frost days (Fig. 3b). Summer days at most stations in China showed an increasing trend (Fig. 3c), and the significant increasing trends, >5 d decade$^{-1}$, generally occurred in the northeastern part of the Inner Mongolia Autonomous Region, in the middle and lower reaches of the Yangtze River, and in most of Yunnan Province. Tropical nights also mostly showed an increasing trend, but the areas with significant increase were mainly concentrated in eastern China, in the southern part of Southwest China, and in the coastal zone of South China (Fig. 3d).

In summary, absolute cold indices for mainland China showed a decreasing trend and, in general, have been declining significantly since the mid-1980s. However, warm indices mainly showed an increasing trend, but significant variation occurred till the mid-1990s. As viewed from a spatial distribution of trends, cold indices showed a more significant decreasing trend in northern China, while primarily in the middle and lower reaches of the Yangtze River and in the southern part of Southwest China the warm index significantly increased.

### 3.2. Extreme value indices

The temporal variations in annual mean maximum and minimum temperatures, as well as in DTR, in the past 48 yr are shown in Fig. 4. Both mean maximum and minimum temperatures showed increasing trends.

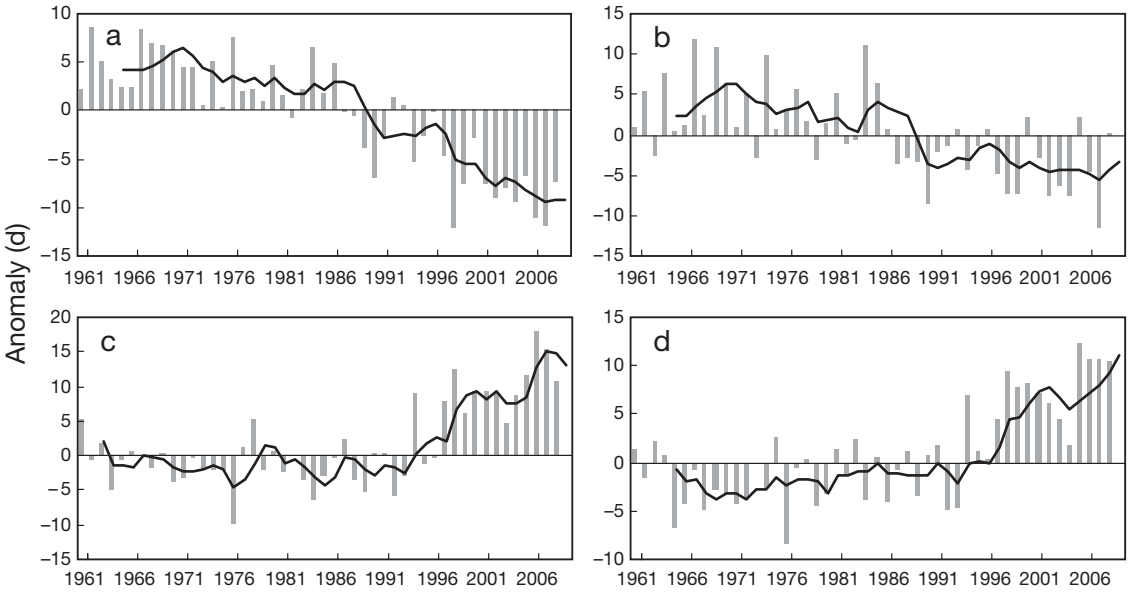


Fig. 2. Anomalies of the country-averaged annual (a) frost days (FD0), (b) ice days (ID0), (c) summer days (SU25), and (d) tropical nights (TR20) in mainland China, 1961–2008. The anomalies are relative to 1971–2000 mean values. The curves are 5 yr running means

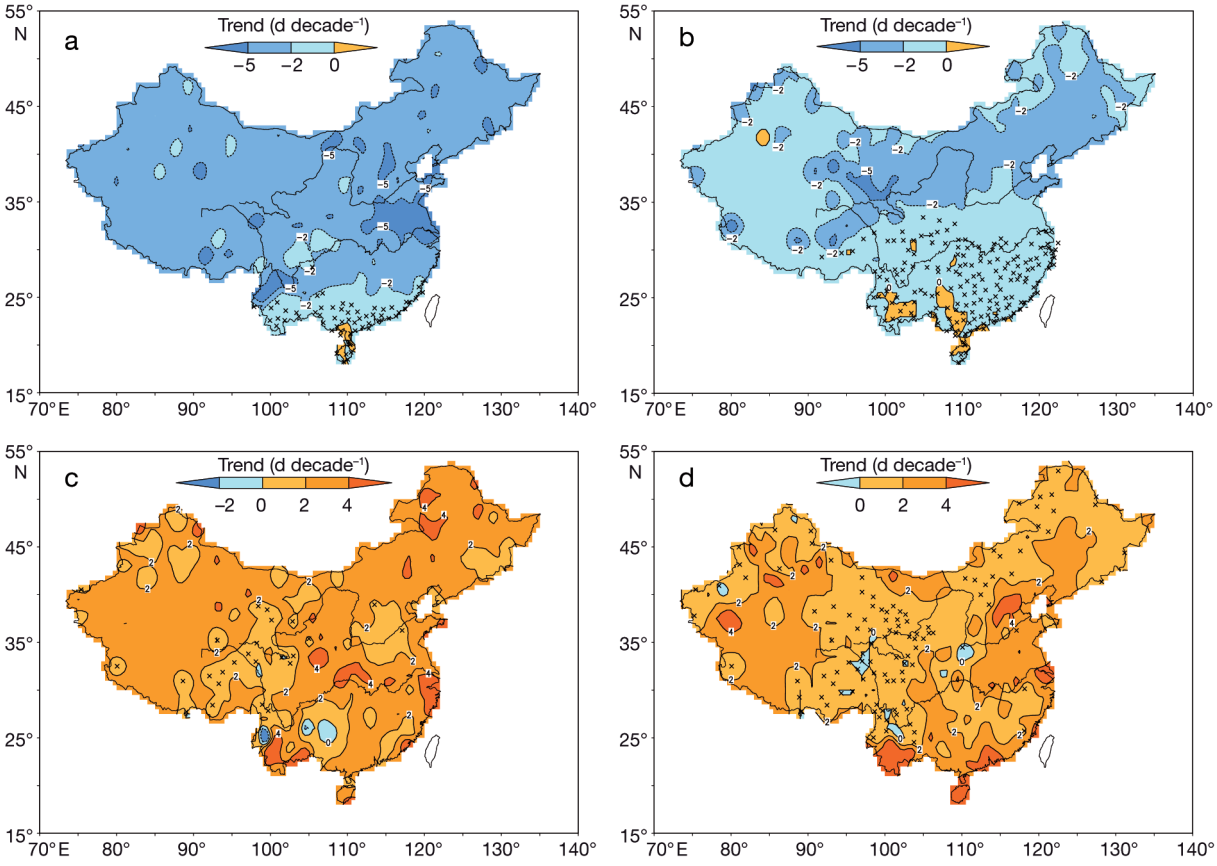


Fig. 3. Trends in the numbers of (a) frost days (FD0), (b) ice days (ID0), (c) summer days (SU25), and (d) tropical nights (TR20) in mainland China, 1961–2008. Crosses denote that linear trends were unavailable due to the sparseness of the extreme temperature events. Data given as d decade$^{-1}$

The maximum temperatures fluctuated prior to the 1990s, and then began to rise significantly. However, the minimum temperature has steadily risen since the late 1970s, and the upward trend became more prominent in the late 1980s. Because of the asymmetry of maximum and minimum temperature variations, DTR underwent a significant decrease. However, the decreasing trend in DTR mainly occurred prior to the mid-1980s, and became insignificant after that time. DTR was linearly reduced by 0.72°C in the country on the whole during the last 48 yr.

Extreme values of daily maximum and minimum temperatures showed increasing trends, and TNn rose more significantly. The increasing trend in TNn was as great as 0.58°C decade$^{-1}$, while that of TXx was only 0.15°C decade$^{-1}$. It is also evident in Fig. 5 that TNn showed an overall increasing trend, with the trend more obvious in the late 1980s and 1990s. Since the beginning of the 21st century, however, TNn has generally been stable or even declining, with the exception of 2007. TXn varied insignificantly before the mid-1980s and then rose slowly. Its variation has been similar to that of TNn since the mid- to late 1980s. However, TNx and TXx showed relatively stable variations prior to the mid-1990s, and after that they rose rapidly and have remained at a high level since 2000.

As Fig. 6a shows, TXx increased in most areas, with the general trend <0.5°C decade$^{-1}$, while the areas with declining trends were mainly in the southeastern part of North China and the middle and upper reaches of the Yangtze River. Compared with TXx, the extent with a downward trend shrunk for TNx (Fig. 6b), while the extent with an upward trend expanded. The areas with increasing trends >0.5°C decade$^{-1}$ were mainly located in northern China. Compared with TXx and TNx, the extents with rising trends of TXn and TNn were generally broader. TXn (Fig. 6c) increased in most areas, especially in Northeast China and in the northern part of Xinjiang province, with the rising trend >0.5°C decade$^{-1}$. TNn (Fig. 6d) rose considerably throughout country, and the increasing trend was >0.5°C decade$^{-1}$ in most regions, with some stations in Northeast China,

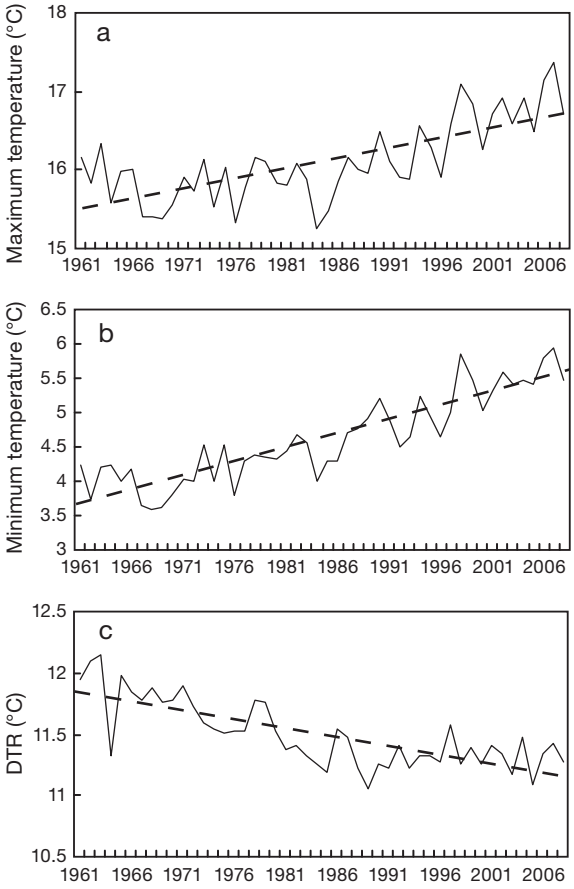


Fig. 4. Country-averaged annual mean (a) maximum temperature, (b) minimum temperature, and (c) diurnal temperature range (DTR) in mainland China, 1961–2008. The dashed lines are linear trends

North China, and the northern part of Xinjiang province reaching 1.0°C decade$^{-1}$ or even more.

In summary, the mean and maximum and minimum values of daily maximum and minimum temperatures showed overall increasing trends, while DTR was significantly decreased. The mean maximum temperature has risen significantly since the 1990s, while the mean minimum temperature began to rise steadily in the late 1970s, and the trend became more prominent in the late 1980s. Because of the asymmetry of maximum and minimum temperature variations, DTR experienced a significant decline, especially prior to the mid-1980s.

TXn and TNn have increased significantly since the mid-1980s, while TXx and TNx have increased rapidly since the mid-1990s. A noteworthy phenomenon was that TNn and TXn have generally showed a stable or even declining trend since 2000, while TNx and TXx have remained at a high level since that time. Significant upward trends in TXx and TNx occurred in northern China, while TXx underwent an obvious downward trend in southern North China and the middle and lower reaches of the Yangtze River. TXn and TNn increased significantly across the whole country, but TNn increased more strongly.

### 3.3. Relative indices

Table 1 shows that cool nights (days) significantly decreased with a trend of –8.23 d decade$^{-1}$ (–3.26 d

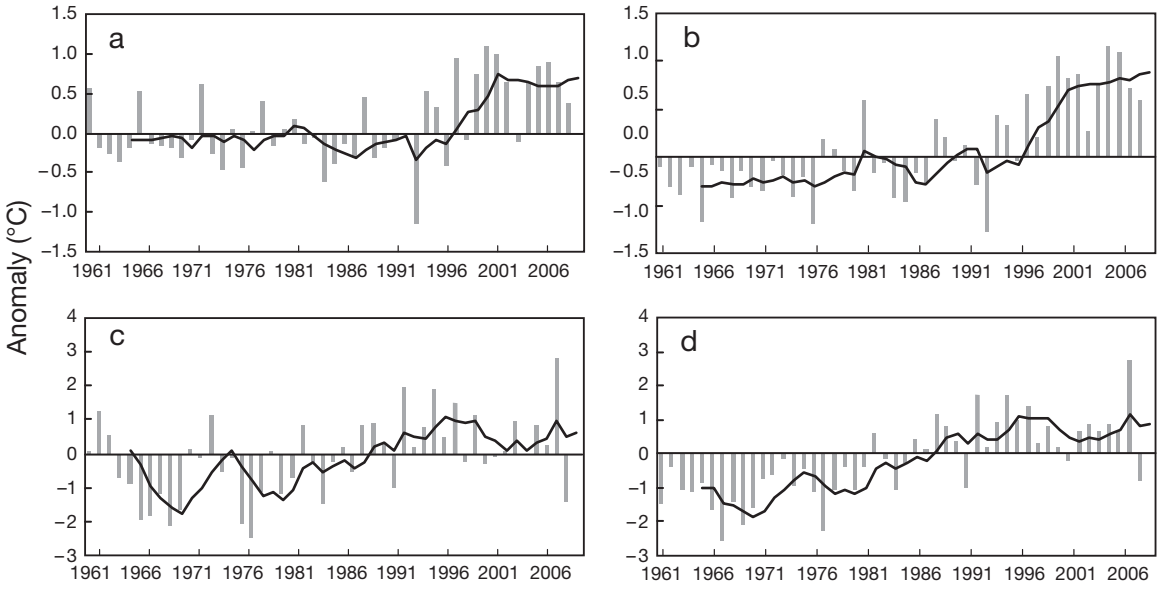


Fig. 5. Anomalies of the country-averaged annual (a) maximum $T_{max}$ (TXx), (b) maximum $T_{min}$ (TNx), (c) minimum $T_{max}$ (TXn), and (d) minimum $T_{min}$ (TNn) in mainland China, 1961–2008. The anomalies are relative to 1971–2000 mean values. The curves are 5 yr running means

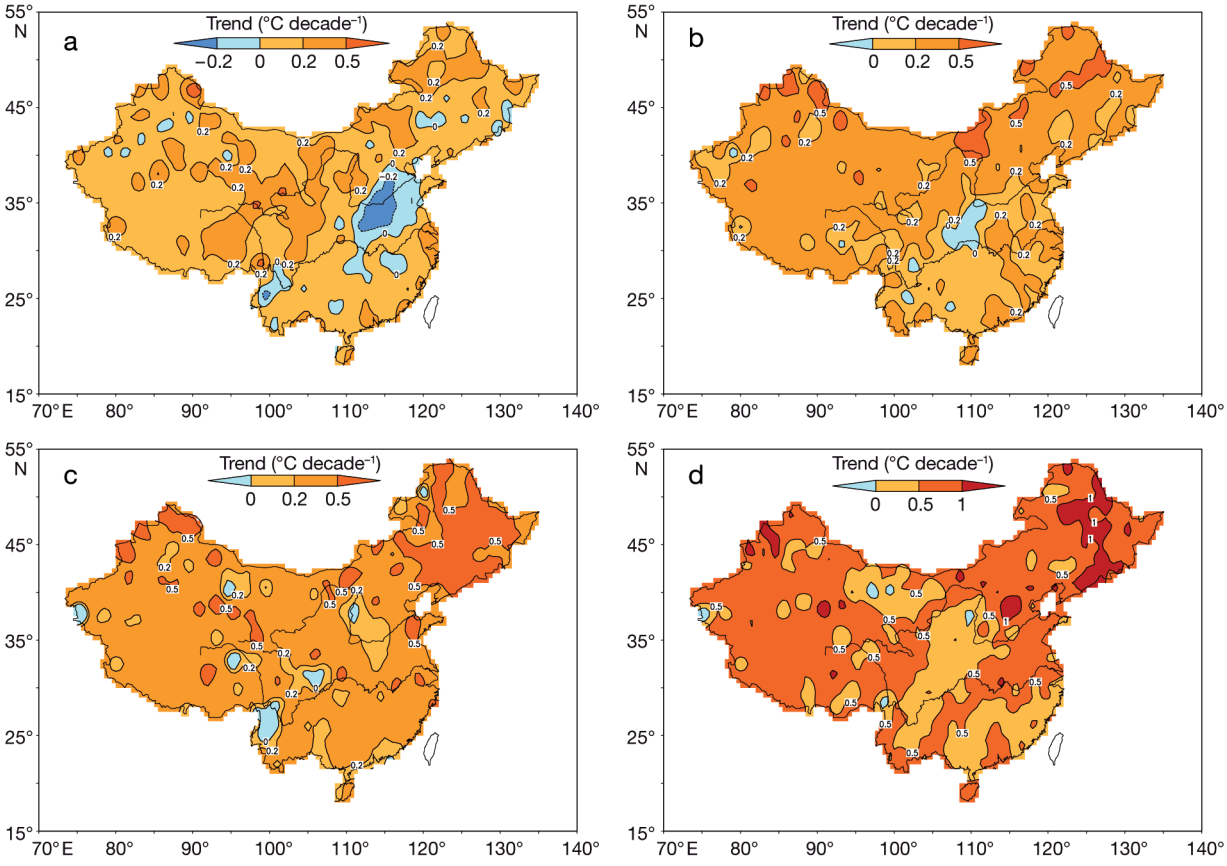


Fig. 6. Trends in distributions of (a) maximum $T_{max}$ (TXx), (b) maximum $T_{min}$ (TNx), (c) minimum $T_{max}$ (TXn), and (d) minimum $T_{min}$ (TNn) in mainland China, 1961–2008. Data given as °C decade$^{-1}$

decade$^{-1}$) during the period 1961–2008, while warm nights (days) significantly increased with a trend of 8.16 d decade$^{-1}$ (5.22 d decade$^{-1}$). Cool days (nights) primarily showed positive anomalies before the late 1980s, followed by a rapid decline, and negative anomalies have been observed for 19 out of 21 yr since 1987 (Fig. 7a,b). Warm days (nights) showed negative anomalies for most years before 1987, followed by positive and negative anomalies, which alternated till the early 1990s and substantially increased after 1994, with a negative anomaly occurring in only 1 yr during the last 15 yr (Fig. 7c,d). More significant changes occurred for cool (warm) nights than for cool (warm) days. These results are generally consistent with what Choi et al. (2009) found for the Asian Pacific region, but the changing trends obtained here are larger, except for cool days, for which both had similar trends. The trends reported here are also a little bit larger than those given by previous Chinese researchers. The difference might have been due to the different datasets, data processing methods, and lengths of the time periods used in the studies.

Spatial characteristics of trends of the relative extreme temperature indices are displayed in Fig. 8. Cool days significantly declined in northern China, and the areas with increasing trends were mainly in Southwest China (Fig. 8a). For cool nights, with a few exceptions in the eastern part of Southwest China, more significant decrease was observed in the country, with most areas registering downward trends of >5 d decade$^{-1}$. Northeast China, the northern part of North China, the eastern part of Northwest China, and the southern part of Southwest China witnessed an even larger decrease of >10 d decade$^{-1}$ (Fig. 8b). Warm days were reduced in a few stations in the central region and the eastern part of Southwest China, and they significantly increased in other regions, notably in northern China, in the southern part of Southwest China, and in coastal areas of South China, with the increasing trend mostly >5 d decade$^{-1}$ (Fig. 8c). Warm nights significantly increased in most regions, with the increasing trend generally >5 d decade$^{-1}$, and the most significant increases can be seen in Northeast China, North China, Southwest China, and in South China coastal areas (Fig. 8d).

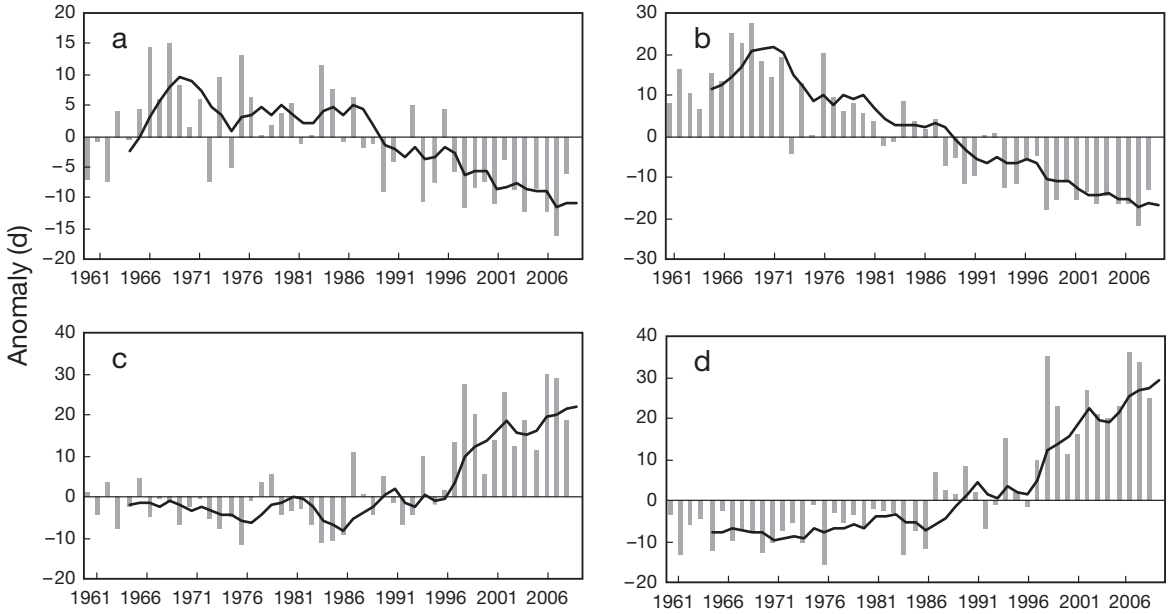


Fig. 7. Anomalies of the country-averaged (a) cool days (TX10p), (b) cool nights (TN10p), (c) warm days (TX90p), and (d) warm nights (TN90p) in mainland China, 1961–2008. The anomalies are relative to 1971–2000 mean values. The curves are 5 yr running means

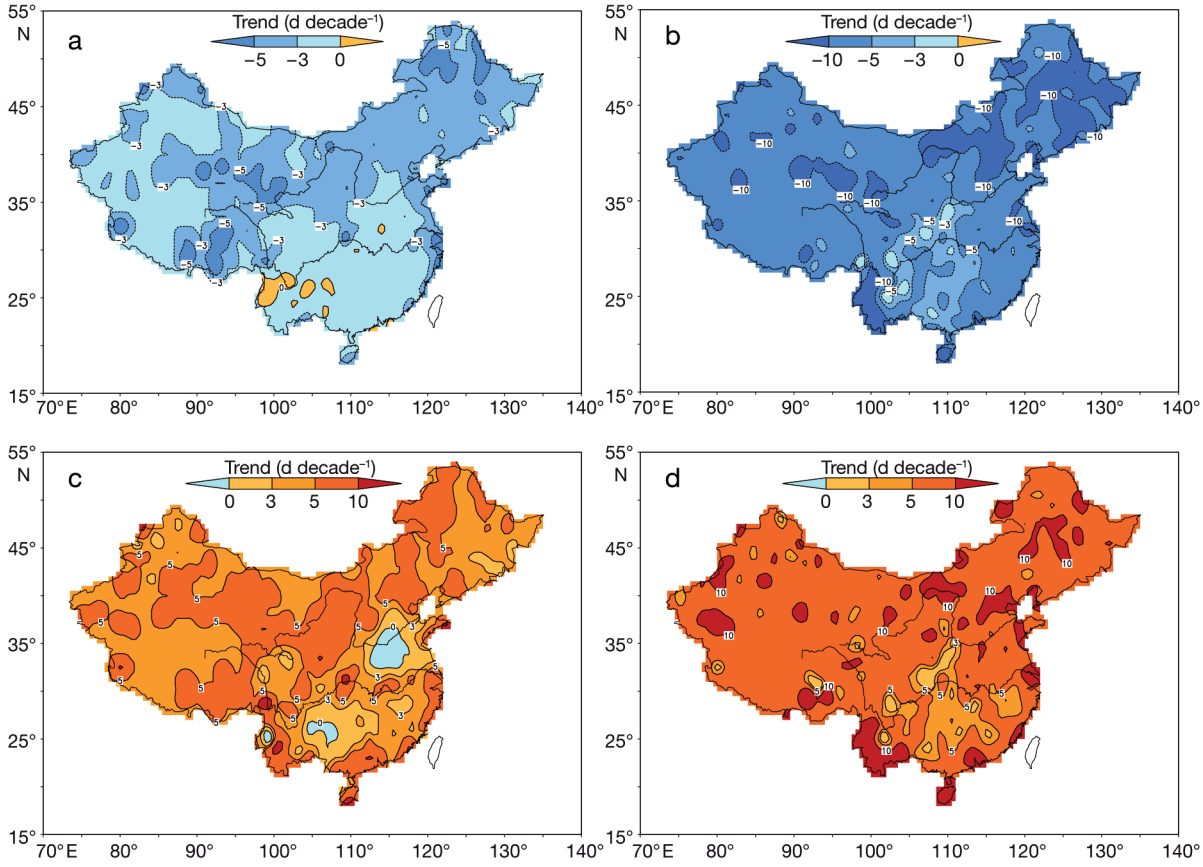


Fig. 8. Trends in distributions of (a) cool days (TX10p), (b) cool nights (TN10p), (c) warm days (TX90p), and (d) warm nights (TN90p) in mainland China, 1961–2008. Data given as d decade$^{-1}$

Those areas with reduced cool days (nights) in the present study were approximately consistent with the research conclusions reached by Qian & Lin (2004), in spite of the fact that the geographical extent in which cool days were significantly reduced was broader, while that showing an increasing trend shrunk. Similar situations could be seen for the areas with increased warm days (nights), except that the extent in which warm days were significantly increased was broader. The study period selected by Qian & Lin (2004) was 1961–2000, and urban stations with populations >500 000 were excluded from their analysis. These might be the main reasons for the differences mentioned above. The decreasing (increasing) trends of the relative cool (warm) indices have become stronger in the past decade, and the urbanization effect on mean and extreme temperatures of national stations, and particularly of big city stations, was significant (Ren et al. 2008, Zhou & Ren 2009).

Therefore, the warm extreme indices have significantly increased, while the cold extreme indices have significantly decreased in the country during the past 48 yr. In addition, the indices related to minimum temperature have changed more significantly than those related to maximum temperature. The frequencies of cool days (nights) showed a rapid decline after the late 1980s, while the frequencies of warm days (nights) rose substantially in the mid-1990s. From a spatial distribution perspective, the relative indices changed more significantly in northern China.

In examining the seasonal change (Table 2), the reduction of cool days (nights) mainly occurred in winter, and the change was the weakest in summer. The most significant increase in frequencies of warm days (nights) occurred in autumn and summer.

Cool winter nights (days) and warm summer days (nights) are good indicators for cold periods and heat waves in climatic applications. Analysis of the 4 series of indices reveals that the most significant changes occurred for cool winter nights and warm summer nights, with respective trends reaching −10.9 and 9.3 d decade$^{-1}$ (Table 2, Fig. 9). The frequencies of cool winter nights (days) were relatively stable before the mid-1980s, but rapidly declined after 1986 and have generally remained at a low level in the last 2 decades (Fig. 9). The frequencies of warm summer (nights) days has continuously increased since the mid-1990s.

Fig. 10a shows that cool winter days significantly declined across the whole country, and the decreasing trends for nearly half of the stations were >5 d decade$^{-1}$. The areas with significant reduction were primarily in northern China, East China, and on the Qinghai-Tibet Plateau. Cool autumn days were reduced in most regions of China, but generally with decreasing trends of <5 d decade$^{-1}$ (data not shown). The extents of areas with significantly decreasing trends were reduced in spring and summer. In summer, cool days even showed increasing trends at nearly half of the stations (data not shown). The areas with increasing trends were mainly in Central and East China. However, cool nights in 4 seasons were significantly reduced in most regions, especially in winter (Fig. 10b), and more than half of the stations showed decreasing trends of >10 d decade$^{-1}$. The areas with significant reductions of cool nights were generally the same as those with reductions of cool days, but the intensity was stronger. During the other seasons, significant reductions in cool nights were also observed for most of the stations in northern China, while increasing trends occurred in some stations in southern China, but only during spring and summer. It is thus obvious that the frequencies of winter cold spells tended to decrease significantly in most regions of China, and a tremendous drop occurred in northern China, East China, and the Qinghai-Tibetan Plateau.

Table 2. Linear trends in seasonal cool nights and warm days in mainland China, 1961–2008. Data are given in d decade$^{-1}$. *: statistically significant at the 0.05 confidence level

| | Cool nights (TN10p) | Cool days (TX10p) | Warm nights (TN90p) | Warm days (TX90p) |
|---|---|---|---|---|
| Spring | −7.6* | −2.5* | 8.1* | 4.9* |
| Summer | −7.0* | −1.4 | 9.3* | 4.8* |
| Autumn | −7.9* | −4.3* | 7.0* | 5.7* |
| Winter | −10.9* | −5.4* | 7.7* | 5.3* |

For warm autumn days, increasing trends were observed in most regions, notably in South China coastal areas, where significant upward trends occurred. Decreasing trends existed for warm winter and spring days in a few regions of Central and East China, while the areas with significant increases were mainly distributed on the Qinghai-Tibet Plateau and in the western part of Southwest China. Except for Central China and a part of South China in which a decreasing trend was observed for warm summer days (Fig. 10c), increasing trends were shown in most of the remaining regions, especially in North China, Northwest China, and in South China coastal areas. Warm nights for all seasons showed increasing trends across the whole country, and the significant increase not only occurred in North China and South-

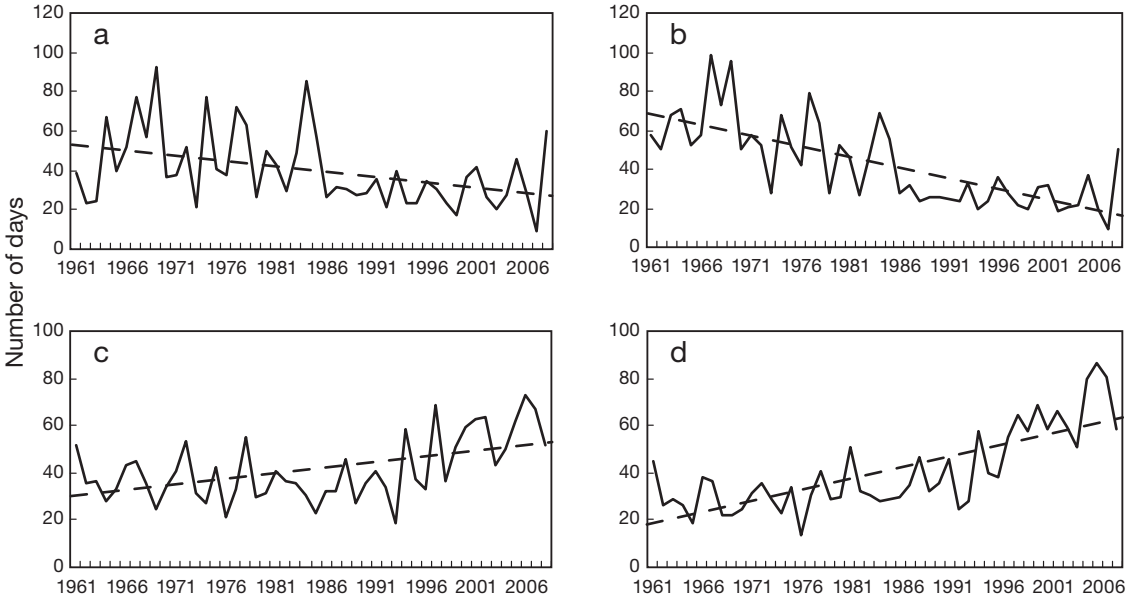


Fig. 9. Country-averaged (a) cool days (TX10p) and (b) cool nights (TN10p) for winter, and (c) warm days (TX90p) and (d) warm nights (TN90p) for summer in mainland China, 1961–2008. The dashed lines are linear trends

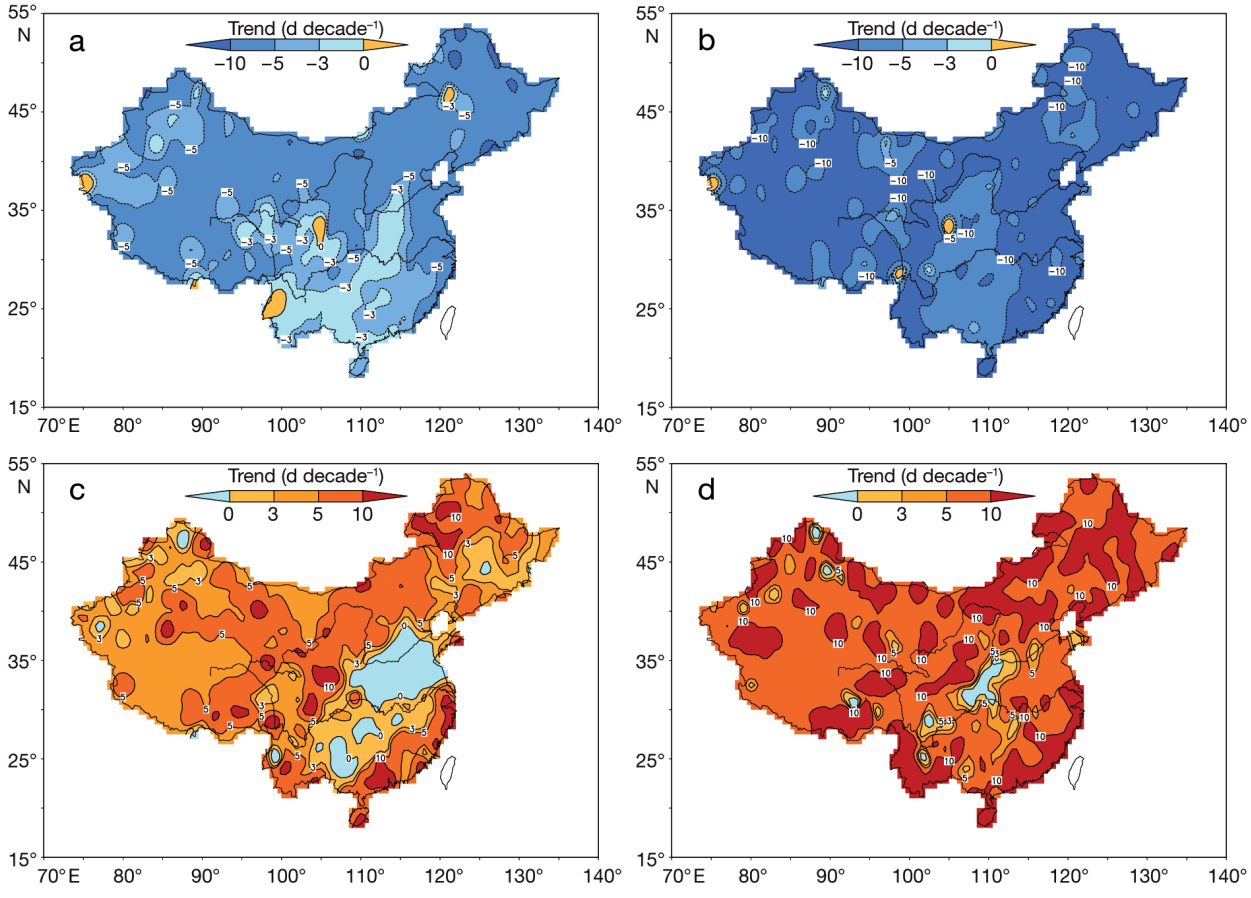


Fig. 10. Trends in (a) cool days (TX10p) and (b) cool nights (TN10p) for winter and (c) warm days (TX90p) and (d) warm nights (TN90p) for summer in mainland China, 1961–2008

west China, but also in South China during summer and autumn. The stations at which warm summer nights were significantly increased were more extensively distributed (Fig. 10d), implying an increasing frequency of summer heat waves at some stations.

## 4. DISCUSSION

We have shown in the present study that, for mainland China on the whole, the indices of extreme warm temperatures have generally evidenced increasing trends, while indices of extreme cold temperatures have shown more significant decreasing trends. Overall these observations are consistent with the findings in previous publications (Yan et al. 2002, Zhai & Pan 2003, Gong & Han 2004, Qian & Lin 2004, Tang et al. 2005), in spite of the fact that the country-averaged linear trends of the index series reported here are usually a bit stronger than those in the previous studies, mainly due to the different data processing methods used and time periods analyzed.

A major issue is the possible urbanization effect on the series of extreme temperature indices. According to analysis of the urbanization effect on mean maximum and minimum temperature trends in North China during the period 1961–2000 conducted by Zhou & Ren (2009), an insignificant urbanization effect existed on the maximum temperature at national stations and at stations with populations of <500 000. However, the region-averaged annual mean minimum temperature series for the national stations in North China was significantly affected by urbanization, with the contribution of urban warming to overall warming reaching >50% (Zhou & Ren 2009). The urbanization effect on the minimum temperature series of medium-sized and small city stations was somewhat weaker, but also statistically significant. Large urbanization effects on the extreme temperatures at the national stations in Shanghai and Beijing have also been reported by Cui et al. (2009) and Zhang et al. (2011). Significantly higher extreme maximum and minimum temperatures, and significantly more high-temperature days were found in the urban area of Shanghai than in its suburbs, while, since the 1980s, low temperature days in the urban area have been significantly reduced compared to those in the suburbs (Cui et al. 2009). In the case of Beijing station, frost days, cool nights, and DTR were significantly reduced between 1960 and 2008 due to the urbanization effect, while warm nights and mean minimum temperature increased significantly (Zhang et al. 2011). The above research results indicate that urbanization had impacts not only on daily and monthly mean temperatures at the national stations, but also particularly on the daily mean maximum and daily minimum temperatures and the resulting series of extreme temperature indices.

In order to better understand the magnitude of the urbanization effect on series of extreme temperature indices in a larger region, we chose North China as a case study to compare differences in a few extreme temperature indices between national stations and rural stations. Table 3 shows the extreme temperature indices of national and rural stations, as well as the urbanization effect and the contribution of the urbanization effect in North China during the period 1961–2008.

It is clear from Table 3 that the changes of the indices related to minimum temperatures were more significant for the national stations than for the rural stations. The urbanization effect on the index series was statistically significant at the 0.05 confidence level for the negative trends of frost days, DTR, cool nights, and cool days, and for the positive trends of summer days, tropical nights, TNx, TNn, and warm nights. For these indices, the contributions of the urbanization effect to the overall trends were also large, ranging from 10 to 100%. The largest contributions come from tropical nights, DTR, TNx, and TNn, which all reached >50%, with DTR reaching 100%. This means that the significant decrease in DTR observed for the national stations in North China was entirely caused by urbanization. This is an interesting finding because previous studies attributed most of the observed decrease in DTR to increasing cloud cover and atmospheric/soil moisture (Dai et al. 1999, Easterling et al. 2000, Duan & Wu 2006) and to the possible influence of aerosols in industrial regions (Stone & Weaver 2003, Zhou et al. 2009).

The urbanization effect exacerbated the trends of the cold and warm indices related to $T_{min}$. However, the urbanization effects of the $T_{max}$-related temperature indices were usually milder and generally did not pass the significance test at the 0.05 confidence level; this situation results from the fact that the urbanization effect on maximum temperature was much weaker and statistically less significant. An insignificant negative urbanization effect on the trends in maximum temperature and warm days might have resulted from the cooling effect of pollutants near the national stations as compared to rural stations. These results are basically consistent with our previous analysis of maximum and minimum temperature changes in North China using a different dataset of rural stations (Zhou & Ren 2009).

Table 3. Comparison of linear trends in series of extreme temperature indices between the national and rural stations in North China, 1961–2008. Data given as days or degrees Celsius per decade. *: statistically significant at the 0.05 confidence level

| | National station ($X_u$) | Rural station ($X_r$) | Urbanization effect ($\Delta X_{ur}$) | Contribution (%) of urbanization effect ($E_u$) |
|---|---|---|---|---|
| **Absolute index** | | | | |
| Frost days (FD0) | −4.17* | −2.29* | −1.88* | 45.1 |
| Summer days (SU25) | 2.52* | 2.24* | 0.28* | 11.1 |
| Ice days (ID0) | −2.32* | −2.56* | 0.24 | −10.3 |
| Tropical nights (TR20) | 2.31* | 0.83* | 1.48* | 64.1 |
| **Extreme value index** | | | | |
| Diurnal temperature range (DTR) | −0.17* | 0 | −0.17* | 100.0 |
| Maximum TX (TXx) | 0.04 | 0.06 | −0.02 | −50.0 |
| Maximum TN (TNx) | 0.26* | 0.1* | 0.16* | 61.5 |
| Minimum TX (TXn) | 0.36* | 0.34* | 0.02 | 5.6 |
| Minimum TN (TNn) | 0.61* | 0.3* | 0.31* | 50.8 |
| **Relative index** | | | | |
| Cool nights (TN10p) | −8.61* | −4.85* | −3.76* | 43.7 |
| Cool days (TX10p) | −3.43* | −3.07* | −0.36* | 10.5 |
| Warm nights (TN90p) | 8.07* | 4.20* | 3.87* | 48.0 |
| Warm days (TX90p) | 3.83* | 3.91* | −0.08 | −2.0 |

It is not clear at present how much effect urbanization processes will have on the series of extreme temperature indices with respect to the national stations in mainland China on the whole. This will be further investigated in our future studies. However, the case of North China implies that the urbanization effect will be not negligible, and more attention should be given to this issue in future studies of global and regional extreme temperature change.

## 5. CONCLUSIONS

In the present paper, analysis was carried out on the temporal changes in 15 extreme temperature indices for mainland China during the last 48 yr. The following conclusions were drawn:

(1) Cold indices, i.e. frost days and ice days, showed a significant decreasing trend, especially after the mid-1980s. However, warm indices, i.e. summer days and tropic nights, generally showed an insignificant increasing trend, in spite of the fact that a significant rising trend did occur after the mid-1990s. The frequencies of cold events decreased more significantly in northern China, while the frequencies of warm events increased significantly only in the middle and lower reaches of the Yangtze River and in southern Southwest China.

(2) The mean and maximum (minimum) values of daily maximum and minimum temperatures showed overall increasing trends, and DTR decreased significantly. The mean maximum temperature began to rise significantly after the 1990s, while the mean minimum temperature had begun to steadily rise as early as the late 1970s. The reduction in DTR mainly occurred before the mid-1980s, however, and the change thereafter became insignificant. TXn and TNn significantly increased after the mid-1980s, while TXx and TNx did not increase until after the mid-1990s. TXx and TNx in northern China rose significantly, but a downward trend was observed in the middle and lower reaches of the Yangtze River and in Southwest China. TXn and TNn significantly increased across the whole country.

(3) Although the warm indices increased significantly and cold indices decreased significantly, the series of the relative indices related to minimum temperature changed more significantly than those related to maximum temperature. The significant reduction of cool nights and days occurred after the late 1980s, while the significant increase of warm nights and days occurred after the mid-1990s. The most significant changes in cool nights and days were in northern China, and the warm nights and days increased more substantially in Southwest China and in the coastal areas of South China.

(4) The significant reduction of cool days and nights mostly occurred in winter, and the frequencies of warm days and nights increased more significantly in autumn and summer. Warm summer days and nights increased more prominently in North China and in the coastal areas of South China. Thus, the winter cold spells tended to decline considerably in most regions of China, notably northern China, East China, and on the Qinghai-Tibet Plateau. The days with extreme high temperatures increased in most regions, mainly in summer, while the nights with extreme high temperatures increased more significantly, resulting in an increase of summer heat waves.

(5) The case study of North China proved that urbanization intensified the downward trend in cold index series and the upward trend in warm indices related to minimum temperature. The urbanization effect on the series of extreme temperature indices was statistically significant for the downward trends

in frost days, DTR, cool nights, and cool days, and for the upward trends in summer days, tropical nights, TNx, TNn, and warm nights. For these indices, the contributions of the urbanization effect to the overall trends ranged from 10 to 100%, with the largest contributions coming from tropical nights, DTR, TNx, and TNn. The decrease in DTR at the national stations in North China was caused entirely by urbanization. However, the urbanization effect was rather weaker on the trends in the indices related to maximum temperatures. The case analysis shows that the urbanization effect on the trends in the series of extreme temperature indices should not be ignored for mainland China, and more attention needs to be given to the issue in future studies.

*Acknowledgements.* The present study was financially supported by the Ministry of Science and Technology of China (2007BAC29B02 and 2007BAC03A01).

## LITERATURE CITED

Alexander LV, Zhang X, Peterson TC, Caesar J and others (2006) Global observed changes in daily climate extremes of temperature and precipitation. J Geophys Res 111:D05109. doi:10.1029/2005JD006290

Brabson BB, Palutikof JP (2002) The evolution of extreme temperatures in the central England temperature record. Geophys Res Lett 29:2163–2166

Choi G, Collins D, Ren GY, Trewin B and others (2009) Changes in means and extreme events of temperature and precipitation in the Asia-Pacific Network region, 1955–2007. Int J Climatol 29:1906–1925

Cui LL, Shi J, Zhou WD (2009) Characteristics of extreme temperature variations and their response to urbanization in Shanghai. Sci Geogr Sin 29:93–97 (in Chinese)

Dai A, Trenberth KE, Karl TR (1999) Effects of clouds, soil moisture, precipitation and water vapor on diurnal temperature range. J Clim 12:2451–2473

Ding T, Qian WH, Yan ZW (2009) Changes in hot days and heat waves in China during 1961–2007. Int J Climatol 30:1452–1462

Ding YH, Ren GY, Shi GY, Gong P and others (2006) National assessment report of climate change. I. Climate change in China and its future trend. Adv Clim Change Res 2:3–8 (in Chinese)

Duan AM, Wu GX (2006) Change of cloud amount and the climate warming on the Tibetan Plateau. Geophys Res Lett 33:L22704. doi:10.1029/2006GL027946

Easterling DR, Evans JL, Groisman PY, Karl TR, Kunkel KE, Ambenje P (2000) Observed variability and trends in extreme climate events: a brief review. Bull Am Meteorol Soc 81:417–425

Gong DY, Han H (2004) Extreme climate events in northern China over the last 50 years. Acta Geophys Sin 59: 230–238 (in Chinese)

Hu YC, Dong WJ, He Y (2007) Progress of the study of extreme weather and climate events at the beginning of the twenty-first century. Adv Earth Sci 22:1066–1075 (in Chinese)

IPCC (Intergovernmental Panel on Climate Change) (2007) Climate change 2007: the physical science basis. Cambridge University Press, Cambridge

Jones PD, Hulme M (1996) Calculating regional climatic time series for temperature and precipitation: methods and illustrations. Int J Climatol 16:361–377

Kendall MG, Gibbons JD (1981) Rank correlation methods, 5th edn. Edward Arnold, London

Klein Tank AMG, Konnen GP (2003) Trends in indices of daily temperature and precipitation extremes in Europe, 1946–99. J Clim 16:3665–3680

Li QX, Liu XN, Zhang HZ, Peterson TC, Easterling DR (2004) Detecting and adjusting temporal inhomogeneity in Chinese mean surface air temperature data. Adv Atmos Sci 21:260–268

Liu XH, Ji ZJ, Wu HB, Yu XJ (2006) Characteristics and interdecadal difference of daily temperature and precipitation extremes in China for the last 40 years. J Trop Meteorol 22:618–624 (in Chinese)

Liu XN, Li QX (2003) Research of the inhomogeneity test of climatological data series in China. Acta Meteorol Sin 17:492–502

Manton MJ, Della-Marta PM, Haylock MR, Hennessy KJ and others (2001) Trends in extreme daily rainfall and temperature in southeast Asia and the south Pacific: 1961–1998. Int J Climatol 21:269–284

Qian WH, Lin X (2004) Regional trends in recent temperature indices in China. Clim Res 27:119–134

Ren GY, Chu ZY, Zhou YQ, Xu MZ and others (2005) Recent progress in studies of regional temperature changes in China. Clim Environ Res 10:701–716 (in Chinese)

Ren GY, Zhou YQ, Chu ZY, Zhang AY, Guo J, Liu XF (2008) Urbanization effects on observed surface air temperature trends in North China. J Clim 21:1333–1348

Ren GY, Feng GL, Yan ZW (2010a) Progresses in observation studies of climate extremes and changes in mainland China. Clim Environ Res 15:337–353 (in Chinese)

Ren GY, Zhang AY, Chu ZY, Zhou JX, Ren YY, Zhou YQ (2010b) Principles and procedures for selecting reference surface air temperature stations in China. Meteorol Sci Technol 38:78–85 (in Chinese)

Ren YY, Ren GY (2011) A remote-sensing method of selecting reference stations for evaluating urbanization effect on surface air temperature trends. J Clim 24:3179–3189

Shi J, Ding YH, Cui LL (2009) Climatic characteristics of extreme maximum temperature in East China and its causes. Chin J Atmos Sci 33:347–358 (in Chinese)

Stone DA, Weaver AJ (2003) Factors contributing to diurnal temperature range trends in twentieth and twenty-first century simulations of the CCCma coupled model. Clim Dyn 20:435–445

Tang HY, Zhai PM, Wang ZY (2005) On change in mean maximum temperature, minimum temperature and diurnal range in China during 1951–2002. Clim Environ Res 10:728–735 (in Chinese)

Vincent LA, Peterson TC, Barros VR, Marino MB and others (2005) Observed trends in indices of daily temperature extremes in South America 1960–2000. J Clim 18: 5011–5023

Yan Z, Jones PD, Davies TD, Moberg A and others (2002) Trends of extreme temperatures in Europe and China based on daily observations. Clim Chang 53:355–392

Yang P, Liu WD, Wang QG, Xiong KG, Hou W (2010) The climate change trend and seasonal characteristics of daily temperature extremes in China for the last 40 years. J Appl Meteorol Sci 21:29–36 (in Chinese)

Ye DX, Zou XK, Zhang Q, Chen XY (2008) An analysis of climatic characteristics of high temperature in the three gorges area. J Trop Meteorol 24:200–204 (in Chinese)

You QL, Kang SC, Li CL, Yan YP, Yan SY (2008) Change in extreme temperature over Sanjiangyuan region in the period from 1961 to 2005. Resour Environ Yangtze Basin 17:233–236 (in Chinese)

Zhai PM, Pan XH (2003) Trends in temperature extremes during 1951–1999 in China. Geophys Res Lett 30: 1913–1916

Zhang AY, Ren GY, Zhou JX, Chu ZY, Ren YY, Tang GL (2010) On the urbanization effect on surface air temperature trends over China. Acta Meteorol Sin 68:957–966 (in Chinese)

Zhang DQ, Qian ZH (2008) Analysis of extreme events in China's temperature in the recent 50 years using a detection method based on medians. Acta Phys Sin 57: 4634–4640 (in Chinese)

Zhang L, Ren GY, Liu J, Zhou YQ, Ren YY, Zhang AY, Feng YW (2011) Urban effect on trends of extreme temperature indices at Beijing Station. Chin J Geophys 54: 1150–1159 (in Chinese)

Zhang X, Yang F (2004) RClimDex (1.0) user manual. Climate Research Branch, Environment Canada, Downsview, Ontario

Zhou LM, Dickinson RE, Dai AG, Dirmeyer P (2009) Detection and attribution of anthropogenic forcing to diurnal temperature range changes from 1950 to 1999: comparing multi-model simulations with observations. Clim Dyn 35:1289–1307

Zhou YQ, Ren GY (2009) The effect of urbanization on maximum and minimum temperatures and daily temperature range in North China. Plateau Meteorol 28:1158–1166 (in Chinese)

*Submitted: February 25, 2011; Accepted: September 13, 2011*

*Proofs received from author(s): November 14, 2011*

# 基于偏态分布的百分位估计公式的建立*

周 云[1)] 侯 威[2)†] 钱忠华[1)] 何文平[2)]

1)(扬州大学物理科学与技术学院,扬州 225009)

2)(国家气候中心,北京 100081)

(2010 年 10 月 25 日收到; 2011 年 2 月 28 日收到修改稿)

顺序统计量将累积概率与数据排序后的位置建立相关联系,可用于估计数据分布的累积概率. 鉴于不同气候要素概率分布存在着不同程度的偏态特征,基于偏态分布条件下的累积概率函数,通过理论推导和数值模拟建立了与偏态指数相关的位置参数的回归模型,从而给出了基于数据偏态特征的经验百分位估计公式. 利用 1980 年—2009年全球夏季逐日平均温度资料,进一步对比分析了偏态百分位估计方法与 Jenkinson 方法下得到的第 90 个百分位值所对应的温度排序后位置的差异.

**关键词**: 顺序统计量, 偏态分布, 百分位

**PACS**: 92. 60. Wc

## 1. 引 言

1977 年,Jenkinson[1] 运用经验排序法给出了基于数据排序后所处位置的累积概率分布的经验估计. 根据该经验估计,对于长度为 $n$ 的时间序列,将这 $n$ 个元素按升序排列,则发生小于或等于排序后第 $m$ 个元素的概率为

$$p = \frac{m - 0.31}{n + 0.38}. \tag{1}$$

若时间序列长度 $n$ 等于 100,那么第 90 个百分位值对应的数据排序后的位置为 90.65,介于元素 $x_{90}$($p$ = 89.35%) 与 $x_{91}$($p$ = 90.35%) 之间. (1)式在应用时无需时间序列的具体统计模型,且计算方便,近年来被广泛应用于各种极端事件百分位阈值的估计以及回归时间的确定等研究中[2—6]. 但值得注意的是,只有当所分析的数据服从或近似服从高斯分布时,利用(1)式才能得到较准确的结果[7,8]. 当某一要素所服从的概率分布函数已知时,则可给出在这一特定分布下累积概率的经验百分位值估计. 如 Goel 等[9] 给出了广义极值分布条件下的经验百分位估计式,该估计式不仅与数据排序后的位置有关,而且还与广义极值分布中的形状参数相关联.

大气系统是一个复杂的耗散的非线性系统[10—17],数学模型总是不可能与实际情况完全一致. 在研究温度时间序列时,通常以高斯分布作为其统计模型,但事实上对于不同的地区,温度序列所表现出的高斯分布特征存在着不同程度的偏态性质,若一概以高斯分布作为其统计模型,势必会在统计及相关的分析过程中带来较大偏差,而偏态分布函数可以用偏态指数来表征偏态分布的特征,从很大程度上可以避免这一问题[18]. 本文以偏态分布函数作为温度时间序列的统计模型,针对偏态分布条件下的累积概率分布函数,通过理论推导和数值模拟建立了温度序列偏态分布条件下的经验百分位估计公式,从而给出与偏态指数相关的经验百分位值估计. 并进一步对比分析了 1980 年—2009 年全球各格点夏季逐日平均温度资料的第 90 个百分位值所对应的温度顺序统计量位置在偏态百分位估计方法和 Jenkinson 估计方法[1] 下的异同.

## 2. 资料和方法

### 2.1. 资 料

本文使用的温度资料来自美国国家环境预报

* 国家自然科学基金(批准号:40930952,41005043)和国家科技支撑计划(批准号:2007BAC29B01)资助的课题。

† 通讯联系人. E-mail: hou_w@ sohu. com

©2011 中国物理学会 Chinese Physical Society 

中心和美国国家大气研究中心联合发布的全球逐日平均温度再分析资料(地面资料),分辨率为 2.5°×2.5°,选取 1980 年—2009 年夏季逐日平均温度为研究对象.

### 2.2. 偏态概率密度函数

采用偏态分布函数作为全球 1980 年—2009 年夏季逐日平均温度资料的统计模型,其概率密度函数为

$$f(x)=\frac{1}{\sqrt{2\pi}\sigma(\mu-a)}\times\exp\left(-\frac{\left(\left(\frac{x-a}{\mu-a}\right)^{\lambda}-1\right)^{2}}{2\sigma^{2}\lambda^{2}}\right)\left(\frac{x-a}{\mu-a}\right)^{\lambda-1}.\quad(2)$$

(2)式由经偏态数据在 Box-Cox 变换后所满足的正态假定条件推导而来,其中 $a$ 为对温度时间序列的平移量,对每个格点上的平移量,本文取为与各格点 1980 年—2009 年夏季逐日平均温度最小值偏差为 0.1 ℃的值,以保证经过 Box-Cox 变换得到的数据皆为正值;$\mu$ 为原始温度时间序列的均值;$\sigma$ 为经 Box-Cox 变换后新序列的标准差;$\lambda$ 为 Box-Cox 变换中通过极大似然法求得的偏态指数,用它表征概率分布的偏态性质. 如图 1 所示,当 $\lambda<1$ (图 1(a)),表明温度时间序列呈正偏分布,分布的右侧平缓,左侧陡峭;当 $\lambda>1$ (图 1(b)),表明温度时间序列呈负偏分布,其分布特征与正偏分布相反. $\lambda$ 值偏离 1 越大,表明分布的偏态性越显著.

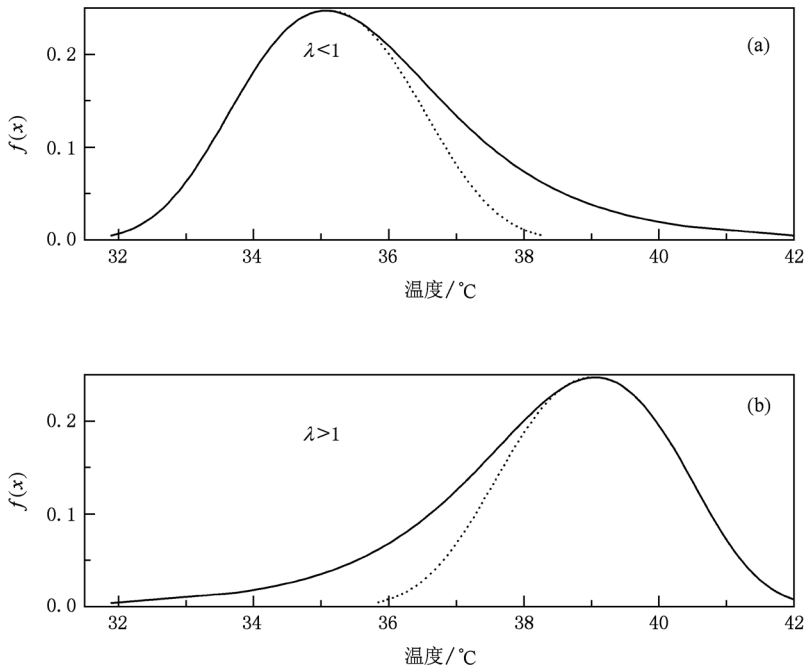


图 1 偏态分布示意图 (a)正偏分布型,(b)负偏分布型

当 $\lambda=1$,表明温度时间序列呈高斯分布,左右两侧对称,此时(2)式即可转化为高斯分布函数

$$f(x)=\frac{1}{\sqrt{2\pi}\sigma(\mu-a)}\exp\left(-\frac{(x-\mu)^{2}}{2\sigma^{2}(\mu-a)^{2}}\right).\quad(3)$$

图 2 为 1980 年—2009 年全球各格点夏季逐日平均温度的偏态指数分布情况. 从图 2 可以看出,全球大部分地区呈现负偏,即 $\lambda>1$,表明夏季发生的最概然温度(偏态分布函数的概率密度最大处所对应的温度,即最有可能发生的温度事件)普遍高于温度序列的均值,夏季更倾向于发生高于均温的温度事件,而低于均温的温度事件的极端程度相对较高,且不容易发生. 其中在 60°S 附近负偏呈现比较明显的带状分布,该区域最概然温度与平均温度的偏离更为明显;而在极地以及赤道附近部分地区则呈现正偏分布,夏季更易发生低于均温的温度事件.

### 2.3. 偏态分布函数

偏态分布函数可由(1)式偏态概率密度函数积分得到,

$$F(x)=\int_{a}^{x}f(x)\,\mathrm{d}x$$

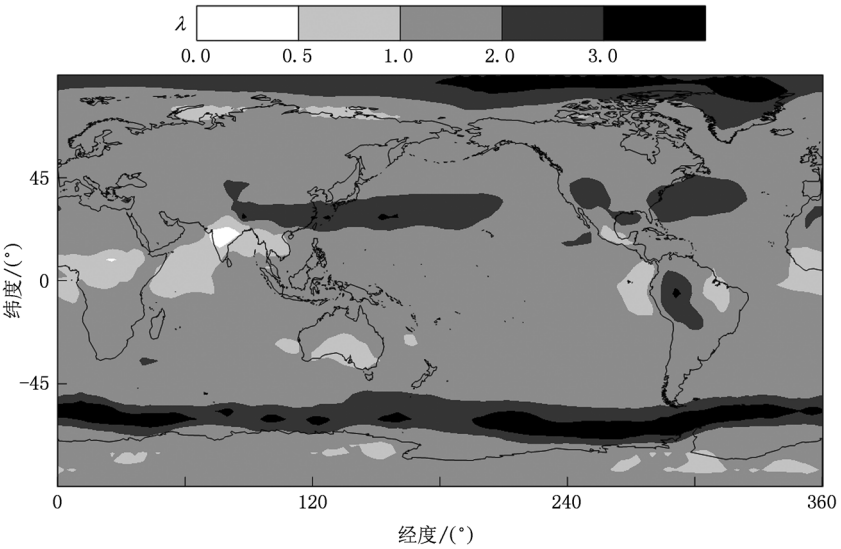


图2 1980年—2009年全球夏季逐日平均温度的偏态指数的空间分布

$$= \int_a^x \frac{1}{\sqrt{2\pi}\sigma(\mu - a)} \times \exp\left(-\frac{\left(\left(\frac{x-a}{\mu-a}\right)^{\lambda} - 1\right)^2}{2\lambda^2\sigma^2}\right)\left(\frac{x-a}{\mu-a}\right)^{\lambda-1} \mathrm{d}x$$

$$= \int_a^x \frac{1}{\sqrt{2\pi}\sigma\lambda} \exp\left(-\frac{\left(\left(\frac{x-a}{\mu-a}\right)^{\lambda} - 1\right)^2}{2\lambda^2\sigma^2}\right) \times \mathrm{d}\left(\frac{x-a}{\mu-a}\right)^{\lambda}. \tag{4}$$

令

$$y = \left(\frac{x-a}{\mu-a}\right)^{\lambda},$$

代入(4)式可得

$$F(x) = \int_0^y \frac{1}{\sqrt{2\pi}\lambda\sigma} \exp\left(-\frac{(y-1)^2}{2\sigma^2\lambda^2}\right)\mathrm{d}y. \tag{5}$$

根据指数函数二次幂的积分公式

$$F(x) = \frac{1}{\sigma\sqrt{2\pi}}\int \exp\left(-\frac{(x-\mu)^2}{2\sigma^2}\right)\mathrm{d}x = \frac{1}{2}\left(1 + \mathrm{erf}\left(\frac{x-\mu}{\sigma\sqrt{2}}\right)\right), \tag{6}$$

可得

$$F(x) = \frac{1}{2}\left(\mathrm{erf}\left(\frac{y-1}{\lambda\sigma\sqrt{2}}\right) + \mathrm{erf}\left(\frac{1}{\lambda\sigma\sqrt{2}}\right)\right). \tag{7}$$

这里 erf(·) 为误差函数,

$$\mathrm{erf}(x) \approx \frac{x}{|x|}\sqrt{1 - \exp\left(-x^2\frac{4/\pi + \alpha x^2}{1 + \alpha x^2}\right)}. \tag{8}$$

可以由(8)式近似求解误差函数,其中 $\alpha \approx 0.14$.

## 3. 理论基础

### 3.1. 顺序统计量

Jenkinson[1]对累积概率给出形如 $P_m = \frac{m+a}{n-b}$ 的估计,这为样本中某一元素对应的百分位与其排序后的位置两者之间建立联系. 这里参数 $a$ 和 $b$ 即为对与百分位值相应的排序后第 $m$ 个元素位置的微调,称为位置参数,需要基于顺序统计量的相关理论来推导并求解位置参数 $a$ 和 $b$. 对样本的 $n$ 个元素,按从小到大排序为 $x_1 \leqslant x_2 \leqslant \cdots \leqslant x_m \leqslant \cdots \leqslant x_n$, 则排序后的序列或其中的部分称为顺序统计量,它主要用于构造样本的经验分布,并估计经验分布的百分位值.

设样本序列的概率密度函数和分布函数分别为 $f(x)$ 和 $F(x)$, 用 $100\alpha$ 代表百分位( $0 < \alpha < 1$ ),累积概率 $F(\xi_\alpha) = \alpha$. 若分布函数 $F$ 已知,则任意 $\alpha$ 对应的百分位值 $\xi_\alpha$ 均可直接确定. 但实际应用中更容易获知样本的经验分布,如何用 $x_m$ 来估计 $\xi_\alpha$, 即对百分位值作经验估计,找出 $p$ 与第 $m$ 个顺序统计量 $x_m$ 之间的关系,使得 $p = F(x_m)$, 是一个需要解决的问题.

设原始的 $n$ 个顺序统计量之间相互独立,其对应的累积概率分别为 $y_1 = F(x_1)$, $\cdots$, $y_n = F(x_n)$, 因分布函数 $F$ 为连续单调递增函数,有

$$y_1 \leqslant \cdots \leqslant y_m \leqslant \cdots \leqslant y_n, \tag{9}$$

则 $y \in [0,1]$, 服从 0—1 之间的均匀分布[19], 即

$$\begin{aligned} f(y) &= 1, \\ F(y) &= y. \end{aligned} \tag{10}$$

$y_m$ 即可视为位于 $[0,1]$ 之间且呈均匀分布的 $n$ 个顺序统计量中的第 $m$ 个元素. 将第 $m$ 个顺序统计量出现 $y_m$ 的概率密度函数表示为 $f_m(y_m)$. $y_m$ 仅作为顺序统计量中的某一个元素发生 $y_m$ 的概率为 $f(y_m)$; 假设在 $y_m$ 之前, $n$ 个样本量中有 $m-1$ 个元素值小于 $y_m$, 其发生概率为 $\frac{n!}{(m-1)!(n-m)!}F(y_m)^{m-1}$; 余下大于 $y_m$ 的 $n-m$ 个元素的发生概率为 $(1-F(y_m))^{n-m}$. 因为假设了 $n$ 个样本量之间相互独立, 故在 $n$ 个顺序统计量中第 $m$ 个元素值为 $y_m$ 的发生概率为

$$\begin{aligned} f_m(y_m) &= \frac{n!}{(m-1)!(n-m)!} f(y_m) \\ &\quad \times F(y_m)^{m-1}(1-F(y_m))^{n-m} \\ &= \frac{n!}{(m-1)!(n-m)!} \\ &\quad \times (y_m)^{m-1}(1-y_m)^{n-m}. \end{aligned} \tag{11}$$

同理, 当已获知样本 $\{x\}$ 的具体分布模型, 在 $n$ 个顺序统计量中出现 $x_m$ 的概率可表示为

$$\begin{aligned} g_m(x_m) &= \frac{n!}{(m-1)!(n-m)!} f(x_m) \\ &\quad \times F(x_m)^{m-1}(1-F(x_m))^{n-m}. \end{aligned} \tag{12}$$

(12)式将依赖于 $x$ 的分布情况.

### 3.2. 基于偏态分布的第 $m$ 个顺序统计量的分布特征

采用以上介绍的方法, 计算得到 1980 年—2009 年夏季逐日平均温度序列的概率密度函数 $f(x)$ ((2)式)及其分布函数 $F(x)$ ((7)式), 代入(12)式后可得到基于偏态分布的第 $m$ 个顺序统计量的概率密度分布 $g_m(x)$. 图 3 所示为基于高斯分布、正偏分布以及负偏分布下的第 $m$ 个顺序统计量的概率密度分布, 横坐标为顺序统计量分布的累积概率 $F(x)$, 图中以样本量 $n$ 取为 30, $m$ 分别取 1, 2, 4, 10, 15, 20, 27, 29, 30.

由图 3(a)可见, 当序列具有高斯分布时, 第 15 个顺序统计量分布的最高概率密度高于其他顺序

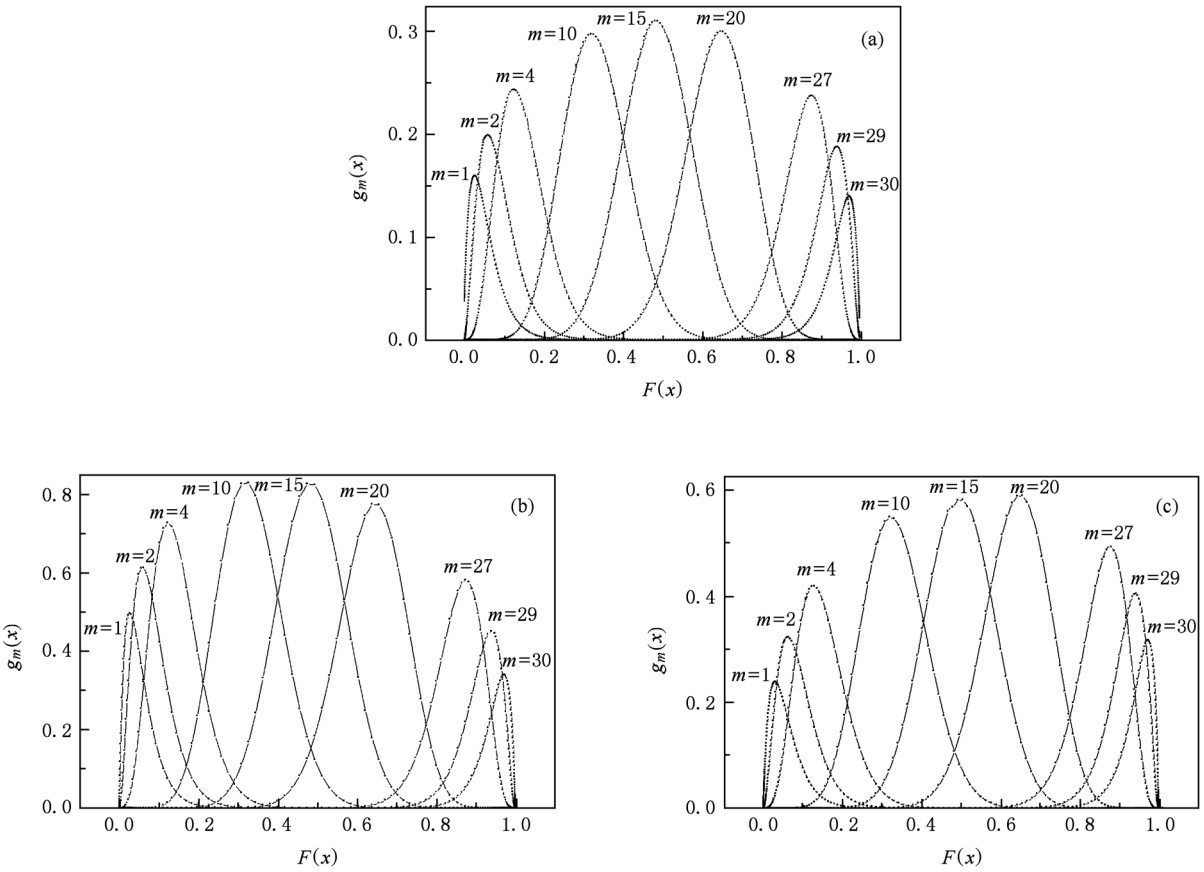


图 3 第 $m$ 个顺序统计量的概率密度分布特征 (a)高斯分布, (b)正偏分布, (c)负偏分布

统计量,其他顺序统计量的分布关于第 15 个顺序统计量分布近似对称,即 $m = 10$ 与 $m = 20$, $m = 4$ 与 $m = 27$ 等等. 且 $m$ 的值越大或越小,越可能出现概率递减. 图 3(b)为序列处于正偏分布时第 $m$ 个顺序统计量的分布特征,此时第 15 个顺序统计量分布中的最高概率密度不再高于其他顺序统计量,而是出现在第 10 个顺序统计量中,其他顺序统计量也不再关于第 15 个顺序统计量对称,在左右对应的顺序统计量分布中左侧分布的最概然概率高于右侧. 而在图 3(c)中,当序列处于负偏分布时,其情况恰与图 3(b)相反,也就是左右对应的顺序统计量分布中右侧分布的最概然概率高于左侧.

## 4. 经验百分位公式的建立

从图 3 可知,当序列处于不同的分布型时,对该序列第 $m$ 个顺序统计量的分布特征具有一定的影响. 而在序列所满足的偏态分布中,偏态指数是表征序列偏态程度的量,据此可以判定,序列中概率分布的偏态指数与第 $m$ 个顺序统计量的分布形式相关联. 第 $m$ 个顺序统计量的分布即代表着某序列第 $m$ 个元素可能出现的值的分布,对第 $m$ 个元素值进行估计,即可进一步对第 $m$ 个元素所对应的累积概率进行估计,从而将排序后元素所对应的位置与其相应累积概率相联系. 而由于第 $m$ 个顺序统计量在越偏离中间位置的顺序统计量时,其分布的偏态程度将越明显,若以均值作为估计值,受极端值的影响也将越显著,以致越偏离于最有可能发生的值. 为此,将第 $m$ 个顺序统计量分布中最高概率密度所对应的值作为对第 $m$ 个元素的估计值.

下面给出建立基于偏态分布的经验百分位公式的步骤.

**步骤 Ⅰ** 选定样本量 $n$.

**步骤 Ⅱ** 选定表征不同分布型的偏态指数 $\lambda$.

**步骤 Ⅲ** 在某一分布型下,对于 $n$ 个顺序统计量中第 $m$ 个值为 $x_m$ 的概率密度函数可由(13)式获得,以 $x_m$ 分布函数中最高概率密度所对应的 $x_m$ 值作为最有可能发生的第 $m$ 个顺序统计量,记为 $x_{m(\max g_m)}$.

**步骤 Ⅳ** 由历史数据的分布函数求解 $F(x_{m(\max g_m)})$,作为对经验百分位 $P_m$ 的估计.

**步骤 Ⅴ** 将 $P_m = \dfrac{m+a}{n-b}$ 写成 $nP_m - m = a + bP_m$,令 $S_m = nP_m - m$,以 $P_m$(即 $F(x_{m(\max g_m)})$)为变量,$S_m$ 为因变量(其中 $m$ 在 1—$n$ 之间取值)建立线性回归方程,得到位置参数 $a$ 和 $b$.

**步骤 Ⅵ** 在已知样本量的情况下,选定不同的分布,即改变偏态指数,重复步骤 Ⅱ—步骤 Ⅴ,得到不同的位置参数 $a$ 和 $b$.

**步骤 Ⅶ** 建立位置参数 $a$ 和 $b$ 关于偏态指数 $\lambda$ 的回归方程.

**步骤 Ⅷ** 选取不同的样本量,重复步骤 Ⅱ—步骤 Ⅶ.

按照以上步骤,即可求得偏态分布的百分位公式.

图 4 为样本量 $n = 100$ 时,不同偏态指数 $\lambda$ 下 $S_m$ 随 $P_m$ 的变化. 由图 4 可知,在 $\lambda$ 取不同值时,$S_m$ 随 $P_m$ 变化的曲线满足不同的线性关系,可由线性拟合得到位置参数 $a$ 和 $b$,且当序列的概率分布从正偏分布向负偏分布变化(即偏态指数 $\lambda$ 值逐渐变大)时,位置参数 $a$ 有增大的趋势,位置参数 $b$ 则有减小的趋势.

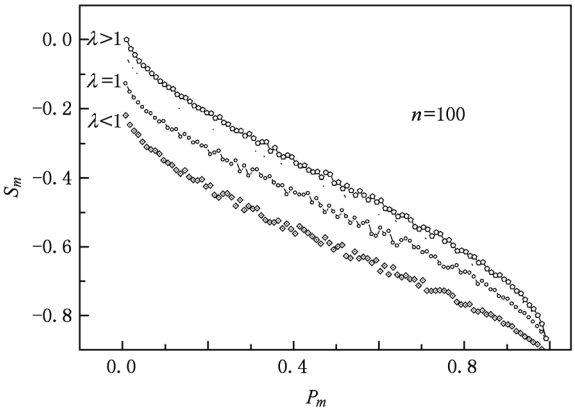


图 4 $S_m$ 随 $P_m$ 的变化

从图 4 中已经获知,位置参数 $a$ 和 $b$ 随偏态指数 $\lambda$ 的变化具有不同的特征,那么它们之间究竟存在的是何种关系呢? 为此,同样以样本量 $n = 100$ 为例,分别建立位置参数 $a$ 和 $b$ 随 $\lambda$ 变化的回归方程. 图 5 所示为位置参数 $a$ 和 $b$ 随偏态指数 $\lambda$ 的变化,基于曲线拟合,位置参数 $a$ 和 $b$ 均可建立关于 $\lambda$ 的指数回归方程,即

$$\begin{aligned} a &= a_0 + a_1\exp(a_2\lambda), \\ b &= b_0 + b_1\exp(b_2\lambda). \end{aligned} \tag{13}$$

对位置参数 $a$ 和 $b$ 拟合较好的 $\lambda$ 范围主要集中在

0.5—3 之间,对于负偏以及正偏相对比较严重的情况,拟合效果相对较差.

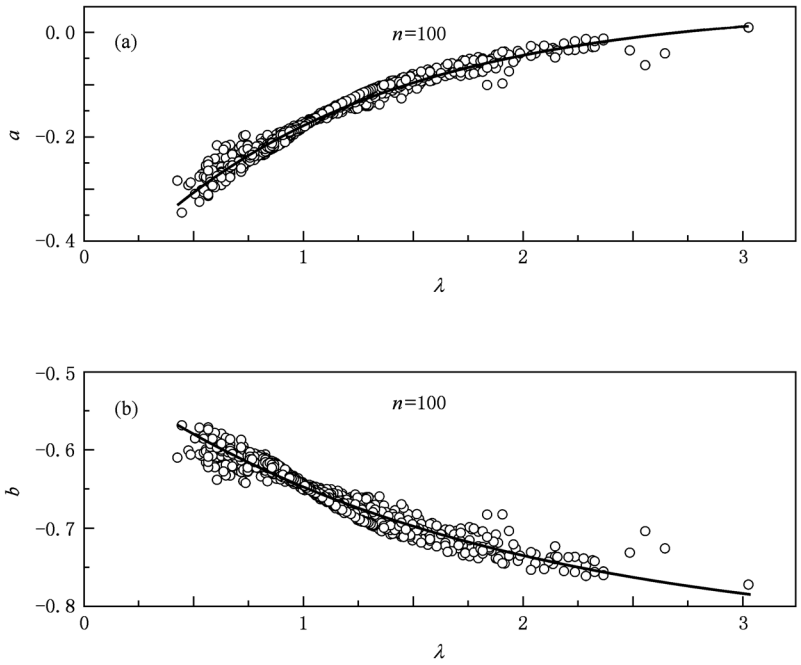


图5 位置参数 $a$ 和 $b$ 随偏态指数 $\lambda$ 的变化 (a)参数 $a$, (b)参数 $b$

表1 不同样本量所得的各项系数

| $n$ | $a_0$ | $a_1$ | $a_2$ | $b_0$ | $b_1$ | $b_2$ |
|---|---|---|---|---|---|---|
| 10 | 0.05856 | −0.62674 | −0.93664 | −0.81255 | 0.39290 | −0.77126 |
| 30 | 0.05669 | −0.59363 | −0.91352 | −0.83076 | 0.37272 | −0.68126 |
| 50 | 0.05481 | −0.57900 | −0.90317 | −0.83461 | 0.36354 | −0.65186 |
| 70 | 0.05183 | −0.56880 | −0.90050 | −0.83887 | 0.35854 | −0.62066 |
| 100 | 0.05057 | −0.55665 | −0.88833 | −0.84378 | 0.35441 | −0.59072 |
| 150 | 0.04979 | −0.54735 | −0.87807 | −0.84958 | 0.35183 | −0.56023 |

表1为选取不同的样本量时所得到的位置参数 $a$ 和 $b$ 关于偏态指数的回归方程的各项系数. 从表1可知,在不同的样本量下所得的系数虽有所不同,但随着样本量不断增加,它们的差异越来越小. 图6显示了各项系数随样本量 $n$ 的变化关系. 经计算,在样本量很大的情况下,各项系数值可最终收敛于一个常数,分别为 $a_0 \approx 0.04793$, $a_1 \approx -0.54480$, $a_2 \approx -0.87394$, $b_0 \approx -0.84915$, $b_1 \approx 0.35186$, $b_2 \approx -0.55255$. 而在样本量 $n \geqslant 300$ 时,各项系数的误差均可控制在 $1 \times 10^{-3}$ 内. 保留上述各项系数小数点后两位小数,将其代入 $P_m = \dfrac{m+a}{n-b}$ 中,可得偏态分布下的百分位公式为

$$P_m = \frac{m - 0.54\exp(-0.87\lambda) + 0.05}{n - 0.35\exp(-0.55\lambda) + 0.85}. \quad (14)$$

至此,已建立与偏态分布相关的经验百分位公式.

值得一提的是,Jenkinson[1] 给出的不考虑具体分布形式的经验百分位公式,是以第 $m$ 个顺序统计量 $x_m$ 概率分布的中值作为第 $m$ 个顺序统计量的估计值时得到的理论公式;而同样在不考虑具体分布形式下,若以第 $m$ 个顺序统计量 $x_m$ 概率分布的均值作为第 $m$ 个顺序统计量的估计值时,所得的经验百分位公式为 $p = \dfrac{m}{n+1}$. 在考虑偏态分布条件下,以第 $m$ 个顺序统计量 $x_m$ 概率分布中最概然概率对应的值作为第 $m$ 个顺序统计量的估计值,以此得到基于偏态分布的经验百分位公式. 当偏态指数 $\lambda = 1$ (代表左右对称的高斯分布),代入(14)式,可得 $p = \dfrac{m-0.175}{n+0.65}$, 其位置参数 $a$ 和 $b$ 与以中值和平均

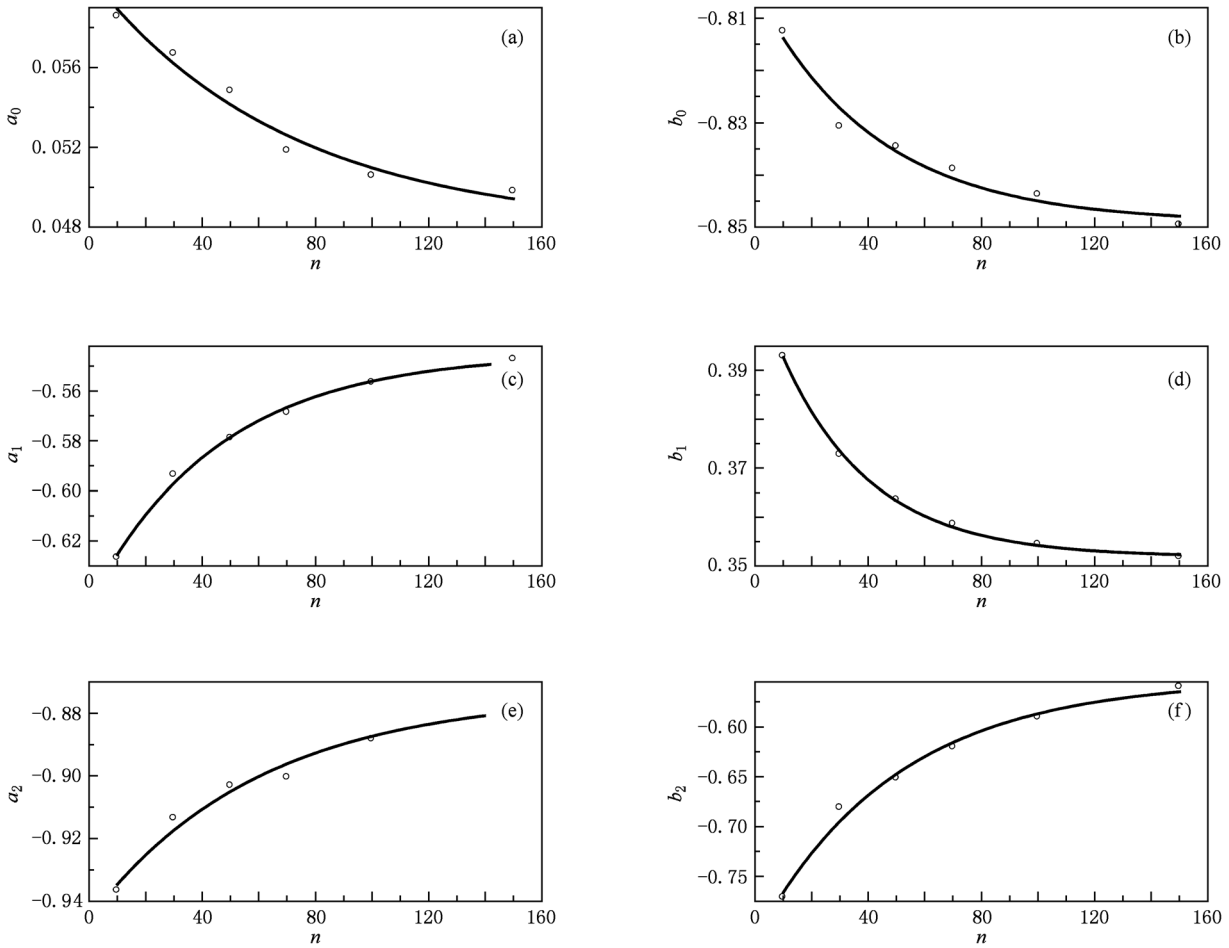


图 6 系数 $a_0, b_0, a_1, b_1, a_2, b_2$ 随样本量 $n$ 的变化 (a) $a_0$, (b) $b_0$, (c) $a_1$, (d) $b_1$, (e) $a_2$, (f) $b_2$

值作为估算值时均有所不同. 由此可知,即使都是在对称分布下,若处理方法不同其位置参数也会有所不同.

## 5. 偏态与 Jenkinson 方法相同百分位下温度顺序统计量位置的比较

Jenkinson 百分位估计式((1)式)虽是在不考虑具体分布的情况下获得,但在一定的条件下有其适用性,是一种比较常用的百分位值估计方法. 在统计模型存在一定的偏态特征时,所得偏态分布下的经验百分位公式((14)式)可针对不同概率分布条件下的百分位值进行估计. 在一定的样本数据下对于某一特定的百分位,Jenkinson 百分位估计方法中对应的顺序统计位置也是确定的,但偏态百分位估计方法中随偏态程度的不同对应的顺序统计量位置也会有所不同. 在大气科学中常根据研究的需要,将温度资料的第 90 个、第 95 个、第 99 个等一些百分位值作为极端高温的阈值[5,6,20],在此方法下百分位值所对应的温度在排序后序列中所处的位置将决定阈值的大小,文中取温度序列的第 90 个百分位值进行研究. 在温度资料满足偏态分布的条件下,第 90 个百分位值所对应的温度在排序后序列中的位置将由于偏态程度的不同而有所差异.

利用(1)和(14)式,对 1980 年—2009 年全球各格点夏季逐日平均温度资料进行百分位估计,比较这两种方法得到第 90 个百分位值对应的温度在排序后序列中位置的差异,将此位置差异用 $\Delta m$ 表示,其分布如图 7 所示. 因 1980 年—2009 年夏季日平均温度资料存在一定的偏态特征,故其在偏态分布条件与 Jenkinson 估计下的第 90 个百分位值所对应的排序后序列中位置差值的分布与图 2 中偏态指数的分布具有紧密的联系. 当偏态指数越小时,其对应的位置差值越大,在处于正偏的赤道附近部分地区,即亚洲大陆北部、非洲北部及其东部海域以及南美附近海域,位置差值在 0.1 乃至 0.15 以上. 在处于负偏的地

区,位置差值在 0.1 以内,在 60°S 附近以及北极地区,即负偏比较明显的地区,位置差值在 0.05 以内.

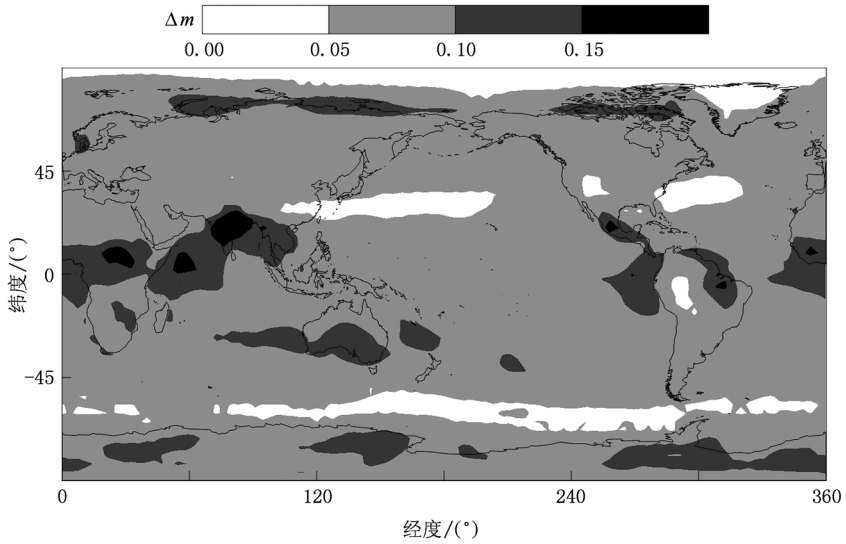


图 7 偏态与 Jenkinson 方法下第 90 个百分位值所对应的位置差异 $\Delta m$ 的分布

## 6. 结 论

本文以偏态分布函数作为温度时间序列的统计模型,针对原始数据序列偏态分布条件下的累积概率函数,通过理论推导和数值模拟建立了偏态分布下的经验百分位公式. 对基于偏态分布的顺序统计量给出简单的经验百分位值估计. 通过相关推导和计算表明,偏态分布下的经验百分位公式与表征偏态程度的偏态指数相关,利用本文得到的百分位公式可以更精确地估计不同分布下的百分位值. 对全球各格点夏季逐日平均温度资料的应用比较表明,当正偏分布越明显,即偏态指数越小时,与 Jenkinson 公式对应的温度顺序统计量位置相差越大.


[1] Jenkinson A F 1977 *Synoptic Climatol. Branch Memo* **58** 41

[2] Horton E B, Folland C K, Parker D E 2001 *Climatic Change* **50** 267

[3] Bonsal B R, Zhang X, Vincent L A, Hogg W D 2001 *J. Climate* **14** 1959

[4] Feng G L, Gong Z Q, Zhi R 2008 *Acta Meteor. Sin.* **66** 892 (in Chinese) [封国林、龚志强、支 蓉 2008 气象学报 **66** 892]

[5] Gong Z Q, Wang X J, Zhi R, Feng G L 2009 *Acta Phys. Sin.* **58** 4342 (in Chinese) [龚志强、王晓娟、支 蓉、封国林 2009 物理学报 **58** 4342]

[6] Feng G L, Wang Q G, Hou W, Gong Z Q, Zhi R 2009 *Acta Phys. Sin.* **58** 2853 (in Chinese) [封国林、王启光、侯 威、龚志强、支 蓉 2009 物理学报 **58** 2853]

[7] Folland C K, Anderson C W 2002 *J. Climate* **15** 2954

[8] Makkonen L 2005 *J. Appl. Meteor. Climatol.* **45** 334

[9] Goel N K, De M 1993 *Stoch. Hydrol. Hydraul.* **7** 1

[10] Hou W, Yang P, Feng G L 2008 *Acta Phys. Sin.* **57** 3932 (in Chinese) [侯 威、杨 萍、封国林 2008 物理学报 **57** 3932]

[11] Zhang D Q, Qian Z H 2008 *Acta Phys. Sin.* **57** 4634 (in Chinese) [章大全、钱忠华 2008 物理学报 **57** 4634]

[12] Feng G L, Dong W J, Gong Z Q, Hou W, Wan S Q, Zhi R 2006 *Nonlinear Theory and Methods on Spatial-temporal Distribution of the Observational Data* (Beijing: China Metrological Press) (in Chinese) [封国林、董文杰、龚志强、侯威、万仕全、支 蓉 2006 观测数据非线性时空分布理论和方法 (北京:气象出版社)]

[13] He W P, Feng G L, Dong W J, Li J P 2005 *Chin. Phys.* B **14** 21

[14] He W P, Feng G L, Wu Q, Wan S Q, Chou J F 2008 *Nonlin. Proc. Geophys.* **15** 601

[15] Feng G L, Yang J, Wan S Q, Hou W, Zhi R 2009 *Acta Meteor. Sin.* **67** 61 (in Chinese) [封国林、杨 杰、万仕全、侯 威、支 蓉 2009 气象学报 **67** 61]

[16] Feng G L, Gao X Q, Dong W J, Li J P 2008 *Chaos Solitons Fract.* **37** 487

[17] Feng G L, Gong Z Q, Zhi R, Zhang D Q 2008 *Chin. Phys.* B **17** 2745

[18] Qian Z H, Feng G L, Gong Z Q 2010 *Acta Phys. Sin.* **59** 7498 (in Chinese) [钱忠华、封国林、龚志强 2010 物理学报 **59** 7498]

[19] Chen X R 2009 *Advanced Mathematical Statistics* (Hefei: University of Science and Technology of China Press) p164 (in Chinese) [陈希孺 2009 高等数理统计学(合肥:中国科学技术大学出版社)第 164 页]

[20] Zhang L, Zhang D Q, Feng G L 2010 *Acta Phys. Sin.* **59** 5897 (in Chinese) [张 璐、章大全、封国林 2010 物理学报 **59** 5897]

# Development of percentile estimation formula for skewed distribution*

Zhou Yun[1)] Hou Wei[2)†] Qian Zhong-Hua[1)] He Wen-Ping[2)]

1) (*College of Physics Science and Technology, Yangzhou University, Yangzhou* 225009, *China*)

2) (*National Climate Center, Beijing* 100081, *China*)

(Received 25 October 2010; revised manuscript received 28 February 2011)

Abstract

Order statistics establishes a relation between the position of the ranked data and corresponding cumulative probability, so it can be used to estimate the cumulative probability. Owing to the fact that different climatological data have different skewness degrees, in this paper, according to the cumulative probability function under the skewed distribution conditions, we perform theoretical analysis and numerical simulation to establish the position parameters of the regression model which are related to skewness index, then give an amperic percentile formula under the skewed distribution. By using the data about the summer temperature in global from 1980 to 2009, we compare the positions of ranked data corresponding to the 90th percentile, which are obtained by this formula and Jenkinson's formula.

**Keywords**: order statistics, skewed distribution, percentile

**PACS**: 92.60.Wc

* Project supported by the National Natural Science Foundation of China (Grant Nos. 40930952, 41005043) and the State Key Program of Science and Technology of China (Grant No. 2007BAC29B01).

† Corresponding author. E-mail: hou_w@sohu.com

# 论文编目索引


1. Yu Chen，Xianyan Chen，Guoyu Ren. 2011：Variation of Extreme Precipitation over Large River Basins in China. *Advances in Climate Change Research*，2(2)：108-114. doi：10.3724/SP.J.1248.2011.00108.
2. Y J Cheng，Y M Tang and D Chen. 2011：Relationship between predictability and forecast skill of ENSO on various time scales. *Journal of Geophysical Research*，116，C12006，doi：10.1029/2011JC007249.
3. 丑洁明，封国林，董文杰. 2011：构建中国应对气候变化的低碳经济发展模式. *气候变化研究进展*，7(1)：48-53.
4. 杜良敏，张培群，周月华，等. 2011：基于非负矩阵和典型相关的场定量预测方法研究. *高原气象*，30(1)：103-108.
5. 冯爱霞，龚志强，王启光，孙树鹏，封国林. 2011：北半球环流系统季节内及年际以上振荡信号的信息传输. *物理学报*，60(5)：059205-9.
6. 冯亚文，任国玉，张　丽，罗华超. 2011：长江上游月降水人工神经网络预测模型. *长江流域资源与环境*，20(1)：40-47.
7. 符　琳，李维京，张培群，张　强，等. 2011：近50年我国冰雹年代际变化及北方冰雹趋势的成因分析. *气象*，37(6)：669-676.
8. Ge Gao，Chongyu Xu，Deliang Chen，et al. 2011：Spatial and temporal characteristics of actual evapotranspiration over Haihe River basin in China. *Stochastic Environmental Research and Risk Assessment*，doi：10.1007/s00477-011-0525-1.
9. 高　荣，钟海玲，董文杰，韦志刚. 2011：青藏高原积雪、冻土对中国夏季降水影响研究. *冰川冻土*，33(2)：254-260.
10. GAO XueJie，SHI Ying，F GIORGI. 2011：A high resolution simulation of climate change over China. *Science China Earth Sciences*，54(3)：462-472. doi：10.1007/s11430-010-4035-7.
11. 龚振淞. 2011：2008年西北太平洋热带气旋活动异常特征及成因分析. *热带气象学报*，27(2)：202-208.
12. GONG Zhiqiang，ZHI Rong，FENG Guolin and ZHANG Qiang. 2011：Dry/Wet Changes and Their Standing Characteristics in China During the Past 531 Years. *Acta Meteorologica Sinica*，25(2)：142-155.
13. GU Weizong，CHEN Lijuan，LI Weijing and CHEN Deliang. 2011：Development of a Downscaling Method in China Regional Summer Precipitation Prediction. *Acta Meteorologica Sinica*，25(3)：303-315.
14. 郭　军，任国玉，任　雨. 2011：近100年天津平均气温与极端气温变化. *高原气象*，30(5)：1399-1405.
15. Guo Y J and Ding Y H. 2011：Impacts of reference time series on the homogenization of radiosonde temperature. *Advances in Atmospheric Sciences*，28(5)：1011-1022. doi：10.1007/s00376-010-9211-3.
16. 何文平，何　涛，成海英，张　文，吴　琼. 2011：基于近似熵的突变检测新方法. *物理学报*，60(4)：049202-9.

17. 何文平，吴　琼，成海英，张　文. 2011：不同滤波方法在去趋势波动分析中去噪的应用比较. *物理学报*，60(2)：029203-9.
18. 黄　琰，封国林，董文杰. 2011：近 50 年中国气温、降水极值分区的时空变化特征. *气象学报*，69(1)：125-136.
19. 季　飞，支　蓉，龚志强，黄建平，冯爱霞. 2011：北太平洋高度场异常关联中心的空间结构特征的研究. *大气科学*，35(4)：721-728.
20. 贾小龙，陈丽娟，龚振淞，王遵娅，等. 2011：2010 年海洋和大气环流异常及对中国气候的影响. *气象*，37(4)：446-453.
21. 贾小龙，梁潇云. 2011：热带 MJO 对 2009 年 11 月我国东部大范围雨雪天气的可能影响. *热带气象学报*，27(5)：639-648.
22. Jia Xiaolong，Chen Lijuan，Ren Fumin and Li Chongyin. 2011：Impacts of the MJO on Winter Rainfall and Circulation in China. *Advances in Atmospheric Sciences*，28(3)：521-533.
23. 金　巍，任国玉，曲　岩. 2011：1961—2008 年东北三省地面气压变化特征. *高原气象*，30(6)：1661-1667.
24. 李　崇，任国玉，高庆先，马占云. 2011：固体废物焚烧处置及其清洁发展机制. *环境科学研究*，24(7)：819-827.
25. 李润春，张秀芝，王丽华，吕心艳，等. 2011：黄河中游地区土壤湿度特征分析. *干旱区研究*，28(1)：85-91.
26. Wei Li，Panmao Zhai，Jinhui Cai. 2011：Research on the Relationship of ENSO and the Frequency of Extreme Precipitation Events in China. *Advances in Climate Change Research*，2(2)：101-107.
27. 梁　萍，丁一汇. 2011：2009 年是空梅吗？*高原气象*，30(1)：53-64.
28. 廖要明，刘绿柳，陈德亮，谢　云. 2011：中国天气发生器模拟非降水变量的效果评估. *气象学报*，69(2)：310-319.
29. 刘　波，肖子牛. 2011：1961—2005 年新疆区域分级雨日(量)的气候特征. *干旱区地理*，34(3)：419-428.
30. 刘海文，丁一汇. 2011：华北夏季降水的年代际变化. *应用气象学报*，22(2)：129-137.
31. 刘海文，丁一汇. 2011：华北汛期降水月内时间尺度周期振荡的年代际变化分析. *大气科学*，35(1)：157-167.
32. 刘海文，丁一汇. 2011：华北汛期大尺度降水条件的年代际变化. *大气科学学报*，34(2)：146-152.
33. 刘绿柳，孙林海，廖要明，杜良敏，李　想. 2011：基于 DERF 的 SD 方法预测月降水和极端降水日数. *应用气象学报*，22(1)：77-85.
34. 刘芸芸，张雪芹. 2011：西北干旱区空中水资源的时空变化特征及其原因分析. *气候变化研究进展*，7(6)：385-392.
35. 刘芸芸，张雪芹，孙　杨. 2011：全球变暖背景下西北干旱区雨季的降水时空变化特征. *气候变化研究进展*，7(2)：97-103.
36. 马金玉，梁　宏，罗　勇，李世奎. 2011：中国近 50 年太阳直接辐射和散射辐射变化趋势特征. *物理学报*，60(6)：069601-14.
37. 马　宁，李跃凤，琚建华. 2011：2008 年初中国南方低温雨雪冰冻天气的季节内振荡特征. *高原气象*，30(2)：318-327.
38. 聂肃平，罗　勇，李伟平，吴统文. 2011：一套新的 30 年全球台站逐日降水资料集：质量控制和评估. *气候变化研究进展*，7(4)：235-242.

39. 裴　翀，宋连春，吴可军，等. 2011：我国综合气象观测运行监控系统的设计与实践. 气象，37(2)：213-218.
40. Ren F，J Liang，G Wu，W Dong and X Yang. 2011：Reliability Analysis of Climate Change of Tropical Cyclone Activity over the Western North Pacific. *J Climate*，24(15)：5887-5898.
41. G Y Ren，Y Chen，X K Zou，Y Q Zhou，Y Y Ren，et al. 2011：Change in climatic extremes over mainland China based on an integrated extreme climate index. *Climate Research*，50(1-2)：113-124. doi：10.3354/cr01023.
42. Ren G Y，Guan Z Y，Shao X M，Gong D Y. 2011：Changes in climatic extremes over mainland China. *Climate Research*，50，105-111. doi：10.3354/cr01067.
43. Guoyu Ren，Hongbin Liu，Ziying Chu，Li Zhang，et al. 2011：Multi-Time-Scale Climatic Variations over Eastern China and Implications for the South-North Water Diversion Project. *Journal of Hydrometeorology*，12，600-617. DOI：10.1175/2011JHM1321.1.
44. HongLi Ren and Feifei Jin. 2011：Niño indices for two types of ENSO. *Geophysical Research letters*，(38)L04704，doi：10.1029/2010GL046031.
45. HongLi Ren，Feifei Jin，Jongseong Kug，Li Gao. 2011：Transformed eddy-PV flux and positive synoptic eddy feedback onto low-frequency flow. *Clim Dyn*，36，2357-2370. DOI：10.1007/s00382-010-0913-0.
46. Yuyu Ren and Guoyu Ren. 2011：A remote-sensing method of selecting reference stations for evaluating urbanization effect on surface air temperature trends. *Journal of Climate*，24(7)：3179-3189. DOI：10.1175/2010JCLI3658.1.
47. 石　英，高学杰，吴　佳，Giorgi F. 2010：华北地区未来气候变化的高分辨率数值模拟. *应用气象学报*，21(5)：580-589.
48. Ying Shi，Xuejie Gao，Jia Wu and F Giorgi. 2011：Changes in snow cover over China in the 21st century as simulated by a high resolution regional climate model. *Environ Res Lett*，6，doi：10.1088/1748-9326/6/4/045401.
49. Ying Shi，Xuejie Gao，Dongfeng Zhang，Filippo Giorgi. 2011：Climate change over the Yarlung Zangboe-Brahmaputra River Basin in the 21st century as simulated by a high resolution regional climate model. *Quaternary International*，244，159-168. doi：10.1016/j.quaint.2011.01.041.
50. 宋艳玲，刘　波，钟海玲. 2011：气候变暖对我国南方水稻可种植区的影响. *气候变化研究进展*，7(4)：259-264.
51. Yanling Song，Christine Achberger and Hans W Linderholm. 2011：Rain-season trends in precipitation and their effect in different climate regions of China during 1961-2008. *Environ Res Lett*，6，doi：10.1088/1748-9326/6/3/034025.
52. SONG Yanling，ZHAO Yanxia and WANG Chunyi. 2011：Changes of Accumulated Temperature，Growing Season and Precipitation in the North China Plain from 1961 to 2009. *Acta Meteorologica Sinica*，25(4)：534-543.
53. 孙朝阳，邵全琴，刘纪远，匡文慧. 2011：城市扩展影响下的气象观测和气温变化特征分析. *气候与环境研究*，16(3)：337-346.
54. 孙　冷. 2011：2010年西北太平洋热带气旋活动特征及成因的初步分析. 气象，37(8)：929-935.
55. SUN Linhai，AI Wanxiu，SONG Wenling，et al. 2011：Study on Climatic Characteristics of China-Influencing Tropical Cyclones. *Journal of Tropical Meteorology*，17(2)：181-186.

56. 孙树鹏，张　璐，侯　威，封国林. 2011：基于非线性相似度量方法研究中国季节划分. *物理学报*，60(2)：029201-7.
57. 唐国利，王绍武，闻新宇，黄建斌. 2011：全球平均温度序列的比较. *气候变化研究进展*，7(2)：85-89.
58. 陶亦为，孙照渤，李维京，李伟平，等. 2011：ENSO与青藏高原积雪的关系及其对我国夏季降水异常的影响. *气象*，37(8)：919-928.
59. 汪　方，丁一汇. 2011：不同排放情景下模拟的21世纪东亚积雪面积变化趋势. *高原气象*，30(4)：869-877.
60. 王启光，封国林，郑志海，支　蓉. 2011：长江中下游汛期降水优化多因子组合客观定量化预测研究. *大气科学*，35(2)：287-297.
61. 王绍武，罗　勇，赵宗慈，闻新宇，黄建斌. 2011：全球气候变暖原因的争议. *气候变化研究进展*，7(2)：79-84.
62. 王　勇，李清泉，沈新勇. 2011：近50 a江淮地区6—7月降水特征分析. *气象科学*，31(1)：73-78.
63. Wang Z L，Zhang H and Shen X S. 2011：Radiative forcing and climate response due to black carbon in snow and ice. *Advances in Atmospheric Sciences*，28(6)：1336-1344. doi：10.1007/s00376-011-0117-5.
64. 王遵娅. 2011：中国冰冻日数的气候及变化特征分析. *大气科学*，35(3)：411-421.
65. 王遵娅，曾红玲，高　歌，陈　峪，等. 2011：2010年中国气候概况. *气象*，37(4)：439-445.
66. 王遵娅，赵珊珊，张　强. 2011：我国冰冻日出现的气象条件分析及其判别模型. *高原气象*，30(1)：158-163.
67. 卫晓东，张　华. 2011：非球形沙尘气溶胶光学特性的分析. *光学学报*，31(5)：0501002-8.
68. 吴　佳，高学杰，石　英，Filippo Giorgi. 2011：新疆21世纪气候变化的高分辨率模拟. *冰川冻土*，33(3)：479-487.
69. 吴　佳，高学杰，张冬峰，石　英，GIORGI F. 2011：三峡水库气候效应及2006年夏季川渝高温干旱事件的区域气候模拟. *热带气象学报*，27(1)：44-52.
70. 吴　军，张称意，徐海根. 2011：《生物多样性公约》下的气候变化问题：谈判与焦点. *生物多样性*，19(4)：400-403.
71. 吴占华，任国玉，徐卫丽，刘瑞兰. 2011：我国北方沙尘天气的气候成因分析. *干旱区地理*，34(3)：429-435.
72. 夏　坤，罗　勇，李伟平. 2011：青藏高原东北部土壤冻融过程的数值模拟. *科学通报*，56(22)：1828-1838.
73. XIA Kun，LUO Yong，LI WeiPing. 2011：Simulation of freezing and melting of soil on the northeast Tibetan Plateau. *Chinese Science Bulletin*，56(20)：2145-2155. doi：10.1007/s11434-011-4542-8.
74. 肖贤俊，何　娜，张祖强，刘怀明，王东晓. 2011：卫星遥感海表温度资料和高度计资料的变分同化. *热带海洋学报*，30(3)：001-008.
75. XIONG Kaiguo，FENG Guolin，HUANG Jianping and CHOU Jifan. 2011：Analogue-Dynamical Prediction of Monsoon Precipitation in Northeast China Based on Dynamic and Optimal Configuration of Multiple Predictors. *Acta Meteorologica Sinica*，25(3)：316-326.
76. H Xu，R Y Taylor and Y Xu. 2011：Quantifying uncertainty in the impacts of climate change on river discharge in sub-catchments of the Yangtze and Yellow River Basins，China. *Hydrol Earth Syst Sci*，15，333－344.
77. 徐雨晴，何吉成，王长科. 2011：33年来中国铁路运输行业的大气污染物排放. *环境科学*，32(5)：

1217-1223.
78. 闫冠华，李巧萍，邢　超. 2011：不同温室气体排放情景下未来中国地面气温变化特征. *南京信息工程大学学报(自然科学版)*，3(1)：36-46.
79. 杨　杰，王启光，支　蓉，封国林. 2011：动态最优多因子组合的华北汛期降水模式误差估计及预报. *物理学报*，60(2)：029204-13.
80. 杨　萍，刘伟东，侯　威. 2011：北京地区极端温度事件的变化趋势和年代际演变特征. *灾害学*，26(1)：60-64.
81. 杨小波，陈丽娟，刘芸芸. 2011：我国降水和气温的分级概率时空分布特征. *应用气象学报*，22(5)：513-524.
82. 杨小波，王永光，梁潇云. 2011：11月气候异常型及前期环流信号. *应用气象学报*，22(3)：275-282.
83. 尹　红，王　靖，刘洪滨，黄　磊，朱海峰. 2011：小兴安岭红松径向生长对未来气候变化的响应. *生态学报*，31(24)：7343-7350.
84. 尹　青，张　华，何金海. 2011：近48年华东地区地面太阳总辐射变化特征和影响因子分析. *大气与环境光学学报*，6(1)：37-46.
85. YIN Shuiqing，LI Weijing，Deliang CHEN，et al. 2011：Diurnal Variations of Summer Precipitation in the Beijing Area and the Possible Effect of Topography and Urbanization. *Advances in Atmospheric Sciences*，28(4)：725-734.
86. 尹宜舟，肖风劲，罗　勇，赵珊珊. 2011：我国热带气旋潜在影响力指数分析. *地理学报*，66(3)：367-375.
87. 尤　红，肖子牛，艾永智. 2011：2008年“2.28”低纬高原强对流成因诊断与数值模拟. *云南大学学报(自然科学版)*，33(2)：172-178.
88. 翟建青，曾小凡，姜　彤. 2011：中国旱涝格局演变(1961—2050年)及其对水资源的影响. *热带地理*，31(3)：237-242.
89. 张德二，陆龙骅. 2011：历史极端雨涝事件研究——1823年我国东部大范围雨涝. *第四纪研究*，31(1)：29-35.
90. 张东启，明　镜，魏文寿. 2011：天山乌鲁木齐河源1号冰川致冷效应的小气候观测. *干旱区地理*，34(3)：449-457.
91. 张　峰，张　华，沈钟平，卫晓东. 2011：一种处理漫射因子的新方法. *物理学报*，60(1)：010702-4.
92. 张　华，吴金秀，沈钟平. 2011：PFCs和SF_6的辐射强迫与全球增温潜能. *中国科学:地球科学*，41(2)：225-233.
93. H Zhang，Z L Wang，Z Z Wang，et al. 2011：Simulation of direct radiative forcing of aerosols and their effects on East Asia climate using an interactive AGCM-Aerosol coupled system. *Climate Dynamics*，DOI:10.1007/s00382-011-1131-0.
94. Hua Zhang，Jinxiu Wu，Peng Lu. 2011：A study of the radiative forcing and global warming potentials of hydrofluorocarbons. *J Quant Spectro & Radiavitive Trans*，112，220-229.
95. ZHANG Hua，WU JinXiu and SHEN ZhongPing. 2011：Radiative forcing and global warming potential of perfluorocarbons and sulfur hexafluoride. *Sciences China Earth Sciences*，54(5)：764-772. doi：10.1007/s11430-010-4155-0.
96. 张　雷，任国玉，刘　江，等. 2011：城市化对北京气象站极端气温指数趋势变化的影响. *地球物理学报*，54(5)：1150-1159.
97. Li Zhang，Min Dong，Tongwen Wu. 2011：Changes in precipitation extremes over Eastern China sim-

ulated by the Beijing Climate Center Climate System Model (BCC_CSM1.0). *Climate Research*, 50, 227-245. doi:10.3354/cr01066.

98. 张　灵，李维京，陈丽娟. 2011：北半球平流层大气环流转型的基本气候特征. *应用气象学报*，22(4)：411-420.

99. ZHAO Shanshan, ZHOU Tianjun, YANG Xiuqun, ZHU Yimin, et al. 2011: Interdecadal Change of the Relationship Between the Tropical Indian Ocean Dipole Mode and the Summer Climate Anomaly in China. *Acta Meteorologica Sinica*, 25(2): 129-141.

100. 赵宗慈，罗　勇，江　滢. 2011：全球大风在减少吗？*气候变化研究进展*，7(2)：149-151.

101. 周波涛. 2011：冬季澳大利亚东侧海温与长江流域夏季降水的联系及可能物理机制. *科学通报*，56(16)：1301-1307.

102. Yaqing Zhou, Guoyu Ren. 2011: Change in extreme temperature event frequency over mainland China, 1961—2008. *Climate Research*, 50, 125-139. doi:10.3354/cr01053.

103. 周　云，侯　威，钱忠华，何文平. 2011：基于偏态分布的百分位估计公式的建立. *物理学报*，60(8)：089201-9.

LCS

气候研究开放实验室